Eulerian modeling and simulation of polydisperse moderately dense coalescing spray flows with nanometric-to-inertial droplets: application to Solid Rocket Motors

F. Doisneau

École Centrale Paris

THÈSE

présentée par

François Doisneau

pour l'obtention du

GRADE de DOCTEUR

Formation doctorale : Énergétique, Mathématiques Appliquées

Laboratoires d'accueil : Département d'Énergétique Fondamentale
et Appliquée (DEFA) de l'ONERA
Laboratoire d'Énergétique Moléculaire
et Macroscopique, Combustion (EM2C)
du CNRS et de l'ECP

Eulerian modeling and simulation of polydisperse moderately dense coalescing spray flows with nanometric-to-inertial droplets: application to Solid Rocket Motors

Soutenue le 11 avril 2013

Jury :	M.	Lemou	M.	Rapporteur
	M.	Simonin	O.	Rapporteur
	M.	Subramaniam	S.	Rapporteur
	M.	Massot	M.C.	Directeur de thèse
	Mme	Laurent	F.	Co-directrice de thèse
	M.	Dupays	J.	Encadrant
	M.	Kuentzmann	P.	Examinateur
	M.	Nicoud	F.	Examinateur
	Mme	Amiet	M.-S.	Invitée
	M.	Fox	R.O.	Invité
	M.	Godfroy	F.	Invité
	M.	Reeks	M.W.	Invité

École Centrale des Arts et Manufactures
Grand Établissement sous tutelle
du Ministère de l'Éducation Nationale
Grande Voie des Vignes
92295 Châtenay-Malabry Cedex
Tél : 33 (1) 41 13 10 00
Télex : 634 991 F EC PARIS

Laboratoire d'Énergétique Moléculaire et Macroscopique, Combustion (E.M2.C.)
UPR 288, CNRS et École Centrale Paris
Tél : 33 (1) 41 13 10 31
Fax : 33 (1) 47 02 80 35

2013 - ECAP0030

Contents

List of Tables

List of Figures

Introduction

Taking into account the two-phase aspects of flows has become a necessity for the development of many combustion devices such as piston engines, turbo shaft or turbojet engines, gas turbines, ramjets, scramjets and liquid rocket engines (LRE). In solid rocket motors (SRM) the effects of a disperse phase, i.e. a large number of roughly spherical inclusions of various sizes, have been considered in nozzle efficiency models since the early studies carried out in the 60's (Marble 1963b; Crowe et al. 1964; Grishin et al. 1969; Kuentzmann 1973b; Sternin 1974). Metal fuel is indeed used to increase the combustion chamber's temperature and the motor's efficiency but burnt residuals are present in the SRM flow under the form of a condensed disperse phase which has a mass fraction exceeding 30 %. It strongly conditions the motor's performances: the disperse phase induces losses in the specific impulse as it tends to accumulate in the chamber, to perturb the nozzle flow and to damage the walls. With the growing use of SRMs from the 80's to propel civil launch vehicles, the concern of motor stability has been added to that of high specific impulse and has triggered new research. The thrust oscillations that are observed in several SRMs are indeed rarely destructive (contrary to LREs) but still undesired. Again the disperse phase plays a strong role on the unsteady behavior of the motor and a fine knowledge of the flow and related physics has been sought to design more stable systems. From these intense research campaigns, the knowledge of SRM physics has experienced significant advances but cannot be considered as completed, as a consequence of two penalizing facts:

- the flow in a SRM is complex;
- the nominal SRM conditions are difficult to reproduce at small scales and to study.

A SRM flow is complex since it features the multi-physics aspects of incompressible and compressible, reactive, two-phase flows, and it encounters correspondingly a wide range of Reynolds numbers, Mach numbers, temperatures, spatial and time scales, and densities. In particular, the disperse phase conditions the flow and encounters in return several complex processes across the combustion chamber: these processes remarkably modify the size distribution of the inclusions, namely melting, agglomeration, combustion, coalescence, break-up and solidification. All these phenomena depend on ambient conditions and flow behavior so the problem is tightly coupled as regards all the physical, non-linear phenomena. Given this, the overall physics and conditions of the problem are to be considered in any approach, either model, experiment or simulation. A SRM flow is difficult to study experimentally as regards the high temperatures and pressures but also the dense and two-phase flow conditions; small scale test beds provide valuable but limited data because propellant combustion and two-phase aspects do not lend themselves to the scaling. So the improvement of motors partly resorts to advanced numerical simulations.

In the research for higher performances, the idea of using nanoparticles of metal fuel as a propellant ingredient has been suggested for their good combustion properties. In addition, the resulting residuals in the flow are expected to be smaller and to have a totally new behavior, possibly reducing the nozzle losses. All these presumed effects must be evaluated. The physics of nanoparticles must be assessed in SRM flow conditions and integrated to a comprehensive modeling.

The disperse phase in SRM two-phase flows is characterized by its high mass ratio, resulting in a strong coupling between the two phases, referred to as two-way coupling. Its volume fraction is still small enough for inclusions to keep a fixed shape and justifies to consider it as a disperse phase. Such flows are referred to as moderately dense in the present work, this to emphasize the necessity to account for two-way coupling while the condense phase is disperse. The disperse phase is also characterized by its widespread size distribution: the bigger droplets have a diameter that can be 100 times larger than the smaller ones. So they obey a very different physics since the ability of droplets to correlate their temperatures and velocities to that of the flow varies as the square of the diameter. Moreover the role of the droplet size is crucial in all the physical processes that the disperse phase encounters and drives: distributed combustion, acoustic coupling, hydrodynamic coupling, advection and slag formation, nozzle losses, radiation. This situation is referred to as polydispersity. The presence of nanoparticle residuals potentially exacerbates the issue. Besides the dynamics of this polydisperse phase is complex and droplets can locally have very different velocities, resulting in particle trajectory crossings (PTC). The situation of multiple velocities is referred to as polykineticity: it occurs very often between droplets of different sizes (and therefore different dynamics) and it occurs in high strain zones for droplets of comparable sizes, if they are sufficiently (say moderately) inertial. So

polykineticity refers in fact to two different aspects: crossings of particles of different sizes is referred to as hetero-PTC and crossings of particles of the same size is referred to as homo-PTC. Finally, polykineticity and high number concentrations, linked to high mass fractions, may induce collisions, leading to the coalescence in the case of liquid droplets, the size distribution of which strongly evolves as a consequence.
The detailed study of existing SRMs, the predictive simulation of newly designed motors and the investigation of nanoparticle propellant require an accurate and efficient strategy to compute SRM flows. Models based on the description of a single-phase do not reproduce well many experimental results (Kuentzmann 1998; Godfroy and Briand 2004), so a modeling and numerical strategy must be developed that treats in detail the SRM two-phase flow, in order to achieve full motor computations. We are looking for an accurate but cost-effective approach, that is also robust for obvious reasons of design comfort and engineer-time sparing. The approach should be able to account for the disperse phase, its interactions with the gas, its polydispersity, some polykinetic features and its complex size evolution all along the motor. To improve the prediction level on performance and stability, the key requirements for numerical simulations are (i) to capture polydispersity and polykineticity and (ii) to achieve a High Performance Computing (HPC) capacity.
The choice of a model for two-phase flows is crucial to fulfill these requirements. The choice of a statistical approach to describe the disperse phase is not questioned as regards the high number of droplets and the low level of knowledge on the initial and boundary conditions. The Williams-Boltzmann equation is the reference statistical approach. It describes conveniently all the characteristics of a disperse phase with numerous degrees of freedom, here size, velocity and temperature; it can be strongly coupled to a continuous description of the gas e.g. with Navier-Stokes equation. The resulting fluid-kinetic approach is potentially the fundamental model for SRM flows, provided the satisfactory physical closures, these being obtained from the knowledge of the behavior of a single droplet. Unfortunately, the fluid-kinetic approach is too costly to address complex cases: (1) the flow features turbulence, the small scales of which are out of reach with today's computational power in the context of a Direct Numerical Simulation (DNS) and (2) the phase space of the disperse phase kinetic approach has too high a dimension. To achieve high-fidelity simulations, solutions are being investigated by many communities to filter out and model the small scales of turbulence and to reduce the kinetic approach's high level of detail. To pursue the latter goal, two essentially different paths are available namely the stochastic-Lagrangian (Monte-Carlo) approach and the Eulerian approach. Both approaches have dragged intense developments during the last decades in both the scientific (Subramaniam 2013; Fox 2012) and the SRM domain (Estivalezes 2011), which proves the complexity of the quandary: considerations of computational convenience mingled with customs distort the decision between these two approaches.
On the one hand, the stochastic-Lagrangian approach is an efficient and popular method in the mechanical engineering community (Subramaniam 2013) as it needs few assumptions and allows in principle an easy implementation: in particular, it requires no modeling effort to account for polydispersity nor any kind of polykineticity. In return it requires:
(L1) a cautious interpretation of numerical results, as convergence is difficult to obtain and to assess;
(L2) a strong effort on numerical methods to achieve properly the two-way coupling;
(L3) a strong effort on numerics and implementation to achieve an efficient parallelization (Garcia 2009).
On the other hand, the Eulerian approach results in the so-called Euler-Euler model where the gas-disperse phase coupling is natural and the parallelization far easier. In return, the method is handicapped by:
(E1) the need for a strong modeling effort to include simultaneously multi-physics aspects;
(E2) the sensitivity of numerical schemes to the peculiar features of transporting a Eulerian disperse phase, namely its hypercompressibility, requiring a careful research for stability and for controlled numerical diffusion;
(E3) the particularly delicate treatment of polykineticity.
These crippling drawbacks did not deter early Euler-Euler approaches for SRMs (Dupays 1996) but in a simplified framework e.g. without polydispersity nor polykineticity. Hopefully the emergence of advanced methods has allowed to overcome some of the original pitfalls:
(E1) methods for the size variable have progressively eased the capture of polydispersity and the related physics, such as moment methods (Marchisio and Fox 2005; Fox et al. 2008; Kah 2010) and the Multi-Fluid method (Laurent and Massot 2001; de Chaisemartin 2009) which solves the question of polykineticity for droplets of different sizes i.e. hetero-PTC;
(E1)' the phenomenon of coalescence has been included in the Multi-Fluid method (Laurent et al. 2004) and in some moment methods (Fox et al. 2008);
(E2) the qualification of realizable second order transport schemes for a hypercompressible disperse phase have unlocked the possibility for advanced, robust and complex simulations (de Chaisemartin 2009; Le Touze et al. 2012; Larat et al. 2012);
(E3) Eulerian methods have been developed for polykineticity: algebraic closures for the treatment of Random Uncorrelated Motion have been developed (Fevrier et al. 2005; Masi 2010) as well as many high order moment methods on the velocity variable such as QMOM (Desjardins et al. 2008), EMVM (Kah

2010), CQMOM (Yuan and Fox 2011) or MG (Chalons et al. 2010) and these methods answer in part to the issue of homo-PTC and are still under investigation (see for instance Vié et al. 2012).

So Eulerian methods have reached a good level of maturity and are used in more and more applications (Boileau et al. 2008; Kah 2010; Sierra Sanchez 2012).

In the prospect of accurately describing the two-phase flow of a SRM, possibly with nanoparticle residuals, the following issues must be tackled:

1. the efficient computation of coalescence in a Eulerian framework:
2. the robust and accurate coupling of the two phases;
3. the improvement of the model towards polykineticity for droplets with the same size;
4. the assessment of the peculiar physics of nanoparticle transport;

together with the reduced modeling of (two-phase) turbulence. These model and method improvements must be implemented in an overall approach to treat so-called moderately dense coalescing nano-to-inertial two-phase flows.

First the Eulerian coalescence strategies currently available are costly and they lack the required flexibility to bear advanced droplet models; the latter physics being crucial. Higher order methods in size are promising to treat both aspects of cost-efficiency and advanced modeling. Nonetheless should they be assessed but the algorithms must be improved to comply with the requirements of high performance computation (HPC).

Second the Euler-Euler approach encounters numerical resolution difficulties for small droplets, namely stiffness: many numerical strategies achieve accuracy or even stability at the cost of very small time steps. This expense of resource is nonetheless an extra-cost but also a fundamentally ill-suited strategy: the stiff physics of the smaller droplets is sometimes trivial (equality of velocity and temperature to that of the gas) and brute force methods may remain inaccurate in a stiff context e.g. by rendering an erroneous asymptotic regime. As the relaxation times of small particles are small, all the particle quantities that are solved have to be updated very fast, which must be treated in a specific numerical way. A preliminary work on the model and method is desirable for stiff problems to spare cost and increase accuracy.

Third polykineticity occurs when the flow features velocity fluctuations (inhomogeneities and unsteadiness) and when the disperse phase includes droplets with enough inertia: at worst, droplets of the same size can cross and this homo-PTC occurs for a significant proportion of the droplets when they enter the nozzle. If hetero-PTC has been presented as solved by MF methods so that coalescence can be treated for low-inertia droplets, the case of homo-PTC is more complex: the usual Eulerian approaches generate numerical artifacts referred to as δ-shocks (de Chaisemartin 2009). These discrepancies can be tolerated in some cases of application of an Euler-Euler approach but they are difficult to handle when assessing two-way coupling effects. So they must be treated on the one hand. On the other hand, the Eulerian multi-velocity approaches presented before account for polykineticity with different trade-off on the complexity and the level of detail which may not be adapted to our objective, while the methods themselves may not be robust enough to be implemented in industrial codes: some attempts end up in industrial successes (Boileau et al. 2008) but acknowledge discrepancies due to combined model and numerical issues (Dombard 2011; Sierra Sanchez 2012); moreover the combination of polykineticity and polydispersity treatments can impose a complex and costly algebra. To describe the SRM physics, the detail of the velocity distributions is not needed but only the characteristic size of the structures resulting from droplet crossing and a rough estimate of the relative velocities in order to compute coalescence source terms. These informations are missing in the usual Eulerian simulations. Simoes (2006) attempted to account for uncorrelated particle velocities in a SRM with a Eulerian formalism based on algebraic closures: the approach raises some modeling questions e.g. as regards two-way coupling but it raises also numerical issues; besides, it has the potential to account for coalescence though this has not been furthered and has been successfully extended to the so-called Large Eddy Simulation (LES) formalism (Boileau et al. 2008) which is a promising reduced model for turbulence.

Fourth the presence of nanoparticle residuals requires to account for their peculiar physics: the evolution of the overall size distribution is extremely sensitive to Brownian motion which presumably enhances coalescence. Unfortunately, nanoparticle coalescence is described in a formalism that does not comply to the statistical description so that an effort to adapt the models is needed. Moreover the exact processes affecting nanoparticles are not known, at least in a SRM. Whenever the detailed physics is known, its numerical treatment must be revised since the phenomena presumably introduce fast time scales compared to that of the SRM. So nanoparticles raise both modeling and method issues.

The achievements of the present thesis are now listed. We have focused on the resolution of two-phase flows in a context where no reduced turbulence model is applied, as a prerequisite for a full resolution. The four remaining subjects, which have been defined as crucial for the improvement of high-fidelity simulations for SRMs, have been tackled one after the other, by applying the following methodology: a mathematical modeling of the problem is proposed and complemented by a numerical analysis to assess the well-posedness and the model peculiarities; this study guides the definition of a numerical strategy; the developed model and methods are then extensively validated in an academic context; the approach is implemented in an industrial-oriented code, namely the CEDRE code developed at ONERA (Refloch et al. 2011) and applicative

computations are performed to assess the approach's overall relevance. The CEDRE code is an interesting platform to assess such developments as it features multi-physics solvers on unstructured grids and is fully parallelized.

1. The choice of the Eulerian Multi-Fluid framework to efficiently treat polydispersity and the related physics is discussed and justified after a review of the (numerous) existing methods for disperse phase flows: among the Monte-Carlo, moment and sampling methods, the sectional discretization at the basis of the Multi-Fluid method offers a satisfactory level of detail as regards the accuracy-complexity trade off. A particular method referred to as Two Size Moment Multi-Fluid (TSM) is selected and the coalescence terms are modeled in this context. As regards numerics, two size closures are discussed and the corresponding methods are developed in order to compute in an efficient way the source terms, especially the coalescence ones which have *a priori* a complex algebra. The TSM is then implemented in an in-house research code named TUYA, in which its accuracy and convergence are assessed versus another Multi-Fluid method on a case featuring a strong coupling between transport and coalescence. The new method is validated thanks to an analytical model purposely derived, which is to be published in a paper in preparation (Doisneau and Laurent 2013). The new method is also verified versus available experimental results. The ability to solve efficiently for coalescence is then assessed in CEDRE. This work has led to the first complex SRM computations to capture coalescence: it was presented during the ICMF Conference, Tampa, USA (Doisneau et al. 2010) and has been published in the Journal of Computational Physics (Doisneau et al. 2013) where the numerical methods are detailed and analyzed and the efficiency of the strategy in complex computations is assessed. The ability to capture efficiently coalescence in contexts with such a complex dynamics is a breakthrough which is promising for other domains. Besides, source terms for the presumed PDF modeling of break-up have also been studied in the context of the TSM to include the modeling and method improvements discussed for coalescence sources. An industrial strategy to capture break-up has emerged, in the prospect of assessing the physics of particles in a SRM nozzle and in other industrial configurations such as for icing (Murrone and Villedieu 2011): a publication is in preparation to present achievements and practical computations.
2. Facing the stiffness introduced by small droplets and the need to achieve two-way coupling even for polydisperse cases, a more accurate, robust and flexible time integration strategy has been developed for Eulerian methods in the case of high mass loadings for the disperse phase, which is a major issue in SRMs. From considerations on the different physical timescales of a polydisperse, strongly coupled compressible flow, a new method is tailored in collaboration with A. Sibra. It is based on operator splitting which is particularly suited for unsteady cases, is remarkably easy to handle, and allows to mix explicit, implicit and adapted time steps for the integration of the different operators. The method is especially useful for small droplets as it accounts efficiently for stiff relaxation times without strong numerical constraints on time steps. It is therefore used for SRM computations and allows to account for the first time in a detailed way for the smallest droplets present in the domain. The new method has been validated versus a purposely derived analytical method, after its implementation in an in-house research code named SAP1, dedicated to assessing two-way coupling methods, with advanced numerical schemes. The method and this comprehensive validation were presented in the Joint Propulsion Conference, San Diego, USA (Doisneau et al. 2011) and a publication is submitted to the Journal of Propulsion and Power (Doisneau et al. 2013), where the overall strategy to capture unsteady two-way coupling in polydisperse flows is discussed as regards SRM computations. The method can moreover be extended to split other source terms and to account for the various couplings at best, which has allowed for instance SRM computations with a detailed restitution of small droplets, and their coalescence with bigger droplets having a very different size: an application to a realistic motor has been published in a special issue "Combustion for Aerospace Propulsion" of the Comptes Rendus Mécaniques (Doisneau et al. 2013). The new method is believed to be efficient for the coupling of multiple and complex physics in unsteady cases so the approach is particularly promising, e.g. for multi-physics platforms such as CEDRE.
3. The approach of homo-PTC has been considered in a way that yields a sufficient level of detail for SRMs without compromising cost, flexibility and robustness. A new high order velocity model was introduced for disperse phase flows by Vié et al. (2014), referred to as the Anisotropic Gaussian velocity closure (AG), and it has been extensively assessed and qualified in the context of a collaborative work with A. Vié. We have indeed shown that polykineticity is sufficiently well described to capture:
   - the spatial size of droplet clouds in the nozzle, allowing to assess correctly the two-way coupling effect;
   - the intensity of local relative velocities -as linked to dispersion-, allowing to compute coalescence.

   This new velocity model raises numerical issues on transport: a transport scheme is proposed for structured meshes and validated, and time strategies are suggested: the transport scheme is validated in a research code named AG2D. Coalescence is included and the behavior of the model for the case

of two coalescing jets is assessed and validated versus a point-particle DNS: the new Eulerian method is indeed implemented in an in-house code named SAP2 and the research code Asphodele (Reveillon and Demoulin 2007b; Thomine 2011) is used for the point-particle DNS reference, based on a collision detection algorithm. This comprehensive validation of AG with coalescence has been published in the Proceedings of the CTR Summer Program (Doisneau et al. 2012) as a breakthrough to assess polykinetic coalescence. In addition, the test case is a simplified vision of the coalescence issue raised in a SRM nozzle so this work completes the toolbox of models for polydispersity and coalescence, in the case of homo-PTC. The AG model is presented as a good candidate to estimate more accurately two-phase losses in SRMs. This model is promising for treating transport and crossing at small scale in many other contexts (Vié et al. 2012). A publication is in preparation (Vié et al. 2014) to validate the AG model for turbulent flows and in particular to quantify its ability to reproduce the spray characteristic scales, energies and relative velocities. The study of this closure to assess the two-way coupling in a nozzle flow with homo-PTC is also in preparation. These works prove the need and feasibility of such an approach for industrial computations but the adaptation is not straightforward, when considering the numerical effort still needed to solve AG on unstructured meshes (Sabat et al. 2013; Sabat 2015). So this development is a promising modeling and numerical method contribution and further studies are required to apply it to an industrial context.

4. In another aspect of the present contribution, the peculiarities of nanometric droplets have been thoroughly considered and their physics has been stated: peculiarities on transport and coalescence have been identified. The former effect is classically accounted for in the Brownian theory. The issue is then to provide a comprehensive modeling of coalescence in nano-micro droplet mixtures: this is possible thanks to the versatility of the MF formalism so a hybrid Multi-Fluid approach has been developed, where the ensemble of the droplets are coupled through coalescence and through their effect on the carrier gas. The hybrid model has been implemented and tested in CEDRE and a publication on the physics of hybrid nano-micro mixtures is in preparation (Doisneau et al.). In addition, a prospective study was carried out on a two-way coupling model for nanoparticles in free molecular regime: the similarity of the statistical equation for particles and gas molecules has attracted modeling efforts onto the derivation of a strongly coupled two-phase nanoparticle description from a fully kinetic formalism, which sheds light on the detailed physics such as out-of-equilibrium particle transport. Such detailed models are believed to be useful to assess the local physics of nanoparticle flows in a SRM. The study has yielded fundamental results that support the models that are eventually used but the prospective two-way coupling model is not deployed so that its derivation is presented in Appendix D to ease the reading of the manuscript.

All these model and method improvements allow to perform SRM computations which shed light on several issues, namely two-phase losses and hydrodynamic instability. The effect of polydispersity on the physics of a SRM is assessed in the case of a LP10 sub-scale motor, including the effect of coalescence. Thanks to the improvements in models and methods for either polydispersity, coalescence and two-way coupling, SRM computations have been performed that prove the improvement in the high-fidelity two-phase simulation capability. These results have been presented at the European Conference on Aerospace Science (Doisneau et al. 2011) and have allowed to assess the crucial role of polydispersity and coalescence on instability levels in a complex case of inert particle-driven instability confirmed by an experiment (Dupays et al. 2008). In particular, the efficiency for sprays including small droplets is proven: the new time integration strategy has indeed enabled the simulation of SRMs featuring stiff droplet models. This proves to be useful for a P230 full scale computation, which features 1 μm-droplets. These results have been presented at the INCA Advanced Combustion Colloquium (Doisneau et al. 2011) and published in Doisneau et al. (2013). Thanks to the methods allowing robust small droplet computations and to the new modeling for nano-micro droplet mixtures, we obtain results on motors with nanometric combustion residuals as regards size distribution evolution and two-phase loss assessment. Finally, the level of validation of CEDRE has increased, thanks to the use of a large experimental database on ODP, that has been compared to the LP10 computations. Comparisons between different numerical approaches for two-phase flows are also performed e.g. Eulerian versus Lagrangian simulations (Doisneau et al. 2013). Finally the CEDRE code and its ability to treat coalescence are verified versus an experiment and an analytical solution in Doisneau et al. (2013).

With the ability to treat efficiently moderately dense nano-to-inertial coalescing sprays, the CEDRE code is ready to perform a new high standard type of simulations. In addition, many recent advances for the simulation of two-phase flows in SRMs such as the consideration of turbulent dispersion of droplets (Simoes 2006), the modeling of aluminum combustion (Sibra 2014), the ability to perform high standard stochastic-Lagrangian computations as a complimentary approach (Estivalezes 2011) suggest to reconsider the experimental data available on either disperse phase and motor behavior in order to mutually enlighten the simulation tool and the physics of the system. As a remark the advances on numerical capabilities for two-phase flows thanks to Euler-Euler approaches have also yielded progress in other domains: let us cite another example of a two-way coupled disperse phase in a complex ambience in the case of liquid rocket

engines, where a Eulerian approach in CEDRE has yielded overwhelming advances (Le Touze et al. 2012). During the Stanford CTR Summer Program, a collaboration with N. Rimbert yielded interesting prospective results on the atomization of a moderately dense flow, for which experiments had been conducted at LEMTA (Université de Lorraine). Taking benefit from the acquired skills on moment methods for disperse phase with two-way coupling and with break-up, a prospective study on the fundamental and reduced treatment of primary and secondary atomization in turbulence was published in the Proceedings of the CTR Summer Program (2012) (Rimbert et al. 2012). A modeling framework for turbulent two-way coupled atomization is introduced that accounts in an efficient way for the transient shape of disperse liquid structures. This study has allowed to explore the limits of the presumed PDF approach for break-up, of the sphericity assumption and the additional modeling efforts that are required by the source terms of moderately dense two-phase flows. It is an interesting opening in the possibilities of Eulerian disperse phase modeling and shows the potential of the proposed approach to other areas of research. Accounting for disperse phase break-up in SRM simulations e.g. for two-phase nozzle loss prediction is however out of the scope of the present work so that the model is presented in Appendix C for the sake of legibility.

The manuscript is organized in five parts that are the context, the models for two-phase flows, some specific models for nanoparticle flows, the related numerical methods for transport, polydispersity and two-way coupling treatment and some applicative computations.

The context of SRMs is presented in Part I. The detail of SRM physics is thoroughly reviewed in Chapter 1 in order to introduce the mains issues and to show the impact of two-phase flows. The complexity of SRM flows is shown to call for a comprehensive multi-physics approach with a fine level of resolution to account for the many non-linearities and couplings between the laminar-to-turbulent-to compressible flow, combustion, disperse phase and structure: the modeling and design of a SRM is proven to resort to high-fidelity approaches in the context of a decrease of the experimental resource. An insight on the strategies to achieve high-fidelity modeling is then given in Chapter 2, on with the recent achievements, which allows to conclude on the modeling needs to capture accurately the role of the disperse phase.

Models for moderately dense polydisperse two-phase flows are presented in Part II, which is divided in two chapters describing reference modeling and four chapters on modeling contributions of the present thesis. The specificities of disperse two-phase flows, their classification and some models from the literature are presented in Chapter 3 while their level of detail is discussed; the kinetic (statistical approach) is retained as regards the efficient capture of polydispersity and coalescence; the issues of model reduction for turbulence are presented but the framework of a fluid-kinetic DNS is defined and chosen as a modeling goal of the thesis and as a desirable starting point for high-fidelity SRM computations. Approaches to reduce the level of detail of the kinetic model are discussed in Chapter 4 among which the Euler-Lagrange approach, as well as polydisperse and polykinetic Euler-Euler approaches: the Eulerian Multi-Fluid model is chosen for its flexibility on size-conditioned physics and ease to treat two-way coupling, while some developments towards polykineticity are needed. The peculiarities of two-way coupling with Euler-Euler approaches are finally assessed, as a desirable feature for our approach to capture. As regards polydispersity, a particular MF model referred to as TSM is introduced and discussed in Chapter 5 for its ability to be more accurate on size at a reasonable cost; the coalescence and break-up TSM terms are derived. As regards polykineticity, a high order velocity method is presented in Chapter 6 and its behavior as regards homo-PTC is discussed and compared to other methods; its structure as a fluid model is studied; the AG coalescence terms are derived and written for the MF formalism; the method is finally analyzed in the context of two-way coupling and presented as a satisfactory, robust and accurate approach for moderately-inertial, coalescing and two-way coupled cases such as that of a SRM nozzle. To close this part and with the constant concern to improve and to validate the model and methods, various analytical models have been derived, for isolated physical phenomena, namely two-phase acoustics and coalescence, and they are presented in Chapter 7; first the derivation of an analytical description of polydisperse acoustics, as an extension of a classical formula from Temkin and Dobbins (1966) which has been used to validate monodisperse solvers Dupays (1996), is a powerful approach to validate the two-way coupling that arises in polydisperse two-phase flows, this in a harsh, unsteady context; second, the detailed study of coalescence allows to derive analytical models which ideally validate the numerical strategy developed for coalescence; these reduced order models are exploited in the corresponding validation chapters.

Models dedicated to nanoparticle flows are presented in Part III, with a chapter overviewing methods from the literature and two chapters of contributions. The general issues raised by nanoparticle flows are discussed and the models are reviewed in Chapter 8; the approaches for particles in continuous and free molecular regimes are distinguished and detailed: the first one corresponds to Brownian motion, which has consequences on transport and coalescence and the second concerns a kinetic regime. In Chapter 9, a comprehensive model is derived that allows to treat mixtures of nanoparticles and usual microparticles when coupled by coalescence: this approach hybridizes the models chosen to account for nanoparticles physics and the TSM method developed to treat efficiently polydispersity.

Part IV is dedicated to the numerical methods for moderately dense polydisperse two-phase flows: the

first chapter presents the available methods and developments are proposed and validated in the three following chapters. A review of the numerical peculiarities and related methods linked to the simulation of Eulerian models for disperse phase is done in Chapter 10: (i) the issue of hypercompressibility is discussed as regards the solutions provided by the literature, and the models presented in Part II are shown to need such numerical developments; (ii) a time integration strategy for strong coupling is then presented, that allows to treat efficiently and separately the physical and phase space, without defiling the couplings; (iii) techniques to accurately compute the dynamics of the phase space and the related source terms are finally discussed and the class of quadrature methods, together with advanced time integrators for Ordinary Differential Equations, are identified as needed for the efficient integration of phase space source term. Chapter 11 presents a numerical method to account for particle transport, in the context of the AG closure; a second order scheme is introduced for structured grids and validated on several complementary configurations. Chapter 12 is dedicated to a new splitting approach for the two-way coupled gas-disperse phase system; the method, based on operator splitting, is suggested from the consideration of the flow physics and is proven to be accurate for several unsteady, two-way coupled configurations, thanks to a verification on an academic case versus an analytical solution derived in Chapter 7 for acoustics and to a cross-comparison with another method on a complex SRM case; the benefit of the method on robustness and computational efficiency is also presented; so the new strategy is a breakthrough as regards two-way coupling and allows Euler-Euler approaches to achieve one of their fundamental potentials. Numerical methods for size source term computation are then introduced in Chapter 13, based on quadrature approaches in order to allow a high level of flexibility on source term modeling; accounting for advanced, non-linear closures is indeed needed for industrial computations; the numerical methods are validated on academic cases with the analytical solutions derived in Chapter 7 for coalescence, with a point-particle DNS simulation, and with an experimental result.
Finally, Part V presents applicative computations on SRMs. Once validated, the previous improvements on coalescence, two-way coupling and nanometric coalescence have been implemented in the CEDRE code, a mixed industrial and research code presented in Chapter 14. We highlight that the developments for moderately inertial regimes and homo-PTC are not implemented as either the model and the method are not mature enough. However several improvements of CEDRE have been conducted. The new strategy for low-inertia coalescing two-way coupled sprays allows to perform new SRM computations: the effect of polydispersity on the physics of a SRM is assessed in Chapter 15, including the effect of coalescence and a wide range of steady, unsteady, realistic and strongly polydisperse cases are studied, possibly compared to stochastic-Lagrangian simulations. The new modeling for nano-micro droplet mixtures, coupled to the new robust integration, is presented and discussed in Chapter 16, before concluding on the overall work.

This Ph.D. was directed by Marc Massot[1], Frédérique Laurent[2], and Joël Dupays[3]. It counted on the close collaboration of Angelo Murrone[4], Alaric Sibra[5], Aymeric Vié[6], and Nicolas Rimbert[7].

This work was supported by:
- a Ph.D. grant from the Délégation Générale de l'Armement, agency of the French Ministry of Defence (M.S. Amiet technical monitor).

Furthermore it was carried out thanks to:
- an ONERA fundamental research program, PEA NANO-MOLEN2 (leader Y. Fabignon 2009-2012);
- a France-Stanford grant (project leaders P. Moin & M. Massot 2011-2012).

The financial and material support from EM2C all along the Ph.D. thesis and the support from the Center for Turbulence Research during the Summer Program 2012 are greatly acknowledged.

[1]Laboratoire EM2C - UPR CNRS 288, École Centrale Paris, Grande Voie des Vignes, 92295 Chatenay-Malabry Cedex, France (marc.massot@ecp.fr)

[2]Laboratoire EM2C - UPR CNRS 288, École Centrale Paris, Grande Voie des Vignes, 92295 Chatenay-Malabry Cedex, France (frederique.laurent@ecp.fr)

[3]ONERA, Département d'Énergétique Fondamentale et Appliquée (DEFA) - BP 81000, 91120 Palaiseau Cedex, France (joel.dupays@onera.fr)

[4]ONERA, Département d'Énergétique Fondamentale et Appliquée (DEFA) - BP72, 29 avenue de la Division Leclerc FR-92322 Chatillon Cedex, France (angelo.murrone@onera.fr)

[5]ONERA, Département d'Énergétique Fondamentale et Appliquée (DEFA) - BP 81000, 91120 Palaiseau Cedex, France – Laboratoire EM2C - UPR CNRS 288, École Centrale Paris, Grande Voie des Vignes, 92295 Chatenay-Malabry Cedex, France (alaric.sibra@onera.fr)

[6]Laboratoire EM2C - UPR CNRS 288, École Centrale Paris, Grande Voie des Vignes, 92295 Chatenay-Malabry Cedex, France (aymeric.vie@ecp.fr)

[7]LEMTA - UMR 7563, ESSTIN, Université de Lorraine - Boulevard des Aiguillettes, BP 70239, 54506 Vandoeuvre Cedex, France (nicolas.rimbert@esstin.uhp-nancy.fr)

Part I

Two-phase flows in SRMs: Modeling and Simulation objectives

Chapter 1

Context and physics of Solid Rocket Motors

We introduce the applicative context of solid rocket motors (SRMs) by describing their structure and characteristics, some SRM-propelled vehicles, the related industries and the general technical problems raised by SRMs. We then focus on the phenomenology of the SRM internal flow and the general aspects of its modeling. We finally state that a detailed description and resolution of the two-phase flow inside the chamber is essential to capture and predict the most important SRM features.

1.1 General context and issues

The typical structure of SRMs is described as well as their characterization before presenting the main applications and the related industries. Three benchmark SRMs are then detailed. The context presentation is concluded by an overview of the problems posed by SRM designing.

1.1.1 Motor Description

A SRM is a reaction engine that discharges a fast moving jet generating thrust in accordance with Newton's third law. This principle also works in absolute vacuum so it is the key to space travels, as envisioned by the Russian mathematician and physicist Konstantin Tsiolkovski at the end of the XIX$^{\text{th}}$ century, see for instance Tsiolkovski (1903).
Thrust results from the motor's own mass ejected at high speed, this mass corresponding to burnt gases resulting from the pressurized combustion of an energetic material called solid propellant. The hot gases flow through the combustion chamber towards a De Laval nozzle where their pressure decreases as their speed increases: kinetic energy is converted from microscopic (internal) to macroscopic (ensemble) energy.
SRMs are distinguished from liquid rocket engines (LRE) by the fact that the propellant is a solid material, while the propellant of LREs is a liquid that is atomized at the core of the combustion chamber thanks to injectors. A third class of motors, referred to as hybrid, consists in atomizing a liquid (oxidizer) on a solid (reductant) grain. These three types of motors feature very different flows and raise distinct issues.
From now on, we focus on SRMs. We hereafter describe their structure and the overall performance indicators.

1.1.1.1 Motor structure

A SRM is schematically constituted of a casing, usually made of metal or composite materials, at the end of which is fixed a nozzle. It is loaded with a solid propellant grain, separated from the case by a material layer, called internal thermal insulation (PTI, standing for the French "Protection Thermique Interne"), which reduces undesired heat fluxes towards the casing. The grain is hollowed out to form the combustion chamber, which more or less complex shape drives the burn rate. The ignition device, constituted of a small charge of energetic material with an electric ignition lock, is usually located at the front of the combustion chamber and provides the required amount of energy to start the combustion process of the main grain. These features are sketched in Figure 1.1.

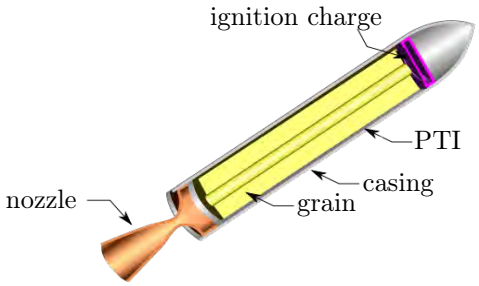

Figure 1.1: *General structure of a SRM (source: Wikipedia).*

1.1.1.2 Propellant requirements

The propellant is the energy-containing material that fuels the SRM. It is composed of thoroughly mixed solid oxidizers and reductants, selected to maximize the gas volume and temperature without any external supply of air. The propellant also contains additives to enhance its structural, combustion and storage properties.
As regards mechanical engineering, the nominal conditions are harsh compared to other combustion-based devices with temperatures around 3500 K and pressures ranging from 5 to 10 MPa. High temperatures and high pressures are required for efficiency reasons. The operating time of a SRM ranges from seconds to minutes.
These harsh conditions justify the need of thermal insulation. In addition, such conditions impose modeling, design and measurement difficulties. In particular, high temperature and pressure conditions are a source of experimental difficulties, presented in § 1.4.1.
In the case where metal particles (typically aluminum) are used to contribute to the chemical reactions, the resulting oxides are liquid and form droplets in the flow.

1.1.1.3 Segmented motors

Because the propellant is difficult to cast in large sizes, large SRMs are often made of several propellant grains called segments. A segmented motor is shown in Figure 1.2.

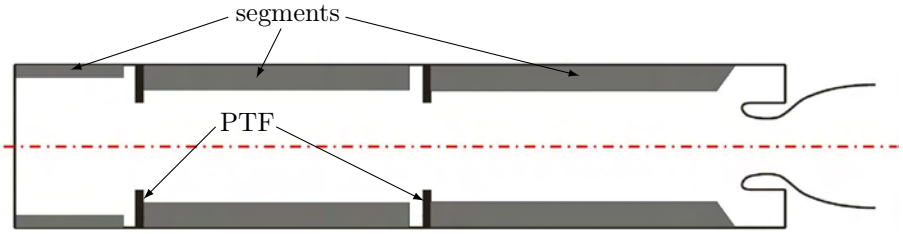

Figure 1.2: *Schematic representation of a segmented motor during firing (Simoes 2006).*

To reduce heat fluxes on the segment faces or towards the casing, the inter-segment is often jointed with a polymer washer referred to as face thermal insulation (PTF standing for the French "Protection Thermique de Face"). The design of the PTF is crucial as it ensures that the grain burns at the surface only, enforcing a given combustion rate. In return, the emergence of the PTF in the chamber during the motor operation has a major impact on the flow. Its phenomenology and the modeling efforts to capture its influence on instabilities are discussed in § 1.2.1.3.

1.1.1.4 Nozzle

The nozzle accelerates the gases, converting heat and pressure into momentum, to achieve thrust according to Eq. (1.2). The classical design chosen to achieve supersonic exhaust velocities is the De Laval nozzle, also named convergent-divergent: the gas velocity increases as pressure drops, from the combustion chamber to the output plane in a continuous way, at subsonic, sonic at the throat and then supersonic regime as shown in Figure 1.3.
The exhaust velocity v_{out}, which drives the motor thrust according to Eq. (1.2) can be computed from chamber conditions and gas properties (Candel 1990):

$$v_{out} = \sqrt{\frac{T_c R}{M}\frac{2\gamma}{\gamma-1}\left[1-\left(\frac{p_{out}}{p_c}\right)^{\frac{\gamma-1}{\gamma}}\right]} \tag{1.1}$$

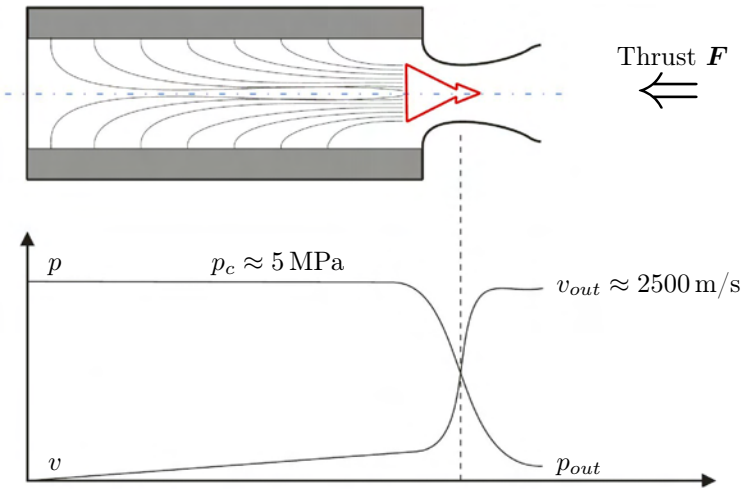

Figure 1.3: *Typical axial velocity and pressure profile along a SRM (Simoes 2006).*

with T_c and p_c the chamber temperature and pressure, p_{out} the exhaust pressure, $R = 8.314\,\mathrm{kJ/mol/K}$ the perfect gas constant, M the exhaust gas molecular weight, and γ the isentropic coefficient.
The gas pressure in the exhaust plan p_{out} also drives the motor thrust, depending on the exterior pressure p_0, according to Eq. (1.2). Depending on both pressures, the nozzle is said to be:

- underexpanded if $p_{out} > p_0$,
- ambient if p_{out} matches p_0,
- overexpanded $p_{out} < p_0$.

Underexpansion and overexpansion translate into a loss in efficiency. However, grossly overexpanded nozzles result in an improved efficiency, considering the economy of weight, but their exhaust jet is unstable.
The nozzle material must withstand the heat fluxes conducted from the gas and radiated by condensed matter, both at high temperatures. So that heat-resistant, carbon-based materials are often used, such as amorphous graphite or carbon-carbon. Some designs include directional control of the exhaust for steering purpose.

1.1.1.5 Performance indicators

The mechanical behavior of a motor is completely determined by its thrust over time, given its mass over time. Thrust $\boldsymbol{F}$ can be computed from the jet characteristics

$$\boldsymbol{F}(t) = \dot{m}\boldsymbol{v}_{out} + (p_{out} - p_0)\boldsymbol{A}_e \tag{1.2}$$

where $\boldsymbol{A}_e$ is the exhaust jet oriented surface, all variables being instantaneous. The vehicle's mass is deduced from the mass flow rate.
Specific impulse I_{sp} is then defined as:

$$I_{sp} = \frac{F}{\dot{m}g} \tag{1.3}$$

where F and $\dot{m}$ are average thrust and mass flow rate and g is the value of gravity acceleration at sea level. The specific impulse has the dimension of a time and is classically used to characterize the motor's performance -and sometimes the propellant's by misuse of language. It corresponds to the time, in seconds, during which the propellant can bear its own weight. It is of crucial importance to characterize non-breathing propelling devices, which have to bear and accelerate all their fuel. So that I_{sp} is often used to compare rocket motors.
By integrating the equation of motion of the vehicle featuring a vehicle mass that varies from M_0 to M_f versus an acceleration $a(t)$, we can compute the velocity variation $\Delta v = v_f - v_0$:

$$\Delta v = v_{out} \ln\left(\frac{M_0}{M_f}\right) - \int_0^{t_f} a(t)\mathrm{d}t \tag{1.4}$$

assuming a steady motor operation i.e. constant mass flow rate and exhaust velocity v_{out}. We note $L(a) = \int_0^{t_f} a(t)\mathrm{d}t$ the loss caused by force fields. Eq. (1.4) is known as Tsiolkovski's equation though it was first derived in Moore (1813). It shows how the fuel mass penalizes the mission, which is either quantified in terms of velocity difference Δv (for an orbit correction), in terms of integral compensation of a specific force

a (for a missile cruise velocity sustain versus atmospheric drag) or both (for a space launch towards a given orbit requiring potential energy gain and orbital velocity).
The orbit is more costly depending on its altitude (or reach time t_f). For instance a typical low earth orbit (LEO) is fairly circular with a radius of 8.7 km and a velocity of 6.8 km/s requiring $(\Delta v)^{LEO} = 7.8\,\text{km/s}$ and an additional $(L)^{LEO} = 2\,\text{km/s}$ for Earth gravity and drag while a typical geosynchronous transfer orbit (GTO) is an ellipse with a semi-major axis of 24.5 km, perigee velocity of 9.9 km/s, apogee velocity of 1.64 km/s and requires an additional $(\Delta v)^{LEO-GTO} = 2.5\,\text{km/s}$. Considering that the vehicle carries its own structure mass M_t or tare mass, the effective payload $M_p = M_f - M_t$ is reduced.

1.1.1.6 Solid Rocket Motor control

SRM thrust laws only depends on design features chiefly geometry, propellant and nozzle. They are determined before flight and the motor is not throttlable, as it is well known and leads sometimes to prefer LREs or hybrid motors. So SRM "control" only relies on fixing the evolution of the chamber pressure. This is achieved by presetting:

- the propellant composition, which defines the gas thermodynamics and the energy release,
- the grain geometry, which defines the burning surface,
- the nozzle geometry and particularly throat diameter.

In addition the knowledge of external pressure conditions p_0, which varies with altitude, is required as they influence the nozzle efficiency according to Eq. (1.2).

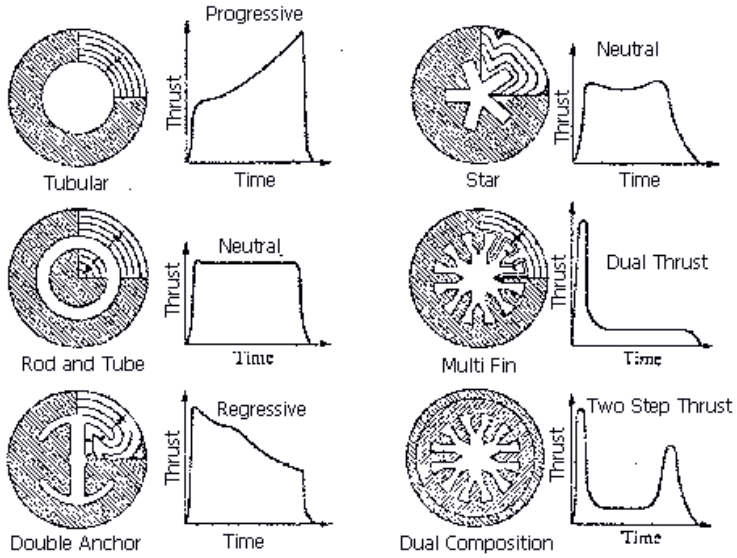

Figure 1.4: *Initial grain geometry, regression contours and corresponding thrust laws (Nakka 2012).*

Figure 1.5: *Star-shaped grain of a P230 1/35 sub-scale test motor named LP10 (source: ONERA).*

The grain geometry appears to be the most reliable and efficient way to control thrust, since varied thrust laws can be so preset as shown in Figure 1.4, excerpted from Nakka (2012).

1.1.2 Applications and industrial context

SRMs are used to propel vehicles and missiles in air or space, generally at high speed, the precise mission eventually being orbit reach, trajectory correction, atmospheric flight, *etc.* In the case of Expendable Launch

Systems (ELV) i.e. vehicles aiming at sending a payload to a given orbit, multiple stages are classically used, eventually based on SRMs but also on LREs and ion thrusters (for upper stages, though, as their thrust is much smaller): they share the common basis of being jet engines able to operate without breathing air.
SRMs are characterized by a relative ease of storage and use. They are also easy to build as long as their size and thrust remain moderate. As a counterpart, their energetic performances (I_{sp}) are moderate compared to LREs and they cannot be stopped or even throttled during operation. The thrust evolution can only be set by design, as discussed in § 1.1.1.6.

1.1.2.1 Space applications

SRMs are widely used for space applications, constituting a stage of ELVs. As part of the stage of an ELV, they are sometimes referred to as "boosters". SRMs are often compared to LREs when it comes to designing a new vehicle. LREs reach a very high specific impulse by using high energy propellant couples such as LH2/LOx or GCH4/LOx (Harrje and Reardon 1972; Culick 1966a; Culick 1988) but are technologically more complex and costly. Typical ELVs are given in Figure 1.6 with their payload: most of them involve SRMs.

Figure 1.6: *Different ELVs.*

The European heavy duty ELV Ariane 5, shown in Figure 1.6 and in Figure 1.7, features SRMs. Its first stage named EAP -standing for Étage d'Accélération à Poudre, built by EADS Astrium ST- is indeed composed of two SRMs named P230. Ariane 5, in its latest version, sizes 52m and 750t and carries a payload of 12t at GTO. It has over 50 % of the commercial satellite market share and achieves an overall reliability of 95 %. The project manager is Arianespace. The P230 SRM is developed under the responsibility of Europropulsion company (owned by SAFRAN Herakles and Avio). The conception phase of the P230 was shared by many French research organisms as well as Italian research organisms. The P230 internal geometry is used in § 15.4.

Figure 1.7: *Left: Ariane 5 on its launch pad – Right: Ariane 5 and its booster stage.*

The European ELV VEGA, shown in Figure 1.6 and in Figure 1.11, is equipped with a first stage based on

a single SRM named P80. The P80 is built by Avio; it is described in § 1.1.3.2. The ELV can send up to 2.3 t in LEO.

1.1.2.2 Strategic military applications

SRMs are also used for strategic military applications, mainly to deliver nuclear warheads from silos or submarines at long range. The French Submarine Launched Ballistic Missiles (SLBM) M45 and M51 are built by EADS Astrium ST, in order to be launched underwater. They are presented inside the submarine and when emerging in Figure 1.8.

Figure 1.8: *Left: M4 in a submarine; Middle: M51 (source: Wikipedia) – Right: M51 test firing (source: DGA).*

The M51 is a three stage missile of 12 m high and weighing over 50 t, which was deployed in 2010. Each propulsive stage, built by SAFRAN Herakles, develops 1800 kN thrust, allowing the missile to reach a cruise speed of 19 km/s. Each missile has a range of over 11, 000 km. The underwater launch phase requires specific conception and modeling.

1.1.2.3 Tactical weapons

Tactical weapons refer to short range rockets (unguided) and missiles (guided), from a few kilometers to a few hundred kilometers. For instance, and with respect to increasing range, there are anti-tank rockets, anti aircraft and anti-ship missiles, cruise missiles (i.e. generating lift) and tactical ballistic missiles for land attack (possibly nuclear). While subsonic missiles can be propelled by turbojets (anti-ship), the fastest missiles can resort to solid propellant or ramjets.
Tactical SRMs are small motors generating small thrust and the issues raised are completely different from those of large SRMs. There are less efforts to reach high I_{sp} and the operating times are short so the casing can be reduced as the pressure in the chamber p_c is lower and overheating is unlikely. Since the chamber dimensions are much smaller, the short chamber residence times rarely allow the use of metal particles (as they would not burn completely) and longitudinal instabilities rarely develop. Still high frequency instabilities may occur with the coupling of the propellant response (see § 1.3.2.3) to acoustic tangential modes, see Lhuillier (1966) and Kuentzmann (1991). Also the use of particles is avoided as hot residuals increase the jet radiative signature, penalizing the degree of stealth against infrared detectors.

1.1.3 Examples of large SRMs

We focus on large SRMs as they raise the most important issues.

1.1.3.1 The P230 SRM

The P230 SRM is used in pair as the first stage of the European ELV Ariane 5. A comprehensive description of its physical and technological concerns, oriented towards two-phase flows and instabilities can be found in Simoes (2006).
Each P230 SRM generates a 7000 kN thrust, allowing Ariane 5's first stage to generate 92 % of the ELV's take-off thrust, while the LRE Vulcain 2 is also lit for reliability reasons. The two P230 operate during 132 s, taking Ariane 5 to an altitude of 60 km. The P230 includes 230 t (Scippa et al. 1996) of 68/18/14 AP/Al/HTPB solid propellant (Biagioni and Austruy 1996) which has a density of 1750 kg/m^3 and a specific energy of 3.0 MJ/kg. The regression rate of the surface depends on the chamber pressure which is constant during most of the operating time (see Figure 1.10), so that the propellant surface has a regression rate which is fairly constant $V_b = 7.4$ mm/s. The regression rate, also referred to as burn rate or recession rate, is defined later in Eq. (1.5) and more details on the general modeling of propellant combustion are given in § 1.2.2.3.

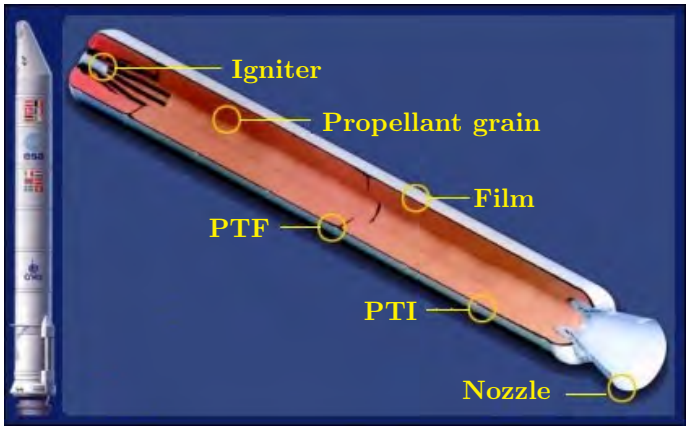

Figure 1.9: *EAP cut (source: Herakles).*

We insist on the fact that the aluminum is incorporated as micrometric particles μAl. The propellant is mixed under vacuum and casted around kernels, into three different segments because of the motor's size (cf. Figure 1.9). A star-shaped grain with 15 branches -see for instance Figure 1.5- ensures a high initial thrust and two cylindrical-conical grains allow a longer combustion tail. The grains are separated by PTF at their edges, shown in Figure 1.9 and sketched during combustion in Figure 1.2. The integrated nozzle is inherited from the M45 strategic motor (Faure et al. 1996). The specific impulse of the motor is $I_{sp} = 273\,\mathrm{s}$ in vacuum.

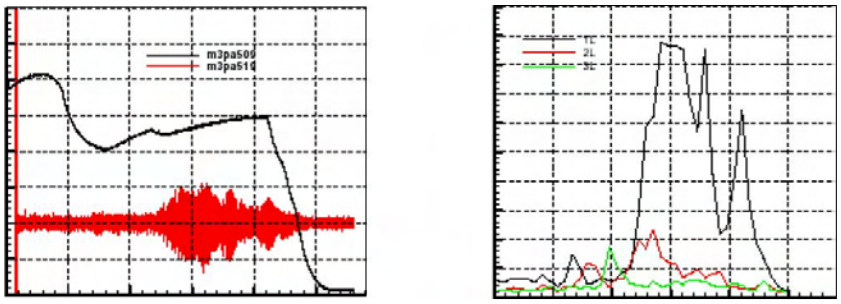

Figure 1.10: *Pressure signals in a P230 – Left: average (black) and unsteady (red) versus time; Right: amplitude of the three first longitudinal modes versus time – Excerpted from Prévost et al. (2001).*

The P230 is a reliable SRM, as the success of Ariane 5 demonstrates, but a phenomenon of thrust oscillations, referred to as TO, occurs regularly and is a major issue. All P230 are equipped with pressure sensors in the front and rear ends which confirm the link between pressure fluctuations and TO (Join-Lambert et al. 1996; Ballereau et al. 2003), with pressure oscillation levels reaching 200 mbars for the first longitudinal mode, around 20 Hz. The detailed study of the P230 unstable behavior is given in Prévost et al. (2001), from which the mean and fluctuating pressure signals are reproduced in Figure 1.10. The P230 pressure features four bursts around 66 s, 95 s, 107 s, and 117 s (Ballereau et al. 2003) with variable amplitudes.
In large SRMs, the scenarios involving hydrodynamic instabilities possibly coupled to longitudinal acoustic modes (e.g. 1L) are regarded as satisfactory. Whereas propellant combustion instabilities (described in § 1.3.2.3) are unlikely to develop regarding the weak propellant response at these low frequencies (Gallier et al. 2002). The American ELV Titan III and IV and the Space Shuttle SRMs featured TO with repeatable frequencies, which were analyzed as a coupled hydrodynamic-acoustic interaction (Brown et al. 1981; Dunlap and Brown 1981; Dotson et al. 1997). The P230 SRM from the European ELV Ariane 5 proved to be unstable during its design phase (Scippa et al. 1994). The ASSM program has concluded that the unstable behavior of the P230 is dominated by hydrodynamic, vortex shedding mechanisms (Fabignon et al. 2000) still influenced by combustion, structure vibration *etc.*
Another issue in the P230 is the accumulation of aluminum oxide residuals in the aft dome region of the motor. This slag accumulation was confirmed experimentally on test benches and can reach 2 t in the P230 (Fabignon 1997) which is significant compared to the 72 t of alumina produced by such a motor (Lavergne et al. 1996) and is also significant compared to the motor's tare mass $M_t^{P230} = 38\,\mathrm{t}$. Slag has stability and performance impacts which are presented in § 1.2.4.1.

1.1.3.2 The P80 SRM

In 1999, the European Space Agency (ESA), motivated by Italy, decided to develop an ELV for small payloads, in order to supplement the capacity range of European vehicles. The P80 is both the first stage of this ELV named VEGA and a low-cost SRM technology demonstrator. Initiated by ESA, the P80 project was entrusted to CNES and the project manager is the Italian manufacturer Avio. The first test bench firing of a P80 was achieved in 2006, initiating a successful one-year test campaign. The P80 SRM was qualified in 2008 and the first VEGA was launched on the 13$^{\text{th}}$ February 2012.

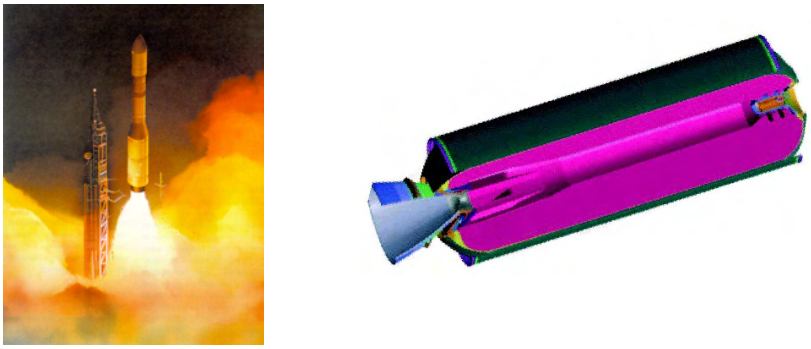

Figure 1.11: *Left: Launch of European light ELV VEGA – Right: Schematic representation of the P80 SRM, first stage of VEGA (source: ESA).*

The P80 is a 3 m diameter SRM, analogously to the standard P230. The energetic material is, as for the P230, an AP/Al/HTPB propellant with a slightly different formulation (69/19/12) therefore still with aluminum particles. The SRM is 10 m long and takes 88 t of propellant. But the main innovations allow a weight reduction: a filament-wound case replaces the traditional steel case, the PTI is made of low density rubber, the nozzle joint is electrically actuated instead of hydraulically, and circlips replace many bolted joints. The ignition system has also been simplified. If similarly applied to the P230, these improvements would allow a gain of 1 t. The P80 finally operates during 110 s, delivering a maximum thrust of about 3040 kN. Remarkably, the P80 features TO, rather in the first part of its operating time.

1.1.3.3 SRMs for Ariane 6

Ariane 6 is an intermediate size ELV (6 to 8 t in GTO) supposed to replace the European intermediate and heavy ELVs (Soyouz and Ariane 5 respectively) by 2022. Ariane 5, though reliable and in a dominant position, suffers from its high cost, in the context of satellite market evolution and arrival of low cost competitors (SpaceX and China). The decision to build Ariane 6 is to be taken in 2014.
The propulsion configuration should be set by ESA in mid-2013: the first stage should be composed of three P135 in a row, the second stage of a unique P135, and the third stage of a re-ignitable LRE called Vinci. The P135 on which this solution should be based is considered among several other SRMs such as the P80 of Vega or a new design called P110. All these SRMs share an architecture inspired from that of the P80: they are made of a single segment to avoid the development of hydrodynamic instabilities caused by the emergence of the PTF in the chamber flow, and the figure in the name stands for the mass of propellant (in metric tonnes).

1.1.4 Issues of large SRMs

The issues of large SRM conception and modeling are related either to their performances, in order to maximize the payload capacity for a given mission, or to their stability, in order to improve the comfort of the payload and reduce the weight of the suppressor devices (DIAS). Performances and stability are of course sought in the limit of an affordable cost (material, process). Environmental issues might gain in importance in the coming years and are briefly discussed. We highlight for each issue the role of the disperse phase, the modeling and simulation of which we aim at improving in the present thesis.

1.1.4.1 Motor performance

The motor performance is measured in terms of I_{sp}, though more thrust is sometimes also required. Thrust is given by Eq. (1.2), and increases with v_{out}: this requires high pressure p_c and temperature T_c in the chamber, which results in wearing out the casing and PTI material. Otherwise, mass flow rate $\dot{m}$ (or A_e) can be increased, this corresponding to oversizing the motor. To increase I_{sp}, it is needed to improve

the motor energetic content and the nozzle efficiency, quantified by the characteristic velocity $C^\star$ and the coefficient C_F according to Eq. (1.15) derived further below.
The motor energetic content can always be increased by resorting to:

- an energetic binder (nitroamines, nitralates, azides, *etc.*),
- new additives (carbon nanotubes, nano-iron),
- a size reduction on existing metal additives (nanoparticles of aluminum are extensively described in the following),
- more metal additives to (partly) replace aluminum: boron (Chen et al. 1993; Ishihara and Brewster 1993), zirconium, magnesium (Ishihara and Brewster 1993), *etc.*)

But the properties (and cost) have to be assessed before deploying a radically new propellant formulation:

- exact combustion behavior (burning rate, propellant response),
- mechanical and thermal properties of the bulk material,
- manufacturing properties (moulding or casting),
- storage, aging and security.

When reformulating a propellant, the metal fuel raises many issues as its combustion and physics in the two-phase flow are poorly predicted. So-called two-phase chemical losses can be reduced with an appropriate coating to avoid surface oxidation (which is presented in § 1.2.2.4) but the combustion behavior is up to now impossible to predict without extensive experimental characterization.
The nozzle yield is already well optimized regarding single-phase flow considerations as single-phase nozzle theory is mature i.e. Eq. (1.13) is a good approximation. However, two-phase nozzle losses remain significant: it can be envisioned to stretch the nozzle in order to improve the two-phase thermal and dynamic equilibrium. But a reduction of the condensed phase particle sizes would result as well in a better equilibrium since the relaxation times strongly decrease with the particle size. Again, the two-phase physics in the chamber is not predictable with today's numerical tools while experiments are costly and of questionable representativeness. The solution of reducing the particle size, possibly down to nanometric particles, in order to reduce the residual size is discussed (Mench et al. 1998; Huang et al. 2005; Meda et al. 2005; Meda et al. 2007; Yetter et al. 2009). If the residual size reduction is observed, it could also yield benefit in terms of slag formation and nozzle erosion as smaller condensed residuals may follow the flow and be evacuated in large proportion, instead of impinging the nozzle wall and filling the aft-dome region. The burning rate of propellants loaded with nanoparticles is significantly different (Mench et al. 1998) which may be a desired feature. Regarding the many different properties with loadings of reduced particle, this solution is still far from adopted.
The role of particles on performances is of first order and undisputed. But predicting the possibly numerous consequences induced by the metal fuel as well as its evolution during firing is difficult.

1.1.4.2 Motor stability

Thrust oscillations (TO) can be observed in large SRMs and are linked to pressure oscillations in the chamber (ODP, standing for the French "Oscillations De Pression"): these phenomena are part of the overall motor stability which is a crucial point. Contrary to LREs where instabilities may lead to wreckage, no such incident occurred in SRM regular flights nor is expected. But TO are still a concern as they can damage the payload. The vibration levels tolerated on Ariane V's payload fairing require the use of suppressor devices (DIAS) and the reinforcement of the satellite structures: this results in extra-weight. The next-generation ELVs are to achieve lower vibration levels and thus stability needs to be predicted during conception (Gallier et al. 2002)
Unfortunately TO modeling and prediction has been a tough topic and only partly solved so far, no exhaustive and comprehensive theory having arisen up to now. Many experimental data was gathered across the world and scenarios involving either acoustic, hydrodynamic and two-phase effects have been developed in parallel. In the following, we will devote part of our studies to instabilities for two reasons: (i) as a hot SRM topic, we review and discuss the role of the disperse phase in ODP in order to assess the particular stability of nanoparticle-based SRMs, (ii) we use part of the abundant ODP data to validate the hereafter developed models and methods on the complex physics of instabilities.

1.1.4.3 Environmental print

In the context of space application development and the potentiality of space tourism, the environmental impact of launchers must be assessed (Soares 2011).
Very toxic formulations where rejected in the past for instance with beryllium (Tavernier et al. 1970) or boron (King et al. 1984) particles as a metal fuel. The latter seem to be still under study in China (Yu 2009). Research on less-polluting propellants were conducted (Finck and Perut 1991; Davenas 1995) e.g. to reduce hydrochloric acid emissions. This shows that environment is a constant concern up to now and is systematically considered as well as security and cost. But the norms get stricter and stricter so new studies

are conducted (Lempert et al. 2009). Today's choices for propellants could be reassessed, depending on future political choices.
Predicting pollutants, which are produced in small quantities (a few ppm), is very difficult and requires a more accurate turbulent chemistry modeling than actually used as well as huge computational resources. The example of nitrogen oxides in air-breathing combustion devices well illustrates the size of the challenge: their prediction has been partly solved in the context of Large Eddy Simulation (LES) with chemistry tabulation and thickened flame models (Schmitt et al. 2007). In our case, the presence of a condensed disperse phase greatly complicates the modeling and is difficult to tabulate. For now, the chemical models in SRM simulations are rustic as they only aim at capturing near-equilibrium states, the main species and the associated overall heat release. Moreover this level of detail on chemical species is rarely sought simultaneously to the resolution of other physics such as the disperse phase: the lack of coupled resolution approaches is discussed in Chapter 2. The use of advanced chemistry models to predict the concentration of pollutants into a comprehensive, two-phase simulation is not scheduled by SRM research and industrial communities. Hopefully, most of the reactions occur in a well known volume that is close to the propellant surface so that the decoupled chemistry models used up to now may provide a satisfactory estimation of these atypical chemical aspects.

1.2 Phenomenology of a SRM

We now describe the phenomena that occur from the propellant surface to the exhaust jet, including reactive and two-phase aspects.

1.2.1 Geometry of the motor

A SRM has a complex geometry that moreover varies in time. These variations may not be taken into account in the context of so-called quasi-steady approximation but they have a major importance for the comprehensive, predictive modeling of SRMs.

1.2.1.1 Complex geometry

The geometry of a SRM chamber is designed to achieve a given thrust law, as said previously: it is therefore complex regarding modeling and CFD meshing. And the relatively simple grain patterns e.g. resulting from the extrusion of the shapes given as an illustration in Figure 1.4, are not the only ones to be used in practice for large SRMs: complex 3D shapes, the so-called finocyl, are casted in the grain, mainly to maximize the propellant loading.
Their role in disrupting some coherent structures of the flow and therefore controling instabilities is suspected: the influence of complex grain shapes on motor stability behavior is currently studied, for instance in the frame of the Ariane 6 program.
As for the nozzle, it is also relatively complex either to achieve a particular flow behavior (e.g. dual bell nozzle for pressure adaptation) or for technical reasons, see § 1.2.1.4. So realistic nozzle geometries, possibly with moving parts, are to be accounted for.

1.2.1.2 Propellant surface regression

The segments are usually designed for the combustion front to remain fairly parallel to the initial surface and to move at a few millimeters per second, towards the outside. The resulting products are therefore injected in the combustion chamber with an opposite velocity as shown in Figure 1.12.

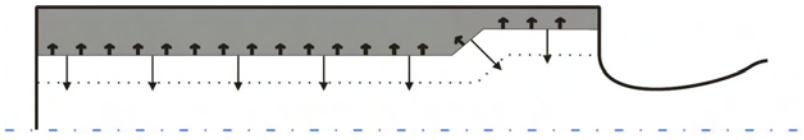

Figure 1.12: *Combustion front and injection velocity.*

To describe the combustion process, assumed to occur mainly at the propellant surface as detailed in § 1.2.2.3, the propellant is often assumed to burn uniformly, at least in average, so that the burning fronts are parallel (Price and Sigman 2000) as shown in Figure 1.12. From the burnt thickness δ_b, we define the regression rate:

$$V_b = \frac{\mathrm{d}\delta_b}{\mathrm{d}t}. \tag{1.5}$$

The regression rate comes from propellant combustion modeling, which is detailed in § 1.2.2.3.
The evolution of the chamber geometry due to the propellant regression has a strong impact on the motor behavior. Of course, the average thrust evolves, as expected when the grain shape was designed, as discussed in § 1.1.1.6. But these changes in geometry also bear side-effects, e.g. the appearance and disappearance of phenomena such as ODP. The appearance of four ODP bursts in the P230 chamber pressure p_c, given in Figure 1.10, is a well known example of the importance of geometry on the SRM behavior.
Numerical approaches should therefore take into account the evolution of the chamber geometry due to the propellant regression. In practice, the quasi-steady assumption is made and a fixed geometry is meshed. This approach does not allow to capture transient phenomena such as oscillations nor bifurcations and hysteresis.

1.2.1.3 PTF emergence and flapping

As said previously, the PTF of segmented motors such as the P230, emerges during SRM operation as the propellant regresses. This obstacle generates a hydrodynamic instability which was first described by Brown et al. (1981) and is referred to as VSO when coupled to the acoustics of the chamber (Vuillot 1995), see § 1.3.2.4 for more details. Its role is moreover complex to assess as it emerges, is deformed and is ablated during the operating time.
This obstacle is nonetheless a source of hydrodynamic instability, but it may also oscillate, the eventuality of a flapping PTF being suggested in the 90s: it is suspected but not proven that flapping couples to flow instabilities, especially VSO. Moreover, the PTF has a complex behavior as it is made of an advanced polymer material, which has to be characterized to include non-linear effects (Cerqueira 2012).
Studies were conducted to develop new PTF geometries numerically (Ballereau et al. 2005) and experimentally (Telara et al. 2005). Stability analysis and numerical simulation (Cerqueira 2012) as well as numerical simulation in turbulent contexts (Richard and Nicoud 2011; Richard 2012) were performed in the context of a flapping PTF and showed the major role of the PTF on the unstable behavior of SRMs.
The main issue is still that very few data is available about the PTF geometry during firing as it is riddled and possibly torn apart by the harsh flow. Regarding the major impact of the PTF on instabilities and its modeling issues, it is envisioned to suppress it in future Ariane 6 designs, and to resort to single-segment architectures, as said in § 1.1.3.3.

1.2.1.4 Mobile nozzle

In many SRMs, the geometry of the nozzle may be changed while operating. This may be done for several reasons:

- to steer the vehicle by changing the motor jet angle,
- to spare space when the motor is not lit (upper stages, submarine storage),
- to adapt the nozzle regime to p_{out} as it varies.

In all these cases, accounting for mobile part kinematics is complex: first the configurations will feature a complex behavior with possibly hysteresis phenomena e.g. flow separation and second, the consideration of fluid-structure interactions may be necessary.

1.2.2 Propellant formulation and combustion

1.2.2.1 Propellant formulation

The propellant is chemically formulated to (i) store the maximum possible energy, (ii) minimize parasitic reactions during storage, (iii) release energy by burning at a given rate, and (iv) guarantee adequate mechanical properties from grain casting to operation including the combustion phase. The components are classically described as fuel, oxidizer, binder and additives.
In the following, we focus on a formulation based on Ammonium Perchlorate (AP) with a hydroxyl-terminated polybutadiene (HTPB) binder. This propellant, referred to as Butalite in the French nomenclature, is often improved by adding aluminum particles, and is then named Butalane in the French nomenclature. The Aluminum particles have a size distribution which is usually a narrow peak around a few micrometers and is, in this case, referred to as μAl.
Butalane formulations are classical for large SRMs thanks to their reliability and ease of storage (Doriath and D'Andrea 1996), either for defense (M45, M51) or for civil (P230, P80, SRB) applications: the P230, for instance, uses a propellant named 68/18/14 AP/μAl/HTPB, where the figures stand for the proportions on the different ingredients. The propellant behavior depends on the packing of its ingredients, which is an active research topic (Knott et al. 2001; Matous et al. 2007) and is illustrated in Figure 1.13.
The use of aluminum is essentially motivated by its high energetic content, yielding high temperatures and high specific impulse, as presented in the following internal ballistic study. The propellant burnt gases are indeed oxidizing after combustion of the AP and binder but slightly reductant after aluminum combustion.

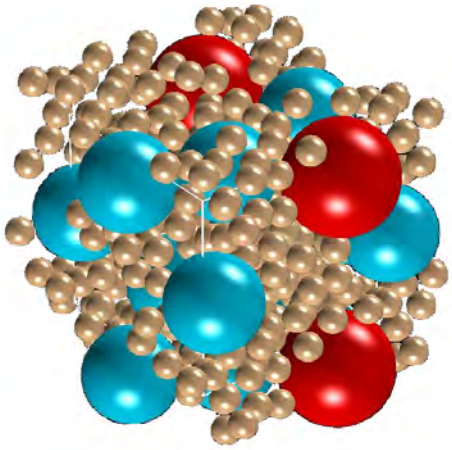

Figure 1.13: *3D illustration of the packing of a Butalane – Aluminum (24 μm, $Y = 18\,\%$ in red) and large AP particles (200 μm, $Y = 40\,\%$ in blue) and small AP particles (6 μm, $Y = 30\,\%$ in copper) – Excerpted from (Knott et al. 2001).*

For instance in the P230, the combustion of a 68/18/14 AP/μAl/HTPB formulation brings the chamber temperature to $T_c = 3400\,\mathrm{K}$ under $P_c = 50\,\mathrm{bar}$ while a similar propellant without aluminum leads to a temperature that is 1000 K below.
But aluminum raises many issues: among these, aluminum particles mostly burn in the chamber and their combustion residuals include aluminum oxide -or alumina- Al_2O_3 under the form of liquid droplets. The presence of this condensed disperse phase, both reactive (metal) and inert (oxide), has major consequences on the physics of the SRM. It has been, for a long time, given credit for damping the oscillations and stabilizing the motor (Summerfield and Krier 1969; Gossant 1993). But the role of the condensed phase seems to be more ambiguous when complex interactions between a disperse phase and hydrodynamic instabilities are observed in the SRM. Depending on the interaction mechanism, the damping effect can be less pronounced than expected by the linear theory (Dupays 1996; Dupays et al. 2000) or even a spectacular and unexpected driving effect can be observed (Ballereau et al. 2003; Simoes et al. 2005; Dupays et al. 2008).
Giving up aluminum without losing performance would require using oxidizers more energetic than AP or energetic binders such as azides, which is still under study. The use of other metal fuels has been widely discussed, such as beryllium which is highly toxic (Tavernier et al. 1970), boron (King et al. 1984; Brown et al. 1995; Dreizin et al. 1999; Yu 2009) which oxides are not inert, or magnesium, ending up to the conclusion that aluminum is the most efficient, most stable, cheapest, safest, best known metal fuel (Yetter et al. 2009). So aluminized propellants are to be used for many years but they still raise research issues such as modeling the disperse phase and the evolution of the resulting two-phase flow. Two-phase aspects of aluminized propellants must be modeled and simulated to improve the next generations of SRMs.

1.2.2.2 Nano-propellants

In the case of metal fuels, nanometric particles can also be incorporated. We refer to nano-propellants for the propellants formulated with nanoparticles of metal fuel. Nanoparticles are defined as particles with an average size below a micrometer, see Chapter 8 for more details. These nanoparticles have interesting new properties compared to classical, rather micrometric, particles but they raise industrial synthesis issues and their modeling is difficult.
Some studies are led on nanometric Boron (Yang et al. 2011) but the most interesting case is the one of aluminum, which nanoparticles are referred to as (nAl). Nanometric aluminum particles have been considered for their energetic properties (Gen et al. 1979; Barbee 1985; Ivanov and Tepper 1997): their use is promising for performance increase, but they are not well known yet and they raise coating and combustion issues discussed in § 1.2.2.4. Nano-propellants can incorporate nAl as an additive or as a substitute of μAl (Meda et al. 2005; Meda et al. 2007; Yetter et al. 2009). Another issue is that of the preparation of the propellant: the specific surface of nAl is so high that the mixing of the propellant is made difficult by the increased viscosity. This effect is such that nAl/μAl mixtures are sometimes preferred because of the difficulty to prepare a propellant with an equivalent mass fraction of pure nAl.
Different types of nAl exist (Bocanegra 2007), namely ALEX and L-ALEX (Aluminum Explosive, uncoated or coated), SteaC, nano Sedoy, *etc.* though the denominations can vary from a research team to another. Moreover structural differences can exist as regards the surface or the size distribution and clustering, as shown in Figure 1.14. For instance, DeLuca et al. (2010) states that the portion of particles below 10 nm has

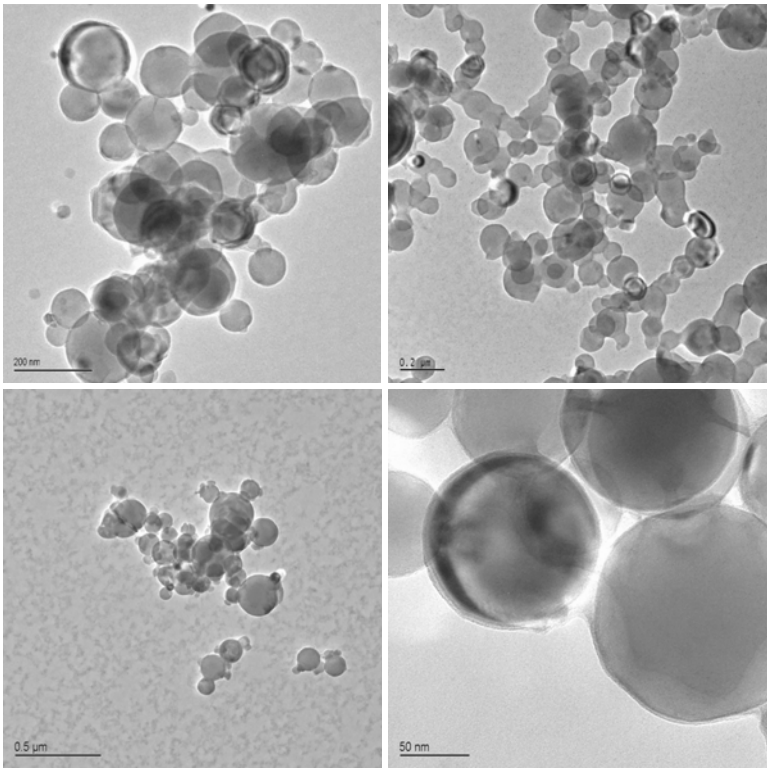

Figure 1.14: *MET imaging of different types of nAl particles – Bottom Right: L-ALEX; Others: research preparations (Bocanegra 2007).*

Path	Average Size	Surface state	Quantities	Reference
EEW	150 nm	uncoated	100 g/h/machine	Gromov et al. (2006)
SP	40 nm	coated	0.5 g/bath	Aït Atmane (2012)
PC	40 to 200 nm	coated or uncoated		DeLuca et al. (2010)
PM	2500 nm	uncoated		DeLuca et al. (2010)

Table 1.1: *Some aluminum nanoparticle synthesis paths and their characteristics.*

an significantly increased reactivity due to its clustered structure. The surface state in general is a major aspect of nAl since it describes nonetheless the energy content but also the reactivity: coated particles will have a lower energy content (depending on the stability of the coating layer) but they are more stable, while uncoated nAl particles may self-ignite or explode at air or water contact (Gromov et al. 2006). The surface state also conditions the trend to sinter or agglomerate during storage (DeLuca et al. 2010). The solution of energetic coatings has been explored e.g. with glycidile polyazoture (PAG).
To control the size and coating properties, the nAl synthesis path is a major issue. Both ascendent and descendent techniques have been considered, based respectively on assembling atomic aluminum or dividing bulk metal. In practice, the synthesis of nAl can be performed by several paths:

- Electric Explosion of a Wire (EEW) (Ivanov and Tepper 1997; Gromov et al. 2006);
- Physical Vapor Deposition (PVD) or condensation (Barbee 1985);
- Chemical Vapor Deposition (CVD) e.g. by reductive elimination of H_2 from aluminum hydrides (Yang et al. 2011);
- Plasma Condensation (PC);
- Solution Precipitation (SP) (Aït Atmane 2012);
- Pneumatic Milling (PM) (DeLuca et al. 2010);
- DC arc discharge; or
- Laser Ablation (LA).

The resulting size characteristics, surface state *etc.* are given in Table 1.1 for mostly used synthesis paths: these paths generate a fairly small deviation of particle sizes (below 1 %). The quantities that can be produced are however far from meeting industrial needs.

1.2.2.3 Propellant surface combustion

Propellant combustion modeling consists in establishing a so-called pyrolysis law, giving the total mass flow rate depending on the chamber conditions, canonically the pressure and the initial temperature $\dot{m}(p_c, T_c^0)$. In this paragraph is discussed the modeling of combustion with the assumption that the propellant combustion mainly occurs close to its surface, though the overall combustion process is more complex when involving metal particles. The flame front has indeed been proven to stabilize at a few millimeters from the wall (Godon 1984; Godon et al. 1992; Most et al. 1996; Beckstead et al. 2007). To this simplification assumption of surface combustion, we add a homogeneity assumption i.e. that the combustion occurs as it would for a homogeneous (or tightly mixed composite) propellant, i.e. with the combustion surface regressing parallel to itself, see § 1.2.1.2.
In nominal conditions and for many propellants, the regression rate V_b defined in Eq. (1.5) can be modeled as a function of p_c according to Paul Vieille -or Saint-Robert- law:

$$V_b = a p_c^n \tag{1.6}$$

where a depends on the initial propellant temperature only and n is referred to as the pressure exponent. We then assume that the presence of metal particles has little influence on the combustion law that is derived, and that the particle effect can be superimposed to the surface combustion model. The surface combustion model can still be slightly modified e.g. by fitting coefficients, in the presence of heterogeneous metal fuel as the latter burns quite close to the surface (Beckstead et al. 2007).
The burnt gas mass flow rate $\dot{m}$ is then:

$$\dot{m} = \rho_{prop} S_b V_b \tag{1.7}$$

where ρ_{prop} is the propellant density and S_b is the instantaneous burning surface. So that the mass flow rate depends on both chemical properties and geometric properties through V_b and S_b respectively.
Several models have been suggested in the literature such as Denison-Baum-Williams (DBW), Beckstead-Derr-Price (BDP), Ward Son Brewster (WSB), or the Thickened Flame (TF) model developed at ONERA (see the reviews of Beckstead et al. (2007) and Rahman (2012)). These models have been validated at nominal pressure (bomb studies, sub-scale "hot gas" motors) and by numerical simulations. The role of turbulence on surface combustion was studied in Apte and Yang (2000). The particular case of low-pressure combustion has also been studied to model accidental situations e.g. after the burst of a motor (Chassagne 2007).
Detailed chemistry should be assessed to retrieve the law and to predict the burnt gases composition and properties: this is possible for simple propellant formulations. Among these, the Ammonium Perchlorate (AP) combustion was described with several chemical mechanism in Meynet (2005), involving up to 37 species in 215 reactions. When including hydrocarbon chemistry (by considering only ethylene precursors C_2H_4), the mechanisms reach 105 species and 659 reactions, though simplified mechanisms exist (Meynet 2005).
For more details on unsteady combustion, we refer to recent works from Rahman (2012) where complex chemistry, complex solid-gas interfaces are accounted for. For instance an advanced acoustic model of the propellant wall behavior, based on the assumed existence of a foam resulting from the organic binder decomposition, is introduced and shown to play a significant role.

1.2.2.4 Nano-aluminized propellant combustion

Among the issues raised by SRM modeling, it has been discussed in § 1.1.4.1 the possibility of reducing the particle size below micrometric scales.
Recent reviews on nanoparticle propellant combustion have recently been done (Yetter et al. 2009; De Luca et al. 2011). The presence of reactive nanoparticles has a significant effect on propellant burning rates even when mixed with more common micro-particles (Mench et al. 1998; Lessard et al. 2001; Dokhan et al. 2002). Nanoparticles increase propellant combustion rates in the case of pure nAl (Mench et al. 1998) and in the case of mixtures (Dokhan et al. 2002). The so-called ALEX type nAl is also used in the formulation of explosives (Ritter and Braun 2001).
The precise mechanism of nanoparticle combustion in the propellant differs significantly, due to the following peculiarities:

- the particle surface/volume ratio is much higher,
- the melting point is lower, and
- the thermo-mechanical properties of a nano-propellant are very different.

The particle surface/volume ratio is very high compared to micronic formulations, which presumably increases reactivity. The melting temperature of the particle is lowered as exterior atoms have a significant effect compared to bulk ones: this is known as the Kelvin effect and is described by a classical theory, given in

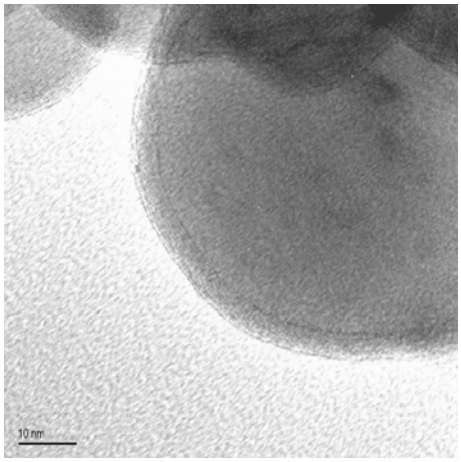

Figure 1.15: *MET imaging of the oxide layer on a particle of nAl SEDOY (Bocanegra 2007).*

Diameter	$Y^0_{\mathrm{Al}}(\%)$	$Y^0_{\mathrm{Al_2O_3}}$ (%)	T_c (K)	$C^\star$ (m/s)	I_{sp} (s)
30 μm	17,984	0,016	3395	1583	255,6
10 μm	17,953	0,047	3394	1582	255,6
5 μm	17,905	0,095	3392	1582	255,5
2 μm	17,764	0,236	3387	1580	255,2
1 μm	17,531	0,469	3378	1577	254,7
500 nm	17,076	0,924	3359	1571	253,7
300 nm	16,488	1,512	3334	1563	252,3
200 nm	15,783	2,217	3303	1552	250,7
125 nm	14,593	3,407	3247	1535	247,9
100 nm	13,852	4,148	3210	1523	246,0
75 nm	12,701	5,299	3148	1504	243,1
50 nm	10,675	7,325	3030	1469	237,6
40 nm	9,363	8,637	2948	1445	233,8

Table 1.2: *Energetic content of a propellant with monodisperse Al particles depending on their average size – Mass fractions Y computed assuming a 3 nm oxide layer (computed with COPPELIA).*

§ 8.3.4. In the case of aluminum, more precise estimations were obtained by molecular dynamics simulations indicating that the melting temperature can be as low as 400 K (Alavi and Thompson 2006), compared to the 933 K of the bulk aluminum melting temperature. This may increase the reaction rate.
The presence of nanoparticles modifies the thermomechanical properties of the propellant, which are crucial as regards storage, security, and propellant combustion. In particular, the modification of thermal conductivity by nanoparticles has a major impact on the propellant response, and therefore on combustion instabilities (see § 1.3.2.3). This feature has not been assessed.
Aluminum, even before being mixed into propellant, has always an oxide layer. The layer is visible in Figure 1.15 and its thickness is presumably driven by the diffusion of oxygen in aluminum oxide. This layer is proven to have a constant thickness, estimated to 3 nm by Yetter et al. (2009). This may reduce the reactivity but has a much more direct impact on the motor, as discussed below.
The presence of an oxide layer on particles incorporated to a propellant raises an issue on motor performance which is referred to as two-phase chemical loss. A mass of aluminum oxide can be estimated, that corresponds to the oxide layer naturally present before combustion. Typical estimations assume the following material densities $\rho_{\mathrm{Al}} = 2700\,\mathrm{kg/m^3}$ and $\rho_{\mathrm{Al_2O_3}} = 3965\,\mathrm{kg/m^3}$ at ambient temperature. This inert mass has an effect on the propellant energetic content, reducing $C^\star$. Moreover smaller particles have a higher surface/volume ratio so the effect is size-dependent, negligible for micronic particles but significant when nanometric ones are used. This effect can be quantified using a chemical equilibrium code developed at ONERA (COPPELIA) according to a methodology recalled in § 2.1.1. Some results are shown in Table 1.2 for a 68/18/14 AP/Al/HTPB propellant (Ariane 5 type): as expected, T_c, $C^\star$ and I_{sp} decrease when the particle size decreases. However these results only account for the two-phase chemical loss while the nozzle loss cannot be assessed simply, requiring complex modeling or even a full CFD approach.

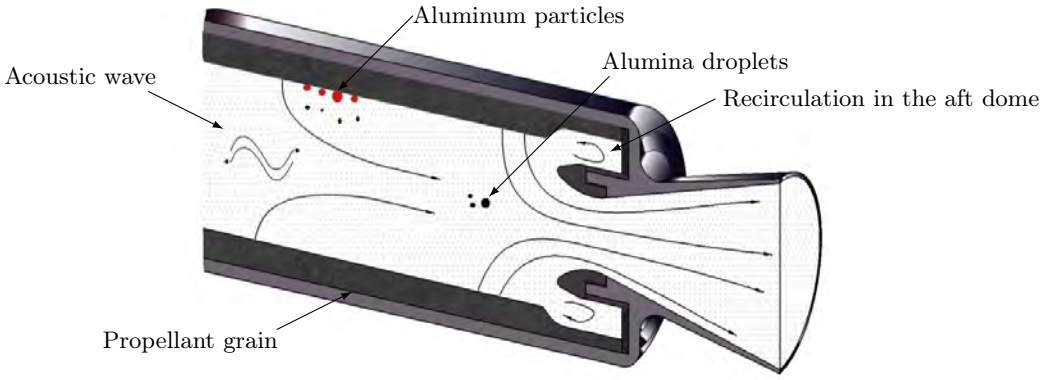

Figure 1.16: *CAO of a booster rear-end with integrated nozzle (courtesy: J. Dupays).*

1.2.3 Description of the flow in the chamber

The chamber flow of a SRM is very complex and here described. It includes a disperse phase, which has nonetheless a complex behavior but a strong influence on the flow and the SRM operating conditions. So a fine understanding of the motor, including ODP, is proven to require the modeling of the flow as two-phase.

1.2.3.1 Nature of the flow

The chamber flow is modeled as injected from the wall constituted by the propellant surface. The wall slowly regresses (V_b is of order of a few mm/s, see § 1.2.1.2) so the gas injection velocity is of a few m/s due to the mass density ratio between solid propellant and hot gases produced. Of course, the flow can include condensed matter, which is discussed hereafter. The flow accelerates due to the small chamber section compared to the wall surface: this surface ratio referred to as the strangling coefficient K is a crucial parameter of the motor and is defined later in Eq. (1.18).
The velocities are moderate enough for the flow to remain incompressible in the chamber and laminar in a significant part of the chamber (Beddini 1981). Turbulence still plays an important role:

- during transient phases (especially ignition),
- on the interaction between flow hydrodynamics and acoustics,
- on two-phase modeling,

which is detailed in § 1.3.2.2. In the latest case, the role of particles on turbulence, has not been assessed in SRMs. It is a tough subject in general and roughly theorized (Elghobashi 1991): particles may enhance or damp turbulence depending on their size, larger or smaller than the Kolmogorov scale. Direct simulations start to give an insight on this complex physics, see for instance Burton and Eaton (2005).
The development of two-phase models dealing with turbulence in a two-way coupling context is discussed in § 3.6.2. As expected in the nozzle, the Mach number Ma increases to one at the throat and beyond Ma = 2.5 in the exhaust plane.

1.2.3.2 Particle dragging within the chamber

When metal fuel is used, metal particles (in combustion) and oxide particles (inert) are present in the chamber flow as a disperse phase of condensed matter, referred to as inclusions. Inclusions are dragged from the propellant into the chamber by burnt gases as the grain regresses, which we refer to as "injection". They are carried away by the flow -metal particles burn in some part of the chamber, while oxide particles, often liquid (e.g. alumina), travel in the chamber and may coalesce or break-up- until their ejection by the nozzle, as illustrated in Figure 1.16. So the disperse phase is both reactive and inert and is the place of many physical phenomena. To model the chamber flow, the knowledge of inclusion characteristics when leaving the propellant is crucial:

- mass flow rate (or injection rate),
- chemical state (oxide mass fraction),
- temperature (liquid or solid, enthalpy),
- size distribution, and
- velocity.

The aluminum injection rate is conditioned by the propellant regression rate. Due to the proportion of aluminum in the propellant, the condensed phase has always a strong mass fraction. High mass loadings have major consequences, as discussed below in the case of the chamber flow. The strong impact of a high mass loading is general to all disperse phase flows: such flows are referred to as moderately dense and their characteristics and modeling is extensively discussed in § 3.1.4.

The particle chemical state and temperature are related to its combustion phenomenon. Injection velocity remains a modeling issue as it influences the residence times in a surprisingly strong way: as particles accelerate sharply all along the motor, to a small initial velocity corresponds a residence time at the wall vicinity that is long compared to the one in the chamber and in the nozzle *a fortiori*, this being illustrated in a simple case in § 13.2.1.4. The particle injection velocity also drives the thickness of the distributed combustion zone, therefore playing a role on particle combustion in general and ITHAC (presented in § 1.3.2.5) in particular.
Finally the size distribution of the inclusions appears to play a major role on the chamber and the nozzle physics and is discussed hereafter. In SRMs in general, the effect of polydispersity, i.e. widespread particle sizes, is very significant. The size distribution strongly depends on the packing topology, ambient conditions, and propellant combustion (particularly heat and mass transfer), wether they foster agglomeration at the surface or not Duterque and Lambert (1998); Duterque et al. (1999). So that aluminum leaves the surface with various sizes, as illustrated in Figure 1.17, depending nonetheless on the dispersion of the initial size and combustion process intensity but moreover on the propensity of aluminum to agglomerate at the very surface of the grain (Trubert 2000; Srinivas and Chakravarthy 2007). Experimental results show the dependency of the agglomeration process (Babuk et al. 2001):

- on the physical and mechanical properties of the propellant binder,
- on the particle sizes of the metal fuel,
- on the type of coating of the original metal particles, and
- on the type and particle size of oxidizer in the propellant.

The modeling of particle characteristics, when emerging from the propellant, is crucial for further modeling. The so-called "pocket model", validated for μ-Al, bases the agglomerate sizes on the pocket volumes provided by the largest oxidizer particles in which aluminum particles aggregate and melt (Cohen 1983): the pockets strongly depend on the propellant packing, which is therefore thoroughly studied and modeled, typically by stochastic approaches (Gallier 2009). Very little data is available on size distribution considering that direct and indirect measurement are difficult (Kuentzmann 1973b). We keep in mind that three possible model size distributions have been suggested for aluminized propellant inclusions on semi-empirical bases: monodisperse, bimodal and lognormal.

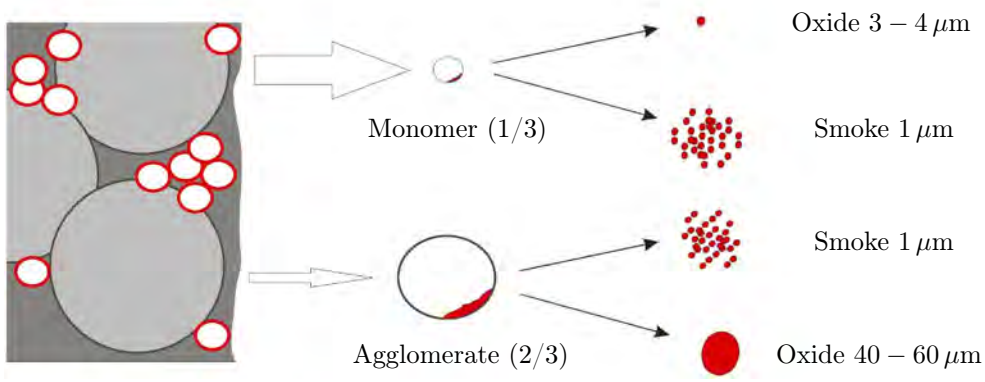

Figure 1.17: *Aluminum and aluminum oxide dragging from propellant surface combustion (case of Ariane 5) – White: Metal Al, Red: Oxide (from Duterque 1998).*

The monodisperse description is modeled by one infinitely thin distribution or Dirac δ-function:

$$M(S) = \alpha_1 \delta(S - S_1) \tag{1.8}$$

where S is the droplet surface variable, S_1 the mode surface and α_1 its density. It can be seen as a simplification hypothesis, but also as a simple model for polydispersity, provided that the considered diameter is a well-chosen moment of the effective distribution, see § 3.1.2 for details and limits of this approach. A particular monodisperse approach, consisting in accounting for the bigger particles with a unique size and treating the smaller ones with the so-called Equivalent Gas approach (see § 3.2.4.2) can be efficient for simple cases, see § 4.7.5.
The bimodal behavior, early described by Price (1984a), can be explained by the simultaneous dragging and coexistence of agglomerates and monomer particles as shown in Figure 1.17, excerpted from Duterque and Lambert (1998). The bimodal distribution is modeled by two infinitely thin distributions or Dirac δ-functions:

$$BM(S) = \alpha_1 \delta(S - S_1) + \alpha_2 \delta(S - S_2) \tag{1.9}$$

where S_1 and S_2 are the two mode surfaces and α_1 and α_2 their densities. This distribution is used in applicative cases in § 13.2.4.

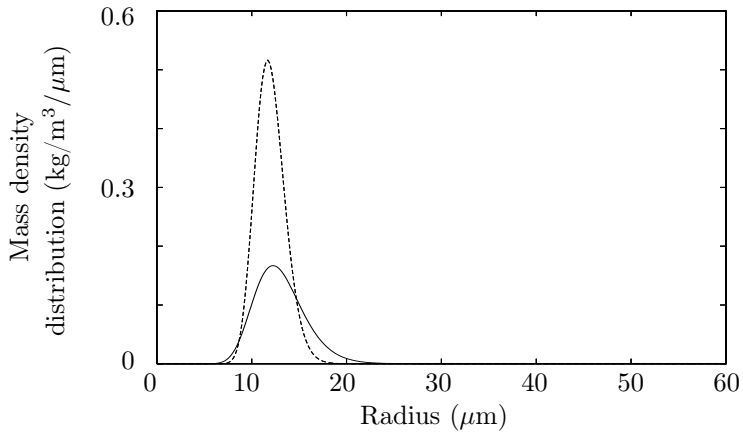

Figure 1.18: *Lognormal droplet mass distributions with $S_{LN} = 1600\,\mu m^2$ used as boundary condition in the nozzle test case – **Solid**: $m_0 = 1.06\,kg.m^{-3}$ and $\sigma_{LN} = 1.5$; **Dashed**: $m_0 = 2\,kg.m^{-3}$ and $\sigma_{LN} = 1.3$.*

The lognormal distribution, used for instance by Salita (1994), can rather be explained by agglomeration statistics, yielding a self-similar profile similar to those of some coalescence regimes, as detailed in § 8.3.3.5. When parameterized in droplet surface variable, the lognormal distribution reads:

$$LN(S) = \frac{1}{S\sqrt{2\pi}\log(\sigma_{\mathrm{LN}})} \exp\left[-\frac{1}{2}\left(\frac{\log(S) - \log(S_{\mathrm{LN}})}{\log(\sigma_{\mathrm{LN}})}\right)^2\right] \tag{1.10}$$

where S_{LN} is called the geometric average surface and σ_{LN} is called the geometric standard deviation. These parameters must not be mistaken for the usual moments of a distribution, they are of empirical use. In the following, we will write lognormal distributions on the surface variable, without loss of generality. As an illustration, two distributions plotted on the radius are given in Figure 1.18, which are used in Chapter 13. Other distribution laws, e.g. Rosin-Rammler (Beck and Watkins 2002; Jones and Watkins 2012), *etc.*, may be considered.

1.2.3.3 Particle transport and size evolution

The modelings suggested in § 1.2.3.2 are often used for inert and reactive simulations, as injection boundary conditions. And if the disperse phase size distribution at injection is complex, it evolves in the chamber as a consequence of many different phenomena, and it strongly conditions the flow, according to the so-called size/velocity coupling, which is detailed in § 3.1.3.5.

The size distribution of the inclusions strongly influences their transport and heating in the chamber, as the momentum and heat fluxes are proportional to the particle surface. As the particles have a heavy mass ratio (see § 3.1.4 for the detailed description of high mass loading effects) the flow must be considered as requiring a full coupling treatment. Remarkably, the disperse phase has a strong impact on the overall hydrodynamic structure and acoustic ambience in the chamber. Morover, so-called acoustic reemission can occur from the nozzle, this term designing in fact several mechanisms, from noise emitted by vortices and entropic waves swallowed by the nozzle (Marble and Candel 1977), to vortices hitting the nozzle wall or penetrating the recirculation zone.

The chamber turbulence also conditions the particle transport, resulting in particle turbulent dispersion (Simoes 2006). As inclusions are at very high temperature, their radiation is significant and must be accounted for (Dupays 1996; Joumani 2001; Duval 2002). The thermal coupling of particles and radiation is crucial in the ignition phase and extensively modeled, see for instance Tang and Brewster (1992). The dynamics coupling of particles and radiation is discussed more particularly in Duval et al. (2004). As an illustration, the dynamics coupling is often neglected but it is shown in general cases to generate behaviors, unseen in single-phase flows (Zamansky et al. 2012). Besides, the overall SRM propellant combustion is strongly affected by radiation (Tang and Brewster 2001).

Transport is also influenced by collisions. As the disperse phase travels in the chamber, collisions occur, with a strong dependence on the flow structure: they are favored in vortical and strain zones. And their rate increases with particle density. Typical collision rates are given for the P230 in Figure 1.19, which confirm this behavior. Collisions occur when particles come close to each other with a relative velocity: as there is a carrier gas flow all around at least one of the particles, they may dodge each other as illustrated in Figure 3.17, resulting in a decrease of the collision rate, often modeled through a collision efficiency term. Particles dodging each other may still have an influence on their transport, this being referred to as quasi-collisions by O'Rourke (1981) but rarely accounted for. But when collisions occur, they result in coalescence,

Figure 1.19: *Collision rate in the P230 SRM– 2D Lagrangian computation from Estivalezes (2010) with the CEDRE code (ONERA).*

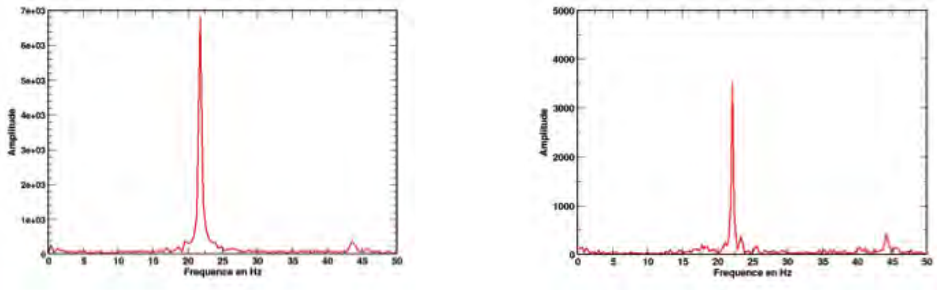

Figure 1.20: *Pressure spectrum in a two-phase P230 simulation – Left: without coalescence; Right: with coalescence – 2D Lagrangian computation (CEDRE code, ONERA).*

stretching, or reflexion which are illustrated in Figure 3.20. The ratio between these phenomena can be modeled, e.g. through a so-called coalescence efficiency coefficient. Collision and coalescence efficiencies are difficult to obtain in SRM conditions. A modeling is suggested for collision in § 3.3.3. So that quasi-collisions, rebounds, stretching and reflexion are often neglected compared to coalescence, which is on the contrary cited as a major phenomenon in SRMs (Sambamurthi et al. 1984).
The phenomena that modify size are classically:

- evaporation, nucleation and combustion,
- coalescence,
- break-up.

Evaporation plays a role in the combustion of aluminum (Dreizin 2003) but evaporation of the oxides is negligible i.e. Al_2O_3 saturation temperature is very high. In pure oxygen and under 1 bar, Glassman and Yetter (2008) have estimated $T_{vol}^{Al_2O_3} = 4000\,K$; some authors assess that Al_2O_3 is decomposed in SRM ambience at high temperature (Glassman 1960; Bucher et al. 1999). Other studies provide temperatures ranging from 3600 K (Orlandi 2002) to 4400 K (Widener and Beckstead 1998).
But combustion of the metal has consequences on size, as discussed in § 1.2.3.4 along with models for this so-called distributed combustion. The phenomenon of nucleation of metal oxide particles (Hermsen and Dunlap 1969) also occurs, bringing in very small particles which are visible as a thick smoke. Nucleation is poorly documented but a modeling is suggested for SRMs by Liang and Beckstead (1998). Finally, break-up does not occur significantly in the chamber.
As for coalescence, it occurs significantly and modifies the size distributions in a sensible way: as an illustration, this has consequences on ODP levels as shown in Figure 1.20. In accordance with the size/velocity coupling, the evolution of size distribution due to coalescence strongly modifies the chamber flow, as illustrated in Figure 1.21. Among all these size-modifying phenomena, coalescence is considered to have, in the case of alumina residuals, a major impact on the motor dynamics (Traineau et al. 1997): it may influence ODP, as they are sensitive to polydispersity, and it surely modifies two-phase lag losses in the nozzle. The experimental study of coalescence in hot gas motors is made difficult by the fact that particles are disrupted in the nozzle while direct measurement in the chamber is up to now impossible. A test campaign consisting in freezing the liquid disperse phase with a helium coolant in the chamber has yielded the only results, though mitigated (Traineau et al. 1992).
In the case of nanoresiduals -either coming from nano-propellant residuals, or produced by combustion and nucleation as smokes- the particular physics of transport is to be reassessed as Brownian physics comes into play. But moreover, coalescence is presumably strongly modified as it depends on number densities -which are much higher for small particles at constant mass fraction- and particle relative velocities -which are macroscopically smaller but microscopically significant due to Brownian agitation. So the size of a disperse phase resulting from nano-propellant combustion is not easily predictable. If the impact on two-phase nozzle losses has been anticipated to be favorable and the impact on ODP is presumably strong, a strong coalescence challenges these *a priori* conclusions.
As a conclusion, several phenomena contribute to polydispersity in the chamber (initial particle distribution, surface combustion, distributed combustion, coalescence, break-up) and they are a key point to capture the physics of SRMs.

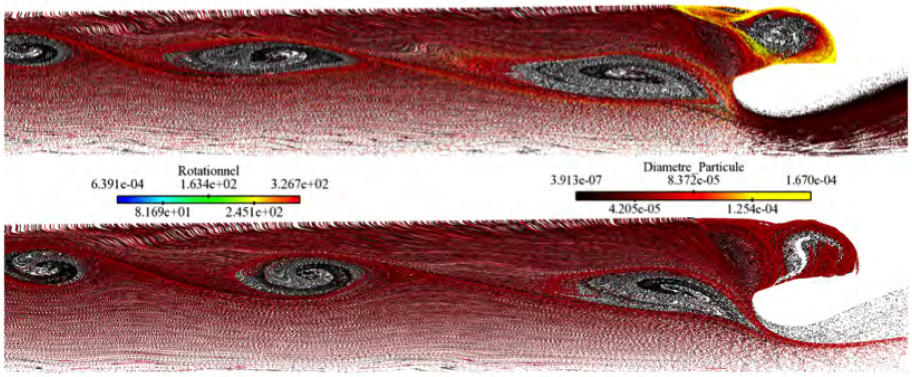

Figure 1.21: *Vorticity and particle size in the P230 SRM with coalescence (top) and without (bottom) – 2D Lagrangian computation (CEDRE code, ONERA).*

Figure 1.22: *Ignited aluminum droplets ejected from the propellant surface. (source: ONERA).*

1.2.3.4 Metal particle distributed combustion

Metal particle combustion occurs all along its way in the chamber so it is referred to as distributed combustion (Braithwaite et al. 1984; Beckstead 1987; Brooks and Beckstead 1995; Dupays et al. 2000; Fabignon et al. 2003; Sabnis 2003). The heat release can strongly interact with the flow, with feedback possibly leading to Thermo-Acoustic Instabilities (ITHAC), see § 1.3.2.5. Distributed combustion is a modeling issue, e.g. regarding chemical mechanism for it occurs in partially burnt gases (Marion et al. 1996; Legrand et al. 2000; Orlandi 2002).

The overall mechanism of aluminum particle combustion in propellant burnt gases is very complex and, unfortunately very difficult to study. But it has been early studied (Hermsen 1981a; Cohen 1983; Price 1984a) and is now described by complete physical mechanisms (Widener and Beckstead 1998; Dupays et al. 2000; Burton et al. 2000; Fabignon et al. 2003; Beckstead et al. 2007; Puri 2008; Washburn et al. 2008). The ejection of ignited droplets from the propellant surface is a complex phenomenon, illustrated in Figure 1.22, which has been described as follows. Once the particles and aggregates are dragged from the wall -or kind of foam- they encounter various phenomena at a given distance from it:

(i) they melt within the propellant and possibly agglomerate Trubert (2000);
(ii) they leave the propellant and keep on melting and oxidizing so that an aluminum oxide cap forms at their surface Beckstead (2002);
(iii) they then cross the propellant flame front, and heat up suddenly, causing them to ignite;
(iv) they keep on burning on a distance which depends mainly on their initial size (but also on the oxidizer and gas composition);
(v) they end up as liquid alumina droplets at physico-chemical equilibrium.

Aluminized propellant combustion is by itself an active research topic (Brooks and Beckstead 1995; Beckstead et al. 2007; Maggi et al. 2011) which aims at evaluating ignition, combustion characteristics *etc.* but also particle size distribution in the chamber (Jeenu et al. 2010). The heat release rate is influenced by the ambient temperature, pressure, chemical composition and the flow surrounding the droplet, as studied for a single droplet (Marion et al. 1996; Liang and Beckstead 1998; Orlandi 2002) and the aspects of aluminum particle combustion in a turbulent gaseous field are also studied Corcoran et al. (2013). Complex reaction

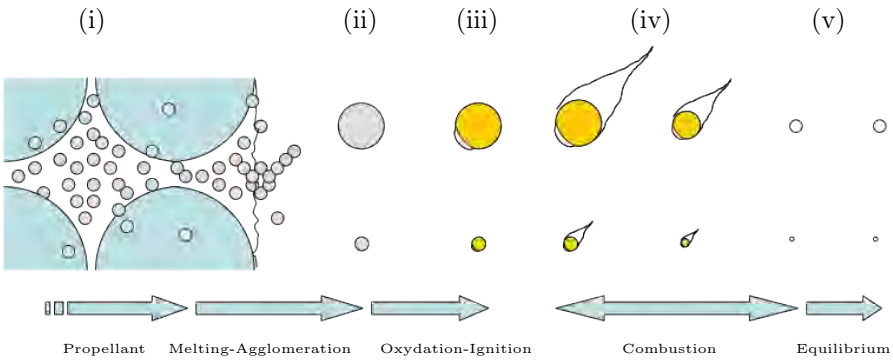

Figure 1.23: *Mechanism of aluminum particle evolution from propellant to chamber (courtesy: J. Dupays).*

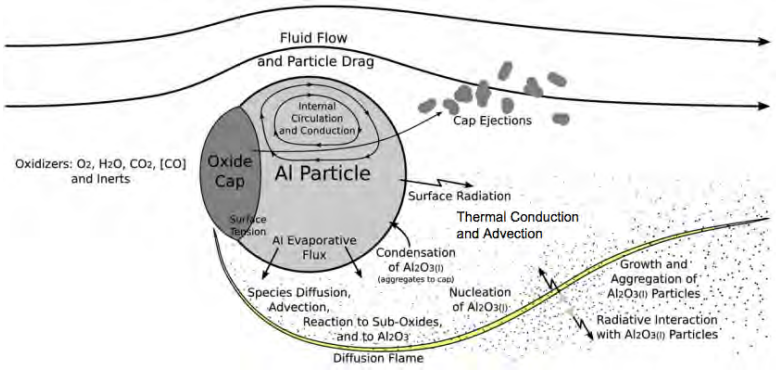

Figure 1.24: *Mechanism of aluminum particle combustion (Washburn et al. 2010).*

schemes for aluminum combustion have been derived for aluminum in surrogate oxidizers (Swihart and Catoire 2000; Bocanegra 2007), a typical one featuring 33 species and 89 reactions. The complete chemical process, involving aluminum particle combustion which can be both homogeneous and heterogeneous, in a propellant ambience, has however not been studied. So aluminum combustion is usually modeled as occurring in the gas phase, with a simple chemistry, e.g. a two-step mechanism, or a simplified mechanism e.g. the one used by Dupays et al. (2000) with 8 species and 9 reactants. Mass transfers are modeled based on the d2-law, see § B, have long been used but seem inexact. By analogy with the d2-law, an empirical dn-law with an exponent $n = 1.8$ is eventually more relevant (Dupays et al. 2000; Beckstead 2002; Fabignon et al. 2003; Huang et al. 2009).

Droplet combustion also depends on the droplet composition and structure. As an oxide cap forms, combustion is perturbed so the cap must be modeled, depending on the size and history of the droplet (Dupays et al. 2000; Beckstead 2002; Fabignon et al. 2003): this leads to the need for bi-species two-phase modelings and for their implementation in numerical codes (Sibra 2014). Droplet internal state also plays a role as the droplet surface temperature of big droplets depends on wether temperature is stratified in a conductive limit, or homogenized by convection through Hill vortices (Johns and Beckmann 1966). The thermo-mechanical behavior of the particle also plays a role in its combustion (Rosenband 2004). The combustion of metal particles is illustrated in Figure 1.24 and models are discussed in § B.2.4.

In the context of a P230-like propellant, Cesco (1997) assumes that the aluminum particles dragged into the chamber are bimodal, in the spirit of the physics described Figure 1.17, and the following orders of magnitude are given: monomers burn in 5 ms which is negligible compared to a P230 residence time of 200 ms. Since bigger agglomerates may build up, some droplets can burn in a significant part of the chamber -e.g. droplets with a diameter of 100 μm burn in 40 ms. Correct modeling requires the knowledge of aluminum particle combustion in partially burnt gases, referred to as distributed combustion and described hereafter. Agglomerates are estimated to represent one third of the aluminum mass. The inclusion sizes are presumed to depend on the initial aluminum particle sizes (Briand 2003): the small particle inclusions have a diameter of a few microns or less and are considered as smokes; the agglomerate inclusions are of a few tens of microns.

1.2.3.5 Nanoparticle combustion

The distributed combustion of nano-propellants has been described as complex (Huang et al. 2005; De Luca et al. 2005; Yetter et al. 2009). In the case of nanoparticle injection, this combustion changes significantly as shown in Huang et al. (2009), whose results are reproduced in Figure 1.25. It has also been studied in Puri (2008). For nAl, a dn-law with an exponent between 0.25 and 0.49 can be fitted, based on experimental

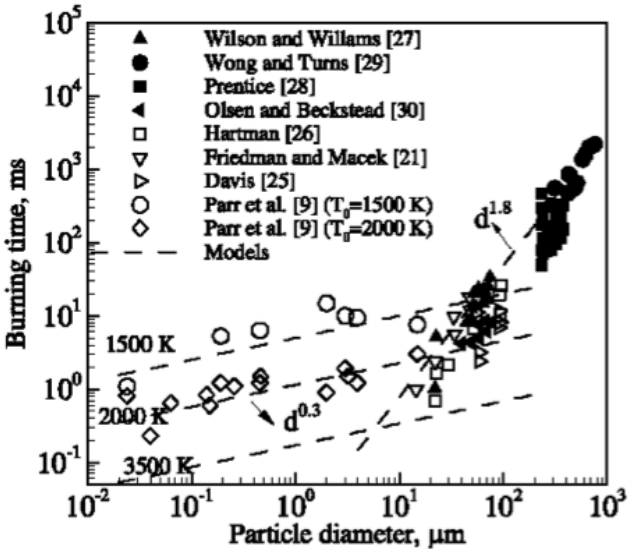

Figure 1.25: *Different combustion laws depending on the aluminum particle sizes (Huang et al. 2009).*

considerations but with bold assumptions on the particle size evolution, in particular the absence of agglomeration (Bocanegra 2007; Huang et al. 2009). A new chemistry has also to be assessed for comprehensive modelings of nAl combustion, still in a simplified chemical environment (Bocanegra 2007).
The question to know if group combustion occurs, as it does for hydrocarbon droplet combustion in air (Candel et al. 1999; Sirignano 2010), has not been tackled: it may have a sensible effect in the case of nanoparticles.
Distributed combustion however occurs on a very short distance as burning times are short. So the use of nanoparticles may be assumed to reduce ITHAC but further study of this physics and modeling is to be done.

1.2.4 Nozzle and exhaust jet

1.2.4.1 Structure erosion and slag formation

Because of their inertia, the droplets can hit the chamber walls, especially when entering the nozzle. The riddling contributes to damaging the structure walls, which are already weakened by the extreme temperatures and harsh chemical ambience. Eventually, alumina droplets settle and form a liquid film at the front of the nozzle. This alumina film yields a thermo-chemical insulation of the wall material that can further damage the internal structure.
In the case of a submerged nozzle or any similar cavity, aluminum oxide droplets can be collected from the approach flow and trapped. A slag of molten aluminum oxide then accumulates (Johnston et al. 1994; Whitesides et al. 1995; Fabignon 1997) as shown in Figure 1.16; the flow that stagnates in the aft dome region also contributes to slag formation (Cesco et al. 1996). Slag accumulation occurs for instance in the P230 presented in § 1.1.3.1 and has been studied numerically (Godfroy and Guéry 1997a; Godfroy and Guéry 1997b; Le Helley et al. 2000; Villedieu et al. 2000) and experimentally (Tòth 2008). Slag raises stability issues: ELV balancing is compromised if the two-motors fill up differently and trajectory control is perturbed if sloshing motion of molten alumina becomes significant. In addition, slag material can be ejected intermittently towards the nozzle eroding it (Burakov and Sandu 1997) and yielding pressure drops in the chamber or exciting ODP (Martin 1995; Whitesides et al. 1995). But slag also raises issues of efficiency: the slag mass does not contribute to thrust while it remains in the motor tare mass (Fabignon 1997), thus reducing I_{sp}.
In the case of nano-propellants, the size of the flow inclusions is still to be assessed. If the droplets are smaller than those of classical propellants, they will follow the main flow towards the nozzle and be better evacuated, limiting nozzle erosion and slag formation.

1.2.4.2 Secondary break-up

The flow is strongly accelerated in the nozzle, as shown in Figure 1.3. At the same time, temperature decreases strongly, eventually below the fusion temperature of the metal oxide. For aluminum oxide for instance, $T_f^{Al_2O_3} = 2300\,\mathrm{K}$ while a typical value of the throat temperature is $T^\star = 2000\,\mathrm{K}$. Thus the oxide particles can become solid before passing the throat, depending on the temperature lag.

So the disperse phase encounters a strong aerodynamical strain which leads to break-up. The phenomenology is however different for liquid (secondary atomization) and solid particles (fragmentation). The modeling of break-up is discussed in § 3.3.4: it is shown to be difficult and moreover in a two-way coupling context, as that of the nozzle. A modeling strategy for liquid secondary atomization is introduced in Appendix C in the perspective of treating a complex interaction between a spray and its turbulent carrier phase.

1.2.4.3 Exhaust jet issues

The exhaust jet, starting from the diverging part of the nozzle and stretching up to several kilometers behind the vehicle, plays a priori no role regarding specific impulse or ODP but it raises radiation and noise issues. The description of the plume should also be detailed, for environmental considerations (Kovalev 2002).
The SRM exhaust jet emits strong electromagnetic radiations. In particular, the infrared part of the spectrum is a defense issue as it is used to detect and identify vehicles and missiles and is referred to as its signature (Mahulikar et al. 2007). The radiation is partly due to afterburning of the exhaust gases as illustrated in Figure 1.27 with the presence of the radical species $OH^\star$. Solving for afterburning requires advanced chemistry and the modeling of a plasma -still a cold plasma, allowing to use the electroneutral simplification (Rax 2005). So the carrier phase modeling is tough. But the disperse phase plays a major role (Kovalev 2002). It modifies the shape of the jet, see for instance Figure 1.27 for a comparison with and without particles, and the particles themselves emit intense radiations as they are very hot. The study of SRM signatures is an active research topic (Simmons and DeBell 1961; Hao et al. 2003) and the knowledge of the effect of particles is explicitly required (Racine 1991; Kovalev 2002). Hermsen (1981b)'s law yields a d_{43} average diameter (as defined in § 3.1.2.3) depending on nozzle conditions and based on a break-up dominated mechanism. It is often used as a simple model to predict particle size and therefore radiation. But this semi-empirical law is not accurate enough for todays applications.

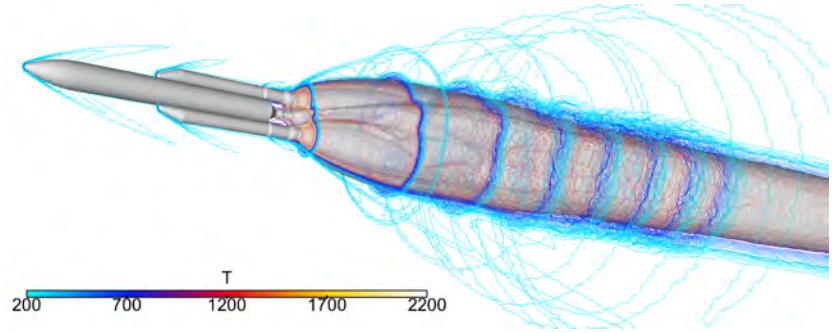

Figure 1.26: *Nose-to-tail reactive and two-phase simulation of Ariane 5 at* 30 *km with the CEDRE code (courtesy: P. Grenard).*

During the take-off of an ELV, two types of acoustic waves can damage the payload that are the ignition overpressure (IOP) and the duct overpressure (DOP), coming from the vents shown in Figure 1.7. These waves are damped on their way back to the payload fairing by spraying water all around the vehicle. A prediction of the IOP by numerical simulation is highly desirable: this requires to capture SRM ignition but also the unsteady out-of-chemical-equilibrium exhaust flow as after-burning (or re-ignition) has been identified as a leading mechanism, see Dargaud (2013) and references therein. The jet noise steady radiation is also an issue, but rather an environmental one as noise does not propagate back towards the vehicle during flight since there are no surrounding noise reflectors, and the vehicle moves at supersonic speed or in vacuum. Finally the disperse phase has not been identified yet as playing a crucial role in either IOP, DOP or acoustic emissions of SRMs.

1.3 Detailed physics and low-order models for SRMs

The phenomenology of a SRM has been described. But phenomena such as instabilities can occur that result from the coupling of the previous physics. This complex phenomenology is now described and general models are drawn, that are referred to as low-order, since they allow to link global quantities and output data such as performance indicators or stability criteria. Low-order models do not account for physics at the local (or microscopic) scale, which allows them to give a clear view of the general phenomena. Moreover such approaches do not require computational power but they are limited, as shown in § 1.4. To these extents, low-order models oppose to high-fidelity models, presented in Chapter 2, which provide a more detailed level of resolution with a high number of degrees of freedom but require high performance computing (HPC).

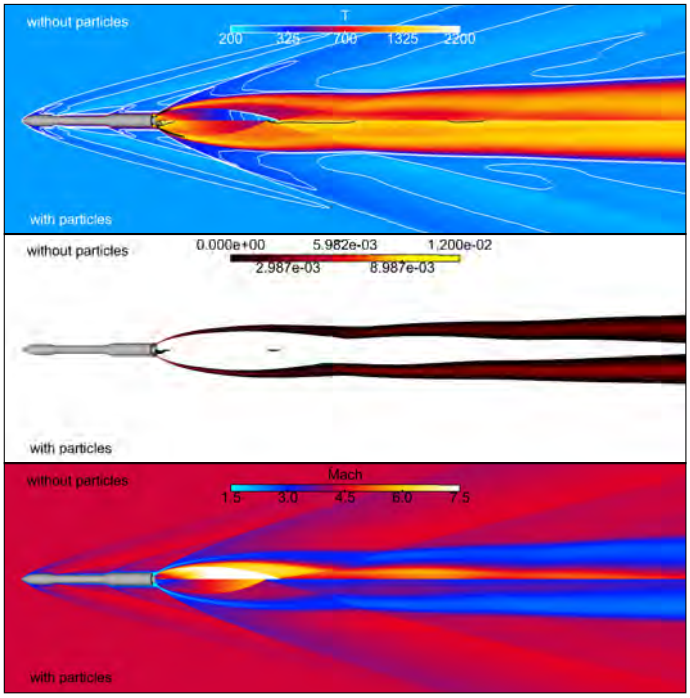

Figure 1.27: *Nose-to-tail reactive and two-phase simulation of VEGA at 30 km with the CEDRE code – Fields of gas temperature (top), $OH^\star$ radical species (middle), and Mach number (bottom) without and with particles (courtesy: P. Grenard).*

These models are engineer-like approaches in steady (or quasi-steady) and unsteady regimes: their limits are discussed. The quasi-steady regime, is defined to allow eventual temporal variations as long as they occur slowly compared to chamber residence times, this allowing the perturbations to be evacuated smoothly. The quasi-steady regime, allows to extend steady analysis to determine thrust as a function of time but it is not suitable for instability studies. All along this survey of the state of the art, we highlight the important and partly non-modeled role of the disperse phase, which is summed up at the end of the section.

1.3.1 Internal ballistic at steady regime

Internal ballistic aims at describing the phenomena inside a chamber leading to the expulsion of material from it. In the case of a SRM, the goal is simply to describe the thrust $\boldsymbol{F}$ and the ejection velocity $\boldsymbol{u}_{out}$ as a function of time. The simple notions hereafter developed are excerpted from Simoes (2006) and disregard the question of propellant geometry and chemistry but the interested reader can also refer to Kuentzmann (1973b), Lucas (1993), or Gossant (1993).
The following modeling is performed at steady regime and all the relations assume isobaric combustion in the entire chamber, and isentropic flow of a perfect gas through the nozzle. Quasi-steady assumptions are extended by Giraldi (2006), where a corresponding internal ballistic modeling is developed and implemented in a numerical tool.
As for two-phase aspects, they are ignored in most steady models, even though possible extensions of the theory allow to understand a small part of two-phase issues, namely two-phase lag losses presented in § 1.3.1.5.

1.3.1.1 Thrust

Thrust results from the pressure forces of ambient and combustion gases on a closed surface around the SRM according to Eq. (1.2). For a given ambient pressure p_{ext}, thrust is maximum if the combustion gas output pressure p_{out} is equal to p_{ext} (ambient nozzle), the latter varying with the altitude. When this condition is satisfied, thrust increases as p_{ext} decreases and thrust becomes maximum in vacuum. In quasi-steady regime, p_{out} and the jet section A_{out} can be proportionally linked to the chamber pressure p_c and the throat section A_t so that thrust can be expressed:

$$F = C_F p_c A_t \tag{1.11}$$

with a dimensionless proportional constant C_F. It is referred to as the thrust coefficient and characterizes the nozzle's efficiency. It depends on the isentropic coefficient γ_{gas}, its expression can be found in Sutton and Biblarz (2011).

1.3.1.2 Simple propellant combustion modeling

The propellant combustion has been described as a surface process in the previous section, leading to the knowledge of the flow rate depending on the chamber pressure as given in Eq. (1.7). The mass flow rate can also be expressed through the nozzle:

$$\dot{m} = C_D p_c A_t \tag{1.12}$$

with C_D a flow rate coefficient. In a simplified approach and for a perfect gas, C_D only depends on the gas chamber temperature T_c and its properties:

$$C_D = f(\gamma_{\text{gas}}) \times \sqrt{\frac{M_{\text{gas}}}{RT_c}} \tag{1.13}$$

with T_c ranging from 2000 to 3700 K, $R = 8.314\,\text{kJ/mol}$ the perfect gas constant and M_{gas} the molecular weight. Defining a propellant characteristic velocity $C^\star = C_D^{-1}$ yields a fundamental relation from Eq. (1.11) and Eq. (1.12):

$$F = \dot{m} C_F C^\star \tag{1.14}$$

where appear the contributions of flow rate $\dot{m}$, nozzle efficiency C_F and propellant energy potential $C^\star$ to the motor thrust F.
From the expression of thrust in terms of propellant and nozzle efficiencies in Eq. (1.14), the specific impulse defined in Eq. (1.3) can be written:

$$I_{sp} = \frac{C_F C^\star}{g} \tag{1.15}$$

which allows to compare motors with different specifications by combining features from the propellant and the nozzle. This reveals the necessity to use propellants with high characteristic velocities $C^\star$ and therefore high combustion temperatures T_c according to Eq. (1.13). To this extent, the incorporation of aluminum powder as a strong reductant rises significantly the combustion temperature (Tavernier et al. 1970), say from more than 1000 K. The resulting specific impulse remains below 300 s, which is weak compared to LOx-LH2 LREs (up to 435 s) or even LOx-RP1 LREs (up to 360 s), but is remarkably reproducible (Faure et al. 1996).
Finally, the last important quantity that is the chamber pressure p_c can be computed from Eq. (1.7) and Eq. (1.12) in quasi-steady regime:

$$\rho_{prop} S_b V_b = C_D p_c A_t \tag{1.16}$$

Increasing the burning surface S_b increases the flow rate and therefore the pressure, which can be expressed from the combustion law Eq. (1.6):

$$p_c = \left(\rho_{prop} a C^\star \frac{S_b}{A_t} \right)^{\frac{1}{1-n}}. \tag{1.17}$$

1.3.1.3 Motor operating point

From combustion and nozzle behavior, we can define the motor operating point. The constraint $n < 1$ on the pressure exponent of combustion law avoids extinction and explosion events and allows a stable operating point. Practically, an exponent below 0.5 is recommended. The unique motor operating point is naturally found in a flow rate-pressure diagram as the intersection point between the (concave) combustion law Eq. (1.6) and the mass balance Eq. (1.7), which is shown in Figure 1.28.
The strangling coefficient K is defined as the ratio of the burning front area to the throat section

$$K = \frac{S_b}{A_t} \tag{1.18}$$

and defines the instantaneous operating point for a given motor. So that a variation of K, either intended to set thrust over time or fortuitous -sudden change in the burning front or throat choking- leads to a new operating point with new values for chamber pressure p_c' burning rate V_b' as illustrated in Figure 1.28.

1.3.1.4 A simple and steady model: the Taylor flow

The Taylor flow is a classical approach to model the steady state flow in a SRM chamber. It features the main SRM characteristics of wall injection and cylindrical symmetry so that the flow is constrained to flow axially.

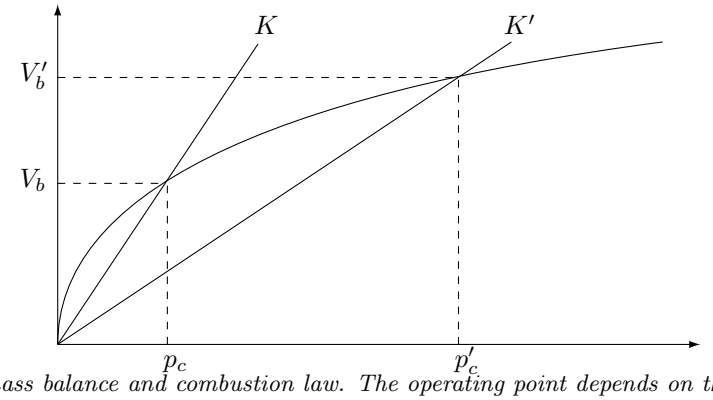

Figure 1.28: *SRM mass balance and combustion law. The operating point depends on the strangling coefficient K.*

This configuration is peculiar to SRMs and is met nowhere else in flow physics to the author's knowledge: a comparison is possible to a case of crowd dynamics where a train empties at a platform. In Low-Mach regime, the problem is referred to as the Taylor flow as a classical analytical solution was derived by Taylor (1956). It was first applied to non-viscous SRM flows by Culick (1966b). For steady regime modeling, it has rather a historical value but it has a crucial importance as it is the ground state for turbulence studies (see § 1.3.2.2) and hydrodynamic stability analysis (see § 1.3.2.4). We here focus on the case of a cylinder but many peculiarities of this flow, as a model for SRM flows, are also featured in plane geometries as long as they feature wall injection, as studied by Varapaev and Yagodkin (1969): these flows are referred to as non-parallel (Varapaev and Yagodkin 1970; Varapaev et al. 1973).

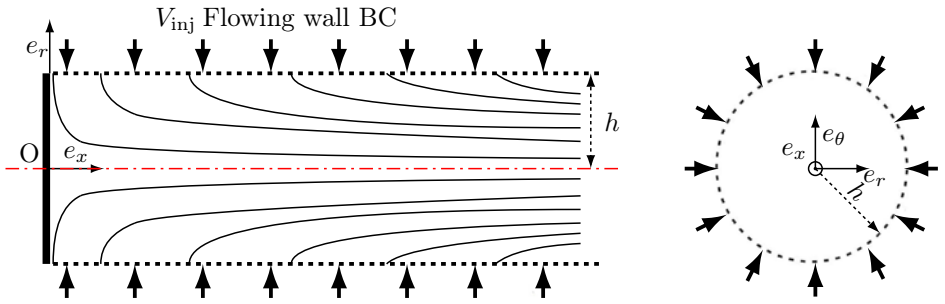

Figure 1.29: *Parameters and analytical streamlines of the Taylor flow.*

We assume a cylindrical combustion chamber with an inert flow injected normally from the wall at V_{inj} uniform: the flow is deflected and gets a longitudinal velocity which increases as shown in Figure 1.3. The analytical solution reads in cylindrical coordinates (Taylor 1956):

$$\left\{\begin{array}{ll} U_x = & V_{\text{inj}}\pi x \cos\left(\dfrac{\pi}{2}r^2\right) \\ U_r = & -\dfrac{V_{\text{inj}}}{r}\sin\left(\dfrac{\pi}{2}r^2\right), r \in [0,h] \\ U_\theta = & 0 \end{array}\right. \tag{1.19}$$

where V_{inj} is the injection velocity and U_x, U_r and U_θ are the axial, radial and azimuthal velocities respectively. The streamlines are sketched in Figure 1.29. The pressure field reads:

$$P = -\frac{\pi^2 x^2}{2} - \frac{1}{r^2}\sin^2\left(\frac{\pi}{2}r^2\right) + P_0 \tag{1.20}$$

From the original approach of the Taylor flow many analytical paths have been explored to assess specific aspects of the flow. Full-Mach solution can be derived (Clavin 1996) with small benefit and analytical solutions in more complex cases are presented in Griffond (2001) and in Griffond and Casalis (2001), for unsteady cases in Majdalani and Van Moorhem (2001), with regressing walls in Zhou and Majdalani (2002), with headwall injection (Majdalani and Saad 2007) but many assumptions remain: single-phase, non reactive, cylindrical geometry, rotation symmetry, no nozzle effect *etc.*

1.3.1.5 Simple assessment of two-phase losses in the nozzle

The occurrence of solid or liquid inclusions in the exhaust leads to a reduction in performance for a number of reasons, as analyzed by Nakka (1984):

- the condensed inclusions cannot perform any expansion work and therefore do not contribute to the acceleration of the exhaust flow,
- the higher effective molecular weight of these products lowers the propellant efficiency $C^\star$,
- due to thermal inertia, the heat of the condensed phase is partly ejected out of the nozzle before its transfer to the surrounding gases, and is therefore not converted into kinetic energy (particle thermal lag),
- likewise momentum inertia limits particle acceleration in the nozzle, the condensed phase exiting at a lower velocity than the gases (particle velocity lag).

These different types of losses have also been analyzed and modeled by Jackson and Davidson (1983) in the case of steam in nozzles. Two-phase nozzle losses in SRMs are crucial to model when metal fuel propellants are used (Kuentzmann 1973b): this problem has motivated a wide range of research on two-phase nozzles as soon as in the 60's (Gilbert et al. 1962; Marble 1963b; Crowe et al. 1964; Grishin et al. 1969; Kuentzmann 1973b) and then on (Sternin 1974; Vasenin et al. 1986; Vasenin et al. 1995). Among the effects listed above, the two latter ones are referred to as lag losses and are discussed in detail below.

Internal ballistic models can account in a simple way for a condensed phase in two limit regimes:

- equilibrium: the disperse phase and the gas are in permanent dynamic and thermal equilibrium, which is equivalent to assuming infinitely fast exchanges;
- frozen particles: the disperse phase does not exchange with the gas and the lags are maximum.

These two limit approaches are controlled by the relative position of the particle relaxation times compared to the flow characteristic time, their ratio forming Stokes numbers, which are detailed in § 3.1.2.1. The flow characteristic time in the chamber is large for most particle sizes but it becomes small in the nozzle, which goes to a Mach number Ma ~ 2.5, with a typical strain $\epsilon = 10^{-5}\,\mathrm{s}^{-1}$. We can write this fact in terms of Stokes numbers:

$$\mathrm{St}_\omega \ll \mathrm{St}_\epsilon \tag{1.21}$$

where St_ω is based on a chamber perturbation of pulsation ω and St_ϵ is based on a nozzle strain rate ϵ. This relation is true for any size of particle. But Stokes numbers increase with particle size: the frozen particle approach is valid for infinite Stokes numbers and is rarely relevant in the nozzle, if only break-up would occur. The equilibrium approach was suggested in the 50's (Kliegel 1959) and is relevant for a part of the typical sizes of particles in a SRM. It is based on the derivation of a modified molecular weight M_{eq}, heat capacity $c_{p,eq}$, and isentropic coefficient γ_{eq} depending on the particle mass fraction Y_p according to the one fluid Equivalent Gas approach presented in § 3.2.4.2. We highlight that the sound speed in these conditions is simply:

$$c_{eq} = \sqrt{\gamma_{eq} \frac{R}{M_{eq}} T_{eq}}. \tag{1.22}$$

Additional details about the calculation of these modified parameters may be found in Hoglund (1962).

Particles encountering $\mathrm{St}_\epsilon \sim 1$ i.e. a tuned inertia in the nozzle, yield strong drag and heat lag losses. The equilibrium approach does obviously not give insight on the lag losses: they have been crudely assessed also by Kliegel (1959) for a 1D flow by assuming fixed lags but such approach is relevant in short sections of the nozzle such as the throat. Marble (1963b) introduces a more complete approach for particle lag losses. The flow of a gas-particle mixture through the nozzle is analyzed under the approximation that the particle slip velocity is small compared with the average mixture velocity, using one-dimensional gas dynamics, the Stokes drag law, and corresponding approximations for the heat transfer between solid and gas phase. The evolution equations defining the pressure distribution giving the minimum impulse loss due to particle lag is formulated and solved for nozzles of prescribed mass flow, length, and of given exit pressure or area. The throat section of the optimum nozzle is considerably elongated and more gradual than that of the conventional nozzle. The velocity and temperature lags are much lower (about 1/3) in the throat region than those in the conventional nozzle. The impulse loss of the optimum nozzle was, however, reduced only about 30% below that of the conventional nozzle. So contouring of the nozzle to improve gas-particle flow performance will result in only very modest gains. To sum up, Marble (1963b) states that a stretched nozzle can be considered to allow a smoother relaxation of particle velocity and temperature, achieving a higher efficiency. Such nozzle contours for minimum two-phase losses are also discussed in Nakka (1984): it is concluded that they avoid lag losses which otherwise penalize the nozzle yield up to one third. But particles optimized nozzles are heavier and cumbersome so such solutions are usually disregarded. Still the impulse losses calculated for optimum nozzles can be used as a rough but convenient approximation for the impulse losses in conventional nozzles having the same area ratio or pressure ratio.

All these approaches assume a 1D flow: Hermsen (1981b) has extended the approach to assess radial lags but the results remain mitigated. In addition inertial (high Stokes) droplets encounter crossings (see § 3.1.3)

which complicates the analysis: the average velocities and densities are then difficult to assess. Finally, the weakness of all these approaches is the inaccurate knowledge of the particle sizes compared to such sensible physics: the evolution of the disperse phase in the chamber has been presented as complex, impeding a fine knowledge of particle sizes but the occurrence of break-up and coalescence within the nozzle moreover blurs the analysis. Attempts to model particle size evolution in the nozzle under coalescence (Crowe and Willoughby 1967; Marble 1967; Jenkins and Hoglund 1969; Kuentzmann 1969; Grishin et al. 1969; Tishin and Khairutdinov 1971; Kraiko and Shraiber 1974; Ivanov and Ivanova 1976), under break-up (Kovalev and Fomin 1982) or under both phenomena (Podvysotskii and Shraiber 1975; Hermsen 1981b; Averin et al. 2003) remain inaccurate.
The two-phase losses in the nozzle raise modeling issues and they seem to require a high-fidelity approach while they are crucial to be predicted in the perspective of determining and reducing I_{sp} losses.

1.3.2 Unsteady chamber regimes

Unsteady chamber regimes are modeled in two contexts: ignition and motor instabilities. The latter is the most important: instabilities resulting in ODP, occur in many SRMs and are the source of energetic, guidance and goal performance issues. For instance, Ariane 5 encounters oscillation bursts which require suppressor devices, see § 1.1.4.2. ODP should be predicted quantitatively regarding their frequency, their level and their triggering.
The modeling of unsteady chamber regimes requires fine modeling and advanced tools. Apart from some rare analytical models, unsteady regimes resort to numerical simulation. The difficulty to describe unsteady physics at a predictive level is such that up to now, existing technologies have often been improved instead of developing new motors.

1.3.2.1 Ignition

Ignition is a particular unsteady regime which requires a careful modeling (Caveny et al. 1980): the goal is the accurate prediction of correct fixing versus extinction, misfire, or over-pressure and some side-effects such as IOP (see § 1.2.4.3). The difficulty to model ignition is compensated in practice by two facts:

- SRM ignition is reliable *de facto*,
- large SRMs are ignited at first so that a launch may be postponed in case of a misfire.

To account for this process, the ignition device must be modeled first: it triggers a very unsteady and inhomogeneous process with strong compressible effects and complex chemistry. The unsteady flow field depends on ignition delay, propellant ignition, flame spreading, and chamber filling/pressurization (Johnston 1995). Radiation must be taken into account, especially when modeling laser ignition devices (Yan et al. 2001) and to evaluate the heat flux received by remote and confined propellant areas, where convective effects are minor.
The levels of turbulence in the flow at the first times after ignition, while pressure builds up, play a role that is more significant than in permanent regime (Fiedler et al. 2005). In this complex context, unsteady heating of the device must be accounted for, but the thermal transfers at the wall (propellant) have to be assessed accurately. Finally peculiarities such as nozzle transition from subsonic to supersonic must be treated at the boundaries.
As a conclusion, the ignition process is complex. Computation methodologies exist, rather for high-fidelity models, but the main stumbling points are:

- the flow rate from the ignition device,
- the thermodynamics model for the out-of-equilibrium flow of the ignition device,
- the propellant grain ignition itself,
- the heat fluxes and thermal losses at the wall,
- the radiative properties of the combustion products (Duval et al. 2004).

1.3.2.2 Turbulence

The flow in a SRM has a peculiar turbulent structure: unlike other combustion chambers where turbulence is required to enhance mixture and combustion, turbulence is not desired in SRMs as combustion occurs at the propellant surface. In large SRMs still, the flow is likely to transition towards turbulence as the motor is long and there are many sources of disturbance.
The knowledge of turbulence is compulsory to determine:

- the transfers at the walls i.e. friction and heat flux,
- the reaction rates,
- the oscillatory levels,
- the mass of condensed matter entrapped by cavities (Cesco 1997),

- the particle impingement rate in the nozzle.

We highlight that turbulence modeling is needed to assess motor stability (Kourta 1999) since turbulence plays a role on oscillatory levels.
Unfortunately, transition occurs at a fairly intermediate position in large SRMs so that the turbulent regimes are remarkably complex: a "young" turbulence (Ha Minh 1987) is at work and the determination of the transition location and conditions is required. Modeling the transition and such young turbulence is known as particularly tedious.
Numerical simulations (Beddini 1981; Beddini 1986) have allowed to identify three regimes before that of fully developed turbulence:

- laminar ($x/h < 5$) with a Taylor-Culick like velocity profile;
- first transition ($5 < x/h < 10$) with a significant turbulence $\sqrt{k} > 0.1 v_x$ but with laminar persistency i.e. the average axial velocity profile is the one of the laminar regime;
- second transition ($x/h > 10$ to 20) where the axial velocity profile is that of a turbulent internal flow.

The first transition can be theorized in a linear framework (Varapaev and Yagodkin 1969). The second transition is more complex to study but it is also the most important as it induces an increase in friction, heat flux and reaction rates (Beddini 1981).
From the Taylor flow geometry, we can define some Reynolds numbers:

$$\mathrm{Re}_s = \frac{hV_{\mathrm{inj}}}{\nu_{\mathrm{gas}}}, \quad \overline{\mathrm{Re}} = \frac{h\overline{V}(x)}{\nu_{\mathrm{gas}}}, \quad \text{or} \quad \mathrm{Re}_c = \frac{hV(x, r=h)}{\nu_{\mathrm{gas}}} \tag{1.23}$$

with h the cylinder radius, ν_{gas} the gas viscosity and a velocity which can be the injection velocity, the axial velocity averaged on a radius, or the centerline (or maximum) axial velocity. The surface Reynolds number can be linked to the average axial one:

$$\overline{\mathrm{Re}}(x) = \frac{x}{h}\mathrm{Re}_s \tag{1.24}$$

as the latter is based on a velocity that integrates the effect of injection from 0 to x. As for Re_c, it is linked to the surface Reynolds number Re_s in Beddini (1986)'s diagram, see Figure 1.30, which allows to locate the second transition, and is established from experimental results (Olson 1964; Yagodkin 1967; Huesmann and Eckert 1968; Dunlap et al. 1974; Yamada et al. 1976). The above scenario is still under study and has been challenged in recent works (Gazanion 2014).

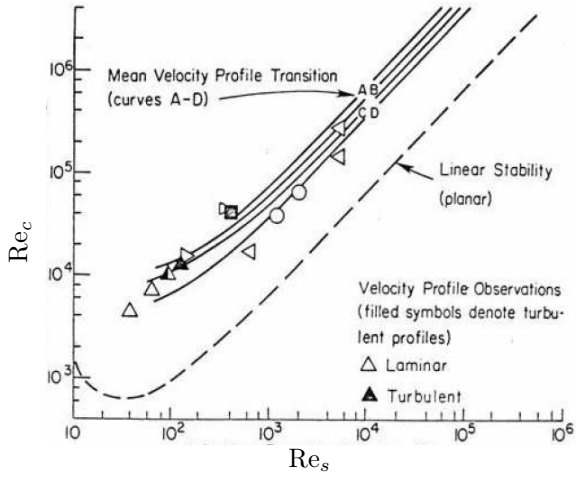

Figure 1.30: *Beddini's experimental chart for SRM turbulence transition.*

We highlight that the previous results and the quantitative study of turbulence in SRMs are conducted in cold gas experiments e.g. on the VECLA test bed (Avalon and Lebon 1993; Avalon and Lambert 2010). While in hot gas conditions, no measurements are accurate enough: flow visualizations have not been worked out. Hot gas pressure measurements, though unable to yield structural information on turbulence, proved that the turbulence levels are much higher than in non-reactive flows. Since the original approach of Beddini (1977), the role of several phenomena on promoting transition and increasing levels has been discussed such as acoustic ambience (Lee and Beddini 1999) or propellant combustion noise (Dupuy 2012). We also highlight the potential role of the disperse phase inclusions in fostering transition through their fitful injection, their turbulent wakes and their noisy combustion or in delaying it through damping effects. None of these effects have been quantified up to now.
In parallel with experimental efforts, numerical simulations are conducted to assess turbulence and its effects with high-fidelity models: such approaches are discussed in § 2.1.3.2, as well as the need to couple them with high-fidelity models for other physical aspects.

1.3.2.3 Propellant combustion instabilities (CI)

Propellant combustion instabilities (CI) -sometimes simply referred to as combustion instabilities- where observed experimentally in early motors, see a review in Price (1984b). They occur when the surface combustion of the propellant features an unsteady response that is tuned to a periodic excitation: coupling with the acoustic ambience can then occur (Kuentzmann 1991; Gossant 1993; Lupoglazoff and Vuillot 1996) and results in ODP. Reviews on unsteady propellant combustion and instabilities can be found in De Luca and Price (1992) and in Culick and Yang (1992).
Propellant combustion instabilities are modeled through linear acoustic budgets (Hart and Mc Clure 1965; Culick 1966a) or fluctuating energy budgets (Flandro 1985; Radenac 2011), which yield instability frequencies but not their levels. The main contributions of chamber, nozzle and disperse phase damping (Gossant 1993; Vuillot and Lupoglazoff 1996) are to be modeled as well as the propellant response, e.g. through a transfer function in linear theory (Baum and Denison 2012; Rahman 2012). A propellant response transfer function can be defined: it matches the pressure exponent from the combustion law of Eq. (1.6) for low frequencies such as the P230 instabilities. In general, such responses depend strongly on the solid propellant unsteady thermal behavior, and their derivation is very different from that of the steady combustion models, given in § 1.2.2.3. It depends strongly on the heterogeneous properties linked to propellant packing (Buckmaster et al. 2005). The derivation of propellant response functions was also performed on the basis of linear models for an unsteady flow (Clavin and Lazimi 1992). Stability charts can be established, that depend on the propellant response model, to analyze the most complex cases.
These instabilities are often of high frequency -around 1 kHz- so that they do not occur in large SRMs (Kuentzmann 1991). This conclusion has for instance been stated for the P230 in Gallier et al. (2002). Still combustion instabilities are crucial in the context of small SRMs so they have been studied experimentally in the prospect of validating models and characterizing propellants e.g. with an exciting device at the exhaust driving in Kuentzmann and Laverdant (1984).

1.3.2.4 Hydrodynamic instabilities (HI)

Hydrodynamic instabilities (HI) correspond to periodic detachment of coherent structures resulting in ODP. A simplified hydrodynamic model based on a linear analysis of the Taylor flow, see § 1.3.1.4, and three vortex shedding mechanisms is classically invoked as a ground analysis, see a review on vortex shedding in Vuillot (1995). This analysis is nonetheless relevant but also convenient since it is purely hydrodynamic and does not need to consider reactive aspects in the modeling nor in the experiments, the latter being performed on simple, cold gas facilities that are easily equipped.

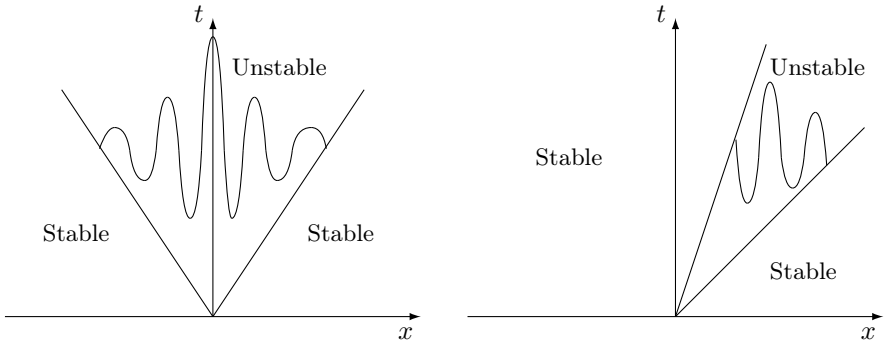

Figure 1.31: *Absolute instability (left) and convective instability (right) in 1D space-time diagram.*

Linear stability analysis of Taylor-like flows are a classical approach for SRM instability prediction (Ugurtas 2000; Anthoine 2000; Griffond 2001; Griffond and Casalis 2001). These flows feature only convective instabilities (Favray 1999; Ugurtas 2000) so that a perturbation does not interfere with its source but grows downstream as shown in Figure 1.31. The instabilities predicted by linear analysis are observed as they gather into coherent structures or vortices and three generating mechanisms were identified in the ASSM/POP program (Vuillot 1998; Kuentzmann 2001) that are angle, obstacle and parietal vortex shedding. They are referred to as VSA, VSO and VSP respectively after their French acronyms and are described in detail below. The first two are natural consequences of the finite perturbations initiated by wall angles or any obstacles such as a PTF but the third is of peculiar kind: a critical abscissa x_c exists beyond which any infinitesimal perturbation of the injected flow is amplified. As a result, real SRMs are subject to hydrodynamic instabilities nonetheless whenever the geometry is complex or a protruding obstacle exists but also as soon as the chamber is sufficiently long. These three vortex shedding mechanisms have been demonstrated to appear in cold gas and real motor experiments and in numerical simulations. They do not exclude each other but they are now presented separately.

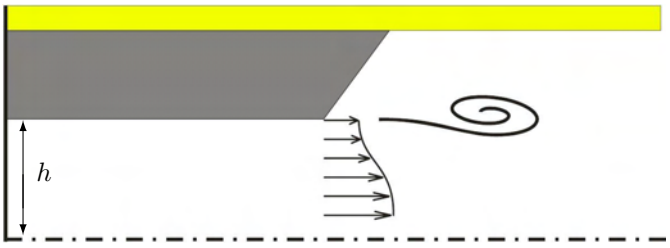

Figure 1.32: *Illustration of the angle vortex shedding (VSA).*

VSA is due to a sudden increase in the chamber section e.g. at the edge of a segment, even when chamfered: a shear layer appears and the axial velocity profile features an inflexion point, a necessary condition for instabilities according to Rayleigh's theorem (Charru 2011). A convective instability can develop towards the nozzle as shown in Figure 1.32, and has been often observed, in experiments on real motors such as the C1x at ONERA (Dupays 1996), on laboratory scale 2D facilities at ESPCI (Favray 1999), on cold gas test beds such as called VIOLETTE (Goncalves de Miranda 2000), and in simulations (Dupays 1996; Lupoglazoff and Vuillot 1998b). So VSA should be considered as likely as soon as the propellant grain presents an angle. For instance the unstable behavior of a French SLBM stage was proven to originate from VSA in Ribereau and Le Breton (1995) whereas research had been oriented towards combustion instabilities.

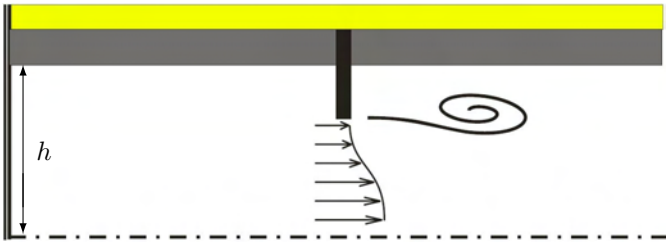

Figure 1.33: *Illustration of the obstacle vortex shedding (VSO).*

VSO appears when an obstacle generates a velocity profile with an inflexion point as shown in Figure 1.33. VSO was demonstrated to occur experimentally in early campaigns (Brown et al. 1981; Shu et al. 1986), on the MICAT1 bench at ENSMA (Couton et al. 1996; Vetel 2001), at the VKI (Anthoine et al. 2000), and at ONERA with the LP3 and LP6 sub-scale motor firings (Hylkema et al. 2011). In the latter case, the role of grain PTF was extensively studied depending on their material, position and shape (Traineau et al. 1997; Prévost et al. 2000) since PTFs that protect the forward segment faces emerge during combustion and act as diaphragms. The VSO is strongly coupled to the PTF, and possibly to PTF flapping as explained in § 1.2.1.3. The parameters of the PTF are so sensitive that a change in materials during Ariane 5's lifetime has increased the ODP levels by $25-50\,\%$. A characterization of the PTF elastomer was recently conducted to include the vibration of the obstacle in experiments and simulations (Cerqueira 2012).

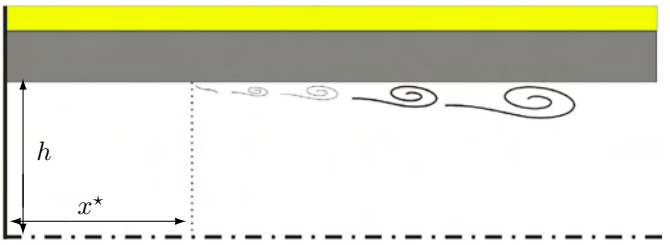

Figure 1.34: *Illustration of the parietal vortex shedding (VSP).*

At the beginning of the 2000's VSA and VSO were considered as the main instabilities of American and European large SRMs respectively, the obstacle in the case of VSO being the PTF at the inter-segment junction. But for the P230, the actual levels do not match the VSO levels predicted by experiments (Traineau et al. 1997) and simulations (Lupoglazoff and Vuillot 1996), so that the above scenario is challenged. In the meantime a natural instability of Taylor-like flows, the VSP, suggested by Varapaev and Yagodkin (1969) but then considered as weak, was observed to play a major role in long SRMs. The role of VSP was proven thanks to numerical evidence (Lupoglazoff and Vuillot 1996) and to experimental campaigns on P230, SSM1, LP6, and LP10 sub-scale motors (Godfroy and Tissier 1993; Lupoglazoff and Vuillot 1993; Godfroy and Tissier 1994; Cagnon et al. 1997). VSP is up to now considered as predominant, though VSA and VSO are still

thought to play a role (Ballereau and Godfroy 2009; Ballereau et al. 2011). A linear stability-based theory has been specifically developed for the prediction of VSP (Casalis et al. 1998; Griffond et al. 2000; Griffond 2001) and is based on a critical abscissa $x^\star \approx 8h$, shown in Figure 1.34, after which the flow is unstable at a given frequency. The number of unstable frequencies then increases with position which allows VSP to easily couple with other instabilities when motors are long. This theory has been confirmed numerically (Casalis et al. 2000) and experimentally on laboratory scale facilities (Guéry et al. 2000), on cold gas test beds such as rectangular duct VECLA (Avalon et al. 1998; Avalon and Lambert 2000; Ugurtas 2000; Griffond et al. 2000; Ugurtas et al. 2000) shown in Figure 1.35 and axisymmetrical duct VALDO (Avalon and Lambert 2000) at ONERA, 1/30 sub-scale P230 (Anthoine 2000) and 1/15 sub-scale P230 (Tòth 2008) at VKI. VSP has also been observed on dedicated hot gas experiments such as the LP9 1/35 P230 sub-scale motor (Prévost and Vuillot 1998; Prévost et al. 2000) and retrospectively on other sub-scale motors such as the LP6.

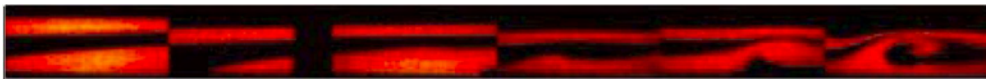

Figure 1.35: *Visualization with PLIF diagnostic in the VECLA test bed (Avalon and Lambert 2000).*

The vortex shedding mechanisms are well theorized, but they are not sufficient to retrieve the occurrence and levels of instabilities. The general acoustic ambience is presumably involved (Kourta 1996; Lupoglazoff and Vuillot 1996; Lupoglazoff and Vuillot 1998a; Avalon et al. 1998; Vuillot and Casalis 2000) with many sources such as propellant combustion or geometry noise but the frequencies are first related to the chamber modes: longitudinal harmonics are mainly considered with a $kL/2$ wavelength, L the chamber length and k an integer, since the choked throat behaves like a wall. This scenario was examined numerically (Vuillot 1995; Lupoglazoff and Vuillot 1996) and experimentally (Anthoine 2000; Anthoine et al. 2000), the levels being maximized when the vortex shedding is tuned on acoustic modes. A coupled hydro-acoustic model was suggested by Flandro (1973) and developed in Flandro (1986), based on VSO, acoustic reemission from the nozzle throat and interaction with a second obstacle (Culick and Magiawala 1979). But the nozzle acoustic reemission covers many phenomena, from noise emitted by vortices and entropic waves swallowed by the nozzle (Marble and Candel 1977), to vortices hitting the nozzle wall or penetrating the recirculation zone. This requires an advanced modeling, which takes the nozzle shape into account. A hydro-acoustic coupling was also exposed for VSA (Favray 1999) and for VSP (Ugurtas et al. 2000) and a VSO-VSP coupling was exposed numerically (Godfroy and Briand 2005) and experimentally (Vetel 2001).
Finally the overall scenario is a feedback mechanism locked on the previous hydrodynamic and/or acoustic instability frequencies. The frequencies can jump from a mode to another (Anthoine 2000). Moreover, since the geometry evolves during propellant combustion, a series of triggering and cut-off may occur and matches the observed oscillation bursts.
The levels are still not predicted so that fluid-structure interaction (Richard and Nicoud 2011), turbulence (Kourta and Ha Minh 1995; Silvestrini et al. 1995; Chaouat and Schiestel 2000; Gallier et al. 2004; Dupuy 2012), disperse phase combustion (Lupoglazoff et al. 2000; Ballereau et al. 2003), and inert disperse phase effect (Dupays et al. 2008) are still investigated.
The identified control parameters are then:

- grain geometry,
- metal fuel size distribution,
- thermal protection (PTF) (Godfroy and Briand 2005).

1.3.2.5 Thermoacoustic instabilities (ITHAC): an effect of the reactive disperse phase.

The distributed combustion may play a crucial role on the levels of oscillations in the chamber, when so-called Thermo-Acoustic Instabilities occur (ITHAC). A scenario has indeed been elaborated, according to which burning droplets release mass, momentum and a moreover significant amount of energy in the gas in a coupled way as regards the acoustic ambience. This scenario resembles that of Rijke (1859)'s tube, which has been purposely studied by Raun and Beckstead (1993) in the prospect of the application to military SRMs. This would lead to a new type of ODP instability, resulting in TO.
Numerical simulations taking into account reactive particles such as in Lupoglazoff et al. (2000) and in Ballereau et al. (2003) showed that the distributed combustion of aluminum particles had an effect on oscillations. The coupling occurs preferentially with acoustic modes (Gallier et al. 2009; Gallier and Godfroy 2009; Casalis et al. 2011; Radenac 2013) so it is referred to as a Thermo-Acoustic Instability for the fluctuating heat release rate $\dot{q}'$ couples to acoustic modes: the occurrence of an instability can be assessed by a straightforward use of the Rayleigh criterion. The significance and relevance as regards ITHAC of the interaction between hydrodynamic structures (vortex shedding) and the distributed combustion is still discussed in the community. In both cases, though ITHAC is strictly speaking a combustion instability this

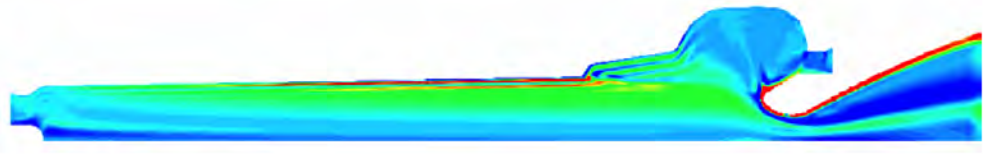

Figure 1.36: *P80 vorticity featuring ITHAC – Eulerian computation with the CPS code from Herakles (courtesy: S. Gallier).*

term is disregarded to avoid the confusion with the propellant combustion instabilities described in § 1.3.2.3. In the purely acoustic understanding of ITHAC, the control parameters are:

- the position and thickness of the combustion zone -which strongly depend on the flow conditions- as well as the particle size and temperature;
- the aluminum heat of reaction;
- the thickness of the acoustic boundary layer;

as assessed numerically (Gallier et al. 2009; Gallier and Godfroy 2009). The addition of a thermo-acoustic stability integral in the acoustic balance theory of Culick (1966a), then referred to as Fluctuating Energy Balance (Radenac 2013), gives theoretical insight on a proposed mechanism, according to which acoustic boundary layer creates high acoustic velocities that enhance heat release from burning aluminum particles (Gallier and Godfroy 2009; Radenac 2013).
The overall coupled effects between reactive particles and a reactive flow are very complex, proving a non-linear, threshold behavior. General knowledge and modeling is scarce: the classical but limited criterion for instabilities due to Rayleigh (1896):

$$Q_R(x) = \frac{1}{T}\int_0^T p'(x,t)\dot{q}'(x,t)\mathrm{d}t > 0 \tag{1.25}$$

where p' is the fluctuating pressure of the acoustic field and T a period is still used nowadays, for ITHAC and in other combustion instability problems, despite a century of active research to build a comprehensive theory (Nicoud and Poinsot 2005). This criterion can be integrated on the chamber volume and compared to the integrated sources of damping to forecast stability.
As said previously, the P230 is believed to feature ITHAC though it is not the main source of oscillation. On the contrary, the P80 is much more studied regarding ITHAC which appears as an exacerbated 1L mode at the beginning of the firing, as simulated in Gallier et al. (2009) (see also Gallier and Godfroy (2009)). On the contrary, vortex shedding is less feared as the motor is shorter. The vorticity in a P80 is given in Figure 1.36 as an illustration of such phenomenon. As a conclusion, the ITHAC scenario is suspected but not proven: in the particular case of the P80, its unstable behavior shares many similarities with ITHAC-proved simulations so additional studies are planned on the subject (Sibra 2014).

1.3.2.6 General coupling of an inert disperse phase to ODP

The disperse phase plays a major role regarding velocity and temperature lags: combustion residuals, though chemically inert, require an important share of the modeling effort to predict ODP.
There are two couplings that can occur between ODP and an inert disperse phase: the disperse phase directly modifies the chamber acoustic properties but it can also modify the hydrodynamics and the vortex shedding, bringing them close to an acoustic mode. In both cases, the parameter that characterizes the interaction between particles and flow structures is proven to be the droplet size: it conditions heat and momentum transfer times, which are to be compared to acoustic and flow characteristic times, as detailed in § 3.1.2.1.
Another effect has been pointed out by Summerfield and Krier (1969), which results in damping. It consists in a modification of the propellant response function induced by the accumulation and the melting of aluminum particles at the propellant surface. However, as highlighted by Price (1971), this effect, mainly observed for frequencies below 2000 Hz, is probably of secondary importance. So we focus on two-phase acoustics and hydrodynamics.

1.3.2.7 A linear model for particle damping

The damping role of particles in the motor has been early suspected and presented as dominant in Summerfield and Krier (1969), this conclusion being strongly criticized by Price (1971) and retracted since then. Still, the damping effect of the condensed phase is important and can be assessed simply.
We now derive a classical analytical model for some simple cases of two-phase acoustics. ODP is here modeled as acoustic waves propagating in the chamber. The dispersion and damping effects of the disperse phase on acoustics can be assessed with the following model. Indeed, the thermal and velocity lags yield

enthalpy and momentum transfers that influence the propagation of acoustic waves, introducing additional dissipation and dispersion, as accounted for by classical linear theory (Temkin and Dobbins 1966).
This linear acoustic approach is classical for waves in monodisperse sprays. It can be used to test numerical schemes (Morfouace and Tissier 1995; Dupays 1996) in a monodisperse case. We consider a monochromatic wave with a pulsation ω propagating in a spray that is homogeneous when at rest. We can determine analytically the solution by assuming a decaying plane wave structure. We define the speed of sound in the gas alone $c_0 = \sqrt{\gamma r T_0}$ where γ is the isentropic coefficient and r is the specific constant of the gas. The corresponding wave number is $k_0 = \omega/c_0$ and the wave period $\tau_\omega = 2\pi/\omega$. Defining the complex wave number $\underline{k} = k_1 + ik_2$, we are interested in decaying harmonic solutions with the following form:

$$\boldsymbol{u}_g(t,x) = \sin(\omega t - k_1 x)\exp(-k_2 x)\boldsymbol{u}_g^0. \tag{1.26}$$

Temkin and Dobbins (1966) have considered conservation equations for the gas and for a phase of monodisperse particles, both interacting through drag and heat transfer. A dispersion relation for decaying harmonic waves can be derived for droplets of size S:

$$\left(\frac{\underline{k}}{k_0}\right)^2 = \left(1 + \frac{\mu}{1 - i\omega\tau^{\boldsymbol{u}}(S)}\right)\frac{\left(1 + \frac{\mu\kappa}{1-i\omega\tau^T(S)}\right)}{\left(1 + \frac{\mu\gamma\kappa}{1-i\omega\tau^T(S)}\right)} \tag{1.27}$$

with μ the particle mass loading i.e. the ratio of droplet bulk density to gas density and $\kappa = c_{p,l}/c_{p,g}$ the pressure heat capacity ratio. We note that $k_1/k_0 = c_0/c(\omega)$ with $c(\omega)$ the effective speed of sound in the spray. Temkin and Dobbins also suggest to define dimensionless coefficients to quantify attenuation and dispersion:

$$\begin{cases} \alpha^\star = \dfrac{2k_2}{\mu k_0} \\ \beta^\star = \dfrac{1}{\mu}\left[\left(\dfrac{k_0}{k_1}\right)^2 - 1\right] \end{cases} \tag{1.28}$$

where $\alpha^\star$ is a dimensionless attenuation, independent of μ for moderate loadings and $\beta^\star$ is a dimensionless dispersion, null for asymptotically big droplets. From this equation, two dimensionless groupings $\mathrm{St}_\omega = \omega\tau^{\boldsymbol{u}}(S)$ and $\mathrm{St}^\theta_\omega = \omega\tau^T(S)$ naturally appear that are the acoustic Stokes number St_ω and the thermal acoustic Stokes number $\mathrm{St}^\theta_\omega$, which is generally close to St_ω, see § 7.1.

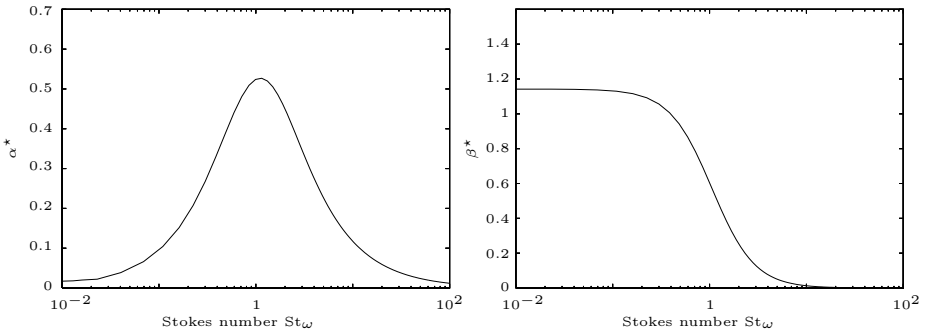

Figure 1.37: *Attenuation $\alpha^\star$ and dispersion $\beta^\star$ of a monochromatic acoustic wave in a monodisperse spray versus the acoustic Stokes number St_ω.*

We plot in Figure 1.37 the attenuation and dispersion coefficients as functions of the Stokes number St_ω, which is proportional to the dynamic Stokes number and is defined in § 7.1. Dispersion is related to the speed of sound:

- at very high St_ω, the speed of sound is the one of the gas alone c_0 and the particulate phase is decoupled from the gas;
- at very low St_ω, the speed of sound converges to c_{eq} that is the speed of sound in an homogeneous mixture of gas and particles at equilibrium, consistently to the steady nozzle models of § 1.3.1.5 and to the general two-phase equilibrium model referred to as Equivalent Gas and presented in § 3.2.4.2.

As for attenuation, it is null for extreme values of Stokes numbers, referred to as "untuned" regimes while $\alpha^\star$ reaches a maximum for $\mathrm{St}_\omega = 1$. Another local maximum, usually smaller, appears when the thermal and the dynamic times are separated by more than a decade.
An extension to evaporating and reactive cases (Dupays 2000; Dupays and Vuillot 2002; Sibra 2014) can be performed at the cost of hypotheses on the heat and mass transfer mechanisms: it yields another peak

	CI	HI	ITHAC
Wall Combustion	$\oplus$		
Carrier phase	$+$	$\oplus$ $+$	
Inert disperse phase	$-$	$\oplus$ $-$	$-$
Dist. combustion		$\oplus$ $\ominus$	$\oplus$
Turbulence	$\ominus$	$\ominus$	$\ominus$

Table 1.3: *Instability models and couplings:* $\oplus$ *non-linear;* $+$ *linear;* $-$ *linear damping.*

linked to the mass transfer characteristic time, which can correspond to both attenuation or amplification depending on the regime. An extension to cases with a non trivial mean flow is also possible, using a fluctuating perturbation method (Culick 1975). This approach does not account for the hydrodynamic response to polydispersity: droplets of different sizes are segregated by the flow coherent structures -and can condition them- in a feedback mechanism.
As a conclusion, the linear theory, that accounts for the attenuation and dispersion effects of a homogeneous distribution of particles on a pure acoustic wave, can be used to predict similar effects of the disperse phase in any unstable regime (CI, HI, ITHAC). Unfortunately the particles, even inert, can have in these cases a more complex, non-linear role, possibly leading to thresholding, amplification, mode selection *etc.* as described below.

1.3.2.8 Non-linear coupling of an inert disperse phase to HI

In the particular case of HI, the damping role of the disperse phase can of course be assessed with the previous approach and it appears to be incontrovertible. But observations lead to think that a driving effect can be more important (Dupays 1996), especially in reactive conditions (Lupoglazoff et al. 2002; Gallier et al. 2009). At this stage, it is tempting to develop a manichean point of view: inert Al_2O_3 droplets would tend to damp pressure oscillations while burning aluminum droplets would tend to drive them through ITHAC. The impact of an inert condensed phase on pressure oscillations is however numerically shown to be more complex (Ballereau et al. 2003; Godfroy and Briand 2004; Simoes et al. 2005) and particularly not so profitable (Jézéquel and Prévost 2007; Dupays et al. 2008). As a preliminary remark, most of the experimental observations of the particulate damping phenomenon relate to high frequency instabilities, often effectively treated by adding a minimal amount of small refractory particles in the propellant.
Above all, conclusions for lower frequency instabilities generated by hydrodynamic disturbances are more qualified. First, Féraille (2004) showed, thanks to a linear stability analysis of a two-phase flow with parietal injection, that inert particles may sometimes drive the instabilities following the displacement of the stability curve. Second, experimental studies conducted on the so-called C1xb setup, exhibited the ambiguous role of the condensed phase. This motor is subject to combustion instabilities due to a coupling between the acoustics of the chamber and VSA (Dupays 1996). A damping effect is observed in perfect accordance with the linear theory below a threshold loading around 10 %; above this threshold, a driving effect is observed experimentally and confirmed numerically, the condition being a tuned size of particles i.e. $St_\omega \sim 1$; finally above 20 % particles in mass, the oscillations are totally damped, exhibiting a second threshold (Dupays et al. 2000). These threshold effects are in direct conflict with the linear theory.

1.3.2.9 Summary of instability modeling

The known instability mechanisms presented above are summed up in Table 1.3 on with the related physical aspects. Among all these phenomena, the disperse phase is proven to have a strong and complex impact. Regarding the major dependency of these instability mechanisms on particle sizes, the idea of modifying particle sizes has been contemplated to limit ODP and is discussed in the following examples:

- Simoes (2006) has suggested to use 5 μm particles of μAl in the P230 but warns that coalescence must first be proven to be weak to get a satisfactory effect;
- the use of large particles could have the same effect and could be cheaper but this idea is not applicable in practice (Godfroy and Briand 2004; Simoes et al. 2005) due to differences in the combustion regime, increased erosion, *etc.*;
- finally nAl particles are studied for strategic applications and have a great potential, but the questions on coalescence are raised again.

All these scenarios remain hypothetical solutions as long as they are not backed, at least, by numerical evidence.
As a conclusion, experiments and many numerical results prove that the disperse phase has a complex impact on ODP. A damping effect generally occurs and is acknowledged but some motors experience an overall driving effect of particles. Though the driving effect theory has been criticized in Italy (Stella et al.

2005), it has been retrieved in numerical simulations (Dupays et al. 2008). Modeling effort still seems necessary to identify the dominant mechanisms but the knowledge of size distribution is crucial to exploit current models and elaborate future ones.

1.4 Towards the improvement of SRM knowledge

The technical difficulties of experiments are overviewed to justify the recourse to numerical simulations. The questions left unanswered by the SRM phenomenology presented above, are summed up, and modeling needs are discussed.

1.4.1 Necessity and limits of experiments

1.4.1.1 An incontrovertible approach

SRM characterization has to do with fluid mechanics, chemical reactions, multiple couplings *etc.*, reaching a complexity level that yields non-linear effects and emergent phenomena, and ending in predictability problems. Because of this complex physics, SRMs are described by a theory that "fits" to the known (i.e. tested) regimes. This choice is guided by the intuition that the fundamental mechanisms at stake have been well identified. But this does not guarantee either that the physical model perimeter is correctly defined for these regimes or that the physical model is appropriate for other regimes. So SRM design should resort to experiments and test beds when it comes to new configurations.
For instance the numerous cold gas experiments on SRM configurations listed in § 1.3.2.4 allowed HI to be identified as a major ODP mechanism in the P230 and theorized through vortex shedding theory. In addition down-scaled SRMs or so-called "hot gas" test beds have always been a valuable and incontrovertible tool in the study of ODP mechanisms: the numerous configurations tested at ONERA over the last 20 years, through more than 130 experiments as reviewed in Hylkema et al. (2011), have contributed to the determination of ODP mechanisms and pave the way to TO reduction through industrial system modification and new design.
Finally scale one experiments -including direct measurements on operating motors- have been up to now a major source of data for design and modeling. The P230, the SRMU, and the P80 have systematically been instrumented and their firings analyzed, yielding a wide data and supporting a large part of the present knowledge on SRMs (Brown et al. 1981; Dunlap and Brown 1981; Dotson et al. 1997; Ballereau and Godfroy 2009). The strong need for full-scale SRM results is symptomatic of both the complexity of the flow and the difficulty to handle the operating conditions.
For the same reasons of complex physics, the numerical codes should be considered for their ability to reproduce the experimental results and if not, the reason should be known.

1.4.1.2 Technical limitations of experiments

The difficulties to get detailed and accurate experimental results on SRMs are briefly discussed.
On the one hand, experiments on SRMs yield little information since the chamber ambience is very hot, two-phase and reactive, which makes measurements intractable, and under high pressure, which makes optical diagnostics quite complicated. Attempts to achieve optical access and measurement in hot-gas test beds are envisioned under the condition of developing new break-through laser diagnostics.
On the other hand, the representativeness of experimental test beds is a major issue: experimental results do not systematically allow to predict the behavior of a whole, full scale system. First, the physics is not always completely reproduced by experiments: in the case of SRMs, the combustion and the two-phase features are the most difficult to get e.g. many tests are performed in cold-gas. Second, the experiment scale may not allow some phenomena to occur in the same regimes: hydrodynamics (especially VSA and VSO), turbulence, and two-phase features are noticeably sensitive to the size of the system and do not scale in the same proportions. For instance, sub-scale experiments come in good agreement with single phase simulations such as in the case of the LP6 (Hylkema et al. 2011), whereas similar simulations of the P230 systematically underestimate oscillation levels. These discrepancies between full scale and sub-scale representativeness raise scaling issues regarding flow time scales compared to those of particles and their combustion, this question being discussed in Tòth (2008) and in Hylkema et al. (2011). Still poorly scaled experiments can be used as intermediate class tests for code validation.
So experiments are costly on full scale and even on sub-scale motors. The cost of an experiment campaign is always significant and no scale savings can be done; on the contrary numerical simulations allow parametric studies and a better rate of reconversion of the developed features.

1.4.2 Need for numerical simulation with high-fidelity models

1.4.2.1 Rise of numerical simulation

Experiments are incontrovertible to guarantee successful design and optimization. A satisfactory experimental database can possibly be achieved and kept up to date with sustained experimental efforts and thanks to continuous improvements in experimental possibilities (materials, techniques) and measurement techniques (accuracy, data storage and processing).
For economical reasons, the experimental approach is on the decline while simulation is more and more developed and used. As a matter of fact, SRM design and optimization today relies on modeling and numerical abilities. The scientific and technical advances today resort to "Numerical experimentation", an approach which is as tantalizingly as ambiguously rich since the extrapolation from validated configurations to new results is easy and immediate but potentially misleading.
For this reason numerical simulations are up to now used, not for design, but for research purposes: they are applied to identify dominant physical mechanisms, which are confirmed by experimental facilities. The identification of the VSP mechanism, as described in § 1.3.2.4, is exemplary of this strategy. And the same numerical preliminaries are applied to do the spadework for ITHAC understanding.

1.4.2.2 Need for reactive aspects

Since a SRM is a chemical motor, the conversion mechanism occurs through complex reactions: at the level of the propellant, at the level of aluminum particles and possibly at the level of the exhaust jet.
We have presented current modelings for these three phenomena and we have highlighted that different levels of modeling are available by assessing the number of reactions and species that are involved in typical reduced chemistry models.
But as soon as coupled phenomena are investigated, simpler chemistry models are used, which does not enable to capture all the physics and threatens the predictability of the approach.

1.4.2.3 Need for hydrodynamic improvement

As regards hydrodynamics, the fluid models that are available and classically used are not questioned to approach SRM flows. But the phenomena of interest, e.g. instabilities, are very sensitive to the coupling to turbulence, to chemical reactions and to the disperse phase. They are also very sensitive to the initial and boundary conditions.
This raises three questions to conclude on the effective level of detail needed

- the role of turbulence, chemistry, and the disperse phase must be assessed;
- the uncertainty on the conditions requires a fine analysis of the sensitivity of the flow to perturbations at the wall, principally those generated by the solid propellant combustion;
- the many roles of the structure and its geometry on the flow must be evaluated.

1.4.3 Modeling needs for two-phase aspects

We now recapitulate the issues raised by the disperse phase to highlight the need for its detailed modeling.
We have seen that the disperse phase plays a major role in SRMs in all the aspects:

- aluminum particles partly drive combustion kinetics and efficiency,
- their combustion is the source of ITHAC and may interact with HI,
- combustion residuals -though chemically inert- take an important part of the modeling effort to predict HI,
- the formation of an accumulated slag,
- they determine the nozzle efficiency.

The different mechanisms and their effects are summed up below.

1.4.3.1 Two-phase losses

In the previous paragraphs, many losses on performance have been attributed to the disperse phase.
The so-called two-phase chemical losses are due to the presence of particles of already oxidized and unburnt metal.
Two-phase slag losses correspond to propellant mass that is not ejected through the nozzle: the condensed matter accumulated in the slag has delivered its chemical energy but has not played its role on thrust, and increases the tare mass in a way that strongly penalizes the motor's performance.
Finally, two-phase lag losses correspond to dissipation due to drag and heat fluxes between gas and particles, that lower the nozzle efficiency.

1.4.3.2 Two-phase effect on stability

We have seen that the condense phase is involved in several recognized and supposed instability mechanisms. First the metal fuel distributed combustion is envisioned as fostering ITHAC and may interact with HI. Second the disperse phase is strongly coupled to the hydrodynamic structures and to the acoustic modes of the chamber flow so that it plays a role on all the instabilities (ODP and ITHAC). This role can be both damping and driving, according to mechanisms that are not completely clarified. Third a more subtle mechanism -prone to trigger instabilities- is the transit of clusters of condensed matter through the nozzle, reemitting perturbations and noise. But the formation of clusters (i.e. disperse phase spatial structures) is coupled to the chamber dynamics through a coupling to the hydrodynamics and through the intermittent ejection of slag material. This retroaction mechanism can therefore exacerbate unstable behaviors.

1.4.3.3 Nanoparticle peculiarities

The phenomenology of nano-propellants is peculiar:

- a larger mass fraction of initial oxide influences the propellant energy content (two-phase chemical loss becomes significant),
- nanoparticle burning rates are different,
- the overall propellant burning rate is enhanced (pseudo-catalytic effect, role of radiation),
- the disperse phase has a different size distribution (nano-residual formation),
- the disperse phase has a different dynamics (velocities and temperatures relaxed but Brownian diffusion),
- the disperse phase encounters a different evolution of its size distribution (due to potentially increased coalescence),

So the behavior of nano propellant SRMs is particularly tricky to assess and is mainly thought to be:

- a reduction of two-phase losses,
- an undefined impact on ODP,
- a reduction of ITHAC, and
- a reduction of slag formation and nozzle erosion.

All these benefits are still hypothetical as long as fine modeling and simulation of nano-propellant based motors has not been performed.

1.4.4 Conclusion on the need for high-fidelity models

The physics of a SRM is complex and the disperse phase plays a first rank role, through various couplings and a rich dynamics. To capture this physics accurately, high-fidelity models are needed to account for physics at a local scale, namely the complex interaction of chemistry and particles with the flow. Some strategies based on high-fidelity models are presented in the following chapter. High-fidelity models may inspire refinements for the low-order models but a comprehensive approach is believed to be needed to understand the physics and allow efficient design.

Chapter 2

A review of strategies for SRM high-fidelity modeling

The physics of a SRM is very complex for who wants to predict accurately performances and stability of the motor. To complete the analytical approaches and the models of Chapter 1, a wide range of high-fidelity models have been developed: they usually account in detail for a part of the physics which has been analyzed to drive a studied phenomenon. We show that the level of accuracy and predictability which is from now desired, requires a comprehensive approach, that solves high-fidelity models in a coupled fashion. And the accurate description of the disperse phase is shown to be incontrovertible.

2.1 High-fidelity models for SRMs

High-fidelity models refer to models where some aspects are taken into account in detail: such approaches translate into equations which depend on space, time and possibly other variables. They are generally intended to be solved with numerical approaches.
Facing the complex phenomenology, such high-fidelity models emphasize different aspects of the physics of SRMs. We aim at briefly presenting them, as well as their limitations. This to show the need for a comprehensive modeling and possibly well suited numerical approaches.
Several aspects of the problem have already been identified and developed independently: propellant combustion (Rahman 2012), particle injection conditioned by the packing (Knott et al. 2001), burnt gas hydrodynamics (Lupoglazoff and Vuillot 1996), 3D geometry (e.g. finocyl), turbulence, aluminum distributed combustion (Lupoglazoff et al. 2002; Sibra 2014), slag accumulation dynamics (Cesco 1997) and fluid/structure coupling (Richard and Nicoud 2011), but they should ultimately be coupled as showed by Vuillot (1998) and Parsons et al. (2000). Computation capacity, memory, visualization etc. have progressed but a fully coupled, unsteady simulation has not been reached up to now.

2.1.1 Chemical equilibrium calculations

Chemical equilibrium computations have been the first numerical approaches applied to SRMs. They aim at assessing the energy content of the motor, given the chemical complexity of the propellant that is used. These approaches started in the 70's and all the current methods are inspired from the original approach of Gordon and McBride (1971). The COPPELIA code at ONERA and the OPHELIE code at Herakles are based on such approaches.
Ultimately, chemical equilibrium models establish the energy budget of the motor at steady state, equivalent to finding the $C^\star$ in the formalism of Eq. (1.15) and the performance of the motor is deduced by proper assumptions on C_F. In practice such approaches allow to assess the temperature and molar mass of the burnt gases as well as the chamber pressure from the initial chemical components, provided that the code is fed with adequate thermochemical data. The JANAF and CHEMKIN II data bases (Chase et al. 1985; Kee et al. 1990) are often used. But some components which are rarely used in industry (e.g. boron) and are therefore not well known as regards their thermochemical properties, may generate species that are not tabulated.
Simple assumptions are made to take into account the condensed inclusions. They limit the validity of the approach to moderate mass fractions. Moreover these approaches cannot account for disperse phase losses, nor unsteadiness (instability). The chemical equilibrium computations remain however a precious tool for SRM designing as long as rate controlled physics is not involved. Finally, the now traditional chemical approach used can be a source of inspiration to include chemistry in more complete codes.

2.1.2 Chamber stability analysis

The original approach to motor stability is the so-called Acoustic Energy Budget (Hart and Mc Clure 1965; Culick 1966a). It was extended to all kinds of perturbation structures, not only acoustic modes and is then referred to as Fluctuating Energy Budget (Flandro 1985; Flandro 1986; Radenac 2011).
Fluctuating Energy Budget can include chamber, nozzle and disperse phase damping, providing that their response can be modeled (Gossant 1993; Vuillot and Lupoglazoff 1996). In the case of propellant combustion instabilities, the propellant response is accounted for e.g. through a transfer function in linear theory (Baum and Denison 2012; Rahman 2012). Such approaches can predict some instability frequencies but not their levels.
Still SRM stability is not well predicted as important modes are missing (Vuillot and Lupoglazoff 1996), even with improvements such as the inclusion of vortex shedding (Flandro 1986), particularly VSP (Flandro and Majdalani 2003). Efforts towards the inclusion of more two-phase effects are done (Radenac 2011) e.g. in the context of ITHAC modeling.
A comprehensive approach to linear stability has been purposely developed for SRMs from the work of Griffond and Casalis (2001): it is referred to as Biglobal Analysis (Chedevergne et al. 2006) and a review of its achievements can be found in Chedevergne et al. (2012).

2.1.3 Single-phase flow computations

Single-phase flow approaches consist in treating the flow in the chamber and the nozzle with a fluid model such as Navier-Stokes equations, possibly multi-species and/or with an Equivalent Gas approach for the disperse phase. Such a model is detailed in § A. Several aspects of SRM flows have been investigated with single-phase computations and there is a wealth of literature on the subject.

2.1.3.1 Early computations

The Equivalent Gas approach (EG), is used to assess simply the effect of particles. It results in a single-phase modeling, more details being provided in § 3.2.4.2.
The first computations of a full chamber and nozzle were performed in 2D and allowed to confirm the general hydrodynamic behavior, such as the existence of VSA and VSO (Lupoglazoff and Vuillot 1992). But these early computations eventually led to the discovery of a new type of hydrodynamic instability, peculiar to wall injection and SRMs, the VSP (Lupoglazoff and Vuillot 1996; Lupoglazoff and Vuillot 1998b).

2.1.3.2 Capturing turbulence

The role of turbulence is important and badly known as explained in § 1.3.2.2. It has been assessed continuously, though in the context of single phase flows.
The Direct Numerical Simulation of SRM turbulence was attempted (Nicoud 1995; Venugopal 2003; Chedevergne et al. 2012) but not in the context of a complete geometry, which is out of reach. In the perspective of performing efficient numerical simulations including turbulence, modeled approaches have therefore been envisioned, namely in the RANS formalism (Chaouat 1994) and in the LES formalism (Silvestrini et al. 1995; Silvestrini 1996; Najjar et al. 2002; Apte and Yang 2003; Wasistho and Moser 2005; Dupuy 2012).
The RANS approach has yielded lukewarm results either in cold gas (Avalon et al. 2000) and in reactive cases (Gallier et al. 2004). And it is pursued in the context of advanced models e.g. second order non-linear stress models (Chaouat and Schiestel 2005), or SAS models (Menter and Egorov 2010): it can be fitted satisfactorily whenever the transition point is known. As for LES approaches, which aim at avoiding fitting, today's sub-grid scale closures struggle to reproduce the small knowledge that is available.
The influence of many sources of perturbation on the turbulence transition point can be strong such as that of wall roughness, propellant flow rate fluctuations, combustion processes, or disperse phase (see § 1.3.2.2): DNS studies are planned to understand the mechanisms while modeling approaches have been developed, based on dedicated noise injection at the wall Dupuy (2012). In general, the development of two-phase turbulent models is an active and challenging area of scientific research and is briefly discussed in § 3.6.2.

2.1.3.3 Fluid-structure coupled simulations

The role of fluid-structure interaction has been assessed in many different contexts:

- propellant surface regression (Fiedler et al. 2001), which plays an obvious role on flow patterns and chamber resonance,
- PTF flapping (see § 1.2.1.3) (Della Pieta et al. 2001; Richard and Nicoud 2011; Errera et al. 2011; Cerqueira 2012; Richard 2012), which was proven to excite ODP through VSO,

- casing vibration (Errera et al. 2011), which acts as an ODP damper (Richard and Nicoud 2011; Richard 2012),
- mobile nozzle deployment, which may trigger flow separation,
- PTI spoiling and breach.

2.1.3.4 Conclusion on single-phase flow approaches

The numerical resolution of a single-phase flow allows to model many phenomena, that can be verified separately versus simplified experiments. The ability to simulate each phenomenon (hydrodynamics, acoustics, turbulence, complex geometry evolution) independently has reached a satisfactory level of maturity.
However, since the disperse phase is then accounted for with equilibrium models (detailed in § 3.2.4.2), many two-phase aspects are missed such as the driving of oscillations or the linear damping of acoustic waves (see § 4.7.5 for more details on the latter aspect).

2.1.4 Two-phase flow computations

Two different strategies have been explored in the literature to address the detailed physics of two-phase SRM flows. These two strategies are referred to as Euler-Lagrange and Euler-Euler, where the carrier phase is always modeled with a Eulerian approach, to benefit from the experience from single-phase computations. The existence of two very different paths to address the disperse phase illustrates the difficulty to find a satisfactory approach. Euler-Lagrange and Euler-Euler achievements in SRMs are now overviewed.

2.1.4.1 Euler-Lagrange approaches

The Euler-Lagrange technique for disperse two-phase flows typically resorts to a fluid approach for the gas phase coupled to a Direct Simulation Monte-Carlo approach for the disperse phase. This approach is detailed in § 4.2.
The two-phase flow in SRMs was early assessed with Euler-Lagrange approaches, as regards slag accumulation (Cesco et al. 1996; Cesco 1997) or turbulent flow (Gailliegue 1998). The two-phase acoustic interaction was evaluated with an Euler-Lagrange approach (Cai et al. 2003), including a two-phase turbulence model, the SSM model (Shuen et al. 2004). Distributed combustion has been included in simulations (Sabnis 2003): the interest for this feature has now increased as it is at the origin of ITHAC. The role of particle radiation has also been taken into account with an Euler-Lagrange approach (Duval 2002; Duval et al. 2004).
Models including coalescence were developed very early for Euler-Lagrange approaches (Hylkema 1999), that could be used in realistic geometries only recently (Estivalezes 2010; Estivalezes 2011) because of the computational cost. The latter reference provides 3D unsteady computations of a P230 with coalescence. In these cases, the relevance of Euler-Lagrange approaches in massively parallel architectures is discussed in § 4.2.3 and a practical illustration is given in § 15.4.

2.1.4.2 Euler-Euler approaches

The Euler-Euler technique for disperse two-phase flows resorts to a fluid approach for the gas phase coupled to a similar Eulerian approach for the disperse phase, some typical Eulerian approaches being presented in Chapter 4.
Because of the limits of equilibrium approaches, slightly out-of-equilibrium methods were developed to render velocity lags (Ferry and Balachandar 2001; Ferry and Balachandar 2002) and temperature lags (Ferry and Balachandar 2005) and their effects on the flow, partly achieving two-way coupling (Ferry and Balachandar 2001).
The Eulerian approach for two-phase turbulent flows in the context of LES was introduced by Fevrier et al. (2005) and used for SRM computations (Simoes et al. 2005; Simoes 2006).
The role of polydispersity, known to be crucial as detailed in § 3.1.2, has been assessed in the case of ODP by Dupays et al. (2008) and where its calculated impact has been confirmed by comparison to a hot gas sub-scale experiment. But the results are very dependent on size distribution input data, as discussed in § 1.2.3.2 and on the evolution of size under coalescence. So that approaches that can account for the evolution of droplet sizes under injection, combustion and coalescence are desirable. Coalescence is modeled in the present thesis and computations are led in § 15.3.2.3 to extend the results of polydispersity impact on ODP when coalescence occurs.
The numerical simulation of ITHAC was performed in Gallier et al. (2009) and in Gallier and Godfroy (2009) by taking into account the propellant surface regression thanks to a deforming mesh approach. Comprehensive approaches, including polydispersity and advanced aluminum combustion modeling are developed to capture ITHAC (Sibra 2014).

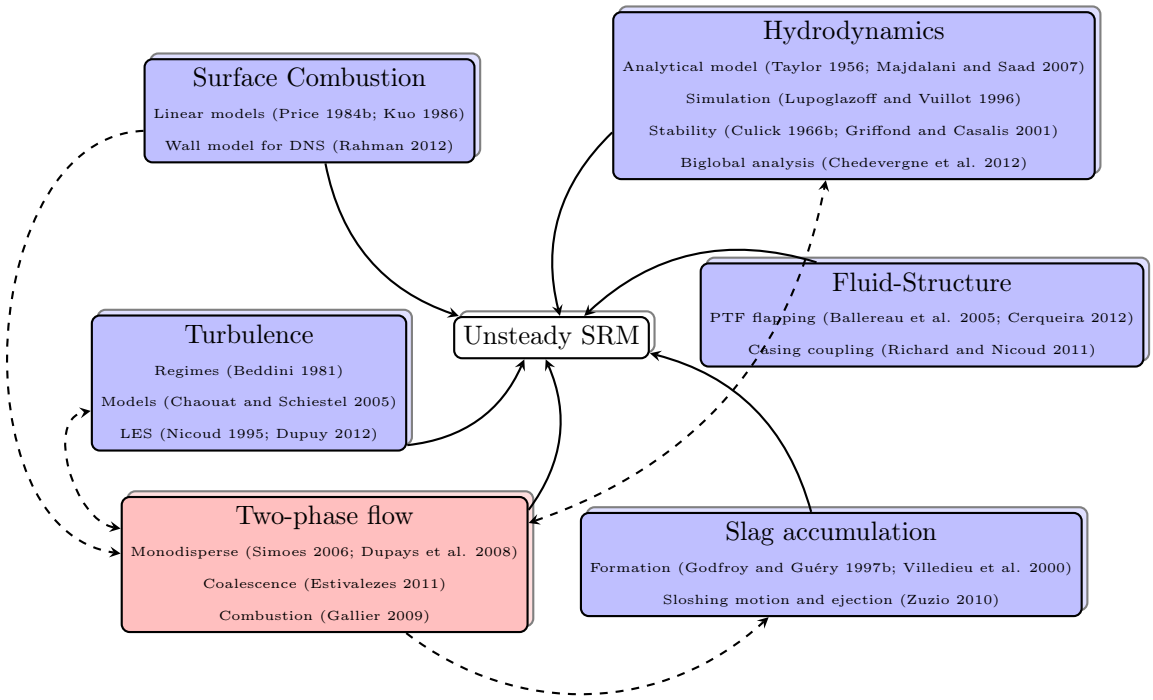

Figure 2.1: *High-fidelity simulation achievements as the ingredients for an unsteady SRM predictive simulation – Two-Phase coupling needs: - - -.*

2.1.5 Conclusions on SRM numerical approaches

As said previously, the simulation ability of many phenomena considered independently (hydrodynamics and acoustics, turbulence, complex geometry, chemistry) has reached a satisfactory level of maturity. Yet single-phase approaches do obviously not render the peculiar behavior of two-phase flows, e.g. the velocity and temperature lags, and their effects on the flow.
We have described the state of the art of the numerical simulations that are able to render two-phase aspects: different approaches are still under development. This shows that SRM two-phase flow simulation is not mature and requires efforts at each level: modeling, numerical methods and validation. In the present thesis, we propose to improve models and methods as regards the disperse phase and its coupling to the gas.
In the long-run, the objective is to couple all the single-phase features to satisfactory two-phase models, as illustrated in Figure 2.1, in order to achieve predictive simulations. A comprehensive CFD approach is sought, that could solve two-phase aspects (both inert and reactive) and account for turbulence, moving meshes and complex chemistry.

2.2 Some modeling prospects for simulation

The success of the inclusion of polydispersity related features (coalescence, break-up), for SRM computations must not hide the remaining developments needed to achieve predictive simulations.

2.2.1 Aluminum distributed combustion

The treatment of aluminum distributed combustion by a polydisperse Eulerian approach is highly desirable to design future motors and predict ITHAC. This requires a modeling effort but also finely designed numerical methods: capturing accurately coupling and unsteadiness is needed in the general context of instabilities. These demanding numerical features must still be developed in the context of HPC for industrial simulations so they must resort to efficient methods. These developments are done at ONERA in the context of a PhD Thesis (Sibra 2014).

2.2.2 Towards two-phase LES

The treatment of turbulence is not a priority in SRMs as its effects have been identified as limited. But it will become more and more important, provided that the desired levels of accuracy on computations increase continuously, and that computation capacities allow to tackle it.

The use of Large Eddy Simulation (LES) is the only reasonable approach, considering that DNS cost is out of reach.
It is well-known in single-phase turbulence that LES requires numerical methods that are specific. As an illustration, accurate and well-known schemes (as regards dissipation and dispersion) are chosen to prevent the scheme to introduce some unexpected effects that could be interpreted as physical (e.g. scheme dissipation), while explicit filtering procedures are envisioned to increase the level of control on the physics.
In the case of the high mass loadings of the disperse phase, such as in SRMs, it is conceivable that the very structure of the turbulence is partly driven by the disperse phase. Yet, the modeling of moderately dense turbulent flows is still an active research topic, as discussed in § 3.6.2.
Finally, the cost of LES in a two-phase context, as it features complex geometries, with fine meshes *etc.* promises to be important, compared to the usual SRM computations. For instance, these simulations are necessarily 3D, while many cases are computed in 2D up to now: attempts of 3D computations with a Lagrangian approach proved to be costly and to require a compromise on Lagrangian convergence levels (Estivalezes 2011).

2.2.3 Other prospects

In the context of a high number of degrees of freedom, more modeling is required to account for the correlations between phenomena, which are unknown *a priori*.
Non-linear coupled phenomena need to be finely modeled e.g. combustion-radiation-chemistry coupling (Lecanu 2005). In the case of two-phase flows, new behaviors emerge and again no superposition principles can prevail e.g. the case of two-phase flows with radiation generating new kinds of turbulent structures (Zamansky et al. 2012).
Moving meshes and remeshing techniques are needed, as they proved to be efficient techniques to address geometry effects which are themselves physically significant. For instance, they are remarkably needed for propellant regression, which is discussed in § 1.2.1.2, PTF flapping, which is a major VSO source (see § 1.2.1.3), and mobile parts, as discussed in § 1.2.1.4.
A coupling with propellant combustion modeling, using advanced models and wall boundary conditions (Rahman 2012) is desirable. In particular, the latter conditions depend on the propellant packing, which aspects should be included in the simulations.
The treatment of shock-droplet interaction also requires further modeling e.g. in the case of ignition (Benkiewicz and Hayashi 2002) but also for the modeling of the nozzle flow (Crowe et al. 1964). However the methods used to reach the required accuracy, see for instance (Oran and Boris 2001; Benkiewicz and Hayashi 2002; Billet et al. 2008), are not compliant with the efficiency needs of HPC.

2.3 Conclusion on high-fidelity simulation needs

As a general conclusion of SRM modeling, high-fidelity approaches are necessary, due to the complex physics, to assess performances as well as stability. And the accurate description of the disperse phase and the two-way coupling with the carrier phase is particularly desirable.
This requires a well chosen model and method to describe in detail the complex physics of the disperse phase, especially its polydisperse features: the method must be nonetheless accurate but also:

- flexible to allow the inclusion of many physical models, in a coupled way,
- compliant with the requirements of HPC to allow detailed computations,
- robust to spare so-called engineer-time.

The following chapters are devoted to the detailed description of two-phase approaches and to the choice of a well-suited one for SRM modeling. Chapter 3 presents the different levels of modeling while Chapter 4 gives methods to solve the so-called "fluid-kinetic approach", which is finally retained. Finally Chapter 5 and Chapter 6 propose a detailed study and the development of relevant methods to practically solve the chosen model.

Figure 2.2: *Ariane 5 take-off. (source: ESA)*

Part II

Models and methods for moderately dense polydisperse two-phase flows

Chapter 3

Disperse two-phase flow modeling

The general aspects and the phenomenology of two-phase flows are presented and the specific case of disperse phase flows is introduced. The notions of polydispersity, polykineticity and dense flows are detailed as well as some elements to classify disperse phase flows. The precise modeling of two-phase flows is then considered. We first consider the case of continuum mechanics, where the carrier phase modeling is presented as well as the various levels of description of two-phase flows. In particular the closures at the level of spherical particles are described. Second, general aspects of statistical modeling are presented before extensively considering the kinetic modeling of a disperse phase. The fluid-kinetic model is finally chosen as our basis approach for a disperse phase strongly coupled to a gas and some issues are discussed as a conclusion, such as the level of detail chosen as regards turbulence.

3.1 Classification of two-phase flows

A wealth of literature exists on two-phase flows, classifying their complex regimes and deriving fundamental and modeled equations (Ishii 1975; Crowe et al. 1998; Drew and Passman 1999; Sirignano 2010; Ishii and Hibiki 2010; Kah 2010). The phenomenology and the regimes of two-phase flows are described.

3.1.1 Phase topology

3.1.1.1 Definition of phases

The notion of phase is more complex than it seems and has received several definitions, see for instance Landau and Lifshitz (1988). It is first defined as a region of the thermodynamic parameter space of a substance where the free energy is an analytic function: the usual concepts of liquid state, gas state, and the different states of a solid (crystals, amorphous *etc.*) obviously tally with this definition. A substance can evolve, within the same phase, by smooth thermodynamic changes; on the contrary it evolves from a phase to another by discontinuous jumps of some thermodynamic parameters, so-called phase transitions. So the borders of the phases in a thermodynamic phase diagram are the transition lines.
By extension, we consider as phase the spatial region where the matter is present under the form of a unique thermodynamic phase, although the thermodynamic functions may not be uniform throughout the phase. The spatial borders of a multiphase system are the interfaces. They are characterized by specific physical phenomena e.g. light diffraction between two transparent media, which makes the interface familiarly easy to spot.
The material densities of the phases are local quantities corresponding to the mass density of pure phase i, defined as

$$\rho_i(\boldsymbol{x}) = \frac{m_i(\boldsymbol{x})}{\mathcal{V}_i(\boldsymbol{x})} \tag{3.1}$$

where $\mathcal{V}_i(\boldsymbol{x})$ is a control volume containing only phase i and $m_i(x)$ the mass of i within $\mathcal{V}_i(\boldsymbol{x})$, as shown in Figure 3.1. Material densities are independent of the two-phase status of the flow and correspond to the actual thermophysical properties of the phase material: we use in the following ρ_g to refer to the gas, ρ_l for any liquid, ρ_{Al} for aluminum, and $\rho_{\mathrm{Al_2O_3}}$ for aluminum oxide.
Quantities are then defined for the multiphase flow. The volume fraction α_i of a phase is defined on a local volume of two-phase mixture $\mathcal{V}(\boldsymbol{x})$:

$$\alpha_i(\boldsymbol{x}) = \frac{\mathcal{V}_i(\boldsymbol{x})}{\mathcal{V}(\boldsymbol{x})} \tag{3.2}$$

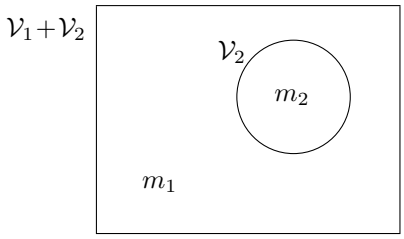

Figure 3.1: *Control volumes for the definition of phasic quantities of a multiphase flow.*

with $\mathcal{V}(\boldsymbol{x}) = \sum_i \mathcal{V}_i(\boldsymbol{x})$, the volume average being performed on a sufficiently large volume to get a smooth function of $\boldsymbol{x}$. And the mass fractions read:

$$Y_i(\boldsymbol{x}) = \frac{m_i(\boldsymbol{x})}{m(\boldsymbol{x})} \tag{3.3}$$

where the $m_i(\boldsymbol{x})$ are the masses enclosed by $\mathcal{V}_i(\boldsymbol{x})$ with $m(\boldsymbol{x}) = \sum_i m_i(\boldsymbol{x})$. They are all extensive quantities. We finally define the multiphase flow density ρ:

$$\rho(\boldsymbol{x}) = \frac{m(\boldsymbol{x})}{\mathcal{V}(\boldsymbol{x})} = \frac{\sum_i m_i(\boldsymbol{x})}{\sum_i \mathcal{V}_i(\boldsymbol{x})} \tag{3.4}$$

which yields the fundamental relation

$$\rho Y_i = \rho_i \alpha_i. \tag{3.5}$$

3.1.1.2 Interface

The space evolution of the interface needs to be modeled as well as the transfers that occur through it: classical laws, that are applicable in most cases, are provided below. In many problems of interest, unfortunately, the interface geometry is very complex and requires averaging, statistical, or even fractal mathematical methods. In many fluid simulations moreover, the interface results in a discontinuity of some variables.
The shape of the interface, its curvature and wrinkles, in brief its complexity are driven by the competition between surface tension and strain as estimated by a Weber number. Weber numbers compare dynamic forces to surface ones, as estimated by the surface tension σ_{lg}. With L a characteristic length of the interface, such comparison can either resort to a liquid Weber if dynamic forces on the interface are mostly provoked by the motion of the liquid:

$$\mathrm{We}_L^l = \frac{\rho_l L \mid \boldsymbol{u}_l - \boldsymbol{u}_g \mid^2}{\sigma_{lg}} \tag{3.6}$$

or to an aerodynamic Weber number if the liquid moves as an ensemble against a gas flow:

$$\mathrm{We}_L^a = \frac{\rho_g L \mid \boldsymbol{u}_l - \boldsymbol{u}_g \mid^2}{\sigma_{lg}}. \tag{3.7}$$

Weber numbers are static criterions i.e. accounting for the interface equilibrium; whereas the interface dynamics comes down to the value of the Ohnesorge number Oh:

$$\mathrm{Oh}_L = \frac{\mu_l}{\sqrt{\sigma_{lg}\rho_l L}} \tag{3.8}$$

implying the viscosity μ_l of the liquid material and which relates the viscous forces to surface tension ones. The interface may also feature complex behaviors due to surface tension wherever it gets into contact with walls, which requires specific modeling: see for instance the case of membranes, emulsions, *etc.* (Lepercq-Bost et al. 2008; Lepercq-Bost et al. 2010). Droplets in a gas feature complex capillary and wetting properties (Quéré et al. 1990; De Gennes et al. 2003), which are still an active research topic, in order to find materials that ensure non-sticking (Quéré 2005), bouncing (Richard et al. 2002), self-propelling (Bico and Quéré 2002), *etc.* unconventionnal properties, that are interesting for various applications e.g. fabrics and mechanical engineering. The wall contact properties are often discussed in the gravity field and resort to capillary numbers.
To conclude, it is highlighted that two-phase flow modeling strongly depends on the interface topology. It conditions the transfers between the phases and therefore the overall dynamics of the flow.

Figure 3.2: *Visualization of the primary atomization of two jets – Left: experiment (ESPCI); Right: interface tracking simulation (Pr. Zaleski).*

3.1.1.3 General case of separate phases

When the interface is complex and none of the two phases has a remarkable geometry, the flow is said to be separate-phase. In this case, the bulk kinetic energy is significant compared to the interface energy.
These flows are widely studied as they occur in oil extraction, nuclear thermo-hydraulics and so forth: a complete literature on two-phase pipe flows exists, for which flow regime charts (churn, plug, slug *etc.*) have been built and the corresponding transfer laws have been established from mass flow rates, see for instance Delhaye (2008) and Kah (2010). These flows are also a focal point of energy conversion systems as they occur in the atomization process (Lefebvre 1989) so that they have received particular attention, see for instance Gorokhovski and Herrmann (2008) and Le Chenadec (2012).
The increase of the interface density under specific flow conditions, is referred to as atomization: the modeling issues are detailed in Appendix C, where a new modeling strategy is suggested. Let us discuss for now only the main aspects of atomization, in the context of the present overview. The liquid Weber number We_L^l is the key parameter of primary atomization and the aerodynamic Weber number We_L^a rather describes secondary atomization. These Weber numbers characterize the density of interface at equilibrium as regards surface tension and dynamic efforts. So they reflect the intensity of the atomization process and therefore its multi-scale character: We_L^l and We_L^a play a similar role for atomization as the Reynolds number Re does for turbulence, indicating the number of relevant degrees of freedom of the system.
Disperse phase flows, hereafter described, can result from the primary atomization process. The modeling of pure disperse flows is eased by the fact that the interface topology is fixed and is most of the time weakly coupled to the surrounding flow. But when both regimes simultaneously occur, typically during the atomization process itself, it is remarkably difficult to account in detail for the separated phase domain and to account efficiently for the spray regime. The modeling of such transition is a key point in mastering many separate-phase flows (Kah 2010), especially those where atomization is expected and where the resulting disperse phase is the desired final state, e.g. for combustion.
In the case of a SRM, the issue of separate-phase flows occurs in very specific regions, for the modeling of slag accumulation (see § 1.2.4.1). In addition, such approaches can be a source of inspiration to model the break-up of dense flows, as attempted in Appendix C. But the peculiarities of separate-phase flows are still mostly disregarded in the present overview, and we focus on disperse phase flows from now on.

3.1.1.4 Particular case of a disperse phase

A specific two-phase flow regime is of particular interest in the present work: a phase is diluted enough -i.e. with not too high a volume fraction- to allow distinct packets to form and the flow is smooth enough for the packets to be spherical. This regime is referred to as disperse and the non-continuous phase is the disperse phase.
The disperse phase can have a lower material density such as in bubbly flows but if it has the highest material density, it has a significant impact on the dynamics of the flow as it balances its low volume fraction by a significant mass fraction, having a particular role regarding momentum, heat, or species.
Contrary to the case of separate-phase flows, a direct interface resolution can be avoided in the case of a disperse phase flow, if the inclusions are spherical enough. Hence the computation cost is no longer linked to the Weber number. Moreover, thanks to the sphericity of the inclusions, (or the constancy of their shape in the case of particle-laden flows) the inclusions have so few degrees of freedom that volume average approaches are convenient and statistical approaches, based on kinetic theory, become possible.
Among the possible configurations for disperse phases, the case of a continuous liquid with disperse gaseous inclusions is briefly presented. So-called bubbly flows have been widely studied in the context of nuclear power plants, for instance. The boiling crisis that may occur in pressurized water reactors triggers the formation of bubbles that modify the wall heat flux in an sensitive way (Lemonnier and Rowe 1988; Lemonnier and Selmer-Olsen 1992; Delhaye 2008).

Regarding the very low mass fraction of bubbles, they do not modify the momentum and the energy of the flow -at least for a reasonable volume fraction- but they play a central role on the properties of the bulk flow, modifying turbulence, viscosity and heat transfers *etc.* A remarkable illustration of the role of a gaseous disperse phase on the two-phase medium properties is the peculiar acoustics of bubbly flows, with sound waves traveling in an unprecedented way (Drew and Passman 1999).
The case of bubbly flows is no longer discussed and we now consider the case of condensed inclusions.

3.1.1.5 Gas with disperse condensed inclusions

When the continuous phase is gaseous, the disperse phase is liquid (aerosol, fog, mist, spray) but solid inclusions can often be modeled with the same approaches (particles, sand, smoke, dust, haze), as long as a clear-cut interface can maintain itself: the disperse phase is then referred to as condensed to highlight its higher density. A classification of particle-laden flows is suggested in Guazzelli (2003). For instance the following mechanical engineering applications feature a disperse condensed phase:

- hydrocarbon fuel is most of the time injected as a liquid phase in the combustion chamber (direct injection piston engines, aeronautical and gas turbine burners, industrial furnaces),
- the combustion residuals of metal fuels in solid rocket motors remain condensed (even in the very high chamber temperatures),
- the liquid fuel of LREs is atomized and burns as a liquid at engine start and if operated at a sub-critical pressure.

So the case of liquid jet atomization is a major issue. An experimental injection, given in Figure 3.3, shows how the atomization process starts with a characteristic separate-phase flow but ends up as a disperse two-phase flow or spray, which is the very purpose of atomization i.e. to increase the exchange surface of the liquid phase. In SRMs however, the process that leads to the presence of a disperse phase is not atomization but the dragging of disperse particles from the propellant surface, and their combustion, as presented in Chapter 1.

Figure 3.3: *Generation of a polydisperse spray from the primary atomization of a jet – Experiment by C. Dumouchel (CORIA).*

Let us consider a two-phase with a gaseous $i = g$ phase and a disperse, condensed phase $i = c$. The assumption of a disperse phase translates into $\mathcal{V}_c \ll \mathcal{V}_g$ so that the volume fractions as defined in Eq. (3.2) can be assessed:

$$\alpha_c \ll 1 \quad \text{and} \quad \alpha_g \approx 1. \tag{3.9}$$

In the case of moderately dense sprays, still, the disperse phase mass fraction, as defined in Eq. (3.3), is considered to be significant by definition so that

$$Y_c = \mathscr{O}(1) \quad \text{as well as} \quad Y_g = \mathscr{O}(1). \tag{3.10}$$

So we get the simplified relation:

$$\rho = \rho_g + \alpha_c \rho_c \tag{3.11}$$

after neglecting the volume occupied by the condensed phase thanks to Eq. (3.9).
Along with the mass fraction, another way to describe the respective mass occupation of the two phases is to define the mass loading:

$$C = \frac{m_c}{m_g} \tag{3.12}$$

which indicates the predominance of the disperse phase compared to the carrier phase. The following relation is always verified:

$$C = \frac{Y_c}{1 - Y_c} \tag{3.13}$$

and it shows the origin of a frequent confusion between mass fraction and mass loading, since the two numbers are very close for small mass fractions. For denser cases however, they are very different as the mass fraction is limited to 1 while the mass loading may take any positive value.

3.1.2 Size dispersion: Polydispersity

Polydispersity refers to the fact that the inclusions have many different sizes: therefore it mostly applies to disperse phase flows. Polydispersity is opposed to monodisperse sprays and is a common feature of particle-laden flows and sprays (Mugele and Evans 1951) but its strength and the ways to quantify it depend on the application. We consider from now on the case of spherical inclusions, the geometry of which is therefore parameterized by a unique variable, either radius r, surface S, or volume v.

3.1.2.1 Phenomenology of polydispersity

The particles exchange mass, momentum and enthalpy with the carrier phase at a rate which depends on the interface density. Thus the particle size is a crucial parameter for this physics and the particle size distribution drives the two-phase flow dynamics. Characteristic momentum and heat transfer time scales, noted $\tau^{\boldsymbol{u}}(S)$ and $\tau^T(S)$ respectively are compared to a typical evolution time of the gas τ_g through the so-called Stokes numbers:

$$\mathrm{St} = \frac{\tau^{\boldsymbol{u}}(S)}{\tau_g} \quad \text{and} \quad \mathrm{St}^\theta = \frac{\tau^T(S)}{\tau_g}. \tag{3.14}$$

We distinguish a dynamic and a thermal Stokes number as they may be different; however, momentum and heat transfers always occur with respect to the particle surface and are very close in most cases. In addition, the velocity and temperature relaxation times always decrease with the square of the particle diameter. The Stokes number is a dimensionless parameter of crucial importance for particles in a flow: it is universally used in the literature but its definition may vary, depending on the chosen time τ_g for the gas.

3.1.2.2 Defining effective polydispersity

A more pragmatic definition of polydispersity consists in considering it as effective (or recognized) in the following case: particles of different sizes -in the sense that they yield significantly different behaviors regarding a given phenomenon- are present in a substantial amount.
If it depends on the particle size, a physical phenomenon may be proportional, to the surface (e.g. exchanges) to the volume (e.g. inertia) or to any other function of size. So polydispersity becomes troublesome when physical phenomena are considered, that have different dependencies.
This is the case in SRMs, see for instance (Kovalev 2002), for which the problem is clearly multi-scale: some typical characteristic times are presented in Table 3.3 as an illustration. Effective polydispersity then raises many modeling issues (Sellens 1989; Babinsky and Sojka 2002), for which we propose detailed solutions in the present thesis.
The issue and the quantification of effective polydispersity is discussed for the particular aspects of two-phase acoustics in § 7.1.3.

3.1.2.3 Size modeling on average

Even though particles with different sizes have different behaviors, the overall effect of the spray may sometimes be represented through a monodisperse model spray, given a well-chosen diameter (Loth 2000; Alderliesten 2004a; Alderliesten 2004b), as illustrated in Peirano and Leckner (2000) for the general case of fluidized bed flows. Otherwise if the particle heterogeneity of sizes leads to a physical behavior that is not observed with any monodisperse spray, then polydisperse approaches are mandatory. This is necessarily the case when:

- the particle response to at least two phenomena varies in a different way with particle size,
- the particle response is non-linear (size coupling).

This is the case in SRMs as distributed combustion, acoustics and hydrodynamics have a dependency to different particle size functions.
In industrial contexts, the knowledge of size distribution is rarely complete: an average diameter has to be approximated and then becomes the sole parameter. A size distribution function $\kappa^{(\phi)}$ is considered, e.g.

Category	Regime	$\mathrm{St}/\mathrm{St}_c$
Very small	neglected inertia	$\ll 1$
Small	low-inertia	< 1
Medium	moderate-inertia	~ 1
Large	high-inertia	> 1

Table 3.1: *Particle categories and the associated vocabulary.*

depending on the particle radius $\phi = r$, in which case $\kappa^{(r)}$ is expressed in $[\mathrm{m}^{-3}.\mu\mathrm{m}^{-1}]$. A size moment M_p^I of order p on an interval $I = [r_1, r_2]$ can then be defined:

$$M_p^I(\kappa^{(r)}) = \int_I r^p \kappa^{(r)}(r)\mathrm{d}r \tag{3.15}$$

besides $\kappa^{(s)}(S)\mathrm{d}S = \kappa^{(r)}(r)\mathrm{d}r$ so that the relation can be written in surface variable with $I = [S_1, S_2]$:

$$M_p^I(\kappa^{(s)}) = \int_I \left(\sqrt{\frac{S}{4\pi}}\right)^p \kappa^{(s)}(S)\mathrm{d}S \tag{3.16}$$

We also define the average diameters of order $p - q$ from the particle diameter $d = 2r$ as:

$$(d_{pq})^{p-q} = \frac{\int_I d^p \kappa^{(d)}(d)\mathrm{d}d}{\int_I d^q \kappa^{(d)}(d)\mathrm{d}d} \tag{3.17}$$

which read from the moments:

$$(d_{pq})^{p-q} = \pi^{\frac{q-p}{2}} \frac{M_p^I(\kappa^{(s)})}{M_q^I(\kappa^{(s)})}. \tag{3.18}$$

As an illustration, the d_{32} is commonly used and referred to as the Sauter Mean Diameter.

3.1.3 Velocity dispersion: Polykineticity

In the lineage of the importance of polydispersity, we qualitatively highlight the main behavior differences brought about by particles of different sizes regarding local velocity distributions: the co-existence of several velocities at a location is a peculiarity of the disperse phase, referred to as polykineticity. This fact is opposed to monokineticity i.e. one velocity for all the particles in a given vicinity. Sainsaulieu (1995a) and de Chaisemartin (2009) describe monokineticity as a velocity equilibrium for the disperse phase, by analogy with the local thermodynamical equilibrium in the kinetic theory of gases, yielding a hydrodynamical limit. In return polykineticity corresponds to an out-of equilibrium state. The different regimes of occurrence of polykineticity are now assessed and the main consequences are described.

3.1.3.1 Different categories of polykineticity

As the velocity relaxation time increases with particle size, we expect that small particles will have a velocity close to the gas while bigger particles will have their own velocity, conditioned by their history. Particle advection is then classified in different regimes that depend on the dynamic Stokes number St. Whatever the detailed structure of the flow, we can distinguish particles of a given size in different regimes so that particles of this given size have velocities that are locally:

(i) equal to the gas velocity (or non significantly deviated),
(ii) significantly deviating from the gas velocity but correlated altogether,
(iii) significantly deviating from the gas velocity but slightly dispersed around a unique velocity,
(iv) more or less uncorrelated.

The corresponding particles are referred to as (i) very small, (ii) small, (iii) medium and (iv) large. In the following, we designate either the category of particles, the inertial regime or the Stokes number, according to an equivalence of vocabulary given in Table 3.1.

As an illustration, we consider a polydisperse spray featuring all these regimes, the typical size-velocity PDF is expected to have a form as the one described in Figure 3.4, where it can be seen that size-conditioned velocity distributions become more complex as inertia grows. The typical modeling characteristics that are required to capture this complexity are summed up in Table 3.2, with the corresponding degrees of freedom (DoF) that should be taken into account, accordingly to the levels of correlation described above.

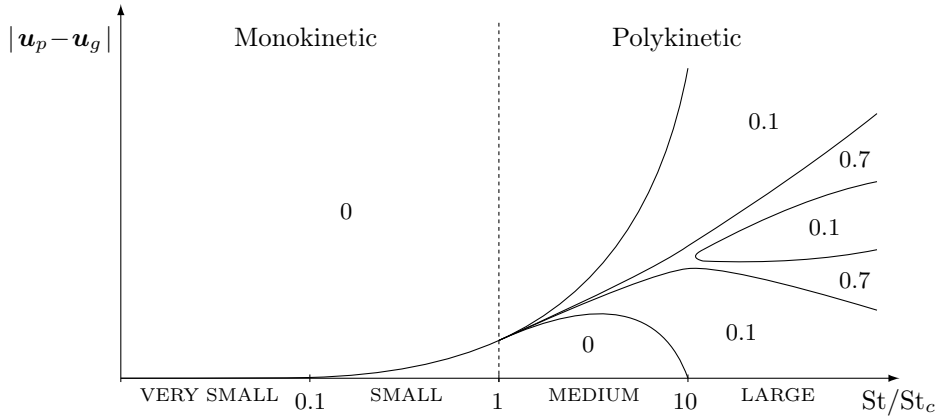

Figure 3.4: *Typical size-velocity PDF as a chart of the different inertial regimes.*

Category	DoF	Relaxed quantities	homo-PTC
Very small	none	aver. to gas, disp. to 0	No
Small	aver.	disp. to 0	No
Medium	aver., disp.	distrib. shape	Small scale
Large	whole distrib.	none	Large scale

Table 3.2: *Particle categories and the associated physics (for velocities or temperatures) at a given particle size.*

One of the main purposes of the above classification is to categorize the so-called Particle Trajectory Crossing phenomenology. Polykineticity occurs when the flow features any kind of velocity fluctuations (inhomogeneity and unsteadiness): vortices, strain, turbulence drive polykineticity to adopt different structures but a characteristic time can always be worked out and noted τ_g. Depending on the authors, the gas time scale can be based:

- on fixed scales with a physical meaning, e.g. Kolmogorov's turbulent scale (Kolmogorov 1941);
- on the mathematical definition of the local strain rate.

These approaches yield a critical Stokes number above which crossings occur, e.g. $\mathrm{St}_c = 1/(2\pi N_d)$ for Taylor-Green vortices (see § 11.4.2) where N_d is the dimension of the physical space.
The occurrence of significant slip velocities for inertial particles has been assessed in a turbulent field by Simonin et al. (2002). As an illustration in a Taylor-Green vortex, Figure 3.5 shows the velocity vectors: the existence of a slip velocity between particles and the gas, due to particle inertia, brings the latter to form singularities. Figure 3.6 gives the particle velocities in a radial cut in Taylor-Green vortices for different sizes: the velocities are smooth and null at the edge up to $\mathrm{St} = \mathrm{St}_c$ but discontinuities appear, and multivariate velocities occur above.
As for SRMs, all the crossing regimes are encountered, possibly in different regions of the motor for a given particle size, as the motor includes vortices, strain and turbulence with very different characteristic times. They are illustrated in Figure 3.11, based on a typical particle behavior.
Finally, a dispersion of particle temperatures can also occur, depending on the thermal Stokes number St^θ. As temperature does not directly influence the particle transport, temperature dispersion is less emphasized

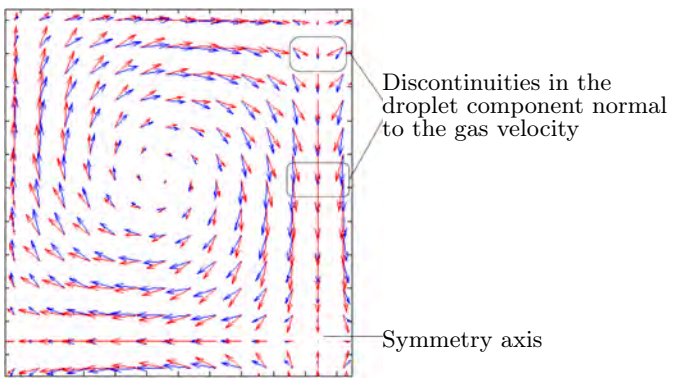

Figure 3.5: *Velocity fields for the gas flow (Blue) and particles with $St = 4St_c$ (Red) showing a centrifugal component yielding velocity discontinuities and possibly concentration singularities (courtesy: S. de Chaisemartin).*

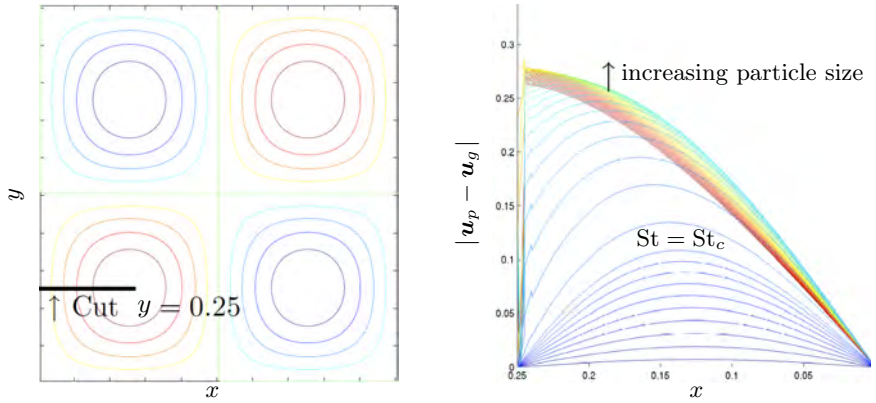

Figure 3.6: *Gas streamlines (left) and particle slip velocities in a radial cut for different sizes (right) in Taylor-Green vortices (courtesy: S. de Chaisemartin).*

but its phenomenology gains importance in the context of two-phase turbulent flows and is extensively discussed and modeled in Masi (2010), see also Dombard (2011).

3.1.3.2 Lag estimation for small particles

Crowe et al. (1998) suggest an interesting approach to estimate the velocity and temperature of a particle, which is however valid only for low-inertia regimes.
In the case of the relaxation of a single quantity in a flow, the following dynamic model is analyzed

$$\frac{\mathrm{d}\boldsymbol{u}_p}{\mathrm{d}t} = \frac{\boldsymbol{u}_g - \boldsymbol{u}_p}{\tau_p^{\boldsymbol{u}}} \tag{3.19}$$

where the characteristic variation time for $\boldsymbol{u}_g$ is τ_g. This yields the following estimation:

$$\frac{u_g}{u_p} \sim 1 + \mathrm{St} \tag{3.20}$$

which corresponds to the following approximation:

$$|\,\boldsymbol{u}_p - \boldsymbol{u}_g\,| \sim \mathrm{St}\,|\,\boldsymbol{u}_g\,| \tag{3.21}$$

or the following bracketing:

$$u_g(1 - \mathrm{St}) < u_p < u_g(1 + \mathrm{St}) \tag{3.22}$$

These velocity estimations depend on size and can be used to assess crossings and collisions for droplets of different sizes (hetero-DTC defined below), as done in Chapter 9.
The same approach can be used to evaluate temperature lags:

$$\frac{T_g}{T_p} \sim 1 + \mathrm{St}^\theta \tag{3.23}$$

which corresponds to the following approximation:

$$|\,T_p - T_g\,| \sim \mathrm{St}^\theta T_g \tag{3.24}$$

or the following bracketing:

$$T_g(1 - \mathrm{St}^\theta) < T_p < T_g(1 + \mathrm{St}^\theta) \tag{3.25}$$

For medium and large particles, this analysis does not hold since inertia induces a departure from the gas that is significant.

3.1.3.3 Phenomenology of trajectory crossing

Particle trajectory crossing (PTC), also referred to as Droplet Trajectory Crossing (DTC), is the possibility for particle trajectories to cross each other. In the context of a mesoscopic modeling based on volume averages i.e. a change in the scale of the representation, particles in the microscopic vicinity are treated at once at the modeling level so that PTC rather refers to multivariate particle velocities in a given vicinity.

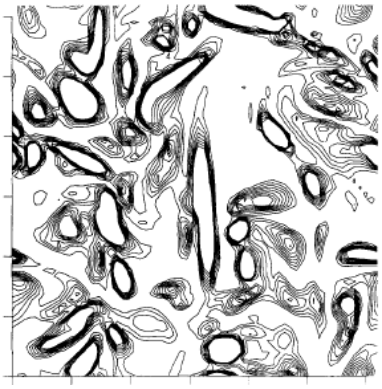

Figure 3.7: *Segregation (also referred to as preferential concentration) in a one-way coupled turbulent flow (Squires and Eaton 1991b).*

In the context of a mesoscopic modeling based on ensemble averages, i.e. a statistical modeling, crossings result in locally multivariate velocities, and in collisions, depending on the modeled cross-section. These two visions raise issues related to the models and are discussed in § 4.5.
So crossings are linked to the ability of particles to have significantly different velocities in a same region of the flow. As the particles tend to correlate their velocities at different rates according to their size in a given flow, it is natural to expect a major influence of size: while all the very small particles have the gas velocity, small, medium and large particles have a velocity depending on their size so that they do cross if their sizes are significantly different. This is referred to as "hetero-PTC" i.e. PTC at different sizes. In addition, medium and large particles may encounter crossings even for particles of the same size, which is referred to as "homo-PTC", PTC at same size: this is due to the fact that medium and large particles are defined to take a large time compared to that of the gas to correlate their velocities so this correlations weakly or never occur. Medium particles are distinguished from large ones by the fact that PTC occurs only at a small scale compared to the space scales of the problem: once a filtering length is defined (e.g. the typical size of mesh cells), the velocities of particles encountering small scale crossings remain correlated on a distance smaller than the filtering length. Whereas large particles encounter large scale crossings, i.e. their velocities after a crossing remain correlated on a significant distance. The notion of small and large scale crossings is discussed in § 6, where a modeling is proposed for the case of small scale crossings. The notion of small scale is size dependent as LES can be for turbulence (Vié et al. 2013).
As a remark, in system featuring symmetry axes (or walls), the occurrence of homo-PTC for a given inertia is expected nonetheless in non-uniform flow regions (vortices and strain) but also near these symmetry axes (or walls if rebounds occur): particles with enough inertia are prone to having a normal velocity component, which is opposite for the particles coming from the other side (or those reflected), so that the trajectories inescapably cross.

3.1.3.4 Remarks on clustering and hypercompressibility

Let us highlight that particle inertia is linked to the trend of particles to form clusters, also referred to as segregation or preferential concentration, as first described by Squires and Eaton (1991a) (see also Squires and Eaton 1991b). For instance, segregation in a turbulent field is shown in Figure 3.7. The issue of segregation has been studied in the case of the contra-rotative vortices of Taylor-Green in de Chaisemartin (2009) (see § 11.4.2 for a more complete description of the case) and the following behavior has been described according to size:

- particles with low inertia do not reach the possible crossing locations (e.g. low vorticity zones) in a fast enough time;
- particles with a slightly subcritical Stokes concentrate significantly as shown in Figure 3.8, but without crossing;
- particles with $\mathrm{St} = \mathrm{St}_c$ come and exactly accumulate in the crossing locations;
- particles with a slightly supercritical Stokes number also concentrate significantly as shown in Figure 3.9, but after crossing;
- particles with a very high inertia go far beyond the crossing locations so they do not accumulate.

In the general case, segregation is maximum for $\mathrm{St} \sim \mathrm{St}_c$. At a mesoscopic scale i.e. when considering a local concentration of particles modeled as a fluid, segregation can be seen as a hypercompressibility feature of the model fluid: depending on the dynamics of the underlying gas, which drives the motion of the particles fluid, the concentration field becomes strongly non-uniform.

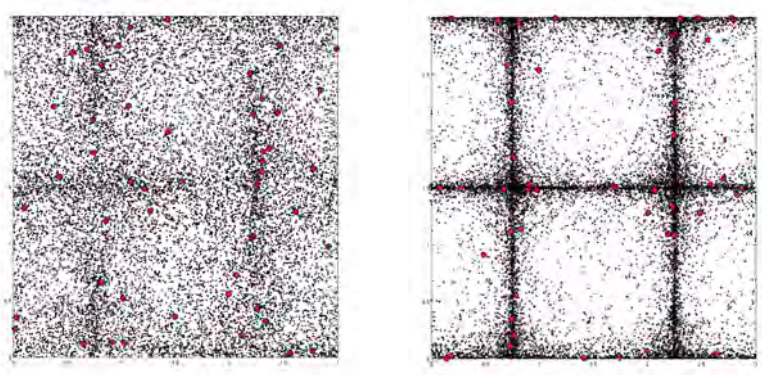

Figure 3.8: *Particles in Taylor-Green vortices at different times for $St = 0.75St_c$ (Lagrangian simulation starting with a uniform concentration).*

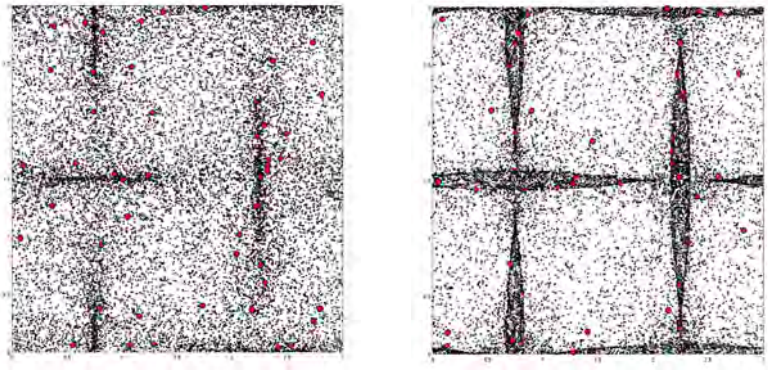

Figure 3.9: *Particles in Taylor-Green vortices at two different times for $St = 7.5St_c$ (Lagrangian simulation starting with a uniform concentration).*

The peculiar space representation of hypercompressible media can be described as accumulations with far-from-one density ratios at the edges. The point of these vacuum and accumulation zones is that the related segregation, features key aspects of the physics of the disperse phase. As an illustration, Zamansky et al. (2012)'s recent study on buoyancy driven turbulence proves a two-way coupling between the turbulent and particle structures. Segregation is crucial as it conditions all the disperse phase physics so it needs to be captured accurately by models (e.g. to evaluate the source terms).
In the case of a SRM for instance, particle space structures with length scales conditioned by hydrodynamic modes are observed (and hypothetically acoustic modes too). Such space structures play a strong role on the physics: they are for instance supposed to be at the origin of the triggering and amplification of ODP, a suggested mechanism (but not the only one) being the periodic passage of particle clusters in the nozzle, which reemits coherent noise.
The issues raised by segregation in the context of a Eulerian modeling are discussed in § 4.3.2.3.

3.1.3.5 Size-Velocity coupling

As we have shown in § 3.1.2.1, the particle size has a major impact on the dynamics of particles, and yields a particle velocity distribution, size-correlated for small particles, and more complex due to homo-PTC for large and very large particles. Besides, a velocity distribution induces crossings and possibly coalescence in the case of DTC i.e. for liquid particles. This yields a modification in the particle size distribution. So we have a two-way coupled mechanism of size-velocity coupling, as illustrated in Figure 3.10.
This strongly coupled mechanism is difficult to capture and requires modeling and method effort. We give in § 13.2.1.3 an illustration of this mechanism and the proposed set of methods allows to capture this coupled phenomenon accurately.

3.1.3.6 Conclusions on polykineticity

As a conclusion, polykineticity has various consequences and should be carefully accounted for. The phenomenology of polykineticity is strongly dependent on size and we have introduced size categories. It is clear that several modeling approaches are needed, that are dedicated to the specificities of particles of different inertia, as suggested in Ferry and Balachandar (2001). In the following, we focus on very small, small and

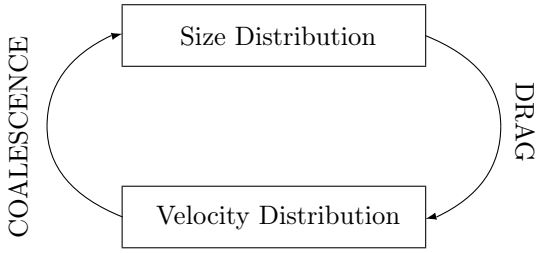

Figure 3.10: *Size-velocity coupling mechanism illustration*

large particles and we refer to the latter as moderately inertial while very small particles belong *de facto* to the nanometric size range and are referred to accordingly.

3.1.4 Disperse phase loading

The proportion of condensed phase in the flow is quantified in terms of mass fraction Y_i as mass conditions also momentum and energy ratios. The flow structure and its entire modeling are completely modified, depending on the mass loading. We describe the different classifications, depending on the mass fraction and on the volume fraction. The case of moderately dense sprays is put forward and consequences are drawn as regards modeling and simulation.

3.1.4.1 Classifications

A classification suggested by O'Rourke (1981) distinguishes sprays, mainly based on their volume fraction α_c and considers four categories of sprays:

- very thin, which can be modeled with a one-way coupling,
- thin, which features two-way coupling,
- thick, which features two-way coupling, so-called quasi-collisions (O'Rourke 1981) and collisions,
- churning, which features complex interfaces and is rather considered as a separate-phase flow here.

Elghobashi (1991) also bases his classification on volume fraction with a threshold between one and two-way coupling at $\alpha_c = 10^{-6}$ and a threshold between dilute (non-colliding) and dense (colliding) sprays at $\alpha_c = 10^{-3}$. O'Rourke (1981) rather refers to dense regimes when a retrocoupling to the gas occurs through liquid volume occupation.
Crowe et al. (1998) introduce dimensionless numbers to assess the strength of mass, momentum and energy coupling between the two phases. In our moderately dense but inert case, we focus on momentum and energy transfers. The momentum coupling index is the ratio between the drag force and the momentum flux of the gaseous phase:

$$\Pi^u = \frac{\alpha_c \rho_c L^3 (u_p - u_g)/\tau^{\boldsymbol{u}}}{\rho_g u_g^2 L^2} = \frac{C}{1 + \mathrm{St}} \tag{3.26}$$

where the velocity difference has been assessed from Eq. (3.21), therefore in the context of small particles. Similarly to momentum, the heat coupling index is the ratio between the heat flux and the energy flux of the gaseous phase:

$$\Pi^T = \frac{\alpha_c \rho_c L^3 (T_p - T_g)/\tau^T}{\rho_g u_g c_{p,g} T_g L^2} = \frac{C}{1 + \mathrm{St}^\theta} \tag{3.27}$$

where the temperature difference has been assessed from Eq. (3.24), therefore in the context of small particles. In the context of evaporation (only for liquid droplets), Crowe et al. (1998) define the mass coupling index as the ratio between the mass flux coming from evaporation and the mass flux flowing per unit volume:

$$\Pi^m = \frac{n_l L^3 \dot{m}}{\rho_g u_g L^2} = \frac{C}{\mathrm{St}_m} \tag{3.28}$$

where n_l is the number concentration of liquid droplets and where St_m is defined from a characteristic evaporation time τ_{evap}. The heat coupling index is the ratio between the heat flux brought by the evaporating mass and the energy flux of the gaseous phase:

$$\Pi^T_{evap} = \frac{n_l L^3 \dot{m} L_v}{\rho_g u_g c_{p,g} T_g L^2} = \Pi^m \frac{L_v}{c_{p,g} T_g} \tag{3.29}$$

Smallest droplet Stokes time $\tau^{\boldsymbol{u}}(r_1)$	1μs
Big droplet Stokes time $\tau^{\boldsymbol{u}}(r_2)$	10ms
First acoustic mode	50ms
Eddy revolution time	50ms
Significant regression time	1s
Motor operating time	120s

Table 3.3: *Typical timescales in a P230 motor.*

where L_v is the liquid latent heat of evaporation.
We will not hereafter attempt to classify spray regimes more in detail but we will consider the occurrence of two-way coupling based on a mass fraction criterion $Y_c > 10^{-3}$, which complies the approach of Crowe et al. (1998) based on $\Pi^u > 10^{-3}$ and $\Pi^T > 10^{-3}$ for our moderate Stokes particles. The occurrence of volume occupation coupling is quantified by a volume fraction criterion $\alpha_c > 10^{-1}$.
As for collisions, they can have various results ranging from rebounds to coalescence or agglomeration. The effect of rebounds on the flow brings Tsuji (2007) to introduce three regimes:

- collision free flows,
- collision dominated flows, and
- contact dominated flows.

Our case of application is not dense enough and brings us to consider that the direct effect of collisions on the flow is negligible: particle-particle interactions, even if present, will not be the main phenomena driving the trajectories, as opposed to dense sprays or fluidized beds. However, when coalescence occurs, it should be taken into account for the size evolution has major consequences on the flow. The occurrence of collisions (and possibly coalescence) cannot be conditioned to static criterions and requires the knowledge of the dynamics of the flow so that collision times have to be evaluated as suggested by O'Rourke (1981). This approach is mostly retained in the following work: characteristic times are evaluated, depending on the context, see § 7.2 for a detailed study of coalescence intensity estimation. However, the volume fraction gives a first estimate of the collision intensity and can be taken as a first indication that collisions will occur in our moderately dense cases.

3.1.4.2 Moderately dense two-phase flows

Disperse two-phase flows are referred to as moderately dense when there is a strong impact of two-way coupling of mass, momentum, heat and species whereas the condensed phase still has a negligible volume occupancy in the flow (typically $\alpha_c < 1\%$).
Based on the average volume and mass fraction in a SRM, we consider that a SRM spray is subjected in most of the chamber to:

- a strong two-way coupling through drag and heat exchange,
- collisions and coalescence because of DTC,
- but a negligible retrocoupling through volume occupancy as the volume fraction is below 1%.

In correlation with the latter point, droplet-droplet interactions, even if present, will not be the main phenomena driving the trajectories, as opposed to dense sprays or fluidized beds.
In particular SRMs feature moderately dense flows and we focus in the present thesis on the modeling of such regimes. Moderately dense flows are indeed characterized by the so-called two-way coupling, which requires robust and accurate modeling and methods.

3.1.5 SRM case: nano-to-inertial moderately dense disperse phase flow

The flow in a SRM is mainly a two-phase, disperse phase flow with liquid droplets in the chamber and solid particles at the nozzle output, as extensively described in § 1.2.3.
Let us now consider an illustration of the various time scales introduced by the disperse phase: Table 3.3 gives some typical time scales of the physics in a P230 SRM. The disperse phase features in this case droplets of sizes r_1 and r_2 with an initial size ratio of 100. Such remarkably bimodal distributions serve as a basis for the classical approach to polydispersity in SRMs since they have been observed and formation mechanisms have been suggested, as discussed in § 1.2.3.2.
In a spray, we usually have $\rho_l \sim 10^3 \rho_g$, in accordance with a condensed phase. The liquid alumina cloud of a SRM has an average mass fraction of $Y_l = 0.35$ but, considering $\rho_l = 2,800\text{kg/m}^3$ and a typical density for the gas is $\rho_g = 5\text{kg/m}^3$, the liquid volume fraction is of order of $\alpha_l = 10^{-4}$. The situation is more complex because of non-uniformities of the flow: a 2D simulation shows that the volume fraction varies significantly with space, yielding relatively empty zones and zones with $\alpha_l = 10^{-3}$, as shown in Figure 3.12.

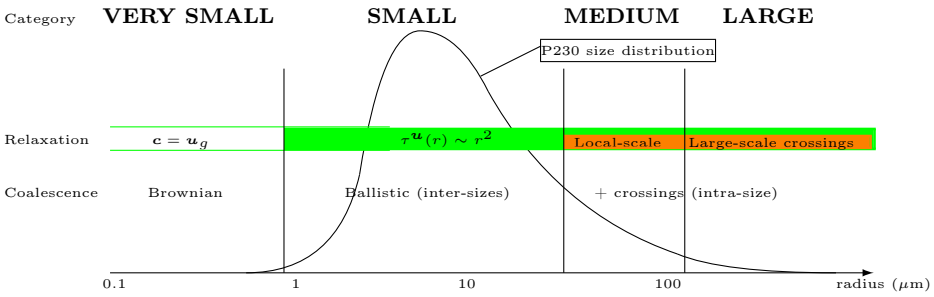

Figure 3.11: *Phenomena to be accounted for depending on droplet size*

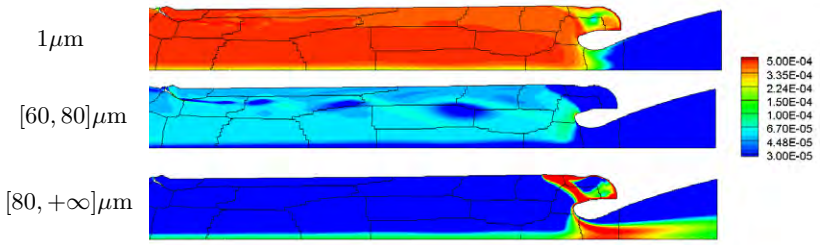

Figure 3.12: *Alumina droplet volume fractions in a portion of P230 with coalescence – Eulerian simulation with CEDRE (Doisneau et al. 2013).*

We have presented the general aspects of multiphase flows among which the fact that they are multi-scale. We consider several scales of space in a SRM, which we consider as clearly separate:

- microscopic: atoms and molecules typically 10^{-9} m,
- interfacial: around a droplet i.e. $\approx 10^{-6}$ m,
- mesoscopic: intermediate scale where the flow varies little but droplets are sufficiently numerous to allow a statistical description $\approx 10^{-4}$ m,
- macroscopic: a control volume of $\approx 10^{-2}$ m,

to which we add the scale of the motor, of several meters and the scale of the plume of several hundreds of meters. In some cases, the scale separation is not sufficient to allow the definition of the mesoscopic scale, which prevents the use of statistical approaches and commands instead a direct resolution of the problem, with its exact, deterministic initial and boundary conditions, at the cost of a loss of robustness of the predictibility. In the following, we rely on this scale separation to recourse to a statistical approach of the disperse phase.

The flow features an important mass loading and is considered as moderately dense. Polydispersity is effective everywhere and polykineticity should be taken into account for:

- hetero-PTC occurs everywhere as a direct consequence of polydispersity,
- homo-PTC occurs at the vortices' edges and in the nozzle

These crossings generate coalescence and size-velocity coupling is significant.

As a consequence, we refer to SRM flows as

- nanometric to moderately inertial,
- moderately dense,

for polydisperse/polykinetic and heavy mass loading reasons respectively. These features should all be included carefully in the chosen modeling approach.

We consider in addition the number concentration of particles: since the disperse phase volume fraction can reach 0.1% and droplet diameters are small (a few tens of micrometers), the number of droplets per unit volume can be estimated:

$$N_p = \frac{\alpha_c}{\frac{4}{3}\pi r^3} \approx 10^{11}\mathrm{m}^{-3}. \tag{3.30}$$

This high number has also consequences on the choice of a modeling approach.

3.2 Continuum mechanics approaches for disperse two-phase flows

Continuum mechanics is based on the derivation of conservation equations with space averaging of some quantities: the space averaging acts as a filter, smearing out the undesired level of detail so that the equations are finally written at the macroscopic level. The continuous system is derived to also fulfill some given

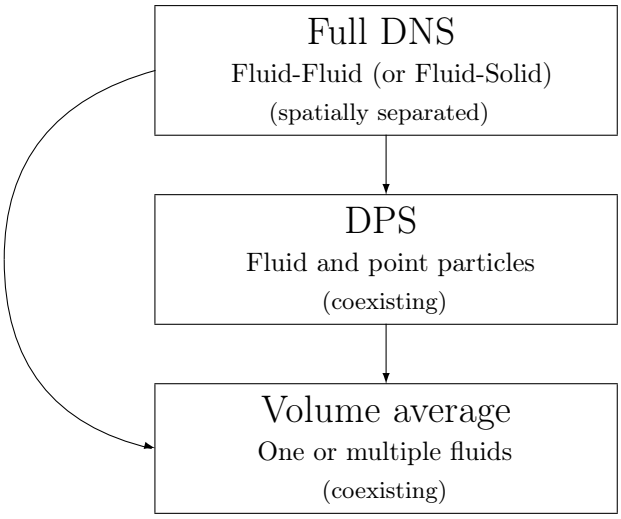

Figure 3.13: *Hierarchy of continuum mechanics models for disperse two-phase flows*

properties such as hyperbolicity and the existence of an entropy (Woods 1975). This approach has been strictly theorized by Truesdell (1966).
In the case of two-phase flows, depending on the scale of space filtering, the level of detail of the model can be very different, resulting in a hierarchy presented in Figure 3.13 and which main models are described in the following paragraphs.
Disperse two-phase flows can be modeled with different levels of detail, which we present from the most detailed, microscopic, to the most blunt, macroscopic ones. First, we briefly present so-called "DNS at the particle level" methods that can be used for separate-phase flows as well: they prove to yield too much detail and to be costly for a full SRM computation. Then, some closures are given for the integral effect of a particle in a surrounding fluid that can be obtained either analytically or from the previous approaches. We finally present the so-called "Discrete Particle Simulation" that can be used for disperse phase flows and two-fluid models, that give a macroscopic, volume average description of two-phase flows.
The passage from local properties at the microscopic level to continuum mechanics models at the macroscopic level is achieved by a volume average i.e. a change of scale. If the averaging volume $\mathcal{V}(\boldsymbol{x}, \Delta x)$ is centered on a physical space point $\boldsymbol{x}$ and has a Δx extension, then a given quantity Φ can be defined locally:

$$\Phi(t, \boldsymbol{x}) = \frac{1}{\mathcal{V}(\boldsymbol{x}, \Delta x)} \int_{\mathcal{V}(\boldsymbol{x}, \Delta x)} \phi(t, \boldsymbol{x}', \boldsymbol{c}') \mathrm{d}\boldsymbol{x}' \mathrm{d}\boldsymbol{c}' \tag{3.31}$$

from a microscopic function $\phi(t, \boldsymbol{x}', \boldsymbol{c}')$. It is local as compared to the entire system which physical extension spans the entire physical subspace of Γ, and provided that particles spend enough time in $\mathcal{V}(\boldsymbol{x}, \Delta x)$.
This method can be applied to derive the equations for a single phase fluid, namely the Navier-Stokes equations. As a preliminary model at the basis of many approaches, we consider the continuum mechanics approach for a single fluid. To model such a continuous phase, as well as any usual gas or liquid, Lagrangian approaches can be considered, e.g. smoothed particle methods (Cottet and Mas-Gallic 1990; Magni and Cottet 2012). But we here choose a Eulerian approach: the Navier-Stokes equations for a multi-species (or multicomponent) reactive flow. This system is extensively described in Appendix A. The Euler equations -a more simple, non-dissipative system of equations which physics is included in the Navier-Stokes approach- are also considered in some parts of the thesis for the basic analysis of models (Sainsaulieu 1993). These fluid models are the basis for either one-fluid modeling and for the gas description within two-fluid and fluid-kinetic modelings, as presented now.

3.2.1 Direct numerical simulation at the particle level

We briefly present methods that give access to the detailed information of the fluid flow at the interface level. These methods can be referred to as "full DNS" and are used for instance by Faure et al. (2009), Apte et al. (2009), or Shardt and Derksen (2012). They have a prohibitive cost for a direct use in our applications.

3.2.1.1 Fluid-fluid DNS

A family of approaches is designated as fluid-fluid DNS: these approaches, valid for liquid condensed phases, simply perform the resolution of the flow with spatially separated (non-coexisting) fluid equations, given from single fluid models, as presented in Appendix A. The fluid-fluid interface then results from the evolution of

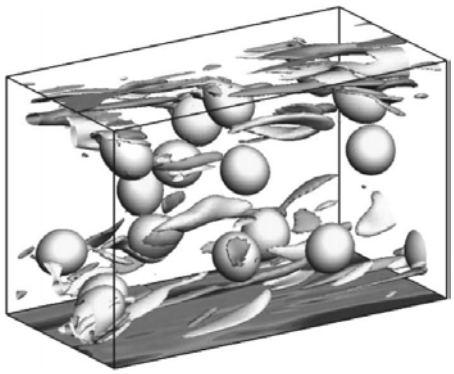

Figure 3.14: *DNS of a gas-liquid flow (courtesy: G. Tryggvason).*

both fluids, requiring no additional information on the interface shape. Each fluid influences the other one through boundary conditions written at the interface. A typical computation result is given in Figure 3.14. Approaches based on particular methods, work for incompressible flows (hydrodynamics) featuring an interface, see for instance the Smoothed Particle Hydrodynamics (Monaghan 1992) and the SPH-ALE formalism in Leduc (2010). But in general cases, the position of the interface must be solved accurately to impose satisfactory boundary conditions for both fluid domains (Scardovelli and Zaleski 2003).
Additional knowledge on the interfaces is provided to separate-phase flow simulations by several techniques:

- front tracking method (Unverdi and Tryggvason 1992; Popinet and Zaleski 1999),
- level-set (Sussman et al. 1994), or
- volume of fluid (Rider and Kothe 1998).

Each of these methods raises many numerical issues and improvements are provided by many authors (Gueyffier et al. 1999; Herrmann 2005; Olsson and Kreiss 2005; Tryggvason et al. 2006; Menard et al. 2007; Desjardins et al. 2008; Tryggvason et al. 2010; Zuzio and Estivalezes 2011; Le Chenadec and Pitsch 2013a; Le Chenadec and Pitsch 2013b). Moreover, such computations raise numerical stability issues such as the appearance of numerical oscillations (Fedkiw et al. 1999) which have required much research and are still under study (Le Chenadec and Pitsch 2013b).
The complexity of the interface of separate-phase flows has been presented as increasing with the Weber number in § 3.1.1.3: so the Direct Numerical Simulation (DNS) cost in the context of an interface tracking approach increases with the Weber number (Lebas et al. 2009). The high level of detail of such flows can be seen in Figure 3.2. For our applications, fluid-fluid DNS cannot be used for cost reasons. Hopefully it provides excessively refined information compared to what is needed as the phase is disperse: the inclusion shape is well known and does not need to be a DoF of the problem. This is not true in specific regions where the flow is dense e.g. in the aft dome cavity and the nozzle for the resolution of slag accumulation: in these zones, a separate phase flow approach should be considered.
In the spirit of LES for single phase turbulence, intermediate approaches, where an average interface is resolved while small scale unevenness, such as wrinkles, is modeled, has still to be defined, to provide an affordable trade off for industrial computations (Pai and Subramaniam 2006; Demoulin et al. 2007; Gorokhovski and Herrmann 2008; Herrmann 2010; Jibben and Herrmann 2012; Chesnel et al. 2012).
An interesting answer to the limitation of both separate phase approaches and disperse phase approaches has been provided with the coupling of a Eulerian separate-phase description for the simulation of the liquid core primary atomization with a stochastic-Lagrangian description of the dispersed phase, in regions distant from the injector nozzle, done in the solver Eulerian Lagrangian Spray Atomization (ELSA) (Vallet et al. 2001; Vallet and Borghi 2002; Demoulin et al. 2007). Other attempts of such hybridization were made (Tomar et al. 2010; Zuzio 2010; Zuzio et al. 2013).

3.2.1.2 Fluid DNS around solid bodies

The principle of this second type of full DNS approach is to solve for a fluid around solid (not deformable) bodies: the method is sometimes referred to as Fully Resolved Simulation in the context of solid particles (Apte et al. 2009) but can also be used for a disperse liquid at low We_L^a. The solid bodies can be fixed or may move depending on the forces from the surrounding flow. The treatment of the solid bodies is done with appropriate boundary conditions e.g. they are meshed or immersed boundary conditions are applied (Xu and Subramaniam 2010).
This approach can be used to solve the settling of a group of particles, as the interaction of particles through their wakes generates a long range interaction and modifies the physical properties of the system (settling velocities).

This approach is costly, its cost linearly increasing with the number of particles. It is well suited when the modeling effort is important e.g. for settling but when particles have few properties, a less detailed approach should be considered.

3.2.1.3 Achievements and computational cost

Full DNS approaches are used to capture complex physics: they notably allow to render group effects (Derksen 2012). For instance in sedimentation, the coupling between the wakes of particles is well known to significantly modify the settling velocity of a group of particles compared to an isolated one (Tory et al. 1999). Another example is group combustion which arises in specific conditions and where the flame structure and the overall dynamics is strongly linked to the organization of the cloud and its evolution at large scale (Sirignano 2010). The issue of group effects is also present in crowd modeling (Maury et al. 2010). For all these group effects, the resolution of the flow at the level of each particle is required

- as it strongly departs from that of a single particle,
- as it has an influence on macroscopic dynamics.

Besides, the exact numerical resolution of interfaces is still a research topic, especially for the purpose of:

- DNS computations to improve and validate models and correlations,
- mesoscopic approaches,
- first stage of a mesoscopic approach with coupling to a disperse phase approach.

For instance in the case of a heavy loading of liquid, the complex shape of the interface can be solved during coalescence process by such methods, see for instance Luret et al. (2010).
It is unfortunately very difficult to solve for a macroscopic system with a full DNS approach, regarding the high cost of the methods so these methods are not considered for our problem. They can still be used to give an insight on complex cases e.g. those described above and to validate models, intended to be implemented in more affordable approaches.

3.2.2 Discrete Particle Simulation

The Discrete Particle Simulation (Lagrangian DPS) is a deterministic Lagrangian approach of the disperse phase (Riley and Patterson 1974; Zhu et al. 2007). The method resembles the "DNS around solid body" approach previously described in § 3.2.1.2 except that the effect of particle volume occupation on the surrounding fluid flow is not resolved: the method is sometimes referred to as point-particle DNS (Pai and Subramaniam 2012). In the following this method is referred to as Lagrangian DPS, to highlight its numerical similarities to the so-called stochastic-Lagrangian (see § 4.2), though their fundamental origins and meaning are different.
The fluid equations presented in Appendix A are used to model the continuous, carrier phase of the two-phase flow: they are defined everywhere in space. The disperse phase is treated by individual, physical particles, which location is exactly resolved. The particles are assumed to be point-wise i.e. they have no volume occupation and their influence on the gas phase is described by the addition of local source terms in the gas phase equations (Riley and Patterson 1974). This model is relevant for a disperse phase that is dilute enough. However if collisions occur, they can be detected as soon as the two particles come into contact with respect to their actual sizes and the effect of collisions can still be accounted for with a good-level of detail, provided that the flow at the particles' very surface (wake) does not play a role.
The method is now described in detail, as it is used in the present thesis as a reference for the validation of a statistical approach for the coalescence in a moderately inertial spray, the results being presented in § 13.4. The meaning of DPS solutions compared to statistical ones is also discussed in this prospect.

3.2.2.1 Description of DPS

The Lagrangian DPS approach, introduced by Riley and Patterson (1974), is a deterministic resolution of a particulate problem, therefore very different from the statistical approach based on Eq. (3.123). Most of the first numerical studies were dedicated to solid particle dispersion (Squires and Eaton 1991a; Elghobashi and Truesdell 1992). The extension to evaporating droplets in turbulent flows has been provided in Mashayek et al. (1997) as well as in Reveillon et al. (1998) and in Miller and Bellan (1999) and has been used in combustion applications by the same authors (Mashayek 1998; Miller and Bellan 2000; Reveillon and Vervisch 2005; Fréret et al. 2013). This method, is mainly used in DNS configurations, where all the droplets contained in the physical domain can be tracked.
In this approach, each particle i among N_p corresponds to a physical particle transported thanks to the ODEs of its center of mass position $\boldsymbol{x}_{pi}$, velocity $\boldsymbol{u}_{pi}$, size S_{pi}, and temperature θ_{pi}:

$$\partial_t \boldsymbol{x}_{pi} = \boldsymbol{u}_{pi}; \quad \partial_t S_{pi} = R_{pi}; \quad \partial_t \boldsymbol{u}_{pi} = \boldsymbol{F}_{pi}; \quad \partial_t \theta_{pi} = H_i \tag{3.32}$$

where the sources in the ODEs depend on the particle variables as well as the local gas properties.
Drag and heating are computed from Eq. (3.51) and Eq. (3.59) and with the particle's local variables. The local drag force on a particle reads:

$$\boldsymbol{F}_i(t) = \boldsymbol{F}(\boldsymbol{u}_{pi}, \boldsymbol{u}_g(t, \boldsymbol{x}_{pi}), S_{pi}) \tag{3.33}$$

and heating reads:

$$H_i(t) = H(\theta_{pi}, T_g(t, \boldsymbol{x}_{pi}), S_{pi}). \tag{3.34}$$

3.2.2.2 Point-particle coupling to the gas

The gas equations are to be coupled to the DPS description of the disperse phase: when the liquid phase is described with point particles, its influence on the gas phase can be described by a source term addition in the gas phase equations (Dupays 2006a): this corresponds to the assumption that the disperse phase is dilute enough.
From the single phase gas system composed of Eq. (A.1), Eq. (A.2), (A.4), and (A.6) in the case of Navier-Stokes equations, we form the two-phase gas system of equations by adding the disperse phase source terms:

$$\left\{\begin{array}{l} \partial_t \rho_g + \partial_{\boldsymbol{x}} \cdot (\rho_g \boldsymbol{u}_g) = S^m \\ \partial_t (\rho_g Y_k) + \partial_{\boldsymbol{x}} \cdot (\rho_g \boldsymbol{u}_g Y_k) = -\partial_{\boldsymbol{x}} \cdot \left(\rho_g Y_k \boldsymbol{u}_k^{\text{diff}}\right) + M_k \dot{\omega}_k + S_k^m, \quad k \in [\![1, n_s]\!] \\ \partial_t \left(\rho_g \boldsymbol{u}_g\right) + \partial_{\boldsymbol{x}} \cdot (\rho_g \boldsymbol{u}_g \otimes \boldsymbol{u}_g) = \partial_{\boldsymbol{x}} \cdot \boldsymbol{T} + \rho \boldsymbol{a} + \boldsymbol{S}^{\text{mom}} \\ \partial_t \left(\rho_g e_g\right) + \partial_{\boldsymbol{x}} \cdot (\rho_g \boldsymbol{u}_g e_g) = \boldsymbol{T} : \partial_{\boldsymbol{x}} \boldsymbol{u}_g - \partial_{\boldsymbol{x}} \cdot \boldsymbol{q} + S^{\text{e}} \end{array}\right. \tag{3.35}$$

with the relations:

$$\sum_{k=1}^{n_s} Y_k = 1, \ \sum_{k=1}^{n_s} S_k^m = S^m \ \text{ and } \ \sum_{k=1}^{n_s} \rho_g Y_k \boldsymbol{u}_k^{\text{diff}} = 0 \tag{3.36}$$

and S_k^m, $\boldsymbol{S}^{\text{mom}}$, and S^{e} are the disperse phase mass, momentum and heat source terms due to the evaporated mass of liquid in species k, to the drag force and to the term of enthalpy. The latter is due to heating and to the work of the drag force. In general, the disperse phase mass source term can render mass exchanges with particles due to evaporation and possibly homogeneous chemical reactions such as the presence of flame fronts surrounding the droplet; they may also include mass transfers due to heterogeneous chemical reactions i.e. at the droplet surface. Finally, the thermodynamical relations as well as the species and heat fluxes are computed similarly as for a single phase flow, described in Appendix A.
As an illustration, we give the expression of the Lagrangian DPS evaluation of the mass source term S_k^m in the gas equation for mass conservation. In this DPS context with mono-component droplets, we can reconstruct a Eulerian field provided a volume of space $V(\boldsymbol{x}, \Delta x)$ considered at location $\boldsymbol{x}$ and for a filter size Δx:

$$S^{\text{species}} = S^m = \frac{1}{V(\boldsymbol{x}, \Delta x)} \sum_{\boldsymbol{x}_{pi} \in V(\boldsymbol{x}, \Delta x)} \rho_l \mathrm{d}_t \mathcal{V}(S_{pi}(t)) \tag{3.37}$$

where we sum over all the particles i such that $\boldsymbol{x}_{pi}$ belongs to the space volume at a distance Δx around $\boldsymbol{x}$ and where $\mathcal{V}(S)$ stands for the volume of a particle of surface S.

3.2.2.3 Case of collisions

The occurrence of collisions or coalescence is assessed deterministically with a collision detection algorithm. Since all the trajectories are computed, the effects of velocity correlations are intrinsically accounted for so that no efficiency correction is required. The impact parameter is also available as all the information on the trajectories of the two partners is computed. So that the collision regime can be assessed even if the inter collision times are small: the method can describe denser regimes than the usual Boltzmann equation.
In case of a collision, the velocities are modified, as required by the corresponding regime i.e. rebound, stretching, or coalescence (see § 3.3.3 for a detailed modeling of these regimes and their occurrence). In the case of coalescence, each collision produces a unique particle out of two, according to the transformations (3.73).
We briefly describe the collision detection algorithm used in the following and refer to Thomine (2011) for further details. Transport is divided in time steps, which need to be small enough to avoid more than one collision per particle. The collision detection algorithm determines for each particle if the particles in a neighborhood are to collide. The neighborhood is chosen to reduce the cost of the algorithm significantly below the theoretical limit $N_p(N_p - 1)$. The DPS algorithm proceeds on a time step as follows:

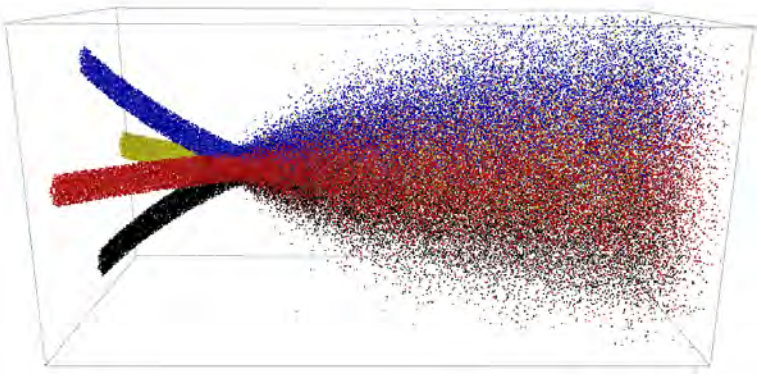

Figure 3.15: *DPS of four particle jets with elastic collisions (Thomine 2011).*

1. collision detection;
2. time resolution of Eq. (3.32) with a 3rd order Runge-Kutta method;
3. position and velocity update for colliding particles.

As an illustration, a computation of jets of colliding particles, performed with a DPS approach with the Asphodele code (Reveillon and Demoulin 2007b) is presented in Figure 3.15, excerpted from Thomine (2011). DPS is used in the following for validation purpose. As the case is solved in 2D, the DPS approach must be adapted: all collisions are considered to occur in 2D, which is exact as soon as all the initial centers of mass and velocity vectors belong to the same plane. We therefore adapt the statistical kernel of the Eulerian approach, as well as the collision detection algorithm of the Lagrangian DPS in order to perform strictly 2D computations.

3.2.2.4 Comparison to statistical approaches

The remaining question is how to compare DPS to kinetic-based approaches (introduced in § 3.5), as the DPS is not based on a kinetic approach. Indeed, in this framework, DPS can be seen as one realization of a statistical description. An ensemble averaging of DPS solutions oughts to retrieve the statistical fields.
We will thus use this method to assess the ability of the statistical approach described below (more precisely of the models derived from it and given in Chapter 4) to reproduce the global physics of considered configurations, achieving comparisons between the chosen statistical methods and Lagrangian DPS on global quantities. These comparisons will especially allow to assess the efficiency of the Eulerian description of spray polydispersity and moreover of coalescence, which is a delicate topic. DPS comparison provides a strong validation for statistical approaches of collisions and coalescence.
As a remark, we recall the point made by de Chaisemartin (2009) that, in a non-colliding and one-way coupling case, DPS can also be seen as one realization of a stochastic-Lagrangian description (see § 4.2) if the latter is driven by stoichiometry. We highlight that this is the only resemblance between Lagrangian DPS and stochastic-Lagrangian.

3.2.2.5 Deterministic issues

Initial Conditions and Boundary Conditions can be deterministic. But they are more often modeled by using a stochastic approach, considering the poor knowledge that is available for these conditions in real applications.
In the context where a stochastic injection is performed, the DPS has a very different meaning: it becomes a realization of a statistical system. It is useful for group effects though it achieves in these cases a less accurate description than full-DNS (see § 3.2.1.3). DPS is also used to compute disperse two-phase turbulence cases and dense collision studies, as discussed in the following paragraph but it must be highlighted that the approach loses its relevance for problems that are far from ergodicity, with influent rare events.
The direct comparison between such a deterministic approach and a Eulerian statistical approach, especially when particle interactions are present or for unsteady turbulent flows, may lead to serious difficulties, which will not be studied here and we refer to Pai and Subramaniam (2012) for further considerations. First, the DPS results must be projected on the Eulerian grid for comparison. Second ensemble-averaging is required to have comparable, statistical data. This averaging is *a priori* performed on many DPS realizations, using random initial and boundary conditions, is generally needed. However, in statistically steady configurations, time-averaging one DPS realization and considering the steady state of the Eulerian simulation yield comparable quantities. On the contrary, the comparison of statistical and DPS approaches for unsteady cases will require to ensemble average several realizations of the latter to perform a consistant comparison.

3.2.2.6 Achievements and computational cost

The DPS method can be used to study complex physics as it yields one realization of the flow. On the contrary statistical approaches, described below in § 3.4, yield macroscopic quantities that are average and therefore difficult to interpret in some cases.
Group effects can still be rendered, though in a less accurate way than full-DNS approaches. For disperse phases with collisions in particular, DPS allows to study in detail turbulent as well as dense aspects. First the role of turbulence on collisions is not well known and the study of DPS realizations is sufficient to analyze new collision probabilities, as done in Wunsch et al. (2008), with the aim of developing statistical models (Wunsch et al. 2009; Wunsch 2009). Second, DPS can be used for dense collision cases since it remains valid when the intercollision time becomes close to the collision interaction time: as said previously the method does not account for the volume effect of particles on the fluid, but the collision detection algorithm can still be set to detect two particles coming into contact. In fact this is done most of the time and this makes DPS accurate as regards collisions in dense cases. Such dense collisions are extensively described in Drew and Passman (1999) and bring along new physical behaviors, which are well known to occur for instance in fluidized beds (Peirano and Leckner 1998) and has been observed with DPS (Tsuji et al. 1993; Tsuji et al. 1998).
The cost of the method is $\mathscr{O}(n)$ for most linear operations and can reach $\mathscr{O}(n^2)$ for the collision detection algorithm. So the method is rarely used for complex macroscopic problems. The high number of droplets in a SRM, see relation (3.30), proves that it is not reasonable to describe the droplet trajectories deterministically. The stochastic-Lagrangian approach (extensively described in § 4.2) allows to overcome the issue of large numbers of particles and that of the collision cost: statistical collision algorithms have been developed to reduce the cost down to $\mathscr{O}(n)$ (see § 4.2.2.1).
In addition in complex macroscopic problems, initial conditions and correlations are very difficult to evaluate deterministically. Finally, the complete physics of each of these droplets is not relevant to evaluate the motor's behavior so the DPS approach is rather used as a reference method to assess the relevance of other modeling approaches and assumptions.

3.2.3 Two-Fluid volume average models

A wide range of methods for two-phase flows can be derived from volume averages (Ishii 1975; Delhaye and Achard 1977; Marle 1982; Nigmatulin 1990; Lhuillier 1992; Zhang and Prosperetti 1994; Zhang and Prosperetti 1997; Prosperetti and Tryggvason 2007; Kah 2010). The averaging process is performed on a volume large enough to contain both phases, and small enough compared to the length scales desired to be solved (Nigmatulin 1979). A number of macroscopic quantities are then accounted for with distinct Eulerian conservation equations. So the two phases are described as fluids (see § 3.4.2.1 for the definition of a fluid model) that virtually coexist, for all the quantities are defined at every location in space. We briefly describe some models, which can be used in their general form for separate as well as for disperse phase flows.
Back to the general case of separate-phase flows, models based on volume average have to be introduced whenever it becomes impossible to describe in detail the interfaces and to account for the transfers at local scale. These approaches generate closure problems as transfer terms within the averaging volume have macroscopic effects that should be taken into account, so that models are required for closure. On the contrary the closure problem is eased when the liquid phase can be assumed as disperse, some authors resorting to particle-level closures such as those given in § 3.3.
The complexity of two-fluid models partly holds in the number of conserved quantities, so this number is sometimes used to designate the model. However strong qualitative differences exist depending on the chosen closures for exchange terms. As for all continuum mechanics approaches, hyperbolicity and entropic properties are sought as a sign of well-posedness (Nigmatulin 1990).

3.2.3.1 Two-fluid models for separate-phase flows

The most general approaches with two fluids account for the conservation of mass, momentum and energy of both fluids and add an equation for a volume fraction to describe the local scale topology of the flow: they are therefore referred to as seven-equation models. This level of detail is rather required for separate phase flows. The first seven-equation model to be derived, the so-called Baer and Nunziato (1986) model, was originally designed to model the gas-solid front propagation in explosives and has raised a variety of applications, see a review in Kah (2010). This model is still used in highly compressible two-phase contexts (Saurel and Abgrall 1999). The issue is then to close the transfer terms since the interface is only coarsely known through the average volume fractions: the closure is strongly conditioned by the physical process that is accounted for. The seven-equation model entails numerical peculiarities which have aroused a wide literature (Saurel and Abgrall 1999; Saurel and Le Metayer 2001; Ambroso et al. 2012).

Some two-phase regimes do not require to account for the local volume fraction and are then referred to as six-equation models. The two-fluid model of Ishii (1975) is dedicated to liquid-vapor bubble flows occurring in cooling networks of nuclear plants, in normal or accidental functioning. This model is of course composed of six equations:

$$\left\{\begin{array}{l}\partial_t(\alpha_g\rho_g)+\partial_{\boldsymbol{x}}\cdot(\alpha_g\rho_g\boldsymbol{u}_g)=\Gamma_g\\ \partial_t(\alpha_g\rho_g\boldsymbol{u}_g)+\partial_{\boldsymbol{x}}\cdot(\alpha_g\rho_g\boldsymbol{u}_g\otimes\boldsymbol{u}_g)=-\partial_{\boldsymbol{x}}\cdot(\alpha_g p_g)+\partial_{\boldsymbol{x}}\cdot(\alpha_g\boldsymbol{\Pi}_g)+\boldsymbol{F}_{gl}\\ \partial_t(\alpha_g\rho_g e_g)+\partial_{\boldsymbol{x}}\cdot(\alpha_g\rho_g\boldsymbol{u}_g e_g)=-\partial_{\boldsymbol{x}}\cdot(\alpha_g\boldsymbol{u}_g p_g)+\partial_{\boldsymbol{x}}\cdot(\alpha_g\boldsymbol{q}_g)+\partial_{\boldsymbol{x}}\cdot(\alpha_g\boldsymbol{\Pi}_g\boldsymbol{u}_g)+H_{gl}\\ \partial_t(\alpha_l\rho_l)+\partial_{\boldsymbol{x}}\cdot(\alpha_l\rho_l\boldsymbol{u}_l)=\Gamma_l\\ \partial_t(\alpha_l\rho_l\boldsymbol{u}_l)+\partial_{\boldsymbol{x}}\cdot(\alpha_l\rho_l\boldsymbol{u}_l\otimes\boldsymbol{u}_l)=-\partial_{\boldsymbol{x}}\cdot(\alpha_l p_l)+\partial_{\boldsymbol{x}}\cdot(\alpha_l\boldsymbol{\Pi}_l)+\boldsymbol{F}_{lg}\\ \partial_t(\alpha_l\rho_l e_l)+\partial_{\boldsymbol{x}}\cdot(\alpha_l\rho_l\boldsymbol{u}_l e_l)=-\partial_{\boldsymbol{x}}\cdot(\alpha_l\boldsymbol{u}_l p_l)+\partial_{\boldsymbol{x}}\cdot(\alpha_l\boldsymbol{q}_l)+\partial_{\boldsymbol{x}}\cdot(\alpha_l\boldsymbol{\Pi}_l\boldsymbol{u}_l)+H_{lg}\end{array}\right. \tag{3.38}$$

where the interface exchange terms Γ_k, the pressures p_k, the stress tensors $\boldsymbol{\Pi}_k$, the heat fluxes $\boldsymbol{q}_k$, the momentum exchange terms $\boldsymbol{F}_{kk'}$, and the energy exchange terms $H_{kk'}$ must be modeled. In the literature, this model can be found under two different options:

- One of the phases is considered incompressible. Thus only the gas phase has an equation of state, and the pressure of the mixture is taken as the gas pressure,
- Both phases are compressible, and the closure is realized by forcing mechanical equilibrium (pressure equilibrium) between the phases.

The compressible context is a classical approach for two-phase flows (Drew and Passman 1999).
From the six-equation model, some approaches for separate phase flows have focused on the additional modeling of the density of interface, as it conditions mass, momentum and heat transfers. This approach comes in replacement of the volume fraction equation in the seven-equation model which is difficult to close. Ishii (1975) suggested that the interface surface density Σ should obey a transport equation having the following form:

$$\partial_t\Sigma+\partial_{\boldsymbol{x}}\cdot(\Sigma\boldsymbol{u}_\Sigma)=S_\Sigma \tag{3.39}$$

where $\boldsymbol{u}_\Sigma$ is the transport velocity of the interface surface density (equal to $\boldsymbol{u}_i$, the transport velocity of the volume fraction), and S_Σ a source term taking into account the different phenomena creating or destroying interfacial area, such as coalescence or breakup, phase change or interfacial stretching. Ishii (1975) wrote this equation for a population of identical (but not necessary spherical) bubbles. Morel (1997)'s objective was to derive such an equation without assuming any particular geometrical configuration in the interfaces, and therefore to prove that it could be applied independently of the flow regime. This development was based on the work of Candel and Poinsot (1990), who wrote an equation on a flame surface density, in order to account for its stretching. As a by-product of his work, the rigorous mathematical expression of the transport velocity $\boldsymbol{u}_\Sigma$ was established and the method was applied to the combustion of liquid sprays by Jay et al. (2006). Besides a relaxed approach of this type has been used in a RANS formalism for liquid jet atomization (Vallet and Borghi 1999), with the assumption that the Reynolds and Weber numbers were large.

3.2.3.2 Two-fluid models for disperse phase flows

While the seven-equation models provide a description of the interface with either a volume fraction or an interface density equation, they are too complex and not used in practice for disperse phase flows. On the contrary, six-equation models are interesting for disperse-phase flows as the information on interface is better known e.g. through the assumption of an average droplet diameter.
Sainsaulieu (1995b) has extensively studied the mathematical properties of the compressible six-equation model, still with explicit closures derived with a disperse phase assumption; see also Sainsaulieu and Larrouturou (1992) for the corresponding numerical methods. Such two-fluid model with a disperse phase closure has been applied for instance to the simulation of atomization and combustion in LREs (Zamuner and Lecourt 1995).
The dilute bi-fluid model is a particular two fluid model with the assumption that $\alpha_l \ll 1$ so that $\alpha_g = 1$ (Nigmatulin 1990). The system of equations is then greatly simplified compared to the six-equation model Eq. (3.38), as the local volume fractions do not need to be solved, so that they vanish and the system reads:

$$\left\{\begin{array}{l}\partial_t\rho_g+\partial_{\boldsymbol{x}}\cdot(\rho_g\boldsymbol{u}_g)=0\\ \partial_t(\rho_g\boldsymbol{u}_g)+\partial_{\boldsymbol{x}}\cdot(\rho_g\boldsymbol{u}_g\otimes\boldsymbol{u}_g)=-\partial_{\boldsymbol{x}}p_g+\partial_{\boldsymbol{x}}\cdot\boldsymbol{\Pi}_g-\boldsymbol{F}_{lg}\\ \partial_t(\rho_g e_g)+\partial_{\boldsymbol{x}}\cdot(\rho_g\boldsymbol{u}_g e_g)=-\partial_{\boldsymbol{x}}\cdot(\boldsymbol{u}_g p_g)+\partial_{\boldsymbol{x}}\cdot(\boldsymbol{\Pi}_g\boldsymbol{u}_g)+\partial_{\boldsymbol{x}}\cdot\boldsymbol{q}_g-(H_{lg}+(\boldsymbol{u}_l-\boldsymbol{u}_g)\cdot\boldsymbol{F}_{lg})\\ \partial_t\rho_l+\partial_{\boldsymbol{x}}\cdot(\rho_l\boldsymbol{u}_l)=0\\ \partial_t(\rho_l\boldsymbol{u}_l)+\partial_{\boldsymbol{x}}\cdot(\rho_l\boldsymbol{u}_l\otimes\boldsymbol{u}_l)=\boldsymbol{F}_{lg}\\ \partial_t(\rho_l e_l)+\partial_{\boldsymbol{x}}\cdot(\rho_l\boldsymbol{u}_l e_l)=H_{lg}\end{array}\right. \tag{3.40}$$

where $\boldsymbol{F}_{gl}$ and H_{gl} ensure the coupling between the two fluids and need to be modeled: they depend *a priori* on the structure of the gas-liquid interface. This model is particularly suited for disperse-phase flows, as the existence of stable spherical droplets is partly linked to the fact that the volume fraction is low.
Approaches similar to the dilute bi-fluid model where used by Temkin and Dobbins (1966) with the closures of spherical droplets. Jackson and Davidson (1983) focused on strongly coupled disperse phase flows with a six-equation model. A link between the bi-fluid model and the equations arising from moment methods for the statistical approach has been established by Laurent and Massot (2001): this link illustrated in the particular case of dilute models in § 4.3.

3.2.3.3 Linearized lag models

A hierarchy of simpler two-fluid models can be derived from the six-equation model for the corresponding relevant contexts by assuming successive equilibria between temperatures and pressures: this allows to reduce the number of equations. This hierarchy is discussed in Kah (2010). A particular class of approaches is referred to as drift-flux models, where the velocities of the two phases are close to an equilibrium but a mean drift must still be solved (Ambroso et al. 2008). This approach is suitable even for highly compressible two-phase contexts (Saurel et al. 2012).
We focus on such models in the context of a disperse phase: when the particle velocity and temperature fields are not resolved, they can still be reconstructed based on a Taylor expansion of the drag force and the heat transfer, linked to the velocity and temperature estimations performed for small droplets in § 3.1.3.2. This type of modeling has been developed by Ferry and Balachandar (2001) and is referred to as the Eulerian Equilibrium Model (EEM). In the case of a linearized velocity lag model, the truncation error increases with the Stokes number (Ferry and Balachandar 2001; Ferry and Balachandar 2002). In a similar way, the particle temperature field can be estimated (Ferry and Balachandar 2005). These models are originally one-way coupled but a two-way extension is discussed in § 4.7.5.
For moderately dense sprays, this type of modeling is said to be extendable to two-way coupling (Ferry and Balachandar 2001). Other expansions were performed by directly considering two-way coupling (Druzhinin 1994; Druzhinin 1995) but with a partial knowledge of the flow so they are available for simple configurations only.

3.2.4 One-fluid volume average models

Two-phase models can be derived by a volume average approach when considering macroscopic quantities for a mixture of the two-phases: this relies on strong equilibrium assumptions between the two-phases. They are referred to as one-fluid models as they solve for a unique "fluid" at every location: these models can be seen in the prolongation of the two-fluid model hierarchy as models where all the two-phase quantities are relaxed.
One-fluid models are also referred to as mixture models or Homogeneous Equilibrium Models (HEM) (Kah 2010).

3.2.4.1 General frame of one-fluid models

One-fluid models are based on dynamic and thermodynamic equilibrium assumptions between the phases: there are no slip velocities and no temperature differences between the phases.
Mean physical quantities are solved (density, velocity, temperature but also molar mass, heat capacity, viscosity) for the two-phase flow itself which is treated as a fluid that is a mixture of the two phases:

$$\begin{aligned} &\rho_m = \rho_g\alpha_g + \rho_l\alpha_l \\ &\rho_m\boldsymbol{u}_m = \rho_g\alpha_g\boldsymbol{u}_g + \rho_l\alpha_l\boldsymbol{u}_l \\ &\rho_m e_m = \rho_g\alpha_g e_g + \rho_l\alpha_l e_l \end{aligned} \tag{3.41}$$

with e_k the total energy of phase $k \in \{g, l\}$. The equivalent fluid is solution of a system of equations for a single-phase flow:

$$\left\{ \begin{array}{l} \partial_t\rho_m + \partial_{\boldsymbol{x}}\cdot(\rho_m\boldsymbol{u}_m) = 0 \\ \partial_t(\rho_m\boldsymbol{u}_m) + \partial_{\boldsymbol{x}}\cdot(\rho_m\boldsymbol{u}_m\otimes\boldsymbol{u}_m) = -\partial_{\boldsymbol{x}}p_m + \partial_{\boldsymbol{x}}\cdot\boldsymbol{\Pi}_m \\ \partial_t(\rho_m e_m) + \partial_{\boldsymbol{x}}\cdot(\rho_m e_m\boldsymbol{u}_m) = -\partial_{\boldsymbol{x}}\cdot(p_m\boldsymbol{u}_m) + \partial_{\boldsymbol{x}}\cdot(\boldsymbol{\Pi}_m\boldsymbol{u}_m) + \partial_{\boldsymbol{x}}\cdot\boldsymbol{q}_m \end{array} \right. \tag{3.42}$$

where p_m is an equivalent pressure, $\boldsymbol{\Pi}_m$ is an equivalent stress tensor, and $\boldsymbol{q}_m$ is an equivalent heat flux.
The equation of state (EOS) applies then to the mixture, and is different from pure fluid EOS. Various types of EOS have been proposed and are briefly discussed in the following. As a remark, we highlight that computational methods dedicated to single phase flows can be directly used, as long as the peculiarities of the present EOS are properly treated. To ensure that slip velocities and temperature differences are

null, momentum and heat transfers are virtually instantaneous, at least at the resolved time scale, which corresponds to equilibrium between the two phases. In addition, no mass transfers can be resolved, though some transformations (e.g. depending solely on mixture temperature) can be accounted for, by modifying the EOS. To sum up, no exchange term is explicitly solved.
So that mixture models can be used to model processes where exchanges between phases are not significant, or, if important, taken into account simply through the model. Although the use of mixture models is limited to very special cases, under clear and identified assumptions on the flow, it allows in these cases an efficient resolution (Moreau 2006; Kah 2010).

3.2.4.2 Equivalent gas

The so-called Equivalent Gas model (EG) is a particularly simple mixture model where the two-phase medium behaves as a perfect gas.
We get the following EOS, similar to Eq. (A.8) for a perfect gas:

$$p_m = \rho_m \frac{R}{M_m} T_m = \rho_m (\gamma_m - 1) \left(E_m - \frac{\boldsymbol{u}_m^2}{2} \right) \tag{3.43}$$

but with modified thermophysical properties.
We now express the thermophysical properties in the case of a mixture of species i either gaseous g or condensed c. The mixture molar mass M_m is computed with the mass of all the species, either gaseous or condensed but with the gas density:

$$M_m = \frac{1}{\sum_{\mathrm{g}} n_i} \sum_{\mathrm{g\ \&\ c}} M_i n_i, \tag{3.44}$$

while the equivalent heat capacity includes all the species:

$$c_{p,m} = \sum_{\mathrm{g\ \&\ c}} c_{p,i} Y_i. \tag{3.45}$$

We get a speed of sound in the two-phase medium:

$$c_m = \sqrt{\gamma_m \frac{R}{M_m} T_m}. \tag{3.46}$$

3.2.4.3 Other EOS models for complex physics

In complex cases, the use of a non-perfect equation of state allows to account for more physical phenomena. The first type corresponds to cubic equations reproducing the liquid-vapor phase diagram. In the case of a cubic EOS, for example the Van der Waals equation, the hyperbolic character of the system might be lost in the mixture domain, where the two phases coexist (Kah 2010).
Some authors also use combinations of EOS of pure fluids to build the mixture EOS while tabulated models or an equation resulting from a combination of EOS for pure fluid are always hyperbolic. But on the other hand, other problems appear, for example the inability of the model to take into account metastable states (Le Métayer 2003).

3.2.4.4 Limitations of equilibrium models

The simplicity of the mixture model (made of the Euler or Navier-Stokes system of equations, plus an EOS for the mixture) comes with severe limitations.
For cavitation problems, the thermodynamic equilibrium assumption forbids the study of metastable cases. Besides, as assumed by Morel (1997), mass transfer is assumed to be instantaneous, but this is not always correct, see for example evaporation front in liquid phase studied in Le Métayer (2003). Moreover, some cavitation problems can be solved making the exact opposed hypothesis, i.e that the kinetic of transfer is very slow, even null, see for instance Barberon and Helluy (2005); Davies et al. (1994).
In the case of a disperse phase, the Equivalent Gas approach is well known and relevant for very low Stokes numbers. The use of EG models for SRM flows has been discussed in § 1.3.1.5, where it has been shown that models needed at least to capture a velocity and temperature lag between the two-phases to assess properly some properties such as two-phase losses. So the EG approach for SRM is limited to steady state computations and thermodynamics computing (see § 2.1.1). An alternative approach, referred to as Partial Equivalent Gas consists in considering only a fraction of the disperse phase as part of the Equivalent Gas: this modeling approach is rather used to overcome numerical peculiarities (e.g. of the smallest droplets) and it is discussed as a numerical approach in § 4.7.5.

3.3 Modeling at the level of a single particle

The integral physics at the level of a single particle in a fluid can be assessed simply by solving the Navier-Stokes equations, presented in Appendix A, around a solid body, or by the use of empirical correlations. This approach allows to replace the physical particle by a point-particle, encountering the integral effects hereafter computed and exerting on the fluid the corresponding response.
The point-particle position is then referred to as $\boldsymbol{x}_p$, its velocity $\boldsymbol{u}_p$ and its temperature T_p. It receives and renders source terms from and to the fluid at position $\boldsymbol{x}_p$, which can be computed with the correlations detailed in this section. These correlations can be used in the DPS approach as well as in statistical approaches *qua* closures. They are expressed per particle unit mass, considering a particle of radius r_p at location $\boldsymbol{x}_p$, at velocity $\boldsymbol{u}_p$ and temperature T_p.
Since we focus on chemically inert particles in the present work, the momentum and heat transfers are presented, as well as the collision and break-up approaches. While the case of coupled heat and mass transfer, e.g. evaporation or combustion, is presented in Appendix B for the sake of legibility.

3.3.1 Momentum transfer

The forces that act on a particle, due to the surrounding gaseous flow, are presumably complex but they can be modeled in a simple and classical way as soon as particles are assumed to be spherical and isolated i.e. not influenced by their neighbors. Studies have been conducted experimentally and numerically to model the flow around a sphere, the total drag force and the heat transfers.
In the BBO approach, standing for Basset-Boussinesq-Oseen, see for instance (Sangani et al. 1991; Dupays 2005; Michaelides and Roig 2011), drag force is decomposed in a viscous drag, a pressure gradient effect, an added mass term, and a history term. In the following and for reasons of compatibility with the statistical approach, we only consider the viscous drag effect (Laurent and Massot 2001).

3.3.1.1 Drag force in Stokes regime

The first drag expression, for viscous or creeping flows around a sphere, is due to Stokes (1846) and reads $6\pi\mu_g r_p(\boldsymbol{u}_g - \boldsymbol{u}_p)$ for a particle so that the drag force per unit mass can be written:

$$\boldsymbol{F}^{\mathrm{St}}(\boldsymbol{u}_p, \boldsymbol{u}_g, r_p) = \frac{(\boldsymbol{u}_g - \boldsymbol{u}_p)}{\tau^{\boldsymbol{u}}} \tag{3.47}$$

where the drag time is defined as:

$$\tau^{\boldsymbol{u}} = \frac{2\rho_l r_p^2}{9\mu_g}. \tag{3.48}$$

The particular Reynolds number measures the dominancy of convection on diffusion and reads:

$$\mathrm{Re}_p = 2r_p \left\| \boldsymbol{u}_g - \boldsymbol{u}_p \right\| / \nu_g \tag{3.49}$$

so that Stokes' law is correct when $\mathrm{Re}_p < 1$, which is known as Stokes' regime.

3.3.1.2 Convective correction

When Re_p gets higher, a convective correction is required such as the Schiller-Naumann correction (Schiller and Naumann 1935):

$$\boldsymbol{F} = \boldsymbol{F}^{\mathrm{St}} \left(1 + 0.15\mathrm{Re}_p^{0.687}\right) \tag{3.50}$$

or sometimes written in an archaic form $\left(1 + \frac{\mathrm{Re}_p^{2/3}}{6}\right)$. Since the drag force in convective regime depends on the square of the velocity difference, a more general form is sometimes written thanks to a dimensionless coefficient called drag coefficient C_D:

$$m_p \boldsymbol{F}(\boldsymbol{u}_p, \boldsymbol{u}_g, r_p) = C_D \beta_p \frac{\rho_g}{2} \left| \boldsymbol{u}_g - \boldsymbol{u}_p \right| (\boldsymbol{u}_g - \boldsymbol{u}_p) \tag{3.51}$$

where $\beta_p = \pi r_p^2$ is the cross-section of the sphere alone. The drag coefficient C_D is then:

$$C_D = \begin{cases} 24\mathrm{Re}_p^{-1} & \text{if } \mathrm{Re}_p < 1 \\ 24\mathrm{Re}_p^{-1}\left(1 + 0.15\mathrm{Re}_p^{0.687}\right) & \text{if } \mathrm{Re}_p < 10^3 \\ C_{D,1} & \text{if } 10^3 < \mathrm{Re}_p < 10^5 \\ C_{D,2} & \text{if } 10^5 < \mathrm{Re}_p \end{cases} \tag{3.52}$$

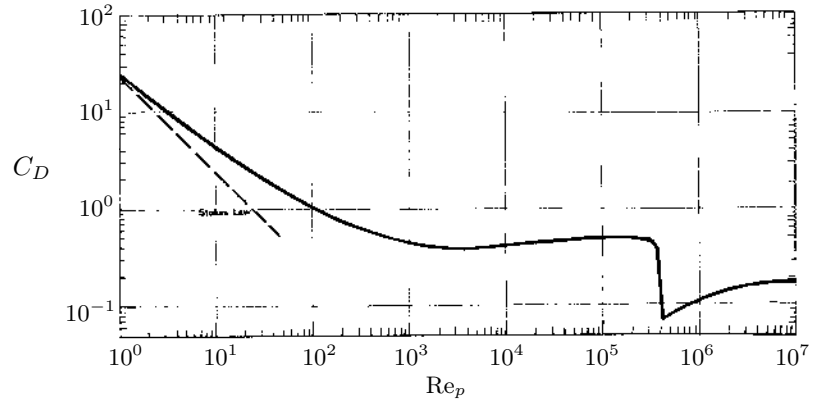

Figure 3.16: *Dimensionless drag coefficient versus Reynolds number (Clift et al. 1978).*

where $C_{D,1} \approx 0.445$ measures drag in the first turbulent regime and $C_{D,2} \approx 0.2$ measures drag in the second turbulent regime i.e. after the drag crisis point. The evolution of drag on a sphere is described by the law given in Figure 3.16.
In a SRM, particles are small enough to maintain Re_p out of the turbulent regime. In fact, Stokes' law is valid in most of the chamber and the particular Reynolds number eventually reaches $\mathrm{Re}_p = 500$ in the nozzle where Schiller-Naumann's correction is needed and sufficient.

3.3.1.3 Characteristic momentum transfer time

From the drag force relations, a characteristic momentum transfer time can be deduced which is simply $\tau^{\boldsymbol{u}}$ in Stokes regime: we highlight the fact that this characteristic time increases with the square of the particle radius. Equivalently it is proportional to the particle surface.
The characteristic time can be generalized when convection effects are sensible, though it will depend on Re_p.
For polydisperse sprays, the transfer source terms can be averaged on size so that the laws can be written as depending on an average size. A characteristic time is then defined for a polydisperse spray as that of a monodisperse phase which retrieves the polydisperse average transfer term.

3.3.2 Heat transfers

3.3.2.1 Conduction-convection heating

The same analysis can be conducted for heat transfer thanks to the analogy between the momentum and the heat equation. In Stokes' regime, the heat transfer per unit mass reads

$$H^{\mathrm{St}}(T_p, T_g, r_p) = c_{p,l}\frac{T_g - T_p}{\tau^T} \text{ with } \tau^T = \frac{3}{2}\mathrm{Pr}_g\frac{c_{p,l}}{c_{p,g}}\tau^{\boldsymbol{u}} \tag{3.53}$$

where we assume a constant heat capacity $c_{p,l}$ for the liquid phase, and where Pr_g is the Prandtl number for the gas:

$$\mathrm{Pr}_g = \frac{\nu_g}{D_g^T} = \frac{\mu_g c_{p,g}}{\lambda_g} \tag{3.54}$$

We then define the droplet Nusselt number as the dimensionless transfer coefficient:

$$\mathrm{Nu} = \frac{H}{H^{\mathrm{St}}} = \frac{m_p H}{2\pi r_p \lambda_g (T_g - T_p)} \tag{3.55}$$

which can be used to express correlations. This definition matches the usual droplet Nusselt one:

$$\mathrm{Nu} = \frac{2r_p h}{\lambda_g} \tag{3.56}$$

where h is the heat transfer coefficient yielding a linear transfer law $h(T_g - T_p)$ per unit surface. Eq. (3.53), which describes heat transfer in Stokes' regime, is equivalent to the dimensionless relation:

$$\mathrm{Nu} = 2. \tag{3.57}$$

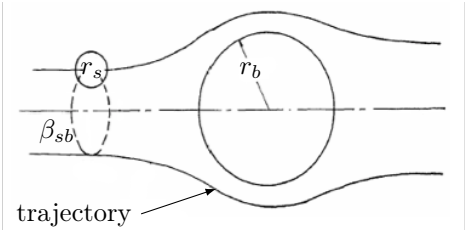

Figure 3.17: *Origin of collision efficiency corrections – Trajectory of a small droplet r_s following the near-flow of a bigger droplet r_b.*

A convective correction due to Ranz and Marshall (1952) can be considered for the same range of Re_p than Eq. (3.50):

$$\mathrm{Nu} = 2 + 0.6\mathrm{Re}_p^{\frac{1}{2}}\mathrm{Pr}_g^{\frac{1}{3}}. \tag{3.58}$$

so that heating reads for $\mathrm{Re}_p < 1000$:

$$H^{\mathrm{RM}}(T_p, T_g, r_p) = c_{p,l}\frac{T_g - T_p}{\tau^T}(1 + 0.3\mathrm{Re}_p^{\frac{1}{2}}\mathrm{Pr}_g^{\frac{1}{3}}). \tag{3.59}$$

3.3.2.2 Radiative transfer

In the case of radiative transfers, a basis model is suggested in Tang and Brewster (1992). Simpler models may be considered (Dupays 1996): the radiative heat transfer per unit mass for a grey body of emissivity ϵ_p^{R} (independent of the wavelength) reads for a black-body gas (Solonenko and Krylov 1987; Zhou et al. 1994):

$$H^{\mathrm{Rad}}(T_p, T_g, r_p) = 3\epsilon_p^{\mathrm{R}}\sigma_{\mathrm{Stefan}}\frac{T_g^4 - T_p^4}{\rho_l r_p}. \tag{3.60}$$

and for the gas as a grey body with an ϵ_g^{R} (Siegel and Howell 1972):

$$H^{\mathrm{Rad}}(T_p, T_g, r_p) = \frac{3\sigma_{\mathrm{Stefan}}}{1/\epsilon_p^{\mathrm{R}} + 1/\epsilon_g^{\mathrm{R}}}\frac{T_g^4 - T_p^4}{\rho_l r_p}. \tag{3.61}$$

Advanced radiation modeling can be found in Duval et al. (2004). Particle radiation is not considered in the following work.

3.3.2.3 Characteristic heating time

From the heat transfer relations, a characteristic heat transfer time can be deduced in the spirit of the characteristic momentum transfer one. It is simply τ^T in Stokes regime: again this characteristic time increases with the square of the particle radius. Equivalently it is proportional to the droplet surface.
The heat transfer time is sensitive to convection when the mechanism is that of conduction and is similarly sensitive to Re_p, while the radiative transfer time is not sensitive to convection.
In the case of polydispersity, an average approach for heat can be done similarly to that for momentum.

3.3.3 Deterministic modeling of collision

In the same spirit than for transfers, collisions are now modeled for their integral effect on particle trajectories, the effect on the surrounding fluid being neglected.

3.3.3.1 Two-particle trajectory correlation

Because the carrier flow can influence two particles about to collide, their exists a correlation of their velocities before collision, that may influence the collision itself. It is equivalent to consider that droplets may dodge each other due to the gas flow surrounding them, as shown in Figure 3.17. Collision efficiency is then a parameter that decreases the possibility of a collision. The determination of collision efficiency laws thus require knowledge of local gas parameters such as density ρ_g or viscosity μ_g.
We consider the case of unbalanced droplet sizes with a bigger particle of radius r_b and a smaller particle of radius r_s. In this specific case, two collision efficiency models are suggested on empirical basis (Hylkema 1999; Achim 1999; D'Herbigny and Villedieu 2001; Dufour 2005), namely from Langmuir (1948) and Beard

and Grover (1974). These laws strongly depend on the bigger droplet particle Reynolds number Re_p and on a dimensionless number k which reads:

$$k = \frac{2\rho_l r_s^2 \mid \boldsymbol{u}_b - \boldsymbol{u}_s \mid}{9\mu_g r_b}. \tag{3.62}$$

The number k is the ratio of the smaller droplet relaxation time $\tau^{\boldsymbol{u}}(r_s)$ to its residence time in the bigger droplet influence zone $\tau^R = \frac{r_b}{|\boldsymbol{u}_b - \boldsymbol{u}_s|}$. In the case of low particle Reynolds numbers, Langmuir (1948) gets the following expression with a numerical approach:

$$\begin{cases} E_1(k) &= 0 & \text{if } k \leq 1.214, \\ E_1(k) &= \left(1 + \dfrac{3\ln(2k)}{2(k-1.214)}\right)^{-2} & \text{otherwise} \end{cases} \tag{3.63}$$

whereas for high particle Reynolds numbers, they get:

$$\begin{cases} E_2(k) &= 0 & \text{if } k \leq 0.0833, \\ E_2(k) &= \dfrac{k^2}{(k+0.5)^2} & \text{otherwise.} \end{cases} \tag{3.64}$$

For intermediate cases they assume the following interpolation:

$$\mathfrak{E}_{\mathrm{LB}}(k, \mathrm{Re}_p) = \frac{E_1(k)}{1 + \mathrm{Re}_p/60} + \frac{(\mathrm{Re}_p/60)E_2(k)}{1 + \mathrm{Re}_p/60}. \tag{3.65}$$

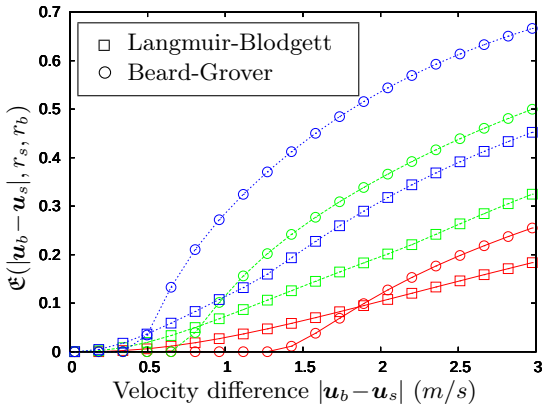

Figure 3.18: *Two collision laws selected for SRM applications with $r_b = 150\mu m$ (Solid: $r_s = 2\mu m$, Dashed: $r_s = 3\mu m$; Dotted: $r_s = 4\mu m$)*

Beard and Grover (1974) suggest to increase the accuracy of formula (3.65) which results from a simple interpolation between two limits. For this purpose, they use a numerical solution of the incompressible Navier-Stokes equations in order to determine the gaseous flow surrounding the bigger droplet depending on the Reynolds number. They can therefore evaluate precisely the forces on the smaller droplet and compute its trajectory. For $\mathrm{Re}_p \in [0, 400]$ it yields:

$$\mathfrak{E}_{\mathrm{BG}}(k, \mathrm{Re}_p) = \frac{4}{\pi^2}[\arctan(\max(H(k, \mathrm{Re}_p), 0))]^2, \tag{3.66}$$

where

$$\begin{aligned} H &= 0.1465 + 1.302Z - 0.607Z^2 + 0.293Z^3, \\ Z &= \ln(k/k_0), \\ k_0 &= \exp(-0.1007 - 0.358\ln(\mathrm{Re}_p) + 0.0261[\ln(\mathrm{Re}_p)]^2). \end{aligned}$$

Typical collision efficiency values with these two laws are given in Figure 3.18.

3.3.3.2 Geometric parameters of a collision

When a collision occurs between two droplets, the dynamics strongly depends on the geometric parameters of the collision. To describe the collision regimes, we consider dimensionless versions of the geometric parameters.

The impact parameter b is the dimensionless distance between the trajectories of the droplet centers:

$$b = \frac{I}{r_s + r_b} \tag{3.67}$$

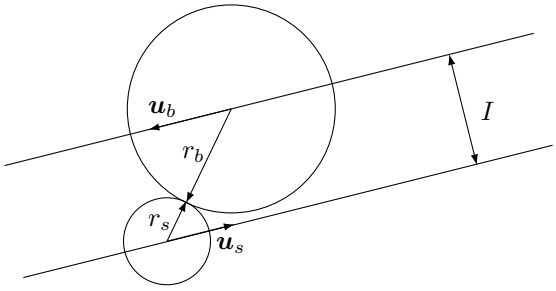

Figure 3.19: *Geometric parameters of a binary collision.*

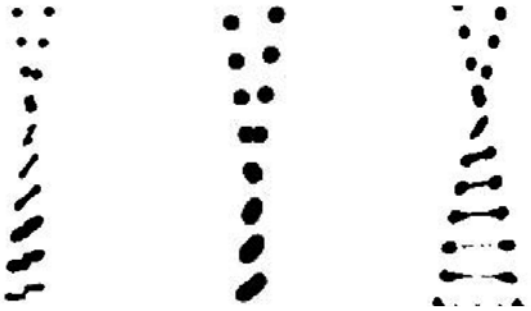

Figure 3.20: *Illustration of reflexion, coalescence, and stretching of two colliding droplets (Qian and Law 1997).*

that describes the eccentricity of the collision: $b = 0$ is a frontal collision while b close to one corresponds to a skimming collision. The radius ratio also plays an important role, which reads:

$$\Delta r = \frac{r_s}{r_b} \tag{3.68}$$

to ensure that it is between 0 and 1.
In a collision of liquid droplets, the surface energy of the two droplets tends to preserve their shapes and to impede deformations. So that the collision regime depends on the comparison of surface energy to relative kinetic energy. This is done with a liquid Weber number as defined in Eq. (3.6):

$$\mathrm{We}^l_{coll} = \frac{\rho_l r_b \mid \boldsymbol{u}_s - \boldsymbol{u}_b \mid^2}{\sigma_{lg}} \tag{3.69}$$

computed on the biggest droplet radius r_b and with the relative droplet velocity.

3.3.3.3 Regimes after collision

In the case of solid particles, the regime is that of rebounds, the latter being generally modeled as elastic and without any effects of rotation.
In the case of liquid droplets, experiments where conducted by Qian et al. (1997) and numerical simulation by Mashayek et al. (2003); Tanguy and Berlemont (2005) to assess the consequences of liquid droplet collision. There are three remarkable regimes after a collision according to Qian and Law (1997)'s study as illustrated in Figure 3.20. These regimes must be described finely as they have very different consequences. While Brazier-Smith et al. (1972) only considers the stretching, which he refers to as "rotation" separation, Ashgriz and Poo (1990) include the three regimes and their occurrence has been correlated to the impact parameter b, as summed up in Figure 3.21. The critical impact parameters are conditioned on the collisional Weber number and on the relative size ratio so that we have finally:

- separation by reflexion if $b < b_1(\mathrm{We}^l_{coll}, \Delta r)$,
- separation by stretching if $b > b_2(\mathrm{We}^l_{coll}, \Delta r)$,
- coalescence otherwise i.e. if $b \in [b_1(\mathrm{We}^l_{coll}, \Delta r), b_2(\mathrm{We}^l_{coll}, \Delta r)]$.

The values for the critical impact parameters have been widely studied for water droplet as they condition rain modeling and other important applications e.g. nuclear accident cooling (Rabe 2009; Foissac 2011). A water regime chart is reproduced in Figure 3.22. In the case of aluminum oxide droplets in a SRM, the early model of Brazier-Smith et al. (1972), treating only stretching, is said to be sufficient (Achim 1999; Hylkema 1999; Dufour 2005).

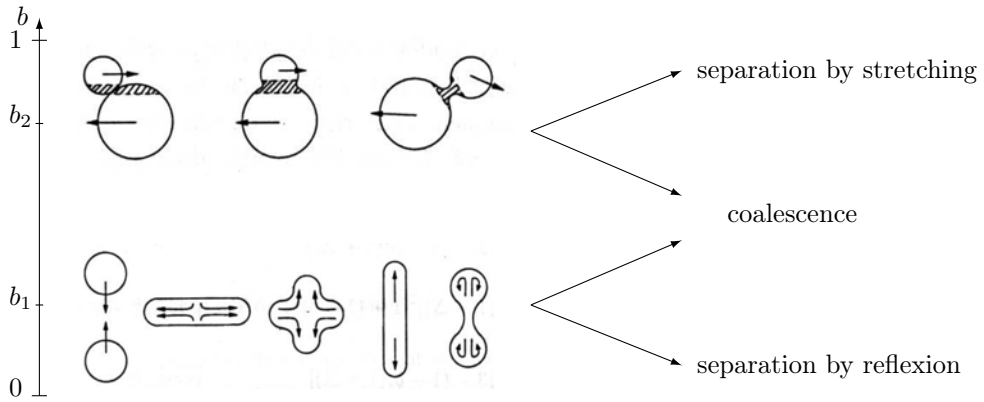

Figure 3.21: *Phenomenology of extreme impact parameter collisions (Courtesy: P. Achim).*

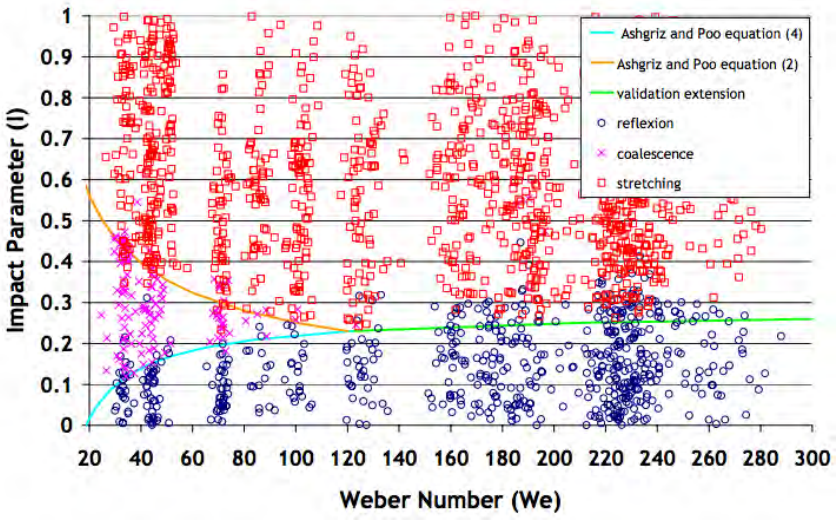

Figure 3.22: *Collision regimes as predicted by a theoretical model (Ashgriz & Poo) and experimental results (Rabe 2009).*

3.3.3.4 Description of separation regimes

The separation regimes are usually modeled as follows. In both separation cases, the amount of exchanged mass is neglected so that there is no evolution of the droplet sizes:

$$\begin{cases} r_s' = r_s \\ r_b' = r_b \end{cases} \tag{3.70}$$

As a consequence, we consider no evolution for enthalpy or any other conservative property of the droplet. As for velocities, we have in the case of reflexion:

$$\begin{cases} \boldsymbol{u}_s' = \boldsymbol{u}_s \\ \boldsymbol{u}_b' = \boldsymbol{u}_b \end{cases} \tag{3.71}$$

while we have in the case of stretching:

$$\begin{cases} \boldsymbol{u}_s' = \boldsymbol{u}_s - \dfrac{2r_b^3}{r_b^3 + r_s^3}((\boldsymbol{u}_s - \boldsymbol{u}_b)\cdot\boldsymbol{n})\boldsymbol{n} \\ \boldsymbol{u}_b' = \boldsymbol{u}_b + \dfrac{2r_s^3}{r_b^3 + r_s^3}((\boldsymbol{u}_s - \boldsymbol{u}_b)\cdot\boldsymbol{n})\boldsymbol{n} \end{cases} \tag{3.72}$$

where $\boldsymbol{n} = \frac{\boldsymbol{u}_s - \boldsymbol{u}_b}{|\boldsymbol{u}_s - \boldsymbol{u}_b|}$ is the normalized vector carrying the relative velocity.

3.3.3.5 Description of coalescence

After coalescence, only one droplet remains that contains all the mass of the two precursor droplets. If densities are the same for all droplets, we have relations for the volume and momentum conservation:

$$\begin{cases} v = v^\star + v^\diamond \\ v\boldsymbol{u}_p = v^\star \boldsymbol{u}_p^\star + v^\diamond \boldsymbol{c}^\diamond \end{cases} \tag{3.73}$$

Besides, the coalescence process corresponds to a perfectly inelastic collision so that kinetic energy, as well as any other higher order velocity moment, are not conserved. These high order moments can be deduced from the momentum relation:

$$(v\boldsymbol{u}_p)^k = (v^\star \boldsymbol{u}_p^\star + v^\diamond \boldsymbol{c}^\diamond)^k \tag{3.74}$$

and Eq. (3.74) does not bring any additional microscopic information compared to Eq. (3.73). The dissipated relative kinetic energy may lead to an increase of temperature, especially if liquid density is high such as metal droplets (Mathiaud 2006).
As for the droplet enthalpy, the new droplet hosts the entire enthalpy of the precursors:

$$vh = v^\star h^\star + v^\diamond h^\diamond \tag{3.75}$$

and we do not account for relative kinetic energy transformed into internal energy by viscous efforts in the droplet nor for surface tension variation.

3.3.4 Secondary break-up modeling

Secondary break-up occurs when the flow surrounding a particle is too strong and the shear tears the particle apart. In the same spirit than for collisions, this break-up process is modeled for its effect on the particle. The integral effect on the fluid is also discussed.

3.3.4.1 Static stability of solid particles

It can occur for solid particles and is then sometimes referred to as erosion. The static stability of particles in a flow is assessed by comparing the aerodynamic forces to the cohesion forces of the solid. These forces are computed differently, depending on the type of solid (aggregate, glass, polycristal, monocristal, *etc.*) and resort from material science.
In the case of solid aluminum oxide particles in the nozzle, the occurrence of solid particle break-up has not been evaluated. The overall effect of the nozzle on such particles has been assessed by an empirical correlation due to Hermsen (1981b). But the precise mechanism is not known, either liquid, solid phase break-up or both.

3.3.4.2 Static stability of droplets

We focus on the case of liquid droplets. The break-up of droplets corresponds to the process of secondary atomization.
Break-up of liquid droplets is driven by the ratio of capillary forces versus aerodynamic forces. So the aerodynamic Weber number is considered, as defined in Eq. (3.7) based on the droplet diameter as a characteristic length and on the gas density. It is noted We:

$$\mathrm{We}(r) = \frac{\rho_g 2r \mid \boldsymbol{u}_p - \boldsymbol{u}_g \mid^2}{\sigma_{lg}} \tag{3.76}$$

where the liquid-gas surface tension is noted σ_{lg}.
The droplet Weber number arises from the comparison of the maximum pressure that can exist around a droplet according to Bernoulli's formula:

$$\Delta p^{max} = \frac{1}{2}\rho_g \mid \boldsymbol{u}_p - \boldsymbol{u}_g \mid^2 \tag{3.77}$$

to Laplace's formula for interfacial pressure:

$$p^{int} - p^{ext} = 2\frac{\sigma_{lg}}{r} \tag{3.78}$$

which gives a pressure increase $\delta p = 2\epsilon_r \frac{\sigma_{lg}}{r}$ linked to a deformation of the droplet $\epsilon_r = \delta r / r$. The balance of the aerodynamic pressure of Eq. (3.77) and the pressure increase gives the following relation:

$$\mathrm{We} = 8\epsilon_r \tag{3.79}$$

so that a critical Weber We_c arises from the definition of a maximum deformation $\epsilon_{r,c}$: it gives a purely static criterion for droplet stability. Some authors (O'Rourke and Amsden 1987; Achim 1999) take $\epsilon_{r,c} = 1$ while others consider $\mathrm{We}_c \approx 12$ (Pilch and Erdman 1987; Hsiang and Faeth 1992; Schmelz and Walzel 2003).

3.3.4.3 Dynamics of breakage

A slight correction to include dynamics is done in Pilch and Erdman (1987), resulting in the correlation:

$$\mathrm{We}_c = 12(1 + 0.77\mathrm{Oh}^{1.6}) \tag{3.80}$$

where the Ohnesorge number Oh is defined by Eq. (3.8).
The evolution of droplets after break-up is discussed in (Pilch and Erdman 1987; Hsiang and Faeth 1993; Gelfand 1996; Shraiber et al. 1996).
The use of a typical break-up time τ_0 allows to define a break-up frequency $\nu_{\mathrm{bu}} = \tau_0^{-1}$. The break-up time can be assessed from the typical time for momentum propagation suggested by Ranger and Nicholls (1968):

$$\tau_0 = \frac{2r}{\mid \boldsymbol{u}_g - \boldsymbol{u}_p \mid} \sqrt{\frac{\rho_l}{\rho_g}}. \tag{3.81}$$

Pilch and Erdman (1987) give a correlation between τ_{bu} and τ_0:

$$\tau_{\mathrm{bu}} = \begin{cases} 6(\mathrm{We} - 12)^{-0.25} & \text{if } 12 < \mathrm{We} < 18 \\ 2.45(\mathrm{We} - 12)^{0.25} & \text{if } 18 < \mathrm{We} < 45 \\ 14.1(\mathrm{We} - 12)^{-0.25} & \text{if } 45 < \mathrm{We} < 351 \\ 0.766(\mathrm{We} - 12)^{0.25} & \text{if } 351 < \mathrm{We} < 2670 \\ 5.5 & \text{if } 2670 < \mathrm{We}. \end{cases} \tag{3.82}$$

While Hsiang and Faeth (1992) suggest

$$\tau_{\mathrm{bu}} = 5\tau_0 \tag{3.83}$$

Nigmatulin (1990) suggests:

$$\tau_{\mathrm{bu}} = \frac{6(1 + 1.5\mathrm{Oh}^{0.74})}{(\ln(We))^{\frac{1}{4}}}\tau_0 \tag{3.84}$$

where the introduction of the Oh allows to account for an additional break-up delay linked to the viscosity of the liquid.

To account more finely for the effects of liquid viscosity, the TAB model (Taylor Analogy Break-up) (O'Rourke and Amsden 1987; Baranger 2004b) describes the dynamics of the break-up process by considering the amplification of oscillations at the droplet surface. For the n-th oscillation mode, which amplitude is ϵ_n, a non-linear analysis yields:

$$\mathrm{d}_{tt}\epsilon_n + \frac{2(n-1)(2n+1)\mu_l}{\rho_l r^2}\mathrm{d}_t\epsilon_n + \frac{n(n-1)(n+2)\sigma_{lg}}{\rho_l r^3}\epsilon_n = \frac{\rho_g \mid \boldsymbol{u}_g - \boldsymbol{u}_p \mid^2}{3\rho_l r} \tag{3.85}$$

where the r.h.s. is a forcing term that increases oscillation amplitudes. This method yields in addition details on the fragment number and sizes, which can be linked to the modes. Again a parameter must be set, that is a critical value of amplitude $\epsilon_{n,c}$ to determine the occurrence of break-up. But model results compare well to experimental results on break-up times. It is implemented in the KIVA II code (Amsden et al. 1989), see also Baranger (2004b); Baranger (2004a); Baranger et al. (2005).

3.3.4.4 Break-up effects on the fluid

Depending on the modeling taken for the fragment velocities, the effect of sudden drag forces can be included. So that the retrocoupling on the gas should be taken into account.
We also highlight that the above modeling is valid if the local flow field around each particle is not too perturbed by the disperse phase so the break-up physics becomes difficult to assess in a moderately dense context. A modeling step in this direction is performed in Appendix C, where some transient aspects of break-up are included, giving promising possibilities of smoothly taking into account the coupling between the break-up process of the disperse phase and the gas velocity field evolution, in a filtered framework.

3.4 Statistical modeling: general aspects of kinetic theory

Statistical modeling relies on ensemble (or statistical) averages, in contrast with continuum mechanics modeling which relies on volume averages. The goal is to reduce the information carried by the numerous particles to the only relevant one of ensemble behaviors.

3.4.1 From the N-particle system to reduced NDFs

We consider a system of N particles with N very large: it is either estimated by Eq. (3.30) for particles in a spray or with the Avogadro number $\mathscr{N}_a$ for atoms in a macroscopic volume of fluid.

3.4.1.1 Deterministic approach at the microscopic level

Each particle, denoted by the subscript i, is described by few degrees of freedom (DoF) that evolve in time, e.g. *a minima* its position $\boldsymbol{x}_i(t)$ and velocity $\boldsymbol{c}_i(t)$. So the particle system has $6N$ DoFs in total and its state is exactly described by a point in a $6N$-dimensional space called the Γ phase space with $\Gamma = \mathbb{R}^{6N}$. For classic particles encountering an external force $\boldsymbol{F}^{\mathrm{ext}}$ per unit mass and a particle-particle interaction force $\boldsymbol{F}_{ij}$ per unit mass that depends on the relative distance $|\boldsymbol{x}_i - \boldsymbol{x}_j|$, the equations of motion at the microscopic level read:

$$\begin{cases} \mathrm{d}_t\boldsymbol{x}_i(t) = \boldsymbol{c}_i(t) \\ \mathrm{d}_t\boldsymbol{c}_i(t) = \boldsymbol{F}_i^{\mathrm{ext}}(t) + \displaystyle\sum_{\substack{j=1 \\ j\neq i}}^{N} \boldsymbol{F}_{ij}(t) \end{cases} \tag{3.86}$$

With these N sets of equations, the corresponding dynamical system is classically described by a trajectory, which, in our case, lives in Γ. This trajectory has the property to never intersect itself. The property of ergodicity is the fact that the trajectory is dense in an isoenergetic sub-manifold of Γ: this property is much desired to describe the system as it allows the equivalence of time and ensemble averaging (Reif 1965).

3.4.1.2 Statistical modeling

We want to avoid describing all the details of the system and, instead, to follow some of the quantities that emerge at the macroscopic scale. These quantities define a state at the macroscopic level and they are not as numerous as the micro-DoFs. So a macroscopic state can be reached thanks to many different underlying microscopic configurations (Pottier 2007). We now focus only on these macroscopic variables: we compute them as ensemble averages, i.e. an average over many copies of the initial system, possibly evolving differently at the microscopic scale, but similarly at the macroscopic scale: this idea, due to Gibbs, allows to smooth out

the undesired fluctuations from the temporal behavior of the macroscopic quantities. The number of ensembles to consider is large enough for the microscopic state points to be dense in Γ. We thus adopt a statistical point of view, introducing a multiple-particle joint distribution function $f^N(t, \boldsymbol{x}_1, \boldsymbol{x}_2, ..., \boldsymbol{x}_N, \boldsymbol{c}_1, \boldsymbol{c}_2, ..., \boldsymbol{c}_N)$ that is normalized to 1 (Balian 1992; Dupays 2006b; Pottier 2007):

$$\int_\Gamma f^N(t, M)\mathrm{d}M = 1 \tag{3.87}$$

where $M = (\boldsymbol{x}_1, ...\boldsymbol{x}_N, \boldsymbol{c}_1, ...\boldsymbol{c}_N)$. A macroscopic quantity Φ can be computed by integrating on Γ a function ϕ depending on the microscopic DoFs:

$$\Phi(t) = \int_\Gamma \phi(M) f^N(t, M)\mathrm{d}M. \tag{3.88}$$

The evolution of an N-particle system is then given by the Liouville equation for the NDF in $6N$ phase space:

$$\partial_t f^N + \sum_{i=1}^{N} \boldsymbol{c}_i \cdot \partial_{\boldsymbol{x}_i} f^N + \sum_{i=1}^{N} \left(\boldsymbol{F}_i^{\text{ext}} + \sum_{\substack{j=1 \\ j\neq i}}^{N} \boldsymbol{F}_{ij} \right) \cdot \partial_{\boldsymbol{c}_i} f^N = 0 \tag{3.89}$$

which originates from the conservation of the number of points in Γ and renders all the microscopic evolution equations of System (3.86).

3.4.1.3 The BBGKY hierarchy

We define the s^{th} order marginal PDFs:

$$f^s(\boldsymbol{x}_1, ...\boldsymbol{x}_s, \boldsymbol{c}_1, ...\boldsymbol{c}_s) = \int_{\text{Part}_s(\Gamma)} f^N(t, \boldsymbol{x}_1, ...\boldsymbol{x}_N, \boldsymbol{c}_1, ...\boldsymbol{c}_N)\mathrm{d}M_s \tag{3.90}$$

where $M_s \in \text{Part}_s(\Gamma) = \text{Vect}(\boldsymbol{x}_{s+1}, ...\boldsymbol{x}_N, \boldsymbol{c}_{s+1}, ...\boldsymbol{c}_N)$. By integration over each subspace $\text{Part}_s(\Gamma)$, the Liouville equation can be transformed into a chain of equations in which the first equation connects the evolution of one-particle PDF f^1 to the two-particle PDF f^2, the second equation connects f^2 to f^3, and generally the s^{th} equation connects to the $(s+1)$-particle PDF:

$$\partial_t f^s + \sum_{i=1}^{s} \boldsymbol{c}_i \cdot \partial_{\boldsymbol{x}_i} f^s + \sum_{i=1}^{s} \left(\boldsymbol{F}_i^{\text{ext}} + \sum_{\substack{j=1 \\ j\neq i}}^{s} \boldsymbol{F}_{ij} \right) \cdot \partial_{\boldsymbol{c}_i} f^s = -\sum_{i=1}^{s} (N-s) \int \boldsymbol{F}_{is+1} \cdot \partial_{\boldsymbol{c}_i} f^{s+1} \mathrm{d}\boldsymbol{x}_{s+1} \mathrm{d}\boldsymbol{c}_{s+1} \tag{3.91}$$

where identical (indiscernible) particles are often considered to simplify the particle-particle interaction term, yielding $\boldsymbol{F}_{is+1} = \boldsymbol{F}_{js+1}$ for all i and j different from $s+1$. This chain of equations is named BBGKY hierarchy as an acronym for the authors who contributed to its finding (Pottier 2007). The system is an exact approach to the Liouville equation. It is therefore redundant but it is practical to build approximations by truncation of the chain when some particle correlations are neglected.
The most celebrated example of the utility of the BBGKY hierarchy consists in closing the first equation of the hierarchy by assuming:

$$f^2(t, \boldsymbol{x}_1, \boldsymbol{x}_2, \boldsymbol{c}_1, \boldsymbol{c}_2) \approx f^1(t, \boldsymbol{x}_1, \boldsymbol{c}_1) f^1(t, \boldsymbol{x}_2, \boldsymbol{c}_2) \tag{3.92}$$

which means that the particles are totally uncorrelated before collisions. The BBGKY hierarchy is then entirely defined by the knowledge of a one-particle Probability Density Function (PDF) evolving in a 6-dimensional space called μ-phase space according to the equation:

$$\partial_t f^1 + \boldsymbol{c}_1 \cdot \partial_{\boldsymbol{x}_1} f^1 + \boldsymbol{F}_1^{\text{ext}} \cdot \partial_{\boldsymbol{c}_1} f^1 = -(N-1) \int \boldsymbol{F}_{12} \cdot \partial_{\boldsymbol{c}_1} f^1(t, \boldsymbol{x}_1, \boldsymbol{c}_1) f^1(t, \boldsymbol{x}_2, \boldsymbol{c}_2) \mathrm{d}\boldsymbol{x}_2 \mathrm{d}\boldsymbol{c}_2. \tag{3.93}$$

3.4.1.4 The Boltzmann equation

The Boltzmann equation features the appropriate level of statistical information to describe many particle systems, from those with intense (but still binary) collisions to those, more dilute which are collisionless.
We now note $f = \sum_{i=1}^{N} f^1 = N f^1$ the number density function (NDF), obtained by summing the one-particle PDF in order to describe N indiscernible particles (Villani 2002): its phase space variables are $\boldsymbol{x}$ and $\boldsymbol{c}$, supported by the μ-phase space.

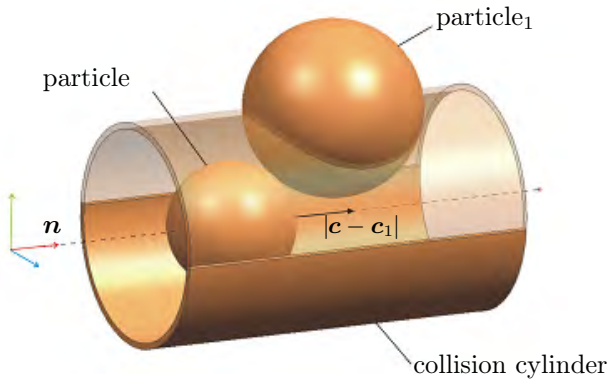

Figure 3.23: *Collision cylinder and geometric cross-section in the case of a hard sphere potential.*

The Boltzmann-Grad limit is defined as the limit of an infinite system of point particles:

$$\begin{cases} N \to +\infty \\ r \to 0 \\ Nr^2 = cst \end{cases} \tag{3.94}$$

where it is crucial to keep a finite cross section Nr^2 at the limit in order to achieve a finite particle-particle interaction probability.
If the particle-particle interactions occur during a very short time τ', compared to the intercollision time τ_0 and to the system's macroscopic evolution time Δt, the one-point PDF Eq. (3.93) yields an evolution equation for f known as the Boltzmann equation:

$$\partial_t f + \boldsymbol{c} \cdot \partial_{\boldsymbol{x}} f + \boldsymbol{F}^{\text{ext}} \cdot \partial_{\boldsymbol{c}} f = \mathcal{C}(f, f) \tag{3.95}$$

where $\mathcal{C}$ models the particle-particle interaction integral of the r.h.s. of Eq. (3.93). The particle-particle interaction term is now a collision term that renders two-particle interactions in an infinitely short time and in an infinitely small physical volume: collisions are instantaneous and local.
The collision probability is proportional to the local velocity difference $\mid \boldsymbol{c} - \boldsymbol{c}_1 \mid$, to the local densities of particles $f(t, \boldsymbol{x}, \boldsymbol{c})$ and $f(t, \boldsymbol{x}, \boldsymbol{c}_1)$ and to the cross-section β: this result is obtained by considering the volume of the cylinder that is swept by particles with rectilinear trajectories as illustrated in Figure 3.23. The collision term reads:

$$\mathcal{C}(f, f) = \iint \left[f(t, \boldsymbol{x}, \boldsymbol{c}') f(t, \boldsymbol{x}, \boldsymbol{c}_1') - f(t, \boldsymbol{x}, \boldsymbol{c}) f(t, \boldsymbol{x}, \boldsymbol{c}_1) \right] |\boldsymbol{c} - \boldsymbol{c}_1| \, \beta \mathrm{d}\boldsymbol{c}_1 \mathrm{d}\boldsymbol{c}_1' \tag{3.96}$$

where $\boldsymbol{c}'$ and $\boldsymbol{c}_1'$ are post collisional velocities defined so that the collisions are perfectly elastic:

$$\begin{cases} \boldsymbol{c}' + \boldsymbol{c}_1' = \boldsymbol{c} + \boldsymbol{c}_1 \\ \boldsymbol{c}'^2 + \boldsymbol{c}_1'^2 = \boldsymbol{c}^2 + \boldsymbol{c}_1^2 \end{cases} \tag{3.97}$$

These microscopic collision functions render the property of microreversibility. Microreversibility coupled to independency of the collision probabilities of Eq. (3.92), constitutes what is referred to as molecular chaos (Boltzmann 1872). Molecular chaos is at the origin of macroscopic irreversibility, see Villani (2002) for an extensive review on the mathematical properties of kinetic theory approaches.
Finally the cross section β contains the physics of the particle-particle interaction: it can be for instance considered in the context of hard spheres as the geometric cross section:

$$\beta = \pi (r + r)^2 \tag{3.98}$$

though other potentials can also be considered (Grad 1949; Drew and Passman 1999).

3.4.2 A hierarchy of fluid models

The Boltzmann equation, given in Eq. (3.95), has too large a phase space to be directly solved in many cases. Reduced approaches give birth to a wide range of models which are referred to as fluid as they account for macroscopic quantities that depend only on space and time. This hierarchy of models is described in the numerous cases of gases and for other particle systems, as it gives an insight on how to reduce statistical model, reduction which we aim at performing in the following chapters.

3.4.2.1 Definition of a fluid model

The passage from the particle model at microscopic level to the fluid model at the macroscopic level is achieved by an ensemble average. It is a major difference with continuum mechanics where volume averaging was used to perform a change of scale. A macroscopic quantity $\Phi(t, \boldsymbol{x})$ can be built locally (in physical space) (Bardos et al. 1991):

$$\Phi(t, \boldsymbol{x}) = \int_{\mathbb{R}^3} \phi(t, \boldsymbol{x}, \boldsymbol{c}) \mathrm{d}\boldsymbol{c} \tag{3.99}$$

from a microscopic function $\phi(t, \boldsymbol{x}, \boldsymbol{c})$ which is local in physical and phase spaces. It is local as compared to the entire system which physical extension spans the entire physical subspace of Γ.
We quantify the intensity of collisions through a Knudsen number:

$$\mathrm{Kn} = \frac{l_0}{\Delta x} = \frac{\tau_0}{\Delta t} \tag{3.100}$$

where l_0 and τ_0 are the mean free path and the intercollision time and Δx and Δt are a flow characteristic length and time.
If the Knudsen number is sufficiently small, collisions allow the velocity distribution to get close to an equilibrium on the characteristic distance Δx. We can describe the system's evolution as follows: information is transported at the macroscopic level, i.e. on a distance Δx, by free streaming particles and it is absorbed in $\boldsymbol{x} + \Delta \boldsymbol{x}$ instantly i.e. faster than Δt thanks to collisions with the particles already present.
The equilibrium distribution in each subsystem $\mathcal{V}(\boldsymbol{x}, \Delta x)$ has a form that is conditioned by the collision operator so it is presumably independent of $\boldsymbol{x}$. But it is parametrized with few quantities that are $\boldsymbol{x}$-dependent, defined at the macroscopic level thanks to Eq. (3.99), just like in thermodynamics. So the state of the system is defined by space dependent macroscopic quantities, this being the definition of a fluid model. The kinetic aspect i.e. a dependence on microscopic velocities $\boldsymbol{c}$ has vanished.

3.4.2.2 Collisional regimes

Different fluid models can be established from the kinetic level, in a hierarchy based on the level of collisions i.e. the Knudsen number (Villani 2002). This number represents the importance of particle-particle collisions relatively to free transport (Struchtrup 2005). A review on collisional regimes is done by Mathiaud (2006). We perform an overview of the most classical levels.
The Chapman-Enskog expansion, detailed below in § 3.4.3, allows to derive a hierarchy of fluid models:

- Euler,
- Navier-Stokes,
- Burnett (Agarwal et al. 2001; Shan et al. 2006),
- super Burnett and augmented Burnett (Struchtrup 2005) *etc.*

and the theory includes tools to compute the transport properties of the fluids (Ferziger and Kaper 1972; Giovangigli 1999). The Euler equations read:

$$\left\{ \begin{array}{l} \partial_t \rho + \partial_{\boldsymbol{x}} \cdot (\rho \boldsymbol{u}) = 0 \\ \partial_t (\rho \boldsymbol{u}) + \partial_{\boldsymbol{x}} \cdot (\rho \boldsymbol{u} \otimes \boldsymbol{u} + p \boldsymbol{I}) = 0 \\ \partial_t (\rho E) + \partial_{\boldsymbol{x}} \cdot (\rho E \boldsymbol{u} + p \boldsymbol{u} \boldsymbol{I}) = 0 \end{array} \right. \tag{3.101}$$

with the macroscopic quantities

$$\begin{pmatrix} \rho \\ \rho \boldsymbol{u} \\ \rho E \end{pmatrix} = \int \begin{pmatrix} 1 \\ \boldsymbol{c} \\ c^2 \end{pmatrix} f(\boldsymbol{c}) \mathrm{d}\boldsymbol{c} \tag{3.102}$$

and where $p = \rho(E - \frac{\boldsymbol{u}^2}{2})$ happens to be given by the perfect gas equation of state. The Euler system does not include dissipative fluxes. The next level corresponds to the Navier-Stokes equations, already presented in the context of continuum mechanics in Appendix A, which derivation through kinetic theory can be found in (Giovangigli 1999; Ern and Giovangigli 1994; Massot 1996). We recall their form with the current notations:

$$\left\{ \begin{array}{l} \partial_t \rho + \partial_{\boldsymbol{x}} \cdot (\rho \boldsymbol{u}) = 0 \\ \partial_t (\rho \boldsymbol{u}) + \partial_{\boldsymbol{x}} \cdot (\rho \boldsymbol{u} \otimes \boldsymbol{u} + \boldsymbol{\Pi}) = 0 \\ \partial_t (\rho E) + \partial_{\boldsymbol{x}} \cdot (\rho E \boldsymbol{u} + \boldsymbol{u} \cdot \boldsymbol{\Pi} + \boldsymbol{q}) = 0 \end{array} \right. \tag{3.103}$$

where $\boldsymbol{\Pi}$ is the strain tensor and $\boldsymbol{q}$ is the heat flux vector. They are often closed with simple Newton and Fourier assumptions:

$$\begin{array}{l} \boldsymbol{\Pi} = \mu \left(\partial_{\boldsymbol{x}} \boldsymbol{u} + \partial_{\boldsymbol{x}}^T \boldsymbol{u} \right), \\ \boldsymbol{q} = \lambda \partial_{\boldsymbol{x}} T, \end{array} \tag{3.104}$$

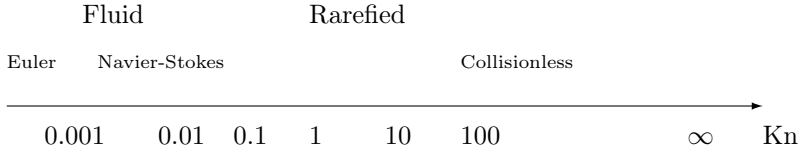

Figure 3.24: *Regimes of the Boltzmann equation depending on collision intensity (Knudsen).*

with μ and λ transport coefficients that correspond respectively to the dynamic viscosity and the thermal conductivity.
Maxwell transfer equations for moments, i.e. the system resulting from the raw integration of Eq. (3.95) versus $\psi = (1, \boldsymbol{c}, c^2)^T$, yield a class of fluid models

$$\begin{cases} \partial_t \rho + \partial_{\boldsymbol{x}} \cdot (\rho \boldsymbol{u}) = 0 \\ \partial_t (\rho \boldsymbol{u}) + \partial_{\boldsymbol{x}} \cdot (\rho \boldsymbol{u} \otimes \boldsymbol{u} + p \boldsymbol{I}) = 0 \\ \partial_t (\rho E) + \partial_{\boldsymbol{x}} \cdot (\rho E \boldsymbol{u} + p \boldsymbol{u} \boldsymbol{I}) = \Xi \end{cases} \tag{3.105}$$

which can be solved using a simplified model for the integral collision term Ξ. A typical linear model is the Bhatnagar-Gross-Krook (BGK) approximation for collisions (Bhatnagar et al. 1954):

$$\Xi = \frac{1}{\tau_0}(f^{(0)} - f) \tag{3.106}$$

with τ_0 a modeled collision time and $f^{(0)}$ an equilibrium distribution e.g. the Maxwellian given in Eq. (3.119). This model was extended to slight anisotropy with the ES-BGK formalism, see (Andries et al. 2002). The collision term Ξ can also be accounted for with a moment method (Levermore 1996; Levermore and Morokoff 1998).
Another approach due to Grad (1949) and based on a Hilbert expansion yields another class of fluid models, which are useful for hypersonic and rarefied gas dynamics (high Kn) and are an active topic of research but they raise realizability issues. Attempts to regularize the Grad solutions can be found in (Struchtrup and Torrilhon 2003; Torrilhon and Struchtrup 2004; Torrilhon 2010).

3.4.2.3 Examples of fluid models for gases

Kinetic theory has originally been developed for gases, at first speculating the existence of underlying molecules (Boltzmann 1872) and then taking inspiration from them (Enskog 1917). The Knudsen number allows to distinguish several fluid models, which are used in many applications. They correspond to the hydrodynamical regime and a review of fluid model derivations can be found in Bardos et al. (1991). The particle system can be considered as a continuous flow as long as $\mathrm{Kn} \ll 1$. The collisional hierarchy is illustrated in Figure 3.24 and some applications of the classical fluid models for gas flows are given as an illustration.
A flow can be described very accurately by the Euler equations when $\mathrm{Kn} < 10^{-3}$. This model, also known as perfect fluid aerodynamics in reference to the absence of dissipative fluxes, is used to solve infinite Reynolds number problems. For instance, the flow around a plane can be so computed, when the effect of boundary layers on the flow can be neglected: transfers (drag) towards the object can be assessed from the knowledge of the velocity at the edge of the boundary layer (one-way coupling). An iterative protocol can possibly be considered for a weak coupling between the bulk flow and the boundary layer.
The Navier-Stokes equations describe flows up to $\mathrm{Kn} < 10^{-2}$. They are very useful in most gas and liquid applications and have been widely studied: the matter of the existence and unicity of their solution has been tackled many times since Chorin (1968).
On the contrary, when $\mathrm{Kn} > 0.1$, the rate of collisions is not significant enough to ensure that the flow is close to an equilibrium. This occurs in hypersonic flows (typically $\mathrm{Ma} > 5$) (Magin and MacCormack 2009), rarefied gas dynamics (typically $p < 1\,\mathrm{Pa}$) (Cercignani 2000), and microfluidics (typically $\Delta x < 1\,\mu\mathrm{m}$) (Frezzotti et al. 2009). In such cases, the particle flow can be described with other fluid models, e.g. among the ones given previously, but four issues arise:

- the models are not systematically mathematically well posed, in the sense of unconditional hyperbolicity,
- the models are difficult to solve,
- the transport coefficients are not well known,
- the models are not very accurate approximations.

In systems that are strongly out-of-equilibrium, another approach is to come back to the Boltzmann equation. But the latter, with its high-dimensional phase space and its highly non-linear integral collision term, is very

difficult to solve up to now. Moment methods are explored (Desvillettes 1993; Struchtrup 2005) but the Boltzmann equation is sometimes approached with simplified collision operators e.g. BGK or a reduction of the phase space dimension if possible.
The flow model also depends on the microscopic physics, which conditions the transport coefficients for instance. Models for β can be of hard sphere type, see Eq. (3.98), while simplified models such as Maxwell molecules can be integrated analytically (Drew and Passman 1999; Villani 2002). In the case of dense gases, the theory must be adapted to include multiple collisions and altered potentials (Drew and Passman 1999). These extensions allow to retrieve real gas effects such as covolume coefficient modeling minimum occupancy, complex potentials which account for the various Van der Waals effects (Keesom, Debye and London forces).

3.4.2.4 Fluid models for particle systems

Finally, the theory is valid for any large system of particles and a crucial point is that it can be used for disperse phase flows: the phase space can be enriched with any kind of internal DoFs, which eventually yields the so-called Williams-Boltzmann equation, detailed in § 3.5.
Particle systems have collision times τ_0 that are typically much larger than that of gas molecules. So that an equilibrium approach may seem awkward at first glance but it is relevant in many cases, either due to the tranquilizing presence of an underlying gaseous phase or due to significant collisions. Equilibrium regimes for particles are extensively studied, including collisional regimes, in Mathiaud (2006).
But particle systems can either be considered on large time scales, as classically done in astronomy. In two-phase disperse flows, the dynamics of the system is to be considered but we may take advantage of pseudo-equilibria imposed by the underlying carrier phase, see for instance the case of Brownian Motion in § 8.4.2. In the absence of a significant carrier phase, the particles behave like a granular flow if very collisional (dense), this topic being a wide research area (Rao et al. 2008).

3.4.3 Chapman-Enskog expansion

Different techniques have been listed above to yield approximations of the kinetic equation for near-equilibrium cases, namely Chapman-Enskog, Hilbert, and Grad expansions. We focus on the Chapman-Enskog expansion as we use it in Chapter 8 to study a Fokker-Planck equation describing nanoparticles and in Chapter 9 to get a kinetic-kinetic formalism for strongly coupled nanoparticle-fluid flows.
From the seminal work of Chapman (1916); Enskog (1917); Chapman (1918), the Chapman-Enskog expansion yields several modeling levels as described in Chapman and Cowling (1939) reedited regularly (Chapman and Cowling 1970; Chapman and Cowling 1990) and (Grad 1958; Ferziger and Kaper 1972; Cercignani 1988; Cercignani et al. 1994; Massot 1996; Giovangigli 1999; Magin and MacCormack 2009).

3.4.3.1 Principle

The Chapman-Enskog expansion is an asymptotic expansion based on a collision frequency, or another small parameter η, that yields a hierarchy of approximations which depend only on time t and space $\boldsymbol{x}$ through average, macroscopic quantities (Massot 1996; Pottier 2007) e.g. density, hydrodynamic velocity, temperature *etc.*. We can write any kinetic equation with a symbolic notation for the collision operator:

$$\partial_t f + \boldsymbol{c}\cdot\partial_{\boldsymbol{x}} f + \boldsymbol{F}\cdot\partial_{\boldsymbol{c}} f = \frac{1}{\eta}\mathcal{J}(f,f) \tag{3.107}$$

where the collision operator reads, for the Boltzmann equation Eq. (3.95):

$$\mathcal{J}^{\mathrm{B}}(f,g) = \mathcal{C}(f,g) \tag{3.108}$$

for all functions $f(\boldsymbol{c})$ and $g(\boldsymbol{c})$ and with $\mathcal{C}(f,g)$ defined from Eq. (3.96).
The lower order approximation is naturally the equilibrium distribution, noted $f^{(0)}$, i.e. the distribution that cancels the collision operator:

$$\mathcal{J}(f^{(0)},f^{(0)}) = 0 \tag{3.109}$$

and the expansion has the form

$$f = f^{(0)}(1+\eta\phi^{(1)}+\eta^2\phi^{(2)}+...) \tag{3.110}$$

where the $\phi^{(i)}$ are constrained as follows

$$\int f^{(0)}\phi^{(i)}\mathrm{d}\boldsymbol{c} = \int \boldsymbol{c} f^{(0)}\phi^{(i)}\mathrm{d}\boldsymbol{c} = \int c^2 f^{(0)}\phi^{(i)}\mathrm{d}\boldsymbol{c} = 0 \tag{3.111}$$

in the fluid reference frame. These constraints mean that f and $f^{(0)}$ yield the same local density, hydrodynamic velocity and temperature, and that the zeroth order approximation is a local equilibrium distribution. The dissipative fluxes are null at this order and the hydrodynamics is that of a perfect fluid.
The first order approximation comes out when writing the kinetic equation at zeroth order and developing the collision operator on $\phi^{(1)}$. By solving the first order equation, one gets an expression of $\phi^{(1)}$ versus $f^{(0)}$ and the affinities. The first order yields the instantaneous dissipative fluxes and the equations of hydrodynamics. This class of solutions is referred to as normal solutions (Grad 1958), and any solution is proven to converge towards these solutions after a time of the order of the collision time (typically $\eta = 10^{-10}$ s in a gas at normal conditions).

3.4.3.2 Collision Invariants

Collision invariants ψ are microscopic quantities that are conserved by the collision operator so that we can write the microscopic collision relation for particles 1 and 2:

$$\psi_1 + \psi_2 = \psi_1' + \psi_2' \tag{3.112}$$

with the usual exponent $'$ for post-collision quantities. As a consequence, any linear combination of collision invariants is also a collision invariant and the macroscopic quantity $\int \boldsymbol{\psi} f \mathrm{d}\boldsymbol{c}$ is conserved by $\mathcal{J}$.
In the case of Boltzmann's equation, the collision operator models micro-reversible collisions so that matter (number or mass), momentum and kinetic energy are conserved by collisions:

$$\psi = \begin{pmatrix} 1 \\ \boldsymbol{c} \\ c^2 \end{pmatrix} \tag{3.113}$$

which yields:

$$\begin{pmatrix} n(t,\boldsymbol{x}) \\ \boldsymbol{u}(t,\boldsymbol{x}) \\ 2e(t,\boldsymbol{x}) \end{pmatrix} = \int \boldsymbol{\psi} f(t,\boldsymbol{x},\boldsymbol{c}) \mathrm{d}\boldsymbol{c}. \tag{3.114}$$

We retrieve as a consequence that the Boltzmann collision operator conserves mass, momentum and kinetic energy at the microscopic level.
It can be shown that the collision invariants of Boltzmann's equation in 3D belong to a vector space of dimension 5 (Ferziger and Kaper 1972; Massot 1996; Pottier 2007).

3.4.3.3 Zeroth order and Maxwellian distribution

One introduces the mathematical entropy:

$$\mathscr{H} = \int f \log f \mathrm{d}\boldsymbol{c} \tag{3.115}$$

and its temporal derivative (Ferziger and Kaper 1972):

$$\frac{d\mathscr{H}}{dt} = -\frac{1}{4} \int (f'^2 - f^2) \left[\log(f'^2) - \log(f^2)\right] \mid \boldsymbol{c}_1 - \boldsymbol{c}_2 \mid \mathrm{d}\boldsymbol{c}_1 \mathrm{d}\boldsymbol{c}_2 \tag{3.116}$$

which is negative and is null at equilibrium (Magin and MacCormack 2009):

$$\frac{d\mathscr{H}}{dt} \leq 0 \tag{3.117}$$

this result constituting the celebrated H-theorem.
As a consequence the quantity $\log(f'^2) - \log(f^2)$ cancels at equilibrium and is therefore a collision invariant, implying the following constraint:

$$\log f \in \mathrm{span}\{1, \boldsymbol{c}, c^2\} \tag{3.118}$$

which yields after integration the equilibrium distribution:

$$f^{(0)} = n(t,\boldsymbol{x}) \left(\frac{m}{2\pi k_B T(t,\boldsymbol{x})}\right)^{\frac{3}{2}} \exp\left(\frac{-m(\boldsymbol{c} - \boldsymbol{u}(t,\boldsymbol{x}))^2}{2k_B T(t,\boldsymbol{x})}\right) \tag{3.119}$$

where $e = k_B T/m$ and $k_B = 1.3806503 \times 10^{-23}\,\mathrm{m^2.kg.s^{-2}.K^{-1}}$ is the Boltzmann constant. Eq. (3.119) is known as the Maxwell-Boltzmann distribution or Maxwellian.
The properties of the equilibrium solution, which has been explicitly computed in Eq. (3.119), can be used to solve the $\phi^{(i)}$. Moreover the resolution steps yield a hierarchy of dynamic equations for the fluid. They are deduced from the so-called resolubility criterion: for the equation of a given order, the resolubility criterion is the constraint on the r.h.s. to be in the image of operator $\mathcal{J}$.

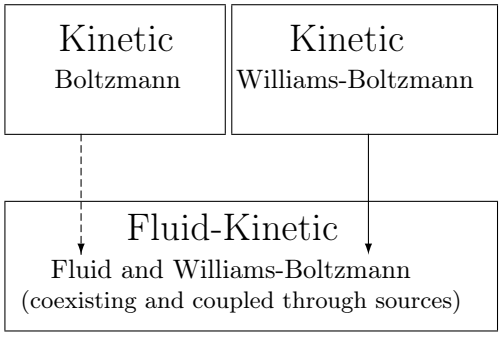

Figure 3.25: *Hierarchy of kinetic models for disperse two-phase flows.*

3.4.3.4 Conclusion on the Chapman-Enskog expansion

The Chapman-Enskog expansion allows to derive fluid equations and thermophysical properties from kinetic equations. Approaches such as the Hilbert expansion or the Grad expansion can also be used in other contexts.
This approach is used in the present thesis: in § 8.4.2.3, the equations of a set of particles submitted to Brownian motion are derived from a Fokker-Planck equation; in Appendix D fluid equations are derived in the case of a two-phase mixture of nanometric particles at free molecular regime in a gas, from a kinetic modeling both at the gas and at the nanometric particle levels.

3.5 The fluid-kinetic approach for disperse two-phase flows

We now introduce a statistic description for the disperse phase which is referred to as kinetic because of the analogy with the kinetic theory of gases introduced by Boltzmann (1872), see § 3.4.1.4.
We consider a carrier phase made of a large ensemble of particles at low Knudsen so that it is a continuous fluid at the macroscopic level, see § 3.4.2.2. It is *a priori* also a fluid at the level of the disperse phase inclusions, except in Appendix D.
The fluid equations presented in Appendix A are used to derive a continuous model for the carrier phase of the two-phase flow: they are defined in the whole space. The disperse phase is then modeled by a kinetic equation, also defined in the whole space. The disperse phase is assumed to be dilute enough so that its influence on the gas phase can be described by local source term addition in the gas phase equations Kuentzmann (1973a); Dupays (2006a) and such source terms are described in § 3.5.1.5.

3.5.1 Kinetic modeling of a disperse phase

3.5.1.1 A statistical approach

The statistical approach is recommended when the droplets can be considered through few degrees of freedom. They are then represented as point particles and the information on the degrees of freedom is stored in a number density function (NDF) noted f as derived in § 3.4.1.4.
The statistical approach is void if

- rare events condition the observable dynamics (e.g. in a two-phase counter-flow flame, when big droplets intermittently cross the flame front yielding large scale perturbations);
- long-range interactions occur between the inclusions e.g. wake effect in settling problems (Crowe et al. 1998).

3.5.1.2 Basis assumptions on droplets

The following simplification assumptions are made:

- the droplets are spherical: surface tension is dominant versus the surrounding hydrodynamic forces, as quantified by the aerodynamic Weber number given in Eq. (3.7).
- droplets are assumed to have a homogeneous composition and no internal motion.

The size parameter ϕ is generally taken as the radius r, the surface $S = 4\pi r^2$ or the volume $v = \mathcal{V}(r) = 4/3\pi r^3$ of the droplets. The infinitesimal droplet number $\mathrm{d}N = f^r(r)\mathrm{d}r = f^s(S)\mathrm{d}S = f^v(v)\mathrm{d}v$ is expressed in all variables so that the three NDFs f^r, f^s and f^v are linked by the relation (Laurent and Massot 2001):

$$f^r(t,\boldsymbol{x},\boldsymbol{c},\theta,r) = 8\pi r f^s(t,\boldsymbol{x},\boldsymbol{c},\theta,S) = 4\pi r^2 f^v(t,\boldsymbol{x},\boldsymbol{c},\theta,v). \tag{3.120}$$

So the NDF is simply noted f in the following, keeping in mind that it can depend on any size parameter as soon as the pre-factor is considered.
When modeling the droplet with an infinite conductivity hypothesis (Abramzon and Sirignano 1989; Laurent and Massot 2001), we can choose to parametrize the droplet internal state with the only temperature variable. Its state function is then the enthalpy, which only depends on T and reads:

$$h(\theta) = h_{\text{ref}} + \int_{\theta_{\text{ref}}}^{\theta} c_{p,l}(\theta')\mathrm{d}\theta' \tag{3.121}$$

where $c_{p,l}(\theta)$ is the droplet heat capacity and the index "ref" denotes a reference state.

3.5.1.3 The Williams-Boltzmann equation

The entire information of the disperse phase is included in the number density function (NDF) so that:

$$f(t, \boldsymbol{x}, \boldsymbol{c}, \theta, \phi)\mathrm{d}x\mathrm{d}\boldsymbol{c}\mathrm{d}\theta\mathrm{d}\phi \tag{3.122}$$

is at time t the probable number of droplets at a location $\boldsymbol{x}$ in a $\mathrm{d}\boldsymbol{x}$-neighborhood of $\boldsymbol{x}$, with a velocity $\boldsymbol{c}$ in a $\mathrm{d}\boldsymbol{c}$-neighborhood of $\boldsymbol{c}$, with a temperature θ in a $\mathrm{d}\theta$-neighborhood of θ, and with a size parameter ϕ in a $\mathrm{d}\phi$-neighborhood of ϕ. The velocity $\boldsymbol{c}$ is sometimes decomposed in cartesian components $\boldsymbol{c} = (c_1\ c_2\ c_3)^T$. If $\mathrm{d}\boldsymbol{x}$ is an elementary volume of the physical space, the infinitesimal volume $\mathrm{d}\boldsymbol{c}\mathrm{d}\theta\mathrm{d}\phi$ is an elementary volume of the phase space.
The kinetic equation or Williams-Boltzmann equation or sometimes Generalized Population Balance Equation simply expresses that the total derivative of the NDF is due to integral source terms (Williams 1958):

$$\partial_t f + \partial_{\boldsymbol{x}} \cdot (\boldsymbol{c} f) + \partial_{\boldsymbol{c}} \cdot (\boldsymbol{F} f) + \partial_\theta \left(\frac{H}{c_{p,l}} f \right) + \partial_\phi (R_s f) = \mathfrak{B} + \mathfrak{C} \tag{3.123}$$

that are break-up $\mathfrak{B}$, usually depending linearly on f, and collisions $\mathfrak{C}$, usually depending quadratically on f. The modeling effort also consists in closing the different rates of change:

- $\boldsymbol{F}$ is the droplet acceleration usually due to drag,
- H is the enthalpy change rate usually due to heating,
- R is the size evolution, due to evaporation for instance,

so that the two-phase flow is completely modeled by gas equations given in Eq. (A.1), (A.2), (A.4), and (A.6), coupled to the kinetic Eq. (3.123) for the disperse phase. The exchange source terms, expressed as integrals on the droplet NDF are discussed in § 3.5.1.5.

3.5.1.4 Kinetic transfer closures

To close the drag, heating and evaporation terms, we can directly use the correlations for a single drop, given in § 3.3.
For instance the drag per unit mass is taken as that of a single droplet:

$$\boldsymbol{F}(t, \boldsymbol{x}, \boldsymbol{c}, \phi) = \boldsymbol{F}(\boldsymbol{u}_p, \boldsymbol{u}_g(t, \boldsymbol{x}_p), \phi_p) \tag{3.124}$$

for all t as long as $\boldsymbol{x}_p = \boldsymbol{x}$ and $\phi_p = \phi$ and where $\boldsymbol{F}(\boldsymbol{u}_p, \boldsymbol{u}_g(t, \boldsymbol{x}_p), \phi_p)$ is given from Eq. (3.51).

3.5.1.5 Retrocoupling source terms

As said previously, the fluid-kinetic approach assumes point-particles: the disperse phase is dilute enough to have a coupling only through source terms on the conservative quantities.
The gas system composed of Eq. (A.1), Eq. (A.2), (A.4), and (A.6) in the case of Navier-Stokes equations is recalled:

$$\begin{cases} \partial_t \rho_g + \partial_{\boldsymbol{x}} \cdot (\rho_g \boldsymbol{u}_g) = S^m \\ \partial_t (\rho_g Y_k) + \partial_{\boldsymbol{x}} \cdot (\rho_g \boldsymbol{u}_g Y_k) = -\partial_{\boldsymbol{x}} \cdot \left(\rho_g Y_k \boldsymbol{u}_k^{\text{diff}} \right) + M_k \dot{\omega}_k + S_k^m, \quad k \in [\![1, n_s]\!] \\ \partial_t \left(\rho_g \boldsymbol{u}_g \right) + \partial_{\boldsymbol{x}} \cdot (\rho_g \boldsymbol{u}_g \otimes \boldsymbol{u}_g) = \partial_{\boldsymbol{x}} \cdot \boldsymbol{T} + \rho \boldsymbol{a} + \boldsymbol{S}^{\mathbf{mom}} \\ \partial_t \left(\rho_g e_g \right) + \partial_{\boldsymbol{x}} \cdot (\rho_g \boldsymbol{u}_g e_g) = \boldsymbol{T} : \partial_{\boldsymbol{x}} \boldsymbol{u}_g - \partial_{\boldsymbol{x}} \cdot \boldsymbol{q} + S^{\text{e}} \end{cases} \tag{3.125}$$

with the relations:

$$\sum_{k=1}^{n_s} Y_k = 1, \ \sum_{k=1}^{n_s} S_k^m = S^m \ \text{ and } \ \sum_{k=1}^{n_s} \rho_g Y_k \boldsymbol{u}_k^{\text{diff}} = 0 \tag{3.126}$$

while the thermodynamical relations as well as the species and heat fluxes are computed similarly as for a single phase flow, described in Appendix A.
The overall disperse two-phase system is always written to be conservative as regards mass, momentum and energy. The source terms in the gas equations are computed as integrals of the disperse phase kinetic sources (Laurent and Massot 2001; Laurent et al. 2004). The mass transfer source terms are due to evaporation or chemical reactions and read:

$$S^m(t,\boldsymbol{x}) = -\int_{\mathbb{R}^+}\int_{\mathbb{R}^+}\int_{\mathbb{R}^3} \rho_l \, R_s \, \partial_\phi \mathcal{V}(\phi) \, f(t,\boldsymbol{x},\boldsymbol{c},\theta,\phi) \mathrm{d}\boldsymbol{c}\mathrm{d}\theta\mathrm{d}\phi \tag{3.127}$$

where $\mathcal{V}(\phi)$ is the droplet volume, while the species transfer term reads:

$$S_k^m(t,\boldsymbol{x}) = -\int_{\mathbb{R}^+}\int_{\mathbb{R}^+}\int_{\mathbb{R}^3} \rho_l \, R_k \, \partial_\phi \mathcal{V}(\phi) \, f(t,\boldsymbol{x},\boldsymbol{c},\theta,\phi) \mathrm{d}\boldsymbol{c}\mathrm{d}\theta\mathrm{d}\phi \tag{3.128}$$

where R_k is the evaporation rate, broken down to match the appropriate gaseous species. The momentum transfer source term reads:

$$\begin{aligned}\boldsymbol{S}^{\mathbf{mom}}(t,\boldsymbol{x}) = -\int_{\mathbb{R}^+}\int_{\mathbb{R}^+}\int_{\mathbb{R}^3} \rho_l \Big[& \mathcal{V}(\phi)\boldsymbol{F}(t,\boldsymbol{x},\boldsymbol{c},\phi) \\ & + \boldsymbol{c}\, R_s \, \partial_\phi \mathcal{V}(\phi) \Big] f(t,\boldsymbol{x},\boldsymbol{c},\theta,\phi) \mathrm{d}\boldsymbol{c}\mathrm{d}\theta\mathrm{d}\phi\end{aligned} \tag{3.129}$$

and is due to the drag force but also the momentum contribution of the evaporated mass. The energy transfer source term is due to heating, evaporative contribution and to the work of the drag force:

$$\begin{aligned}S^{\mathrm{e}}(t,\boldsymbol{x}) = -\int_{\mathbb{R}^+}\int_{\mathbb{R}^+}\int_{\mathbb{R}^3} \rho_l \Big[& \mathcal{V}(\phi) \left[\mathrm{H}(t,\boldsymbol{x},\theta,\phi) + (\boldsymbol{c}-\boldsymbol{u}_g)\cdot\boldsymbol{F}(t,\boldsymbol{x},\boldsymbol{c},\phi)\right] \\ & + h(\theta)\, R_s \, \partial_\phi \mathcal{V}(\phi) \Big] f(t,\boldsymbol{x},\boldsymbol{c},\theta,\phi) \mathrm{d}\boldsymbol{c}\mathrm{d}\theta\mathrm{d}\phi\end{aligned} \tag{3.130}$$

here $(\boldsymbol{c}-\boldsymbol{u}_g(t,\boldsymbol{x}))\cdot\boldsymbol{F}$ is the work of the drag force of a single particle, which is exclusively transmitted to the gas, as a reasonable assumption. Please note that the definition of the enthalpy of vapor species k must comply that of the liquid.
If the spray has a mass fraction that is low enough, the retrocoupling terms can be neglected: this approach is referred to as one-way coupling. On the contrary for moderately dense sprays, as defined in § 3.1.4, these terms should be taken into account and the disperse two-phase system is then strongly coupled: the problem is said to be two-way coupled.
Two-way coupling introduces peculiarities that require specific modeling and numerical methods, as discussed in § 4.7.

3.5.2 Kinetic collision operators

The modeling of collisions cannot be done directly from its deterministic model of § 3.3.3. We build a collision operator that complies with the statistical modeling.

3.5.2.1 Collision probability

The kinetic modeling for the collision operator is taken from Hylkema and Villedieu (1998) with the following assumptions (Laurent et al. 2004):
[HC1] We only take binary collisions into account.
[HC2] The mean collision time is very small compared to the inter-collision time.
[HC3] Mass, momentum and droplet enthalpy are preserved during collisions.
Hypotheses [HC1] and [HC2] result from the small liquid phase volume fraction in the context of moderately dense sprays. Hypothesis [HC3] is a classical conservation hypothesis for most types of collisions, including inelastic collisions and coalescence (which is perfectly inelastic).
Collisions are assessed in a statistical context by a collision flow rate that depends on a cross-section, classically taken as the geometric cross-section as illustrated in Figure 3.23, and a relative velocity so that the collision kernel reads:

$$\mathfrak{K}_{\mathrm{coll}}(\boldsymbol{c}^\diamond,\boldsymbol{c}^\star,v^\diamond,v^\star) = \mathfrak{E}\pi(r^\diamond + r^\star)^2 \, |\boldsymbol{c}^\diamond - \boldsymbol{c}^\star| \, . \tag{3.131}$$

This collision kernel is directly inspired from the one in the Boltzmann collision operator given in Eq. (3.96) as it assumes straight line (ballistic) trajectories in-between two collisions and a hard sphere-like interaction. Whenever the gas surrounding the particles should play a role in the occurrence of collision events, a collision

efficiency correction $\mathfrak{E} < 1$ is considered to account for the surrounding gas flow effect, which is equivalent to reducing the swept volume as illustrated in Figure **??**. This probability factor models the correlation of droplet velocities immediately before a collision. As a remark, the collision efficiency correction would be void in the classical kinetic theory of gases since no carrier phase can perturb the ballistic collision mechanism. For disperse phase flows, the simplest approach is to neglect this effect and to consider $\mathfrak{E} = 1$. This simplifies the computation but a small error on growth rate is amplified when coalescence is intense and droplet size growth significant. So that models given in § 3.3.3.1 should be considered. Besides, the simulation of real 2D disperse phases i.e. with particles which centers and velocity vectors all belong to the same plan, has an impact on collision probability modeling, the geometric cross section becoming $\beta(r^\star, r^\diamond) = r^\diamond + r^\star$.
After a collision, different regimes can occur, especially for liquid droplets, which are detailed below, see § 3.3.3.3 for the modeling of the transition between the different regimes. We now introduce the operators used in the kinetic vision to account for collision effects: these operators usually separate disappearance and creation terms according to $\mathfrak{C} = \mathfrak{C}^+ - \mathfrak{C}^-$, and they are written to ensure the desired conservation properties.

3.5.2.2 Rebound operator

Inclusions may bounce on each other so that only their velocities are modified, see § 3.3.3.4. Bouncing occurs systematically after a collision in the case of solid particles.
Let us now consider hard sphere collisions between the particles. The rebound term can be modeled using the generalized hard-sphere Boltzmann inelastic, binary-collision operator (Cercignani 1988; Fox et al. 2008):

$$\begin{aligned}\mathfrak{C}^+_{reb} &= \int_0^\infty \iint_{\mathbb{R}^3,\mathbb{R}^+} \frac{f(t,\boldsymbol{x},\boldsymbol{c}'',\theta,v) f(t,\boldsymbol{x}^\star,\boldsymbol{c}^{\star\prime\prime},\theta^\star,v^\star)}{\alpha(v,v^\star)^2} \mathfrak{K}_{\text{coll}}(\boldsymbol{c},\boldsymbol{c}^\star,v,v^\star)\, |\boldsymbol{g}\cdot\boldsymbol{n}|\, \mathrm{d}\boldsymbol{n}\mathrm{d}\boldsymbol{c}^\star\mathrm{d}v^\star \\ \mathfrak{C}^-_{reb} &= \int_0^\infty \iint_{\mathbb{R}^3,\mathbb{R}^+} f(t,\boldsymbol{x},\boldsymbol{c},\theta,v) f(t,\boldsymbol{x}^\star,\boldsymbol{c}^\star,\theta,v^\star) \mathfrak{K}_{\text{coll}}(\boldsymbol{c},\boldsymbol{c}^\star,v,v^\star)\, |\boldsymbol{g}\cdot\boldsymbol{n}|\, \mathrm{d}\boldsymbol{n}\mathrm{d}\boldsymbol{c}^\star\mathrm{d}v^\star\end{aligned} \tag{3.132}$$

where $\boldsymbol{n} = (\boldsymbol{x} - \boldsymbol{x}^\star)/|\boldsymbol{x} - \boldsymbol{x}^\star|$ is the unit vector in the direction between the droplet centers, $\boldsymbol{g} = \boldsymbol{c} - \boldsymbol{c}^\star$ is the velocity difference before collision, and $0 \leq \alpha \leq 1$ is the coefficient of restitution with the property $\alpha(v,v^\star) = \alpha(v^\star,v)$. The integration on $\boldsymbol{x}^\star$ is equivalent to integrating on an impact parameter. For elastic rebounds, $\alpha = 1$. The surface S^+ is the unit half sphere on which $\boldsymbol{g}\cdot\boldsymbol{n} > 0$ (i.e., velocity differences that result in collisions). The collision cross section is:

$$\beta(v,v^\star) = \beta(v^\star,v) = \pi\left(r(v) + r(v^\star)\right)^2. \tag{3.133}$$

The double-prime variables denote values before the inverse collision, which are defined in terms of the pre-collision values by Fox et al. (2008):

$$\begin{aligned}\boldsymbol{c}'' &= \boldsymbol{c} - \frac{v(S^\star)(1+\alpha(v,v^\star))}{\alpha(v,v^\star)(v+v^\star))}(\boldsymbol{g}\cdot\boldsymbol{n})\boldsymbol{n}, \\ \boldsymbol{c}^{\star\prime\prime} &= \boldsymbol{c}^\star + \frac{v(S)(1+\alpha(S,S^\star))}{\alpha(v,v^\star)(v+v^\star))}(\boldsymbol{g}\cdot\boldsymbol{n})\boldsymbol{n}.\end{aligned} \tag{3.134}$$

where the droplet volume is $v(S) = S^{3/2}/(6\sqrt{\pi})$. Note that we have assumed in Eq. (3.132) and Eq. (3.134) that the droplet volumes do not change during a rebound event (i.e. $v'' = v' = v$ and $v^{\star\prime\prime} = v^{\star\prime} = v^\star$).
By analogy with the BGK model presented in § 3.4.2.2 to account in a simple linear way for the effect of collisions, a linear model for particle collisions can be considered though it is valid in the particular case of intense collisions, for pure rebound regimes and for monodisperse size distributions only. It reads (Fox et al. 2008):

$$\mathfrak{C}^{\text{BGK}}_{reb} = \frac{1}{\tau_c}(f_{\text{eq}} - f) \tag{3.135}$$

when considering the equilibrium distribution function f_{eq} and the characteristic collision time τ_c of the particles in the flow. The latter is complex to estimate as it depends on properties of the surrounding flow and of the disperse phase, mainly number concentration and inertia. Complex consequences of collisions on the particle transport can be modeled, resulting in other types of readily integrated collision terms, see for instance Abbas et al. (2006) and Abbas (2008).

3.5.2.3 Stretching operator

The physics of stretching can be treated with the operator $\mathfrak{C}_{str}$ which has a structure close to that of the rebound operator $\mathfrak{C}_{reb}$ given in Eq. (3.132) but where the velocity transformation Eq. (3.72) must be enforced.

3.5.2.4 Coalescence operator

The coalescence operator at the kinetic level is developed as $\mathfrak{C}_{coal} = \mathfrak{C}^+_{coal} - \mathfrak{C}^-_{coal}$ where $\mathfrak{C}^+_{coal}$ and $\mathfrak{C}^-_{coal}$ respectively correspond to the quadratic integral operators associated with creation and destruction of droplets due to coalescence. Considering two precursor droplets of volumes $v^\star$ and $v^\diamond$ colliding to form a new droplet of volume v, the kinetic coalescence operators read (Hylkema and Villedieu 1998; Hylkema 1999):

$$\begin{aligned}
\mathfrak{C}^+_{coal} &= \frac{1}{2}\iint_{\boldsymbol{c}^\star,\theta^\star}\int_{v^\star\in[0,v]} f(t,\boldsymbol{x},\boldsymbol{c}^\diamond,\theta^\diamond,v^\diamond)f(t,\boldsymbol{x},\boldsymbol{c}^\star,\theta^\star,v^\star)\mathfrak{K}_{\text{coll}}(\boldsymbol{c},\boldsymbol{c}^\star,v^\diamond,v^\star)J\mathrm{d}v^\star\mathrm{d}\boldsymbol{c}^\star\mathrm{d}\theta^\star,\\
\mathfrak{C}^-_{coal} &= \iint_{\boldsymbol{c}^\star,\theta^\star}\int_{v^\star} f(t,\boldsymbol{x},\boldsymbol{c},\theta,v)f(t,\boldsymbol{x},\boldsymbol{c}^\star,\theta^\star,v^\star)\mathfrak{K}_{\text{coll}}(\boldsymbol{c},\boldsymbol{c}^\star,v,v^\star)\mathrm{d}v^\star\mathrm{d}\boldsymbol{c}^\star\mathrm{d}\theta^\star,
\end{aligned} \tag{3.136}$$

where $v^\diamond = v - v^\star$, $v^\diamond\boldsymbol{c}^\diamond = v\boldsymbol{c} - v^\star\boldsymbol{c}^\star$, $v^\diamond h(\theta^\diamond) = vh(\theta) - v^\star h(\theta^\star)$ are pre-collisional parameters,

$$J = (v/v^\diamond)^{n_d+1}c_{p,l}/c^\diamond_{p,l} \tag{3.137}$$

is the Jacobian of the mapping $(v,\theta,\boldsymbol{c}) \to (v^\diamond,\theta^\diamond,\boldsymbol{c}^\diamond)$ with n_d the dimension of the velocity phase space, $c_{p,l} = c_{p,l}(\theta)$ and $c^\diamond_{p,l} = c_{p,l}(\theta^\diamond)$. The kernel is the collision kernel presented in Eq. (3.131).
The coalescence operator obviously depends only on $(r,\boldsymbol{c},\theta)$. We check that we have the following relations:

$$\int_{\mathbb{R}^+}\begin{pmatrix}1\\ v\\ \boldsymbol{c}v\\ hv\end{pmatrix}\mathfrak{C}^+_{coal}(t,\boldsymbol{x},\boldsymbol{c},\theta,r)\mathrm{d}\boldsymbol{c}\mathrm{d}\theta\mathrm{d}v = \int_{\mathbb{R}^+}\begin{pmatrix}\frac{1}{2}\\ v\\ \boldsymbol{c}v\\ hv\end{pmatrix}\mathfrak{C}^-_{coal}(t,\boldsymbol{x},\boldsymbol{c},\theta,r)\mathrm{d}\boldsymbol{c}\mathrm{d}\theta\mathrm{d}v \tag{3.138}$$

of mass, momentum, and enthalpy local conservation while number is reduced by coalescence itself.

3.5.2.5 Full collision operator

A full collision operator accounting for all the collision regimes can be defined as soon as the transition between the different regimes is treated at the kinetic level. The transition can be based on a so-called coalescence efficiency $\mathfrak{E}_{coal}$ in order to be compatible with the statistical modeling (Hylkema 1999). The choice of $\mathfrak{E}_{regime}$ depends directly on the model, chosen for instance among those of § 3.3.3.3.
This efficiency must be *a priori* integrated within the various collision operators, as it depends on the phase space variables. But Dufour (2005) has shown for usual models that $\mathfrak{E}_{regime}$ can be integrated analytically so that the full collision operator reads:

$$\mathfrak{C} = \mathfrak{E}_{reb}\mathfrak{C}_{reb} + \mathfrak{E}_{str}\mathfrak{C}_{str} + \mathfrak{E}_{coal}\mathfrak{C}_{coal} \tag{3.139}$$

where $\mathfrak{E}_{reb}$, $\mathfrak{E}_{str}$, and $\mathfrak{E}_{coal}$ depend on b_1 and b_2, as defined by the models of § 3.3.3.3.
We now formulate the assumption:
[HC4] Every collision leads to coalescence.
which is used for all the following developments as a simplification. We keep in mind that the different regimes can be taken into account but we focus on modeling and methods for coalescence so we assume $\mathfrak{E}_{reb} = 0$ and $\mathfrak{E}_{str} = 0$. The collision operator used in the thesis is therefore treated as equal to the coalescence one:

$$\mathfrak{C} = \mathfrak{C}_{coal} \tag{3.140}$$

and we take the notation:

$$\mathfrak{K}_{\text{coal}} = \mathfrak{K}_{\text{coll}}. \tag{3.141}$$

3.5.2.6 Estimation of coalescence intensity

At this point, we can make quantitative remarks on the physics of coalescence that will be helpful to design relevant test cases in the following. We link coalescence intensity to the droplet rate of growth since coalescence is hereafter the only phenomenon to modify the droplet size. We define a local droplet growth time $\overline{\tau}^G(t,\boldsymbol{x},v)$ for a given size v:

$$\frac{1}{\overline{\tau}^G(t,\boldsymbol{x},v)} = \int_0^v\frac{v^\star}{v}\iint_{\boldsymbol{c}^\star,\theta^\star} f(t,\boldsymbol{x},\boldsymbol{c}^\star,v^\star,\theta^\star)\mathfrak{K}_{\text{coal}}(|\boldsymbol{c}-\boldsymbol{c}^\star|,v,v^\star)\mathrm{d}\boldsymbol{c}^\star\mathrm{d}v^\star\mathrm{d}\theta^\star \tag{3.142}$$

based on the coalescence rate with all the droplets that are smaller than v and weighted by the partner's relative volume $v/v^\star$: this time can be very different from a collision time, for instance it is null for very small droplets since they do not grow by themselves but are absorbed by bigger ones.

This is a local and instantaneous definition but it gives an insight into the intensity of coalescence: after a time $\overline{\tau}^G(t,\boldsymbol{x},v)$ and if all the conditions persist, droplets of size v (which have not coalesced with a bigger droplet) have encountered a volume growth of v i.e. their volume has doubled. The local growth time can be plotted as a chart to analyze the zones where coalescence is intense. Similarly, its evolution in time gives insight into the unsteadiness of coalescence.
The growth time decreases -or equivalently coalescence intensifies- when either collision partner densities, velocity differences or collision efficiencies increase. We can define a coalescence Knudsen number Kn_g as the ratio of the global growth time to a typical flow time: coalescence is intense when Kn_g is close to one or smaller. This definition is analogous to the classical Knudsen number that measures the dimensionless collision frequency (Ferziger and Kaper 1972; Struchtrup 2005) except that the velocity difference must be resolved in our ballistic coalescence case instead of coming from microscopic agitation. The importance of coalescence is measured by the dimensionless volume growth according to the use of $\overline{\tau}^G$. The characteristic flow time that is used to define Kn_g can be a particle residence time τ^R in the volume of interest: we then define coalescence intensity as the growth of a particle in the considered volume, which is rather a Lagrangian point of view.

3.5.3 Secondary break-up

The modeling of break-up cannot be done directly from its deterministic model of § 3.3.4 because such models are not immediately compatible with statistical approaches. We build a break-up operator $\mathfrak{B}$ that complies with the statistical modeling.
A kinetic approach, introduced in Dufour et al. (2003) and detailed in Dufour (2005) considers a break-up frequency equal to

$$\nu_{\mathrm{bu}}(\boldsymbol{c},r,\boldsymbol{u}_g)=\frac{\mathbb{1}_{[\mathrm{We}_c,+\infty[}}{\tau_{\mathrm{bu}}(r)} \tag{3.143}$$

where the critical Weber number We_c and the characteristic break-up time have been defined and modeled in § 3.3.4.

3.5.3.1 Presumed PDF closure for size

A convenient way to account for the evolution of the size distribution (Dufour 2005) is to assume a size PDF for the fragments, which settles instantaneously when break-up criteria are satisfied. The presumed PDF for size is noted $g_{\mathrm{bu},\phi}(\phi;\boldsymbol{c}^\star,\phi^\star,\boldsymbol{u}_g)$, with an internal coordinate that is the daughter droplet size ϕ and a dependency on the flow and mother velocity through $\boldsymbol{c}^\star$, $\phi^\star$, and $\boldsymbol{u}_g$. This PDF is normalized to ensure mass conservation:

$$\int r^3 g_{\mathrm{bu},\phi}(r;\boldsymbol{c}^\star,\phi^\star,\boldsymbol{u}_g)\mathrm{d}r = r^{\star 3} \qquad \forall \boldsymbol{c}^\star,\phi^\star,\boldsymbol{u}_g. \tag{3.144}$$

In the following models, the dependency of $g_{\mathrm{bu},\phi}$ has been accounted for through the mother droplet Weber number $\mathrm{We}^\star=\mathrm{We}(\boldsymbol{c}^\star,\phi^\star,\boldsymbol{u}_g)$. For the radius size distribution O'Rourke and Amsden (1987) suggest an exponential shape:

$$g^{OA}_{\mathrm{bu},\phi}(r,\mathrm{We}^\star)=\alpha\exp\left(\frac{r}{r_d(\mathrm{We}^\star)}\right) \tag{3.145}$$

while Dufour (2005) suggests an exponential shape versus droplet surface:

$$g^{D}_{\mathrm{bu},\phi}(S,\mathrm{We}^\star)=\frac{\alpha}{8\pi}\exp\left(\frac{-\gamma(\mathrm{We}^\star)^2}{4\pi}S\right). \tag{3.146}$$

The two parameters of each of the above PDFs must be closed with respect to mass conservation of Eq. (3.144) but also to provide at least one satisfactory size moment for the daughter fragments: the r_{32} is chosen, as defined in Eq. (3.17). We detail the case of Eq. (3.145) where we get $r_d=3r_{32}$ and $\alpha=27(r^\star)^3/(2r_{32}^4)$. So the r_{32} of the correlation can be fixed freely. It happens that experimental correlations from Wert (1995) provide a satisfactory value:

$$\frac{r_{32}(\mathrm{We}^\star)}{r^\star}=0.32(\mathrm{We}^\star)^{-\frac{1}{3}}\begin{cases}\left(\dfrac{4.1}{(\mathrm{We}^\star-12)^{\frac{1}{4}}}\right)^{\frac{2}{3}} & \text{if } 12<\mathrm{We}^\star<18\\ \left(\dfrac{2.45\sqrt{\mathrm{We}^\star-12}-1.9}{(\mathrm{We}^\star-12)^{\frac{1}{4}}}\right)^{\frac{2}{3}} & \text{if } 18<\mathrm{We}^\star<45\\ \left(\dfrac{12.2}{(\mathrm{We}^\star-12)^{\frac{1}{4}}}\right)^{\frac{2}{3}} & \text{if } 45<\mathrm{We}^\star\end{cases} \tag{3.147}$$

3.5.3.2 Presumed PDF closure for velocity

As for the velocity distribution after break-up noted $g_{\mathrm{bu},u}$, a presumed PDF approach is also used though less experimental data is generally available on velocity to close it. Hsiang and Faeth (1992) suggest a size-correlated distribution:

$$g^{HF}_{\mathrm{bu},u}(\boldsymbol{c};\phi,\boldsymbol{c}^\star,\phi^\star,\boldsymbol{u}_g) = \delta\left(\boldsymbol{c}-\boldsymbol{u}^{\mathrm{bu}}(\phi,\boldsymbol{c}^\star,\phi^\star,\boldsymbol{u}_g)\right) \tag{3.148}$$

where the size-dependent velocity reads

$$\boldsymbol{u}^{\mathrm{bu}}(r,\boldsymbol{c}^\star,\phi^\star,\boldsymbol{u}_g) = \boldsymbol{u}_g + \frac{\boldsymbol{c}^\star-\boldsymbol{u}_g}{1+2.7\left(\sqrt{\frac{\rho_l}{\rho_g}}\frac{r^\star}{r}\right)^{\frac{2}{3}}}. \tag{3.149}$$

Such closure is based on the reasonable assumption that the smaller the fragments the closer their velocity is to the one of the gas.
It is worth highlighting that this velocity closure obviously does not preserve momentum:

$$\int r^3\boldsymbol{u}^{\mathrm{bu}}(r,\boldsymbol{c}^\star,r^\star)g_{\mathrm{bu},\phi}(r,\mathrm{We}^\star)\mathrm{d}r \neq r^{\star 3}\boldsymbol{c}^\star \tag{3.150}$$

and the break-up process is modeled as a dissipative process, where most of the deceleration on small droplets due to drag is included in the phase space transport performed by the operator. Such approach smoothens the stiffness of the model: indeed break-up creates instantaneously very small droplets far from their dynamic equilibrium; the model could decelerate the fragments by a direct resolution of drag but it would have to do this in a very short time, especially for the smallest fragments.
The approach is valid in one-way coupling but raises an issue in a two-way coupling context. The modeling of break-up in a two-way coupling context is, in a more general extent, delicate as the Weber number in the vicinity of the spray is presumably perturbed.

3.5.3.3 Break-up operator

The kinetic operator is formally splitted in disappearance and creation terms $\mathfrak{B} = \mathfrak{B}^+ - \mathfrak{B}^-$. The kinetic break-up terms can be closed with the following expressions:

$$\begin{aligned}\mathfrak{B}^- &= \nu_{\mathrm{bu}}(\boldsymbol{c},\phi,\boldsymbol{u}_g)f(t,\boldsymbol{x},\boldsymbol{c},\phi,\theta)\\ \mathfrak{B}^+ &= \iint_{\boldsymbol{c}^\star,\theta^\star}\int_{\phi^\star>\phi}\nu_{\mathrm{bu}}(\boldsymbol{c}^\star,\phi^\star,\boldsymbol{u}_g)f_{\mathrm{bu}}(\boldsymbol{c},\phi;\boldsymbol{c}^\star,\phi^\star,\boldsymbol{u}_g)f(t,\boldsymbol{x},\boldsymbol{c}^\star,\phi^\star,\theta^\star)\,\mathrm{d}\phi^\star\mathrm{d}\boldsymbol{c}^\star\mathrm{d}\theta^\star\end{aligned} \tag{3.151}$$

where one needs to model the fragment NDF $f_{\mathrm{bu}}(\boldsymbol{c},\phi;\boldsymbol{c}^\star,\phi^\star,\boldsymbol{u}_g) = g_{\mathrm{bu},\phi}(\phi;\boldsymbol{c}^\star,\phi^\star,\boldsymbol{u}_g)g_{\mathrm{bu},u}(\boldsymbol{c};\phi,\boldsymbol{c}^\star,\phi^\star,\boldsymbol{u}_g)$. The dependency on the flow and mother droplet velocity can be reduced to that on the mother droplet Weber number $\mathrm{We}^\star = \mathrm{We}(\boldsymbol{c}^\star,\phi^\star,\boldsymbol{u}_g)$ e.g. with the above models, hereafter summed up:

- the break-up frequency ν_{bu}, a model being suggested by Hsiang and Faeth (1993),
- the fragment distribution shape f_{bu} (O'Rourke and Amsden 1987; Dufour 2005),
- the fragment Sauter mean radius (Wert 1995),
- the fragment velocity distribution $\boldsymbol{u}^{\mathrm{bu}}$ (Hsiang and Faeth 1993).

3.5.3.4 Extension to dynamic models

To overcome the limitation of instantaneous break-up models, a progress variable can be added to the phase space in order to describe the dynamics of the break-up process.
Another approach is to add a NDF, and its kinetic equation, to describe the population of metastable structures and the dynamics of their evolution. This second approach is retained in Rimbert et al. (2012) and is presented in Appendix C.

3.6 Conclusion on the fluid-kinetic approaches

The kinetic model of Eq. (3.123), coupled to the Navier-Stokes equations, constitutes our reference model, which is closed (Laurent and Massot 2001; Fox 2012). This so-called "fluid-kinetic" modeling frame can then be specified as regards the level of detail on either the gas fields and the disperse phase statistical field: we first define a Direct Numerical Simulation Level of this approach by opposition to many attempts to filter out some scales and model their effects. We then detail a set of assumptions that we keep from now on and we conclude on the need for additional modeling and closure to provide a reasonably costly and detailed approach.

3.6.1 Definition of a DNS level for the fluid-kinetic description

3.6.1.1 The Fluid-Kinetic DNS

The resolution of fluid-kinetic (or fluid-fluid) coupled equations for the disperse two-phase flow will be referred to as Direct Numerical Simulation (DNS), as long as the structures of the gas flow, linked to the geometry, are resolved. In this definition of DNS (Fox 2012), modeling is tolerated that corresponds to the unresolved (microscopic) scales at the level of the droplet surface e.g. their wake. Conversely, this means that we will not introduce any modeling for either the gas or the disperse phase turbulence (Laurent and Massot 2001; Fox 2012).

3.6.1.2 The MEF formalism

In the case where the flow produces crossings (homo-PTC), it is tantalizing to account for the local multivariate velocity distribution in a reduced way.
From the ideas of Simonin (1996) the Mesoscopic Eulerian Formalism (MEF) considers a quantity to describe at the statistical level the multivariate status of the velocities: the so-called Random Uncorrelated Motion (RUM). The difficulty is that the corresponding PDF has no reason to have a particular form, contrary to Gas Dynamics and its Euler closure, which is in the hydrodynamical equilibrium. So the MEF formalism considers a PDF that is conditioned by a realization of the gas flow-field (Fevrier 2000; Fevrier et al. 2005). The extension of the MEF approach to unresolved anisothermal effects has been suggested (Masi 2010; Dombard 2011; Masi and Simonin 2012).
The MEF can then be written at the macroscopic level: with moment equations featuring unclosed RUM tensor terms, the resulting approach is Eulerian. The tensor closures for unresolved scale transport are performed by analogy with Reynolds' tensor (Kaufmann et al. 2004; Masi 2010), so that the approach is sometimes referred to as an algebraic closure method of moments (ACBMM): the knowledge of the underlying kinetic distribution is never assessed.
When noting the streaming operator $\mathscr{D}(\cdot) = \partial_t \cdot + \partial_{x_j} \bar{u}_{p,j} \cdot$, the MEF equations read:

$$\begin{aligned} \mathscr{D}(\bar{n}_p) &= 0 \\ \mathscr{D}(\bar{n}_p \bar{u}_{p,i}) &= -\frac{\bar{n}_p}{\bar{\tau}_p}(\bar{u}_{p,i} - u_{f,i}) - \partial_{x_j} \bar{n}_p \delta R_{p,ij} \\ \mathscr{D}(\bar{n}_p \delta R_{p,ij}) &= -2\frac{\bar{n}_p}{\bar{\tau}_p}\delta R_{p,ij} - \bar{n}_p \delta R_{p,kj}\partial_{x_k}\bar{u}_{p,i} - \bar{n}_p \delta R_{p,ik}\partial_{x_k}\bar{u}_{p,j} - \partial_{x_k}\bar{n}_p \delta Q_{p,ijk} \end{aligned} \tag{3.152}$$

where the physics of RUM is featured by the velocity tensor $\delta R_{p,ij}$. This tensor admits a decomposition in:

$$\delta R_{p,ij} = \delta R^{\star}_{p,ij} + \frac{2}{3}\delta\theta_p \delta_{ij} \tag{3.153}$$

where $\delta R^{\star}_{p,ij}$ is to be modeled. Two closures were suggested:

- VISCO $\delta R^{\star}_{p,ij} = -\frac{2}{3}\widetilde{\tau}_p \delta\theta_p S^{\star}_{p,ij}$ by Pr. Simonin,
- AXISY-C $\delta R^{\star}_{p,ij} = \mathrm{sign}(III_s)\left(\frac{2}{3}\right)^{\frac{1}{2}} 2\delta\theta_p \frac{S^{\star}_{p,ij}}{\sqrt{II_s}}$ in Masi (2010)

where II_s and III_s are the second and third invariants of the symmetric tensor $S^{\star}_{p,ij}$:

$$S^{\star}_{p,ij} = \frac{1}{2}\left[\partial_{x_j}\bar{u}_{p,i} + \partial_{x_i}\bar{u}_{p,j} - \frac{2}{3}\partial_{x_k}\bar{u}_{p,k}\delta_{ij}\right]. \tag{3.154}$$

The second modeling is considered as the best as it can render energy backscattering from the sub-grid to resolved velocities. The model is validated on a statistically homogeneous and isotropic turbulence or HIT (Fevrier et al. 2005) and on a decaying turbulence field (Kaufmann et al. 2008).
The resulting Eulerian approach is a moment method based on a statistical approach. It corresponds to a DNS approach as long as all the gas scales are resolved, though a part of the particle velocities is not resolved but modeled: the crossings which are treated are deterministic in the sense that they occur because of a fully resolved gas scale, but they are treated in a statistical sense throughout the RUM. The MEF approach has obtained several successes in applicative computations: it was used for SRM simulation by Simoes (2006) and is extended to the treatment of turbulence in LES simulations as detailed below.

3.6.2 Approaches for two-phase turbulence

Depending on the conditions of the flow, namely the Reynolds number, the Navier-Stokes equations can feature a very complex time and space structure, referred to as turbulence (Monin and Yaglom 1971; Tennekes and Lumley 1972): a major issue is the ability of the smallest scales to play a role on source terms (e.g. by enhancing mixing) and on the larger flow scales (backscattering). The overall effect on two-phase flows, e.g.

spatial dispersion (Tchen 1947; Reeks 1977; Fevrier et al. 2005) and clustering (Squires and Eaton 1991a; Squires and Eaton 1991b), is correctly accounted for (when disregarding the scales of the particle wakes) by a full resolution of the fluid-kinetic approach referred to as DNS and discussed above. But when some scales cannot be resolved, modeling issues arise. The goal is then to introduce consistent and accurate "filtered" models, where the effects of the scales that are not accounted for are properly modeled.

3.6.2.1 Filtered approaches for single phase turbulence

Facing the cost of solving all the scales, many approaches have been suggested to model the small scales and reduce the cost. Among these, the Reynolds Average Navier-Stokes approach (RANS) and the Large Eddy Simulation (LES) are often introduced as filtered approaches to replace a complete resolution or DNS.
The RANS approach is based on a time average used to filter all the scales, yielding steady state equations; a version named URANS allows slowly varying evolutions, as long as they are not linked to the turbulent phenomenon itself. These approaches consist in transporting additional quantities to describe in a statistical point of view the unresolved scales: for instance turbulent kinetic energies of the so-called Reynolds tensor, that is second order velocity moments, play in RANS a similar role as the pressure and strain in the usual Euler closure. The main difference with Boltzmann's assumption for Euler equations is that the small turbulent scales are not close enough to an equilibrium distribution to allow the use of structural properties (e.g. isotropy) so they keep their tensorial structure and the associated fluxes require a complex, non-linear treatment. After decades of research, the modeling of RANS closures is still an active research topic (Chaouat and Schiestel 2005; Rumsey and Jeyapaul 2012; Pecnik et al. 2012).
The LES approach is based on a spectral/spatial filtering that removes the space scales and no additional quantity is generally transported: the effect of unresolved scales is modeled from the knowledge of the resolved ones, for instance with a structural assumption (Smagorinsky 1963; Nicoud and Ducros 1999) or a scale similarity assumption (Germano et al. 1991). The choice of the latter model strongly depends on the configuration. In practice, the space filtering is generally worked out to be as small scale as the computational resources allow, for the models to behave accurately and to limit their impact (Sagaut 1998; Pope 2000; Poinsot and Veynante 2011).

3.6.2.2 Issue of unresolved scales for the disperse phase

Whatever method is used, the reduced approach for the Navier-Stokes equation provides filtered fields which mimic the local ones but are not satisfactory to close the sources in the kinetic equation. Ideally, the local values of the gaseous field would be used but the modeling of turbulent two-phase flows resorts to closing the kinetic sources with some information from the gas unresolved scales, either modeled (LES) or transported (RANS). The derivation of a transport equation for the NDF of droplets in turbulent flows has been the subject of many researches in the past two decades (Reeks 1991; Pandya and Mashayek 2002; Mashayek and Pandya 2003; Reeks 2005; Fox 2012).
A RANS filtering of the kinetic equation led Reeks (1992) to suggest the following closure:

$$\partial_t\langle f\rangle + \partial_{\boldsymbol{x}}\cdot(\boldsymbol{c}\langle f\rangle) + \partial_{\boldsymbol{c}}\cdot(\langle F\rangle\langle f\rangle) = -\partial_{\boldsymbol{c}}\left(\lambda_R\partial_{\boldsymbol{x}}\langle f\rangle + \mu_R\partial_{\boldsymbol{c}}\langle f\rangle\right) \tag{3.155}$$

where λ_R and μ_R are related to the turbulent correlations of the gas and to the particle Stokes number. A similar approach was performed by Zaichik et al. (2009) in the context of LES. These closures go along with an equilibrium assumption on the velocity distribution conditioned by size. They allowed Réveillon et al. (2002) to derive, a semi-kinetic system of conservation laws (as presented in § 4.4.1 for laminar cases), taking in this case the moment of order 0, 1 and 2 in velocity, see also Massot et al. (2004) and Massot (2007). But the form of the equilibrium assumption is discussed.
Since the local gas scales (mainly velocity) are so important to the kinetic equation, it has been suggested to include an additional variable in the phase space of the kinetic equation to embody the gas velocity at the particle location (see for instance Minier and Peirano 2001; Simonin et al. 2002). The resulting joint PDF then reads:

$$f(t,\boldsymbol{x},\boldsymbol{c},\boldsymbol{c}_s) \qquad \text{so that} \qquad \int f(t,\boldsymbol{x},\boldsymbol{c},\boldsymbol{c}_s)\mathrm{d}\boldsymbol{c}_s = f(t,\boldsymbol{x},\boldsymbol{c}) \tag{3.156}$$

which resumes the usual PDF after integration on the gas velocity variable. The evolution of $\boldsymbol{c}_s$ then requires a modeling linked to the flow structure itself: it often resorts to evolution equations based on a stochastic process (Hyland et al. 1999; Minier and Peirano 2001; Pai 2007; Zeren and Bedat 2009). This approach can be extended to the fluctuations of temperature (Couzinet 2008).
Facing the difficulties to link fluid and particle velocity correlations with the previous PDFs, methods based on two-point PDFs, are introduced (Pai and Subramaniam 2009). Such methods allow to account for space

correlations, in accordance with the assumption that turbulence features coherent structures (Holmes et al. 2012). In return, they are complex to handle and to close.
The existence of unresolved scales for the gas goes presumably hand in hand with unresolved scales for the disperse phase, which can be accounted for as regards their consequences on moments of the NDF (Ma and Ahmadi 1990). The MEF formalism can bear a RANS-type filtering but this formulation is criticized for discrepancies as regards academic turbulence test cases (Xu and Subramaniam 2006). The MEF formalism also bears a LES-type filtering of its macroscopic equations (Kaufmann et al. 2004): the first practical formulation of a two-phase flow LES is to be found in Moreau (2006), who has worked out a modeling for the filtered terms in the MEF context. Many works were then devoted to LES of solid particles (Moreau 2006; Riber 2007; Vié 2010) and completed by studies on monodisperse sprays in reacting flows (Riber et al. 2006; Boileau 2007; Lamarque 2007). An extension of LES for polydisperse spray is proposed in Mossa (2005), with a size presumed PDF (see § 4.4.2) and the most promising polydisperse approach is the extension to Multi-Fluid methods (see § 4.4.5) performed by Vié (2010) (see also Vié et al. 2013). It is a rare example of turbulent model to have obtained several successes in complex applicative computations: it was used for instance for the transient simulation of ignition in an aeronautical burner with a monodisperse spray by Boileau et al. (2008) and for the simulation of internal combustion engines and aeronautical burners with polydisperse sprays by (Vié 2010).
As a conclusion on the filtered two-phase models, the closures remain coarse as regards the non-linear phenomena: size-conditioned physics such as combustion is investigated in the prospect of yielding turbulent closures. Such closures have been suggested in RANS context (Réveillon et al. 2002; Massot et al. 2004; Reveillon et al. 2004).

3.6.2.3 Case of collisions

Turbulent modeling of collisions and coalescence has been an active research topic because of the need to predict rain drop formation (Langmuir 1948; Saffman and Turner 1956; Wang et al. 2006). In general, the occurrence of collisions is sensitive to the small scales of the flow so collision modeling is particularly critical in reduced approaches (Fede 2004; Fede and Simonin 2006).
Coalescence rates can be assessed from the raw knowledge of local turbulent kinetic energy, as done in the early work of Saffman and Turner (1956):

$$\mathcal{P}_{\text{coal}}^{\text{turb}}(r^\star, r^\diamond) = 1.30(r^\star + r^\diamond)^2(\epsilon/\nu_g)^{\frac{1}{2}} \tag{3.157}$$

where ϵ is the Turbulent Kinetic Energy (transported in many RANS modeling) and ν_g is the gas kinematic viscosity. This approach is only valid for particles that are smaller than the Kolmogorov scale η_K, with a response time shorter than the smallest eddy time

$$\tau^{\boldsymbol{u}} < \tau_K$$

and for particles that have balanced sizes i.e.

$$\Delta r = \frac{r_s}{r_b} > \frac{1}{2}. \tag{3.158}$$

Further developments of this RANS-like approach can be found (Abrahamson 1975; Ashgriz and Givi 1987) and has been pursued in the context of LES (Wang et al. 1998). The coupling to other phenomena such as gravity is also studied (Dodin and Elperin 2002).
The joint-PDF approach has naturally been contemplated to model collisions (Fede et al. 2002; Zaichik et al. 2003; Zaichik et al. 2009), as it gives a (modeled) value for the local gas velocity. Methods based on joint-PDF approaches can be found in a Eulerian resolution framework (Belt and Simonin 2009) as well as in a stochastic-Lagrangian one (Wunsch et al. 2009; Wunsch 2009). The case of coalescence has also been treated by these authors.

3.6.2.4 Case of two-way coupling

In the case of moderately dense loadings, the modeling is far from completed: the use of standard fluid-kinetic equations is valid for DNS but the modeling is difficult to achieve.
At best, both closures for the gas and the particles must be redesigned and at worst, the modeling must be questioned such as in the case of the MEF (Zeren and Bedat 2009; Zeren 2010), where the PDF conditioning on a realization is troublesome.
As an illustration, an identified two-phase effect such as the enhancement of turbulence by inertial particles (Elghobashi 1991), has not been assessed and is a tough subject in general, its actual occurrence being theorized in rare models (Druzhinin 2001). Some recent advances have been done in Pai and Subramaniam (2012).

3.6.3 Modeling retained in the present work

The treatment of turbulent two-phase flows with a filtered approach is a goal for the community but the models are not mature enough and active research is conducted. So we choose to focus on the fluid-kinetic DNS framework. We define a set of simplification assumptions. The model can theoretically be solved directly, as it is closed, but the level of detail is too high and the model too costly for such approaches to yield results in practical configurations.

3.6.3.1 Choice of a fluid-kinetic DNS

The definition of a proper framework for two-phase filtered approach is crucial provided that:

- the configurations of interest almost always feature turbulence (the case of SRMs is discussed in § 1.3.2.2);
- the available computer resources do not allow any type of DNS for real cases.

From now on, the models and methods that are presented apply to the fluid-kinetic DNS. If some modeling work is done to render for instance crossings, it is not performed as an algebraic closure within macroscopic equations (ACBMM such as the MEF) but velocity distributions are explicitly assumed at the kinetic level. The resulting macroscopic equations belong to a class of models referred to as a Kinetic Based Moment Methods (KBMM) and they can also be solved at a DNS level i.e. with fully resolved gas fields (provided that the closure errors are neglected). The DNS resolution of macroscopic equations is referred to as fluid-fluid DNS (not to be confused with the full-DNS described in § 3.2.1 where an interface does exist).
The choice of a DNS strategy in the following is nonetheless motivated by the DNS computations we aim at performing as a first step in understanding the physics of SRMs but also because efficient DNS is an incontrovertible starting point for disperse two-phase flow simulations. The adaptation of the model and methods to LES relies indeed most of the time on theory and DNS tools. Thus, the present contribution focuses on a DNS of the fluid-kinetic coupled system of equations.

3.6.3.2 General assumptions of the present work

We consider a disperse phase of liquid droplets, though the approach can apply, with the relevant adaptations of some sources, to solid particles in the case of burning aluminum or solidified residuals at the output. Some simplification assumptions are recalled or introduced to be used in the following work.
First, the droplets are spherical, except in some infinitely fast transient regimes of coalescence and break-up. This allows to describe them with a unique size parameter.
Second, the dilatation of droplets and particles under temperature or pressure variations are neglected so that we have:

$$\rho_l = cst. \tag{3.159}$$

This allows to use descriptions in size, consistently to mass conservation without any tedious algebra.
Third, coalescence is the only phenomenon that is accounted for when collisions of liquid droplets occur, accordingly to [HC4] (see § 3.5.2). The treatment of other collision regimes can still be included later.

3.6.3.3 Need for further modeling and method

The fluid-kinetic approach can theoretically be solved e.g. with a finite volume discretization of the entire phase space. In practice such approach is costly and would only allow a coarse mesh in each direction, limiting the accuracy to a level that is not acceptable. For instance, it has been possible to solve Boltzmann's equation by a direct resolution only for a limited phase space (5D and a half) and still with a coarse grid.
Several approaches can then be envisioned: stochastic-Lagrangian, size sampling, moment methods, sectional methods *etc.*, each being adapted to specific cases. We describe them in Chapter 4 and discuss the choice of a method adapted for SRM simulation.
It is worth highlighting that some of the methods that are presented in the following chapter may result in (systems of) fluid systems of equations: the corresponding approaches are then referred to as fluid-fluid, and the usual resolution methods are referred to as Euler-Euler. So a DNS resolution (in the sense of § 3.6.1.1) of the fluid-fluid model will provide, as long as the additional reduction assumptions are valid, the same level of accuracy as a DNS of the fluid-kinetic approach. This DNS framework which we adopt is a starting point for larger scale simulations and LES developments.

Chapter 4

Strategies for the resolution of the kinetic equation in two-way coupled fluid-kinetic systems

We present different strategies to reduce the level of detail of the kinetic equation in the context of a fluid-kinetic approach. The strategies that are presented can still account for either issues of polydispersity and of multiple velocities or temperatures: the corresponding assumptions are discussed as regards their restrictions. The impact of such choices on the applicability of the models for a practical resolution is also discussed. We particularly focus on the ability of each strategy to account efficiently for moderately dense two-phase flows since the two-way coupling is difficult to render: two-way coupling yields physics peculiarities that we describe and which must be accounted for by the chosen approach.

4.1 Introduction

We have chosen the fluid-kinetic formalism -i.e. the Williams-Boltzmann equation, coupled to a fluid carrier phase- to account for the moderately dense, polydisperse nanometric-to-moderately inertial two-phase flow that occurs in the chamber and the nozzle of a SRM.
The derivation of a reduced model from the kinetic model for the disperse phase is a crucial point but it must be done under the following constraints:

1. account for polydispersity;
2. account for polykineticity;
3. account for two-way coupling;
4. comply with HPC.

These features induce sensible differences in the reduction treatment compared to that of a kinetic equation in gas dynamics, presented in § 3.4.2. First, polydispersity results is an additional dimension, and the velocity and source terms depend strongly on the size variable, according to the description given in § 3.1.2.1. Second, the reduction cannot be based on collisional considerations, contrary to the approach of Mathiaud (2006) leading to models in a hydrodynamic limit, and polykineticity is characteristic of out-of-equilibrium systems, as discussed in § 3.1.3: the effect of drag may still bring a pseudo-equilibrium for small particles as illustrated in Figure 3.4. The particular case of disperse phase velocity equilibrium in Brownian motion is presented in § 8.4.2.2.
The kinetic vision of polykineticity in the Boltzmann-Grad limit is compared to that of a volume average vision for a system of finite size particles as regards crossings in Figure 4.1: multivariate velocities are shown to arise respectively from ensemble averaging and from volume averaging. Kinetic polykineticity is also linked to a statistical vision of collisions as shown in Figure 4.2. Anyway this far-from-equilibrium situation requires its own specific resolution methods.
The reduction of the kinetic level of detail relies either on sampling methods (stochastic-Lagrangian, Multi-Class), on moment methods (QMOM, DQMOM), or on discretization methods (sectional), as detailed in the present chapter. In the case of a disperse phase, the practical methods happen to be structured in two families that are Lagrangian and Eulerian methods. Lagrangian methods are based on a stochastic Monte-Carlo discretization of all the phase space and physical space variables. The resulting disperse two-phase flow method is sometimes referred to as Euler-Lagrange to recall that the carrier gas is solved with a Eulerian method. Eulerian methods are based on various techniques (sampling, moments, or sectional) where the variables remain Eulerian fields that satisfy transport equations: contrary to stochastic-Lagrangian

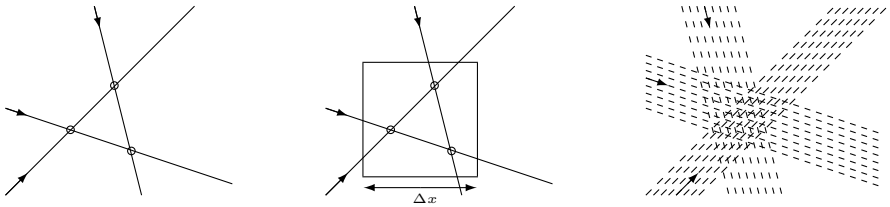

Figure 4.1: *Two-visions of polykineticity – Left: Crossings for a finite number of finite size particles involve exactly two trajectories; Center: Volume average yields multi-crossing; Right: Statistical (Boltzmann-Grad limit) model intrinsically accounts for polykineticity.*

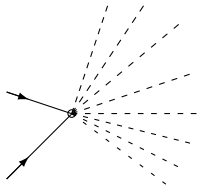

Figure 4.2: *Statistical collisions yield ensemble velocity dispersion.*

approaches -where the phase space can be freely sampled-, some correlations need to be assumed between the kinetic variables, to allow the computation of the moments.
Both Lagrangian and Eulerian families of methods are now described, the latter being decomposed in monokinetic and polykinetic methods as the ability to treat polykineticity is a strong dividing line for Eulerian methods. The question of accounting for two-way coupling in the context of HPC is shown to guide the choice of resorting to a model reduction strategy.

4.2 The stochastic-Lagrangian approach

The stochastic-Lagrangian method, also referred to as Direct Simulation Monte-Carlo (DSMC) is based on a stochastic Monte-Carlo discretization of all the NDF variables, which makes the method powerfully versatile.

4.2.1 Background of stochastic-Lagrangian approach

The stochastic-Lagrangian description has been introduced in two different contexts. On the one hand it has been developed to supply DPS in configurations where the high number of physical droplets prevents to use one numerical particle for each droplet, given the high computational cost associated. In this framework, each numerical particle, also called parcel, represents several physical droplets. This approach has been first described in Crowe et al. (1977) and introduced for fuel spray and referred to as Stochastic Parcel (SP) in O'Rourke (1981), extending the work of Dukowicz (1980). This method is referred in Crowe et al. (1998) as the discrete element method, and as a multicontinua method in Sirignano (2010), where the parcels are defined as classes of droplets. The computational cost of this method is obviously linked to the chosen number of tracked parcels: the SP method aims at coarsening the DPS description and the number of statistical parcels is thus set by the computational cost limitation, without drawing any links with kinetic level of description. The cost of the method is thus well controlled, and it is therefore broadly used to compute industrial configurations but its rigorous meaning is doubtful.
On the other hand, the stochastic-Lagrangian method can be seen as a resolution method of the Williams-Boltzmann kinetic Eq. (3.123) as stated by Subramaniam (2001). This approach is called DSMC and is also introduced for rarefied gas in Bird (1994). This approach aims at describing the evolution of the spray NDF moments, and thus a high number of statistical particles (Subramanian 2000) are needed to obtain a converged solution. The numerical particle has a weight associated, adapted to the needed refinement: this weight is a real number so a numerical parcel may represent a fraction of physical droplet. This method provides directly the ensemble average, in terms of initial condition, and then the reconstructed Eulerian fields correspond to the same level of information than the one provided by a Eulerian method. The difference between the two visions is only the level of refinements provided. Indeed, the convergence expected in the DSMC method demands a high number of statistical particles, leading to a higher refinement level than in DPS.
Stochastic-Lagrangian methods are implemented for instance in the KIVA II code (Amsden et al. 1989) and are used in many industrial computational codes at present (Hylkema 1999; Rüger et al. 2000; Iliopoulos et al. 2003; Desjardins and Pepiot 2009; Desjardins and Capecelatro 2011) such as the CEDRE code (Dupays

et al. 2000; Murrone and Villedieu 2011).

4.2.2 Lagrangian equations and approaches

We present the stochastic-Lagrangian method in the framework of a resolution approach for the statistical description of the spray.
It then consists in approximating -or sampling- the NDF with a finite number I of parcels i, each parcel having a position $\boldsymbol{x}_{pi}$, a size S_{pi}, a velocity $\boldsymbol{c}_{pi}$, and a temperature T_{pi}, as follows:

$$f(t,\boldsymbol{x},\boldsymbol{c},\theta,S) = \sum_{i\in[1,I]} w_{pi}\delta(\boldsymbol{x}-\boldsymbol{x}_{pi}(t))\delta(S-S_{pi}(t))\delta(\boldsymbol{c}-\boldsymbol{c}_{pi}(t))\delta(\theta-T_{pi}(t)) \tag{4.1}$$

where $w_{pi} \in \mathbb{R}$ is a weight. With this approached NDF for Eq. (3.123), the terms of the PDE decouple, yielding a set of ODEs but the r.h.s. maintains a coupling between all the ODEs. In a two-way coupling context, the mass transfer, drag force and heat transfer terms also achieve an indirect coupling between all the parcels through the gas equations.
In a dilute context and if no collisions occur, there are exactly I decoupled systems of ODEs:

$$\partial_t \boldsymbol{x}_{pi} = \boldsymbol{c}_{pi}; \quad \partial_t S_{pi} = R_{pi}; \quad \partial_t \boldsymbol{c}_{pi} = \boldsymbol{F}_{pi}; \quad \partial_t \theta_{pi} = H_{pi}. \tag{4.2}$$

A deterministic integration of the particle trajectories can be performed using the local and instantaneous gas velocity. The method has also been widely used to simulate turbulent particle flows, on with stochastic dispersion models (Minier and Peirano 2001; Peirano et al. 2006; Marchioli et al. 2006; Vinkovic et al. 2006; Chibbaro and Minier 2008) so that the ODEs then feature a stochastic term and require a specific numerical treatment.
If a coupling between the particles occurs either through collisions, coalescence, or two-way coupling, the situation is very different. For instance in the CEDRE code, Eq. (3.123) is not solved in practice but split into three steps (Murrone and Villedieu 2011) that are:

- transport in the physical space,
- transport in the phase space, and
- collision and break-up.

In the transport step, the r.h.s. of Eq. (3.123) decouples for each parcel i in the system of ODEs given in Eq. (4.2), which has to be solved with a method that respects the coupling to the gaseous phase. An unconditionally stable first order scheme may be chosen to do so e.g. in CEDRE (Murrone and Villedieu 2011).

4.2.2.1 Collision algorithms

In the collision step, pairs of particles are randomly chosen among each cell and their state is modified according to the so-called collision algorithm. Many such algorithms have been widely proposed and studied (O'Rourke 1981; Bird 1994; Hylkema and Villedieu 1998; Hylkema 1999; Sommerfeld 1999; Schmidt and Rutland 2000; Rüger et al. 2000). They all suppose that the computational domain is divided into cells, or control volumes, which are small enough to consider that the droplet distribution function is almost uniform over them. They do not need to match a mesh cell and are presumably larger.
As an illustration we give the algorithm used in Hylkema and Villedieu (1998) and in Laurent et al. (2004) for pure coalescence. It consists of the following three steps:

1. For each computational cell C_J, containing N_J parcels, we choose randomly, with a uniform distribution law, $N_J/2$ pairs of parcels ($N_J - 1/2$, if N_J is odd).
2. For each pair p, let p_1 and p_2 denote the two corresponding parcels with the convention $n_{p1} \geq n_{p2}$, where n_{p1} and n_{p2} denote the parcel numerical weights. Then for each pair p of the cell C_J, we choose randomly an integer ν_p, according to the Poisson distribution law:

$$P(\nu_p) = \frac{\lambda_{12}}{\nu_p!}\exp(-\lambda_{12}) \tag{4.3}$$

with

$$\lambda_{12} = \frac{n_{p1}(N_J-1)\Delta t}{\mathcal{V}(C_J)}\mathfrak{K}_{\text{coal}}(|\,\boldsymbol{u}_{p1}-\boldsymbol{u}_{p2}\,|, r_{p1}, r_{p2}) \tag{4.4}$$

where $\mathcal{V}(C_J)$ is the volume of the cell C_J and r_{p1}, r_{p2} are the radii of the parcels p_1, p_2. The coefficient λ_{12} represents the mean number of collision, during $N_J - 1$ time steps, between a given droplet of the parcel p_2 and any droplet of the parcel p_1. Note that a given pair of parcels is chosen, in average, every $N_J - 1$ time steps.

3. If $\nu_p = 0$, no collision occurs during this time step between the parcels p_1 and p_2. Otherwise, if $\nu_p > 0$, the parcel p_1 undergoes ν_p coalescences with the parcel p_2 and the outcome of the collision is treated as follows. First the weight n_1 of the parcel p_1 is replaced by $n'_{p1} = n_{p1} - n_{p2}$ and its other characteristics are left unchanged. If $\nu_p \leq 0$, the parcel p_1 is removed from the calculation. Secondly, the velocity $\boldsymbol{u}_{p2}$ and the volume v_{p2} of the parcel p_2 are replaced by

$$v'_{p2} = v_{p2} + \nu_p v_{p1}, \quad \boldsymbol{u}'_{p2} = \frac{v_{p2}\boldsymbol{u}_{p2} + \nu_p v_{p1}\boldsymbol{u}_{p1}}{v_{p2} + \nu_p v_{p1}}, \tag{4.5}$$

and its weight n_2 is left unchanged.

Let us mention that, for each time step and each control volume C_J, the computational cost of this algorithm behaves like $\mathscr{O}(N_J)$. This is a great advantage compare to O'Rourke (1981)'s method, which behaves like $\mathscr{O}(N_J^2)$. Another algorithm, with the same features, is introduced by Schmidt and Rutland (2000).

To obtain a good accuracy, the time step Δt, must be chosen small enough to ensure that the number of collisions between two given parcels, p_1 and p_2, is such that for almost every time: $\nu_p n_{p2} \leq n_{p1}$. The average value of ν_p being λ_{12}, this constraint is equivalent to the condition:

$$\frac{n_{p2} N_J \Delta t}{\mathcal{V}(C_J)} \mathfrak{K}_{\text{coal}}(|\,\boldsymbol{u}_{p1} - \boldsymbol{u}_{p2}\,|, r_{p1}, r_{p2}) \ll 1. \tag{4.6}$$

The method also requires a sufficient number of parcels per integration cell. This is discussed in Chapter 15 for stochastic-Lagrangian computations of coalescing SRMs.

4.2.2.2 Initial and boundary conditions of a stochastic-Lagrangian computation

A specific attention must be devoted to the initial and boundary conditions of such a method, since they define the number of numerical particles in the domain and therefore the method's cost and accuracy. The initial and boundary conditions must be sufficiently accurate realizations of the real initial and boundary distribution functions. Moreover, these conditions should be random but (unavoidable) imperfections in the conditions threaten the quality of the solution.

Two methods can be used to compute a realization of a given NDF f^0 (de Chaisemartin 2009; Thomine 2011):

- (i) simulating a uniform distribution on the support of f^0 and adjusting the weights to obtain the correct distribution;
- (ii) simulating directly the mass distribution, $\frac{\rho_l}{6\sqrt{\pi}} S^{\frac{3}{2}} f^0$, through a rejection method (de Chaisemartin 2009) with numerical particles having weights representing the same mass density.

The first method, albeit easier to implement, induces particles with a very small mass density and thus little efficiency in terms of computational cost. Furthermore, this method, based on a uniform distribution, describes with the same precision the whole distribution, whereas the second, leading to a mass of droplets linked with the number density function form, gives a better precision for the main part of the size phase space, while it coarsens the resolution for the tails of the distribution where few droplets are likely to be found. The second method gives thus a better global precision.

4.2.3 Properties and issues of numerical approaches for Euler-Lagrange strategies

To solve a disperse two-phase flow, the stochastic-Lagrangian approach is often coupled to a Eulerian approach for the carrier gas phase: we refer to this strategy as Euler-Lagrange for this coupling induces model and method peculiarities compared to other fields where stochastic-Lagrangian is thought out to be used alone. The general numerical aspects of Euler-Lagrange simulations are here assessed in the perspective of choosing a strategy for two-phase flows, especially moderately dense ones.

4.2.3.1 Accuracy on phase space variables

On one hand, the stochastic-Lagrangian method does not assume any correlations between the phase space variables, contrary to the Eulerian methods presented after: the variables of the parcels are intrinsically uncorrelated with that of other parcels. This means that the method can solve any types of crossings in phase space. For velocities for instance, the method *a priori* allows any type of particle trajectory crossings (PTC), including those occurring on symmetry axes, close to a wall or at the rim of vortices.

On the other hand, the fact that the method can solve crossings does not ensure that a given numerical discretization will do so. More parcels are needed to ensure a satisfactory convergence when degrees of freedom such as polydispersity, polykineticity or unsteadiness are sought. But the use of more parcels is

costly in terms of CPU and memory so that the actual number of parcels in a practical computation may not be sufficient to ensure convergence, as discussed below.
The criterion for a simulation to represent accurately significant physics, e.g. crossings, is called convergence. Unfortunately, there is no obvious evidence for a given solution that convergence is not gained.

4.2.3.2 Convergence

Convergence is the main concern about Monte-Carlo methods. It should be examined regarding each effective degrees of freedom (e.g. effective polydispersity criterion for the size variable): it is a very important point to consider the complexity (and cost) of the problem related to the sensitivity of the solution to dispersion in the phase space variables (Garg et al. 2009).
On the contrary, the complexity of the problem is not at all related to the *a priori* size of the phase space as it can be often heard: physical (effective) correlations can and will occur between phase space variables. The choice of a stochastic-Lagrangian approach allows not to bother about them but they are still useful to reduce noise and to gain a satisfactory level of convergence easily. Such correlations are exploited by Eulerian approaches.
Convergence can be evaluated by performing several realizations with the same initial and boundary conditions (in a statistical sense) and comparing the deviation of the solution. Such deviation is referred to as statistical noise. Convergence studies are rarely performed for industrial computations, the resources rather being used to maximize the number of parcels.

4.2.3.3 Accuracy on transport

Since the parcel trajectories are computed separately, they may account for particle trajectory crossing (PTC). In collisional cases, the collision rates are computed and enforced so that only a representative fraction of the parcels collide while the remaining part may account for PTC.
The complete and natural knowledge of trajectories allows to model easily and in the detail the elementary physics of particles (collisions, wall interactions such as rebound etc.)
No numerical diffusion is introduced regarding transport since ODEs are to be integrated, ODE solvers introducing very little error in general. But coupling terms require a non-local (at the droplet scale) computation of terms (drag, collisions) and the required projection step introduces such diffusion. So numerical diffusion is still introduced by the gas two-way coupling and the collision algorithm since source terms have to be evaluated on the Eulerian mesh.

4.2.3.4 Accuracy on two-way coupling

Accounting for two-way coupling with an Euler-Lagrange raises two issues.
First, the ODEs for the parcels are no longer independent but coupled through the gas equation. The quantities must ideally be relaxed simultaneously for all the particles at a given location and for the underlying gas, the latter transmitting information at the velocity of its fastest eigenvalue to the surrounding gas and parcels. Numerical procedures rarely achieve such strong coupling, since it is interesting to keep the ODEs as decoupled so that splitting-like techniques are employed. This can compromise the accuracy of two-way coupling which is achieved with dedicated methods at the cost of additional efforts (Capecelatro and Desjardins 2013). Let us note that collision and coalescence also yield such local coupling that requires fine-tuned numerical methods.
Second, in a high performance computing context, possibilities of vectorization/parallelization or implicitation are limited for Euler-Lagrange simulations. The particle load balance is particularly difficult to achieve (Garcia 2009). The parcels must indeed often communicate with the underlying fluid but they move in the domain in a way that is difficult to predict (at least for the load balance algorithm). As a result parcels that are computed by a given CPU must be dispatched to other ones according to a complex process, which does not comply with efficiency requirements of parallel architecture.

4.2.4 Euler-Lagrange achievements

Subramaniam (2013) has performed a review on the abilities of the Euler-Lagrange strategies. Such simulations are widely used for disperse two-phase flows. They are remarkably efficient on dilute sprays so we do not insist on these aspects and we discuss the practical use of Euler-Lagrange strategies in contexts featuring collisions or two-way coupling.

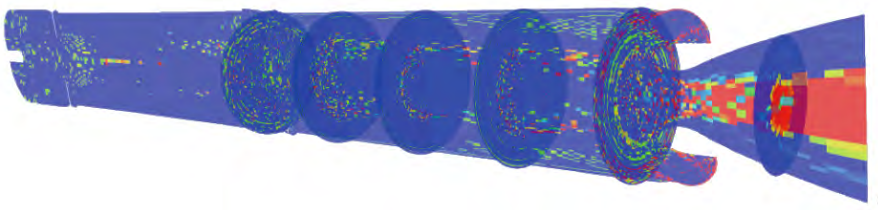

Figure 4.3: *Particle d_{32} in the P230 SRM with coalescence – 3D stochastic-Lagrangian computation (CEDRE code, ONERA).*

4.2.4.1 Collisions and coalescence

The Euler-Lagrange strategy has been used to assess the effect of collisions and coalescence in academic cases (Rüger et al. 2000; Sommerfeld 2003).
The Euler-Lagrange technique is also used for the simulation of realistic SRMs, as stated in § 2.1.4.1: coalescence has been accounted for by Estivalezes (2010) in a 2D context as well as in a 3D context (Estivalezes 2011). As an illustration, such SRM two-phase computation performed on a 3D domain is presented in Figure 4.3.

4.2.4.2 Two-way coupling

The Euler-Lagrange technique has also been used in turbulent two-way coupling contexts (Pai and Subramaniam 2006; Garg et al. 2007), again in academic configurations.
It has proven its ability to account for two-way coupling in SRM contexts (Estivalezes 2010; Estivalezes 2011).

4.2.4.3 Conclusion on Euler-Lagrange approaches

The Euler-Lagrange technique has been presented: it is a convenient and usual strategy for two-phase flows. As regards practical use, its flexibility is compound by the convergence caveat. If efforts are made to overcome the convergence and parallelization difficulties in order to perform larger computations, the approach is anyway needed as regards its flexibility, to assess complex cases, e.g. with unknown correlations. As an alternate approach for the fluid-kinetic model, it can be used for cross validations: this approach is used to validate a new Euler-Euler method in § 13.2.4 and in applicative computations in Chapter 15, where its convenience for practical SRM computations is assessed.
However, in HPC contexts, achieving coalescence or two-way coupling is tedious and this drawback is discussed in the final section of the chapter. The method is implemented in industrial codes such as CEDRE (Murrone and Villedieu 2011) as it is efficient for some industrial cases. But the use of Euler-Euler approaches is promising and recommended in strongly coupled cases: the Euler-Lagrange approach comes as a preliminary, validation approach. This validation strategy based on accessible, first step Euler-Lagrange computations is the one we adopt in Chapter 15.

4.3 Fundamental Eulerian approach: the monokinetic closure

Instead of discretizing all the kinetic DoFs with parcels as in the stochastic-Lagrangian approach, we can consider to discretize variables of the phase space solely, while keeping their Eulerian representation as fields of moments, to describe the disperse phase: this is the principle of Eulerian methods.
We now present and discuss a fundamental Eulerian method which is monokinetic and monodisperse. It can be seen as a method where the velocity and size DoFs are discretized by one sample. This method is discussed for it features one of the main issues of all Eulerian methods: their hypercompressibility.

4.3.1 The monodisperse monokinetic approach

The monodisperse and monokinetic approach is introduced. Some related historical approaches, which do not take into account the various inclusion sizes, are presented.

4.3.1.1 Fundamental closure and conservation system

The fundamental closure for the Williams-Boltzmann equation consists in assuming a simple form for the NDF:

$$f(t,\boldsymbol{x},\boldsymbol{c},\theta,S) \approx n(t,\boldsymbol{x})\delta(\boldsymbol{c}-\boldsymbol{u})\delta(S-S_0)\delta(\theta-T) \tag{4.7}$$

with $\boldsymbol{u}(t,\boldsymbol{x})$ a single velocity (monokinetic), $S_0(t,\boldsymbol{x})$ a single size (monodisperse), and $T(t,\boldsymbol{x})$ a single temperature (monothermal) for all particles at a given location $(t,\boldsymbol{x})$. Size-modifying phenomena such as evaporation, coalescence, or break-up cannot be taken into account with such restrictive assumptions.
By substituting the assumed NDF and integrating at the kinetic level Eq. (3.123) versus all the phase space variables that ought to be removed from the explicit resolution, the fundamental system for a disperse phase is then (Laurent and Massot 2001):

$$\left\{\begin{array}{rcl} \partial_t n & + & \partial_{\boldsymbol{x}}\cdot(n\boldsymbol{u}) = 0 \\ \partial_t(n\boldsymbol{u}) & + & \partial_{\boldsymbol{x}}\cdot(n\boldsymbol{u}\otimes\boldsymbol{u}) = n\overline{\boldsymbol{F}} \\ \partial_t(nh) & + & \partial_{\boldsymbol{x}}\cdot(nh\boldsymbol{u}) = n\overline{\mathrm{H}} \end{array}\right. \tag{4.8}$$

where $n(t,\boldsymbol{x})$ is the particle density, $\boldsymbol{u}(t,\boldsymbol{x})$ their local velocity, and $h = h(T)$ their enthalpy.
The drag force and heat transfer are then simply assesses for a droplet at $\boldsymbol{u}$, T, and S_0 so that $\overline{\boldsymbol{F}} = \boldsymbol{F}(S_0,\boldsymbol{u}_g,\boldsymbol{u})$ and $\overline{\mathrm{H}} = H(S_0,T_g,T)$, e.g. taking H and F from Eq. (3.51) and Eq. (3.59).

4.3.1.2 Links to other approaches

Such a statistical approach has been used for applicative cases in the monokinetic limit: the so-called dusty gas approach (Marble 1963a; Marble 1970) is a monodisperse formulation and the early polydisperse approach of Kuentzmann (1973a) includes coalescence and was used to describes the equations of a disperse phase in a SRM.
The rigorous derivation of the monokinetic, monodisperse model (Nigmatulin 1990; Laurent and Massot 2001) has established the link with the two-fluid models (see § 3.2.3), provided that the closures are those of spherical droplets.
The transport part of the equation is the same as the Pressureless Gas Dynamics (PGD) as stated by de Chaisemartin (2009), a model which is widely used in astronomy, and also referred to as the sticky particle equation. The detail and issues are discussed below. The PGD can be seen as the limit of the Euler system, given in § 3.101, and the underlying distribution is then a generalized Maxwell-Boltzmann distribution at zero temperature and therefore zero pressure. From this point of view, the model is well defined as the limit of a standard fluid model.
However it can also be seen as the limit of a velocity QMOM approach (see § 4.5.1) with one peak. We retrieve from this point of view the singular behavior of the monokinetic model since all the multi-peak approaches are weakly hyperbolic (Chalons et al. 2012).

4.3.1.3 Treatment of polydispersity in average

We have seen in § 3.1.2.3 that a polydisperse phase can sometimes be treated by using an appropriate average radius. In these cases, the previous description of Eq. (4.8) can be used by setting S_0 to fit the desired average quantity. Still, depending on the type of average quantity that is used and the dispersion in the original size distribution, the drag and heating terms may be inaccurately evaluated.
However when polydispersity becomes effective, i.e. in many applications, the size parameter is of paramount importance and should be described in a more detailed manner. The monokinetic assumption is compatible with a detailed treatment of polydispersity: in § 4.4.1 and the following sections, we present approaches that account in detail for the dynamics of different particle sizes and are therefore referred to as polydisperse. But first let us analyze the peculiar dynamics that results from the monokinetic approach, in a monodisperse frame for the sake of clarity.

4.3.2 The Pressureless Gas Dynamics: a reference description

System (4.8) describes the DNS of an ensemble of particles, which velocities are locally correlated altogether. When disregarding the thermal part and focusing on velocities, its dynamics follows the so-called Pressureless Gas Dynamics (Zel′dovich 1970; Bouchut 1994):

$$\left\{\begin{array}{rcl} \partial_t\rho & + & \partial_{\boldsymbol{x}}\cdot(\rho\boldsymbol{u}) = 0 \\ \partial_t(\rho\boldsymbol{u}) & + & \partial_{\boldsymbol{x}}\cdot(\rho\boldsymbol{u}\otimes\boldsymbol{u}) = 0 \end{array}\right. \tag{4.9}$$

which is now discussed as it is a representative minimum model.

From a mathematical point of view, the PGD system is weakly hyperbolic (Bouchut et al. 2003; de Chaisemartin 2009), and it features as a consequences δ-shocks and vacuum zones. The formation of vacuum zones is naturally linked to the zero pressure and raises issues when a numerical approximation is sought, see § 10.2, while δ-shocks raise both numerical and modeling issues, the latter being described hereafter.

4.3.2.1 Kinetic equivalence

The PGD system is proven (Bouchut 1994) to be equivalent to the kinetic equation Eq. (3.123) with monodisperse and monokinetic initial conditions, as long as singularities do not occur. The occurrence of such events is evaluated by Jabin (2002) and is linked to crossings and their occurrence is quantified by de Chaisemartin (2009), according to a criterion based on the Stokes number. The classification made in § 3.1.3.1 consists in separating particles in:

- very small and small ones, for which crossings do not occur and the PGD is therefore able to describe exactly the transport physics of these categories of particles;
- medium and large particles for which crossings occur after a given time so the PGD will render δ-shocks at some locations, leading to an inaccurate description of the system.

The principle of a critical Stokes, as defined by de Chaisemartin (2009), to separate these two regimes and to delimitate the sizes for which the first crossings occur is retained, as discussed in § 3.1.3.1.

4.3.2.2 Issues of δ-shocks

A δ-shock is a measure-type solution corresponding to a finite accumulation of mass on a sub-manifold of topological degree strictly below that of the physical space (e.g. a sheet or a curve in 3D). When modeling a disperse phase at high Kn, the occurrence of δ-shocks is an artifact of the model, corresponding to failed attempts of PTC, the mass of crossing particle clouds agglomerating (de Chaisemartin 2009).
The PGD models the physical behavior of sticky particles i.e. particles which coalesce with an infinite cross section e.g. at the hydrodynamic limit described by a zero Knudsen number. In our case, where particles can have a Knudsen number above 0.1 (or infinite), the physical solution consists in letting part (all) of the particles pursue their trajectories after the crossing point. On the contrary the PGD model for particles brings along δ-shocks that are in this case unphysical accumulations. The δ-shocks consolidate all the mass and momentum of the crossing clouds as if we were in the hydrodynamical regime. These two regimes of sticking and crossing are illustrated in Figure 4.4.

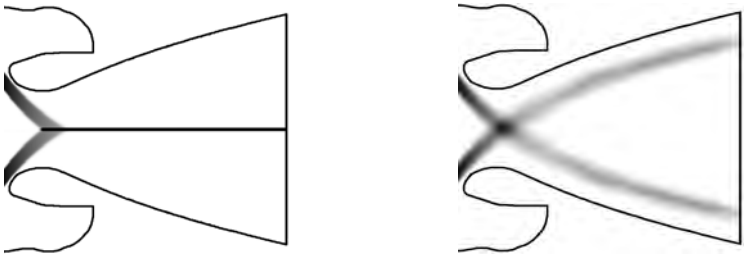

Figure 4.4: *Illustration of a monokinetic or $Kn = 0$ crossing jet (left) versus a fully resolved $Kn = +\infty$ crossing jet (right).*

The formation of a δ-shock corresponds to the destruction of relative kinetic energy within the particle system, in accordance with the fact that there is no conservation equation for kinetic energy in the model. This description of the disperse phase overestimates segregation.
Of course coalescence only occurs if there are collisions i.e. if there are trajectory crossings: the latter occur for particles with sufficient inertia. In practical computations, the occurrence of δ-shocks is sometimes tolerated as long as it does not perturb the physics of interest. This is particularly true for low inertia particles (Massot et al. 2009; de Chaisemartin et al. 2009; de Chaisemartin 2009). Since the particle concentrations and relative velocities are erroneous in the vicinity of a δ-shock, the use of PGD modeling for $\mathrm{St} > \mathrm{St}_c$ is strongly discrepant:

- in a coalescing context as discussed in § 13.4;
- in a two-way coupling context, as discussed in § 15.2.3.3.

4.3.2.3 Hypercompressibility and model singularities

As a first intuitive approach, let us make a thought experiment: by moving particles closer to each other, a cloud of particles can be brought to occupying a smaller volume without consequences (e.g. particle deformation and mechanical stress). In practice, the underlying carrier phase dominates the behavior of the

disperse phase which is subjugated through the drag force (up to a given inertia) so that the gas velocity field drives the compression of the particle phase. This fact is rendered by the Eulerian models and the corresponding situation is referred to as Hypercompressible Gas Dynamics (HGD), and the PGD is the canonical limit of HGD.
Hypercompressibility results in segregation, and the level of segregation depends on the particle inertia, as introduced in § 3.1.3.4. Capturing the characteristic size of such clusters raises many model and method issues. For instance the PGD tends to transform any (physical) accumulation into a (spurious) singularity: any disperse phase with $\mathrm{St} \geq \mathrm{St}_c$ will result in δ-shocks in the crossing zones and such singularities are the print of homo-PTC. The concentration of particles in a Homogeneous Isotropic Turbulence (i.e. with several time scales) is presented in Figure 4.5 and Figure 4.6 as resolved by a stochastic-Lagrangian and a monokinetic Eulerian approach. In a low enough inertia case, the PGD perfectly matches the (reference) stochastic-Lagrangian approach as shown in Figure 4.5 so the monokinetic assumption is satisfactory. For a higher inertia, the PGD can yield δ-shocks in the vortical zones while the Lagrangian approach will always render the crossings and the structures have a finite width, as shown in Figure 4.6. So the monokinetic assumption can become erroneous and can introduce singularities above St_c, depending on the effective local scale and the unsteadiness.

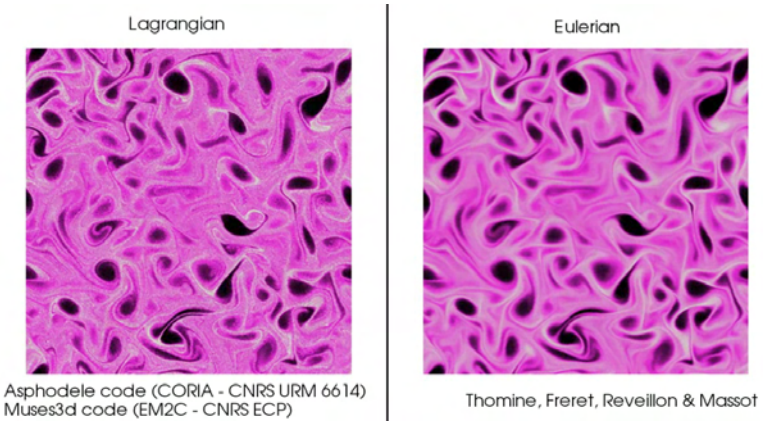

Figure 4.5: *Particle concentration in HIT for* $St = 0.2St_c$.

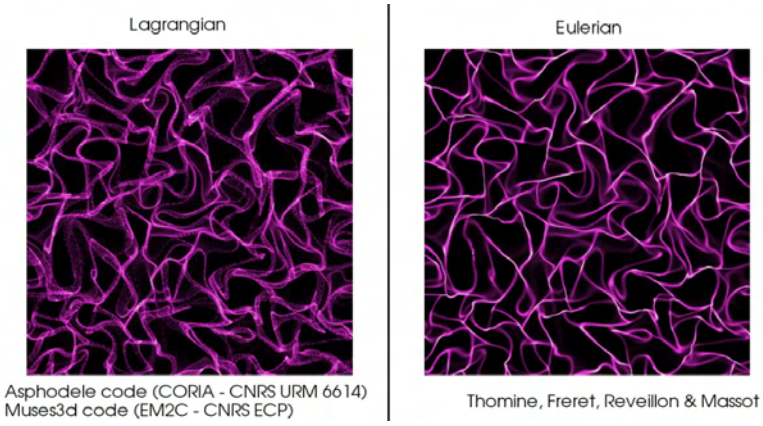

Figure 4.6: *Particle concentration in HIT for* $St = St_c$.

As a conclusion, the peculiar behavior of hypercompressibility is rendered by the Eulerian monokinetic closure up to $\mathrm{St} = \mathrm{St}_c$. Above this limit, the PGD yields model singularities and the clusters are abnormally infinitely thin, so that segregation can be overestimated. As regards numerical difficulties, the model singularities of PGD come in addition to the hypercompressible features of disperse phase flows, as discussed in § 10.2.

4.3.2.4 Beyond the PGD modeling

Particle flows can be modeled by many Eulerian equations, for instance:

- PGD (see Eq. (4.9)) models laminar particle flows;
- AG (see Eq. (6.14)) models small scale crossings with a pressure tensor;
- moment methods on Reeks' Eq. (3.155) yields a fluid system that accounts for a turbulent velocity dispersion with a stress tensor in the RANS framework (Réveillon et al. 2002) or in the LES framework

(Vié et al. 2013);
- the MEF of Eq. (3.152) accounts for a crossing and turbulent velocity dispersion with a strain tensor.

In laminar regime, the monokinetic closure models a dilute or moderately dense disperse phase as PGD: it is the most simple model that features the hypercompressible pathologies.
Polykinetic closures yield a particle stress tensor e.g. a particle pressure (Simoes 2006). This stress can either render deterministic (resolved) crossings (homo-PTC as defined in § 3.1.3.3) or unknown sub-grid scale crossings, yielded by unresolved turbulence in LES for instance. The main point is that, if the Stokes number based on the Kolmogorov time scale is close to one, high segregation effects occur, leading to the formation of vacuum zones and stiff accumulations without homo-PTC: such effects can be reproduced in DNS using a monokinetic closure, which leads again to the PGD system; but in reduced turbulent approaches, a HGD behavior occurs. The structure of the convective part of the disperse phase equations is then similar to Euler equations but the pressure is much weaker while the drag force dominates the flow so singularities similar to that of PGD occur.
To deal with the complex dynamics of particles in turbulent flows, several closures have been proposed in the literature, see Vié et al. (2012) and references therein. For instance, the Mesoscopic Eulerian Formalism (MEF) presented in § 3.6.1.2 renders homo-PTC through a strain tensor (particle pressure and viscosity) that is closed algebraically. The validity of the closures introduced up to now to deal with filtered turbulent scales has not been fully demonstrated yet, and is an active research topic. Whatever the closure, the particle system features HGD.
So hypercompressibility is a common feature of particle flow models as it is a physical characteristic of most disperse phases. The Eulerian models are able to render it accurately but possibly with the introduction of singularities and erroneous characteristic lengths in the case of PGD.

4.3.2.5 Two-way coupling of a hypercompressible medium

When a hypercompressible medium is coupled to a more regular fluid, the drag force *a priori* prevents particles from getting close to each other and the appearance of strong gradients depends on the flow topology. We focus on moderately dense flows, where the coupling is achieved through source terms, and we disregard dense flows where the volume occupancy plays an additional role e.g. in the dense models presented in § 3.2.3.
The coupling to another medium is done through source terms of mass, momentum and energy, as discussed in § 3.5.1.5, possibly yielding a non-equilibrium state, e.g. as regards the relaxation described in § 4.7.4.2, or as regards chemistry. For instance:
- in a supersonic nozzle, the particles are in strong dynamic and thermal lag so they deliver a strong momentum and energy source term.
- when burning, fuel droplets (or aluminum particles) generate a significant mass and heat release towards the gas.

But the presence of a smooth phase coupled through drag has a strong effect on the space structure of the hypercompressible phase, as the latter has a weak self-dynamics. For instance vortices yield, as soon as droplets are inertial enough, a remarkable segregation, corresponding to strong density gradients.
As a conclusion, it is crucial to preserve the space structures of the disperse phase to achieve a detailed enough description of its physics and to achieve predictive simulations, since the space density conditions the sources.

4.4 Eulerian polydisperse approaches with a monokinetic closure

We now present a class of Eulerian approaches based on the monokinetic closure and including strategies to describe the size variable and its related physics.

4.4.1 Eulerian polydisperse approach with continuous size-conditioning

We present a method, described and referred to as semi-kinetic in Laurent and Massot (2001), where the NDF is approached by assuming that its degrees of freedom are all conditioned by size. The phase space is then reduced to a one-dimensional sub-manifold, still depending on the external conditions: the size-conditioned variables are controlled by evolution equations.

4.4.1.1 Choice of the conserved moments

For this purpose, we only consider moments in the velocity and temperature variables at a given time, a given position and for a given droplet size that are the droplet number density, the average momentum, and

the average enthalpy:

$$n\begin{pmatrix}1\\ \boldsymbol{u}\\ h\end{pmatrix}=\iint\begin{pmatrix}1\\ \boldsymbol{c}\\ h(\theta)\end{pmatrix}f(t,\boldsymbol{x},\boldsymbol{c},\theta,S)\mathrm{d}\boldsymbol{c}\mathrm{d}\theta \tag{4.10}$$

which indeed depend only on $(t,\boldsymbol{x},S)$. We can now define a notation for an effective temperature T so that the disperse phase formally uses the same relation to compute its enthalpy moment $h=h(T)$ than individual droplets. We highlight that

$$T\neq n^{-1}\iint\theta f\mathrm{d}\boldsymbol{c}\mathrm{d}\theta \tag{4.11}$$

a priori.

In order to close the system, the following assumptions are introduced:

[HV1] For a given size S and location $(t,\boldsymbol{x})$, the only characteristic velocity is the average $\boldsymbol{u}(t,\boldsymbol{x},S)$.

[HV2] The velocity dispersion around $\boldsymbol{u}(t,\boldsymbol{x},S)$ is zero in each direction, whatever the point $(t,\boldsymbol{x},S)$.

[HT1] For a given size S and location $(t,\boldsymbol{x})$, the only characteristic temperature is the average $T(t,\boldsymbol{x},S)$.

[HT2] The temperature dispersion around $T(t,\boldsymbol{x},S)$ is zero whatever the point $(t,\boldsymbol{x},S)$.

It is equivalent to presume the following form of NDF:

$$f(t,\boldsymbol{x},\boldsymbol{c},\theta,S)=n(t,\boldsymbol{x},S)\delta(\boldsymbol{c}-\boldsymbol{u}(t,\boldsymbol{x},S))\delta(\theta-T(t,\boldsymbol{x},S)). \tag{4.12}$$

4.4.1.2 Discussion on the monokinetic hypotheses

The set of hypotheses [HV1] and [HV2] known as the monokinetic hypothesis has been introduced in Laurent and Massot (2001) and is equivalent to reducing the velocity distribution support to a one dimensional submanifold parameterized by droplet size. It is correct when $\tau^{\boldsymbol{u}}(S)$ is small compared to the gas characteristic dynamic time (de Chaisemartin et al. 2007; Massot et al. 2009; de Chaisemartin et al. 2009; de Chaisemartin 2009), the ratio of these two times forming the dynamic Stokes number St. This assumption is a pseudo-equilibrium one equivalent to a hydrodynamic limit, not imposed by collisions, but by the drag of the underlying carrier phase (Kah 2010).

These two hypotheses yield errors in the advection term if the Stokes number is close to one or higher but are correct below this limit as demonstrated extensively by comparisons to stochastic-Lagrangian references in one-way coupled complex combustion cases (de Chaisemartin 2009; Fréret et al. 2010; Fréret et al. 2013). The question of dense sprays of inertial particles remains open.

Hypotheses [HV1] and [HV2] can also yield errors in the source terms which depend directly on velocity such as coalescence or drag retroaction -in a two-way coupling context- if the Stokes number is too high.

Hypotheses [HT1] and [HT2] are similarly introduced in Laurent and Massot (2001) so that temperatures are locally correlated for droplets of a given size. They are correct when the thermal Stokes number formed, with $\tau^T(S)$, is smaller than one, as well as the dynamic Stokes number. Otherwise, errors occur in temperature-dependent source terms such as evaporation or heating retroaction in a two-way coupling context.

4.4.1.3 Semi-kinetic conservation equations

By substituting the assumed NDF and integrating at the kinetic level Eq. (3.123) versus all the disregarded phase space variables ($\boldsymbol{c}$ and θ), we get a system of conservation equations called the semi-kinetic model (Laurent and Massot 2001):

$$\left\{\begin{array}{rcl}\partial_t n+\partial_{\boldsymbol{x}}\cdot(n\boldsymbol{u}) & = & \mathscr{B}^{n-}+\mathscr{B}^{n+}+\mathscr{C}^{n-}+\mathscr{C}^{n+}\\ \partial_t(n\boldsymbol{u})+\partial_{\boldsymbol{x}}\cdot(n\boldsymbol{u}\otimes\boldsymbol{u}) & = & n\overline{\boldsymbol{F}}+\mathscr{B}^{u-}+\mathscr{B}^{u+}+\mathscr{C}^{u-}+\mathscr{C}^{u+}\\ \partial_t(nh)+\partial_{\boldsymbol{x}}\cdot(nh\boldsymbol{u}) & = & n\overline{\mathrm{H}}+\mathscr{B}^{h-}+\mathscr{B}^{h+}+\mathscr{C}^{h-}+\mathscr{C}^{h+}\end{array}\right. \tag{4.13}$$

where the coalescence terms are provided by Laurent et al. (2004).

4.4.1.4 Semi-kinetic transfer source terms

The kinetic transfer terms of Eq. (3.51) and Eq. (3.59) are integrated at the semi-kinetic level so that we can write a semi-kinetic transfer vector:

$$\begin{pmatrix}0\\ n\overline{\boldsymbol{F}}(t,\boldsymbol{x},\boldsymbol{u},S)\\ n\overline{\mathrm{H}}(t,\boldsymbol{x},T,S)\end{pmatrix}=\iint_{(\mathbb{R}^+)^2}\begin{pmatrix}0\\ \boldsymbol{F}(\boldsymbol{c},\boldsymbol{u}_g(t,\boldsymbol{x}),S)\\ \mathrm{H}(\theta,T_g(t,\boldsymbol{x}),S)\end{pmatrix}f(t,\boldsymbol{x},\boldsymbol{c},\theta,S)\mathrm{d}\boldsymbol{c}\mathrm{d}\theta. \tag{4.14}$$

In the case of closures that are linear in $\boldsymbol{c}$ and θ, e.g. in Stokes regime Eq. (3.47) and Eq. (3.53), the semi-kinetic transfer terms are computed with $\boldsymbol{c} = \boldsymbol{u}(t,\boldsymbol{x})$ and $\theta = T(t,\boldsymbol{x})$, and S the size variable so that drag simply reads:

$$\overline{\boldsymbol{F}}(t,\boldsymbol{x},\boldsymbol{u},S) = \boldsymbol{F}(\boldsymbol{u}(t,\boldsymbol{x}),\boldsymbol{u}_g(t,\boldsymbol{x}),S) \tag{4.15}$$

and heating simply reads:

$$\overline{\mathrm{H}}(t,\boldsymbol{x},T,S) = H(T_p(t,\boldsymbol{x}),T_g(t,\boldsymbol{x}),S). \tag{4.16}$$

4.4.1.5 Semi-kinetic break-up operator

In the semi-kinetic framework, the break-up operator yields the evolution rate of the zeroth and first order moments of the velocity phase space.
We perform the semi-kinetic velocity integration on the break-up terms given in Eq. (3.151), so that the Multi-Fluid break-up terms read, when omitting the $(t,\boldsymbol{x})$ dependency:

$$\begin{aligned}
\begin{pmatrix}\mathscr{B}^{n-}\\ \mathscr{B}^{u-}\\ \mathscr{B}^{h-}\end{pmatrix} &= \begin{pmatrix}1\\ \boldsymbol{u}\\ h\end{pmatrix} \nu_{\mathrm{bu}}(\boldsymbol{u},S,\boldsymbol{u}_g) n(t,\boldsymbol{x},S) \\
\begin{pmatrix}\mathscr{B}^{n+}\\ \mathscr{B}^{u+}\\ \mathscr{B}^{h+}\end{pmatrix} &= \int_{S^\star>S} \nu_{\mathrm{bu}}(\boldsymbol{u}^\star,S^\star,\boldsymbol{u}_g) g_{\mathrm{bu},\phi}(S;\boldsymbol{u}^\star,S^\star,\boldsymbol{u}_g) n(t,\boldsymbol{x},S^\star) \begin{pmatrix}1\\ \boldsymbol{u}^{\mathrm{bu}}(S,\boldsymbol{u}^\star,S^\star,\boldsymbol{u}_g)\\ h(T^\star)\end{pmatrix} \mathrm{d}S^\star
\end{aligned} \tag{4.17}$$

where we have noted $\boldsymbol{u}(S^\star) = \boldsymbol{u}^\star$ and $T(S^\star) = T^\star$.

4.4.1.6 Semi-kinetic coalescence operator

In the semi-kinetic framework, the coalescence operator yields the evolution rate of the zeroth and first order moments of the velocity phase space.
Coalescence phenomenon has no particular reason to preserve the velocity and temperature distributions as Dirac δ-functions. To preserve the monokinetic and zero-dispersion assumptions, these integrals have been evaluated with a formal dispersion which is constrained to be zero: this projection step is detailed in Laurent et al. (2004). The same demonstration can be done for the temperature distribution. Both these projections are consistent with the size-conditioned relaxations induced by drag and heat transfers, with the same criteria as for the validity of the monokinetic (monothermal) assumption i.e. the Stokes numbers must be below one.
So these terms finally read, when omitting the $(t,\boldsymbol{x})$ dependency:

$$\begin{aligned}
\begin{pmatrix}\mathscr{C}^{n-}\\ \mathscr{C}^{u-}\\ \mathscr{C}^{h-}\end{pmatrix} &= n(v) \begin{pmatrix}1\\ \boldsymbol{u}\\ h\end{pmatrix} \int_{v^\star\in[0,+\infty[} n(v^\star)\beta(v,v^\star) I_{vel}(\boldsymbol{u},\boldsymbol{u}^\star)\mathrm{d}v^\star \\
\begin{pmatrix}\mathscr{C}^{n+}\\ \mathscr{C}^{u+}\\ \mathscr{C}^{h+}\end{pmatrix} &= \int_{v^\star\in[0,v]} n(v^\diamond)n(v^\star) \begin{pmatrix}1\\ \frac{v^\star\boldsymbol{u}^\star+v^\diamond\boldsymbol{u}^\diamond}{v^\star+v^\diamond}\\ \frac{v^\star h^\star+v^\diamond h^\diamond}{v^\star+v^\diamond}\end{pmatrix} \beta(v,v^\star) I_{vel}(\boldsymbol{u}^\star,\boldsymbol{u}^\diamond)\mathrm{d}v^\star
\end{aligned} \tag{4.18}$$

where I_{vel} is the partial collisional integral, computed with the size correlated velocities:

$$I_{vel}(\boldsymbol{u}^\star,\boldsymbol{u}^\diamond) = |\boldsymbol{u}^\star - \boldsymbol{u}^\diamond|\ \mathfrak{E}(|\boldsymbol{u}^\star - \boldsymbol{u}^\diamond|, v^\star, v^\diamond) \tag{4.19}$$

where we have noted $\boldsymbol{u}(r^\star) = \boldsymbol{u}^\star$, $\boldsymbol{u}(r^\diamond) = \boldsymbol{u}^\diamond$, $h(r^\star) = h^\star$, and $h(r^\diamond) = h^\diamond$. In the particular case where we consider $\mathfrak{E} = 1$, we get $I_{vel}(\boldsymbol{u}^\star,\boldsymbol{u}^\diamond) = |\boldsymbol{u}^\star - \boldsymbol{u}^\diamond|$.

4.4.1.7 Cost of the semi-kinetic method

The phase space of the semi-kinetic system has too high a dimension as it has a continuous dependency on size, with a presumably complex dynamics regarding this variable. So the approach is too costly and is never used directly. Different modeling approaches have been proposed, which rely on the semi-kinetic basis such as sampling approaches (§ 4.4.3) or sectional approaches (§ 4.4.5).

4.4.2 Eulerian polydisperse approach with presumed PDFs

Another way to obtain a description of the size distribution is to presume a PDF for the size variable, as suggested in Babinsky and Sojka (2002). The idea is to presume a form for the size distribution and to solve the evolution of a set of parameters of this distribution. This form is linked to particular distributions: they can correspond to experimentally justified shapes or to simplified modeling approaches (Jones and Watkins 2012), but they have to be related to a given physics.
Nevertheless, this approach suffers severe limitations, such as the impossibility to account for the diversity of droplet velocities, which is one of the first features of polydispersity. Other limitations are now discussed.
The presumed PDF approach was extensively studied in the case of evaporation in Mossa (2005). It proved to be of limited stability and accuracy. Indeed it is necessary to presume a form of the spray NDF, for instance a log-normal form, and to resolve the evolution of this log-normal parameters. Nevertheless, the form of the NDF is not conserved through evaporation: an initially log-normal distribution evaporating has no reason to stay a log-normal distribution. Therefore severe singularities occur in the equations governing the evolution of the log-normal parameters.
The idea can be extended to the break-up phenomenon since typical distributions are retrieved experimentally (see § 3.5.3.1). The case of coalescence is also interesting provided the existence of attracting distributions or self-similar regimes: the existence of such regimes depends on the kernel as described in Chapter 7.

4.4.3 Eulerian polydisperse approach with size sampling

The size sampling approach (Laurent and Massot 2001; BenDakhlia 2001), also referred to as Multi-Class method (Murrone and Villedieu 2011), or Lagrangian-in-size method, considers the NDF as sampled regarding the size variable, yielding I classes of particles of same size. It is based on class assumptions, which can be related to the monokinetic hypothesis presented in § 4.4.1.2 so that sampling can be derived from the semi-kinetic approach.

4.4.3.1 Principle of sampling

The sampling approach is based on the following approximate NDF:

$$f(t,\boldsymbol{x},\boldsymbol{c},\theta,S)=\sum_{i\in[1,I]} N_i(t,\boldsymbol{x})\delta(S-S_{pi}(t,\boldsymbol{x}))\delta(\boldsymbol{c}-\boldsymbol{u}_i(t,\boldsymbol{x}))\delta(\theta-T_i(t,\boldsymbol{x})) \tag{4.20}$$

where S_{pi}, T_i and $\boldsymbol{u}_i$ are respectively the droplet size, temperature and velocity at the location $(t,\boldsymbol{x})$. With this form, particles with the same size, velocity, and temperature are gathered into classes where i is the index of a class: the classes perform a sampling of the NDF over the whole phase space. Because particles of a given size S_{pi} have the same velocity and temperature at a given location, the size-velocity (or temperature) correlations can be considered as accounted similarly as in the semi-kinetic approach so that sampling can be thought as being derived from it i.e. under the monokinetic assumption. Conversely the sampling approach requires at least the same validity conditions as the semi-kinetic approach, that is a low inertia.
Each class behaves as a fluid which number density is N_i and the terms S_{pi}, T_i and $\boldsymbol{u}_i$ are respectively the droplet size, temperature and velocity, which are equal for all droplets of a class. These variables are in fact Eulerian fields since they only depend on $(t,\boldsymbol{x})$, the corresponding equations describing the local evolution of droplet sizes, temperatures and velocities, due to the droplet closures coupled to the local gas state, with space and time derivatives only. The method is therefore described as a Lagrangian-in-size approach. The Lagrangian size samples are represented as Dirac δ-functions in the size phase space, see Figure 4.7. This is a significant simplification compared to kinetic models where dependencies and derivatives are taken against every phase space variable (Sainsaulieu 1995b).
The form of the NDF given in Eq. (4.20) raises the issue nonetheless of velocity crossings but also of size and temperature crossings: so the context in which the method is used must be thoroughly assessed to avoid singularities.

4.4.3.2 Conservation equations

The conservation equations for the disperse phase are obtained by integrating the approximated NDF of Eq. (4.20) in the semi-kinetic System (4.13), a rigorous approach should use distribution theory techniques, that are described in Schwartz (1987). A complete derivation of the sampling model, as well as applications to combustion, can be found in Laurent and Massot (2001) (see also BenDakhlia and Giovangigli 2000 and

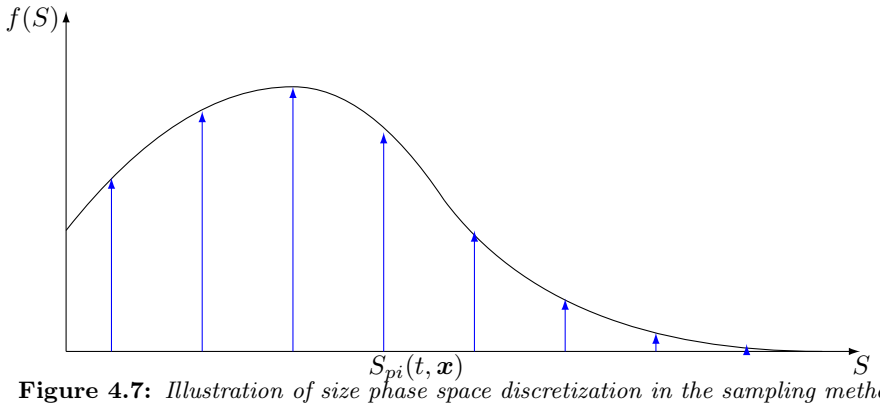

Figure 4.7: *Illustration of size phase space discretization in the sampling method.*

Ben-Dakhlia et al. 2002). The system reads, when disregarding collisions, coalescence and break-up:

$$\begin{cases} \partial_t N_i + \partial_{\boldsymbol{x}} \cdot (N_i \boldsymbol{u}_i) = 0 \\ \partial_t \rho_i + \partial_{\boldsymbol{x}} \cdot (\rho_i \boldsymbol{u}_i) = \dot{m}_i \\ \partial_t (\rho_i \boldsymbol{u}_i) + \partial_{\boldsymbol{x}} \cdot (\rho_i \boldsymbol{u}_i \otimes \boldsymbol{u}_i) = \rho_i \overline{\boldsymbol{F}}(S_{pi}) + \dot{m}_i \boldsymbol{u}_i \\ \partial_t (\rho_i h_i) + \partial_{\boldsymbol{x}} \cdot (\rho_i \boldsymbol{u}_i h_i) = \rho_i \overline{\mathrm{H}}(S_{pi}) + \dot{m}_i h_i \end{cases} \tag{4.21}$$

where $\rho_i = N_i \rho_l \mathcal{V}(S_{pi})$ so that the number and mass equations are in fact redundant, provided S_{pi}.
The mass, momentum and heat source terms are evaluated as they depend on the sample droplet variables.
The size evolution is computed directly from the characteristics, as illustrated in Figure 4.8.
A continuous size evolution e.g. due to evaporation can be considered. The class size parameter S_{pi} evolves identically for all droplets of the class: the size is therefore a Lagrangian variable of the problem, described by an ODE which depends on the conditions at $(t, \boldsymbol{x})$.

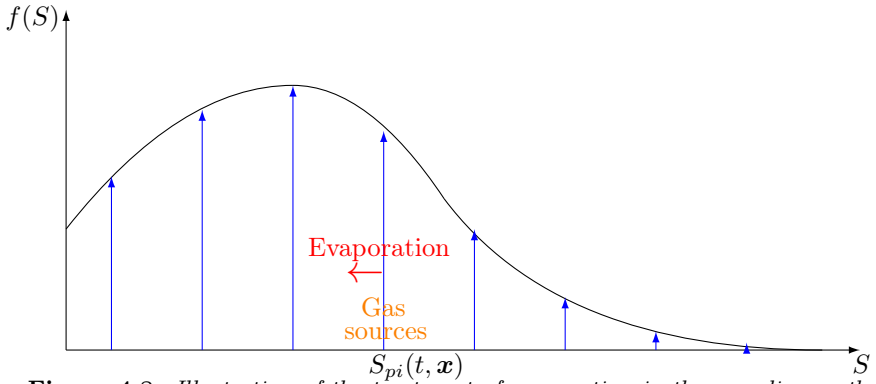

Figure 4.8: *Illustration of the treatment of evaporation in the sampling method.*

4.4.3.3 Peculiarities of non-local operators

The size sampling method is not compatible with integro-differential operators yielding a non-local transport in size phase space and a continuous size spectra, e.g. $\mathfrak{B}$ and $\mathfrak{C}$. As the approach is discretized regarding size with Dirac δ functions, the non-local transport cannot be accounted for properly: the size evolution due to r.h.s. sources (coalescence, break-up) is poorly rendered due to the fact that the samples have no particular reasons to match the new sizes. Apart from the approach of Vasenin et al. (1995) which is yet complex, break-up and coalescence are never considered in sampling approaches. Conversely this technique is avoided when it comes to modeling discrete size-changing phenomena.
The case of collisions with rebounds is similarly intractable as they induce a non-local transport in the velocity phase space.

4.4.3.4 Accuracy, applications and limitations

The Multi-Class approach can yield a satisfactory representation of the disperse phase size distribution, prevented that enough classes are considered and that they correspond to relevant points. Choosing a satisfactory sampling of a given distribution is a classical problem but here, it is coupled to the question of predicting the correct evolution of the spray, given such a distribution, which is a tough non-linear and implicit problem. So size samples are often chosen empirically. The choice also raises computational cost issues such as in the case of the local disappearance of a class due to "complete" evaporation *etc.*.

Multi-class methods are classical to treat a phase space variable such as vehicle types in traffic flow models (Wong and Wong 2002), or particle sizes in multiphase flow models: they have been widely used in academic (BenDakhlia and Giovangigli 2000; Laurent and Massot 2001) and applied contexts (Konan et al. 2010), and especially in SRM two-phase flow modeling (Chang 1980; Dash and Thorpe 1981; Johnston et al. 1994; Daniel 2000). The sampling method is implemented in the CEDRE code as it provides a convenient approach for evaporation so it is used to simulate realistic SRMs to assess aluminum combustion (Dupays et al. 2001). But this method is intractable to tackle integral terms except at the cost of strong modal simplifications (Vasenin et al. 1995; Rayapati et al. 2011). Since size sampling does not easily account for coalescence or break-up, this approach is disregarded for the high-fidelity SRM computations we aim at performing.

4.4.4 Eulerian polydisperse approaches with moments

Moment methods refer to any resolution method for a kinetic equation that uses the mapping between the distribution and some of its moments computed on the whole size phase space. Moment methods can be applied to the size variable, in which case the moments are integrated on $\mathbb{R}^+$; moments computed on size intervals can also be used but the method is then referred to as a "sectional" method, the latter being described in § 4.4.5.
The main issue in moment methods is that the evolution equations of the chosen moments may involve other moments, possibly unclosed.

4.4.4.1 The univariate QMOM for size

A way to close the system of equations describing the moments' evolution is to use a quadrature formula to compute the unknown high order moments as a function of low order moments. A method called Quadrature Method of Moments or QMOM (McGraw 1997; Wright et al. 2001; Marchisio et al. 2003) is inherited from moment methods for fluid-particle systems derived from Population Balance Equations, reviewed in Ramkrishna and Fredrickson (2000).
The original QMOM approach consists in transporting and conserving a set $(M_k)_k$ of $2N_p$ size moments. The size moments $M_k(t,\boldsymbol{x}) = \int_{\mathbb{R}^+} \xi^k f(t,\boldsymbol{x},\xi)\mathrm{d}\xi$ are defined as usual with k belonging to the moment index set $\mathcal{N}$ and of course $\mathrm{card}(\mathcal{N}) = 2N_p$. The moments are often chosen as the consecutive, lowest integer order moments i.e. $\mathcal{N} = [0, 1, ..., 2N_p - 1]$ so that the quadrature is exact for any polynomial function of degree $2N_p - 1$ or lower: this is a reasonable goal since any smooth enough function can be locally approached by such a polynomial, with an accuracy that increases with the degree. QMOM is therefore expected to be more accurate when using more nodes, the counterpart being a higher cost and a more difficult inversion.
The univariate QMOM method is described as follows. The NDF form is assumed to be that of a sum of Dirac δ-functions in size (Marchisio et al. 2003) while the velocity and temperature is locally the same for all particles:

$$f(t,\boldsymbol{x},\boldsymbol{c},\theta,\xi) = \delta(\boldsymbol{c}-\boldsymbol{u}(t,\boldsymbol{x}))\delta(\theta - T(t,\boldsymbol{x}))\sum_{i=1}^{N_p}\omega_i(t,\boldsymbol{x})\delta(\xi-\xi_i(t,\boldsymbol{x})). \tag{4.22}$$

with N_p is the number of peaks, ω_i the weights, and ξ_i the abscissae. The unique velocity and temperature for all particles is a limitation of the original QMOM approach, which make it suitable for aerosols but not for significantly polydisperse sprays. After integration of the kinetic equation Eq. (3.123), the evolution of the k^{th} order size moment is given by:

$$\partial_t M_k + \partial_{\boldsymbol{x}}(\boldsymbol{u}M_k) = \int_{\xi,\boldsymbol{c},\theta} \xi^k Q(\xi,\boldsymbol{c},\theta) f(t,\boldsymbol{x},\boldsymbol{c},\theta,\xi)\mathrm{d}\xi\mathrm{d}\boldsymbol{c}\mathrm{d}\theta \tag{4.23}$$

where $Q(\xi,\boldsymbol{c},\theta)$ stands for any kinetic source term. The evolution of the NDF is described by $2N_p + 2$ equations i.e. those of the conserved size moments and those of the overall velocity and temperature.
The NDF reconstruction is assessed as the weights ω_i and the abscissae ξ_i are linked to the conserved, low order moments through a system:

$$M_k = \sum_{i=1}^{N_p}\omega_i\xi_i^k, \quad k\in\mathcal{N} \tag{4.24}$$

that can be inverted with the product difference (PD) algorithm (McGraw 1997) or with Wheeler (1974)'s method. Thanks to this quadrature, the unclosed integral terms are computed as:

$$\int_{\xi,\boldsymbol{c},\theta}\xi^k Q(\xi,\boldsymbol{c},\theta)f(t,\boldsymbol{x},\boldsymbol{c},\theta,\xi)\mathrm{d}\xi\mathrm{d}\boldsymbol{c}\mathrm{d}\theta = \sum_{i=1}^{N_p}\omega_i(t,\boldsymbol{x})Q(\xi_i(t,\boldsymbol{x}),\boldsymbol{u}(t,\boldsymbol{x}),T(t,\boldsymbol{x})). \tag{4.25}$$

In particular from the quadrature formula, the non-conserved moments can be computed simply:

$$M_\alpha = \sum_i^{N_p} \omega_i \xi_i^\alpha, \qquad \alpha \in \mathbb{R}. \tag{4.26}$$

Such size QMOM approaches are evaluated for coalescence and/or break-up in Marchisio et al. (2003), in Estrada and Cuzzi (2008) and for turbulent cases in Belt and Simonin (2009). High order transport schemes can be developed, see for instance Vikas et al. (2011); Kah (2010); Kah et al. (2012). To overcome the limitation of a unique velocity, multivariate QMOM methods have been developed to account for the size velocity correlations and they are discussed in § 4.6.1. Multivariate QMOM can also be used to describe the complex shape of aggregates though multiple size parameters e.g. surface and volume (Wright et al. 2001; Fan et al. 2004). Let us finally present the Direct QMOM approach (DQMOM), which uses the same reconstruction as QMOM but the abscissae and weights ω_i et ξ_i are transported instead of the moments (Marchisio and Fox 2005). More details can be found in Marchisio and Fox (2007). DQMOM is more efficient as regards computational cost since the reconstruction computations need to be done less often. In return, the numerical errors introduced by practical transport schemes threaten realizability so the method can become unstable, especially when the monokinetic hypothesis is not strongly verified and δ-shocks start to appear. DQMOM approaches have been evaluated to capture the size distribution evolution under coalescence in laminar (Fox 2006; Fox et al. 2008) and turbulent cases (Belt and Simonin 2009). Comparisons between DQMOM and the Multi-Fluid approach (presented below) were performed in Fox et al. (2008) which prove that DQMOM is efficient for coalescence but much less for evaporation. This latter limitation is due to the inaccurate description of the droplet flux in $S = 0$.

4.4.4.2 Pivot methods

Pivot methods consist in the choice of discrete sizes (the pivots) to assess the integral source terms of a disperse phase statistical description (Kostoglou and Karabelas 1994; Kumar and Ramkrishna 1996a). These approaches are here defined as a category that is distinct from sampling (Multi-Class) method for they are not based on a NDF reconstruction (contrary to sectional methods, which are presented below) but they still allow to tackle some continuous aspects (contrary to class methods), though in an *ad hoc* fashion. To do so, all these methods perform some mathematical treatment to cast the integral terms into moment evolution equations evaluated at the pivots' locations, under the constraint of conserving a given set of moments of the whole NDF (global moments). As a consequence, the method is computationally efficient (few or none integrals are assessed) and accurate for a small set of global moments but it does not enforce local (sectional) accuracy and it is therefore unable to describe the details of the NDF. For instance Kostoglou and Karabelas (1994) refers to these methods as "zero order methods" to emphasize the fact that the NDF cannot be approached with arbitrary accuracy. Pivot methods are used to treat agglomeration and breakage, because these phenomena tend to multiply the number of modes and are costly to treat with a sampling approach. In addition, an identical velocity and temperature must often be assumed for all the sizes, which is a strong limitation.
Pivot methods are commonly used to solve Population Balance Equations (PBEs) (Gelbard et al. 1980; Kostoglou and Karabelas 1994; Kumar and Ramkrishna 1996a; Pope and Howard 1997; Puel et al. 2003; Wen et al. 2005) which are 0D or homogeneous, but they are rarely applied to multidimensional (heterogeneous) contexts (Bove et al. 2005; Netzell et al. 2007; Cheng et al. 2012). As an illustration, we tally the following groups of pivot methods:

- In early methods reviewed by Kostoglou and Karabelas (1994) and by Kumar and Ramkrishna (1996a) discrete size samples are considered and integral terms are computed as pointwise evaluations with corrections applied to overcome the mass conservativity issues raised by the projection discrepancies of the physical modes onto the numerical classes.
- In the "fixed pivot technique" described by Kumar and Ramkrishna (Kumar and Ramkrishna 1996a; Ramkrishna and Fredrickson 2000) or in improved versions such as the "high order class method" (Alopaeus et al. 2006) or the "cell average technique" (Kumar et al. 2006) the integral terms are computed at the class locations, e.g. with quadrature techniques, but these integrations are *ad hoc* and are not explicitly linked to an underlying size distribution that would be consistent for all the terms of the equation.
- A "moving pivot technique" has also been suggested by Kumar and Ramkrishna (1996b) to increase accuracy and it preserves similarly some moments of the global size distribution.

The pivot methods are cost-effective approaches but we disregard them for the general frame is constraining and not rigorous enough as regards transport.

4.4.4.3 MOMIC

In the MOMIC method (Frenklach 2002; Frenklach 2009), a set of global moments is again conserved and the size distribution is reconstructed to bring the following closure for the positive order moments:

$$M_k = \exp\left(\sum_i a_i \xi_i\right) \tag{4.27}$$

where a_i are Lagrange coefficients that enforce the conservation of the known moments. The negative order moments require another interpolation (Frenklach 2002).
In the context of a 0D approximation, a typical Population Balance Equation then reads:

$$\begin{cases} \mathrm{d}_t M_0 = R_0 - G_0 \\ \mathrm{d}_t M_1 = R_1 + W_1 \\ \mathrm{d}_t M_2 = R_2 + G_2 + W_2 \\ \vdots \\ \mathrm{d}_t M_k = R_k + G_k + G_k \end{cases} \tag{4.28}$$

where R, G, and W are the nucleation, coagulation and surface growth terms respectively.
This method was extended to particles with various (non-spherical) shapes in Balthasar and Frenklach (2005). It describes accurately the size variable but at the cost of a complex algebra, yielding realizability problems.

4.4.4.4 Hybrid moment methods

A method referred to as HMOM (hybrid method of moments) is introduced in Mueller et al. (2009a); Mueller et al. (2009b) which is based on the following size reconstruction:

$$n(t, \boldsymbol{x}, v) = N_0 \delta(v_0 - v) + \sum_i^{N_p} \omega_i \delta(v - v_i) \tag{4.29}$$

with the following moments

$$M_k = N_0 v_0^k + \exp\left(\sum_i a_i \xi_i\right) \tag{4.30}$$

It therefore couples a MOMIC approach with a single peak at v_0. It is designed to capture the bimodal features of many soot models, namely the existence of a typical precursor size v_0, with larger aggregates that are polydisperse and may evolve in size.
The use of a fixed value for v_0 is a good approximation, with the constraint:

$$N_0 = \lim_{\alpha \to +\infty} \left(\frac{M_{-\alpha}}{v_0^{-\alpha}}\right) \tag{4.31}$$

This method is used in HPC configurations for soot modeling (Mueller and Pitsch 2012; Bisetti et al. 2012).

4.4.4.5 High order size moment methods

High order moment methods are considered to get a satisfactory description of particle size distribution in the disperse phase. The principle is to replace the continuous size dependency of the semi-kinetic system by discrete integral quantities, usually integer moments of a size parameter ϕ (Laurent 2006; Yuan et al. 2012):

$$\begin{pmatrix} m_0 \\ m_1 \\ m_2 \\ \vdots \\ m_N \end{pmatrix} = \int_{\mathbb{R}^+} \begin{pmatrix} 1 \\ \phi \\ \phi^2 \\ \vdots \\ \phi^N \end{pmatrix} n(t, \boldsymbol{x}, \phi) \mathrm{d}\phi \tag{4.32}$$

with N the number of moments of the method. The integration of System (4.13) versus the moment vector yields a system of $N+2$ conservation equations for the moments:

$$\partial_t \begin{pmatrix} m_0 \\ m_1 \\ m_2 \\ \vdots \\ m_N \\ m_\xi \boldsymbol{u} \\ m_\xi h \end{pmatrix} + \partial_{\boldsymbol{x}} \cdot \begin{pmatrix} m_0 \boldsymbol{u} \\ m_1 \boldsymbol{u} \\ m_2 \boldsymbol{u} \\ \vdots \\ m_N \boldsymbol{u} \\ m_\xi \boldsymbol{u} \otimes \boldsymbol{u} \\ m_\xi h \boldsymbol{u} \end{pmatrix} = \begin{pmatrix} 0 \\ 0 \\ 0 \\ \vdots \\ 0 \\ m_\xi \overline{\boldsymbol{F}} \\ m_\xi \overline{\mathrm{H}} \end{pmatrix} \tag{4.33}$$

where m_ξ is the mass moment so that $\xi \in \mathbb{Z}$ depends on the choice of ϕ. If $\phi = r$ or $\phi = v$, ξ is equal to 3 or 1 respectively so that mass is a conserved moment. If $\phi = S$, $\xi = \frac{3}{2}$ so that m_ξ has to be reconstructed. Because there is only one velocity moment and one temperature moment, all the particles are transported with a unique velocity and assuming a unique temperature, whatever their sizes. The evolution of the velocity and temperature moments is assessed for an average size, which is accurately estimated thanks to the detailed information on the local size distribution.

The mathematical properties of such methods and their accuracy regarding size have been assessed in Laurent (2006). Realizability issues are raised as the moment space in which the moment vector lives is a restriction of $(\mathbb{R}^+)^N$: numerical methods (e.g. transport schemes) must be carefully developed to avoid approximations of the moment vector that would be out of the moment space, resulting in stability and accuracy failures.

The Eulerian Multi-Size Method (EMSM), introduced by Massot et al. (2010) and developed in Kah (2010) (see also Kah et al. (2012)), takes $\phi = S$ and considers the first four moments. In the context of the EMSM, the question of high order, accurate and realizable transport schemes was resolved for $N = 4$, see Kah et al. (2012). The EMSM has been more particularly developed for evaporating cases, where the evaluation of the source term requires the knowledge of the size distribution in $S = 0$. While point-wise knowledge of the underlying distribution is difficult to get with moments (which are global), the EMSM reconstruction $n^{\mathrm{ME}}(S)$ uses the entropy maximization (Mead and Papanicolaou 1984), and a numerical method has been carefully developed to allow a stable and accurate resolution of evaporating sprays (Massot et al. 2010; Kah 2010; Kah et al. 2012).

Still, high order size methods offer poor knowledge of velocities, as they locally account for only one velocity for all the disperse phase. High order methods for size-velocity coupling are discussed below. Similarly the temperature information is very reduced in high order moment methods. So the cases of application correspond to those where a fine knowledge of size is required but neither velocity nor temperature play a significant role.

4.4.4.6 Polydispersity with high order in size-conditioned velocity

In the context of the continuous description of the size variables provided by the high order size methods of moments above, a unique velocity moment has been up to now associated to a size interval. This allows to achieve a first order reconstruction of the velocity distribution conditioned by size. Vié et al. (2013) has introduced the so-called Correlated Size-Velocity Method or CSVM to increase the accuracy of the EMSM as regards velocity, based on high order velocity-conditioned-by-size moments.

Back to the semi-kinetic level, the monokinetic closure allocates one velocity $\boldsymbol{u}(S)$ per size S with the corresponding NDF, given in § 4.12. The semi-kinetic system then solves for a size distribution $n(S)$, and a velocity distribution $\delta(\boldsymbol{c} - \boldsymbol{u}(S))$. To account for size velocity couplings cross-moments are introduced:

$$M^{i,pqr} = \int_{\mathbb{R}^+} \iiint_{\mathbb{R}^3} S^i c_1^p c_2^q c_3^r \widetilde{f}(s, \boldsymbol{c}) \mathrm{d}S \mathrm{d}\boldsymbol{c} \tag{4.34}$$

At the EMSM level, size is reconstructed on the sections with the maximum entropy distribution $n^{\mathrm{ME}}(S)$ but CSVM then introduces a velocity reconstruction with the following form:

$$\boldsymbol{u}(t, \boldsymbol{x}, S) = \boldsymbol{u}_g + \boldsymbol{A}(t, \boldsymbol{x}) S + \boldsymbol{B}(t, \boldsymbol{x}) S^2. \tag{4.35}$$

In the previous form the three directions are decoupled so that we do not need consider cross-moments in the velocity components. In accordance with both the EMSM requirements and the number of parameters in the velocity reconstruction, the following moments are chosen:

$$\begin{pmatrix} & M^{0,000} & \\ & M^{1,000} & \\ & M^{2,000} & \\ & M^{3,000} & \\ M^{0,100} & M^{0,010} & M^{0,001} \\ M^{1,100} & M^{1,010} & M^{1,001} \end{pmatrix} \tag{4.36}$$

which makes 10 in 3D, while we would only need 6 moments in 1D and 8 in 2D. Thanks to the direction decoupling, the vector notation $\boldsymbol{M}^{i,p} = (M^{i,p00}\ M^{i,0p0}\ M^{i,00p})^T$ is no longer ambiguous and is used from now on. The reconstruction process can be performed as follows. Given the availability of $M^{0,0}$, $M^{1,0}$, $M^{2,0}$, and $M^{3,0}$ the size distribution can be reconstructed, in a first step, with the same algorithm than in classical EMSM approaches. In a second step, the velocity moments in a section must ensure the following relations:

$$\left\{ \begin{array}{ll} \boldsymbol{M}^{0,1} = & \boldsymbol{u}_g M^{0,0} + \boldsymbol{A} M^{1,0} + \boldsymbol{B} M^{2,0} \\ \boldsymbol{M}^{1,1} = & \boldsymbol{u}_g M^{1,0} + \boldsymbol{A} M^{2,0} + \boldsymbol{B} M^{3,0} \end{array} \right. \tag{4.37}$$

which is an invertible system as there are only two unknowns $\boldsymbol{A}$ and $\boldsymbol{B}$.
We finally get the following conservation equations, written without coalescence nor break-up:

$$\partial_t \begin{pmatrix} M^{0,0} \\ M^{1,0} \\ M^{2,0} \\ M^{3,0} \\ \boldsymbol{M}^{0,1} \\ \boldsymbol{M}^{1,1} \end{pmatrix} + \partial_{\boldsymbol{x}} \begin{pmatrix} M^{0,1} \\ M^{1,1} \\ M^{2,1} \\ M^{3,1} \\ \boldsymbol{M}^{0,2} \\ \boldsymbol{M}^{1,2} \end{pmatrix} = \begin{pmatrix} 0 \\ 0 \\ 0 \\ 0 \\ \boldsymbol{F}_k^0 \\ \boldsymbol{F}_k^1 \end{pmatrix} \tag{4.38}$$

where all the moments are known except $\boldsymbol{M}^{0,2}$, $\boldsymbol{M}^{1,2}$, $\boldsymbol{M}^{2,1}$, and $\boldsymbol{M}^{3,1}$ which can be reconstructed. The source terms (drag, possibly heating) may also require more size moments, which can still be computed from the knowledge of the size and velocity reconstructions (Massot et al. 2009; Kah 2010).

4.4.5 The Eulerian Multi-Fluid model

The Eulerian Multi-Fluid model (MF), also referred to as "sectional" method, was developed in Laurent and Massot (2001) to account for the droplet size in a continuous and affordable manner. It is inspired from the seminal work of Tambour (1980), furthered in Silverman et al. (1991); Greenberg et al. (1993). But the origin and assumptions of the Multi-Fluid model have been precisely presented in Laurent and Massot (2001), proving it to derive from the semi-kinetic model. And the potential of the method was developed since then e.g. with extension to coalescence (Laurent et al. 2004).
We here focus on particle size modeling, and the dynamics of size-conditioned DOFs (velocity and temperature) but sectional methods can also be used for other phase space DOFs such as energy levels for collision modeling in hot plasmas, see for instance Trautmann and Wanner (2003).

4.4.5.1 Discretization of size phase space

The Multi-Fluid model relies indeed on the choice of a discretization for the droplet size phase space:

$$0 = S_0 < S_1 < \cdots < S_{N_{\text{sec}}} = \infty \tag{4.39}$$

where N_{sec} is the number of sections. The system of conservation laws is then average over each fixed size interval $[S_{k-1}, S_k[$, called section. The set of droplets in one section can be seen as a "fluid" for which conservation equation are written, the sections exchanging mass, momentum and enthalpy. The principle of sectional discretization is shown in Figure 4.9 and can be seen as a finite volume method on the size dimension, continuous size-variation source terms (e.g. evaporation) resulting in fluxes at the edges of the size cells.

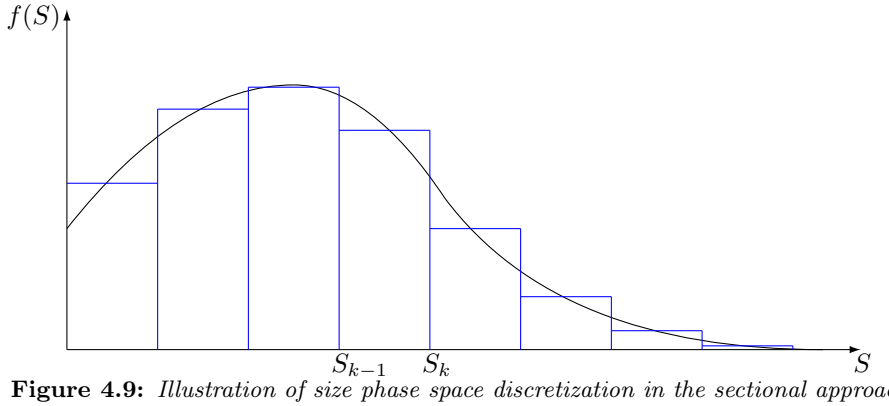

Figure 4.9: *Illustration of size phase space discretization in the sectional approach.*

4.4.5.2 Sectional velocity closure

In order to close the system, the following assumptions are introduced:

[HV3] In each section, the velocity does not depend on the size of the droplets.

[HT3] In each section, the temperature does not depend on the size of the droplets.

We choose for assumption [HV3] the notation $\boldsymbol{u}(t,\boldsymbol{x},S) = \boldsymbol{u}_k(t,\boldsymbol{x})$ to designate the constant velocity distribution in section k. Hypothesis [HT3] is similarly introduced here and is equivalent to presuming $h(T(t,\boldsymbol{x},S)) = h_k(t,\boldsymbol{x}) = h(T_k(t,\boldsymbol{x}))$ as a constant enthalpy distribution in section k, and the corresponding effective temperature $T_k(t,\boldsymbol{x})$ which allows to define the sectional specific heat capacity $\bar{c}_{p,k} = c_{p,l}(T_k)$. The validity of these assumptions is linked to the strength of polydispersity in each section, which is quantified in a section by comparing the smallest to the biggest Stokes numbers. If the dynamic Stokes number spectrum is too wide, [HV3] and [HT3] no longer hold while only [HT3] fails for a wide thermal Stokes number spectrum. In both cases, the discretization must then be refined, as discussed in Doisneau et al. (2011); Doisneau et al. (2013) in the particular case of acoustics in polydisperse two-phase flows, or high order methods such as the CSVM method (see § 4.4.4.6) must be used as discussed below.

4.4.5.3 Sectional size closure

We finally assume

[HS1] In each section, the form of n as a function of S is presumed.

which allows to reduce the size distribution information in each section at $(t,\boldsymbol{x})$ to a set of moments of S, the number of which depends on the choice of the $(\kappa_k)_k$ set of size presumed form functions.

Several methods were developed that are based on different forms of presumed functions for [HS1]. We hereafter present the so-called One Size Moment method (OSM), where a one-parameter function in each section decouples size dependence ${}^1\kappa_k(S)$ and space-time dependence $m_k(t,\boldsymbol{x})$, yielding a first order size distribution convergence with the number of sections. This is the classical Multi-Fluid method which has been developed and validated for evaporating cases (Laurent and Massot 2001) and in coalescing cases (Laurent et al. 2004). A higher order method with two size moments is presented in Chapter 5.

The OSM then solves for size moments calculated on the sections, the equations of which are derived by integrating the semi-kinetic System (4.13). Please note that the more parameters the presumed function has, the more moments one needs. The choice of refining the size distribution description with a high order moment method for a finer resolution of polydispersity therefore increases the computational cost. In the context of evaporation, the generalization to more moments can allow to reduce the number of sections to one (Kah 2010; Massot et al. 2010; Kah et al. 2012), yielding a high order size moment method, described previously. Regarding coalescence, only OSM has been validated (Laurent and Massot 2001) so far as explained in the introduction.

The OSM Multi-Fluid model assumes a fixed size profile in each section, as shown in Figure 4.9, therefore decoupling size and space dependency. The following notation therefore specifies [HS1] in each section k:

$$n(t,\boldsymbol{x},S) = m_k(t,\boldsymbol{x})\,{}^1\kappa_k(S) \tag{4.40}$$

where m_k is the mass concentration of droplets in the k^{th} section, in such a way that:

$$\int_{S_{k-1}}^{S_k} {}^1\kappa_k(S)\frac{\rho_l}{6\sqrt{\pi}}S^{3/2}\mathrm{d}S = 1. \tag{4.41}$$

Such an approach only focuses on one moment of the distribution in the size variable: the moment in terms of mass is chosen because it is conserved by all the phenomena of interest except evaporation.

Please note that the distribution on the last section is a decreasing exponential with a fixed coefficient. This choice allows the final section to treat the bigger droplets but requires not to host a significant part of the mass for the sake of accuracy. It is well suited for evaporating sprays, the size support of which never extends (Laurent and Massot 2001). This is though a major limitation when coalescence occurs since bigger droplets are generated. Comparisons to results provided by the Two Size Moment method when this final, unbounded section is "active" are discussed in § 13.2.4.

4.4.5.4 Multi-Fluid conservation equations

The conservation equations for the k^{th} section result from the integration of the mass moment of the semi-kinetic System (4.13) in each section k and reads, without mass transfer:

$$\left\{\begin{array}{rcl} \partial_t m_k + \partial_{\boldsymbol{x}}\cdot(m_k\boldsymbol{u}_k) & = & {}^1\mathrm{B}_k^{m+} - {}^1\mathrm{B}_k^{m-} + {}^1\mathrm{C}_k^{m+} - {}^1\mathrm{C}_k^{m-} \\ \partial_t(m_k\boldsymbol{u}_k) + \partial_{\boldsymbol{x}}\cdot(m_k\boldsymbol{u}_k\otimes\boldsymbol{u}_k) & = & m_k\,{}^1\boldsymbol{F}_k + {}^1\boldsymbol{B}_k^{u+} - {}^1\boldsymbol{B}_k^{u-} + {}^1\boldsymbol{C}_k^{u+} - {}^1\boldsymbol{C}_k^{u-} \\ \partial_t(m_k h_k) + \partial_{\boldsymbol{x}}\cdot(m_k h_k\boldsymbol{u}_k) & = & m_k\,{}^1\mathrm{H}_k + {}^1\mathrm{B}_k^{h+} - {}^1\mathrm{B}_k^{h-} + {}^1\mathrm{C}_k^{h+} - {}^1\mathrm{C}_k^{h-} \end{array}\right. \tag{4.42}$$

where ${}^1\boldsymbol{F}_k$ is the average drag force per unit mass on a section and ${}^1\mathrm{H}_k$ is the average heat transfer per unit mass so that we get the transfer vector:

$$m_k \begin{pmatrix} 0 \\ {}^1\boldsymbol{F}_k \\ {}^1\mathrm{H}_k \end{pmatrix} = \int_{S_{k-1}}^{S_k} \begin{pmatrix} 0 \\ \overline{\boldsymbol{F}}(t,\boldsymbol{x},\boldsymbol{u},S) \\ \overline{\mathrm{H}}(t,\boldsymbol{x},T,S) \end{pmatrix} m_k {}^1\kappa_k(S)\mathrm{d}S \tag{4.43}$$

The total system thus counts n_d+2 times more equations to be solved on the space domain than the number of sections with n_d the dimension of the physical space. The gas-droplet coupling times ${}^1\overline{\tau}_k^u$ and ${}^1\overline{\tau}_k^T$ are fixed as soon as the size discretization is given.
An error on the disperse phase velocity and temperature dynamics occurs, especially if the droplet mass of the size distribution that is approximated in a section is supposed to be concentrated close to a section boundary.

4.4.5.5 Remarks on Multi-Fluid integral source terms

At the Multi-Fluid level, the reconstructed form of the size distribution $n(S)=\sum_k m_k {}^1\kappa_k(S)$ is used so that the integration of any size function $\Psi(S)$ on the whole size phase space can be transformed into a sum of elementary sectional integrals:

$$\int n(S)\Psi(S)\mathrm{d}S = \sum_k m_k \int_{S_k}^{S_{k-1}} {}^1\kappa_k(S)\Psi(S)\mathrm{d}S. \tag{4.44}$$

This decomposition is used for break-up terms as well as for coalescence terms, as these sources are integrated at the kinetic level on all the possible partner sizes $\phi^\star \in \mathbb{R}^+$. The corresponding integration operations on the sections result from the sectional decomposition of the coalescence partner integral from the kinetic level and it should not be confused with the sectional integration of the system, that has been done on the semi-kinetic size variable ϕ.
The source terms can also be expressed as a function of some d_{pq}, the latter given in Eq. (3.17). In practice, the d_{pq} can be computed by integration of the size reconstruction.

4.4.5.6 Multi-Fluid break-up terms

From the break-up expressions (4.17), the Multi-Fluid integration operates by substituting the reconstructed form of $n(S)=\sum_k m_k {}^1\kappa_k(S)$ and integrating on the semi-kinetic size variable ϕ, so that the creation sources can be seen as sums of elementary integrals on the sections hosting mother droplets:

$$\begin{pmatrix} {}^1\mathrm{B}_k^{m+} \\ {}^1\boldsymbol{B}_k^{u+} \\ {}^1\mathrm{B}_k^{h+} \end{pmatrix} = \sum_{i=k}^{N_{\mathrm{sec}}} \begin{pmatrix} {}^1\mathrm{Q}_{ik}^{m+} \\ {}^1\boldsymbol{Q}_{ik}^{u+} \\ {}^1\mathrm{Q}_{ik}^{h+} \end{pmatrix} \tag{4.45}$$

where the elementary integrals read:

$$\begin{pmatrix} {}^1\mathrm{Q}_{ik}^{m+} \\ {}^1\boldsymbol{Q}_{ik}^{u+} \\ {}^1\mathrm{Q}_{ik}^{h+} \end{pmatrix} = \int_{S^\star=S_{i-1}}^{S^\star=S_i} \int_{S=S_{k-1}}^{S=S_k} \begin{pmatrix} 1 \\ \boldsymbol{u}^{\mathrm{bu}}(S;\boldsymbol{u}_i,S^\star,\boldsymbol{u}_g) \\ h(T_i) \end{pmatrix} m_i {}^1\kappa_i(t,\boldsymbol{x},S^\star) \times \nu_{\mathrm{bu}}(\boldsymbol{u}_i,S^\star,\boldsymbol{u}_g)\, f_{\mathrm{bu}}(S;\boldsymbol{u}_i,S^\star,\boldsymbol{u}_g)\mathrm{d}S\mathrm{d}S^\star \tag{4.46}$$

and have the property:

$${}^1\mathrm{Q}_{ik}^{m+} = h(T_i) {}^1\mathrm{Q}_{ik}^{h+} \tag{4.47}$$

which is useful to spare computational resource.
As for the disappearance terms, they can be directly integrated on the sections:

$$\begin{pmatrix} {}^1\mathrm{B}_k^{m-} \\ {}^1\boldsymbol{B}_k^{u-} \\ {}^1\mathrm{B}_k^{h-} \end{pmatrix} = \int_{S_{k-1}}^{S_k} m_k \begin{pmatrix} 1 \\ \boldsymbol{u}_k \\ h(T_k) \end{pmatrix} {}^1\kappa_k(t,\boldsymbol{x},S)\nu_{\mathrm{bu}}(\boldsymbol{u}_k,S,\boldsymbol{u}_g)\mathrm{d}S \tag{4.48}$$

The following relations between disappearance and creation emphasize mass conservation:

$$\begin{pmatrix} {}^1\mathrm{B}_k^{m-} \\ {}^1\boldsymbol{B}_k^{u-} \\ {}^1\mathrm{B}_k^{h-} \end{pmatrix} = \sum_{i=1}^{N_{\mathrm{sec}}} \begin{pmatrix} {}^1\mathrm{Q}_{ki}^{m+} \\ \boldsymbol{u}_k {}^1\mathrm{Q}_{ki}^{m+} \\ h_k {}^1\mathrm{Q}_{ki}^{m+} \end{pmatrix} \tag{4.49}$$

where enthalpy is conserved by the break-up operator:

$$ {}^{1}\mathrm{B}_k^{h-} = \sum_{i=1}^{N_{\mathrm{sec}}} {}^{1}\mathrm{Q}_{ki}^{h+}. \tag{4.50} $$

while momentum is not conserved by the operator:

$$ {}^{1}\boldsymbol{B}_k^{u-} \neq \sum_{i=1}^{N_{\mathrm{sec}}} {}^{1}\boldsymbol{Q}_{ki}^{u+} \tag{4.51} $$

due to the projection of daughter droplet velocities on to $\boldsymbol{u}^{\mathrm{bu}}(S;\boldsymbol{u}_i,S^\star,\boldsymbol{u}_g)$ and as described at the kinetic level in § 3.5.3.2.
For mass and enthalpy practical computations, Eq. (4.49) are preferred to the integral ones of Eq. (4.48) in order to enforce conservation.

4.4.5.7 Multi-Fluid coalescence terms

For each section k, the coalescence creation terms result from a double integration: on the whole colliding partner size space at the kinetic level in Eq. (3.136) and on the concerned section at the Multi-Fluid level. Yet the second dependency will not coincide with the section after mapping the natural variables of the two precursor colliding partners i and j. When splitting the integration domain thanks to the continuity of section partitioning, one gets elementary integrals Q_{ijk}, triply indexed with the two precursor section numbers i and j and the destination section number k. The corresponding elementary integration domains are illustrated in Figure 4.10 and defined as:

$$ \mathscr{D}_{ijk} = \left\{ r^\star, r^\diamond \middle\| r_i < r^\star < r_{i+1} \ ; \ r_j < r^\diamond < r_{j+1} \ ; \ r_k^3 < r^{\star 3} + r^{\diamond 3} < r_{k+1}^3 \right\} \tag{4.52} $$

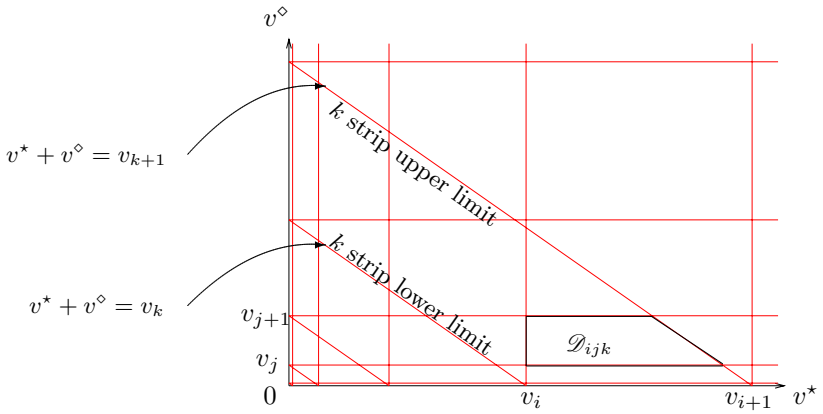

Figure 4.10: *Domains $\mathscr{D}_{ijk}$ on which coalescence terms are integrated.*

4.4.5.8 Remarks on coalescence in the OSM method

We focus on the possibility of factorizing the coalescence terms in the particular case of the OSM method in order to optimize their computations. We need to assume the collision efficiency as independent of velocities: the context of [HC4] with $\mathfrak{E} = 1$ is a particular and convenient case. So we note this limited efficiency $\widetilde{\mathfrak{E}}$ as it does not allow the same modeling flexibility as the general form.
The coalescence integrals Q_{ijk} then take the following form after factorizing the mass moments m_i and m_j (Laurent and Massot 2001):

$$ \begin{pmatrix} {}^{1}\mathrm{Q}_{ijk}^{\star} \\ {}^{1}\mathrm{Q}_{ijk}^{\diamond} \end{pmatrix} = \iint_{\mathscr{D}_{ijk}} \rho_l \frac{4}{3}\pi \begin{pmatrix} r^{\star 3} \\ r^{\diamond 3} \end{pmatrix} {}^{1}\kappa_i(r^\star)\,{}^{1}\kappa_j(r^\diamond)\widetilde{\mathfrak{E}}\pi(r^\star + r^\diamond)^2 \mathrm{d}r^\star \mathrm{d}r^\diamond. \tag{4.53} $$

As for the disappearance terms, they can also be computed as sums of the elementary creation integrals and must be so to ensure the conservation of matter. After some algebra, the coalescence terms ${}^{1}\mathrm{C}_k^{m+}$, ${}^{1}\mathrm{C}_k^{m-}$,

${}^1\boldsymbol{C}_k^{u+}$, ${}^1\boldsymbol{C}_k^{u-}$, ${}^1\mathrm{C}_k^{h+}$ and ${}^1\mathrm{C}_k^{h-}$ read (Laurent et al. 2004):

$$\begin{aligned}
\begin{pmatrix} {}^1\mathrm{C}_k^{m+} \\ {}^1\boldsymbol{C}_k^{u+} \\ {}^1\mathrm{C}_k^{h+} \end{pmatrix} &= \sum_{i=1}^{k} m_i \sum_{j=1}^{i} m_j \, |\boldsymbol{u}_i - \boldsymbol{u}_j| \left\{ \begin{pmatrix} 1 \\ \boldsymbol{u}_i \\ h_i \end{pmatrix} {}^1\mathrm{Q}_{ijk}^{\star} + \begin{pmatrix} 1 \\ \boldsymbol{u}_j \\ h_j \end{pmatrix} {}^1\mathrm{Q}_{ijk}^{\diamond} \right\}, \\
\begin{pmatrix} {}^1\mathrm{C}_k^{m-} \\ {}^1\boldsymbol{C}_k^{u-} \\ {}^1\mathrm{C}_k^{h-} \end{pmatrix} &= m_k \begin{pmatrix} 1 \\ \boldsymbol{u}_k \\ h_k \end{pmatrix} \sum_{j=1}^{N_{\mathrm{sec}}} m_j \, |\boldsymbol{u}_j - \boldsymbol{u}_k| \sum_{i=1}^{N_{\mathrm{sec}}} {}^1\mathrm{Q}_{kji}^{\star}.
\end{aligned} \tag{4.54}$$

The integrands of the Q_{ijk} integrals depend only on size parameters r, $r^\star$ and $r^\diamond$ thanks to [HS1]. This allows the Q_{ijk} integrals to be pre-computed as soon as the section limits and the $({}^1\kappa_k)_k$ are given, i.e. once and for all at the beginning of a simulation, the advantages and limits of which are discussed in § 13.1.5.
As an application of the characteristic times suggested in § 3.5.2.6 we introduce sectional droplet growth times ${}^1\overline{\tau}_k^G$ for each section k. They reads, based on definition of Eq. (3.142):

$${}^1\overline{\tau}_k^G = \frac{4/3\rho_l \pi \bar{r}_k^3}{\sum_{i=1}^{k-1} m_i \pi (\bar{r}_k + \bar{r}_i)^2 \, |\boldsymbol{u}_k - \boldsymbol{u}_i|} \tag{4.55}$$

where $\bar{r}_i$ are average radii on section i.

4.4.5.9 Multi-Fluid evaporation terms

The Multi-Fluid model can be seen as a finite volume method in the 1D size variable phase space: evaporation, which corresponds to a transport operator, must be treated with a method that resorts to numerical schemes for finite volume transport.
In this context, the evaporation terms for the OSM MF method have been derived and are presented in detail in de Chaisemartin (2009).

4.4.5.10 High order in the sections

The high order methods presented in § 4.4.4.5 and in § 4.4.4.6 can be adapted straightforward to the Multi-Fluid method, provided that the moments become sectional:

$$M_k^{i,pqr} = \int_{S_{k-1}}^{S_k} \iiint_{\mathbb{R}^3} S^i c_1^p c_2^q c_3^r \widetilde{f}(s, \boldsymbol{c}) \mathrm{d}S \mathrm{d}\boldsymbol{c} \tag{4.56}$$

and that the reconstruction forms are limited to the section intervals.
At the Multi-Fluid level, size is reconstructed on the sections with any form $\kappa_k(S)$, e.g. a sectional entropy maximization $n_k^{\mathrm{ME}}(S)$ and the velocity is reconstructed

$$\widetilde{\boldsymbol{u}}(t, \boldsymbol{x}, S) \approx \sum_{i=1}^{N_{\mathrm{sec}}} \boldsymbol{u}_k(t, \boldsymbol{x}, S) \mathbb{1}_{[S_{k-1}, S_k[}(S) \tag{4.57}$$

with the velocity form inspired from Eq. (4.35):

$$\boldsymbol{u}_k(t, \boldsymbol{x}, S) = \boldsymbol{u}_g + \boldsymbol{A_k} S + \boldsymbol{B_k} S^2. \tag{4.58}$$

Again in this form the three velocity directions are decoupled so that we do not need consider cross-moments in the velocity components; we consider a vector notation and choose for instance the following moments in each section:

$$\begin{pmatrix} M_k^{0,000} \\ \dots \\ M_k^{p-1,000} \\ \boldsymbol{M}_k^{0,1} \\ \boldsymbol{M}_k^{1,1} \end{pmatrix} \tag{4.59}$$

with p the number of size moments that must comply with the number of parameters in the size form $\kappa_k(S)$ and two non-trivial velocity moments that comply with the choice of Eq. (4.58). The velocity moments in a section must ensure:

$$\begin{cases} \boldsymbol{M}_k^{0,1} = & \boldsymbol{u}_g M_k^{0,0} + \boldsymbol{A_k} M_k^{1,0} + \boldsymbol{B_k} M_k^{2,0} \\ \boldsymbol{M}_k^{1,1} = & \boldsymbol{u}_g M_k^{1,0} + \boldsymbol{A_k} M_k^{2,0} + \boldsymbol{B_k} M_k^{3,0} \end{cases} \tag{4.60}$$

which is an invertible system as there are only two (vector) unknowns $\boldsymbol{A_k}$ and $\boldsymbol{B_k}$.
We finally get the following conservation equations in the section without coalescence nor break-up:

$$\partial_t \begin{pmatrix} M_k^{0,0} \\ \dots \\ M_k^{p-1,0} \\ \boldsymbol{M}_k^{0,1} \\ \boldsymbol{M}_k^{1,1} \end{pmatrix} + \partial_{\boldsymbol{x}} \begin{pmatrix} M_k^{0,1} \\ \dots \\ M_k^{p-1,1} \\ \boldsymbol{M}_k^{0,2} \\ \boldsymbol{M}_k^{1,2} \end{pmatrix} = \begin{pmatrix} 0 \\ 0 \\ 0 \\ 0 \\ \boldsymbol{F}_k^0 \\ \boldsymbol{F}_k^1 \end{pmatrix} \tag{4.61}$$

where the unknown (un-transported) moments have to be reconstructed.

4.4.5.11 Conclusion on the Multi-Fluid model

The Multi-Fluid model is a sectional approach allowing a versatile treatment of the size variable: it can treat continuous (evaporation) and non-local (coalescence and break-up) size evolution. The transfers among sections are illustrated in Figure 4.11. The reconstruction of the size distribution allows to treat rigorously the size dependency of all the terms of a given problem since the kinetic equation is integrated over the sections, performing a partitioning of the whole size space. Properties, such as the conservation of a set of local (in space) moments, are then enforced independently on each section and the combination of the reconstructed NDFs converges towards the exact NDF. This allows the MF method to deal with phenomena such as coalescence -which modeling is highly needed in SRM simulations- contrary to the Multi-Class methods described in § 4.4.3. Moreover the continuous treatment of the size variable is done in a way that is consistent at the section level to the treatment of other phenomena (drag, heating), which makes a strong difference with the pivot methods described in § 4.4.4.2 used for PBEs, which conserve a few global properties. The MF model treats particle inertia independently in each section so it can capture, with respect to polydispersity, acoustics and unsteady hydrodynamics thanks to the fact that it is spatially resolved.
So the MF method achieves an accurate treatment of size distributions for a large size range including inertial particles/droplets in a CFD framework: it is more accurate and rigorous than other Eulerian methods as regards polydispersity when multiple phenomena including inertia occur. The method also provide a fairly detailed description of the size-conditioned velocities and temperatures compared to high order moment methods, which proves to be useful to capture the dynamics of a widespread distribution (in the sense of effective polydispersity).

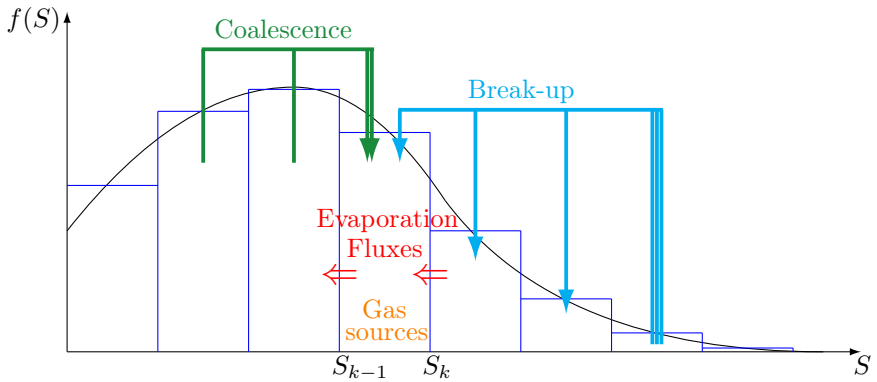

Figure 4.11: *Transfer of conserved quantities in size phase space with MF approach.*

As an accurate and flexible method, the Multi-Fluid strategy is used in several research and industrial codes:

- in MUSES3D, a research platform on Eulerian methods (see § 10.5.1);
- in CEDRE (an industrial-oriented code presented in § 14.1), with a Two Size Moment method;

and has inspired a polydisperse extension of an approach implemented in AVBP (Vié 2010). Some achievements of the multi-fluid model are presented in Figure 4.12, with MUSES3D.

4.4.6 Conclusion on polydispersity with Eulerian approaches

4.4.6.1 Accounting for the size distribution and hetero-PTC

The treatment of the size variable has received several developments: sampling, sectional and moment methods have interesting qualities and are used in many contexts. The choice of a particular method is then guided by the inertial regime of the disperse phase as discussed now.
The polydisperse approaches previously presented are based on the monokinetic closure. The monokinetic closure systematically yields a PGD-like behavior which accounts efficiently for the dynamics of so-called

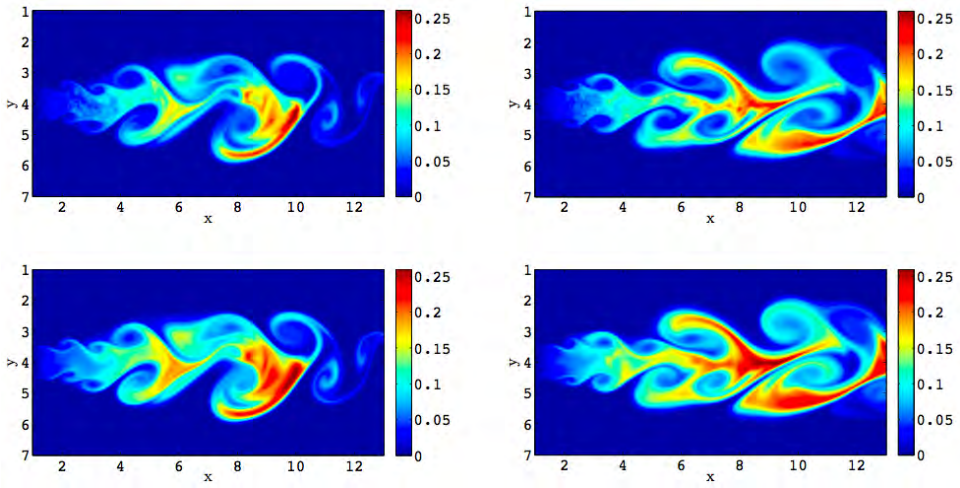

Figure 4.12: *Comparison of the gas-phase fuel mass fraction at times* $t = 15$ *(left) and* $t = 20$ *(right) – Top: stochastic-Lagrangian method with* $30,000$ *droplets. Bottom: Eulerian Multi-Fluid model on* $400 \times 200 \times 10$ *mesh with MUSES3D (de Chaisemartin 2009).*

small particles. These particles can encounter hetero-PTC, which is perfectly accounted for by the semi-kinetic model (though it is too costly) and correctly accounted for by sampling and sectional methods, depending on their level of refinement.
High order size moment methods have *a priori* a unique velocity for the whole size spectrum so they cannot account for hetero-PTC: they are chosen for negligible-inertia regimes such as for soots. High order size-conditioned-velocity methods such as the CSVM have then been proposed to cope with this caveat.

4.4.6.2 Limits of the monokinetic closure for homo-PTC

The monokinetic assumption, performed at the semi-kinetic level, totally impedes to account for homo-PTC, as extensively discussed above. So all the previous approaches are unable to deal with medium or large particles. They yield spurious δ-shocks instead of the expected crossings, similarly to the monodisperse monokinetic approach presented in § 4.3.
We now present polykinetic approaches in the following section, which are designed to cope with the issue of homo-PTC. These models are first written for a given size.

4.5 Eulerian polykinetic approaches conditioned on size

We now focus on polykinetic approaches to treat homo-PTC. So that the issue of polydispersity is *a priori* decoupled. We keep in mind that the polykinetic approaches below can be superimposed to polydisperse approaches.

4.5.1 Eulerian polykinetic approach with QMOM

The quadrature moment methods presented for the size variable in § 4.4.4.1 can also be used to evaluate the velocity variable. The peculiarity in this case is the same as for the complete equation set, that is the fact that the underlying kinetic function is multivariate and that some cross-moments must be accounted for to render the correlations among the variables (Yoon and Mc Graw 2004). The problem of multivariate cases and the adapted choice of moments is detailed in Fox (2009) (see also Fox (2006); Fox and Vedula (2009)).

4.5.1.1 The univariate QMOM for the velocity variable

Because the QMOM method presented in § 4.4.4.1 is valid for a univariate distribution, it can be applied to $f(t, \boldsymbol{x}, \boldsymbol{c})$ with one internal coordinate, i.e. for a one-dimensional case. We also consider an isothermal monodisperse spray so we disregard size and temperature. We follow a set $(M_k)_k$ of $2N_p$ velocity moments, defined as $M_k(t, \boldsymbol{x}) = \int_{\mathbb{R}} \boldsymbol{c}^k f(t, \boldsymbol{x}, \boldsymbol{c}) \mathrm{d}\boldsymbol{c}$ with k belonging to the moment index set $\mathcal{N}$. Again, the set $\mathcal{N} = [0, 1, ..., 2N_p - 1]$ is preferred to ensure polynomial reconstructions. The evolution of the k^{th} order velocity moment is given by:

$$\partial_t M_k + \partial_{\boldsymbol{x}} M_{k+1} = \int_{\boldsymbol{c}} \boldsymbol{c}^k Q(\boldsymbol{c}) f(t, \boldsymbol{x}, \boldsymbol{c}) \mathrm{d}\boldsymbol{c}. \tag{4.62}$$

with $Q(\boldsymbol{c})$ any kinetic source term. The distribution function is taken with the following shape:

$$f(t,\boldsymbol{x},\boldsymbol{c}) = \sum_{i=1}^{N_p} \omega_i(t,\boldsymbol{x})\delta(\boldsymbol{c}-\boldsymbol{u}_i(t,\boldsymbol{x})). \tag{4.63}$$

where the weights and abscissae are linked to the low order moments:

$$\int_{\boldsymbol{c}} f(t,\boldsymbol{x},\boldsymbol{c})\mathrm{d}\boldsymbol{c} = \sum_{i=1}^{N_p} \omega_i \boldsymbol{u}_i^k \tag{4.64}$$

through a system that can again be inverted with the product difference (PD) algorithm (McGraw 1997) or with Wheeler (1974)'s method. The source terms in the transport equation are closed with the quadrature formula:

$$\int_{\boldsymbol{c}} Q(\boldsymbol{c})f(t,\boldsymbol{x},\boldsymbol{c})\mathrm{d}\boldsymbol{c} = \sum_{i=1}^{N_p} \omega_i(t,\boldsymbol{x})Q(\boldsymbol{u}_i(t,\boldsymbol{x})) \tag{4.65}$$

and also the non-conserved M_{2N_p+1} moment which appears from the streaming operator is closed with the relation

$$M_\alpha = \sum_{i}^{N_p} \omega_i \boldsymbol{u}_i^\alpha, \qquad \alpha \in \mathbb{R}. \tag{4.66}$$

The great advantage of this method is its ability to describe particle trajectory crossings (PTC). Indeed when particles are crossing, there are two different velocities at the same point, which can be accounted for as soon as there are two peaks in the reconstruction i.e. $N_p = 2$. Whereas presumed velocity PDF presented in the previous paragraph, as they describe an equilibrium distribution around a mean velocity, cannot describe this out of equilibrium case.

4.5.1.2 Multivariate QMOM

The limitation of the original QMOM method to univariate distributions is penalizing when it comes to the use of velocity QMOM for the description of polykineticity because the problems of interest are 3D. The multivariate extension of QMOM is desirable to treat distribution functions with several internal coordinates. From the ideas of Fox (2008), the method has been used with two-peaks per physical space dimension and referred to as Eulerian Multi-Velocity Model (EMVM) by Kah et al. (2010) (see also Massot et al. 2009; Kah 2010), which results are presented in Figure 4.13.

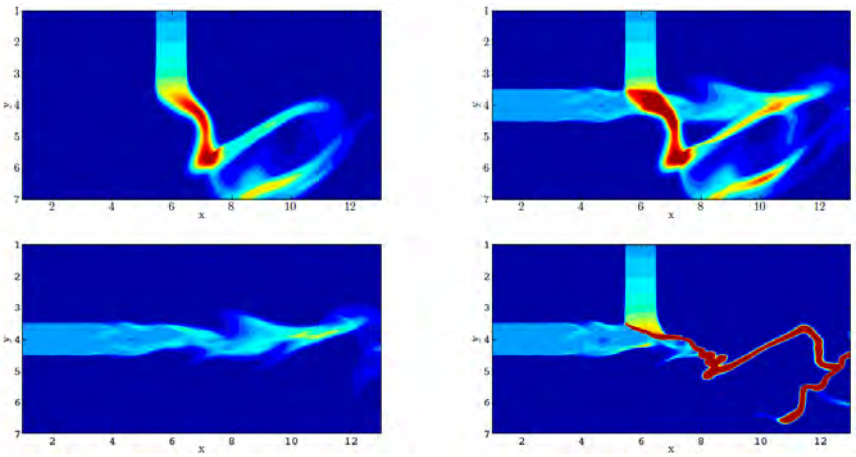

Figure 4.13: *Total number density of two particle jets with MUSES3D – Top left: Vertical jet with EMVM; Bottom left: Horizontal jet with EMVM; Top right: Two crossing jets with EMVM; Bottom right: Two crossing jets with a monokinetic closure(Kah 2010).*

A third order QMOM method, using $2n_d$ quadrature nodes, n_d being the dimension of the physical space, can deal with configurations where PTC occur (Fox 2008). Nevertheless, this method encounters reconstruction problems and must be regularized (Kah et al. 2010). In addition, it cannot be applied to spray simulation, where nonetheless $n_d > 1$ but also distribution functions have more internal coordinates such as size and temperature.

$St \lll 1$	$St \ll 1$	$St < St_c$	$St > St_c$
EG	EEM	Monokinetic	KBMM
		MF	ACBMM

Table 4.1: *Models for the treatment of polykineticity at different levels.*

4.5.1.3 Eulerian polykinetic approach with CQMOM

The difficulty to close multivariate quadrature approaches has led Yuan and Fox (2011) to define a Conditional Quadrature Method of Moments (CQMOM), which has first been applied to the description of the three dimensional velocities of a polykinetic spray. The closure of the NDF is based on Dirac δ-functions so that it has the same form as in QMOM approaches. The inversion procedure from a set of moments is however different.
In practical computations, numerical diffusion brings many different velocities to coexist so that CQMOM tends to form δ-shocks, whatever the number of peaks that are chosen (Chalons et al. 2012). A typical CQMOM approach with two-peaks in each direction requires to control 12 moments in 2D. This method is promising for moderate-to-high inertia sprays.

4.5.2 Eulerian polykinetic approach with Multi-Gaussian

In order to cope with the singularities that occur with Dirac δ-function reconstructions, it has been suggested to use functions with a continuous support. A simple function as regards its moments is the Gaussian function and it achieves a minimum entropy reconstruction. But inertial sprays have been described by many authors as far from a Gaussian equilibrium so the multi-peak aspect is a desired feature. So a bi-Gaussian reconstruction has been first used by Chalons et al. (2010) to describe inertial sprays in 1D.
The difficulty that arises in multi-dimensional contexts to reconstruct a suitable bi-Gaussian function in each direction has led Vié et al. (2011) to use a directionally-conditioned algorithm inspired from the CQMOM to achieve the Multi-Gaussian method.
The Multi-Gaussian method is up to now one of the velocity moment methods that controls the more velocity moments (up to 16 in 2D) therefore achieving potentially the most detailed and accurate approach for polykineticity.

4.5.3 Conclusion on Eulerian polykinetic approaches

Many polykinetic closures have been developed in the recent years to account for homo-PTC. Their ability to treat small scale or large scale crossings i.e. medium or large droplets is under discussion as well as the development of efficient numerical methods. All of these methods are currently under study and have not been implemented in industrial codes yet: the maturity of Eulerian polykinetic approaches is not satisfactory to do this.
A classification of the methods has been suggested in (Vié et al. 2012) as regards their ability to treat inertial particles, as quantified by an average Stokes number:

- a family of methods based on the choice of an underlying kinetic distribution shape are referred to as Kinetic Based Moment Methods (KBMM) and include QMOM and Multi-Gaussian presented above,
- while other authors explore the possibility of closing the unknown velocity moments at the macroscopic level, leading to a family referred to as Algebraic Closure Based Moment Methods (ACBMM).

This classification is recalled in Table 4.1 and enriched with equilibrium approaches (see § 3.2.3) that are the Equivalent Gas (EG) and a linearized-lag model, the Eulerian Equilibrium Model (EEM).

4.6 Hybrid Eulerian approaches for a polykinetic polydisperse phase

The Eulerian methods presented above can be combined to increase the level of detail of the model. The objective is to account simultaneously for polydispersity, hetero-PTC and homo-PTC.

4.6.1 Fully polykinetic polydisperse approach: the multivariate QMOM

We present a method that treats all the directions of the phase space at once. The multivariate QMOM approach (see § 4.5.1 has been suggested to fulfill the task of accounting for both polydispersity and polykineticity in a fully coupled way but the quadrature is difficult to perform with so many dimensions. In this case the approximation of the NDF is extended from QMOM to a multivariate distribution (Marchisio and

Fox 2005):

$$f(t,\boldsymbol{x},S,\boldsymbol{c},T)=\sum_{i=1}^{N}\omega_i\delta(S-S_i)\delta(\boldsymbol{c}-\boldsymbol{u}_i)\delta(T-T_i) \tag{4.67}$$

where N is the number of Dirac δ-functions and ω_i is the weight of the node i. Achieving this multivariate quadrature is yet troublesome. The DQMOM approach has been furthered in the multivariate context. The weights ω_i and abscissae $(S_i,\boldsymbol{u}_i,T_i)$ then are Eulerian fields governed by the following conservation equations:

$$\begin{aligned}&\partial_t\omega_i+\partial_{\boldsymbol{x}}\cdot(\omega_i\boldsymbol{u}_i)=a_i\\&\partial_t(\omega_iS_i)+\partial_{\boldsymbol{x}}\cdot(\omega_iS_i\boldsymbol{u}_i)=b_i\\&\partial_t(\omega_iS_i\boldsymbol{u}_i)+\partial_{\boldsymbol{x}}\cdot(\omega_iS_i\boldsymbol{u}_i\otimes\boldsymbol{u}_i)=c_i\end{aligned} \tag{4.68}$$

where the source terms (a_i,b_i,c_i) are obtained from the source terms of the Williams equation Eq. (3.123). It results in a $5n\times5N$ linear system giving these source terms. The moments of the distribution are then given by (Fox et al. 2008):

$$M_{k\mathbf{l}m}=\int_S\int_{\boldsymbol{c}}\int_T S^k\boldsymbol{u}^{\mathbf{l}}T^m f(t,\boldsymbol{x},S,\boldsymbol{c},T)\mathrm{d}S\mathrm{d}\boldsymbol{c}\mathrm{d}T=\sum_{n=1}^{N}\omega_nS_n^k\boldsymbol{c}_n^{\mathbf{l}}T_n^m \tag{4.69}$$

where $M_{k\mathbf{l}m}$ is the moment of order k in size, $\sum(l_i)$ in velocity and m in temperature.
The multivariate QMOM approach raises stability, accuracy and cost issues. If accepting to lose the size-velocity correlations, any size moment method can be combined straightforward to a polykinetic closure. For instance, the combination of the EMSM size method (with 4 size moments) with a QMOM method (the EMVM with 4 velocity moments) is performed and discussed by Kah (2010).

4.6.2 Size-discretized hybrid approaches

Instead of treating the directions at once, a discretization can be performed on the size variable: it can either resort to sampling or sectional techniques.
The accessible subspaces of the size-velocity phase space are presented for typical methods as an illustration in Figure 4.14.

4.6.2.1 Extensions for polydispersity

The fundamental methods for polydispersity, presented in § 4.4 are (i) size moment methods which explore the whole size variable at a given velocity (therefore unable to account for hetero-PTC); (ii) sampling methods; and (iii) sectional methods which are piece-wise continuous in size, at different velocities. The first possible hybridization consists in using a high order size moment method on the continuous support of the sectional discretization: this approach is promising as:

- it increases the size accuracy of the sectional method, allowing to reduce the number of sections;
- it allows moment methods to treat hetero-PTC.

In Chapter 5, we develop a sectional method with two size moments per section to achieve such benefits.

4.6.2.2 Extensions for polydisperse polykineticity

The fundamental methods for polykineticity, presented in § 4.5, are (iv) velocity moment methods; (v) sampled velocity moment methods; and (vi) sectional methods with high order velocity methods. The latter approaches are very attractive since they deal with both hetero-PTC and homo-PTC; many combinations are possible and Kah (2010) has suggested to use a Multi-Fluid method with an EMVM velocity treatment in each section: This development has been implemented in the MUSES3D code (see § 10.5.1). In Chapter 6, we introduce a new velocity moment method named Anisotropic Gaussian (AG) and we use it in the context of a two-size moment Multi-Fluid method.

4.6.2.3 Extensions for size-velocity correlations

Finally, we consider methods that can account for size-velocity correlations.
A first idea is to extend the QMOM approach but with conditional quadratures according to the ideas of Yuan and Fox (2011): this case corresponds to sweeping the $\boldsymbol{u}_p$–S space as in (vii).
To increase accuracy on velocity conditioned by size in a continuous way, the CSVM method can be considered, which has been detailed in § 4.4.4.6 and is illustrated in (vii). It is designed for hetero-PTC (and

cannot treat homo-PTC). Its accuracy on size can be increased, not by sampling since a continuous size variable is required, but by a sectional discretization as shown in (ix). Since the CSVM has the algebra of a 4 size moment method, we introduce in Chapter 5 a two size moment Multi-Fluid method with velocity correlations to achieve a second order size-velocity method. The new method inspired from CSVM is designed to be accurate on hetero-PTC, and it is developed in the context of coalescence.

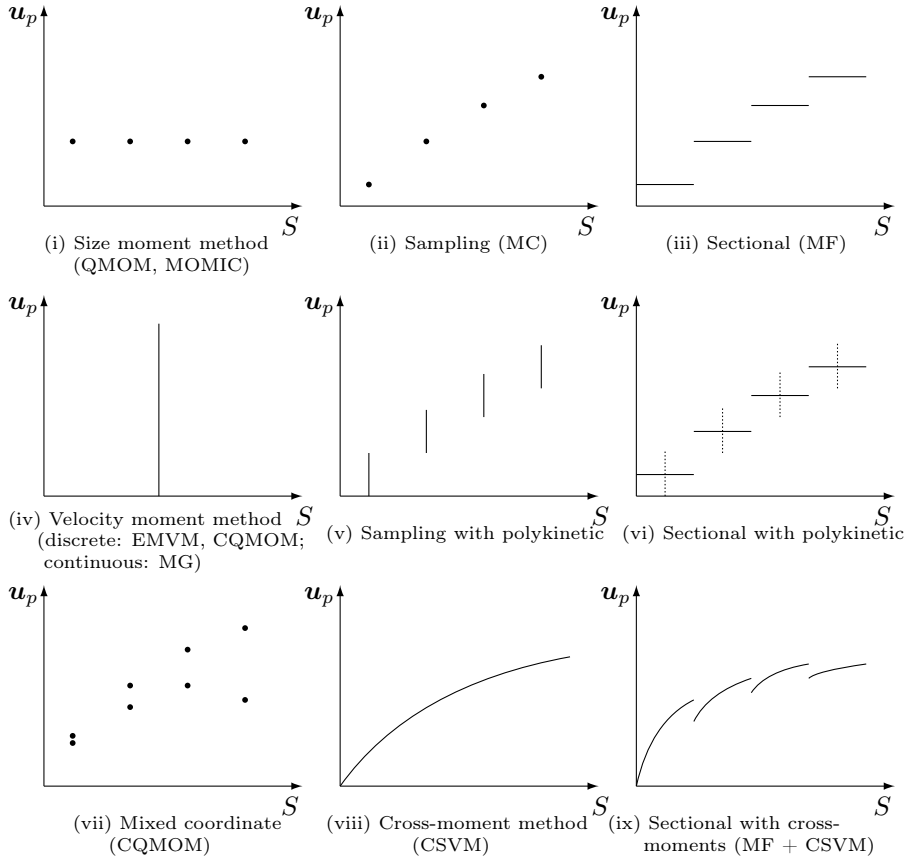

Figure 4.14: *Accessible $\boldsymbol{u}_p$–S subspace to various Eulerian methods.*

4.6.2.4 Flexibility of the discretized methods

As a conclusion on hybrid methods, we emphasize that the choice of discretized methods introduces a convenient flexibility on the modeling.
We focus on sectional approaches, which are more complete than sampling ones. The hybridization provides many types of modeling, either more accurate on size, velocity (homo-PTC), or size-velocity correlations (hetero-PTC) than the classical Multi-Fluid model. But the approaches (and related assumptions) performed in each section are independent from that of the other sections so that the hybridization can be performed in a new prospect: the model and related level of detail can be chosen different in each section. An additional modeling effort is then required to treat exchange source terms between differently modeled particles.
The use of different models with size is relevant in the context described in § 3.1.3.1, where inertia grows with size and where homo-PTC occurs non-significantly for small particles, at small scale for medium particles and at large scale for large particles. The general idea of using different models for different particle sizes has been contemplated for a long time: Ferry and Balachandar (2001) suggested to use a linearized lag model, a monokinetic closure, and a stochastic-Lagrangian method for small to large particles; but as we tend to show here, the wide spectrum of particle sizes and their physics can all be treated with Eulerian approaches. The swapping between different Eulerian descriptions of polykineticity has been attempted by Boileau et al. (2010) (see also Boileau et al. (2010)).

4.7 Fluid-fluid approaches for strong coupling

We now study some peculiarities of such fluid-fluid models. A Eulerian monokinetic approach is chosen and the effects of polydispersity are examined in the context of the Multi-Fluid method, yielding a set of fluid equations for the sections, strongly coupled to the fluid equations for the carrier gas.

4.7.1 A choice governed by two-way coupling

4.7.1.1 Practical issue of two-way coupling

When disregarding the detailed structure of the above descriptions, it remains that there are Euler-Lagrange and Euler-Euler approaches to reduce the fluid-kinetic model presented and chosen in Chapter 3.
Following many authors, it has been stated that the stochastic-Lagrangian approach is highly flexible but raises convergence issues when coalescence occurs and when two-way coupling must be practically rendered. These issues are not prohibitive as recent computations of 3D coalescing SRM cases testify (Estivalezes 2011).
But we assume that the Euler-Lagrange method is not as promising as the Euler-Euler method for full-scale high-fidelity simulations. The latter method requires the user to make the relevant assumptions preliminarily and explicitly by choosing the closures, correlations and methods, which is tedious but guarantees in return convergence, and fully mastered limitations. Moreover achieving practically two-way coupling has been described as more natural in a HPC context for Euler-Euler methods: parallelization can be achieved straightforward as the two-phases are described with the same types of equations.
The peculiarities of two-way coupling has led many applicative cases of moderately dense two-phase flows to be approached by Euler-Euler simulations (Dupays et al. 2001; Le Touze et al. 2012). This choice is followed in the present work.

4.7.1.2 Retained approaches

In the following, we mainly focus on the Multi-Fluid method, which has proven to be efficient in industrial codes; the sectional discretization has also been presented as very flexible so extensions of the method are considered. Methods are developed in most of the present work in the context of low-inertia disperse phases. We keep in mind that some discrepancies may appear in high strain zones, namely in the nozzle of the SRM. To cope with the particular case of moderately inertial disperse phases, we also work on a polykinetic method. The general QMOM approach has been presented as weakly hyperbolic, which threatens robustness. So we develop a new method, which we want to capture some physical features of homo-PTC at a reasonable cost: the Anisotropic Gaussian closure is introduced in Chapter 6, and gives promising results on crossing jets (Chapter 11) and coalescing crossing jets (Chapter 12).
In the context of moderately dense two-phase flows, the Eulerian reduction of kinetic-fluid approach leads to a two-way coupled fluid-fluid approach which is now discussed.

4.7.2 A model fluid-fluid system

4.7.2.1 Choice of a reference fluid model

We focus on a Eulerian model with two-way coupling where polydispersity has been treated with a sectional approach, with N_{sec} sections. Whatever the number of size moments in each section, they are treated as passive scalars as regards transport. So we can focus on a method with one size moment per section. As for the velocity moments, we have discussed in § 4.3.2 the fact that the monokinetic closure features all the peculiarities of disperse phase flows, namely hypercompressibility.
So the reference Eulerian model as regards a polydisperse two-way coupled disperse phase with low-inertia droplets ($\text{St} < \text{St}_c$) is the OSM Multi-Fluid model, as fully validated by de Chaisemartin (2009) on academic configurations, stochastic Lagrangian reference cases and experiments.

4.7.2.2 Polydisperse Euler-PGD approach

When adding the gas System (3.125) to the N_{sec} sectional systems of equations (4.42), we obtain the following OSM MF system, coupled through drag and heating source terms and valid for moderately dense sprays:

$$\left\{\begin{array}{l}
\partial_t \rho_g + \partial_{\boldsymbol{x}}\cdot(\rho_g \boldsymbol{u}_g) = 0 \\
\partial_t(\rho_g \boldsymbol{u}_g) + \partial_{\boldsymbol{x}}\cdot(\rho_g \boldsymbol{u}_g \otimes \boldsymbol{u}_g) = -\partial_{\boldsymbol{x}} p - \displaystyle\sum_{k=1}^{N_{\text{sec}}} m_k \boldsymbol{F}_k \\
\partial_t(\rho_g e_g) + \partial_{\boldsymbol{x}}\cdot(\rho_g e_g \boldsymbol{u}_g) = -p\partial_{\boldsymbol{x}}\cdot\boldsymbol{u}_g - \displaystyle\sum_{k=1}^{N_{\text{sec}}} m_k \text{H}_k + \sum_{k=1}^{N_{\text{sec}}} m_k \boldsymbol{F}_k(\boldsymbol{u}_g - \boldsymbol{u}_k) \\
\left.\begin{array}{l}
\partial_t m_k + \partial_{\boldsymbol{x}}\cdot(m_k \boldsymbol{u}_k) = 0 \\
\partial_t(m_k \boldsymbol{u}_k) + \partial_{\boldsymbol{x}}\cdot(m_k \boldsymbol{u}_k \otimes \boldsymbol{u}_k) = m_k \boldsymbol{F}_k \\
\partial_t(m_k h_k) + \partial_{\boldsymbol{x}}\cdot(m_k h_k \boldsymbol{u}_k) = m_k \text{H}_k
\end{array}\right\} \quad k \in [\![1, N_{\text{sec}}]\!]
\end{array}\right. \tag{4.70}$$

where the disperse phase sources, namely evaporation, coalescence and break-up have been ommited for the sake of clarity. To assess two-way coupling features, the Euler equations for the gas carrier phase

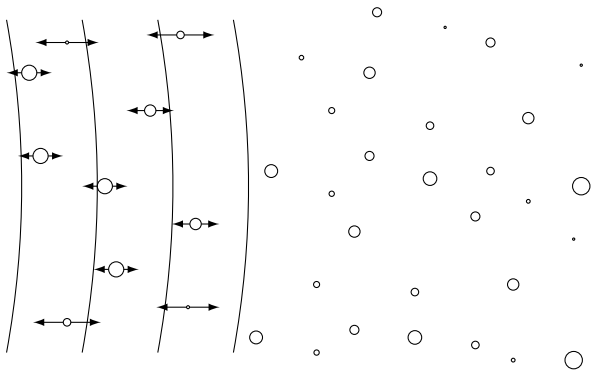

Figure 4.15: *Particle motion in a large wavelength – Illustration of two-phase acoustics hypotheses.*

are considered, for the sake of legibility. The resulting system is indeed similar to the one written with Navier-Stokes and described in § 3.5.1.5 as regards two-way coupling. The vanishing diffusion terms can be obtained in the limit of a high Reynolds number, which remains compliant with a viscous drag force around the particles i.e. any reasonable Re_p. Anyway the generalization to Navier-Stokes, namely NS-PGD, is straightforward.
System (4.70) has been written to ensure the conservation of total momentum and total energy. Yet, drag and heat transfer between the droplets and the gas yields local dissipation regarding velocity and temperature differences.
We study the peculiarities of two-way coupling in compressible regimes, among which two-phase acoustics is carefully described.
We also prove the existence of an equilibrium state, which can be studied with an entropy equation. This fact needs to be quantitatively rendered, so that the two-phase model and method must be chosen carefully, as discussed in § 4.7.5.

4.7.3 Two-phase acoustics and compressible regimes

4.7.3.1 Definition of two-phase acoustics

Acoustic waves are elastic waves propagating longitudinally thanks to compressibility of the continuous, carrier phase. When the carrier phase features a disperse phase (homogeneous at rest or not), e.g. a fog, the wave may propagate in a very similar way as in a single phase fluid: this requires in fact large wavelengths compared to the inclusions. We refer to these conditions as two-phase acoustics conditions.
In two-phase acoustics, there are no perceptible effects of the interface shape: the inclusions do not generate reflection at their surface and do not encounter refraction within the condensed medium.
Considering the independency to interface shape together with the negligible effect of volume occupation, the so-called two-phase acoustics is consistent with the vision of two-way coupling through exchange source terms only, as described in § 3.5.1.5. The condense phase locally reacts to the passing wave by moving and shifting its temperature as a whole, yielding momentum and heat transfers through drag and heating. The ensemble motion of inclusions under the passage of a perturbation of larger wavelength is sketched in Figure 4.15.
Finally, our definition of two-phase acoustics is limited to linear regimes: the motion (or heating of particles) is of small enough amplitude to generate negligible perturbations in the compressible medium.

4.7.3.2 Polydisperse acoustics

The more general case of polydisperse acoustics refers to two-phase acoustics in polydisperse inclusions. The impact of polydispersity on acoustics-spray interaction is presumably complex but few studies are available while many authors suggest equivalent diameter approaches such as in Peirano and Leckner (2000).
These approaches are not suitable when the physical phenomena involve very different levels and time scales of interaction between the phases depending on the size of the droplet/particles, see § 3.1.2.2.

4.7.3.3 Peculiarities of two-phase acoustics and other two-way compressible features

The manifestation of two-way coupling in compressible regimes may be categorized as follows:
(i) dissipation and dispersion of acoustic waves in two-phase media,
(ii) acoustic disturbance yielded by condensed phase transport and heating,
(iii) interactions of the gaseous flow structures with the dynamics of particles.

Feature (i) matches the perimeter of two-phase acoustics as local dissipation and dispersion allow to characterize exactly the linear behavior of an acoustic wave in a disperse two-phase medium with inclusions smaller than the wave length. Feature (i) must be captured, e.g. to assess instability damping, see § 1.3.2.6.
Feature (ii) is significant in non-linear regimes. The latter has a wider definition than for single-phase acoustics: it includes the usual case when velocity perturbations are close to the speed of sound, (or p' close to p_0), but also cases when particle slip velocities are close to the speed of sound (and $T_k - T_g$ close to T_g). These situations are encountered in compressible flows and when particles are inertial enough. Feature (ii) must be captured to assess accurately noise ambience, e.g. for instability triggering.
Feature (iii) refers to complex cases where flow structures e.g. vortices become coupled to particle structures e.g. preferential concentration. In these cases, the two-phase acoustic behavior is expected to couple to the flow. These features are complex and are desirable to capture in order to predict instabilities.

4.7.4 Dissipation in fluid-fluid approaches

4.7.4.1 Entropy equation

We consider the gas specific entropy s_g and the section specific entropies s_k to define a mixture entropy $\rho s = \rho_g s_g + \sum_{k=1} m_k s_k$ and its flux $F_s = \rho_g s_g \boldsymbol{u}_g + \sum_{k=1} m_k s_k \boldsymbol{u}_k$ and we derive from Gibbs' relations for each phase the following entropy budget for System (4.70) for regular solutions:

$$\partial_t \rho s + \partial_{\boldsymbol{x}} F_s = \sum_{k=1} \frac{m_k}{T_g \overline{\tau}^u_k} (\boldsymbol{u}_g - \boldsymbol{u}_k)^2 + \sum_{k=1} \frac{m_k \overline{c}_{p,k}}{\overline{\tau}^T_k} \frac{(T_g - T_k)^2}{T_g T_k}. \tag{4.71}$$

The entropy equation (4.71) has two-phase source terms corresponding to the irreversibility of heat transfer and viscous effects close to the droplets. These transfers at the microscopic level have a significant effect on the two-phase dynamics (and have here been modeled through drag and heating) even when the transfers at the bulk level of the gas have not (and may not be modeled such as with Euler equations).

4.7.4.2 Existence of a local equilibrium

The entropy source terms are positive which proves that the coupled system locally converges towards dynamic and thermal equilibrium. The local equilibrium state cancels the entropy source terms and is naturally found to be the state where the velocities of all phases are equal to $\boldsymbol{u}_{eq}$ and the temperatures are equal to T_{eq}, which read:

$$\begin{aligned} \rho_{eq} \boldsymbol{u}_{eq} &= \rho_g \boldsymbol{u}_g + \sum_k m_k \boldsymbol{u}_k \\ \rho_{eq} c_{v,eq} T_{eq} &= \rho_g c_{v,g} T_g + \sum_k m_k \overline{c}_{p,k} T_k \end{aligned} \tag{4.72}$$

where $\rho_{eq} = \rho_g + \sum_k m_k$ and $\rho_{eq} c_{v,eq} = \rho_g c_{v,g} + \sum_k m_k \overline{c}_{p,k}$. The convergence of the variables of System (4.70) towards this local equilibrium state is exact in 0D. But it is also a good approximation if not far from equilibrium when considering convection. This trend to reduce the velocity and thermal differences is responsible for the attenuation of acoustic waves which is the main specificity of two-phase acoustics, along with dispersion due to velocity and temperature lag. Numerical methods which pretend solving two-phase acoustics should therefore capture this convergence efficiently. Typical numerical approaches are analyzed regarding this problematic in the following.
In polydisperse sprays, the equilibrium state depends on the gas variables and all the disperse phase ones, which confirms that the resulting coupling is total among all phases, as explained in § 10.3.2.4.

4.7.5 Failure of equilibrium models to capture dissipativity

We discuss the necessity to solve the gas and particle velocities and temperatures to properly capture dissipation. The limits of some equilibrium approaches (described in § 3.2.4), namely the Equivalent Gas (EG), the Eulerian Equilibrium Model (EEM), and the Partial Equivalent Gas (PEG) are developed.

4.7.5.1 Comments on equilibrium models

A full equilibrium model, i.e. assuming a homogeneous density of particles constantly at dynamic and thermal equilibrium with the gas, is a classical first approach for two-phase flows and is referred to as Equivalent Gas (EG), see § 3.2.4.2.
Because velocities and temperatures are assumed at equilibrium at all times, dissipation is not considered. In other terms, the entropy source terms of Eq. (4.71) depend on velocity and temperature differences, which

are no longer resolved in the EG equations. In the particular case of acoustic waves -which is fully studied in the following section- no attenuation occurs and the speed of sound is constantly equal to c_{eq} that is the speed of sound in a mixture of density ρ_{eq} and heat capacity $c_{v,\text{eq}}$. Since these facts are true only for very small droplets, EG fails to capture crucial two-phase acoustics features such as dissipation for most droplet sizes.

4.7.5.2 Case of linearized lag models

Since velocity and temperature differences are crucial variables for dissipation, linearized lag models have been derived (see § 3.2.3.3) to assess simply for them. For moderately dense sprays, this type of modeling is said to be extendable to two-way coupling (Ferry and Balachandar 2001) which could allow to directly compute dissipation. The velocities and temperatures are then formally assessed with an equivalent mixture density and specific heat: the approach is similar to EG and the velocity and temperature differences still suffer a truncation error so that the practical results depart with Stokes numbers even when below one, which is not satisfactory in a part of the chamber and in the nozzle.
Other expansions were performed by directly considering two-way coupling (Druzhinin 1994; Druzhinin 1995) but with a partial knowledge of the flow so they are available for simple configurations only. Anyway, the extension to polydispersity or particle-particle collisions was never performed. So that near-equilibrium approaches are potentially not suited for capturing dissipation in industrial configurations.
Besides, the extension of linearized lag models to polydispersity or particle-particle collisions and coalescence was never performed so that the approach is of limited interest for high-fidelity SRM cases.

4.7.5.3 Partial Equivalent Gas model for polydisperse sprays

Up to now, the two-way coupling is properly rendered only when both particle and gas variables are solved such as in the dusty gas modeling (Marble 1970), valid for monodisperse cases. The Multi-Fluid models have this feature and they are valid for polydisperse cases as well as for collision-coalescence.
An idea to avoid stiffness of small droplets is to combine full resolution strategies, such as MF, to EG in order to force the small droplets at equilibrium. Such techniques are referred to as Partially Equivalent Gas (PEG). This technique has been used in several SRM computations to deal with the small combustion residuals without encountering numerical issues, as well with Eulerian (Dupays et al. 2008) than with stochastic-Lagrangian (Sabnis 2003) approaches of the disperse phase.
An approach referred to as PEG-MF is considered in § 15.3 where a part of the disperse phase mass at injection, corresponding to the droplets with $\text{St} \ll 1$ everywhere, is transferred to the gas according to the EG technique and the rest is considered with its polydispersity with a MF technique. The same limitations exist as for EG i.e. the "unresolved" disperse phase must effectively be close to equilibrium at all time for the method to remain accurate. This technique is classically used in SRM simulations to get rid of the small droplet stiffness. We then highlight that small particle evaporation, chemical reaction, coalescence or radiation are difficult to account for in PEG-MF since the particles are perfectly mixed and indistinguishable from the gas: the knowledge of the size distribution, as influenced by these phenomena, is poorly rendered. A solution is then to treat size bins as species in the mixture.

4.7.6 MF methods for polydisperse acoustics

Polydisperse acoustics, as described in § 4.7.3.1 is proven in § 12.3.2.1 to be a feature that is difficult to capture by numerical approaches and a preliminary step to capture two-way compressible effects. It also yields useful test cases for the benchmarking of moderately dense two-phase approaches. The modeling in the context of monokinetic assumptions is discussed and numerical solutions are compared to an analytical approach.
We discus the ability of Eulerian models based on monokinetic hypotheses to capture polydisperse acoustics.

4.7.6.1 Case of a continuous size variable

First of all, we state that polydisperse acoustics is completely and exactly captured by the semi-kinetic model.
Back to the definition of two-phase acoustics, the inclusions encounter velocity and temperature variations that are due to the passage of a wave which has a large wavelength compared to themselves. So that, at a given location, inclusions that have the same initial temperatures and velocities will evolve due to the same sources. They evolve with a dynamics that is conditioned by size. So that inclusions of a given size and at a given point remain at the same velocity and temperature.
The size-conditioned description of velocities and temperatures made by the semi-kinetic model is therefore well-suited for polydisperse acoustics.

In convective cases, the uniqueness of velocities and temperatures remains as long as homo-DTC do not occur, which is a limit of the semi-kinetic model anyway.

4.7.6.2 Effect of size discretization

At the Multi-Fluid level, the particle size distribution is discretized and a unique velocity is assumed on each size interval. So the acoustic response of a polydisperse spray, as defined in § 4.7.3.3 is only approached, since droplets with a slightly different dynamics are treated as having the same velocities and temperatures. Convergence is gained if the section width in terms of Stokes number is not too large which is the reciprocal property of the "effective polydispersity" criterion given in § 3.1.2.2 Whatever the number of size moments in the section, all sectional methods that rely on a unique velocity moment to capture droplet dynamics in the section should converge at the same rate as regards velocity: they are of same (first) order regarding polydisperse acoustics problems. Yet high order size moment methods provide a better estimation of the average relaxation times: their values can be initialized exactly while their evolution is estimated at second order in size discretization. On the contrary for the OSM method, the relaxation times are fixed once for all as soon as the section bounds are chosen. So high order size moment are more accurate on polydisperse acoustics. They are therefore better for coarsely discretized cases i.e. low numbers of sections.
As a remark, a two-size moment method is the cheapest method -in the sense of minimum in terms of number of moments- to provide the accurate, bound-independent, resolution of characteristic times and other size dependent integrals. Higher order methods, e.g. EMSM feature a better estimation of the size distribution but at a higher cost (for a given number of sections) due to the number of moments and the related algebra.
To complete these remarks on two-phase acoustics with discretized methods, a sectional convergence study is provided in § 7.1.3.3 on an analytical approach of quasi-uniform non-rotational acoustics.

4.7.7 Conclusion on fluid-fluid approaches for SRMs

As a conclusion, we have chosen a basis model to treat nano-to-inertial moderately dense disperse phase flows in a HPC context.
An Euler-Euler method is chosen to reduce the fluid-kinetic approach as it allows a convenient treatment of two-way coupling in HPC: a feature of two-way coupling has been identified as crucial, namely dissipation, so the numerical resolution strategy must be designed to capture it.
The method is based on a Multi-Fluid model, since it can account efficiently for the size-conditioned physics of the wide spectrum of droplets: a reasonable level of accuracy is provided on size-conditioned velocities and temperature, which allows to render hetero-PTC, coalescence and break-up. This method is moreover flexible as regards the implementation of advanced closures for the physical phenomena, and different closures can be used in the sections, allowing to treat efficiently size-conditioned physics. We introduce in the following two improvements for the method.
The Multi-Fluid method as presented above requires however the use of a large number of sections to be accurate: we introduce in Chapter 5 a higher order method in size to reduce the cost. The accuracy/complexity trade off is discussed.
The case of moderately-inertial particles is not well treated by the usual monokinetic closure: we introduce in Chapter 6 a new polykinetic closure that provides a description of homo-PTC with just enough detail as regards the level of inertia of the biggest SRM particles; the treatment of coalescence and two-way coupling are assessed in this case for the method to assess the SRM nozzle flow.

Chapter 5

Accuracy and flexibility on size: Two-Size moment MF methods

An accurate method is needed to capture polydispersity at the compromise of computational cost, but also ease of implementation and flexibility. Instead of increasing the number of sections, we present methods that rely on solving two size moments in each section, in order to increase the accuracy without compromising too much computational efficiency. The method is promising to be efficient, and to be applicable in a flexible way, which makes it suitable for complex computations of industrial problems.

5.1 General principles of TSM methods

The general ideas of Multi-Fluid methods for polydisperse sprays have been introduced in the previous chapter, see § 4.4.5. The One Size Moment (OSM) method was presented as it was the first MF method to be derived (Laurent and Massot 2001), the first to be used (Laurent et al. 2004; de Chaisemartin 2009; Kah 2010) and the most simple that can be imagined.
In this part, we propose an improvement of the MF method based on the ability of sectional approaches to be hybridized: it consists in solving two size moments per section and is therefore referred to as Two Size Moment method (TSM). The general principles are exposed hereafter and two particular approaches are presented. Their efficiency is discussed in the following sections, as well as some achievements.
This work is a modeling contribution developed in the prospect of capturing polydispersity and coalescence efficiently in an industrial context: it has been published in Doisneau et al. (2013).

5.1.1 Treatment of size variable at the Multi-Fluid level

5.1.1.1 Choice of two size moments

We introduce the Two Size Moment formalism for Multi-Fluid approaches. It consists in transporting two size moments, e.g. number and mass instead of one -usually mass- (Dufour 2005; Laurent 2006).
The size moments M_k^1 and M_k^2 are defined from the choice of the size parameter ϕ and the order, relatively to ϕ, of each moment. So that we have on each section k

$$\begin{pmatrix} M_k^1 \\ M_k^2 \end{pmatrix} = \int_{\phi_{k-1}}^{\phi_k} \begin{pmatrix} \phi^{i_1} \\ \phi^{i_2} \end{pmatrix} n(t, \boldsymbol{x}, \phi) \mathrm{d}\phi \tag{5.1}$$

where M_k^1 and M_k^2 are of order i_1 and i_2 respectively and where the size discretization is done according to the standard Multi-Fluid one, given in Eq. (4.39). We give the link between some physical quantities and the moments in Table 5.1.
In the following, we will focus on methods that are able to solve for number and mass moments, whatever ϕ. Still we make a choice $\phi = S$ for the sake of clarity.

5.1.1.2 Need for reconstruction

In moment methods, an underlying reconstruction is considered for two purposes:

- to close the terms that depend on moments which are not conserved,
- to close the terms that depend on point-wise values of the number density function.

	$\phi = r$		$\phi = S$		$\phi = v$	
	power	coef.	power	coef.	power	coef.
Number	0	1	0	1	0	1
Radius	1	1	1/2	$1/\sqrt{4\pi}$	1/3	$(3/(4\pi))^{\frac{1}{3}}$
Surface	2	4π	1	1	2/3	$(6\sqrt{\pi})^{\frac{2}{3}}$
Mass	3	$\rho_l 4\pi/3$	3/2	$\rho_l/(6\sqrt{\pi})$	1	ρ_l

Table 5.1: *Spray-average physical quantities as moments of the size variable ϕ – Power k and coef. α express quantity q with the form $q = \alpha\phi^k$.*

To close the size dependent terms, the TSM method introduces a two-parameter function in each section noted ${}^2\kappa_k(t, \boldsymbol{x}, S)$ which is used to approximate the size distribution:

$$n(t, \boldsymbol{x}, S) \approx \widetilde{n}(t, \boldsymbol{x}, S) = \sum_{k=0}^{N_{\text{sec}}} {}^2\kappa_k(t, \boldsymbol{x}, S) \mathbb{1}_{[S_{k-1}, S_k[} \tag{5.2}$$

It is referred to as a reconstruction as it is deduced from the knowledge of some moments in the section, number and mass in our case. It is computed from the knowledge of the transported moments, in a way that should ensure their conservation.
The general method has been validated for evaporating cases (Dufour 2005; Dufour and Villedieu 2005; Laurent 2006) and analyzed by Laurent (2006). We validate the approach for coalescence in Chapter 13.

5.1.2 Treatment of size-conditioned variables

5.1.2.1 Sectional monokinetic assumption

The other hypotheses in the section remain as in the OSM method: there is a unique velocity for a given size, corresponding to the monokinetic assumption [HV1] and [HV2]. This unique velocity is considered constant on the whole size interval, corresponding to the sectional monokinetic assumption [HV3].
So the local ensemble velocities $\boldsymbol{u}$ are reconstructed as piecewise constant functions of size:

$$\boldsymbol{u}(t, \boldsymbol{x}, S) \approx \widetilde{\boldsymbol{u}}(t, \boldsymbol{x}, S) = \sum_{i=1}^{N_{\text{sec}}} \boldsymbol{u}_k(t, \boldsymbol{x}) \mathbb{1}_{[S_{k-1}, S_k[}(S) \tag{5.3}$$

in the context of the Dirac velocity distribution introduced in Eq. (4.12):

$$f^u(t, \boldsymbol{x}, \boldsymbol{c}, S) = n(t, \boldsymbol{x}, S)\delta(\boldsymbol{c} - \boldsymbol{u}(t, \boldsymbol{x}, S)). \tag{5.4}$$

The same assumptions are taken for temperatures T, with a unique temperature for the whole size interval:

$$T(t, \boldsymbol{x}, S) \approx \widetilde{T}(t, \boldsymbol{x}, S) = \sum_{i=1}^{N_{\text{sec}}} T_k(t, \boldsymbol{x}) \mathbb{1}_{[S_{k-1}, S_k[}(S) \tag{5.5}$$

in the context of the Dirac temperature distribution introduced in Eq. (4.12):

$$f^T(t, \boldsymbol{x}, \theta, S) = n(t, \boldsymbol{x}, S)\delta(\theta - T(t, \boldsymbol{x}, S)). \tag{5.6}$$

resulting from [HT1], [HT2] and [HT3].
Finally, we have the following NDF at the Multi-Fluid level:

$$\widetilde{f}(t, \boldsymbol{x}, \boldsymbol{c}, \theta, S) = \widetilde{n}(t, \boldsymbol{x}, S)\delta(\boldsymbol{c} - \widetilde{\boldsymbol{u}}(t, \boldsymbol{x}, S))\delta(\theta - \widetilde{T}(t, \boldsymbol{x}, S)). \tag{5.7}$$

We leave the notation $\sim$ in the following and we keep in mind the discrete nature of the system and the fact that the reconstructed NDF is a piecewise size function.

5.1.2.2 A first order but accurate approximation of velocity

The piecewise constant velocity reconstruction $\widetilde{\boldsymbol{u}}$ converges to the semi-kinetic size-conditioned velocity $\boldsymbol{u}$ at first order in the section discretization.
Similarly, the piecewise constant temperature reconstruction $\widetilde{T}$ converges to the semi-kinetic size-conditioned velocity T at first order in the section discretization.

The extension to a more accurate method in velocity and temperature conditioned by size, using cross-moments is discussed in § 5.4.
Although the OSM and TSM methods both have a first order reconstruction on velocity and temperature, TSM achieves a more accurate velocity and temperature resolution, thanks to the increased accuracy on size.
While OSM computes drag and heating with a fixed reconstruction, TSM computes these terms with a size distribution that is better described inside each section. Moreover the quality of the size reconstruction has a strong impact on the velocity and temperature errors since drag and heating times $\tau^{\boldsymbol{u}}$ and τ^T usually depend on the square of the droplet radius. So the Two Size Moment method achieves a better, more accurate, approximation of velocity and temperature.

5.1.3 Conservation equations for TSM methods

The method is based on two size moments that are conserved, so that the equations do not depend on the type of reconstruction, which is used only for closure purpose. So the TSM systems can be presented in the general case, while size reconstructions are discussed in § 5.3.
The conservation equations for the k^{th} section read:

$$\left\{\begin{array}{rcl} \partial_t n_k + \partial_{\boldsymbol{x}}\cdot(n_k\boldsymbol{u}_k) & = & {}^2\mathrm{B}_k^{n+} - {}^2\mathrm{B}_k^{n-} + {}^2\mathrm{C}_k^{n+} - {}^2\mathrm{C}_k^{n-} \\ \partial_t m_k + \partial_{\boldsymbol{x}}\cdot(m_k\boldsymbol{u}_k) & = & {}^2\mathrm{B}_k^{m+} - {}^2\mathrm{B}_k^{m-} + {}^2\mathrm{C}_k^{m+} - {}^2\mathrm{C}_k^{m-} \\ \partial_t(m_k\boldsymbol{u}_k) + \partial_{\boldsymbol{x}}\cdot(m_k\boldsymbol{u}_k\otimes\boldsymbol{u}_k) & = & m_k\,{}^2\boldsymbol{F}_k + {}^2\boldsymbol{B}_k^{u+} - {}^2\boldsymbol{B}_k^{u-} + {}^2\boldsymbol{C}_k^{u+} - {}^2\boldsymbol{C}_k^{u-} \\ \partial_t(m_k h_k) + \partial_{\boldsymbol{x}}\cdot(m_k h_k\boldsymbol{u}_k) & = & m_k\,{}^2\mathrm{H}_k + {}^2\mathrm{B}_k^{h+} - {}^2\mathrm{B}_k^{h-} + {}^2\mathrm{C}_k^{h+} - {}^2\mathrm{C}_k^{h-} \end{array}\right. \tag{5.8}$$

where the heat and momentum source terms ${}^2\boldsymbol{F}_k$ and ${}^2\mathrm{H}_k$ are integrated similarly as for the One Size Moment method, see § 5.2.1, while the coalescence and break-up source terms are computed in a different way, see § 5.2.4 and § 5.2.3.
The sectional system features one more moment, thus counting $N_d + 3$ equations, with N_d the dimension of the physical space.
As more size information is available in the section, we get better estimations of the source terms. For instance, drag and heating have characteristic times that are more accurately predicted.
For a fixed number of sections, the increase in cost of TSM compared to OSM is limited to one additional moment to be transported. Most of the method's cost then lies in the more complex algebra of reconstruction and source term computation. The aim of the TSM method is of course to benefit from the improved accuracy to reduce the number of sections. These features are discussed in the following while algorithms are developed in Chapter 13 and the overall cost is assessed in Chapter 15.

5.2 Source terms in TSM formalism

The size dependent source terms are computed for all the conserved moment equations. They are computed with respect to the conserved moments, which is achieved thanks to the knowledge of the size reconstruction. The latter is detailed in § 5.3.

5.2.1 Drag and heating

5.2.1.1 Usual integration

We get the vector for TSM transfer terms by usual integration of the semi kinetic transfer terms given in Eq. (4.14):

$$m_k \begin{pmatrix} 0 \\ 0 \\ {}^2\boldsymbol{F}_k \\ {}^2\mathrm{H}_k \end{pmatrix} = \int_{S_{k-1}}^{S_k} \begin{pmatrix} 0 \\ 0 \\ \overline{\boldsymbol{F}}(t,\boldsymbol{x},\boldsymbol{u},S) \\ \overline{\mathrm{H}}(t,\boldsymbol{x},T,S) \end{pmatrix} \frac{\rho_l S^{\frac{3}{2}}}{6\sqrt{\pi}}\, {}^2\kappa_k(S)\mathrm{d}S. \tag{5.9}$$

where the sectional velocity can be taken as $\boldsymbol{u}_k(t,\boldsymbol{x})$ thanks to Eq. (5.42) while $T(t,\boldsymbol{x},S) = T_k(t,\boldsymbol{x})$ thanks to Eq. (5.48).

5.2.1.2 Expression of the characteristic times

The characteristic times ${}^2\overline{\tau}_k^u$ and ${}^2\overline{\tau}_k^T$ are linked to the corresponding source terms.
These times are now space and time dependent as the size distribution within a section can vary. So they depend on the reconstruction parameters. The velocity and temperature dynamics are better evaluated,

especially if the droplet mass of the size distribution that is approximated in a section is supposed to be concentrated close to a section boundary.
In linear cases such as Stokes' regime, they read:

$$\frac{m_k}{\overline{\tau}_k^u} = \int_{S_{k-1}}^{S_k} \frac{1}{\tau^{\boldsymbol{u}}(t,\boldsymbol{x},S)} \frac{\rho_l}{6\sqrt{\pi}} S^{\frac{3}{2}} {}^2\kappa_k(S)\mathrm{d}S \tag{5.10}$$

and

$$\frac{m_k}{\overline{\tau}_k^T} = \int_{S_{k-1}}^{S_k} \frac{1}{\tau^{T}(t,\boldsymbol{x},S)} \frac{\rho_l}{6\sqrt{\pi}} S^{\frac{3}{2}} {}^2\kappa_k(S)\mathrm{d}S \tag{5.11}$$

with usually $\overline{\tau}_k^T = \frac{3}{2}\frac{c_{p,l}}{c_{p,g}}\mathrm{Pr}_g \overline{\tau}_k^u$, so that the knowledge of characteristic times is algebraically equivalent to the knowledge of the source terms, with the correspondence:

$$\begin{aligned} {}^2\boldsymbol{F}_k(t,\boldsymbol{x},\boldsymbol{u}_k) &= \frac{\boldsymbol{u}_g(t,\boldsymbol{x}) - \boldsymbol{u}_k}{\overline{\tau}_k^u(t,\boldsymbol{x})} \\ {}^2\mathrm{H}_k(t,\boldsymbol{x},T_k) &= \overline{c}_{p,k}\frac{T_g(t,\boldsymbol{x}) - T_k}{\overline{\tau}_k^T(t,\boldsymbol{x})}. \end{aligned} \tag{5.12}$$

5.2.2 Evaporation

As it was the case for the OSM method, the TSM Multi-Fluid method can be seen as a finite volume method in size. But the associated transport scheme must account for the second order reconstruction within the sections (playing the role of cells).
In this context, the evaporation terms for the TSM MF method have been derived and are presented in detail in Dufour (2005), see also Dufour and Villedieu (2005), Laurent (2006) and Laurent (2013) for the Aff-TSM method. The use of such approaches has been extended to aluminum combustion modeling by Sibra et al. (2013) for SRM applications.

5.2.3 Secondary break-up

Secondary break-up is a source term that is linear on the NDF at the kinetic level, see Eq. (3.151). Yet it features an integration on all the droplets that possibly break-up.

5.2.3.1 Expression as linear combinations of elementary integrals

The break-up terms for the TSM have been derived by Dufour (2005). They result in linear combinations in the same way than for the OSM method:

$$\begin{pmatrix} {}^2\mathrm{B}_k^{n+} \\ {}^2\mathrm{B}_k^{m+} \\ {}^2\boldsymbol{B}_k^{u+} \\ {}^2\mathrm{B}_k^{h+} \end{pmatrix} = \sum_{i=k}^{N_{\mathrm{sec}}} \begin{pmatrix} {}^2\mathrm{Q}_{ik}^{n+} \\ {}^2\mathrm{Q}_{ik}^{m+} \\ {}^2\boldsymbol{Q}_{ik}^{u+} \\ {}^2\mathrm{Q}_{ik}^{h+} \end{pmatrix} \tag{5.13}$$

where the elementary integrals read:

$$\begin{pmatrix} {}^2\mathrm{Q}_{ik}^{n+} \\ {}^2\mathrm{Q}_{ik}^{m+} \\ {}^2\boldsymbol{Q}_{ik}^{u+} \\ {}^2\mathrm{Q}_{ik}^{h+} \end{pmatrix} = \int_{S^\star=S_{i-1}}^{S^\star=S_i} \int_{S=S_{k-1}}^{S=S_k} \begin{pmatrix} 1 \\ \frac{\rho_l}{6\sqrt{\pi}} S^{\star\frac{3}{2}} \\ \frac{\rho_l}{6\sqrt{\pi}} S^{\star\frac{3}{2}} \boldsymbol{u}^{\mathrm{bu}}(S;\boldsymbol{u}_i,S^\star,\boldsymbol{u}_g) \\ \frac{\rho_l}{6\sqrt{\pi}} S^{\star\frac{3}{2}} h(T_i) \end{pmatrix} {}^2\kappa_i(t,\boldsymbol{x},S^\star) \times \nu_{\mathrm{bu}}(\boldsymbol{u}_i,S^\star,\boldsymbol{u}_g)\ f_{\mathrm{bu}}(S;\boldsymbol{u}_i,S^\star,\boldsymbol{u}_g)\mathrm{d}S\mathrm{d}S^\star \tag{5.14}$$

where it can be seen that:

$${}^2\mathrm{Q}_{ik}^{h+} = h(T_i){}^2\mathrm{Q}_{ik}^{m+}. \tag{5.15}$$

As for the disappearance terms, they can be directly integrated on the sections:

$$\begin{pmatrix} {}^2\mathrm{B}_k^{n-} \\ {}^2\mathrm{B}_k^{m-} \\ {}^2\boldsymbol{B}_k^{u-} \\ {}^2\mathrm{B}_k^{h-} \end{pmatrix} = \int_{S_{k-1}}^{S_k} \begin{pmatrix} 1 \\ \frac{\rho_l}{6\sqrt{\pi}} S^{\frac{3}{2}} \\ \frac{\rho_l}{6\sqrt{\pi}} S^{\frac{3}{2}} \boldsymbol{u}_k \\ \frac{\rho_l}{6\sqrt{\pi}} S^{\frac{3}{2}} h(T_k) \end{pmatrix} {}^2\kappa_k(t,\boldsymbol{x},S)\nu_{\mathrm{bu}}(\boldsymbol{u}_k,S,\boldsymbol{u}_g)\mathrm{d}S \tag{5.16}$$

The following relations between disappearance and creation emphasize mass conservation:

$$\begin{pmatrix} {}^2\mathrm{B}_k^{m-} \\ {}^2\boldsymbol{B}_k^{u-} \\ {}^2\mathrm{B}_k^{h-} \end{pmatrix} = \sum_{i=1}^{N_{\mathrm{sec}}} \begin{pmatrix} {}^2\mathrm{Q}_{ki}^{m+} \\ \boldsymbol{u}_k\, {}^2\mathrm{Q}_{ki}^{m+} \\ h_k\, {}^2\mathrm{Q}_{ki}^{m+} \end{pmatrix} = \begin{pmatrix} 1 \\ \boldsymbol{u}_k \\ h_k \end{pmatrix} \sum_{i=1}^{N_{\mathrm{sec}}} {}^2\mathrm{Q}_{ki}^{m+} \tag{5.17}$$

where enthalpy is conserved by the break-up operator:

$${}^2\mathrm{B}_k^{h-} = \sum_{i=1}^{N_{\mathrm{sec}}} {}^2\mathrm{Q}_{ki}^{h+}. \tag{5.18}$$

while momentum is not conserved by the operator:

$${}^2\boldsymbol{B}_k^{u-} \neq \sum_{i=1}^{N_{\mathrm{sec}}} {}^2\boldsymbol{Q}_{ki}^{u+}. \tag{5.19}$$

due to the projection of daughter droplet velocities on to $\boldsymbol{u}^{\mathrm{bu}}(S;\boldsymbol{u}_i,S^\star,\boldsymbol{u}_g)$ and as described at the kinetic level in § 3.5.3.2.
The most important point is to be emphasized is that number is not conserved at all by the break-up operator:

$${}^2\mathrm{B}_k^{n-} \neq \sum_{i=1}^{N_{\mathrm{sec}}} {}^2\mathrm{Q}_{ki}^{n+} \tag{5.20}$$

which was not visible in the OSM method, as number was not a conserved moment anyway.

5.2.3.2 Practical computational aspects

The numerical methods to assess the disappearance integrals are that of linear integrals.
The mass disappearance term is not integrated in practice but computed as the sum of the creation terms to enforce conservation versus numerical errors. The momentum and enthalpy losses can be computed straightforward with Eq. (5.17), instead of evaluating the integrals of Eq. (5.16). Therfore, ${}^2\mathrm{B}_k^{n-}$ is the only disappearance term that needs to be computed. This results from the non-conservation of the droplet number, intrinsic to break-up processes.
As for creation terms, number, mass and momentum elementary integrals must be computed while enthalpy can be related to mass creation thanks to Eq. (5.15).
We finally highlight that momentum is not conserved: the break-up process is written in a non-conservative form, intrinsically accounting for stiff drag effects on the small fragments, as explained in § 3.5.3.2. This modeling point is profitable for the upcoming numerics.
The numerical methods to assess the creation integrals terms are still considered as linearly difficult as the arrival section integral is performed on a presumed PDF, with the whole section as integration interval.

5.2.4 Quadratic source terms: case of coalescence

5.2.4.1 Expression of the coalescence terms

Since the time and space dependency of the size-distribution functions ${}^2\kappa_k(t,\boldsymbol{x},S)$ is no longer factorizable as was m_k in the One Size Moment method, the Q_{ijk} integrals must be computed at each time step in each cell on $\mathscr{D}_{ijk}$. Let us introduce the notation:

$$\Psi^{ij}(r^\star,r^\diamond,|\boldsymbol{u}_i-\boldsymbol{u}_j|) = {}^2\kappa_i(S(r^\star))\,{}^2\kappa_j(S(r^\diamond))\pi(r^\star+r^\diamond)^2\ |\boldsymbol{u}_i-\boldsymbol{u}_j|\ \mathfrak{E}(r^\star,r^\diamond,|\boldsymbol{u}_i-\boldsymbol{u}_j|) \tag{5.21}$$

where the $(t,\boldsymbol{x})$ dependency has been dropped. The coalescence integrals have a different homogeneity than in the One Size Moment method. They now include the number or mass information and read:

$$\begin{pmatrix} \mathrm{Q}_{ijk}^{n} \\ \mathrm{Q}_{ijk}^{\star} \\ \mathrm{Q}_{ijk}^{\diamond} \end{pmatrix} = \iint_{\mathscr{D}_{ijk}} \begin{pmatrix} 1 \\ \frac{\rho_l}{6\sqrt{\pi}} S^{\star\frac{3}{2}} \\ \frac{\rho_l}{6\sqrt{\pi}} S^{\diamond\frac{3}{2}} \end{pmatrix} \Psi^{ij}(r^\star,r^\diamond,|\boldsymbol{u}_i-\boldsymbol{u}_j|)\mathrm{d}r^\star\mathrm{d}r^\diamond \tag{5.22}$$

The coalescence source terms ${}^2\mathrm{C}_k^{n+}$, ${}^2\mathrm{C}_k^{n-}$, ${}^2\mathrm{C}_k^{m+}$, ${}^2\mathrm{C}_k^{m-}$, ${}^2\boldsymbol{C}_k^{u+}$, ${}^2\boldsymbol{C}_k^{u-}$, ${}^2\mathrm{C}_k^{h+}$ and ${}^2\mathrm{C}_k^{h-}$ are still written as direct

sums of the "(i,j,k) integrals" and therefore read:

$$\begin{pmatrix} {}^2\mathbb{C}_k^{n+} \\ {}^2\mathbb{C}_k^{m+} \\ {}^2\boldsymbol{C}_k^{u+} \\ {}^2\mathbb{C}_k^{h+} \end{pmatrix} = \sum_{i=1}^{k}\sum_{j=1}^{i-1} |\boldsymbol{u}_i - \boldsymbol{u}_j| \left\{ \begin{pmatrix} \frac{1}{2}\mathbb{Q}_{ijk}^{n} \\ \mathbb{Q}_{ijk}^{\star} \\ \boldsymbol{u}_i \mathbb{Q}_{ijk}^{\star} \\ h_i \mathbb{Q}_{ijk}^{\star} \end{pmatrix} + \begin{pmatrix} \frac{1}{2}\mathbb{Q}_{ijk}^{n} \\ \mathbb{Q}_{ijk}^{\diamond} \\ \boldsymbol{u}_j \mathbb{Q}_{ijk}^{\diamond} \\ h_j \mathbb{Q}_{ijk}^{\diamond} \end{pmatrix} \right\},$$
$$\begin{pmatrix} {}^2\mathbb{C}_k^{n-} \\ {}^2\mathbb{C}_k^{m-} \\ {}^2\boldsymbol{C}_k^{u-} \\ {}^2\mathbb{C}_k^{h-} \end{pmatrix} = \sum_{j=1}^{N_{\text{sec}}}\sum_{i=1}^{N_{\text{sec}}} |\boldsymbol{u}_j - \boldsymbol{u}_k| \begin{pmatrix} \mathbb{Q}_{kji}^{n} \\ \mathbb{Q}_{kji}^{\star} \\ \boldsymbol{u}_k \mathbb{Q}_{kji}^{\star} \\ h_k \mathbb{Q}_{kji}^{\star} \end{pmatrix}. \tag{5.23}$$

5.2.4.2 Comments on TSM coalescence

As shown in System (4.42) and System (5.8), drag, heat transfers and coalescence yield spatially located source terms in the Multi-Fluid equations, analogous to chemical source terms for instance. In the Two Size Moment method, these source terms must be evaluated by relevantly accurate integrations on the size distribution inside each section. A key issue for the Two Size Moment method is to compute the coalescence source terms for each section, in each cell and at each time step with a good cost over accuracy compromise, which is discussed in § 13.1.5.

5.3 Size reconstruction

5.3.1 Reconstruction constraints

Two Size Moment methods use a two-parameter ${}^2\kappa_k(t,\boldsymbol{x},S)$ function instead of [HS1] which yields an accurate description of size: it is second order in size distribution convergence but the fully coupled problem may still be solved at first order due to the treatment of velocity and temperature conditioned by size with no cross-moments. Still the method features an interesting gain on accuracy.

5.3.1.1 Conservation constraints

$$\begin{cases} \displaystyle\int_{S_{k-1}}^{S_k} {}^2\kappa_k(t,\boldsymbol{x},S)\mathrm{d}S = n_k(t,\boldsymbol{x}) \\ \displaystyle\int_{S_{k-1}}^{S_k} {}^2\kappa_k(t,\boldsymbol{x},S)\frac{\rho_l}{6\sqrt{\pi}}S^{3/2}\mathrm{d}S = m_k(t,\boldsymbol{x}) \end{cases} \tag{5.24}$$

5.3.1.2 Realizability constraints

The only realizability condition for a couple of size moments (n_k, m_k) in a section is to be positive and to correspond to an average diameter that is in the size interval:

$$\begin{cases} n_k > 0 \text{ or } n_k = m_k = 0 \\ m_k > 0 \text{ or } n_k = m_k = 0 \\ m(S_{k-1}) \leq \frac{m_k}{n_k} \leq m(S_k) \end{cases} \tag{5.25}$$

with S_k the section bounds expressed in surface and $m(S_k) = \frac{\rho_l S_k^{\frac{3}{2}}}{6\sqrt{\pi}}$ the section bounds expressed in mass.
In the following, two approaches are considered, the first one is based on an exponential reconstruction and the second one on a linear reconstruction.

5.3.2 Exponential reconstruction: the Exp-TSM method

5.3.2.1 Reconstruction function

The Exp-TSM MF method is based on a two-parameter exponential approximation of the size distribution in each section. The method has been validated for evaporating cases (Dufour and Villedieu 2005). This means that [HS1] then reads, for $S \in [S_{k-1}, S_k[$:

$${}^2\kappa_k(t,\boldsymbol{x},S) = a_k(t,\boldsymbol{x})\exp(-b_k(t,\boldsymbol{x})S) \tag{5.26}$$

where $(a_k(t,\boldsymbol{x}), b_k(t,\boldsymbol{x}))_k$ yields two moments per section $(n_k(t,\boldsymbol{x}), m_k(t,\boldsymbol{x}))_k$ that must ensure Eq. (5.24). Regarding realizability, the choice of an exponential function ensures the positivity of the distribution function as soon as $a_k \geq 0$.
It is proven to be well suited for evaporation, which requires mass flux information at the section boundary.

5.3.2.2 Exponential reconstruction properties

On the other hand, a problem known as realizability emerges from the fact that the transported quantities are the $(n_k, m_k)_k$ while all source terms are computed by integration of ${}^2\kappa_k(t, \boldsymbol{x}, S)$ on S, therefore requiring $(a_k, b_k)_k$. The inversion of the previous system as well as all PDE resolution and integration numerical methods must respect realizability conditions on the sections. Practically, $(m_k/n_k)_k$ ratios are conditioned by the k^{th} section boundaries since they drive information on average droplet volume. The $(a_k, b_k)_k$ inversion algorithm was improved to reduce its cost and to increase its reliability and is detailed in § 13.1.2.
The two size moment Eulerian Multi-Fluid method transports two size moments for section k but the properties that have to be averaged on section $[S_{k-1}^{3/2}, S_k^{3/2}]$ are computed assuming a two parameter exponential reconstruction for (n_k, m_k). The constraints of Eq. (5.24) require to compute the reconstruction parameters as follows:

$$\left\{\begin{array}{ll} b_k = & g_k^{-1}\left(\frac{m_k}{n_k}\right) \\ a_k = & \left\{\begin{array}{ll} \frac{n_k b_k}{\exp(-b_k S_{k-1})-\exp(-b_k S_k)} & \text{if } b_k \neq 0 \\ \frac{n_k}{S_k - S_{k-1}} & \text{if } b_k = 0 \end{array}\right. \end{array}\right. \tag{5.27}$$

where we have noted the auxiliary function $g_k(b)$ defined for $b \in \mathbb{R}^+$:

$$g_k(b) = \frac{\rho_l}{6\sqrt{\pi}} \frac{\int_{S_{k-1}}^{S_k} S^{\frac{3}{2}} \exp(-bS)\mathrm{d}S}{\int_{S_{k-1}}^{S_k} \exp(-bS)\mathrm{d}S}. \tag{5.28}$$

An analytical expression can be derived for g_k (Dufour 2005):

$$g_k(b) = \frac{\rho_l/(6\sqrt{\pi})}{1-\exp(-b\Delta S)} \left\{\begin{array}{l} \left[S_{k-1}^{\frac{3}{2}} - S_k^{\frac{3}{2}} \exp(b\Delta S) + \frac{3}{2b}\left(S_{k-1}^{\frac{1}{2}} - S_k^{\frac{1}{2}} \exp(b\Delta S)\right)\right. \\ \left. + \frac{3\sqrt{\pi}}{4} \frac{\exp(bS_{k-1})}{b^{\frac{3}{2}}} \left(\mathrm{erf}\sqrt{bS_k} - \mathrm{erf}\sqrt{bS_{k-1}}\right)\right] \quad \text{if } b > 0 \\ \left[S_{k-1}^{\frac{3}{2}} - S_k^{\frac{3}{2}} \exp(b\Delta S) + \frac{3}{2b}\left(S_{k-1}^{\frac{1}{2}} - S_k^{\frac{1}{2}} \exp(b\Delta S)\right)\right. \\ \left. + \frac{3\sqrt{\pi}}{4b^{\frac{3}{2}}} \left(\exp(b\Delta S)\mathrm{daw}\sqrt{-bS_k} - \mathrm{daw}\sqrt{-bS_{k-1}}\right)\right] \quad \text{if } b < 0 \end{array}\right. \tag{5.29}$$

where $\Delta S = S_k - S_{k-1}$, where the error function erf is defined as:

$$\mathrm{erf}(\zeta) = \frac{2}{\sqrt{\pi}} \int_0^\zeta \exp(-t^2)\mathrm{d}t \tag{5.30}$$

and where the Dawson function daw is defined as:

$$\mathrm{daw}(\zeta) = \frac{2\exp(-\zeta^2)}{\sqrt{\pi}} \int_0^\zeta \exp(t^2)\mathrm{d}t. \tag{5.31}$$

5.3.2.3 Suitability as a reconstruction

The function $g_k(b)$ depends only on b_k. It is a strictly monotonic function and has the two limits:

$$\left\{\begin{array}{l} \lim\limits_{b\to-\infty} g_k(b) = \frac{\rho_l}{6\sqrt{\pi}} S_k^{\frac{3}{2}} \\ \lim\limits_{b\to+\infty} g_k(b) = \frac{\rho_l}{6\sqrt{\pi}} S_{k-1}^{\frac{3}{2}} \end{array}\right. \tag{5.32}$$

so that g_k is a bijection from $\mathbb{R}$ to $]m(S_{k-1}), m(S_k)[$. As a consequence it is invertible and System (5.27) has a unique solution.
The exponential function Eq. (5.26) is therefore admissible as a reconstruction.

5.3.3 Positive affine reconstruction: the Aff-TSM method

The Aff-TSM MF method is also based on a two-parameter approximation of the size distribution in each section. An early version was suggested in Laurent (2006) but the one presented here is simpler and more efficient, as analyzed in Laurent (2013). The choice of an affine function is not straightforward because of the positivity realizability constraint: a positivity constraint must be enforced with the corresponding inversion algorithm to be developed.

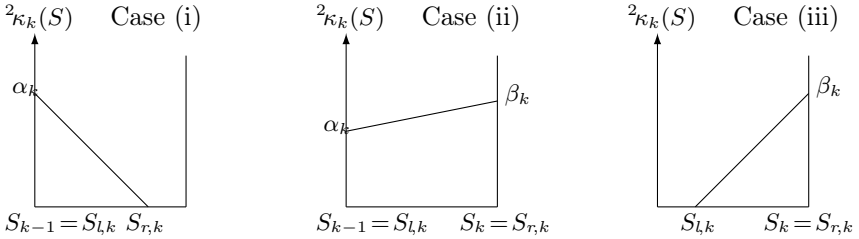

Figure 5.1: *The three possible cases for the positive affine reconstruction and their two respective relevant parameters.*

5.3.3.1 Reconstruction function

We now define the positive affine reconstruction. We consider the following form of a distribution for $S \in [S_{k-1}, S_k[$:

$$^2\kappa_k(t,\boldsymbol{x},S) = \begin{cases} 0 & \text{if } S_{k-1} < S < S_{l,k}(t,\boldsymbol{x}) \\ \alpha_k(t,\boldsymbol{x})\dfrac{S_{r,k}(t,\boldsymbol{x}) - S}{S_{r,k}(t,\boldsymbol{x}) - S_{l,k}(t,\boldsymbol{x})} & \\ +\beta_k(t,\boldsymbol{x})\dfrac{S - S_{l,k}(t,\boldsymbol{x})}{S_{r,k}(t,\boldsymbol{x}) - S_{l,k}(t,\boldsymbol{x})} & \text{if } S_{l,k}(t,\boldsymbol{x}) \le S \le S_{r,k}(t,\boldsymbol{x}) \\ 0 & \text{if } S_{r,k}(t,\boldsymbol{x}) < S < S_k \end{cases} \tag{5.33}$$

which allows a threshold at 0 i.e. it is piecewise affine. It is defined with four parameters that are α, β, S_l and S_r. To define completely the positive affine reconstruction, a condition is added to the latter form:

[R1] Only one bound is allowed to be different from a section bound so that only three cases can occur, as presented in Figure 5.1.

[R2] The reconstruction $^2\kappa_k$ is a continuous function of S on $]S_{k-1}, S_k[$.
These assumptions allow the reconstruction to be well-posed, as discussed below.

5.3.3.2 Number of parameters

The positive affine reconstruction is defined from the form given in Eq. (5.33) which has four parameters α, β, S_l and S_r but condition [R1] is enforced. As a consequence, only two parameters are finally relevant for the reconstruction, depending on the case: either two coefficients in case (ii) which is purely affine or one coefficient and a bound in cases (i) and (iii), which are piecewise affine.
In fact, these conditions are equivalent to fixing only two reel parameters P_1 and P_2 e.g. by considering:

- $P_1 := \alpha$ and $P_2 := -S_r$ if in case (i) so that $\beta = 0$ and $S_l = S_{k-1}$,
- $P_1 := \alpha$ and $P_2 := \beta$ if in case (ii) so that $S_l = S_{k-1}$ and $S_r = S_k$,
- $P_1 := -S_l$ and $P_2 := -\beta$ if in case (iii) so that $\alpha = 0$ and $S_r = S_k$.

With this algorithm, it can be seen that the knowledge of the case is given by the sign of P_1 and P_2 and the two relevant parameters can then be deduced.

5.3.3.3 Determination of the cases

There are three possible cases for the positive affine reconstruction:
(i) a constant zero domain at the right of the section,
(ii) no zero, or
(iii) a constant zero domain at the left,
as showed in Figure 5.1. We now assess the occurrence of these cases depending on the two moments.
The reduced average volume are now considered from the moments:

$$\widetilde{v}_{30} = \frac{6\sqrt{\pi}}{\rho_l}\frac{m_k}{n_k} \tag{5.34}$$

and we consider the following bounds:

$$\begin{aligned} \widetilde{v}_1 &= S_{k-1}^{\frac{3}{2}} \\ \widetilde{v}_2 &= \frac{2(S_k S_{5/2} - S_{7/2})}{\Delta S^2} \\ \widetilde{v}_3 &= \frac{2(S_{7/2} - S_{k-1} S_{5/2})}{\Delta S^2} \\ \widetilde{v}_4 &= S_k^{\frac{3}{2}} \end{aligned} \tag{5.35}$$

with the notations $\Delta S = S_k - S_{k-1}$, $S_{5/2} = \frac{2}{5}(S_k^{\frac{5}{2}} - S_{k-1}^{\frac{5}{2}})$ and $S_{7/2} = \frac{2}{7}(S_k^{\frac{7}{2}} - S_{k-1}^{\frac{7}{2}})$.
It can then be proven (Laurent 2013) that case (i) corresponds exactly to the algebraic condition:

$$\widetilde{v}_1 \leq \widetilde{v}_{30} \leq \widetilde{v}_2 \tag{5.36}$$

case (ii) occurs exactly when:

$$\widetilde{v}_2 < \widetilde{v}_{30} < \widetilde{v}_3. \tag{5.37}$$

and case (iii) occurs exactly when:

$$\widetilde{v}_3 \leq \widetilde{v}_{30} \leq \widetilde{v}_4. \tag{5.38}$$

5.3.3.4 Suitability as a reconstruction

The previous study proves that the three cases map the interval $[m(S_{k-1}), m(S_k)]$ so:

- the proposed affine reconstruction allows to account for any (n_k, m_k) couple that respects the basic realizability condition given in Eq. (5.25);
- any reconstruction corresponds to a couple (n_k, m_k).

The positive affine description is therefore proven to be admissible as a reconstruction.

5.3.4 Remarks on reconstructions and efficiency

Figure 5.2 shows a lognormal size distribution as approximated by the piecewise constant, the exponential and the positive affine reconstructions, respectively from OSM, Exp-TSM and Aff-TSM methods. The OSM reconstruction is obviously less accurate while the TSM reconstructions are different from each other.
But the aim of TSM methods is to conserve two moments and not directly to fit the size distribution (though these two aspects are linked). So that it should not be assessed whether a method is better based on the fact that its reconstruction is close to the original size distribution or not. Indeed the two methods are similar in a pure numerical analysis framework: both reconstructions respect number and mass in each section at the accuracy of the reconstruction algorithm.

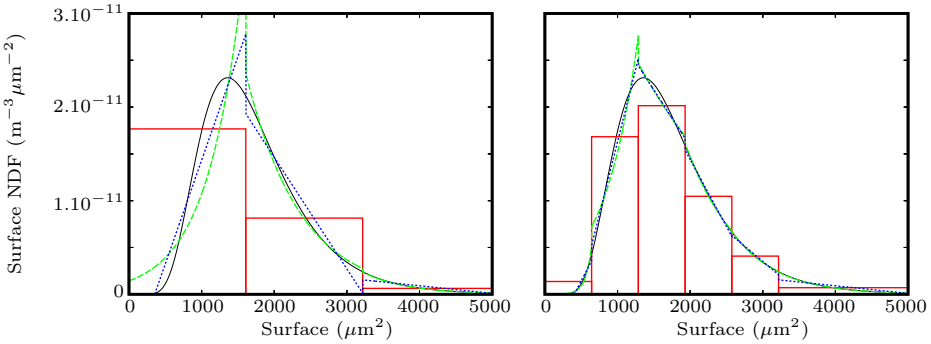

Figure 5.2: *Illustration of NDF reconstruction for OSM (boxes), Exp-TSM (– –), Aff-TSM (· · ·) with 3 sections (left) and with 6 sections (right) – Reference NDF (—) is lognormal in surface with* $S_{LN} = 1600\,\mu m^2$ *and* $\sigma_{LN} = 1.5$.

So TSM methods will differ in the practice of a CFD code only regarding truncature errors, algorithm efficiency and pure algebraic cost. This is discussed in § 13.1.

5.4 Increasing the accuracy on velocity

To increase the accuracy on velocity, we develop an approach to render size-velocity correlations, inspired from the CSVM developed by Vié et al. (2013), see § 4.4.4.6.
As CSVM can be seen as an extension of EMSM, the following method extends TSM and is referred to as Correlated Size-Velocity Two Size Moment method (CSVTSM).
The fact that the approach is defined on sections allows to treat cases where the Stokes numbers vary significantly within the section. In link with the definition of effective polydispersity in § 3.1.2.2, polydispersity can indeed induce strong differences of size-correlated quantities within the section and high order approaches are required to remain accurate without increasing the number of sections.
The method is designed to account efficiently for size-conditioned dynamics: it is expected to be fully second order in size and velocity but with a simpler algebra than the CSVM. Since it accounts efficiently for hetero-PTC, it is particularly suited for coalescing cases, so that the terms are hereafter computed. The model is promising and a publication is in preparation, but it is not used in the rest of the work.

5.4.1 Accounting for size-velocity correlations

We take inspiration from CSVM approach presented in § 4.4.4.6 and from its extension to sectional methods presented in § 4.4.5.10 to introduce a high order velocity and temperature approach to complete the TSM method. In addition, the coalescence terms are computed. This approach is relevant in the prospect of reducing the number of sections, as sought by the TSM method.

5.4.1.1 Choice of moments

We need to account for size velocity couplings so we introduce again the cross-moments in the section:

$$M_k^{i,pqr} = \int_{S_{k-1}}^{S_k} \iiint_{\mathbb{R}^3} S^i c_1^p c_2^q c_3^r \widetilde{f}(s,\boldsymbol{c}) \mathrm{d}S\mathrm{d}\boldsymbol{c} \tag{5.39}$$

If the shape of the velocity reconstruction is well chosen, the three velocity directions can be decoupled so that we do not need consider cross-moments in the velocity components. In the following the triple direction indices in $M_k^{i,pqr}$ are dropped for a vector notation $\boldsymbol{M}_k^{i,p} = (M_k^{i,p00}\ M_k^{i,0p0}\ M_k^{i,00p})^T$. The following moments are then chosen in the section:

$$\begin{pmatrix} M_k^{0,0} \\ M_k^{3/2,0} \\ \boldsymbol{M}_k^{0,1} \\ \boldsymbol{M}_k^{3/2,1} \end{pmatrix} \tag{5.40}$$

in accordance with both the TSM requirements and the number of parameters in the chosen velocity reconstruction. So that there is a need to transport 4 moments in 1D, 6 in 2D and 8 in 3D. We note that if the constant velocity reconstruction had been chosen, we would have the relation $M_k^{3/2,100} = M_k^{0,100} M_k^{3/2,000}$ which would allow the use of only 3 moments, yielding back the standard TSM method. We finally get the following conservation equations, written in 1D and in the case of coalescence but without break-up:

$$\partial_t \begin{pmatrix} M_k^{0,0} \\ M_k^{3/2,0} \\ \boldsymbol{M}_k^{0,1} \\ \boldsymbol{M}_k^{3/2,1} \end{pmatrix} + \partial_{\boldsymbol{x}} \cdot \begin{pmatrix} \boldsymbol{M}_k^{0,1} \\ \boldsymbol{M}_k^{3/2,1} \\ \boldsymbol{M}_k^{0,2} \\ \boldsymbol{M}_k^{3/2,2} \end{pmatrix} = \begin{pmatrix} 0 \\ 0 \\ \boldsymbol{F}_k^0 \\ \boldsymbol{F}_k^{3/2} \end{pmatrix} + \begin{pmatrix} \mathrm{C}_k^{0,0+} \\ \mathrm{C}_k^{3/2,0+} \\ \boldsymbol{\mathrm{C}_k^{0,1+}} \\ \boldsymbol{\mathrm{C}_k^{3/2,1+}} \end{pmatrix} - \begin{pmatrix} \mathrm{C}_k^{0,0-} \\ \mathrm{C}_k^{3/2,0-} \\ \boldsymbol{\mathrm{C}_k^{0,1-}} \\ \boldsymbol{\mathrm{C}_k^{3/2,1-}} \end{pmatrix} \tag{5.41}$$

where all the moments are known except $\boldsymbol{M}_k^{0,2}$ and $\boldsymbol{M}_k^{3/2,2}$ which have to be reconstructed.

5.4.1.2 A size-velocity dependent closure

Back to the semi-kinetic level, the monokinetic closure allocates one velocity $\boldsymbol{u}(S)$ per size S with the corresponding NDF, given in § 4.12. The semi-kinetic system then solves for a size distribution $n(S)$, and a velocity distribution $\boldsymbol{u}(S)$.
At the Multi-Fluid level, size is reconstructed on the sections with any reconstruction ${}^2\kappa_k(S)$ and the velocity is reconstructed

$$\widetilde{\boldsymbol{u}}(t,\boldsymbol{x},S) \approx \sum_{i=1}^{N_{\mathrm{sec}}} \boldsymbol{u}_k(t,\boldsymbol{x},S) \mathbb{1}_{[S_{k-1},S_k[}(S) \tag{5.42}$$

where the velocity reconstructions now depend on size. We choose the following velocity form:

$$\boldsymbol{u}_k(t,\boldsymbol{x},S) = \boldsymbol{u}_g + \boldsymbol{A_k} S + \boldsymbol{B_k} S^2 \tag{5.43}$$

which is the same form as a form suggested by Vié et al. (2013) for the original CSVM approach.

5.4.1.3 Reconstruction

Given the availability of a number $M_k^{0,0}$ and a mass moment $M_k^{3/2,0}$, the size distribution can be reconstructed, in a first step, with the same algorithm than in classical TSM approaches.
In a second step, the velocity moments in a section must ensure the following relations:

$$\begin{cases} \boldsymbol{M}_k^{0,1} = & \boldsymbol{u}_g M_k^{0,0} + \boldsymbol{A_k} M_k^{1,0} + \boldsymbol{B_k} M_k^{2,0} \\ \boldsymbol{M}_k^{3/2,1} = & \boldsymbol{u}_g M_k^{3/2,0} + \boldsymbol{A_k} M_k^{5/2,0} + \boldsymbol{B_k} M_k^{7/2,0} \end{cases} \tag{5.44}$$

which is an invertible system as there are only two (vector) unknowns $\boldsymbol{A_k}$ and $\boldsymbol{B_k}$. The size moments of order 1, 2, 5/2 and 7/2 can indeed be reconstructed from the knowledge of ${}^2\kappa_k(S)$ so that the velocity reconstruction follows.

5.4.1.4 Source terms

We consider, as an illustration, the integration of a velocity dependent source term such as Stokes' drag:

$$\begin{pmatrix} \boldsymbol{F}_k^0 \\ \boldsymbol{F}_k^{3/2} \end{pmatrix} = \int_{S_{k-1}}^{S_k} \begin{pmatrix} 1 \\ \frac{\rho_l}{6\sqrt{\pi}} S^{\frac{3}{2}} \end{pmatrix} \frac{^2\kappa_k(S)}{\tau^{\boldsymbol{u}}(S)} \left(\boldsymbol{u}_g - \left[\boldsymbol{u}_g + \boldsymbol{A_k} S + \boldsymbol{B_k} S^2\right]\right) \mathrm{d}S \tag{5.45}$$

which simplifies by linearity of the velocity dependence and which reads, when assuming a characteristic time $\tau^{\boldsymbol{u}}(S) = \rho_l S/(18\pi\mu_g)$:

$$\begin{cases} \boldsymbol{F}_k^0 = & -\dfrac{18\pi\mu_g}{\rho_l}(\boldsymbol{A_k} M_k^{0,0} + \boldsymbol{B_k} M_k^{1,0}) \\ \boldsymbol{F}_k^{3/2} = & -3\sqrt{\pi}\mu_g(\boldsymbol{A_k} M_k^{3/2,0} + \boldsymbol{B_k} M_k^{5/2,0}) \end{cases} \tag{5.46}$$

again the unknown moments of order 1 and 5/2 can be reconstructed from the knowledge of $^2\kappa_k(S)$. In the case of a convective correction, an additional velocity dependency results from the particular Reynolds Re_p so that the term reads:

$$\begin{pmatrix} \boldsymbol{F}_k^0 \\ \boldsymbol{F}_k^{3/2} \end{pmatrix} = \int_{S_{k-1}}^{S_k} - \begin{pmatrix} 18\pi/\rho_l \\ 3\sqrt{\pi} S^{\frac{3}{2}} \end{pmatrix} {}^2\kappa_k(S)\mu_g(\boldsymbol{A_k} + \boldsymbol{B_k} S) \left[1 + 0.15 \left(\frac{\rho_g S^{\frac{1}{2}} |\boldsymbol{A_k} S + \boldsymbol{B_k} S^2|}{2\sqrt{\pi}\mu_g} \right)^{0.687} \right] \mathrm{d}S \tag{5.47}$$

and these integrals formally correspond to the need for non-transported size moments. The latter can be computed from the knowledge of the size reconstruction, whatever their order, even non-integer.

5.4.1.5 Case of temperature

Temperature can be reconstructed at second order on the section with the exact same approach as for velocities:

$$\widetilde{T}(t, \boldsymbol{x}, S) \approx \sum_{i=1}^{N_{\mathrm{sec}}} T_k(t, \boldsymbol{x}, S) \mathbb{1}_{[S_{k-1}, S_k[}(S) \tag{5.48}$$

with the temperature form:

$$T_k(t, \boldsymbol{x}, S) = T_g + A_k^T S + B_k^T S^2. \tag{5.49}$$

We suggest to conserve a zeroth $M_k^{0,000,1}$ and first order in mass $M_k^{3/2,000,1}$ temperature moment, with the following definition for temperature moments:

$$M_k^{i,pqr,t} = \int_{S_{k-1}}^{S_k} \iiint_{\mathbb{R}^3} S^i c_1^p c_2^q c_3^r h(\theta)^t \widetilde{f}(s, \boldsymbol{c}) \mathrm{d}S \mathrm{d}\boldsymbol{c} \mathrm{d}\theta \tag{5.50}$$

. The temperature/velocity correlations do not need to be accounted for since
(1) they are accounted for through size correlations, by transitivity,
(2) they have no physical meaning by themselves.
The conservation system then reads, for the chosen moments and with the vector notation:

$$\partial_t \begin{pmatrix} M_k^{0,0,0} \\ M_k^{3/2,0,0} \\ \boldsymbol{M}_k^{0,1,0} \\ \boldsymbol{M}_k^{3/2,1,0} \\ M_k^{0,0,1} \\ M_k^{3/2,0,1} \end{pmatrix} + \partial_{\boldsymbol{x}} \begin{pmatrix} \boldsymbol{M}_k^{0,1,0} \\ \boldsymbol{M}_k^{3/2,1,0} \\ \boldsymbol{M}_k^{0,2,0} \\ \boldsymbol{M}_k^{3/2,2,0} \\ \boldsymbol{M}_k^{0,1,1} \\ \boldsymbol{M}_k^{3/2,2,1} \end{pmatrix} = \begin{pmatrix} 0 \\ 0 \\ \boldsymbol{F}_k^0 \\ \boldsymbol{F}_k^{3/2} \\ H_k^0 \\ H_k^{3/2} \end{pmatrix} \tag{5.51}$$

where coalescence terms have been removed for the sake of legibility. The source terms may require to reconstruct other temperature moments. The temperature reconstruction routine can be performed similarly as for velocity, provided that two temperature moments are transported.
We now detail the most likely forms for source terms. As usual, they are computed with an integration versus the size variable so that a linear, Stokesian heating term reads:

$$^2\mathrm{H}_k = \frac{(T_g - T_p)}{\tau^T} \tag{5.52}$$

while a convective-corrected term such as the Ranz-Marshall heating of Eq. (3.58) has also a velocity dependent part through Re_p which must be replaced by the velocity correlation and therefore reads:

$$\begin{pmatrix} H_k^0 \\ H_k^{3/2} \end{pmatrix} = \int_{S_{k-1}}^{S_k} - \begin{pmatrix} 18\pi/\rho_l \\ 3\sqrt{\pi} S^{\frac{3}{2}} \end{pmatrix} \frac{2c_{p,l}\,{}^2\kappa_k(S)}{3c_{p,g}\mathrm{Pr}_g} \mu_g(A_k^T S + B_k^T S^2) \left[1 + 0.3 \left(\frac{\rho_g S^{\frac{1}{2}} |\boldsymbol{A_k} S + \boldsymbol{B_k} S^2|}{2\sqrt{\pi}\mu_g} \right)^{\frac{1}{2}} \mathrm{Pr}_g^{\frac{1}{3}} \right] \mathrm{d}S \tag{5.53}$$

5.4.2 Coalescence terms

5.4.2.1 Role of velocity in the coalescence integrals

Since the velocity reconstruction has a size dependency, we can no longer factorize the velocity dependent terms in the coalescence integrals at the semi-kinetic level. The kinetic velocity difference $|\,\boldsymbol{c}^\star - \boldsymbol{c}^\diamond\,|$ should be left in the coalescence integral at the multi-fluid level and replaced by its reconstructed, size dependent expression before size integration:

$$|\,\boldsymbol{c}^\star - \boldsymbol{c}^\diamond\,| = |\,\boldsymbol{u}_i(S^\star) - \boldsymbol{u}_j(S^\diamond)\,| = |\,\boldsymbol{A_i}S^\star + \boldsymbol{B_i}S^{\star 2} - \boldsymbol{A_j}S^\diamond - \boldsymbol{B_j}S^{\diamond 2}\,| \tag{5.54}$$

where we see that the gas velocity vanishes.

5.4.2.2 Elementary integrals

Compared to the case of first order in velocity given in Eq. (5.22), the elementary integrals now feature the non-factorized velocity differences:

$$\begin{pmatrix} \mathrm{Q}^n_{ijk} \\ \mathrm{Q}^\star_{ijk} \\ \mathrm{Q}^\diamond_{ijk} \\ \boldsymbol{Q}^u_{ijk} \\ \boldsymbol{Q}^{u\star}_{ijk} \\ \boldsymbol{Q}^{u\diamond}_{ijk} \end{pmatrix} = \iint_{\mathscr{D}_{ijk}} \begin{pmatrix} 1 \\ m(S^\star) \\ m(S^\diamond) \\ \boldsymbol{u}_g + \boldsymbol{A_i}S^\star + \boldsymbol{B_i}S^{\star 2} \\ \left(\boldsymbol{u}_g + \boldsymbol{A_j}S^\diamond + \boldsymbol{B_j}S^{\diamond 2}\right) m(S^\star) \\ \left(\boldsymbol{u}_g + \boldsymbol{A_i}S^\star + \boldsymbol{B_i}S^{\star 2}\right) m(S^\diamond) \end{pmatrix} {}^2\kappa_i(S^\star)^2\kappa_j(S^\diamond)\,\left|\boldsymbol{A_i}S^\star + \boldsymbol{B_i}S^{\star 2} - \boldsymbol{A_j}S^\diamond - \boldsymbol{B_j}S^{\diamond 2}\right| \pi(r^\star + r^\diamond)^2 \mathrm{d}S^\star \mathrm{d}S^\diamond \tag{5.55}$$

and the velocity moments must be integrated in addition. The coalescence terms are then combined as follows:

$$\begin{pmatrix} \mathrm{C}^{0,0+}_k \\ \mathrm{C}^{3/2,0+}_k \\ \mathrm{C}^{\boldsymbol{0,1+}}_{\boldsymbol{k}} \\ \mathrm{C}^{\boldsymbol{3/2,1+}}_{\boldsymbol{k}} \end{pmatrix} = \sum_{i=1}^{k}\sum_{j=1}^{i} \left\{ \begin{pmatrix} \frac{1}{2}\mathrm{Q}^n_{ijk} \\ \mathrm{Q}^\star_{ijk} \\ \frac{1}{2}\boldsymbol{Q}^u_{ijk} \\ \boldsymbol{Q}^{u\star}_{ijk} \end{pmatrix} + \begin{pmatrix} \frac{1}{2}\mathrm{Q}^n_{ijk} \\ \mathrm{Q}^\diamond_{ijk} \\ \frac{1}{2}\boldsymbol{Q}^u_{ijk} \\ \boldsymbol{Q}^{u\diamond}_{ijk} \end{pmatrix} \right\}$$

$$\begin{pmatrix} \mathrm{C}^{0,0-}_k \\ \mathrm{C}^{3/2,0-}_k \\ \mathrm{C}^{\boldsymbol{0,1-}}_{\boldsymbol{k}} \\ \mathrm{C}^{\boldsymbol{3/2,1-}}_{\boldsymbol{k}} \end{pmatrix} = \sum_{j=1}^{N_{\mathrm{sec}}}\sum_{i=1}^{N_{\mathrm{sec}}} \begin{pmatrix} \mathrm{Q}^n_{kji} \\ \mathrm{Q}^\star_{kji} \\ \boldsymbol{Q}^u_{kji} \\ \boldsymbol{Q}^{u\star}_{kji} \end{pmatrix}. \tag{5.56}$$

5.4.2.3 Remarks for practical computation

In practical cases, coalescence is computed with a 2D quadrature approach, see § 13.1.5 which requires to evaluate the integrand as many times as there are nodes. The use of the second order velocity reconstruction requires to compute the velocity difference as a function of size and to compute more terms, though quite simple: but the structure of the coalescence algorithm does not need to be changed, nor the quadrature itself, thanks to the general fact that quadratures are point-wise integrations.
Another difference arises from the fact that velocity differences are now accounted for within a section. So there are non-null coalescence terms for a section with itself, which are computed similarly as the usual terms: they describe the evolution of size due to coalescence in the section, resulting -if taken alone- in a decrease of the number at constant mass. Again, this does not require a specific algorithm and it must just be checked, when adapting a classical TSM method, that the computation of these "diagonal terms" has not been disabled in the routines.
So the upgrade of TSM into CSVTSM is straightforward and the additional computational cost, even with coalescence, is presumably mostly limited to the transport of more moments and the execution of a more complex transport scheme, as the one described in Vié et al. (2013).

5.5 Conclusions on the TSM approach

As a general conclusion, the TSM method allows to compute size information more accurately in the sections, at the cost of transporting an additional moment and performing some inversions and integral computations. It is still a versatile technique with both a reasonably high accuracy and a relatively simple algebra compared to higher order methods. As the accuracy on size is high, some cases will require higher size-correlated

velocity and temperature information, which the method allows: the CSVTSM method has been derived in this spirit, and proves the versatility of the Two Size Moment method.
In the following we qualify and use the TSM method with a single velocity moment per section. The detail of the needed algorithms and the efficiency of the TSM approach are presented in Chapter 13 and some applicative computations are performed in Chapter 15 and Chapter 16.

Chapter 6

A new model for moderately-inertial sprays: the Anisotropic Gaussian velocity closure

We introduce a new velocity closure for Eulerian modeling to account for homo-PTC, at least on small scales, and to treat the possible coalescence that follows. By transporting more velocity moments, the relative kinetic energy between droplets of the same size is estimated, avoiding the sticky particle behavior of PGD and the corresponding singularities.

6.1 The Anisotropic Gaussian velocity closure

We aim at developing a method that can account for polydispersity, coalescence, two-way coupling with the gas, and possibly break-up and evaporation, regardless of the structure of the mean flow and turbulence. For moderately inertial particles of a given size feature crossings, which is referred to as homo-PTC and is incompatible with the usual monokinetic closure, the treatment of the velocity variable must be revised. From a collaborative work with A. Vié, a velocity closure referred to as Anisotropic Gaussian (AG) has been discussed and assessed for moderately inertial disperse phase flows: this velocity closure requires few velocity moments compared to the CQMOM and MG approaches presented in § 4.5 and is therefore thought to be an interesting development for industrial simulations.

6.1.1 Motivation and objectives

6.1.1.1 Need for a Eulerian method compatible with polydispersity

Eulerian approaches have been presented as well adapted for two-way coupling and HPC. Among these the Multi-Fluid (MF) methods and especially the TSM method are shown to account efficiently for the complex size dependent physics of the disperse phase. Unfortunately this approach for size is based on a monokinetic closure which is inaccurate for moderately-inertial sprays and can deteriorate the estimation of coalescence and retrocoupling, see § 4.3.2.2. So a monokinetic based approach can yield strong discrepancies in the estimation of specific impulse loss in a SRM nozzle.

6.1.1.2 A moment method based on a velocity closure

A new Eulerian model is introduced for moderately-inertial particles. The method is a Kinetic Based Moment Method (KBMM) since it consists in assuming an underlying kinetic closure and to conserve some moments to reconstruct it: we choose an Anisotropic Gaussian velocity closure (AG) which parameters are conditioned by size. This closure, also referred to as "10-moment Gaussian" was introduced by (Levermore and Morokoff 1998) for rarefied gas dynamics since it controls all the second order velocity moments and it maximizes entropy (see a complete discussion in Vié et al. 2014). This approach was extended and applied to moderate-inertia particle-laden flows in Vié et al. (2014) in order to capture small scale PTC, and compared to the so-called Algebraic Closure Based Moment Methods (ACBMM) in Vié et al. (2012). Vié et al. (2014) provide further discussions on the necessity of an entropy formalism.
As a moment method, it can be seen as a higher order method as regards velocity compared to monokinetic based ones: the form of the closure does not necessarily need to be interpreted as having a physical meaning e.g. it does not need to correspond to a real velocity PDF, as met in moderately inertial regimes. In return,

it is a good choice considering the arguments of Levermore and Morokoff (1998) in the prospect of controlling moments of second order at most with an entropy principle on the related system.

6.1.1.3 Further issues and use of the model

The new model is designed to be hyperbolic: it no longer describes a PGD-like behavior but still a hypercompressible behavior, the physical aspects of which are detailed in § 4.3.2.3. To make things short, the hypercompressibility of the new approach is characterized by vacuum zones and zero pressure zones, alternated with weak pressure zones (and anisotropy) and these peculiarities require a well-suited numerical approach, of a new type. The connection of pressure zones with zero pressure ones has been discussed in Boileau et al. (2010) and Boileau et al. (2010). We introduce the minimum ingredients to tackle the resolution of the new model in Chapter 11, still on structured grids.
The model is then implemented in a 2D structured research code to assess its potential and validate it, see Chapter 11. It is also implemented in a 2D polydisperse code to study the resolution of coalescence in crossflows, see Chapter 13. So the model is fully characterized and validated on structured grids but the issue of its application to industrial contexts is not yet tackled in the present work.

6.1.2 Anisotropic Gaussian closure at the semi-kinetic level

The statistical analysis of the disperse phase through the Williams-Boltzmann Eq. (3.123), coupled to a carrier fluid, is still our ground model. The kinetic equation was up to now reduced by considering the monokinetic hypothesis, which fails when homo-PTC occurs, i.e. for moderately inertial sprays. We introduce a new velocity approach that is dedicated to moderately-inertial sprays and from which can be derived a family of polydisperse models.

6.1.2.1 Moment conservation equations

To reduce the size of the phase space, we choose to solve for velocity moments of order two at most. Still this allows to account for a little more information on local relative particle velocities than in the monokinetic context. Ten velocity moments, stored in a vector $\mathcal{M}$ are then needed to be conserved in 3D, which are generated by integration of the vector of kinetic velocity polynomials $\mathfrak{M}^u(\boldsymbol{c})$; they read

$$\mathcal{M} = \begin{pmatrix} M_{000} \\ M_{100} \\ M_{010} \\ M_{001} \\ M_{200} \\ M_{110} \\ M_{020} \\ M_{101} \\ M_{011} \\ M_{002} \end{pmatrix}, \qquad \mathfrak{M}^u(\boldsymbol{c}) = \begin{pmatrix} 1 \\ c_1 \\ c_2 \\ c_3 \\ c_1^2 \\ c_1c_2 \\ c_2^2 \\ c_1c_3 \\ c_2c_3 \\ c_3^2 \end{pmatrix}. \tag{6.1}$$

These moments are at most second order and include all the pure second order directional velocity moments and all the cross-directional velocity moments.
After integration of the kinetic Eq. (3.123) with respect to the kinetic velocity variable $\boldsymbol{c}$, we get the system of conservation equations with source terms:

$$\partial_t \mathcal{M} + \partial_{\boldsymbol{x}} \cdot \boldsymbol{\mathcal{F}}(\mathcal{M}) = \mathcal{S}(\mathcal{M}) + \mathscr{C}(\mathcal{M}, \mathcal{M}) + \mathscr{B}(\mathcal{M}) \tag{6.2}$$

where the flux vector $\boldsymbol{\mathcal{F}} = (\mathcal{F}_1\ \mathcal{F}_2\ \mathcal{F}_3)^T$ depends on unresolved and unclosed (for now) third order moments. The source term vector $\mathcal{S}$ here describes drag and depends on known moments if a linear form is chosen for drag e.g. Stokes. Otherwise, drag is not closed. The coalescence term $\mathscr{C}(\mathcal{M}, \mathcal{M})$ and the break-up term $\mathscr{B}(\mathcal{M})$ also are not closed. So in the general case, transport and sources are unclosed.

6.1.2.2 The 10-moment Gaussian closure

To solve the terms depending on unclosed moments, the 10-moment Gaussian velocity closure which was suggested by Levermore and Morokoff (1998) is chosen. We assume the following NDF form (Vié et al. 2014):

[HV1] $$f(t, \boldsymbol{x}, \boldsymbol{c}, S) = n(t, \boldsymbol{x}, S)\mathscr{N}(\boldsymbol{c}; \boldsymbol{u}(t, \boldsymbol{x}, S), \boldsymbol{\Sigma}(t, \boldsymbol{x}, S)) \tag{6.3}$$

where $\mathscr{N}$ is a joint Gaussian distribution (Levermore and Morokoff 1998) with $\boldsymbol{u} = (u_1\ u_2\ u_3)^T$ its center and $\boldsymbol{\Sigma} = (\sigma_{ij})$ its 3×3 covariance matrix, taken symmetric:

$$\mathscr{N}(\boldsymbol{c};\boldsymbol{u},\boldsymbol{\Sigma}) = \frac{\det(\boldsymbol{\Sigma})^{-\frac{1}{2}}}{(2\pi)^{\frac{1}{2}N_d}} \exp\left(-\frac{1}{2}(\boldsymbol{c}-\boldsymbol{u})^T\boldsymbol{\Sigma}^{-1}(\boldsymbol{c}-\boldsymbol{u})\right) \tag{6.4}$$

where N_d is again the dimension of the physical space. The covariance matrix must respect some realizability conditions that are the strict positivity of the diagonal coefficients σ_{ii} and of $\det(\boldsymbol{\Sigma})$, in link with its entropies, presented below.
Nonetheless are all the moments close and fixed by the parameters of the Gaussian closure, but they can be expressed relatively simply, as polynomials of the parameters $\boldsymbol{u}$ and $\boldsymbol{\Sigma}$ of the velocity closure: this simplicity is one reason for the choice of a Gaussian closure, which has a simple algebra and allows to reduce the cost. In particular, it appears from the expressions of the second order moments that these "energies" can be split in:

- a macroscopic energy u_iu_j linked to the mean velocities;
- a "microscopic" energy σ_{ij} linked to the agitation velocities.

In the following of our approach, both average velocity $\boldsymbol{u}(t,\boldsymbol{x},S)$ and dispersion $\boldsymbol{\Sigma}(t,\boldsymbol{x},S)$ are conditioned by size, accordingly to the semi-kinetic approach.

6.1.2.3 Expression of the moments in 2D

For the sake of clarity, we now detail the method in 2D so we need to transport only six moments:

$$\mathcal{M} = \begin{pmatrix} M_{00}\\ M_{10}\\ M_{01}\\ M_{20}\\ M_{11}\\ M_{02}\end{pmatrix} = n\begin{pmatrix} 1\\ u_1\\ u_2\\ u_1^2+\sigma_{11}\\ u_1u_2+\sigma_{12}\\ u_2^2+\sigma_{22}\end{pmatrix}. \tag{6.5}$$

The flux vector $\boldsymbol{\mathcal{F}} = (\mathcal{F}_1\ \mathcal{F}_2)^T$ depends, as said previously, on unresolved, third order moments that can be computed from $\boldsymbol{u}$ and $\boldsymbol{\Sigma}$ thanks to the Gaussian profile:

$$\mathcal{F}_1 = n\begin{pmatrix} u_1\\ u_1^2+\sigma_{11}\\ u_1u_2+\sigma_{12}\\ u_1^3+3u_1\sigma_{11}\\ u_1^2u_2+2u_1\sigma_{12}+u_2\sigma_{11}\\ u_1u_2^2+u_1\sigma_{22}+2u_2\sigma_{12}\end{pmatrix},\quad \mathcal{F}_2 = n\begin{pmatrix} u_2\\ u_1u_2+\sigma_{12}\\ u_2^2+\sigma_{22}\\ u_1^2u_2+u_2\sigma_{11}+2u_1\sigma_{12}\\ u_1u_2^2+2u_2\sigma_{12}+u_1\sigma_{22}\\ u_2^3+3u_2\sigma_{22}\end{pmatrix} \tag{6.6}$$

where space fluxes of the second order moments happen to be third order velocity moments, which are well known for a Gaussian profile. The source term vector $\mathcal{S}$ can be expressed in the case of Stokes' law:

$$\mathcal{S} = \frac{n}{\tau^{\boldsymbol{u}}}\begin{pmatrix} 0\\ -u_1+u_{g,1}\\ -u_2+u_{g,2}\\ 2u_1u_{g,1}-2u_1^2-2\sigma_{11}\\ u_1u_{g,2}+u_2u_{g,1}-2u_1u_2-2\sigma_{12}\\ 2u_2u_{g,2}-2u_2^2-2\sigma_{22}\end{pmatrix} \tag{6.7}$$

while the other source terms are detailed below.
The phase space of an AG velocity PDF is given for a 2D case in Figure 6.1, where it can be seen that the contours are ellipses.

6.1.2.4 Remarks on creation and relaxation of dispersion

We discuss the notion of velocity dispersion from a macroscopic point of view and its creation in the context of a compression flow field. The role of drag is presented as fundamental in the overall physics of the AG approach.
From the simple form of the Stokesian drag of Eq. (6.7), (which describes the ultimate step of the evolution towards an equilibrium as the particle slip velocity becomes smaller and smaller) a simple equation can be derived for each σ_{ij} by elimination of the macroscopic kinetic energy $n\boldsymbol{u}_i\boldsymbol{u}_j$:

$$\partial_t(n\sigma_{ij}) + \partial_{\boldsymbol{x}}\cdot(n\sigma_{ij}\boldsymbol{u}) = -\frac{1}{3}n\sigma_{ij}\partial_{\boldsymbol{x}}^{Sym}\boldsymbol{u} - \frac{n\sigma_{ij}}{\tau^{\boldsymbol{u}}} \tag{6.8}$$

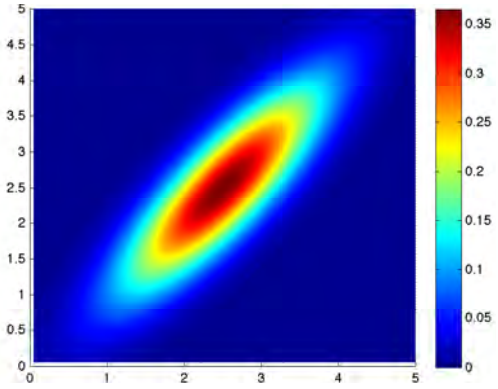

Figure 6.1: *AG velocity PDF for* $\sigma_{11} = 1$, $\sigma_{22} = 0.8$ *and* $\sigma_{12} = 0.75$.

where all the other sources are neglected. The l.h.s. of this equation describes the conservation of dispersion during transport at the local macroscopic velocity while the r.h.s. features two sources for dispersion:

- increase (decrease) due to the compression (expansion) velocity field $-\partial_{\boldsymbol{x}}^{Sym}\boldsymbol{u} > 0$ (< 0);
- relaxation due to drag towards zero at a rate $\tau^{\boldsymbol{u}}$.

This gives an overall view of the physics of AG: compressive velocity fields induce a tightening of the streamlines, possibly leading to crossings, which are accounted for by a velocity dispersion; besides, dispersion is continuously destroyed by drag, which practically tends to correlate the local particle velocities together. As a conclusion, drag plays a fundamental role in the relevance of our model. Since the Gaussian velocity closure is only an approximation, the model describes at best the physics of the disperse phase in the zones where dispersion is null i.e. when the underlying Gaussian is in fact a Dirac δ-function. Moderately-inertial sprays correspond to moderate Stokes numbers so drag is still significant: the dispersion remains moderate and the error limited. Whereas for higher Stokes numbers, drag is weak, the dispersion is high and the error induced by an approximate velocity closure becomes significant.

6.1.3 Transport model of AG

In order to study the properties of the new transport, we temporarily consider a monodisperse closure so that the size-conditioned density $n(t, \boldsymbol{x}, S)$ becomes a usual fluid density $\rho(t, \boldsymbol{x})$ in physical space.

6.1.3.1 Tensor form

The convection part of the system reads in tensorial form:

$$\begin{cases} \partial_t \rho + \partial_{\boldsymbol{x}} \cdot (\rho \boldsymbol{u}) = 0 \\ \partial_t (\rho \boldsymbol{u}) + \partial_{\boldsymbol{x}} \cdot (\rho \boldsymbol{u} \otimes \boldsymbol{u} + \boldsymbol{P}) = 0 \\ \partial_t (\rho \boldsymbol{E}) + \partial_{\boldsymbol{x}} \cdot ((\rho \boldsymbol{E} + \boldsymbol{P}) \otimes \boldsymbol{u}) = 0 \end{cases} \tag{6.9}$$

where $\otimes$ is the symmetric outer product. This form is valid in any dimension.
The equation of state reads in tensor form:

$$\rho \boldsymbol{E} = \frac{1}{2} \rho \boldsymbol{u} \otimes \boldsymbol{u} + \frac{1}{2} \boldsymbol{P} \tag{6.10}$$

where the pressure tensor is defined analogously to the Euler equation pressure:

$$\boldsymbol{P} = \rho \boldsymbol{\Sigma}. \tag{6.11}$$

6.1.3.2 Cartesian form

This system can also be written in cartesian coordinates e.g. in 2D:

$$\begin{cases} \partial_t \rho + \partial_x (\rho u_1) + \partial_y (\rho u_2) = 0 \\ \partial_t (\rho u_1) + \partial_x (\rho u_1^2 + p_{11}) + \partial_y (\rho u_1 u_2 + p_{12}) = 0 \\ \partial_t (\rho u_2) + \partial_x (\rho u_1 u_2 + p_{12}) + \partial_y (\rho u_2^2 + p_{22}) = 0 \\ \partial_t (\rho E_{11}) + \partial_x ((\rho E_{11} + p_{11}) u_1) + \partial_y (\rho E_{11} u_2 + p_{12} u_1)) = 0 \\ \partial_t (\rho E_{22}) + \partial_x (\rho E_{22} u_1 + p_{12} u_2) + \partial_y ((\rho E_{22} + p_{22}) u_2) = 0 \\ \partial_t (\rho E_{12}) + \partial_x (\rho E_{12} u_1 + (p_{11} u_2 + p_{12} u_1)/2) + \partial_y (\rho E_{12} u_2 + (p_{22} u_2 + p_{12} u_2)/2) = 0 \end{cases} \tag{6.12}$$

where the equation of state reads:

$$\rho E_{ij} = \frac{1}{2} \rho u_i u_j + \frac{1}{2} p_{ij} \tag{6.13}$$

6.1.3.3 Eigenstructure, hyperbolicity and entropies

The previous transport system Eq. (6.9) can also be projected on a chosen direction, e.g. $\boldsymbol{x}$ in order to yield a 6-equation system with partial derivatives of x only:

$$\begin{cases} \partial_t \rho + \partial_x(\rho u_1) = 0 \\ \partial_t(\rho u_1) + \partial_x(\rho u_1^2 + p_{11}) = 0 \\ \partial_t(\rho u_2) + \partial_x(\rho u_1 u_2 + p_{12}) = 0 \\ \partial_t(\rho E_{11}) + \partial_x((\rho E_{11} + p_{11})u_1) = 0 \\ \partial_t(\rho E_{22}) + \partial_x(\rho E_{22} u_1 + p_{12} u_2) = 0 \\ \partial_t(\rho E_{12}) + \partial_x(\rho E_{12} u_1 + (p_{11} u_2 + p_{12} u_1)/2) = 0 \end{cases} \tag{6.14}$$

The introduced formalism allows to directly deduce the eigenvalues, as well as hyperbolicity and entropies. The present presentation and 1D restriction are inspired from Berthon (2006), while some subtleties of the multidimensional formulation are studied in (Larat and Massot 2014) and will be essential for unstructured mesh simulation. The 1D aspects are sufficient for the Cartesian meshes we aim at using in Chapter 11. System (6.14) is hyperbolic and admits the set of eigenvalues (Berthon 2006):

$$\boldsymbol{\lambda}_x = \left(u_1, \quad u_1, \quad u_1 + \sqrt{\frac{p_{11}}{\rho}}, \quad u_1 - \sqrt{\frac{p_{11}}{\rho}}, \quad u_1 + \sqrt{\frac{3p_{11}}{\rho}}, \quad u_1 - \sqrt{\frac{3p_{11}}{\rho}} \right)^T. \tag{6.15}$$

The eigenvalue u_1 has two orders of multiplicity and is associated to a linearly degenerated field. The other eigenvalues have one order of multiplicity. The eigenvalues $u_1 \pm \sqrt{\frac{3p_{11}}{\rho}}$ are associated to genuinely nonlinear fields and the eigenvalues $u_1 \pm \sqrt{\frac{p_{11}}{\rho}}$ are associated to linearly degenerate fields.
System (6.14) is also associated to two entropy families. Considering:

$$s_{11} = \frac{p_{11}}{\rho^3} = \frac{s_{11}^2}{\rho^2}, \qquad s_{12} = \frac{p_{11}p_{22} - p_{12}^2}{\rho^4} = \frac{s_{11}s_{22} - s_{12}^2}{\rho^2} \tag{6.16}$$

a family of convex functions $\mathcal{F}(s_{11})$ and $\mathcal{G}(s_{12})$ resulting from the composition of the logarithm function and a functional that has some identified properties (Berthon 2006), as well as entropy fluxes $u_1\,\mathcal{F}(s_{11})$ and $u_1\,\mathcal{G}(s_{12})$ yield Lax entropy pairs of System (**??**) and satisfy:

$$\begin{aligned} &\partial_t \rho \mathcal{F}(s_{11}) + \partial_x \left(u_1\,\mathcal{F}(s_{11}) \right) \leq 0 \\ &\partial_t \rho \mathcal{G}(s_{12}) + \partial_x \left(u_1\,\mathcal{G}(s_{12}) \right) \leq 0. \end{aligned} \tag{6.17}$$

Such an approach allows to treat the shocks that can naturally appear in Eulerian moment models and also to rely on the large literature devoted to Godunov-like schemes. The entropy conditions are needed to rule out unphysical solutions, their growth must be respected by any numerical scheme to obtain the physical solutions. The entropy conditions are used in § 11.1.1 to define realizability and to design a transport scheme.

6.1.4 Treatment of source terms

While the treatment of coalescence is detailed in § 6.3, we briefly discuss the other source terms.

6.1.4.1 Drag source term

The drag source term is easily expressed in the context of a linear, Stokesian expression, see Eq. (6.7).
In the case of velocity dependent closures, e.g. Schiller-Naumann, the knowledge of the velocity distribution allows to close the term by performing an additional integration on the velocity reconstruction.

6.1.4.2 Heat source term

The model as written up to now does not include the treatment of particle enthalpy and heat transfers. We suggest to use a monokinetic assumption for temperature [HT1] and [HT2]. A higher order method can be considered whenever temperature dispersion is of interest (Couzinet 2008; Masi 2010). But we limit for now our approach to the mean temperature as the dispersion does not play, in our case, a role on transport nor on complex source terms.
In the context of a monokinetic closure for temperature, heat transfers are assessed similarly as for the usual case as long as they do not depend on velocities. In the case of velocity dependent closures, e.g. the Ranz-Marshall law which depends on Re_p, the knowledge of the velocity distribution allows to close the term.

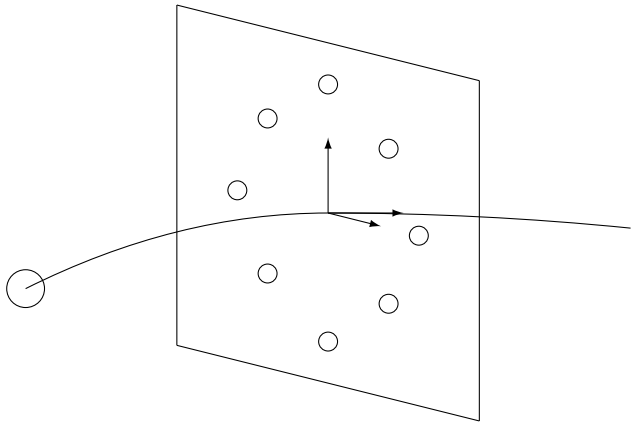

Figure 6.2: *A modeling for the post-break-up velocities – Assumption of a dispersion in the normal plane to the trajectory.*

6.1.4.3 Evaporation

The extension to evaporation is not discussed but is straightforward as evaporation terms depend mostly on the size variable. In addition, the transfers of velocities and energies from a section to another are treated with the usual conservative approach.
For simple cases such as the d2-law, there is no dependence on velocity and the terms are unchanged compared to a monokinetic cases. For advanced cases with convective correction, the knowledge of the velocity distribution allows to close the terms.

6.1.4.4 Break-up

The extension to break-up is performed as follows: the computation of the break-up rates is straightforward as we have the knowledge of the velocity distribution.
The main difficulty comes from the fact that the evolution of velocities for the fragments during the break-up process are not well known. In the presumed PDF break-up approach, presented in § 3.5.3.1, the velocity evolution during break-up is mainly modeled, as instantaneous and the resulting velocities are assessed with an experimental closure. We do not have such correlations for velocity dispersions.
We suggest two physical leads to model the break-up induced dispersion:

- (i) dispersion appears in the plane orthogonal to the mother droplet velocities (see Figure 6.2), rendering the burst of the structure (rim, bag *etc.*);
- (ii) dispersion is negligible in all directions as the droplets are much smaller so their inertia is negligible.

The occurrence of case (ii) can be confirmed by checking the daughter droplet Stokes number. Whatever modeling is chosen, we recall that the velocity evolution in such modelings is non-conservative *a priori*. Momentum conservation must be enforced purposely in two-way coupling cases, whenever the chosen presumed PDFs are still valid, as regards the mass and volume fractions.

6.2 Comparative study of velocity closures

6.2.1 Fundamental case of two crossing jets

To assess the behavior of the AG approach compared to a monokinetic one when a crossing occurs, a model problem is considered of two jets of particles that cross. The case is assumed to occur:

- at infinite Knudsen so that the two clouds do not interact;
- at infinite Stokes so that the gas does not relax the particle velocities at all.

The latter simplification assumption is that of infinite inertia so that no space scale is introduced by the gas relaxation, the AG model is therefore not well suited, as discussed in § 6.1.2.4, but it has still an interesting behavior to illustrate its features.
The exact case is described as follows: two jets flow at the same velocity in the same plane and cross with an angle 2α. In the appropriate cartesian system of coordinates, they both come from the left, they are symmetrical with respect to the $\boldsymbol{x}$-axis and meet at the origin.
This test case is studied as regards coalescence in § 7.4. However the infinite Stokes hypothesis is not consistent with moderately inertial sprays, where drag plays a role. So a similar test case with a Stokes number not too far from one is used for a transport test case in § 11.3, and again for coalescence in § 13.4.

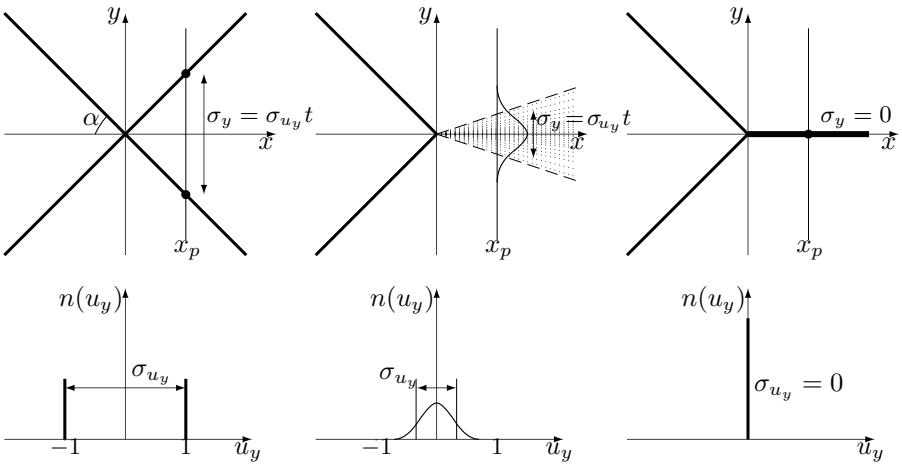

Figure 6.3: *Spray trajectories and y velocity component distribution at origin when homo-PTC occurs with infinite inertia – Left: Bikinetic ($Kn = +\infty$ effective); Middle: single-peak with dispersion (Euler or AG); Right: Monokinetic (Classical MF).*

6.2.2 Response of different Eulerian models to the crossing

The ability to reproduce the velocity distribution at the origin of the crossing (and therefore the modeling level) conditions the spray repartition for $x > 0$: the latter depends on the number of velocity moments that are resolved at the semi-kinetic level.
We perform an *a priori* analysis of the characteristics at the crossing location. First, the x velocity component is exactly resolved whatever the model since it is equal and constant for particles of both jets before and after crossing. Second, the y velocity component does not evolve from its value at the origin i.e. attributed by the model closure. The spatial distribution in a y-wise cut at $x_p \geq 0$ can then be assessed and it is a homothety of the y velocity component distribution at the origin. Figure 6.3 illustrates how this case is resolved with three different approaches, based on this analysis.
The numerical solution of the problem with different approaches is given in Figure 6.4 for comparison purpose but is not needed.

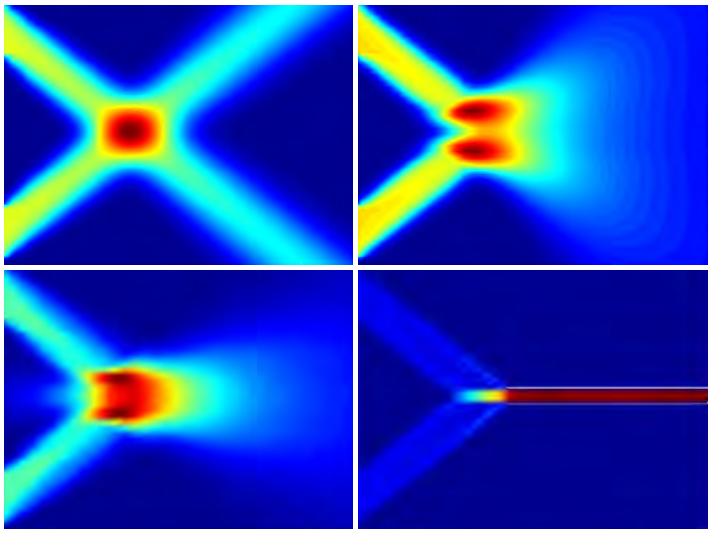

Figure 6.4: *Computation of homo-PTC treatment for $Kn = +\infty$ depending on the velocity reconstruction – Top left: two velocities; Top right: Anistoropic Gaussian; Bottom left: Isotropic Gaussian; Bottom right: monokinetic.*

6.2.2.1 Monokinetic response to the crossing

In the classical monokinetic context, we solve only one first order velocity moment (a vector). Coexisting velocities are therefore averaged for momentum conservation reasons so we can not account for deterministic particle trajectory crossings (homo-PTC): the equivalence between the kinetic and the semi-kinetic level is eventually broken and an unphysical δ-shock appears (§ 4.3.2.2).
The case of two crossing jets has been studied with a monokinetic closure by Kah (2010). The relative macroscopic kinetic energy between the two jets is lost and the out-of-equilibrium physics is not rendered.

The δ-shock is advected at a velocity corresponding to the average momentum, in the $\boldsymbol{x}$-direction This analysis is illustrated in Figure 6.3, right.
This type of computation is reproduced in Figure 6.4, where it can be seen that the space discretization has an additional impact on the δ-shock discrepancy: the numerical δ-shock has a characteristic length (its width) which is conditioned by the mesh.

6.2.2.2 Single peak response

Single peak models are defined as models where the underlying velocity distribution has a unique maximum. In single peak models, the relative macroscopic kinetic energy is transferred towards a microscopic one i.e. dispersion by the means of energy conservation. Let us analyze how the single peak models behave after a crossing.
The particle density in a y-cut after the crossing point is continuous. It here features a Gaussian shape as a consequence of the characteristic trajectories of particles from the origin, which have been allocated a Gaussian velocity distribution. This fact is illustrated in Figure 6.3, middle.
The distinction is made between the Euler equations (presented in Eq. (3.101)) which correspond to an underlying isotropic Gaussian distribution and AG. The first one conserves a unique energy and the flux is computed from a single "pressure" while the second one conserves directional energies and has directional "pressures". The consequences can be compared in the computations of Figure 6.4, where the Euler closure produces a flux in all directions, while the AG one has a repartition only in the $x > 0$ half-plane. This indicates that energy has not been transferred to another direction than y; let us quantify this fact.
If we define the y-directional space moments:

$$M_p^y(x) = \int y^p n(x,y) \mathrm{d}y \tag{6.18}$$

it appears in this simple case that AG has the same $M_p^y(x)$ moments than the exact solution for p up to 2, while Euler has an unsatisfactory space repartition corresponding to an erroneous spatial dispersion in the y-cuts. This loss is due to the repartition of energy in all the directions. So back to the characteristics analysis of Figure 6.3, the AG spatial dispersion M_2^y, noted σ_y, matches that of the exact solution. As a conclusion, the AG closure is the only one to feature the correct space length scale in the y-direction, thanks to its ability to preserve the anisotropy of the case.
As a general conclusion when homo-PTC occurs, the loss of relative kinetic energy in the resolved velocity flux is recovered by the dispersion (induced by the velocity divergence), which yields in return an additional flux. This flux can be isotropic $p\mathbf{I}$ with Euler or directional with AG but only the latter reproduces well the space structures as the energy is redistributed in the corresponding direction only. This justifies the choice of a model which includes anisotropy: the initial particle problem is very different from standard (isotropic) gas dynamics since there is no physical phenomenon (e.g. collisions) on which we can rely to re-isotropize the unresolved velocities. In return, drag is used to relax the velocities towards the monokinetic, fundamental state, as stated in § 6.1.2.4.

6.2.2.3 Multi-peak response

Multi-peak approaches are those with multiple maxima in the velocity reconstruction: QMOM, CQMOM and MG correspond to this definition, see § 4.5.
In principle, all these approaches can render the exact physics of the crossing case since the exact distribution (at the kinetic level) can be reproduced exactly by these methods. This is illustrated in Figure 6.3, left, where the velocity distribution at origin is reproduced as two Dirac δ-functions, whatever the multi-peak closure.
In terms of moments, rendering such a crossing corresponds to the ability to preserve some third order (skewness) velocity moments.
The effective solution with a multi-peak approach is shown in Figure 6.4 and it matches the exact solution of two jets that do not interact at all.

6.3 Coalescence with AG: rendering a velocity-based source term

We describe the coalescence source terms in the AG formalism and extend it to an affordable approach that is discretized in size, thanks to the Multi-Fluid formalism. The TSM method is chosen as it allows to reduce significantly the number of sections.
The method is then implemented in a research code for validation purpose, the results being presented in § 13.4. A semi-analytical validation and a comparison to a Lagrangian DPS (see § 3.2.2) are performed on a crossing jet case in order to qualify the proposed approach and assess its potential.

6.3.1 Motivation

Capturing collision rates and possibly coalescence is crucial and becomes difficult in the situation of homo-PTC, as the system is strongly multivariate.
Thanks to the AG closure, the collision rates can be computed with the second order velocity moment information in each direction at crossing locations. The reduction of the formalism regarding size variable is done with a MF approach based on a Two Size Moment reconstruction that allows to use few sections and limits the cost in the perspective of industrial computations. We then propose an integration algorithm for the complex velocity integrals arising in the coalescence terms.

6.3.2 AG coalescence operator

6.3.2.1 A usual semi-kinetic form

Considering the kinetic modeling of the coalescence operator given in § 3.5.2.4, the AG coalescence operator is obtained by substituting the velocity closure of Eq. (6.4):

$$\begin{aligned}\mathscr{C} = \frac{1}{2}\iint_{\mathbb{R}^{2N_d}}\int_{v^\star\in[0,v]} \mathcal{C}\left(\boldsymbol{c}^\star,\boldsymbol{c}^\diamond\right) n(v^\star)\mathscr{N}(\boldsymbol{c}^\star;v^\star)n(v^\diamond)\mathscr{N}(\boldsymbol{c}^\diamond;v^\diamond)\mathfrak{K}_{\text{coal}}(v^\star,v^\diamond,\boldsymbol{c}^\star,\boldsymbol{c}^\diamond)\mathrm{d}v^\star\mathrm{d}\boldsymbol{c}^\star\mathrm{d}\boldsymbol{c}^\diamond \\ -n(v)\iint_{\mathbb{R}^{2N_d}}\int_{v^\star\in[0,+\infty[}\mathcal{M}^u(\boldsymbol{c})\mathscr{N}(\boldsymbol{c};v)n(v^\star)\mathscr{N}(\boldsymbol{c}^\star;v^\star)\mathfrak{K}_{\text{coal}}(v,v^\star,\boldsymbol{c},\boldsymbol{c}^\star)\mathrm{d}v^\star\mathrm{d}\boldsymbol{c}^\star\mathrm{d}\boldsymbol{c}\end{aligned} \tag{6.19}$$

where the velocity distributions are conditioned by size through their macroscopic parameters e.g. $\mathscr{N}(\boldsymbol{c}^\star;v^\star) = \mathscr{N}\big(\boldsymbol{c}^\star;\boldsymbol{u}(v^\star),\boldsymbol{\Sigma}(v^\star)\big)$ and where $\mathcal{C}$ is the coalescence creation function vector that renders the transformations of coalescence on microscopic variables, from the relations defined in Eq. (3.73) and in Eq. (3.74) for the second order moments. Remarkably the latter are not conserved, as a property of coalescence which is perfectly inelastic.

6.3.2.2 Velocity formalism

To handle the coalescence terms, the moment formalism is detailed. The microscopic coalescence transformations are regrouped in a vector:

$$\mathcal{C}(\boldsymbol{c}^\star,\boldsymbol{c}^\diamond) = \begin{pmatrix} 1 \\ (v^\star c_1^\star + v^\diamond c_1^\diamond)/v \\ (v^\star c_2^\star + v^\diamond c_2^\diamond)/v \\ (v^\star c_1^\star + v^\diamond c_1^\diamond)^2/v^2 \\ (v^\star c_1^\star + v^\diamond c_1^\diamond)(v^\star c_2^\star + v^\diamond c_2^\diamond)/v^2 \\ (v^\star c_2^\star + v^\diamond c_2^\diamond)^2/v^2 \end{pmatrix} \tag{6.20}$$

keeping in mind that $v = v^\star + v^\diamond$
The above vector can be decomposed, in the present modeling, as a vector $\mathfrak{P}$ of linear combinations of one among the following size monomials:

$$\mathcal{C}^s(v^\star,v^\diamond) = (1 \;\; v^\star/v \;\; v^\diamond/v \;\; v^{\star 2}/v^2 \;\; v^\star v^\diamond/v^2 \;\; v^{\diamond 2}/v^2)^T \tag{6.21}$$

and one among the second order velocity monomials:

$$\mathcal{C}^u(\boldsymbol{c}^\star,\boldsymbol{c}^\diamond) = (1 \;\; \boldsymbol{c}_1^\star \;\; \boldsymbol{c}_1^\diamond \;\; \boldsymbol{c}_2^\star \;\; \boldsymbol{c}_2^\diamond \;\; \boldsymbol{c}_1^{\star 2} \;\; \boldsymbol{c}_1^{\diamond 2} \;\; \boldsymbol{c}_1^\star\boldsymbol{c}_1^\diamond \;\; \boldsymbol{c}_2^\star\boldsymbol{c}_2^\diamond \;\; \boldsymbol{c}_1^\star\boldsymbol{c}_2^\diamond \;\; \boldsymbol{c}_2^\star\boldsymbol{c}_1^\diamond)^T. \tag{6.22}$$

This decomposition formally reads:

$$\mathcal{C}(\boldsymbol{c}^\star,\boldsymbol{c}^\diamond) \triangleq \mathfrak{P}\big(\mathcal{C}^s(v^\star,v^\diamond),\mathcal{C}^u(\boldsymbol{c}^\star,\boldsymbol{c}^\diamond)\big) \tag{6.23}$$

and allows to compute separately velocity and size integrals in the following. We highlight that this is not possible in correlated size-velocity methods, such as § 5.4.2.

6.3.3 Multi-Fluid approach with the Anisotropic Gaussian velocity closure

The second modeling step leads to the so-called Eulerian Multi-Fluid model (Laurent and Massot 2001), here applied to the previous semi-kinetic approach with AG.

6.3.3.1 Usual sectional discretization

We choose a discretization $0 = S_0 < S_1 < \cdots < S_{N_{\text{sec}}} = +\infty$ for the droplet size phase space and we average System (6.2) over each fixed size interval $\mathscr{S}_k = [S_{k-1}, S_k[$, called section. The set of droplets in one section can be seen as a "fluid" for which conservation equations are written, the sections exchanging mass, momentum and enthalpy. In order to close the system, assumptions are introduced in each section k:

[HS1] The form of $n(S) = \kappa_k^s(S)$ is presumed.

[HV2] The form of $\mathscr{N}$ is fixed as $\mathscr{N}_k$ so that $\big(\boldsymbol{u}(S), \boldsymbol{\Sigma}(S)\big) = \big(\boldsymbol{u}_k, \boldsymbol{\Sigma}_k\big)$.

We consider the TSM Multi-Fluid approach which is described in Chapter 5 so the distributions chosen for [HS1] have two parameters and the two corresponding moments are number n_k and mass m_k, generated by integration versus the moment generator vector

$$\mathcal{M}_k^s(S) = \begin{pmatrix} 1 \\ \frac{\rho_l}{6\sqrt{\pi}} S^{\frac{3}{2}} \end{pmatrix} \tag{6.24}$$

on the section interval $\mathscr{S}_k$.

6.3.3.2 TSM-AG conservation equations

The TSM formalism has been chosen for size and its equations are presented without loss of generality as the AG velocity approach can be adapted to any size formalism, though with extra-work in the case of coupled size velocities. The resulting model is referred to as TSM-AG.

After integration of System (6.2) on the $\mathscr{S}_k$, we get the Multi-Fluid systems:

$$\partial_t \mathcal{M}_k + \partial_{\boldsymbol{x}} \cdot \boldsymbol{\mathcal{F}}_k(\mathcal{M}_k) = \mathcal{S}_k(\mathcal{M}_k) + \mathscr{C}_k\big((\mathcal{M}_i)_{1,N_{\text{sec}}}\big) \tag{6.25}$$

acting on the vector of the variables of section k:

$$\mathcal{M}_k = \begin{pmatrix} n_k \\ m_k \\ m_k u_{k1} \\ m_k u_{k2} \\ m_k(u_{k1}^2 + \sigma_{k11}) \\ m_k(u_{k1}u_{k2} + \sigma_{k12}) \\ m_k(u_{k2}^2 + \sigma_{k22}) \end{pmatrix} \tag{6.26}$$

which counts seven (eleven) elements in 2D (3D).

6.3.3.3 TSM-AG coalescence terms

The coalescence terms are now size and velocity integrals decomposed as sums thanks to the continuity of the size partitioning in sections:

$$\mathscr{C}_k\big((\mathcal{M}_i)_{i=1,N_{\text{sec}}}\big) = \sum_{i+j=k} \mathfrak{P}_{\text{MF}}\left(\mathcal{I}_{ij}^u, \mathcal{I}_{ijk}^s\right) - \sum_{i,j} \mathfrak{P}_{\text{MF}}\left(\mathcal{I}_{ki}^u, \mathcal{I}_{kij}^s\right) \tag{6.27}$$

where the two terms have been integrated in the context of the creation terms, the disappearance terms being recombined to ensure mass conservation. We highlight that $\mathfrak{P}_{\text{MF}}$ is still a vector of linear combinations of multivariate size and velocity monomials but with respect to the required size moments at the Multi-Fluid level:

$$\mathcal{C}_{\text{MF}}^s = (1 \;\; v^\star \;\; v^\diamond \;\; v^{\star 2}/v \;\; v^\star v^\diamond/v \;\; v^{\diamond 2}/v) \tag{6.28}$$

The velocity integrals:

$$\mathcal{I}_{ij}^u = \iint_{(\boldsymbol{c}^\star, \boldsymbol{c}^\diamond) \in \mathbb{R}^{2N_d}} \mathcal{C}^u\left(\boldsymbol{c}^\star, \boldsymbol{c}^\diamond\right) \mathscr{N}_i(\boldsymbol{c}^\star) \mathscr{N}_j(\boldsymbol{c}^\diamond) \beta^u(\boldsymbol{c}^\star, \boldsymbol{c}^\diamond) \mathrm{d}\boldsymbol{c}^\star \mathrm{d}\boldsymbol{c}^\diamond \tag{6.29}$$

have been integrated twice on the velocity phase space and the size integrals:

$$\mathcal{I}_{ijk}^s = \iint_{(S^\star, S^\diamond) \in \mathscr{D}_{ijk}} \mathcal{C}_{\text{MF}}^s(S^\star, S^\diamond)\, \kappa_i^s(S^\star)\, \kappa_j^s(S^\diamond) \beta^s(S^\star, S^\diamond) \mathrm{d}S^\star \mathrm{d}S^\diamond \tag{6.30}$$

have been integrated on a section and on a portion of the partner size space. Yet the first dependency does not coincide with any section after mapping onto the colliding partners i and j. So domains are defined to ensure mass conservation (Laurent et al. 2004; Doisneau et al. 2013), as illustrated in Figure 4.10, and they are triply indexed with the two precursor section numbers i and j and the destination section number k. This form shows the decoupling between size and velocity integrals.

6.3.3.4 Remarks on numerical approach for coalescence integrals

Since the velocity reconstruction $\mathscr{M}_k(\boldsymbol{c};\boldsymbol{u}_k,\boldsymbol{\Sigma}_k)$ and size reconstruction $\kappa_k^s(S)$ change at each time and location, we need to compute the coalescence integrals very often and for each pair of sections.
The size integrals (6.30) on $\mathscr{D}_{ijk}$ are as complex as in any TSM MF approach (as long as no size-velocity correlations are accounted for) so we use the same method for all the size integrals, described in § 13.1.5.
The velocity integrals require a specific development as the AG model is the first model with a complex velocity reconstruction to include coalescence terms. These developments are presented in § 13.4.

6.4 Coupling AG to the gas

Accounting for two-way coupling is crucial for AG as we have developed the model to deal with moderately inertial sprays in order to treat the nozzle of a SRM.
The extension to two-way coupling is now performed. The source terms for the disperse phase and the gas are computed. A numerical strategy for HPC can be built, resorting to splitting techniques presented in Chapter 12. This numerical approach is successfully assessed for two-phase acoustics and are promising for the stiff coupling between sections, generated by coalescence.

6.4.1 Full system for two-way coupled AG

6.4.1.1 General system

We consider a TSM-AG system fully coupled to the gas equations, say Euler equations. The disperse phase particle enthalpy is treated with [HT1] and [HT2] assumptions, yielding a single equation for enthalpy. The full system reads, without considering the size phase space sources:

$$\left\{\begin{array}{l}
\partial_t\rho_g+\partial_{\boldsymbol{x}}\cdot(\rho_g\boldsymbol{u}_g)=0\\
\partial_t(\rho_g\boldsymbol{u}_g)+\partial_{\boldsymbol{x}}\cdot(\rho_g\boldsymbol{u}_g\otimes\boldsymbol{u}_g)=-\partial_{\boldsymbol{x}}p-\displaystyle\sum_{k=1}m_k\boldsymbol{F}_k\\
\partial_t(\rho_g e_g)+\partial_{\boldsymbol{x}}\cdot(\rho_g e_g\boldsymbol{u}_g)=-p_g\partial_{\boldsymbol{x}}\cdot\boldsymbol{u}_g-\displaystyle\sum_{k=1}m_k\mathrm{H}_k-\sum_{k=1}m_k\mathrm{Trace}(\boldsymbol{F}_k^E)\\
\left.\begin{array}{l}
\partial_t n_k+\partial_{\boldsymbol{x}}\cdot(n_k\boldsymbol{u}_k)=0\\
\partial_t m_k+\partial_{\boldsymbol{x}}\cdot(m_k\boldsymbol{u}_k)=0\\
\partial_t(m_k\boldsymbol{u}_k)+\partial_{\boldsymbol{x}}\cdot(m_k\boldsymbol{u}_k\otimes\boldsymbol{u}_k+\boldsymbol{P}_k)=m_k\boldsymbol{F}_k\\
\partial_t(m_k\boldsymbol{E}_k)+\partial_{\boldsymbol{x}}\cdot((m_k\boldsymbol{E}_k+\boldsymbol{P}_k)\otimes\boldsymbol{u}_k)=m_k\boldsymbol{F}_k^E\\
\partial_t(m_k h_k)+\partial_{\boldsymbol{x}}\cdot(m_k h_k\boldsymbol{u}_k)=m_k\mathrm{H}_k
\end{array}\right\}\quad k\in[\![1,N_{\mathrm{sec}}]\!]
\end{array}\right.\tag{6.31}$$

where the retrocoupling terms to the gas are computed as usual, see § 3.5.1.5 but with the TSM-AG size and velocity closures so a new term $\boldsymbol{F}_k^E$ must be integrated to account for relaxation in the disperse phase energy equation.
The effect of drag non-linearities on the coupling is not assessed as the system becomes linear when it gets closer to the equilibrium. We highlight that the non-linear regime is important in the nozzle, where the Schiller-Naumann non-linear correlation is valid.

6.4.1.2 Linear coupling

We assume linear Stokesian transfers and we finally get the following model system:

$$\left\{\begin{array}{l}
\partial_t\rho_g+\partial_{\boldsymbol{x}}\cdot(\rho_g\boldsymbol{u}_g)=0\\
\partial_t(\rho_g\boldsymbol{u}_g)+\partial_{\boldsymbol{x}}\cdot(\rho_g\boldsymbol{u}_g\otimes\boldsymbol{u}_g)=-\partial_{\boldsymbol{x}}p-\displaystyle\sum_{k=1}m_k\frac{\boldsymbol{u}_g-\boldsymbol{u}_k}{\overline{\tau}_k^u}\\
\partial_t(\rho_g e_g)+\partial_{\boldsymbol{x}}\cdot(\rho_g e_g\boldsymbol{u}_g)=-p\partial_{\boldsymbol{x}}\cdot\boldsymbol{u}_g-\displaystyle\sum_{k=1}m_k\frac{T_g-T_k}{\overline{\tau}_k^T}-\sum_{k=1}m_k\frac{\mathrm{Trace}(\boldsymbol{u}_g\otimes\boldsymbol{u}_k-\boldsymbol{E}_k)}{\overline{\tau}_k^u}\\
\left.\begin{array}{l}
\partial_t m_k+\partial_{\boldsymbol{x}}\cdot(m_k\boldsymbol{u}_k)=0\\
\partial_t(m_k\boldsymbol{u}_k)+\partial_{\boldsymbol{x}}\cdot(m_k\boldsymbol{u}_k\otimes\boldsymbol{u}_k+\boldsymbol{P}_k)=-m_k\dfrac{\boldsymbol{u}_k-\boldsymbol{u}_g}{\overline{\tau}_k^u}\\
\partial_t(m_k\boldsymbol{E}_k)+\partial_{\boldsymbol{x}}\cdot((m_k\boldsymbol{E}_k+\boldsymbol{P}_k)\otimes\boldsymbol{u}_k)=-m_k\dfrac{\boldsymbol{E}_k-\boldsymbol{u}_g\otimes\boldsymbol{u}_k}{\overline{\tau}_k^u}\\
\partial_t(m_k h_k)+\partial_{\boldsymbol{x}}\cdot(m_k h_k\boldsymbol{u}_k)=m_k\dfrac{T_g-T_k}{\overline{\tau}_k^T}
\end{array}\right\}\quad k\in[\![1,N_{\mathrm{sec}}]\!]
\end{array}\right.\tag{6.32}$$

The System (6.32) describes a modeled two-way coupling for moderately inertial cases and is referred to as "Euler-AG". It features source terms that are very similar to the usual ones of "Euler-PGD", given in System (4.70).
The gas energy equation sees an additional contribution due to the energy dissipated by the relaxation of dispersion which is of the form

$$\sum_{k=1} m_k \boldsymbol{F}_k^E - \sum_{k=1} m_k \boldsymbol{F}_k \cdot (\boldsymbol{u}_g - \boldsymbol{u}_k) = \sum_{k=1} m_k \frac{\mathrm{Trace}(\boldsymbol{e}_k)}{\frac{1}{\tau_k^u}} \tag{6.33}$$

and is presumably negligible compared to the work of the drag force applied to the resolved velocity.

6.4.2 Hyperbolicity of Euler-AG system

6.4.2.1 Hyperbolicity of an Euler-AG system

The new system is very close to the usual Euler-PGD one but it has a slightly different structure as the AG systems are strictly hyperbolic while PGD was only weakly hyperbolic. The hyperbolicity of an Euler-AG system is proven as a result of the hyperbolicity of the two sub-systems, which are only coupled through source terms.

6.4.2.2 Comparison to the usual Euler-PGD system

First, let us state that the Euler-AG system retrieves the Euler-PGD in the "zero-temperature" limit i.e. when the covariance matrix $\boldsymbol{\Sigma}$ tends to zero. Contrary to Euler-PGD, the Euler-AG transport part conserves the energies which is a major difference: dissipation of particle relative kinetic energy occurs only with the source terms.
We moreover suggest to consider the non-convective ("acoustic") eigenvalues of the disperse phase, given in Eq. (6.1.3.3), as very weak. The spray is still a hypercompressible medium in which acoustic waves propagate very slowly so in first approximation they can be neglected and the behavior of the system can be associated to that of the two-way coupled Euler-PGD, as regards peculiar behaviors, the only difference consisting in the absence of δ-shocks and the ability to assess the sprawl of crossing clouds. So thin and dense structures may occur, but their thickness is driven by physical aspects contrary to the case of δ-shocks: the AG model features a more satisfactory behavior and is well-posed, though it is still hypercompressible. The practical issues raised by hypercompressibility have been discussed in Chapter 4.3.2.3.

6.4.3 Conclusion on two-way coupled moderately inertial sprays

The Anisotropic Gaussian can be two-way coupled to the carrier phase in a similar way to other Eulerian models. In its two-way coupled model form, Euler-AG, features source terms that are very close to those of the usual monokinetic closure Euler-PGD. But in addition, the system is hyperbolic so the structures are always well-defined and unphysical δ-shocks do not occur. So the new AG model is well-suited to treat moderately inertial cases when they are also moderately dense: the accurate treatment of crossing zones is presumably required to assess correctly the retrocoupling and the overall two-phase flow dynamics, which AG can do efficiently while the usual monokinetic closure would bring in discrepancies.

6.5 Conclusions on the AG model

As a conclusion, the Anisotropic Gaussian velocity closure is well-suited to account for homo-PTC. The method is promising for moderately dense polydisperse two-phase flows, to treat the portion of droplets that has a significant enough inertia, because the AG model, which can account for coalescence and two-way coupling, is compliant with the Multi-Fluid method for polydispersity.
A numerical scheme for physical transport on structured grids is developed in Chapter 11, to study the method on academic cases. The numerical strategies developed in Chapter 12 for a high-fidelity two-way coupling of Euler-PGD can also be used for Euler-AG. A strategy for coalescence is developed and validated in Chapter 13. From this series of developments the AG model is fully validated on academic cases for crossing dynamics, two-way coupling and coalescence and further studies are required to apply it to an industrial context.

Chapter 7

Specifically isolated physics in various asymptotics: simplified models with detailed resolution for validation purpose

In this chapter, some specific physical phenomena are considered as isolated: models are derived in various asymptotics as a basis for physical analysis or for the validation of high-fidelity approaches. A first development deals with two-way coupling in the simplified context of the linear propagation of a small perturbation in a disperse two-phase medium: an existing formula for monodisperse cases is classically used to validate numerical approaches, and we extend it to polydisperse cases. A second and third developments deal with polydispersity through the study of a size distribution evolution under coalescence in two asymptotics: the case of hetero-DTC coalescence is studied to assess the characteristic time of size variation of some model size distributions, then the case of a bimodal distribution allows some analytical developments. In a fourth study, coalescence is finally estimated in the case of homo-DTC for a small collision rate.

7.1 Harmonic approach for quasi-uniform non-rotational sprays

We address the exact physics of acoustics in sprays and the relevance of MF methods in such contexts, in the context of a collaborative work with A. Sibra. The following linear acoustic case is a classical approach for waves in monodisperse sprays: both gas and disperse phase are uniform at rest and a non-rotational perturbation propagates, yielding a disturbance that is small compared to the quantities at rest so that the fields remain quasi-uniform. This definition will correspond in the following to the term two-phase acoustics. This physics can be used to test numerical schemes (Morfouace and Tissier 1995; Dupays 1996) in a monodisperse case since it has an analytic solution. It is here extended to polydisperse sprays in order to be the basis of quantitative evaluation of the new numerical strategy -this evaluation being performed in § 12.3. Then, the ability of MF methods to account for polydisperse acoustics is shown and the effect of size discretization is studied to draw some firm conclusions on size discretization requirements.

7.1.1 Classical dispersion relation for a monodisperse spray

7.1.1.1 Harmonic approach

We consider a monochromatic wave with a pulsation ω propagating in a spray that is homogeneous when at rest. If its amplitude is small enough for the propagation to remain linear, we can determine analytically the solution by assuming a decaying plane wave structure. This approach is analogous to the single-phase acoustics where the Euler equations can be linearized (Morse and Ingard 1987) except that the single-phase acoustics encounters no decay.
We note the speed of sound in the gas alone $c_0 = \sqrt{\gamma r T_0}$ where γ is the isentropic coefficient and r is the specific constant of the gas. The corresponding wave number is $k_0 = \omega/c_0$ and the wave period $\tau_\omega = 2\pi/\omega$. Defining the complex wave number $\underline{k} = k_1 + ik_2$, we are interested in decaying harmonic solutions with the following form:

$$\boldsymbol{u}_g(t,x) = \sin(\omega t - k_1 x)\exp(-k_2 x)\boldsymbol{u}_g^0. \tag{7.1}$$

7.1.1.2 Dispersion relation for a monodisperse spray

Temkin and Dobbins (1966) have considered conservation equations for the gas and for a phase of monodisperse particles, which are formally equivalent to a 1-section MF system, both interacting through drag and heat transfer. These transfers can be written in Stokes regime as a consequence of the linearity hypothesis. A dispersion relation for decaying harmonic waves is then derived for a monodisperse spray of droplets of size S_0:

$$\left(\frac{k}{k_0}\right)^2 = \left(1 + \frac{C}{1 - i\omega\tau^{\boldsymbol{u}}(S_0)}\right) \frac{\left(1 + \frac{C\chi_p}{1-i\omega\tau^T(S_0)}\right)}{\left(1 + \frac{C\gamma\chi_p}{1-i\omega\tau^T(S_0)}\right)} \tag{7.2}$$

with C the particle mass loading i.e. the ratio of droplet bulk density to gas density and $\chi_p = c_{p,l}/c_{p,g}$ the pressure heat capacity ratio. We note that $k_1/k_0 = c_0/c(\omega)$ with $c(\omega)$ the effective speed of sound in the spray. Temkin and Dobbins also suggest to define dimensionless coefficients to quantify attenuation and dispersion:

$$\begin{cases} \alpha^\star = \dfrac{2k_2}{Ck_0} \\ \beta^\star = \dfrac{1}{C}\left[\left(\dfrac{k_0}{k_1}\right)^2 - 1\right] \end{cases} \tag{7.3}$$

7.1.1.3 Dimensionless groupings

We can define acoustic Stokes numbers that are Stokes numbers based on an acoustic characteristic time. From Eq. (7.2), two dimensionless groupings naturally appear:

$$\mathrm{St}_\omega = \omega\tau^{\boldsymbol{u}}(S_0) \quad \text{and} \quad \mathrm{St}^\theta_\omega = \omega\tau^T(S_0) \tag{7.4}$$

that are the acoustic Stokes number St_ω and the thermal acoustic Stokes number $\mathrm{St}^\theta_\omega$. The latter is generally close to St_ω, as explained in § 3.1.2.1.

7.1.1.4 Response of a monodisperse spray

Figure 7.3 (dotted) shows the dissipation and dispersion coefficients plotted versus the wave frequency, which is proportional to the dynamic Stokes number. At low St_ω, the speed of sound converges to c_{eq} that is the speed of sound in an homogeneous mixture of gas and particles at equilibrium. It can be computed with the equivalent mixture density and the gas compressibility.
Dissipation reaches a maximum for $\alpha^\star$, when $\mathrm{St}_\omega \sim 1$. Another local maximum, usually smaller, can be distinguished if the thermal time is not so close to the dynamic time. In all the following conditions, $25\,\mu$m diameter droplets yield $\mathrm{St}_\omega = 1$ for a wave frequency around 700 Hz. As a remark, a similar development can be done in the context of evaporating droplets, which shows another attenuation peak, linked to the evaporation time: the corresponding dispersion relation is derived in Dupays (2000), (see also Dupays and Vuillot 2002). The evaporating case is not studied here.
Finally at very high Stokes number, the dimensionless dispersion coefficient tends to zero, so that the speed of sound is the one of the gas alone c_0. In this regime the particulate phase is decoupled from the gas: this fact complies with the analysis of Crowe et al. (1998) presented in § 3.1.4.1 according to which the momentum and heat coupling indices defined in Eq. (3.26) and Eq. (3.27) tend to zero:

$$\begin{aligned} &\lim_{\mathrm{St}\to+\infty} \Pi^u = 0, \\ &\lim_{\mathrm{St}^\theta\to+\infty} \Pi^T = 0. \end{aligned} \tag{7.5}$$

7.1.2 Extension for polydisperse sprays

7.1.2.1 Polydisperse acoustics with MF methods

An acoustic wave propagating in a quiet monodisperse or polydisperse spray yields drag force and heat transfer that are local and only depend on droplet size. The initial condition being the same for droplets of the same size, their velocity and temperature will evolve in the same way so the monokinetic assumptions [HV1], [HT1], [HV2] and [HT2] are exact regarding polydisperse acoustics. And so is the semi-kinetic model. We can therefore derive an extension of the formula for polydisperse sprays in a MF context (Sibra 2011):

$$\left(\frac{k}{k_0}\right)^2 = \left(1 + \sum_k \frac{C_k}{1 - i\omega\overline{\tau}^u_k}\right) \frac{\left(1 + \sum_k \frac{C_k\chi_p}{1-i\omega\overline{\tau}^T_k}\right)}{\left(1 + \sum_k \frac{C_k\gamma\chi_p}{1-i\omega\overline{\tau}^T_k}\right)} \tag{7.6}$$

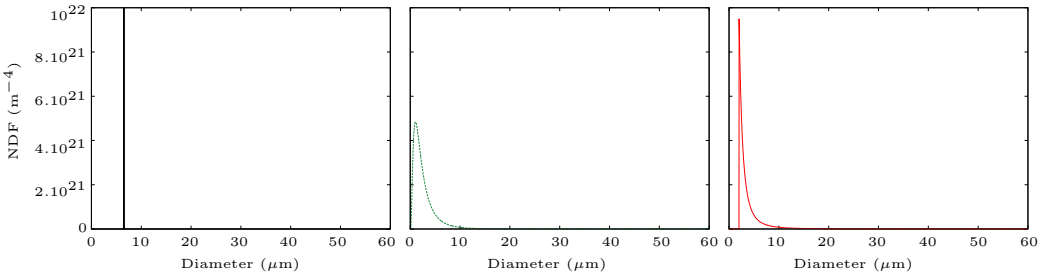

Figure 7.1: *Different number density functions (NDF) with the same total bulk density and average diameter d_{31} – Left: Dirac size distribution (monodisperse); Middle: lognormal size distribution; Right: window size distribution.*

where $C_k = m_k/\rho_g$.

7.1.2.2 Continuous formulation

Formula (7.6) converges towards a continuous formulation:

$$\left(\frac{k}{k_0}\right)^2 = \left(1 + \int_{\mathbb{R}+} \frac{\rho_l}{\rho_g} \frac{S^{\frac{3}{2}}}{6\sqrt{\pi}} \frac{n(S)}{1 - i\omega\tau^{\boldsymbol{u}}(S)} \mathrm{d}S\right) \frac{\left(1 + \int_{\mathbb{R}+} \frac{\rho_l}{\rho_g} \frac{S^{\frac{3}{2}}}{6\sqrt{\pi}} \frac{\chi_p n(S)}{1-i\omega\tau^T(S)} \mathrm{d}S\right)}{\left(1 + \int_{\mathbb{R}+} \frac{\rho_l}{\rho_g} \frac{S^{\frac{3}{2}}}{6\sqrt{\pi}} \frac{\gamma\chi_p n(S)}{1-i\omega\tau^T(S)} \mathrm{d}S\right)} \tag{7.7}$$

which is intrinsic and does not require the MF formalism and hypotheses. It is however subjugated to the semi-kinetic hypotheses.

7.1.2.3 Verification on asymptotic limits

The above relations can be studied in the limit of distributions of very small or very big droplets. We define $\mathrm{St}_{\omega,\min}$ and $\mathrm{St}_{\omega,\max}$ the acoustic Stokes number of the smallest and biggest droplet of the spray respectively. In the particular case of small mass loadings $\mu \ll 1$, we recover two limits of attenuation stated by Temkin and Dobbins (1966) (see also Harrje and Reardon 1972):

$$\alpha^\star = \begin{cases} \omega\bar{\tau}^u_{53} + (\gamma-1)\chi_p\omega\bar{\tau}^T_{53} & \mathrm{St}_{\omega,\max} \ll 1 \\ \dfrac{1}{\omega\bar{\tau}^u_{31}} + (\gamma-1)\chi_p\dfrac{1}{\omega\bar{\tau}^T_{31}} & \mathrm{St}_{\omega,\min} \gg 1 \end{cases} \tag{7.8}$$

which depend each on a specific moment of the droplet size distribution $\bar{d}_{pq}$ through the relaxation times noted e.g. $\bar{\tau}^u_{pq} = \rho_l \bar{d}^2_{pq}/(18\mu_g)$. In general cases yet, approaches based on such global moments will fail as said previously.

7.1.3 Response of some typical sprays

7.1.3.1 Response of some sprays with typical size distributions

We consider the three size distributions shown in Figure 7.1, a monodisperse distribution, a lognormal distribution -the form of which is classical in solid propulsion Price (1984a)-, and a window distribution. These distributions are chosen to have the same average diameter $d_{31} = 6.53\,\mu$m. The exact attenuation and dispersion induced by these sprays on acoustic waves are shown in Figure 7.3, as computed from the analytical relation of Eq. (7.7). Compared to the classical response of a monodisperse spray, polydisperse sprays have a wider attenuation range but a lower attenuation maximum. Moreover the response of the lognormal spray is more biased for low frequencies than the one of the window spray as a consequence of the lognormal size distribution tail. As a conclusion, polydispersity has an impact on acoustic waves as soon as it has a significant mass of droplets with Stokes numbers separated by at least one decade, which we refer to as "genuine polydispersity".

7.1.3.2 Exact responses

Polydispersity is shown to have an impact on acoustic waves, as discussed in § 4.7.3.2. Figure 7.1. It can be considered as "effective polydispersity" (as defined in § 3.1.2.2) regarding acoustics as soon as it has a significant mass of droplets with Stokes numbers separated from at least two decades.

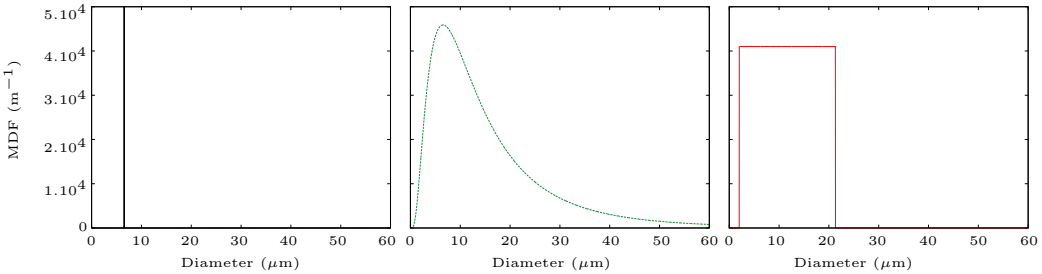

Figure 7.2: *Different mass density functions (MDF = $4/3\pi r^3 NDF$) with the same total bulk density and average diameter d_{31} – Left: Dirac size distribution (monodisperse); Middle: lognormal size distribution; Right: window size distribution.*

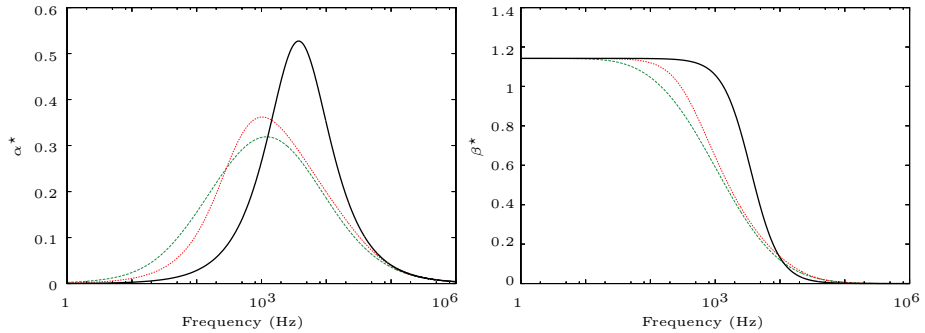

Figure 7.3: *Attenuation $\alpha^\star$ and dispersion $\beta^\star$ of a monochromatic acoustic wave in a polydisperse spray – **Solid**: Dirac size distribution (monodisperse); Dotted: window size distribution; Dashed: lognormal size distribution.*

7.1.3.3 Sectional accuracy study

We now assess some aspects of the convergence of the MF method towards the two-phase acoustic response: we focus on the ability of the method to render accurately the shape of the dispersion relation with a low number of sections.

There is a wide variety of options to parameterize the MF, e.g. the number of conserved moments and the form of the reconstruction. The discretization method has to be carefully chosen, especially with a wide size distribution such as the lognormal one presented in Figure 7.1, which tail corresponds to a significant widening of the mass distribution (see Figure 7.2). The accuracy of sectional approaches is performed with four types of systematic discretization techniques:

- the so-called Constant Δr discretization method defines equal radius intervals,
- the so-called Constant ΔS discretization method defines equal Surface intervals,
- the so-called Geometric discretization method has bounds defined by $r_k = r_0 R^k$ with $R > 0$,
- and the so-called Fixed mass Δr discretization method has its bounds $(r_k)_k$ defined to enclose a constant amount of mass in each section k:

$$m_k = \int_{r_k}^{r_{k+1}} r^3 f(r) \mathrm{d}r = m_{tot}/N_{\mathrm{sec}}.$$

These four approaches are illustrated in Figure 7.4 in the case of a 4 section discretization of the lognormal distribution of Figure 7.1. The Constant ΔS discretization method makes the first section very wide while the three other sections host very little mass; the Constant Δr discretization method also suffers from the fact that the lognormal distribution is skewed on the right. The Geometric and the Fixed mass Δr methods discretize more finely the small sizes: they adapt better to the lognormal skewness, the Fixed mass Δr discretization having a balanced amount of mass in each section by construction.

We first consider the window distribution from Figure 7.1 and we choose OSM with a ${}^1\kappa_k(r) = cst$. The size phase space is discretized with intervals of constant width as regards the variable r, which is a simple and natural first approach. The convergence of the acoustic response with such a discretization is shown in Figure 7.5 and is satisfactory with as few as 4 sections.

We now consider the lognormal distribution from Figure 7.1: this distribution is wider in terms of mass repartition (MDF) as shown in Figure 7.2. The convergences of the acoustic responses with the four discretizations for the lognormal spray are given in Figure 7.7, 7.6, 7.8, and 7.9 respectively. The constant Δr and constant ΔS methods yield poorer results than the Geometric and the Fixed mass Δr methods. The two latter discretizations are more complex but they guarantee a better (equal for the Fixed mass method) repartition of mass within each section. Finally, we consider the approximate response with a Fixed mass Δr discretization and the exact d_{31} computed from the lognormal distribution on the section in Figure 7.10:

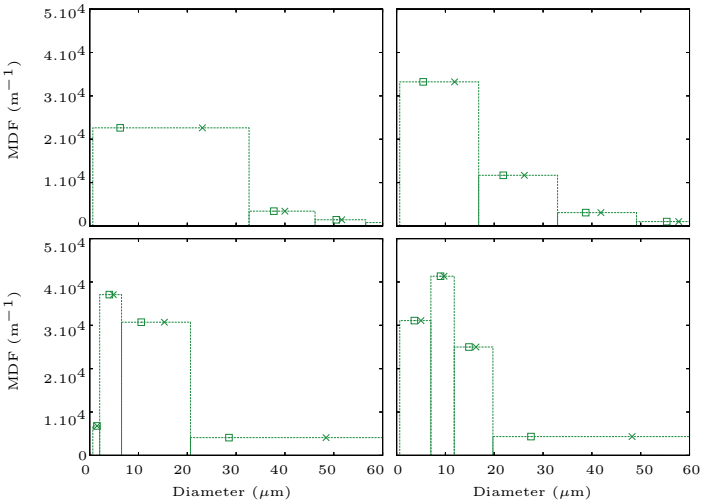

Figure 7.4: *Four methods of discretization/reconstruction for the lognormal distribution using 4 sections; - - - section bounds with area proportional to mass; ×: d_{31} computed with $\kappa(r) = cst$; □: exact d_{31} – Top Left: Constant ΔS discretization method; Top Right: Constant Δr discretization method; Bottom Left: Geometric discretization method; Bottom Right: Fixed mass Δr discretization method.*

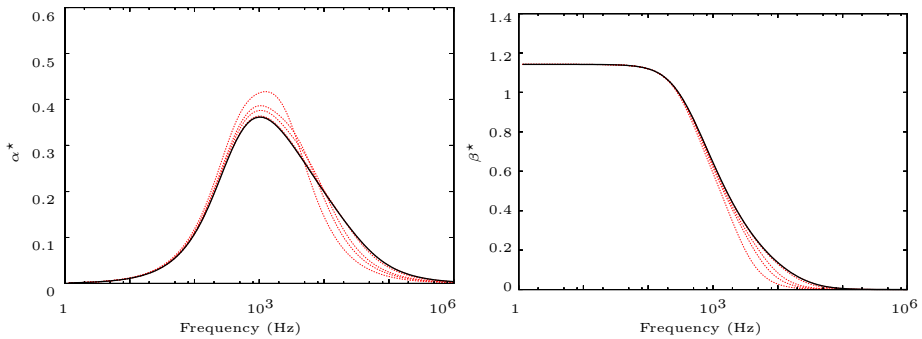

Figure 7.5: *Attenuation $\alpha^\star$ and dispersion $\beta^\star$ of a monochromatic acoustic wave in a polydisperse window spray – Dotted: MF with 2, 3, 4, and 10 sections with constant Δr; **Solid**: reference.*

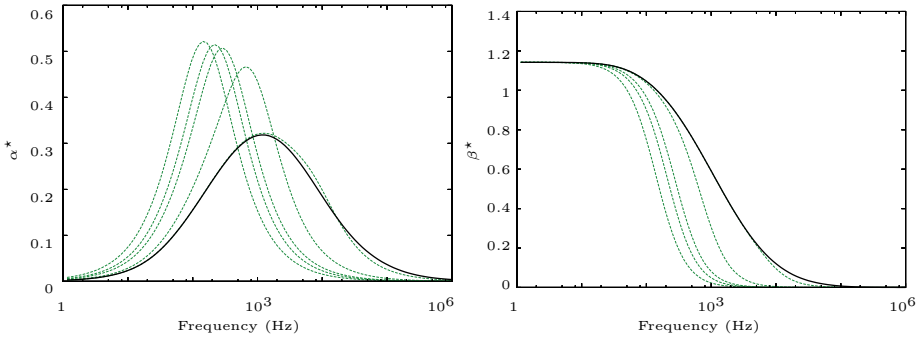

Figure 7.6: *Attenuation $\alpha^\star$ and dispersion $\beta^\star$ of a monochromatic acoustic wave in a polydisperse lognormal spray – Dashed: MF with 2, 3, 4, 10, and 100 sections with constant ΔS; **Solid**: reference.*

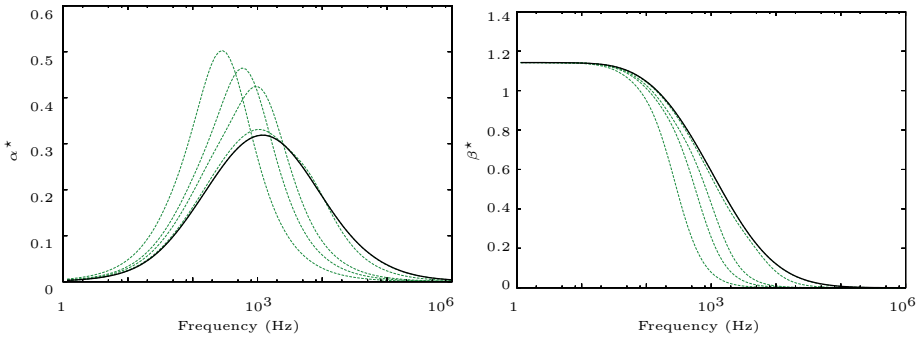

Figure 7.7: *Attenuation $\alpha^\star$ and dispersion $\beta^\star$ of a monochromatic acoustic wave in a polydisperse lognormal spray – Dotted: MF with 2, 3, 4, and 10 sections with constant Δr; **Solid**: reference.*

the accuracy at low numbers of sections is remarkably good.
As a conclusion, the Geometric discretization method and the Fixed mass Δr discretization method, as well as the use of an accurately reconstructed d_{31} strongly improve the accuracy of MF, which provides a satisfactory response with as few as 4 sections. This satisfactory response is obtained with a coarse size discretization for either the window distribution and a strongly biased distribution, namely the lognormal one. MF methods are efficient to treat polydisperse two-phase acoustics, even with a low number of sections: the discretization technique must be well-chosen, depending on the width and complexity of the spray's size distribution.

7.1.4 Conclusions on the linear theory

As a conclusion, the linear acoustic theory gives the key to polydisperse two-phase acoustics that is the exact solution of acoustics in a two-phase, quasi-uniform non-rotational medium through attenuation and dispersion coefficients. This theory has been extended to polydispersity, which first gives practical insight on how to handle MF discretizations to capture two-phase acoustics, and second allows high standard validations of high-fidelity approaches for two-way coupled disperse two-phase flows.
As a remark, the non rotational linear approach is limited to cases with uniform initial droplet repartition whereas the Multi-Fluid method -which can capture polydisperse acoustics accurately and reduce stiffness- is spatially resolved and no linearization is performed so it naturally captures the physics of rotational flows and non-linear waves. Moreover, such theory does not handle non-uniform cases: the segregation of droplets

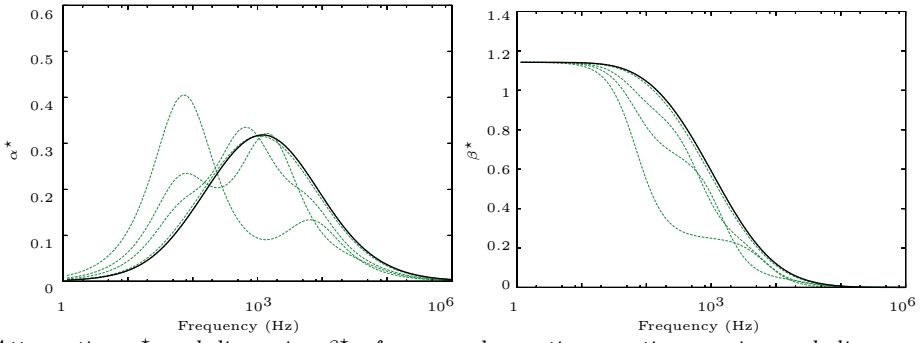

Figure 7.8: *Attenuation $\alpha^\star$ and dispersion $\beta^\star$ of a monochromatic acoustic wave in a polydisperse lognormal spray – Dotted: MF with 2, 3, 4, and 10 sections with Geometric discretization method; **Solid**: reference.*

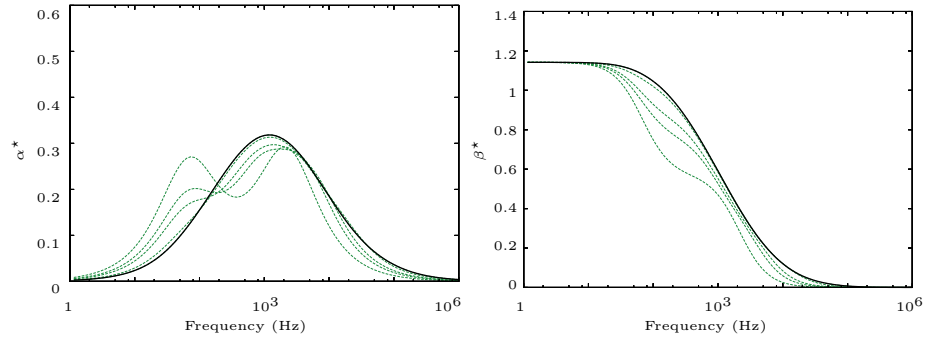

Figure 7.9: *Attenuation $\alpha^\star$ and dispersion $\beta^\star$ of a monochromatic acoustic wave in a polydisperse lognormal spray – Dotted: MF with 2, 3, 4, and 10 sections with Fixed mass Δr discretization method; **Solid**: reference.*

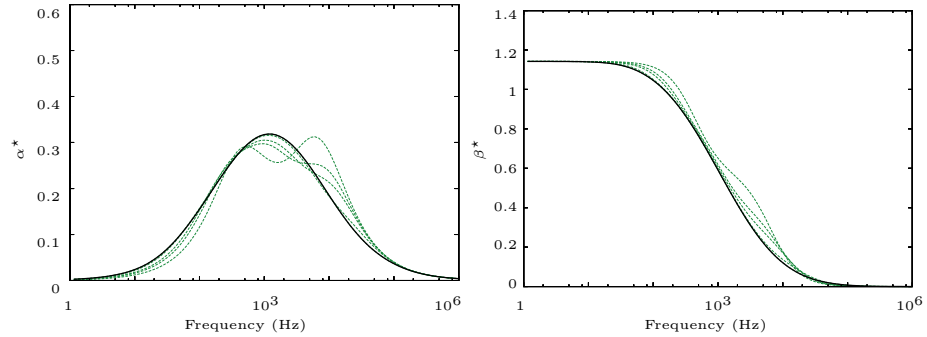

Figure 7.10: *Attenuation $\alpha^\star$ and dispersion $\beta^\star$ of a monochromatic acoustic wave in a polydisperse lognormal spray – Dotted: MF with 2, 3, 4, and 10 sections with Fixed mass Δr discretization method and exact r_{31}; **Solid**: reference.*

by the flow, droplet inhomogeneities and structures having significant effects on acoustic waves. Neither does it handle non-linear effects of wave propagation. So these interesting results are inadequate for many applications, especially solid rocket motors, where inhomogeneities and non-linearities are important.
So the theory is mostly useful for code validation purpose: two-phase acoustics brings into play all the physics of two-phase flows as well as their coupling. Challenging a code on such a simple case as wave propagation in a quasi-uniform medium allows to evaluate its ability to capture accurately all the gas-particle couplings. In the particular case of the Multi-Fluid method, a convergence study is led in § 7.1.3.3 to assess the requirements on size discretization. The responses to some typical size distributions that are here computed are finally used as reference solutions in § 12.3.

7.2 Characteristic growth times for hetero-DTC coalescence

In the prospect of assessing coalescence intensity in realistic cases, we develop some approximations to assess the characteristic coalescence growth time $\overline{\tau}^G$ and its corresponding coalescence Knudsen number Kn_g, defined in § 3.5.2.6.
Because it is the source of coalescence, we must estimate the velocity difference: this is performed only in the case of small droplets -as defined in § 3.1.3.1- since velocities can be linked to sizes in that case through the velocity estimation given in Eq. (3.21).

7.2.1 Stability of a monodisperse distribution

According to the size-velocity coupling mechanism, described in § 3.1.3.5, a polydisperse spray in a non-uniform or unsteady flow encounters an increase in its velocity dispersion, resulting in coalescence and increasing the size-dispersion: for a monodisperse spray, the existence of a small size dispersion is therefore unstable.
We consider a spray of number concentration n_0 that is initially monodisperse at r_0 and monokinetic. The surrounding flow is initially at $\boldsymbol{u}_g$ and varies in a time τ_g. We now consider a slight size dispersion δr. Because of drag, the velocity difference between the smallest and the largest droplets rapidly becomes:

$$\gamma \sim |\boldsymbol{u}^\star - \boldsymbol{u}| = |\,\mathrm{St}^\star - \mathrm{St}\,|\,u_g \approx \frac{4\rho_l r_0 \delta r u_g}{9\mu_g} \tag{7.9}$$

thanks to the velocity estimation given in Eq. (3.21) for small droplets. The time required for droplets of size r_0 to acquire a size $r_0 + \delta r$ i.e. to absorb by coalescence a relative volume $(r_0+\delta r)^3/r_0^3 \sim 3\delta_r/r_0$, is

assessed from Eq. (3.142):

$$\tau^G(r_0) = \frac{3\delta_r/r_0}{4\pi r_0^2 \gamma n_0/2} \tag{7.10}$$

where half of the concentration $n_0/2$ is allocated to the collision partners. We finally get by substituting Eq. (7.9):

$$\tau^G(r_0) = \frac{27\mu_g}{8\rho_l r_0^4 u_g \pi n_0} \tag{7.11}$$

which can be written for a mass concentration of droplets m_0:

$$\tau^G(r_0) = \frac{9\mu_g}{2m_0 r_0 u_g}. \tag{7.12}$$

This time is to be compared to the flow time τ_g, then forming a coalescence Knudsen number:

$$\mathrm{Kn}_g = \frac{9\mu_g}{2m_0 r_0 \tau_g u_g} \tag{7.13}$$

to assess the stability of a monodisperse spray of small droplets as regards size-velocity coupling.

7.2.2 Estimation of an average growth time in polydisperse cases

7.2.2.1 Form of an average growth time

We aim at characterizing the configurations for comparison purposes so a more general growth time is to be defined, based on average quantities:

$$\overline{\tau}^G(v) = \frac{m_p(v)}{\bar{M}\bar{\beta}\bar{\gamma}\bar{\mathfrak{E}}} \tag{7.14}$$

where $m_p(v)$ is the mass of a particle of size v. We have noted $\bar{M}$ an average total mass concentration, $\bar{\beta}$ an average cross-section, $\bar{\gamma}$ an average velocity difference, and $\bar{\mathfrak{E}}$ an average collision efficiency. All these quantities are estimated to be representative on a volume and a period of interest, their order of magnitude being generally well known and not too variable. Except velocity differences that are notably responsive since they are here the reason for coalescence to happen.
Such a time has been presented in the case of a Multi-Fluid approach in Eq. (4.55).

7.2.2.2 Case of a nozzle

We consider a nozzle flow with a rate of strain ϵ, homogeneous to $[\mathrm{s}^{-1}]$. The Stokes number reads $\mathrm{St}_\epsilon = \epsilon\tau^{\boldsymbol{u}}(r)$, yielding the average velocity difference:

$$\begin{aligned} \bar{\gamma} &= \epsilon \boldsymbol{u}_g \, |\tau^{\boldsymbol{u}}(r) - \tau^{\boldsymbol{u}}(r^\star)| \\ &= \bar{\epsilon}_g \bar{u}_g \mid \tau^{\boldsymbol{u}}(v) - \bar{\tau}^u \mid \end{aligned} \tag{7.15}$$

where $\bar{\epsilon}_g$ and $\bar{u}_g$ are an average strain rate and velocity of the gas and $\bar{\tau}^u$ is an average dynamic time of the disperse phase. Finally the size v used for $\overline{\tau}^G(v)$ is chosen as the most represented at the entrance of the volume of interest.
In SRM nozzles, the gas accelerates from subsonic to supersonic regime on a very short distance, yielding high velocity differences but small residence times. In the decelerating nozzle that is considered in § 13.2.4, the residence time is much higher so that we take small velocity differences to keep a comparable coalescence intensity. The Kn_g are estimated in the following to characterize the different configurations regarding coalescence.

7.2.3 Conclusion on hetero-DTC estimation

The characteristic growth time can be assessed from average collision parameters. Once compared to a typical residence time, the importance of coalescence can be estimated.
The methods suggested above require to make some choices and assumptions but they yield an interesting insight on the physics of the system under consideration. They are used to preliminarily quantify coalescence intensity in the nozzle test case of § 13.2.4 and in the applicative computations of Chapter 15.

7.3 Bimodal linearized coalescence: an analytical model

In order to assess an analytical coalescence model, we now investigate the case of a bimodal spray i.e. where two significantly different sizes are present. This corresponds of course to a case of hetero-DTC, where the velocities can be assessed accurately as they are very different and weakly perturbed by the coalescence process. Moreover, since the coalescence mostly occurs among droplets of different sizes, the model may be linearized as soon as a significant difference in concentrations exists between the two populations. The framework of such a linearization is that of order degenerescence in chemical kinetics where a second order reaction becomes a pseudo-first-order reaction if one of the components is majority and therefore its concentration quasi-constant (Connors 1990).
We consider a configuration inspired from D'Herbigny and Villedieu (2001)'s experiment, which features coalescence within a bimodal spray. We derive an original analytical approximation in the particular D'Herbigny case in order to calculate the mean volume and volume standard deviation of the big droplet distribution. The main idea is to take advantage of the fog droplet monodispersity to foretell the big droplet discrete accessible sizes and to project their NDF on these sizes, thus reducing the phase space dimension by discretizing on size "modes".

7.3.1 The D'Herbigny experiment

The D'Herbigny experiment (D'Herbigny and Villedieu 2001) consists in the growth of a big droplet falling through a fog of smaller droplets. The main features are summed up in Figure 7.11. Details about the experimental device can be found in D'Herbigny and Villedieu (2001). We only specify that the average injection radius of the bigger droplets is $r_b = 150\,\mu$m and their initial velocity $\boldsymbol{u}_s = 3\,$m/s thanks to a piezoelectric injector. The fog droplet radius $r_s \in [2\,\mu\text{m},4\,\mu\text{m}]$ is much smaller. These conditions bring the efficiency law parameters Re_p and k, defined in Eq. (3.49) and Eq. (3.62) respectively, close to typical SRM ones. The growth time for the big droplets is $\overline{\tau}^G = 1.1\,$s when assuming $\mathfrak{E} = 1$ and $C_v = 60$ppm for the small droplet concentration. The residence time in the tunnel is $\tau^R = 1.7\,$s for the big droplets so that $\text{Kn}_g = 0.6$. The experiment results are presented in Figure 7.12.

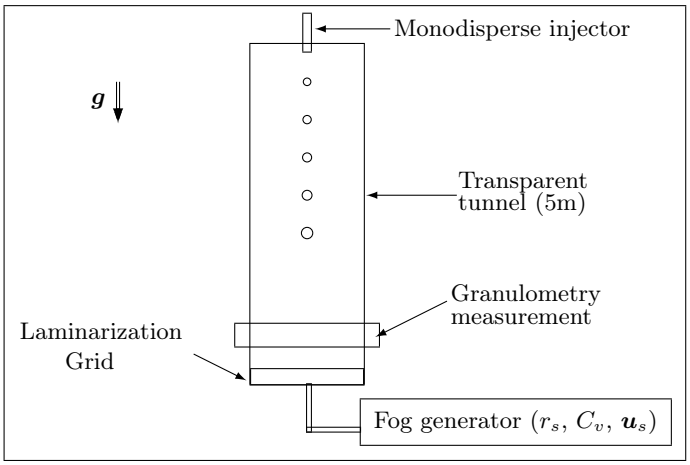

Figure 7.11: *D'Herbigny experimental device (ONERA).*

7.3.2 General description of two size populations

We describe the disperse phase at the semi-kinetic level, i.e. with size and size-conditioned velocities that are accounted for continuously. We exploit the size separation between big and small droplets to determine equations for both populations.

7.3.2.1 Two populations with separated size scales

Since the droplets belonging to the fog have a constant volume ($v = v_s$) and the bigger droplets can only grow by coalescence ($v \geq v_b$), let us first split the semi-kinetic NDF $n(t,z,v)$ regarding the size support as follows:

$$\begin{aligned} n_s(t,z,v) &= n(t,z,v = v_s) \\ n_b(t,z,v) &= n(t,z,v \geq v_b) \end{aligned} \tag{7.16}$$

where z is the 1D space coordinate. Of course, $n = n_s + n_b$.

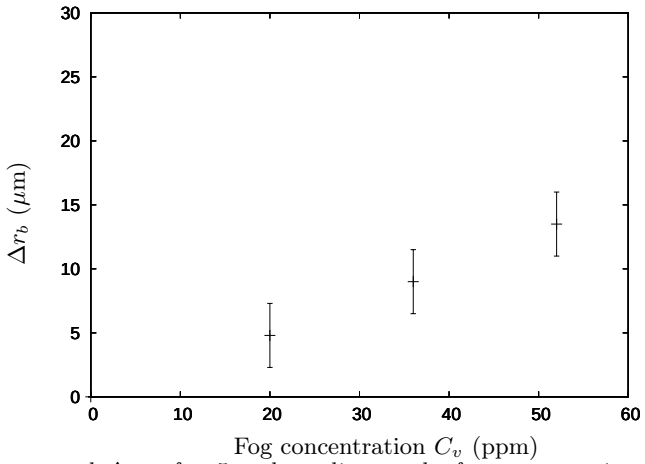

Figure 7.12: *Radius growth Δr_b after 5 m depending on the fog concentration C_v with experimental errorbars.*

The fog is described by the semi-kinetic System (4.13), written for the two populations, and where thermal evolutions are neglected:

$$\text{Small}\begin{cases} \partial_t n_s + \partial_z \cdot (n_s \boldsymbol{u}) = & Q_n^+(n_s,n_s) - Q_n^-(n_s,n_s) \\ & +Q_n^+(n_b,n_s) - Q_n^-(n_b,n_s) \\ & +Q_n^+(n_s,n_b) - Q_n^-(n_s,n_b) \\ \partial_t(n_s\boldsymbol{u}) + \partial_z \cdot (n_s \boldsymbol{u}\otimes\boldsymbol{u}) = n_s\overline{\boldsymbol{F}} & +Q_u^+(n_s,n_s) - Q_u^-(n_s,n_s) \\ & +Q_u^+(n_b,n_s) - Q_u^-(n_b,n_s) \\ & +Q_u^+(n_s,n_b) - Q_u^-(n_s,n_b) \end{cases} \tag{7.17}$$

$$\text{Big}\begin{cases} \partial_t n_b + \partial_z \cdot (n_b \boldsymbol{u}) = & Q_n^+(n_s,n_b) - Q_n^-(n_b,n_s) \\ & +Q_n^+(n_b,n_s) - Q_n^-(n_s,n_b) \\ \partial_t(n_b\boldsymbol{u}) + \partial_z \cdot (n_b \boldsymbol{u}\otimes\boldsymbol{u}) = n_b\overline{\boldsymbol{F}} & +Q_u^+(n_s,n_b) - Q_u^-(n_s,n_b) \\ & +Q_u^+(n_b,n_s) - Q_u^-(n_b,n_s) \end{cases}$$

where the coalescence terms have been developed for the two populations. The term $\overline{\boldsymbol{F}}$ stands here for the sum of the forces on droplets i.e. drag and gravity.
We now make the fundamental hypothesis:
[He1] n_b is much smaller than n_s.
This allows us to separate the scales of the two different populations of small and big droplets.

7.3.2.2 Steadiness of the small droplet population

First, the coalescence terms involving (n_b, n_b), i.e. describing coalescence of big droplets together, are of order two so that they are too small to be taken into account. Second, coalescence terms involving (n_s, n_s) vanish since small droplets all have the same velocity, thanks to the monokinetic hypothesis [HV1].
So the small droplet equations from System (7.17) can be truncated as follows, at order 0:

$$\begin{cases} \partial_t n_s + \partial_z \cdot (n_s \boldsymbol{u}) = & 0 \\ \partial_t(n_s\boldsymbol{u}) + \partial_z \cdot (n_s \boldsymbol{u}\otimes\boldsymbol{u}) = & n_s\overline{\boldsymbol{F}} \end{cases} \tag{7.18}$$

Considering negligible forces in the zeroth order momentum equation i.e. neglecting gravity for the fog which sediments too slowly, the small droplet velocity is constant. Choosing the fog as the reference frame, we have $\boldsymbol{u}(v_s) = 0$.
Finally the zeroth order mass equation shows that small droplets have a constant concentration which makes the problem steady as long as the injection conditions are. We shall therefore consider:

$$n_s(t,z,v) = \alpha_s \delta(v - v_s) \tag{7.19}$$

which means that the small droplet fog remains monodisperse and uniform.

7.3.2.3 Evolution of the big droplet population

From System (7.17), we now consider the big droplet equations, which lower order terms happen to be of order one. First the term $Q_n^-(n_s, n_b)$ treats the disappearance of small droplets so it vanishes on the big

droplet size support. Second, $Q_n^+(n_b, n_s) = Q_n^+(n_s, n_b)$ and $Q_u^+(n_b, n_s) = Q_u^+(n_s, n_b)$ due to the form of the coalescence operator so that:

$$\left\{ \begin{array}{rl} \partial_z \cdot (n_b \boldsymbol{u}) = & 2.Q_n^+(n_s, n_b) - Q_n^-(n_b, n_s) \\ \partial_z \cdot (n_b \boldsymbol{u} \otimes \boldsymbol{u}) = & n_b \overline{\boldsymbol{F}} + 2.Q_u^+(n_s, n_b) - Q_u^-(n_b, n_s) \end{array} \right. \tag{7.20}$$

With the previous hypotheses on the fog features, one can easily calculate the remaining coalescence terms, where we have considered $\mathfrak{E} = 1$:

$$\begin{array}{rl} Q_n^+(n_s, n_b) = & \alpha_s n_b(z, v - v_s)\beta(v - v_s, v_s)\ |\boldsymbol{u}(v - v_s)|\ /2 \\ Q_n^-(n_b, n_s) = & \alpha_s n_b(z, v)\beta(v, v_s)\ |\boldsymbol{u}(v)| \\ Q_u^+(n_s, n_b) = & \alpha_s n_b(z, v - v_s)\beta(v - v_s, v_s)\boldsymbol{u}(v - v_s)\ |\boldsymbol{u}(v - v_s)|\ (v - v_s)/(2v) \\ Q_u^-(n_b, n_s) = & \alpha_s n_b(z, v)\beta(v, v_s)\boldsymbol{u}(v)\ |\boldsymbol{u}(v)| \end{array} \tag{7.21}$$

7.3.2.4 Big droplet velocity drift

We now make a continuity assumption on velocities so that, considering the very small size of the fog droplets ($v_s \ll v_b$), we have:

[He2] $\boldsymbol{u}(v - v_s) \approx \boldsymbol{u}(v)$ for $v \geq v_s$.

Replacing the momentum equation by a linear combination of the two equations in System (7.20), the big droplet evolution system is finally composed of number and velocity equations that are decoupled:

$$\left\{ \begin{array}{rl} \partial_z n_b(z, v) = & \alpha_s[\beta(v - v_s, v_s)n_b(z, v - v_s) - \beta(v, v_s)n_b(z, v)] \\ 0 = & n_b(z, v)\overline{\boldsymbol{F}} - \alpha_s\beta(v - v_s, v_s)\boldsymbol{u}(z, v)\ |\boldsymbol{u}(z, v)|\ n_b(z, v - v_s)\dfrac{v_s}{v} \end{array} \right. \tag{7.22}$$

with the boundary condition:

$$\left\{ \begin{array}{l} n_b(z = 0, v) = \alpha_b \delta(v - v_b) \\ \boldsymbol{u}(z = 0, v = v_b) = \boldsymbol{u}_0 \end{array} \right.$$

where α_b is the big droplet number density and $\boldsymbol{u}_0$ their velocity at the boundary.

Let us rewrite the decoupled momentum equation in System (7.22) to characterize the bigger droplet behavior in the D'Herbigny conditions:

$$n_b(z, v)\overline{\boldsymbol{F}} = \alpha_s\beta(v - v_s, v_s)\boldsymbol{u}(z, v)\ |\boldsymbol{u}(z, v)|\ n_b(z, v - v_s)\frac{v_s}{v} \tag{7.23}$$

The rhs models the effect of coalescence with the static fog droplets. Absorbing static mass induces a momentum dilution i.e. a slow down. When neglecting this effect, this equation reduces to a classic dynamic balance ($\overline{\boldsymbol{F}} = 0$) which, in our case, means that the drag force compounds the weight. Therefore, droplets do reach a terminal velocity but this limit velocity increases with the droplet size since the Stokes number depends on the size. To illustrate this fact, Figure 7.13 shows the evolution of the big droplet velocity in the D'Herbigny configuration computed with the Two Size Moment method, supposing that droplets are injected with an initial velocity of 3 m/s. The black curve is the dynamic equilibrium solution ($\overline{\boldsymbol{F}} = 0$) for the corresponding droplet Sauter mean radius: they both increase. Finally, the slight overestimation yielded by the terminal velocity approach comes from neglecting the so-called momentum dilution. This difference is no longer negligible when coalescence becomes intense. See the case in Figure 7.13, right of a $C_v = \alpha_s v_s = 60$ ppm fog where the terminal velocity is 45 % overestimated.

Now that we have discussed the evolution of velocity, confirming that the big droplet distribution slowly increases with size, let us solve the mass equation by projecting it on size modes.

7.3.3 Modal resolution

7.3.3.1 Existence of size modes

A remarkable point in the bimodal limit condition is that it yields size modes: the volume increment is quantified by the small droplet volume v_s. Thus the big droplet volume v can only take the following values:

$$v_k = v_b + kv_s \ ; \ k \in \mathbb{N}. \tag{7.24}$$

Let us rewrite the big droplet size distribution:

$$n_b(z, v) = \sum_{k=0}^{+\infty} n_k(z)\delta(v - v_k). \tag{7.25}$$

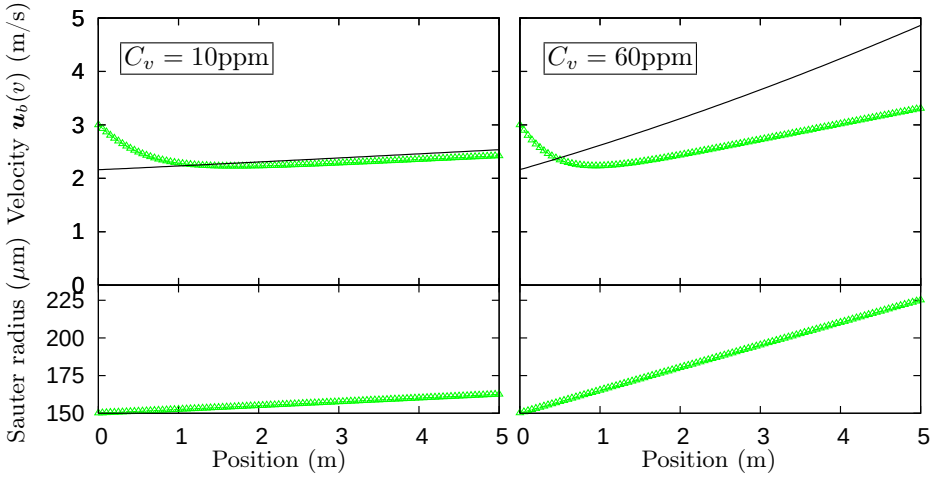

Figure 7.13: *Velocity and Sauter Mean Radius along the tunnel computed with the Two Size Moment method with* $\mathfrak{E} = 1$ *(*Δ*) and terminal velocity (**black**) corresponding to the computed Sauter Mean Radius – Left:* $C_v = 10ppm$*; Right:* $C_v = 60ppm$*.*

This observation allows us to exactly project the number equation from System (7.22) on the size modes:

$$\left\{\begin{array}{rl} \mathrm{d}_z n_0(z) = & -\frac{1}{\tilde{z}} b_0 n_0(z) \\ \mathrm{d}_z n_1(z) = & \frac{1}{\tilde{z}}[b_0 n_0(z) - b_1 n_1(z)] \\ \vdots & \\ \mathrm{d}_z n_k(z) = & \frac{1}{\tilde{z}}[b_{k-1} n_{k-1}(z) - b_k n_k(z)] \end{array}\right. \tag{7.26}$$

with the boundary conditions $n_0(0) = \alpha_b$ and $n_k(0) = 0, k \geq 1$ and where we have defined:

$$\epsilon = \frac{v_s}{v_b}\ , \qquad b_k = [(1+k\epsilon)^{\frac{1}{3}} + \epsilon^{\frac{1}{3}}]^{\frac{2}{3}}\ , \qquad \text{and} \qquad \tilde{z}^{-1} = \alpha_s \pi \left(\frac{3 v_b}{4\pi}\right)^{\frac{2}{3}}. \tag{7.27}$$

In the context of a purely modal evolution of the big droplets, the NDF evolution equation has become a system of ODEs for the number of each mode.

7.3.3.2 Coalescence lengths

We highlight that the $\tilde{z}/b_k$ are lengths that define the typical coalescence lengths or mean coalescing free paths for droplets n_k. Consider now another length criterion, that evaluates the importance of volume growth rate for the initial class of big droplets:

$$\mathcal{L}_g = \frac{v_b}{v_s}\frac{\tilde{z}}{b_0}. \tag{7.28}$$

If $\tilde{z}/b_0$ is the typical travel length of a big droplet between two coalescing collisions with a fog droplet that is a mean free path regarding coalescence, we need v_b/v_s times more distance for a big droplet to absorb enough matter to double her own volume. Length $\mathcal{L}_g$ gives the length after which the big droplet average volume has significantly changed because of coalescence. This length is defined as was the growth time $\overline{\tau}^G$ in § 7.2. This means that the dimensionless number that describes coalescence intensity in the D'Herbigny configuration is a coalescence Knudsen number $\mathrm{Kn}_g = \mathcal{L}_g/z$ based on a length, for instance the length of the tunnel, in accordance with the steadiness of the problem.
To solve System (7.26), we consider two modelings whether z is small or big compared to $\mathcal{L}_g$ which allows us to neglige the cross-section variations with size or not.

7.3.4 First analytical growth formulae for bimodal coalescence

7.3.4.1 The constant β growth model

As a first estimation, we assume that $b_i = b_0$ and the collision lengths are all equal to z_0. We formalize this temporary hypothesis:
[He3] the collision lengths $\tilde{z}/b_k$ are all equal to $z_0 = \tilde{z}/b_0$.

This is equivalent to assuming the cross-section $\beta(v_k, v_s) = \beta(v_b, v_s) = \beta$ constant so [He3] is valid only when the big droplet size does not vary too much i.e. $z \ll \mathcal{L}_g$. System (7.26) can now be integrated recursively, yielding the following modal densities:

$$n_k(z) = \alpha_b \frac{1}{k!} \left(\frac{z}{z_0}\right)^k \exp(-z/z_0) \tag{7.29}$$

In fact, the modal densities follow Poisson's law with z/z_0 being the law parameter. This means that after traveling a $z = kz_0$ distance in the fog, the most probable droplet size is $v_k = v_b + kv_s$ which corresponds exactly to k coalescence events.

7.3.4.2 Size moment evolution

In this first modeling, with β constant, we can analytically evaluate the moments of the distribution $n_b(z, v) = \sum n_k(z)\delta(v - v_k)$ by direct summation of the analytical number density of Eq. (7.29). The average volume reads:

$$\overline{v}(z) = \frac{\int v n_b(z, v)\mathrm{d}v}{\int n_b(z, v)\mathrm{d}v} = v_b + v_s \frac{z}{z_0} \tag{7.30}$$

and the size distribution standard deviation reads:

$$\sigma^2(z) = \frac{\int (v - \overline{v})^2 n_b(z, v)\mathrm{d}v}{\int n_b(z, v)\mathrm{d}v} = v_s^2 \frac{z}{z_0} \tag{7.31}$$

The model validity domain is limited to small deviations of $\tilde{z}/b_k$ from z_0 i.e. $\overline{v}(z) \approx v_b$. This corresponds to a coalescence number criterion $v_s z/z_0 \ll v_b$ which retrieves the condition on coalescing length:

$$z \ll \mathcal{L}_g$$

This first model yields an increasing size dispersion for the big droplets. This dispersion is intrinsic to the way droplets grow, independently of any velocity or cross-section variations. Moreover the resulting distribution is, as discussed below, fairly Gaussian as it is a Poisson law with a high parameter. This invalidates any monodisperse approach for the D'Herbigny configuration.

7.3.4.3 Constant β model approximation

We also note that Poisson's law can be approximated with a normal distribution with very good match as soon as $z/z_0 > 5$ which is clear in Figure 7.14, bottom. This fact eases computations for high z.
Besides, this case is computed versus a Multi-Fluid approach in § 13.2.3.1.

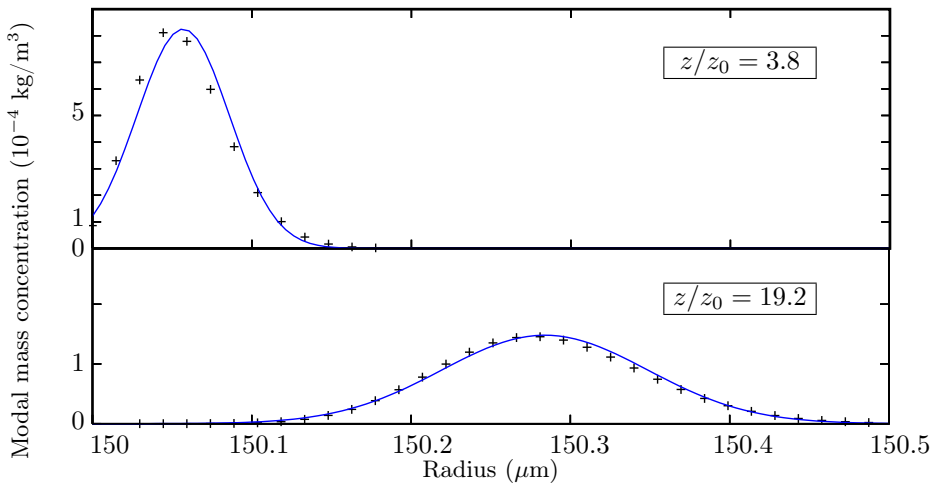

Figure 7.14: *Poisson's law (+) compared to Normal law (—) for $z/z_0 = 3.8$ (top) and $z/z_0 = 19.2$ (bottom).*

7.3.5 Second analytical growth formulae for bimodal coalescence

7.3.5.1 Variable β growth model

As a second and broader modeling, we now solve System (7.26) with the exact i.e. variable $\beta(v_k, v_s)$ coefficients. We thus remove hypothesis [He3]. We still have $n_0(z) = \alpha_b \exp(-s_0 \frac{z}{\tilde{z}})$ and we can prove by

induction that:

$$n_k(z) = \alpha_b \sum_{i=0}^{k-1} \frac{b_{k-1}}{b_k - b_i} \lambda_{ik-1} [\exp(-b_i \frac{z}{\tilde{z}}) - \exp(-b_k \frac{z}{\tilde{z}})] \ , \ k \geq 1 \tag{7.32}$$

where we have the following notation for the λ_{ik} coefficients, for $k \geq 1$:

$$\lambda_{ik} = \frac{\prod_{j=0}^{k-1} b_j}{\prod_{\substack{j=0 \\ j \neq i}}^{k} (b_j - b_i)}. \tag{7.33}$$

No further analytical expression has been derived from this formula, which has to be computed directly or at least approximated as done in the following.

7.3.5.2 Model comparison

We compare the constant β and variable β models in a case with large $\mathcal{L}_g$ in Figure 7.15. This case shows strong differences between the two cases, proving that the variation of the cross-section has a significant effect in this case of bimodal coalescence.

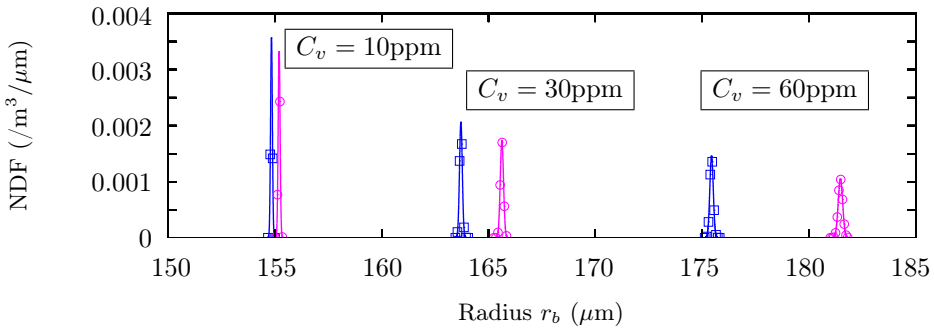

Figure 7.15: *NDF after 2 m in a 10, 30 and 60 ppm fog – □: constant β model; ○: variable β model.*

7.3.6 Conclusion on bimodal coalescence

As a conclusive remark, the form of the coalescence equation is classical and complex enough to have yielded many studies. Especially, mathematical studies have been performed in the frame of self-similar distributions (van Dongen and Ernst 1988; Park and Lee 2001; Calvo and Jabin 2011) i.e. time-size distributions that can be reduced to a single dependency parameter.
The bimodal coalescence case is a much simpler case, especially as the size support is discrete. Still it is an interesting case for validation purpose as it is quite complex -the size distribution evolves in a non-trivial way- and it features a detailed analytical solution, from which high order moments such as size dispersion can be computed. A publication of the analytical study is in preparation (Doisneau and Laurent 2013).
It is used as a strong validation tool for a MF approach of coalescence in Chapter 13 and its level of detail allows nonetheless to validate the high-fidelity approach but to assess features such as the numerical diffusion in size of the resolution method.

7.4 Characteristic time and modes for homo-DTC coalescence

We now focus on the case of homo-DTC coalescence. The simplest case that can be considered is that of a monodisperse spray: coalescence is spatially coupled but at the location where the first crossing occurs, all the quantities are known and coalescence can be assessed exactly. After the crossing location, size and velocity evolve: they can be assessed on a distance where non-linear coalescence effects are not significant. So the case that is studied can be described as a modal but polykinetic coalescence case.

7.4.1 Two crossing jets in a crossflow

7.4.1.1 Presentation of the case

We consider a 2D case of two jets injected at a velocity $(u_0, \pm v_0)$ whose trajectories cross because of the droplet inertia before being bent by a gaseous co-flow of velocity $(u_0, 0)$.
The spray is here characterized by two dimensionless numbers:

- a Stokes number that determines the curvature of each jet and the way they cross;
- a Knudsen number that gives the intensity of collisions and therefore coalescence.

7.4.1.2 Stokes number to characterize the crossing

The Stokes number is defined as the ratio $\mathrm{St} = \tau_0^{\boldsymbol{u}}/\tau_m$ where $\tau_0^{\boldsymbol{u}}$ is the Stokes time associated to the injected particles and $\tau_m = \eta_0/v_0$ is the time required for a particle to meet the centerline at constant velocity v_0 from an initial distance of the centerline η_0. Noticeably, a finite inertia droplet encountering Stokes drag travels exactly a distance $\tau_0^{\boldsymbol{u}} v_0$ in the vertical direction before stopping so that:

$$\mathrm{St} = \frac{\tau_0^{\boldsymbol{u}} v_0}{\eta_0} \tag{7.34}$$

is a ratio of lengths and droplets with $\mathrm{St} > 1$ are the only one to cross the centerline.

7.4.1.3 Knudsen number to characterize coalescence intensity

We then define a coalescing Knudsen number inspired from that of § 3.5.2.6. But in the case of monodisperse homo-DTC coalescence, it matches a collision Knudsen number $\mathrm{Kn}_g = (\nu_{\mathrm{coal}}\tau_{ol})^{-1}$ where ν_{coal} is a coalescence frequency and τ_{ol} is a flow characteristic time, here the time during which the two jet footprints overlap. In a crossflow that is initially monodisperse, it reads:

$$\mathrm{Kn}_g \;=\; \frac{\rho_l r_0 \,|\,\boldsymbol{u}_0\,|}{12 m_0 v_0 d_0} \tag{7.35}$$

where the initial state is described by r_0 the droplet radius, ρ_0 the initial mass concentration, d_0 the width of each jet and $|\,\boldsymbol{u}_0\,|$ the injection velocity norm.

7.4.2 Modal coalescence estimation for large Knudsen

We assume an initial particle concentration in each jet that yields:

$$\mathrm{Kn}_g \gg 1.$$

So coalescence is weak and very few new droplets are created.

7.4.2.1 Existence of modes

The coalescence terms are then linearized by neglecting

1 the mass taken from the initial section
2 the interactions between two non-initial sections.

Because of the initial monodisperse condition, coalescence yields size modes, i.e., droplets, with an integer multiple $k\mathcal{V}(r_0)$ of the initial droplet volume $\mathcal{V}(r_0)$ so the size distribution is discrete.

7.4.2.2 Analytical formula

This gives immediately a semi-analytical estimation of the droplets produced at the exit of the crossing as proportional to Kn_g. So the formula reads for the section concentrations after the crossing, thanks to the mode/section equivalence:

$$m_{k+1} = \frac{1}{\mathrm{Kn}_g} m_k \tag{7.36}$$

this being written indifferently in total mass or mass concentration thanks to the sufficient homogeneity of the problem.

7.4.3 Conclusion on homo-DTC coalescence analysis

The coalescence in two crossing jets is an interesting test case as it represents a very far from equilibrium velocity configuration, the anisotropy being very high compared to multiple crossing cases. This test case is therefore a good case to assess complex polykinetic configurations.
The linear formula that is derived for this case is used in Chapter 13 where polykinetic coalescence is studied. This provides a first insight on the validity of the solver. However the dynamics of this case in a fully non-linear regime ($\mathrm{Kn}_g \leq 1$) is much more complex so a full validation resorts to a high-fidelity approach (a DPS simulation is chosen).

7.5 Conclusion on the analytical models for isolated physics

Some specific physical phenomena have been considered as isolated and analytical models are derived in some of their asymptotic regimes:

- the polydisperse two-phase acoustic asymptotics embraces the main aspects of a moderately dense polydisperse case,
- the bimodal coalescence asymptotics allows to validate some aspects of hetero-DTC, as a typical case of the coalescence of low-inertia droplets, and
- the crossing coalescence linearized asymptotics gives some insight on homo-DTC, as it is a typical case of moderate-inertia coalescence.

So the previous models form a complete toolbox for the validation of a strategy for moderately dense nano-to-inertial coalescing two-phase flows.

Part III

Modeling flows of nanometric particles and droplets

Chapter 8

Nanoparticle flow modeling

We here present general aspects of nanoparticles, by describing the types and applications as well as the issues they raise. We then focus on the modeling of flows laden with nanoparticles and two classical modeling angles are introduced: aerosol theory that is the science of non-inertial disperse phase flows, and general aspects of Brownian theory.

8.1 Introduction on nanoparticle flows

The modeling of nanoparticle transport in a gas flow has been presented in § 1.4.3.3 as mandatory to predict the improvements and pitfalls of nanopropellants for SRMs.
In addition, a regain of interest on nanoparticles is observed in various applications, due to the recent advances in nanotechnologies. The issues raised by nanoparticle flows must then be tackled for process design and safety assessment as soon as nanoparticles are involved. This is both necessary and difficult when considering the peculiar physics of nanoparticle flows, and the difficulties to get quantitative experimental data.
In the present chapter, issues and modeling for nanoparticle flows are gathered from the literature. It is stated that two modeling regimes are classically distinguished, based on the nanoparticle size: the diffusive regime and the free molecular regime.
From this state-of-the art, the modeling needs for SRMs are identified and corresponding modeling efforts made in the present thesis are developed in the following chapters of Part III.

8.2 Context of nanoparticles and their applications

We briefly present nanoparticles, their sources and the motivations for their studies that are their remarkable properties and their potential health effects. Nanoparticles are currently an area of intense research (Roco 1999; Gaffet 2008) due to a wide variety of potential applications as biomedical, optical and electronic fields, composite materials, this interest going back to the 1990s when the National Nanotechnology Initiative was launched in the USA. Nanoparticles may exhibit size-related properties that differ significantly from those observed in fine particles or bulk materials. While "micro" has come to mean anything small, nano emphasizes the atomic granulometry that produces the unique phenomena observed in nanoscience. After defining nanoparticles, we detail their sources and the health issues.

8.2.1 Definitions and sources of nanoparticles

Nanoparticles, formerly referred to as ultrafine particles (Granqvist and Buhrman 1976), correspond conventionally to particles with a size below a few 100 nm. By particle, nanotechnology understands a small object, excluding molecules, that behaves as a whole unit in terms of its transport and properties. The term nanoparticle can sometimes refer to objects with only one dimension of the nano range, we prefer the term "nanofiber", "nanotube" or at least "high aspect ratio" when one dimension is bigger than the two others.
Anyway, nanoparticles are assumed to be transportable freely, and should be distinguished from nanostructured materials where the nano elements are fixed and cannot spread within a gas or fluid carrier. For instance nano-films -with two non-nano dimensions- are not considered here.
Other specific terms are used in the literature, that highlight a specificity of the considered nanoparticles:

- Nanoclusters have at least one dimension between 1 and 10 nm and a narrow size distribution.
- Nanopowders are agglomerates of ultrafine particles, nanoparticles, or nanoclusters.

- Nanometer-sized single crystals, or single-domain ultrafine particles, are often referred to as nanocrystals.
- We refer to dispersed nanometric droplets as nanosprays.

Depending on the mode of production, nanoparticles can have a narrow size distribution and be considered as monodisperse. Yet, their very small sizes often bring along Brownian agitation and high number concentrations so that agglomeration occurs, possibly yielding widespread distributions which have sometimes been interpreted as lognormal. Another reading of this observed lognormal behavior is that the residence time in a dense, agglomeration-prone zone is distributed after Brownian diffusion, yielding lognormal sizes (Kiss et al. 1999).

8.2.1.1 Natural nanoparticle sources

The main source of nanoparticles on earth is natural: 90 % of the aerosols in the atmosphere results from desert dusts, volcano ashes, sea salt, sulfates emitted by plankton, biomass burning residuals, and nitrates, rose and carried by the winds.
About half of the atmospheric aerosol is minerals from deserts and mainly silica SiO_2. And half of this mass is under the from of compact particles smaller than 2.5 μm (d'Almeida and Schütz 1983; Shi et al. 2005). There are ten main desertic zones identified worldwide as responsible for this particle production. Mineral particles are also proven to carry microorganisms, several hundreds of them being known to resist UVs during their intercontinental trips in the atmospheric circulation (Buzea et al. 2007).
Mineral-laden wind bursts are visible from satellites as well as volcano erupted material and large forest fire plumes. These aerosols absorb sun radiation and can also scatter it back to space.
Natural particles are also studied on other planets and space bodies such as the Moon and Mars, where nanoparticles have been detected (Taylor et al. 2005).

8.2.1.2 Urban nanoparticles

The remaining 10 % of atmospheric particles are from human origin. But this average ratio does not tell anything about the strong non-uniformity that exists: particle concentrations are very high in cities and mostly due to human activities. Remarkably, industrial disposal is not identified as a significant source of nanoparticles (Buzea et al. 2007; Stone et al. 2007)
Urban transports are a major source of particles (Westerdahl et al. 2005), with combustion residuals of internal combustion engine (ICE) exhausts, brake wear and tire debris. Combustion residual particles from ICEs, composed of hydrocarbons such as polyaromatic hydrocarbons (PAH), reach concentrations of 1500 particles/cm^3 (d'Almeida and Schütz 1983) and range from 20 to 130 nm for diesel engines and from 20 to 60 nm for gasoline engines. They are typically spherical (Sioutas et al. 2005). Brake wear debris size around 1 μm and are composed of various metal (Fe, Cu, Ba) and non-metal (Si, K, Ca, Ba) particles as well as organic and mineral (asbestos) fibers (Rogge et al. 1993; Sternbeck et al. 2002; Sanders et al. 2003). Tire debris and road dust contain several hundreds of organic species (Rogge et al. 1993) but it is generally accepted that these particles are large ($> 10\,\mu$m) compared to PAH nanoparticles produced by combustion and other high temperature sources (Sheu et al. 1997).
Another source, though sporadic, of nanoparticles is building demolition. In the case of old buildings, the resuspension of asbestos fibers is to be feared but demolition always yields high levels of particles below 10 μm anyway (Stefani et al. 2005). As an illustration, the adverse health effects of the World Trade Center collapse on September 11, 2001, have been widely studied up to now and Carbon Nanotubes (CNT) have been found in dust samples and exposed population lungs (Wu et al. 2010).

8.2.1.3 Indoor nanoparticles

Solid fuel combustion is used for cooking by a rough 50 % of the world's population and produces a misestimated indoor pollution (Wagner et al. 2010).
Indoor particle pollution also results from cigarette smoke, in which particles ranging from 100 to 700 nm and composed of 100, 000 chemical components can be found (Ning et al. 2006).
Even combustion-free transports such as metropolitan railway networks raise particle issues as brake wear debris are confined e.g. in subway corridors, where they can concentrate. The composition of brake debris and the associated particle sizes have already been given above.
Asbestos became increasingly popular among manufacturers and builders in the late 19th century because of its sound absorption, average tensile strength, its resistance to fire, heat, electrical and chemical damage, and affordability (for electrical insulation hotplate wiring and in building insulation). When asbestos is used for its resistance to fire or heat, the fibers are often mixed with cement (resulting in fiber cement) or woven into fabric or mats. Yet asbestos fibers become airborne in specific and well-defined conditions such

as asbestos mining, building and decontamination. Finally, asbestos fibers are well-known to provoke strong adverse effects (since 1906), this as they include nanofibers (Jolicoeur et al. 1981).

8.2.1.4 Engineered nanoparticles

Among the topics of interests in nanoparticles, carbon nanotubes (CNT) are a trendy one, which is presented in the following section.
For the production of high performance ceramics (medical applications) nanopowders are used that improve mechanical properties of fine ceramics and lowers sintering temperature. Yet, unlike regular micronic powders, the preparation of ready-to-sinter nanopowders requires to control deagglomeration so they are produced and stored in liquid suspensions to control and limit agglomeration. Such powders are typically composed of Al_2O_3, Y_2O_3, or ZrO_2.
Metallic nanoparticles are used for their optical properties (Fedlheim and Foss 2001) while metallic oxides are used in cosmetics (e.g. sunscreens) (Donaldson et al. 2004): nanoscale TiO_2 and ZnO become transparent to visible light while they are able to absorb and reflect UV light.

8.2.1.5 Engineered nanoparticles: case of CNTs

CNTs exhibit remarkable properties regarding mechanical strength, thermal and electrical conductivity, chemical chelation (like fullerenes). Further improvement in tensile strength, multi-wall synthesis yielding MWCNT are expected.
They are currently used in composite structure materials (bicycle components, vessel frame and hull, wind turbines, skis, ice hockey sticks, baseball bats, hunting arrows, surfboards), tips for atomic force microscope probes and bone scaffolding in tissue engineering. They are promising for many structural applications (ropes[1], textile), in electrical circuits (CNT wires, CNT FETs, battery and ultracapacitor electrodes, solar cell junctions), for hydrogen storage, for surface treatment (radar absorption), as antennas in medical applications of tumor surgery etc.
Up to now, they are synthesized by arc discharge or plasma, Chemical Vapor Deposition (CVD) (see (Dichiara 2012) for Carbon Nanotube synthesis), milling *etc.* The case of aluminum nanoparticle synthesis has been discussed in § 1.2.2.2.

8.2.2 Some issues of nanoparticles related to their transport

The transport of nanoparticles is a major issue: as soon as they become airborne they are convected but they also tend to diffuse due to their small size. The modeling of such phenomenon is hitherto not predictive enough regarding the nanoparticle transport modeling needs at the heart of health and safety concerns.

8.2.2.1 Soots

Soots result from the combustion of carbon rich fuels, e.g. wood and fossil fuels. In internal combustion engines (ICE), levels of soots should be predicted as they are pollutants and as they induce side-effects such as coke-up. The following phases have been identified and studied:

- formation steps (Bockhorn 1994; Blanquart et al. 2009);
- nucleation;
- growth (Mueller et al. 2009a);
- agglomeration (Mueller et al. 2009b); and
- oxidation (causing a reduction in size),

which depend on a fine knowledge of the transport mechanisms at the smallest scales.
Since ICEs cannot be considered as well-stirred, these mechanisms are indirectly conditioned by transport. They are moreover very dependent on temperature and concentration (Blanquart and Pitsch 2009) so the turbulent reactive contexts that occur are harsh to render with high-fidelity (Bisetti et al. 2012; Mueller and Pitsch 2012). Soot modeling in turbulence (Zucca et al. 2006; Netzell et al. 2007) and the coupling of soot models with radiation (Dorey 2012; Hernandez et al. 2013) have been studied in advanced computation contexts, but with simple transport modeling.

8.2.2.2 Nanoparticles in industrial processes

Many industrial processes feature nanoparticles: their agglomeration, their deposition, or their overall synthesis (Dichiara et al. 2012; Dichiara and Bai 2012; Dichiara 2012) must be accounted for. In the case of their synthesis, it is crucial to predict and control the agglomeration rates in the reactor (Friedlander 1999).

[1] Let us mention Arthur C. Clarke's visionary idea of a space elevator made of a single diamond crystal.

A particular industrial concern is that of health and safety (Gaffet 2009): processes involving nanoparticles (either as an intermediate product or a by-product) must be qualified as regards health and safety requirements. The transport and deposition of such particles must be controlled and possible air cleaning (e.g. electrostatic filters) must be deployed. There are then two main troubles: the security norms and criteria are based on very few experience or models and the cleaning devices are not efficient for all sizes.

8.2.2.3 Nanoparticles in human respiratory system

The study of particle transport in the human respiratory system is a strong and active concern (Moussa 2009). And the case of nanoparticles needs again to be treated specifically: Particles below $10\,\mu$m can reach the deepest gas exchange surfaces (Lippmann 1990). Advanced studies are conducted including turbulence, geometry branching effects, see for instance Li and Ahmadi (1995) or Ahmadi (2009).

8.2.2.4 Dusts

The issue of nanoparticle dusts is not new and has raised many efforts to understand its influence on health, climate *etc.* But the concerns are also strong in space exploration: extraterrestrial dust (Moon, Mars) is indeed very abundant and it raises technological issues as it tends to stick to electrostatically charged surfaces such as astronaut space suits and solar panels.

8.2.2.5 Particular case of nanosprays

Nanodroplets in suspension have a wide range of applications such as maskless lithography, rapid prototyping, spotting, and biological analysis technologies. The use of nanoparticles in SRMs is contemplated for combustion reasons but the resulting nanospray must be modeled, as discussed in Chapter 1, to predict the possible effects on the SRM flow:

- a reduction of two-phase losses,
- an undefined impact on ODP,
- a reduction of ITHAC, and
- a reduction of slag formation and nozzle erosion.

The issues of transport and coalescence are crucial to predict these aspects, by improving the knowledge on the size distribution, which is crucial. The transport and coalescence of nano sprays can be assessed with tools that are close to those for transport and agglomeration of nanoparticles.

8.2.3 Health concerns of nanoparticles

Nanoparticles, whatever the type, have raised health concerns in the last decades with the emergence of nanosciences and engineered nano-materials. A wide literature related to nanoparticle toxicity has therefore appeared, see for instance (Buzea et al. 2007; Brayner 2008) and more specifically engineered nano-material risks (Gaffet 2011; Misra et al. 2012). Though some nanoparticles may have benefits for humans, they are examined suspiciously in manufactured goods and systematically considered as a pollution if airborne released.

8.2.3.1 Toxicity criteria

The potentially strong toxicity of nanoparticles results both from their ability to migrate deeply in the body and from the enhanced reactivity due to their large specific surface.
The penetration of nanoparticles in the organism occurs by three main ways given with the related diseases that are known:

- inhaled nanoparticles provoke asthma, bronchitis, emphysema, lung cancer and neurodegenerative diseases (Parkinson's, Alzheimer's),
- gastrointestinal tract provokes Crohn's disease and colon cancer,
- skin penetration provokes podoconiosis.

Their small size allows nanoparticles to translocate in the body, to pass the cell wall (either directly, by means of vacuoles or by Na^+/K^+ pump) and to interact with any part of the cell. When inhaled, nanoparticles pass the various filters (hairs) and remain in suspension down to the alveolus.
Damage mechanisms then occur that are detailed in Buzea et al. (2007) and are:

- oxidative stress and release of antioxidants,
- inflammation,
- DNA damage,
- nervous, lymphatic, or endocrinal system uptake.

A complete study on nanoparticle cytotoxicity is given in Soto et al. (2005). It has also been said that nanoparticles can carry and introduce easily toxic compounds and microorganisms, therefore playing an indirect toxic role.
Reciprocally, the body is able to eliminate the intruders, the rate of which is referred to as the clearance. Clearance occurs by translocation in the organism, but also phagocytosis (mainly through the action of macrophages) and the so-called mucociliary escalator in the lungs (Brain et al. 2009).

8.2.3.2 Examples of harmful nanoparticles

Among the previous examples of nanoparticles, remarkable adverse health effects of some of them are now described.
The nature of combustion nanoparticles (soots and CNTs) and their role on health is studied in Evelyn et al. (2003), and the role of high aspect ratio particles is again proven particularly harmful. Indoor pollution causes most casualties (Wagner et al. 2010) but is paradoxically assumed to be benign to the environment. Buzea et al. (2007) states that the natural, renewable status of wood is a cause for the underestimation of wood fire harm.
The cosmetics industry has always been less monitored than the pharmaceutical industry, and many nanoparticles have been incorporated without any test campaign, solely on the basis that micro particles of the same compounds are innocuous. Unfortunately, adverse effects were recently identified in widely used nanoparticles such as TiO_2 (Rehn et al. 2003).
Asbestos causes a wide range of cancers (mesothelioma etc.) after long exposures (Jolicoeur et al. 1981) so the risk is nowadays well known and limited. Metal nanoparticles constitute an industrial hazard for workers in the production factories (Duffin et al. 2007; Park et al. 2007). Volcanic soils are related to podoconiosis, an acute and chronic inflammation of the lower limbs in which nanoparticles are accumulated, having penetrated through their bare feet. Lunar dusts have early been studied (Batsura et al. 1981) and are proven to cause lung disease such as pneumoconiosis.

8.2.4 Conclusion and need for fine modeling

As a conclusion, nanoparticles raise complex issues that require a complete modeling strategy. Processes involving nanoparticles are roughly modeled up to now. Although engineered nanoparticles may be a technological chance, their dispersion through gases and liquids as well as their toxicology must be assessed: on the basis of the nanoparticle material, morphology (size, shape e.g. aspect ratio) but also aging.
The effect of the particle chemical composition is detailed in Brain et al. (2009). The particle size drives the penetration ability and the deposition rate but also the clearance rate (e.g. macrophages have a size of $20\,\mu$m). The particle aspect ratio (Lippmann 1990) plays also a major role with the general idea that the higher, the most harmful e.g. asbestos fiber toxicity strongly depends on their size and shape, the relations being well listed (Jolicoeur et al. 1981). And a surprising concentration-decreasing effect is put forward in Churg et al. (1998) and in Gurr et al. (2005), based on the idea that high concentrations promote agglomeration and that the resulting clusters may have a reduced impact.
Essentially, the exact knowledge of the nanoparticle size distribution should be modeled with care at all the stages: we focus on the modeling of transport of nanoparticles as it is an important and less studied topic.

8.3 General theory of aerosols adapted to nanoparticle case

Aerosols designate disperse two-phase flows where the inclusions have a negligible inertia. Aerosols have many technological applications including aerosol sprays; dispersal of pesticides; medical treatment of respiratory illnesses and in combustion technology. Aerosol science covers a wide range of topics, such as generation and removal of aerosols, technological application and their impacts on the environment and people.
We consider the possibility to treat nanoparticles through aerosol theory. The main models are presented and the limitations for nanoparticles are discussed.

8.3.1 Aerosol transport

The theory of aerosol and its transport is described in many books (Fuchs 1964; Hinds 1982; Hidy 1984; Nigmatulin 1990; Williams and Loyalka 1991; Willeke and Baron 1993; Seinfeld and Pandis 1998; Friedlander 2000; Baron and Willeke 2001). In some extents, aerosol models are close to disperse two-phase flow models, though inertia plays a major role in the latter, while inertia is neglected for aerosols. Brownian effects may then occur.

8.3.1.1 Transport equation

Aerosols are usually described as a monospecies concentration n for which a transport equation can be written at fluid velocity $\boldsymbol{u}_g$:

$$\partial_t n + \partial_{\boldsymbol{x}} \cdot (\boldsymbol{u}_g n) = \partial_{\boldsymbol{x}} \cdot (D \partial_{\boldsymbol{x}} n) \tag{8.1}$$

This equation was derived by Smoluchowski (1916). It is retrieved from the Fokker-Planck equation written at an underlying kinetic level in § 8.4.2.3.
This formalism accounts for the transport of a dilute aerosol by the carrier phase. The effect of a moderately dense disperse phase on the carrier phase cannot be assessed easily. So the resulting model for a disperse two-phase flow is one-way coupled.

8.3.1.2 Diffusion

The diffusion of aerosol particles in their carrier medium is due to molecular agitation and results in a transport that tends to homogenize the particle density. It is most of the time treated in a long time asymptotics with a flux proportional to a concentration gradient. The diffusion coefficient is assessed in the Brownian theory, as presented in § 8.4.1, by the Stokes-Einstein formula:

$$D = \frac{kT_g}{6\pi\mu_g r_p} \tag{8.2}$$

with k the Boltzmann constant, T_g and μ_g the gas temperature and viscosity, and r_p the particle radius.
A correction for agglomerates can be considered (Friedlander 2000) from the knowledge of the agglomerates' shape e.g. their fractal dimension, defined in § 8.3.3.2. The diffusion coefficient is the standard one for $D_f = 3$ while it should be corrected to include porosity and string effects, according to the work of Tandon and Rosner (1995).

8.3.1.3 Friction coefficient

Friction f is a proportionality coefficient between the drag force and slip velocity:

$$\boldsymbol{F} = f\boldsymbol{u}_{\text{slip}}. \tag{8.3}$$

Since inertia is not considered for aerosols, the drag force does not need to be computed to solve the particle convective transport. But its knowledge remains necessary as friction is a limiting process, the effect from which results various equilibria, e.g. settling velocity v_s of an isolated particle, Brownian diffusion *etc.*
In general, when particles encounter a body force such as gravity weight $m_p g$, non Galilean force $m_p a_{\bar{g}}$, buoyancy, electrical force $q\boldsymbol{E}$ for a charged particle q in an exterior field $\boldsymbol{E}$, *etc.* a settling velocity can be computed by considering an equilibrium state. For instance in the case of drag, buoyancy and gravity, we have:

$$\boldsymbol{v}_s = \frac{2(\rho_l - \rho_g)\boldsymbol{g} r_p^2}{9\mu_g}. \tag{8.4}$$

The link between the diffusion coefficient and the slip coefficient is explained in § 8.4.1.

8.3.1.4 Thermophoresis

Thermophoresis is defined as the transport of particles due to temperature gradients. It has been envisioned theoretically by Waldman and Schmitt (1966) and studied experimentally (Talbot et al. 1980; Eisner and Rosner 1985).
We note that thermophoresis depends on temperature gradients. In practice, it is significant for strong gradients e.g. in a flame front. The typical numerical approach of a SRM is done with modeled flame fronts so that thermophoresis is not to be directly accounted for.
Thermophoresis may still have significant effects:

- in BC modeling e.g. propellant combustion,
- in droplet modeling e.g. aluminum distributed combustion,
- at the sub-grid scale level, e.g. to induce preferential concentration, promoting coalescence *etc.*.

Let us highlight the particular role that thermophoresis is assumed to play at the scale of a burning aluminum microscopic droplet in a SRM (Fabignon et al. 2003): thermophoretic transport of nano droplets (or smokes) is the cause of a Stefan flux that influences the chemical equilibrium and the overall burning rate.

8.3.2 Remarks on coupling terms

By analogy with the micrometric inclusions, we now discuss heat and mass transfers, though the question is not envisioned in these terms for aerosols.

8.3.2.1 Drag and heating

For aerosol particles, the momentum transfer through drag is so fast that drag does not need to be modeled itself and the average transport is considered at the carrier phase velocity.
As for heat transfers, nanoparticles are most of the time at thermal equilibrium with the surrounding carrier phase for the same reasons of fast relaxation. The role of radiation is however particularly important, bringing the aerosol to an equilibrium with the radiative ambience. Its modeling is made difficult by the fact that the particle shape can be complex. The case of soot in a combustion chamber is representative of these peculiarities.
So the momentum and heat source terms are rarely treated (except in the case of radiation) while the mass source terms can become significant.

8.3.2.2 Mass transfers

Mass transfers for aerosols are treated with similar tools as for droplets and particles (presented in § B).
Compared to usual inclusions, surface effects are dominant so that heterogeneous chemistry often needs to be taken into account. Some particles have particular surface properties or shape (e.g. soot) which must be taken into account and need further modeling.
In addition, chemistry or evaporation kinetics may become significant compared to the other phenomena.

8.3.3 Multicomponent and polydisperse aerosols

The chemical composition and size distribution of particles in aerosols can be complex and its modeling is now discussed.

8.3.3.1 Superposition of aerosol equations

In case multiple species are simultaneously airborne (multicomponent aerosols), we just need to consider n_k concentrations with their corresponding equations, where k is the species index.
In case of polydispersity, the sizes present in an aerosol can be described with the same techniques as for two-phase polydispersity: samples, sections or size moments can be used. The classes or bins n_k are transported simultaneously with the corresponding volume v_k. A continuous representation of size is possible through the size distribution $n(v)$. In this case, the transport equation is the usual aerosol one, but conditioned by size. Moment methods are then possible (Marchisio and Fox 2005), such as those described in Chapter 4.
A conditioning by chemical composition can also be done, as detailed in Friedlander (2000).

8.3.3.2 Shape description

Considering an agglomerate of size r, made of N_p primary particles of radius r_0 where:

$$N_p \sim \left(\frac{r}{r_0}\right)^{D_f} \tag{8.5}$$

the D_f exponent, referred to as fractal dimension, characterizes the stacking up. For a compact or well-sintered agglomerate, we have $D_f = 3$ while $D_f = 1$ for a linear agglomerate, chain or polymer (Friedlander 2000).
Non-spherical particles are often found when the agglomeration process is significant and they require careful modeling (see for instance Jeong and Choi 2003a). Multivariate statistical descriptions can be considered (Cheng et al. 2008) but they are out of the scope of this work. Soots in ICE are notoriously non spherical.

8.3.3.3 Agglomeration, coalescence, coagulation

Agglomeration is the process of two particles coming to permanent contact, coalescence (liquid case) is the merging of the interfaces towards a unique spherical one (sintering designates a fairly similar process for solid particles). Coagulation is sometimes used to describe both agglomeration and coalescence occurring at once.
Agglomeration can lead to non-spherical aggregates while coalescence leads to spherical liquid droplets.
In the following, we use the term coalescence, keeping in mind that the rates can be modeled similarly for agglomeration and coalescence.

8.3.3.4 Description of coalescence: Smoluchowski's master equations

Smoluchowski (1916) describes the evolution of the number of particles of different sizes due to coalescence in a spatially homogeneous case, i.e. a well-stirred reactor. He defined a set of coupled master equations, in the sense that a master equation describes the time-evolution of a system, which can be modeled as being in exactly one of countable number of states at any given time. The states correspond to finite bins or modes, accounting for particles with either an integer number of monomers (for agglomerates) or an integer multiple of a monomer volume (for coalescence and coagulation products). The coalescence process itself, i.e. the transport from a bin to another, is assessed statistically, which requires to evaluate collision probabilities. The latter depend on microscopic velocity differences between particles.
Smoluchowski's master equations result in a system of non-linear equations that read:

$$\left\{\begin{array}{ll} \mathrm{d}_t n_1 = & -\sum_{j=1}^{+\infty} \beta(1,j) n_1 n_j \\ \vdots & \\ \mathrm{d}_t n_k = & \frac{1}{2} \sum_{\substack{i=1 \\ j=k-i}}^{+\infty} \beta(i,j) n_i n_j - n_k \sum_{j=1}^{+\infty} \beta(k,j) n_j \\ \vdots & \end{array}\right. \tag{8.6}$$

where $\beta(i,j)$ is the coalescence kernel. In the case of coalescence, the number of monomers i and j are replaced by volume variables v_i and v_j and coalescence ensures the conservation of volume $v_k = v_i + v_j$. A continuous representation of sizes allows then to write:

$$\partial_t n(v) = \frac{1}{2} \int_{v^\diamond = v - v^\star} \int_{v^\star=0}^{+\infty} \beta(v^\star, v^\diamond) n(v^\star) n(v^\diamond) \mathrm{d}v^\star - \int_{v^\star=0}^{+\infty} \beta(v, v^\star) n(v) n(v^\star) \mathrm{d}v^\star \tag{8.7}$$

where $v^\diamond = v - v^\star$. This equation is referred to as a Population Balance Equation (PBE).
The modeling of β to close the coalescence equation has a strong influence on the dynamics of coagulation, as discussed below. Smoluchowski originally suggested a brownian coagulation kernel, as presented in § 8.4.4.2, but other kernels exist, depending on the particle size, that are obtained from various theories e.g. in free molecular regime from the kinetic theory § 8.5.1.2 or empirical laws on size. Because of the small inertia of nanoparticles, the interaction potential at close distance plays a role on the coagulation kernel, which makes its modeling difficult, as discussed in § 8.4.5.3.

8.3.3.5 Coalescence asymptotics

The asymptotics of coalescence has been long-time studied either as a mathematical topic: self-similar solutions are an efficient and popular approach, see a review in van Dongen and Ernst (1988). And as a physical topic, it has been studied to predict size distributions or explain observed behaviors. The case of pigment particle distributions (TiO_2) is for instance under study (Tsantilis et al. 2002; Spicer et al. 2002)
As regards the mathematical properties of the coalescence asymptotic solution, a strong dependence on the kernel is observed and has led to many researches on properties e.g. existence of such solutions, gelation transition (Friedlander and Wang 1966; Lai et al. 1972; Drake 1976; Park and Lee 2001; Leyvraz 2003)
Facing the complexity of the solution of the coagulation equation, bimodal approaches have been tested (Chatzi and Kiparissides 1992; Jeong and Choi 2001; Jeong and Choi 2003b; Jeong and Choi 2005; Ziegler and Wolf 2005) for their ability to allow linearization (as discussed and exploited in § 7.3).

8.3.3.6 Accounting for coalescence with transport

If non uniformity is to be considered, the previous equations can be extended to spatial dependency. The master equation is rarely written so, since it then features a high number of PDEs to be solved. The PBE extended to space dependency is referred to as Generalized Population Balance Equation (GPBE): it has a high dimensional phase space (though lacking the three dimensional velocity DOF compared to Williams-Boltzmann equations) and can be solved by appropriate discretizations, described in Chapter 4.

8.3.4 Size dependency of the closures

As for disperse two-phase flows, closures are very dependent on the relative size of the particles.
The unusual properties of nanoparticles evolve smoothly with size, down to the level when quantum effects appear. From then, the exact atomic structure of the particle must be known since a discontinuous behavior occurs due to quantum confinement effects in material with electron delocalization:

- quantized energy spectrum,
- magnetic moments even when the corresponding bulk material is non-magnetic (gold, platinum, palladium),
- quantified changes in the ability to accept and donate electrons, resulting in modified catalytic abilities.

8.3.4.1 Collision cross-sections

The collision cross-sections describe nearby nanoparticle interactions.
In the case of nanoparticles, short range forces have to be assessed. Moreover, particles with a slight electrical charge can encounter deviations from the usual geometric cross-section.

8.3.4.2 Curvature effect

Mass transfers at the surface are perturbed when curvature becomes strong i.e. for small particles.
For instance, the well known Kelvin effect is the fact that smaller particles need a higher ambient relative humidity to maintain equilibrium than bigger ones would. Relative humidity for equilibrium can be determined with a saturation vapor pressure p_s above a small particle at equilibrium that is different from the p_0 saturation vapor pressure above a flat surface of the same liquid. The Kelvin equation for saturation vapor pressure above a curved surface is (Gyarmathy 1963; Gyarmathy 1982; Young 1995):

$$\ln\left(\frac{p_s}{p_0}\right) = \frac{2\sigma_l M}{RT_p\rho_l r_p} \tag{8.8}$$

with r_p the droplet radius, σ_l the surface tension, ρ_l the density of the liquid, T_p the droplet surface temperature, M the molar mass of the gaseous mixture, and R the molar perfect gas constant.

8.3.4.3 Surface effects

Nanoparticles encounter remarkably strong surface effects in the following sense. Surface atoms and molecules have altered properties compared to bulk atoms and molecules and the ratio of outer/inner molecules depends on particle size.
For instance, the lower binding energy of outer atoms results in the reduction of the melting point (e.g. for gold), accounted for through Gibbs-Thomson equation.
Compared to a 10 μm particle a 10 nm particle has its reactivity enhanced 1000-fold.
The idea of coating particles is classical in nano science and it may yield interesting results but complicates the analysis as regards size.

8.3.4.4 Conclusion and regimes

In the following, nanoparticles are treated distinctly from usual, inertial particles: the limit diameter is noted d_N, and its definition is discussed in Chapter 9.
For nanoparticles, the transport is very dependent on the relative size of the particles. This is quantified by a Knudsen number which compares the particle diameter d_p to the mean free path of the carrier fluid l_0:

$$\mathrm{Kn}_d = \frac{l_0}{d_p} \tag{8.9}$$

marking the transition from a continuous surrounding fluid to a molecular discrete environment. For air in the standard conditions, the mean free path is typically $l_0 \approx 70$ nm. For burnt gases in a SRM chamber, $l_0 \approx 15$ nm.
There are then two regimes for nanoparticles (see Figure 8.1):

- the diffusive or Brownian regime where Brownian motion occurs,
- the so-called free molecular regime or FMR (Friedlander 2000).

These two regimes are discussed in the two following sections and detailed models are provided. A synthesis is presented in the final section of the chapter as well as interpolation approaches and formulae for particles in between the two regimes.

8.4 Modeling particles in diffusive regime: Brownian particles

We consider the case of particles which are small enough to encounter Brownian motion but are still larger than the mean free path of the carrier phase so they have:

$$\mathrm{Kn}_d \ll 1.$$

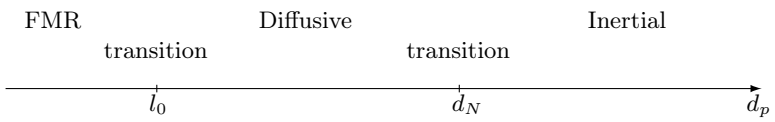

Figure 8.1: *Regimes of particle and nanoparticle flows.*

This regime is sometimes designated as continuous for the fluid surrounding the particles is a continuous medium at the scale of the particles themselves.
The modeling effort on such particles has been intense, triggered by the ease to observe Brownian motion. To account for the discontinuous and random effect of gas molecules on the particles, a stochastic modeling is used that complies to the statistical formalism, yielding the Fokker-Planck equation.

8.4.1 Near-equilibrium approach of Brownian Motion

8.4.1.1 Definition and historical insight

Brownian motion (or pedesis) is a physical phenomenon corresponding to the chaotic motion of a particle in a fluid, observable when the particle is sufficiently small. It was first observed by Robert Brown for particles within plant pollen (Brown 1828), then theorized and quantified in Einstein (1905) and the theoretical formula was confirmed experimentally (Perrin 1908; Perrin 1910), being then considered as a strong proof of the atomic theory. Brownian motion results indeed from permanent collisions of the invisible particles constituting the fluid (atoms, molecules) on the "observable" particle which is larger. The large particle trajectory is jagged as the fluid particles have various momenta.
Brownian motion also refers to a mathematical object: a stochastic process which can be used to model the corresponding, physical phenomenon as well as many others such as temperature fluctuations, price in financial market modeling *etc.* The mathematical process is also named Wiener process.

8.4.1.2 Practical aspects of Brownian motion

Nanoparticles encounter Brownian motion, which can be seen as regards the related aspects of dispersion, diffusion, and dissipation. These three phenomena are caused by collisions between particles and gas molecules, the latter being smaller but at higher (thermal) velocities. Dispersion corresponds to the fact that the particles have several, very different velocity values with time. Diffusion corresponds to the fact that a group of particles expands as the particles move in all directions (random walk), but the center of mass of the cloud does not move, as illustrated in Figure 8.2. Finally, dissipation corresponds to the fact that a particle with a relative motion tends to stop in the gas reference frame as it encounters more collisions on its forward face than on its rear.
Linking the third aspect with the first two -which are naturally linked- may seem awkward; however, it is an essential and characteristic feature of Brownian motion: dissipation occurs at a rate that is linked to velocity and position fluctuations: this principle is enforced by the fluctuation-dissipation theorem (Callen and Greene 1952; Kubo 1966; Greffet 2008; Pottier 2007). On the contrary, turbulent transport of particles does not satisfy the fluctuation-dissipation theorem since the local velocity dispersion can be linked to spatial correlations of the turbulent field (Reeks 1988) while dissipation is permanently linked to the friction coefficient.
Chandrasekar (1943) has shown that the number density function of particles encountering a Brownian random walk tends to a Gaussian which deviation increases with time. This solution for the NDF is analogous to that of a temperature field encountering isotropic heat conduction.

8.4.1.3 The Langevin equation

A classical phenomenological model has been introduced by Langevin (1908). In a Lagrangian point of view, the position of a particle $\boldsymbol{x}_p$ of mass m_p is assessed by accounting for the effect of the surrounding fluid through two distinct contributions:

$$m_p \partial_{tt} \boldsymbol{x}_p = -m_p \gamma \partial_t \boldsymbol{x}_p + \boldsymbol{F}_p(t) \tag{8.10}$$

where the first contribution is a usual fluid drag of coefficient γ and $\boldsymbol{F}_p$ is a random force so that Langevin's equation is a first historical example of stochastic equation (Pottier 2007).
The random force $\boldsymbol{F}_p$ is then a steady process:

$$\langle \boldsymbol{F}_p(t) \rangle = 0 \tag{8.11}$$

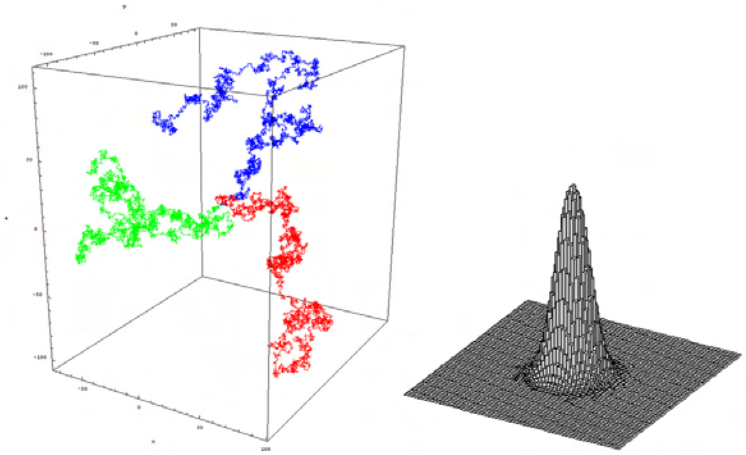

Figure 8.2: *Random walk in* $\mathbb{Z}^3$ *(step* $10,000$*) (left) – NDF in* $\mathbb{Z}^2$ *(step* 60*)*

and moreover its autocorrelation function is assumed to be a Dirac δ-function (Pottier 2007):

$$\langle \boldsymbol{F}_p(t)\boldsymbol{F}_p(t+\tau)\rangle = 2Dm_p^2\delta(\tau) \tag{8.12}$$

to account for the complete independence of two successive trajectory strokes i.e. the force imposed by the underlying molecules is a white noise. This assumption is linked to the scale separation between the collision time and the relaxation time and therefore to the idea that the particle is "heavy" compared to molecule and matches the requirement $\mathrm{Kn}_d \ll 1$.
The Langevin equation describes the complete evolution of particles in Brownian conditions: it allows to determine the time for such particles to reach a steady state, say to thermalize, and to quantify the fluctuations in such steady state, matching the observations of Brownian motion.
At steady state, the velocity dispersion σ can be assessed as the RMS of the velocity process

$$\sigma^2 = \langle \boldsymbol{c}^2\rangle = \frac{\int \boldsymbol{c}^2 f \mathrm{d}\boldsymbol{c}}{\int f \mathrm{d}\boldsymbol{c}} \tag{8.13}$$

and the thermal equilibrium leads to the following equality:

$$\frac{1}{2}m_p\langle \boldsymbol{c}^2\rangle = \frac{3}{2}kT_g \tag{8.14}$$

with $k = 1.3806503 \times 10^{-23}\,\mathrm{m}^2.\mathrm{kg/s}^2/\mathrm{K}$ the Boltzmann constant. We get finally

$$\sigma = \sqrt{\frac{3kT_g}{m_p}}. \tag{8.15}$$

8.4.1.4 Thermodynamic modeling

From considerations on the thermodynamics of a system of particles and an analogy with the osmotic pressure, Einstein (1905) then introduces the form of the coefficient:

$$D = \frac{kT_g}{f} \tag{8.16}$$

see also Einstein (1926). This coefficient is linked to the thermal energy at the molecular level, in accordance with the description of Brownian motion as caused by collisions with molecules. The steady regime of Brownian motion is then legitimately referred to as a thermalization.
In addition, the stokesian friction coefficient can be used in the context of the Brownian theory (Friedlander 2000), which is universally linked to the fluid viscosity in Stokes regime (Stokes 1846) and then reads

$$f = 6\pi\mu_g r_p \tag{8.17}$$

for a particle of radius r_p. This expression is the same as the one used to write the drag force in the general case of Eq. (3.47), while the Schiller-Naumann or turbulent drag expressions are never relevant for these small particles. Stokes' friction coefficient is said to be applicable for r_p below a micrometer (Friedlander 2000) and as long as $\mathrm{Kn}_d \ll 1$ i.e. down to the continuous limit again.

So coefficient D finally reads:

$$D = \frac{kT_g}{6\pi\mu_g r_p}. \tag{8.18}$$

which is consistent with Eq. (8.2). It finally is a diffusion coefficient consistent with the aerosol transport Eq. (8.1): it describes the trend for a cluster of particles to homogenize in space, at a rate that increases when particle size decreases.
As a conclusion, the Brownian motion can be described by a stochastic-Lagrangian (i.e. particular) theory through the Langevin model, still based on thermodynamics i.e. near equilibrium considerations. Remarkably, the stochastic vision is equivalent to a PDF description, as it was the case for disperse phase modeling. So that, after describing the orders of magnitude in a SRM, the Eulerian formulation of this Brownian theory can be detailed: it is based on the so-called Fokker-Planck equation and the aerosol Eq. (8.1) can be retrieved and its analysis furthered.

8.4.1.5 Case of a SRM

The mean free path in a SRM chamber has been assessed as $l_0 \approx 15\,\text{nm}$ for burnt gases. This shows that the continuous regime is mostly relevant. From the formulae of Eq. (8.18) and of Eq. (8.15), we can give some orders of magnitude in typical SRM conditions for the velocity dispersion in Table 8.1 and the diffusion coefficient in Table 8.2.

r_p (μm)	0.1	1	10
$T_g = 398\,\text{K}$	4.10^{-2}	10^{-3}	4.10^{-5}
$T_g = 3000\,\text{K}$	0.1	3.10^{-3}	10^{-4}

Table 8.1: *Values of σ (m/s) in SRM burnt gases.*

r_p (μm)	0.1	1	10
$T_g = 398\,\text{K}$	3.10^{-11}	3.10^{-12}	3.10^{-13}
$T_g = 3000\,\text{K}$	2.10^{-10}	2.10^{-11}	2.10^{-12}

Table 8.2: *Values of D (m^2/s) in SRM burnt gases.*

We highlight that the Brownian diffusion coefficient is very small by considering two examples:

- Assuming a SRM chamber with a characteristic size of $L = 1\,\text{m}$, a particle with a radius of 100 nm diffuses through the distance L in a time $T = 5.10^9\,\text{s}$.
- Assuming a particle residence time in the chamber $\tau^R_{\text{chamber}} = 10\,\text{ms}$, the characteristic distance of diffusion is $\delta = 1.4\,\mu\text{m}$.

8.4.2 Fokker-Planck equation

We consider a modeling for Brownian particles that is equivalent to the previous Langevin model, but in an Eulerian framework: the statistical modeling of Brownian motion with a Brownian stochastic term results in a Fokker-Planck equation.

8.4.2.1 Deriving the Fokker-Planck equation

We describe the Brownian particles statistically through there NDF $f(t, \boldsymbol{x}, \boldsymbol{c}, S)$ where the droplet temperature is not solved as it is close to that of the gas (as discussed in § 8.3.2.1 for aerosols). The NDF follows a kinetic equation:

$$\partial_t f + \boldsymbol{c} \cdot \partial_{\boldsymbol{x}} f + \partial_{\boldsymbol{c}} \left(\widetilde{\boldsymbol{F}} f \right) = \mathfrak{C}. \tag{8.19}$$

The gas-particle coupling term $\widetilde{\boldsymbol{F}}$ requires particular care as it includes the fluctuating effect of collisions between the gas and the particles, which we aim at capturing. The source term $\mathfrak{C}$ renders the particle-particle collisions. We consider again time scales that are big compared to the collision time which corresponds to $\text{Kn}_d \ll 1$. This means that in a DNS context, the gaseous field has deterministic (well defined) and continuous values of velocity and temperature at each location. Whereas at the microscopic level which we do not want to describe, the gas-droplet coupling occurs only because of molecule collisions, which yield at the same time

momentum fluctuation and dissipation so that the rate of change of velocity is modeled with a Langevin force per unit mass:

$$\widetilde{\boldsymbol{F}} = \boldsymbol{F} + \boldsymbol{B} \tag{8.20}$$

where $\boldsymbol{F}$ is the deterministic part corresponding to dissipation and $\boldsymbol{B}$ is a stochastic term modeling fluctuations so its average is null $\langle \boldsymbol{B}(t) \rangle = 0$. The average force $\boldsymbol{F}$ is given by the usual Stokes law, considering its relaxation time $\tau^{\boldsymbol{u}}(S)$:

$$\boldsymbol{F}(t, \boldsymbol{x}, \boldsymbol{c}, S) = \frac{\boldsymbol{u}_g(t, \boldsymbol{x}) - \boldsymbol{c}}{\tau^{\boldsymbol{u}}(S)} \tag{8.21}$$

where $\boldsymbol{u}_g(t, \boldsymbol{x})$ is the local gas velocity. As for $\boldsymbol{B}(t)$, it models a Brownian motion so its autocorrelation function is isotropic

$$\int_0^{+\infty} \langle \boldsymbol{B}(t) \otimes \boldsymbol{B}(t+\tau) \rangle \mathrm{d}\tau = q(t)\mathbf{I}. \tag{8.22}$$

Since the considered timescales are big compared to the collision time, we assume that $\boldsymbol{B}(t)$ is totally uncorrelated as for Eq. (8.12):

$$q(t) = 2D\delta(0) \tag{8.23}$$

which is equivalent to having the spectrum of a white noise. So the random motion is treated equivalently as for the Langevin model.
From a Cramers-Moyal expansion (Risken 1996; Pottier 2007), the white noise modeling for $\boldsymbol{B}$ is proven to yield the following equation from Eq. (8.19) for the NDF, when assuming $\mathfrak{C} = 0$:

$$\partial_t f + \boldsymbol{c} \cdot \partial_{\boldsymbol{x}} f + \partial_{\boldsymbol{c}} \left(\frac{\boldsymbol{u}_g - \boldsymbol{c}}{\tau^{\boldsymbol{u}}(S)} f \right) = \partial_{\boldsymbol{c}} \cdot (D \partial_{\boldsymbol{c}} f) \tag{8.24}$$

known as the Fokker-Planck equation. This formalism statistically accounts for the overall effect (drag and Brownian diffusion) of the gas on the particles but the retrocoupling on the gas cannot be deduced easily. So a resulting model for a disperse two-phase flow will necessarily be one-way coupled.
As a remark, similar equations can be derived for underlying processes which have a non-zero correlation time that feature mixed derivatives $\partial_{\boldsymbol{cx}}$ and are referred to as generalized Fokker-Planck equations, as stated by Reeks (1988) for turbulence.

8.4.2.2 Pseudo-collision-operator and equilibrium distribution

Let us consider the dimensionless form of Eq. (8.24):

$$\partial_t f + \boldsymbol{c} \cdot \partial_{\boldsymbol{x}} f = \frac{1}{\eta} \partial_{\boldsymbol{c}} \cdot [(\boldsymbol{c} - \boldsymbol{u}_g) f + \widetilde{D} \partial_{\boldsymbol{c}} f] \tag{8.25}$$

where $\widetilde{D}$ is the dimensionless coefficient of Brownian diffusion and η is the dimensionless relaxation time i.e. the Stokes number of the particles.
Let us write the r.h.s. $\mathcal{J}^{\mathrm{FP}}$ and treat it formally as a collision operator so that Eq. (8.25) reads:

$$\partial_t f + \boldsymbol{c} \cdot \partial_{\boldsymbol{x}} f = \frac{1}{\eta} \mathcal{J}^{\mathrm{FP}}(f). \tag{8.26}$$

The Fokker-Planck collision operator features a very different physics from Boltzmann's collision operator Eq. (3.108): Boltzmann's operator models elastic collisions, preserving mass, momentum and kinetic energy while the Fokker-Planck operator is conservative regarding mass only.
The Fokker-Planck equation can be seen as a linear model to account for the effect of collisions with molecules of the gas. As a result, the collision invariant theory applies only for mass so that we have:

$$\begin{aligned} &\int f^{(0)} \mathcal{J}^{\mathrm{FP}}(f) d\boldsymbol{c} = 0 \\ &\int \boldsymbol{c} f^{(0)} \mathcal{J}^{\mathrm{FP}}(f) \mathrm{d}\boldsymbol{c} \neq 0 \\ &\int \frac{1}{2} c^2 f^{(0)} \mathcal{J}^{\mathrm{FP}}(f) \mathrm{d}\boldsymbol{c} \neq 0. \end{aligned} \tag{8.27}$$

As a sum of drag and Brownian motion operators, $\mathcal{J}^{\mathrm{FP}}$ has non conservative effects on the particle velocities which can be illustrated as follows:

- the drag part dissipates momentum if the particle phase has a slip velocity,
- the Brownian part increases agitation from a completely still distribution of particles.

It can be shown that the Maxwellian distribution (see Eq. (3.119)) centered on $\boldsymbol{u}_g$ and with a dispersion $\widetilde{D}$:

$$f^{(0)}(t,\boldsymbol{x},\boldsymbol{c}) = \frac{n}{\sqrt{2\pi\widetilde{D}}}\exp\left(-\frac{(\boldsymbol{c}-\boldsymbol{u}_g)^2}{2\widetilde{D}}\right). \tag{8.28}$$

is the steady solution of Eq. (8.25). In addition, the equilibrium distribution $f^{(0)}$ carries all the macroscopic information as we have the constraints Eq. (3.111), with the particular values:

$$\begin{aligned}
&\int f^{(0)} d\boldsymbol{c} = n \\
&\int \boldsymbol{c} f^{(0)} \mathrm{d}\boldsymbol{c} = \boldsymbol{u}_g \\
&\int c^2 f^{(0)} \mathrm{d}\boldsymbol{c} = \widetilde{D}.
\end{aligned} \tag{8.29}$$

8.4.2.3 Chapman-Enskog expansion of the Fokker-Planck equation

A Chapman Enskog expansion, is performed on the Fokker-Planck equation to retrieve the classical fluid modeling for aerosols, in particular the Smoluchowski Eq. (8.1).
The Chapman-Enskog expansion is a technique that yields close to equilibrium solutions; it has been described in § 3.4.3 for the Boltzmann equation in a collisional regime. Benefiting from the fact that the Fokker-Planck equation has a pseudo-collision operator yielding an equilibrium, we can legitimate Chapman-Enskog expansion, where the parameter η (similar to a Stokes number) is very small for small particles. This is to be linked to the small Knudsen numbers for Boltzmann's collisional regimes.
We decompose f in the formalism of Chapman Enskog as done in Eq. (3.110):

$$f = f^{(0)}(1 + \eta\phi^{(1)} + \eta^2\phi^{(2)} + ...)$$

with the constraints of Eq. (3.111) for $i \geq 1$:

$$\begin{aligned}
&\int f^{(0)}\phi^{(i)} \mathrm{d}\boldsymbol{c} = 0 \\
&\int \boldsymbol{c} f^{(0)}\phi^{(i)} \mathrm{d}\boldsymbol{c} = \boldsymbol{0} \\
&\int c^2 f^{(0)}\phi^{(i)} \mathrm{d}\boldsymbol{c} = 0.
\end{aligned} \tag{8.30}$$

We substitute the expansion Eq. (3.110) in Eq. (8.26):

$$\partial_t[f^{(0)}(1 + \eta\phi^{(1)} + \eta^2\phi^{(2)})] + \boldsymbol{c}\cdot\partial_{\boldsymbol{x}}[f^{(0)}(1 + \eta\phi^{(1)} + \eta^2\phi^{(2)})] = \frac{1}{\eta}\mathcal{J}^{\mathrm{FP}}(f^{(0)}(1 + \eta\phi^{(1)} + \eta^2\phi^{(2)})) \tag{8.31}$$

where the term η^{-1} factorized in the r.h.s. will shift its order.
In accordance with the Chapman Enskog methodology, the zeroth order describes the equilibrium, valid at times η^{-1}:

$$\mathcal{J}^{\mathrm{FP}}(f^{(0)}) = 0 \tag{8.32}$$

where $f^{(0)}$ is the Maxwellian distribution derived previously. This solution satisfies the equality case in the H-theorem, presented in § 3.4.3.3, i.e. it minimizes entropy. It can be moreover demonstrated that

$$(\boldsymbol{c} - \boldsymbol{u}_g)f^{(0)} + \widetilde{D}\partial_{\boldsymbol{c}}f^{(0)} = 0 \tag{8.33}$$

The first level of the Chapman Enskog expansion, which describes the timescales of order η, is obtained by eliminating the equilibrium collision term $\mathcal{J}^{\mathrm{FP}}(f^{(0)}) = 0$:

$$\partial_t f^{(0)} + \boldsymbol{c}\cdot\partial_{\boldsymbol{x}}f^{(0)} = \mathcal{J}^{\mathrm{FP}}(f^{(0)}\phi^{(1)}) \tag{8.34}$$

thanks to the fact that $f^{(0)}$ belongs to the kernel of $\mathcal{J}^{\mathrm{FP}}$.
From the resolubility criterion (see § 3.4.3.3) of the first level Eq. (8.34), which is linked to mass conservation, we get:

$$\begin{aligned}
\mathscr{F}(\phi^{(1)}) &= \frac{1}{f^{(0)}}\partial_{\boldsymbol{c}}\cdot[(\boldsymbol{c}-\boldsymbol{u}_g)(f^{(0)}\phi^{(1)}) + \widetilde{D}\partial_{\boldsymbol{c}}(f^{(0)}\phi^{(1)})] \\
&= (\boldsymbol{u}_g - \boldsymbol{c})\partial_{\boldsymbol{c}}\phi^{(1)} + \widetilde{D}\partial_{\boldsymbol{cc}}\phi^{(1)}
\end{aligned} \tag{8.35}$$

with the notation $\mathscr{F}(\phi^{(1)}) = \frac{\mathcal{J}^{\mathrm{FP}}(f^{(0)}\phi^{(1)})}{f^{(0)}}$. Besides, we define the function Ψ from the l.h.s. of Eq. (8.34) which is developed as regards the peculiar velocity:

$$\Psi = \frac{1}{f^{(0)}}\left[\partial_t f^{(0)} + \boldsymbol{c}\cdot\partial_{\boldsymbol{x}} f^{(0)}\right] = \partial_t \log(f^{(0)}) + \boldsymbol{c}\cdot\partial_{\boldsymbol{x}}\log(f^{(0)}) \tag{8.36}$$

The resolubility criterion of Eq. (8.34) then formally reads:

$$\mathscr{F}(\phi^{(1)}) = \Psi \tag{8.37}$$

To make use of the resolubility criterion, we need to show that $\mathscr{F}$ is a self-adjoint operator. Let $\langle\phi,\psi\rangle = \int f^{(0)}\phi\psi \mathrm{d}\boldsymbol{c}$ be the scalar product in the Hilbert space of the functions of $\boldsymbol{c}$. We shall prove that the bilinear operator $\mathscr{F}$ is self-adjoint for $\langle\cdot,\cdot\rangle$ i.e. $\langle\mathscr{F}(\phi),\psi\rangle = \langle\phi,\mathscr{F}(\psi)\rangle$.

Proof Let us integrate Eq. (8.35):

$$\int f^{(0)}\psi\mathscr{F}(\phi^{(1)})\mathrm{d}\boldsymbol{c} = \underbrace{\int f^{(0)}\psi(\boldsymbol{u}_g-\boldsymbol{c})\partial_{\boldsymbol{c}}\phi^{(1)}\mathrm{d}\boldsymbol{c}}_{(1)} + \underbrace{\int f^{(0)}\psi\widetilde{D}\partial_{\boldsymbol{cc}}\phi^{(1)}\mathrm{d}\boldsymbol{c}}_{(2)} \tag{8.38}$$

where the r.h.s. is developed as

$$\begin{aligned}
(1) &= -\int\phi^{(1)}\partial_{\boldsymbol{c}}\left[f^{(0)}\psi(u_g-v)\right]\mathrm{d}v\\
&= -\int\phi^{(1)}\frac{\boldsymbol{u}_g-\boldsymbol{c}}{\widetilde{D}}f^{(0)}\psi(\boldsymbol{u}_g-\boldsymbol{c})\mathrm{d}\boldsymbol{c} - \int\phi^{(1)}f^{(0)}\partial_{\boldsymbol{c}}\psi(\boldsymbol{u}_g-\boldsymbol{c})\mathrm{d}\boldsymbol{c} + \int\phi^{(1)}f^{(0)}\psi\mathrm{d}\boldsymbol{c}\\
(2) &= -\widetilde{D}\int\partial_{\boldsymbol{c}}(f^{(0)}\psi)\partial_{\boldsymbol{c}}\phi^{(1)}\mathrm{d}\boldsymbol{c}\\
&= -\widetilde{D}\int\frac{\boldsymbol{u}_g-\boldsymbol{c}}{\widetilde{D}}f^{(0)}\psi\partial_{\boldsymbol{c}}\phi^{(1)}\mathrm{d}\boldsymbol{c} - \widetilde{D}\int f^{(0)}\partial_{\boldsymbol{c}}\psi\partial_{\boldsymbol{c}}\phi^{(1)}\mathrm{d}\boldsymbol{c}\\
&= -\int\phi^{(1)}f^{(0)}\psi\mathrm{d}\boldsymbol{c} + \int\phi^{(1)}\frac{\boldsymbol{u}_g-\boldsymbol{c}}{\widetilde{D}}f^{(0)}\psi(\boldsymbol{u}_g-\boldsymbol{c})\mathrm{d}\boldsymbol{c} + \int\phi^{(1)}f^{(0)}\partial_{\boldsymbol{c}}\psi(\boldsymbol{u}_g-\boldsymbol{c})\mathrm{d}\boldsymbol{c}\\
&+ \int f^{(0)}\phi^{(1)}(\boldsymbol{u}_g-\boldsymbol{c})\partial_{\boldsymbol{c}}\psi\mathrm{d}\boldsymbol{c} + \int\widetilde{D}\int f^{(0)}\phi^{(1)}\partial_{\boldsymbol{cc}}\psi\mathrm{d}\boldsymbol{c}
\end{aligned} \tag{8.39}$$

The proof is finally concluded:

$$\begin{aligned}
\int f^{(0)}\psi\mathscr{F}(\phi^{(1)})\mathrm{d}\boldsymbol{c} &= \int f^{(0)}\phi^{(1)}(\boldsymbol{u}_g-\boldsymbol{c})\partial_{\boldsymbol{c}}\psi\mathrm{d}\boldsymbol{c} + \int\widetilde{D}\int f^{(0)}\phi^{(1)}\partial_{\boldsymbol{cc}}\psi\mathrm{d}\boldsymbol{c}\\
&= \int f^{(0)}\phi^{(1)}\mathscr{F}(\psi)\mathrm{d}\boldsymbol{c}
\end{aligned} \tag{8.40}$$

The resolubility criterion is reformulated as an algebraic constraint by using the self-adjoint property of $\mathscr{F}$: Ψ must belong to the orthogonal complement of the kernel of $\mathscr{F}$. As the kernel is here reduced to the dimensionless mass 1, Eq. (8.34) finally reads:

$$\langle 1,\Psi\rangle = \int f^{(0)}\left[\partial_t\log(f^{(0)}) + \boldsymbol{c}\cdot\partial_{\boldsymbol{x}}\log(f^{(0)})\right]\mathrm{d}\boldsymbol{c} = 0 \tag{8.41}$$

Integrating Eq. (8.37) and eliminating the r.h.s. thanks to Eq. (8.41) yields a unique scalar macroscopic equation:

$$\partial_t n + \partial_{\boldsymbol{x}}\cdot(n\boldsymbol{u}_g) = 0 \tag{8.42}$$

which describes mass conservation on a timescale where diffusion fluxes are neglected and where the velocity is trivially $\boldsymbol{c} = \boldsymbol{u}_g$. A similar reasoning on the Boltzmann equation would yield the Euler equations, which indeed describe the dynamics of a gas where dissipative fluxes i.e. viscous and heat transfers are neglected. The second level of the Chapman Enskog expansion describes the timescales of order η^2:

$$\partial_t(f^{(0)}\phi^{(1)}) + \boldsymbol{c}\cdot\partial_{\boldsymbol{x}}\cdot(f^{(0)}\phi^{(1)}) = \mathcal{J}^{\mathrm{FP}}(f^{(0)}\phi^{(2)}) \tag{8.43}$$

An analogous approach with a resolubility criterion yields a macroscopic equation on mass n, the so-called Smoluchowski equation (Smoluchowski 1916; Chandrasekar 1943):

$$\partial_t n + \partial_{\boldsymbol{x}}\cdot(n\boldsymbol{u}_g) = \eta\partial_{\boldsymbol{x}}\cdot(\boldsymbol{V}_d) \tag{8.44}$$

where $\boldsymbol{V}_d$ is a drift velocity of particles which reads

$$\boldsymbol{V}_d = \int f^{(0)}\phi^{(1)}(\boldsymbol{c}-\boldsymbol{u}_g)\mathrm{d}\boldsymbol{c}. \tag{8.45}$$

It can be checked that $\boldsymbol{c}$ cannot be a collision invariant for $\mathcal{J}^{\mathrm{FP}}$ that is

$$\int f^{(0)}\phi^{(1)}\boldsymbol{c}\mathrm{d}\boldsymbol{c} \neq 0 \tag{8.46}$$

which would otherwise nullify $\boldsymbol{V}_d$ and yield the previous order Eq. (8.42).
To find $\boldsymbol{V}_d$, the new value of $\phi^{(1)}$ must be explicitly solved. Eq. (8.37) can be developed with the peculiar velocity:

$$\mathscr{F}(\phi^{(1)}) = \Psi = \partial_t \log f^{(0)} + \boldsymbol{u}_g\cdot\partial_{\boldsymbol{x}}\log f^{(0)} + \boldsymbol{c}\cdot\partial_{\boldsymbol{x}}\log f^{(0)} \tag{8.47}$$

which can be factorized:

$$\begin{array}{rcccccc} \Psi & = & \dfrac{1}{n^{(0)}}D_t n^{(0)} - \dfrac{\boldsymbol{u}_g-\boldsymbol{c}}{\sigma}\cdot D_t\boldsymbol{u}_g + \boldsymbol{c}\cdot\dfrac{\partial_{\boldsymbol{x}}n^{(0)}}{n^{(0)}} - \dfrac{\boldsymbol{c}\cdot(\boldsymbol{u}_g-\boldsymbol{c})}{\sigma}\partial_{\boldsymbol{x}}\boldsymbol{u}_g & & & & \\ & = & \left(\dfrac{\boldsymbol{c}^2}{\sigma}-1\right)\partial_{\boldsymbol{x}}\boldsymbol{u}_g & + & \dfrac{\boldsymbol{c}}{\sigma}\cdot D_t\boldsymbol{u}_g & + & \boldsymbol{c}\cdot\dfrac{\partial_{\boldsymbol{x}}n^{(0)}}{n^{(0)}} \\ & = & \Psi^u & + & \Psi^p & + & \Psi^n \end{array} \tag{8.48}$$

by considering the material derivative at hydrodynamic velocity $D_t\boldsymbol{u}_g = \partial_t\boldsymbol{u}_g + \boldsymbol{u}_g\cdot\partial_{\boldsymbol{x}}\boldsymbol{u}_g$. A decomposition of $\phi^{(1)}$ in the gradients is now performed:

$$\phi^{(1)} = \phi^n\frac{\partial_{\boldsymbol{x}}n^{(0)}}{n^{(0)}} + \phi^p D_t\boldsymbol{u}_g + \phi^u\partial_{\boldsymbol{x}}\boldsymbol{u}_g. \tag{8.49}$$

The Fokker-Planck equation is one of the rare cases where the gradients can be explicitly expressed, thanks to the linearity of $\mathscr{F}$:

$$\begin{cases} \mathscr{F}(\phi^n) = \boldsymbol{c} \\ \mathscr{F}(\phi^p) = \dfrac{\boldsymbol{c}}{\sigma} \\ \mathscr{F}(\phi^u) = \dfrac{\boldsymbol{c}^2}{\sigma} - 1 \end{cases} \tag{8.50}$$

After substitution of Eq. (8.50), we get

$$(\boldsymbol{u}_g-\boldsymbol{c})\partial_{\boldsymbol{c}}\phi^{(i)} + \widetilde{D}\partial_{\boldsymbol{cc}}\phi^{(i)} = \Psi^i\ , \qquad i\in\{n,p,u\} \tag{8.51}$$

where

$$\begin{cases} \phi^n = -\boldsymbol{c} \\ \phi^p = -\dfrac{\boldsymbol{c}}{\sigma} \\ \phi^u = \dfrac{(\boldsymbol{u}_g-\boldsymbol{c})^2}{\sigma} \end{cases} \tag{8.52}$$

so that Eq. (8.49) reads:

$$\phi^{(1)} = -\boldsymbol{c}\frac{\partial_{\boldsymbol{x}}n^{(0)}}{n^{(0)}} - \frac{\boldsymbol{c}}{\sigma}D_t\boldsymbol{u}_g + \frac{(\boldsymbol{u}_g-\boldsymbol{c})^2}{\sigma}\partial_{\boldsymbol{x}}\boldsymbol{u}_g \tag{8.53}$$

The drift velocity is that of a diffusion:

$$\begin{array}{rcl} \boldsymbol{V}_d & = & \displaystyle\int f^{(0)}\phi^{(1)}(\boldsymbol{c}-\boldsymbol{u}_g)\mathrm{d}\boldsymbol{c} \\ & = & \displaystyle\left[\int f^{(0)}(\boldsymbol{c}-\boldsymbol{u}_g)\mathrm{d}\boldsymbol{c}\right]\frac{\partial_{\boldsymbol{x}}n^{(0)}}{n^{(0)}} \\ & & \displaystyle-\left[\int f^{(0)}\frac{\boldsymbol{c}}{\sigma}(\boldsymbol{c}-\boldsymbol{u}_g)\mathrm{d}\boldsymbol{c}\right]D_t\boldsymbol{u}_g \\ & & \displaystyle+\left[\int f^{(0)}\frac{(\boldsymbol{u}_g-\boldsymbol{c})^2}{\sigma}(\boldsymbol{c}-\boldsymbol{u}_g)\mathrm{d}\boldsymbol{c}\right]\partial_{\boldsymbol{x}}\boldsymbol{u}_g \\ & = & \displaystyle-\sigma n^{(0)}\frac{\partial_{\boldsymbol{x}}n^{(0)}}{n^{(0)}} + 0\cdot\partial_{\boldsymbol{x}}\boldsymbol{u}_g - n\frac{\sigma}{\sigma}D_t\boldsymbol{u}_g \end{array} \tag{8.54}$$

and the final equation at this order reads:

$$\partial_t n^{(1)} + \partial_{\boldsymbol{x}}\cdot(n^{(1)}\boldsymbol{u}_g) = \eta\partial_{\boldsymbol{x}}\cdot(\sigma\partial_{\boldsymbol{x}}n^{(1)}) + \eta\partial_{\boldsymbol{x}}\cdot(n^{(1)}D_t\boldsymbol{u}_g). \tag{8.55}$$

The last term of the r.h.s. is understood as a perturbation due to the non galilean states of the hydrodynamic reference frame and vanishes if $\boldsymbol{u}_g$ is uniform.

8.4.2.4 Retrieving the Aerosol limit

As a conclusion, Eq. (8.1) is retrieved from the Fokker-Planck equation, which is therefore the relevant underlying kinetic representation for the Smoluchowski equation. This approach has been performed in more complex cases by Chavanis et al. (2004).
When η is small, the Fokker-Planck pseudo-collision operator is dominated by dispersion effects due to Brownian motion. Information on particle average velocity is no longer needed as the slip is negligible. So convection can be computed with the gas velocity.
This allows to consider:

$$\boldsymbol{u} = \boldsymbol{u}_g \text{ and } \sigma = \sigma_{\mathrm{Br}}$$

where σ_{Br} is given by Eq. (8.15). In this context, velocity average and dispersion are always relaxed and it is sufficient to solve Smoluchowski (1916)'s equation :

$$\partial_t n + \partial_{\boldsymbol{x}} \cdot (n\boldsymbol{u}_g) = \partial_{\boldsymbol{x}} \cdot D\partial_{\boldsymbol{x}} n \tag{8.56}$$

where it can be shown that $3D = \sigma_{\mathrm{Br}}^2 \tau^{\boldsymbol{u}}(S)$ so that D matches the mass diffusion coefficient due to Brownian microscopic agitation defined in Eq. (8.18).

8.4.3 Brownian thermophoresis

The phenomenon of thermophoresis, presented in § 8.5.1.3 as playing an important role in aluminum combustion modeling for instance, is defined as the transport of particles due to temperature gradients.
In the standard theory, this oriented transport superimposes to the isotropic Brownian motion; still they both originate from the collisions with the fluid molecules. Thermophoresis can be crudely explained by the fact that the fluid molecules are agitated with a varying strength along the temperature gradient so that they transfer to the particle a non-zero average impulsion, oriented from hot to cold regions.
For particles in a diffusive regime i.e. $\mathrm{Kn}_d \ll 1$, Talbot et al. (1980) suggests:

$$F_T = -\frac{3\pi\mu_g 2d_p H_T \nabla T}{2\rho_g T} \tag{8.57}$$

so that the thermophoretic velocity reads:

$$c_T = -\frac{1}{2}\nu_g H_T \frac{\nabla T}{T} \tag{8.58}$$

where ∇T is the temperature gradient. H_T is a correction factor for the temperature gradient within the particle that depends on the ratio of particle and fluid heat conductivities $r = \lambda_g/\lambda_l$:

$$H_T = \frac{2.34}{1 + 3.42\mathrm{Kn}_d} \frac{r + 2.18\mathrm{Kn}_d}{1 + 2r + 4.36\mathrm{Kn}_d}. \tag{8.59}$$

8.4.4 Brownian coalescence

In the Brownian regime, particles are prone to coalesce together because of their agitated motion. We now discuss the classical modeling approach for Brownian coalescence.

8.4.4.1 Issue of scale separation

The modeling for the coalescence of inertial particles has been done at the kinetic level (see § 3.5.2.4) but in the Brownian regime, the Fokker-Planck equation deals with particles for which the velocities are correlated on a time that is small compared to the particle-particle inter collision time. So the equilibrium velocity distribution, together with the local average particle concentration, is not satisfactory to assess collision frequencies.
In the following, we do not attempt to solve for the velocities. So the velocity kernel for coalescence is unclosed. An heuristic model is considered to replace velocity differences, based on the continuous formulation of Smoluchowski's master equation, described in § 8.3.3.4: a macroscopic flux is sought to close the coalescence kernel by an analytical formula. This modeling of coalescence terms is valid as long as the effect of coalescence on the velocity distribution is weak enough not to perturb the equilibrium described in Eq. (8.28).

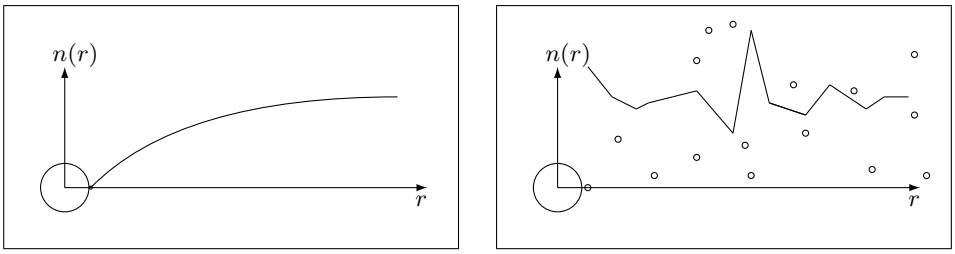

Figure 8.3: *Particle space repartition in the diffusive (left) and kinetic (right) regimes*

8.4.4.2 Classical theory: the diffusive kernel

We now consider the hydrodynamic limit of Eq. (8.24) i.e. we disregard transient regimes, which lead to the Brownian equilibrium. In this limit, the transport part results in the Smoluchowski equation:

$$\partial_t n + \partial_{\boldsymbol{x}} \cdot (n \boldsymbol{u}_g) = \partial_{\boldsymbol{x}} \cdot D \partial_{\boldsymbol{x}} n + Q_n \tag{8.60}$$

as stated in § 8.4.2.4 and the treatment of coalescence is a continuous model for Smoluchowski's master equation, presented in § 8.3.3.4, for which the kernel is unclosed. The coalescence term is not assessed as the limit of a kinetic coalescence term since the exact behavior of the latter, together with that of the correlation function is not evaluated. So that Smoluchowski (1916) resorts to a closure of Q_n, built by the direct resolution of a diffusive equation in the particle vicinity. The macroscopic coalescence term reads from the empirical Eq. (8.7):

$$\begin{aligned} Q_n = & \int_{v^\star \in [0,v]} n(t,\boldsymbol{x},v^\diamond) n(t,\boldsymbol{x},v^\star) \mathfrak{K}_{\text{coal}}(v^\diamond, v^\star) \mathrm{d}v^\star \\ & - n(t,\boldsymbol{x},v) \int_{v^\star \in [0,+\infty[} n(t,\boldsymbol{x},v^\star) \mathfrak{K}_{\text{coal}}(v, v^\star) \mathrm{d}v^\star \end{aligned} \tag{8.61}$$

and it has a similar form to that of the semi-kinetic terms of Eq. (4.18).
When the carrier phase is a continuous fluid i.e. $\mathrm{Kn}_d \ll 1$, the classical diffusive kernel of Smoluchowski (1916) prevails and reads:

$$\mathfrak{K}^{\text{Df}}_{\text{coal}}(r^\star, r^\diamond) = 4\pi \left(D^\star + D^\diamond\right)\left(r^\star + r^\diamond\right) \tag{8.62}$$

which can be expressed from the particle sizes and gas properties thanks to the knowledge of the Brownian diffusion coefficient of Eq. (8.18):

$$\mathfrak{K}^{\text{Df}}_{\text{coal}}(r^\star, r^\diamond) = \frac{2kT_g}{3\mu_g}\left(\frac{1}{r^\star} + \frac{1}{r^\diamond}\right)\left(r^\star + r^\diamond\right). \tag{8.63}$$

The theoretical background of this approach was completed by Chandrasekar (1943). A clarification and a synthesis were done by Fuchs (1964) (see also Friedlander 2000). This kernel is obtained by solving a usual Brownian transport equation for particles towards a test particle, the corresponding flux yielding the kernel. This resolution assumes that Smoluchowski's equation applies on a scale comparable to that of the inter particle distance, which goes hand in hand with the assumption that collisions occur rarely enough not to perturb the Brownian equilibrium
Diffusion indeed occurs due to a lower density compared to the average (lack of particles) in the surrounding of a reference particle, as illustrated in Figure 8.3, left. This lack, due to the absorbing boundary condition imposed near the reference particle is balanced by Brownian diffusion, but too slowly so that the criterion is rather a comparison between coalescence and diffusion times τ_c and τ_d, analogously to diffusion limited reactions. The existence of a density gradient at the particle wall is the consequence of the scale separation between Brownian transport dynamics and Brownian coalescence dynamics. The macroscopic coalescence rate is obtained as a diffusion flux at the reference particle wall.

8.4.4.3 Derivation of the diffusive kernel

We now present the derivation of this term as performed by Fuchs (1964). Considering particles of diameter $r^\diamond$, having a concentration $n^\diamond$ and a diffusion coefficient $D^\diamond$, the coalescence rate with a unique particle of radius $r^\star$ is the total flux of particles $\diamond$ at the absorbing spherical boundary $\mathcal{S}_{r^\star + r^\diamond}$ of radius $r^\star + r^\diamond$:

$$\Phi = \oint_{\mathcal{S}_{r^\star + r^\diamond}} \mathcal{F}(n^\diamond) \cdot \mathrm{d}\mathbf{S} \tag{8.64}$$

where the flux is the one of a conservation equation:

$$\frac{\partial n^\diamond}{\partial_t} + \nabla \cdot \mathcal{F}(n^\diamond) = 0 \tag{8.65}$$

In the non slip case, the diffusion equation reads almost everywhere:

$$\frac{\partial n^\diamond}{\partial_t} - \nabla \cdot (D^\diamond \nabla n^\diamond) = 0 \tag{8.66}$$

shows the flux to be purely diffusive i.e. a gradient. The uniformity far from the particle allows Fuchs (1964) to evaluate n at steady state

$$n^\diamond(\rho) = n^\diamond_\infty - (n^\diamond_\infty - n'^\diamond)\frac{r^\star + r^\diamond}{\rho} \tag{8.67}$$

where $n^\diamond_\infty$ is the unperturbed value and $n'^\diamond = n^\diamond(r^\star + r^\diamond)$ is the value close to the border. The gradient along the radial direction can be evaluated:

$$\nabla n^\diamond \cdot \mathbf{e}_r = \left(\frac{\mathrm{d}n^\diamond}{\mathrm{d}\rho}\right)_\rho = (n^\diamond_\infty - n'^\diamond)\frac{r^\star + r^\diamond}{\rho^2} \tag{8.68}$$

and especially

$$\left(\frac{\mathrm{d}n^\diamond}{\mathrm{d}\rho}\right)_{\rho = r^\star + r^\diamond} = \frac{(n^\diamond_\infty - n'^\diamond)}{r^\star + r^\diamond} \tag{8.69}$$

this value of the concentration gradient being illustrated in Figure 8.3, right as the slope of the concentration at the boundary. The total flux reads, by using the spherical symmetry and the absorbing condition $n' = n(r^\star + r^\diamond) = 0$:

$$\Phi = 4\pi(r^\star + r^\diamond)^2 \left(\frac{\mathrm{d}n^\diamond}{\mathrm{d}\rho}\right)_{\rho = r^\star + r^\diamond} = 4\pi n^\diamond_\infty (D^\star + D^\diamond)(r^\star + r^\diamond) \tag{8.70}$$

where the diffusion coefficient can be modified to account for the $\star$ particle diffusion coefficient $D^\star$ by additivity, for reasons of statistical independence of both diffusion processes (Fuchs 1964).

8.4.4.4 Brownian-ballistic transition

It has been stated above that for sufficiently small particles Brownian coalescence occurs, while for sufficiently large particles the mechanism is ballistic coalescence (Chapter 3). In fact this distinction is a simplification that practically renders the domination of one or another mechanism and there clearly exists particle sizes for which both mechanisms are significant: the problem then arises of how to calculate the coalescence kernel when Brownian and ballistic effects combine.

We highlight that the passage from a regime to another is not strictly speaking a transition since Brownian and inertial collisions originate from distinct phenomena: in the domain of domination of one mechanism, the other mechanism still occurs but it is too weak and can be neglected. Whereas in a transition such as the one between kinetic and diffusive Brownian coalescence, two different modeling approaches are involved to describe a unique phenomenon in the two "pure domains" while a third formalism may be needed in transition regime.

This raises three observations on the Brownian-ballistic transition:

- the transition criterion depends on the relative strength of Brownian and ballistic coalescence, which have independent sources;
- the transition zone's width depends on the way Brownian and ballistic coalescence vary with particle size;
- there is no need to introduce a new modeling frame in the transition regime.

This Brownian-ballistic "transition" is discussed in detail in Chapter 9 where it is designated as nano-micro transition for the Brownian particles of interest have a rather nanometric size and the ballistic ones a micrometric size.

8.4.5 Treating Brownian coalescence at the kinetic level

To treat coalescence at the kinetic level, an additional modeling effort must be done compared to usual non-Brownian particles to account for the scale separation between Brownian motion and inter-collision times.

8.4.5.1 Fokker-Planck equation with coalescence

We consider again the Fokker-Planck Eq. (8.24) as a base model for the disperse phase:

$$\partial_t f + \boldsymbol{c}\cdot\partial_{\boldsymbol{x}} f + \partial_{\boldsymbol{c}}\left(\frac{\boldsymbol{u}_g - \boldsymbol{c}}{\tau^{\boldsymbol{u}}(S)} f\right) = \mathfrak{C} + \partial_{\boldsymbol{c}}\cdot(D\partial_{\boldsymbol{c}} f) \tag{8.71}$$

where $\mathfrak{C}$ is the coalescence term. In the regime where the Fokker-Planck equation is valid, collisions of particles with gas molecules are much more frequent than with other particles. In addition, when a particle coalesces with another, the local particle density is perturbed on a long enough time compared to the mean free path of particles. As a consequence, the average concentration, together with the equilibrium velocity distribution cannot be used to assess the collision probability, as in usual kinetic systems: the correlations must be accounted for.
Coalescence terms can be accounted for in the kinetic formulation similarly to § 3.5.2.4 except that we take a more general form of the collision probability:

$$\begin{aligned}\mathfrak{C}(f^{(2)}) = &\frac{1}{2}\iint_{\boldsymbol{x}^\star,\boldsymbol{c}^\star}\int_{v^\star\in[0,v]} f^{(2)}(t,\boldsymbol{x},\boldsymbol{c}^\diamond,v^\diamond,\boldsymbol{x}^\star,\boldsymbol{c}^\star,v^\star)\,|\boldsymbol{c}^\diamond-\boldsymbol{c}^\star|\,\beta(v^\diamond,v^\star)J\mathrm{d}v^\star\mathrm{d}\boldsymbol{x}^\star\mathrm{d}\boldsymbol{c}^\star\\ &+\iint_{\boldsymbol{x}^\star,\boldsymbol{c}^\star}\int_{v^\star} f^{(2)}(t,\boldsymbol{x},\boldsymbol{c},v,\boldsymbol{x}^\star,\boldsymbol{c}^\star,v^\star)\,|\boldsymbol{c}-\boldsymbol{c}^\star|\,\beta(v,v^\star)\mathrm{d}v^\star\mathrm{d}\boldsymbol{x}^\star\mathrm{d}\boldsymbol{c}^\star\end{aligned} \tag{8.72}$$

where the molecular chaos assumption of Eq. (3.92) has been removed, so that collision probabilities resort to the two-point NDF $f^{(2)}$.

8.4.5.2 Two-point NDF

The introduction of a two-point NDF $f^{(2)}$ for laminar two-phase flow has been suggested by Batchelor (1972) to account for long-range interactions that lead to a group sedimentation velocity (see also Batchelor 1982; Batchelor and Wen 1982; Batchelor 1986). The approach has been extended to the case of gravity-induced coalescence (Schowalter 1982; Feke and Schowalter 1984; Melik and Fogler 1984; Wen et al. 1991). These authors rather focus on the two-point PDF p_2 defined as:

$$f^{(2)}(t,\boldsymbol{x},\boldsymbol{c}^\diamond,v^\diamond,\boldsymbol{x}^\star,\boldsymbol{c}^\star,v^\star) = f(t,\boldsymbol{x},\boldsymbol{c}^\diamond,v^\diamond)f(t,\boldsymbol{x},\boldsymbol{c}^\star,v^\star)p_2(t,\boldsymbol{r},\boldsymbol{c}^\star,v^\star,\boldsymbol{c}^\diamond,v^\diamond) \tag{8.73}$$

where $\boldsymbol{r} = \boldsymbol{x}^\star - \boldsymbol{x}$ is the distance between the centers of the two-particles. The correlation PDF then follows its own evolution equation (Wang and Wen 1990):

$$\begin{cases}\partial_t p_2 + \partial_{\boldsymbol{r}}\left(p_2\partial_t\boldsymbol{r} - p_2\boldsymbol{D_2}\cdot\partial_{\boldsymbol{r}}\cdot\left(\dfrac{\Phi_2}{kT_g}\right) - \boldsymbol{D_2}\cdot\partial_{\boldsymbol{r}}p_2\right) = 0\\ p_2(|\boldsymbol{r}| = r_1 + r_2) = 0\\ p_2(|\boldsymbol{r}|\to+\infty) = 1\end{cases} \tag{8.74}$$

where $\boldsymbol{D_2}$ is the Brownian relative diffusion coefficient and Φ_2 is the inter particle potential. The l.h.s. is null because the disperse phase is dilute enough to neglect the perturbations induced by three particle collisions. The dilution allows also to assume a steady state so that:

$$p_2\partial_t\boldsymbol{r} - p_2\boldsymbol{D_2}\cdot\partial_{\boldsymbol{r}}\left(\frac{\Phi_2(\boldsymbol{r})}{kT_g}\right) - \boldsymbol{D_2}\cdot\partial_{\boldsymbol{r}}p_2 = 0 \tag{8.75}$$

must be solved.

8.4.5.3 Modeling the short range interaction

The interaction potential function Φ_2 first describes the impenetrable aspect of the particle so the potential function goes to infinity when $|\boldsymbol{r}| < r_1 + r_2$. The repulsive part of the potential also deals with the electric charges at the particles surface (Feke and Schowalter 1984). In addition, the interaction potential is of paramount importance to describe in detail the effective occurrence of coalescence: the potential must have a minimum at some distance $|\boldsymbol{r}_0| \gtrsim r_1 + r_2$ to describe the attractive effect between the particles, typically due to Van der Waals forces. Indeed, in the context of a competition between cohesion forces of an agglomerate and Brownian agitation, which brings particles close to each other and can also indifferently separate them, the depth of the potential gap and its width characterize the stability of the agglomerate. Since the particles do not interact at long range, the Φ_2 is constant at $\boldsymbol{r}\to+\infty$. The Lennard-Jones potential (Lennard-Jones 1924; Giro and Guardia 1985) is a potential which is typical to describe chemical bonds and which suits to describe agglomerating particles; it is presented in Figure 8.4 and reads:

$$\Phi_2^{LJ} = K^{LJ}\left(\left|\frac{\boldsymbol{r}_0}{\boldsymbol{r}}\right|^{12} - 2\left|\frac{\boldsymbol{r}_0}{\boldsymbol{r}}\right|^{6}\right) \tag{8.76}$$

where K^{LJ} is the depth of the well and also drives its width.
A finer level of description of the particle-particle interaction can be reached with the advances of quantum chemistry, but the scale separation is such that a full resolution of the orbitals is intractable. Still the modeling can be led with so-called coarse-graining approaches (Markutsya et al. 2008; Markutsya et al. 2012), which reconcile particle modeling and chemical bond modeling.

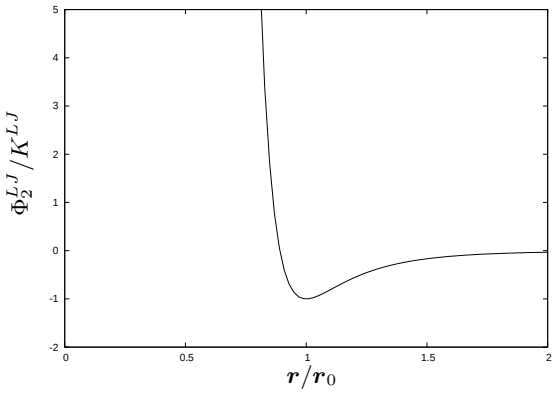

Figure 8.4: *Lennard-Jones potential.*

In the case of agglomeration in solution (e.g. for colloids), the ionic force of the solvent also plays a role so that the interaction potential must account for this effect. The DLVO theory, accounting for the combined effect of Van der Waals and double layer forces solves this issue. In gases, the effect of the carrier phase on the potential is not considered.

8.4.5.4 Conclusion

On the one hand the kinetic level accounts for:
- the transient aspects of non-equilibrium velocity and density distributions,
- the short range particle-particle interactions.

as soon as the scale separation is treated. Moreover this approach is valid whatever the particle size i.e. for any Kn_d. Finally the modeling of coalescence at the macroscopic level performed in Eq. (8.61) can be retrieved from the kinetic level. In return, the resolution of a kinetic equation and moreover of an additional two-point particle PDF equation to close the collision term is difficultly tractable.
On the other hand the resolution of macroscopic equations with an empirical closure for the coalescence kernel based on the diffusive model, discussed in § 8.4.4, is specific to the Brownian regime i.e. $l_0 < d_p < d_N$. To account for short range interactions, Spielman (1970) suggests a correction to the Brownian diffusive kernel:

$$\frac{\mathfrak{K}_{\mathrm{coal}}^{\mathrm{Df}}}{\mathfrak{K}_{\mathrm{coal}}} = 4 \int_{r=|r^\star+r^\diamond|}^{+\infty} \frac{\exp(\Phi_2/kT_g)\mathrm{d}r}{r^2 C(r)} \tag{8.77}$$

where Φ_2 is an interaction potential (with spherical symmetry) and $C(r)$ is a mobility function that reflects hydrodynamic interactions between particles separated by a center-to-center distance r. But the macroscopic approach has still the major drawback of being specific to a regime.

8.5 Modeling particles in Free Molecular Regime

The free molecular regime (FMR) is the regime of particles featuring:

$$\mathrm{Kn}_d \gg 1$$

so that the particles encounter a significant time of free flight in between two collisions with gas molecules. The conclusions on Brownian regime, previously drawn, are that a specific modeling is required in the FMR. The FMR modeling is now discussed.

8.5.1 Kinetic modeling for the strict FMR

For FMR particles, the transport regime is studied directly in the framework of kinetic theory:

$$\partial_t f + \boldsymbol{c} \cdot \partial_{\boldsymbol{x}} f + \partial_{\boldsymbol{c}} \left(\widetilde{\boldsymbol{F}} f \right) = \mathfrak{C}. \tag{8.78}$$

8.5.1.1 Friction coefficient

From kinetic theory, Epstein (1924) provides the friction coefficient by an analytical computation which is valid again for $\mathrm{Kn}_d \gg 1$:

$$f_{Ep} = \frac{2}{3} d_p^2 \rho_g \left(\frac{2\pi k T_g}{m_p}\right)^{\frac{1}{2}} \left[1 + \frac{\pi \alpha_\theta}{8}\right] \tag{8.79}$$

where α_θ is the so-called accommodation coefficient. This coefficient is defined as the fraction of gas molecules that encounter a thermal i.e. isotropic reflexion, assuming that only thermal and specular reflexion occur.

8.5.1.2 Kinetic coalescence

In the FMR, particles are assumed to follow trajectories which are straight lines on a distance which is significant compared to a target particle so the collision is assessed by a kinetic collision kernel, based on one-particle NDFs, in which the velocity is the equilibrium velocity distribution i.e. a Maxwellian distribution. This case is opposed to that of a diffusive regime as regards the fact that the particle density is not smooth at the scale of the particle, as illustrated in Figure 8.3, right. In comparison with the Brownian regime, there is not a scale separation between particle-gas mean free path and particle-particle mean free path so the molecular chaos assumption holds and the coalescence term is based on the usual Boltzmann collision probability:

$$\begin{aligned}\mathfrak{C}(f,f) = &\frac{1}{2}\int_{\boldsymbol{c}^\star}\int_{v^\star\in[0,v]} f(t,\boldsymbol{x},\boldsymbol{c}^\diamond,v^\diamond) f(t,\boldsymbol{x},\boldsymbol{c}^\star,v^\star)\ |\boldsymbol{c}^\diamond - \boldsymbol{c}^\star|\ \beta(v^\diamond,v^\star) J \mathrm{d}v^\star \mathrm{d}\boldsymbol{c}^\star \\ &+ \int_{\boldsymbol{c}^\star}\int_{v^\star} f(t,\boldsymbol{x},\boldsymbol{c},v) f(t,\boldsymbol{x},\boldsymbol{c}^\star,v^\star)\ |\boldsymbol{c} - \boldsymbol{c}^\star|\ \beta(v,v^\star) \mathrm{d}v^\star \mathrm{d}\boldsymbol{c}^\star\end{aligned} \tag{8.80}$$

The kinetic coalescence kernel has a geometric part that is the basic hard sphere one with geometric cross sections.
When moving to a macroscopic model for a size distribution n, similar to the semi-kinetic model of § 4.4.1, the term reads:

$$\begin{aligned}\mathscr{C}(n,n) = &\frac{1}{2}\int_{v^\star\in[0,v]} n(t,\boldsymbol{x},v^\diamond) n(t,\boldsymbol{x},v^\star) \mathfrak{K}^{\mathrm{K}}_{\mathrm{coal}}(v^\diamond,v^\star) J \mathrm{d}v^\star \\ &+ \int_{\boldsymbol{c}^\star}\int_{v^\star} f(t,\boldsymbol{x},v) f(t,\boldsymbol{x},v^\star) \mathfrak{K}^{\mathrm{K}}_{\mathrm{coal}}(v,v^\star) \mathrm{d}v^\star\end{aligned} \tag{8.81}$$

the velocity distribution can be integrated as it is explicitly known to be the Maxwellian distribution after a very short time. The velocity part of the kernel results from the integration on isotropic Gaussian velocity distributions:

$$\mathfrak{K}^{\mathrm{K}}_{\mathrm{coal}}(v^\diamond,v^\star) = \left(\frac{3}{4\pi}\right)^{\frac{1}{6}} \left(\frac{6kT_g}{\rho_l}\right)^{\frac{1}{2}} \left(\frac{1}{v^\star} + \frac{1}{v^\diamond}\right)^{\frac{1}{2}} (v^{\diamond\frac{1}{3}} + v^{\star\frac{1}{3}})^2. \tag{8.82}$$

A correction can be considered in the case of a more complex potential such as for charged particles (repellant) or Van der Waals forces (attractive) (Fuchs 1964).

8.5.1.3 Kinetic thermophoresis

Thermophoresis, presented in § 8.5.1.3 and quantified above for Brownian particles, also occurs in FMR.
In the case of particles in FMR i.e. $\mathrm{Kn}_d \gg 1$, the kinetic theory of gas/particle mixtures yields the analytical expression of the thermophoresis velocity (Waldman and Schmitt 1966):

$$\boldsymbol{c_t} = \frac{-3\pi\nu_g \nabla T_g}{4(1+\pi\alpha_\theta/8)T_g} \tag{8.83}$$

where α is again the accommodation coefficient.

8.5.1.4 Macroscopic model

A macroscopic model can be derived from the previous kinetic model, where the Gaussian equilibrium imposed by gas-particle collisions plays a central role in diffusion and other transport phenomena, as well as coalescence:

$$\partial_t n + \partial_{\boldsymbol{x}} \left(n(\boldsymbol{u}_g + \boldsymbol{c_t})\right) = \partial_{\boldsymbol{x}} \cdot (D \partial_{\boldsymbol{x}} n) + \mathscr{C}(n,n). \tag{8.84}$$

Similarly to the Smoluchowski equation and to the Fokker-Planck equation, this formalism statistically accounts for the overall effect of the gas on the particles but the retrocoupling on the gas cannot be deduced easily. So a resulting model for a disperse two-phase flow will necessarily be one-way coupled.

8.5.2 FMR-Brownian transition

The approach for FMR is very different from that of the Brownian regime and no comprehensive and efficient approach has been suggested. The domain of transition:

$$\mathrm{Kn}_d \sim 1.$$

is quite large and of major importance since the coalescence process bring particles from FMR to cross the transition. The only approach that has yielded some successes is based on interpolation formulae between the different regimes.

8.5.2.1 Friction coefficient in the transition regime

To assess the friction coefficient in FMR-Brownian transition, a slip correction on the continuous coefficient $f_C = \frac{f_{\mathrm{St}}}{C(\mathrm{Kn}_d)}$ is proposed by Cunningham (1910) and also by Knudsen and Weber (1911) with:

$$C(\mathrm{Kn}_d) = 1 + \mathrm{Kn}_d \left(A_1 + A_2 \exp\left(-\frac{A_3}{2\mathrm{Kn}_d} \right) \right) \tag{8.85}$$

where values for A_1, A_2, and A_3 have been determined by Millikan (1923) and by Davies (1945) for air and more recently in Kim et al. (2005). The correction is plotted in Figure 8.5.

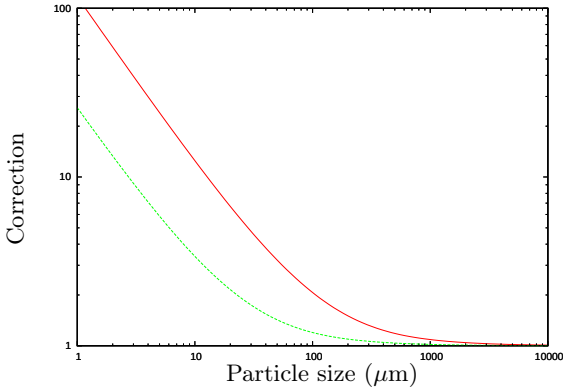

Figure 8.5: *Cunningham's correction with Davies (1945)'s coefficients for particles in transition regime – Solid: $l_0 = 70\,nm$; Dashed: $l_0 = 15\,nm$.*

8.5.2.2 Coalescence in the transition regime

Assessing the coalescence rates for particles in the transition between kinetic and diffusive regimes i.e.

$$d_p \approx l_0$$

is remarkably difficult.
The kinetic and diffusive regimes are two different modelings of the same fundamental process that is coalescence under thermal agitation. They can not coexist in the sense that the Brownian "diffusive" approach cannot be hybridized with the kinetic one, due to the separation of scales and the need for an equilibrium state in the Brownian description.
This is the exact contrary of the Brownian-inertial transition described in § 8.4.4.4:

- the transition zone is wide;
- the transition criterion is an intrinsic parameter Kn_d;
- both modeling frames are not satisfactory.

So modeling the transition is important and difficult.
Attempts to model kinetic-diffusive transition are numerous, mainly through interpolation formulae such as in Fuchs (1964). The matter of coalescence in the FMR-Brownian transition is also treated in Kim et al. (2003) and in Azarov and Veshchunov (2010). Gopalakrishnan et al. (2011) suggests to use techniques similar to the interpolation formulae for the transition of nanoparticles to treat diffusion-limited chemical reactions of large non-spherical molecules.
Because it is not particular to any regime, the kinetic approach based on a two point PDF presented in § 8.4.5 can potentially treat this transition in a general way, provided that the correlation function is solved.

8.6 Conclusion on nanoparticle flow modeling

8.6.1 Issue of additional scale separation

When the particle size gets closer to the mean free path of the carrier phase, the particles encounter effects that are usually relegated to the atomic level, and which would be treated together with the collisional equilibrium of the carrier phase. The kinetic modeling of nanoparticles is made difficult because the scaling is changed compared to usual micrometric ones: in short, nanoparticles interact with the collisional scales of the carrier phase, and the resulting agitation influences transport and coalescence. For the latter, the scales of agitation are however separated from the scales of particle-particle collision. Suspensions of nanoparticles have been modeled with several heterogeneous approaches, due to this scale separation and moreover to the various regimes they encounter as summed up in Figure 8.1.
A new insight on nanoparticle coalescence modeling has been introduced by Veshchunov (2010b) (see also Veshchunov 2011) as well as Veshchunov (2010a) and Veshchunov and Azarov (2012) where the authors present a so-called "new approach" for Brownian coalescence: the issues of such separations of scale are discussed but an empirical modeling is proposed, with a specific derivation of models for each case.
We rather consider an extended kinetic approach based on a two-point PDF, to comply the usual kinetic and diffusive closures at the macroscopic level. Coalescence models can be directly derived from the two-point PDF approach, presented in § 8.4.5, if a tractable approach is found.

8.6.2 Summary of successes and issues of nanoparticle flow modeling

Two regimes are classically identified for nanoparticle-laden flows that are the Brownian and the FMR regime. Their common features are peculiar transport and coalescence properties. They are well quantified by classical theories.
The transition between the two-regimes is however a strong modeling issue. In polydisperse cases (enhanced by coalescence), providing a synthetic approach is therefore difficult.

8.6.3 Modeling needs for SRM flows

Considering that the mean free path $l_0 \approx 15\,\text{nm}$ is very low in a SRM, the issue of FMR-Brownian transition is not a major one.
SRM flows are however characterized by a strong mass loading, which may compromise the validity of the kinetic and Brownian models, which are one-way coupling models as presented above. In general, a comprehensive theory is sought that can account for the complex transport of nanoparticles, two-way coupling, and coalescence. A fully kinetic model is derived in Appendix D in the prospect of shedding light on this physics.
The other issue in SRMs is the coexistence of Brownian (nano) and inertial (micro) droplets so that the transition is crucial to model as regards coalescence in order to capture accurately resulting the size distribution. A practical approach of this question is discussed in Chapter 9 and a hybrid model is derived in the framework of Eulerian Multi-Fluid methods.

Chapter 9

A mesoscopic model for nano-micro mixture flows

The simultaneous presence of nanometric droplets, encountering Brownian motion, and micrometric droplets, encountering inertial effects, can be accounted for separately with various dedicated models. But coalescence then occurs between all particles and must be treated at once. In this chapter, we focus on deriving a coalescence model common to all sizes of particles and which couples the chosen approaches for nano and micro particles. First is given an overview of the issues raised by such mixtures. Second the available coalescence kernels presented previously are assessed. Third a new kernel is derived to treat coalescence between a Brownian and a ballistic particle. From this, a model is finally proposed for nano-micro mixture flows by abutting dedicated models for both regimes and coupling them with the appropriate kernels.

9.1 Issues of nano-micro mixtures

The presence of a large amount of both nanometric and micrometric particles raises several issues: the physics of these two types of particles are very different but they both influence the carrier phase flow in a two-way coupled manner and they interact all together, notably through coalescence.

9.1.1 Definition of nano and micro classes

The overall study deals with mixtures of particles with varied sizes: we particularly need to focus on the interactions between particles with heterogeneous sizes, which we define as particles behaving with different physics. And we still need to account for interactions between particles with the same physics, which we refer to as homogeneous in size.
In the following, we use the term nanometric (or nano) to designate any particle that has negligible inertia. And by micrometric (or micro), we consider any particle which encounters significant inertia effects. This classification is not absolutely related to particle size, and depends rather on the flow conditions but the choice of the names "nano" and "micro" is adapted to the particular configuration of SRMs. It also happens in many other applications that the transition range is around $1\,\mu$m (Friedlander 2000). These terms are convenient to clearly distinguish the physics of relaxed but agitated droplets on one hand and of monokinetic and ballistic droplets on the other hand. We discuss in § 9.2.3 the orders of magnitude and the transition criteria.
We recall that for particles with negligible inertia, coalescence is fostered by Brownian motion; while for inertial particles, coalescence is said to be ballistic since the particles have fairly free flight trajectories in the meantime of two collisions. The relative velocities governing collisions are driven by the macroscopic flow.

9.1.2 Choice of a modeling level for nanoparticles

We have discussed in § 8.6.1 the peculiarities of kinetic modeling of collisional Brownian sprays: depending on the particle size, the separation between the particle collision scales and gas molecule collision scales requires a specific kinetic modeling with the additional resolution of a two-point NDF. In § 8.4.5, such a model has been proposed from a Fokker-Planck equation in the context of a fluid modeling for the carrier phase. In § D.5.2, the same type of approach has been assessed for the fully kinetic model of Appendix D so that two-way coupling can be described in detail, and the out-of-equilibrium particle transport terms can be treated from fundamental collision considerations. In both cases, the recourse to a two-point NDF allows the model to account naturally for the Brownian-ballistic transition.

These two formalisms yield a rich but complex overall model so we now resort to a more tractable approach. Smoluchowski (1916)'s early approach for Brownian coalescence is satisfactory when the agitation and coalescence scales are separated. Two limiting regimes exist for a disperse phase in a carrier gas, as discussed in Chapter 8:

- free molecular regime: particles are free of all interaction with the fluid molecules most of the time.
- diffusive: particles encounter many collisions with the molecules at a single time, all the time.

The classical criterion to separate these regimes is a Knudsen number (Fuchs 1964; Friedlander 2000) which we recall:

$$\mathrm{Kn}_d = \frac{\lambda_0}{d_p}$$

where $\lambda_0 = 1/(n\sigma)$ is the mean free path of the carrier phase molecules. But recent works (Veshchunov 2010b) have questioned the historical modeling hypotheses and conclusions.

9.1.3 Coalescence in nano-micro mixtures

We have stated that collisions and coalescence had a strong influence on dense nano-micro mixtures. Coalescence among all types of particles is intense as the number concentrations are high due to the significant mass concentrations and moreover due to the small size of the nanoparticles. This intense overall phenomenon then couples both types of particles together and brings their sizes to evolve:

- the coupling between all the types of particles needs to be accounted for;
- the size evolution is crucial to capture, since the physics and the models to be chosen are strongly dependent on size.

The modeling for micrometric particle collisions is written at the kinetic level as ballistic collisions i.e. in a free flight regime due to inertia (see Chapter 3) while for nanometric particles we meet the difficulty of choosing the correct modeling hypotheses and coalescence kernel in the Brownian regime. This point has been tackled historically in the literature (see § 8.4.4) and the Brownian kernel is based on a macroscopic resolution of the particle flux at the particle boundary. However none of these approaches can be readily used:

- neither to determine the behavior of two particles with sizes that range within the transition between Brownian and ballistic regimes.
- nor to describe coalescence between a nanometric and a micrometric particle.

We focus on these two issues in § 9.2, which follows.

9.2 Issues of the nano-micro coalescence transition

To elaborate a model for the overall coalescence process within a mixture of Brownian and inertial droplets, we need first to assess the models available for each regime separately.

9.2.1 Analysis of the existing coalescence kernels

We now briefly summarize all the coalescence kernels $\mathfrak{K}_{\mathrm{coal}}$. The particularity of the competition between agitation (unresolved) and ballistic (resolved) coalescence is that the second one completely depends on the flow so that no a priori estimation of its order of magnitude can be given, except in the case where turbulence is the source (Zaichik and Alipchenkov 2008), bringing this inertial coalescence back to an unresolved phenomenon.

In both cases, coalescence is assessed statistically, which requires to evaluate the probability that a coalescence event occurs: a coalescence kernel is computed based on the number of probable coalescence events per unit time and per unit particle concentration. Such a kernel depends on microscopic velocity differences between particles.

9.2.1.1 Kinetic kernel

In the classical theory of Brownian coalescence, the kinetic approach for coalescence prevails when the particle encounters few interactions between two particle-particle collisions, which corresponds to the free molecular regime. The criterion used is $\mathrm{Kn}_d \gg 1$ and the kinetic coalescence Brownian reads (Smoluchowski 1916; Smoluchowski 1917; Fuchs 1964; Friedlander 2000):

$$\mathfrak{K}^{\mathrm{K}}_{\mathrm{coal}}(r^\star, r^\diamond) = (r^\star + r^\diamond)^2 \left[\frac{6kT_g}{\rho_l}\left(\frac{1}{r^{\star 3}} + \frac{1}{r^{\diamond 3}}\right)\right]^{\frac{1}{2}} \tag{9.1}$$

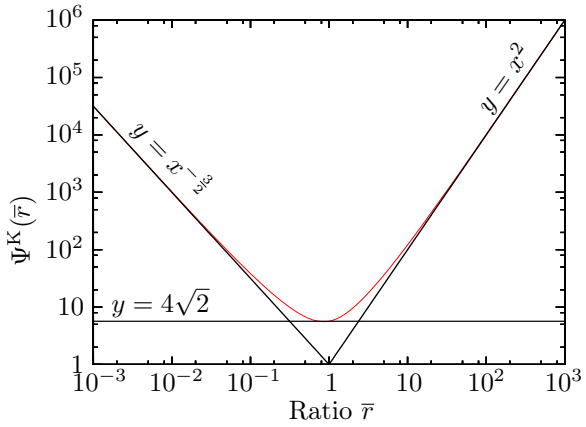

Figure 9.1: *Dimensionless kinetic kernel versus radius ratio.*

which has already been given in Eq. (8.82). For particles with similar sizes $r^\star = r^\diamond = r$, the kernel evolves as $r^{\frac{1}{2}}$.
To treat particles with significantly different sizes, the size ratio $\overline{r} = r^\diamond/r^\star$ is defined. We consider the notation:

$$\sqrt{r^\star}\Psi^{\mathrm{K}}(r^\star, r^\diamond) = (r^\star + r^\diamond)^2 \left(\frac{1}{r^{\star 3}} + \frac{1}{r^{\diamond 3}}\right)^{\frac{1}{2}} \tag{9.2}$$

where Ψ^{K} is a dimensionless function and we perform an asymptotic study versus $\overline{r}$:

$$\Psi^{\mathrm{K}}(\overline{r}) = \frac{(1+\overline{r}^3)^{\frac{1}{2}}(1+\overline{r})^2}{\overline{r}^{\frac{3}{2}}} \sim \begin{cases} \overline{r}^{-\frac{3}{2}} & \text{if } \overline{r} \ll 1 \\ 4\sqrt{2} & \text{if } \overline{r} \sim 1 \\ \overline{r}^2 & \text{if } \overline{r} \gg 1 \end{cases} \tag{9.3}$$

as presented in Figure 9.1.

9.2.1.2 Diffusive kernel

In the diffusive regime, i.e. when $\mathrm{Kn}_d \ll 1$, we get the kernel presented in Eq. (8.63):

$$\mathfrak{K}^{\mathrm{Df}}_{\mathrm{coal}}(r^\star, r^\diamond) = \frac{2kT_g}{3\mu_g}\left(\frac{1}{r^\star} + \frac{1}{r^\diamond}\right)(r^\star + r^\diamond)\,. \tag{9.4}$$

For particles with similar sizes $r^\star = r^\diamond = r$, it is noteworthy that the kernel is a constant and reads:

$$\mathfrak{K}^{\mathrm{Df}}_{\mathrm{coal}}(r, r) = \frac{8kT_g}{3\mu_g}.$$

The diffusive kernel often is crudely presented as a "constant" kernel (Friedlander 2000) but an asymptotic study shows that this is no longer true for significantly unbalanced droplets.
To treat particles with significantly different sizes, the size ratio $\overline{r} = r^\diamond/r^\star$ is considered again. We take the notation:

$$\Psi^{\mathrm{Df}}(r^\star, r^\diamond) = \left(\frac{1}{r^\star} + \frac{1}{r^\diamond}\right)(r^\star + r^\diamond) \tag{9.5}$$

where Ψ^{Df} is also a dimensionless function and we perform again an asymptotic study versus $\overline{r}$:

$$\Psi^{\mathrm{Df}}(\overline{r}) = \frac{(1+\overline{r})^2}{\overline{r}} = \overline{r} + 2 + \frac{1}{\overline{r}} \sim \begin{cases} \overline{r}^{-1} & \text{if } \overline{r} \ll 1 \\ 4 & \text{if } \overline{r} \sim 1 \\ \overline{r} & \text{if } \overline{r} \gg 1 \end{cases} \tag{9.6}$$

as presented in Figure 9.2.

9.2.1.3 Ballistic kernel

If the particle velocity is resolved macroscopically, we can use this macroscopic velocity directly to evaluate the collision-coalescence kernel. The coalescence associated to resolved velocity differences is referred to as ballistic coalescence and its kernel reads for two particle classes $\star$ and $\diamond$:

$$\mathfrak{K}^{\mathrm{bal}}_{\mathrm{coal}} = |\,\boldsymbol{u}^\star - \boldsymbol{u}^\diamond\,|\,\pi(r^\star + r^\diamond)^2 \tag{9.7}$$

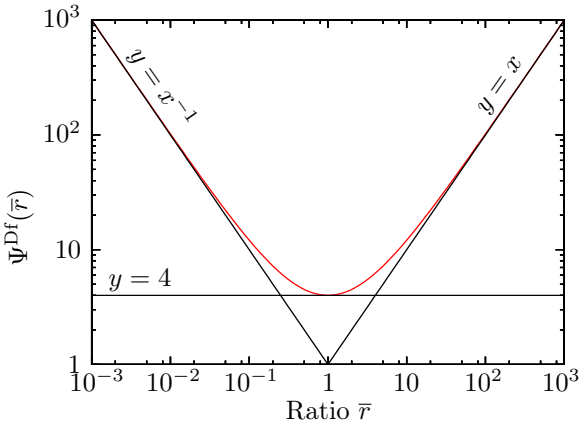

Figure 9.2: *Dimensionless diffusive kernel versus radius ratio.*

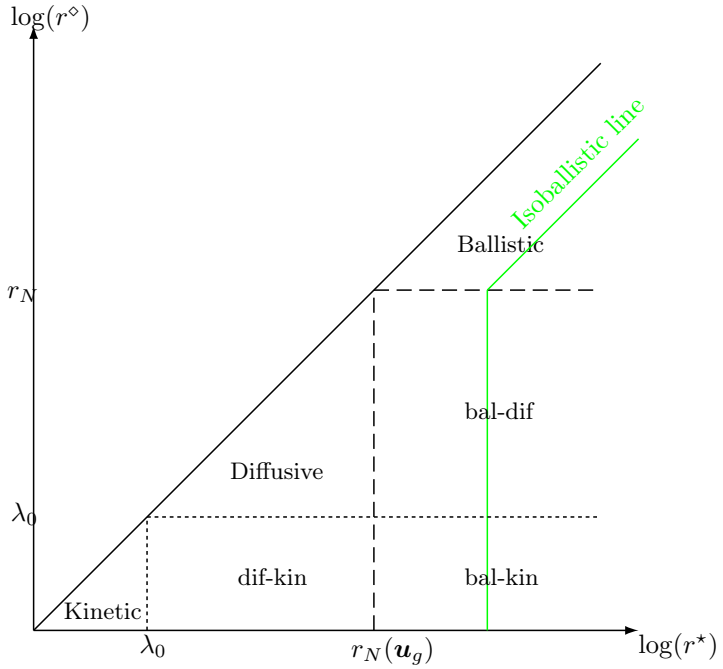

Figure 9.3: *Polydisperse coalescence kernel chart.*

where it can be seen that the resolved velocities $\boldsymbol{u}^\star$ and $\boldsymbol{u}^\diamond$ are strongly dependent on the flow. The asymptotic behavior of the kernel can be immediately addressed as quadratic, whether the droplets have balanced sizes or not.

9.2.1.4 Conclusion on the fundamentally different approaches

The coalescence kernel is computed with radically different approaches depending on if the regime is FMR, diffusive or ballistic: the FMR and ballistic kernels are defined at the kinetic level, while the diffusive one has already encountered an integration on velocity distributions, and is valid only at the semi-kinetic level. For these different regimes and models, the asymptotic behaviors are different as studied previously and the kernels have no particular reason to connect at the transition point nor to be described by one or the other model:

- the issue of the FMR-diffusive transition has been discussed in § 8.5.2;
- the ballistic coalescence process may interfere with coalescence occurring at unresolved level (turbulent, microscopic). So it seems that coalescence intensity cannot be estimated *a priori* or even compared to the microscopic processes in order to assess the regime, as suggested in § 9.1.3.

Small particles have a resolved velocity that is close to the one of the gas. Yet they can still coalesce thanks to microscopic (unresolved) phenomena such as Brownian agitation, for which we note the coalescence kernel $\mathfrak{K}^{\mathrm{bro}}_{\mathrm{coal}}$.

Moreover, in the case of a polydisperse spray, the two partners may be described by a different regime so that coalescence is to be assessed in these new hybrid cases, which are recapitulated in Figure 9.3. In the prospect of modeling SRMs, particles in FMR are disregarded from now on.

9.2.2 Simple models for the nano-micro transition

We now present general considerations on nano-micro transition modeling. To this extent the ballistic coalescence kernel is noted $\mathfrak{K}_{\text{coal}}^{\text{bal}}$ and the Brownian coalescence kernel is noted $\mathfrak{K}_{\text{coal}}^{\text{bro}}$. In practical cases, particles close to the nano-micro transition are in diffusive regime so that $\mathfrak{K}_{\text{coal}}^{\text{bro}} = \mathfrak{K}_{\text{coal}}^{\text{Df}}$ but this particular point is not necessary for the following modeling.

9.2.2.1 Independency-assumed transition kernel

We can assume that ballistic coalescence and Brownian coalescence are completely independent though they do not amplify or inhibit each other too much. This assumption is classical in the absence of any modeling approach and leads to simply adding the two kernels:

$$\mathfrak{K}_{\text{coal}}^{\text{bro+bal}} = \mathfrak{K}_{\text{coal}}^{\text{bro}} + \mathfrak{K}_{\text{coal}}^{\text{bal}}. \tag{9.8}$$

The independency-assumed transition kernel is sometimes referred to as the sum kernel.

9.2.2.2 Competition-assumed transition kernel

A competition may settle as the particle density in the surrounding of the target particle may be depleted because of one of the two simultaneous coalescence mechanisms. In the case of a competition between the two mechanisms, we may simply write:

$$\mathfrak{K}_{\text{coal}}^{\text{bro/bal}} = \max(\mathfrak{K}_{\text{coal}}^{\text{bro}}, \mathfrak{K}_{\text{coal}}^{\text{bal}}). \tag{9.9}$$

The competitive transition kernel is sometimes referred to as the max kernel.

9.2.2.3 RMS transition kernel

Instead of adding the two kernels as if they were independent, they can be treated as if their quadratic means were additive, by analogy with many statistical situations or with physical problems where efficient quantities are defined. The overall kernel is then the root means square (RMS) of the elementary kernels:

$$\mathfrak{K}_{\text{coal}}^{\text{RMS}} = \sqrt{(\mathfrak{K}_{\text{coal}}^{\text{bro}})^2 + (\mathfrak{K}_{\text{coal}}^{\text{bal}})^2}. \tag{9.10}$$

The RMS kernel is often met in aerosol literature; it has for instance been suggested in Silberberg (1979) but it is criticized by Simons et al. (1986) as less accurate than the sum kernel.

9.2.2.4 Bracketing the transition kernel

It is reasonable to assume that the two phenomena do not inhibit each other and that they do not amplify each other. So the transition coalescence kernel is bounded by the sum (independency) and max (competition) kernels, as follows:

$$\max(\mathfrak{K}_{\text{coal}}^{\text{bro}}, \mathfrak{K}_{\text{coal}}^{\text{bal}}) \leq \mathfrak{K}_{\text{coal}} \leq \mathfrak{K}_{\text{coal}}^{\text{bro}} + \mathfrak{K}_{\text{coal}}^{\text{bal}}. \tag{9.11}$$

This empirical bracketing can be used to check the relevance of a modeling approach. Whenever a model yields a kernel that comes out of this bracketing, such a result should be justified by the existence of an inhibition or amplification mechanism.

9.2.2.5 Limits of such simple approaches

The previous approaches are justified neither by theory nor by experiment. The orders of magnitude have been empirically considered as satisfactory. But considering the suspicion that the two phenomena are not independent, it is necessary to base such a kernel on a comprehensive theory.
As an illustration, let us consider the case of a transition to turbulent coalescence: its source is simple as it can be quantified with an exogenous parameter such as the turbulent kinetic energy. Zaichik and Alipchenkov (2008) have studied the Brownian-inertial transition in the case of turbulent flows: it is shown from a comprehensive theory that the Brownian and turbulent coalescence modelings are not independent so that the transition is not a simple summation.

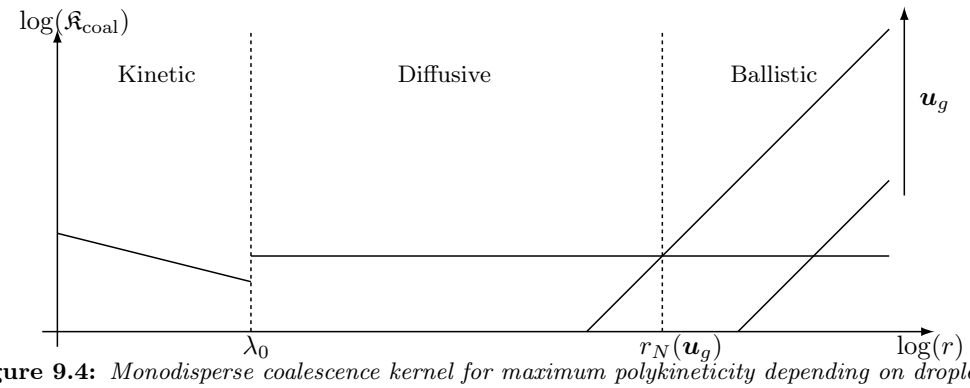

Figure 9.4: *Monodisperse coalescence kernel for maximum polykineticity depending on droplet radius*

9.2.3 Orders of magnitude for transition with independency assumption

It has been stated that the ballistic kernel is negligible for nanoparticles and that the Brownian kernel is negligible for microparticles: so the sum kernel is valid far from the transition. The transition zone can then be defined as the zone where the sum kernel is not valid.
Also the latter region is suspected to be narrow enough so that its particle size transition range can be assessed by using the sum kernel. This approach is retained below and the transition size is computed, using different assumptions on the inertial particles.

9.2.3.1 Estimating the ballistic coalescence with maximum polykineticity

We first consider a monodisperse case with a droplet radius r. Droplets of the same size are shown to have their velocities bounded by the gaseous velocity, see Eq. (3.21):

$$|\,\boldsymbol{u}_p - \boldsymbol{u}_g\,| \leq \mathrm{St}\,|\,\boldsymbol{u}_g\,|\,. \tag{9.12}$$

We assume a flow with an average velocity u_g, that maximizes the ballistic coalescence, case which we refer to as maximum polykineticity. In this configuration the ballistic velocity difference $\gamma = |\,\boldsymbol{u}^\star - \boldsymbol{u}^\diamond\,|$ can be expressed:

$$\gamma = 2\mathrm{St}u_g \tag{9.13}$$

with St increasing like r^2: assuming the above velocity difference is referred to as the maximum polykineticity hypothesis. The ballistic coalescence kernel then reads:

$$\mathfrak{K}^{\mathrm{bal}}_{\mathrm{coal}}(\text{monodisperse,polykinetic}) = 2\mathrm{St}\,|\,\boldsymbol{u}_g\,|\,\pi(2r)^2 = 16\pi u_g \frac{\rho_l r^4}{9\mu_g \tau_g}. \tag{9.14}$$

The nanometric coalescence occurs either in kinetic or in diffusive regime, depending on the mean free path λ_0:

$$\mathfrak{K}^{\mathrm{bro}}_{\mathrm{coal}}(\text{monodisperse}) = \begin{cases} \sqrt{2}\pi\sigma(r)(2r)^2 &= \sqrt{\dfrac{9\pi k T_g}{\rho_l}}\, r^{\frac{1}{2}} & \text{if } r < \lambda_0 \\ 4rD(r) &= \dfrac{8kT_g}{3\pi\mu_g} & \text{otherwise.} \end{cases} \tag{9.15}$$

The evolution of these two coalescence kernels is then shown in Figure 9.4.
Since $\mathfrak{K}^{\mathrm{bal}}_{\mathrm{coal}}$ is proportional to r^4 the coalescence kernel is dominated by ballistic coalescence only for droplets bigger than a critical radius r_N which reads:

$$r_N^4 = \frac{3kT_g}{2\pi^2\rho_l}\frac{\tau_g}{u_g} \tag{9.16}$$

and depends on the flow through u_g and τ_g.

9.2.3.2 Estimating the ballistic coalescence with monokineticity

We now consider a completely monokinetic case so that droplets of the same sizes cannot coalesce. We have to consider polydisperse coalescence between a droplet of size $r^\star$ and a droplet of size $r^\diamond$ and the ballistic velocity difference γ is bounded as follows:

$$|\,\mathrm{St}^\star - \mathrm{St}^\diamond\,|\,\boldsymbol{u}_g \leq \gamma \leq |\,\mathrm{St}^\star + \mathrm{St}^\diamond\,|\,\boldsymbol{u}_g \tag{9.17}$$

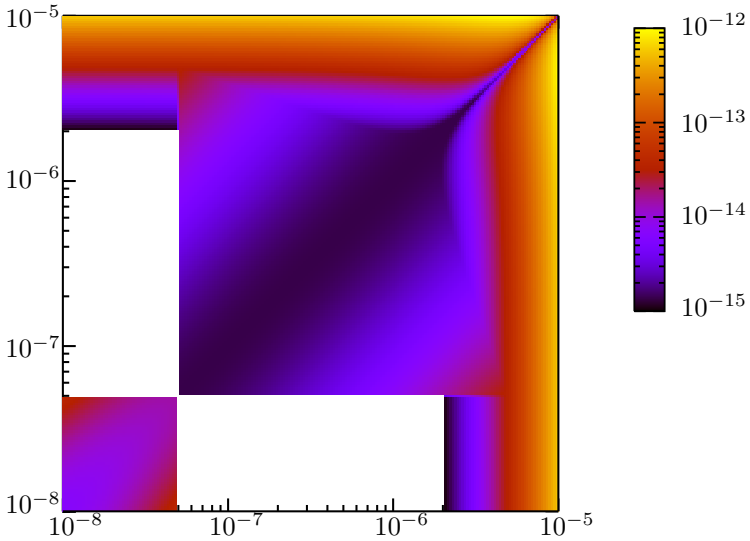

Figure 9.5: *Polydisperse coalescence kernel (m^3/s) for monokinetic sprays ($u_g = 5\,m/s$, $T_g = 3600\,K$, $\mu_g = 96.10^{-6}\,Pa.s$, $\lambda_0 = 50\,nm$, $\rho_l = 1600\,kg/m^3$- – The dif-kin domain has not been represented for no kernel is known.*

	nano	transition	micro
nano	diffusive	?	?
transition	×	?	?
micro	×	×	ballistic

Table 9.1: *Categories of coalescence in a nano-micro mixture – ? designates cases that are still to be modeled and × is treated by symmetry.*

though monokineticity invites to rather consider the lower bound.
The domains of coalescence are recapitulated in Figure 9.3. We define the isoballistic line as an iso-contour of ballistic kernel: it follows the $r^\star + r^\diamond$ iso-contours in the purely ballistic domain "bal-bal" and then follows a $r^\star$ iso-contour in the hybrid domain "bal-bro". We show the orders of magnitude of the direct summation kernel in a numerical application case in Figure 9.5.

9.2.4 Conclusion on nano-micro coalescence issues

In the case of fairly homogeneous particle sizes, the coalescence modeling and kernels have been devised in previous chapters and they have been recalled and analyzed above. The focal point to describe nano-micro mixtures is then to model coalescence between heterogeneous sizes of particles in the sense that:

- the bigger ones are animated by a slip velocity due to their inertia,
- while the smaller ones encounter Brownian agitation at zero mean slip.

Moreover because of the existence of "transition" particles which encounter both Brownian agitation and inertia, a set of cases emerges that are all gathered in Table 9.1.
The different heterogeneous coalescence cases that have been identified feature different modeling issues: Brownian and ballistic agitation contribute simultaneously to coalescence but they are probably not independent though they are probably weakly coupled. The trouble is that these phenomena are modeled with incompatible approaches and a transition kernel has not been derived to our knowledge. In particular the cases featuring "transition particles" are a conundrum for the behavior of a single particle in transition needs itself to be assessed.
Ultimately the evaluation of a generalized kernel that accounts for both Brownian and ballistic effects is sought in order to implement a unique formula in codes and to account for all regimes without *ad hoc* criteria. In the following section, this goal is reached for the FMR-ballistic transition. But in practical SRM cases, the transition is rather between diffusive and ballistic particles, which case is examined in § 9.4.

9.3 Extension of the kinetic kernel towards the ballistic regime

We consider the extension of the kinetic kernel in the case of significant inertia of particles in FMR. This case requires that particle-particle collisions dominate particle-gas collisions, see § D.2, which is not reached in practical SRM cases. Still it is a collisional regime which transition can be explicitly assessed as the non-inertial and inertial regimes are both modeled with a kinetic formalism.

9.3.1 A common modeling basis: two kinetic approaches

We can find a generalized kernel, adapted to both ballistic and FMR coalescence regimes thanks to the strong similarity between the two approaches. These approaches both feature free flight between two collisions so that they can be based on the kinetic integral Eq. (3.136), rewritten hereafter:

$$\begin{aligned} Q^+ &= \frac{1}{2}\iint_{\boldsymbol{c}^\star, v^\star \in [0,v]} f(t,\boldsymbol{x},\boldsymbol{c}^\diamond,v^\diamond) f(t,\boldsymbol{x},\boldsymbol{c}^\star,v^\star)\,|\boldsymbol{c}^\diamond-\boldsymbol{c}^\star|\,\pi\left(r^\star+r^\diamond\right)^2 J \mathrm{d}v^\star \mathrm{d}\boldsymbol{c}^\star \\ Q^- &= \iint_{\boldsymbol{c}^\star, v^\star} f(t,\boldsymbol{x},\boldsymbol{c},v) f(t,\boldsymbol{x},\boldsymbol{c}^\star,v^\star)\,|\boldsymbol{c}-\boldsymbol{c}^\star|\,\pi\left(r+r^\star\right)^2 \mathrm{d}v^\star \mathrm{d}\boldsymbol{c}^\star \end{aligned} \tag{9.18}$$

where $v^\diamond = v - v^\star$, $v^\diamond \boldsymbol{c}^\diamond = v\boldsymbol{c} - v^\star \boldsymbol{c}^\star$ are the pre-collisional parameters, J is the Jacobian from the mapping $(v,\boldsymbol{c}) \to (v^\diamond, \boldsymbol{c}^\diamond)$: $J = (v/v^\diamond)^{n_d+1}$ and n_d is the dimension of the velocity phase space.
In the Ballistic regime, the velocity distribution, which is a marginal of the NDF, is conditioned exogenously (by the flow) so that there is a macroscopic equation that allows to solve its evolution. As for the velocity distribution in FMR regime, it results from interactions with molecules and is not known macroscopically but it can be described as an endogenous consequence of the macroscopic state of the carrier fluid, if the system is locally at a thermodynamic equilibrium: the velocity distribution can be modeled.
A kernel $\mathfrak{K}_{\mathrm{coal}}$ can then be defined as soon as it is possible to write the following factorization at the macroscopic level (here at the semi-kinetic level described in § 4.4.1):

$$\mathscr{C}^{n+} = \frac{1}{2}\int_{v^\star\in[0,v]} n(t,\boldsymbol{x},v^\diamond) n(t,\boldsymbol{x},v^\star) \mathfrak{K}_{\mathrm{coal}}(v^\diamond,v^\star,P^\diamond,P^\star)\mathrm{d}v^\star$$

$$\mathscr{C}^{n-} = \int_{v^\star} n(t,\boldsymbol{x},v) n(t,\boldsymbol{x},v^\star) \mathfrak{K}_{\mathrm{coal}}(v,v^\star,P,P^\star)\mathrm{d}v^\star$$

where the velocity part has been integrated versus $\boldsymbol{c}^\star$ and $\boldsymbol{c}^\diamond$ so that there is only a remaining dependency on sets of macroscopic parameters $P^\star$ and $P^\diamond$ of the velocity distributions. In the particular case where a partial velocity distribution $\psi(\boldsymbol{c},P)$ can be factorized from the NDF $f(t,\boldsymbol{x},\boldsymbol{c},v) = n(t,\boldsymbol{x},v)\psi(\boldsymbol{c},P)$, it is possible to factorize the kernel in a velocity and a size part:

$$\mathfrak{K}_{\mathrm{coal}}(v^\diamond,v^\star,P^\diamond,P^\star) = \beta(v^\star,v^\diamond) I_{vel}(P^\diamond,P^\star)$$

where the velocity part reads:

$$I_{vel}(P^\diamond,P^\star) = \int_{\boldsymbol{c}^\star,\boldsymbol{c}^\diamond} |\boldsymbol{c}^\diamond-\boldsymbol{c}^\star|\,\psi(\boldsymbol{c}^\star,P^\star)\psi(\boldsymbol{c}^\diamond,P^\diamond)\mathrm{d}\boldsymbol{c}^\star\mathrm{d}\boldsymbol{c}^\diamond \tag{9.19}$$

while the size part can be for instance $\beta(v^\star,v^\diamond) = \pi(r^\star+r^\diamond)^2$ in the case of a geometric cross-section.

9.3.2 Analytical expression for the general kernel

In the FMR, the equilibrium velocity distribution is Gaussian, centered on the hydrodynamic velocity and dispersed according to the carrier fluid macroscopic temperature (see § 8.4.2.2). In the ballistic regime, it is a δ-Dirac function centered on an exogenous macroscopic velocity as soon as the particles have a low enough inertia, as discussed in § 4.3. Both cases can therefore be described as limits of a Gaussian distribution shifted by the macroscopic (resolved) velocity $\boldsymbol{u}$. This multi-purpose distribution, noted $\mathscr{N}(\boldsymbol{c},\boldsymbol{u},\sigma)$ where σ depends on the fluid temperature with respect to Eq. (8.15), can nonetheless describe the velocity distribution in FMR and in inertial regime but also in the transition zone as a matter of fact. In the following, we can further the computation of a hybrid kernel and the dependency on σ is omitted for the sake of legibility.
From the integration of the Boltzmann kernel of Eq. (3.136) versus velocity given in its general form in Eq. (9.19) and assuming a shifted-Gaussian velocity distribution i.e. $f(t,\boldsymbol{x},\boldsymbol{c},v) = n(t,\boldsymbol{x},v)\mathscr{N}(\boldsymbol{c},\boldsymbol{u})$, we can build a macroscopic kernel which reads:

$$\mathfrak{K}^{\text{K-B}}_{\mathrm{coal}}(r^\star,r^\diamond,\boldsymbol{u}^\star,\boldsymbol{u}^\diamond) = \pi(r^\star+r^\diamond)^2 \int_{\boldsymbol{c}^\star,\boldsymbol{c}^\diamond} |\boldsymbol{c}^\diamond-\boldsymbol{c}^\star|\,\mathscr{N}(\boldsymbol{c}^\star,\boldsymbol{u}^\star)\mathscr{N}(\boldsymbol{c}^\diamond,\boldsymbol{u}^\diamond)\mathrm{d}\boldsymbol{c}^\star\mathrm{d}\boldsymbol{c}^\diamond \tag{9.20}$$

This hybrid coalescence kernel can be computed as an analytic expression in 1D cases:

$$\begin{aligned} \mathfrak{K}^{\text{K-B}}_{\mathrm{coal}}(r^\star,r^\diamond,\boldsymbol{u}^\star,\boldsymbol{u}^\diamond) = \quad & \pi(r^\star+r^\diamond)^2 \left[|\,\boldsymbol{u}^\diamond-\boldsymbol{u}^\star\,| \,\mathrm{erf}\left(\frac{|\,\boldsymbol{u}^\star-\boldsymbol{u}^\diamond\,|}{\sqrt{2(\sigma^{\star 2}+\sigma^{\diamond 2})}}\right)\right. \\ & \left. + \frac{\sqrt{2(\sigma^{\star 2}+\sigma^{\diamond 2})}}{\sqrt{\pi}} \exp\left(-\frac{|\,\boldsymbol{u}^\star-\boldsymbol{u}^\diamond\,|^2}{2(\sigma^{\star 2}+\sigma^{\diamond 2})}\right)\right] \end{aligned} \tag{9.21}$$

which can be considered as the product of a geometrical cross section by a velocity integral, as stated above. We now check that the ballistic and FMR limits are accounted for by the hybrid kernel previously computed in the 1D case. In the limit of no average velocity, we have:

$$\mathfrak{K}^{\text{K-B}}_{\text{coal}}(r^\star, r^\diamond, 0, 0) = \frac{\sqrt{2(\sigma^{\star 2} + \sigma^{\diamond 2})}}{\sqrt{\pi}} \pi (r^\star + r^\diamond)^2$$

where the velocity dispersion is computed as:

$$\sigma = \sqrt{\frac{3kT_g}{m_p}} = \sqrt{\frac{3kT_g}{\frac{4}{3}\rho_l \pi r^3}}$$

and yields back the FMR kinetic kernel $\mathfrak{K}^{\text{K}}_{\text{coal}}(r^\star, r^\diamond)$ given in Eq. (9.1). In the limit of no dispersion $\sigma^\star = \sigma^\diamond = 0$, we have:

$$\mathfrak{K}^{\text{K-B}}_{\text{coal}}(r^\star, r^\diamond, \boldsymbol{u}^\star, \boldsymbol{u}^\diamond) = \pi (r^\star + r^\diamond)^2 \, | \, \boldsymbol{u}^\diamond - \boldsymbol{u}^\star \, |$$

which kernel features the velocity integrals of Eq. (4.19) found at the semi-kinetic level for inertial particles.

9.4 Extension of the diffusive kernel towards the ballistic regime

We consider two sets of particles $\star$ and $\diamond$, of unbalanced sizes so that $r^\star > r^\diamond$. They are described at the semi-kinetic level, i.e. they have ensemble velocities $\boldsymbol{u}^\star$ and $\boldsymbol{u}^\diamond$ respectively. Because $\diamond$ is a nanoparticle, we can write $\boldsymbol{u}^\diamond = \boldsymbol{u}_g$, the carrier fluid ensemble velocity.

9.4.1 Detail of the diffusive kernel derivation

Let us consider how a slip velocity can modify the diffusion kernel in the classical approach. In the reference frame of the $\star$ particle, the fluid and the nanoparticles move at $\boldsymbol{u}^\star - \boldsymbol{u}_g$ far from the big particle. In the neighborhood of the big particles, the convection-diffusion equation derived by Fuchs (1964) can apply:

$$\partial_t n^\diamond + \partial_{\boldsymbol{x}} \cdot (n^\diamond \boldsymbol{u}^\diamond_{\text{loc}}) = \partial_{\boldsymbol{x}} \cdot (D \partial_{\boldsymbol{x}} n^\diamond) \tag{9.22}$$

where $D = D^\star + D^\diamond$ but $\boldsymbol{u}^\diamond_{\text{loc}}(\boldsymbol{x}) \neq \boldsymbol{u}^\star - \boldsymbol{u}_g$ is non-uniform. Because $\diamond$ is a nanoparticle i.e. it has strictly no inertia, we can go further and consider that the local particle velocity field is the same as the local carrier fluid velocity:

$$\boldsymbol{u}^\diamond_{\text{loc}}(\boldsymbol{x}) = \boldsymbol{u}_{g,\text{loc}}(\boldsymbol{x})$$

We can finally consider the problem at steady state. The flux of particles $\diamond$ towards the boundary of a particle $\star$ now reads:

$$\mathcal{F}_{n^\diamond} = n^\diamond \boldsymbol{u}_{g,\text{loc}} - D \partial_{\boldsymbol{x}} n^\diamond \tag{9.23}$$

and looses its spherical symmetry, compared to the pure diffusion case treated in § 8.4.4.3. The kernel must therefore be computed with its general expression (8.64):

$$\Phi = \oint_{\mathcal{S}_0} (n^\diamond \boldsymbol{u}_{g,\text{loc}} - D \partial_{\boldsymbol{x}} n^\diamond) \cdot \mathrm{d}\mathbf{S} \tag{9.24}$$

where $\mathcal{S}_0$ is a sphere of radius $r_0 = r^\star + r^\diamond$, with the new solution $n^\diamond$ for the convection-diffusion problem. We need to study the convection-diffusion case sketched in Figure 9.7 to find the generalized kernel. In particular, we check the relevance of assuming independence between the convective collisions and the diffusive ones (i.e. negligible inhomogeneities) and the accuracy of adding the two classical diffusive and ballistic kernels.

9.4.2 Monodimensional approach

First let us see what happens in a 1D case, with the notation u for $\boldsymbol{u}_{g,\text{loc}}$. In steady state, the mass conservation becomes a flux conservation which reads on both sides of the domain:

$$\mathcal{F}_{n^\diamond}(\pm x > r_0) = \mathcal{F}_{n^\diamond}(\pm \infty) \tag{9.25}$$

and yields two ODEs:

$$n^\diamond u + D \partial_{\boldsymbol{x}} n^\diamond = n^\diamond(\pm\infty) u, \qquad \pm x > r_0 \tag{9.26}$$

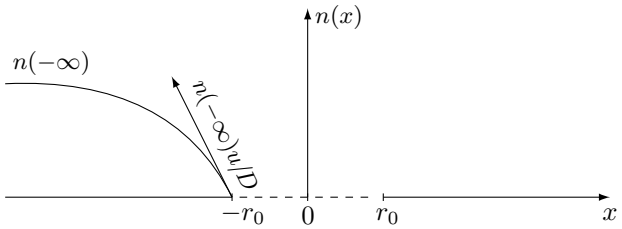

Figure 9.6: *Convection-diffusion problem around a 1D absorbing sphere.*

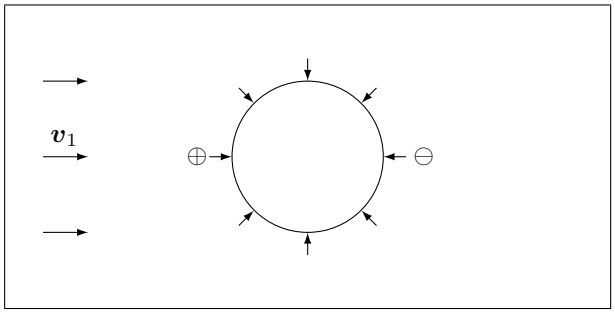

Figure 9.7: *Convection-diffusion problem around a 2D absorbing sphere – Fluxes (→) and density inhomogeneities (⊕, ⊖).*

for which the condition $n(-r_0 < x < r_0) = 0$ acts as a Dirichlet boundary condition which yields:

$$n^\diamond(x) = \begin{cases} n^\diamond(-\infty)\left[1 - \exp\left(-\dfrac{u}{D}(x + r_0)\right)\right] & \text{if } x < -r_0 \\ n^\diamond(+\infty)\left[1 - \exp\left(+\dfrac{u}{D}(x - r_0)\right)\right] & \text{if } x > r_0. \end{cases} \tag{9.27}$$

The first solution is acceptable and corresponds to a flux at the particle boundary obviously equal to $n^\diamond(-\infty)u$. This solution is shown in Figure 9.6. But the second part of the solution explodes in an unphysical way, except for the trivial solution $n^\diamond(x > r_0) = 0$: it predicts no particles downstream. Moreover, the diffusion coefficient no longer drives the flux at the sphere boundary, which is equal to the convective flux at infinity. So the 1D approach is ill suited to model our problem.

9.4.3 Multidimensional approach

9.4.3.1 Necessity of a by-pass dimension

The 1D approach shows that the ability of partners to skirt the target particles (by-pass effect) are necessary to model faithfully the convection-diffusion process. So a satisfactory resolution of the problem at the local, target particle scale should be 2D or even 3D.

9.4.3.2 Thermal analogy approach

This approach, valid in 3D, consists in using the classical convective correlations. If the particles are small enough to neglect their slip velocity with the carrier gas, their concentration n is just a transported quantity, analogous to the internal energy $\rho e = \rho c T$ of an incompressible fluid. The diffusive flux $-D\partial_{\boldsymbol{x}} n^\diamond$ is compared to the thermal diffusion $-\kappa\partial_{\boldsymbol{x}} T$. Finally the convective velocity can be imposed as $\boldsymbol{u}_{g,\text{loc}}$ previously was or solved with the Navier-Stokes equations around the sphere.
The most subtle part of the analogy is the absorbing boundary condition. Imposing a zero concentration at the boundary is equivalent to imposing the temperature (phase change for instance) and is numerically difficult. Heat transfers are most often modeled with conduction-convection fluxes at the wall that are source terms of the form $-h(T - T_0)$. Analogously, we define a mass flux $-h(n^\diamond(r_0) - n^\diamond)$, so that the thermal analogy is settled as follows:

$$\partial_t n^\diamond + \partial_{\boldsymbol{x}}\left(n^\diamond \boldsymbol{u}_{g,\text{loc}} - D\partial_{\boldsymbol{x}} n^\diamond\right) = \begin{cases} -h(n^\diamond(r_0) - n^\diamond) & \text{on the sphere boundary} \\ 0 & \text{elsewhere.} \end{cases} \tag{9.28}$$

This problem is again to be solved at steady state. Imposing a zero density inside the sphere requires obviously $n^\diamond(r_0) = 0$. As for the value of h, it is linked to a coagulation characteristic rate: we see for instance that imposing $n^\diamond(r_0) = 0$ is equivalent to taking $h = +\infty$ so that we understand the difficulty of the zero concentration condition. So the model is closed under the condition of correctly modeling h.

As a remark, a modified boundary condition has been assessed by Zaichik and Alipchenkov (2008) for a Brownian-Turbulent transition case.
But the interest of such an analogy lies in the fact that the problem has been solved globally, since the need for a total flux at the wall is classic. The method is based on the use of correlations which are available for the mass and for the thermal convection-diffusion problem and provide a global (macroscopic) modeling at steady state: we can estimate the wall surface flux with a difference between the non-perturbated value $n^\diamond$ and the sphere value $n^\diamond(r_0)$, given a h_{macro}:

$$\mathcal{F}_{n^\diamond}(r_0) = -h_{\text{macro}}\left(n^\diamond - n^\diamond(r_0)\right) \tag{9.29}$$

which is, in the end, an averaged value. The Sherwood number Sh (also called the mass transfer Nusselt number) defined by:

$$\text{Sh} = h_{\text{macro}} L/D \tag{9.30}$$

expresses the dimensionless mass gradient at the wall where the characteristic length is the sphere diameter $L = 2r_0$. A simple correlation for Sh that is analogous to the Ranz-Marshall correlation reads:

$$\text{Sh} = 2 + 0.6\text{Re}^{\frac{1}{2}}\text{Sc}^{\frac{1}{3}},\ 0 \leq \text{Re} < 200,\ 0 \leq \text{Sc} < 250 \tag{9.31}$$

with the Reynolds number $\text{Re} = uL/\nu_g$ and the Schmidt number $\text{Sc} = \mu_g/D$. It is close to the Froessling correction.
If we consider a dimensioned version of this relation, we can evaluate the total flux towards the sphere:

$$\Phi = 4\pi r_0^2 h_{\text{macro}} n_\infty \tag{9.32}$$

where the coefficient is evaluated thanks to the Ranz-Marshall analogy:

$$h_{\text{macro}} = \frac{D}{r_0}\left(1 + 0.3\left(\frac{2r_0\,|\,\boldsymbol{u}^\diamond - \boldsymbol{u}^\star\,|}{\nu_g}\right)^{\frac{1}{2}}\left(\frac{\nu_g}{D}\right)^{\frac{1}{3}}\right) \tag{9.33}$$

For a negligible Reynolds i.e. $|\,\boldsymbol{u}\,| \to 0$, Fuchs' diffusive formula is retrieved:

$$\begin{aligned}\Phi_0 &= n(\infty)4\pi r_0^2 \frac{D}{r_0} \\ &= n(\infty)4\pi D r_0\end{aligned} \tag{9.34}$$

and the general flux with a convective correction reads:

$$\Phi = \Phi_0\left(1 + 0.3\left(\frac{2r_0\,|\,\boldsymbol{u}^\diamond - \boldsymbol{u}^\star\,|}{\nu_g}\right)^{\frac{1}{2}}\left(\frac{\nu_g}{D}\right)^{\frac{1}{3}}\right) \tag{9.35}$$

9.4.4 Conclusion on the diffusive-ballistic transition modeling

9.4.4.1 A new kernel for non-transitional nano-micro heterogeneous coalescence

It has been identified above that non-transitional heterogeneous coalescence can be described as a convection-diffusion problem. This approach opposes to the advection-diffusion analogy suggested by Simons et al. (1986), for which the computation has been recently furthered and corrected (Sajo 2008; Sajo 2010). The advection-diffusion approach indeed replaces $\boldsymbol{u}_{g,\text{loc}}$ by $\boldsymbol{u}^\diamond_{\text{ext}}$ in Eq. (9.23)

$$\mathcal{F}_{n^\diamond} = n^\diamond \boldsymbol{u}^\diamond_{\text{ext}} - D\partial_{\boldsymbol{x}} n^\diamond \tag{9.36}$$

where $\boldsymbol{u}^\diamond_{\text{ext}}$ is uniform and exogenous so that the problem can be solved analytically. This exogenous velocity can be the settling velocity as in the original work of Simons et al. (1986) but we could consider to use the slip velocity $\boldsymbol{u}^\diamond_{\text{ext}} = \boldsymbol{u}^\star - \boldsymbol{u}^\diamond$ for our ballistic particles. This latter case would correspond to a macroscopic approximation, equivalent to assume that the small particle velocity field in the neighborhood of the big particle is unperturbed by the fluid flow around this big particle. This simplification was justified to extract an analytical solution but we do not retain it because we have found an empirical solution to the more accurate convection-diffusion modeling.
As for transition particles, inertia plays a role for the small particles so it is now necessary to solve:

$$\mathcal{F}_{n^\diamond} = n^\diamond \boldsymbol{u}^\diamond_{\text{loc}} - D\partial_{\boldsymbol{x}} n^\diamond \tag{9.37}$$

with $\boldsymbol{u}^{\diamond}_{\rm loc}$ the small particle velocity field, which has its own evolution equation, featuring a drag force $\boldsymbol{F}(\boldsymbol{u}^{\diamond}_{\rm loc}, \boldsymbol{u}_{g,\rm loc})$ with the surrounding gas flow. So that this flux computation requires to solve the full steady problem for the particles $\diamond$:

$$\left\{ \begin{array}{l} \partial_{\boldsymbol{x}}(n^{\diamond}\boldsymbol{u}^{\diamond}_{\rm loc} - D\partial_{\boldsymbol{x}} n^{\diamond}) = 0 \\ \partial_{\boldsymbol{x}}(n^{\diamond}\boldsymbol{u}^{\diamond}_{\rm loc} \times \boldsymbol{u}^{\diamond}_{\rm loc}) = n^{\diamond}\boldsymbol{F}(\boldsymbol{u}^{\diamond}_{\rm loc}, \boldsymbol{u}_{g,\rm loc}) \end{array} \right. \tag{9.38}$$

where $\boldsymbol{u}_{g,\rm loc}$ can be taken as the gas velocity field around a sphere in the absence of particles (i.e. the same as for the thermal analogy) as long as the one-way coupling assumption holds. This problem, referred to as inertial convection-diffusion has not been solved.
As a conclusion, we suggest the following hybrid kernel for diffusive-ballistic coalescence from the previous study of a convection-diffusion problem:

$$\mathfrak{K}^{\rm D\text{-}B}_{\rm coal}(r^{\star}, r^{\diamond}) = 4\pi(D^{\star} + D^{\diamond})(r^{\star} + r^{\diamond}) \left(1 + \frac{0.3\sqrt{2(r^{\star} + r^{\diamond})\,|\,\boldsymbol{u}^{\star} - \boldsymbol{u}^{\diamond}\,|}}{\nu_g^{\frac{1}{6}}(D^{\star} + D^{\diamond})^{\frac{1}{3}}} \right) \tag{9.39}$$

so that $\Phi = n^{\diamond}\mathfrak{K}^{\rm D\text{-}B}_{\rm coal}(r^{\star}, r^{\diamond})$ and:

$$\mathscr{C}(r) = \int n^{\diamond} n^{\star} \mathfrak{K}^{\rm D\text{-}B}_{\rm coal}(r^{\star}, r^{\diamond}) J \mathrm{d}r^{\diamond}$$

provided that $r^{\star}$ and $r^{\diamond}$ are in the nano-micro range. We can for instance consider a micro droplet $\star$ and a nano droplet $\diamond$, so that $\boldsymbol{u}^{\diamond} = \boldsymbol{u}_g$.

9.4.4.2 Junction with the homogeneous coalescence regimes

The hybrid "bal-dif" kernel, between a ballistic and a Brownian, diffusive particle obviously tends towards the pure "dif-dif" one when the particles become small:

$$\mathfrak{K}^{\rm D\text{-}B}_{\rm coal}(r^{\star}, r^{\diamond}) \to \mathfrak{K}^{\rm Df}_{\rm coal}(r^{\star}, r^{\diamond}) \quad \text{when } r^{\star} \to \text{nano} \tag{9.40}$$

as we have $\boldsymbol{u}^{\star} - \boldsymbol{u}^{\diamond} \to 0$.
But the "bal-dif" kernel has no reason to converge towards the "bal-bal" kernel: this is due to the fact that the convective correction for the diffusion equation is valid in a given range of Reynolds numbers that has no particular link with the limit of validity of the pure ballistic kernel.
We consider the case of minimum polykineticity for small droplets i.e.

$$|\,\boldsymbol{u}^{\star} - \boldsymbol{u}^{\diamond}\,| \approx |\,\mathrm{St}^{\star} - \mathrm{St}^{\diamond}\,|\; u_g$$

so that we can write the hybrid kernel as a function of $r^{\star}$ and $r^{\diamond}$:

$$\begin{aligned} \mathfrak{K}^{\rm D\text{-}B}_{\rm coal}(r^{\star}, r^{\diamond}) &= \frac{2kT_g}{3\mu_g}\left(\frac{1}{r^{\star}} + \frac{1}{r^{\diamond}}\right)(r^{\star} + r^{\diamond}) \left(1 + \frac{0.3\sqrt{2(r^{\star} + r^{\diamond})\rho_l \boldsymbol{u}_g\,|\,r^{\star 2} - r^{\diamond 2}\,|}}{18\mu_g \nu_g^{\frac{1}{6}} \left(\frac{2kT_g}{3\mu_g}\left(\frac{1}{r^{\star}} + \frac{1}{r^{\diamond}}\right)\right)^{\frac{1}{3}}} \right) \\ &= \frac{2kT_g}{3\mu_g}\left(\frac{1}{r^{\star}} + \frac{1}{r^{\diamond}}\right)(r^{\star} + r^{\diamond}) \left(1 + \frac{0.3\sqrt{2\rho_l \boldsymbol{u}_g (r^{\star} + r^{\diamond})^2\,|\,r^{\star} - r^{\diamond}\,|}}{18\mu_g \nu_g^{\frac{1}{6}} \left(\frac{2kT_g}{3\mu_g}\right)^{\frac{1}{3}} \left(\frac{1}{r^{\star}} + \frac{1}{r^{\diamond}}\right)^{\frac{1}{3}}} \right) \end{aligned} \tag{9.41}$$

to compare to the ballistic kernel in this case:

$$\begin{aligned} \mathfrak{K}^{\rm B}_{\rm coal}(r^{\star}, r^{\diamond}) &= \frac{\pi\rho_l \boldsymbol{u}_g}{18\mu_g}(r^{\star} + r^{\diamond})^2\,|\,r^{\star 2} - r^{\diamond 2}\,| \\ &= \frac{\pi\rho_l \boldsymbol{u}_g}{18\mu_g}(r^{\star} + r^{\diamond})^3\,|\,r^{\star} - r^{\diamond}\,| \end{aligned} \tag{9.42}$$

9.5 A hybrid MF model for nano-micro sprays

The nanometric droplets present in the mixture are not treated at the kinetic level (Fokker-Planck) as we are at (Gaussian) equilibrium. Instead, both nanometric and micrometric droplets are described by semi-kinetic models and coupled with the hybrid coalescence kernel introduced in Eq. (9.39), which is indeed written at the semi-kinetic level.
We consider the critical radius r_N below which particles are relaxed regarding average velocity towards the gas velocity and regarding dispersion towards Brownian agitation.

9.5.1 Hybridization at the semi-kinetic level

9.5.1.1 Nano model

We consider the number density $n(r)$ of droplets of size $r < r_N$ which is described by Smoluchowski's equation, extended to all sizes:

$$\partial_t n + \partial_{\boldsymbol{x}} \cdot (n \boldsymbol{u}_g) = \mathscr{C}_{nano} + \mathscr{C}^-_{D-B} + D \partial_{\boldsymbol{x}} n, \qquad r \leq r_N \tag{9.43}$$

where $D = \frac{kT_g}{6\pi\mu_g r}$ comes from Eq. (8.18) and the coalescence integrals read:

$$\mathscr{C}_{nano} = -\int n(r) n(r^\star) \mathfrak{K}^{\mathrm{Df}}_{\mathrm{coal}}(r, r^\star) \mathrm{d}r^\star + \frac{1}{2} \int n(r^\star) n(r^\diamond) \mathfrak{K}^{\mathrm{Df}}_{\mathrm{coal}}(r^\star, r^\diamond) J \mathrm{d}r^\star \tag{9.44}$$

and

$$\mathscr{C}^-_{D-B} = -\int n(r) n(r^\star) \mathfrak{K}^{\text{D-B}}_{\mathrm{coal}}(r, r^\star) \mathrm{d}r^\star \tag{9.45}$$

The latter term describes the disappearance of nano droplets due to their coalescence with micro ones.

9.5.1.2 Micro model

We consider the number density $n(r)$ of droplets of size $r > r_N$ which is described by a system inspired from the semi-kinetic System (4.13):

$$\left\{ \begin{array}{l} \partial_t n + \partial_{\boldsymbol{x}} \cdot (n \boldsymbol{u}) = \mathscr{C}_{micro} + \mathscr{C}^+_{D-B} \\ \partial_t n \boldsymbol{u} + \partial_{\boldsymbol{x}} \cdot (n \boldsymbol{u} \otimes \boldsymbol{u}) = \mathscr{C}_{micro,nu} + \mathscr{C}^+_{D-B,nu}, \qquad r > r_N \\ \partial_t nh + \partial_{\boldsymbol{x}} \cdot (nh \boldsymbol{u}) = \mathscr{C}_{micro,nh} + \mathscr{C}^+_{D-B,nh} \end{array} \right. \tag{9.46}$$

where the coalescence integrals read:

$$\begin{aligned} \mathscr{C}_{micro} = \quad & -n(r) \int n(r^\star) \mathfrak{K}^{\mathrm{B}}_{\mathrm{coal}}(r, r^\star) \mathrm{d}r^\star \\ & + \frac{1}{2} \int n(r^\star) n(r^\diamond) \mathfrak{K}^{\mathrm{B}}_{\mathrm{coal}}(r^\star, r^\diamond) J \mathrm{d}r^\star \\ \mathscr{C}_{micro,nu} = \quad & -n(r) \boldsymbol{u}(r) \int n(r^\star) \mathfrak{K}^{\mathrm{B}}_{\mathrm{coal}}(r, r^\star) \mathrm{d}r^\star \\ & + \frac{1}{2} \int n(r^\star) n(r^\diamond) \frac{v^\star \boldsymbol{u}^\star + v^\diamond \boldsymbol{u}^\diamond}{v^\star + v^\diamond} \mathfrak{K}^{\mathrm{B}}_{\mathrm{coal}}(r^\star, r^\diamond) J \mathrm{d}r^\star \\ \mathscr{C}_{micro,nh} = \quad & -n(r) h(r) \int n(r^\star) \mathfrak{K}^{\mathrm{B}}_{\mathrm{coal}}(r, r^\star) \mathrm{d}r^\star \\ & + \frac{1}{2} \int n(r^\star) n(r^\diamond) \frac{v^\star h^\star + v^\diamond h^\diamond}{v^\star + v^\diamond} \mathfrak{K}^{\mathrm{B}}_{\mathrm{coal}}(r^\star, r^\diamond) J \mathrm{d}r^\star \end{aligned} \tag{9.47}$$

and

$$\begin{aligned} \mathscr{C}^+_{D-B} &= \frac{1}{2} \int n(r^\diamond) n(r^\star) \mathfrak{K}^{\text{D-B}}_{\mathrm{coal}}(r, r^\star) \mathrm{d}r^\star \\ \mathscr{C}^+_{D-B,nu} &= \frac{1}{2} \int n(r^\diamond) n(r^\star) \frac{v^\star \boldsymbol{u}_g + v^\diamond \boldsymbol{u}^\diamond}{v^\star + v^\diamond} \mathfrak{K}^{\text{D-B}}_{\mathrm{coal}}(r, r^\star) \mathrm{d}r^\star \\ \mathscr{C}^+_{D-B,nh} &= \frac{1}{2} \int n(r^\diamond) n(r^\star) \frac{v^\star h(T_g) + v^\diamond h^\diamond}{v^\star + v^\diamond} \mathfrak{K}^{\text{D-B}}_{\mathrm{coal}}(r, r^\star) \mathrm{d}r^\star \end{aligned} \tag{9.48}$$

The latter term describes the appearance of new micro droplets from nano-micro coalescence: their mass is taken from Eq. (9.43). The overall system is conservative as regards mass, thanks to a compliant computation of $\mathscr{C}^-_{D-B}$ and $\mathscr{C}^+_{D-B}$.

9.5.2 Hybrid Multi-Fluid approach

9.5.2.1 Size discretization

The Multi-Fluid models rely on the choice of a discretization $0 = S_0 < S_1 < \cdots < S_{N_{\mathrm{sec}}} = \infty$ for the droplet size phase space and the averaging of the conservation law system over each fixed size interval $[S_{k-1}, S_k[$, called section. The set of droplets in one section can be seen as a "fluid" for which conservation equation are written, the sections exchanging mass, momentum and enthalpy.
In our case, we choose one of the section bounds to match the nano-micro transition: we define k_c so that $r_{k_c} = r_N$.

9.5.2.2 One size moment hybrid Multi-Fluid method

The OSM Multi-Fluid model is derived with the same assumptions than for its usual derivation (see § 4.4.1). As for the Brownian sections, they have relaxed velocities $\boldsymbol{u}_k(t,\boldsymbol{x}) = \boldsymbol{u}_g(t,\boldsymbol{x})$ and temperatures $T_k(t,\boldsymbol{x}) = T_g(t,\boldsymbol{x})$, $k \leq k_c$.
The conservation equations for the k^{th} section result from the integration of the mass moment for the Smoluchowski Eq. (8.60) in each section $k \leq k_c$:

$$\partial_t m_k + \partial_{\boldsymbol{x}}\cdot(m_k\boldsymbol{u}_g) = \mathrm{C}^m_{nano,k} - \mathrm{C}^-_{D-B,k}\ , \quad k \in [\![1,k_c]\!] \tag{9.49}$$

and for the dispersed semi-kinetic System (9.43) in each section $k > k_c$:

$$\left\{\begin{array}{l} \partial_t m_k + \partial_{\boldsymbol{x}}\cdot(m_k\boldsymbol{u}_k) = \mathrm{C}^{m+}_{D-B,k} + \mathrm{C}^m_{micro,k} \\ \partial_t(m_k\boldsymbol{u}_k) + \partial_{\boldsymbol{x}}\cdot(m_k\boldsymbol{u}_k\otimes\boldsymbol{u}_k) = m_k{}^1\boldsymbol{F}_k + \mathrm{C}^{mu+}_{D-B,k} + \mathrm{C}^{mu}_{micro,k}\ , \quad k \in [\![k_c+1, N_{\mathrm{sec}}]\!] \\ \partial_t(m_k h_k) + \partial_{\boldsymbol{x}}\cdot(m_k h_k\boldsymbol{u}_k) = m_k{}^1\mathrm{H}_k + \mathrm{C}^{mh+}_{D-B,k} + \mathrm{C}^{mh}_{micro,k} \end{array}\right. \tag{9.50}$$

where the coalescence disappearance terms are computed similarly to the usual ones, but with the appropriate kernels, and the creation ones distribute mass between the nano and micro sections.

9.5.2.3 Two size moment hybrid Multi-Fluid method

A hybrid TSM method can be derived similarly to that of Chapter 5.
The conservation equations now result from the integration of the number and mass moment for the Smoluchowski Eq. (8.60) in each section $k \leq k_c$:

$$\left\{\begin{array}{l} \partial_t n_k + \partial_{\boldsymbol{x}}\cdot(n_k\boldsymbol{u}_g) = \mathrm{C}^n_{nano,k} - \mathrm{C}^{n+}_{D-B,k}\ , \quad k \in [\![1,k_c]\!] \\ \partial_t m_k + \partial_{\boldsymbol{x}}\cdot(m_k\boldsymbol{u}_g) = \mathrm{C}^m_{nano,k} - \mathrm{C}^{m+}_{D-B,k} \end{array}\right. \tag{9.51}$$

and for the dispersed semi-kinetic System (9.43) in each section $k > k_c$:

$$\left\{\begin{array}{l} \partial_t n_k + \partial_{\boldsymbol{x}}\cdot(n_k\boldsymbol{u}_k) = \mathrm{C}^{n+}_{D-B,k} + \mathrm{C}^n_{micro,k} \\ \partial_t m_k + \partial_{\boldsymbol{x}}\cdot(m_k\boldsymbol{u}_k) = \mathrm{C}^{m+}_{D-B,k} + \mathrm{C}^m_{micro,k}\ , \quad k \in [\![k_c+1, N_{\mathrm{sec}}]\!] \\ \partial_t(m_k\boldsymbol{u}_k) + \partial_{\boldsymbol{x}}\cdot(m_k\boldsymbol{u}_k\otimes\boldsymbol{u}_k) = m_k{}^2\boldsymbol{F}_k + \mathrm{C}^{mu+}_{D-B,k} + \mathrm{C}^{mu}_{micro,k} \\ \partial_t(m_k h_k) + \partial_{\boldsymbol{x}}\cdot(m_k h_k\boldsymbol{u}_k) = m_k{}^2\mathrm{H}_k + \mathrm{C}^{mh+}_{D-B,k} + \mathrm{C}^{mh}_{micro,k} \end{array}\right. \tag{9.52}$$

where the source terms and especially $\mathrm{C}_{micro,k}$ are computed as in § 5.2.4.

9.5.3 Discussion on dispersion orders of magnitude

The nano droplet agitation has an effect on coalescence but not on the spray dynamics since diffusion is absolutely negligible. Above this radius, a standard semi-kinetic system with a zero dispersion assumption is sufficient up to a Stokes that is not too high. Below this radius, Smoluchowski's Eq. (8.60) is considered and averaged on the sections.

9.6 Illustration of the Brownian-ballistic coalescence dynamics on an academic case

We present some numerical results obtained with a research code, as an illustration of the peculiar features of coalescence in nano-micro mixtures. The code and the configuration that are used are presented later in § 13.2.1 and are used for a complete validation of the model and method for micrometric cases.

9.6.1 Brief presentation of the case

9.6.1.1 A case with velocity differences

We consider a polydisperse spray in a gaseous field:

$$u_z(z) = \frac{z_0^2 u_z(z_0)}{z^2} \tag{9.53}$$

that decelerates, independently from the disperse phase (one-way coupling). The flow is permanently fed so the case is at steady state.
On the one hand, the deceleration imposed to the inertial droplets is different depending on their size so that velocity differences appear. On the other hand, the Brownian droplets perfectly follow the gas so they are all convected at the gas velocity, whatever their sizes. Coalescence occurs between inertial droplets due to the velocity differences that appear, while Brownian droplets encounter Brownian coalescence due to their agitation.

9.6.1.2 Numerical configuration

We consider an initially bimodal distribution with droplets of radius 10 μm and 20 μm. The disperse phase is modeled with a hybrid MF approach, derived in § 9.5. In the code, both an OSM and an Exp-TSM method are used. The transition between Brownian and ballistic droplets is fixed at $r_N = 12\,\mu$m so that a relaxed model is used below this size. As a remark, this large value for transition is obtained in the particular case of a large residence time and a "slowly" varying flow, inducing relatively weak ballistic coalescence.
The transition kernel that is used is an additive one, presented in Eq. (9.10) and based on the assumption of independence between the Brownian and the ballistic coalescence mechanisms. This kernel is an approached model that still allows to assess the dynamics of Brownian-ballistic mixtures.

9.6.2 Results

The results are presented for mass concentration distributions in Figure 9.8 and for velocities in Figure 9.9. The velocities follow a smooth behavior, which means that the transition radius r_N is reasonably chosen.
Thanks to the bimodal initial distribution, three distinct coalescence phenomena can be observed from the evolution of size distributions:

- Auto-coalescence occurs among Brownian droplets: the first mode (around 12 μm) is clearly visible because it results from purely monodisperse droplets.
- Coalescence between Brownian and ballistic droplets is observed as it widens the ballistic peak, still in a continuous way as the size difference is significant.
- Purely ballistic coalescence occurs later because the inertial velocity differences need more length to settle. It results in the appearance of a tail for the ballistic peak.

These three "isolated" coalescence facts occur simultaneously in more complex cases, as a consequence of the non-linearity of coalescence. But we highlight that Brownian coalescence can be seen as enhancing the usual ballistic coalescence because it widens the distributions, therefore increasing the velocity differences in hetero-DTC cases.

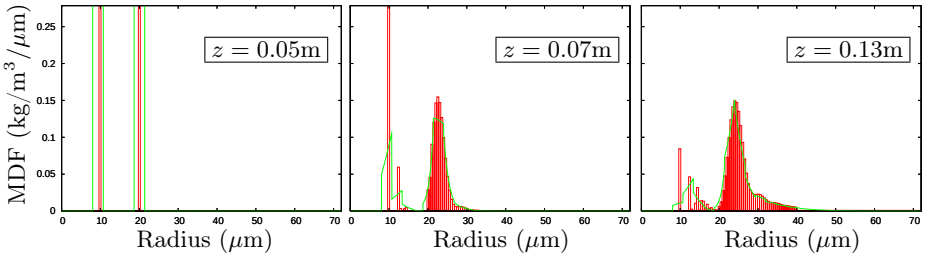

Figure 9.8: *Mass concentration distribution at different abscissa - Boxes:One size moment hybrid MF with* 80 *sections; Line: Two size moment hybrid MF with* 16 *sections.*

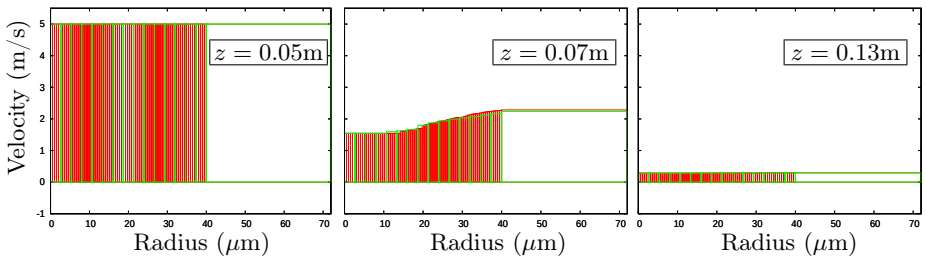

Figure 9.9: *Velocity per section at different abscissae - Boxes: One size moment hybrid MF with* 80 *sections; Boxes: Two size moment hybrid MF with* 16 *sections.*

9.6.3 Conclusion on the mixture case

In the context of a Multi-Fluid approach, the model differences between Brownian and ballistic particles can be accounted conveniently thanks to the sectional discretization, provided a satisfactory kernel. The peculiarities of coalescence in such mixtures is illustrated on an example case and the complex behavior is shown. The role of Brownian particles in enhancing coalescence is exhibited.

9.7 Conclusion

In the framework of a hybridization between a kinetic spray model and Smoluchowski's equation, the modeling of a coalescence kernel is crucial. The physics of the resulting mixtures is complex. Several paths are explored to connect the two regimes and a promising approach based on empirical closures, classical for convection-diffusion problems is derived. The validation of this approach is necessary but out of the scope of this work.

Part IV

Numerical methods for Euler-Euler two-way coupled polydisperse two-phase flow simulations

Chapter 10

Numerical methods for moderately dense polydisperse two-phase flows

We describe efficient and accurate numerical strategies from the literature that can be used for HPC simulation of two-way coupled disperse two-phase flows. Such flows generate a stiff multi-scale and coupled problem, the dynamics of which we aim at capturing, so time strategies are assessed in regards. First, a major specificity of disperse phase flows is hypercompressibility: it is difficult to treat due to the potential occurrence of accumulations and singularities. Hence the space transport resolution strategy is to be designed accordingly and depends on the purpose of the method, namely for structured or unstructured meshes. Second, time integration strategies for multi-scale problems are then presented: the choice of splitting methods is motivated by the need (i) to preserve mathematical properties of the system, (ii) to comply to the existing code structures, and (iii) to either account for, or to overcome the multiple time scales in a way that accurately reproduces the overall physics. Third, facing the high-dimensional phase space of a disperse phase, a strategy for the integration of the source terms with respect to the internal couplings and dynamics is finally discussed. Based on the conclusions drawn from the previous three areas, the contributions of the present work are highlighted as well as their impact in the several codes for research and applicative computations that we have used and improved.

10.1 Introduction

10.1.1 Approaching multi-scale evolution PDEs with complex dynamics

Numerical methods are at the heart of CFD concerns. The simulation of two-phase flows with an Euler-Euler approach nonetheless relies on an efficient and accurate strategy for the carrier fluid -which is a vast topic (Anderson 1995; Lomax et al. 2001; Chung 2010; Refloch et al. 2011) and is not discussed here- but requires also a specific treatment of the Eulerian disperse phase equations. Besides, the choices and the structure of the carrier gas solver may influence the strategy for the disperse phase.

The space transport resolution strategy is discussed as regards the model: all the Eulerian disperse phase models feature indeed a peculiar behavior, which is referred to as hypercompressibility, the origin of which has been presented in § 3.1.3.4: mass accumulations may occur, depending on the dynamics of the underlying gas flow. When modeled by Eulerian approaches, these mass accumulations may in addition result in singularities, as presented in § 4.3.2.3. The disperse phase concentration field in physical space, together with its accumulations and singularities, is said to be multi-scale. Specific numerical methods are required to cope with accumulations i.e. to describe them robustly, accurately and to account for the related physics i.e. their effects on the flow and on the sources. Hypercompressibility is at the origin of the early failure in the application of Euler-Euler methods for two-phase flows but the appropriate methods, linked to the spatial numerical resolution strategy, are under development, with successes on structured meshes.

The problem we are tackling is also a dynamical and evolving one because of its complex phase space and the presence of multiple couplings: various time scales arise from both intrinsic dynamics such as the source terms in polydisperse media and the coupling to the multi-scale space repartition. So the problem is stiff. Well-suited time integration strategies are then necessary and they are discussed based on their ability to render all the scales, the dynamics and the couplings and at which cost they do so. In particular, the two-way coupling that arises in moderately dense cases requires a careful integration of the overall system though in our moderately dense case, the coupling occurs only through source terms.

With a well chosen strategy, the evolutions within the phase space can be considered alone but they require also a careful treatment and a strategy to account accurately and efficiently for dynamics and internal

couplings between size, velocity, temperature and the gas variables. In our case polydispersity is effective and the evolution of the phase space variables, as conditioned by size, has a stiff and complex dynamics (drag, heat exchange, coalescence). Within most of the droplet size spectrum, the physics remains size-conditioned, which allows the use of a MF formalism and partly simplifies the resolution criteria as far as accuracy is concerned. So stiffness of the dynamics in the phase space can be anticipated depending on the particle sizes that are present while two-way coupling remains a stiffness factor that is difficult to forecast.

10.1.2 Duality of research and industrial codes

Numerical methods and their implementation happen to have been developed in two different directions, which we designate as:

- research simulations, and
- industrial simulations.

Research simulations are designed and performed to study a given problem: the geometry is simplified e.g. a box with Homogeneous Isotropic Turbulence, a jet, a step, *etc.* in order to focus on some isolated physical phenomena, possibly with advanced models and a fine level of resolution. A detailed and exhaustive post-processing is amenable to a study of the full spectrum of scales, still within a reasonable volume of data and computational time.

Industrial simulations are performed to assess a realistic configuration, where the multiple physics is to be accounted for and where the complex geometry plays a key role: so a refined level of detail is needed. In many applications as in SRMs, the geometry is complex (see § 1.2.1.1) and may evolve with time, so non-structured meshes are mandatory (Scherrer et al. 2011; Kah et al. 2013). In many cases (turbulent simulation, multi-physics) many degrees of freedom are required: they reach today billions of points e.g. in aeronautical configurations (Moureau et al. 2011). In return, the models and methods are chosen to be less detailed and the mostly desired qualities are robustness and short pre-processing and restitution times.

As for the outputs, the simulation is ultimately performed to capture the main features of the configuration, e.g. as regards quantities post-processed as integrals (total drag, heat flux, mean temperature at a point, mass flow rate through a section, average pressure). The reference simulation can be the "one-night computation" for engineering design or the validation computation which takes a few weeks and should prove a satisfactory behavior of the full system.

The limit between research and industrial simulations is not bold: some detailed studies are led on complex configurations e.g. semi-industrial cases, with experimental results featuring realistic parts of a device (Sanjosé et al. 2008; Dupays et al. 2008). But each type of approach requires adapted numerical methods. The space discretization strategy can be good criterion to distinguish the two approaches:

- structured grids are used for research simulations;
- unstructured meshes are used for industrial simulations.

The first ones are adapted to accurate methods on simple geometries while the second ones are adapted to complex geometries. This distinction is not a rule but we carry on the analysis on this simplified basis.

10.1.3 Requirements of HPC

High Performance Computing (HPC) refers to an ensemble of features that should be achieved by a computation to allow it to cope with systems that have numerous degrees of freedom and require accuracy (Dowd et al. 1998). In our case, we more precisely refer to massively parallel computations of high-fidelity models with efficient and accurate methods.

To increase the fidelity of a computation, two strategies can be explored that are high order methods, requiring a low number of DoFs but featuring complexity and low order methods, requiring a high number of DoFs but with simple algorithms. As today's computational power is still not sufficient to reach the desired level of detail, several techniques such as LES for turbulence have been used to model part of the DoFs. So the parameterization of a computation is carried out in order to refine at best the meshing of the space, for a given computational power. As a simplified illustration on transport, a twofold refinement of a 3D space transport resolution strategy may result in a 2^4 times higher cost (as the time step must often also be divided by 2 for most convection schemes). As a consequence, the evolution towards a reliable computation is slow, even with the spectacular increase in CPU power.

High-fidelity computations in fluid dynamics and mechanical engineering are performed with relatively high order schemes (Gourdain et al. 2009; Haider et al. 2011), but a fine mesh is still required to capture multi-scale physical phenomena, demanding high computational power and large data storage capacity: the problem is well known for single phase turbulence.

This computational paradigm requires parallel and even massively parallel architectures, the parallelization being often achieved by domain decomposition. This entirely conditions the models and methods from their design to their implementation: it requires compact spatial schemes to reduce communications, while the

implementation must be done including shared and/or distributed memory instructions (e.g. OpenMP and MPI).

10.1.4 Our objectives

Because the industrial codes and some large research codes are designed and improved on long periods and by several developers, the most generic, convenient, and reliable strategies are sought when it comes to implementing new methods and to including the new models needed. But methods are rarely fully generic so in practice, the new developments are oriented by the existing material. This liability and legacy constraint is strong as regards the space transport resolution strategy (structured or unstructured formulation), and the time integration is as well constrained. So we aim at developing methods which are compatible and which require minimum modifications on the existing code.
A brief overview of the available methods is done. However the matters of defining a strategy for:

- transport in the physical space,
- global time integration, and
- phase space dynamics integration,

are not decoupled -even if the splitting technique that is finally chosen helps to do so- because the physics is coupled at some of the smallest scales. So the choices are related to our particular case: the multi-scale physics and the coupling with transport yielding hypercompressibility require to develop a specific strategy to respect both the physics at all scales and the realizability, robustness and cost constraints, together with achieving a good (potentially tunable) cost accuracy trade-off and with remaining compliant for HPC. The requirements imposed by HPC on the numerical strategy and methods are discussed along the three parts.

10.2 Strategies for the transport in physical space of hypercompressible flows

The strategy for the transport in physical space is now discussed in the context of a Eulerian treatment of the disperse phase: the goal is then to transport some of its moments in an accurate way as regards the mathematical peculiarities, the potential multi-scale aspects i.e. accumulation (and possibly singularity) formation and the realizability issues.
The Eulerian modeling of a disperse phase consists in hyperbolic or weakly hyperbolic transport equations for some moment quantities of the NDF, as presented in detail in Chapter 4. This fact is true regardless of the treatment of the phase space. So the following discussion is held for the transport in physical space, decoupled from the phase space dynamics, provided that a time strategy is chosen, that respects all levels of couplings.

10.2.1 General constraints of disperse phase transport in physical space

We discuss the numerical issues of the transport in physical space, as it is often the numerical focal point of a flow simulation and as it is particularly tedious to treat in disperse phase cases.

10.2.1.1 Hypercompressibility and multi-scale physics

The disperse phase dynamics has been presented as hypercompressible in § 4.3.2.3: the problem is multi-scale since particle concentration accumulations (such as δ-shocks described in § 4.3.2.2) occur and can be very thin (infinitely in the case of PGD). The accumulations that may arise must nonetheless be handled (for robustness), but also accounted for accurately and their multi-scale stiff physical effects must be rendered.
Numerically speaking, the following concerns arise unfortunately:

- accumulations are difficult to treat because of their steepness;
- singularities raise similar concerns and are model limitations;
- the vacuum zones may not be rendered accurately due to numerical diffusion, and positivity is difficult to preserve (very limited oscillation is then admitted in low-density areas);
- the smearing and destruction of mixing structures can be a major drawback of Eulerian approaches.

As a result some standard numerical strategy, schemes and source integration used for Gas Dynamics (GD) cannot be directly generalized to Hypercompressible Gas Dynamics (HGD).
A high quality solution accurate for the accumulations and coping with singularities is required, so either a refined mesh or an accurate method must be considered (Fréret et al. 2010; Martinez 2009). To spare degrees of freedom and cost, a high order transport scheme, yielding a low level of diffusion, should be used. This is rarely achieved in Euler-Euler simulations because high-order methods may be unstable in the presence of the strong gradients of singularities. For instance de Chaisemartin (2009) states that many high

order transport schemes developed for Euler or Navier-Stokes equations are ill-suited for the disperse phase because of the peculiarities of PGD that are vacuum zones and singularities.

10.2.1.2 Realizability constraints for transport in physical space

The set of equations of the hypercompressible medium describes the transport of moments of the medium. A given set of moments is not realizable, or equivalently, no NDF possesses these moments means that the set of moments is not admissible to describe the system: realizability issues result in method stability and accuracy problems. The problem of realizability impacts the choice of a numerical method since moments cannot evolve independently: numerical errors must keep a given level of consistency.
The most important realizability constraint is that of positivity of the density. This constraint also exists for Euler systems but it is not so restrictive in the context of reasonably compressible flows. In hypercompressible media yet the existence of vacuum zones and strong density gradients permanently threatens positivity.
Other realizability constraints do exist for high order methods. As regards size moments, the realizability constraints increase when moving from the OSM to the TSM and to the EMSM. Realizability constraints of the TSM methods are presented in § 5.3.1.2, while higher order methods such as EMSM are studied in Kah (2010) and Kah et al. (2012). To ensure a realizable transport for the TSM, a scheme has been developed Dufour (2005); de Chaisemartin (2009) and is presented in Chapter 13.
As regards velocity moments, the realizability constraints increase when moving from the monokinetic closure to QMOM or MG (the methods being presented in § 4.5. As for the AG model (introduced in Chapter 5), the positivity of the diagonal dispersions and of the determinant of the Gaussian covariance matrix must be enforced. These aspects are discussed in Chapter 11 and a transport method is developed for the AG formalism.
As a general lesson on realizability, high order moment methods (i.e. with at least second order moments) introduce strong constraints on the transport schemes, to ensure realizability (Vié et al. 2013).

10.2.1.3 Conclusion

Accounting for accumulations and singularities raises the following numerical issues:

- the physical space transport imposes simultaneously an accurate scheme and a fine mesh (leading to a restrictive CFL constraint);
- the realizability can be threatened by localized numerical errors especially for high order moment methods.

The space transport resolution strategy has therefore to be defined with caution, with respect to these constraints. Because the problem is multi-scale, an accurate scheme is required to capture these structures at a reasonable cost: the trade-off is then to design a high order scheme which is robust enough and preserves realizability.
Numerical schemes for transport in physical space are now discussed. The space description of the field depends on space discretization, e.g. the mesh (characterized by a typical size Δx) and on the in-cell representation. The numerical strategies that have been developed are very different depending on the class of mesh, namely structured or unstructured, so we present the approaches for these two cases separately.

10.2.2 Strategies for structured grids

The question of deriving accurate and robust schemes for hyperbolic equations has been tackled for a long time on structured grids. The space description of the fields is briefly presented as it is not crucial for structured meshes: it can either resort to finite difference (FD), finite volume (FV) or finite element (FE) methods, which makes differences in the conserved quantities and the evaluation of derivatives and integrals. These descriptions are detailed below for unstructured meshes as the choice is then crucial.

10.2.2.1 Dimensional splitting

For structured grids, the dimensional splitting approach, also referred to as Alternate Dimension Integration (ADI) method (Briley and McDonald 1977; LeVeque 2002), has been introduced to bring back to a 1D vision. This approach is however limited to second order in time and raises issues about losses in the directional coupling. The proper implementation of boundary conditions in a splitting context is also a research topic. The overall strategy is still more accurate than a multidimensional integration (LeVeque 2002) e.g. it is less dissipative as it allows to transport in each direction with an adapted CFL. It allows moreover a convenient implementation as it uses 1D methods, repeated in multiple directions.

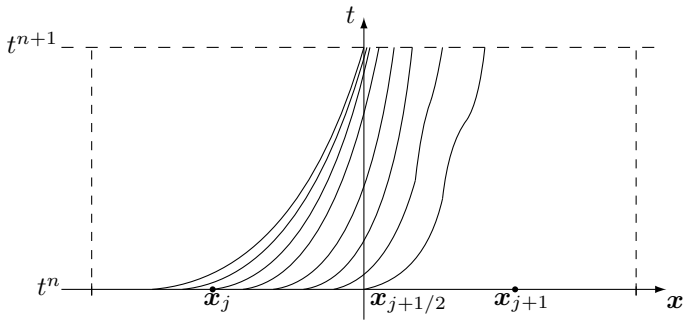

Figure 10.1: *Characteristics of a non-linear, coupled problem: a kinetic scheme approximates these underlying characteristics to integrate the flux passing through the boundary $\boldsymbol{x}_{j+1/2}$ on one time step.*

10.2.2.2 Evaluation of the fluxes at the cell boundaries: general aspects

To update the values of the variable fields, numerical fluxes are computed at the boundaries of the cells. They should satisfy conservation and consistency properties. They can be directly computed from derivatives estimated for the field but the accuracy and stability of the method are then threatened near singularities. To avoid this issue, Godunov's approach was introduced (Godunov 1959): the discontinuities at the cell interfaces are treated as physical ones and a simplified problem is solved in correspondence: the Riemann problem. The Riemann solver can be either exact, in which case it is often non-linear and may require an iterative method or approached, in which case many techniques are given in Toro (2009).
The numerical methods for compressible flows were limited to order one according to Godunov's theorem but Van Leer (1979) proved that higher order were possible in the smooth area at the cost of a non-linear limitation close to the singularities: the MUSCL approach was introduced, based on high order reconstructions to estimate more accurately the conditions of a Riemann problem at the interface. The question of the accurate integration on time can be included in the space transport resolution strategy. On the one hand, the numerical fluxes can be computed as instantaneous and this value used by the time scheme as a low order estimation of the flux on the time step: the schemes then have a high order in space and time but the time representation is poor so the overall strategy is not accurate (large convergence constant). On the other hand, coupled time-space approaches may be achieved to increase the overall accuracy: kinetic schemes (Deshpande et al. 1998) or ADER (Toro 2009), which is based on the generalized Riemann problem have been suggested.

10.2.2.3 Early compressible schemes

As a first idea to treat hypercompressibility, we focus on schemes for compressible flows. MacCormack (1969)'s scheme, which achieves second order with an acceptable level of diffusion and has been widely applied to simulate hypersonic flows, has been used for a disperse phase in SRMs, described with the PGD (Dupays 1996).
A wide literature of schemes was then issued for compressible flows e.g. the AUSM and AUSM$^+$ (Liou and Steffen 1993; Liou 1996). But the corresponding treatments are adapted to GD and its level of compressibility so they are not strict enough to ensure robustness and positivity for HGD, e.g. when vacuum zones and singularities coexist.

10.2.2.4 Kinetic schemes

In the quest for accuracy, space-time strategies where derived, that reduce the error to the space representation.
Kinetic schemes (Deshpande et al. 1998) are well suited for space-time approaches, as a good information on the time evolution of the boundary flux is reconstructed from the characteristics, see Figure 10.1. When represented in 1D thanks to ADI, characteristics can indeed be easily assessed and an integration along the reconstructed characteristics is performed, possibly in an exact way. From these considerations, (Estivalezes and Villedieu 1996) introduced a high order Strong Stability Preserving scheme for disperse phases. In the case of GD however, kinetic schemes bring a significant level of diffusion, especially as far as contact are concerned.

10.2.2.5 Kinetic scheme for the PGD

The PGD has been approached properly in disperse phase contexts only recently and on structured grids: de Chaisemartin (2009) has proposed such a kinetic scheme, based on the seminal work of Bouchut et al.

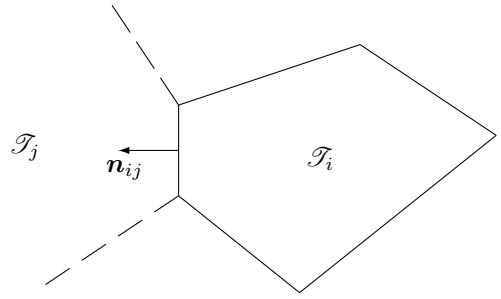

Figure 10.2: *Fluxes in a non-structured, generic mesh.*

(2003). The second order scheme is very accurate (provided that CFL$\sim$ 1) and robust for the description of the disperse phase multi-scale aspects. It is detailed in § 13.1.1, as we use it in research codes to transport the moments of the TSM method. Because the kinetic scheme comes back to the underlying kinetic level, it allows to take strictly into account the dynamics of collisionless particles.
The kinetic approach retained by de Chaisemartin (2009) reaches second order thanks to a MUSCL-type reconstruction with a slope limitation and uses the underlying kinetic equation to obtain an exact evaluation in time of the fluxes at each interface. The resulting scheme has the important property of intrinsically preserving the natural properties at PDE level for the PGD system: the positivity of the number density and a discrete maximum principle on the velocity, which is not the case with classical linear high order finite volume schemes. This approach has been used for the DNS of turbulent particulate flows, and has also been adapted to more complex moment methods for polydisperse flows (Kah 2010).

10.2.2.6 Towards an approach for AG

The AG is a new model for the DNS of a moderately inertial disperse phase, introduced in Chapter 6. The model is strictly hyperbolic but features HGD, as it describes a disperse phase.
Because its pressure stresses have *a priori* a complete freedom on anisotropy, the model features in addition peculiarities that require further studies: the numerical space transport resolution strategy is assessed on structured meshes as a first step. As regards the 1D system, Berthon (2006) has suggested a first order scheme that preserves the entropy. But the resolution at second order is desirable to account efficiently for the multi-scale aspects of the moderately inertial disperse phase.

10.2.2.7 Conclusion

The peculiarities of HGD compared to GD have led to the use of kinetic schemes on structured meshes. This strategy is efficient enough for PGD to allow robust and accurate computations of disperse phase fields: as an illustration, consider the level of accuracy of such strategies in the turbulent case of Figure 4.6 where singularities produced by the PGD modeling are captured with a reasonable mesh. In the case of the AG closure, a second order scheme is developed in Chapter 11. Connecting such polykinetic approaches to PGD and vacuum zones is a remaining issue, introduced and discussed in Boileau et al. (2010): the robust and accurate treatment of interface zones is done by resorting to arbitrary clipping parameters, but this approach is difficult to generalize to the connection of other polykinetic methods with vacuum and PGD zones.

10.2.3 Unstructured meshes

The numerical schemes for transport in physical space on unstructured meshes are more complex to handle and often less accurate compared to those of structured meshes. For instance the order is often limited to three or four for stability and compactness reasons. Moreover, the time approach cannot be improved by ADI techniques.

10.2.3.1 Complex mesh description

The finite difference (FD) approach consists in a direct estimation of derivatives from Taylor expansions: this approach is useful for simple differential operators (e.g. space divergence on structured meshes, which results in a sum of space derivatives) where arbitrarily high order can be reached. In the same favorable geometries, spectral approaches take benefit of the information of the whole domain to estimate the operators, provided that the basis functions (e.g. harmonic) are compatible with the boundary conditions.
For arbitrary geometries, we rather refer to finite volume or finite element techniques. The finite volume (FV) approach consists in storing the average value of the fields on the cell volume (LeVeque 2002). Since

the ensemble of the cells is a partition of the physical space, this method is well adapted for conservativity. Thus FV is often used in CFD e.g. because mass conservation is vital and source terms can be evaluated in an intuitive form. On the one hand the most common formulation, sometimes designated as cell-centered, stores an average value on the cell, which is close to the value at the center of the cell. On the other hand the so-called cell vertex formulation uses the mesh cell as control volume but redistribute the quantities at the nodes for storage and possibly scheme computation. A node centered formulation uses the dual mesh as a control volume and the node for cell-center-like operation. To achieve higher order, in-cell representation can be upgraded with linear or polynomial piecewise representation such as in the celebrated MUSCL approach suggested by Van Leer (1979) and the WENO approach (Shu 1998; Qiu and Shu 2002).
The finite element (FE) approach consists in storing a projection of the field on a set of basis functions, with a non-zero value on compact domains, the elements (cells). Depending on the properties of the basis functions, there are Petrov-Galerkin, Discontinuous Galerkin *etc.* but these methods are not discussed here and a detailed description is provided by Donea and Huerta (2003).

10.2.3.2 Flux integration for genuine multidimensional problems

Multi-dimensional finite volume high order methods often reconstruct a high order value of the variables at the location of the intersection between the face and the segment connecting the cell centers. The total flux through the face is then computed by multiplying the point-wise reconstructed value by the face surface, which can be considered as a first order quadrature.
In multidimensional cases with cartesian meshes, resorting to dimensional splitting allows such a first order space quadrature to achieve a fairly accurate computation of the flux through the face as this flux is quite uniform on the face, unperturbed by transport in other dimensions. But for generic meshes, with complex geometry and without dimensional splitting, the flux may vary strongly on the faces of the mesh. Low order face integrations then introduce errors.
Non-structured approaches rarely resort to high order integration on the faces, inducing a loss in accuracy. This poorly resolved spatial vision is the main source of inaccuracy in unstructured schemes.

10.2.3.3 Cell-centered formulations

We focus on FV approaches with a cell-centered formulation. From the knowledge of average (conserved) quantities on the cell, the local values are reconstructed to compute the numerical fluxes. The reconstructions may introduce an unphysical increase in the so-called variation (Van Leer 1979) which threatens maximum principles, the entropy properties and realizability. So that the reconstructed values are often limited e.g. by a slope limiter in MUSCL schemes.
A natural extension of the FV MUSCL scheme (Van Leer 1979) on generic fully generic, unstructured meshes is used in the CEDRE code for any Mach number flows (Courbet et al. 2011) and it can reach order four (Haider et al. 2011).
The second order version was extended to disperse phase transport (Murrone and Villedieu 2011) by using similar reconstructions, still with a cautious reconstruction to achieve robustness (Le Touze et al. 2012), and a specific flux scheme, but with standard slope limiter functions. The difference between first and second order transport of the disperse phase in CEDRE is illustrated in a 2D case in Figure 10.3. The ability of the CEDRE code to deal with multi-physics problems is detailed in Errera et al. (2011). Still, this scheme achieves poor space time representation due to the geometric complexity of unstructured meshes. Higher order formulations are under developments (Haider et al. 2011) with promising results as regards accuracy, robustness and HPC compliancy thanks to the good compactness of the formulation.
Inspired by the situation for structured meshes, a kinetic scheme was developed for PGD on unstructured meshes (and possibly ALE formalism) in Kah et al. (2012) and extended to two-way coupling cases by Emre (2013); Kah et al. (2013). It has all the desirable realizability properties and achieves a second order integration of the fluxes, while relying on a constant state Runge-Kutta time integration. But it has a reduced accuracy compared to structured grid schemes, though it is still second order in space and time.

10.2.3.4 Cell-vertex formulations

Classical centered schemes, either finite volume or finite element, require artificial diffusion to stabilize the computation. The case of cell-vertex formulations is interesting since it has been explored in industrial codes to achieve high order schemes.
For instance, the AVBP code is an unstructured solver (Moureau et al. 2005; Gourdain et al. 2009) based on low-dissipation centered schemes, third-order in space and time and belonging to the Two-step Taylor Galerkin (TTG) family (Colin and Rudgyard 2000; Lamarque 2007). The AVBP code features an approach for turbulent disperse phase flows the Mesoscopic Eulerian Formalism or MEF (see § 3.6.1.2), which is solved using one of the two following numerical schemes:

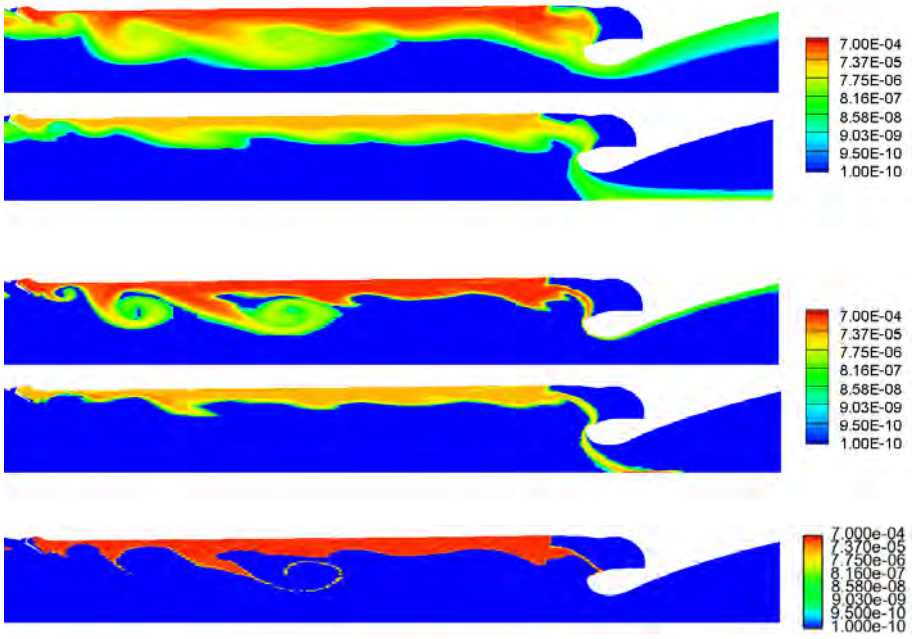

Figure 10.3: *Volume fractions of alumina particles in a SRM– Top: small and medium particles with first order transport scheme; Middle: small and medium particles with second order transport scheme; Bottom: both sizes with stochastic-Lagrangian.*

- Positive Streamwise Invariant (PSI) which is very dissipative,
- Two-step Taylor Galerkin Colin (TTGC) which is accurate but requires the use of artificial viscosity.

The TTG schemes are indeed unstable and always require artificial viscosity. The latter is applied in two steps (CERFACS 2011):

- Target zones of under-resolved gradients are first detected using one of Jameson et al. (1981)'s or Colin (2000)'s sensor,
- Operators are then applied to the targeted zones with a combination of a "shock capturing" term, based on a 2^{nd} order diffusion operator, and a "background dissipation" term, based on a 4^{th} order diffusion term or bilaplacian.

Due to its singular behavior, the disperse phase is resolved with a specific stabilization method (Martinez 2009), adapted from Colin (2000) but applying on specific variables with a tuned sensor. This approach, based on very accurate, unstable schemes, stabilized with artificial viscosity is not optimal for at least two reasons:

- it requires to tune several parameters, making the computations difficult to understand, describe and reproduce.
- it does not prevent the occurrence of realizability failures (negative densities, high velocity oscillations *etc.*), the computation ending up with an unphysical though converged solution.

The latter issue is remarkably sensitive for instability assessment, where hysteresis phenomenon may be triggered unwillingly.

Regarding parallel performance, the AVBP solver is a highly efficient massively parallel CFD solver (Gourdain et al. 2009) It has been validated for a large range of applications (Selle et al. 2004; Vermorel et al. 2007; Lacaze et al. 2009). In the case of disperse phase flows, the strategy has allowed industrial computations in a one-way coupling context: in a monodisperse case (Boileau et al. 2008) as well as in polydisperse cases (Vié 2010; Vié et al. 2013), the latter being illustrated in Figure 10.4. The limits of the stabilized procedure for a hypercompressible disperse phase have been discussed recently as regards numerical diffusion and segregation (Vié 2010; Dombard 2011; Sierra Sanchez 2012): overdissipation can become sensible on particle statistics such as segregation.

10.2.3.5 ALE formalism for moving meshes

The Arbitrary Lagrangian-Eulerian formalism (ALE) has been developed to account for moving and deforming meshes (Donea et al. 2004).

It is implemented in the IFP-C3D code developed at IFP (Bohbot et al. 2009) to describe Diesel injection in engines where the piston can move and strongly compress the chamber volume. A Eulerian approach for disperse phase flows is implemented in IFP-C3D, namely the EMSM (Kah 2010) (which deals with 4 size moments).

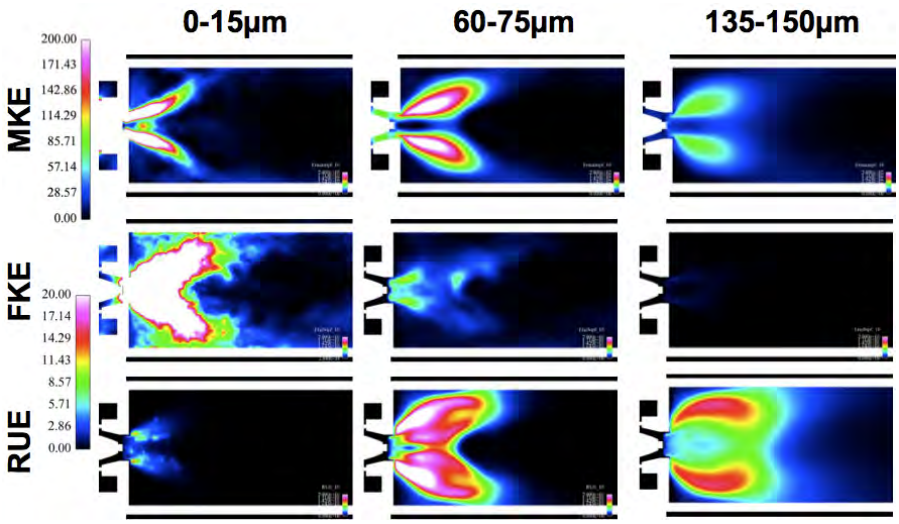

Figure 10.4: *Disperse phase size-conditioned energies in the MERCATO semi-industrial burner – Eulerian computation with the polydisperse MEF, evaporation and combustion with the AVBP code (Vié 2010).*

A transport scheme developed in Kah et al. (2013) achieves the disperse phase transport at second order in space and time on unstructured, moving meshes, with a satisfactory preservation of realizability. The code also bears two-way coupling. This proves the validity of Eulerian approaches in the ALE formalism.

10.2.3.6 Stability for transport in physical space

The matter of stability of a scheme becomes sensitive when it comes to strongly heterogeneous fields e.g. for hypercompressible flows. Most high order methods hardly deal with steep gradients. Stabilization techniques are then used and result in a locally reduced accuracy: they either lower the order or the constant of the scheme convergence to achieve stability.
If low order schemes are disregarded as they generate too much numerical dissipation, the main issue of a high order scheme is linked to numerical dispersion: overshoots and undershoots can appear, the latter being deadly, close to vacuum zones featured by HGD.

10.2.4 Conclusion on strategies for transport in physical space

The issue of the physical space transport of a disperse phase requires a fine-tuned strategy considering the peculiarities of hypercompressibility: the treatment of singularities in an accurate and robust way is crucial. Strategies for structured and unstructured meshes have been reviewed.
On structured grids, the case of PGD is treated (de Chaisemartin 2009) but other cases have not been studied such as AG. The general orientation of accurate and robust kinetic schemes of order two is however efficient for hypercompressible problems with strong realizability constraints. Efforts are then oriented towards advanced strategies implying adaptive mesh techniques: Automatic Mesh Refinement techniques, initially introduced by Berger and Oliger (1984) and Multi-Resolution (Mallat 1989) are an active topic (Duarte et al. 2012).
On unstructured meshes, two strategies are explored in industrial codes, namely MUSCL-type FV in CEDRE (Le Touze et al. 2012) and stabilized high order cell-vertex in AVBP (Martinez 2009). In FV approaches, the reconstruction may introduce an unphysical increase in the so-called variation (Van Leer 1979) so that the reconstructed values are often limited e.g. by a slope limiter in MUSCL schemes. In centered schemes, artificial viscosity is used to damp the high frequency artifacts (wiggles and oscillations). The peculiarities of HGD require dedicated methods which are often very dissipative and reduce the accuracy on mass accumulations e.g. their characteristic sizes and concentration ratio. The principle of such stabilization methods is to add an amount of artificial dissipation that is lower (together with the scheme's numerical dissipation) than the physical dissipation present in the original system (Gourdain et al. 2009). Of course in hypercompressible systems, the pressure and strain terms play the role of physical dissipation but they are weak, as highlighted previously. So methods are difficult to properly stabilize i.e. without compromising the physics.
The need for advanced methods is strong and other paths are evaluated for HGD (as well as for GD). The potential advances on unstructured meshes are an interesting example: residual distributed scheme (RDS) formulations have been studied for GD (Larat 2009; Abgrall et al. 2011), while for the simulation of PGD, a Discontinuous Galerkin (DG) formulation was introduced by Larat et al. (2012), based on recent works

(Zhang and Shu 2010; Zhang et al. 2012). This example seems to be the first high order, high accuracy scheme to simulate PGD properly on unstructured grids and work is going on (Sabat et al. 2013; Sabat 2015): the DG strategy is promising for HPC thanks to its accuracy and compactness.

10.3 Time strategy for multi-physics problems

We discuss the issues and existing strategies to perform a time integration of dynamical and evolutive problems with a complex phase space and many strong couplings.
The stiffness of the system is characterized at first. The choice of a time strategy has a strong impact on the level of detail and the scales that the method can capture; the time strategy moreover conditions the numerical methods for physical and phase space. Two time-integration strategies are then retained and presented, either a fully coupled or an operator splitting strategy.
So the time integration strategy must be chosen consistently:

- to the desired physics (to properly resolve the entire spectrum of scales responsible for the main physical phenomena), and
- to the underlying effective physics (as stiffness threatens accuracy and robustness).

In the context of our choice and in addition to allowing an efficient coupling between the physical and phase space dynamics, the time strategy needs to be adapted to the existing code and to HPC requirements.

10.3.1 General aspects of stiffness of polydisperse moderately dense two-phase flows

The physics of two-phase flows is complex and multi-scale. Physical and phase space dynamics are considered (through transport, drag, heat transfer, coalescence which experience a large spectrum of time scales) and the related stiffness, as defined physically in Curtiss and Hirschfelder (1952) and mathematically in Hairer and Wanner (1996), must be accounted for when designing the numerical strategy.

10.3.1.1 Stiffness of phase space dynamics

The most important source of stiffness in a disperse two-phase flow is polydispersity: it introduces multiple time scales, often varying with the square of the particle radius. This aspect is detailed in the case of the Multi-Fluid model for transport in § 10.3.2 and also as regards phase space coupling in § 10.3.2.5. Let us highlight that the Multi-Fluid method is derived in a suitable way as regards size stiffness since all the phase space variables are conditioned by size and the particles are gathered in sections of small size spanning.
Two-way coupling is also an issue provided the wide range of densities and the multi-scale structure of the flow. Some areas of the problem feature very high source terms with a wide diversity of time scales: evaporation, reaction, combustion, coalescence, break-up *etc.* Moreover the associated closures are often non-linear, which complicates the analysis and makes the integration strategies versus phase space and time even more sensitive to stiffness. In this context, the strong couplings are also considered as non-linearities by themselves due to the existence of feedback mechanisms between the disperse and carrier phases.
Capturing this stiff dynamics requires nonetheless to have a fine tuned time strategy but also to compute accurately the two-way coupled source terms for the disperse phase, possibly treated as several fluids, and for the gas.
To the authors' knowledge, the literature does not mention these numerical specificities for moderately dense sprays. For instance in the context of monokinetic closures, the numerical peculiarities of PGD can bring in unphysical singularities (see § 4.3.2.2): in a two-way coupling context, these singularities would generate a singular retrocoupling towards the gas -or an arbitrarily strong retrocoupling in a spatially discretized context- as highlighted in Doisneau et al. (2013). This requires at least robust schemes if the impact of the singularities remains limited, whereas additional modeling is needed if the two-way coupling is significant in such zones. This is highlighted in § 15.2, where a SRM nozzle generates crossings and δ-shocks on the axis of the nozzle. Though this accumulation is due to incorrect modeling of droplet crossing in many cases, it can still occur for specific particle inertia. The nozzle two-phase losses are presumably very different, with the existence of particle concentrated packets compared to the case of a homogeneous mist.

10.3.1.2 Stiffness of physical space transport

From the multi-scale nature of the disperse phase, the transport in physical space is also stiff. The moments are indeed transported with many time scales due to the presence of various velocities and the latter change very fast due to the stiffness in phase space previously described (arising from stiff source terms and strong couplings). In the same time, the gas encounters sudden variations as the stiff source terms exert a strong

retrocoupling in the case of moderately dense sprays. The physical space transport is therefore a problem with multiple time scales, which is *a priori* coupled to the phase space dynamics.

10.3.1.3 First conclusions

The resolution of a polydisperse moderately dense two-phase flow is a fully coupled problem with many space and time scales. So the overall modeling and time strategy must be carefully designed: we now consider the particular case of a Multi-Fluid approach, where the fact that the variables are conditioned by size allows a hierarchy in time resolution.

10.3.2 Stiffness of dynamics in MF systems

As a starting point, the kinetic level describes a continuous range of scales for all the phase space variables, with a fully detailed description of the couplings. There are no *a priori* assumptions of dominant dependencies.

10.3.2.1 Effect of size-conditioning and size discretization

Thanks to size-conditioning, the semi-kinetic system has a continuous range of time scales for convection through $\boldsymbol{u}(S)$ and for relaxation through $\tau^{\boldsymbol{u}}(S)$ and $\tau^T(S)$, controlled by size $S \in \mathbb{R}^+$. Stiffness is then linked to these scales but also to the effective particle densities that are related and to the local gas dynamics.
In the MF approach, sizes are discretized so that velocities, temperatures and time scales are average for a group of droplets in the size interval. The discrete spectrum still spans a large range of times scales so the system remains stiff. Yet we highlight the fact that discretization gathers the scales of the smallest and biggest droplets into the first and last sections respectively. This narrows the time scale spectrum. The level of size discretization that is required to capture the physics, and the treatment of stiffness are discussed in § 7.1.3.3. Finally, the stiffness of MF methods as regards gas coupling is qualified at first by the range of $\tau_1^{\boldsymbol{u}}$ (τ_1^T) to $\tau_{N_{\text{sec}}}^{\boldsymbol{u}}$ ($\tau_{N_{\text{sec}}}^T$).

10.3.2.2 Time scales for convection and sources

An overview of two-phase flow spatial discretization for resolution purposes is provided in § 10.2. Once a space discretization is chosen, in relation with hypercompressibility and the accumulation characteristic lengths, a time scale appears for the gas, that in return conditions stability and accuracy of the numerical methods. The most relevant scale for the gas, noted τ_g, is defined as the time required for the fastest perturbation to cross the length of a mesh cell Δx:

$$\tau_g = \frac{\Delta x}{c_0 + \mid \boldsymbol{u}_g \mid}.$$

This characteristic time is compared to the integration time step to build the CFL stability criterion, crucial for most numerical transport schemes. But it also has a physical meaning: the gas variables in a cell -which are coupled in a compressible approach- cannot change faster than τ_g, if the fields are smooth and when neglecting the effect of source terms.
A convective time scale can be defined similarly for each section, based on the average particle velocity $\boldsymbol{u}_k$:

$$\overline{\tau}_k^c = \frac{\Delta x}{\mid \boldsymbol{u}_k \mid}. \tag{10.1}$$

This time scale only drives the particle convection and is often much bigger than τ_g. It is also the basis of the stability/accuracy criterion of the particle transport scheme. In the following, we will use $\overline{\tau}_k^c$ to refer to the convection scale of the section with the highest velocity, which will be the most problematic, keeping in mind that all these scales are generally slower than the gas scale τ_g, except for supersonic flows.

10.3.2.3 Local scales

Each section has also a dynamic and a thermal relaxation time, which come from the drag and heat transfer laws. These times noted $\overline{\tau}_k^u$ and $\overline{\tau}_k^T$ are generally close so we consider the smaller time as the reference time scale of a section $\overline{\tau}_k$:

$$\overline{\tau}_k = \min\{\overline{\tau}_k^u, \overline{\tau}_k^T\}.$$

It is useful to distinguish droplets on their ability to react to acoustic disturbances so we call:

- **slow particles** those which relax slower than the gas varies in a cell ($\overline{\tau}_k > \tau_g$);
- **fast particles** those which relax faster than the gas varies in a cell ($\overline{\tau}_k < \tau_g$).

For other applications, modeling particle-particle interactions, evaporation, etc. yield additional time scales. The example of growth times due to coalescence is given in § 7.2. They also add coupling links between the sections: collisions lead to momentum transfer, evaporation, coalescence or break-up lead to mass, momentum and heat transfer, etc. but these phenomena are not considered here.

10.3.2.4 Coupling and scales

In System (4.70), the conservation equations of all the phases are coupled through the gas phase. This is schematically summed up in Figure 10.5.

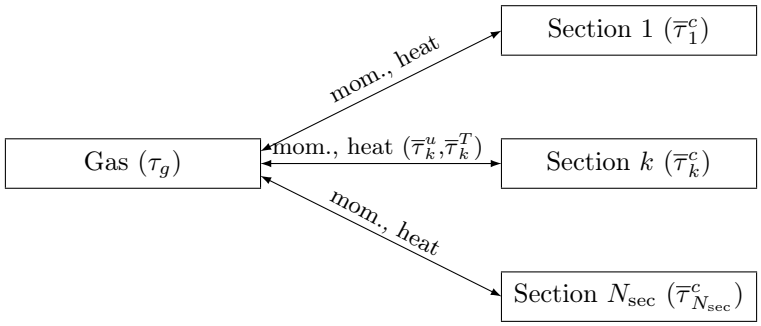

Figure 10.5: *Gas and Multi-Fluid equation coupling and time scales – Case without size phase space sources for the disperse phase.*

So the problem features $3N_{\text{sec}} + 1$ time scales and is tightly coupled. This requires a careful strategy to render the two-phase physics. For polydisperse sprays, we define the minimum relaxation time scale:

$$\tau_{\min} = \min\{\overline{\tau}_k\}$$

so that only $N_{\text{sec}} + 2$ time scales are relevant to characterize the coupling stiffness: the gaseous and liquid convection scales τ_g and $\overline{\tau}_k^c$ and the relaxation scale $\tau_{\min}$.
The evolution of all these time scales depending on droplet size is given in Figure 12.1 for typical SRM. In these cases, meshes are defined with nozzle cell sizes that typically yield $\tau_g > 10^{-6}$s. With classical alumina loadings, $\tau_{\min}$ generally remains above τ_g but it becomes troublesome for loadings of micronic droplets and falls below 10^{-8}s for propellants with nano-aluminum loadings. To sum up, stiffness emerges from the fast scales that lie in acoustics with τ_g, and in polydispersity with $\tau_{\min}$.
The coupling study for Multi-Fluid systems is furthered as regards phase space source terms in § 12.5.

10.3.2.5 Source-induced couplings among the fluids

The study on the stiffness of Multi-Fluid systems as regards coupled transport and coupling sources conducted previously is furthered to show how the phase space source terms induce coupling among the sections.
The size phase space terms can be either due to:

- evaporation which results in fluxes, coupling sections as shown in Figure 10.6,
- coalescence which results in sources, coupling sections as shown in Figure 10.7,
- break-up which results in sources, coupling sections as shown in Figure 10.7.

These new couplings are performed by operators which are local in space so that the ACS strategy can *a priori* be used. The only remaining concern is the position of the characteristic times compared to Δt_{c} and Δt_{a} and the existence, or not, of rapidly attracting equilibrium sub-manifolds.

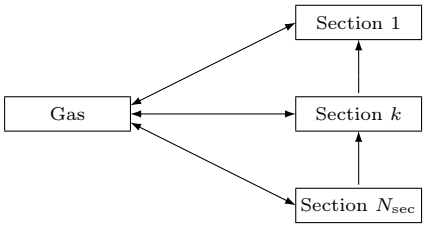

Figure 10.6: *Gas and Multi-Fluid equation couplings – Case with evaporation.*

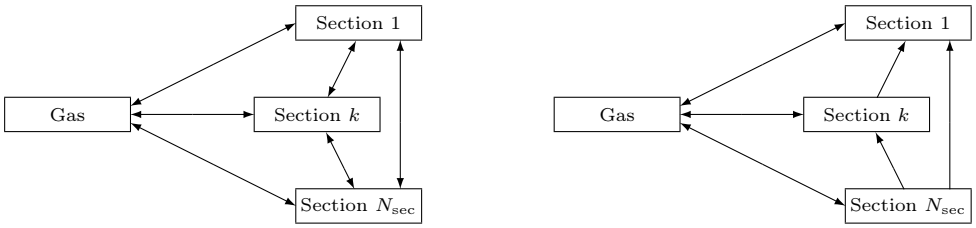

Figure 10.7: *Gas and Multi-Fluid equation couplings – Left: Case with coalescence; Right: Case with break-up.*

10.3.2.6 Conclusion on stiffness in MF systems

The previous study shows how the Multi-Fluid approach for a two-way coupled system yields a coupled problem and what structure it has.
In addition to that introduced by the mass accumulations in physical space (see § 10.2.1.1), stiffness arises:

- from the presence of sections with very different time scales, coupled to a gas with its own scales;
- from the interactions among these sections due to phase space sources.

This is revealing of the general multi-scale nature of the system, and is complimentary to the multi-scale space structures. The situation of stiffness due to various coupling time scales also requires a cautious treatment and we now review some existing strategies.

10.3.3 Time strategy based on an integration at once

The first approach that achieves two-way coupling is a simultaneous time integration of the liquid and gas operators, space fluxes being considered as time dependent source terms.

10.3.3.1 Time integration methods

Hundsdorfer and Verwer (2007) offer a general view of time integration for multi-scale PDEs. The usual time stepping techniques are either explicit or implicit and are very often based on Runge-Kutta integrators (Butcher 1987). Implicit integration achieves a better stability and allows to smear out some undesired transient phenomena, this at the cost of a non-linear algebra resulting in the inversion of large dimensional systems.

10.3.3.2 Explicit strategy

When using explicit time integrations, the time step must be smaller than the smallest characteristic time. The two-phase system is stiff, as said in § 10.3.2, so that there are several orders of magnitude between this small scale and the biggest scales leading to a high cost of this approach.
However this approach introduces little error on the physics, and especially the couplings are all preserved, so that this technique is preferred, for highly coupled, complex problems (see for instance Billet et al. 2008) or when the entire dynamics of an unsteady problem is sought, e.g. when the whole spectrum of scales is affecting the overall phenomenon.

10.3.3.3 Implicit strategies

An overall implicit approach can improve stability at higher time steps, and so reduce the cost needed to reach a given final time. Implicit strategies are often used in the case of single-phase flows for instance to find a steady state or to get rid of fast dynamics such as acoustics: such a strategy works even for unstructured meshes (Selva 1998). The numerical task is then harsh to achieve an all-at-once implicit integration of two-phase flow systems because the number of variables and their cross-dependencies increase the scheme's complexity.
Moreover the physics of coupling may not be rendered properly. For unsteady phenomena, with numerous time scales e.g. due to the intrinsically multi-scale nature of the problem, the fast scales are usually unresolved or one has to rely on adaptive time stepping which will be most of the time too costly.
In stiff context, IMEX strategies have been developed (Sommeijer et al. 1997; Verwer and Sommeijer 2004; Hundsdorfer and Ruuth 2007) and adapted to reactive flows (Najm et al. 1998) to integrate some scales explicitly and others implicitly, the latter scales having a neglected impact on the accuracy of the studied physics (see a review in Duarte 2011). These strategies are interesting since they solve the stiffness issue in an accurate way. But their implementation requires a complete reworking of the code and the implicitation of a part of the operators may impose a large memory occupancy and intense CPU work and communications during the computations.

10.3.3.4 Conclusion

We have discussed the motivations for using explicit or implicit time stepping and it has been stated that a multi-scale system requires both. To achieve this, IMEX strategies are accurate but they are not chosen for liability and HPC reasons. We therefore resort to a strategy based on operator splitting techniques, which we present below, and which allows to mix the qualities of explicit and implicit integration methods in a flexible way: the existing codes can be used, the partial implicitation can be performed on smaller operators and therefore at reasonable effort, algebra, memory and cost, and the overall accuracy can be easily controlled.
In addition to the matter of using explicit, implicit or mixed techniques, some advanced techniques need sometimes to be considered. Adaptive time stepping has been studied, when coupled to splitting techniques, by Duarte et al. (2012) for cases where the dynamics introduces varying and unknown scales, e.g. for reactive waves, autoignition problems *etc.* Asymptotic preserving methods (Carrillo et al. 2008; Vié et al. 2013) are needed when the system features a mixed mathematical behavior e.g. turbulent dispersion and Brownian diffusion at $\mathrm{St} \to 0$, resulting in a diffusive limit. In our case, these approaches are not mandatory.

10.3.4 Time strategy based on an splitting techniques

Operator splitting techniques consist in separating the time integration of different operators and to integrate them separately and successively. Such approaches establish a separate vision of the different physical parts of the system, conditioned by time, so that time integration can be performed in an adapted way for each specific operator.
Such methods have been extensively discussed by Duarte (2011) as a convenient approach for the resolution of multi-scale PDEs, under the condition that the splitting structure and time steps are well chosen.

10.3.4.1 Principles of operator splitting

Operator splitting has been theorized in the context of systems of linear differential equations. We briefly present the aspects of splitting theory, more details can be found in Duarte (2011).
Let us consider a general linear initial value problem:

$$\begin{cases} \partial_t \boldsymbol{U} = \mathrm{A}\boldsymbol{U} + \mathrm{B}\boldsymbol{U}, \quad t > 0 \\ \boldsymbol{U}(0) = \boldsymbol{U}_0 \end{cases} \tag{10.2}$$

with linear operators $\mathrm{A}, \mathrm{B} \in \mathcal{M}_m(\mathbb{R})$ where $\mathcal{M}_m(\mathbb{R})$ is the set of real square matrices of size m, $\boldsymbol{U}_0 \in \mathbb{R}^m$ and $\boldsymbol{U} : \mathbb{R} \to \mathbb{R}^m$, for which the exact solution is given by

$$\boldsymbol{U}(t) = \mathrm{e}^{t(\mathrm{A}+\mathrm{B})}\boldsymbol{U}_0, \quad t \geq 0. \tag{10.3}$$

A time operator splitting technique consists in successively solving the evolutionary problems associated with each time operator in an independent way. For System (10.2) this amounts to separately solve problems:

$$\partial_t \boldsymbol{U} = \mathrm{A}\boldsymbol{U}, \quad t > 0 \tag{10.4}$$

and

$$\partial_t \boldsymbol{U} = \mathrm{B}\boldsymbol{U}, \quad t > 0 \tag{10.5}$$

with appropriate initial conditions for each subproblem. Then, for a time discretization given by $t_0 = 0 < t_1 < \cdots < t_N$, the associated time steps or splitting time steps are defined as $\Delta t_n = t_{n+1} - t_n$ for $n = 0, 1, \ldots, N-1$.
Starting from the initial condition of System (10.2): $\boldsymbol{U}_0 = \boldsymbol{U}(0)$, the splitting numerical approximation U_{n+1} of the exact values $\boldsymbol{U}(t_{n+1})$ is computed from the previous $\boldsymbol{U}_n$ for $n = 0, 1, \ldots, N-1$, by means of a composition of $s \geq 1$ independent solutions of Eq. (10.4) and Eq. (10.5) with the recurrence relation:

$$\boldsymbol{U}_{n+1} = \mathrm{e}^{\beta_s \Delta t_n \mathrm{B}} \mathrm{e}^{\alpha_s \Delta t_n \mathrm{A}} \ldots \mathrm{e}^{\beta_1 \Delta t_1 \mathrm{B}} \mathrm{e}^{\alpha_1 \Delta t_1 \mathrm{A}} \boldsymbol{U}_n \tag{10.6}$$

where $\mathrm{e}^{\Delta t \mathrm{A}}\boldsymbol{U}_0$ and $\mathrm{e}^{\Delta t \mathrm{B}}\boldsymbol{U}_0$ are respectively the exact solutions of Eq. (10.4) and Eq. (10.5) for $t \geq 0$ from initial condition $\boldsymbol{U}_0$. The values of the real or complex coefficients of the scheme: $(\alpha_i, \beta_i)_{i=1}^s$ such that $\sum_{i=1}^s \alpha_i = \sum_{i=1}^s \beta_i = 1$ will then define the order of approximation of the method. These splitting schemes can be seen as composition methods for which the general order conditions are well known (see Hairer et al. (2006)).
Let us describe the Baker-Campbell-Hausdorff (BCH) formula on composition of exponentials. For the linear operators A and B, for which their exponentials $\mathrm{e}^{t\mathrm{A}}$ and $\mathrm{e}^{t\mathrm{B}}$ can be understood as a formal series expansion i.e. $\mathrm{e}^{t\mathrm{A}} = \sum_{i \geq 0}^{+\infty} \frac{t^n}{n!} \mathrm{A}^n$, we define the commutator:

$$[\mathrm{A}; \mathrm{B}] = \mathrm{AB} - \mathrm{BA}. \tag{10.7}$$

The main idea is then to find $\mathrm{C}(t)$ such that we can write:

$$\mathrm{e}^{t\mathrm{A}}\mathrm{e}^{t\mathrm{B}} = \mathrm{e}^{t\mathrm{C}(t)} \tag{10.8}$$

This exponential representation is known as the BCH formula. For t small, we have also:

$$\mathrm{C}(t) = t\mathrm{C}_1 + t^2\mathrm{C}_2 + t^3\mathrm{C}_3 + t^4\mathrm{C}_4 + \dots \tag{10.9}$$

The first order splitting, also referred to as Lie splitting, is achieved according to two ways:

$$\boldsymbol{U}^{\mathrm{Lie1}}(t+\Delta t) = \mathrm{e}^{\mathrm{B}\Delta t}\mathrm{e}^{\mathrm{A}\Delta t}\boldsymbol{U}(t) \tag{10.10}$$

or

$$\boldsymbol{U}^{\mathrm{Lie2}}(t+\Delta t) = \mathrm{e}^{\mathrm{A}\Delta t}\mathrm{e}^{\mathrm{B}\Delta t}\boldsymbol{U}(t) \tag{10.11}$$

The first order splittings yield an error, assessed from the BCH formula:

$$\boldsymbol{U}(t+\Delta t) - \boldsymbol{U}^{\mathrm{Lie1}}(t+\Delta t) = -\frac{\Delta t^2}{2}\left\{\mathrm{AB} - \mathrm{BA}\right\}\boldsymbol{U}(t) + \mathscr{O}(\Delta t^3) \tag{10.12}$$

so the local error is therefore of second order so that the global error of the method in first order.
The second order splitting, also referred to as Strang splitting, can be done according to two ways (Strang 1968):

$$\boldsymbol{U}^{\mathrm{Strang1}}(t+\Delta t) = \mathrm{e}^{\frac{1}{2}\mathrm{A}\Delta t}\mathrm{e}^{\mathrm{B}\Delta t}\mathrm{e}^{\frac{1}{2}\mathrm{A}\Delta t}\boldsymbol{U}(t) \tag{10.13}$$

or

$$\boldsymbol{U}^{\mathrm{Strang2}}(t+\Delta t) = \mathrm{e}^{\frac{1}{2}\mathrm{B}\Delta t}\mathrm{e}^{\mathrm{A}\Delta t}\mathrm{e}^{\frac{1}{2}\mathrm{B}\Delta t}\boldsymbol{U}(t). \tag{10.14}$$

The second order splittings yield an error but at third order:

$$\boldsymbol{U}(t+\Delta t) - \boldsymbol{U}^{\mathrm{Strang1}}(t+\Delta t) = \frac{\Delta t^3}{24}\left[\mathrm{A};\left[\mathrm{A};\mathrm{B}\right]\right]\boldsymbol{U}(t) - \frac{\Delta t^3}{12}\left[\mathrm{B};\left[\mathrm{B};\mathrm{A}\right]\right]\boldsymbol{U}(t) + \mathscr{O}(\Delta t^4) \tag{10.15}$$

so that the method is globally of second order. If each operator is solved with a numerical strategy that is at least second order in time, the suggested Strang splitting (Strang 1968) ensures a second order convergence with Δt as long as the solution is regular and the time step is smaller than all the physical scales (Descombes and Massot 2004).

10.3.4.2 Practical application

In practical cases, the fastest scales are not always part of the dynamics of interest of the problem: when an equilibrium sub-manifold exists -e.g. the velocities and temperatures equating that of the gas, as discussed in § 4.7.4.2- the timescale describing the relaxation towards it may not be relevant, especially for very small droplets which relax fast.
The choice and order of operators in a splitting technique is linked to the existence of such equilibrium sub-manifold in some operators: the output solution should respect such equilibrium sub-manifolds at best so that the corresponding operators shall be performed at the end, as suggested in a study by Descombes and Massot (2004).
If explicit methods require a time step below the fastest phenomenon to achieve stability, implicit methods require a complex algebra to evaluate the full Jacobian of the system and to invert it (Selva 1998).
The overall time integration must meet various requirements linked to the discretization of the operators: the time integration should be performed at the same order than space discretization to achieve time consistency (Allaire 2005; Duarte 2011) and high order space schemes often need high order time integration for stability reasons e.g. WENO schemes (Wang and Spiteri 2008). The phase transport operators must achieve positivity on density, maximum principle on velocity and temperature etc.
Operator splitting techniques can be used for unsteady problems with multiple time scales. The principle of splitting techniques is to define operators in a system of equations and to integrate them consecutively. The benefit is twofold compared to an all-at-once integration. First, the numerical methods used for one operator can meet their theoretical specifications (stability, positivity, maximum principle etc.).
Second, time steps that are internal to each numerical operator are subjected to the only numerical stability conditions of their respective numerical schemes. The major drawback is that the splitting time step Δt has to be chosen specifically for the configuration that is solved, in order to control the splitting error (Duarte

2011). This overall time step has to be based on physical time scales of the coupling phenomena. Splitting the operators often yields pure convection, diffusion, relaxation (or reaction) problems. The first ones can be integrated classically with an order-compliant method and the CFL requirements apply. The relaxations are due to sources and are mostly local problems (except for radiation); they are possibly stiff e.g. for small droplets.
Third, as regards liability, splitting techniques are considered as a more flexible approach to keep the existing solvers while they still allow to achieve a robust resolution with a controlled accuracy on the strong couplings. So splitting techniques are good candidates to fulfill the accuracy, realizability and flexibility under liability and HPC requirements.

10.3.4.3 The Balanced Weak Coupling: a classical but limited approach

We now consider an approach that is based on operator splitting: it is classical but not efficient for two-way coupling. Its critical analysis is a basis for the development of a strategy in Chapter 12.
A convenient technique for small mass loadings of particles is here referred to as the Balanced Weak Coupling (BWC). On a time step Δt_{BWC}, it consists in computing the particle phase alone, assuming that the gas is frozen as in one way coupling approaches. Source terms are then reinjected in the gas equations to ensure total momentum and energy conservation on the time step. In this sense, the technique can be considered as a splitting technique with modified source terms. The key parameter of this technique is the ratio of the integration time step to the particle relaxation time $\tau_{\min}$:

$$K_{\mathrm{BWC}} = \frac{\Delta t_{\mathrm{BWC}}}{\tau_{\min}} \tag{10.16}$$

which drives the quality of the coupling.
For 0D cases, this method ensures correct convergence to the equilibrium values whatever K_{BWC} as shown in Figure 10.8. For small mass loadings C, the frozen gas hypothesis is correct on all time steps as shown on the top left graph in Figure 10.8 because particles little perturb the gas so $\boldsymbol{u}_g$ and $\boldsymbol{u}_{eq}$ are close. But when one increases the mass loading (bottom left) or increases the time step above the relaxation time ($K_{\mathrm{BWC}} = 2$, top right), the error on the transient values becomes significant. Finally, large oscillations can appear for high mass loadings and long time steps as shown in the bottom right graph. The BWC technique encounters accuracy problems for $K_{\mathrm{BWC}} > 1$.

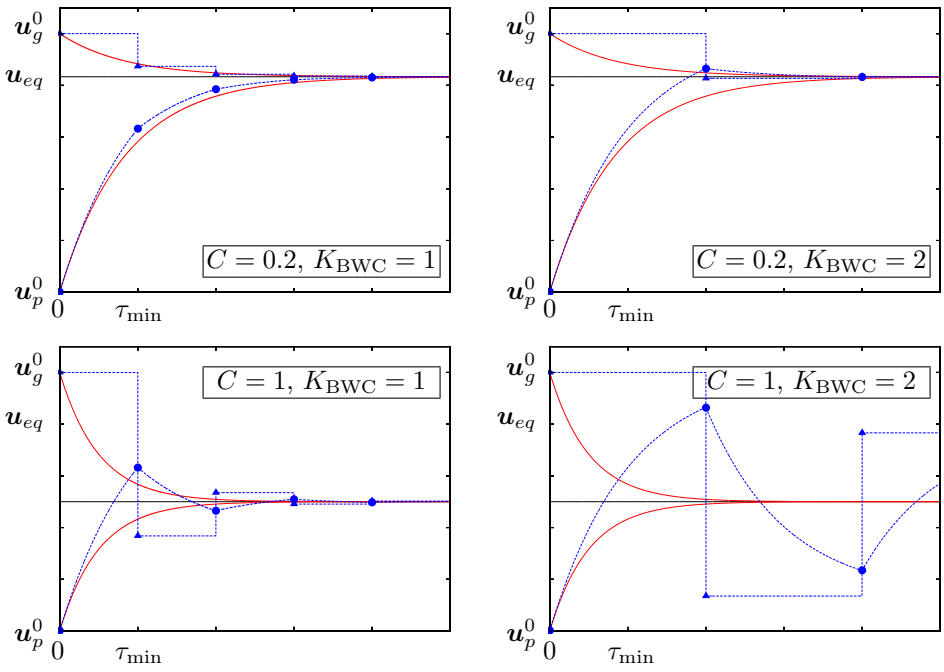

Figure 10.8: *BWC computation of a 0D gas-particle relaxation case for different mass loadings and different K_{BWC} – Δ: gas; ∘: particles; Line: exact solution for each phase.*

The 0D study illustrated in Figure 10.8 shows that BWC oscillates and converges difficultly for high mass loading 0D cases. Moreover in higher dimension cases, transport in physical space is performed at each time step with the computed transient velocities, which are poorly evaluated. Moreover, high mass loading zones can be created during a computation such as at the edge of vortices so that the BWC is also inaccurate that

are dilute in an average sense as soon as the flow is likely to generate droplet segregation and therefore zones of strong mass loading.
As a conclusion, it is shown that because of stiffness and coupling, a first approach for solving System (4.70) would be to integrate the whole set of equations with a time step shorter than the smallest time scale of the spray. For slow particles, this approach introduces no additional constraints compared to a single-phase case since the fastest time scale is the one of the gas. With an explicit time integration for instance, recommended for unsteady solution determination and parallel computation, the integration time step has anyway to be smaller than τ_g for CFL stability requirement. With an implicit integration, CFL should also remain moderate, for accuracy purpose. But for small droplets, the integration time step can be severely constrained by $\tau_{\min}$ which decreases like the square of the mean droplet diameter in the section. We suggest in the following a numerical strategy where the time step is adapted regarding error criteria to reduce computational cost.

10.3.5 Conclusions on time stepping

In the case of a two-way coupled multi-scale system e.g. a moderately dense polydisperse two-phase flow, for which the unsteady evolution is sought, the time strategy must be carefully assessed. For liability reasons, we focus on the two following usual approaches.
On the one hand, "integration at once" strategies have the following drawbacks:

- they can become costly to overcome stiffness, either with small time steps if explicit or with complex algebra if implicit;
- they may not achieve the requirements of the numerical methods related to the physical and phase space transport parts, namely order and realizability.

On the other hand splitting techniques are flexible as regards cost and algebra requirements and property enforcement but they may deteriorate accuracy, especially on the physics of the coupling.
The flexibility is of paramount importance for multivariate problems with coupled dimensions and also for the practical implementation of complex physics. In splitting methods, accuracy is set by the splitting time step so few parameters are needed. As for liability, the existing code is kept with minimum modifications. The coupling properly achieved as regards the desired physics and the existing stiffness.
Splitting techniques are promising to time-integrate efficiently the complex problem of transport in physical space, of two-way coupling and phase space dynamics but the approach must be well designed. Let us assume that the decoupling between physical space and phase space is done correctly to capture all the levels of coupling. A technique to do so is introduced in Chapter 12. We now focus on the numerical strategy for the description of the phase space dynamics, when decoupled.

10.4 Strategy for evolution in the phase space

The evolution within the phase space is characterized by a complex dynamics and the models are very sensitive to inaccurate methods. The overall time strategy based on splitting has been designed to allow the decoupling of the transport in physical space from the evolution in phase space. So that the evolution in phase space is local in physical space. The time integration strategy of this proper dynamics must still be assessed: advanced time integrators are required to preserve the properties and overcome the phase space stiffness (presented in § 10.3.2). In addition, the terms describing the time evolution in the phase space involve integrals of an underlying NDF which must be reconstructed: quadrature techniques are introduced to compute the phase space terms efficiently. The overall strategy must be carefully designed since realizability issues threaten the robustness of the algorithms.

10.4.1 Peculiarities of the phase space problem with moment methods

Let us introduce the peculiarities of the overall problem of evolution in the phase space.

10.4.1.1 Phase space variables

Compared to a standard fluid, a disperse phase is described by additional parameters for sizes, velocities and temperatures. The phenomena treating their evolution, possibly with couplings among them, are accounted for by terms referred to as operating in the phase space: in two-way coupling contexts, the dynamics in phase space includes the gas variables of density, velocity, temperature, and species concentration. The phase space dynamics features the same peculiarities as that of the physical space, i.e. stiffness, couplings and realizability issues.
We disregard the phase space at the kinetic level and focus on the phase space for the retained Eulerian model: its geometry and the numerical issues depend on the retained method, namely on the chosen moments.

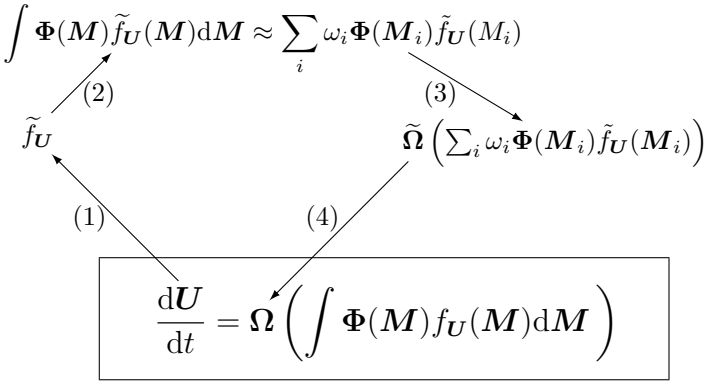

Figure 10.9: *Numerical strategy for the phase space dynamics with a moment method: (1) reconstruction, (2) phase space integration (e.g. through quadratures), (3) source computations to allow (4) the time integration of the system.*

Models and methods for the size variable as well as for the velocity (and temperature) variable have been presented in Chapter 4 as well as the associated moments to be conserved. We have focused our work on Multi-Fluid methods, which can be seen as a numerical approach to discretize the size variable: the TSM method, presented in Chapter 5 is thus a second order approach in size, as demonstrated for evaporation in Laurent (2006), with two size moments per section and several sections. As for the velocity, it is approached either with the monokinetic closure (see § 4.3) or the AG closure (see Chapter 6) which require respectively 3 and 9 velocity moments per section in 3D. The temperature requires 1 additional moment. And the gas introduces some mass fraction quantities (for evaporation and reaction), density, 3 velocities and temperature.

10.4.1.2 Treating the phase space as a local problem

From the original full PDEs, the time strategy has allowed to decouple the evolution in phase space from the space transport. As a major consequence, the result of this strategy is a full compliancy with HPC and particularly parallelization by domain decomposition.
It may seem artificial to decouple the dynamics of the phase space from that of the physical space, since the velocity variable characterizes the transport in physical space while some phase space terms depend on local variables. But the time splitting integration strategies allow to treat them separately, in the limit of a short enough time stepping. In the following, we assume that such decoupling holds and focus on the phase space evolution strategy.

10.4.1.3 Non-linear problem of moment dynamics

Because the evolution in phase space is rendered by source terms (drag, heating, evaporation, coalescence, break-up), the corresponding equations are Ordinary Differential Equations (ODEs), possibly non-linear and coupled on all the variables described previously. For instance, the size-velocity coupling resulting from drag and coalescence has been presented in § 3.1.3.5 and must be captured to assess the SRM dynamics.
Let us note the vector of variables of the phase space $\boldsymbol{U}$ in the context of moment methods, so that the phase space problem reads:

$$\partial_t \boldsymbol{U} = \mathbf{\Omega}. \tag{10.17}$$

The peculiarity of the phase space evolution with moment methods is that the sources $\mathbf{\Omega}$ depend on integral terms of the underlying NDF f, which can only be estimated as $f_{\boldsymbol{U}}$ from the knowledge of the transported moments $\boldsymbol{U}$ (in the context of a moment method), and is finally reconstructed as $\widetilde{f}_{\boldsymbol{U}}$ with a numerical inversion method.
So the problem is complex due to the peculiar need to integrate the sources on a unknown function, which is reconstructed from the variables themselves. This dependency loop is summed up in Figure 10.9 and the strategies for time integration, reconstruction and integral computation are discussed below.

10.4.1.4 Realizability

Realizability issues originate from the fact that the NDF itself must be positive. In addition for moment methods, the admissible moment space is presumably complex (Kah 2010).
The numerical errors of the various approximations may bring the approximated solutions for the moments not to respect the constraints i.e. to be non-realizable. So robustness is difficult to achieve in the context of the complex evolution in phase space and all the previously described numerical approximation steps must be designed carefully:

(1) reconstructing a NDF,
(2) computing the integrals on the phase space,
(3) computing the source terms, and
(4) (discrete) time-stepping in a stiff context,

The realizability issue is very strong when the system spends some time at the edge of the moment space, where the realizability is mostly fragile: this occurs very often e.g. for steep initial distributions (Dirac) or when a section is emptied by evaporation, coalescence, *etc.*
Realizability has been assessed for high order moment methods by Kah (2010) and specific techniques have been designed. For instance, a significant advance in the case of size moments is the introduction of reduced moments, the canonical moments, which belong to a cube, and the expression of numerical methods on these moments to ensure a robust treatment. In the following, we do not need to use such a modified set of moments but we still need to design a strategy for reconstruction, integration and source term computation that is robust, accurate and cost-effective.

10.4.2 Need for dedicated time integration strategies

A major aspect of the dynamics in phase space is that it is strongly coupled and in a non-linear way. To render accurately and robustly the multiple couplings and overcome stiffness, dedicated time integrators are required.

10.4.2.1 Use of stable and accurate integrators for stiff problems

The desired properties for an advance time integrator are:

- A and L stability (Hairer and Wanner 1996),
- adaptive time stepping to ensure that the effects of fast dynamics can be captured, and
- a one-step implementation.

The latter aspect is linked to the overall splitting strategy: multistep methods (e.g. LSODE Hindmarsh 1980) are inaccurate in their first iterations, and this inaccurate situation is encountered, in our splitting strategy, after each coupling of the phase space resolution to the physical transport.
Runge-Kutta techniques can be used if the time steps are small enough, which is efficient in the case of non-stiff phase space dynamics. A one-step strategy referred to as RADAU5 has been developed to ensure all the previous properties in the case of stiff systems and to provide a solution with a fixed accuracy thanks to an adapted time step (Hairer and Wanner 1996): it can be used for complex systems with unknown eigenvalues such as chemical reactions or coalescence. However, facing the impossibility to compute an analytical Jacobian for Ω, implicit strategies resort to numerical estimations of the Jacobian, which efficiency depends on the smoothness of the overall reconstruction/integral computation strategy. In cases where all the eigenvalues are real, explicit integrators such as ROCK4 (Abdulle 2002) can be used such as in the case of discretized diffusion terms, as suggested by Duarte (2011).

10.4.2.2 Conclusion on phase space time-stepping

Again, the choice of a time-stepping technique is particular to the models that are retained to describe polydispersity, polykineticity and the physics of the disperse phase (coalescence, evaporation *etc.*).

10.4.3 Peculiar aspects of reconstruction

The reconstruction step is the evaluation of a NDF $\widetilde{f}_{\boldsymbol{U}}$ from the moments $\boldsymbol{U}$, in order to compute the source terms.
Because of the many constraints of a reconstruction (positivity and unicity), the forms that are used as functions are often non-linear. Moreover, the constraints of the reconstruction problem are of integral type so that the problem is complex. Performing a reconstruction then resorts to an implicit formulation. And because of the large size of the phase space, and of the choice of advanced time-stepping techniques, the reconstruction is to be performed presumably many times so the technique must be efficient.
For instance, in the case of the Exp-TSM method (see § 5.3.2) which is implemented in CEDRE, an iterative inversion technique is performed on integrals which are computed analytically Dufour (2005): this method penalizes the overall efficiency of the approach. In the case of the Aff-TSM method (see § 5.3.3) an iterative inversion is also used but the corresponding function to invert is a polynomial integral, which can be assessed analytically at a low cost, so the overall cost of the iterative method is acceptable. In both case, the iterative method has been chosen for its fast convergence: Ridders' method (Press et al. 1992) is satisfactory.

10.4.4 Computing the integral terms of the phase space

The numerical approximations of the source terms in the ODE system of the phase space are noted:

$$\boldsymbol{\Omega} \approx \tilde{\boldsymbol{\Omega}} \left(\int \boldsymbol{\Phi}(\boldsymbol{M}) \widetilde{f}_{\boldsymbol{U}}(\boldsymbol{M}) \mathrm{d}\boldsymbol{M} \right) \tag{10.18}$$

to recall that they are computed from integrations on the kinetic variables $\boldsymbol{M}$. Their effective numerical computation must be done in accordance with accuracy, stability and cost efficiency requirements to which must be added a compliance with the architecture and the HPC strategy. From the previous choice of an advanced time integrator, the source terms must be computed several times so efficient approaches must be designed.

10.4.4.1 Principles of quadrature techniques for integrals

Source terms are used to describe the discrete evolution as regards the kinetic variables e.g. due to coalescence and break-up, drag and heating, evaporation *etc...* In the context of Multi-Fluid methods, these source terms are computed as integrals of the previously reconstructed NDF on the whole section so the numerical methods that are related mainly resort to integration techniques.
As regards the complexity of such source terms, which may involve variable changes and advanced, non-linear closures with many dependencies, we suggest the use of point-wise integration techniques i.e. techniques that do not require the evaluation of integrals or derivatives.
Composite integrations such as fractional quadratures (i.e. quadratures on sub-intervals) or Romberg's method (Press et al. 1992) achieve integrations with a fixed and arbitrary precision so they can be very accurate. In return, they require the computation of the point-wise function many times. Composite methods are useful when a low level of complexity is needed and can be supplied by a high level of repetition. So they are not efficient as regards cost in the context of advanced time integrators, since the latter require the composite integration to be done many times.
In our context, we suggest the use of quadrature techniques (Abramowitz and Stegun 1964; Gautschi 1996; Zwillinger 2003), which require the evaluation of the function to integrate at given points and few points are needed to achieve a reasonable accuracy. So that quadrature techniques:

- are well-suited for terms with a complex form as they are based on point-wise evaluations;
- fulfill rather the cost requirement as regards the cost/accuracy trade-off, since few points can be used.

As a result, the integral terms become sums, which are formally noted:

$$\int \boldsymbol{\Phi}(\boldsymbol{M}) \widetilde{f}_{\boldsymbol{U}}(\boldsymbol{M}) \mathrm{d}\boldsymbol{M} \approx \sum_i \omega_i \boldsymbol{\Phi}(\boldsymbol{M}_i) \tilde{f}_{\boldsymbol{U}}(M_i). \tag{10.19}$$

Since the practical implementation of quadrature techniques does not depend on the underlying function, the latter can be easily changed in the context of the development of a new physical closure. We highlight however that the accuracy of the quadrature depends on the integrated functions, mainly its smoothness: this issue is practically met for the integration of exponential functions in § 13.1.4.3 and of a norm functions in § 13.3.1. In return, quadrature methods are less accurate than methods which include a partial knowledge of the integrated functions e.g. analytical integrations, but the latter techniques are rarely applicable in practical contexts.
We finally highlight that, in the case of coalescence, the source terms have a complex combinatorial, requiring particularly efficient methods to cope the numerous integrals to compute: their number increases also with N_{sec}^2.

10.4.4.2 Kinetic integration technique

Some phenomena are described at the kinetic level by derivatives of kinetic variables: they correspond to a continuous evolution in the phase space e.g. due to evaporation, condensation or some cases of break-up modeling as a continuous process (see for instance Appendix C).
In the context of Multi-Fluid methods, continuous size terms result in fluxes at the edge of the sections, which require the knowledge of the point-wise value of the size distribution at the edge:

$$\int_{M-}^{M+} \partial_{\boldsymbol{M}} \left(\boldsymbol{\Psi}(\boldsymbol{M}) \widetilde{f}_{\boldsymbol{U}}(\boldsymbol{M}) \right) \mathrm{d}\boldsymbol{M} \approx [\boldsymbol{\Psi} \widetilde{f}_{\boldsymbol{U}}]_{M-}^{M+} \tag{10.20}$$

and more precisely, its integral value on a time step is desired.
From the knowledge of the kinetic dynamics, thanks to a reconstruction of the NDF, such terms can then be computed with a kinetic scheme i.e. from the knowledge of the characteristics in phase space (Dufour and

Villedieu 2005; Laurent 2006): the kinetic scheme then achieves an integration on time and on the phase space variable of interest, at a fixed accuracy.
The kinetic schemes are very sensitive to the type of reconstruction and the order of the method (Massot et al. 2010). They have to be re-designed specifically when new phenomena are to be considered: for instance (Sibra 2014) has designed a specific method for evaporation and condensation in a two-way coupling context.

10.4.4.3 Couplings in phase space: multivariate cases

The case of multivariate functions, possibly non-factorizable, translates the existence of couplings in the phase space: these couplings may require to be treated accurately if they participate to the overall dynamics.
The computation of multiple integrals in the context of quadrature techniques is based on Fubini's theorem: the quadratures are embedded, resulting in a multiple summation which cost increases like the power of the dimensionality. The cost issue occurs for instance for coalescence velocity integrals with the AG method (see § 13.3.1): the integration of a complex non-linear function is to be performed on $\mathbb{R}^6$ so that the quadrature must be chosen under a strict cost constraint.
In the case of multivariate dynamics i.e. with several moments that are coupled together, a direct treatment can be performed by a coupled reconstruction/integration technique and brute force integrations: the evolution of all the moments can be assessed simultaneously to capture strong dynamic couplings as in rare examples on size and velocity Kah et al. (2010). But realizability issues become complex when too many moments are involved and the issue of performing a quadrature that respects all the moments is strong: multivariate quadrature methods can for instance be chosen but they require specific developments, such as CQMOM (Yuan and Fox 2011), for inversion and realizability concerns. So strategies with conditioned variables are preferred for accuracy, robustness and algebra complexity reasons. These methods are dependent on the physics that is treated. For instance for the three velocity components, the CQMOM technique (Yuan and Fox 2011) allows a conditional treatment, that eases the inversion.
So the treatment of a strongly coupled multivariate phase space is possible but requires fine-tuned methods to be accurate, and realizability is a strong issue. The decoupling of phase space variables (as soon as when choosing the moment method) should be done each time it is possible, as regards accuracy, to allow the use of simpler, more robust and cost-effective methods.

10.4.5 Conclusion on numerical strategy for phase space evolution

As a conclusion, the physics of the phase space must be treated, which is an additional feature compared to usual flows, which count at most chemical reactions in the case of multicomponent reactive flows.
Thanks to quadrature techniques and kinetic schemes, phase space terms can be computed accurately as regards their multiple dependencies and integrated with advanced time methods. However, the complex dynamics of the phase space and the variety of methods to describe the phase space information require the numerical methods to be developed in a way that is specific to the modeling approach. To this extent, the robustness of well-chosen ODE integrators and the flexibility of the quadrature techniques are salutary.
The integration of complex, multivariate source terms is a first issue. The sources must be computed with respect to the realizability conditions so the methods must be accurate and specific. The combinatorial resulting from the numerous interactions between all the resulting fluids, and the no less numerous variables of integration require efficient methods: quadrature integrations are satisfactory to treat complex functions and must be carefully extended to multivariate cases. Finally, facing a complex algebra, the new hardware evolutions such as the many core architectures may offer interesting possibilities of computing complex terms.
The general aspects of stiffness and coupling are another issue, which is not developed any further here. But it is highlighted that the phase space terms may condition the time strategy, discussed previously.

10.5 Various codes used in the thesis and their initial status

The numerical strategy for two-way coupling polydisperse two-phase flows is now briefly discussed in the context of some existing codes at the beginning of the present thesis.

10.5.1 Example of a research code strategy: MUSES3D

The MUSES3D code is a generic platform dedicated to the evaluation of Eulerian spray models and methods. It was initiated by de Chaisemartin (2009) and co-developed with L. Fréret and the EM2C Math team. The MUSES3D code has proven the efficiency of Eulerian approaches for a disperse phase as modeled by the PGD de Chaisemartin (2009). It accurately treats hypercompressibility for low to moderate Stokes thanks to work on algorithms in time.

MUSES3D operates on 1D, 2D and 3D structured grids for the simulation of Eulerian disperse phase equations, provided a gas flow field: the code is one-way coupled. Physical transport is solved on structured grids with finite volume schemes: the PGD is captured accurately and at second order thanks to the Bouchut scheme. The code provides the possibility to assess the methods on several configurations:

- Taylor-Green vortices with periodic boundary conditions,
- frozen turbulent field,
- HIT,
- free jet.

As for the time integration strategy, it must be adapted to treat the multiple time-scales of transport in physical space and of phase space dynamics, which are stiff as usual. The strategy chosen for MUSES3D consists in a splitting technique, which is eased by the fact that the code is one-way coupled. This allows the Bouchut transport scheme to operate at CFL ~ 1 to reduce numerical diffusion and the phase space time integration to be performed efficiently as regards realizability.

The MUSES3D code has been written so that its enrichment with new resolution methods, can directly be brought in its structure. This has the advantage of focusing on the sole coding work of the method itself, inheriting the various model frameworks, and the configurations for test cases. The One Size Moment Multi-Fluid method is implemented, as well as higher order methods such as EMSM and CSVM. Multi-velocity methods such as DQMOM are also implemented. The code also proposes various numerical schemes when considering the same model. Whatever the method, no approach for coalescence is implemented in MUSES3D so far.

The Asphodele code is devoted to the simulation of spray combustion. It is developed by J. Reveillon at CORIA (Reveillon and Demoulin 2007b; Reveillon 2007; Thomine 2011). It features a Low-mach solver for the carrier gas phase, a stochastic-Lagrangian (Direct Simulation Monte-Carlo) approach and a Lagrangian DPS approach for the disperse phase. It has been successfully coupled to MUSES3D, allowing detailed cross-validations of Euler-Euler and Euler-Lagrange strategies in a one-way coupling context. The Asphodele code also operates alone. Its DPS solver is used in Chapter 13 to validate the AG strategy for coalescence: the deterministic algorithm, based on collision detection, provides a strong and interesting validation point of view, compared to our statistical approach.

MUSES3D is a representative example of the strategy for polydisperse two-phase flows that we have discussed in the present chapter. It has also initiated the use of splitting techniques for the efficient treatment of both the physical transport and phase space dynamics with dedicated methods. In addition, the code has been optimized through High Performance Computing (HPC) techniques, allowing to evaluate the multi-fluid method efficiency in a parallel framework (Fréret et al. 2010; Fréret et al. 2012), and also to address more realistic configurations. This parallel framework is transparent for the implementation of a new spray model. So that the code is a test platform for Euler-Euler methods in HPC, and the developments of the present thesis are to be evaluated with thus tool.

10.5.2 Research code on coalescence

To study and validate coalescence models and methods in the framework of Eulerian methods, a research code named TUYA has been developed by F. Laurent, which features a One Size Moment MF method and the corresponding coalescence strategy. The code solves a one-way coupled spray in a pre-defined configuration. The achievements of this code are the complete qualification of the OSM MF method for coalescence (Laurent et al. 2004).

10.5.3 Initial state of the CEDRE code

10.5.3.1 Existing strategy in the CEDRE code

The CEDRE code is a multi-physics platform for unstructured generic meshes (Courbet et al. 2011). It is extensively presented in Chapter 14 so only its main features are discussed here. The space discretization is a Finite-Volume one and the disperse phase, when solved with a Eulerian approach, is transported with a first order scheme. while the space fluxes are computed on the faces with a solver based on the resolution of the Riemann problem. The time integration strategy is based on exchange source terms at the end of gas and disperse phase split time steps. This strategy is in fact close to the BWC described in § 10.3.4.3 and it is not satisfactory for two-way coupling, as proven in Chapter 12. The disperse phase polydispersity can be treated with a TSM method but no resolution of coalescence is provided.

10.5.3.2 Extension to second order transport

A second order transport scheme has been developed in the mean time of the thesis by Le Touze et al. (2012) Figure 10.3 shows a SRM case solved with a Eulerian approach with either a first order and a second order

transport scheme: the lower level of diffusion in the latter case allows the second order scheme to render much steeper and denser structures in the vortices and in the nozzle. Nonetheless is the particle repartition (and segregation) better solved when the liquid structures are captured, but sources are accounted for more accurately: two-way coupling and coalescence, strongly depend on concentration, absolutely require spatial accuracy for concentrations and velocities to be accurate. The previous example also shows that coalescence and retro-coupling are stronger with a more accurate scheme. In return, the overall robustness of the numerical strategy is challenged when higher accuracy is achieved for moderately dense sprays.

10.5.3.3 Conclusion on industrial needs

In additional to the FV approach of CEDRE, various strategies have been tested for disperse two-phase flows on unstructured meshes. Space discretization is indeed a limiting and key point: the finite volume approach of CEDRE and the ALE kinetic scheme (Kah 2010) of IFP-C3D (Bohbot et al. 2009) are up to now limited to second order while the higher order cell-vertex approach of AVBP encounters stabilization difficulties. Whenever the achieved order is two, the overall accuracy is still lower than with structured, fine-tuned schemes (e.g. kinetic) which are much more accurate as regards the space-time description. So unstructured simulations of hypercompressible flows can difficultly account for the detail of the accumulations. The accuracy/robustness trade-off of these "high-order" schemes for unstructured meshes is however still satisfactory for industrial computations.
Two-way coupling is also limiting because the time integration strategies are developed under liability constraints. For instance, two-way coupling is accounted for with CEDRE but in a way that is neither robust nor accurate. Finally, the industrial codes do not feature the resolution of advanced source terms such as those of coalescence.

10.6 Conclusion and proposed developments

As a conclusion, three aspects of the numerical strategy for Euler-Euler approaches have been identified to generate numerical issues: the space transport resolution strategy, the time integration, and the phase space dynamics resolution. The existing approaches to solve these aspects have been presented. New methods are then developed in the present work, that we introduce below: these new methods are used, together with the existing approaches, to build research codes for validation purpose, and they are then implemented in CEDRE. The new methods are briefly introduced below and they are presented in detail, with their achievements, in the following chapters of Part IV. they are separated in improvements for the physical space strategy (Chapter 11), improvements for the overall time integration space strategy (Chapter 12) and improvements for the phase space strategy (Chapter 13).

10.6.1 Modeling efforts on physical space transport strategy

Fine-tuned numerical methods are required to treat the specific hypercompressible aspects of the disperse phase: significant advances have been obtained for PGD on structured grids and have inspired practical implementations on unstructured meshes, partly successful for industrial computations. The second order Bouchut scheme, described in § 13.1.1, is efficient for structured grids.
In the context of the development of a research code on two-way coupling, named SAP1 and presented in § 12.3.1, the second order Bouchut scheme has been implemented. This choice is motivated by the desire to use very accurate methods and schemes, in order to study time strategies, free of numerical errors from the other numerical methods.
But the polykinetic case (for moderately inertial particles) is still at stake. In this direction, the AG model has been introduced in Chapter 6 to cope with the δ-shocks by conserving the disperse phase energy and rendering it as anisotropic pressures. We present in Chapter 11 a second order strategy for AG transport on structured grids. It is implemented, tested and validated in a dedicated code referred to as AG2D presented in § 11.3.1: thanks to the quality of the transport strategy, these results prove the AG model to be efficient for homo-PTC, and the model is promising for industrial codes, provided a strategy for unstructured meshes.

10.6.2 Modeling efforts on time strategy

The time-integration strategy must be designed to account accurately for:

- a multivariate problem with many strong couplings;
- a multi-scale problem with many complex dynamics.

The splitting strategies have been presented as accurate and flexible enough (as regards implicitation, liability and HPC) to achieve a satisfactory time integration but the splitting must be done carefully.

From these considerations, a new strategy called ACS is introduced in Chapter 12 to account in an efficient and robust way for the two-way coupling of unsteady polydisperse cases, two-way coupling being a major aspect of moderately dense disperse two-phase flows.
The research code SAP1 (§ 12.3.1) is developed specifically to evaluate time strategies for two-way coupling in a fully non-linear context. The ACS is studied and validated versus an analytical formula for two-phase acoustics, which is a very strict test case and proves the strategy to be very accurate on dissipation at a reasonable cost. The results are presented in Chapter 12) ACS is implemented in the industrial code CEDRE for applicative computations. The validation in CEDRE is also successful and provided in Chapter 12. The new time strategy is tested in a realistic SRM case, where it shows its relevance in reducing the cost when fast particles are present. ACS is also tested in a case featuring many accumulations and a strong and stiff two-way coupling: it proves again to be satisfactory, as shown in § 12.4.2.
So this method is flexible enough to be used in both a research code and an industrial code. Finally the method is proven to be adaptable and efficient for other couplings resulting from phase space physics, such as coalescence. This is presented at the end of Chapter 12 and applicative results are again given in Chapter 15.

10.6.3 Modeling efforts on phase space dynamics strategy

Finally a strategy has been described to capture the complex dynamics and compute the source terms of a moderately dense polydisperse two-phase flow. This also requires advanced numerical methods due to the phase space degrees of freedom that the chosen methods (MF) try to render with high-fidelity. Thanks to the (numerous) quadrature techniques for numerical integration and to kinetic schemes in the phase space variables, the phase space terms can be evaluated accurately, as long as the methods are respectful of the models' algebras and the corresponding realizability constraints.
We introduce in Chapter 13 a set of quadrature integration techniques for reconstruction, drag, break-up and coalescence in the frame of the TSM method, (precisely chosen for its flexibility as regards the computation of such terms). Depending on the TSM reconstruction, different quadratures are chosen: for instance, a new adaptive quadrature is dedicated to the Exp-TSM method in order to cope with its non-linear reconstruction. The methods are implemented in the TUYA code to be validated. They are then implemented in SAP1 and CEDRE for polydisperse studies on two-way coupling, coalescence, and both, which prove their efficiency and flexibility. These improvements altogether with ACS, allow CEDRE to achieve applicative computations of two-way coupling polydisperse two-phase flows in Chapter 15 and Chapter 16.
In Chapter 13, we also introduce a quadrature dedicated to the computation of coalescence high order velocity integrals. It has to be carefully designed because of the peculiarity of the norm function and the high dimension of the integration space. The method is tested and validated on a coalescing case with the AG strategy within the code SAP2 (a research code using the same transport schemes than AG2D, see § 13.4.1). SAP2 treats the coalescence source terms thanks to both the size quadratures of the TSM and the velocity quadratures of AG so the code can account for polydispersity and coalescence in moderately inertial cases i.e. featuring homo-DTC. The results prove the approach to be robust and efficient, and therefore promising to treat the bigger droplets in SRMs, e.g. to assess more accurately specific impulse losses.

Chapter 11

Transport scheme for AG velocity closure

The AG model, introduced in Chapter 6 to treat moderately-inertial sprays and small scale crossings, is analyzed and a second order accurate transport scheme is developed. The model and scheme are then implemented in a research code and studied as regards academic cases to prove the validity of the approach as regards moderately inertial disperse phase modeling and of the numerics as regards research computations: the good behavior on segregation and velocity statistics is proven and promising for an efficient treatment of coalescence and coupling to the gas.

11.1 Numerical requirements driven by the modeling goal

The AG model has been introduced in Chapter 6 to cope with the δ-shocks that occur for moderately inertial disperse phases i.e. with $\mathrm{St} > \mathrm{St}_c$. In other terms this model is promising to treat homo-PTC. It is based on the resolution of the System (6.9):

$$\left\{\begin{array}{l} \partial_t \rho + \partial_{\boldsymbol{x}} \cdot (\rho \boldsymbol{u}) = 0 \\ \partial_t (\rho \boldsymbol{u}) + \partial_{\boldsymbol{x}} \cdot (\rho \boldsymbol{u} \otimes \boldsymbol{u} + \boldsymbol{P}) = 0 \\ \partial_t (\rho \boldsymbol{E}) + \partial_{\boldsymbol{x}} \cdot ((\rho \boldsymbol{E} + \boldsymbol{P}) \otimes \boldsymbol{u}) = 0 \end{array}\right. \tag{11.1}$$

where $\otimes$ is the symmetric outer product. And the model system that is considered is the directional System (6.14), i.e. after directional splitting:

$$\left\{\begin{array}{l} \partial_t \rho + \partial_x (\rho u) = 0 \\ \partial_t (\rho u_1) + \partial_x (\rho v^2 + p_{11}) = 0 \\ \partial_t (\rho u_2) + \partial_x (\rho uv + p_{12}) = 0 \\ \partial_t (\rho E_{11}) + \partial_x ((\rho E_{11} + p_{11}) u) = 0 \\ \partial_t (\rho E_{22}) + \partial_x (\rho E_{22} u + p_{12} v) = 0 \\ \partial_t (\rho E_{12}) + \partial_x (\rho E_{12} u + (p_{11} v + p_{12} u)/2) = 0. \end{array}\right. \tag{11.2}$$

To retrieve the characteristic crossing widths described in § 4.3.2.3, the principle of AG is to conserve all the disperse phase energies E_{ij} (second order velocity moments) and to render their effect as anisotropic pressures p_{ij}. The two types of quantities are linked together by relations resulting from an anisotropic Gaussian velocity closure, given in Eq. (6.4).
We now present a second order strategy for the transport of AG on structured grids. The strategy is valid for monodisperse distributions and straightforward extended to the transport of sections in a Multi-Fluid context. The transport strategy is implemented, tested and validated in a research code named AG2D. This space strategy is also implemented in the SAP2 code which treats polydispersity and coalescence, the latter phenomenon being studied in Chapter 13. This work has been performed in collaboration with A. Vié in a publication to come (Vié et al. 2014).

11.1.1 Realizability constraints of the AG model

As regards velocity moments, which are defined in Eq. (6.1), the AG model must ensure the positivity of the diagonal dispersions and of the determinant of the Gaussian covariance matrix (see § 6.1.3).
This results in the constraints on the moments which reads in 1D:

$$M_2 M_0 - M_1^2 > 0 \tag{11.3}$$

and in 2D:

$$\begin{cases} M_{20}M_{00} - M_{10}^2 > 0 \\ M_{02}M_{00} - M_{01}^2 > 0 \\ \det\begin{pmatrix} M_{20}M_{00} - M_{10}^2 & M_{11}M_{00} - M_{10}M_{01} \\ M_{11}M_{00} - M_{10}M_{01} & M_{02}M_{00} - M_{01}^2 \end{pmatrix} > 0. \end{cases} \tag{11.4}$$

These constraints can also be seen as entropy conditions, with the entropies defined in § 6.1.3.3.

11.1.2 Issue of numerical diffusion

The Eulerian modeling of clouds of particles often resorts to density fields with a poor smoothness, for the particle density has no particular reason to homogeneize in space, once clusters are formed, as discussed in Chapter 3. The density field may encounter large variations, featuring at worst vacuum zones and stiff accumulations. Unfortunately the numerical approximation of such Eulerian models is difficult to achieve accurately: singularities are difficult to capture robustly and spurious diffusion tends to be added unwillingly, as discussed in Chapter 10. In the case of the AG model, we aim at developing a numerical scheme for transport in physical space that preserves the characteristic length in the crossing zones. The spurious numerical diffusion must then result in a widening that is negligible compared to these lengths. In other terms, the energy introduced by the scheme must at all times be smaller than the directional microscopic energies that account for the physics of the crossing zone. In the following, a particular care is given to develop an accurate scheme and this aspect is assessed in the various test cases.

11.2 Transport scheme

In this work, a splitting strategy is used, as suggested in § 10.2.2: the convection part and source part are treated separately using an Alternate Lie splitting, which is second order in time (LeVeque 2002). The convective part is also solved using a dimensional splitting. The splitting is used because it it easier to develop solvers that are proven to be realizable for each element of the full equation.
Then, we derive a second order MUSCL-HLL scheme with conservative reconstruction of primitive variables $\mathcal{U} = (\rho, u, v, \sigma_{11}, \sigma_{12}, \sigma_{22})^T$. This method is composed of two main steps:

1. Reconstruction: each variable is reconstructed within each cell to calculate interface values;
2. Flux evaluation: the fluxes are evaluated using the interface values with a first order flux. Using a RK2 method for the time integration, it provides a second order scheme in space and time.

In the present work we propose a reconstruction of the primitive variables ρ, u, and $\mathbf{\Sigma}$ because realizability conditions such as positivity of the energy are easier to impose on primitive variables. We also impose that our reconstruction is conservative i.e. the integral over the cells of the inner reconstruction is equal to the cell value, such as for kinetic schemes in Bouchut et al. (2003), which is not classical in MUSCL schemes (Berthon 2006).

11.2.1 Second order MUSCL/HLL scheme

A second order numerical scheme can be obtained by using the MUSCL strategy (Van Leer 1979). This method is composed of two main steps:

1. the reconstruction: each variable is reconstructed within each cell. This way, interface values can be evaluated,
2. the fluxes: the fluxes are evaluated using the interface values, with a first order flux. Using a Runge-Kutta method for the time integration, it gives a high order scheme in space and time.

In the present work, we propose a conservative reconstruction of the primitive variables ρ, u, and $\mathbf{\Sigma}$, which is helpful to ensure the realizability of the moment set. The main issue with this type of reconstruction is that the slopes modify the average cell values of the moments, which imposes complex constraints on the slope evaluation. Hereafter, we first define the corrected cell values (still with respect to conservativity) which are needed to evaluate the slope ensuring positivity and/or maximum principles. Then the slope evaluation strategy is detailed. Finally, the flux evaluation and the time integration are presented.

11.2.1.1 Conservativity and corrected cell values

To achieve a second order in space scheme, linear reconstructions are envisioned. A previous work from Berthon (2005) has been devoted to the evaluation of several reconstruction strategies in the perspective of MUSCL schemes for Euler equations. In the present work, we propose a new reconstruction based on central moments, which has the advantage of being conservative and realizability-preserving. We consider a finite

volume discretization over the x dimension into cells of characteristic size Δx. The reconstructed variables for the cell j are the density, the mean velocity and the covariance matrix:

$$\begin{array}{lcl}
\tilde{\rho}_j(x) & = & \overline{\rho}_j + D_{\rho_j}(x - x_j) \\
\tilde{u}_j(x) & = & \overline{u}_j + D_{u_j}(x - x_j) \\
\tilde{v}_j(x) & = & \overline{v}_j + D_{v_j}(x - x_j) \\
\tilde{\sigma}_{11,j}(x) & = & \overline{\sigma}_{11,j} + D_{\sigma_{11,j}}(x - x_j) \\
\tilde{\sigma}_{12,j}(x) & = & \overline{\sigma}_{12,j} + D_{\sigma_{12,j}}(x - x_j) \\
\tilde{\sigma}_{22,j}(x) & = & \overline{\sigma}_{22,j} + D_{\sigma_{22,j}}(x - x_j)
\end{array} \tag{11.5}$$

where $\tilde{\cdot}$ designates the cell-reconstructed variables, and $\overline{\cdot}$ and $D_{\cdot}$ designate the linear reconstruction parameters.
Classically, this type of reconstruction is done without a conservativity constraint (Berthon 2005), because it is just needed to evaluate the fluxes at the interface. But as our aim is to ensure the realizability of the moments through the moment evolution, a conservative reconstruction guarantees that the fluxes will not affect realizability. Conservativity imposes to consider a corrected cell value for each reconstructed variable noted $\overline{\cdot}$. The subsequent constraints are the following:

$$M_{kl,j} = \frac{1}{\Delta x}\int_{x_{j-1/2}}^{x_{j+1/2}} \tilde{M}_{kl,j}(x)\mathrm{d}x. \tag{11.6}$$

Then, for each moment, we get:

$$\begin{array}{rcl}
M_{00,j} & = & \rho_j, \\
M_{10,j} = \rho_j\overline{u}_j + D_{\rho_j}D_{u_j}\dfrac{\Delta x^2}{12}, & & \\
M_{01,j} = \rho_j\overline{v}_j + D_{\rho_j}D_{v_j}\dfrac{\Delta x^2}{12}, & & \\
M_{20,j} & = & \rho_j(\overline{u}_j^2 + \overline{\sigma}_{11,j}) + \left(\rho_j D_{u_j}^2 + D_{\rho_j}\left(2\overline{u}_j D_{u_j} + D_{\sigma_{11,j}}\right)\right)\dfrac{\Delta x^2}{12}, \\
M_{11,j} & = & \rho_j(\overline{u}_j\overline{v}_j + \overline{\sigma}_{12,j}) + \left(\rho_j D_{u_j}D_{v_j} + D_{\rho_j}\left(\overline{u}_j D_{u_j} + \overline{v}_j D_{v_j} + D_{\sigma_{12,j}}\right)\right)\dfrac{\Delta x^2}{12}, \\
M_{02,j} & = & \rho_j(\overline{v}_j^2 + \overline{\sigma}_{22,j}) + \left(\rho_j D_{v_j}^2 + D_{\rho_j}\left(2\overline{v}_j D_{v_j} + D_{\sigma_{22,j}}\right)\right)\dfrac{\Delta x^2}{12}.
\end{array} \tag{11.7}$$

The corrected cell values are then:

$$\begin{array}{lcl}
\overline{\rho}_j & = & \rho_j \\
\overline{u}_j & = & u_j - \dfrac{D_{\rho_j}D_{u_j}}{\rho_j}\dfrac{\Delta x^2}{12} \\
\overline{v}_j & = & v_j - \dfrac{D_{\rho_j}D_{v_j}}{\rho_j}\dfrac{\Delta x^2}{12} \\
\overline{\sigma}_{11,j} & = & \sigma_{11,j} - \dfrac{\Delta x^2}{12}D_{u_j}^2\left(1 + \dfrac{\Delta x^2}{12}\dfrac{D_{\rho_j}}{\rho_j}\right) - \dfrac{\Delta x^2}{12}\dfrac{D_{\rho_j}D_{\sigma_{11,j}}}{\rho_j} \\
\overline{\sigma}_{12,j} & = & \sigma_{12,j} - \dfrac{\Delta x^2}{12}D_{u_j}D_{v_j}\left(1 + \dfrac{\Delta x^2}{12}\dfrac{D_{\rho_j}}{\rho_j}\right) - \dfrac{\Delta x^2}{12}\dfrac{D_{\rho_j}D_{\sigma_{12,j}}}{\rho_j} \\
\overline{\sigma}_{22,j} & = & \sigma_{22,j} - \dfrac{\Delta x^2}{12}D_{v_j}^2\left(1 + \dfrac{\Delta x^2}{12}\dfrac{D_{\rho_j}}{\rho_j}\right) - \dfrac{\Delta x^2}{12}\dfrac{D_{\rho_j}D_{\sigma_{22,j}}}{\rho_j}
\end{array} \tag{11.8}$$

11.2.1.2 Slope evaluation strategy

The slope evaluation is complex because inappropriate slopes can lead to unrealizable corrected cell values. Moreover, whereas positivity of the central moments can be easily ensured, the positivity of the determinant of the covariance matrix imposes a complex non-linear constraint. In the following, a slope evaluation strategy is proposed, which ensures all the realizability constraints for the flux evaluation at the cell interfaces.
First we treat the density, to which a minmod limiter is applied with an additional positivity constraint:

$$D_{\rho_j} = \frac{1}{2}\left(\mathrm{sign}(\rho_{j+1} - \rho_j) + \mathrm{sign}(\rho_j - \rho_{j-1})\right)\min\left(\frac{\rho_{j+1} - \rho_j}{\Delta x}, \frac{\rho_j - \rho_{j-1}}{\Delta x}, \frac{2\rho_j}{\Delta x}\right) \tag{11.9}$$

Second for the velocities, two types of constraints are imposed: a minmod limiter that takes into account the modification of the cell value (Bouchut et al. 2003) and two additional constraints to ensure the positivity

of the energies:

$$\begin{aligned} D_{u_j} = \quad & \frac{1}{2}\left(\text{sign}(u_{j+1}-u_j)+\text{sign}(u_j-u_{j-1})\right) \\ & \times \min\left(\frac{|u_{j+1}-u_j|}{\Delta x(1-\frac{D_{\rho_j}}{\rho_j}\frac{\Delta x}{6})}, \frac{|u_j-u_{j-1}|}{\Delta x(1+\frac{D_{\rho_j}}{\rho_j}\frac{\Delta x}{6})}, D_{u_j}^{\max,\sigma_{11}}, D_{u_j}^{\max,\sigma_{22}}\right) \end{aligned} \tag{11.10}$$

where

$$D_{u_j}^{\max,\sigma_{11}} = \sqrt{\frac{\sigma_{11,j}}{\frac{\Delta x^2}{12}\left(1+\frac{\Delta x^2}{12}\frac{D_{\rho_j}}{\rho_j}\right)}}, \quad D_{u_j}^{\max,\sigma_{22}} = \sqrt{\frac{\sigma_{22,j}}{\frac{\Delta x^2}{12}\left(1+\frac{\Delta x^2}{12}\frac{D_{\rho_j}}{\rho_j}\right)}} \tag{11.11}$$

while the slope for the velocity v is retrieved by analogy. Moreover the resulting slopes must keep the positivity of the corrected determinant within the cell:

$$\overline{\sigma}_{11,j}\overline{\sigma}_{22,j} - \overline{\sigma}_{12,j}^2 > 0 \tag{11.12}$$

By developing each term we rewrite Eq. (11.12):

$$H = \sigma_{11}D_{v_j}^2 + \sigma_{22}D_{u_j}^2 - 2\sigma_{12}D_{u_j}D_{v_j} < \frac{\sigma_{11}\sigma_{22}-\sigma_{12}^2}{\frac{\Delta x^2}{12}\alpha}. \tag{11.13}$$

If $H < 0$, the condition is always satisfied. If $H > 0$ and if this condition is not fulfilled by the first slope evaluation, a correction factor $\gamma \in [0,1]$ is introduced:

$$D_{u_j}^{new} = \gamma D_{u_j}^{old}, \qquad D_{v_j}^{new} = \gamma D_{v_j}^{old} \tag{11.14}$$

$$\gamma \quad = \min\left(1, \sqrt{\frac{\sigma_{11}\sigma_{22}-\sigma_{12}^2}{\frac{\Delta x^2}{12}\left(1+\frac{\Delta x^2}{12}\frac{D_{\rho_j}}{\rho_j}\right)H}}\right) \tag{11.15}$$

Third, the slopes of the covariance matrix are evaluated. The following quantities are introduced to simplify the notations:

$$\begin{aligned} \sigma_{11}^* &= \sigma_{11,j} - \frac{\Delta x^2}{12}D_{u_j}^2\left(1+\frac{\Delta x^2}{12}\frac{D_{\rho_j}}{\rho_j}\right) \\ \sigma_{12}^* &= \sigma_{12,j} - \frac{\Delta x^2}{12}D_{u_j}D_{v_j}\left(1+\frac{\Delta x^2}{12}\frac{D_{\rho_j}}{\rho_j}\right) \\ \sigma_{22}^* &= \sigma_{22,j} - \frac{\Delta x^2}{12}D_{v_j}^2\left(1+\frac{\Delta x^2}{12}\frac{D_{\rho_j}}{\rho_j}\right) \end{aligned} \tag{11.16}$$

We impose a minmod slope evaluation that satisfy the positivity of the energies:

$$\begin{aligned} D_{\sigma_{11,j}} &= \frac{1}{2}\left(\text{sign}(\sigma_{11,j+1}-\sigma_{11,j})+\text{sign}(\sigma_{11,j}-\sigma_{11,j-1})\right) \\ & \times \min\left(\frac{|\sigma_{11,j+1}-\sigma_{11,j}|}{\Delta x(1-\frac{D_{\rho_j}}{\rho_j}\frac{\Delta x}{6})}, \frac{|\sigma_{11,j}-\sigma_{11,j-1}|}{\Delta x(1+\frac{D_{\rho_j}}{\rho_j}\frac{\Delta x}{6})}\right) \end{aligned} \tag{11.17}$$

This limitation does not ensure the positivity of the determinant, which is a quadratic function of the position:

$$\begin{aligned} \Delta(x) = \quad & \overline{\sigma}_{11}\overline{\sigma}_{22} - \overline{\sigma}_{12}^2 + \left(\overline{\sigma}_{11}D_{\sigma_{22,j}} + \overline{\sigma}_{22}D_{\sigma_{11,j}} - 2\overline{\sigma}_{12}D_{\sigma_{12,j}}\right)x \\ & + \left(D_{\sigma_{11,j}}D_{\sigma_{22,j}} - D_{\sigma_{12,j}}^2\right)x^2 > 0 \end{aligned} \tag{11.18}$$

After developing each term we finally get:

$$\begin{aligned} \sigma_{11}^*\sigma_{22}^* - (\sigma_{12}^*)^2 \quad & + \left(x - \frac{\Delta x^2}{12}\frac{D_{\rho_j}}{\rho_j}\right)\left(\sigma_{11}^*D_{\sigma_{22,j}} + \sigma_{22}^*D_{\sigma_{11,j}} - 2\sigma_{12}^*D_{\sigma_{12,j}}\right) \\ & + \left(x - \frac{\Delta x^2}{12}\frac{D_{\rho_j}}{\rho_j}\right)^2\left(D_{\sigma_{11,j}}D_{\sigma_{22,j}} - D_{\sigma_{22,j}}^2\right) > 0 \end{aligned} \tag{11.19}$$

Defining the following quantities:

$$\begin{aligned} \Delta^* &= \sigma_{11}^* \sigma_{22}^* - \left(\sigma_{12}^*\right)^2 \\ A &= \sigma_{11}^* D_{\sigma_{22,j}} + \sigma_{22}^* D_{\sigma_{11,j}} - 2\sigma_{12}^* D_{\sigma_{12,j}} \\ B &= D_{\sigma_{11,j}} D_{\sigma_{22,j}} - D_{\sigma_{22,j}}^2 \end{aligned} \tag{11.20}$$

we can re-write Eq. (11.19):

$$\Delta^* + A\left(x - \frac{\Delta x^2}{12}\frac{D_{\rho_j}}{\rho_j}\right) + B\left(x - \frac{\Delta x^2}{12}\frac{D_{\rho_j}}{\rho_j}\right)^2 > 0 \tag{11.21}$$

As the goal of the reconstruction strategy is to evaluate the value at the cell interfaces, we impose a condition weaker than Eq. (11.21):

$$\begin{aligned} &\Delta^* + A\left(\frac{\Delta x}{2} - \frac{\Delta x^2}{12}\frac{D_{\rho_j}}{\rho_j}\right) + B\left(\frac{\Delta x}{2} - \frac{\Delta x^2}{12}\frac{D_{\rho_j}}{\rho_j}\right)^2 > 0 \\ &\Delta^* + A\left(-\frac{\Delta x}{2} - \frac{\Delta x^2}{12}\frac{D_{\rho_j}}{\rho_j}\right) + B\left(-\frac{\Delta x}{2} - \frac{\Delta x^2}{12}\frac{D_{\rho_j}}{\rho_j}\right)^2 > 0 \end{aligned} \tag{11.22}$$

A new correction factor $\beta \in [0,1]$ is introduced:

$$D_{\sigma_{11,j}}^{new} = \beta D_{\sigma_{11,j}}^{old}, \qquad D_{\sigma_{22,j}}^{new} = \beta D_{\sigma_{22,j}}^{old}, \qquad D_{\sigma_{12,j}}^{new} = \beta D_{\sigma_{12,j}}^{old} \tag{11.23}$$

If $\beta = 0$, the determinant is positive everywhere, so that there is always an admissible value of β. If the determinant is not positive without correction, the highest $\beta \in [0,1]$ is chosen among the ones that satisfies the positivity of the determinant at each interface of the cell:

$$\begin{aligned} &\Delta^* + \beta A\left(\frac{\Delta x}{2} - \frac{\Delta x^2}{12}\frac{D_{\rho_j}}{\rho_j}\right) + \beta^2 B\left(\frac{\Delta x}{2} - \frac{\Delta x^2}{12}\frac{D_{\rho_j}}{\rho_j}\right)^2 > 0 \\ &\Delta^* + \beta A\left(-\frac{\Delta x}{2} - \frac{\Delta x^2}{12}\frac{D_{\rho_j}}{\rho_j}\right) + \beta^2 B\left(-\frac{\Delta x}{2} - \frac{\Delta x^2}{12}\frac{D_{\rho_j}}{\rho_j}\right)^2 > 0 \end{aligned} \tag{11.24}$$

The slope evaluation is complex because the slopes can lead to unrealizable corrected cell values. Moreover whereas the positivity of the central moments can be easily ensured, the positivity of the covariance matrix determinant imposes a complex non-linear constraint. Our slope evaluation satisfies the positivity of the density, the diagonal components of $\mathbf{\Sigma}$, as well as its determinant. This limitation also imposes a maximum principle on each variable to avoid the generation of spurious oscillations.

11.2.2 Fluxes and time integration

Such a Riemann problem can be solved using first order approximate Riemann solvers. This strategy has been extensively studied in Berthon (2005) for the Euler equations using several reconstruction strategy. In the following we will use the same method: we will use the reconstruction strategy to evaluate the states at the interfaces and we will consider a piecewise constant reconstruction in each cell. Then we will solve the Riemann problem at each interface using a first order HLL scheme Harten, Lax, and van Leer (1983) and finally embed it into a second order in time Runge Kutta scheme.
Once the reconstruction strategy is provided, one has to decide how to solve the generalized Riemann problem (GRP) at each cell interface (Toro 2009). A classical strategy is to use a MUSCL scheme (Van Leer 1979): instead of solving the GRP, it solves a classical Riemann problem for which each state is defined as the right and left states at the interface position, given by the reconstruction strategy. Such a Riemann problem can be solved using first order approximate Riemann solvers. This strategy has been extensively studied in Berthon (2005) for the Euler equations using several reconstruction strategies. In the following we resort to the same method: we will use the reconstruction strategy to evaluate the states at the interfaces and we will consider a piecewise constant reconstruction in each cell. Then we will solve the Riemann problem at each interface using a first order HLL scheme (Harten et al. 1983) and finally embed it into a second order in time Runge-Kutta scheme.
The main idea of the HLL solver is to simplify the full Riemann problem. The solution of the Riemann problem is sought to be composed of the initial states at each side of the interface $\mathcal{M}_L$ and $\mathcal{M}_R$, and one intermediate state, which is a non-linear combination of the states, between the minimum and maximum eigenvalues of the Jacobian of the fluxes at the interface. Once this intermediate state is found, the fluxes can be evaluated. Considering the moment equations for the advection in one direction:

$$\partial_t \mathcal{M} + \partial_x \mathcal{F}(\mathcal{M}) = 0 \tag{11.25}$$

Integrating Eq. (11.25) over x direction across one interface , one gets the intermediate state:

$$\mathcal{M}^* = \frac{\mathcal{M}_L - \mathcal{M}_R}{\lambda_{min} - \lambda_{max}} - \frac{\mathcal{F}(\mathcal{M}_L) - \mathcal{F}(\mathcal{M}_R)}{\lambda_{min} - \lambda_{max}} \tag{11.26}$$

which permits to compute the fluxes at the interface:

$$\begin{aligned} \mathcal{F}^{HLL}(\mathcal{M}_L, \mathcal{M}_R) = \quad & \frac{1}{2}\left(\mathcal{F}(\mathcal{M}_L) + \mathcal{F}(\mathcal{M}_R)\right) \\ & -\frac{1}{2}|\lambda_{min}|\left(\mathcal{M}^* - \mathcal{M}_L\right) - \frac{1}{2}|\lambda_{max}|\left(\mathcal{M}_R - \mathcal{M}^*\right) \end{aligned} \tag{11.27}$$

Finally, the integration in time is performed using a 2-step Runge-Kutta method:

$$\begin{cases} \mathcal{M}_j^{n+1/2} = \mathcal{M}_j^n - \frac{1}{2}\frac{\Delta t}{\Delta x}\left(\mathcal{F}_{j+1/2}^n - \mathcal{F}_{j-1/2}^n\right) \\ \mathcal{M}_j^{n+1} = \mathcal{M}_j^n - \frac{\Delta t}{\Delta x}\left(\mathcal{F}_{j+1/2}^{n+1/2} - \mathcal{F}_{j-1/2}^{n+1/2}\right) \end{cases} \tag{11.28}$$

The realizability of the scheme is proven if:

1. using the linear reconstruction of the primitive variable to evaluate a piecewise constant reconstruction leads to realizable states,
2. the HLL scheme is realizable,
3. the Runge-Kutta scheme is realizable.

In our case the realizability proof is provided in Vié et al. (2014). Thanks to the realizable linear reconstruction and the 2-step Runge-Kutta method, the final scheme is second order accurate in time and space, and always keeps the moments realizable.

11.3 Evaluation of the AG closure for moderately inertial sprays

We now validate the AG method and the scheme on academic cases. The case of two crossing jets allows to evaluate the detailed behavior of the method when a unique crossing occurs: the importance of anisotropy is shown and the method is proven to preserve a characteristic length and the directional energy. Then we study the case of Taylor-Green vortices, where multiple crossings occur: the case is again strongly structured and the method is compared versus an isotropic closure to show its efficiency. The AG closure and the second order scheme are finally assessed in a turbulent field, where it is shown that the statistics behave well.

11.3.1 In-house code for polykinetic studies: the AG2D code

The AG2D code is an in-house code initiated by A. Vié to study moderately inertial to inertial sprays with Eulerian methods. The transport scheme for the Anisotropic Gaussian velocity closure has been co-developed with A. Vié. This scheme, presented in § 11.2, applies on finite volume structured meshes, and operates in 2D thanks to a dimensional splitting. The code has then a very simple treatment of the phase space, which consists in one-way coupling drag, computed with an analytical implicit method.

11.3.2 Two jets in a compressive field

In the literature pressure-like models developed in the context of ACBMM have been tested in the context of turbulent flows (Riber et al. 2006; Kaufmann et al. 2008; Dombard 2011; Masi and Simonin 2012; Sierra Sanchez 2012; Masi et al. 2013), where the turbulent mixing generates multiple and complex crossings. While such configurations are of particular interest for final turbulent applications, they do not assess the behavior of the model for the most simple crossing scenario: the crossing between two trajectories. This simple scenario is the building element of what happens in a turbulent case so we propose to set up a specific test case.

To investigate this scenario we consider a situation where the strain rate of the gaseous carrier field will generate PTC for the particulate phase. This test case has already been investigated in 1D (de Chaisemartin 2009; Massot 2007), and here in its 2D version. By injecting particles in the gaseous field from two positions we will generate, depending on the relaxation time of the particles, a two-trajectory crossing. In the following we detail this configuration as well as its analytic Lagrangian solution. We thus analyze the results for the AG model, emphasizing on the description of the spatial distribution of the number density as well as on the energy budget.

11.3.2.1 Configuration description and analytical solution

We consider a carrier phase with the given velocity field in a Cartesian frame $(x, y) \in [0; H] \times [0, L]$:

$$\begin{pmatrix} u_g \\ v_g \end{pmatrix}(x, y) = \begin{pmatrix} u_{g0} \\ -\epsilon y \end{pmatrix} \tag{11.29}$$

so that it flows constantly in the x-direction at a velocity u_{g0} from left to right but with a compressive velocity field in the y-direction i.e. velocities oriented towards $y = 0$. The rate of strain on the $y = 0$ axis of symmetry is $\epsilon = \left|\frac{\partial v_g}{\partial y}(y = 0)\right|$. If we inject particles at time $t = 0$ and at $x = 0$ at the velocity:

$$\begin{pmatrix} U_{p0} \\ V_{p0} \end{pmatrix} = \begin{pmatrix} u_{g0} \\ 0 \end{pmatrix} \tag{11.30}$$

that is at equilibrium with the x-component of the gas velocity, they move uniformly in the the x-direction. But they also accelerate in the y-direction and migrate towards the center according to the Lagrangian equations:

$$\begin{aligned} \mathrm{d}_t Y_p &= V_p \\ \mathrm{d}_t V_p &= F(V_p, V_{g@p}) \end{aligned} \tag{11.31}$$

where the drag force F is taken in Stokes' regime and reads in the velocity field of Eq. (11.29):

$$F(V_p, V_{g@p}) = -\frac{1}{\tau_p}(V_p - V_{g@p}) = -\frac{1}{\tau_p}\left(V_p + \epsilon Y_p\right). \tag{11.32}$$

Collapsing the Lagrangian equations yields a scalar second order equation that describes the the y-motion in a frame that moves along the x-axis:

$$\mathrm{d}_{tt} Y_p + \frac{1}{\tau_p}\mathrm{d}_t Y_p + \frac{\epsilon}{\tau_p} Y_p = 0. \tag{11.33}$$

The solution, when defining $\omega^2 = \frac{1}{4}\left|\frac{1}{\tau_p^2} - \frac{4\epsilon}{\tau_p}\right|$:

$$\begin{pmatrix} X_p \\ Y_p \end{pmatrix}(t) = \begin{pmatrix} U_{p0} t \\ Y_{p0} \exp\left(-\dfrac{t}{2\tau_p}\right) \begin{cases} \exp(-\omega t) & \text{if St} \leq \text{St}_c \\ \cos(-\omega t) & \text{otherwise.} \end{cases} \end{pmatrix} \tag{11.34}$$

oscillates if the determinant is negative. So we define a Stokes number:

$$\text{St} = \epsilon \tau_p \tag{11.35}$$

that yields oscillations if above the critical value $\text{St}_c = \frac{1}{4}$ (de Chaisemartin 2009). We define a space period $\lambda = 2\pi U_g/\omega$ that is relevant in the horizontal direction.
First, the particles converge towards the center in a characteristic time that is $2\tau_p$ which corresponds to a characteristic length $\Lambda = 2U_g\tau_p$ in the x-direction. Second, if particles are injected at, at least, two different ordinates Y_{p1} and Y_{p2}, PTC occurs as soon as oscillation occurs that is $\text{St} > \text{St}_c$.
When multiplying Eq. (11.33) by velocity, one get after integration an equation on the specific energy of a particle:

$$\frac{\mathrm{D}}{\mathrm{D}t}\left(\frac{\dot{Y_p}^2}{2} + \frac{\epsilon}{\tau_p}\frac{Y_p^2}{2}\right) = -\frac{1}{\tau_p}\dot{Y_p}^2 \quad \text{with} \quad \dot{Y_p} = \frac{\mathrm{d}Y_p}{\mathrm{d}t} \tag{11.36}$$

where one recognizes a kinetic energy $e_c = \frac{1}{2}\dot{Y_p}^2$ and a potential energy $e_p = \frac{\epsilon}{2\tau_p}Y_p^2$. The latter comes from a part of the drag force, which has been split in a conservative and a non-conservative part. The potential is high when particles are far from the centerline and minimum when particles are at the center i.e. in the zone of dead water. The sum of these two energies is the mechanical energy, that decreases due to the non-conservative part of the drag force.
We finally define two tools dedicated to the analysis of the two-jet configuration: the y-integration operator and the notion of orbitals. To quantitatively compare the different approaches we define the y-integration operator over a quantity $\cdot$:

$$< \cdot >_y = \int_{y_0}^{y'} \cdot \ \mathrm{d}y', \tag{11.37}$$

where y_0 is the y-ordinate of the centerline. The cumulative number density reads:

$$\psi(x,y) = \frac{< \rho(x,y') >_y}{< \rho(x,y') >_{+\infty}}, \tag{11.38}$$

and is a number (per square length). An α%-orbital is then defined as a sub-manifold of the $x-y$ plane containing the center line and which encloses α% of the total number of particles at every x-position.

11.3.2.2 Eulerian simulation

We now consider a domain $H = 2\,\mathrm{m}$ and $L = 6\,\mathrm{m}$. The mesh is 1000×400 cells. The gas flow has an x-velocity $u_g = 0.2\,\mathrm{m/s}$ and a y-strain $\epsilon = 1\,\mathrm{s}^{-1}$. Two particle jets of width $\delta = 0.2\,\mathrm{m}$ are injected at y-ordinates $y_1 = 0.5\,\mathrm{m}$ and $y_2 = 1.5\,\mathrm{m}$ with $U_{l,inj} = U_g = 0.2\,\mathrm{m/s}$ and $V_{l,inj} = 0$. The particle Stokes number is $\mathrm{St} = 5 = 20\mathrm{St}_c$, which is sufficient to let homo-PTC occur.
In Figure 11.1 the steady solution of the AG model is represented. The white lines represent the limits of the 100%-orbital of the analytical solution described by Eq. (11.34). Results show that even if before the first crossing Lagrangian and Eulerian are in very good agreement, after the first crossing, the AG solution is distributed between the two extremal Lagrangian orbitals. However the number density is still enclosed, and reproduces the length scales (amplitude and spacing) of the crossing even if it cannot capture the details of it.

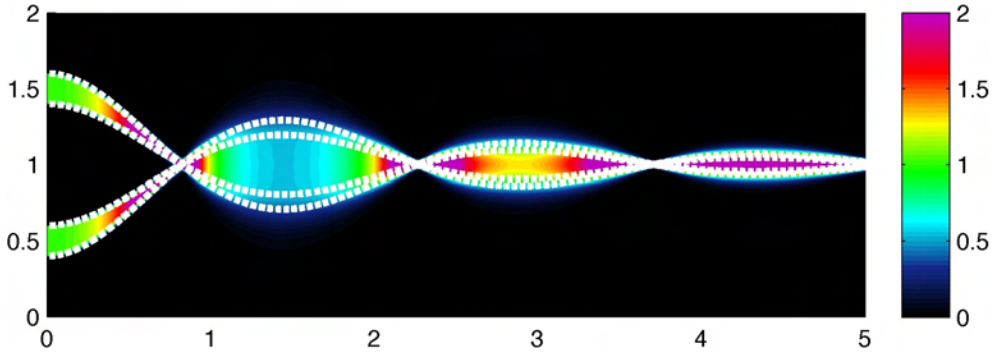

Figure 11.1: *Steady solution of two inertial particle jets ($St = 20$) injected in a compressive velocity field: Particle number density (m^{-3}). White lines represent the lower and upper Lagrangian trajectories for each jet.*

After the first crossing, the AG model looses the detailed information of the velocity distribution, projecting it with respect to the second order moments onto the maximum entropy distribution (in the information sense). In fact, it destroys the information that is not reproduced by the reconstructed NDF. To exhibit this information loss, we propose to replace the two jets by one jet which as a Gaussian spatial distribution in the y-direction. Therefore the injection condition at $x = 0$ is described by the following spatial distribution:

$$\rho_{inj}(y) = \frac{2\delta}{\sqrt{2\pi\sigma_{inj}}} \exp\left(-\frac{(y-1)^2}{2\sigma_{inj}}\right), \qquad \sigma_{inj} = \int_0^H \rho(y) U_{p0} \mathrm{d}y. \tag{11.39}$$

Results for the Gaussian injection are represented in Figure 11.2. Again white lines represent the extremal orbitals of the Lagrangian solution. Here before the first crossing the Eulerian and Lagrangian solutions are no longer equivalent. After the first crossing however, the Eulerian solution of the Gaussian jet becomes similar to the one of the two-jet configuration:

- most of the number density is enclosed in-between the Lagrangian trajectories,
- internal energy is generated at each crossing events.

The Gaussian jet and the two-jet configuration look similar after the first crossing, which has destroyed a part of the information of the injection conditions.
We can estimate the number of particles that are enclosed in-between two y-ordinates thanks to the y-integral defined in Eq. (11.37). Since the problem is symmetric, $\psi(x,y)$ is also symmetric in the y-direction. Results are represented in Figure 11.3. As qualitatively assessed, before the first crossing, the two-jet configuration locates the number density well, while the Gaussian injection condition results in a spreading. After the first crossing both injection conditions give a smeared solution. The 80%-orbitals are the same, close to the extremal orbitals of the Lagrangian solution. The 99%-orbitals differ after the first crossing, but they end up to be similar after the second crossing. Thus both two-jet and Gaussian-jet configurations become equivalent in terms of number density after crossing.

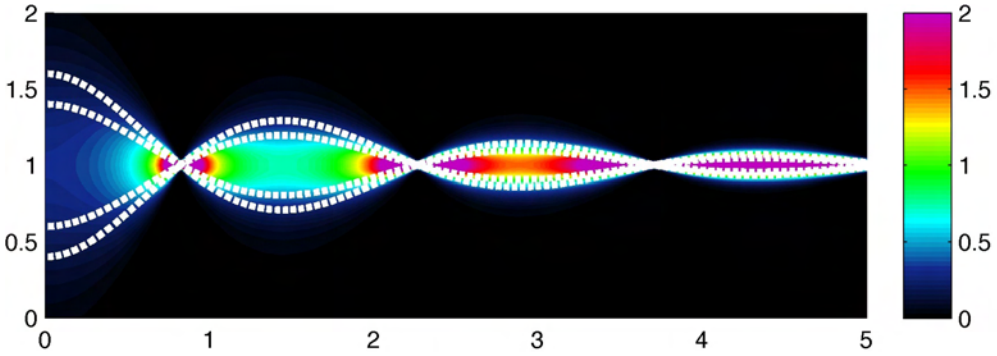

Figure 11.2: *Steady solution of Gaussian particle jet ($St = 20$) injected in a compressive velocity field: Particle number concentration (m^{-3}). White lines represent the lower and upper Lagrangian trajectories for each jet.*

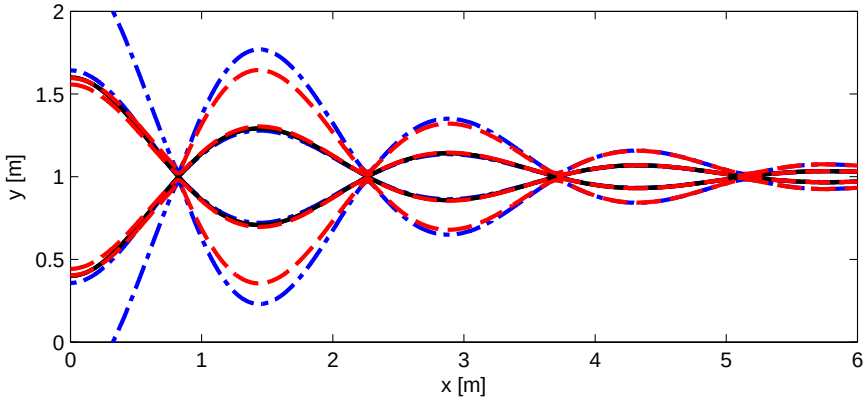

Figure 11.3: *Statistics of the jet configurations into a gaseous compressive field: isolines of cumulative number density for the two-jet analytical solution (100%, black line), the two-jet AG solution (80% and 99%, red lines), and the Gaussian-jet AG solution (80% and 99%, blue lines).*

To further analyze the behavior of the model on both configuration, the mean, integral, and potential density-weighted energies integrated over the y-direction are plotted against the x-direction in Figure 11.4. Results show that the evolution of the energy is reproduced with a good precision compared to the Lagrangian solution. Even before the first crossing, two-jet and Gaussian-jet configuration are identical. It demonstrates that the AG model preserves the information of the second order moments at each crossing event, discarding any higher order information such as the third order central moments.

11.3.3 Conclusion on the model

In conclusion of this test case results demonstrate the main drawback of the AG model: it cannot capture the density distribution generated by deterministic crossings such as in the present configuration. However, when the crossing is generated because of the drag force of a straining gaseous flow field, the particle trajectories are enclosed in manifolds that correspond to a specific space scale. The AG model is able to reproduce this scale, and it captures the width of the crossing and its energetic behavior. Another interesting property of the AG model is that, after a crossing it does not allow to determine if the crossing has been generated by a deterministic event, such as a two-jet crossing, or an ensemble of initial/boundary conditions totalizing the same zero, first and second order spatial moments.
So AG is able to render the characteristic size -and therefore particle concentrations- and the kinetic energy of a particle cloud in the neighborhood of a homo-PTC. The size of the neighborhood depends on the dissipation induced by the carrier phase flow and therefore on the particle inertia. From this spatially structured case with a unique crossing, we now move towards cases featuring multiple crossing zones: the Taylor-Green vortices generate localized mixing zones and the Homogeneous Isotropic Turbulence introduces a more complex mixing.

11.4 Application to model turbulence fields

The ability of the model to reproduce one crossing event has been evaluated: the Anisotropic Gaussian closure can be used to cope with PGD singularities and to account for the characteristic size of the crossing

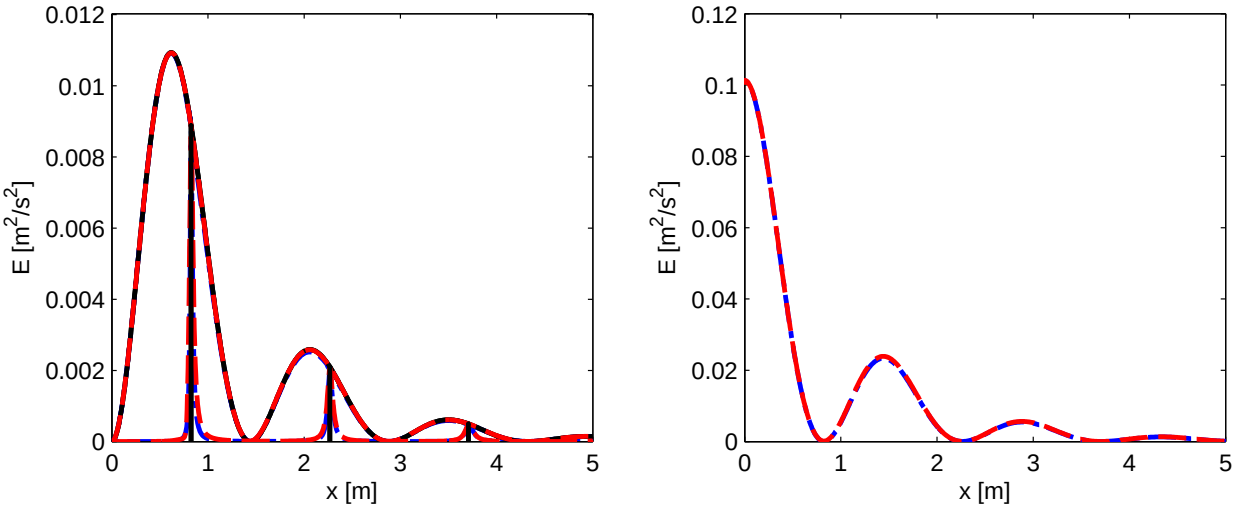

Figure 11.4: *Statistics of the jet configurations into a gaseous compressive field: mean and internal energies (left, the upper curves are for mean energy, the lower for internal energy), and potential energy (right) for the Lagrangian solution (black continuous line), the AG solution of the two-jet (red dashed line) and the full jet (blue dot-dashed line) configurations.*

zone and the characteristic density within it. We now investigate two more complex cases where several crossing events are encountered:

- The 2D Taylor-Green vortices: this test case features four contra-rotative vortices with periodicity. It is interesting because it is composed of one scale, and the conditions for PTC are easy to determine. Furthermore the Lagrangian solution exhibits different structures that correspond to simple or multiple crossings, that are of interest for real turbulent flows. It is an intermediate case between laminar and fully turbulent cases, because in a turbulent field, the particulate phase interacts with a full spectrum of scales, each of them having a specific interaction with the particles. Finally it is also a good test case to demonstrate the quality of the numerics.
- The 2D Decaying Homogeneous Isotropic Turbulence: the physics of this test case is relevant for realistic applications. The turbulence of the carrier phase generates multiple crossing events everywhere in the domain, that are impossible to treat separately in the Eulerian vision of the flow: the validation of Eulerian strategies requires to investigate their ability to treat such superimposed scales. The first level of real turbulent flows is the Homogeneous Isotropic Turbulence, for which the spectrum of scales is well-known. Moreover, we choose a decaying turbulence to assess the interaction of particles with unsteady time scales.

In the following, we compare the AG model to a Lagrangian solution with 10 million particles. We also investigate the importance of the anisotropy of the model by comparing to the results of the Isotropic Gaussian model. Actually this model is obtained by assuming that the energy tensor $\mathbf{\Sigma}$ is isotropic, leading to the Euler equations. This model is the simplest one that can be used to reproduce PTC. Its main advantage is that less moments are solved, as only one second order moment is needed: the total energy. However, as it has been shown in the two-crossing jet case, crossing events are highly anisotropic, and this model could reveal to be inaccurate.

To analyze the results, we use two tools:

- Instantaneous fields: first, the spatial distribution of particles is investigated. This is the primary information that we want to capture, and the double jet case has shown that the AG is not able to reproduce details, but can capture scales of the flow. We then want to verify if it is still the case in turbulent-like conditions, where multiple crossing events can be found at each location.
- Statistics: to evaluate quantitatively the ability of the Eulerian approaches to reproduce the Lagrangian reference, three statistics of the flow are investigated: the segregation, the mean central energy and the mean total energy. The segregation evaluates the generation of stiff accumulation and vacuum zones. It is of particular importance, for example for dense flows, where the local concentration is a leading term to evaluate the coalescence source term, or for the combustion of droplets, where the inhomogeneities of the droplet phase highly influence the whole process. Mean total and central energies are also helpful to determine if the coupling between the gas and the particle phases is well resolved. Here we evaluate the statistical quantities on a fixed reference mesh of 64^2 cells on which all results are projected, for

which Lagrangian results are statistically converged. They are expressed as:

$$g_{pp} = \frac{\{\rho^2\}}{\{\rho\}^2}, \quad \delta\tilde{\Theta}_p = \frac{\{\rho(\sigma_{11}+\sigma_{22})\}}{2\{\rho\}}, \quad \tilde{E}_p = \frac{\{\rho(E_{11}+E_{22})\}}{2\{\rho\}}, \tag{11.40}$$

where g_{pp} is the segregation, $\delta\tilde{\Theta}_p$ the mean central energy, $\tilde{E}_p$ the mean total energy, and $\{.\}$ the spatial averaging operator over the whole domain using the quantities projected on a 64^2-cell mesh.

11.4.1 Introduction of an isotropic reference model for comparison purpose

We now introduce the Isotropic Gaussian model (IG), which transport part exactly matches that of the Euler equations (see System (3.101)).
In the context our numerical validations, we use the same scheme and code structure for IG than for AG, except that energies are redistributed fairly in all directions.
This results in using the following moments (in 2D) for the reconstruction process to compute the fluxes:

$$\begin{cases} M_{20}^{IG} = M_{10}^2 + \frac{1}{2}\left(M_{20} - M_{10}^2 + M_{02} - M_{01}^2\right) \\ M_{02}^{IG} = M_{01}^2 + \frac{1}{2}\left(M_{20} - M_{10}^2 + M_{02} - M_{01}^2\right) \\ M_{11}^{IG} = M_{10}M_{01}/M_{00} \end{cases} \tag{11.41}$$

The IG model preserves the energies as well but it is not able to render anisotropy: an isotropic pressure occurs, whatever direction the compression is. These aspects are illustrated in the discussion on the response of different Eulerian models in § 6.2.2: the IG behavior is shown, for a unique crossing in Figure 6.4.

11.4.2 Taylor-Green vortices

To analyze the ability of modeling approaches to reproduce the dynamics of particles in turbulent flows, the Taylor-Green vortices (TG) are a helpful test case. It consists in four contra-rotative vortices of the same scale. Such a test case is interesting because it permits to figure out how a particulate phase interacts with one gas phase scale. It is an intermediate case between laminar and fully turbulent cases, because in a turbulent field, the particulate phase will interact with a full spectrum of scales, each of them having a specific interaction with the particles.
The gas velocity field of the TG is the following:

$$\begin{aligned} u_g(x,y) &= \sin(2\pi x)\cos(2\pi y) \\ v_g(x,y) &= -\cos(2\pi x)\sin(2\pi y) \end{aligned} \tag{11.42}$$

The dynamics of particles generated by a drag coupling with TG is characterized by a critical Stokes number $\mathrm{St}_c = 1/8\pi$ as defined in de Chaisemartin (2009). Below this limit particles stay in their initial vortex and do not encounter PTC. Above this limit particles have a sufficient inertia to leave their initial vortex. They will generate PTC, which scales becomes larger as the Stokes number increases. In the following we will investigate TG for three Stokes numbers: $\mathrm{St} = \mathrm{St}_c$, $5\mathrm{St}_c$, and $10\mathrm{St}_c$. The solution obtained by a Lagrangian Tracking is considered as the reference. Isotropic (IG) and Anisotropic Gaussian (AG) closures will be investigated, to highlight the importance of the central energy partition in each direction that is done by AG and not by IG. If it is not mentioned the mesh size is composed of 256^2 equi-distributed cells.

11.4.2.1 Instantaneous fields

First, the number density field obtained at time $t = 4$ is compared for each method and each Stokes number, respectively in Figure 11.5, Figure 11.6, and Figure 11.7. At $\mathrm{St} = \mathrm{St}_c$, the number density field has the same structure for each simulation, i.e. a stiff accumulation of particles in the lowest vorticity zones. Eulerian solutions (IG and AG) are equivalent, which is expected because at this Stokes number, no homo-PTC occurs. This implies that no central energy is generated, and the two models behave like PGD. Compared to the stochastic-Lagrangian reference, the two Eulerian models feature a diffused solution but the diffusion length decreases with the mesh refinement.
At $\mathrm{St} = 5\mathrm{St}_c$, homo-PTC are expected, so the model will generate a central energy. Whereas at $\mathrm{St} = \mathrm{St}_c$, the number density field are highly similar for each model, this is no more the case at $\mathrm{St} = 5\mathrm{St}_c$. In Figure 11.6, the structures generated by each simulation are relatively different. At this Stokes number, the stochastic-Lagrangian reference generates two types of structures: four stiff equilibrium manifolds (EM) out of the low vorticity zones, which are the long-time solution of the particle system of ODEs in TG, and larger mixing zones where droplets are traveling around the low vorticity zones without being attracted inside one

of the equilibrium manifolds. The two Eulerian approaches are able to capture the mixing zones but do not reproduce the EM. To capture the EM, an Eulerian approach must be able to reproduce exactly the PTC between two trajectories, which is not the case for one-velocity-node Eulerian approaches[1]. Finally even if IG and AG solutions are different, the best solution among the Eulerian approaches cannot be discriminated by solely considering the number density field. However looking at the results for $\mathrm{St} = 10\mathrm{St}_c$ clearly shows that the IG closure no longer reproduces the characteristic width of the mixing zones, contrary to AG.

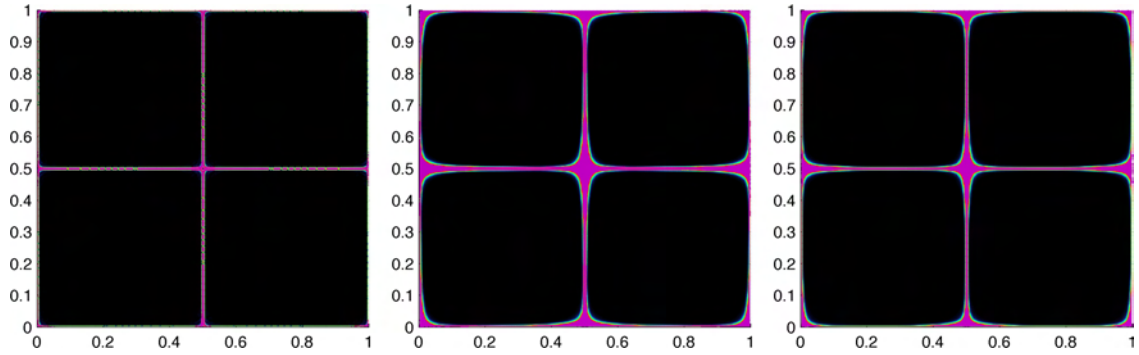

Figure 11.5: *Taylor-Green Vortices for $St = St_c$: number density field at time $t = 4$ for the stochastic-Lagrangian (left), and the Eulerian isotropic (center) and anisotropic (right) Gaussian closures.*

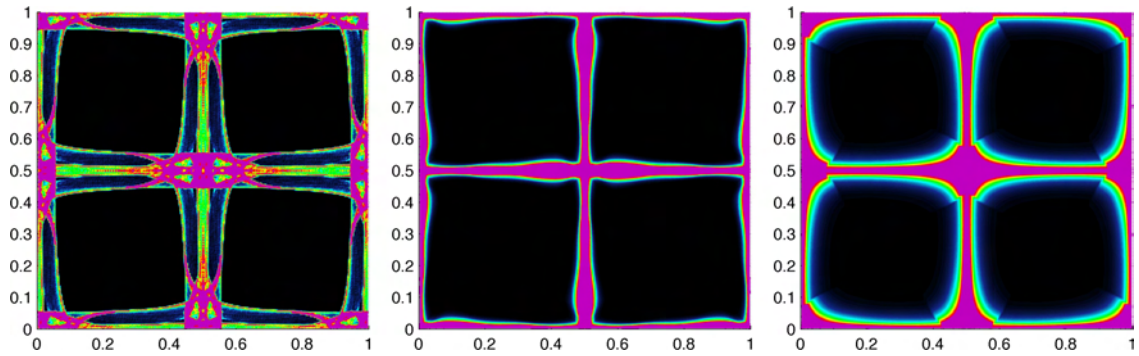

Figure 11.6: *Taylor-Green Vortices for $St = 5St_c$: number density field at time $t = 4$ for the stochastic-Lagrangian (left), and the Eulerian isotropic (center) and anisotropic (right) Gaussian closures.*

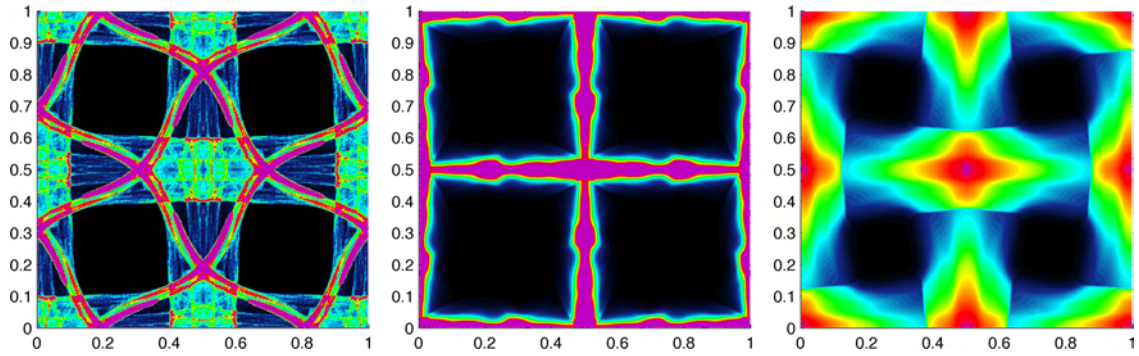

Figure 11.7: *Taylor Green Vortices for $St = 10St_c$: number density field at time $t = 4$ for the stochastic-Lagrangian (left), and the Eulerian isotropic (center) and anisotropic (right) Gaussian closures.*

To further analyze the behavior of both Eulerian model, the central moments are plotted for $\mathrm{St} = 10\mathrm{St}_c$ at $t = 4$ in Figure 11.10, Figure 11.9, and Figure 11.10 for AG, IG and stochastic-Lagrangian respectively. These results highlight that the velocity distribution of the crossing zones is clearly anisotropic in the stochastic-Lagrangian reference. Considering that the energy level is sufficiently high to influence the dynamics, it is then logical that the AG model is better than the IG model to capture such physics.

[1]In Yuan and Fox (2011); Laurent et al. (2012) more nodes have been used and it permits to capture such structures.

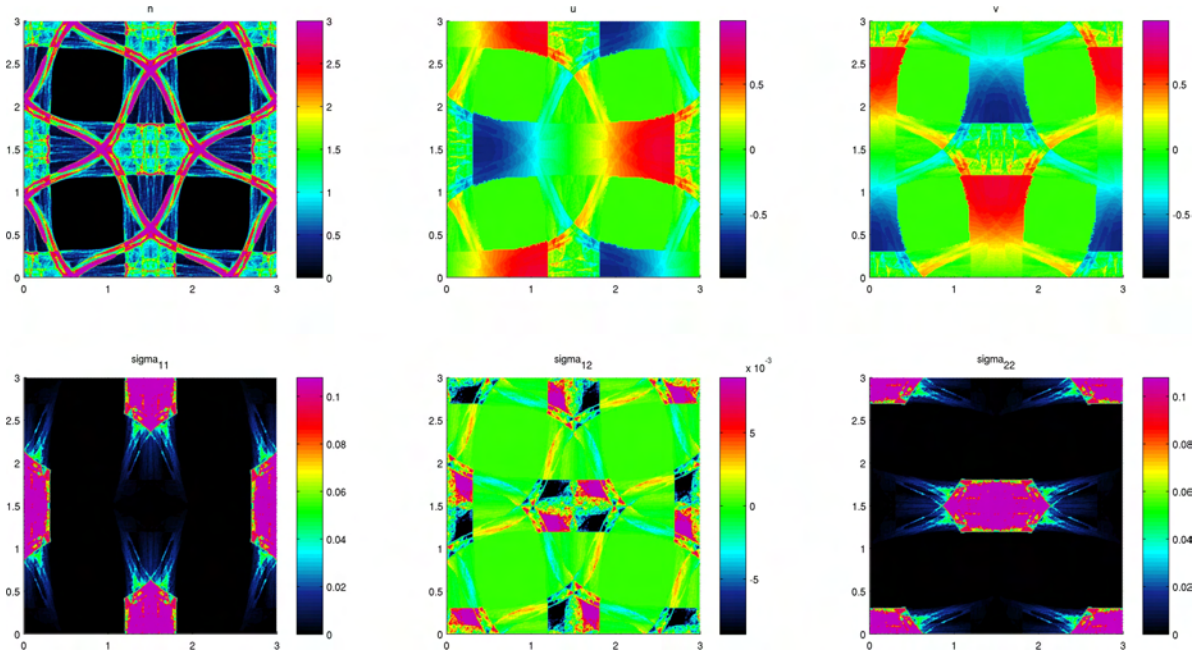

Figure 11.8: *Taylor Green Vortices for $St = 10St_c$ for the stochastic-Lagrangian at time $t = 4$: number density field (upper left), mean x-velocity (upper center), mean y-velocity (upper right), xx-covariance (lower left), xy-covariance (lower center) and yy-covariance lower right).*

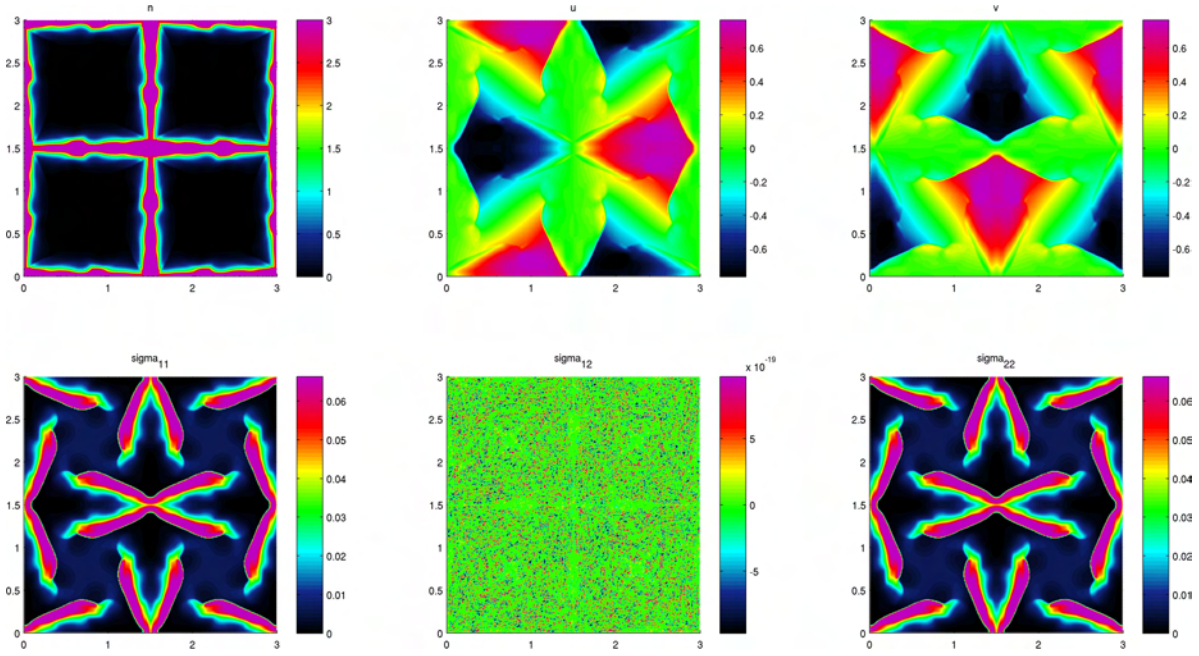

Figure 11.9: *Taylor Green Vortices for $St = 10St_c$ for the Eulerian Isotropic Gaussian closure at time $t = 4$: number density field (upper left), mean x-velocity (upper center), mean y-velocity (upper right), xx-covariance (lower left), xy-covariance (lower center) and yy-covariance lower right).*

11.4.2.2 Statistics

In the following of the two-jet crossing case, we further investigate the behavior of our models by means of statistical quantities namely the segregation and the energy budget. Statistics are plotted in Figure 11.11-11.13 for $\mathrm{St} = \mathrm{St}_c$, $5\mathrm{St}_c$, and $10\mathrm{St}_c$.

At $\mathrm{St} = \mathrm{St}_c$, the segregation is high due to the accumulation of particles in low vorticity zones. The mean central energy is relatively small compared to the mean total energy. Both IG and AG reproduce the profile of the time evolution but they do not recover the same levels. The segregation is underestimated by both models, AG giving the best result compared to the Lagrangian reference. The mean central energy is well captured by both approaches but the mean total energy is better captured by AG, which can be directly linked to the segregation results: as we consider phase-average values, missing the description of the

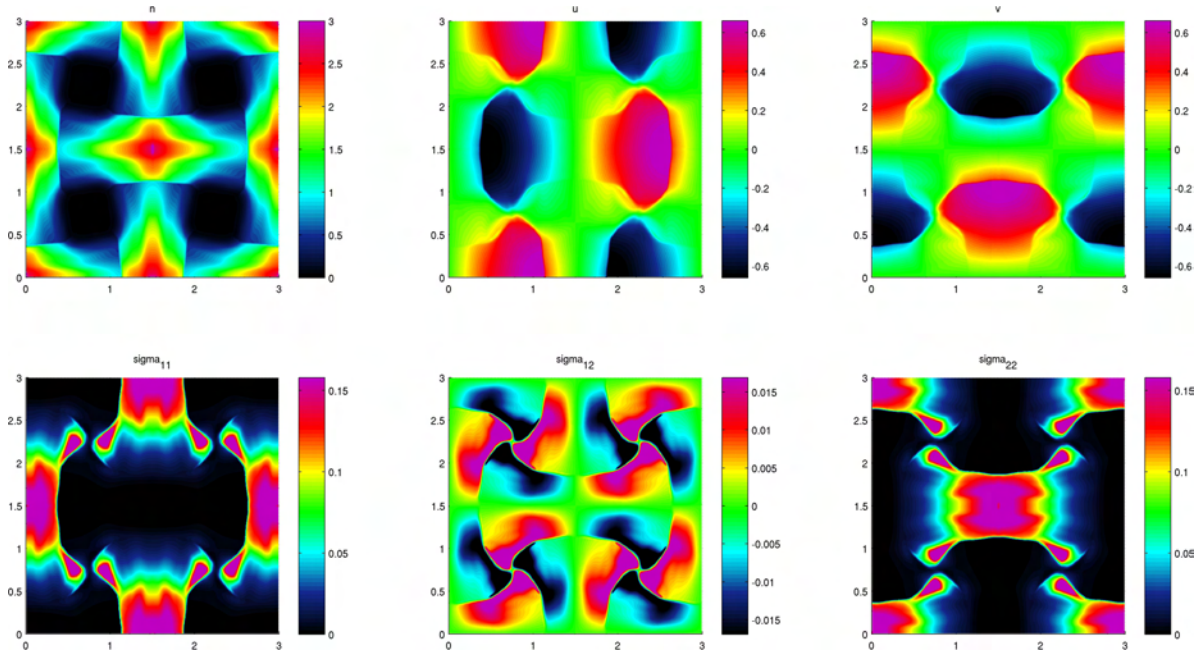

Figure 11.10: *Taylor Green Vortices for $St = 10St_c$ for the Eulerian Anisotropic Gaussian closure at time $t = 4$: number density field (upper left), mean x-velocity (upper center), mean y-velocity (upper right), xx-covariance (lower left), xy-covariance (lower center) and yy-covariance lower right).*

segregation will limit the ability to capture the mean total energy, which is also sensitive to the segregation. At $St = 5St_c$ the AG captures well all the statistics under study, whereas the IG overestimates the segregation. This is a consequence of the underestimation of the mean central energy: actually, the internal energy generates the width of the structures and in the case of IG this energy is too small to capture the correct width.
At $St = 10St_c$, the IG closure again strongly overestimates the segregation, whereas the AG leads to good results but for a short time only. In terms of energy, the results of AG are again only predictive for a short time, the long-time behavior being missed by both Eulerian approaches.

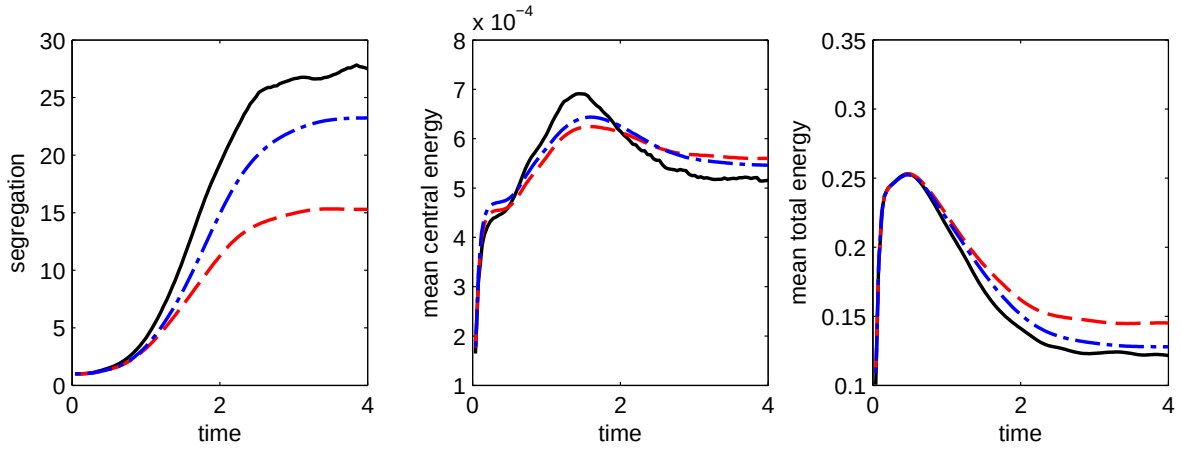

Figure 11.11: *Taylor Green Vortices for $St = St_c$: time evolution of the segregation (left), mean central energy (center), and mean total energy (right) for the stochastic-Lagrangian (black full line), the Eulerian Isotropic (red dashed line) and Anisotropic (blue dot-dashed line) Gaussian closures.*

To conclude on the TG case, compared to the stochastic-Lagrangian reference, the AG gives better results than the IG, because the anisotropy of the velocity distribution is mandatory to reproduce the directional information within homo-PTC zones. In terms of instantaneous field or statistics, AG leads to satisfactory results for moderate Stokes number but at high Stokes number the method becomes less predictive.

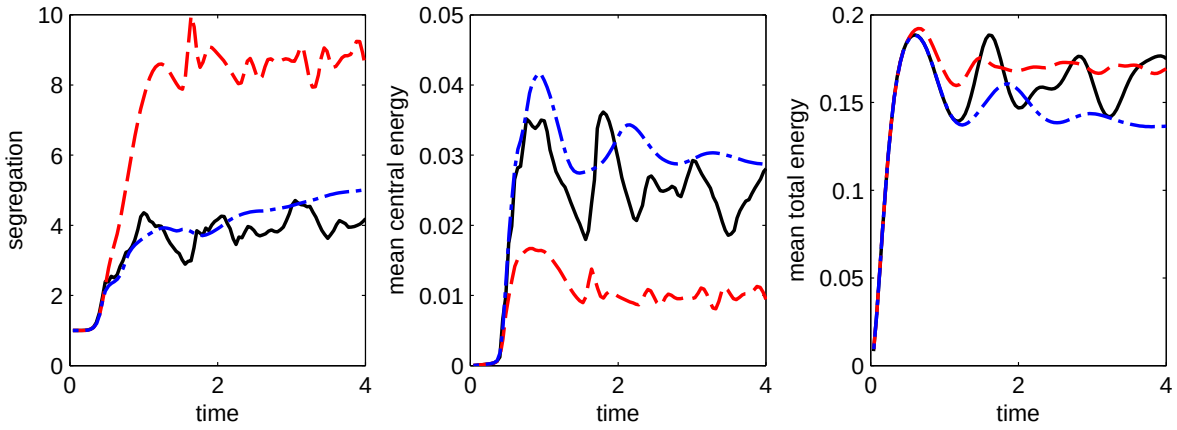

Figure 11.12: *Taylor Green Vortices for $St = 5St_c$: time evolution of the segregation (left), mean central energy (center), and mean total energy (right) for the stochastic-Lagrangian (black full line), the Eulerian Isotropic (red dashed line) and Anisotropic (blue dot-dashed line) Gaussian closures.*

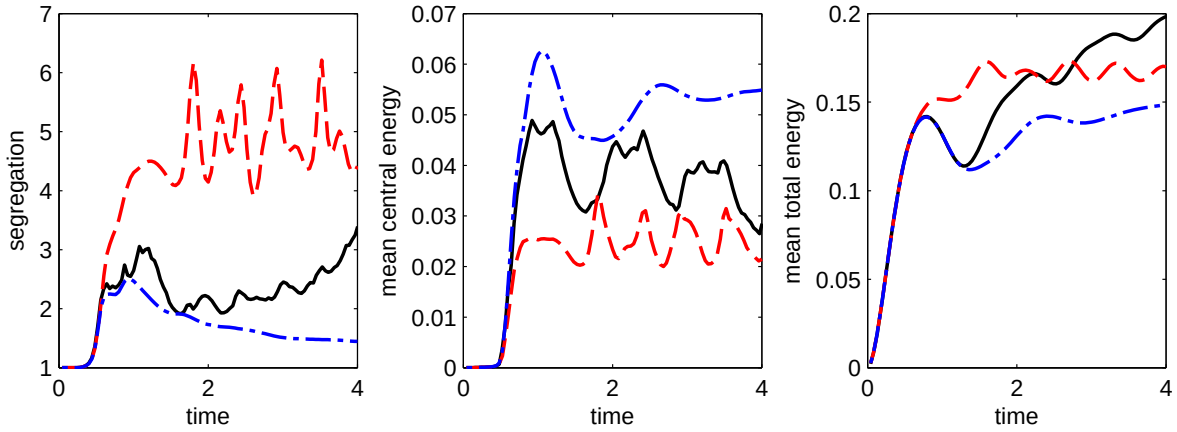

Figure 11.13: *Taylor Green Vortices for $St = 10St_c$: time evolution of the segregation (left), mean central energy (center), and mean total energy (right) for the stochastic-Lagrangian (black full line), the Eulerian Isotropic (red dashed line) and Anisotropic (blue dot-dashed line) Gaussian closures.*

11.4.3 Decaying Homogeneous Isotropic Turbulence

The Homogeneous Isotropic Turbulence (HIT) case is closer to real applications than the TG case. The gaseous flow field consists in a full spectrum of space and time scales, whereas TG has a unique and steady scale, and is time-evolving so that the large-scale sweeping of small scales is present. Such a case is a mandatory step for each modeling method before going to more complex applications and is extensively investigated in the literature (Reeks 1977; Squires and Eaton 1991b; Zaichik and Alipchenkov 2003; Fevrier et al. 2005; Kaufmann et al. 2008).
Here we consider a flow field generated by the Asphodele code (see § 10.5.1). All quantities are non-dimensional. The domain is 3×3. we investigate instantaneous solutions as well as spatial-averaged statistics. The parameters of the turbulent field at $t = 0$ are listed in Table **??**. The evolution of the mean kinetic energy and the Kolmogorov time scale are plotted in Figure **??**, showing that the present HIT is decaying in energy, leading to an increasing Kolmogorov time scale.

Re_t	u_t	ϵ	η_K	l_{int}	τ_K	τ_{int}
7.12	0.1	0.01	0.022	0.1	0.36	1.0

Table 11.1: *Turbulence properties at time $t = 0$.*

In the following the Stokes number will be considered as the ratio of the relaxation time of particles to the Kolmogorov time scale at $t = 0$:

$$\mathrm{St} = \frac{\tau_p}{\tau_K}.$$

This Stokes number is the most relevant in our case, as we will start with equal velocities for gas and

disperse phases at $t = 0$, so that crossings are generated at time $t = 0$. Similarly to TG case, we investigate instantaneous solutions as well as space-average statistics.

11.4.3.1 Instantaneous fields

The instantaneous flow field at time $t = 3.6$ is plotted in Figure 11.14, Figure 11.15, and Figure 11.16 for St $= 1$, 5 and 10 respectively. Similarly as in the TG case, negligible homo-PTC is expected at St $= 1$ and the two Eulerian simulations therefore give similar results, all comparable to the stochastic-Lagrangian reference though being more diffusive. At St $= 5$, the stochastic-Lagrangian result exhibits mixing zones like in the TG case, where particles oscillate around the low vorticity zones, but no long-time equilibrium manifolds, which cannot be captured by neither IG nor AG. The two Eulerian approaches capture the mixing zones, but their widths are closer to the stochastic-Lagrangian ones with the AG model. At St $= 10$, these structures become wider, and again the AG model leads to better results.

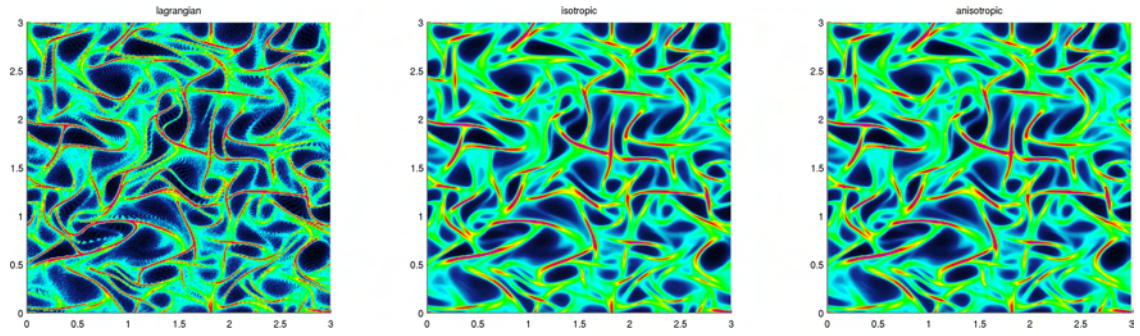

Figure 11.14: *HIT case for St $= 1$: number density field at time $t = 3.6$for the stochastic-Lagrangian (left), and the Eulerian isotropic (center) and anisotropic (right) Gaussian closures.*

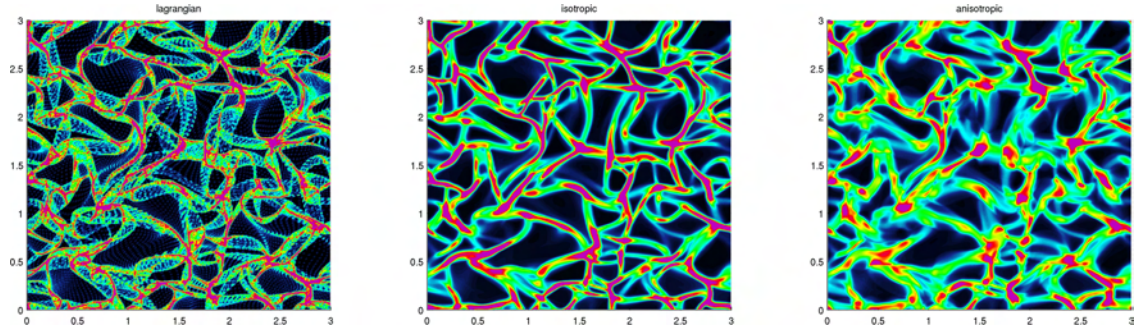

Figure 11.15: *HIT case for St $= 5$: number density field at time $t = 3.6$for the stochastic-Lagrangian (left), and the Eulerian isotropic (center) and anisotropic (right) Gaussian closures.*

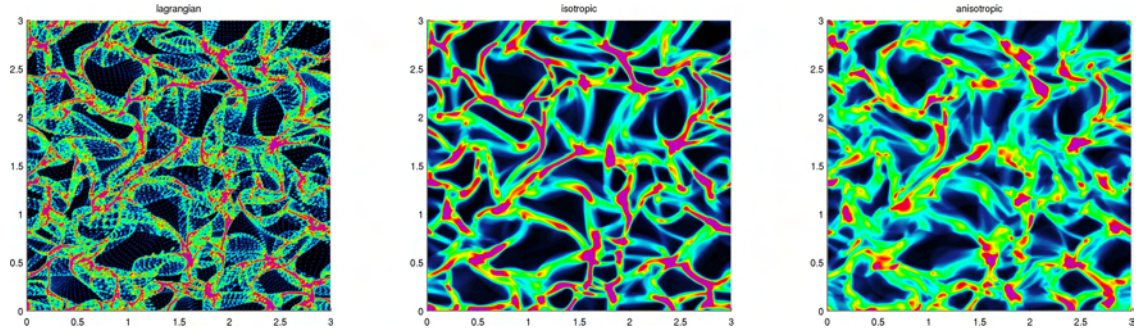

Figure 11.16: *HIT case for St $= 10$: number density field at time $t = 3.6$for the stochastic-Lagrangian (left), and the Eulerian isotropic (center) and anisotropic (right) Gaussian closures.*

11.4.3.2 Statistics

We investigate the same statistics as the TG case, i.e. the segregation, the mean central energy and the mean total energy. For St $= 1$, the two Eulerian model give the same results. The comparison with the stochastic-

Lagrangian reference is satisfactory, even if the segregation is slightly underestimated. For St = 5, the two models give now different results. The AG model underestimates the segregation while overestimating the mean central energy, whereas the IG model has an opposite behavior. However the mean total energy is well reproduced only by the AG model. The analysis is the same for St = 10.
To better estimate the quality of the model, we perform in Figure 11.20 a mesh sensitivity analysis for all statistics at St = 10. Compared to the TG case, where the generated scales of the particulate phase are relatively wide, the scales generated by the HIT case are small compared to the mesh size. The results show that refining the mesh, thus reducing the numerical diffusive, tends to increase the segregation and to decrease the mean central energy. Whereas the mesh refinement degrades the IG results, AG results are more and more closer to the stochastic-Lagrangian results. It clearly shows the importance of the numerical methods for Eulerian models: second order schemes are a minimum requirement for turbulent computations. Less dissipative second order scheme based on Discontinuous Galerkin methods are in development (Larat et al. 2012) and higher order schemes could be envisioned.

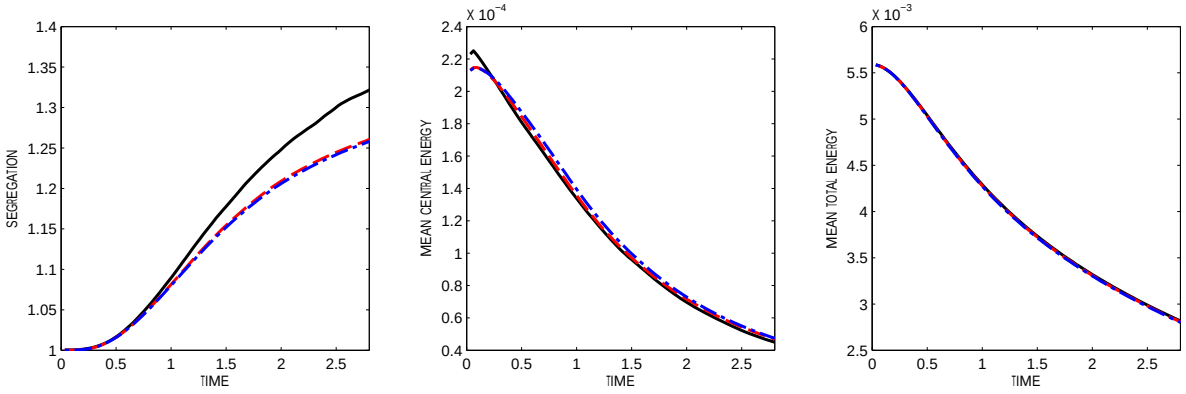

Figure 11.17: *HIT case for St = 1: time evolution of the segregation (left), mean central energy (center), and mean total energy (right) for the stochastic-Lagrangian (black full line), the Eulerian Isotropic (red dashed line) and Anisotropic (blue dot-dashed line) Gaussian closures.*

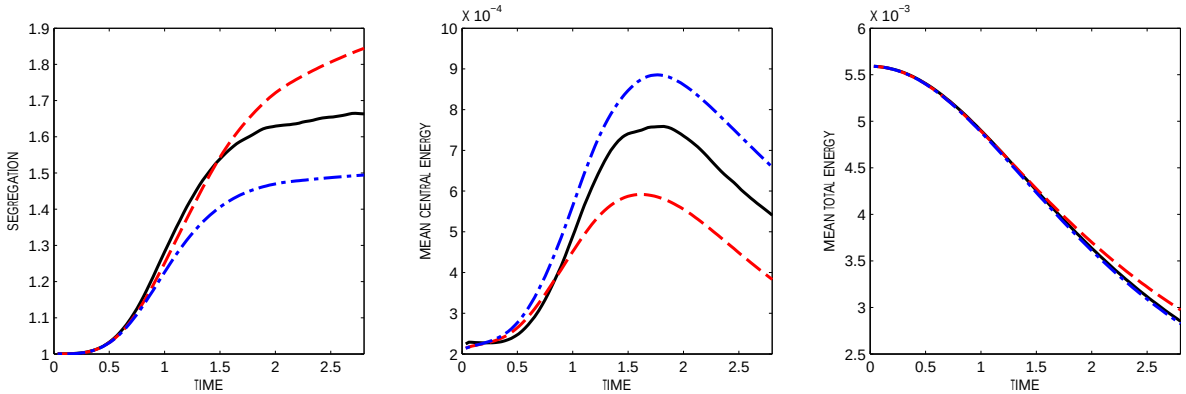

Figure 11.18: *HIT case for St = 5: time evolution of the segregation (left), mean central energy (center), and mean total energy (right) for the stochastic-Lagrangian (black full line), the Eulerian Isotropic (red dashed line) and Anisotropic (blue dot-dashed line) Gaussian closures.*

11.5 Conclusion

The AG model is validated in many types of flows featuring homo-PTC: the validations are performed on the spatial structure of the number concentrations, but also on the statistics, such as segregation and energy, which strongly condition the source terms e.g. coalescence.
First an injection case into a compressive gaseous carrier flow field has been investigated. Such a configuration couples transport and drag in such a way that the fluid particle phase can be considered as hypercompressible for a range of Stokes number involving inertial particles. This case provides of good model for PTC generation in turbulent flows. Results show that the AG model is not able to reproduce the details of deterministic crossings in terms of number density spatial distribution. However it captures at least the right scale and

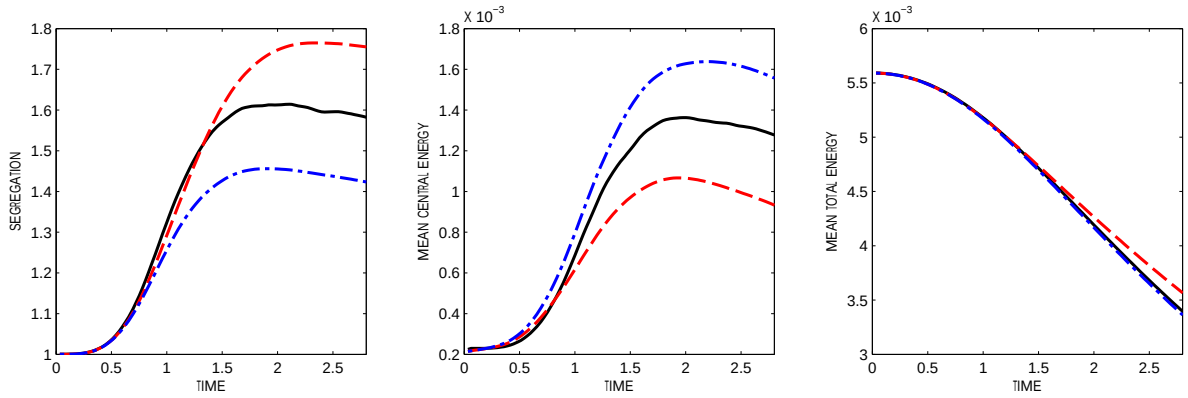

Figure 11.19: *HIT case for $St = 10$: time evolution of the segregation (left), mean central energy (center), and mean total energy (right) for the stochastic-Lagrangian (black full line), the Eulerian Isotropic (red dashed line) and Anisotropic (blue dot-dashed line) Gaussian closures.*

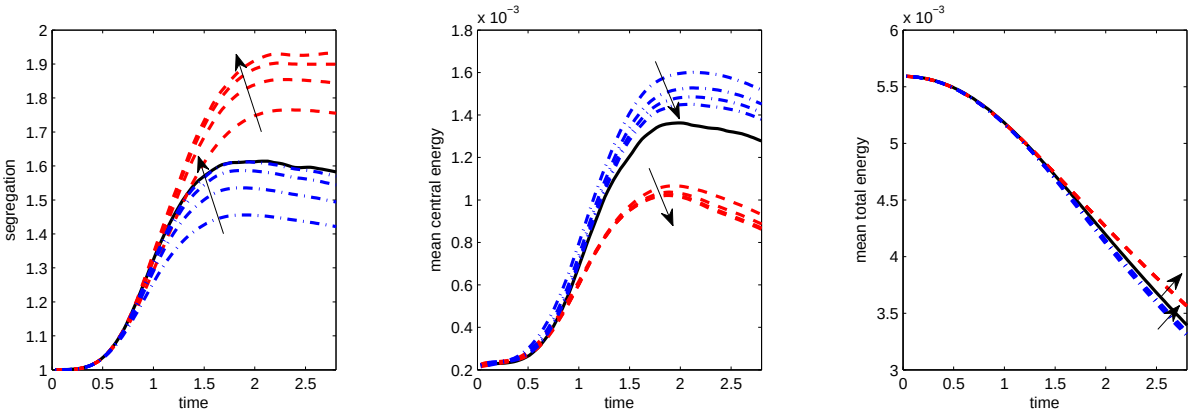

Figure 11.20: *HIT case for $St = 10$, impact of the mesh on statistics: time evolution of the segregation (left), mean central energy (center), and mean total energy (right) for the stochastic-Lagrangian (black full line), the Eulerian Isotropic (red dashed line) and Anisotropic (blue dot-dashed line) Gaussian closures. Arrows indicates growing meshes for each Eulerian model (from 256^2 to 2048^2 cells).*

the right energetic behavior. Moreover, an important aspect of this model is that, after a crossing event, it "destroys" part of the information before the crossings, only keeping the information on zero-to-second order moments in space. Thus the spatial behavior of this model is directly linked to the velocity phase space description.

Second the AG model has been evaluated on 2D turbulent-like test cases. Both Anisotropic and Isotropic Gaussian closures have been compared and we have shown the importance of having a full description of the pressure tensor in order to properly predict the segregation of particles, a key feature for combustion application for example. In the Taylor Green vortices the two Eulerian models are not able to get the details of the spatial distribution. However as in the injection case the AG model captures the characteristic scales of the flow, where IG cannot. In the decaying turbulence the AG model renders a more relevant segregation than IG. Moreover a mesh sensitivity analysis shows that the AG results reproduce the Lagrangian solution, whereas IG does not. The partition between mean and internal energies is also better capturer by the AG model and the mesh sensitivity analysis again demonstrates that AG model reproduces the Lagrangian solution.

In conclusion the AG model in conjunction with the accurate MUSCL/HLL scheme that has been proposed are an interesting robust strategy for the simulation of particle laden flows. However, some aspects of the results have to be understood as consequences of the modeling approach: such a presumed-velocity-PDF approach is not supposed to capture the full range of scales but to reproduce some statistical quantities correctly at the scale of the crossings. Moreover the impossibility to make the difference between deterministic crossings and the variability imposed by initial/boundary conditions after the crossing event has to be kept in mind in the interpretation of the results. It has also been shown that such an approach is robust for shear layers, compared to ACBMM methods (Vié et al. 2012).

The good behavior of AG can be summed up as follows:

- AG never generates singularities when crossings occur,
- AG captures the minimum information on crossings,

- AG can however not capture the exact information of deterministic crossings (e.g. bimodal),
- AG captures efficiently the mixing zones where many crossings occur.

The method is promising for two-way coupling and for homo-DTC coalescence, the latter phenomenon being studied in Chapter 13. As a remark, the coupling of AG with a LES approach is also promising since the disperse phase's velocity distribution limit when $\mathrm{St} \to 0$ is an anisotropic Gaussian with its covariance equal to that of the gas sub-grid scale energy, so the coupling is straightforward.

Chapter 12

Achieving two-way coupling for unsteady moderately dense polydisperse two-phase flows

A new time integration is introduced to accurately capture two-way coupling in the context of polydisperse sprays. The resolution of two-way polydisperse flows is first studied in the particular context of two-phase acoustics. This approach brings a quantitative verification of the new strategy versus an analytical formula. The new strategy is then validated in cases featuring convection, and its robustness is shown in various cases. The treatment of disperse phase sources with a similar splitting strategy is finally developed.

12.1 Introduction

The motivations to develop a new time integration strategy originate from the multi-scale, strongly coupled nature of polydisperse moderately dense two-phase flows. For instance the MF method described in § 4.4.5 achieves an accurate treatment of size distributions for a large size range including inertial particles/droplets in a CFD framework. But computing transport in physical space for both the gas and the particle sections, and eventually capturing the coupling at all time scales, is computationally expensive, especially for unsteady problems. So we seek a MF method:

- that features an accurate treatment in the sections in order to reduce their number,
- that allows to avoid taking a small time step when small, low inertia particles are involved.

For size accuracy high order MF methods exist with reconstructed size distributions converging towards the NDF at order one (Laurent and Massot 2001), two (Doisneau et al. 2013), or even four (Kah et al. 2012) and the time integration method must respect the properties of these methds. For coupling, efforts must be done to allow the use of larger time steps. In the context of dense sprays, the stiffness of small particles has been identified and occurs similarly by means of short velocity and heat relaxation times (Burman and Sainsaulieu 1995). Numerical approaches based on modifications at the Riemann solver level allow to capture accurately all the waves in the asymptotic limit of small particles (Béreux and Sainsaulieu 1997) but it is complex to design methods suited and accurate for all the size range (Béreux 1996).

The time integration strategies presented in Chapter 10 resort either to an *a priori* approach (the fully coupled integration) or to a pragmatic approach guided by computational requirements and liability constraints (the BWC approach, described in § 10.3.4.3). The BWC which is used in some industrial codes allows indeed to keep the structure of the liquid and gas solvers, as written for a one-way coupled context. If the fully coupled integration is incompatible with HPC, the latter is inaccurate and unstable for fast particles and for moderate to strong mass loadings.

So a strategy has been developed and studied for our polydisperse strongly coupled case: the operator splitting technique gives flexibility and allows to control the error of the method: it is well suited for two-way coupling and is efficient for small particles (with fast scales) since it is robust and accurate even with a reasonable time step. This strategy is the result of a collaborative work with A. Sibra: it has been published in Doisneau et al. (2013). Its results on unsteady, fully coupled SRM cases e.g. instabilities are proven to be satisfactory, and especially its ability to deal with the unsteady transport of moderately dense sprays: this aspect is fundamental and results are presented on an academic case in § 12.4 and this features moreover plays a strong role to capture the two-way coupling in a nozzle and assess the two-phase effects and the specific impulse losses.

All these results are promising enough for the method to be extended to complex phase space source terms, the latter yielding a strong coupling between the sections. The structure of the complex couplings generated by such sure terms is presented below, in § 12.5. The method has indeed been used when coalescence occurs (Doisneau et al. 2013) and unsteady results are satisfactory and presented in Chapter 15. The approach is also furthered by Sibra (2014) to account for aluminum combustion in SRMs and predict complex unsteady and coupled phenomena such as ITHAC (see § 1.3.2.5).

12.2 The Acoustic-Convection Splitting: a sound and adaptable strategy

A new strategy is designed to preserve all the physical features of the two-phase flow. It is based on a two-stage operator splitting to decouple particle convective phenomena from two-phase acoustics. This technique is referred to as the acoustic-convection splitting (ACS). The work of this section was presented in Doisneau et al. (2011) and published in Doisneau et al. (2013).

12.2.1 Context

12.2.1.1 A model representative of polydisperse moderately dense flows

We consider System (4.70) as a model for our two-way coupled polydisperse problem. It is written with an Euler system of equations for the gas phase but the method can be extended to Navier-Stokes equations straightforward. It is reproduced here for the sake of legibility:

$$\left\{\begin{array}{l} \partial_t \rho_g + \partial_{\boldsymbol{x}}\cdot(\rho_g \boldsymbol{u}_g) = 0 \\ \partial_t(\rho_g \boldsymbol{u}_g) + \partial_{\boldsymbol{x}}\cdot(\rho_g \boldsymbol{u}_g \otimes \boldsymbol{u}_g) = -\partial_{\boldsymbol{x}} p - \displaystyle\sum_{k=1} m_k \boldsymbol{F}_k \\ \partial_t(\rho_g e_g) + \partial_{\boldsymbol{x}}\cdot(\rho_g e_g \boldsymbol{u}_g) = -p\partial_{\boldsymbol{x}}\cdot\boldsymbol{u}_g - \displaystyle\sum_{k=1} m_k \mathrm{H}_k + \sum_{k=1} m_k \boldsymbol{F}_k(\boldsymbol{u}_g - \boldsymbol{u}_k) \\ \left.\begin{array}{l} \partial_t m_k + \partial_{\boldsymbol{x}}\cdot(m_k \boldsymbol{u}_k) = 0 \\ \partial_t(m_k \boldsymbol{u}_k) + \partial_{\boldsymbol{x}}\cdot(m_k \boldsymbol{u}_k \otimes \boldsymbol{u}_k) = m_k \boldsymbol{F}_k \\ \partial_t(m_k h_k) + \partial_{\boldsymbol{x}}\cdot(m_k h_k \boldsymbol{u}_k) = m_k \mathrm{H}_k \end{array}\right\} \quad k \in [\![1, N_{\mathrm{sec}}]\!] \end{array}\right. \tag{12.1}$$

with Stokes closures for the transfer terms, without loss of generality, as long as the time integration method chosen for these sources deals with a general form of drag and heat transfer. The OSM Multi-Fluid model is used as a minimum representation of the peculiarities of polydisperse moderately dense sprays. The numerical peculiarities of PGD can then bring in unphysical singularities, which are troublesome in two-way coupling contexts as regards the model (see § 4.3.2.2) and the numerical method (see § 10.3.1.1). Polykinetic closures are developed to solve this issue. But we here discuss and develop a method that ensures two-way coupling between the gas and a disperse phase modeled with PGD eventhough discrepancies can be expected when δ-shocks form, keeping in mind that our numerical approach has however been designed to remain relevant for new modelings, e.g. polykinetic closures. Indeed the strategy can be directly extended to higher order size or velocity moment methods. It is done so as regards a high order size moment method in the industrial computations achieved below, since the CEDRE code features the TSM method. The inclusion of coalescence and break-up is straightforward and the case of coalescence is described afterwards.

12.2.1.2 Choice of a splitting method

To approach the above model system, a numerical method based on operator splitting is introduced: this ensures a robust and accurate two-way coupling for moderately dense sprays. The splitting techniques have been introduced and discussed in § 10.3.4.1

The new method is referred to as Acoustic-Convective Splitting (ACS) since it has been designed to treat efficiently the fast scales of acoustics in a two-phase context. Its benefits on cost and accuracy are quantified on two-phase acoustics. In complex flows however, two-way coupling unsteadiness has a similar sensitivity to polydispersity so the method is *a priori* well adapted for SRM cases.

12.2.2 Operator formalism

We consider the conservative variable vector $\boldsymbol{U}(t) \in \mathbb{R}^{3N_{\mathrm{sec}}+3}$:

$$\begin{array}{rl} \boldsymbol{U}(t) & = [\boldsymbol{U}_g, (\boldsymbol{U}_k)_{k=1,N_{\mathrm{sec}}}]^T(t) \\ & = [\rho_g, \rho_g \boldsymbol{u}_g, \rho_g e_g, (m_k, m_k \boldsymbol{u}_k, m_k h_k)_{k=1,N_{\mathrm{sec}}}]^T(t) \end{array} \tag{12.2}$$

so that the coupled gas and disperse phase system given in System (12.1) can be written as a time marching operator $\mathcal{S}$ applying on $\boldsymbol{U}$:

$$\boldsymbol{U}(t+\Delta t) = \mathcal{S}(\Delta t)\boldsymbol{U}(t). \tag{12.3}$$

and depending on the time step Δt.
System (12.1), where coalescence and break-up are not considered for simplicity, is considered as composed of transport operators $\mathscr{T}_g$ and the $\mathscr{T}_k$'s and a relaxation operator $\mathscr{R}_{g\sum k}$:

$$\mathcal{S} = \left\{ \mathscr{T}_g + \left(\sum_{k=1}^{N_{\text{sec}}} \mathscr{T}_k \right) + \mathscr{R}_{g\sum k} \right\} \tag{12.4}$$

with the non-classical notation according to which the sum of operators is the fully coupled, exact operator. All these sub-operators apply on $\boldsymbol{U}$ so that we can equivalently write System (12.1) between t and $t+\Delta t$:

$$\begin{aligned} \boldsymbol{U}(t+\Delta t) &= \mathcal{S}(\Delta t)\, \boldsymbol{U}(t) \\ &= \left\{ \mathscr{T}_g + \left(\sum_{k=1}^{N_{\text{sec}}} \mathscr{T}_k \right) + \mathscr{R}_{g\sum k} \right\}(t)\, \boldsymbol{U}(t). \end{aligned} \tag{12.5}$$

where the operators include boundary conditions so they may depend on time t.

12.2.2.1 Gas transport

The gas transport operator $\mathscr{T}_g$ accounts for full-Mach gaseous dynamics (convection and acoustics). Though it applies on $\boldsymbol{U}$, it does not modify the other phases' variables. It can be written as an equivalent system of Partial Differential Equations:

$$\mathscr{T}_g \left\{ \begin{array}{c} \partial_t \rho_g + \partial_{\boldsymbol{x}} \cdot (\rho_g \boldsymbol{u}_g) = 0 \\ \partial_t (\rho_g \boldsymbol{u}_g) + \partial_{\boldsymbol{x}} \cdot (\rho_g \boldsymbol{u}_g \otimes \boldsymbol{u}_g) = -\partial_{\boldsymbol{x}} p \\ \partial_t (\rho_g e_g) + \partial_{\boldsymbol{x}} \cdot (\rho_g e_g \boldsymbol{u}_g) = -p \partial_{\boldsymbol{x}} \cdot \boldsymbol{u}_g \end{array} \right. \tag{12.6}$$

12.2.2.2 Section transport

The N_{sec} transport operators $\mathscr{T}_k$ account for the particle convection of the sections. Each operator k applies on $\boldsymbol{U}$ but modifies only the k variables: it does not modify the other phases' variables so that transport occurs independently for all the "fluids".
It can be written as an equivalent system of Partial Differential Equations:

$$\mathscr{T}_k \left\{ \begin{array}{c} \partial_t m_k + \partial_{\boldsymbol{x}} \cdot (m_k \boldsymbol{u}_k) = 0 \\ \partial_t (m_k \boldsymbol{u}_k) + \partial_{\boldsymbol{x}} \cdot (m_k \boldsymbol{u}_k \otimes \boldsymbol{u}_k) = 0 \\ \partial_t (m_k h_k) + \partial_{\boldsymbol{x}} \cdot (m_k h_k \boldsymbol{u}_k) = 0 \end{array} \right. \tag{12.7}$$

12.2.2.3 Relaxation transport

The relaxation operator $\mathscr{R}_{g\sum k}$ describes drag and heating between the gas and the disperse phase. It can be written as the equivalent system of PDEs:

$$\mathscr{R}_{g\sum k} \left\{ \begin{array}{l} \partial_t \rho_g = 0 \\ \partial_t (\rho_g \boldsymbol{u}_g) = -\displaystyle\sum_{k=1}^{N_{\text{sec}}} m_k \boldsymbol{F}_k \\ \partial_t (\rho_g e_g) = -\displaystyle\sum_{k=1}^{N_{\text{sec}}} m_k \mathrm{H}_k + \sum_{k=1}^{N_{\text{sec}}} m_k \boldsymbol{F}_k (\boldsymbol{u}_g - \boldsymbol{u}_k) \\ \left. \begin{array}{l} \partial_t m_k = 0 \\ \partial_t (m_k \boldsymbol{u}_k) = m_k \boldsymbol{F}_k \\ \partial_t (m_k h_k) = m_k \mathrm{H}_k \end{array} \right\} \quad k \in [\![1, N_{\text{sec}}]\!] \end{array} \right. \tag{12.8}$$

which modifies all the variables of $\boldsymbol{U}$ except ρ_g and the m_k.
This operator ensures the coupling between each section and the gas, corresponding to the relaxation of the dynamic and thermal quantities by drag and heating towards the equilibrium described in § 4.7.4.2. As a consequence, all the "fluids" are coupled together, this fact being discussed previously and illustrated in Figure 10.5.
Still this coupling is local in space since convection is not considered. The relaxation operator has two major features:

- local conservation of mass, total momentum and total energy of the spray.
- attraction towards an equilibrium state described by formula (4.72).

12.2.3 A two-stage splitting strategy

We suggest a two-stage splitting based on the following time scale hierarchy: disperse phase convection generally yields the slowest scales while the fastest scales are some of the gas transport, namely the ones linked to acoustic waves. The relaxation scales are to be linked to the acoustic scales in order to account for two-phase acoustics.
The notations for the splitting schemes are those of § 10.3.4.1 but we note $e^{A\Delta t} = A(\Delta t)$ and $e^{(A+B)\Delta t} = \{A + B\}(\Delta t)$ for the sake of legibility.

12.2.3.1 Remarks on disperse phase transport

We want to assess the displacement of particles in an acoustic field of pulsation ω which we refer to as acoustic displacement Δx_p^ω.
The acoustic wave is characterized by a local velocity which fluctuates:

$$\boldsymbol{u}_g(t) = \boldsymbol{u}'_g \sin(\omega t) \tag{12.9}$$

where $|\boldsymbol{u}'_g| = u'_g = p'_g/(\rho_{g0} c_0)$ so that the fluid particles of the gas encounter a displacement of $\Delta x^\omega = 2\frac{u'_g}{\omega}$
For the acoustic wave to remain in linear regime it is required to have $u'_g \ll c_0$ (Morse and Ingard 1987) or equivalently $\Delta x^\omega \ll \lambda^\omega/\pi$ with λ^ω the wave length. If the linear limit is set to $u'_g/c_0 = 10^{-2}$, it corresponds to a sound pressure level of 153 dB at atmospheric pressure and around 190 dB at a typical SRM chamber pressure.
We decompose the particle velocity:

$$\boldsymbol{u}_p(t) = \boldsymbol{u}_{p0}(t) + \boldsymbol{u}'_p(t) \tag{12.10}$$

where $\boldsymbol{u}'_p$ is a perturbation imposed by the passage of an acoustic wave. According to the properties of the drag equation, the particles oscillate within $[-\boldsymbol{u}'_g, \boldsymbol{u}'_g]$ and $\boldsymbol{u}_p(t) = \boldsymbol{u}_g(t)$ at the limit of $\mathrm{St} = 0$. So that their maximum displacement is the one of the fluid particles of the gas:

$$\Delta x_p^\omega = \Delta x^\omega = 2\frac{u'_g}{\omega}. \tag{12.11}$$

We consider cases where the mesh size Δx is large compared to the particle displacement Δx_p so that the acoustic displacement is not seen i.e. filtered by the space discretized Eulerian equations of the disperse phase.
Of course, for the acoustic wave to propagate in the discretized problem, we need Δx to be smaller than the acoustic wave length λ^ω so that we finally have the bracketing:

$$\Delta x_p^\omega < \Delta x < \lambda^\omega \tag{12.12}$$

which ensures to filter the material displacements but not the wave.
From this statement, we develop a time integration strategy based on the separation between the scales of the acoustic wave and the scales of particle convection (due to non-acoustic velocity): the purely convective velocity $\boldsymbol{u}_{p0}$ is assumed to generate a significant transport at the mesh scale Δx while the acoustic displacement $\boldsymbol{u}'_p$ does not. The latter is therefore not solved by the new strategy.

12.2.3.2 Acoustic operator

We focus on the resolution of two-phase acoustics in the reference frame of the disperse phase i.e. $\boldsymbol{u}_{p0} = 0$. According to the above considerations, particle convective transport does not need to be solved.
Two-phase acoustics was defined in § 4.7.3 as the interaction between gaseous compressible effects and the disperse phase, in the case of perturbations with a wave-length wider than the particles sizes. This physics is described by the acoustic operator:

$$\mathscr{A}_{g\sum k} = \left\{\mathscr{T}_g + \mathscr{R}_{g\sum k}\right\} \tag{12.13}$$

where no disperse phase transport is performed.
The dynamics of this operator has a characteristic time Δt_a.

12.2.3.3 Disperse phase convection splitting

In cases where the disperse phase convection is significant, we want to solve the effects of $\boldsymbol{u}_{p0} \neq 0$ on transport. So the disperse phase transport is performed thanks to the $\mathscr{T}_k$ operators defined in Eq. (12.7), integrated with a splitting strategy again. This transport occurs presumably with a time step for each section $\overline{\tau}_k$ slower than the two-phase acoustics phenomena of characteristic time Δt_a. This hypothesis reads:

[S1] $\overline{\tau}_k > \Delta t_\mathrm{a}$, $k \in [\![1, N_\mathrm{sec}]\!]$
and is true in many configurations. It must be highlighted that [S1] is presumably wrong in a supersonic flow, which is discussed below.
In the context where [S1] is valid, we perform a splitting of the acoustic and disperse phase transport operator. It can be performed according to of the approaches described in § 10.3.4.1, namely a Lie splitting:

$$\mathcal{S}^\mathrm{Lie}(\Delta t_\mathrm{c}) = \mathscr{A}_{g\sum k}(\Delta t_\mathrm{c}) \left\{ \sum_{k=1}^{N_\mathrm{sec}} \mathscr{T}_k \right\} (\Delta t_\mathrm{c}) \tag{12.14}$$

or a Strang splitting:

$$\mathcal{S}^\mathrm{Strang}(\Delta t_\mathrm{c}) = \mathscr{A}_{g\sum k}\left(\frac{\Delta t_\mathrm{c}}{2}\right) \left\{ \sum_{k=1}^{N_\mathrm{sec}} \mathscr{T}_k(\Delta t_\mathrm{c}) \right\} (\Delta t_\mathrm{c}) \;\; \mathscr{A}_{g\sum k}\left(\frac{\Delta t_\mathrm{c}}{2}\right). \tag{12.15}$$

where the order is chosen to perform the acoustics operator at last, for reasons explained below.
If each operator is solved with a numerical strategy that is at least second order in time, the suggested Strang splitting (Strang 1968) ensures a second order convergence with Δt_c towards $\mathcal{S}$ as long as the solution is regular: this is not the case in the presence of shock waves.
The convective splitting time step Δt_c is chosen to allow disperse phase convection to occur at its physical time scale which matches numerical criterion of the transport scheme:

$$\Delta t_\mathrm{c} \sim \overline{\tau}_k^c.$$

In addition the disperse phase transport solver is called less often than in a fully coupled strategy which spares CPU resources.

12.2.3.4 Acoustic operator splitting

We now focus on the acoustic operator itself, which we may approximate with first or second order splitting strategies. The first order Lie splitting reads:

$$\mathscr{A}^\mathrm{Lie}_{g\sum k}(\Delta t_\mathrm{a}) = \mathscr{R}_{g\sum k}(\Delta t_\mathrm{a}) \;\; \mathscr{T}_g(\Delta t_\mathrm{a}) \tag{12.16}$$

and the Strang splitting:

$$\mathscr{A}^\mathrm{Strang}_{g\sum k}(\Delta t_\mathrm{a}) = \mathscr{R}_{g\sum k}\left(\frac{\Delta t_\mathrm{a}}{2}\right) \mathscr{T}_g(\Delta t_\mathrm{a}) \;\; \mathscr{R}_{g\sum k}\left(\frac{\Delta t_\mathrm{a}}{2}\right). \tag{12.17}$$

where the order is chosen to perform the relaxation operator at last, in order to account better for the attraction towards the equilibrium state (Descombes and Massot 2004). Relaxation is indeed the only physical phenomenon that attracts towards an equilibrium sub-manifold, as shown in § 4.7.4.2, so that the corresponding operator should always be applied last for accuracy purpose.
The two-phase acoustic operator $\mathscr{A}_{g\sum k}$ performs the gas transport and the relaxation, assuming that the particles encounter acoustic effects locally and do not need to be convected on this time scale, as discussed in § 12.2.3.1. This is proven in the following to yield a satisfactory resolution of two-phase acoustics.

12.2.3.5 Time step prescription strategy

Let us now consider the requirements on the splitting time step Δt_a, which ensures the level of coupling between the gas and the particles and is therefore referred to as the coupling time step. It is set to follow the largest time scale (corresponding to the slowest phenomenon) between gas-particle relaxation and gas acoustics:

$$\Delta t_\mathrm{a} = \max\left\{K_p \tau_\mathrm{min}; K_g \tau_g\right\} \tag{12.18}$$

where K_g and K_p are security coefficients, which values are addressed later. It is indeed not necessary to ensure a coupling at so large a frequency that either the gas or the slowest particles cannot react. So τ_min is used for sprays involving only slow particles since it is larger but τ_g is used as soon as fast particles are present. Finally the coupling time step is never smaller than the gas one which allows to spare CPU resources and it can become very large when particles are big and do not react fast.
There is however an upper bound for the coupling time step, imposed by the wave period τ_ω for stability reasons. The relaxation operator should capture the average value of the acoustic wave so a minimum number of coupling instants are imposed in a period:

$$\Delta t_\mathrm{a} < \frac{\tau_\omega}{4} \tag{12.19}$$

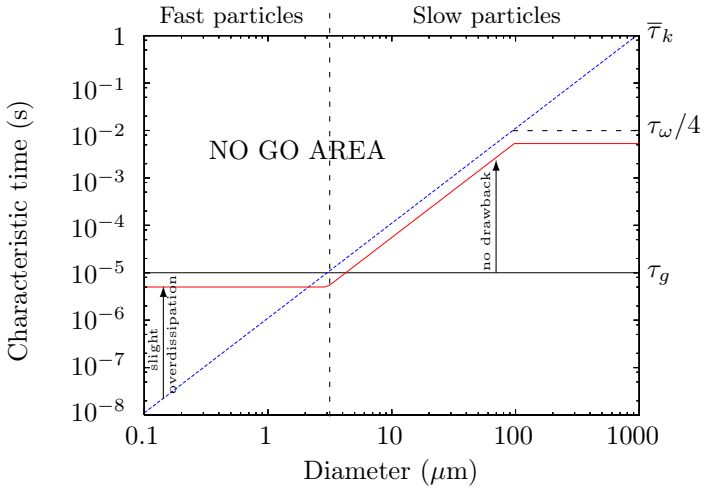

Figure 12.1: *Typical acoustics time scales plotted versus particle diameter – **Black**: gas time τ_g; Dotted: typical particle relaxation time τ_{min} (BWC timestep must be smaller); Red: prescribed acoustic time step Δt_a for ACS with $K_g = K_p = 0.5$.*

which avoids offsetting the equilibrium value of the two-phase system.
The evolution of the prescription for Δt_a depending on the smallest particle size is illustrated in Figure 12.1 with typical values for K_g and K_p.

12.2.3.6 Summary of the ACS features

The ACS strategy operates on a time step defined with the smallest disperse phase convective scale Δt_c:

$$\boldsymbol{U}(t+\Delta t_\mathrm{c}) = \mathcal{S}^{\mathrm{ACS}}(\Delta t_\mathrm{c})\boldsymbol{U}(t) \tag{12.20}$$

and the full system operator is approached by

$$\mathcal{S}^{\mathrm{ACS}}(\Delta t_\mathrm{c}) = \mathscr{A}_{g\sum k}\left(\frac{\Delta t_\mathrm{c}}{2}\right)\left\{\sum_{k=1}^{N_\mathrm{sec}}\mathscr{T}_k\right\}(\Delta t_\mathrm{c})\ \ \mathscr{A}_{g\sum k}\left(\frac{\Delta t_\mathrm{c}}{2}\right) \tag{12.21}$$

where we decompose the acoustic operator

$$\mathscr{A}_{g\sum k}(\Delta t_\mathrm{c}) = \left\{\mathscr{A}_{g\sum k}(\Delta t_\mathrm{a})\right\}^{\Delta t_\mathrm{c}/\Delta t_\mathrm{a}} \tag{12.22}$$

in order to solve it with respect to a two-phase acoustic time scale Δt_a:

$$\mathscr{A}_{g\sum k}(\Delta t_\mathrm{a}) = \mathscr{R}_{g\sum k}\left(\frac{\Delta t_\mathrm{a}}{2}\right)\mathscr{T}_g(\Delta t_\mathrm{a})\ \ \mathscr{R}_{g\sum k}\left(\frac{\Delta t_\mathrm{a}}{2}\right). \tag{12.23}$$

We choose Δt_c as an integer multiple of Δt_a and we have of course $\Delta t_\mathrm{a} < \Delta t_\mathrm{c}$ thanks to the scale separation hypothesis [S1].
This hierarchy is based on that of the chamber of a SRM, where [S1] is correct but is not valid in the nozzle because the gas and the particle flow are supersonic (see the orders of magnitude of typical SRMs in Table 12.2 and in Chapter 15): in the first case, the method brings an improvement on accuracy, robustness and cost (the latter by reducing the disperse phase time step) and in the second case, the method sets $\Delta t_\mathrm{a} = \Delta t_\mathrm{c}$ and it brings an improvement only on accuracy and robustness, the cost being similar to other methods. An advanced time strategy can be envisioned, that consists in using different time steps in the chamber and in the nozzle (at the cost of some algebra to time interpolate at the boundaries of the domains): the ACS strategy would then allow to reduce cost in the chamber.
This method is appropriate for smooth gaseous fields but discontinuous states can introduce strong variations in short times that are not compatible with the time steps suggested splitting techniques. This requires to check that the disperse phase velocities have not varied too much during $\mathscr{A}_{g\sum k}$, which for instance can be done for smooth fields with an embedded error control method (Duarte 2011; Descombes et al. 2011; Duarte et al. 2012). Such adaptive methods are not discussed here since we work with acoustic cases. In general, a strategy based on operator splitting and relatively large time steps is valid in the absence of discontinuities e.g. even for choked nozzles. Furthermore to treat discontinuities such as shocks, time steps smaller than all the scales are required (Billet et al. 2008). In these cases, which are out of the scope of this work, the mesoscopic treatment of multiphase flows with shocks requires additional modeling.

The ACS technique has been designed to decouple the stability and accuracy issues for unsteady strongly coupled two-phase problems. It yields the following advantages:

- the overall coupling time step Δt_c is prescribed only regarding accuracy on disperse phase transport;
- the acoustic time step Δt_a is prescribed only regarding two-phase dissipation/dispersion accuracy;
- all the operators are implemented as modules having their own adapted time integration methods.

Finally, the ACS approach is flexible enough to consider other physical phenomena through operator splitting such as coalescence, break-up or evaporation. These approaches are described in § 12.5.

12.3 Study and validation of the ACS versus two-phase acoustics

The ACS strategy has been designed to preserve the features of two-phase acoustics. We now perform a verification on such physics so that all the test cases of the present section feature a uniform repartition of the disperse phase at rest, while the gas, uniform at rest, carries an acoustic wave i.e. a non-rotational perturbation. So the analytical approach developed in § 7.1 can be used.
The approach is implemented in a research code. The ACS is also implemented in CEDRE: it is evaluated in simple cases, and we choose not to separate the acoustic and convective scales so that $\Delta t_a = \overline{\tau}_k$. A feasibility demonstration in complex cases is also performed with CEDRE and presented in § 12.4.3.

12.3.1 In-house code for two-way coupling studies: the SAP1 code

The ACS is implemented in a research code referred to as SAP1 in order to validate the strategy and evaluate its performance on a two-phase acoustic test case.

12.3.1.1 Objectives of SAP1

The SAP1 code is a 1D code that solves polydisperse moderately dense two-phase flows. It is an in-house code designed to test and analyze time integration strategies for Euler-Euler two-way coupling and in particular splitting strategies. High performance numerical methods are implemented for all the Eulerian transport operators in order to minimize their numerical error: this allows to isolate and study the splitting error. These high quality numerical methods are chosen to be very well-suited to the requirements of acoustics, achieving very low dissipation and dispersion no matter their cost. The SAP1 code is then used to completely verify the previously designed strategy called ACS.

12.3.1.2 Disperse phase schemes

The SAP1 code solves for a polydisperse phase, using the One Size Moment Eulerian Multi-Fluid approach. Since we do not study size phase space transfers (coalescence, break-up, evaporation), this approach is sufficient. It can even be proven to be equivalent to any high-order-in-size method with the same number of sections as long as the relevant d_{pq} for drag is the same: this can be done if reconstruction κ or the set of bounds is well chosen.
Each section is decoupled regarding transport so we can define the schemes to approach the $\mathscr{T}_k$ operators separately. A second order Bouchut space time scheme is used (Bouchut et al. 2003; de Chaisemartin 2009): it is specifically adapted to solve PGD on structured meshes, as discussed in § 10.2.
The Bouchut scheme ideally operates with a CFL condition that is close to 1, to minimize numerical diffusion. Thanks to the two-stage splitting of the ACS technique, we can increase Δt_c to solve the section convection with high CFL_k which limits numerical diffusion in physical space as studied in § 12.4.1.

12.3.1.3 Gaseous phase and coupling

To model the moderately dense aspect, the disperse phase is coupled to a compressible gas solver.
The gas transport scheme is based on WENO5 space fluxes (Shu 1998) integrated with a third order explicit Runge-Kutta method (RK3) to generate very low numerical diffusion (Wang and Spiteri 2008). This scheme can handle shock waves but this feature is not used in the present work.
The relaxation step is performed with an advanced time-stepping method, as suggested in § 10.4.2: it is based on RADAU5, which is a fixed error implicit RK5 solver for ODEs with adaptive time step (Hairer and Wanner 1996). This method is A-stable and L-stable and is thus specifically designed for stiff ODEs. Besides, the Geneva group around E. Hairer has provided a very efficient implementation of such implicit RK methods, which we use here. So the time integration of the relaxation step is performed at a fixed precision and it does not require any manual setting of the time step, even for fast particles.

12.3.2 Presentation of the acoustic case

Accounting for two-phase acoustics is a demanding ability so it is a good criterion to evaluate the quality of the coupling that is achieved between the gas and the disperse phase. We therefore use the classical acoustic theory given in Eq. (7.2) as well as the polydisperse dispersion relation derived in § 7.1.3 to assess the performance of the suggested numerical strategy regarding the couplings. This validation approach based on two-phase acoustics is detailed in § 7.1.4.

12.3.2.1 Two-phase acoustics as a benchmark for two-way coupling

The two-way coupling that occurs in moderately dense two-phase flows between the carrier gas and the disperse phase requires well-suited numerical methods, all the more for unsteady flows. The particular case of two-phase acoustics is a good benchmark test case for two-way coupling approaches.
We have described in § 4.7.3.3 the main characteristics of the compressible regime of a moderately dense disperse two-phase flow which we recall:

(i) dissipation and dispersion of acoustic waves in two-phase media,
(ii) acoustic disturbance yielded by condensed phase transport and heating,
(iii) interactions of the gaseous flow structures with the dynamics of particles.

Capturing all these phenomena requires a robust approach, accurate on source terms and rendering a high-fidelity resolution of the compressible carrier phase.
Many two-phase approaches from the literature are proven to account inaccurately for (i): some methods are described and the reasons for their failure are exposed in § 4.7.5. A two-phase approach that accounts for heat and mass transfers may render the lags that are at the origin of dissipation and dispersion, but whenever it does, the numerics has to be very accurate:

- In the same way as with usual acoustics, low order schemes often introduce dissipation while accurate schemes may be dispersive, as discussed in Chapter 10.
- In addition, inaccuracies in source term evaluation and integration versus time introduce numerical dissipation and dispersion.

Since these flaws are remarkably sensitive with acoustic studies, two-phase acoustics yields very demanding cases for codes.
Two-phase acoustics is a tough problem, that requires high level methods. This, to solve the same aspects as the other non-linear two-way coupling features (ii) and (iii). So it is considered as a reference problem among unsteady cases, and we use it extensively to benchmark our numerical approaches and the codes we use.

12.3.2.2 Choice of the analytical formula

We consider a quasi-uniform non-rotational spray, as described in § 7.1. It is polydisperse so we can use the continuous dispersion relation derived in Eq. (7.7), provided the analytical expression of the size distribution. The approached but algebraic relation given in Eq. (7.6) is preferred, with a sufficiently fine grid to be more converged than the test discretizations. We treat the case of different distributions.

12.3.2.3 Acoustic case numerical description

Let us now describe the acoustic wave and the numerical parameters used for both configurations. We consider a 1D acoustic wave of a given frequency of 1000Hz, with a small relative amplitude of 10^{-4} so that its propagation remains linear and the Stokes regime valid. In SRM conditions of 3600K and 50bar, the speed of sound in a burnt gas mixture is $c_0 = 1275$m/s. The mixture has a dynamic viscosity $\nu_g = 8.855.10^{-5}$Pa.s. The particle density is $1766\,\mathrm{kg/m^3}$ and the mass loading is set to a high value of $\mu = 0.394$. The domain length is set to 25.51m which allows 20 periods in average for the propagative case, as illustrated in Figure 12.2.
For monodisperse distributions, the response can be plotted versus the acoustic Stokes number and we can change the particle diameter in order to sweep the acoustic Stokes number range without changing the frequency and the mesh. But for polydisperse distributions, the distribution is fixed and the mesh is changed; the response is plotted versus the excitation wave frequency.
A 1D 2000-cell mesh is used, corresponding to a spatial resolution of 100 points per wavelength (ppw). Using 100 ppw ensures for SAP1 as well as for CEDRE that numerical attenuation of the acoustic waves is lower than the two-phase attenuation for all cases. Such a space discretization also allows to increase the accuracy on the post-processing of attenuation and dispersion. We insist on the fact that the post-processing is done carefully since attenuation $\alpha^\star$ and dispersion $\beta^\star$, as defined in Eq. (7.3), are very sensitive: a simple approach based on local extremum tracking can be used to estimate amplitude decrease and wavelength, respectively linked to the $\alpha^\star$ and $\beta^\star$ coefficients but errors due to discretization must be minimized e.g. by interpolation.

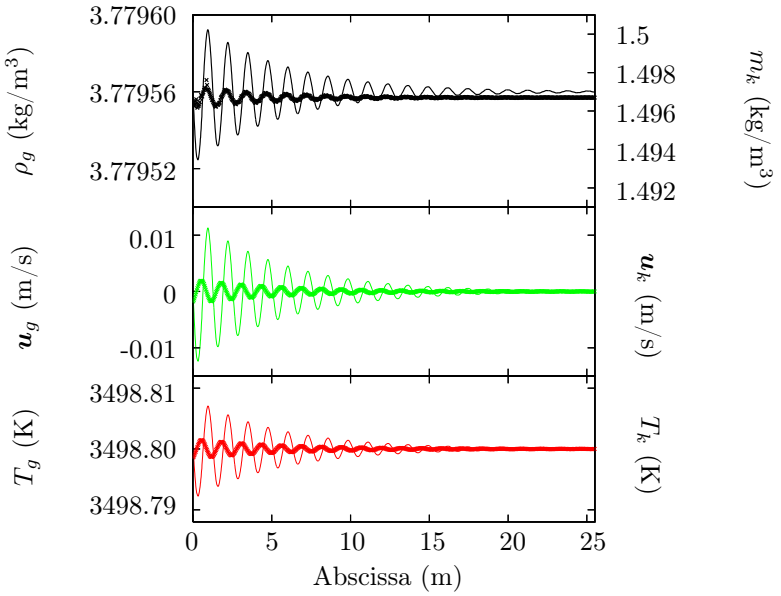

Figure 12.2: *Propagation test case for $St_\omega = 20$ – Gas variables (thin line) and disperse phase variables (+) once the wave has completely penetrated*

A fitting of the best decaying sinus to the signal, e.g. with a least square method, can be used to increase accuracy on the coefficients.

12.3.3 Tuning of the ACS

We consider in this section two test cases for ACS: the first one is based on an evanescent propagation and shows the ability of the method to reproduce the dissipation and dispersion of an acoustic wave according to the analytical formulae. The acceptable limits of the security coefficients are assessed. The second one is quite similar but in a moving reference frame to test the validity of decoupling disperse phase transport from two-phase acoustics. The validation is then performed on the industrial-oriented code CEDRE to show that the ACS, once implemented with practical numerical methods, is still efficient.

12.3.3.1 Splitting error for fast particles

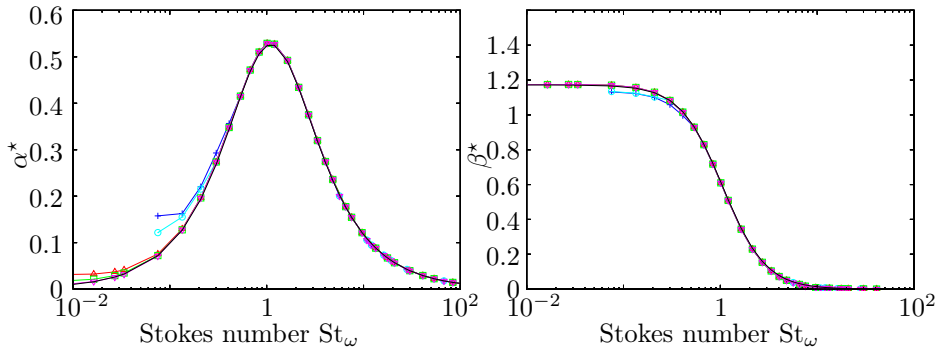

Figure 12.3: *Attenuation and dispersion for different coupling time steps (Monochromatic wave, monodisperse spray, SAP1 code, $K_p = 0.25$) – **Line**: analytic; +: $K_g = 2$; ○: $K_g = 1$; Δ: $K_g = 0.9$; □: $K_g = 0.5$; ▽: $K_g = 0.2$.*

We show in Figure 12.3 the attenuation $\alpha^\star$ and dispersion $\beta^\star$ for different values of the K_g coefficient. First, the computation can give arbitrary results when $K_g > 1$ for very fast particles as shown on both curves of Figure 12.3, this corresponds to the fast particle "no go area" illustrated in Figure 12.1. Second, an erroneous constant attenuation is yielded below a size depending on the value of K_g, as shown on the left curve in Figure 12.3. This overdissipation seems acceptable as soon as $K_g \leq 0.9$ and the analytical result is satisfactorily recovered for $K_g = 0.2$.
An analytical study of the acoustic splitting error which is not detailed here confirms that this over-dissipation plateau for fast particles is naturally yielded by the splitting itself. Such a study allows us to completely control the acoustic splitting error and is presented in a more mathematically oriented contribution in Sibra

(2014).

12.3.3.2 Splitting error for slow particles

The margin on the relaxation time, K_p, depends on the numerical method used to compute the relaxation operator. We have conducted a numerical study with a simple relaxation approach that suggests to set $K_p \leq 0.5$ to ensure an accuracy on dissipation and dispersion better than 1% but the details are not provided for the sake of legibility.
We consider that the computation can fail for most methods when $K_p > 1$ which corresponds to the "no go area" illustrated in Figure 12.1. Finally the prescription of K_p is not a key issue since it only allows to spare calling the relaxation module, which is not costly.

12.3.4 Verification of the ACS

The quality of the two-phase acoustics depends on the splitting time steps that are chosen for ACS, as said in § 12.3.3. The level of accuracy depends on the choice of K_g if there are fast particles and on K_p otherwise. We hereafter make an empirical study of the splitting error with SAP1. The chosen test case is a pure acoustics one where the two-phase dispersion relation derived in this work and given in Eq. (7.2) for monodisperse and in Eq. (7.6) for polydipserse cases applies.

12.3.4.1 Monodisperse two-phase acoustics validation

Results for SAP1 with typical security coefficients ($K_p = K_g = 0.5$) are compared to the analytical solution. The results are given together with those of a further in Figure 12.4. There is an excellent agreement of SAP1 results. The high order numerical methods in SAP1 allow an error smaller than 1% on both $\alpha^\star$ and $\beta^\star$ which is very good, regarding the sensitivity of these coefficients.

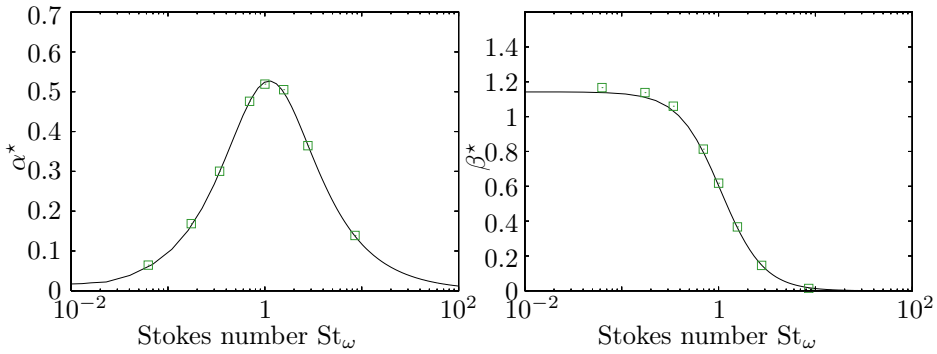

Figure 12.4: *Attenuation and dispersion of a monochromatic acoustic wave in a monodisperse spray – **Line**: analytic; □: SAP1 (ACS splitting).*

12.3.4.2 Polydisperse two-phase acoustics validation

A polydisperse case is now considered and we use the window size distribution that is presented in Figure 7.1. We sweep a frequency range so the mesh has to be rescaled for each point. The polydisperse case is performed with SAP1 and the results are given in Figure 12.5, using 10 sections which is enough to capture polydisperse acoustics with a very good level of accuracy on the acoustic response as discussed in § 7.1.3.3. As shown in this previous study, the MF method handles naturally polydisperse cases as linear combinations of monodisperse cases so the present test case is just a formal check of the code, the numerical performances being already evaluated in the monodisperse case. The results on dissipation and dispersion for SAP1 are correct, which validates the approach for polydisperse sprays too.
This test case, along with the previous monodisperse one, prove the efficiency and accuracy of the splitting technique to treat the acoustic operator $\mathscr{A}_{g\sum k}$. This approach is more general than the ACS itself, and it does not require the splitting of the disperse phase convection part to work. It is assumed that the previous results could have been obtained without separating the disperse phase convection. This other feature of the ACS is evaluated hereafter.

12.3.4.3 Accuracy of the ACS on acoustics with disperse phase convection

We now consider an acoustic disturbance, propagating in a spray with ensemble motion. This disturbance has the same characteristics as the previous propagating wave but it has a shorter space-time extension.

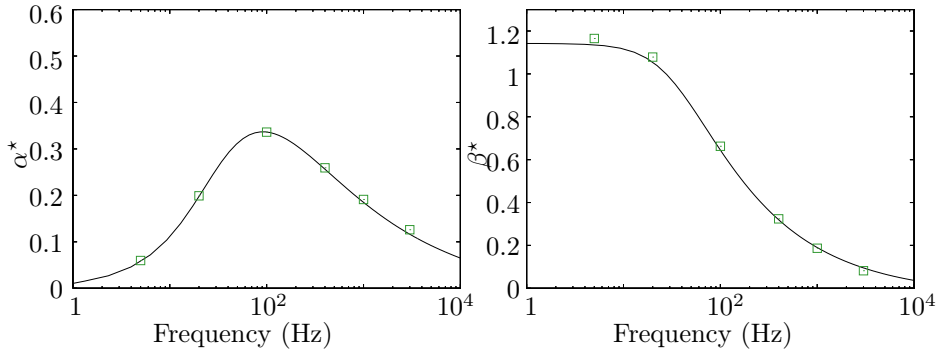

Figure 12.5: *Attenuation and dispersion of a monochromatic acoustic wave in a polydisperse spray – **Line**: analytic; □: SAP1 (ACS splitting,* 10 *sections).*

Convection occurs for both disperse phase and gas which is equivalent to changing the reference frame. The test case is thus trivial as regards the model and it yields the same dispersion relation than Eq. (7.2).
Yet for numerical codes, the space translation corresponding to convection is far from trivial as shown previously in Figure 12.10. The acoustic disturbance is a 3-period sine profile that propagates in a spray with ensemble motion at velocity $\boldsymbol{u}_g = \boldsymbol{u}_p = 150\,\mathrm{m/s}$. We choose a 3-period profile to ease result post-processing. The initial conditions for the gas are shown in Figure 12.6 while the spray is initially uniform.

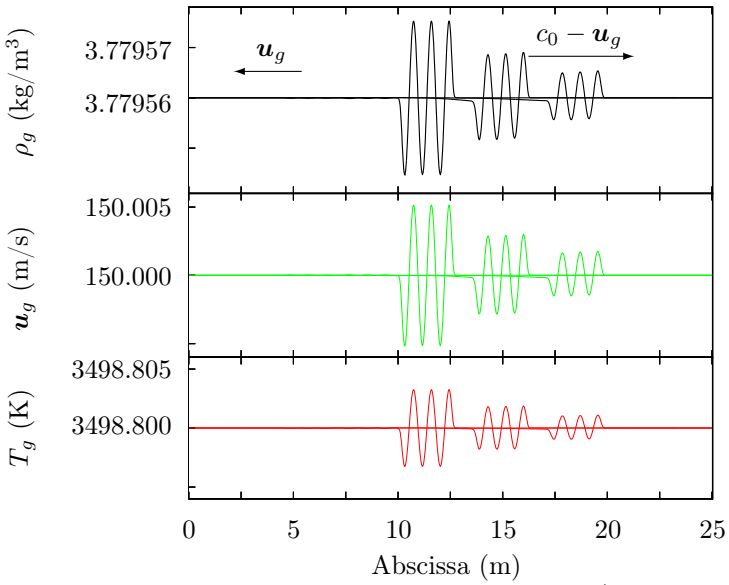

Figure 12.6: *Convective test case – Gas variables at three moments (Initial state: centered 3-period sine profile)*

The test case is performed with a monodisperse phase and the results can be plotted versus the acoustic Stokes number. Figure 12.7 presents the results for SAP1 with ACS only for dissipation. As for dispersion, no post-processing has been developed for complexity reasons. The results on dissipation that are presented match very well with the analytical attenuation, which validates the principle of two-stage splitting technique introduced with ACS.
The case of polydisperse two-phase acoustics in a moving reference frame is not performed. There is indeed no need to study a polydisperse case because sections are naturally decoupled as regards transport in physical space.

12.3.5 Evaluation of ACS in an industrial code

We now evaluate the performances of the ACS with an industrial-oriented code: CEDRE. The code is extensively presented in Chapter 14.

12.3.5.1 Remarks on numerical methods

Compared to SAP1, the CEDRE code is an industrial code which aims at exploiting ACS instead of validating it. The numerical methods are designed to be less costly and to work on non-structured meshes so they

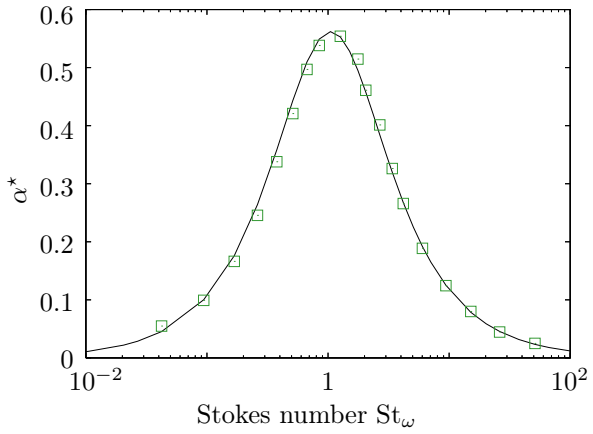

Figure 12.7: *Attenuation of a propagative sine profile in a monodisperse spray with ensemble motion – **Line**: analytic; □: SAP1 with ACS, $K_g = 0.9$ and $\mu = 0.106$.*

introduce small but visible errors in two-phase acoustics.
The difference in the number of moments in size between SAP1 and CEDRE has no incidence on the following monodisperse cases and small incidence on the polydisperse cases for the reasons given in § 4.7.6.2. Finally, the conditions of the acoustic studies make the comparison possible between SAP1 and CEDRE.
Since we perform a comparison between BWC and ACS in CEDRE, we arbitrarily choose a time step that is $\Delta t_c \omega = 2$ for both methods, defining the limit between fast and small particles at $\mathrm{St}_\omega = 2$.

12.3.5.2 Monodisperse validation

Results on acoustic wave attenuation and dispersion for the propagative case (Figure 12.2) in a monodisperse medium with CEDRE with BWC and CEDRE with ACS are compared to the analytical formula. The results are shown in Figure 12.8. The ACS in CEDRE yields very good results so its acoustic part is here validated. The BWC in CEDRE doesn't yield satisfactory results below a given acoustic Stokes number.

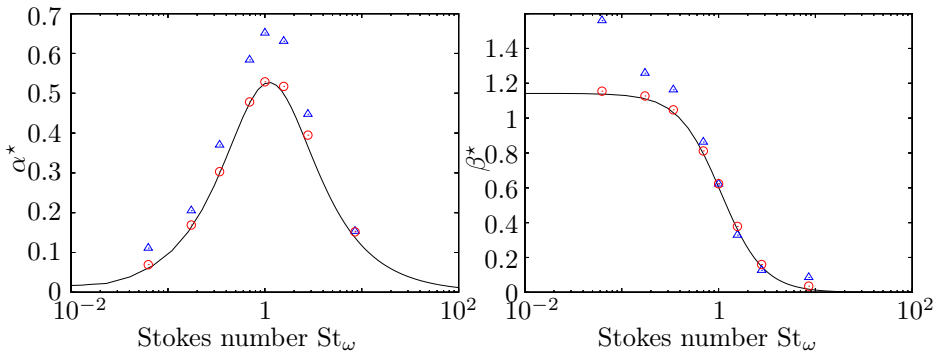

Figure 12.8: *Attenuation and dispersion of a monochromatic acoustic wave in a monodisperse spray – **Line**: analytic; Δ: CEDRE (BWC technique); ○: CEDRE (ACS splitting).*

The limit is here $\mathrm{St}_\omega < 2$, this particular value being linked to the integration time step that is chosen for our test case: the range of over-dissipative particles corresponds exactly to the fast particles. So the BWC is over-dissipative when the particle relaxation time is close to the integration time step or smaller, as expected regarding the errors on instantaneous velocity differences in the 0D test case given in Figure 10.8.

12.3.5.3 Polydisperse validation

Results on acoustic wave attenuation and dispersion in a polydisperse medium with CEDRE with ACS are compared to the analytical formula in Figure 12.9. The test case is the same as the one presented in § 12.3.4 for SAP1: the distribution is again the window size distribution that is presented in Figure 7.1. The ACS in CEDRE still yields very good results which is expected as explained previously. Test cases have been performed down to 5 Hz, which is a very low frequency that requires many iterations, considering the wide scale separation between the wave pulsation ω and the chosen time step.
We highlight that the test case is too costly to be performed in a reasonable time with the BWC approach (detailed in § 10.3.4.3) because of the presence of very small particles introducing small time scales. The

BWC has therefore not been assessed in this polydisperse case.

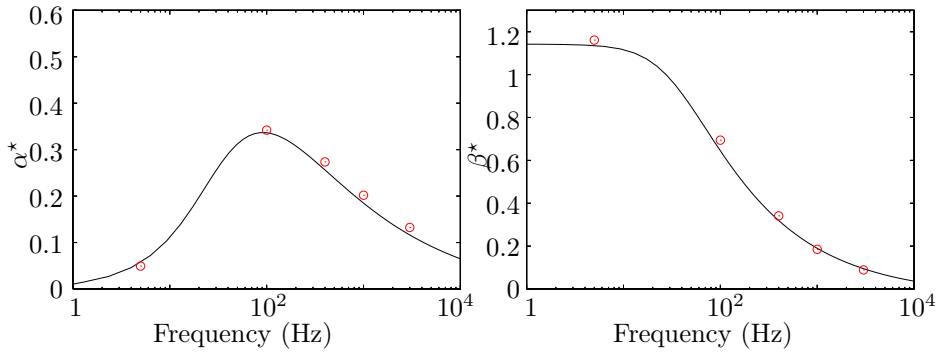

Figure 12.9: *Attenuation and dispersion of a monochromatic acoustic wave in a polydisperse spray – **Line**: analytic; ○: CEDRE (ACS splitting).*

12.3.5.4 Conclusion on the acoustic study in an industrial code

The ACS in CEDRE has proven to be accurate and is validated: the ACS approach in a code which has industrial features can handle monodisperse and polydisperse two-phase acoustics accurately. The two-phase acoustics case in a moving reference frame is not performed with CEDRE because of the complexity of the initial condition, that cannot be easily imposed, but the ability of the code to treat convection is assessed below. We highlight the fact that these acoustics test cases are highly sensitive to inaccurate numerical methods so the previous test case is regarded as very satisfactory.
Moreover the polydisperse case proves that the ACS is able to deal with fast particles while the BWC requires a much smaller time step so the method is, as expected, less costly for fast particles.

12.4 Demonstration of ACS with non-uniform disperse phase transport

We examine the performances of the ACS splitting in the case of a transport of a non-uniform disperse phase: this corresponds for instance to the case of a cluster of particles. The case of a non-uniform disperse phase is of course the most general case.

12.4.1 Capturing convection with the ACS

As exposed previously, the convective splitting allows to use time steps that are adapted to the disperse phase convection operator. But disperse phase convection has small impact in our previous test case since the wave amplitude is small: disperse phase velocity remains below $10^{-4}c_0$ in the pure acoustic cases presented before. We here test the ACS technique on a case featuring significant disperse phase convection.
In general cases where disperse phase convection is performed at sensible velocities, disperse phase structures have a significant impact so they have to be preserved by the numerical scheme. The disperse phase transport scheme has to have a low level of dissipation. Excessively refined time steps can introduce numerical diffusion. The disperse phase transport scheme can have an ill-suited time step imposed by acoustics if a coupled strategy is chosen. This generates an important numerical diffusion with most transport schemes. With ACS, the disperse phase convection time step can be taken bigger which solves this issue.
As an illustration, we perform a numerical test case with the SAP1 code on the evolution of a window-shaped cluster of particles when purely convected. We compare its convection by a second order scheme either when the time step is conditioned (e.g. by acoustics) to the case when it can be chosen freely thanks to ACS. The results are presented in Figure 12.10. The cluster that is convected at $\mathrm{CFL}_k = 0.081$ -due to a time step that is constrained by gas physics- is smeared: the Bouchut transport scheme is ill-suited for such low CFL numbers and it operates at best with a CFL close to one, which is a classical requirement for this class of kinetic schemes (Massot et al. 2009; de Chaisemartin 2009). The cluster convected with the same scheme but in ACS time integration framework is much better preserved, simply because the scheme now operates at $\mathrm{CFL}_k = 0.94$, at the user's choice. With ACS indeed the best CFL can be chosen for transport, as the strategy decouples the operators.

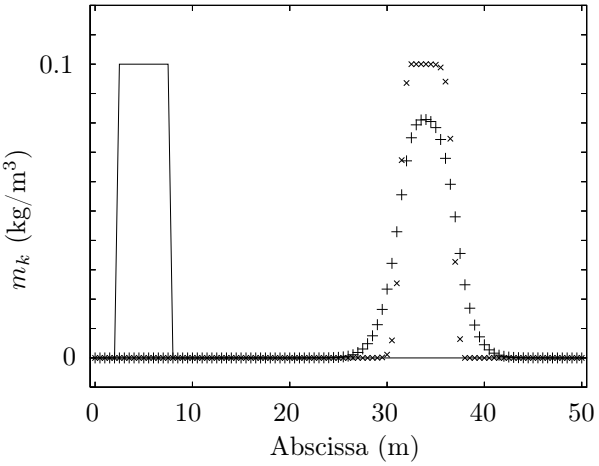

Figure 12.10: *Convection of a disperse phase cluster with a time step driven by acoustics (window cluster convected at 30m/s, second order Bouchut scheme, SAP1 code) – + disperse phase transport at $CFL_k = 0.081$; × disperse phase transport at $CFL_k = 0.94$; — : initial state.*

12.4.2 Spray mixing layer test cases

We perform numerical test cases based on a jet injected in a still gas. Because of the strong mass loading of particles, the disperse phase exerts a strong retrocoupling, entraining the gas on its way and generating a shear layer. So this configuration is relevant to assess the ability of the method to deal with strong mass loadings. As for the physical behavior, it is close to the one of a mixing layer for two non-miscible fluids with a high density ratio. The configuration is highly unsteady.
The conditions of the presented computation (boundaries, upstream flow) are not realistic enough to allow physical interpretations but the case is a numerical benchmark for two-way coupling. The case is demanding for the numerical method since singularities occur. So the robustness of ACS as a time strategy for two-way coupling of multi-scale problems is shown. We compute the test case with the CEDRE code, using a second order scheme that resolves well the strong accumulations and singularities which occur: this test case is a reference as regards the ability of the code to ultimately deal with two-way coupling disperse two-phase flows.

12.4.2.1 Results with a symmetric domain

We consider a disperse two-phase jet with the following characteristics for the gas:
- density $\rho_g = 0.07\,\mathrm{kg/m^3}$, and
- viscosity: $\mu_g = 9.1 \times 10^{-5}\,\mathrm{kg/m^3}$,

and for the particles:
- density $\rho_l = 1000\,\mathrm{kg/m^3}$,
- size $r_p = 100\,\mu\mathrm{m}$,
- mass concentration $\rho_l = 0.007\,\mathrm{kg/m^3}$, and
- particle relaxation time $\tau^{\boldsymbol{u}} = 6.10^{-3}\,\mathrm{s}$.

The dimensioned parameters to describe the case are:
- jet width $d = 2\,\mathrm{m}$,
- particle injection velocity $u_{p0} = 500\,\mathrm{m/s}$,

so the gas time scale is $\tau_g = d/u_{p0} = 4.10^{-3}\,\mathrm{s}$. The dimensionless parameters are then:
- the Reynolds number $\mathrm{Re}_d = 1.5 \times 10^6$,
- the particle mass fraction: $Y_p = 0.1$,
- the particle mass loading: $C = 0.1$,
- the Stokes number: $\mathrm{St} = 1.5$, and
- the coupling parameter: $\Pi^u = C/(1 + \mathrm{St}) = 0.1$.

The mesh is structured (Cartesian) with $10,000$ cells, this for accuracy purposes but the computations could as well be performed on unstructured meshes; it has been generated with Gmsh (Geuzaine and Remacle 2009). A horizontal symmetry axis is assumed which is a strong hypothesis that is not completely satisfactory. The results with equilibrium injection are presented in Figure 12.11 and the case with still gas at the jet level are presented in Figure 12.12.
The appearance of Kelvin-Helmholtz instabilities, cascading into complex vortical structures is remarkably visible in the equilibrium case, see Figure 12.11.

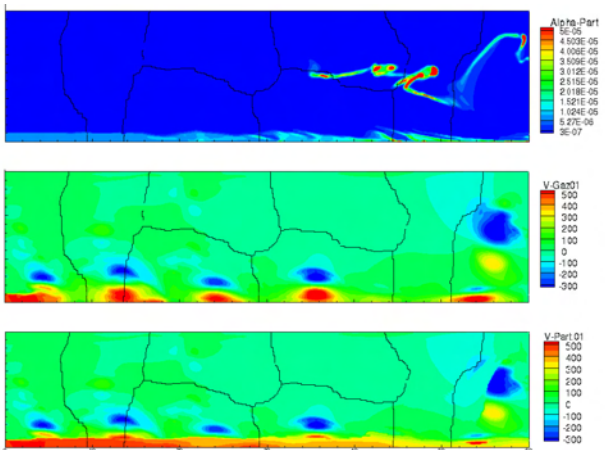

Figure 12.11: *Mixing layer of a moderately dense jet at dynamic equilibrium – Eulerian simulation with CEDRE (ACS).*

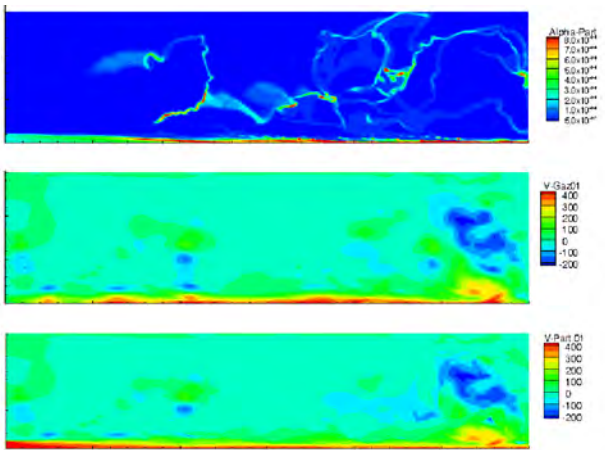

Figure 12.12: *Mixing layer of a moderately dense jet in a still gas – Eulerian simulation with CEDRE (ACS).*

12.4.2.2 Conclusions on robustness and remarks on PTC

The case presented in Figure 12.12 exhibits many δ-shocks. In this case, the monokinetic approach is at its limit as PTC occurs, see § 3.1.3.3. The case should be treated with a polykinetic approach, such as the ones described in § 4.5 or the AG (see Chapter 6).
Though the results are erroneous due to PTC, the case is interesting to demonstrate the robustness of the approach in such cases: δ-shocks can appear in a portion of the domain, which may not compromise the accuracy of a monokinetic computation, depending on the desired results. So a numerical method much cope with δ-shocks, which is difficult as regards the strong source terms that are generated.
The ACS proves to improve the robustness in these cases while BWC cannot work out such a computation.

12.4.3 Unsteady SRM realistic case

We illustrate the robustness and the accuracy of the ACS strategy on a 2D unsteady polydisperse moderately dense case with a complex geometry and hydrodynamic structures. This test case consists in a SRM seeded with polydisperse particles ranging from large, slightly inertial particles to very small particles behaving like tracers and therefore belonging to the "Equivalent Gas" assumption validity domain (see § 4.7.5.3). This is a tough case with various time scales linked to flow scales and particle polydispersity. The study of the space discretization errors is beyond the scope of the present contribution, accordingly to the methodology used for similar studies on splitting methods (Duarte et al. 2012). In a number of applications indeed, the maximal level of space refinement is set by the computational capabilities so we investigate the new numerical strategy solely for the resolution of a semi-discretized problem on a fixed, "most refined" mesh: in our case, this mesh is far from that of a DNS which is intractable anyway, but it is still a mesh that is used in practical SRM simulations. Once the space (mesh) and size (MF) discretizations are chosen, the time resolution is to be done, for a stiff dynamical system associated to the semi-discretized problem. The abilities of BWC and ACS to deal with the multi-scale features of the problem are assessed. The methodology to prove the time accuracy of the method consists in a comparison between ACS and BWC, presented in § 4.7.5: the latter is

indeed a validated approach and it is considered with a time step belonging to the domain of its convergence so BWC can be considered as a reference.
Considering a time step adapted to the fastest flow time scales i.e. the supersonic nozzle flow, we perform two types of simulations: validation and efficiency test cases. In the validation test case, used as a reference we get rid of the stiffness of very small particles with the MF-PEG method -since they feature $St \ll 1$ everywhere- and we prove ACS to match BWC results. In the efficiency test case, the smaller particles are fully and "explicitly" solved within a fourth section by a MF approach -which is therefore stiffer- and ACS retrieves the previous results while BWC departs. Another efficiency test case is finally performed: a MF simulation with even smaller (nano) particles allows ACS to retrieve the reference results, as expected since very small and nano particles both behave like tracers. On the same nano simulation with the same time step, BWC crashes and requires, as expected, an overall time step smaller than the nano particle relaxation time. This validates ACS and proves its accuracy and robustness, with larger time steps than BWC for very small (or nano) particles.

12.4.3.1 Case description and numerical configuration

We consider a SRM case featuring a coupling between acoustic and hydrodynamic instabilities. The considered motor, called LP10, was fired with solid particles at a temperature that prevents them from encountering size evolution so that their distribution is well known and the two-phase effect can be accurately studied. The flow in the chamber is subject to Parietal Vortex Shedding, a hydrodynamic instability coupled to the acoustic mode of the chamber as discovered in Lupoglazoff and Vuillot (1996), theorized in Casalis et al. (1998), and actively studied up to now (Fabignon et al. 2003; Cai et al. 2003; Chu et al. 2003; Casalis et al. 2011; Chedevergne et al. 2012). For this specific LP10 case, a driving effect of inert particles on instability levels has been observed experimentally (Jézéquel and Prévost 2007) and numerically (Dupays et al. 2008). The strong impact of polydispersity on acoustic levels has been demonstrated in Doisneau et al. (2011) with the CEDRE code. No other simulation of this case has been led up to now. The simulation of the LP10 instabilities requires capturing flow and spray spatial structures as well as their coupling, these issues being the ones we aim at tackling, this with a more efficient and still accurate method.

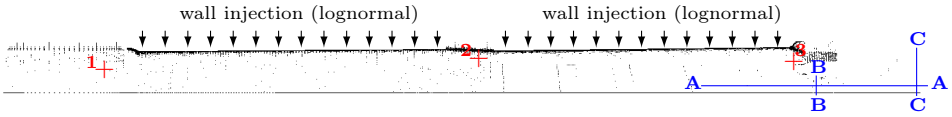

Figure 12.13: *Deformed-structured* 27,000 *cell mesh of the LP10 geometry (**Arrow**: injection;* **Line***: cut; +: pressure sensor).*

The LP10 simulation is performed with CEDRE on a 2D axisymmetrical representation of an LP10 motor fired during an experimental campaign. A multi-species Navier-Stokes formulation is used, for which the generalization of the splitting strategy can be done. Efficient splitting strategies are indeed qualified for convection-reaction-diffusion equations in any regimes in Duarte et al. (2012); but in our case diffusion is slower than convection since the Reynolds numbers are high and the boundary layers are coarsely meshed and no reactions occur so we choose to time-integrate the viscous operator simultaneously to the carrier gas convection. This approach is satisfactory in our particular regime and it is convenient to implement as it complies to the legacy of the CEDRE code. With the present mesh, representing the geometry of the propellant grain, assumed steady at a given time of the firing, the instability spectrum has well-defined modes based on a monochromatic fundamental. The simulation takes place at a time when the most intense instabilities are observed. The simulated time is long enough to perform a harmonic study of the instabilities. At this time, the forward cylindrical grain has totally burnt so that no flow comes from the front end. The simulation takes place on the deformed-structured 27,000 cell mesh already used in previous studies (Doisneau et al. 2011) and shown in Figure 12.13. No propellant combustion is modeled: gas and particles are injected at a fixed surface flow rate of $16.01\,\mathrm{kg/m^2/s}$ and a fixed temperature of $2255\,\mathrm{K}$ from the two walls representing the two propellant segments. The boundary condition ensures that the normal pressure gradient is null, which determines the gas density and velocity.
Particles are chemically inert, non coalescing because solid and they are at equilibrium with the burnt gas flowing from the propellant. The same lognormal distribution based on experimental particle data is injected from both segments to render polydispersity. In the MF approach, the size phase space is discretized in four sections with the diameter bounds 0, 3.33, 6.66 and $10\,\mu\mathrm{m}$, which is enough to capture polydispersity for a lognormal distribution according to the accuracy study performed in § 7.1.3.3 on analytical acoustic solutions. We refer to the corresponding particles as very small VS, small S, medium M and large L particles. In the MF-PEG approach, the size phase space is discretized in three sections with the diameter bounds 3.33, 6.66 and $10\,\mu\mathrm{m}$ while the surface flow rate at the wall corresponding to VS particles is accounted for with an EG

Category	Bounds (μm)	$\bar{d}_k^{30}$ (μm)	$\overline{\mathrm{St}}_{\omega,k}$	$\overline{\mathrm{St}}_{\epsilon,k}$	Flow rate (kg/m^2/s)
N	$[0, 3.33[$	0.20	2.10^{-4}	0.3	0.15
VS	$[0, 3.33[$	0.60	2.10^{-3}	2.8	0.15
S	$[3.33, 6.66[$	5.02	0.51	8.10^{2}	0.17
M	$[6.66, 10[$	8.14	1.34	2.10^{3}	0.30
L	> 10	12.83	3.33	4.10^{3}	0.61

Table 12.1: *Particle injection conditions*

$\tau_N^{\boldsymbol{u}}$ Stokes time	0.1
Time step Δt_a	0.2
Time step Δt_c	0.2
Nozzle CFL time (Full Mach)	0.6
$\tau_{VS}^{\boldsymbol{u}}$ Stokes time	1.7
Nozzle strain-rate-based time	30
$\tau_S^{\boldsymbol{u}}$ Stokes time	120
$\tau_M^{\boldsymbol{u}}$ Stokes time	320
Eddy revolution time	750
$\tau_L^{\boldsymbol{u}}$ Stokes time	780
First acoustic mode (L/2)	1500
Typical simulation time	500,000

Table 12.2: *Timescale hierarchy (μs), exhibiting stiffness.*

technique. BWC and ACS strategies are considered for MF and MF-PEG cases. Finally, a MF computation is performed with nano N particles instead of VS particles. The details on injection and Stokes numbers for the different particle categories are given in Table 12.1.

The case is very stiff since (i) the chamber flow is slow while the nozzle flow is supersonic, and (ii) the disperse phase is strongly polydisperse. In the chamber, the characteristic flow times are associated to hydrodynamic instabilities and more precisely vortex revolution times but also to the fundamental acoustic wave period ω. In our case in fact, the two phenomena are locked so that their characteristic times are linked: we can qualify particle behavior in the chamber with an acoustic Stokes number $\overline{\mathrm{St}}_{\omega,k}$. In the nozzle, the characteristic time is linked to the gas acceleration and is defined as the inverse of an average strain rate $\epsilon = (u_g(x') - u_g(x))/(x' - x)$. We consider its maximum value $\epsilon_\mathrm{max} = 3.10^4\,\mathrm{s}^{-1}$ and the particle behavior in the nozzle is qualified with the corresponding nozzle Stokes number $\overline{\mathrm{St}}_{\epsilon,k}$. The gas has a viscosity $\nu_g = 7.057.10^{-5}$Pa.s and the particles are made of zirconium oxide with $\rho_l = 6100\,\mathrm{kg/m}^3$. So we can sort the problem's characteristic times as given in Table 12.2. We insist on the fact that the particle time scales are estimated with dynamic Stokes times $\tau_k^{\boldsymbol{u}}$ while Schiller-Nauman corrections are used for strong slip velocities and can be linked to shorter values for the time scales. Moreover the thermal times can be smaller, especially with the Ranz-Marshall correction. So the hierarchy given in Table 12.2 is only indicative.

The two-phase simulation starts from a steady state of the single phase gaseous flow field. With the chosen mesh, the most restrictive CFL time is $\tau_g = 6.10^{-7}$s. and the splitting time steps are $\Delta t_\mathrm{c} = \Delta t_\mathrm{a} = 2.10^{-7}$s, being equal because of the coupling between acoustic and convective aspects in the supersonic nozzle. This yields the gas security coefficient $K_g = 1/3$. In the MF-PEG approach, the smallest section time is $\tau_\mathrm{min} = \tau_S^{\boldsymbol{u}} = 1.2.10^{-4}$s which yields a particle security coefficient $K_p = 1/600$. In the MF approach, the smallest section time is $\tau_\mathrm{min} = 1.7.10^{-6}$s which yields a particle security coefficient $K_p = 1/9$. Once again, these security coefficients are based on Stokes time but the relaxation is faster when Re_p is large due to drag and heat corrections.

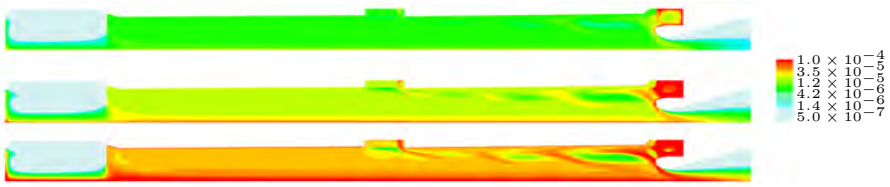

Figure 12.14: *Instantaneous volume fraction per section in LP10 with CEDRE (MF-PEG ACS (top to bottom: S, M and L particles).*

When the particles are injected, the pressure builds up to a new value of average pressure. We give instantaneous particle volume fraction fields in Figure 15.13 for the PEG-MF ACS as an illustration. Their structure matches the one of the BWC results. As expected in classical analysis, the three particle sizes behave differently in the gaseous vortices: the smaller particles featuring a uniform repartition while more inert particles from section three are ejected from the vortices. This behavior complies to the particles' respective acoustic Stokes numbers $\overline{\mathrm{St}}_{\omega,k}$, see Table 15.2, because the vortices are, in this particular case, tuned on the acoustic instability so their revolution time is equal to the wave period.
Finally, the computation with nanoparticles N instead of VS yields the same results for ACS, regarding chamber acoustics and nozzle dynamics. On the contrary, the nanoparticle N computation crashes with BWC. This shows the improvement on robustness brought by the new ACS strategy when stiffness is introduced by very low inertia particles.

12.4.3.2 Dynamic study in the nozzle

We perform a quantitative comparison between the four computations MF-PEG and MF on the instantaneous hydrodynamic data along the three cuts in the nozzle given in Figure 12.13.

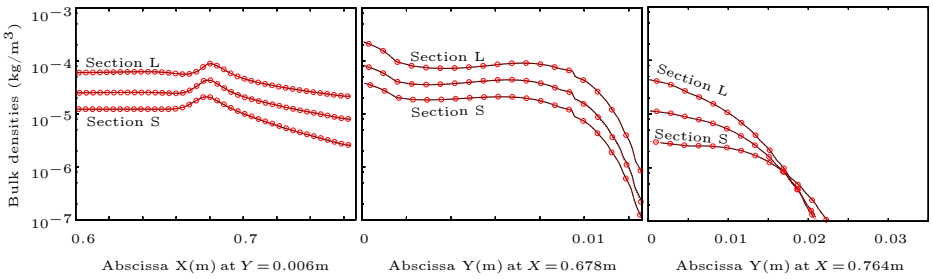

Figure 12.15: *Particle mass concentrations along cuts (left: cut A-A, middle: cut B-B, right: cut C-C)* – **Solid***: MF-PEG BWC (reference);* ○*: MF-PEG ACS.*

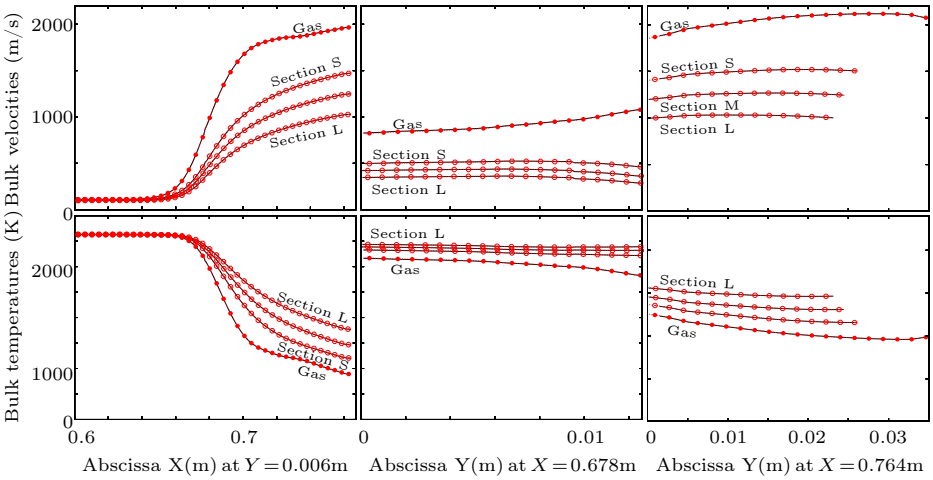

Figure 12.16: *Velocities and temperatures along cuts (left: cut A-A, middle: cut B-B, right: cut C-C)* – **Solid***: MF-PEG BWC (reference);* ○*: MF-PEG ACS – Empty symbols: disperse phase; Full symbols: gas.*

We first compare the two MF-PEG approaches. Regarding particle mass concentrations, given in Figure 12.15, the MF-PEG results match perfectly between BWC and ACS. Along the A-A cut, concentrations increase and decrease after the throat. The B-B and C-C cuts show that the particle concentrations are maximum on the centerline and decrease as we get closer to the wall. Regarding velocities and temperatures, given in Figure 12.16, the MF-PEG results also match perfectly between BWC and ACS. Along the A-A cut, the gas velocity increases as the temperature decreases, and the particles follow partially this behavior, but with differences that increase with the particle size. We recall that the three resolved sections S, M and L feature $\overline{\mathrm{St}}_{\epsilon,k} \gg 1$ so that this behavior, i.e. wall depletion, velocity and temperature lag, is as characteristic of very inertial particles in the nozzle. The B-B and C-C cuts also prove ACS and BWC to match perfectly. Finally the ACS reproduces perfectly the BWC results when particles have a relaxation time that is large compared to the numerical time step i.e. $K_p \gg 1$: so the validity and accuracy of ACS is proven to time integrate space and size semi-discretized SRM problems.
We now compare the two MF approaches and we keep a MF-PEG result as a reference. Regarding particle mass concentrations, given in Figure 12.17, the ACS results match very well to the reference while BWC

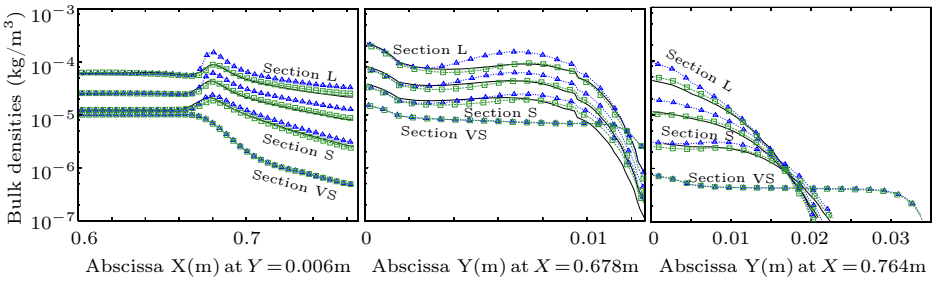

Figure 12.17: *Particle mass concentrations along cuts (left: cut A-A, middle: cut B-B, right: cut C-C) –* **Solid***: MF-PEG reference (BWC);* Δ*: MF BWC;* □*: MF ACS.*

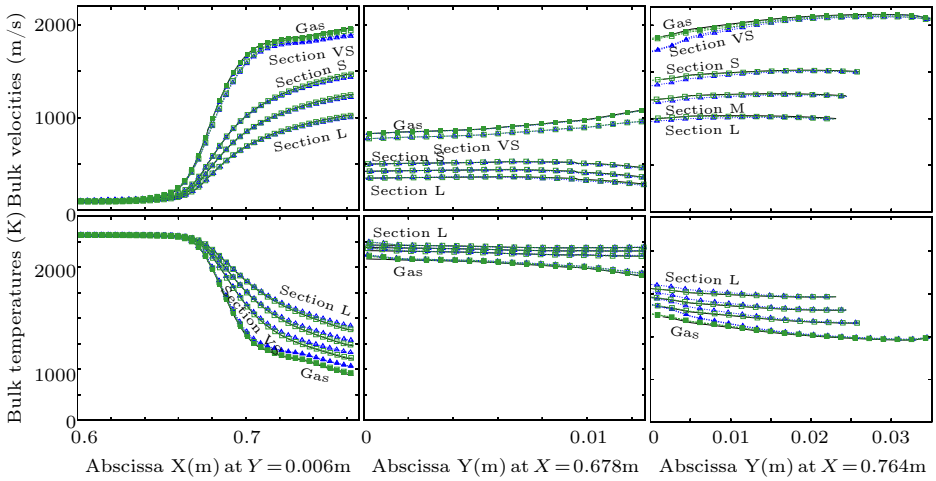

Figure 12.18: *Velocities and temperatures along cuts (left: cut A-A, middle: cut B-B, right: cut C-C) –* **Solid***: MF-PEG reference (BWC);* Δ*: MF BWC;* □*: MF ACS – Empty symbols: disperse phase; Full symbols: gas.*

ones depart. Along the A-A cut, concentrations increase and decrease after the throat especially for the VS particles which dilute much more in the diverging part of nozzle. The BWC overestimates S, M, and L concentrations in the diverging part. The B-B and C-C cuts now show that the VS particle concentration is very uniform in nozzle sections, compared to inertial particles (S, M, L). Regarding velocities and temperatures, given in Figure 12.18, the ACS results also match the reference well and the BWC results still depart. Along the A-A cut, the ACS gas velocity and temperature match the reference, contrary to BWC. The VS particle temperature as resolved by ACS sticks perfectly to the gas and the ACS VS velocity matches well the gas, according to the analysis of its $\overline{\mathrm{St}}_{\epsilon,k}$; the inertial sections in ACS match perfectly the corresponding sections of the reference, which is computed in a PEG approach: this is natural as soon as the gas fields are similar in MF and MF-PEG. On the contrary, the BWC which has not well resolved the gas yields discrepancies on all the sections. The B-B and C-C retrieve these results: ACS matches the reference perfectly except for the VS velocities at throat which have a slight lag; the BWC has velocity and temperature discrepancies at the output, close to the centerline. Finally the ACS reproduces very well the reference results with a MF approach, even with a security coefficient $K_p = 1/9$, which is not so low; the slight difference at the throat is presumably due to the fact that the PEG hypothesis is at its limit of validity. On the contrary, the BWC results for the MF approach depart from the PEG reference so BWC is proven to be inaccurate when time steps are close both to particle relaxation times and flow characteristic times, which is not satisfactory in a perspective of cutting computational costs.

12.4.3.3 Harmonic study

To study the instabilities, data is gathered during the steady regime and a harmonic analysis is performed on three pressure signals, measured at the front, the inter-segment and at the rear of the chamber. The spectra are shown in Figure 12.19 for the four computations. The structure of the modes is similar and typical of a longitudinal steady mode: harmonics are integer multiples of a unique fundamental wave and they decrease quasi-linearly for sensors 1 and 3. They match very well, with differences on the first two peaks below 0.5%. So the use of ACS or BWC in this case has no influence on the harmonic behavior of the problem. We link this result to the fact that the chosen time step is far below the acoustic time scales of the problem so that BWC or ACS are not challenged. While proofs of ACS accuracy on two-phase acoustics have been given in § 12.3.4, and the strategy has been validated in CEDRE, see § 12.3.5, the ACS strategy is now qualified to

capture unsteady two-way coupled hydrodynamics and acoustics.

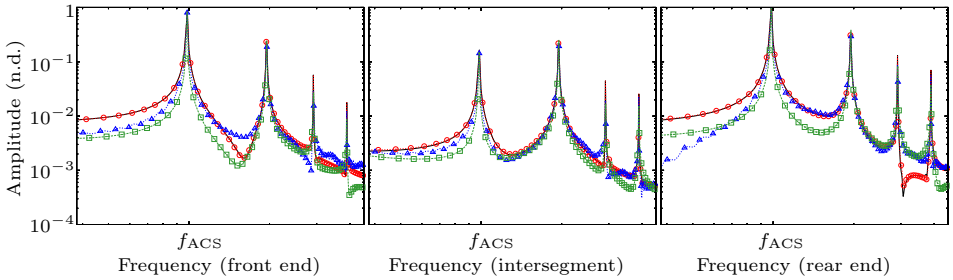

Figure 12.19: *Spectra of pressure signal non dimensioned by the ACS highest peak – Left: front-end sensor (1); Middle: middle sensor (2); Right: rear-end sensor (3)* – – **Solid***: MF-PEG BWC (reference);* ○*: MF-PEG ACS;* Δ*: MF BWC;* □*: MF ACS.*

12.4.3.4 Conclusion on ACS for SRM simulations

The ACS method is proven to be well suited for SRM simulations. It solves accurately the two-way coupled convection problem in the nozzle while BWC needs a smaller time step to meet the same level of accuracy. It is robust and accurate with a splitting time step based on the flow convective scale, whatever scales are introduced by the spray; in comparison, BWC needs to base its time step on the smallest time scale, which may be imposed by the disperse phase. With such a time step, constrained by the supersonic nozzle, and such a discretization, the acoustic in the chamber is over-resolved so no difference is observed between BWC and ACS; but the monochromatic wave studies have proven ACS to be more accurate than BWC on two-phase acoustics too, when time steps are close to the acoustic time. So this allows ACS to spare cost in further SRM configurations.

12.5 Splitting the disperse phase source terms

The ACS method is briefly described in the context of source terms and particularly of coalescence.
The ACS is a two stage splitting based on the following time scale hierarchy: disperse phase convection generally yields the slowest scales while the fastest scales are gas transport scales, which include acoustic waves. The relaxation scales, that are drag and heat transfers between the disperse phase and the gas, are to be linked to the acoustic scales in order to account for two-phase acoustics.

12.5.1 Case of coalescence

Coalescence, as a physical phenomenon, strongly modifies the size distribution and therefore the dynamics of moderately dense sprays. It is crucial to account for it in the context of a moderately dense time strategy, which is done below for ACS.

12.5.1.1 Operator definition

We first define the coalescence operator $\mathscr{C}_{\sum k}$:

$$\mathscr{C}_{\sum k}\left\{\begin{array}{l}\partial_t m_k = {}^2\mathrm{C}_k^{m+} - {}^2\mathrm{C}_k^{m-} \\ \partial_t (m_k \boldsymbol{u}_k) = {}^2\boldsymbol{C}_k^{u+} - {}^2\boldsymbol{C}_k^{u-} \\ \partial_t (m_k h_k) = {}^2\mathrm{C}_k^{h+} - {}^2\mathrm{C}_k^{h-}\end{array}\right. \quad k \in [\![1, N_{\mathrm{sec}}]\!] \tag{12.24}$$

which couples all the sections together but is local in space. Again, the PDE is written for the OSM without loss of generality.

12.5.1.2 Need for a time scale assessment

The coalescence time scales must be estimated in order to choose the way the operator is included in the splitting approach.
This question is remarkably difficult to tackle as $\mathscr{C}_{\sum k}$ is a non-linear operator. Its dynamics has never been studied. The estimation of coalescence times performed in § 3.5.2.6 and prolongated for the Multi-Fluid approaches yields an indication on physical times scales but does not provide a comprehensive analysis, potentially ignoring hidden fast scales and the detailed effect of the exact size distribution.

The coalescence operator can be placed at the upper stage of the ACS splitting if the characteristic times of coalescence are slow enough compared to Δt_c. This can still be checked by a trial and error method.
In the case when $\mathscr{C}_{\sum k}$ is computed with an explicit time integration, the integration will fail as soon as a fast time scale is excited. With an implicit, unconditionally stable method, the integration may be accurate enough if the time scales that are ran over correspond to fast but not significant modes. Still, the strong non-linearity of coalescence impedes a general study of time scales. Linearly degenerate cases can however be considered with techniques presented in § 7.3 or in § 7.4.

12.5.1.3 Structure of the coalescence splitting

We can rewrite the moderately dense polydisperse system of equations as an operator, in the spirit of Eq. (12.21):

$$\mathcal{S}_{\text{coal}}^{\text{ACS}}(\Delta t_c) = \mathscr{A}_{g\sum k}\left(\frac{\Delta t_c}{2}\right)\left\{\sum_{k=1}^{N_{\text{sec}}}\mathscr{T}_k\right\}(\Delta t_c)\ \ \mathscr{A}_{g\sum k}\left(\frac{\Delta t_c}{2}\right)\ \ \mathscr{C}_{\sum k}(\Delta t_c) \tag{12.25}$$

where $\mathscr{C}_{\sum k}$ has been included through a first order Lie splitting to spare resources, as regards its high numerical cost. The coalescence operator is placed at the beginning of the splitting to allow the acoustic operator to perform the final relaxation towards its equilibrium sub-manifold.

12.5.1.4 Practical implementation and feasibility assessment

Coalescence has been implemented in CEDRE and feasibility has been assessed on a scale 1 Ariane 5 motor, as presented in Chapter 15 and featuring stiffness because of varied particle sizes.

12.5.2 Other phase space terms

The issues and existing solutions for other phase space terms are briefly presented. The splitting strategy used for coalescence does not render fast and strong couplings with other phenomena e.g. relaxation. This is acceptable for the coalescence size-velocity coupling, which has generally large enough time scales compared to the other scales of interest.
The strategy can be applied for break-up terms, but it must be checked that the coupling between break-up and relaxation has not been broken e.g. that the smallest particles that are created are correctly decelerated: part of this modeling can be introduced in the break-up model (see § 3.5.3.2) in which case the coupling is efficiently treated.
The strategy must however be cautiously designed for evaporation, where a strong and fast coupling occurs between size evolution and thermal transfers between the disperse phase and the gas: a more complex splitting strategy is considered by Sibra (2014) in this case.

12.6 Conclusion on the ACS splitting strategy

A new strategy referred to as ACS has been developed for polydisperse moderately dense two-phase flows and extensively tested in general and SRM contexts. The method is ready for use in the CEDRE code.

12.6.1 Improved robustness

The ACS robustness is proven for strongly coupled cases and for particle distributions with fast particles, i.e. particles with a fastest relaxation time than the CFL time.

12.6.2 Improved accuracy

The ACS is accurate as regards two-way coupling as demonstrated extensively for two-phase acoustics and it allows to treat the stiffness of fast particles without penalizing the overall approach.
The approach is evaluated with significant particle transport, possibly featuring two-way coupling and ACS proves to improve the overall robustness of the code, even when momentum is locally dominated by the disperse phase or when δ-shocks form.

12.6.3 Improved cost and flexibility

The ACS approach allows to use time steps that are never smaller than that of the gas CFL one.

It is moreover flexible to implement as the operators are split. For instance the choice of an implicit integration for a given operator requires to compute the partial Jacobian matrix for the operator alone. ACS prove to be very flexible and its implementation is straightforward in HPC codes.
Finally, it can naturally account for other source terms such as coalescence, whenever they yield new couplings, as long as their dynamics is respected.

Chapter 13

Rendering polydispersity and size evolution

The evolution of size distribution, due to coalescence and break-up, is accounted for in the context of TSM Multi-Fluid models, for which efficient algorithms are developed and presented. These algorithms are dedicated to the treatment of size in TSM methods, keeping in mind that they are to be implemented in HPC codes. We present computational studies that validate and qualify TSM approaches for polydispersity: first in the case of low inertia sprays, where the monokinetic closure is sufficient, then for moderately inertial sprays, where the AG approach and the corresponding coalescence closure are used.

13.1 Algorithms for size reconstruction and integration in TSM approaches

TSM approaches have been presented in Chapter 5. They are based on the resolution of equations for two size moments, here number and mass. All the moment methods raise three numerical issues:

1 the moments should remain realizable,
2 the underlying (size) distribution must be reconstructed,
3 source terms must be integrated from the (size) reconstruction.

We therefore recall the main aspects of realizable schemes on structured grids for transport in physical space, as introduced in Dufour (2005) and in de Chaisemartin (2009). We then introduce algorithms for an exponential and a positive affine reconstruction, which are at the root of Exp-TSM and Aff-TSM methods, respectively. We finally introduce integration techniques dedicated to the efficient computation of source terms for each reconstruction technique. The choice of the reconstruction technique is discussed and shown to be crucial, as stated in the general case in § 10.4.3 and moreover, the computation techniques for the source terms are shown to be linked to the choice of a reconstruction.

13.1.1 A finite volume kinetic numerical scheme for space preserving the moment space

The first issue raised by the treatment of a complex disperse phase with moment methods is to transport the moments in a way that necessarily preserves the realizability of the underlying distribution (Kah 2010). In the context of the TSM methods, there are two size moments to transport with respect to the realizability condition which is given in § 5.3.1.2 and corresponds to positivity and a bounded ratio. This condition is not as constraining as for higher order methods, (e.g. EMSM, see § 4.4.4.5) but the numerical scheme still must be well defined.

13.1.1.1 Typical transport equations for a moment method

We present the first and second order numerical schemes used to discretize the pure transport operator for the TSM in the 1D case, described by System (12.7). Because of the conservative form of this system, the finite-volume method (LeVeque 2002) is a natural candidate for its discretization. Moreover, for academic codes, computations are usually enforced in a cartesian mesh and a dimensional splitting algorithm is then used as explained in § 10.2.2.1. Thus, all the directions are solved separately, using a 1D scheme. Let us remark that, for industrial codes such as CEDRE, with unstructured meshes, MUSCL-type cell-center scheme can be derived in a similar manner (Dufour and Villedieu 2005; Kah et al. 2012; Le Touze et al. 2012).

$$\begin{array}{ccc} m_j^n, u_j^n & & m_j^{n+1}, u_j^{n+1} \\ \downarrow & & \uparrow \\ f(t^n, x, u) & \xrightarrow[\Delta t]{\text{exact evolution}} & f(t^{n+1}, x, u) \end{array}$$

Figure 13.1: *Main steps of the kinetic based transport scheme.*

The system is rewritten:

$$\begin{cases} \partial_t m + \partial_x(mu) = 0 \\ \partial_t(mu) + \partial_x(mu^2) = 0 \\ \partial_t(m\phi) + \partial_x(m\phi u) = 0 \end{cases} \tag{13.1}$$

where m is the mass density m_k of the considered section, u is its velocity in the direction x and ϕ is a passive scalar corresponding to an eventual velocity component in another direction in case of directional splitting, to the enthalpy, or to the rate n_k/m_k.

13.1.1.2 General form of the kinetic schemes

System (13.1) is weakly hyperbolic and can produce δ-shocks. The scheme has to be robust enough to capture this kind of singularity, without breaking the positivity of m and the realizability of the moments: the rate n_k/m_k has to belong to $\left]\dfrac{6\sqrt{\pi}}{\rho_l S_k}, \dfrac{6\sqrt{\pi}}{\rho_l S_{k-1}}\right[$. A kinetic-based numerical scheme is then used (de Chaisemartin 2009; Dufour and Villedieu 2005; Kah et al. 2012), based on the ideas developed by Bouchut et al. (2003). It is based on the equivalence, as sketched in Figure 13.1, between the "macroscopic" System (13.1) and the following kinetic equation on $f(t, x, \xi, \zeta)$:

$$\partial_t f + \partial_x(\xi f) = 0, \tag{13.2}$$

with $f(t, x, \xi, \zeta) = m(t, x)\delta(\xi - u(t, x))\delta(\zeta - \phi(t, x))$. This kinetic equation has the exact solution $f(t, x, \xi, \zeta) = f(0, x - \xi t, \xi, \zeta)$.
In order to obtain discrete values over a mesh of constant size Δx, one defines the averages m_j^n, u_j^n and ϕ_j^n for inertial particles, with the usual definitions:

$$m_j^n = \frac{1}{\Delta x}\int_{x_{j-1/2}}^{x_{j+1/2}} m(t_n, x)\,\mathrm{d}x, \tag{13.3}$$

$$m_j^n u_j^n = \frac{1}{\Delta x}\int_{x_{j-1/2}}^{x_{j+1/2}} m_j^n(t_n, x)u(t_n, x)\,\mathrm{d}x, \tag{13.4}$$

$$m_j^n \phi_j^n = \frac{1}{\Delta x}\int_{x_{j-1/2}}^{x_{j+1/2}} m_j^n(t_n, x)\phi(t_n, x)\,\mathrm{d}x. \tag{13.5}$$

The discretized equations are obtained in a conservative form by integrating Eq. (13.2) over $(t, x, \xi, \zeta) \in (t_n, t_{n+1}) \times (x_{j-1/2}, x_{j+1/2}) \times \mathbb{R} \times \mathbb{R}$:

$$m_j^{n+1}\begin{pmatrix} 1 \\ u_j^{n+1} \\ \phi_j^{n+1} \end{pmatrix} = m_j^n \begin{pmatrix} 1 \\ u_j^n \\ \phi_j^n \end{pmatrix} - \frac{\Delta t}{\Delta x}(\boldsymbol{F}_{j+1/2} - \boldsymbol{F}_{j-1/2}). \tag{13.6}$$

where the fluxes $\boldsymbol{F}_{j+1/2}$ can be decomposed in $\boldsymbol{F}_{j+1/2} = \boldsymbol{F}^+_{j+1/2} + \boldsymbol{F}^-_{j+1/2}$ with:

$$\boldsymbol{F}^{\pm}_{j+1/2} = \frac{1}{\Delta t}\int_{t_n}^{t_{n+1}}\int_{\pm\xi\geq 0}\int_{\mathbb{R}} \begin{pmatrix} 1 \\ \xi \\ \zeta \end{pmatrix} \xi\, f(t, x_{j+1/2}, \xi, \zeta)\,\mathrm{d}\zeta\mathrm{d}\xi\mathrm{d}t, \tag{13.7}$$

To evaluate the fluxes, the exact solution of the kinetic scheme is used, which leads to:

$$\boldsymbol{F}^+_{j+1/2} = \frac{1}{\Delta t}\int_{x_{j-1/2}}^{x_{j+1/2}} m(t_n, x)\begin{pmatrix} 1 \\ u(t_n, x) \\ \phi(t_n, x) \end{pmatrix} \mathbb{1}_{\{x, x_{j+1/2} - u(t_n, x)\Delta t \leq x \leq x_{j+1/2}\}}(x)\,\mathrm{d}x, \tag{13.8}$$

and

$$\boldsymbol{F}^{-}_{j+1/2} = -\frac{1}{\Delta t}\int_{x_{j-1/2}}^{x_{j+1/2}} m(t_n,x)\begin{pmatrix}1\\ u(t_n,x)\\ \phi(t_n,x)\end{pmatrix}\mathbb{1}_{\{x,x_{j+1/2}\leq x\leq x_{j+1/2}-u(t_n,x)\Delta t\}}(x)\,\mathrm{d}x. \tag{13.9}$$

These expressions are valid under the CFL condition:

$$\Delta t \sup_x |u(t_n,x)| \leq \Delta x. \tag{13.10}$$

We then have to reconstruct the variables $m(t_n,.)$, $u(t_n,.)$ and $\phi(t_n,.)$ from their averaged values m_j^n, u_j^n and ϕ_j^n on each cell. This reconstruction is wanted to preserve a maximum principle on u and ϕ and the positivity of m in order that the scheme will have the same properties of the averaged variables.

13.1.1.3 Second order kinetic scheme

For the purpose of a second order scheme, piecewise linear reconstructions are considered for m, u and ϕ:

$$\text{for } \; x_{j-1/2}<x<x_{j+1/2} \qquad \left\{\begin{array}{l} m(x) = m_j^n + D_{m_j}(x-x_j,)\\ u(x) = \overline{u_j} + D_{u_j}(x-x_j),\\ \phi(x) = \overline{\phi_j} + D_{\phi_j}(x-x_j).\end{array}\right. \tag{13.11}$$

where $x_j = (x_{j+1/2}+x_{j-1/2})/2$ is the center of the j^{th} cell and where, to simplify the notation, the t_n dependance of each function is implicit. The quantities with bars $\overline{u_j}$ and $\overline{\phi_j}$ are different from the corresponding averaged values u_j^n and ϕ_j^n. In order to have the conservation property, they are defined in such a way that:

$$m_j^n u_j^n = \frac{1}{\Delta x}\int_{x_{j-1/2}}^{x_{j+1/2}} m(x)u(x)\,\mathrm{d}x, \qquad m_j^n\phi_j^n = \frac{1}{\Delta x}\int_{x_{j-1/2}}^{x_{j+1/2}} m(x)\phi(x)\,\mathrm{d}x.$$

They are given by:

$$\overline{u_j} = u_j^n - \frac{D_{m_j}D_{u_j}}{m_j^n}\frac{\Delta x^2}{12} \qquad \overline{\phi_j} = \phi_j^n - \frac{D_{m_j}D_{\phi_j}}{m_j^n}\frac{\Delta x^2}{12}$$

Once the conservativity of the scheme is ensured, the slopes are determined using limiters in order to satisfy maximum principles for the transported quantities and positivity for the number density. In practice, the following slope limiter are used (Bouchut et al. 2003):

$$\begin{aligned}
D_{m_j} &= \frac{1}{2}(\mathrm{sign}(m_{j+1}^n - m_j^n) + \mathrm{sign}(m_j^n - m_{j-1}^n))\\
&\quad \times \min\left(\frac{|m_{j+1}^n - m_j^n|}{\Delta x}, \frac{|m_j^n - m_{j-1}^n|}{\Delta x}, \frac{2m_j^n}{\Delta x}\right),\\
D_{u_j} &= \frac{1}{2}(\mathrm{sign}(u_{j+1}^n - u_j^n) + \mathrm{sign}(u_j^n - u_{j-1}^n))\\
&\quad \times \min\left(\frac{|u_{j+1}^n - u_j^n|}{\Delta x(1-\Delta x D_{m_j}/6m_j^n)}, \frac{|u_j^n - u_{j-1}^n|}{\Delta x(1+\Delta x D_{m_j}/6m_j^n)}\right),\\
D_{\phi_j} &= \frac{1}{2}(\mathrm{sign}(\phi_{j+1}^n - \phi_j^n) + \mathrm{sign}(\phi_j^n - \phi_{j-1}^n))\\
&\quad \times \min\left(\frac{|\phi_{j+1}^n - \phi_j^n|}{\Delta x(1-\Delta x D_{m_j}/6m_j^n)}, \frac{|\phi_j^n - \phi_{j-1}^n|}{\Delta x(1+\Delta x D_{m_j}/6m_j^n)}\right).
\end{aligned} \tag{13.12}$$

The CFL condition is then $\Delta t \max_j |u_j^n| \leq \Delta x$.
Finally, the fluxes can then be evaluated from $m_{j-1/2}^L$, $m_{j-1/2}^R$, $u_{j-1/2}^L$, $u_{j-1/2}^R$, $\phi_{j-1/2}^L$, $\phi_{j-1/2}^R$, the corresponding values of $m(t_n,x)$, $u(t_n,x)$ and $\phi(t_n,x)$ at the left and the right of interface $x_{j-1/2}$ between the cells $j-1$ and j:

$$\begin{aligned}
m_{j-1/2}^L &= m_{j-1}^n + \frac{\Delta x}{2}D_{m_{j-1}}, \quad m_{j-1/2}^R &&= m_j^n - \frac{\Delta x}{2}D_{m_j},\\
u_{j-1/2}^L &= \overline{u_{j-1}} + \frac{\Delta x}{2}D_{u_{j-1}}, \quad u_{j-1/2}^R &&= \overline{u_j} - \frac{\Delta x}{2}D_{u_j},\\
\phi_{j-1/2}^L &= \overline{\phi_{j-1}} + \frac{\Delta x}{2}D_{\phi_{j-1}}, \quad \phi_{j-1/2}^R &&= \overline{\phi_j} - \frac{\Delta x}{2}D_{\phi_j}.
\end{aligned} \tag{13.13}$$

so that (de Chaisemartin 2009):

$$\begin{aligned} \boldsymbol{F}^{+}_{j-1/2} &= \mathbf{U}^{L}_{j-1/2}\alpha^{L}_{j-1/2} - \frac{\Delta t}{2}(\alpha^{L}_{j-1/2})^2\,\Gamma^{+}_{j-1/2}, \\ \boldsymbol{F}^{-}_{j-1/2} &= \mathbf{U}^{R}_{j-1/2}\alpha^{R}_{j-1/2} - \frac{\Delta t}{2}(\alpha^{R}_{j-1/2})^2\,\Gamma^{-}_{j-1/2}, \end{aligned} \tag{13.14}$$

with the following definitions:

$$\mathbf{U}^{L}_{j-1/2} = m^{L}_{j-1/2}\begin{pmatrix} 1 \\ \alpha^{L}_{j-1/2} \\ \phi^{L}_{j-1/2} \end{pmatrix}, \qquad \mathbf{U}^{R}_{j-1/2} = m^{R}_{j-1/2}\begin{pmatrix} 1 \\ \alpha^{R}_{j-1/2} \\ \phi^{R}_{j-1/2} \end{pmatrix}, \tag{13.15}$$

$$\alpha^{L}_{j-1/2} = \frac{(u^{L}_{j-1/2})_+}{1+\Delta t D_{u_{j-1}}}, \qquad \alpha^{R}_{j-1/2} = \frac{(u^{R}_{j-1/2})_-}{1+\Delta t D_{u_j}},$$

with the convention $(y)_+ = \max\{0, y\}$, $(y)_- = \min\{0, y\}$, and

$$\Gamma^{+}_{j-1/2} = \begin{pmatrix} D_{m_{j-1}} \\ -m^{L}_{j-1/2}D_{u_{j-1}} + \alpha^{L}_{j-1/2}D_{m_{j-1}} + \dfrac{\Delta t}{3}D_{m_{j-1}}D_{u_{j-1}}\alpha^{L}_{j-1/2} \\ m^{L}_{j-1/2}D_{\phi_{j-1}} + \phi^{L}_{j-1/2}D_{m_{j-1}} - \dfrac{2\Delta t}{3}D_{m_{j-1}}D_{\phi_{j-1}}\alpha^{L}_{j-1/2} \end{pmatrix} \tag{13.16}$$

as well as

$$\Gamma^{-}_{j-1/2} = \begin{pmatrix} D_{m_j} \\ -m^{R}_{j-1/2}D_{u_j} + \alpha^{R}_{j-1/2}D_{m_j} + \dfrac{\partial_t}{3}D_{m_j}D_{u_j}\alpha^{R}_{j-1/2} \\ m^{R}_{j-1/2}D_{\phi_j} + \phi^{R}_{j-1/2}D_{m_j} - \dfrac{2\partial_t}{3}D_{m_j}D_{\phi_j}\alpha^{R}_{j-1/2} \end{pmatrix}. \tag{13.17}$$

13.1.1.4 Conclusion on transport

The corresponding scheme offers the ability to treat the δ-shocks and vacuum. Furthermore, it guarantees a maximum principle on the velocity and on the passive scalar, as well as the positivity of the density. Moreover, it is second order accurate in space and in time, which is convenient to describe the singularities of the disperse phase in physical space.

13.1.2 Exp-TSM reconstruction algorithm

The Exp-TSM method, described in § 5.3.2, is based on an exponential reconstruction in each section:

$${}^{2}\kappa_k(S) = a_k \exp(-b_k S).$$

13.1.2.1 Reconstruction form inversion

It has been shown in § 5.3.2.2 that the integral system of rank 2 defining the moments from the reconstruction can be written in a form allowing a cascade resolution: the function $g_k = m_k/n_k$ depends only on b_k and can be used as a pivot for elimination resolution.
So the reconstruction process is reduced to the inversion of a function. An analytical expression Eq. (5.29) can be derived for g_k, but not for its reciprocal function, which is therefore inverted numerically.
We consider Ridders' method (Press et al. 1992) which is a method to find a monotonic function's zero and is efficient in our case. It is an iterative method, therefore requiring to compute g_k several times, based on a linearly accelerated dichotomy so the method converges fast and g_k is usually computed around ten times for the required accuracy in practical cases.

13.1.2.2 Computing g_k

The g_k function is explicitly computable thanks to Eq. (5.29) but its expression features the error function or Dawson function. We consider this computation method too costly (see the discussion in § 10.4.3) so we suggest a quadrature approximation of the integral form. The retained quadrature is an adaptive quadrature, and the same as the one discussed and chosen in § 13.1.4, for the same reasons of accuracy and efficiency. We could either use a fixed node quadrature e.g. Newton-Cotes or Gauss-Legendre, but the adaptive quadrature introduced in § 13.1.4.3 is preferred to compute the 3/2 order moment integration. Because of the exponential function in g_k's integrand, an adaptive approach is more accurate than a fixed node quadrature, which achieves a polynomial approximation. The accuracy of the adaptive quadrature in this case is presented in Figure 13.3.

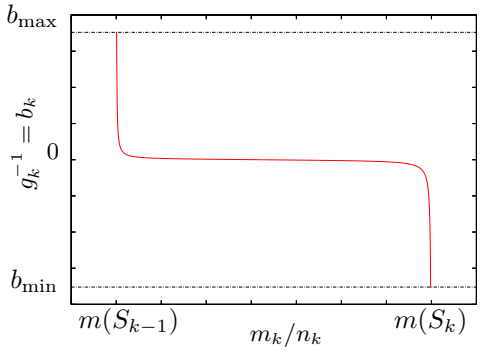

Figure 13.2: *Left: The g_k inverse function with its limiters.*

13.1.2.3 Limitation of the numeric exponentials

To avoid overflow, a constant slope limiter is used in the exponential part of the NDF reconstructions that imposes $\mid b_k \Delta S \mid < K_{\lim}$. Its effect on the accuracy of size distribution reconstructions has been evaluated as very moderate. The shape of the reciprocal function once limited is also presented in Figure 13.2.

13.1.3 Aff-TSM reconstruction algorithm

The Aff-TSM method, described in § 5.3.3, is based on a piecewise affine reconstruction in each section:

$$ {}^2\kappa_k(S) = \begin{cases} 0 & \text{if } S < S_{l,k} \\ \alpha_k \dfrac{S_{r,k} - S}{S_{r,k} - S_{l,k}} + \beta \dfrac{S - S_{l,k}}{S_{r,k} - S_{l,k}} & \text{if } S_{l,k} \leq S \leq S_{r,k} \\ 0 & \text{if } S_{r,k} < S \end{cases} $$

with an additional condition [R1], so that there are three possible cases for the positive affine reconstruction:
(i) a constant zero domain at the right of the section,
(ii) no zero, or
(iii) a constant zero domain at the left,
as stated previously in § 5.3.3.3.

13.1.3.1 Determination of the case

The first goal of the inversion algorithm is to determine to which case belongs a realizable couple (n_k, m_k). This can be done explicitly thanks to the inequalities given in § 5.3.3.3.

13.1.3.2 Inversion

In case (ii), the reconstruction process has to find the affine function that respects two moments, computed between S_{k-1} and S_k which are known: this can be performed analytically:

$$ \begin{cases} \alpha = \dfrac{2n_k(S_{7/2} - S_{5/2}S_{k-1})/\Delta S - m_k \Delta S}{S_{7/2} - S_{5/2}} \\ \beta = \dfrac{-2n_k(S_{5/2}S_k - S_{7/2})/\Delta S + m_k \Delta S}{S_{7/2} - S_{5/2}} \end{cases} \tag{13.18} $$

where ΔS, $S_{5/2}$ and $S_{7/2}$ have been defined in § 5.3.3.3.

n	Non-normalized Weights					Sum	o	C_n
1	1					1	1	-24
2	1					2	1	12
3	1	4				6	3	2880
4	1	3				8	3	6480
5	7	32	12			90	5	1935360
6	19	75	50			288	5	37800000/11
7	41	216	27	272		840	7	1567641600
8	751	3577	1323	2989		17280	7	426924691200/167
9	989	5888	-928	10496		28350	9	62783697715200/37
10	2857	15741	1080	19344	5778	89600	9	458791091483580/173
11	16067	106300	-48525	272400	-260550	427368	11	$653837184.10^{11}/26927$

Table 13.1: *Closed Newton-Cotes coefficients: n/2 first weights (non-normalized), sum and error coefficient.*

In case (i) and (iii), the reconstruction process has to find the affine function that respects two moments, computed between a known and an unknown bound: this requires to find the root of a fifth degree polynomial in $S_{k-1}^{\frac{1}{2}}$ and $S_k^{\frac{1}{2}}$. So we use again Ridders' method.

13.1.3.3 Remarks on inversion cost

As a conclusion, we see that this method requires very few algebra: with only usual operations and no exponentials at all. Some cases require an iterative method for the inversion but the function on which the iteration is performed is polynomial so again very cheap. An inversion with Aff-TSM is therefore more affordable than the similar operation with Exp-TSM, which requires an dedicated quadrature or costly analytic computations.
Limiting the cost of the inversion is all the more important that the inversion is performed at every location, every time step, and for every section. In the context of splitting methods, it may be performed for each operator which is split and changes the size distribution:

- evaporation,
- coalescence,
- break-up,
- and even transport, which possibly mixes states from neighboring cells.

So that the Aff-TSM method has a major advantage on the Exp-TSM from the point of view of cost.

13.1.4 Numerical strategies for size integral computation

As TSM is a moment method, we need to compute many numerical integrals so we describe some quadrature approaches in order to choose the most efficient ones in each case.
We consider in this section the integration of a function ϕ on an interval $[S_a, S_b]$:

$$I = \int_{S_a}^{S_b} \phi(S) \mathrm{d}S. \tag{13.19}$$

13.1.4.1 Newton-Cotes fixed quadrature

As a first quadrature technique, we consider the Newton-Cotes formula of closed type. The 1D n-node closed Newton-Cotes formula approximates integrals as a sum of n point-wise evaluations of the integrand at n predefined abscissae S_i :

$$I = \sum_{i=0}^{n-1} w_i \phi(S_i) + \epsilon_{\mathrm{NC}}^{(n)} \tag{13.20}$$

where $S_i = S_a + \frac{i(S_b - S_a)}{n-1}$ are equi-distributed and include the integration bounds and the w_i are tabulated coefficients. The weights have the symmetry property $w_{n-1-i} = w_i$. We give half of the coefficients in Table 13.1, taken from (Abramowitz and Stegun 1964). The quadrature, as well as any approach involving it, is referred to as (NCn) in the following.
Each Newton-Cotes approach is based on an interpolation of ϕ by its underlying Lagrange polynomial. This yields an error:

$$\epsilon_{\mathrm{NC}}^{(n)} = -\frac{|S_b - S_a|^{o+2}}{C_n} \phi^{(o+1)}(\xi^{(n)}) \tag{13.21}$$

n	Abscissae			Weights			o
1	0			2			2
2		$\pm 1/\sqrt{3}$			1		4
3	0	$\pm 1/\sqrt{3/5}$		$\frac{8}{9}$	$\frac{5}{9}$		6
4		$\pm\sqrt{(3-2\sqrt{6/5})/7}$	$\pm\sqrt{(3+2\sqrt{6/5})/7}$		$\frac{18+\sqrt{30}}{36}$	$\frac{18-\sqrt{30}}{36}$	8
5	0	$\pm\frac{1}{3}\sqrt{(5-2\sqrt{10/7}}$	$\pm\frac{1}{3}\sqrt{(5+2\sqrt{10/7}}$	$\frac{128}{225}$	$\frac{322+13\sqrt{70}}{900}$	$\frac{322-13\sqrt{70}}{900}$	10

Table 13.2: *Gauss-Legendre coefficients: n/2 first weights, sum and error coefficient.*

where $\phi^{(n)}(\xi^{(n)})$ is the n-th derivative of ϕ evaluated at a given $\xi^{(n)} \in [S_a, S_b]$, o is the quadrature's order and C_n is the error coefficient, both given in Table 13.1.
(NCn) achieves a polynomial interpolation which is *a priori* not suited for exponential distributions: this can be seen by considering the error estimate for an exponential form $\phi = \exp(-bS)$, non-dimensionned by a typical estimate of the integral:

$$I_0 = \mid S_b - S_a \mid \exp(-b\xi^{(n)}). \tag{13.22}$$

Eq. (13.21) then becomes:

$$\mathrm{Err}^{\exp}_{(\mathrm{NC}n)} = \frac{\epsilon^{(n)}_{\mathrm{NC}}}{I_0} = \frac{\mid b\Delta S \mid^{o+1}}{C_n}. \tag{13.23}$$

where it is seen that the error increases with the power $o+1$ of $\mid b \mid$.
In the case of these closed Newton-Cotes quadratures, even numbers of quadrature points are disregarded and we resort to (NCn) with n odd.

13.1.4.2 Gauss-Legendre fixed quadrature

We now consider Gauss quadratures and more precisely the Gauss quadrature for a finite closed interval, namely Gauss-Legendre. The 1D n-node Gauss-Legendre formula approximates integrals as a sum of n point-wise evaluations of the integrand at n predefined abscissae S_i :

$$I = \sum_{i=0}^{n-1} w_i \phi(S_i) + \epsilon^{(n)}_{\mathrm{GL}} \tag{13.24}$$

where $S_i = (S_a + S_b)/2 + X_i(S_b - S_a)/2$ do not include the integration bounds and $-1 < X_i < 1$ are the abscissae. They have an analytical expression as well as the weights w_i. We use the symmetry property $X_{n-1-i} = -X_i$ and $w_{n-1-i} = w_i$ to give only half of the coefficients in Table 13.2. The quadrature, as well as any approach involving it, is referred to as (GLn) in the following.
Each Gauss-Legendre approach is based on an interpolation of ϕ by its underlying Legendre polynomial. This yields an error:

$$\epsilon^{(n)}_{\mathrm{GL}} = \frac{\mid S_b - S_a \mid^{2n+1} (n!)^4}{(2n+1)[(2n)!]^3} \phi^{(2n)}(\xi^{(n)}) \tag{13.25}$$

where $\phi^{(n)}(\xi^{(n)})$ is the n-th derivative of ϕ evaluated at a given $\xi^{(n)} \in [S_a, S_b]$, o is the quadrature's order.
(GLn) also achieves a polynomial interpolation which is *a priori* not suited for exponential distributions: we consider the error estimate for an exponential form $\phi = \exp(-bS)$, non-dimensionned by a typical estimate of the integral given in Eq. (13.22) which reads from Eq. (13.21):

$$\mathrm{Err}^{\exp}_{(\mathrm{GL}n)} = \frac{\epsilon^{(n)}_{\mathrm{GL}}}{I_0} = \frac{\mid b\Delta S \mid^{2n} (n!)^4}{(2n+1)[(2n)!]^3}. \tag{13.26}$$

where it is seen that the error increases with the power $2o$ of $\mid b \mid$.

13.1.4.3 Exponentially-adapted quadrature

The previous polynomial quadratures are not well suited for exponential functions, as visible with the error studies Eq. (13.23) and Eq. (13.26). An original approach is to use an exponentially-adaptive n-node quadrature, which we now describe. The quadrature, as well as any approach involving it, is referred to as (ADn) in the following.

We consider the integrand function ϕ as the product of another function and an exponential kernel:

$$\phi = \exp(-bS)\zeta(S) \tag{13.27}$$

so that we can approach with a n-node quadrature:

$$I = \sum_{i=0}^{n-1} w_i \zeta(S_i) + \epsilon_{Ad}^{(n)} \tag{13.28}$$

while the exponential part is included in the quadrature.
This is done by considering constraints under the form of a monomial times the exponential kernel. The moments of the i exponential kernel are computed for p from 0 to $2n-1$:

$$\mathcal{M}_p = \int_{S_a}^{S_b} S^p \exp(-bS)\mathrm{d}S \tag{13.29}$$

which can be done analytically since i is an integer. One then determines the n abscissae S_i and n weights w_i that ensure the moments of order p to be exactly reconstructed:

$$\left\{\begin{array}{lllllll} \mathcal{M}_0 & = w_0 & +w_1 & + & ... & +w_{n-1} \\ \mathcal{M}_1 & = w_0 S_0 & +w_1 S_1 & + & ... & +w_{n-1} S_{n-1} \\ \mathcal{M}_2 & = w_0 S_0^2 & +w_1 S_1^2 & + & ... & +w_{n-1} S_{n-1}^2 \\ \quad\vdots & & & & & \\ \mathcal{M}_{2n-1} & = w_0 S_0^{2n-1} & +w_1 S_1^{2n-1} & + & ... & +w_{n-1} S_{n-1}^{2n-1} \end{array}\right. \tag{13.30}$$

which corresponds to a non-linear system to invert.
System (13.30) is invertible since the $\mathcal{M}_k$ are the moments of a positive function (Gautschi 1996). The abscissae and weights are found with Wheeler (1974)'s method.
The quadrature is called adaptive since the abscissae and weights depend on b. The approximation of $\zeta(S)$ is polynomial of order $2n$:

$$\epsilon_{(\mathrm{Ad})}^{n} = C\frac{(S_b - S_a)^{(2n)}}{(2n)!}\zeta^{(2n)}(\xi^{(n)}) \tag{13.31}$$

with $0 \leq C \leq 1$ depending on b and n. This can be demonstrated from formulae given in Gautschi (1996). In particular, we highlight that the quadrature is exact for polynomials of degree $\leq 2n-1$. The quadrature is exponentially adapted in the sense that the abscissae move towards the side where the exponential kernel is stronger.
Regarding cost, the quadrature spares the computation of the exponentials at the nodes but a minimum of $2n$ exponentials must be computed in most cases for the analytical evaluation of the $2n$ moments M_i. The cost of the algebra to invert System (13.30) grows fast with n. In the particular case of 2 nodes, analytical expressions of abscissae and weights can be used (Desjardins et al. 2008) which reduces significantly the computational cost but in the general case $n \geq 3$, an advanced inversion algorithm must be used such as Wheeler (1974)'s method.

13.1.4.4 Use for inversion

For cost reasons, we have suggested to compute the g_k auxiliary function, which is defined by an integral Eq. (5.28), with a quadrature instead of its analytical expression Eq. (5.29). Cost reduction is all the more crucial that g_k is computed by an iterative process. Moreover the inversion is performed very often, as discussed in § 13.1.3.3.
We suggest the use of (ADn) quadrature to compute the 3/2 order moment. The estimation is not exact but still satisfactory as 3/2 is smaller than n. A computation of g_k with (ADn) is proven to achieve a very accurate result, even with as few as 2 nodes as shown in Figure 13.3 where the error is always below 10^{-5}. On the contrary, fixed-node quadratures yield intolerable errors as soon as b moves from 0, even with a high number of nodes, as illustrated on a similar type of integral with (NC5) and (NC9) in Figure 13.5.
In the Aff-TSM method, no integrals are to be computed in the inversion step.

13.1.4.5 Use for linear sources

From the data of sectional reconstructions, any integral of the form

$$I_k = \int_{S_{k-1}}^{S_k} {}^2\kappa_k(S)\phi(S)\mathrm{d}S \tag{13.32}$$

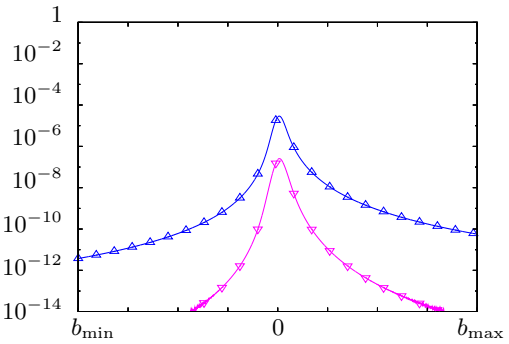

Figure 13.3: *Relative error on $g_k(b)$ – Δ: Ad2; ∇: Ad3; Reference: analytic*

can be computed, e.g. drag force, heat transfer.
Considering $\zeta(S)$ as a source term which must be integrated versus ${}^2\kappa_k(S)$, exponential in the case of Exp-TSM, (ADn) accounts presumably better for cases with steep distributions i.e. where b is far from zero. Indeed the (ADn) quadrature error is independent from b contrary to polynomial ones e.g. (NCn) or (GLn): this can be understood by considering that (ADn) computes the integrals with quadrature points evaluated at adapted abscissae.

13.1.4.6 Case of Break-up

At the Multi-Fluid level, secondary break-up source terms are computed with elementary integrals, see § 5.2.3. For section k, the disappearance terms are 1D integrals on ${}^2\kappa_k$ and they are computed from the creation elementary integrals in practice. But the creation elementary integrals, e.g. ${}^2\mathrm{Q}_{ik}^{m+}$, given in Eq. (5.14), are 2D integrals on the mother section ${}^2\kappa_i$ and on the fragment size distribution $f_{\mathrm{bu}}(S)$, versus the arrival section interval k. This second integration cannot be precomputed as $f_{\mathrm{bu}}(S;\boldsymbol{u}_i,S^\star,\boldsymbol{u}_g)$ also depends on the flow conditions $\boldsymbol{u}_g$ and on the mother droplet size variable $S^\star$ and velocity $\boldsymbol{u}_i$ which is constant.
It happens in some modelings that $f_{\mathrm{bu}}(S)$ is exponential, see for instance the closure of Eq. (3.146). In this case, (ADn) can be used with an adaptation on the break-up coefficient, e.g. $\frac{\gamma^2}{4\pi}$ in the previous closure. The quadrature must be embedded in the upper, mother integration one, which can be also adaptive in Exp-TSM or not in Aff-TSM.

13.1.5 Numerical strategy for TSM coalescence size integrals

13.1.5.1 A difference situation from the OSM method

The One Size Moment expressions given in Eq. (4.53) are double integrals on size variables and their integrands are space and time independent when assuming $\mathfrak{E}=1$. The time/space dependency $m_i(t,x)$ has indeed been factorized. Pre-computing the integrals ${}^1\mathrm{Q}^\star_{ijk}$ and ${}^1\mathrm{Q}^\diamond_{ijk}$ once for all allows to compute the coalescence terms as quadratic combinations of Eq. (4.54), this being possible only in the absence of models depending jointly on droplet sizes and on the flow such as collision efficiency.
The Two Size Moment expressions Q^n_{ijk}, $\mathrm{Q}^\star_{ijk}$ and $\mathrm{Q}^\diamond_{ijk}$ given in Eq. (5.22) are size double integrals that can never be pre-computed.

13.1.5.2 A 2D quadrature strategy

We consider a double integration on the integrand $\Psi^{ij}(S^\star,S^\diamond)$ defined in Eq. (5.21).
Since the integration 2D domain $\mathscr{D}_{ijk}$ is a non trivial polygon in volume variables, see Figure 4.10, we suggest to use a two-level embedded quadrature, which is flexible enough to render accurately the $\mathscr{D}_{ijk}$ polygon. This is all the more important that the size reconstructions ${}^2\kappa_k$ may be very steep, bringing all the physics at an edge of $\mathscr{D}_{ijk}$.
A first direction of integration is chosen, e.g. $S^\star$. The minimum bound across this direction is determined:

$$S^\star_{\min}=\begin{cases} S_{i-1} & \text{if } \mathcal{V}(S_{i-1})+\mathcal{V}(S_j)\geq\mathcal{V}(S_{k-1}) \\ \min(S_i,\mathrm{Surf}(\mathcal{V}(S_{k-1})-\mathcal{V}(S_j))) & \text{otherwise.}\end{cases} \tag{13.33}$$

while the maximum bound reads:

$$S^\star_{\max}=\begin{cases} S_i & \text{if } \mathcal{V}(S_i)+\mathcal{V}(S_{j-1})\leq\mathcal{V}(S_k) \\ \max(S_{i-1},\mathrm{Surf}(\mathcal{V}(S_k)-\mathcal{V}(S_{j-1}))) & \text{otherwise}\end{cases} \tag{13.34}$$

where $\mathrm{Surf}(v)$ is the surface of a particle of volume v and $\mathcal{V}(S)$ is the volume of a particle of surface S. The quadrature nodes $S_l^\star$ are distributed within $[S_{\min}^\star, S_{\max}^\star]$ according to the chosen quadrature approach. For each node l, the second direction $S^\diamond$ is now examined by determining the local minimum bound:

$$S_{\min,l}^\diamond = \begin{cases} S_{j-1} & \text{if } \mathcal{V}(S_l^\star) + \mathcal{V}(S_{j-1}) \geq \mathcal{V}(S_{k-1}) \\ \min(S_j, \mathrm{Surf}(\mathcal{V}(S_{k-1}) - \mathcal{V}(S_l^\star))) & \text{otherwise.} \end{cases} \tag{13.35}$$

while the maximum bound reads:

$$S_{\max,l}^\diamond = \begin{cases} S_j & \text{if } \mathcal{V}(S_l^\star) + \mathcal{V}(S_j) \leq \mathcal{V}(S_k) \\ \max(S_j, \mathrm{Surf}(\mathcal{V}(S_k) - \mathcal{V}(S_l^\star))) & \text{otherwise.} \end{cases} \tag{13.36}$$

Again, the quadrature nodes $S_{lm}^\diamond$ are distributed within each interval $[S_{\min,l}^\diamond, S_{\max,l}^\diamond]$ according to the chosen quadrature approach. As an illustration, the quadrature nodes for (NCn) are presented in a radius-radius diagram in Figure 13.4.
The integration domain and therefore the quadratures nodes can be determined with the above procedure in both cases of exponential and positive affine reconstructions. In the latter case however, accuracy is significantly increased by distributing the nodes within $[S_{l,i}, S_{r,i}]$ and $[S_{l,j}, S_{r,j}]$ instead of $[S_{i-1}, S_i]$ and $[S_{j-1}, S_j]$.

13.1.5.3 Fixed node strategies

We first consider a 2D quadrature strategy with fixed node approaches e.g. (NCn) or (GLn):

$$\iint \Psi^{ij} \mathrm{d}S^\star \mathrm{d}S^\diamond \simeq \sum_{l=0}^{n-1} w_l \sum_{m=0}^{n-1} w_m \Psi^{ij}(S_l^\star, S_{lm}^\diamond) \tag{13.37}$$

The abscissas and weights are fixed and depend on the quadrature. In the case of (NCn), see also § 13.1.4.1, we have

$$\begin{cases} S_l^\star & = S_{\min}^\star + l \dfrac{S_{\max}^\star - S_{\min}^\star}{n-1} \\ S_{lm}^\diamond & = S_{\min,l}^\diamond + m \dfrac{S_{\max,l}^\diamond - S_{\min,l}^\diamond}{n-1} \end{cases} \tag{13.38}$$

while the w_l (and w_m) are tabulated as discussed in § 13.1.4.1. In the case of (GLn), see also § 13.1.4.2, we have

$$\begin{cases} S_l^\star & = \dfrac{S_{\max}^\star + S_{\min}^\star}{2} + X_l \dfrac{S_{\max}^\star - S_{\min}^\star}{2} \\ S_{lm}^\diamond & = \dfrac{S_{\max,l}^\diamond + S_{\min,l}^\diamond}{2} + X_m \dfrac{S_{\max,l}^\diamond - S_{\min,l}^\diamond}{2} \end{cases} \tag{13.39}$$

where the X_l (and X_m) are given from the tabulation of § 13.1.4.2, as well as the w_l (and w_m).
Fixed quadrature strategies are valid for both exponential and positive affine reconstructions. As the nodes are fixed, this strategy imposes a cost mainly consisting in n^2 evaluations of the integrand Ψ^{ij} per source term through the formula: 2D (NCn) and 2D (GLn) approaches achieve a polynomial-accurate interpolation which is *a priori* not suited for the exponential distributions of Exp-TSM.

13.1.5.4 Validation of (ADn) for Exp-TSM

We now consider only the exponential reconstruction of Exp-TSM. The study of (NCn) presented in Figure 13.4 has shown that numerous nodes are needed to be accurate enough on coalescence terms with Exp-TSM. So we qualify the adaptive quadrature strategy.
We re-write the 2D integrand by factorizing its double exponential

$$\Psi^{ij} = {}^2\kappa_i(S^\star) {}^2\kappa_j(S^\diamond) \zeta(S^\star, S^\diamond). \tag{13.40}$$

We highlight that the ζ part varies smoothly with $S^\star$ and $S^\diamond$, for typical cross-section formulae such as that of Eq. (3.131). The 2D exponentially-adapted quadrature formula keeps only the smooth part and reads:

$$\iint \Psi^{ij} \mathrm{d}S^\star \mathrm{d}S^\diamond \simeq \sum_{l=0}^{n-1} w_l \sum_{m=0}^{n-1} w_m \zeta(S_l^\star, S_{lm}^\diamond) \tag{13.41}$$

The abscissae and weights $S_l^\star, w_l$ are computed with b_i and $S_{\min}^\star, S_{\max}^\star$ thanks to the algorithm of § 13.1.4.3. While the n sets of abscissae and weights $S_{lm}^\diamond, w_m$ are computed with b_j and with a pair of bounds $S_{\min,l}^\diamond, S_{\max,l}^\diamond$ for each l abscissa.

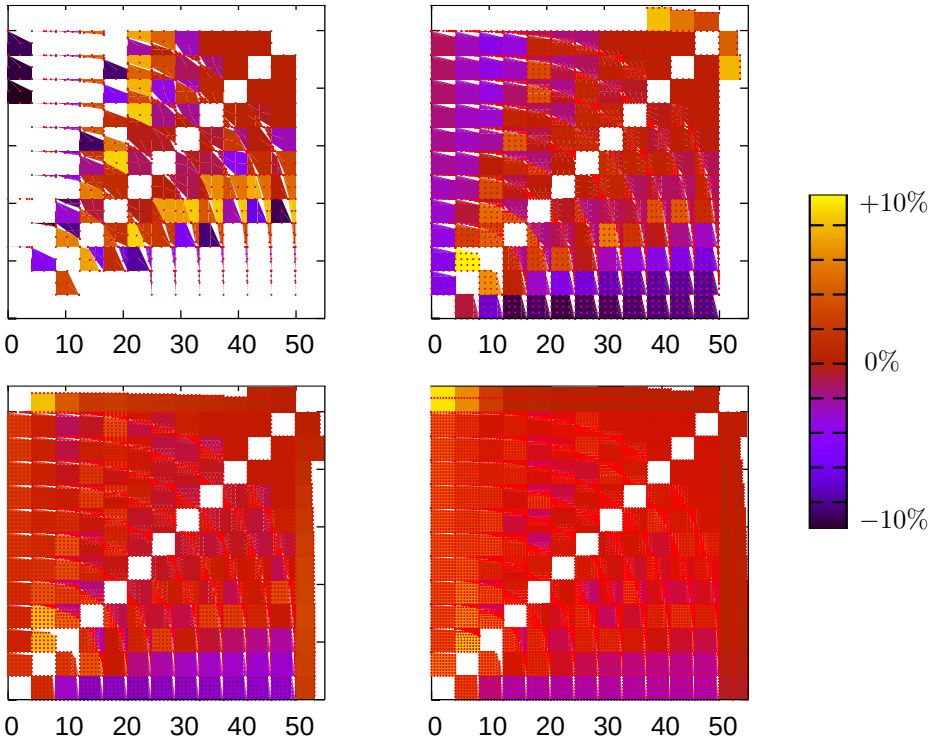

Figure 13.4: *Relative error of the coalescence integrals for Exp-TSM with (NC3), (NC5), (NC7), and (NC9) on a 13 section case – Error between* -10% *and* 10% *and white if out of bounds; Size scales in radius (*μ*m); + quadrature nodes.*

The cost of this embedded adaptive quadratures is rather high compared to fixed quadratures but each adaptive quadrature achieves a $2n^{\text{th}}$ order integration so we can use less nodes compared to the equi-distributed quadrature (NCn): a solution based on (AD2) is efficient thanks to the analytical formulae to invert the system (see § 13.1.4.3). Moreover this approach remains accurate for large values of b, corresponding to steep distributions.

13.1.5.5 Quadrature comparison study

We focus on the Exp-TSM method, for which the choice of a lower order, exponentially adaptive quadrature is envisioned.
We perform a comparison of the suggested quadrature methods on their ability to compute the following integral:

$$I(\beta) = \int_{s_1}^{s_2} S^{\frac{3}{2}} (\sqrt{S^\star} + \sqrt{S})^2 \exp(-\beta S) \mathrm{d}S. \tag{13.42}$$

This function represents a typical coalescence partial 1D integral parametrized by β, which accounts for the exponential parameter that causes integration stiffness.

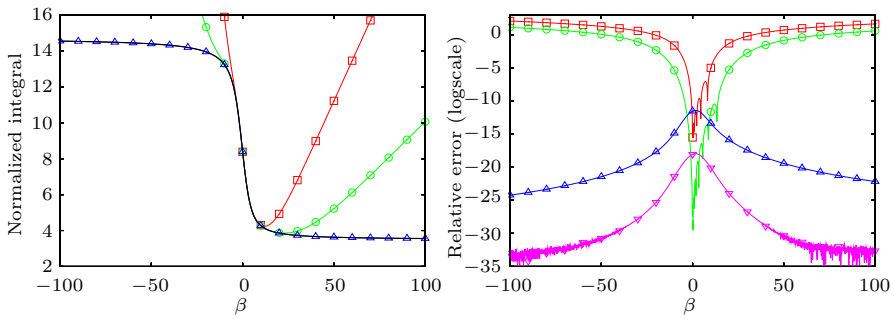

Figure 13.5: *Comparison of quadrature errors (left: absolute; right: relative) on the test integral* $I(\beta)$ *with* $S_1 = 1$, $S_2 = 2$ *and* $S^\star = 0.75$ *– □: NC5; ○: NC9; △: Ad2; ▽: Ad3;* ***Black****: Reference.*

After normalizing $I(\beta)$ by $\int_{s_1}^{s_2} \exp(-\beta S)\mathrm{d}S$ and taking arbitrary numerical values for the integration bounds and the second droplet surface parameter, we show in Figure 13.5 results compared to a reference integral

computed with a 15-stage Romberg method. This proves the failure of fixed-node, polynomial quadratures for moderate to large values of the exponential parameter. The adaptive quadratures behave very well, always achieving a precision better than 10^{-10} with 2 nodes. In the following, we therefore use an adaptive quadrature with 2 nodes (Ad2).

13.2 Validation of TSM methods in the monokinetic framework

Algorithms have been extensively presented, that allow to integrate source terms from the knowledge of size moments. We now implement the methods in an in-house code and perform validations for the computation of complex size evolution.

13.2.1 In-house code for polydisperse studies: the TUYA code

13.2.1.1 Description of the code

The TUYA code is an in-house research code developed to study numerical methods dedicated to polydispersity and size distribution evolution in low-inertia sprays. It features the Exp-TSM and the Aff-TSM Multi-Fluid methods, as well as the OSM Multi-Fluid method as a reference. The original code i.e. before improvement, is detailed in § 10.5.2.
In addition to the behavior of size distribution evolution itself, the code allows to study size-velocity coupling, as defined and presented in § 3.1.3.5, that is the fact that droplet transport depends on droplet size and vice-versa. The coupling feedback loop is closed when velocity differences yield size evolution, typically when coalescence occurs. Evaporation and break-up are also studied.
The code is designed to solve the evolution of a spray in a fixed geometry featuring size-velocity coupling: a pseudo-2D incompressible decelerating nozzle described after. This formally corresponds to the one-way coupling context of an incompressible gas velocity with droplets having their own velocities due to their small inertia. The droplet density has a complex behavior: it is compressible and also depends on velocity, which is coupled to size.

13.2.1.2 Geometry and gas flow

Let us describe the geometry of the test-case: it is a 2D axi-symmetrical diverging conical nozzle (Figure 13.6). It is also described in detail in Laurent et al. (2004).
For the problem to be simpler, an incompressible gas flow is considered. It is taken independent from the particles i.e. the particles are one-way coupled. We neglect the wall viscosity and all other sources of vorticity so the streamlines are straight with well chosen injection conditions. The expressions for the gaseous axial velocity u_z and the reduced radial velocity u_r/r come from the incompressibility and the self-similarity assumptions and they read for $z \geq z_0$:

$$u_z(z) = \frac{z_0^2 u_z(z_0)}{z^2}, \quad \frac{u_r}{r} = \frac{u_z}{z} = \frac{z_0^2 u_z(z_0)}{z^3} \tag{13.43}$$

where $z_0 > 0$ is the coordinate of the nozzle entrance and $u_z(z_0)$ is the fixed axial velocity at the entrance. The velocity, which is plotted in Figure 13.6, decreases since the nozzle diverges.

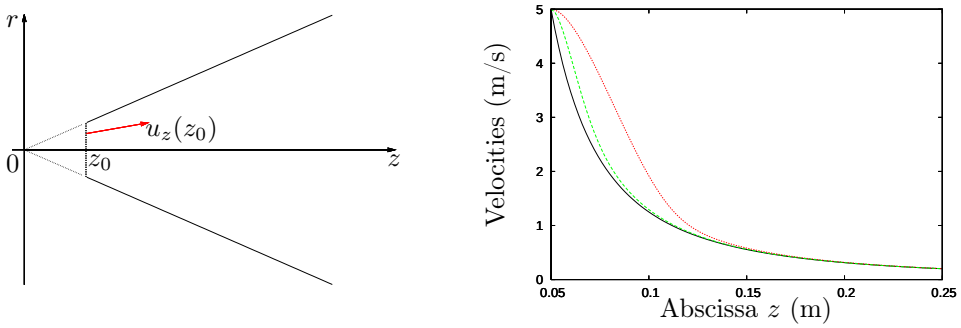

Figure 13.6: *Geometry of a conical 2D self-similar diverging nozzle (Left) and typical velocities in the nozzle (Right) – (Solid): Gas $u_z(z)$; Dashed: Particles of radius $r_1 = 15\,\mu m$ corresponding to a Stokes number St_1; Dotted: Particles with $r_2 = 30\,\mu m$ and $St_2 > St_1$.*

The particles are injected with velocities that are aligned to the gas streamlines so their trajectories are also straight lines. The droplets slow down as the gas decelerates because of drag, as shown in Figure 13.6. For particles with St > 0, the velocities do not match the incompressible flow field Eq. (13.43), so that

compressible effects occur. Since $\boldsymbol{u}(z) > \boldsymbol{u}_g(z)$, we have a reduction in mass densities, as illustrated in Figure 13.7, which complicates the interpretation of results on mass densities.

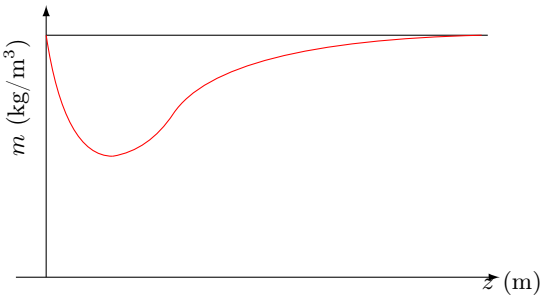

Figure 13.7: *Typical mass evolution along the nozzle for a cloud of particles. It features an expansion effect due to the fact that $\boldsymbol{u}(z) > \boldsymbol{u}_g(z)$, which illustrates the compressibility of the disperse phase.*

13.2.1.3 A decelerating nozzle for coalescence

The droplets are made of alumina, their initial velocity is the one of the gas, their initial temperature, fixed at the one of the gas, is $T_k = 3600\,\mathrm{K}$ and does not change along the trajectories. Since alumina is liquid at this temperature, droplets can coalesce.
As said previously, the droplets slow down with drag, however at a rate depending on their size and inertia, as illustrated in Figure 13.6. This will induce velocity differences, as visible on the velocity graph, and coalescence. The injection velocity conditions the velocity differences and therefore the coalescence intensity though the residence time will decrease proportionally. But the deceleration rate at the entrance of the nozzle $a(z_0) = -2u_z(z_0)/z_0$, which depends on the injection velocity because of the geometry, conditions the strength of the size-velocity coupling so the Kn_g globally increases with $u_z(z_0)$.
When coalescence occurs, the assumption of straight trajectories is not exact. However, even in the case of coalescence, it remains valid in the neighborhood of the centerline (Laurent et al. 2004). We focus our study there.
As a conclusion, the present decelerating nozzle is a simple case still featuring size-velocity coupling, which we aim at capturing in complex configurations.

13.2.1.4 Residence times

Remarkably, the gas residence time in the nozzle τ^R_{nozzle} can be computed analytically, from Eq. (13.43), depending on the output abscissa $z_{\max}$:

$$\tau^R_{\mathrm{nozzle}} = \int_{z_0}^{z_{\max}} \frac{\mathrm{d}z}{u_z(z)} = \frac{1}{3}\frac{z^3_{\max}}{z_0^2 u_z(z_0)} \tag{13.44}$$

since the velocity is analytical and the configuration steady.
This time can be used to estimate the particles' residence times though they will be slightly lower since the particle velocities are above $u_z(z)$ for all z, as shown in Figure 13.6.

13.2.1.5 Numerical features

Let us describe the numerical strategy developed in the research code. The chosen configuration is stationary, 2D axi-symmetrical in space and 1D in droplet size.
The pseudo 2D steady equations describing this configuration, assuming a Stokes law, are those of the Multi-Fluid approaches, with particular transformations thanks to self-similarity. For the One Size Moment method, Eq. (4.42) for section k becomes:

$$\left\{\begin{array}{l} \mathrm{d}_z(m_k\boldsymbol{u}_k) + \dfrac{2m_k\boldsymbol{u}_k}{z} = {}^1\mathrm{C}^{m+}_k - {}^1\mathrm{C}^{m-}_k \\ \mathrm{d}_z(m_k\boldsymbol{u}_k^2) + \dfrac{2m_k\boldsymbol{u}_k^2}{z} = m_k\dfrac{\boldsymbol{u}_g(z) - \boldsymbol{u}_k}{{}^1\tau^u_k} + {}^1\boldsymbol{C}^{u+}_k - {}^1\boldsymbol{C}^{u-}_k \end{array}\right. \tag{13.45}$$

and for the Two Size Moment method, Eq. (5.8) becomes:

$$\left\{\begin{array}{l} \mathrm{d}_z(n_k\boldsymbol{u}_k) + \dfrac{2n_k\boldsymbol{u}_k}{z} = {}^2\mathrm{C}^{n+}_k - {}^2\mathrm{C}^{n-}_k \\ \mathrm{d}_z(m_k\boldsymbol{u}_k) + \dfrac{2m_k\boldsymbol{u}_k}{z} = {}^2\mathrm{C}^{m+}_k - {}^2\mathrm{C}^{m-}_k \\ \mathrm{d}_z(m_k\boldsymbol{u}_k^2) + \dfrac{2m_k\boldsymbol{u}_k^2}{z} = m_k\dfrac{\boldsymbol{u}_g(z) - \boldsymbol{u}_k}{{}^2\tau^u_k} + {}^2\boldsymbol{C}^{u+}_k - {}^2\boldsymbol{C}^{u-}_k \end{array}\right. \tag{13.46}$$

These systems are ordinary differential equation (ODE) systems which we integrate with an error smaller than 2.10^{-4}. This error is defined with the L^∞ norm of the difference on mass concentration repartition to a reference solution.
For coalescence, efficiency laws can be used and are noticed as so. In other cases we use $\mathfrak{E} = 1$ especially for the validations versus other numerical methods.

13.2.2 Verification on the D'Herbigny experiment

We consider a 1D case with experimental results: the experiment conducted by D'Herbigny and Villedieu (2001) aimed at studying the growth of big droplets falling into a fog of small droplets, especially to quantify collision efficiencies. This experiment is extensively described in § 7.3.1 and we here consider the case for it features droplets encountering a strong variation in their size distribution. The simulations are performed with the TUYA code, in which the nozzle's angle is null, in order to reproduce the cylindrical geometry.
We consider simulations with the Two Size Moment Multi-Fluid method in the experiment conditions, though testing six droplet concentration values for the small droplet fog, with C_v from 10 ppm to 60 ppm. We use the three collision efficiency laws described in § 3.3.3.1 i.e. $\mathfrak{E} = 1$, the Langmuir-Blodgett law from Eq. (3.65) and the Beard-Grover law from Eq. (3.66). In Figure 13.8, the measurements from the D'Herbigny experiment are recalled from Figure 7.12 and the computation results are given for the average big droplet radius after 5 m in the fog, depending on its concentration. The simulations show a satisfactory linear dependency of radius growth on fog concentration. This allows us to determine an average collision efficiency coefficient $\bar{\mathfrak{E}}$ given in Table 13.3 for the two empirical laws and for the experiment. The simulation results finally show that collision efficiency laws have a dramatic effect on radius growth, undermining it up to 72 % in the Langmuir-Blodgett case for instance.

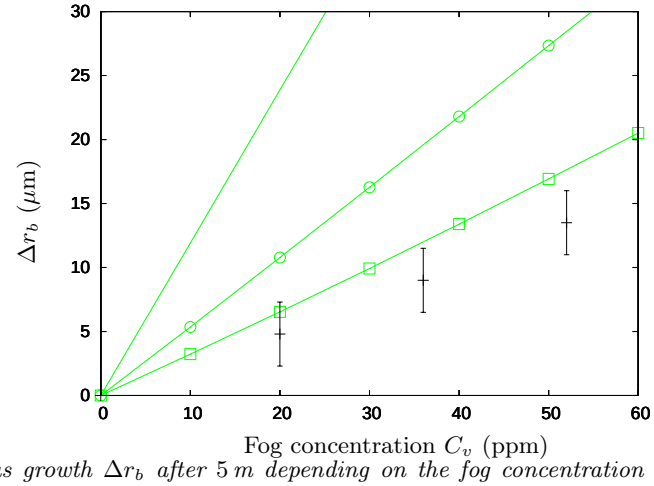

Figure 13.8: *Radius growth Δr_b after 5 m depending on the fog concentration C_v – Solid: Exp-TSM simulation with $\mathfrak{E} = 1$; □: Exp-TSM Moment simulation with Langmuir-Blodgett model; ○: Exp-TSM Moment simulation with Beard-Grover model; **Errorbars**: Experimental.*

	Exp-TSM simulation		Experiment
	Langmuir-Blodgett	Beard-Grover	
Average efficiency	$\bar{\mathfrak{E}}^{\mathrm{LB}} = 0.28$	$\bar{\mathfrak{E}}^{\mathrm{BG}} = 0.46$	$\bar{\mathfrak{E}}^{\mathrm{XP}} = 0.21$

Table 13.3: *Average collision efficiency values in the D'Herbigny configuration*

As for the results of the experiment, they corroborate the linear dependency of radius growth on fog concentration that was proven in § 7.3.1.
They also confirm the dramatic undermining of coalescence by the collision efficiency factor, tending to designate the Langmuir-Blodgett law even-though the experimental average collision efficiency is even smaller than the model forecast. We therefore conclude that coalescence simulations in SRM conditions should take a collision efficiency law into account.
As a conclusion, the D'Herbigny experiment underlines the importance of collision efficiency model. Moreover, though the experimental results are shadowed by uncertainty on collision efficiencies, local fog concentrations and size measurements, their comparison to simulations still provides an ultimate validation of the Two Size Moment method, regarding the linear dependence of growth on fog concentration.

13.2.3 Validation of TSM on steep distributions

13.2.3.1 Modal resolution

We now want to compare the analytical formulae derived in Chapter 7 to simulations and more particularly the variable β formula of Eq. (7.29). So we choose non equidistributed section bounds: the first section encloses the entire small droplet distribution; a dummy section accounts for the gap; the big droplet distribution lives in all the remaining sections, that are of constant width in radius. The number of sections given to specify the discretization of the following simulations is therefore the one of the big droplets that is sections above r_b.
A comparison of formula (7.29) with a fine section grid Two Size Moment simulation in the case of few collisions is given in Figure 13.9 to illustrate the relevance of the analytical model. In this configuration assumption [He3], allowing to use a constant cross section, is perfectly valid as we can verify:

$$\epsilon z/z_0 = v_b/v_s z/z_0 = (50)^{-3} z/z_0 \ll 1. \tag{13.47}$$

Let us add that the modal i.e. discrete nature of the exact distribution is obvious in Figure 13.9 and is correctly captured in our Two Size Moment simulations. Yet, the number of modes increases with z/z_0 and the corresponding number of sections required becomes unsustainable. To explore higher z, we now consider simulations that are modally unresolved because of "coarse" section discretizations, the big droplet distribution being then computed as continuous.

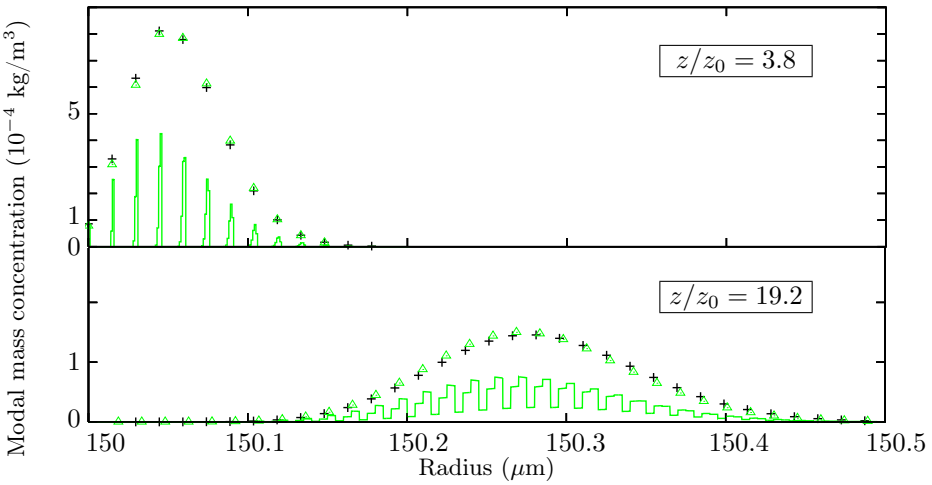

Figure 13.9: *Poisson's law (+) compared to* 200 *section Eulerian Multi-Fluid mass density distribution (histogram) and total mass per mode (△) for* $z/z_0 = 3.8$ *(top) and* $z/z_0 = 19.2$ *(bottom). For analytical validation purposes, this case features a strictly monodisperse fog with* $r_s = 10\,\mu m$.

The results of the β constant model are a first step that confirms the validity of our approach. Yet in the D'Herbigny conditions, one has $z/z_0 \approx 2.10^5$ when $C_v = 60\,\text{ppm}$ while $\frac{v_b}{v_s} \approx 10^5$ so that the coalescence number criterion is not fulfilled. This discrepancy is obvious when comparing the analytical and simulation-derived growth rate laws. Indeed the analytical formula given in Eq. (7.30) gives a linear increase of average volume with C_v, which does not match the linear radius increase obtained numerically and experimentally and showed in Figure 13.8. The constant β model is not satisfactory in the D'Herbigny conditions.

13.2.3.2 Comparison to an analytical formula

We now consider a particular case where the fog volume concentration goes from 10 ppm to 60 ppm and the travelled distance is $z = 2\,\text{m}$. We therefore have $z \gtrsim \mathcal{L}_g$. Let us compare the different model and simulation results. The One Size Moment simulations are performed with 200 sections while using 80 sections for the Two Size Moment ones. The different NDF are given in Figure 13.10 for the One Size Moment, Two Size Moment, constant β and variable β models.
First, we note that the predicted average radii are close except with the constant β model. The constant β model fails, as expected, because $z \gtrsim \mathcal{L}_g$ invalidates [He3] which is equivalent to saying that the big droplet radius variation is too important and requires to reevaluate the impact parameter. The other three models well agree on the radius growth.
They predict an average radius growth Δr_b that is linearly dependent on C_v and is confirmed in Figure 13.8 in § 13.2.2. In contrast, the constant β model predicts a volume growth linearly dependent on fog concentration, which is natural since coalescence intensity is in this case only dependent on C_v.

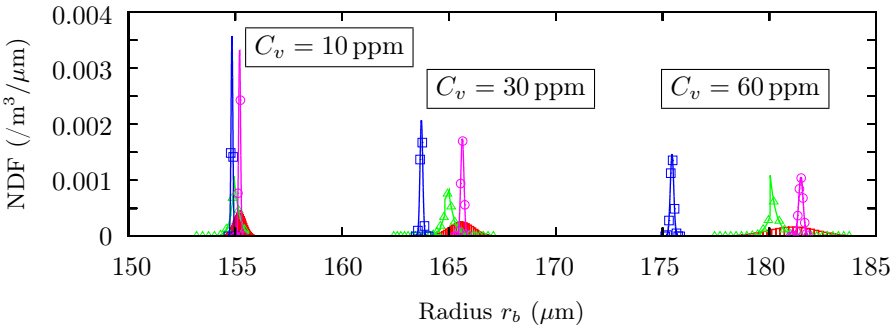

Figure 13.10: *NDF after 2 m in a 10, 30 and 60 ppm fog – Histogram: 200 sections, OSM MF method; △: 80 sections, Exp-TSM MF method; □: constant β model; ○: variable β model.*

13.2.3.3 Illustration of numerical diffusion in size phase space

We now focus on the treatment of the size distribution dispersion. There is a strong difference in Figure 13.10 between a refined One Size Moment simulation where the size distribution is widespread, and a coarser Two Size Moment simulation where the size support remains narrow. The peak widening effect featured by the One Size Moment method increases with fog concentration as visible in Figure 13.10. This widening effect increases also with z.

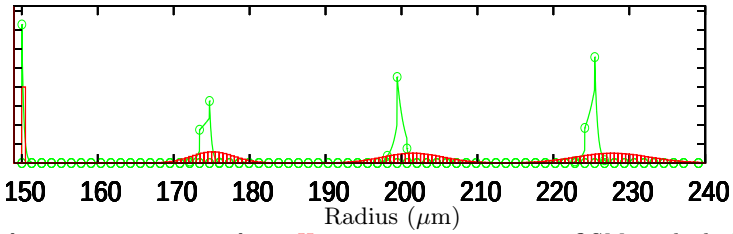

Figure 13.11: *NDF after 2 m in a 60 ppm fog – Histogram: 200 sections, OSM method; △: 80 sections, Exp-TSM method.*

As a general remark, steep distributions are abnormally widespread by MF methods along their way in the size phase space: this is comparable to numerical diffusion in the size phase space. We refer to this effect as numerical diffusion though it results from numerical errors on source terms and not on fluxes. It is remarkable that these test-cases are performed with a high number of sections so the One Size Moment numerical diffusion is unacceptable since it will be even more penalizing in practical cases where size discretizations are coarse. In contrast, the Two Size Moment method brings moderate diffusion in size phase space as shown in Figure 13.10 since widening is smaller to that due to physical size dispersion quantified in our analytical models. The Two Size Moment method handles correctly the D'Herbigny case regarding average size and size dispersion.

13.2.3.4 Conclusion of the validation

As a conclusion, the Two Size Moment Multi-Fluid method, is here proven to be robust and validated thanks to a comparison with analytical formulae, allowing detailed comparison of size distributions. The TSM method is accurate and far less diffusive than the OSM method when dealing with the coalescence of steep size distributions. This feature is relevant for SRM applications where the alumina cloud is sometimes modeled as bimodal (Price 1984a).

13.2.4 Non-linear coalescing case

In this section, we validate the Two Size Moment method by comparing the two Multi-Fluid methods on their ability to describe the dynamics of a coalescing cloud in a size-velocity coupled case. Considering the size/velocity coupling, we need a well-suited test-case, inducing coalescence as well as size-conditioned dynamics and difficult enough to highlight the limitations of the methods. We therefore use the nozzle test-case introduced in Laurent et al. (2004) to challenge the Two Size Moment method and determine for both methods:

- the convergence rate on mass density prediction regarding size discretization,
- the minimum number of sections to capture the physics of size/velocity coupling,

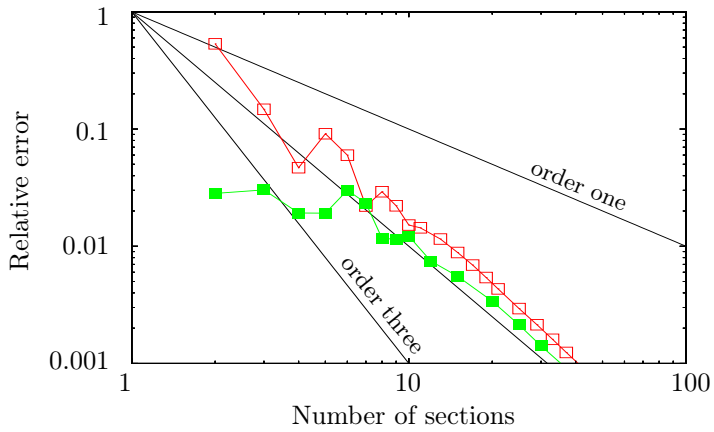

Figure 13.12: *Exp-TSM (NC5) maximum error on total mass concentration compared to a reference case (One Size Moment* 1,000 *sections) – Empty: OSM method; Solid: Exp-TSM with (Ad2) quadrature.*

- the usefulness of the Two Size Moment method in the semi-infinite last section.

We consider a lognormal size distribution in surface, as given in Eq. (1.10) with parameters $m_0 = 1.06\,\mathrm{kg.m^{-3}}$, $S_{\mathrm{LN}} = 1600\,\mu\mathrm{m}^2$ and $\sigma_{\mathrm{LN}} = 1.5$. This corresponds to a sharp distribution centered on a radius of $11.3\,\mu$m as shown in Figure 1.18 and its particular form is justified in some SRM cases, see § 1.2.3.2.
We perform simulations on two different configurations:

- the first configuration studies the convergence and accuracy of the methods on coalescence and spray dynamics in a case that is comparable to the one of a SRM i.e. the size distribution relative shift is moderate. So Kn_g is close to one to keep the average growth small compared to the average size;
- the second configuration assumes a strong average size increase to study the additional benefit of using two size moments in a final, unbounded section. The total injected mass, injection velocity and nozzle length are higher, making Kn_g smaller and increasing coalescence intensity.

13.2.4.1 Asymptotic study

We here study the convergence of the One Size Moment and the Two Size Moment method on liquid mass concentration. We take for the nozzle $z_0 = 0.05$m, $z_{\max} = 0.25\,$m and $u_z(z_0) = 5\,\mathrm{m.s^{-1}}$ so the residence time in the nozzle is $\tau^R_{\mathrm{nozzle}} = 0.4\,$s: these values generate a strong coupling between coalescence and droplet dynamics for the chosen droplet size, which means that the liquid mass density along the nozzle is completely different whether coalescence is considered or not.
The growth time is estimated $\overline{\tau}^G = 0.5\,$s for droplets close to the distribution maximum so that $\mathrm{Kn}_g = 1.3$. This corresponds to the coalescence intensity of a typical SRM case as the ones computed in Chapter 15: the velocity differences and residence times compound each other as discussed in § 7.2. The growth is significant and the size velocity coupling is strong: these severe conditions also make the test-case under consideration a very efficient tool for numerical qualification of the two Eulerian methods.
For the sake of the One Size Moment method accuracy, we define a configuration where coalescence brings negligible mass in the last section so we always take the lower bound of the last section above 50μm.
We give in Figure 13.12 the maximum error on mass density along the nozzle depending on the sectional discretization. This proves the convergence rate of both methods to be of order two. The One Size Moment method has a slightly better convergence constant.
From an applicative point of view, it is crucial to consider the performance of both methods for coarse size discretizations, say below 5 sections. With such a small number of sections, the OSM method can yield errors above 10%. Yet, the Exp-TSM method achieves remarkably accurate computations with always less than 3% relative error on total mass. This applicative advantage of the Two Size Moment method is studied deeply in the following and is the key issue for practical computations.

13.2.4.2 Minimizing the number of sections for practical applications

In the context of industrial codes, we want to use as few sections as possible. We therefore extensively compare both methods on coarse discretization cases regarding their accuracy on size and velocity distribution prediction and mass concentration repartition. For the sake of the One Size Moment method accuracy, we still do not want to transfer too much mass in the last section so we keep the conditions described previously.
We choose the tested numbers of sections: a 5 section test-case illustrates what happens with a very coarse discretization. A 13 section and a 25 section test-cases illustrate the convergence of the method. They are compared to a 53 section One Size Moment run which we use here as a reference solution. These six

simulations are successively compared to the reference solution regarding four data sets: the output size distribution at first, a velocity distribution in the nozzle at second, the total mass and number density along the nozzle axis at third and mass and number in 5 size intervals (or section groupings given in Table 13.4) along the nozzle at fourth.

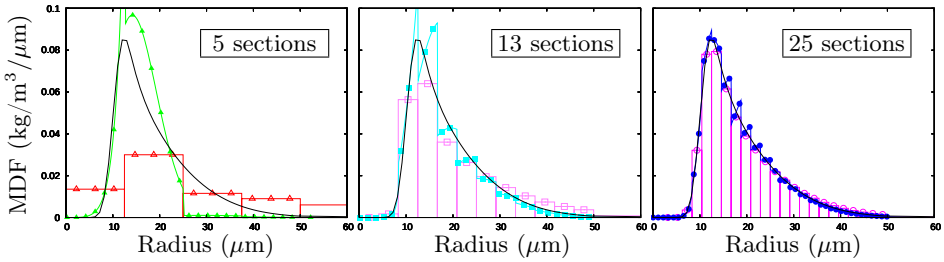

Figure 13.13: *Mass concentration distribution at the nozzle's end ($z = 0.25m$) computed with the OSM (empty symbols) and Exp-TSM method (solid symbols) with 5, 13 and 25 sections and reference (—).*

First, the correct treatment of the size distribution gives an indication on the method's accuracy. We therefore compare the mass concentration distributions at the nozzle output computed with the two methods and with 5, 13 and 25 sections and computed with the 53 section reference test-case in Figure 13.13. With 5 sections, the One Size Moment method strongly overestimates the growth rate while the Two Size Moment method underestimates it. With 13 sections, the trend is the same but the error is smaller. Finally for 25 sections, we consider both methods are roughly converged. The growth rate overestimation by the One Size Moment method for coarse size discretization brings about major consequences for the spray dynamics since the gap of average Stokes number between the bounded sections and the final unbounded section.

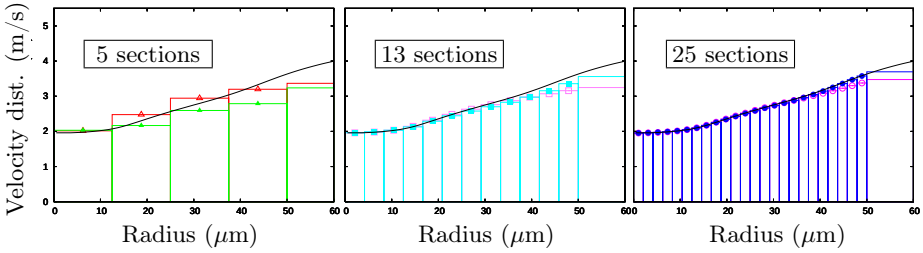

Figure 13.14: *Average velocity distribution at $z = 0.08\,m$ computed with the OSM (empty symbols) and Exp-TSM method (solid symbols) with 5, 13 and 25 sections and reference (**solid line**).*

Second, we check in Figure 13.14 the velocity distributions at an abscissa where the velocity differences and the effect of past coalescence are high. As expected, the smaller droplets have more decelerated as we can see on the reference response. The velocity distribution is observed to be monotonic, according to the monotonicity of the dynamic response time $\tau^{\boldsymbol{u}}(S)$ with size and the injection condition. But its behavior is not a simple law because some droplets, produced by coalescence, have brought their momentum with them to their new size, the velocity of the size then being average through the monokinetic hypotheses [HV1] and [HV2]. We now compare the results with the two approaches and coarse discretizations. In general the error on velocity increases with size, not because of [HV1] and [HV2] which are very correct for the entire Stokes number spectrum that is considered, but because coalescence is underestimated and so is inertia. Then, we observe that the constant velocity reconstruction in each section yields some error, especially in the 5 section case, but we still consider [HV3] as acceptable, the velocity spectrum to be captured in each section being not too wide as required. We finally compare the two approaches together. The velocity behavior is not very well rendered with 5 sections, though the One Size Method gets it right by chance. Then, the velocity distribution is shown to be better rendered with 13 sections by the Two Size Moment method than the One Size Moment method and [HV3] yields little error for both approaches. Finally no error is visible on the graph with the 25 section Two Size Moment method, while the One Size Moment method still has visible error.

Third, let us quantify the influence of the treatment of size and velocity polydispersity on the global dynamics of the spray. Figure 13.15 shows the evolution of mass and number total concentrations along the centerline of the nozzle computed with both Eulerian methods (5, 13, 25 sections) compared to the reference solutions (53 section One Size Moment method and stochastic-Lagrangian reference test-case). For the One Size Moment case, number concentrations are computed considering section average droplet volumes given by integration of the $({}^1\kappa_k)_k$ functions: data are therefore redundant with mass concentration data. We emphasize the fact that good convergence is achieved by the two methods with 25 sections as we can see in Figure 13.15, bottom, which is a close up view on the end of the nozzle and on a very small interval of the Y-coordinate.

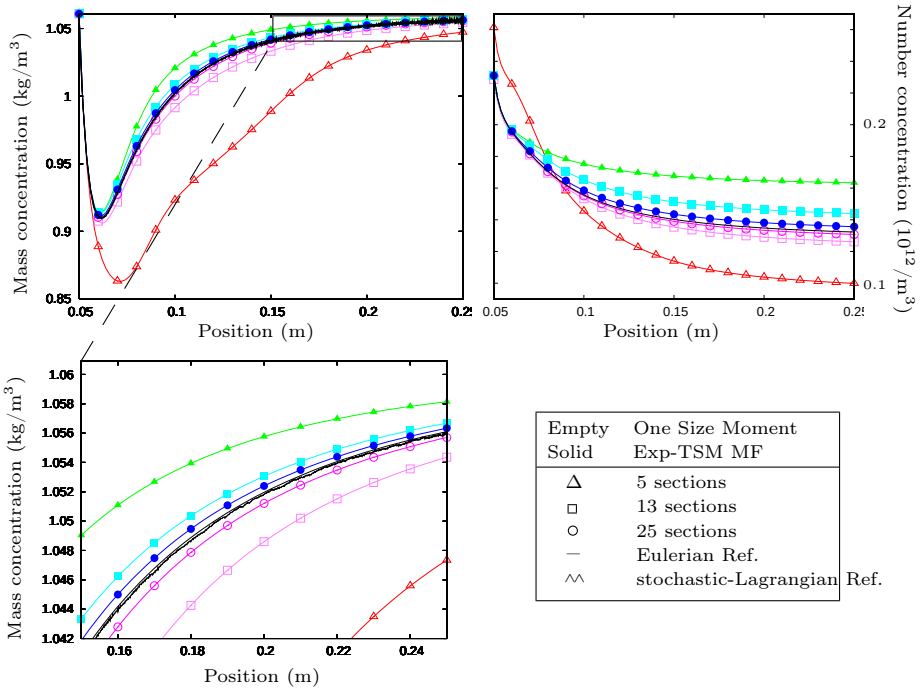

Figure 13.15: *Top: Mass and number concentrations along nozzle – Bottom: close up view on the nozzle's end.*

Group (μm)	5 section case	13 section case	25 section case
G_1=[0, 12.5]	1	1 to 3	1 to 6
G_2=[12.5, 25]	2	4 to 6	7 to 12
G_3=[25, 37.5]	3	7 to 9	13 to 18
G_4=[37.5, 50]	4	10 to 12	19 to 24
G_5 ($> 50\mu$m)	5	13	25

Table 13.4: *Composition of the five section groupings*

The convergence is proven by comparison to a 53 section case performed with the same research code and to a stochastic-Lagrangian simulation result performed with another EM2C code.
Fourth and to compare precisely the effect of polydispersity on dynamics, let us finally consider the evolution of mass and number along the nozzle for five size intervals. These intervals do match with the sections in the 5 section case but correspond to section groupings in the other cases as illustrated in Table 13.4. The evolution of the mass concentration of these groupings along the nozzle is given in Figure 13.16. It is there obvious that the 5 section One Size Moment error on coalescence is severe, especially in the fifth and last grouping G_5 where little mass should be found, as prescribed. The 5 section Two Size Moment method underestimation of size occurs in groups G_3 and G_4 and is more visible here than in Figure 13.13. Yet it has moderate consequences on the total mass evolution as shown in Figure 13.15 because these sections have Stokes numbers that are close enough.
As a conclusion this study validates the Two Size Moment Multi-Fluid method. It also shows that the Two Size Moment method converges to the reference solution with a second order slope as does the One Size Moment method but reveals to have, in this configuration, much smaller error when using few sections. Since the error on mass never exceeds 3% with the Two Size Moment method, this method yields acceptable dynamical response with as few as 2 sections which is most appreciated for industrial simulations.
Yet the test-case was limited to bounded sections in order to facilitate comparisons to the One Size Moment method. In the next paragraph, we evaluate the benefit of using two size moments in the final, unbounded section.

13.2.4.3 Two Size Moment method for the unbounded section

We shall now evaluate the impact of using the Two Size Moment method on an unbounded final section. We therefore change the injection conditions to intensify coalescence. The injection velocity is now $U(z_0) = 500\,\mathrm{m/s}$. The origin of the injection is still $z_0 = 0.05\,\mathrm{m}$ but the length of the nozzle is increased and $z_{\max} = 1.05\,\mathrm{m}$. The initial injected mass concentration is increased to $m_0 = 2\,\mathrm{kg.m^{-3}}$ with $S_{\mathrm{LN}} = 1600\mu\mathrm{m}^2$ and $\sigma_{\mathrm{LN}} = 1.3$ that is a slightly narrower size distribution, also given in Figure 1.18. In these new conditions,

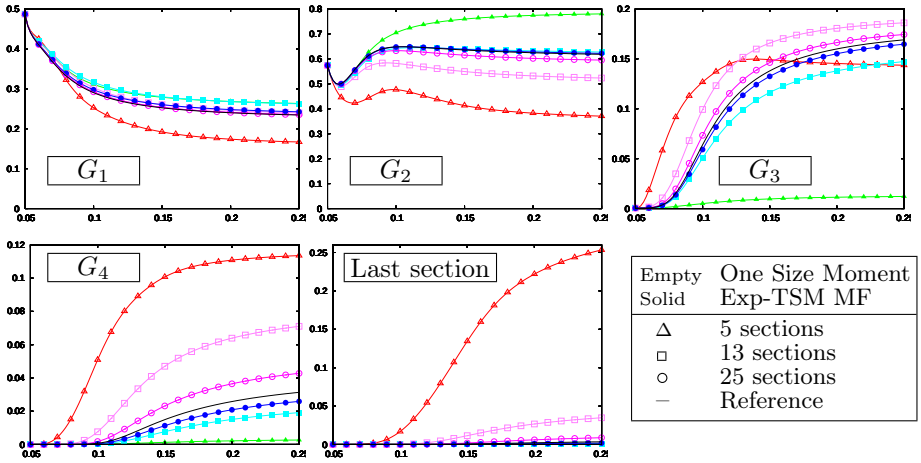

Figure 13.16: *Evolution of mass concentration along the nozzle abscissa z in the four bounded section groupings and in the last section for* 5, 13 *and* 25 *sections.*

the growth time is now $\overline{\tau}^G = 0.5\,\text{ms}$ for droplets close to the distribution maximum and the residence time in the nozzle is $\tau^R_{\text{nozzle}} = 0.3\,\text{s}$ so that $\text{Kn}_g = 0.002$ which is much smaller than the previous case. Coalescence is therefore more intense, as expected. Moreover, the particle inertia i.e. the Stokes number is higher so the velocity differences are higher and remain strong all along the nozzle. So coalescence is much more intense: the size distribution shifts to an average radius that is ten times bigger than previously as shown in Figure 13.17. The lower bound of the final section is set at the same value for all the computations, and below the final average droplet size to assess the final section's particular role.

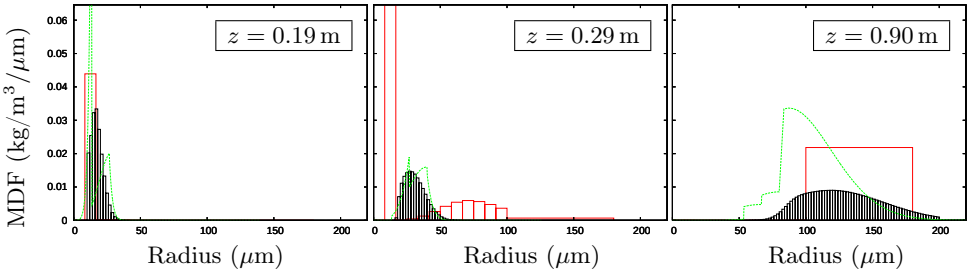

Figure 13.17: *Mass concentration distribution at different nozzle abscissae – Solid: 13 sections, OSM; Dashed: 7 sections, Exp-TSM;* ***Histogram****: reference).*

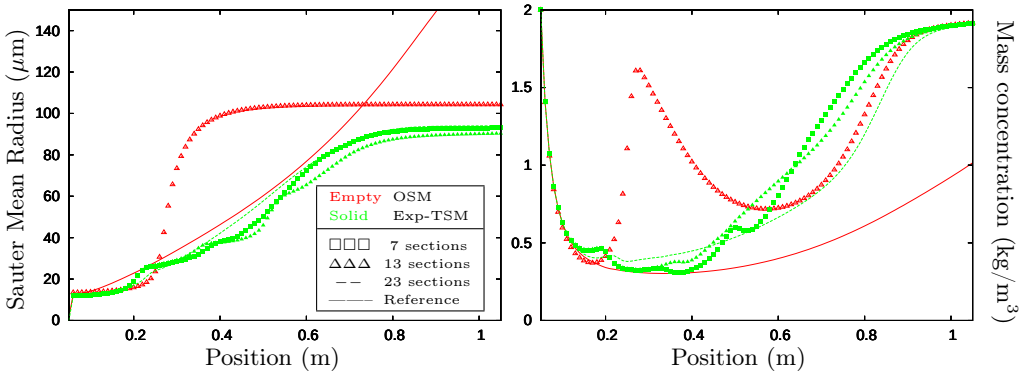

Figure 13.18: *Mass concentration and Sauter Mean Radius along the nozzle.*

The mass concentration and Sauter Mean Radius (SMR) in the new conditions are given in Figure 13.18 and commented in Table 13.5. They allow us to conclude on the versatility of the Two Size Moment method to capture an initially sharp distribution which shifts far from its initial average radius. The SMR failure occurs when too much mass is in the last section: the One Size Moment method requires less than a few percents mass in the last section while the Two Size Moment method allows the SMR to come quite close

to the last section lower bound as shown by the SMR plateaus in Figure 13.18.

Legend	Method	Sections	$r(n_{\text{sec}})$	Mass failure absc.	SMR failure absc.
Solid —	OSM	101	200 μm	reference	reference
Empty Δ	OSM	13	100 μm	0.20 m	0.20 m
Solid □	TSM	7	80 μm	0.50 m	0.70 m
Solid Δ	TSM	13	80 μm	0.60 m	0.70 m
Dashed - -	TSM	23	80 μm	0.80 m	0.70 m

Table 13.5: *Nozzle configurations and result comments.*

The conclusion of this additional study is that a two size moment method implemented in the final unbounded section strongly extends the allowed range for the size distribution which proves to be useful to reduce the number of sections.

13.2.4.4 Remarks on computational time

	1 size moment (pre-computation)	2 size moments Ad2	Ad3	NC5	NC9
5 sections	0.05 s (0.01 s)	4.8 s	13.2 s	5.6 s	10.0 s
13 sections	0.18 s (0.06 s)	20.7 s	88.0 s	26.3 s	56.6 s
25 sections	0.50 s (0.20 s)	80.5 s	356.3 s	100.1 s	220.3 s

Table 13.6: *Computational time on a 2.66 GHz Intel Core 2 Duo CPU.*

To complete the bounded section study with practical computational information, Table 13.6 recapitulates the duration of runs using different computation methods. The space integration cost is negligible compared to the coalescence source term computation so these costs uniquely arise from the coalescence integration method and we can use them to conclude on the efficiency of the different quadratures. First, (Ad2) reveals to be the fastest among the Two Size Moment quadrature methods. Moreover the quadrature cost has no reason to depend on the test-case. Since validations performed all along this study show that (Ad2) brings satisfactory results, this quadrature method is naturally preferred for the Two Size Moment method.
Second, it is obvious that the One Size Moment method is much faster on the nozzle test-case, thanks to coalescence integral pre-computation. For the same number of sections, there are two orders of magnitude of difference on computational cost. For the same level of accuracy, consider the 5 section Two Size Moment simulation and compare it to the 25 section One Size Moment simulation which yields comparable error on mass repartition: the Two Size Moment method is 10 times slower than the One Size Moment method though having 5 times less sections. No firm conclusion regarding the cost in real applications can however be drawn from these numbers since the computational cost of spatial transport in multi-D configurations would then have to be taken into account. This cost is of course severely reduced when using less sections. The final discussion on cost is thus postponed to Chapter 15.

13.2.5 Conclusion on the model and methods

The results of § 13.2.2, § 13.2.3, and § 13.2.4 confirm that Eulerian Multi-Fluid methods can be used to simulate accurately the size distribution evolution of a coalescing spray and its size-conditioned dynamics. When collision efficiency is taken equal to one, the One Size Moment method provides, with a reasonable number of sections -at least 10- very fast results since the coalescence term computations are reduced to quadratic combinations of section masses. The Two Size Moment Multi-Fluid method provides good results with a very coarse size-space discretization (as few as 5 sections) and is far less "diffusive" in size phase space for steep size distributions.
But § 13.2.2 proves also the importance of modeling the collision efficiency factor. The Two Size Moment method features any such modeling for very little additional cost. A general form for coalescence efficiency formulae to be suitable for a pre-computed One Size Moment method are suggested in Laurent et al. (2004) but no classical collision efficiency models can be easily implemented since they require local gas parameters. The One Size Moment method can therefore no longer benefit from pre-computation when including such models.
We finally highlight that the quantitative conclusions that are drawn regarding the performance of the Multi-Fluid section discretization on all these cases totally depends on the respective configurations. First because the Stokes number local spectra, which condition the treatment of velocity and temperature polydispersity

n	Abscissae			Weights			o
1	0			1			0
2		$\pm\sqrt{2}/2$			$1/2$		2
3	0	$\pm\sqrt{6}/2$		$2/3$	$1/6$		4
4		$\pm\sqrt{(3-\sqrt{6})/2}$	$\pm\sqrt{(3+\sqrt{6})/2}$		$\frac{1}{4(3-\sqrt{6})}$	$\frac{1}{4(3+\sqrt{6})}$	6

Table 13.7: *Gauss-Hermite coefficients: n/2 first weights, sum and error coefficient.*

in the sections, varies from a case to another. Second because the coalescence intensity, which conditions the size phase space refinement requirement, varies from a case to another. Since the nozzle test case has levels of polydispersity and coalescence that are comparable to the ones of a SRM, the previous conclusions on the number of sections and on coalescence intensity quantitatively hold for the motor simulations of the following section. Likewise the D'Herbigny experiment has comparable levels of coalescence parameters so the conclusions on coalescence efficiency impact hold. Of course, the qualitative conclusions on the advantages of the Two Size Moment method hold in any case.

13.3 Polykineticity and coalescence: computing AG coalescence source terms

We now focus on coalescence as treated in the TSM-AG formalism, described in § 6.3. The size integrals of Eq. (6.30) on $\mathscr{D}_{ijk}$ are as complex as in any TSM-MF approach (as long as no size-velocity correlations are accounted for) so we use the same method for all the size integrals, described in § 13.1.5. But the velocity integrals are no longer based on monokinetic Dirac δ-functions (which were integrated trivially) but on finite-measure support distributions and they require particular care.

13.3.1 Numerical approach for the velocity integrals

The velocity integrals given in Eq. (6.29) are that of a complex function of two 2D velocity variables. The directions are coupled, at least through the norm function. So we use a 6D quadrature technique (which reduces to 4D for a two-dimensional physical space).

13.3.1.1 Gauss-Hermite fixed quadrature

We need to compute integrals of the form:

$$I = \int_{\mathbb{R}} \phi(c) \exp(-c^2) \mathrm{d}c \tag{13.48}$$

where the support is infinite and were $\exp(-c^2)$ can be factorized so the Gauss-Hermite quadrature is particularly recommended.
We consider the Gauss quadrature for an infinite interval, namely Gauss-Hermite. The 1D n-node Gauss-Hermite formula approximates integrals as a sum of n point-wise evaluations of the integrand at n predefined abscissae c_i :

$$I = \sum_{i=1}^{n} w_i \phi(c_i) + \epsilon_{\mathrm{GH}}^{(n)} \tag{13.49}$$

where c_i are tabulated abscissae. They have an analytical expression as well as the weights w_i, given for instance in Zwillinger (2003). We use the symmetry property $X_{n-1-i} = -X_i$ and $w_{n-1-i} = w_i$ to give only half of the coefficients in Table 13.7. The quadrature, as well as any approach involving it, is referred to as (GHn) in the following.
As regards computational efficiency, the Gauss-Hermite quadrature presents another advantage that is to avoid computing the exponential kernel at the nodes.
Each Gauss-Hermite approach is based on an interpolation of ϕ by its underlying Hermite polynomial. This yields an error:

$$\epsilon_{\mathrm{GH}}^{(n)} = \frac{n!\sqrt{\pi}}{2^n (2n)!} \phi^{(2n)}(\xi^{(n)}) \tag{13.50}$$

where $\phi^{(n)}(\xi^{(n)})$ is the n-th derivative of ϕ evaluated at a given $\xi^{(n)} \in \mathbb{R}$.

13.3.1.2 Smoothness issue

The Gauss quadratures are well known for achieving polynomial approximations which are best for smooth functions. In our case, the norm function is non derivable in 0. This compromises the accuracy of the approach for a low number of nodes, and slows down the convergence with the number of nodes.
Considering the high-dimensional quadrature that is to be performed, this issue is *a priori* serious but the practical study proves the method to require an acceptable number of nodes.

13.3.2 Numerical study of the velocity quadrature

We define a model integral to be representative of the source terms under consideration in a 2D case:

$$I^{2D}(\boldsymbol{u},\boldsymbol{u}^\star,\Sigma,\Sigma^\star)=\int_{\mathbb{R}^2}\int_{\mathbb{R}^2}|\boldsymbol{c}-\boldsymbol{c}^\star|\,\phi(\boldsymbol{c},\boldsymbol{c}^\star)G_\Sigma\left(\boldsymbol{c}-\boldsymbol{u}\right)G_\Sigma\left(\boldsymbol{c}^\star-\boldsymbol{u}^\star\right)\mathrm{d}\boldsymbol{c}\mathrm{d}\boldsymbol{c}^\star \tag{13.51}$$

with G_Σ the centered multivariate Gaussian function with a covariance Σ. It corresponds in fact to the velocity integrals for zeroth order velocity moments.

13.3.2.1 Case of a one-dimensional physical space

In 1D ($c\in\mathbb{R}$, $c^\star\in\mathbb{R}$) the integral I^{1D} is considered instead of I^{2D}:

$$I^{1D}(u,u^\star,\sigma,\sigma^\star)=\int_{\mathbb{R}}\int_{\mathbb{R}}|c-c^\star|\,\phi(c,c^\star)g_\sigma(c-u)\,g_\sigma(c^\star-u^\star)\,\mathrm{d}c\mathrm{d}c^\star \tag{13.52}$$

where g_σ is the centered Gaussian function with a standard deviation σ. In the case where $\phi=1$, we get an analytical expression for the integral:

$$I^{1D}(u,u^\star,\sigma,\sigma^\star)=(u-u^\star)\,\mathrm{erf}\left(\frac{u-u^\star}{\sqrt{2}\sqrt{\sigma^2+\sigma^{\star2}}}\right)+\sqrt{\frac{2}{\pi}}\sqrt{\sigma^2+\sigma^{\star2}}\,\exp\left(-\frac{(u-u^\star)^2}{2(\sigma^2+\sigma^{\star2})}\right) \tag{13.53}$$

which can be approximated via a double or 2D Gauss-Hermite quadrature

$$I_n^{1D}(u,u^\star,\sigma,\sigma^\star)=\sum_{i=1}^{n}\sum_{j=1}^{n}w_iw_j\,|u-u^\star+c_i\sigma-c_j\sigma^\star| \tag{13.54}$$

The relative error $(I^{1D}-I_n^{1D})/I^{1D}$ for this quadrature is plotted for the example case $\phi=1$, $\sigma=0.5$ and $\sigma^\star=1$, versus $u-u^\star$ in Figure 13.19. The maximum error is reached for $u-u^\star=0$, which complies with the fact that the norm function is regular everywhere except in 0: this illustrates the issue of quadrature approaches for non-smooth functions.

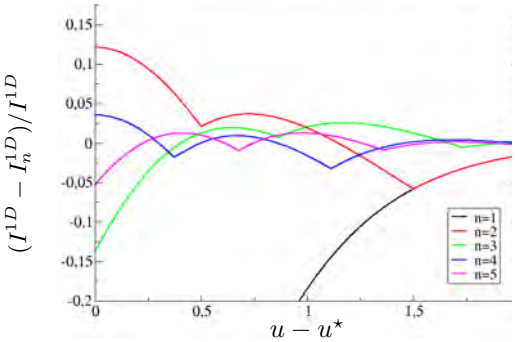

Figure 13.19: *Relative error of the 2D Gauss-Hermite quadrature for a model function $\phi=1$, $\sigma=0.5$ and $\sigma^\star=1$*

13.3.2.2 Case of a two-dimensional physical space

In 2D, the centered Gaussian function G_Σ with a covariance matrix Σ noted as usual:

$$\Sigma=\begin{pmatrix}\sigma_{11}&\sigma_{12}\\\sigma_{12}&\sigma_{22}\end{pmatrix}$$

can be written for $\boldsymbol{c}=(c_1,c_2)^T$:

$$G_\Sigma(\boldsymbol{c})=\frac{1}{2\pi\sqrt{\sigma_{11}\sigma_{22}-{\sigma_{12}}^2}}\exp\left(-\frac{1}{2}\frac{\sigma_{22}c_1^2-2\sigma_{12}c_1c_2+\sigma_{11}c_2^2}{\sigma_{11}\sigma_{22}-{\sigma_{12}}^2}\right) \tag{13.55}$$

For the sake of simplicity and without loss of generality, we take the case $\sigma_{12} = \sigma_{12}^\star = 0$ so that $G_\Sigma(\boldsymbol{c}) = g_{\sqrt{\sigma_{11}}}(c_1) g_{\sqrt{\sigma_{22}}}(c_2)$ et $G_{\Sigma^\star}(\boldsymbol{c}^\star) = g_{\sqrt{\sigma_{11}^\star}}(c_1^\star) g_{\sqrt{\sigma_{22}^\star}}(c_2^\star)$. Considering $\phi = 1$ the integral is re-written, with the notations $g_{\sqrt{\sigma_{ii}}} = g_i$:

$$I^{2D} = \iint \sqrt{(c_1 - c_1^\star)^2 + (c_2 - c_2^\star)^2}\, g_1(c_1 - u_1) g_2(c_2 - u_2) g_{1\star}(c_1^\star - u_1^\star) g_{2\star}(c_2^\star - u_2^\star)\, \mathrm{d}c_1 \mathrm{d}c_2 \mathrm{d}c_1^\star \mathrm{d}c_2^\star \tag{13.56}$$

while the approximation of I^{2D} via a quadruple or 4D Gauss-Hermite quadrature reads:

$$I_n^{2D} = \sum_{i=1}^{n} \sum_{j=1}^{n} \sum_{p=1}^{n} \sum_{q=1}^{n} w_i w_j w_p w_q \sqrt{(u_1 - u_1^\star + c_i \sigma_{11} - c_j \sigma_{11}^\star)^2 + (u_2 - u_2^\star + c_p \sigma_{22} - c_q \sigma_{22}^\star)^2} \tag{13.57}$$

The analytical expression cannot be computed easily in 2D so we plot the evolution of I_n^{2D} with n on an example case to assess convergence. Since the main issue is again raised by the norm function at 0, we assume $u - u^\star = 0 = v - v^\star$ which is expected *a priori* to yield the maximum error. The results are given in Figure 13.20.

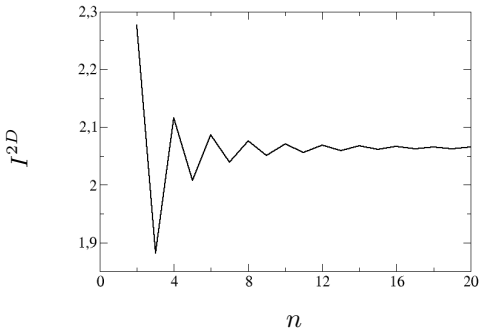

Figure 13.20: *Value of the 4D Gauss-Hermite quadrature for function $\phi = 1$ with $\sigma_{11} = 0.5$, $\sigma_{22} = 0.1$, $\sigma_{11}^\star = 0.2$ and $\sigma_{22}^\star = 0.5$*

13.3.2.3 Choice of a quadrature strategy for velocities

The Gauss-Hermite quadrature is well suited for the present exponential kernel and the infinite size of the integral support but the norm function, which is not smooth, compromises accuracy.
Despite this loss which requires *a priori* more nodes, it is crucial to reduce at most the number of nodes n per quadrature since the total number of quadrature points is n^{2N_d} with N_d the dimension of the physical space. The use of $n = 4$ nodes yields an acceptable maximum error of 2% according to a numerical study on the zeroth order moment of a particular velocity integral.
The integrals for the first and second order velocity moments are not assessed but they feature regular functions of the microscopic velocities in factor of the norm so they presumably do not introduce much more error than the integral which has been studied.
So we choose a 4 node Gauss-Hermite quadrature note (GH4) for all the following developments of AG coalescence.

13.4 Validation of polykinetic coalescence with AG approach

13.4.1 In-house code for polykinetic coalescence: the SAP2 code

The SAP2 code solves the TSM-AG equations on a 2D domain a polydisperse: it can tackle coalescing moderately inertial sprays but two-way coupling is not possible. Polydispersity and coalescence are handled by the Two-Size Moment Multi-Fluid method and small scale crossings by the Anisotropic Gaussian closure in each section.
The 2D domain is a square geometry with a structured finite volume mesh and the transport of the sections is based on the AG2D transport routines presented in § 11.3.1.

13.4.2 Two crossing jets with co-flow: a fundamental case

We consider a 2D case of two jets injected at a velocity $(u_0, \pm v_0)$ whose trajectories cross because of the droplet inertia before being bent by a gaseous co-flow of velocity $(u_0, 0)$. The spray and its coalescence are characterized by two dimensionless numbers as described in § 7.4.1.

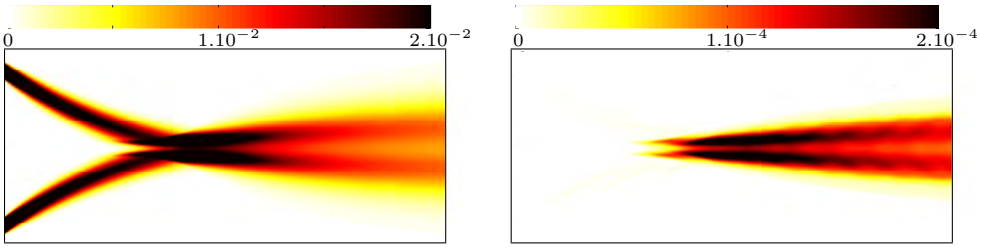

Figure 13.21: *Mass concentration (kg/m^3) for $Kn_{coal} = 100$ with Eulerian approach (Aff-TSM-AG, SAP2 code) – Left: Section 1 (mode 0); Right: Section 2 (mode 1).*

We now set $u_0 = 10\,\mathrm{m/s}$ for the as to flow permanently from left to right. The injection conditions are: two jets wide of $d_0 = 0.01\,\mathrm{m}$ and separated by $2\eta_0 = 0.1\,\mathrm{m}$, of monodisperse particles with $r_0 = 18\,\mu\mathrm{m}$ injected at $u_0 = 10\,\mathrm{m/s}$ and $|\,v_0\,| = 10\,\mathrm{m/s}$. We set the gas viscosity μ_g and the liquid density ρ_l to have $\tau_0^{\boldsymbol{u}} = 7.5\,\mathrm{ms}$ and $\mathrm{St} = 1.5$ so that the two jets cross. Because of the initial monodisperse condition, coalescence yields size modes, i.e., droplets, with an integer multiple $k\mathcal{V}(r_0)$ of the initial droplet volume $\mathcal{V}(r_0)$ so the size distribution is discrete. We here choose a MF discretization for each mode to match exactly one section, e.g., its right bound $\mathcal{V}(S_k) = k\mathcal{V}(r_0)$. As for coalescence intensity, we consider two cases with different $\mathrm{Kn}_{\mathrm{coal}}$ by setting two different injection concentrations m_0: a high Knudsen case which is weakly coalescing and can be linearized and a low Knudsen case which is more complex. To perform these two cases, the new Eulerian model is implemented in a research code called SAP2 and run on a 2D 256^2 grid with 8 sections.

13.4.3 Weakly coalescing case

The first practical case has an initial particle concentration in each jet that yields $\mathrm{Kn}_{\mathrm{coal}} \gg 1$. So coalescence is weak and very few new droplets are created. The coalescence terms are then linearized by neglecting (i) the mass taken from the initial section, and (ii) the interactions between two non-initial sections. This gives immediately a semi-analytical estimation of the droplets produced at the exit of the crossing as proportional to $\mathrm{Kn}_{\mathrm{coal}}$. So the formula reads for the section concentrations after the crossing, thanks to the mode/section equivalence:

$$m_{k+1} = \frac{1}{\mathrm{Kn}_{\mathrm{coal}}} m_k. \tag{13.58}$$

This relation is written indifferently in total mass or mass concentration thanks to the sufficient homogeneity of the problem. A case with $\mathrm{Kn}_{\mathrm{coal}} = 100$ is admissible as weakly coalescing. In this regime, a small mass concentration of droplets of mode 1 ($r_1 = 22.7\,\mu\mathrm{m}$) appears at the right edge of section 2, and even smaller amounts of the following modes appear in the following sections according to (13.58).
On the one hand, we examine the overall dynamics of the problem. First, we consider the infinite Knudsen, i.e. non colliding case, as a reference: its trajectories can be computed analytically as exponentials. Second, we compare it to the infinite Knudsen case with any AG based Eulerian method: most of the mass is enclosed in the analytical trajectories so the spatial repartition is well reproduced, at least regarding the size of the jet characteristic structures thanks to AG presented in Chapter 6 and developed by Vié et al. (2014). Third, we compare the results with finite Knudsen and coalescence given in Figure 13.21: they match the infinite Knudsen Eulerian results, which is relevant since coalescence is too weak to disturb the spray dynamics. So the spray dynamics is well rendered by the new model.
On the other hand, we examine size growth under coalescence: Figure 13.21 shows that the Eulerian mass concentrations in section 2 after the crossing are a hundred times, i.e. about $\mathrm{Kn}_{\mathrm{coal}}$ times, below the ones in section 1. This matches the semi-analytical estimation (13.58) so we get a quantitative validation of the approach for the linearized case. As a conclusion for this crossing jet, spray dynamics is well rendered and coalescence intensity is quantitatively captured by the new Eulerian model.

13.4.4 Non-linear case

We now take $\mathrm{Kn}_{\mathrm{coal}} = 1$. So a significant portion of the droplets encounter coalescence and change size: all droplet modes can significantly interact with themselves and the others so the problem is non-linear and complex. A reference solution is computed with the Asphodele code (Reveillon and Demoulin 2007b; Thomine 2011), using a Lagrangian DPS approach to account for such complexity. The Lagrangian DPS solution has a very complex dynamics, as illustrated on an instantaneous realization in Figure 13.22. We give in Figure 13.24 the mass repartition for the different sections with the new Eulerian approach.
First, we observe that the jet spreads less after the crossing point than for cases with higher Knudsen. Since coalescence corresponds to a perfectly inelastic collision, which destroys the relative kinetic energy of the two

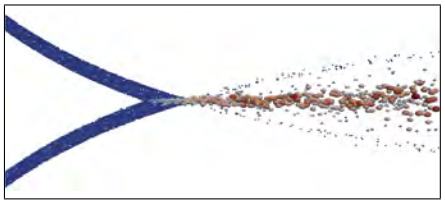

Figure 13.22: *Instantaneous location of particles colored by size for $Kn_{coal} = 1$ with Lagrangian DPS approach (Asphodele code).*

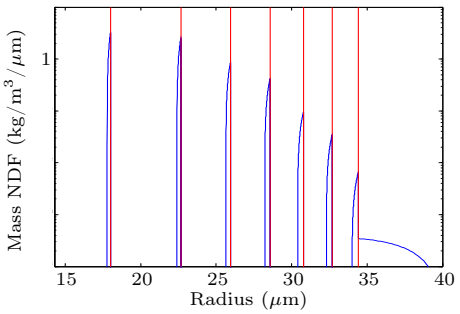

Figure 13.23: *Mass density function (log-scale) at the output on centerline for $Kn_{coal} = 1$ with Eulerian approach (Aff-TSM-AG, SAP2 code).*

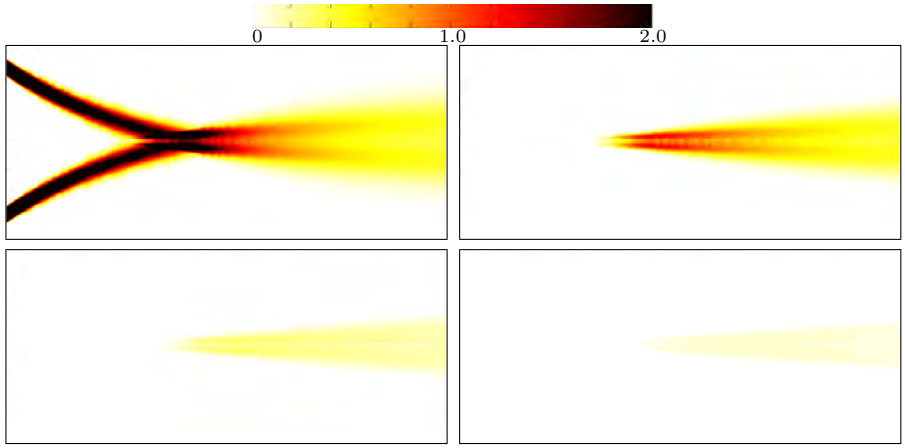

Figure 13.24: *Mass concentration per section with Eulerian approach (SAP2) – Top left to bottom right: section 1 to 4*

jets, the jet angle after crossing is reduced contrary to rebounds which would redistribute kinetic energies and widen the jet angle. In particular, we observe in Figure 13.24 the Eulerian mass repartition of the different sections getting closer to the centerline as the mode number increases. This matches the trend of coalescence to destroy relative kinetic energy since higher sections, i.e., modes have encountered more coalescence. So the jet angle gives quantitative information about the correct treatment of coalescence by the method. We extrapolate that in the case of Kn = 0, we get a δ-shock on the centerline. In the present case of Kn = 1 the Eulerian jet angle compares well to the Lagrangian DPS reference case.
Second, the Eulerian size distribution at the jet output that is given in Figure 13.23 proves that the modes of coalescence are very well captured, the size distribution remaining steep despite a slight numerical diffusion in size phase space. The size discretization has of course been chosen for each mode (up to nine) to match a section, but the two-size moment approach is known to deal efficiently with complex size distributions with a low number of sections. This feature is desired for advanced or industrial computations (Doisneau et al. 2013) and we here show the ability of the new model to do so.
Third, we observe in Figure 13.25 the average d_{30} diameter, as computed with both approaches. The droplet size repartition is well rendered with the Eulerian approach, with the bigger, less agitated droplets on the centerline, and small droplets, which avoided coalescence events, more on the sides. So the complex dynamics of coalescence at a crossing location is captured by the new Eulerian model.

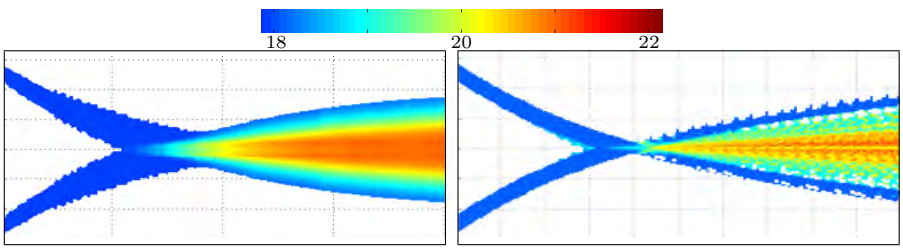

Figure 13.25: *Volume average radius r_{30} (μm) of the overall distribution – Left: Eulerian (SAP2); Right: Time average Lagrangian DPS (Asphodele).*

13.4.5 Conclusion

To conclude on the crossing jet case the configuration appears to have a very complex physics, which can be captured exactly only with a Lagrangian DPS -if that, not for numerous particle cases. But the new Eulerian model renders quantitatively the main features that are size growth, size repartition and jet angle, these quantities being sufficient for industrial applications. In solid rocket motors, for instance, computing the disperse phase retroaction on the flow in the nozzle requires a rough knowledge of the droplet jet inertia and angle after crossing. Moreover, the variety of sizes and trajectories that arises in industrial cases, featuring turbulent flows and many crossings, make Lagrangian DPS simulations difficultly tractable while Eulerian models can approach the dynamics.
The new Eulerian model, based on the Anisotropic Gaussian velocity closure and the Two Size Moment Multi-Fluid method, captures the main features of spreading and coalescence growth when Droplet Trajectory Crossing occurs. This makes it suitable for capturing the dynamics of polydisperse moderately-inertial spray flows with coalescence, especially when such flows become complex, excluding stochastic-Lagrangian and Lagrangian DPS approaches. The approach is valid for structured grid computations and promising for industrial computations thanks to the Two Size Moment method, which allows limiting the number of sections and the cost.

13.5 Conclusions and remarks on high order and flexibility

We have presented in Chapter 5 a method that allows to increase accuracy of the standard, OSM, Multi-Fluid approach for a given number of sections. Algorithms have been described in detail for this method in the present chapter and the method was validated on academic test cases.

13.5.1 Conclusion on coalescence simulation with TSM

Many approaches exist to solve coagulation equations (Kumar and Ramkrishna 1996a; Kumar and Ramkrishna 1996b; Kumar and Ramkrishna 1997; Marchisio and Fox 2005; Kumar et al. 2006; Kostoglou 2007; Estrada and Cuzzi 2008; Kostoglou and Karabelas 2009; Frenklach 2009) as extensively discussed in Chapter 4. The sectional method allows to solve with a reasonable accuracy the size evolution but still to account for velocities in an accurate enough way and to solve the velocities conditioned by size and the corresponding hetero-DTC while many moment methods can only solve coagulation as driven by an external kernel (Brownian or turbulent) but not ballistic kernels.
As a remark, the numerical tools developed for coalescence basically allow to efficiently compute complex combinations of integrals on non-linear functions. These methods can be used for other size/velocity source terms: the case of break-up is remarkably compliant and similar methods have been used; but the results are not presented here.

13.5.2 Discussion on higher order moment methods in the sections

Compared to OSM methods, the TSM methods have allowed to reduce in a sensible way the needed number of sections. Although the overall order of the method is not very high (due to the lack of a high order in velocity), the TSM method is very interesting as a larger part of the physics of interest in our problem lies in the size variable.
Upgrading the number of moments (e.g. using EMSM) requires a more complex algebra for a gain that is presumably not as strong as between OSM and TSM.

13.5.3 Second order in velocity

The use of second order size-velocity correlations such as those of the model derived in § 5.4 for the TSM can be envisioned in a case where the velocity varies strongly within the sections. This can improve the accuracy of the method for a reasonable cost, especially when very few sections are used.

13.5.4 Conclusions on flexibility

As it has been said in this chapter for TSM methods and in § 4.4.4.5 for high order moment methods, moment methods require to compute more or less complex reconstructions and integrations while they encounter realizability constraints: the TSM method is therefore a good compromise since it has:

- an improved accuracy compared to OSM, especially for a low number of sections;
- a good robustness compared to high-order size moment methods;

- a flexible algebra, allowing to account for collision efficiencies straightforward and to add any other type of model.

The TSM method is therefore a good choice for SRM computations, which complies to the requirements of HPC.

Part V

Applicative computations

Chapter 14

The CEDRE code

We present the CEDRE code. It is used for high-fidelity computations: its design allows it to solve research and industrial flow problems with multi-dimensional, complex geometries and multi-physics aspects such as transfers at turbulent boundary layers, combustion, acoustics, compressibility, two-phase flow aspects etc. The CEDRE code is well adapted for SRM computations. Some of the methods presented before are implemented in the code to extend its capacity towards computations featuring coalescence, two-way coupling and nano-micro hybrid disperse phase flows.

14.1 The baseline CEDRE code

The CEDRE code is a multi-physics platform working on general unstructured meshes intended to both advance research and process industrial applications in the fields of energetics and propulsion (Refloch et al. 2011).

14.1.1 General aspects of CEDRE

14.1.1.1 The CEDRE suite

The CEDRE suite is presented in (Refloch et al. 2011). The system includes a graphical user interface for data entry and a set of pre and post processing utilities. The code is organized as a set of solvers, each of which can be used to handle a particular physics, which are coupled together for the computations. The multi-physics resolution is achieved by solvers:

- CHARME is dedicated to reactive gas flows,
- a dispersed phase can be solved with the Eulerian solver SPIREE or the stochastic-Lagrangian solver SPARTE,
- a coupled resolution of solid body thermal conduction can be done with ACACIA,
- and a coupling to liquid films can be performed with FILM,
- radiation can be solved either with a Monte-Carlo approach ASTRE or with a Eulerian approach REA,
- and soots are solved with PEUL.

Other programs can be used to handle other physics that are not part of energetics, such as mechanics, by means of external couplings, using in particular the in-house CWIPI library. The overall software suite is conceived as regards parallel computing, as performance cannot be considered independently from the physics.

14.1.1.2 Applications and achievements

As CEDRE is designed for mechanical engineering configurations, it has achieved a wide range of applications, especially in aeronautics (Scherrer et al. 2011).
Pure fluid approaches are performed with the CHARME solver:

- Aerothermodynamics of turbine blades: RANS, aerothermics, SIBLE wall function, with CHARME;
- Film-cooling of a dump combustor: RANS, fluid/structure aerothermics, reactive, with CHARME;
- Hypersonic vehicle separation: RANS, hypersonic aerodynamics, with CHARME;
- SRM ignition blast wave with afterburning: LES, aeroacoustics, equivalent gas two-phase flow, reactive, with CHARME (Dargaud 2013).;
- Jet noise prediction: LES and aeroacoustics with CHARME-external;
- Flow separation in an over expanded nozzle: RANS and DDES, reactive, with CHARME;
- Aircraft and helicopter icing: RANS two-phase flow, with SPARTE-external (Murrone and Villedieu 2011);

- Flow instabilities in a SRM with turbulence, LES with CHARME;
- Reacting flow in a research ramjet combustor: RANS and LES, reactive, with CHARME
- Reacting flow for SRM afterburning: reactive aeroacoustics and LES with CHARME.

The coupling to a disperse phase, resolved either with a stochastic-Lagrangian approach (SPARTE solver) or with a Eulerian approach (SPIREE solver) was assessed in several configurations:

- Combustion in a multipoint injection burner: RANS, diphasic, reactive, radiation, with CHARME-SPARTE-ASTRE-PEUL (Dorey 2012);
- Combustion in MASCOTTE cryogenic burner: RANS, sub/supercritical fluids, reactive, with CHARME-SPARTE Murrone and Villedieu (2011) and with CHARME-SPIREE (Le Touze et al. 2012);
- role of the disperse phase in SRM flow instabilities, with CHARME-SPIREE (Dupays et al. 2008) and with CHARME-SPARTE (Estivalezes 2010; Estivalezes 2011).

The latter case features a moderately dense phase and requires a fine rendering of the two-way coupling: the Eulerian computation of Dupays et al. (2008) was performed without coalescence and the stochastic-Lagrangian computation of Estivalezes (2011) achieves a coarse convergence.

14.1.1.3 Conclusion

The CEDRE code has proven its capabilities on industrial configurations, for design and development. It is also used for research purpose on semi-industrial experimental bench configurations and on academic cases. We now present the abilities and numerical methods of the carrier and disperse phase, in the context of strongly coupled two-phase flows.

14.1.2 Numerical methods for the carrier phase

14.1.2.1 A general purpose Navier-Stokes solver

It features an aeroacoustic solver allowing a variable isentropic coefficient with a robust solver for advanced chemistry so that the overall code can tackle combustion.
The continuum is a mixture of an arbitrary number of species, each species having its equation of state. The state of the mixture is defined by the densities of the species, together with the total energy and the momentum per unit volume, as given in § A.
In practical applications, velocities may cover a very wide range, from low Mach numbers to hypersonic speeds. Turbulence is present in most simulations and is taken into account in the LES (Bertier et al. 2004) or RANS (Reynolds Averaged Navier-Stokes equations) approach. In the latter case, additional scalar quantities and balance equations are added to the aerothermochemical system to describe the macroscopic properties of turbulence. For most models, these quantities include the mean kinetic energy of turbulence, and an additional scalar may be dissipation, length scale or frequency.

14.1.2.2 Need for generic unstructured meshes

Generic unstructured meshes were originally developed for application domains focused on energetics and propulsion, which are often characterized by very complex geometries.
The setting up of structured hexahedral mesh calculations is regarding as time consuming while many types of automatic mesh generation software gradually became available: tetrahedral meshers first, and then meshers mixing several types of elements, mainly tetrahedra, prisms, pyramids and hexahedra but also hexahedra trimmed by boundaries, hexahedra with refinement, polyhedral mesh obtained as the dual of a tetrahedral original mesh *etc.* Furthermore, the mesh can be subjected to a topological alteration in the course of calculation. Adaptive mesh refinement is a well known example, as well as mesh overlapping, which results in cells that are trimmed in a very general way into various polyhedral shapes, directly used by ALE formalisms.
To cope with this variety of complex meshes, the CEDRE code has been based on its capacity to operate on unstructured generic meshes. This means that the mesh is defined by the faces of its elements, which are used to compute the fluxes in a finite volume formalism. As an obvious consequence, any kind of polygons can be used as long as their faces are defined.

14.1.2.3 Space strategy

Space discretization is described in Courbet et al. (2011):

- the general framework is the cell-centered finite volume approach, on possibly moving and deformable control volumes (ALE formulation);
- interpolation follows a MUSCL type methodology. For each degree of freedom, space derivatives are evaluated algebraically from some neighborhood of the current cell, which allows a polynomial

reconstruction on each cell;
- this reconstruction gives rise to two distinct evaluations of each variable at every point along the interface between two cells. After limitations for monotony, these evaluations are used as input for approximate Riemann solvers;
- cell reconstruction is also the basis for interface gradient and Navier-Stokes flux evaluation.

To spare resource, a unique gradient can be computed on the cell and used for the reconstructions at all faces. This approach proves to be efficient when the mesh is regular enough e.g. cartesian or when the flow is smooth enough e.g. in RANS simulations and some cases. But for torn-down fields, a more accurate and comprehensive approach is used: it is based on the evaluation of a k-exact reconstruction at each face, from the knowledge of the derivatives of order up to k, which can be computed with a compact stencil, limited to the adjacent cell. Compactness is compliant with paralellization and HPC requirements. This method is implemented up to order 4 (Haider et al. 2011), an order that proves to limit numerical dissipation in a critical way. The need for an accurate and local reconstruction is also discussed for the disperse phase transport, below.
Several flux schemes are implemented, which are suited for different cases: Roe's method, ODFI, AUSM+, and HLLC.

14.1.2.4 Time integration

Time integration resorts to the usual Runge-Kutta methods (Marmignon et al. 2011) used in many unsteady simulations. The recourse to explicit approaches is for instance recommended to capture acoustics or transient regimes.
In some cases (low Mach number flows, steady flows), implicit generalizations of these methods can be useful. Euler implicit method can be used at large time intervals when a steady solution is expected. For implicit schemes, large sparse linear systems are solved at each time interval with the help of the Generalized Minimal Residual method or Gmres (Selva 1998).

14.1.2.5 Boundary conditions for SRMs

Many types of boundary conditions are available, including:
- inlet-outlet with various sets of imposed fixed variables and options for swirl, radial equilibrium, mixing plane, non-reflection *etc.*;
- symmetry, axis, no-slip;
- spatial periodicity;
- walls with various heat transfer boundary conditions, and variants for porous walls or solid fuel motors.

For SRMs, it is essential to control the mass fraction: a boundary condition with a fixed mass flow rate has been developed, the temperature being fixed.

14.1.3 Numerical methods for the disperse phase and coupling

As for the disperse phase, CEDRE includes a stochastic-Lagrangian and two Eulerian methods (Murrone and Villedieu 2011) i.e. a Multi-Class or sampling method and a Two Size Moment Multi-Fluid method, namely the Exp-TSM. Only the stochastic-Lagrangian and the Multi-Fluid methods provide the resolution of coalescence.
The code is designed for research and industrial simulations of complex multi-physics problems so the numerical methods are optimized regarding cost and accuracy.

14.1.3.1 Eulerian disperse phase solver

The Eulerian methods in the SPIREE solver allow to solve polydispersity: a Multi-Class method (see § 4.4.3) and a Two Size Moment Multi-Fluid method (see Chapter 5) are well-suited for this. The latter method has a more complex algebra but it solves the size distribution at second order and potentially allows to account for coalescence and break-up. As a remark, both methods can solve for evaporation, though with a very different approach (Lagrangian or finite volume treatment of the size variable in the phase space).
The transport scheme for the Eulerian moments of the disperse phase is the same for both methods and shares the same aspects than that of CHARME. A first order scheme is commonly used for robustness but is not sufficient for many applications, where clustering and singularity characteristic lengths must be captured accurately. A second order MUSCL reconstruction has been developed for disperse phase transport (Le Touze et al. 2012) by using a MUSCL reconstruction close to that of CHARME, still with a cautious reconstruction to achieve robustness but with standard slope limiter functions. The space fluxes are computed on the faces with a solver based on the resolution of the Riemann problem. The space approach is integrated versus time

with a third order implicit Runge-Kutta method (RK3) or its implicit version (RKI3) to extend the stability domain above CFL= 1.
As for the boundary conditions, the Eulerian approach offers simple input and output conditions, in accordance with the PGD modeling resulting from the monokinetic description (either for the Multi-Class and Multi-Fluid approaches): the input condition has DoFs on mass flow rate, velocity and temperature while the output simply removes the outflowing mass (no information can return in PGD). The reflexion conditions (to treat walls and symmetry axes) are intrinsically limited because of the monokinetic assumption and they always generate singularities flowing tangentially.

14.1.3.2 Euler-Euler coupling strategy

The Eulerian solver is coupled to a compressible gas, described by Euler or Navier-Stokes equations and solved with CHARME. The coupling between CHARME and SPIREE can be one-way or two-way (Errera et al. 2011) but we focus on the peculiarities of two-way coupling as we aim at solving moderately dense two-phase flows.
The time integration strategy for the coupled problem is close to the BWC strategy described in § 10.3.4.3: it is flexible and convenient since it is implemented with exchange source terms at the end of the time steps, but not very accurate for two-way coupling nor robust for stiff equations.
A coupled boundary condition allows to assume the disperse phase at some equilibrium, either at dynamic, thermal equilibrium, or both.

14.1.3.3 Stochastic-Lagrangian disperse phase solver

The stochastic-Lagrangian solver SPARTE is based on a Monte-Carlo sampling of the phase space, as presented in § 4.2. The treatment of transport, drag, heating and evaporation is that of Ordinary Differential Equations (ODE) in a one-way coupling case. A one-step implicit strategy can be used.
As for collisions and coalescence, the strategy is that described in § 4.2.2: the computation of coalescence terms is split from the transport and source resolution. The parcel evolution under coalescence is computed with an optimized algorithm that reduces the number of partners to assess and therefore the cost. The incrementation of the data still requires to gather parcel information in a vicinity of the target parcel: this necessitates to have a sufficient number of parcels in the domain, with respect to the singularities of the disperse phase spatial field. Moreover these needed projections introduce numerical diffusion.

14.1.3.4 Euler-Lagrange coupling strategy

In two-way coupling cases, ODEs are still solved for the parcel size, velocity, and temperature, but the resulting mass transfer, drag and heating terms are also used to compute a Eulerian source term to assess the retrocoupling towards the gas. This Eulerian terms are computed on each cell mesh by gathering parcel data (therefore introducing numerical diffusion).
These source terms are communicated to the gas at the end of the time step, in a way that is close to that of BWC. Therefore the coupling may become inaccurate for strong retrocoupling, as illustrated in § 10.3.4.3 for Eulerian cases, and stiffness threatens robustness.
Because accounting for the transport through ODEs introduces a very low level of numerical diffusion and because DSMC may feature noise, the retrocoupling source terms become very stiff when singularities start to form. This may be treated by a relaxation method, which reduces accuracy on the coupling.

14.1.3.5 Conclusions

We discuss the simulation of moderately dense disperse phases two-way coupled cases, the treatment of two-way coupling and some models such as coalescence require some improvements.

14.1.4 Moderately dense achievements

The physics of moderately dense disperse two-phase flows has been assessed with both CHARME-SPARTE and CHARME-SPIREE. We present some polydisperse two-way coupling achievements.

14.1.4.1 Monodisperse achievements

The case of combustion instabilities in a subcritical LRE has been studied by Le Touze et al. (2012) with a Eulerian monodisperse phase of liquid oxygen droplets burning in a hydrogen jet. The very high mass fraction at the output of a modeled primary atomization liquid jet was a major peculiarity that the Euler-Euler method was able to capture, as well as the reactive character of the disperse phase.

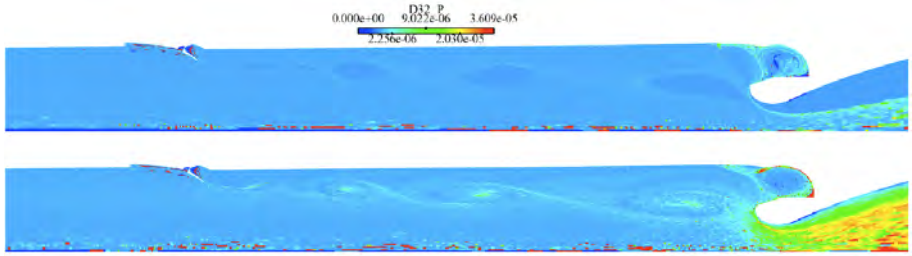

Figure 14.1: *d_{32} diameter in the P230 SRM– 2D computation with CHARME-SPARTE by Estivalezes (2010) – Top: without coalescence; Bottom: with coalescence.*

The structure of a SRM exhaust jet has been assessed with a monodisperse Eulerian approach and the two-way coupling proved the role of particles on it. Results have been given as an illustration in Figure 1.26 for Ariane 5 and for Vega in Figure 1.27.

14.1.4.2 Polydisperse achievements

In the case of SRMs with a detailed resolution of the chamber, polydispersity has been considered as a main feature e.g. to assess instabilities and it was accounted for in the following benchmark computations.
Computations on an unstable sub-scale motor called LP10 with the Multi-Class solver have allowed Dupays et al. (2008) to confirm the driving effect of particles on hydrodynamic instabilities. These computations are furthered in Chapter 15.
Lagrangian computations of the P230 have proven the role of coalescence on the oscillation levels of this full scale motor. A 2D simulation performed in Estivalezes (2010) was the first achievement: some results on collision rates were given in Figure 1.19 and results on size evolution are given in Figure 14.1. A 3D computation was performed in the continuity in Estivalezes (2011): a similar result is given as an illustration in Figure 4.3.

14.2 New methods implemented in CEDRE

The developments of new numerical strategies in Part IV is considered for the CEDRE code.

14.2.1 Implementation of ACS in CEDRE

We focus on the improvement of the coupling strategy between CHARME and SPIREE. This requires to deeply modify the structure of CEDRE, which is fundamentally based on exchange terms between the solvers, transmitted at the end of solver time steps. This implementation has been done with the help of Angelo Murrone.

14.2.1.1 A deep modification of the code

To implement the ACS strategy, presented and validated with the SAP1 code in Chapter 12, it is required to implement in CEDRE a master routine dealing with the time stepping of the CHARME and SPIREE solvers. In addition, a new routine is dedicated to the joint integration of the gas and liquid variables in the context of the relaxation operator, outside of both CHARME and SPIREE; in return, the sources are disabled in the two solvers.

14.2.1.2 A strategy for the relaxation operator

As for relaxation numerical methods, though an analytical solution exists for Stokesian monodisperse sprays, we will use a more general numerical method for the relaxation step in order to easily generalize to polydisperse sprays or non Stokesian transfers. We insist on the fact that, even with multiple sections, operator $\mathscr{R}_{g\sum k}$ is a system of ODEs per discretization point and can be easily solved, though the different particle size characteristic time scales can be very different, therefore yielding a stiff problem: this aspect is discussed in § 10.4. So we use in the following a simple numerical method such as an explicit Runge-Kutta method which is sufficient when the relaxation time step is small enough, corresponding to a K_g below unity (see § 12.3.3.1).

14.2.1.3 A validated strategy

Some validation computations were performed with ACS in CEDRE and have already been presented in Chapter 12.
The strategy allows to capture accurately the attenuation and dispersion of acoustic waves by the disperse phase.
And the code is proven to be more robust in the case of small droplets as well as for higher mass loadings. The convective case proves indeed that the flow can now be resolved robustly, even when the disperse phase drives the flow dynamics i.e. when $C \gtrsim 1$.

14.2.2 Implementation of coalescence in SPIREE

We now focus on implementing coalescence in SPIREE.

14.2.2.1 Method for size integrals

The Two-Size Moment Multi-Fluid method is ideal to implement the validated developments of § 13.1.4 while SPIREE's MF solver is based on an exponential reconstruction.
We introduce both a fixed node Newton-Cotes quadrature strategy (with arbitrary nodes up to 9, see § 13.1.4.1) and an adaptive quadrature (AD2 in § 13.1.4.3). These developments, validated with the TUYA code in Chapter 13 are designed to perform an efficient inversion for the Exp-TSM method and an efficient integration of coalescence in an industrial context e.g. with a very low number of sections.

14.2.2.2 New kernels for nano-micro mixtures

The kernel and the coupling Multi-Fluid methodology developed in Chapter 9 are implemented in CEDRE.

14.2.2.3 Treatment of coalescence in a splitting context

In the context of the ACS, the coalescence terms can be integrated in a split way. The coalescence operator is performed solely at the beginning of a time step in the context of a first order Lie splitting strategy to spare cost: this is detailed in § 12.5.1.
The coalescence operator is integrated versus time with an explicit Runge-Kutta method. Implicit methods are interesting to overcome stiff time scales but they have not been implemented and the explicit strategy has proven to be efficient in the considered cases.

14.2.3 Conclusion on the new developments in CEDRE

The CEDRE code has achieved interesting computations for moderately dense disperse two-phase flows. The presence of both Euler-Euler and Euler-Lagrange strategies in a code is a major feature to perform scientific computations and prospective studies on models and methods.
With the new developments on coalescence and coupling, yielding the ability to treat efficiently moderately dense nano-to-inertial coalescing sprays, the CEDRE code is ready to perform a new high standard type of simulations: studies of polydisperse coalescing sprays for two-phase losses and instabilities are presented in Chapter 15 and for nanometric droplets in Chapter 16.

Chapter 15

Polydisperse moderately dense sprays in SRMs

Applicative computations of realistic SRMs are performed. The first case consists in assessing the flow in a steady model SRM model where coalescence occurs: this gives access to two-phase specific impulse losses in a case where size distribution strongly evolves. The second case is a study on the impact of polydispersity and coalescence on an unstable sub-scale SRM. Capturing the complex behavior of the disperse phase in a strongly coupled, unsteady regime is a major achievement, proving the relevance of the strategy developed in the present thesis for moderately dense polydisperse flows. The third case is a full scale application on a realistic, complex SRM featuring again an unstable behavior but in the presence of a disperse phase that is strongly bimodal and coalesces. The application of the moderately dense and polydisperse numerical strategy to this case is proven to be nonetheless efficient but incontrovertible to treat the stiff source terms that arise with the small droplets in the two-way coupling context.

15.1 Introduction on feasibility and applicative computations

The purpose of this chapter is to present applicative computations on realistic SRM problems. They are performed with the CEDRE code, presented in Chapter 14. In all this part however, a first order transport scheme is used for the particles. The new developments done in the present work and used for the computations are recalled each time they are enabled.
In the context of these developments, applicative computations are intended to provide three levels of results:

1. they achieve the validation of the approach by allowing comparisons to stochastic-Lagrangian computations;
2. they constitute feasibility studies in the sense that they provide informations on the practical applicability of the models and methods assessed or developed in the present thesis, their cost and accuracy in the final context of use;
3. they yield the desired applicative results.

As regards the level of detail of the real SRM flows, the computations are performed with meshes that are refined enough to capture the hydrodynamic structures which appear. But these meshes are too coarse to capture any form of turbulence, which is filtered away by the discretization and the scheme. Such computations are not compliant with the fluid-kinetic DNS context that we have defined in § 3.5 nor with a reduced turbulence approach (LES or RANS) because of the absence of the related models. However these computations still allow:

1. to validate the approach versus stochastic-Lagrangian computations as long as the latter are performed in the same conditions, since both approaches tackle the same underlying fluid-kinetic model, in an under-resolved context;
2. to assess the cost and the practical conditions of use of the new methods and therefore feasibility;
3. to conclude on the trends of physical phenomena.

The following computations are performed on cases with an increasing level of complexity and cost: the first case is steady state, the second case is unsteady and the third case is unsteady and very stiff. The upcoming results demonstrate nonetheless the feasibility and the relevance of the strategy designed in the present work but also the impact of polydispersity and coalescence on two-phase losses and on instabilities. In all the cases, droplets are big enough for coalescence to occur in ballistic regime: no nanometric modeling is enabled.

15.2 Estimation of two-phase losses in SRM

The first SRM simulation is performed on a 2D simplified configuration, yet featuring the main difficulties of SRM typical flows i.e. parietal injection and a supersonic nozzle.
Parietal injection refers here to two-phase mixture injected normally to the wall: it is a classical modeling for the gas and inclusions produced and ejected by the solid propellant combustion. A flow that is injected from a cylindrical wall has indeed the peculiar structure of the Taylor flow as detailed in § 1.3.1.4.
The supersonic nozzle features a compressible flow behavior, that requires an adapted solver: CEDRE allows to solve full-Mach problems. In this case, the ACS is not enabled so that only the developments on coalescence are used.

15.2.1 A steady model SRM: the TEPTEU case

15.2.1.1 Description of the case

The configuration features two injection zones as shown in Figure 15.1: a parietal injection corresponding to the flow coming from the wall that carries small alumina droplets, typical of immediately burnt solid propellant and an axial injection corresponding to the flow coming from the rear, that carries bigger droplets to model burnt and coalesced particles injected upstream. The upper part of the chamber generating these bigger droplets is not solved so that the mesh is significantly shortened. The meeting of these two types of particles may generate coalescence.
A total flow rate of $10\,\mathrm{kg.s^{-1}.m^{-2}}$ models the effect of the propellant combustion from the wall and the effect of the upstream flow from the head end to model. This case involves high velocity gradients in the nozzle, see Figure 15.4 top, which induce size-velocity coupling, similarly to the nozzle test case presented in § 13.2.4.
As for coalescence intensity, it is first estimated with the method discussed in § 7.2. In the chamber, the growth time is about $\overline{\tau}^G = 24\,\mathrm{ms}$ and the residence time $\tau^R_{\mathrm{chamber}} = 10\,\mathrm{ms}$ so that $\mathrm{Kn}_g = 2.4$. In the nozzle, these times are $\overline{\tau}^G = 0.5\,\mathrm{ms}$ and $\tau^R_{\mathrm{nozzle}} = 0.2\,\mathrm{ms}$ so that $\mathrm{Kn}_g = 2.5$. The size distribution is therefore expected to be shifted significantly.

15.2.1.2 Numerical configuration

The simulation takes place on a deformed-structured 1500 cell mesh, see Figure 15.1. When seeking a two-phase flow solution, one usually takes a steady state gas flow field as an initial state.

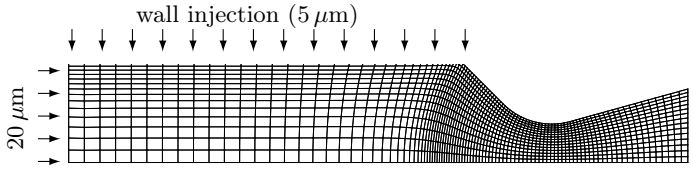

Figure 15.1: *TEPTEU: a deformed-structured* 1500 *cell mesh (Arrows: injection zones).*

The two-phase simulation strictly speaking starts when injecting the disperse phase: a monomodal $5\,\mu$m radius wall injection represents the droplets resulting from recently burnt aluminum particles, directly expelled from the propellant grain, and another roughly monomodal distribution around $20\,\mu$m is injected at the head end to model the previously coalesced droplets (Fabignon et al. 2003). For the purpose of our simulation, the injected volume fractions approximate correctly typical SRM chamber conditions and preserve the dilute spray hypothesis. For the disperse phase, we choose a 5 section discretization (0, 12.5, 21, 25 and $30\,\mu$m) as in the nozzle test case (see § 13.2.4) so that only the first or the second section contain droplets near the injection zones.
A $10^{-2}\,\mathrm{s}$ time interval is required to allow the first droplets to reach the end of the nozzle. With a $10^{-6}\,\mathrm{s}$ time step, $10,000$ iterations are needed.
The gaseous Mach number field, once the permanent two-phase regime is reached, is given in Figure 15.4, bottom; the stationary volume fractions for the five sections are displayed in Figure 15.2. The first section droplets do come from the wall, they fill the combustion chamber and the nozzle, where their volume fraction decreases due to the strong acceleration, which we refer to as dilution. The second section droplets do come from the rear and they are pushed towards the axis by the parietal injection. The three other section droplets are not present close to the wall since they are not injected.

15.2.2 Results with CEDRE

The case is computed with CEDRE. The collision efficiency is not modeled i.e. $\mathfrak{E} = 1$ and no break-up model is enabled so that only coalescence occurs.

15.2.2.1 Results on coalescence

Figure 15.2 shows the creation of bigger particles: coalescence yields droplets in section three as soon as the two injected types of droplets meet; moreover the volume fraction of section three droplets in the chamber is significant which shows the importance of coalescence. Third, even bigger droplets, especially in section four, are created in the nozzle even though acceleration induces there a strong volume fraction dilution.

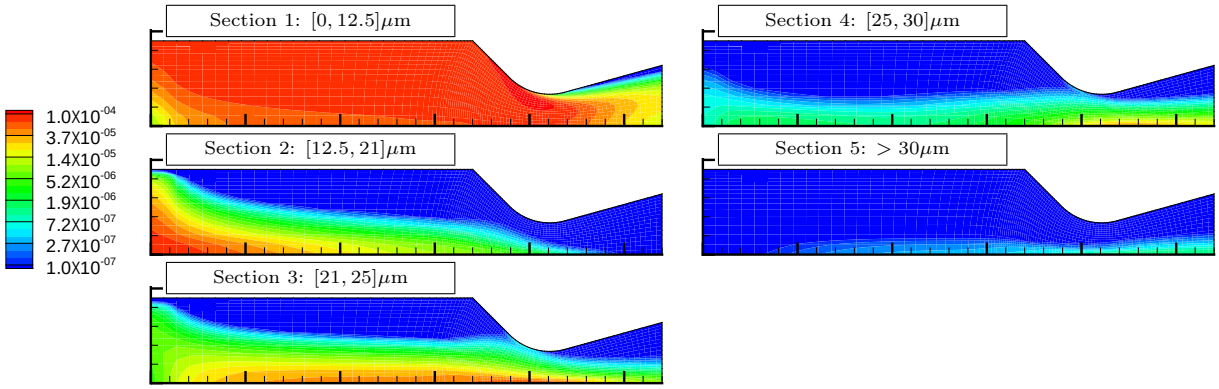

Figure 15.2: *Dispersed phase volume fractions per section.*

15.2.2.2 Eulerian vs. stochastic-Lagrangian computation: size evolution

The stochastic-Lagrangian reference computation is also performed with the CEDRE code. Figure 15.3 shows a mean diameter, the d_{30}, with both simulations: its evolution is correctly predicted by the Eulerian Multi-Fluid method as implemented in CEDRE.

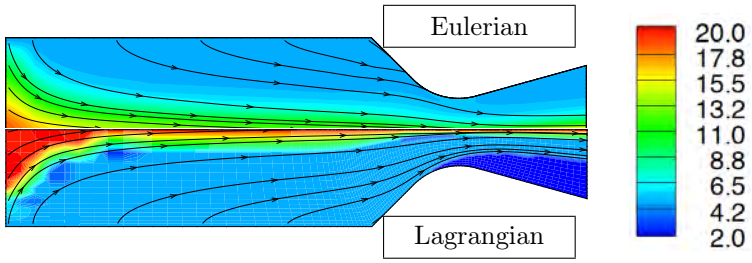

Figure 15.3: *Overall average droplet diameter (d_{30}) and particle streamlines in Eulerian and stochastic-Lagrangian computations.*

The main difference occurs on the axis where the Eulerian model undermines coalescence. Indeed momentum is averaged on each section because of the monokinetic hypotheses [HV1] and [HV2] and thus the Eulerian model is unable to account for particle trajectory crossing among the sections i.e. homo-PTC. This effect is also visible close to the wall where streamlines become tangential. On the contrary, the stochastic-Lagrangian framework naturally handles PTC and can feature any wall rebound model, which allows the particle streamlines to avoid the wall.
Another difference is visible in the nozzle: there are no particles far from the axis in the stochastic-Lagrangian simulation. This is visible when considering the first section volume fraction in Figure 15.2, dark blue convention in Figure 15.3. On the contrary, particles are present almost everywhere in the nozzle with the Eulerian simulation. This reveals that the Eulerian transport scheme is spatially diffusive. This also appears on the size transverse gradient at the rear end of the chamber, which is smoothened. Yet spatial diffusion is rather a matter of numerical method and can be improved by using the second order transport scheme for instance, the latter not being enabled in the present computations.

15.2.2.3 Disperse phase impact on the flow

Figure 15.4 shows that the disperse phase has an impact on the gas flow, in accordance with the two-way coupling enabled in the simulation. Specific impulse loss can therefore be observed with the nozzle Mach number decrease in the presence of droplets.

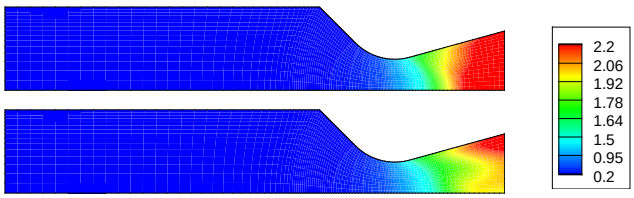

Figure 15.4: *Gaseous Mach number without droplets (top) and with a disperse phase computed with the Two Size Moment method (bottom).*

15.2.2.4 Lagrangian validation on steady two-way coupling

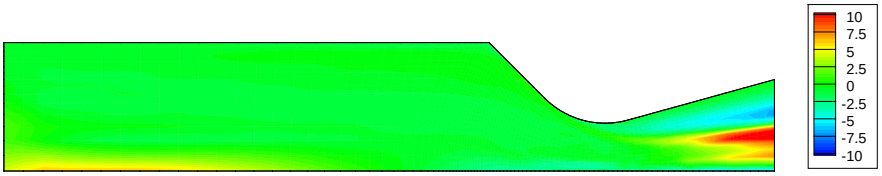

Figure 15.5: *Eulerian relative difference to the stochastic-Lagrangian simulation on the Mach number field (%).*

Figure 15.5 shows the relative error on the Mach Number field compared to the reference stochastic-Lagrangian simulation. Mach number is important to quantify the total specific impulse loss in the nozzle. The defects of the Eulerian Multi-Fluid method, previously commented on the d_{30} evolution, appear here too. Size and velocity prediction errors on the axis imply an overestimation of the Mach number at the rear end. In the nozzle, particle trajectories are axi-parallel and close to the axis, still because of Eulerian momentum averaging, so that the Mach number is overestimated up to 10% in the near-axis zone. Finally, small particle Eulerian diffusion increases flow inertia close to the wall so that the Mach number is slightly underestimated (5%).

15.2.3 Conclusion on the steady case

15.2.3.1 A cross validation

As regards cross comparisons, the Euler-Euler method is validated since it yields results that are satisfactory compared to the Euler-Lagrange approach. However, due to the monokinetic hypothesis and the scheme numerical diffusion, small discrepancies appear on momentum and volume fraction, having up to 10% repercussions on the Mach number in our current configuration.

15.2.3.2 Relevance of Euler-Euler approaches as regards cost

As for the cost, we can also compare the Euler-Euler and Euler-Lagrange strategies. We perform both computations on a single processor AIX platform computation, so the issues of parallel computing are not discussed. The coalescing Euler-Euler approach requires 1 h of wall clock time which corresponds, with a 10^{-6} s time step, to 10,000 iterations and to 360 ms per cycle. This is about 50% more than without coalescence, proving the feasibility of coalescence computations with a TSM method. As a remark, the OSM method would have required more sections, therefore increasing the total number of moments and the cost of transport. As for coalescence, its cost increases with the square of the number of sections and though the OSM allows some optimization when no efficiency is accounted for, the OSM cost on coalescence is much higher if such collision models are accounted for.
With the Euler-Lagrange strategy, the computation takes 6 h, which indicates that the Eulerian approach is relevant as regards cost. A more rigorous cost comparison can however only be performed if level of accuracy is proven to be similar for the Euler-Lagrange and Euler-Euler approaches.

15.2.3.3 Assessing two-phase losses

Let us now discuss the physical insights that the Eulerian computation yields on specific impulse losses. The approach is proven in de Chaisemartin (2009) to be valid for low inertia i.e. small droplets, as defined in § 3.1.3.1. For medium and large sizes, crossings can occur leading, with the Multi-Fluid approach, to δ-shocks. This happens for a small part of the disperse phase in the present case, as shown in Figure 15.2 and has consequences on the gas Mach number as shown in Figure 15.5.
In a strongly two-way coupled situation, such discrepancies cannot be tolerated if a more important proportion of the particles is inertial such as illustrated in Figure 10.3. Indeed the flow encounters a deceleration due to the strong retrocoupling at the level of the δ-shock while the surrounding flow can bypass the centerline particle obstruction. This results in significant modification of the mass flow rate repartition in a nozzle section. Besides, a strong shear appears as the centerline moves slower than the extra-radial annular layers. This does not match the physical behavior.
In these conditions, the physics of the nozzle is badly rendered and the specific impulse losses cannot be assessed. A modeling such as a Eulerian approach based on the Anisotropic Gaussian velocity closure, defined in Chapter 6 can render the characteristic radial dimension of the particle cloud. AG is therefore recommended, depending on the inertia of the disperse phase as it seems remarkably relevant to deal with the homo-DTC issue in the nozzle. And as a remark, assessing the particle inertia at the entrance of the nozzle then relies on the knowledge of coalescence intensity, so both AG and the usual monokinetic closure are to be used in a comprehensive approach of SRMs.

15.3 A new insight on the disperse phase role on SRM instabilities

Instabilities are assessed in the context of unsteady computations, which requires more accurate methods and more computational power than the previous steady computations. To capture the detail of the unsteadiness and in particular the acoustic waves which propagate, we resort to explicit time stepping.
Since the supersonic nozzle features high velocities, the context of an explicit resolution requires to lower the time step, below τ_g.

15.3.1 Influence of polydispersity on instabilities

In this section, we give numerical results of an unstable SRM with a monodisperse and a polydisperse approach. This case has already been used in § 12.4.3 for the validation of the ACS approach. We now perform a study to show the possible impact of polydispersity and we quantitatively compare instability levels to experimental results.
A sub-scale motor called LP10 was fired to bring experimental evidence on the particle driving role on instabilities Jézéquel and Prévost (2007). Dupays et al. (2008) has studied numerically the influence of polydispersity in this case with the Multi-Class solver of CEDRE. We now perform this study with the TSM Multi-Fluid solver and we further it.

15.3.1.1 Experimental setup with solid particles of ZrO_2

To guarantee a fixed and known size distribution of particles everywhere in the motor, the propellant is loaded with inert particles carefully chosen. Zirconium oxide (ZrO_2) powder was selected because of its high melting point which was verified to be above the chamber temperature of a non-aluminized propellant $T_c = 2300\,\mathrm{K}$. The supplied powder was sieved to narrow the size distributions around the chosen mean diameter, i.e. a diameter leading to an acoustic Stokes number St_ω close to one. The number and volume particle size distribution functions before and after the sieving are shown in Figure 15.6. This distribution is then assumed to be perfectly known in the whole chamber.
The mass fraction of particles introduced in the AP/HTPB propellant was fixed at 7 % of the total mass. This amount is sufficient to get an impact of the particulate phase on the motor stability. When comparing the average pressure signal in Figure 15.7 to the one of a firing of a reference propellant without particles, it is confirmed that such a particle loading causes no noticeable modification of the burning rate or of the thermodynamic conditions in the chamber, especially flame temperature and velocity of sound.
Pressure signals are monitored with sensors located at the front end and at the aft-dome region of the rear end of the test rig. Pressure oscillations were observed during the firings. Spectral analyses showed that these oscillations result from a coupling between the acoustics of the chamber (essentially the first axial mode) and a vortex shedding phenomenon. The decrease of the characteristic frequency during a burst and the jump between successive waterfalls are typical signatures of this coupling. As expected, pressure signals in Figure 15.7 show that the instability levels are higher at some point of the firing when adding the particulate phase to the propellant formulation. So the driving effect is supported by firm experimental

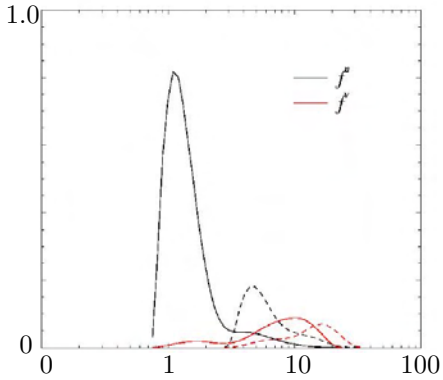

Figure 15.6: *Size distribution of the ZrO_2 particles – Dashed : before sieving; Plain : after sieving*

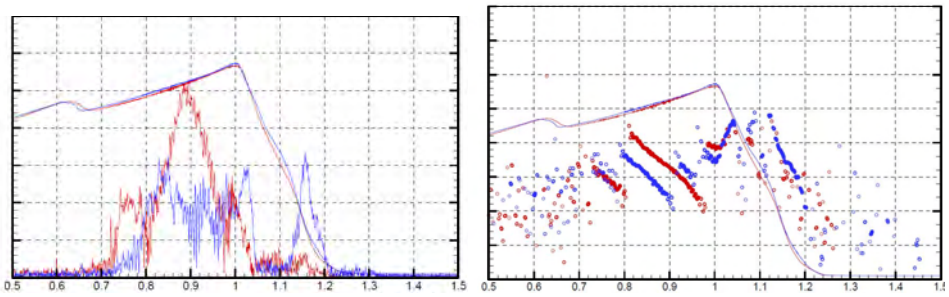

Figure 15.7: *Pressure sensor signal during a LP10 firing – Left: Average pressure (continuous) and fluctuation RMS level; Right: Average pressure (continuous) and instantaneous frequency – Red: Reference propellant; Blue: Sieved ZrO_2 load. (source: ONERA).*

data. The frequency curve of Figure 15.7 also shows that the regime varies quickly. The simulations will therefore be performed with a propellant grain geometry corresponding to the one at the particle-driven burst, assuming that the instability regime is permanent. This is a limitation of the approach since the non-uniform repartition of particles in the chamber is not known at this instant.

15.3.1.2 Inert monodisperse simulation with CEDRE

A LP10 simulation is performed with CEDRE on a 2D axisymmetrical representation of the LP10 sub-scale motor. The simulation takes place at a time when the most intense instabilities are observed, as shown in Figure 15.7. The simulated time is long enough to perform a harmonic study of the instabilities. At this time, the forward cylindrical grain has totally burnt so that no flow comes from the front end. The simulation takes place on a deformed-structured 27,000 cell mesh showed in Figure 15.8. No propellant combustion is modeled: gas and particles are injected at a fixed surface flow rate of $16.01\,\mathrm{kg/m^2/s}$ from the two walls representing the two propellant segments, see Figure 15.8. Particles are part of the burnt gas flow. They are non-coalescing and monodisperse at a diameter yielding $\mathrm{St}_\omega = 0.85$ based on the first longitudinal mode.

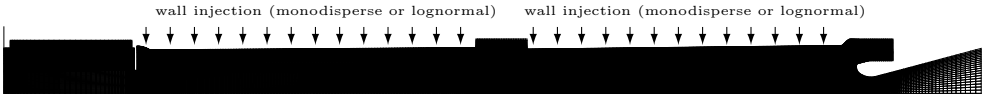

Figure 15.8: *Deformed-structured* 27000 *cell mesh of the LP10 geometry (Arrows: injection zones).*

The evolution of the simulation pressure signal is given in Figure 15.9. The simulation starts from a steady state of the single phase gaseous flow field. The particles are injected at a simulation time $t = 0.4\,\mathrm{s}$. The pressure builds up to a new value of average pressure which is steady after $t = 0.45\,\mathrm{s}$. The instability data is gathered at this new regime, for $0.45\,\mathrm{s} < t < 0.55\,\mathrm{s}$.
The effect of particles on the flow can be checked on the Mach number in Figure 15.10. Nonetheless specific impulse loss is attributable to the particulate phase with a significant Mach number reduction on the axis but we observe Mach number oscillations corresponding to the inhomogeneous particle distribution crossing intermittently the nozzle.

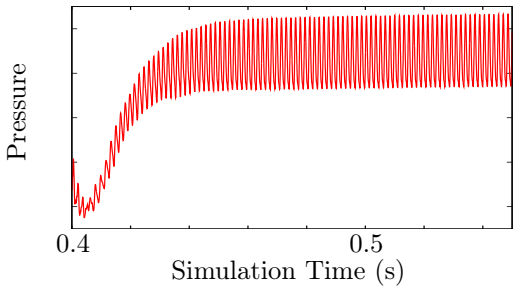

Figure 15.9: *Front end sensor pressure signal when injecting monodisperse particles.*

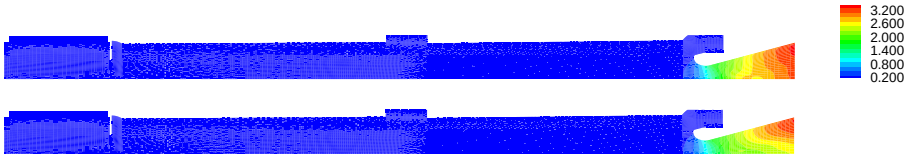

Figure 15.10: *Gaseous phase Mach number – Top: before particle injection; Bottom: with monodisperse solid particles at* $t = 0.514\,s$.

15.3.1.3 Vortices and instability facts

The configuration unsteadiness is visible on this monodisperse computation. The corresponding time scales are given in Table 15.1. When considering the gaseous vorticity field in Figure 15.17, one retrieves the typical VSP hydrodynamic instabilities described in § 1.3.2.4 which occur in long, segmented motors and are strongly coupled to the disperse phase. In the present case, the VSP is tuned on the 1L chamber mode.

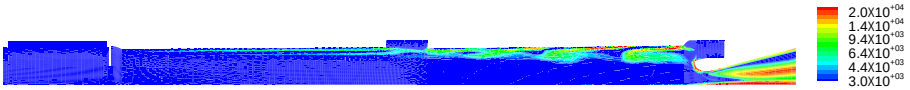

Figure 15.11: *Gaseous phase vorticity module* (s^{-1}) *with monodisperse solid particles at* $t = 0.514\,s$.

The instantaneous volume fraction of the particles is displayed in Figure 15.12 at a simulation time $t = 0.514\,\mathrm{s}$. As expected, segregation is remarkably intense with a factor 10 on volume fractions between the inside and the edge of the vortices. With a Stokes number close to one, most droplets are ejected from the vortices and accumulate at their edges, which results in a structuring effect. Therefore, the failure of linear theories based on homogeneous repartitions for non-coalescing particles is unavoidable. This supports the mechanism that has been suggested in Dupays et al. (2008) to explain the driving effect of some inert particles on instabilities. A coupling between acoustic and hydrodynamic instabilities can occur when $\tau_{acou} = \tau_{VSP}$. Since the structures of VSP are reinforced by particles when $\tau^{\boldsymbol{u}}(S) = \tau_{VSP}$, particles with $\mathrm{St}_\omega \sim 1$ can amplify instability levels. This supports also the necessity of accurately capturing polydispersity.

Figure 15.12: *Volume fraction for solid monodisperse particles with* $d_{30} = 6.5\,\mu m$ *at* $t = 0.514\,s$.

15.3.1.4 Non-coalescing polydisperse simulation

The size phase space is now discretized in three sections with the diameter bounds 3.33, 6.66 and 10 μm. The very small particles are treated with a MF-PEG approach (see § 12.4.3). The same lognormal distribution based on data from the ZrO_2 particles is injected from both segments to render polydispersity. The d_{31} is considered to evaluate a Stokes number $\overline{\mathrm{St}_\omega}$ average on the whole size distribution that is relevant for polydisperse dynamics in Stokes regime as suggested in Peirano and Leckner (2000). The distribution is centered on $d_{31} = 6.5\,\mu$m which ensures $\overline{\mathrm{St}_\omega} = 0.85$. The droplet injection details are given in Table 15.2.
We give instantaneous particle volume fraction fields at $t_s = 0.514\,\mathrm{s}$ in Figure 15.13. As expected, the three droplet sizes react differently to the gaseous vortices, the smaller particles featuring a uniform repartition while more inertial particles from section three are ejected from the vortices. Compared to the monodisperse approach, the d_{30} local value for section three is given in the same figure to show that the particles keep the same size all along their trajectories.

Time step Δt_a	$0.2\,\mu$s
Time step Δt_c	$0.2\,\mu$s
Nozzle CFL time (Full Mach)	$0.6\,\mu$s
$\tau^{\boldsymbol{u}}_{VS}$ acoustic Stokes time	$1.7\,\mu$s
Nozzle strain-rate-based time	$30\,\mu$s
$\tau^{\boldsymbol{u}}_{S}$ acoustic Stokes time	$120\,\mu$s
$\tau^{\boldsymbol{u}}_{M}$ acoustic Stokes time	$320\,\mu$s
Structure revolution time τ_{VSP}	$750\,\mu$s
$\tau^{\boldsymbol{u}}_{L}$ acoustic Stokes time	$780\,\mu$s
First acoustic mode ($2L/c$)	$1500\,\mu$s
Typical simulation time	$500,000\,\mu$s

Table 15.1: *Typical timescales in a LP10 sub-scale motor.*

Table 15.2: *Particle injection conditions*

	Sizes (μm)	d_{30} diameter (μm)	$\overline{\mathrm{St}}_{\omega,k}$	Wall flow rate (kg/m^2/s)
Section 1	$[3.33, 6.66[$	5.02	0.51	0.17
Section 2	$[6.66, 10[$	8.14	1.34	0.30
Section 3	> 10	12.83	3.33	0.61

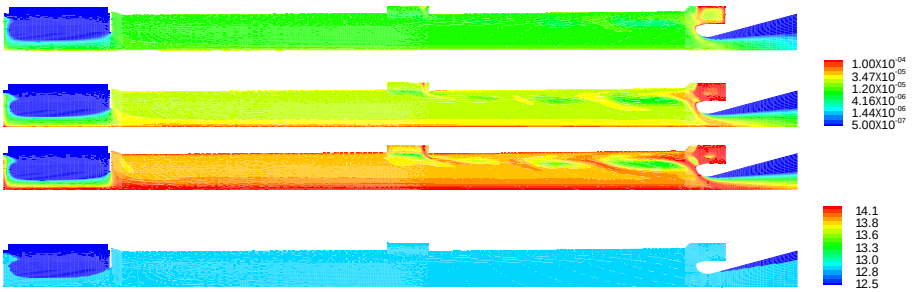

Figure 15.13: *Volume fraction per section and d_{30} mean diameter (μm) of section 3 for solid polydisperse particles at $t = 0.514\,s$.*

The impact of polydispersity on instabilies is shown in Table 15.3 and consists in a 20% drop of pressure oscillation level compared to a monodisperse simulation. The selective repartition mechanism is confirmed and polydispersity has jammed the droplet tuning to the VSP. Moreover, the oscillation level matches very correctly (6%) with the experimental one while the monodisperse simulation shows a 30% overshoot. Accounting for polydispersity with full dynamic resolution proves to be necessary since it seems difficult to find a representative and universal mean diameter whatever the configuration.

15.3.2 Impact of coalescence on instabilities: a modified LP10

We now assume liquid particles of ZrO_2 with the same density as previously. This is of course impossible at the effective chamber temperature but it is a working hypothesis to allow coalescence and study its impact. Regarding coalescence intensity in the chamber, the growth time is about $\overline{\tau}^G = 24\,$ms though the velocity difference can be higher in vortices compared to the average value we take. The residence time in the chamber is $\tau^R_{\text{chamber}} = 20\,$ms but there are vortices in the chamber so that $\mathrm{Kn}_g = 1.2$. In the nozzle, these times are close to those of the TEPTEU case with $\overline{\tau}^G = 0.5\,$ms and $\tau^R_{\text{nozzle}} = 0.2\,$ms so that $\mathrm{Kn}_g = 2.5$.

15.3.2.1 Why a coalescing case?

Coalescence can occur when particles are liquid which corresponds to most cases, that are aluminized propellants. Coalescence can change particle sizes, which are known to condition many phenomena such as gas/particle coupling. We therefore need to gather evidence of the impact of coalescence for further simulations of aluminized propellants.
Our model is based on monokinetic hypotheses so that no coalescence can occur among droplets of a given section but the coalescence phenomenon does happen between different sections. Since the injected droplet size distribution is disperse on the three sections and the flow allows local velocity differences to appear, coalescence will occur between sections as soon as droplets are considered liquid. Moreover it is showed in § 13.2.4 that a discretization as coarse as 3 sections is sufficient to capture basic coalescence size/dynamics

coupling with the TSM method. So we can inject particles with the conditions given in Table 15.2 for polydisperse solid particles. We use the Langmuir-Blodgett collision efficiency model as suggested in § 13.2.2.

15.3.2.2 Coalescing simulation with CEDRE

We give the instantaneous volume fractions per section and the third section d_{30} at $t = 0.514\,\mathrm{s}$ in Figure 15.14. Segregation still occurs as in the polydisperse case. But particles from section three have an average d_{30} diameter of 14.1 μm when crossing the nozzle throat on the centerline. Since they were all injected with a 12.83 μm diameter, they encounter an increase of 1.3 μm due to coalescence in the chamber.

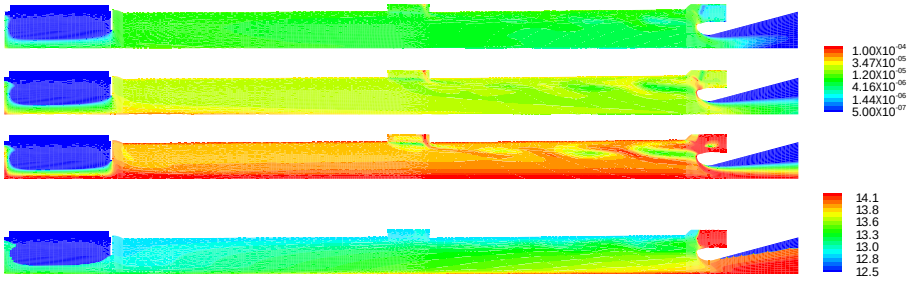

Figure 15.14: *Volume fraction per section and d_{30} mean diameter (μm) of section 3 for liquid polydisperse particles at $t = 0.514\,s$.*

Results not presented here show that the diameter increase reaches 1.8 μm when the collision efficiency is set to one. Not using collision efficiency modeling results in an overestimation of coalescence intensity. So advanced collision efficiency modeling plays a sensitive role.

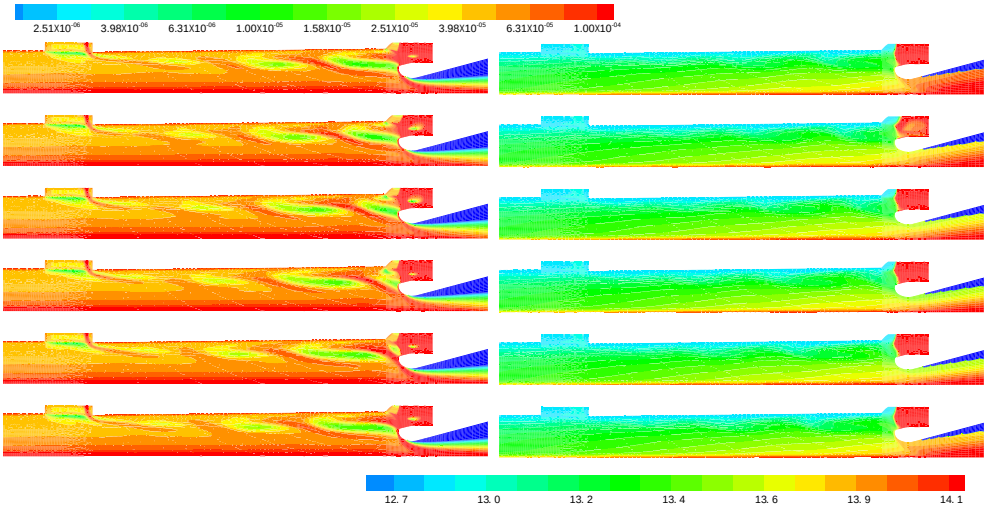

Figure 15.15: *Unsteady coalescence. Left: Volume fraction of the third section particles ($r > 10\,\mu m$). Right: Instantaneous d_{30} of the third section particles ($r > 10\,\mu m$) – Top to bottom : different phases of a cycle (0°, 60°, 120°, 180°, 240° and 300°).*

As shown in Figure 15.15, particles crossing the nozzle throat far from the centerline have a diameter that oscillates with an amplitude of 0.7 μm. This gives evidence of the unsteadiness of coalescence itself since the size of the third section droplets in the nozzle is varying periodically with the instability. This unsteadiness of droplet sizes has presumably minor consequences on instabilities since they are driven by the average droplet size in the chamber, which is here weakly modulated. But unsteady droplet sizes can impact the intensity of the break-up that occurs in the nozzle and consecutively specific impulse loss evaluation or jet signature determination. So the existence of unsteady coalescence is remarkable and incites to a detailed and accurate modeling and resolution of particle-particle interactions.

15.3.2.3 Effect of coalescence on instabilities

Results for monodisperse, polydisperse non-coalescing and polydisperse coalescing cases are compared to experimental pressure in Table 15.3. The diminution of 19% on pressure oscillation levels when assuming that particles can coalesce is presumably due to a significant modification of the droplet size distribution by coalescence. It gives quantitative evidence that coalescence modeling is a crucial issue to capture oscillation

levels in the context of SRM simulation, especially with aluminized propellants where the aluminum oxide droplet mass fraction can exceed 30%. Assuming the instability coupling mechanism recalled previously, the role of coalescence on instabilities is that size variations can detune the particles from the vortices.
With a different initial particle size distribution, having for instance $\overline{\mathrm{St}_\omega}$ much lower than previously, coalescence could bring particles to have a Stokes number closer to one. This growth towards $\overline{\mathrm{St}_\omega} = 1$ should increase instabilities. But this effect competes with a broadening of the size distribution that could reduce the amount of effectively tuned particles thus diminishing the levels. This configuration featuring tuning and broadening has not been tested but shows that coalescence does not necessarily undermine the driving effect of the disperse phase but could as well intensify it.

	Experiment	Monodisperse solid	3 section solid	3 section liquid
Average	100.0	97.8	97.4	97.1
RMS	100.0	129.6	106.4	80.8

Table 15.3: *Recapitulation of dimensionless pressure data at the front sensor (% of experimental value).*

Finally, the main oscillation frequency is the same in the three simulations. The droplet size evolution did not shift the acoustics lock-in of the VSP to an other unstable hydrodynamic mode. But there is no evidence that such a shift due to coalescence could not be observed either for other configurations, with a larger mass fraction or a different distribution size.

15.3.3 Conclusion on instability simulation

15.3.3.1 A cross validation

The studies on the LP10 provide a more limited but still interesting cross validation than that of the TEPTEU: the results are retrieved quantitative compared to those of another Eulerian solver, in the study of Dupays et al. (2008).
A more interesting validation is the one obtained versus the experiment: the results are very satisfactory on oscillation frequencies and moreover, the driving effect is retrieved. The good accordance between the results on oscillatory levels are encouraging but the fact that turbulence is not solved correctly appeal to being cautious since turbulence is known to play a role on instability levels, as discussed in § 1.3.2.2.

15.3.3.2 Relevance of Euler-Euler approaches as regards cost

The numerical features of the 2D SRM simulations and the computational times with and without coalescence are gathered in Table 15.4. Accounting for polydispersity (and eventually coalescence) is nonetheless proven to be necessary, but we show here that it is numerically accessible in the Eulerian Multi-Fluid framework, yielding at most a doubling of the numerical cost for 3 sections with the two size moment method.

Table 15.4: *Compared computational costs of polydispersity and coalescence.*

	Monodisperse solid	3 sections solid	3 sections liquid
Time/cycle (32 CPUs)	360 ms	640 ms	800 ms

These CPU costs prove the resolution of polydispersity to be quite costly with the level of detail of a Multi-Fluid approach but such computations are not at all out of reach: a resolution of polydispersity with coalescence costs less than 3 times that of a monodispere case.
Considering that polydispersity and coalescence are here proven to be compulsory to get the correct physics, the Euler-Euler approach is promising for unsteady moderately dense sprays with a Multi-Fluid approach to capture polydispersity.

15.3.3.3 Assessing instabilities

On the one hand, the Eulerian approach renders the correct oscillation frequency and a qualitative driving effect. On the other hand, we have said above that the results on instability levels are to be taken cautiously, due for instance to the absence of turbulence model.
Since a linear approach such as the Biglobal Analysis, presented in § 2.1.2 yields the instability frequencies, our high-fidelity two-phase approach may seem ill-suited.
But efforts on two-phase simulations must be maintained for two-reasons: first the present Euler-Euler computations are a first step towards comprehensive simulations which aim at shedding light on the detailed structure and on many physical aspects of the flow; second ODP cases such as ITHAC, which features a

coupling with aluminum combustion (see § 1.3.2.5), are not fully assessed and the study of the detailed mechanisms resorts to high-fidelity simulations.
As for this latter aspect, the implementation of a model and numerical strategy to capture aluminum combustion with the TSM approach in CEDRE is on the way (Sibra 2014).

15.4 Numerical simulation of instabilities in the P230 SRM

In this section, we give numerical results from the CEDRE code on a 2D configuration which reproduces the P230 SRM that propels Ariane 5 (see § 1.1.3.1 for a general description of this motor).
This full scale simulation intrinsically features a wide range of time scales. In addition, the modeled disperse phase features small and big droplets with a diameter ratio of 100, so that the case is very stiff. This case is a very good test case to assess the feasibility of ACS, which is enabled. Moreover it happens that it is not possible, with the available ressources, to complete Eulerian computations without ACS. We also perform stochastic-Lagrangian computations of this P230 case, but they are very coarse as regards the parcel discretization.

15.4.1 P230 configuration

The P230 features obstacle vortex shedding (VSO) due to the thermal protection and parietal vortex shedding (VSP), both described in § 1.3.2.4.
The chamber can host acoustic modes and flows through a supersonic nozzle. The propellant is aluminized so the flow contains liquid droplets of aluminum oxide from a zone that is close to the wall down to the nozzle output. The droplet size distribution is modeled as bimodal after combustion (see § 1.2.3.2). We choose to model the spray injection with non-burning aluminum oxide droplets of size d_1 and d_2.

15.4.1.1 A 2D approach

We consider a 2D axisymmetric mesh of the P230 at a specific moment of the grain combustion which is shown in Figure 15.16. It is an unstructured $45,500$ generic cell mesh and the computation is paralellized on 32 domains. We use a coarse mesh, compared to typical SRM meshes with several million points, only to assess the feasibility of complex simulations with an Euler-Euler approach.
For this, we now consider either the possibility of coalescence or not. The simulation starts from a steady state of the single phase gaseous flow field. When the particles are injected, the pressure builds up to a new value of average pressure. The simulated time is long enough to perform a harmonic study of the instabilities. Gas and particles are injected at a fixed surface flow rate from the two walls representing the two propellant segments.

15.4.1.2 Particle injection

The injected liquid flow rate is fairly the same for the two segments. The loading is high since the liquid mass fraction reaches 30% at the injection and can reach much more in the accumulation zones so a two-way coupling approach is required. The small droplets (diameter d_1) represent 90% of the injected mass and the big droplets (diameter d_2) the remaining 10%. The overall number concentration is around $10^{12}\,\mathrm{m}^{-3}$ at the wall and strong velocity differences occur in the flow so coalescence is to be considered. Because of the high density of alumina, the liquid volume fraction is much smaller than one so the liquid volume occupation effect can be neglected, the spray is moderately dense and System (4.70) is relevant.

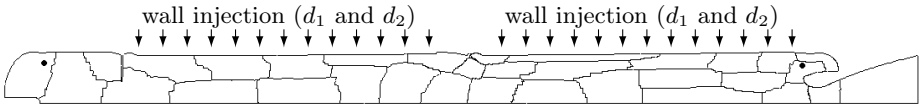

Figure 15.16: *2D axisymmetric geometry and domains of the P230 SRM (· sensor location).*

15.4.1.3 Peculiarities of the case

The case is numerically costly because of the stiffness yielded by the various space and time scales. The motor is indeed more than 25 m long while the smallest hydrodynamic scales are of a few centimeters. Its main instability mode is low frequency around 20 Hz while the small particle response time is close to the microsecond. The injection and nozzle output velocities, respectively a few m/s and Mach 3, introduce time scales with a ratio of about $3,000$. The case is also costly because of the polydisperse coalescing liquid

Smallest droplet Stokes time $\tau^{\boldsymbol{u}}(r_1)$	$1\,\mu s$
Computation time step	$2\,\mu s$
Acoustic CFL time	$10\,\mu s$
Convective CFL time (nozzle)	$30\,\mu s$
Big droplet Stokes time $\tau^{\boldsymbol{u}}(r_2)$	$10,000\,\mu s$
First acoustic mode	$50,000\,\mu s$
Eddy revolution time	$50,000\,\mu s$
Convective CFL time (injection)	$90,000\,\mu s$
Typical computation time	$1,000,000\,\mu s$

Table 15.5: *Typical timescales in a P230 SRM.*

phase. First, it features a strongly bimodal disperse phase: because droplet characteristic times depend on the square of their diameters, this introduces two very different time scales, with a ratio of 10^4. Second, the flow is injected at a very low velocity, encounters hydrodynamic and acoustic instabilities and finally crosses a supersonic nozzle with a high load ratio. We recapitulate all the transport characteristic times in Table 15.5. Since coalescence is a quadratic operator that is intrinsically costly, treating the transport stiffness by solving the smallest scales is definitely out of reach while reducing the cost with an implicit integration for instance would deteriorate accuracy on the unsteady phenomena.
Thanks to the ACS splitting approach, the main time step can be chosen above the small particle response time: this allows to spare an order of magnitude on computational cost without compromising accuracy on the physics of small droplets while most classical coupling methods require a time step below the smallest particle scale for stability reasons, as discussed in § 10.3. The splitting strategy moreover decouples the coalescence intrinsic stiffness from the other time scales, allowing to treat it by a separate integration method if needed.

15.4.1.4 Settings for Eulerian and stochastic-Lagrangian approaches

We now detail the numerical configuration for the size variable in each framework. In the Eulerian Two Size Moment method, the section discretization conditions the simulation's accuracy. For the non-coalescing case two sections are required to solve perfectly the bimodal distribution, no matter what bounds they have, thanks to the Two Size Moment method which can accurately approach the dynamics of any Dirac size distribution. And the two kinds of droplets will not change size during their transport. For the coalescing simulation, the monokinetic hypotheses prevents coalescence from occurring among droplets of the same section. This is relevant if the flow structure prevents PTC for droplets with fairly the same sizes. But the coalescence phenomenon does happen between different sections, which particles have different dynamics. Since the injected droplets are strongly bimodal and the flow yields particle acceleration, coalescence will occur between the two sections. The phase space is then discretized as follows. The first section is defined like in the non-coalescing case since no growth can occur. The second section now ranges from d_2 to $d_3 = 1.3d_2$ to account for the big droplet size increase. A third section is also created to host even bigger droplets that can be created above d_3. Again a coarse discretization of 3 sections is considered to be sufficient to capture the size/dynamics coupling with the TSM.
In the stochastic-Lagrangian computations, the parametrization is the same as in Estivalezes (2010). Numerical particles of the two initial sizes are injected at each wall cell with a period of 4.10^{-4} s. The number of particles per computational domain is however limited to $300,000$. Since we use 32 domains, this allows an average of 200 particles per cell which is said to be enough for the coalescence algorithm to converge (Estivalezes 2010).

15.4.2 Flow topology

15.4.2.1 Gaseous flow

Unsteadiness is visible on the gaseous vorticity field of the non-coalescing case, see Figure 15.17, where one retrieves a strong VSO and VSP along the wall, here tuned on the 1L chamber mode. Both hydrodynamic instabilities are strongly coupled to the disperse phase. The structure is the same with coalescence.

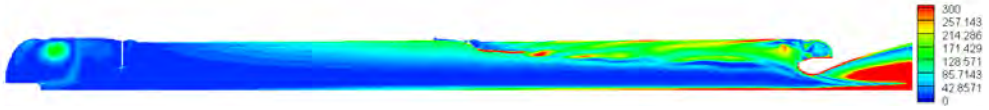

Figure 15.17: *Vorticity (rad/s) in the P230 at $t = 1.46\,s$ without coalescence.*

15.4.2.2 Non-coalescing polydisperse phase

In the non-coalescing case we give Eulerian volume fractions in Figure 15.18 and stochastic-Lagrangian particle repartition in Figure 15.19. The big droplets are segregated out of the vortices, while the small droplets fill most of the chamber. For the same reasons, small and big droplets flow differently throughout the nozzle. This dependence on size motivates a polydisperse approach.

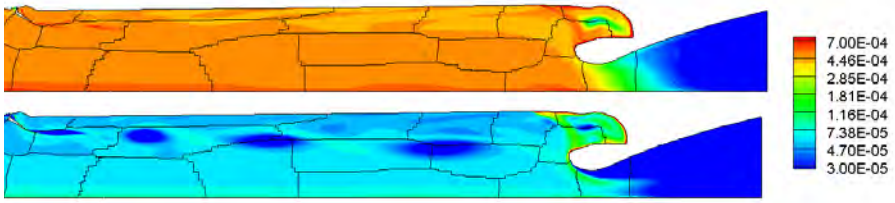

Figure 15.18: *Volume fraction per section (Top: d_1; Bottom: d_2) at $t = 1.09\,s$ without coalescence.*

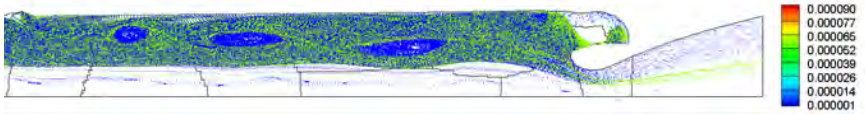

Figure 15.19: *Lagrangian parcel repartition colored by diameter (m) at $t = 1.09\,s$ without coalescence.*

15.4.2.3 Coalescence of the disperse phase

In the coalescing case and for the Eulerian simulation, the instantaneous volume fractions per section are in Figure 15.20. This time, mass is transferred towards the third section, the big droplet mass being completely hosted in this section at the nozzle entrance. This behavior is not immediately visible on the particle repartition of the stochastic-Lagrangian coalescing case, which is presented in Figure 15.21, but bigger particles, resulting from coalescence are indeed present in and after the nozzle, as shown by their coloration.

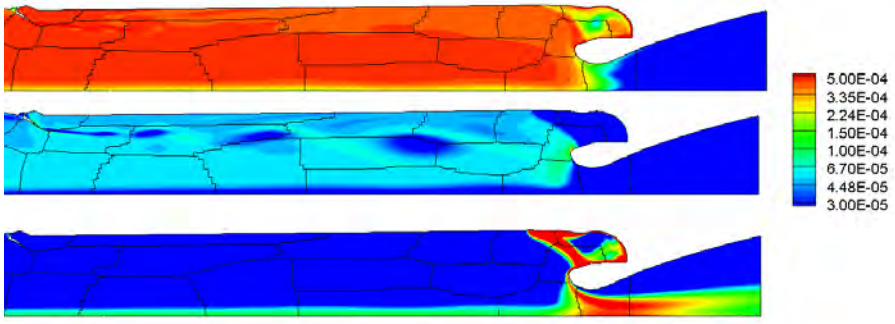

Figure 15.20: *Volume fraction per section (Top: d_1; Middle: d_2 to d_3; Bottom: above d_3) at $t = 0.81\,s$ with coalescence.*

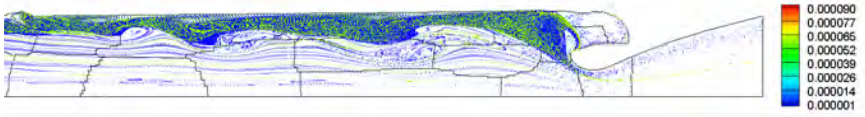

Figure 15.21: *Lagrangian parcel repartition colored by diameter (m) at $t = 0.81\,s$ with coalescence.*

We now consider the evolution of a size moment for the entire droplet distribution. The Eulerian third section d_{30} and the stochastic-Lagrangian overall d_{10} are presented as an illustration in Figure 15.22. In both cases, the most intense coalescence zones are the edges of the vortices, the impact zone of the nozzle wall and the nozzle itself. Moreover coalescence can become so intense that droplet average sizes strongly vary through the domain. The droplet growth can however not be precisely compared since we have different average diameters on different size intervals. Finally Euler-Euler and Euler-Lagrange simulations give comparable

droplet repartition and size. However quantitative comparison is made difficult by the radically different structure of output data.

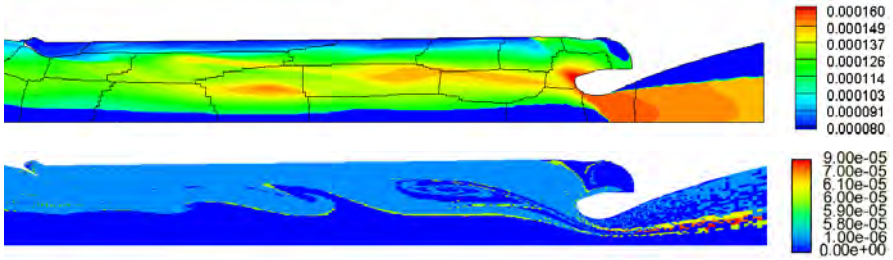

Figure 15.22: *Droplet sizes with coalescence at $t = 0.46\,s$ - Top: Third section d_{30} diameter (m) for the Eulerian simulation; Bottom: Overall d_{10} diameter (m) for the stochastic-Lagrangian simulation.*

15.4.3 Harmonic study

15.4.3.1 Transient regime

The pressure oscillation depends strongly on the flow so we can use it to quantify the effect of coalescence and the differences between the two approaches. The time evolution of the front and rear pressure signals is now described: given in Figure 15.23 for the non-coalescing and coalescing cases. When the particle injection starts, the gaseous flow encounters an additional inertia so the chamber pressure drops whatever the evolution of droplet sizes. But when the droplets reach the nozzle, the flow slows down so that the pressure builds up. It reaches its initial level in the non-coalescing case but stabilizes about 2 bar lower for coalescing particles.

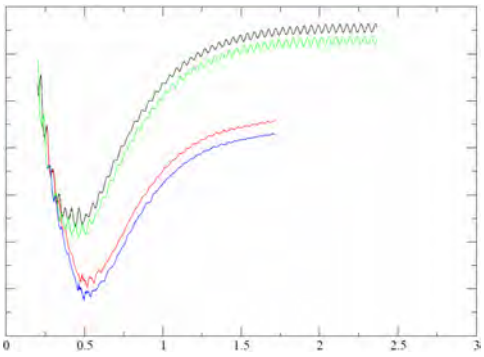

Figure 15.23: *Rear and front pressure evolution with the Eulerian approach - Top: without coalescence; Bottom: with coalescence.*

15.4.3.2 Permanent unstable regime

We now focus on this permanent regime where the average pressure does not vary anymore and only the instability remains. The main values of the pressure signal at permanent regime are given in Table 15.6. Both Eulerian and stochastic-Lagrangian approaches well agree on average pressure in the non-coalescing case and they predict a lower mean pressure at permanent state when coalescence has occurred. This pressure drop can be related to the particle growth. Small particles tend to be in equilibrium with the gas and to increase the chamber pressure while, for the same loading, larger particles tend to stress the deviation from equilibrium and have reduced effects on the pressure. In the asymptotic limit, i.e. for very large particles, the two-phase pressure is similar to the single-phase one. Having said that, a pressure drop of two bars seems to be quite important and may be the sign that coalescence is over-estimated, e.g. due to a 2D simulation. But regarding oscillation levels, they strongly disagree in the non-coalescing case, though they well agree in the coalescing case. The difference is such that the ability to be predictive is still at stake. Further studies are required to understand the differences on instability levels between Eulerian and stochastic-Lagrangian simulations and to complete the cross validation.

Table 15.6: *Dimensionless pressure data (Lagrangian values from ONERA simulations (Estivalezes 2010)).*

		Without coalescence		With coalescence	
		Lagrangian	Eulerian	Lagrangian	Eulerian
Frequency		$1.00 \pm 1\%$	$1.02 \pm 4\%$	$0.99 \pm 2\%$	$1.10 \pm 4\%$
Front sensor pressure	Average	1.00	0.99	0.98	0.95
	RMS	1.0	4.7	1.8	1.6

15.4.4 Conclusion on full scale SRM instability simulation

15.4.4.1 Limits of cross validation

Up to now, Euler-Euler and Euler-Lagrange approaches have yielded comparable results. In the P230 study, the main characteristics are close but significant differences between the Euler-Euler and Euler-Lagrange have been exhibited.
This fact proves a limit of the cross validation strategy: we believe that numerical methods for convergence and coupling are at stake but, provided the cost of the present computations, a convergence study is out of reach.

15.4.4.2 Relevance of Euler-Euler approaches as regards cost

As regards cost and with the levels of resolution chosen above for both methods, the Euler-Euler simulation is much less costly than the Euler-Lagrange one.
In the context of the P230 computations which are parallel, the difference in computational cost is a strong evidence of the relevance of Euler-Euler approaches and especially the TSM Multi-Fluid approach.

15.4.4.3 Assessing the physics of instabilities

The P230 study proves two salient facts about two-phase simulations in SRMs. First, accounting for polydispersity has a major impact on the coupling of hydrodynamic instabilities to acoustics. Its modeling should be carefully done, especially regarding the coupled dynamics of all phenomena involved in a rocket motor.
Second, coalescence plays a front-rank role by modifying size distribution along the flow. For the same reasons as for polydispersity, coalescence requires detailed modeling and simulation. Considering its impact on the overall physics, it is crucial to resolve it accurately.
Finally, the current numerical methods allow to capture details as fine as unsteady coalescence. Both aspects should be considered in SRM simulations and they have been shown to be computable in unsteady complex cases with the Eulerian Multi-Fluid method implemented in CEDRE.

15.5 Conclusion on the feasibility of Eulerian TSM Multi-Fluid SRM simulations

As a global conclusion on these applicative computations, the TSM Multi-Fluid method for polydispersity and coalescence, as developed in Chapter 5 and validated in Chapter 13 is tested on realistic cases through comparisons with experimental measurements as well as with numerical simulations performed with another approach. The feasibility of such an Euler-Euler approach is proven, as well as its relevance as regards computational cost for two-way coupling cases. In the particular case of stiff physics, the new time integration method developed and validated in Chapter 12 is even compulsory.
The previous studies prove that the method is mature and ready to yield satisfactory applicative results on two-phase losses and on instabilities. These results can be improved towards more predictability provided more models and methods:

- Two-phase losses can be assessed more accurately with a model accounting for small scale crossings of inertial droplets: the AG model developed in Chapter 6 and validated in Chapter 11 as regards transport and in Chapter 13 as regards coalescence is promising.
- ODP can be assessed with the additional effect of aluminum combustion: a model and numerical method for strongly coupled reactive disperse phases is under development for CEDRE (Sibra 2014).

As a conclusion, the overall level of predictability of the CEDRE code on SRM physics has increased thanks to improvements on general robustness, two-way coupling, and coalescence.

Chapter 16

Application to SRMs with nanoparticles

From the model and method improvements for nanoparticle coalescence and two-way coupling in stiff cases, we can assess the general behavior of nanoparticles in a motor and prepare further applicative computations. As a conclusion on the ability of CEDRE to compute SRM cases with nanoparticles, we perform a test case with nanoparticles and coalescence.

16.1 A model test case: TEP with NanoAl

We consider a model motor and we assess the behavior of nano-particles in this context.

16.1.1 Description of the case

16.1.1.1 A model SRM

We consider the TEP geometry which is that of a small test bed motor and we assess the case of nanoparticle combustion residuals, assumed to be nanometric droplets of aluminum oxide. The configuration is close to that of the TEPTEU case (see § 15.2) but it features a unique injection zone as shown in Figure 16.1: a parietal injection corresponding to the flow coming from the wall that carries small alumina droplets, typical of immediately burnt solid propellant. The mass flow rate injected from the side wall is $10\,\mathrm{kg.s^{-1}.m^{-2}}$, while the head end is a solid wall.

16.1.1.2 Disperse phase conditions

A monomodal $r_1 = 150\,\mathrm{nm}$ radius wall injection represents the droplets resulting from recently burnt aluminum particles, directly expelled from the propellant grain. For the purpose of our simulation, the injected mass (and volume) fractions approximate correctly typical propellant formulation conditions (provided the total flow rate): the mass fraction of condensed residuals in typical SRM chamber conditions is around $Y_l \approx 35\,\%$, achieving an average volume fraction $\alpha_l \approx 7.10^{-5}$ near the wall. This preserves also the dilute spray hypothesis.
The injected droplets are assumed to have a velocity of a few m/s at a close distance from the wall, as they are dragged by the burnt gases flowing from the propellant. The matter of knowing the size (and the velocity) of the combustion residuals is a major issue, which requires to model the physics of the propellant surface (see § 1.2.3.2 for a discussion in the case of micrometric particles). This is not questioned here.
To assess the stiffness of such nanometric particles, we compute the Stokes time:

$$\tau^{\boldsymbol{u}} = 10^{-9}\,\mathrm{s} \tag{16.1}$$

which we compare to any typical dynamic time in the chamber $\tau_g \sim 10^{-3}\,\mathrm{s,s}$ close to a few ms:

$$\tau^{\boldsymbol{u}} \ll \tau_g \tag{16.2}$$

so the case is very stiff.

16.1.2 Nanoparticle growth estimate in SRM

The objective of this section is to evaluate coalescence intensity for nanoparticles. This is possible since the origin of coalescence is Brownian motion, which is not influenced by the flow dynamics.
First, it is clear that there is no clustering because $\mathrm{St} \ll 1$, (even when considering a Stokes based on the Kolmogorov turbulent time scale) so that the particle number concentration can be considered as fairly homogeneous at local scale..

We now compute a growth estimation formula for monodisperse droplets coalescing because of Brownian motion. The droplets of interest are injected in section 1 with a monodisperse size $r_1 = 150.10^{-9}\,\mathrm{m}$. The volume fraction of injected particles is $\alpha_l = 7.10^{-5}$ which corresponds to a number concentration in the first section $n_1 = 3.5 \times 10^{15}\,\mathrm{m}^{-3}$.
From the gas temperature $T_g = 3600\,\mathrm{K}$, the Brownian diffusion coefficient can be computed:

$$D(r_1) = \frac{2kT_g}{3\mu_g r_1} = 2 \times 10^{-9}\,\mathrm{m}^2.\mathrm{s}^{-1} \tag{16.3}$$

and the Brownian coefficient is taken from the kernel of Eq. (8.63):

$$\mathfrak{K}^{\mathrm{Df}}_{\mathrm{coal}}(r_1, r_1) = 2D(r_1) \times 2r_1 = 1.4 \times 10^{-15}\,\mathrm{m}^3.\mathrm{s}^{-1}. \tag{16.4}$$

So the characteristic coalescence time is:

$$\tau_1^G = \frac{1}{n_1 \mathfrak{K}^{\mathrm{Df}}_{\mathrm{coal}}(r_1, r_1)} = 206\,\mathrm{ms} \tag{16.5}$$

while the residence time of particles is the same as in the TEPTEU case:

$$\tau^R_{\mathrm{chamber}} = 10\,\mathrm{ms} \tag{16.6}$$

which is estimated by assuming that particles are injected at a velocity $u_0 = 1\,\mathrm{m/s}$. As a result, coalescence intensity is quantified by:

$$\mathrm{Kn}_g = 20 \tag{16.7}$$

and the case is weakly coalescing.

16.1.3 Nanoparticle size stability

From the previous estimation, it is seen that particles of 150 nm are "stable" in the chamber flow conditions i.e. they do not remain in the chamber a sufficient time to increase their sizes.

16.1.3.1 Case of other sizes

Let us deduce the behavior of particles with sizes different from r_1. The Brownian diffusion coefficient weakly depends on particle sizes. But the number of particles increases like $n_l \sim r^{-3}$ since we consider a fixed mass (and volume) fraction at injection.
So that smaller particles will coalesce more intensely until they result in particles of size close to this one, while larger particles are even more stable (for the given $\tau^R_{\mathrm{chamber}}$).
So particles of size r_1 are relatively stable in chamber conditions and provided that they are alone.

16.1.3.2 Case of stagnation zones in the flow

The previous stability of r_1 droplets has been stated for droplets injected at u_0, the data of which is a model propellant condition. But the velocity and therefore the residence time in the vicinity of the propellant is not well known: this resorts to both propellant combustion modeling and chamber wall flow modeling.
In practice, long residence times are expected:

- at the wall (possibly);
- in recirculation zones such as in the aft dome region.

These stagnation zones of the flow are crucial to get a clear picture of the size distribution of nanoparticles, while dynamic zones were important for usual microparticles.

16.2 A demonstration computation

We perform a SRM computation featuring nanometric particles, with the CEDRE code.

16.2.1 Objectives

16.2.1.1 Validation of the models and method

A computation is performed with two objectives: the theory that coalescence depends on residence times must be checked and the ability of the CEDRE code to achieve Brownian coalescence simulations must be assessed.

16.2.1.2 Assumption of intensified coalescence

To check the validity of the code implementations, we need the case to feature a significant coalescence.
The coalescence kernel $\mathfrak{K}_{\text{coal}}$ that is used is the one derived in Chapter 9 and corresponds to a hybridized diffusive Brownian kernel $\mathfrak{K}^{\text{Df}}_{\text{coal}}$ and ballistic kernel $\mathfrak{K}^{\text{B}}_{\text{coal}}$.
With such kernel and provided the TEP chamber residence times, the case happens to produce a non-significant size increase, as estimated previously.
To study coalescence, we therefore make an unphysical assumption to increase it: we do not want to change the size or the concentration of particles so the Brownian kernel is modified. We assume:
[B1] $\mathfrak{K}_{\text{coal}} = 10^3 \times \mathfrak{K}^{\text{Df}}_{\text{coal}}$
in order to significantly increase coalescence intensity.

16.2.2 Numerical results

16.2.2.1 Numerical configuration

The simulation takes place on a deformed-structured 1500 cell mesh, see Figure 16.1 and the time integration is performed with the ACS strategy to allow reasonable time steps. When seeking a two-phase flow solution, one usually takes a steady state gas flow field as an initial state.

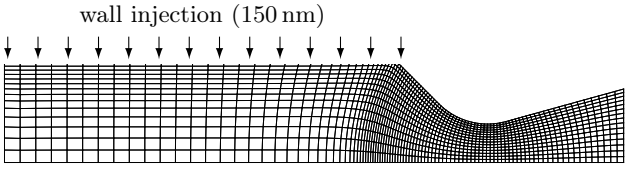

Figure 16.1: *TEP: a deformed-structured* 1500 *cell mesh with side wall injection (arrows).*

The two-phase simulation strictly speaking starts when injecting the disperse phase. For the disperse phase, we choose a 4 section discretization (100, 200, 400, 800 and 1500 nm) and only the first section contains droplets, which size is fixed at $r_1 = 150\,\text{nm}$.
A $10^{-2}\,\text{s}$ time interval is required to allow the first droplets to reach the end of the nozzle. With a $10^{-6}\,\text{s}$ time step, $10,000$ iterations are needed.

16.2.2.2 Results

Results are presented in Figure 16.2 for volume fractions in the different sections. They show that the size increase occurs as soon as the particles are injected from the wall and fairly constantly along their trajectories. The sections 1 to 4 are successively filled with particles as the disperse phase advects in the chamber. When arriving close to the axis, particles have reached a size of a micron, which size they keep down to the nozzle input. They no longer coalesce in the nozzle for three reasons:

- their number concentration decreases due to the acceleration (dilution effect);
- they do not encounter significant Brownian coalescence since the nozzle residence time is much smaller;
- they do not encounter significant ballistic coalescence since their inertia is still very small (and velocity differences are not accounted for within a section by the retained MF model so homo-DTC is not observed).

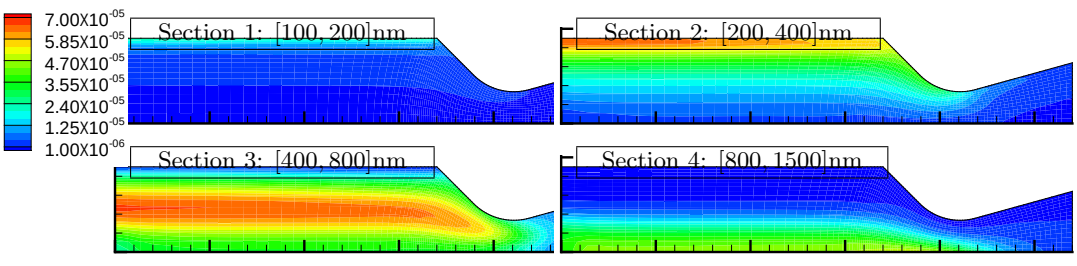

Figure 16.2: *Dispersed phase volume fractions per section* $\mathfrak{K}_{coal} = 10^3 \times \mathfrak{K}^{Df}_{coal}$.

Having a size increase that is regular along the trajectories is a characteristic behavior which is related to the Brownian agglomeration: agglomeration is independent from the flow dynamics and the macroscopic velocities. In most of the chamber, size therefore depends only on the distance from the wall, which translates the residence times of the particles. The dependence on wall distance would no longer be true in long motors since the flow becomes then non-parallel. But the patterns of size increase under Brownian coalescence, as linked to the streamlines, are characteristic of this type of coalescence and are very different from those of ballistic coalescence, where the collision rates depend on the flow dynamics e.g. strain and vortical zones.

16.2.2.3 A satisfactory behavior

The TEP computation has confirmed the ability of the CEDRE code to deal with nanometric droplets and their coalescence. Stiffness is overcome thanks to ACS and coalescence is computed with adapted kernels, while the source term computation method allows a flexible use of kernel models.
The behavior of nanometric droplets is confirmed to be linked to their residence times.

16.3 Modeling needs for nAl motor simulation

From the previous computation, some conclusions are drawn on further studies and modeling needs.

16.3.1 Role of residence time

The role of residence time has been presented as crucial: it can be stated that Brownian coalescence intensity is driven by the residence time. And two zones are identified as featuring a large residence time: the propellant wall and the recirculation zones, namely the cavities.
The velocity boundary condition strongly conditions the residence time and therefore the coalescence intensity of Brownian particles i.e. their Kn_g.

16.3.2 Need to assess physics of the stagnation zones

Coalescence is presumably more intense in stagnation zones.

16.3.2.1 Propellant condition

The boundary condition modeling is crucial, together with a compliant "injection" model, derived from the knowledge of the propellant combustion.

16.3.2.2 Recirculations

Coalescence must also be assessed in the recirculations such as that of the aft dome region.
An significant increase in size of particles entrapped in these zones may result in an faster deposition as a film or, in the case of an ejection of these bigger particles, these zones can be sources of large particles, reemitted in the flow. This may influence the coalescence of the smaller sizes and the dynamics within the nozzle.

16.3.3 Effect of nano-micro coalescence

In the presence of inertial (micronic) droplets, the overall coalescence dynamics is modified. Inertial (micro metric) droplets may result either from the intense coalescence of smaller droplets or from big droplet production at the propellant surface. Indeed the propellant can either feature μAl particles (in the case of mixed nano-micro formulations) or foster surface agglomeration of nAl.
For these cases, the hybrid kernel developed in Chapter 9 is ready to tackle nano-micro mixtures of droplets and their coalescence. Many simulation strategies can be contemplated to assess the dynamics of nano-micro mixtures in SRMs:

1. a polydisperse injection condition (e.g. bimodal);
2. a motor with a modeled head-end flow with micro metric particles (such as the TEPTEU);
3. a motor with a cavity can be used (such as the LP10 or the P230).

The choice of a strategy must be done accordingly to the intuition that a mechanism dominates among the following hypothetic mechanisms:

1. agglomeration at the propellant surface;
2. coalescence during the stagnation at low injection velocity;
3. coalescence within the cavities.

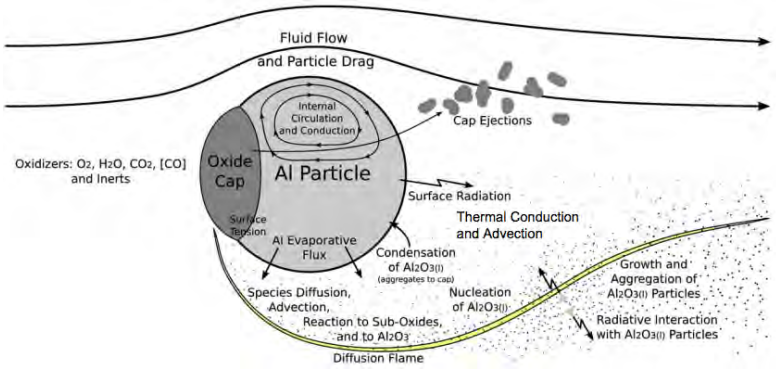

Figure 16.3: *Mechanism of aluminum particle combustion (Washburn et al. 2010).*

16.3.4 Future experimental data

A TEP-like geometry is to be used in the context of an experiment on a nanopropellant: a Bates motor firing is scheduled with research nAl propellants.
Such experiments can bring valuable information on the particle sizes in the chamber, through two aspects:

- a direct measurement of the residual sizes at the output is possible since the chamber particles are presumably very small and weakly altered by their trip through the nozzle;
- the specific impulse losses can be measured through the motor's thrust with a thrust stands and compared to μAl propellant thrust, and to simulation results.

Both approaches allow an indirect analysis of the particle evolution in the chamber but they are detailed enough to assess the relevance of a joint modeling of the effects of propellant combustion and coalescence on the particles sizes.

16.4 Conclusions

The CEDRE code is ready to perform studies on nanoparticle residuals in SRM thanks to the improvements in coalescence (TSM allows an accurate treatment of size increase) and on time integration (ACS allows to compute efficiently fast particles and to overcome stiffness).

16.4.1 Conclusion on nAL SRM simulations

For full motor simulations, the boundary condition as a model of the propellant combustion effect on the particles should be refined.
Provided this, the studies on nanoparticle flows in SRMs can be furthered for motors with mixed nano-micro droplets and for motors with recirculations. Together with experimental results, these studies address the impact of the size reduction of metal fuel particles in SRMs

16.4.2 Other simulation prospects

The study of aluminum combustion is an active research topic, provided the complex physics as discussed in § 1.2.3.4 and illustrated in Figure 16.3.
Among the phenomena that drive aluminum combustion, the retrodiffusion of aluminum oxide is influent: its treatment as nanoparticles (or smokes) can be interesting to determine accurately its role in the combustion process.
At the droplet scale and provided the strong temperature gradients of the flame front, the role of thermophoresis is presumably strong so that the nanoparticle transport model must be improved to account for this coupled effect.

Conclusion

The studies conducted in this work are motivated by the issue of assessing the physics of a SRM with a high fidelity. Capturing two-phase losses is a major goal and accounting for the unsteady regime produced by hydrodynamic instabilities is a highly demanding goal we aim at as a benchmark. The common issues of these cases are imposed by the disperse phase of aluminum oxide droplets, that result from the propellant combustion and travel in the chamber and the nozzle:

- the disperse phase has a high mass loading and is two-way coupled to the carrier phase of burnt gases,
- the disperse phase has a wide range of size droplets with associated complex physics,
- its droplets encounter a size evolution through coalescence.

A discussion on the available models for two-phase flows was conducted to identify the relevant modeling approach and the Eulerian Multi-Fluid approach was chosen for its ability to account efficiently for polydispersity, coalescence, and two-way coupling. A particular method referred to as Two Size Moment Multi-Fluid (TSM) was selected and improved as regards the modeling and numerics: a new reconstruction was discussed and the modeling and dedicated numerical strategies were introduced for coalescence terms in this context. The TSM was then implemented in an in-house research code and in the CEDRE code: its accuracy and convergence were assessed and applicative computations were finally performed. The new method is validated thanks to an analytical model purposely derived and the approach is verified thanks to experimental results. The ability to capture efficiently coalescence in contexts with such a complex dynamics is a breakthrough which is promising for other domains. Besides, source terms for the presumed PDF modeling of break-up have also been studied in the context of the TSM to include the modeling and method improvements discussed for coalescence sources. An industrial strategy to capture break-up has emerged, in the prospect of assessing the physics of particles in a SRM nozzle and in other industrial configurations such as for icing.

A time strategy has been developed and validated to achieve an efficient treatment of the stiff and multi-scale two-phase flow in the context of unsteady two-way coupling. This accurate, robust and flexible time integration strategy is remarkably easy to handle, and allows to mix explicit, implicit and adapted time steps for the integration of the different operators. The method is especially useful for small droplets as it accounts efficiently for stiff relaxation times without strong numerical constraints on time steps. It was therefore used for SRM computations and allowed to account for the first time in a detailed way for the smallest droplets present in the domain, possibly nanometric ones. The method is moreover efficient for the coupling of multiple and complex physics in unsteady cases so the approach is particularly promising, e.g. for multi-physics platforms such as CEDRE.

The approach of homo-PTC has been considered in a way that yields a sufficient level of detail for SRMs without compromising cost, flexibility and robustness. With a high order velocity model, previously introduced for moderately inertial disperse phase flows referred to as the Anisotropic Gaussian velocity closure (AG), we have indeed shown that polykineticity is sufficiently well described to capture: (i) the characteristic width of the centerline droplet cloud in the nozzle, allowing to assess correctly the two-way coupling effect; (ii) the intensity of local relative velocities, allowing to compute coalescence. A transport resolution numerical strategy has been proposed for structured meshes and validated so that the method is applicable for research codes. Coalescence was included in the model and the behavior of the model for the case of two coalescing jets is assessed and validated versus a point-particle DNS: this case is a simplified vision of the coalescence issue raised in a SRM nozzle so this work completes the toolbox of models for polydispersity and coalescence, in the case of homo-PTC and AG is presented as a good candidate to estimate more accurately two-phase losses in SRMs.

In another aspect of the present contribution, the peculiarities of nanometric droplets have been thoroughly considered and their physics has been stated: peculiarities on transport and coalescence have been identified. The former effect is classically accounted for in the Brownian theory. A comprehensive modeling has been developed to account for coalescence in nano-micro droplet mixtures based on the MF formalism: a hybrid Multi-Fluid approach has been developed, where the ensemble of the droplets are coupled through coalescence and through their effect on the carrier gas. The hybrid model has been implemented and tested in CEDRE, allowing to draw the first conclusions and prospects on nano-propellant SRMs. In addition, a prospective

study was carried out on a two-way coupling model for nanoparticles in free molecular regime: the similarity of the statistical equation for particles and gas molecules has attracted modeling efforts onto the derivation of a strongly coupled two-phase nanoparticle description, which sheds light on the detailed physics such as out-of-equilibrium particle transport. Such detailed models are believed to be useful to assess the local physics of nanoparticle flows in a SRM. The study has yielded fundamental results that support the models that are used.

All these model and method improvements have allowed to perform SRM computations which shed light on several issues, namely two-phase losses and hydrodynamic instability. The effect of polydispersity on the physics of a SRM is assessed in the case of a LP10 sub-scale motor, including the effect of coalescence. Thanks to the improvements in models and methods for either polydispersity, coalescence and two-way coupling, SRM computations have been performed that prove the improvement in the high-fidelity two-phase simulation capability. These results have allowed to assess the crucial role of polydispersity and coalescence on instability levels in a complex case of inert particle-driven instability. Thanks to the methods allowing robust small droplet computations and to the new modeling for nano-micro droplet mixtures, we obtain results on motors with nanometric combustion residuals as regards size distribution evolution and two-phase loss assessment. Finally, the level of validation of CEDRE has increased, thanks to the use of a large experimental database on ODP, that has been compared to the LP10 computations. Comparisons between different numerical approaches for two-phase flows were also performed e.g. Eulerian versus stochastic-Lagrangian simulations. In addition to these computations, we have defined physical benchmark cases to assess the improved physical features that are identified: (i) two-phase acoustics, with Temkin and Dobbins (1966)'s formula and related improvements, (ii) bimodal coalescence, with D'Herbigny and Villedieu (2001)'s experiment and analytical formulae, (iii) small scale crossing transport, with analytical validations, and (iv) small scale crossing coalescence, with a DPS validation. The analytical developments that have been done allow to thoroughly validate the models and methods. So the CEDRE code and its ability to treat coalescence and two-way coupling have been verified versus analytical solutions and experimental results, resulting in a high level of confidence of the actual implementations. With the ability to treat efficiently moderately dense nano-to-inertial coalescing sprays, the CEDRE code is ready to perform a new high standard type of simulations.

Interesting prospective results were also obtained on the atomization of a moderately dense flow. Taking benefit from the acquired skills on moment methods for disperse phase with two-way coupling and with break-up, a prospective study on the fundamental and reduced treatment of primary and secondary atomization in turbulence has allowed to explore the limits of the presumed PDF approach for break-up, of the sphericity assumption and the additional modeling efforts that are required by the source terms of moderately dense two-phase flows. It is an interesting prospection on the possibilities of Eulerian modeling and shows the potential of the proposed approach to other areas of research.

In addition to its achievements, this work calls for some short term prospects:

1. The present work has proven the feasibility of applicative computations but the full studies have not been performed: the evaluation of slag accumulation and two-phase I_{sp} losses are now possible with an increased accuracy and robustness, and should be assessed on complete (e.g. 3D) geometries. In the case of two-phase I_{sp} losses, the simulation ability is not available for moderate inertia particles, i.e. which cross in the nozzle, but the case of low inertia particles, as well as nanometric ones, is accessible straightforward. In the latter case, studies are expected shortly to bring some firm conclusions on the effect of nAl in SRM flows, and to guide further research.
2. The AG has been qualified to treat polykineticity, homo-DTC and coalescence, and studies must now be conducted to evaluate the two-way coupling, for which the theoretical background is settled, and to possibly evaluate it in realistic cases such as a supersonic nozzle. This requires to improve the SAP2 code from the developments made for SAP1 (straightforward use of the ACS and the phase space integrator, extension of the compressible gas solver to 2D) and moreover to perform for instance stochastic-Lagrangian comparisons. The goal is to implement the approach in an industrial code to treat the moderately inertial size range, but this requires a careful work on numerical methods for unstructured meshes and for the connection with pressure less zones.
3. The modeling and method developments for secondary break-up are promising to increase the accuracy on both two-phase losses (since break-up occurs in the nozzle) and on slag release interaction with ODP (since the film is atomized in the nozzle). The model that is implemented in CEDRE must be qualified for these phenomena (and coupled to the film solver in the second case).
4. The features of reactive aluminum particles are under study (e.g. to address ITHAC) but the polydisperse case is not yet accessible to industrial simulations: modeling and method developments are under way, that are based on the time-integration improvements for coupling (Sibra 2014). In this context, the implementation of a Aff-TSM method -more robust, accurate and cost-effective than the actual Exp-TSM- and the development and implementation of an advanced time-integrator for the

phase space dynamics in CEDRE are expected to allow an efficient capture of aluminum combustion but also to be beneficial for the other features of the code.

In the medium term, the level of reliability of the models and methods must be increased in the considered regimes.

1. First the input data for full motor simulations must be re-assessed: we have presented the importance for two-phase simulations of size distribution of particles dragged into the chamber, but also the importance of the knowledge of their velocities and their residence time in the propellant vicinity. In addition, the boundary condition plays a crucial role as regards the level of noise and turbulence that is initiated. All these informations can be obtained by studies at a close-up level: packing studies, wall flow and propellant combustion models are to bring in a comprehensive approach for accurate and reliable boundary conditions of full motor simulations.
2. Second, the models for nanometric droplets must be improved e.g. to assess the combustion of an isolated droplet: accounting for thermophoresis, melting temperature *etc.* should be done by *ab initio* modeling. This will allow to assess more accurately the effect of nano droplets of aluminum and oxide on the overall aluminum combustion.
3. Third, the improvements on numerical methods to capture the propellant regression should be included to gain information on the slower dynamics of SRMs: this slow evolution potentially plays a role on the faster physics through hysteresis phenomena.
4. Fourth the role of radiation is crucial at ignition but it can also be important during motor operation: models to assess radiation and its coupling to the flow and the disperse phase are available but studies are just starting with industrial codes, and methods, especially for the complex and strong coupling, are to be improved.

Finally, the validation of the overall approach is incontrovertible in the long term.

1. The validation of the close-up physics models previously discussed must be performed with elementary experiments e.g. at small scale.
2. The validation of the strategy to assess two-phase I_{sp} losses can be performed on small scale SRM such as the Bates-type motor, using a thrust stands: an experiment is scheduled on such a geometry with a propellant including nanometric aluminum particles. Together with the numerical improvements on nanometric inclusions in SRM flows, these experimental results are a major step to address the pros and cons of a size reduction of the residuals in SRMs.
3. As regards the detailed modeling of inclusion size distributions in the motor, gaining access to such information through experiments is still very difficult. Several experimental techniques have been used to gather intact particles such as the rotative trap (which operates in cold gas and is not representative), and the quenching of particles with a cold Helium gas flow to preserve them during their trip through the nozzle (but with a difficulty to assess the success of this preservation technique). In the direction of particle gathering, it is mandatory to operate at realistic chamber pressures so the nozzle cannot be removed, but its destructive effects on particles can be tempered, e.g. by the use of an adapted contour nozzle to reduce lags. In the direction of performing a direct optical access a fine tuning of the diagnostics is to be done to cope with the peculiarities of propellant ambience.

As a conclusion, the models and methods open a path to improve SRM modeling and simulations. Moreover the improvements performed in the CEDRE code and the upcoming works can be straightforward beneficial to other mechanical engineering activities at ONERA:

(i) In the case of air-breathing propulsion, the upcoming improvements in two-phase combustion as well as the treatment of chemical reactions through an adapted time integration method, e.g. splitting the resolution of the species space from that of physical transport, and time-integrating it with dedicated, advanced methods that are stable and robust, will allow the computation of combustion chamber flows with improved accuracy and robustness.

(ii) In the case of liquid rocket engines, the current development of a separate-phase flow solver for primary atomization, added to the ability to treat accurately and robustly a moderately dense disperse phase encountering two-way coupling, secondary break-up and combustion in unsteady regimes are mostly needed. For the latter point, the developments of the present thesis have brought a substantial advance and interesting prospects.

Appendix A

Modeling of a single fluid

The continuum mechanics approach for a single phase fluid is now presented in a Eulerian point of view, since it is a baseline model for most of the two-phase approaches. The so-called Navier-Stokes equations for a multi-species (or multicomponent) reactive flow are indeed the basis for either one-fluid modeling and for the gas description within two-fluid and fluid-kinetic modelings.

A.1 Derivation of fluid equations

The Navier-Stokes equations are Eulerian equations on macroscopic quantities of the fluid, which can be obtained through mass, momentum and energy balances on a control volume Truesdell (1966). This derivation can be found for example, for a general mono-species non-reactive case in Candel (1990), and in Poinsot and Veynante (2011) for reactive multi-species flows. Another way, more mathematical, to obtain these equations is presented in § 3.4.2.2.
The Navier-Stokes equations are a mixed hyperbolic-parabolic system, which mathematical structure is studied for instance in Giovangigli and Massot (1998). We highlight that the latter model applies to combustion which features stiff, non-linear chemistry and a strong coupling to the flow dynamics through stiff heat releases leading to strongly coupled dilatation.

A.2 Multicomponent Navier-Stokes equations

The conservative form of the Navier-Stokes system describes mass, species, momentum and energy conservation. Since $\alpha_c \ll 1$, the gas occupies most of the control volume so the equations are similar to those of a single-phase flow: the representation of the two-phase flow is mesoscopic i.e. the flow scales around the particle (wake *etc.*) are not directly resolved. The effects of particles on the flow are accounted for through source terms based on correlations that should include the physics of the flow in the particle vicinity, assuming that it has similar effects at the macro scale when considering particles in the same state.
The conservation of mass is given by:

$$\partial_t \rho_g + \partial_{\boldsymbol{x}} \cdot (\rho_g \boldsymbol{u}_g) = 0 \tag{A.1}$$

where ρ_g is the gas density, $\boldsymbol{u}_g$ the velocity. Regarding species conservation, we consider n_s species and we have, for species k:

$$\partial_t (\rho_g Y_k) + \partial_{\boldsymbol{x}} \cdot (\rho_g \boldsymbol{u}_g Y_k) = -\partial_{\boldsymbol{x}} \cdot \left(\rho_g Y_k \boldsymbol{u}_k^{\text{diff}}\right) + M_k \dot{\omega}_k, \quad k \in [\![1, n_s]\!] \tag{A.2}$$

where Y_k and $\boldsymbol{u}_k^{\text{diff}}$ are the mass fraction and the diffusion velocity. The term $M_k \dot{\omega}_k$ is the creation rate of species k due to chemical reaction. In a SRM, the chemical reactions among species can be modeled in the context of detailed chemistry such as the one of Ammonium Perchlorate combustion e.g. (Ermolin et al. 1982) or (Rahman 2012) with up to 37 species in 215 reactions.
Mass and momentum conservation principles are expressed as:

$$\sum_{k=1}^{n_s} Y_k = 1 \qquad \text{and} \qquad \sum_{k=1}^{n_s} \rho_g Y_k \boldsymbol{u}_k^{\text{diff}} = 0 \tag{A.3}$$

where $\boldsymbol{u}_k^{\text{diff}}$ is the species diffusion velocity, modeled in § A.4.
The momentum conservation equation reads:

$$\partial_t \left(\rho_g \boldsymbol{u}_g\right) + \partial_{\boldsymbol{x}} \cdot (\rho_g \boldsymbol{u}_g \otimes \boldsymbol{u}_g) = \partial_{\boldsymbol{x}} \cdot \boldsymbol{T} + \rho \boldsymbol{a} \tag{A.4}$$

with the stress tensor $\boldsymbol{T} = -p_g \boldsymbol{I} + \boldsymbol{\tau}$ where p_g is the gas pressure and $\boldsymbol{\tau}$ is the viscous stress tensor. The body force term $\rho \boldsymbol{a}$ depends on $\boldsymbol{a}$ that is the acceleration (due to gravity, non galilean effects *etc.*).
We consider, for the Navier-Stokes system of equations, Newtonian fluids, i.e with a linear isotropic behavior. In the case where volume viscosity is neglected, the stress tensor can be written (Candel 1990):

$$\boldsymbol{\tau} = \mu_g \left(\partial_{\boldsymbol{x}} \boldsymbol{u}_g + \partial_{\boldsymbol{x}} \boldsymbol{u}_g^T \right) - 2\mu_g \partial_{\boldsymbol{x}} \cdot \boldsymbol{u}_g. \tag{A.5}$$

where μ_g is the fluid dynamic viscosity, which is modeled in § A.4. The kinematic viscosity $\nu_g = \mu_g / \rho_g$ is sometimes used as it is homogeneous to a diffusion coefficient.
The conservation equation for energy reads:

$$\partial_t \left(\rho_g e_g \right) + \partial_{\boldsymbol{x}} \cdot \left(\rho_g \boldsymbol{u}_g e_g \right) = \boldsymbol{T} : \partial_{\boldsymbol{x}} \boldsymbol{u}_g - \partial_{\boldsymbol{x}} \cdot \boldsymbol{q} \tag{A.6}$$

with e_g the internal energy of a unit mass and q the heat flux.
The energy flux is given by:

$$\boldsymbol{q} = -\lambda_g \partial_{\boldsymbol{x}} T_g + \sum_{k=1}^{n_s} \rho_g h_k \boldsymbol{u}_k^{\text{diff}} Y_k \tag{A.7}$$

where λ_g is the heat conduction coefficient, modeled in § A.4. It includes a heat diffusion term, classically modeled by Fourier's law and a term associated with different species enthalpy diffusion.

A.3 Thermodynamics of the fluid

Closure relations for the conservation equations can be found through thermodynamical considerations, in Giovangigli (1999) for instance.
The equation of state (EOS) links ρ_g to the thermodynamic quantities of pressure, temperature and composition. The law for perfect gases is

$$\rho_g = \frac{p_g M}{R T_g} \tag{A.8}$$

where R is the perfect gas constant, and M is the molar mass given by:

$$\frac{1}{M} = \sum_{k=1}^{n_s} \frac{Y_k}{M_k}, \tag{A.9}$$

with M_k the molar mass of species k. The internal energy then reads:

$$\rho_g e_g = \sum_{k=1}^{n_s} \rho_k e_k \tag{A.10}$$

where e_k is the internal energy per unit mass of species k given by integration of the volume heat capacity $c_{v,k}$ of species k:

$$e_k(T_g) = e_k^{\text{st}} + \int_{T^{\text{st}}}^{T_g} c_{v,k}(\theta) \mathrm{d}\theta \tag{A.11}$$

where $e_k^{\text{st}} = e_k(T^{\text{st}})$ is the internal energy of formation of species k at standard temperature T^{st}. As a result,

$$\rho_g c_v = \sum_{k=1}^{n_s} \rho_k c_{v,k} \tag{A.12}$$

links the heat capacities.
Specific enthalpy for species k is the defined by:

$$h_k = e_k + r_k T_g \tag{A.13}$$

where $r_k = R/M_k$. As previously,

$$\rho_g h_g = \sum_{k=1}^{n_s} \rho_k h_k. \tag{A.14}$$

By combining the previous relations to the perfect gas EOS we get:

$$h_g = e_g + \frac{RT}{M} = e_g + \frac{p}{\rho_g}. \tag{A.15}$$

The Mayer relation for species k in a perfect gas reads:

$$c_{p,k} = c_{v,k} + r_k. \tag{A.16}$$

so that h_k can also be expressed by a direct integration:

$$h_k(T_g) = h_k^{\mathrm{st}} + \int_{T^{\mathrm{st}}}^{T_g} c_{p,k}(\theta)\mathrm{d}\theta \tag{A.17}$$

where $h_k^{\mathrm{st}} = e_k^{\mathrm{st}} + r_k T^{\mathrm{st}}$ is the standard enthalpy of formation for species k at T^{st} and p^{st}.
The specific entropy is defined for the mixture as the sum of the species entropies:

$$\rho_g s_g = \sum_{k=1}^{n_s} \rho_k s_k \tag{A.18}$$

where the species specific entropy is integrated

$$s_k = s_k^{\mathrm{st}} + \int_{T^{\mathrm{st}}}^{T_g} \frac{c_{pk}(\theta)}{\theta}\mathrm{d}\theta - \frac{R}{M_k}\ln\left(\frac{p_k}{P^{\mathrm{st}}}\right) \tag{A.19}$$

with $s_k^{\mathrm{st}} = s_k(T^{\mathrm{st}}, P^{\mathrm{st}})$ the standard enthalpy for species k at T^{st}. We consider besides Gibbs' function $\mathscr{G}$ for the mixture:

$$\rho_g \mathscr{G} = \sum_{k=1}^{n_s} \rho_k \mathscr{G}_k, \tag{A.20}$$

when defining the species Gibbs function $\mathscr{G}_k$

$$\mathscr{G}_k = h_k - T s_k \tag{A.21}$$

so that we retrieve the classical expression for the gas mixture:

$$\mathscr{G} = h_g - T s_g. \tag{A.22}$$

The specific entropy and Gibbs' function are used to compute the species production rates and the chemical equilibrium.

A.4 Transport coefficients

The dynamic viscosity μ_g accounts for transport at the molecular scale, due to their agitation. It is a crucial parameter as it conditions the flow behavior but also the dynamic interaction with particles through drag force. It can be modeled as a constant for small temperature variations but empirical laws are required when temperature varies strongly e.g. for combustion or nozzles (Dutoya and Matuszewski 2011). Sutherland (1893) suggested the following correlation for viscosity upon temperature:

$$\mu_g(T_g) = \mu_g^0 \left(\frac{T_g}{{T_g}^0}\right)^{\frac{3}{2}} \frac{{T_g}^0 + T_S}{T_g + T_S} \tag{A.23}$$

with a reference temperature ${T_g}^0 = 273,15\,\mathrm{K}$, $\mu_g^0 = 1,711.10^{-5}\,\mathrm{kg/m/s}$ and the Sutherland temperature $T_S = 110,4\,\mathrm{K}$.
The heat conduction coefficient λ_g accounts for heat transport at the molecular level. The Eucken approximation (Hirschfelder et al. 1954) for a polyatomic gas gives λ_g using the viscosity coefficient, the universal gas constant R and the specific heat at constant volume $c_{v,g}$:

$$\lambda_g = \frac{15}{4} R \mu_g \left(\frac{4}{15}\frac{c_{v,g}}{R} + \frac{3}{5}\right) \tag{A.24}$$

For air in the case of a perfect gas, it reads between 100 K and 1900 K:

$$\lambda_g(T) = \lambda_g^0 \frac{\mu_g(T)}{\mu_g^0}\left[1 + 0,00023({T_g} - {T_g}^0)\right] \tag{A.25}$$

with $\lambda_g^0 = 0,0242\,\mathrm{W/m/K}$ (Dupuy 2012).
As for the species transport, the species diffusion velocity $\boldsymbol{u}_k^{\mathrm{diff}}$ can be obtained with an approximation neglecting the Soret effect, i.e. the diffusion of mass due to temperature gradients (Benkiewicz and Hayashi 2002): one needs to solve a linear system of size n_s^2 (Poinsot and Veynante 2011), in each direction at each point and for each time. This resolution is difficult and costly (Ern and Giovangigli 1994), and practically performed with dedicated approaches such as the EGLIB code (Ern and Giovangigli 1995). But many applicative cases are solved with a simpler model to compute the diffusion velocity such as Fick's law:

$$Y_k \boldsymbol{u}_k^{\mathrm{diff}} = -D_k \partial_{\boldsymbol{x}} Y_k \tag{A.26}$$

where D_k is the diffusion coefficient of species k into the mixture. The species conservation law thus becomes:

$$\partial_t(\rho_g Y_k) + \partial_{\boldsymbol{x}} \cdot (\rho_g \boldsymbol{u}_g Y_k) = \partial_{\boldsymbol{x}} \cdot (\rho_g D_k \partial_{\boldsymbol{x}} Y_k) + M_k \dot{\omega}_k + S_k^m, \quad k \in [\![1, n_s]\!] \tag{A.27}$$

One can notice that the first expression of mass conservation that is Eq. (A.1), together with species conservation given by Eq. (A.2), lead to $n_s + 1$ equations for n_s unknowns. The system is thus over-determined and two methods are considered.
First one can solve the species conservation Eq. (A.2) for $n_s - 1$ species and obtain the last species mass fraction Y_{n_s} using Eq. (A.1). Second one can solve Eq. (A.2) for all the species and Eq. (A.1) must be obtained as a computational result. Nevertheless, as explained in (Poinsot and Veynante 2011), the introduction of Fick's law makes these two approaches not equivalent. Actually, Fick's law does not generally ensure global mass conservation, except if the diffusion coefficients for all the species are equal, $D_k = D$ (Giovangigli 1999).
Therefore, in the first approach where global mass conservation is enforced, the mass fraction of the last species Y_{n_s} absorbs all the inconsistencies introduced by Fick's law in the case of different species diffusion coefficients. In the second approach a correction velocity must be added to the convection velocity $\boldsymbol{u}_g$, so that the global mass is conserved. It leads to the modified species conservation equation:

$$\partial_t(\rho_g Y_k) + \partial_{\boldsymbol{x}} \cdot (\rho_g \boldsymbol{u}_g Y_k) = \partial_{\boldsymbol{x}} \cdot \left(\rho_g D_k \partial_{\boldsymbol{x}} Y_k - \rho_g \boldsymbol{u}_g^{\mathrm{cor}} Y_k\right) + M_k \dot{\omega}_k, \quad k \in [\![1, n_s]\!] \tag{A.28}$$

with

$$\boldsymbol{u}_g^{\mathrm{cor}} = \sum_{k=1}^{n_s} D_k \partial_{\boldsymbol{x}} Y_k \tag{A.29}$$

One can refer to Poinsot and Veynante (2011) for more details. As shown in Ern and Giovangigli (1994), this approach is a first order approximation of the exact resolution of diffusion velocity.
In the framework of Fick's law for the diffusion velocity, the heat diffusion encounters the same mass conservation peculiarity. A correction on energy flux E_g^{cor} is introduced by analogy with the correction velocity $\boldsymbol{u}_g^{\mathrm{cor}}$ for the species conservation. We finally have the simplified heat flux:

$$\boldsymbol{q} = -\lambda_g \partial_{\boldsymbol{x}} T_g + E_g^{\mathrm{cor}}, \text{ with } E_g^{\mathrm{cor}} = \sum_{k=1}^{n_s} h_k D_k \partial_{\boldsymbol{x}} Y_k. \tag{A.30}$$

Finally, in the case of multi-species flows the modeling of μ_g and λ_g has to be re-examined (Wilke 1950). Approaches are included in the computation of species diffusions (Ern and Giovangigli 1994).

Appendix B

Heat and mass coupled transfer around a droplet

When mass transfers occur, they necessarily couple to momentum and heat transfers. The drag force modeling may remain correct but the heat transfer is altered since mass transfers often depend on temperature while the transferred mass alters the surface temperature. The problem of mass and heat transfer is therefore a strongly coupled problem.

B.1 Evaporation modeling for a monocomponent droplet

Evaporation occurs at a rate R_s, as defined and used in Eq. (3.123). But the mass transfer yields heat convective flux that is often comparable to the conduction-convection heat transfer rate H so that the overall heat transfer has to be modeled in a way that is coupled to the mass transfer. We recall here the main steps of the models, as described by de Chaisemartin (2009) and more details can be found in Abramzon and Sirignano (1989) and in Versaevel (1996). Monocomponent droplet evaporation produces in the gas a species noted with the specific index v for vapor.

B.1.1 Mass budget

We solve the flow around a spherical droplet of radius r_p depending on the radial coordinate ξ defined so that the abscissa of the droplet surface is $\xi = r_p$. The flow is defined by the fields of gas velocity $\boldsymbol{u}_g(\xi)$, gas temperature $T_g(\xi)$, and vapor mass fraction in the gas phase $Y_v(\xi)$. The unperturbed fields are noted $\boldsymbol{u}_{g\infty}$, $T_{g\infty}$, and $Y_{v\infty}$ while the droplet surface temperature is noted $T_p(r_p)$.
The change rate of the size is linked to droplet mass variation and thus to the total mass flux of vapor at the droplet surface:

$$\dot{m}_{p|s}(r_p) = -\mathrm{d}_t\left(\rho_l \frac{4}{3}\pi r_p^3\right) = -\mathrm{d}_t\left(\frac{\rho_l S_p^{\frac{3}{2}}}{6\sqrt{\pi}}\right) = -\frac{\rho_l S_p^{\frac{1}{2}}}{4\sqrt{\pi}}\mathrm{d}_t S_p = -\frac{\rho_l S_p^{\frac{1}{2}}}{4\sqrt{\pi}} R_S \tag{B.1}$$

We neglect in Eq. (B.1) the dilatation of the droplet, so that $\rho_l = cst$. We therefore need to compute the vapor mass flux to obtain the expression of R_S.
In order to take into account convection cases, i.e. with a relative velocity between the droplet and the gas, we define the thickness δm of a diffusive mass boundary layer. Beyond this distance, the mass vapor mass fraction is taken as a constant: $Y_v(\xi = \delta m) = Y_{v\infty}$. If there is no relative velocity, $\delta m = +\infty$. We also introduce the convective Sherwood number Sh_c:

$$\mathrm{Sh}_c = 2\frac{\delta m}{\delta m - R} \tag{B.2}$$

with R the droplet radius.
We take advantage of the spherical symmetry to derive a 1D formulation. In this framework, the flux $\dot{m}_{p|s}$ can be written (Reveillon and Demoulin 2007a):

$$\dot{m}_{p|s}(r_p) = 4\pi r_p^2 \rho_g \boldsymbol{u}_p(r_p) \tag{B.3}$$

and we thus need to evaluate the quantity $\rho_g \boldsymbol{u}_p(r_p)$ to obtain the size variation rate. To do so, we consider the conservation equations for the momentum of the gas and for the Y_l species, assuming that the evaporation

process is slow enough to consider a steady state and in the limit of no chemical reaction (Sirignano 2010):

$$\begin{cases} \mathrm{d}_\xi\left(\xi^2\rho_g\boldsymbol{u}_g\right)=0 \\ \mathrm{d}_\xi\left(\xi^2\rho_g\boldsymbol{u}_g Y_v\right)=\mathrm{d}_\xi\left(\xi^2\rho_g D_v \mathrm{d}_\xi Y_v\right) \end{cases} \tag{B.4}$$

where Fick's law is used for diffusion of the vapor species in the surrounding gas with a coefficient D_v. The integration of the momentum equation yields:

$$\xi^2\rho_g\boldsymbol{u}_g = \text{constant}. \tag{B.5}$$

and the vapor fraction conservation becomes:

$$\xi^2\rho_g\boldsymbol{u}_g\mathrm{d}_\xi Y_v = \mathrm{d}_\xi\left(\xi^2\rho_g D_v\mathrm{d}_\xi Y_v\right). \tag{B.6}$$

In order to obtain $\rho_g\boldsymbol{u}_g(r_p)$, we will integrate this equation within the diffusive boundary layer. First of all we rewrite Eq. (B.6), introducing the transfer parameter b:

$$\xi^2\rho_g\boldsymbol{u}_g\mathrm{d}_\xi b = \mathrm{d}_\xi\left(\xi^2\rho_g D_v\mathrm{d}_\xi b\right), \quad b=\frac{Y_v(\xi)}{Y_v(r_p)-1}. \tag{B.7}$$

We then integrate between the droplet radius $\xi = r_p$, to the end of the diffusive mass boundary layer $r = \delta m$, where $b = b_\infty$. This integration leads to (Reveillon and Demoulin 2007a):

$$r_p\boldsymbol{u}_g(r_p) = \frac{1}{2}\mathrm{Sh}_c D_v \ln(1+\mathrm{B_M}) \tag{B.8}$$

where we introduced the Spalding dimensionless mass transfer number:

$$\mathrm{B_M} = b_\infty - b_s = \frac{Y_v(r_p)-Y_{v\infty}}{1-Y_v(r_p)} \tag{B.9}$$

leading to

$$\dot{m}_{p|s}(r_p) = 2\pi r_p\rho_g\mathrm{Sh}_c D_v\ln(1+\mathrm{B_M}) \tag{B.10}$$

and combined with Eq. (B.1), it gives the expression for R_s:

$$R_s = 4\pi\frac{\rho_g}{\rho_l}\mathrm{Sh}_c D_v\ln(1+\mathrm{B_M}). \tag{B.11}$$

The Sh_c and $\mathrm{B_M}$ coefficients will depend on the model choice, discussed afterward.

B.1.2 Heat budget

The heat received from the gas ends up in the vapor latent heat, to evaporate a portion of the liquid and in the liquid core, to heat it up. The conductive heat reaching the droplet surface may then be written (Reveillon and Demoulin 2007a):

$$Q_g = \dot{m}_{p|s}L_v + Q_l \tag{B.12}$$

where L_v is the latent heat of evaporation and Q_l the heat absorbed by the liquid core. We recall that only thermal conduction is accounted for, therefore Q_g is given by a conductive flux, possibly modified by convective effects:

$$Q_g = 4\pi r_p^2\lambda_g\mathrm{d}_\xi T_g = 4\pi r_p^2 h\left(T_{g\infty}-T_p(r_p)\right). \tag{B.13}$$

The heat Q_l induces the droplet temperature variation and is thus linked to the temperature change rate:

$$Q_l = m_p c_{p,l}\mathrm{d}_t T_p = m_p H. \tag{B.14}$$

The heat transfer term is thus given by:

$$m_p H = \left(Q_g - \dot{m}_{p|s}L_v\right) = \frac{6\sqrt{\pi}}{\rho_l S_p^{\frac{3}{2}} c_{p,l}}\left(Q_g - \dot{m}_{p|s}L_v\right) \tag{B.15}$$

and its expression is obtained by deriving another expression for $\dot{m}_{p|s}$ by integrating the energy conservation equation over the thermal diffusive boundary layer. To do so we use exactly the same 1D spherical symmetry

context as for the fuel vapor conservation. We define the thermal diffusive boundary layer δT, with $T_g(\delta T) = T_{g\infty}$. We can then write a new expression for the Nusselt number given in Eq. (3.55):

$$\mathrm{Nu}_c = 2\frac{\delta T}{\delta T - r_p}. \tag{B.16}$$

The energy conservation equation can be written:

$$\rho_g \boldsymbol{u}_g \xi^2 \mathrm{d}_\xi(c_{p,g} T_g) = \mathrm{d}_\xi\left(\xi^2 \lambda_g \mathrm{d}_\xi T_g\right) \tag{B.17}$$

and its integration leads to (Reveillon and Demoulin 2007a):

$$\dot{m}_{p|s} = 2\pi r_p \frac{1}{c_{p,g}} \mathrm{Nu}_c \lambda_g \ln(1 + \mathrm{B_T}) \tag{B.18}$$

where we introduce the dimensionless heat transfer Spalding number $\mathrm{B_T}$:

$$\mathrm{B_T} = \frac{\rho_g \boldsymbol{u}_g c_{p,g}}{h}. \tag{B.19}$$

Finally, Eq. (B.13), Eq. (B.14) and Eq. (B.18) yield the following heat transfer:

$$m_p H = 2\pi r_p \lambda_g \left(\mathrm{Nu}(T_{g\infty} - T_p(r_p)) - \frac{L_v}{c_{p,g}} \mathrm{Nu} \ln(1 + \mathrm{B_T})\right) \tag{B.20}$$

with the droplet Nusselt number $\mathrm{Nu} = h 2r_p/\lambda_g$ as defined in Eq. (3.55). Using $\mathrm{Nu} = \mathrm{Nu}_c \ln(1 + \mathrm{B_T})/\mathrm{B_T}$, we finally have:

$$m_p H = \frac{2\pi r_p \lambda_g}{c_{p,g}} \mathrm{Nu}_c \ln(1 + \mathrm{B_T}) \left(\frac{c_{p,g}}{\mathrm{B_T}}(T_{g\infty} - T_p(r_p) - L_v\right) \tag{B.21}$$

Using the two expressions derived for the mass flux $\dot{m}_{p|s}$ i.e. Eq. (B.10) and (B.18), gives:

$$m_p H = 2\pi r_p \rho_g \mathrm{Sh}_c D_v \ln(1 + \mathrm{B_M}) \left(\frac{c_{p,g}}{\mathrm{B_T}}(T_{g\infty} - T_p(r_p)) - L_v\right) \tag{B.22}$$

and

$$\mathrm{B_T} + 1 = (\mathrm{B_M} + 1)^{\frac{\mathrm{Sh}_c}{\mathrm{Nu}_c}\frac{\mathrm{Sc}_v}{\mathrm{Pr}}} \tag{B.23}$$

where the Schmidt number is that of the vapor species:

$$\mathrm{Sc}_v = \frac{\nu_g}{D_v}. \tag{B.24}$$

In the dispersed two-phase flow context, T_∞ is the gas temperature at the droplet position $T_g(\boldsymbol{x}_p)$. We give H expressed in function of the droplet size:

$$m_p H = \frac{6\pi \rho_g}{\rho_l S_p} \mathrm{Sh}_c D_v \ln(1 + \mathrm{B_M}) \left(\frac{c_{p,g}}{\mathrm{B_T}}(T_g(\boldsymbol{x}_p) - T_p) - L_v\right). \tag{B.25}$$

In this expression Sh_c, $\mathrm{B_M}$ and $\mathrm{B_T}$ are still to be modeled.

B.2 Different evaporation models

The coupled heat and mass transfer due to evaporation, as treated above, must be closed thanks to assumptions on the heat transfers.
Internal circulation, such as Hill vortices (Johns and Beckmann 1966), can be considered but it severely complexifies the modeling (Abramzon and Sirignano 1989). If the complex, time dependent, temperature field is not considered, a temperature profile can still be considered (Abramzon and Sirignano 1989; Sirignano 2010; Prud'homme et al. 2010). Nevertheless, these models are not compatible with the kinetic description of the spray, as explained in Laurent and Massot (2001).

B.2.1 Constant temperature model

Among the models with no internal circulation, we cite the constant droplet-temperature model assuming $H = 0$ and the infinite liquid-conductivity model. The first one leads to the well-known d2-law (Godsave 1953; Spalding 1953) where the square of the droplet diameter d_p has a linear regression in time:

$$\mathrm{d}_t(d_p^2) = -K. \tag{B.26}$$

The coefficient K does not depend on the droplet diameter, but depends on local gas conditions. By analogy with this famous law, dn-laws are sometimes introduced with a different exponent n. The absence of relative velocity in these laws yields $\delta m = \infty$ and thus $\mathrm{Sh}_c = 2$. The rate of change of size R_s is thus given by:

$$R_s = 8\pi \frac{\rho_g}{\rho_l} D_v \ln(1 + \mathrm{B_M}). \tag{B.27}$$

The mass transfer number $\mathrm{B_M}$ is obtained by solving a saturation law (Reveillon and Demoulin 2007a) and requires the knowledge of the droplet surface temperature $T_p(r_p)$. Since the temperature is not resolved, we need to compute it. We use the fact that droplet heating is not accounted for, i.e. $H = 0$, giving, from Eq. (B.22):

$$\left(\frac{c_{p,g}}{\mathrm{B_T}(T_p(r_p))} (T_g(\boldsymbol{x}_p) - T_p(r_p)) \right) = L_v(T_p(r_p)). \tag{B.28}$$

Nevertheless in many cases, the d2-law is associated with a constant $\mathrm{B_M}$. This approximation stands if the temperature and pressure of the gaseous carrier phase are uniform and if the vapor concentration is far from the saturation point. Typical values for air-fuel mixtures can be found in Reveillon and Demoulin (2007a).

B.2.2 Infinite conductivity model

A first model taking into account droplet heating, but still not resolving internal conduction, is the infinite liquid-conductivity model. Droplet temperature is uniform, $T_p(r_p) = T_p$, but depends on time. The rate of change of size, R_s, and of temperature, H, are given by Eq. (B.27) and Eq. (B.25), respectively. The mass transfer number $\mathrm{B_M}$ is given by a saturation law determined by the local properties of the flow, see for example (Canneviere 2003). The thermal transfer number $\mathrm{B_T}$ is obtained from $\mathrm{B_M}$, through Eq. (B.23). In order to compute $\mathrm{B_M}$ and $\mathrm{B_T}$, the corrected Sherwood and Nusselt numbers, Sh_c and Nu_c should be evaluated. If no corrections are taken into account, we have, as in the previous model:

$$\mathrm{Sh}_c = \mathrm{Nu}_c = 2. \tag{B.29}$$

In the limit where droplet heating tends to zero, we obtain the previous d2-law model.

B.2.3 Effective conductivity model

To take convection into account, corrections are inserted in Sh_c and Nu_c. We present here two possible choices among several available in the literature, presented for example in Sirignano (2010).
A first choice is to take the empirical corrections from Faeth (1983):

$$\begin{aligned} \mathrm{Sh}_c &= 2 + \frac{0.55 \mathrm{Re}_p \mathrm{Sc}}{(1.232 + \mathrm{Re}_p \mathrm{Sc}^{\frac{4}{3}})^{\frac{1}{2}}}, \\ \mathrm{Nu}_c &= 2 + \frac{0.55 \mathrm{Re}_p \mathrm{Pr}_g}{(1.232 + \mathrm{Re}_p \mathrm{Pr}_g^{\frac{4}{3}})^{\frac{1}{2}}}. \end{aligned} \tag{B.30}$$

A second choice for convection correction insertion is to take the method proposed in Abramzon and Sirignano (1989), where:

$$\begin{aligned} \mathrm{Sh}_c &= 2 + \frac{\mathrm{Sh}_c - 2}{\mathrm{F_M}},\ \mathrm{F_M} = (1 + \mathrm{B_M})^{0.7} \frac{ln(1 + \mathrm{B_M})}{\mathrm{B_M}}, \\ \mathrm{Nu}_c &= 2 + \frac{\mathrm{Nu}_c - 2}{\mathrm{F_T}},\ \mathrm{F_T} = (1 + \mathrm{B_T})^{0.7} \frac{ln(1 + \mathrm{B_T})}{\mathrm{B_T}}. \end{aligned} \tag{B.31}$$

The classical Sherwood and Nusselt numbers are determined using the correlation given in Clift et al. (1978):

$$\begin{aligned} \mathrm{Sh}_c &= 1 + (1 + \mathrm{Re}_p \mathrm{Sc})^{\frac{1}{3}} \psi(\mathrm{Re}_p), \\ \mathrm{Nu}_c &= 1 + (1 + \mathrm{Re}_p \mathrm{Pr}_g)^{\frac{1}{3}} \psi(\mathrm{Re}_p), \end{aligned} \tag{B.32}$$

with

$$\begin{array}{ll} \psi(\mathrm{Re}_p) = 1 & \text{if } \mathrm{Re}_p \leq 1, \\ \psi(\mathrm{Re}_p) = \mathrm{Re}_p^{0.077} & \text{if } 1 < \mathrm{Re}_p < 400. \end{array} \tag{B.33}$$

The use of these correlations requires an iterative procedure, the correction factors, $\mathrm{F_M}$ and $\mathrm{F_T}$ being functions of $\mathrm{B_M}$ and $\mathrm{B_T}$ respectively.

B.2.4 Case of the combustion of metal particles

The combustion of metal particles is peculiar, as discussed in the case of aluminum in § 1.2.3.4. It can occur either in the gaseous phase or in an heterogeneous fashion at the particle surface, depending on the surrounding gas ambience; both modes can even coexist in some regimes. To the models presented in § 1.2.3.4 for aluminum distributed combustion, we can add the model from Law (1973).
These models account for the combustion of a single particle but group effects may be encountered, especially for nanoparticles, which have not been studied. A comprehensive theory of group combustion for hydrocarbon fuel droplets is presented in Sirignano (2010).
In most cases however, chemical reactions occur in the gas phase and this is also true for some two-phase combustion regimes: mass is transferred from the condense phase to the gas according to evaporation, i.e. a mass transfer due to pure phase transformation, and the reactions occur at a distance from the inclusion. We now discuss the case of pure evaporation.

B.3 Remarks on multicomponent droplet evaporation

Multicomponent droplet evaporation has a much complex behavior as the species evaporate at a different rate while the thermophysical properties of the mixture depend on composition in a complex way as discussed in Kee et al. (2011). A numerical approach for multicomponent droplets by methods of moments, see § 4.4.4.1, is developed for HPC simulations (Laurent et al. 2010).

Appendix C

Two-population model for liquid atomization

This appendix presents a prospective work on statistical modeling of liquid atomization, performed with Nicolas Rimbert and published in Rimbert et al. (2012). The purpose is to derive a semi-empirical model that fits the log-Levy experimental droplet distributions of some atomizers by accounting for the transient shape of droplets and their sensitivity to turbulence.

C.1 Introduction

The secondary bag break-up mechanism is described and modeled at a mesoscopic scale using population balance equations as a first step towards industrial simulations of turbulent atomization. A stochastic process accounting for temporality and experimental asymptotics of turbulence-liquid interactions is built with a self similar kernel whereas larger droplets are only subject to a mean-flow-based discrete and instantaneous break-up kernel. For turbulence to influence only the small droplets, they are collected into a second population balance equation and renamed ligaments in relation with their transient shape during the process. The evolution of velocity distributions is introduced in the modeling as a driving parameter of the break-up process. Computations are made for William's full spray equation on simplified cases. Finally the model is reduced to a system of conservation equations in space and time with closed source terms thanks to the Eulerian Multi-Fluid approach, in order to be applicable for more realistic configurations.

C.1.1 Importance of atomization

Turbulent atomization is of paramount importance for mechanical engineering where it requires, most of the time, to be simulated at a mesoscopic level i.e. by disregarding the smallest scales. Indeed Direct Numerical Simulations (DNS) of the liquid-gas interface are intractable for realistic Weber and Reynolds numbers. Even if DNS can give some insight and allow model validations, the development of numerical methods is the main issue (Gorokhovski and Herrmann 2008; Le Chenadec 2012). So Large Eddy Simulation (LES) seems to be the target level of description (Apte et al. 2003). The secondary stage of atomization -where droplets, which have been ripped off the dense core, break-up under the effect of surrounding turbulence- drives the final droplet size distribution so its mesoscopic modeling is the focal point of this contribution.
Turbulent atomization models are scarce and most experimentalists still resort to empirical number density functions (NDF) to describe the resulting size distribution of the droplet mist (Lefebvre 1989). Such NDFs can be directly used to close secondary break-up sources in Population Balance Equations (PBE) (Amsden et al. 1989) and these equations can be generalized to transport and approached by moment methods (Dufour et al. 2003; Doisneau et al. 2013). All these mesoscopic models using presumed NDFs are still popular but, by abandoning all the break-up timescales, they lack temporality and the instantaneous velocity jump from the mother to the daughter droplets, using low-definition empirical laws, is of limited accuracy and brings in numerical convergence issues. Hence a mechanism, even simple, is required to bridge the gap between a microscopic DNS description and the target mesoscopic models in order to properly describe the spray size and velocity distributions.

C.1.2 Two modeling strategies

The wide range of scales in turbulent sprays was early modeled as log-normal, which led eventually Kolmogorov (1941) to devise a stochastic process explaining their widespread appearance. This modeling became famous when used later to describe turbulence intermittencies (between large and small vortices, see Rimbert

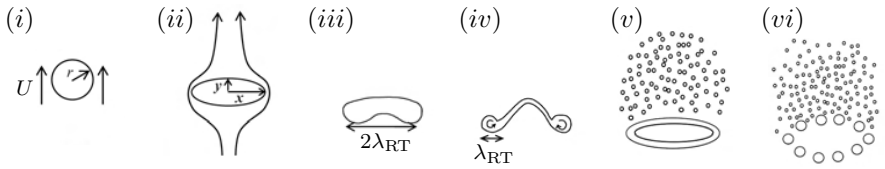

Figure C.1: *The six stages of bag break-up.*

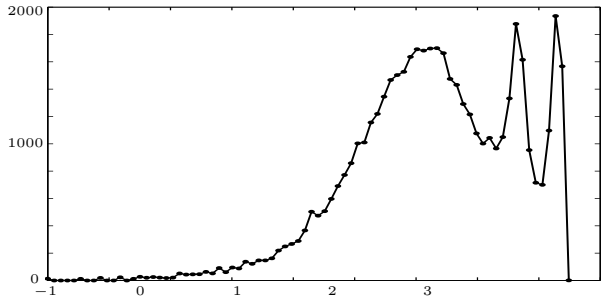

Figure C.2: *Experimental NDF of bag break-up – Size in decimal magnitude,* 0 *stands for* $1\mu m$.

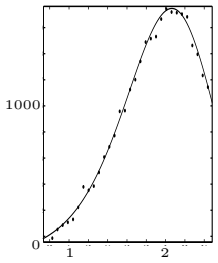

Figure C.3: *Experimental NDF tail (bag mode) fitted by a log-Lévy law* ($\alpha = 1.69$).

(2010) for more details). However when the liquid jet flows rather slowly, classical linear instabilities are well known to govern the mechanism of drop formation and lead to narrow-band spectra.
So these two visions should be merged into a comprehensive theory, based on a consistent description level: ligaments -which have been detected as soon as high-speed imaging became available in the late stage of the atomization process (Pilch and Erdman 1987)- are good candidates as either produced by cascading eddies or subject to capillary instabilities. Theses two visions are partially mapped by Eggers and Villermaux (2008), as far as linear instabilities and ligament reorganization into spherical droplets are concerned, and by Gorokhovski and Herrmann (2008) as far as Kolmogorov theory is concerned. In recent work, Rimbert and Castanet (2011) tried such alliance to explain the experimental classification of secondary break-up made by Faeth's Group in Ann Arbor (Hsiang and Faeth 1995) as well as experimental NDF tails.

C.1.3 Present strategy

In the present work, a mechanism is built through a PBE combining discrete and self-similar break-up kernels: the process' asymptotic distribution matches an experimental NDF while its temporality is based on timescales from classical physical analysis. For the sake of clarity we focus on bag break-up, which asymptotics is a Log-Lévy distribution (a generalization of log-normal laws). The so-forged mechanism is then extended by considering two PBEs in order to separately account for transient ligaments -mostly reorganized by turbulent-surface-tension competition- and for spherical droplets - assumed to be mostly insensitive to turbulence. This leads to a two-layer mesoscopic model which describes a different physics for droplets (discrete break-up) and ligaments (self-similar turbulent reorganization). The role of droplet velocities is then included so that each PBE is generalized into a kinetic equation referred to as GPBE and classically used for the LES of disperse phase flows (Fox 2012). Finally, the compliance of the overall modeling with state-of-the-art moment methods (Massot et al. 2009) is assessed.

C.2 Preliminary modeling secondary atomization

C.2.1 Secondary atomization regimes

The dimensionless parameters that govern the stability of a droplet in a gas stream are the (aerodynamic) Weber number We_d and the Ohnesorge number Oh_d, already defined in Eq. (3.7) and Eq. (3.8) respectively, and here based on the droplet diameter d. Using these two parameters Faeth and co-workers made a thorough investigation of the different kinds of atomization mechanisms (Pilch and Erdman 1987): elongation, bag break-up, umbrella break-up, shear break-up, *etc.*, resulting in a We-Oh map classifying these phenomena (Hsiang and Faeth 1995).

C.2.2 Particular case of bag break-up

For the sake of simplicity, we focus on bag break-up as the lowest-speed break-up regime experimentally listed, and as mostly represented in secondary atomization cascades.

The bag break-up is usually decomposed into six stages shown in Figure C.1 and its temporality is governed by the Rangers & Nichols characteristic time τ_{RN} which describes gas-liquid momentum exchanges (Hsiang and Faeth 1995), and has already been given in Eq. (3.81). The Rayleigh-Taylor length λ_{RT} drives the rim size as the corresponding instability settles in steps (*iii*) and (*iv*). The bag breaks at step (*v*) after $3\tau_{\mathrm{RN}}$ and the rim disrupts at step (*vi*) after $5\tau_{\mathrm{RN}}$, concluding the break-up process so that a characteristic frequency linked to its total duration follows:

$$\nu = \frac{1}{5\tau_{\mathrm{RN}}} = \sqrt{\frac{\rho_g}{\rho_l}}\frac{U}{5d} \tag{C.1}$$

that has been given in Eq. (3.83). We assume the Weber range for bag break-up to be between $\mathrm{We}_b^- = 12$ and $\mathrm{We}_b^+ = 50$ and the parting of the liquid into the rim and the bag to be (R_d,R_l)=(75%, 25%). Radii of the droplets obtained from the break-up of the rim are assumed to be half the radius of the mother droplet -though it could be obtained from other considerations (Zhao et al. 2010). These considerations of volume branching ratio and rim droplet sizes will be used to build the rim-break-up kernel. One of the important results of Rimbert and Castanet (2011) is that, in the bag break-up regime, the small size droplet NDF tail can be adequately fitted by a log-stable Lévy law, an extension of log-normal laws. Figure C.2 depicts the whole NDF and three modes are identified, from right to left: the mother droplet peak, the rim droplet peak and a wider mode of small size droplets resulting from the bag breakage. Figure C.3 shows the fitting of the small size NDF by a log-stable law.
Though log-stable laws were first proposed for turbulent sprays by Novikov and Dommermuth (1997) and then by Rimbert and Séro-Guillaume (2004b), the main advance of the two papers Rimbert (2010) and Rimbert and Castanet (2011) is to give a physical interpretation to the parameters of the law (*e.g.* stability index, scale parameter *i.e.* width). It is therefore possible to cease considering them as fitting parameters. The stability index $\alpha = 1.70$ is related to a model of intermittency based on Self-Avoiding Vortex Random Stretching while the scale and shift parameters are related to the Kolmogorov and Taylor scale of the turbulence through a ligament turbulent reorganization mechanism. The size of the smallest drops is comparable to the Kolmogorov scale $\eta \approx 3\mu m$ and the size of the average drop compares to the estimated Taylor scale $\lambda \approx 137\mu m$. The width of the distribution has been estimated to be $\sigma_{\ln(d)} = 1/2\ln(\lambda/\eta)^{1/\alpha}$.

C.3 A new stochastic process for the description of moderately dense bag break-up

C.3.1 A new process for Break-Up PBEs

In the bag break-up regime, a droplet breaks into two classes of daughter droplets which are taken of equal size as a first approximation. Though the process is somewhat discontinuous (*cf.* the six stages reported in Figure C.1), it is possible to write a continuous-in-time break-up equation by making the balance between the number of parent and daughter drops in a statistical sense. When the parents generate a single class of γ daughter droplets of equal radius $r_\gamma = r/\gamma^{\frac{1}{3}}$ with a frequency ν, the break-up equation reads:

$$\frac{\partial f}{\partial t}(r) = -\nu f(r) + \int_{\mathbb{R}^+} \nu f(r')\gamma\delta_{r_\gamma}(r')\mathrm{d}r' \tag{C.2}$$

where $f(t,r)$ is the NDF of droplets of radius r per unit volume and δ_{r_γ} is Dirac's delta function centered on r_γ. An alternate way of writing the break-up equation is to use a self-similar form (Gorokhovski and Saveliev 2003):

$$\frac{\partial f}{\partial t}(r) = -\nu f(r) + \int_{\mathbb{R}^+} \nu f(r') b(r'/r)\mathrm{d}r'/r' \tag{C.3}$$

where b is the self-similar break-up kernel (most of the time unknown in real applications). Under appropriate hypotheses, the asymptotic behavior of (C.3) is a log-normal NDF therefore relating it to some turbulence cascading mechanism. However, in order to obtain a log-stable law and match experimental results, the kernel must be in the corresponding attraction basin which is roughly equivalent to the following asymptotic behavior:

$$b(r/r') \approx \frac{1}{|\ln(r'/r)|^{\alpha+1}} \tag{C.4}$$

where α is the stability index of the Lévy law. To prevent divergence of integrals, it is either possible to limit this kernel (*e.g.* truncate) or to introduce a constant K_1 such that:

$$\frac{\partial f}{\partial t}(r) = -\nu f(r) + K_0 \int_{\mathbb{R}^+} \nu f(r') \frac{1}{|\ln(r'/r)|^{\alpha+1}}\mathrm{d}r'/r' + K_1 r \frac{\partial f}{\partial r}(r) \tag{C.5}$$

where K_0 is a constant governing the influence of the turbulent peak broadening and K_1 is a constant computed to enforce volume conservation. Although using equation (C.5) over (C.3) combined to a limited form of (C.4) somewhat changes the time dynamics -(C.4) leads to a log-stable law asymptotically while (C.5) leads to it instantaneously-, it does not change the modeling qualitatively and has been chosen in the present work for numerical reasons. In the $\xi = \log_{10}(r)$ space or magnitude space equation (C.5) turns to

$$\frac{\partial f}{\partial t}(\xi) = -\nu f(\xi) + K_0 \int_{\mathbb{R}} \nu f(\xi') \frac{1}{|\xi' - \xi|^{\alpha+1}} \mathrm{d}\xi' + K_1 \frac{\partial f}{\partial \xi}(\xi) \tag{C.6}$$

Note that ν can have a variable value when updating U and d, leading to an increasing frequency as the droplet size decreases, yielding an infinite number of infinitely small particles in a finite time. This is referred to as shattering transition (Ziff and McGrady 1987) and is physically not desirable here so we choose a constant frequency based on the mother droplet size and velocity. Using Weyl's fractional derivative, expressed as follows:

$$\boldsymbol{D}^{\alpha}_{\xi} f(\xi) = \frac{1}{\Gamma(2-\alpha)} \frac{\partial^2}{\partial \xi^2} \int_{\mathbb{R}} f(\xi') \frac{1}{|\xi' - \xi|^{\alpha-1}} \mathrm{d}\xi' \tag{C.7}$$

Eq. (C.6) becomes formally a Fractional Fokker-Planck Equation, for a scale diffusion stochastic process, or can be seen as the generator of the approriate Lévy-Feller semigroup (Rimbert and Séro-Guillaume 2004a), and reads:

$$\frac{\partial f}{\partial t}(\xi) = -\nu f(\xi) + \nu \chi_{\alpha} \boldsymbol{D}^{\alpha}_{\xi} f(\xi) + K_2 \frac{\partial f}{\partial \xi}(\xi) \tag{C.8}$$

where χ_{α} stands for $\sigma^{\alpha} cos(\pi\alpha/2)$ and is roughly equal to unity in our case (and replaces constant K_0). As integro-differential operators in (C.5) and (C.7) are proportional (this can be seen using a Fourier transform), constant K_2 replaces K_1 and must be set equal to $\nu\chi_{\alpha}(4^{\alpha}\Gamma(-\alpha) - 1)/4$ to ensure volume conservation.
We finally have a discrete i.e. instantaneous process (C.2), which we will use to model the rim break-up and the formation of the ligaments from the bag and a continuous process (C.8) which we will use to model the broadening of the ligament mode, presumably in relation with turbulence.

C.4 A two-population kinetic model

C.4.1 Two-Layer PBE model for Droplets and Ligaments

If one considers an initial droplet submitted to equation (C.2) a cascading mechanism naturally occurs as the daughter droplets will themselves be divided into p fragments. It is not the case in the bag break-up mechanism, mostly because the relative velocity of the daughter drops and the surrounding gas is strongly decreasing during the process. A way to prevent daughter structures to break-up with the same mechanism is to separate bag structures into a second population called ligaments. We now use an index $p \in \{d, l\}$ for each population with d referring to droplets and l to ligaments. So the mother droplets break-up into two classes: the rim droplets whose volume ratio is $\gamma_d = 2^3$ according to experimental observations (Rimbert and Castanet 2011) and the bag ligaments whose volume ratio is given by $\gamma_l = 7^3$. Then the bag ligaments are affected by turbulent re-agglomeration and subject to process (C.8). Ligaments are supposed to be fully described by an equivalent diameter when assuming a 1D parametrization of their shape. Though a 2D manifold is required to render at least spheroidal (or cylindrical) shapes, this information was not measured by Rimbert and Castanet (2011) and is not included in the present model for the sake of simplicity. It is therefore of capital importance to presume the topologies of droplets and ligaments for size ξ and for each population p to compute the geometric features that are volumes $\mathcal{V}_p(\xi)$, surfaces $\mathrm{Surf}_p(\xi)$ *etc.* The Population Balance Equations (PBE) on $f_d(\xi)$ and $f_l(\xi)$ finally read:

$$\frac{\partial f_d}{\partial t} = -\nu_d f_d + R_d \int_{\mathbb{R}} \nu_d f_d(\xi') b_d(\xi', \xi) \mathrm{d}\xi' + \mathscr{C}^{ld+}(f_l) \tag{C.9}$$

$$\frac{\partial f_l}{\partial t} = R_l \int_{\mathbb{R}} \nu_d f_d(\xi') b_l(\xi', \xi) \mathrm{d}\xi' - \nu_l f_l + \nu_l \chi_{\alpha} \boldsymbol{D}^{\alpha}_{\xi} f_l(\xi) + K_2 \frac{\partial f_l}{\partial \xi} - \mathscr{C}^{ld-}(f_l) \tag{C.10}$$

where the kernels are noted $b_p = \gamma_p \delta_{\xi_p}(\xi')$ with $\xi_p = \xi - \frac{1}{3}\log_{10}(\gamma_p)$, $\nu_d = 5\tau_{\mathrm{RN}} \mathbf{1}_{[\mathrm{We}_b^-, \mathrm{We}_b^+]}$, $\nu_l = 5\tau_{\mathrm{RN}} \mathbf{1}_{[\mathrm{We}_b^-, \mathrm{We}_b^+]}$ and $\mathbf{1}_{[\mathrm{We}_b^-, \mathrm{We}_b^+]}\big(\mathrm{We}(\xi')\big)$ the characteristic function of the bag break-up domain. The two PBEs are coupled

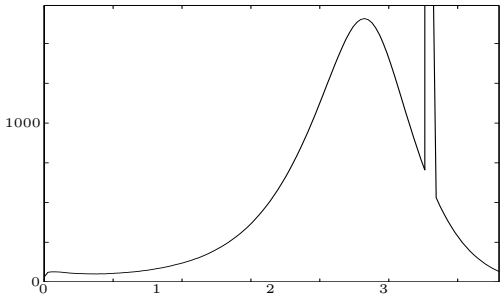

Figure C.4: *Spray NDF with the Two-Layer PBE model.*

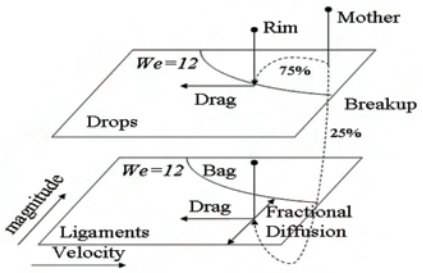

Figure C.5: *Scheme of the two layers containing drops (top) and ligaments (bottom).*

through the discrete break-up creation terms and through the sources $\mathscr{C}^{ld\pm}(f_l)$. The $\mathscr{C}^{ld\pm}$ terms translate the ligaments back to the droplet population once they have reordered, presumably under capillary forces:

$$\mathscr{C}^{ld-}=\nu_c f_l(\xi)\mathbf{1}_{\xi<\xi_0}(\xi) \text{ and } \mathscr{C}^{ld+}=\int_{-\infty}^{\xi_0}\nu_c f_l(\xi')c_l(\xi',\xi)\mathrm{d}\xi' \tag{C.11}$$

with the frequency ν_c linked to the capillary number and the capillary reorganization kernel is given by $c_l=\delta_{\mathcal{V}_l(\xi')}\big(\mathcal{V}_d(\xi)\big)$. The overall system, referred to as Two-Layer PBE model is conservative since:

- the droplet disappearance term $-\nu_d f_d$ is exactly balanced by the (rim) droplet and (bag) ligament discrete creation terms thanks to the branching relation $R_l+R_d=1$,
- the continuous self-similar break-up process is mass conserving by construction,
- the capillary transfer sources ensure $\int_{\mathbb{R}}\mathcal{V}_l(\xi)\mathscr{C}^{ld-}(f_l(\xi))\mathrm{d}\xi=\int_{\mathbb{R}}\mathcal{V}_d(\xi')\mathscr{C}^{ld+}(f_l(\xi),\xi')\mathrm{d}\xi'$.

We now perform a simulation of the Two-Layer PBE model. A discretization of equation (C.10) is done analogously to Rimbert and Séro-Guillaume (2004a) using the algorithm of Gorenflo et al. (2002) for the fractional derivative. We take initial magnitudes of 3.13 ($1350\mu m$), initial velocities of 41m/s and initial Weber numbers of 41 for the mother droplets. In order to prevent subsequent (and spurious) break-up of the daughter rim droplets ($\mathrm{We}_{\mathrm{rim}}=20.5$), We_b^- has been increased to the value of 23, theoretically derived by Rimbert and Castanet (2011). The resulting NDF is depicted in Figure C.4. Note that the mother droplet is not shown on this picture as it has fully disappeared at the end of this atomization process. Since the terms $\mathscr{C}^{ld\pm}$ are not further modeled (ν_c has yet to be determined), they are not considered here and a zero flux boundary condition is imposed instead on the lower end of the magnitude (size) space, in order to prevent the appearance of very small ligaments. This uses the so-called image method (Gorenflo et al. 2002) and ensures mass conservation of the ligaments. The result corresponds to the superposition of the rim droplet peak to the wide ligament mode. If the simulation is left running further there will be an unphysical increase of small droplets on the lower size boundary. So the diffusion process must be stopped adequately e.g. by introducing the terms $\mathscr{C}^{ld\pm}$ to transfer ligaments to the droplet space. Such terms are physically sound as a capillary reformation of droplets and should include the corresponding time scale but their exact form is left for future work.

C.4.2 Accounting for deceleration: Two-Layer GPBE model

To refine the model and cope with the problem of daughter droplet stability more physically, we include the positions $\boldsymbol{x}$ and velocities $\boldsymbol{c}$ in the phase space, leading to Generalized PBEs or GPBEs (Williams 1958). Since Weber numbers depend on $\boldsymbol{c}$, break-up processes are now conditioned on velocities. This results in the Two-Layer GPBE model on $f_p(\xi,\boldsymbol{c})$:

$$\frac{\partial f_d}{\partial t}+\boldsymbol{c}\frac{\partial f_d}{\partial \boldsymbol{x}}+\frac{\partial \boldsymbol{a}_d f_d}{\partial \boldsymbol{c}}=-\nu_d f_d+R_d\iint_{\mathbb{R}^2}\nu_d f_d(\xi',\boldsymbol{c}')b_d(\xi',\boldsymbol{c}',\xi)\beta_d(\xi',\boldsymbol{c}',\boldsymbol{c})\mathrm{d}\xi'\mathrm{d}\boldsymbol{c}'+\mathscr{C}^{ld+}(f_l) \tag{C.12}$$

$$\begin{aligned}\frac{\partial f_l}{\partial t}+\boldsymbol{c}\frac{\partial f_l}{\partial \boldsymbol{x}}+\frac{\partial \boldsymbol{a}_l f_l}{\partial \boldsymbol{c}}= \;& R_l\iint_{\mathbb{R}^2}\nu_d f_d(\xi',\boldsymbol{c}')b_l(\xi',\boldsymbol{c}',\xi)\beta_l(\xi',\boldsymbol{c}',\boldsymbol{c})\mathrm{d}\xi'\mathrm{d}\boldsymbol{c}' \\ & -\nu_l f_l+\chi_\alpha \boldsymbol{D}_\xi^\alpha f_l+K_2\frac{\partial f_l}{\partial \xi}-\mathscr{C}^{ld-}(f_l)\end{aligned} \tag{C.13}$$

The accelerations $\boldsymbol{a}_p(\boldsymbol{c},\xi)$ depend in general on the droplet shape ξ and the relative velocity $\boldsymbol{c}$. For the sake of simplicity, the velocity kernels are taken monokinetic i.e. with a zero dispersion $\beta_p=\delta\big(\boldsymbol{c}-\boldsymbol{u}_p^{bu}\big)$ and the target relative velocity $\boldsymbol{u}_p^{bu}(\xi',\boldsymbol{c}')$ is computed from the mother droplet so that the rim droplets have a Weber number slightly below We_b^- to stop the breakage (Note that the spurious succeeding cascade

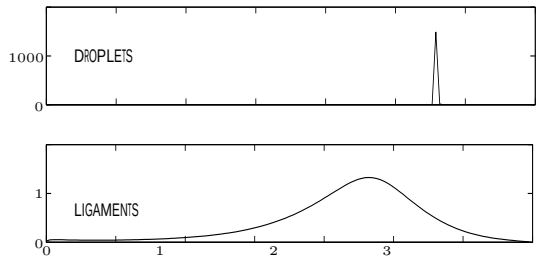

Figure C.6: *NDF of droplets and of ligaments with the Two-Layer GPBE model.*

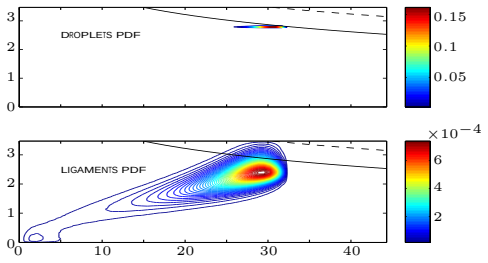

Figure C.7: *NDF in magnitude-velocity space. Dotted and solid line limit* $We_b^- < We < We_b^+$.

of fragmentations of § C.4.1 are naturally eliminated in this process). We highlight that the choice of $\boldsymbol{u}_p^{bu}$ models the integral effect of drag during the discrete break-up process: so it requires a counterpart term for the the carrier phase equations to enforce momentum conservation in a two-way coupling context.
see discussion in § 3.3.4.4
A schematic description of the overall liquid behavior in the two-layer phase space can be found in Figure C.5. The spray break-up is now computed with the Two-Layer GPBE model with the same initial conditions as previously. Because such kinetic equations have a prohibitive cost, we remove the physical space dependence on $\boldsymbol{x}$ by considering the problem homogeneous analogously to well-stirred reactor hypotheses in chemistry and the velocity is 1D. We take for the sake of simplicity $\boldsymbol{a}_p = \boldsymbol{g} - \rho_l \mathrm{Surf}(\xi) C_d |\boldsymbol{c}| \boldsymbol{c}$ with $C_d = 1.0$ for both droplets and ligaments, $\boldsymbol{g}$ stands for the gravity. Results after $5\tau_{\mathrm{RN}}$ are given for the NDF in Figure C.6 and the behavior in phase space can be found in Figure C.7. The shape of the experimental NDF in Figure C.2 is again recovered according to the *ad hoc* choice of the stochastic process.

C.5 Two-population MF model

The Two-Layer GPBE model has been computed with a 0D physical and 1D velocity space for cost-cutting reasons but the full picture is heterogeneous and 3D. The purpose of this section is to show how to reduce the full model to a set of conservation equations on the physical space for the approach to be easily included into CFD softwares e.g. for diesel injection (Kah 2010) or solid rocket motors (Doisneau et al. 2013).

C.5.1 Velocity moment method: the Semi-kinetic Model

In a first step we reduce the Two-Layer GPBE phase spaces to the only droplet size variable. We consider velocity moments that are the number density $n_p = \int_{\mathbb{R}} f_p(\xi, \boldsymbol{c}) \mathrm{d}\boldsymbol{c}$ and the average momentum $n_p \boldsymbol{u}_p = \int_{\mathbb{R}} \boldsymbol{c} f_p(\xi, \boldsymbol{c}) \mathrm{d}\boldsymbol{c}$. In order to close the system, the NDFs are approximated according to a monokinetic hypothesis:

$$f_p(\xi, \boldsymbol{c}) = n_p(\xi) \delta(\boldsymbol{c} - \boldsymbol{u}_p) \tag{C.14}$$

which means that for a given size ξ and location $(t, \boldsymbol{x})$, the only characteristic velocity is the average $\boldsymbol{u}_p(t, \boldsymbol{x}, \xi)$ while the velocity dispersion around $\boldsymbol{u}_p(t, \boldsymbol{x}, \xi)$ is zero in each direction. This assumption is correct when the drag force characteristic time is small compared to the local gas characteristic dynamic time (Massot et al. 2009). This step leads to two systems of conservation equations called semi-kinetic, which read:

$$\begin{cases} \partial_t n_d + \partial_{\boldsymbol{x}} \cdot (n_d \boldsymbol{u}_d) & = -\mathscr{B}^{n_d -} + \mathscr{B}^{n_d d+} & + \mathscr{C}^{n_l d+} \\ \partial_t (n_d \boldsymbol{u}_d) + \partial_{\boldsymbol{x}} \cdot (n_d \boldsymbol{u}_d \otimes \boldsymbol{u}_d) & = -\mathscr{B}^{u_d -} + \mathscr{B}^{u_d d+} & + \mathscr{C}^{u_l d+} + n_d \overline{\boldsymbol{a}}_d \end{cases} \tag{C.15}$$

$$\begin{cases} \partial_t n_l + \partial_{\boldsymbol{x}} \cdot (n_l \boldsymbol{u}_l) & = & \mathscr{B}^{n_d l+} - \mathscr{B}^{n_l -} + \mathscr{B}^{n_l l+} - \mathscr{C}^{n_l d-} \\ \partial_t (n_l \boldsymbol{u}_l) + \partial_{\boldsymbol{x}} \cdot (n_l \boldsymbol{u}_l \otimes \boldsymbol{u}_l) & = & \mathscr{B}^{u_d l+} - \mathscr{B}^{u_l -} + \mathscr{B}^{u_l l+} - \mathscr{C}^{u_l d-} + n_l \overline{\boldsymbol{a}}_l \end{cases} \tag{C.16}$$

where one gets, still with $p \in \{d, l\}$, the average acceleration $n \overline{\boldsymbol{a}}_p = \int_{\mathbb{R}} \boldsymbol{a}_p f \mathrm{d}\boldsymbol{c}$, the break-up disappearance terms $\mathscr{B}^{n_p -} = \nu_p n_p$ and $\mathscr{B}^{u_d -} = \nu_p n_p \boldsymbol{u}_p$ and the break-up creation terms:

$$\begin{aligned} \mathscr{B}^{n_d p+} &= R_p \int_{\mathbb{R}} \nu_d n_d(\xi') b_p(\xi', \xi) \mathrm{d}\xi' & \mathscr{B}^{u_d p+} &= R_p \int_{\mathbb{R}} \nu_d n_d(\xi') b_p(\xi', \xi) \boldsymbol{u}_p^{bu}\big(\xi', \boldsymbol{u}_d(\xi')\big) \mathrm{d}\xi' \\ \mathscr{B}^{n_l l+} &= \nu_l \chi_\alpha \boldsymbol{D}_\xi^\alpha n_l(\xi) + K_2 \frac{\partial n_l}{\partial \xi}(\xi) & \mathscr{B}^{u_l l+} &= \nu_l \chi_\alpha \boldsymbol{D}_\xi^\alpha (n_l \boldsymbol{u}_l)(\xi) + K_2 \frac{\partial n_l \boldsymbol{u}_l}{\partial \xi}(\xi) \end{aligned} \tag{C.17}$$

C.5.2 Size discretization: the Multi-Fluid model

The phase space of the semi-kinetic system has too high a dimension and requires therefore further modeling. So we move to the Eulerian Multi-Fluid (MF) model (Massot et al. 2009). The MF method has already been used for break-up modeling with presumed NDFs by Dufour et al. (2003); Doisneau et al. (2013). We choose two discretizations $-\infty = \xi_{p,0} < \xi_{p,1} < \cdots < \xi_{p,N_p} = \infty$ for the droplet and ligament size phase spaces and we average the conservation law systems (C.15) and (C.16) over each fixed size interval $\mathcal{S}_{p,k} = [\xi_{p,k-1}, \xi_{p,k}[$, called section. The set of droplets or ligaments in one section can be seen as a "fluid" for which conservation equation are written, the sections exchanging mass and momentum. Some size moments are considered, the number of which increases accuracy and cost. In our case and as an illustration, we choose to conserve number and mass $(n_{p,k}\ ,\ m_{p,k}) = \int_{\mathcal{S}_{p,k}} \big(1,\ \rho_l \mathcal{V}_p(\xi)\big) n_p \mathrm{d}\xi$ which corresponds to the Two-Size Moment method, proven to be efficient in industrial simulations with strong droplet distribution variations e.g. due to coalescence (Doisneau et al. 2013). The following size distribution forms are also presumed:

$$n_p(\xi) = \sum_{k=1}^{N_p} \kappa_{p,k}(\xi) \mathbf{1}_{\mathcal{S}_{p,k}}(\xi) \tag{C.18}$$

corresponding to assume in each section a different form for n_p as a function of ξ (e.g. piecewise linear functions), a different velocity $\boldsymbol{u}_{p,k}$ as constant of ξ, and eventually a different shape to define $\mathcal{V}_p(\xi)$, $\mathrm{Surf}_p(\xi)$ *etc.* We finally get conservation equations with source terms for droplets and ligaments of section k:

$$\left\{\begin{array}{ll} \partial_t n_{d,k} + \partial_{\boldsymbol{x}} \cdot (n_{d,k} \boldsymbol{u}_{d,k}) & = -\mathscr{B}_k^{n_d -} + \mathscr{B}_k^{n_d d+} + \mathscr{C}_k^{n_l d+} \\ \partial_t m_{d,k} + \partial_{\boldsymbol{x}} \cdot (m_{d,k} \boldsymbol{u}_{d,k}) & = -\mathscr{B}_k^{m_d -} + \mathscr{B}_k^{m_d d+} + \mathscr{C}_k^{m_l d+} \\ \partial_t (m_{d,k} \boldsymbol{u}_{d,k}) + \partial_{\boldsymbol{x}} \cdot (m_{d,k} \boldsymbol{u}_{d,k} \otimes \boldsymbol{u}_{d,k}) & = -\mathscr{B}_k^{u_d -} + \mathscr{B}_k^{u_d d+} + \mathscr{C}_k^{u_l d+} + m_{d,k} \overline{\boldsymbol{a}}_{d,k} \end{array}\right. \tag{C.19}$$

$$\left\{\begin{array}{ll} \partial_t n_{l,k} + \partial_{\boldsymbol{x}} \cdot (n_{l,k} \boldsymbol{u}_{l,k}) & = \mathscr{B}_k^{n_d l+} - \mathscr{B}_k^{n_l -} + \mathscr{B}_k^{n_l l+} - \mathscr{C}_k^{n_l d-} \\ \partial_t m_{l,k} + \partial_{\boldsymbol{x}} \cdot (m_{l,k} \boldsymbol{u}_{l,k}) & = \mathscr{B}_k^{m_d l+} - \mathscr{B}_k^{m_l -} + \mathscr{B}_k^{m_l l+} - \mathscr{C}_k^{m_l d-} \\ \partial_t (m_{l,k} \boldsymbol{u}_{l,k}) + \partial_{\boldsymbol{x}} \cdot (m_{l,k} \boldsymbol{u}_{l,k} \otimes \boldsymbol{u}_{l,k}) & = \mathscr{B}_k^{u_d l+} - \mathscr{B}_k^{u_l -} + \mathscr{B}_k^{u_l l+} - \mathscr{C}_k^{u_l d-} + m_{l,k} \overline{\boldsymbol{a}}_{l,k} \end{array}\right. \tag{C.20}$$

where the drag terms are $m_{p,k}\overline{\boldsymbol{a}}_{p,k} = \int_{\mathcal{S}_{p,k}} \rho_l \mathcal{V}_p(\xi) \kappa_{p,k}(\xi) \overline{\boldsymbol{a}}_p \mathrm{d}\xi$, the disappearance terms are:

$$\begin{pmatrix} \mathscr{B}_k^{n_p -} \\ \mathscr{B}_k^{m_p -} \\ \mathscr{B}_k^{u_p -} \end{pmatrix} = \int_{\mathcal{S}_{p,k}} \nu_p \begin{pmatrix} 1 \\ \rho_l \mathcal{V}_p(\xi) \\ \rho_l \mathcal{V}_p(\xi) \boldsymbol{u}_{p,k} \end{pmatrix} \kappa_{p,k}(\xi) \mathrm{d}\xi \tag{C.21}$$

the discrete creation terms see the inner integral decomposed (Dufour et al. 2003):

$$\begin{pmatrix} \mathscr{B}_k^{n_d p+} \\ \mathscr{B}_k^{m_d p+} \\ \mathscr{B}_k^{u_d p+} \end{pmatrix} = \int_{\mathcal{S}_{p,k}} R_p \sum_{i=1}^{N_d} \int_{\mathcal{S}_{d,i}} \nu_d \begin{pmatrix} 1 \\ \rho_l \mathcal{V}_d(\xi) \\ \rho_l \mathcal{V}_d(\xi) \boldsymbol{u}_p^{bu}(\xi', \boldsymbol{u}_{d,i}) \end{pmatrix} \kappa_{d,i}(\xi') b_p(\xi', \xi) \mathrm{d}\xi' \mathrm{d}\xi \tag{C.22}$$

and the ligament continuous creation terms are integrals:

$$\begin{pmatrix} \mathscr{B}_k^{n_l l+} \\ \mathscr{B}_k^{m_l l+} \\ \mathscr{B}_k^{u_l l+} \end{pmatrix} = \int_{\mathcal{S}_{l,k}} \nu_l \chi_\alpha \begin{pmatrix} \boldsymbol{D}_\xi^\alpha n_l(\xi) \\ \rho_l \mathcal{V}_l(\xi) \boldsymbol{D}_\xi^\alpha n_l(\xi) \\ \rho_l \mathcal{V}_l(\xi) \boldsymbol{D}_\xi^\alpha n_l(\xi) \boldsymbol{u}_{l,k} \end{pmatrix} \mathrm{d}\xi + \int_{\mathcal{S}_{l,k}} K_2 \begin{pmatrix} \partial_\xi n_l(\xi) \\ \rho_l \mathcal{V}_l(\xi) \partial_\xi n_l \\ \rho_l \mathcal{V}_l(\xi) \partial_\xi n_l \boldsymbol{u}_{l,k} \end{pmatrix} \mathrm{d}\xi \tag{C.23}$$

of first order size derivatives (on the right in (C.23)) that are computed as evaporation terms *i.e.* they become fluxes from/to neighbor sections (Kah 2010) and of fractional derivatives which are in fact integro-differential operators which couple all sections. So the overall system is closed and can be computed with methods from the literature.

C.6 Conclusion on moderately dense break-up modeling

The limits of the presumed PDF approach for break-up, namely the suppression of dynamical aspects of break-up and the arising stiffness of the model can then be overcome: the re-examination of the sphericity assumption, together with additional modeling efforts on stochastic processes for coupled droplet-turbulence interactions, allow to reintroduce a dynamics in the source terms which is a crucial point as regards model and methods in the context of two-way coupling atomization. The experiments conducted at LEMTA give detailed information on the size and velocity of fragments and allows therefore to introduce a first modeling for the coupling dynamics.

This approach is an interesting prospection on the possibilities of Eulerian modeling and shows the potential of the proposed approach to other areas of research.

Appendix D

A kinetic-kinetic approach for two-way coupled nanoparticle flows

A kinetic-kinetic coupled approach is considered to deal with a flow carrying a heavy loading of nanoparticles. The approach yields a new insight on nanoparticle transport, in the context of moderately dense flows, thanks to an expansion based on the mass ratio between gas molecules and nanoparticles.

D.1 Kinetic approach for unbalanced particles

We consider a two-phase disperse flow with nanometric particles. The goal is to shed light on the complex behavior of the two phases by statistically accounting for the interactions between particles and gas molecules, namely the collisions. The Boltzmann and Williams-Boltzmann equations can be chosen to model molecules and particles respectively, at the kinetic level. The molecules are treated through a NDF $f_g(t, \boldsymbol{x}, \boldsymbol{c}_g)$ and the particles are treated through a second NDF $f_p(t, \boldsymbol{x}, \boldsymbol{c}_p, S, T_p)$.
In the following, we do not examine the role of polydispersity nor temperature. If we except the droplet degrees of freedom that are size and internal energy, we formally account for the same physics than that of a gas mixture: the system, as composed of two kinetic equations, is *a fortiori* more complex to solve than the single Boltzmann equation or than the fluid-kinetic approach. In the literature, kinetic equations describing different sorts of particles and coupled through collisions can be found:

- Waldman (1959) has introduced the kinetic theory for multicomponent flows.
- Graille et al. (2009) have described a plasma with out-of-equilibrium translational energies through multiple kinetic equations and they have obtained a well-posed system with an entropy principle, from the consideration of the unbalanced mass between electrons and the other particles (neutrals and ions).
- An unbalanced collisional kinetic approach has also been used to treat aerosols in rarefied gases (Charles and Desvillettes 2009; Charles 2009; Charles et al. 2012).

We therefore focus in the following on a perturbation expansion based on the unbalanced mass ratio between particles and molecules, this being inspired from Graille et al. (2009). The approach allows to derive a fluid-kinetic model that includes the coupling terms between the gas and the particles, the kinetic and fluid levels being presented in Figure D.1. The derivation of the fluid model from both particle and gas coupled kinetic models is to be compared to the usual fluid kinetic approach presented in Figure 3.25, where the gas fluid model is derived alone.

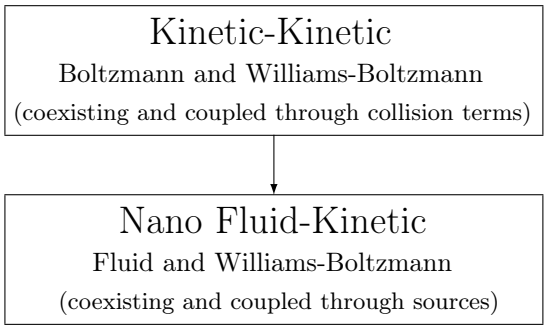

Figure D.1: *Kinetic-kinetic model and derivation of a coupled nanometric disperse two-phase model*

D.1.1 Orders of magnitude and scaling

The orders of magnitude are marked with a 0 exponent. They are now analyzed as they are crucial for the physical understanding of the problem, its dimensionless recasting and the expansion approach.

D.1.1.1 Expansion parameter

The expansion is performed according to the dimensionless parameter ε, defined from the molecule-particle mass ratio:

$$\varepsilon = \sqrt{\frac{m_g^0}{m_p^0}} \tag{D.1}$$

In the following, we refer to molecules as the lightweight population and to particles as the heavyweight population.

D.1.1.2 Microscopic velocities and number concentrations

We assume that heavies and lights have a comparable kinetic energy:

[K1] $$\tfrac{1}{2} m_g^0 (v_g^0)^2 = \tfrac{1}{2} m_p^0 (v_p^0)^2$$

which is an unusual assumption in two-phase flow modeling. In our case, energy is redistributed through molecule-particle collisions and the overall microscopic energy is shared among molecules and particles, provided that the latter are sufficiently small. Whenever particles become too big, they encounter many collisions at once and they no longer react because of their inertia, so that only the average effect of collisions remains, resulting in recovering the usual fluid drag with a weak stochastic motion. The microscopic energy associated to big particles is much smaller than that of the gas and therefore neglected. But here, it is comparable: the nanoparticles are said to be thermalized.
From the microscopic energy equipartition, we get a comparison of the typical velocities:

$$\frac{v_p^0}{v_g^0} = \sqrt{\frac{m_g^0}{m_p^0}} = \varepsilon \tag{D.2}$$

so that particle and gas velocity scales are separated by an order of magnitude. This relation justifies the choice made to define ε, the power 1/2 in Eq. (D.1) corresponds in fact to a scaling in terms of velocity orders. So that ε is the order of magnitude of particle velocities for a unit molecule velocity.
We now focus on number densities. In the case of plasmas, electroneutrality guarantees comparable number densities between lightweight electrons and heavy ions. Our assumption here is rather that mass fractions are comparable so that the number concentrations are strongly separated:

[K2] $$m_g^0 n_g^0 = m_p^0 n_p^0$$

As a consequence, the molecules are remarkably more numerous than the particles:

$$n_p^0 = \varepsilon^2 n_g^0 \tag{D.3}$$

The number density functions are then deduced from Eq. (D.2) and Eq. (D.3):

$$f_i^0 = \frac{n_i^0}{(v_i^0)^3} \quad , \qquad i \in \{g, p\} \tag{D.4}$$

D.1.1.3 Collision cross sections and mean free paths

The cross sections σ_{ij}^0, $(i,j) \in \{g,p\}^2$ render the physics of the molecule-molecule, molecule-particle, and particle-particle collision interactions. They feature a symmetry $\sigma_{pg}^0 = \sigma_{gp}^0$.
They cannot be assessed given the size and number densities so that they should be modeled.
For two-phase computations, the cross sections are put in dimensionless form by using σ_{gg}^0 as a reference since it is usually better known:

$$\begin{aligned} \sigma_{pp}^0 &= \varepsilon^{\chi_1} \sigma_{gg}^0 \\ \sigma_{pg}^0 &= \varepsilon^{\chi_2} \sigma_{gg}^0 \end{aligned} \tag{D.5}$$

We introduce the possible assumptions:

$i\backslash j$	g	p
g	1	$\varepsilon^{-\chi-2}$
p	$\varepsilon^{-\chi}$	$\varepsilon^{-\chi-2}$

Table D.1: *Cross sections σ_{ij}^0 relative positions.*

- equality $\chi_1 = \chi_2 = 0$ as in plasma physics (Graille et al. 2009),
- geometric $\chi_1 = \chi_2 = -\frac{4}{3}$,
- simplification $\chi_1 = \chi_2 = \chi = -1$.

The latter assumptions mimics the geometric decrease but with an integer exponent so we retain this as an assumption:

[K3] $$\sigma_{pp}^0 = \tfrac{1}{\varepsilon}\sigma_{gg}^0$$

The mean free path l_{ij}^0 is defined as the average distance of $i \in \{g, p\}$ between two collisions with $j \in \{g, p\}$. It is computed from the number of collision partners j and the cross-section between i et j:

$$l_{ij}^0 = \frac{1}{n_j^0 \sigma_{ij}^0} \tag{D.6}$$

so that mean free paths can be compared thanks to the number hierarchy of Eq. (D.3) and the cross-section hierarchy of Eq. (D.5), as done in Table D.1.
The mean free path is of course much smaller in the gas than in the particle phase: they are separated by two orders in ε since the latter is much more dilute. The mean free path of a species in its own phase defines the kinetic time:

$$t_g^0 = \frac{l_{gg}^0}{v_g^0} \qquad \text{et} \qquad t_p^0 = \frac{l_{pp}^0}{v_p^0} = \varepsilon^{-\chi-3} t_g^0 \tag{D.7}$$

that is the time which is hypothetically needed for the phase alone to reach an equilibrium state. In a multi-species case, equilibrium may not be reached.

D.1.1.4 Time scales

The choice of the time scale t^0 is crucial as it defines the level of detail of the model. The problem is studied as regards the collision times, which are known as number densities, velocities and cross sections have been estimated.
We choose not to solve for the gas relaxation time in order to get a fluid approach. The gas NDF f_g is assumed to be close to equilibrium, allowing a Chapman-Enskog expansion. So we have to choose a time scale that is large compared to the gas relaxation time of Eq. (D.7):

[K4] $$t^0 = \tfrac{1}{\varepsilon} t_g^0$$

As a consequence, the particle kinetic time is larger compared to the characteristic time of the study

$$t_p^0 = \frac{1}{\varepsilon^{2+\chi}} t^0 \tag{D.8}$$

and f_p is far from its own collisional equilibrium. Still a fluid approach is made possible thanks to the effects of the underlying gas fluid.
For $\chi \geq -1$, we get the following bracketing of the characteristic time between the short gas time and the large particle time:

$$t_g^0 \ll t^0 \ll t_p^0 \tag{D.9}$$

This is a major difference with plasma physics where the two classes of particles are relaxed, therefore yielding two temperatures.

D.1.1.5 Macroscopic scales

We consider the macroscopic densities and velocities for each phase ρ_i et $\boldsymbol{v}_i$, $i \in \{g, p\}$:

$$\begin{aligned} \rho_i &= \int m_i f_i \mathrm{d}\boldsymbol{c}_i \\ \rho_i \boldsymbol{v}_i &= \int m_i f_i \boldsymbol{c}_i \mathrm{d}\boldsymbol{c}_i \end{aligned} \tag{D.10}$$

With $\rho = \rho_p + \rho_g$ the mixture density, we can define the hydrodynamic velocity $\boldsymbol{v}_h$ of the mixture from the mixture momentum $\rho\boldsymbol{v}_h = \rho_p\boldsymbol{v}_p + \rho_g\boldsymbol{v}_g$:

$$\left(\int m_p f_p \mathrm{d}\boldsymbol{c}_p + \int m_g f_g \mathrm{d}\boldsymbol{c}_g\right)\boldsymbol{v}_h = \int m_p f_p \boldsymbol{c}_p \mathrm{d}\boldsymbol{c}_p + \int m_g f_g \boldsymbol{c}_g \mathrm{d}\boldsymbol{c}_g \tag{D.11}$$

The hydrodynamic velocity corresponds to the velocity of the local mixture mass center. It can be seen as the mixture velocity, in the reference of which the two phases may drift.
We define v_h^0 the order of magnitude of the hydrodynamic velocity and we use it as the characteristic macroscopic velocity in order to put the macroscopic velocity scales of the problem in a dimensionless form. The choice of a typical length scale l^0 originates from the choice of a macroscopic velocity and a time scale:

$$l^0 = t^0 v_h^0 \tag{D.12}$$

The order of magnitude of the macroscopic forces per unit mass is noted F^0 and is evaluated with the scales:

$$F^0 = \frac{l^0}{(t^0)^2} \tag{D.13}$$

The chosen time scale allows us to consider the gas distribution close to its equilibrium, see the hierarchy of Eq. (D.9) so that f_g is close to a Maxwell-Boltzmann distribution, which is given in Eq. (3.119). A local temperature can therefore be defined which represents the internal energy of the agitated molecules.
Its order of magnitude is noted T^0, and it can be evaluated either from the knowledge of the molecule microscopic kinetic energy or from the particle microscopic energy, thanks to [K1]:

$$kT^0 = \frac{1}{2}m_g^0(v_g^0)^2 = \frac{1}{2}m_p^0(v_p^0)^2 \tag{D.14}$$

where k is the microscopic Boltzmann constant.

D.1.1.6 Scale recapitulation and comparison

The different orders of magnitude are given in Table D.2 with their orders compared to the reference quantities with exponent 0.

Quantity \ Order	2	1	0	−1	−2	Justification
Dimen. param	ε^2	ε	1	ε^{-1}	ε^{-2}	
Mass	m_g^0		m_p^0			Definition of ε in Eq. (D.1)
Velocity (*low Mach*)			v_p^0	v_g^0		Assumption [K1]
Velocity (*full Mach*)		v_p^0	v_g^0			*idem*
Number density			n_p^0		n_g^0	Assumption [K2]
NDF		f_g^0	f_p^0			Relations (D.2) and (D.3)
Cross-section			σ_{gg}^0	σ_{pp}^0		Assumption [K3]
Time		t_g^0	t^0	t_p^0		Assumption [K4]
Length		l_{gg}^0	l^0	l_{pp}^0		Relation (D.6)
Macro-velocity			v_h^0			

Table D.2: *Relative position of orders of magnitude and reference quantities.*

D.1.2 A change of scale and of reference frame

D.1.2.1 Principle of equation scaling

Dimensionless equations are obtained by dividing variables and equations by their reference quantities: the latter are linked to the orders of magnitudes i.e. defining the first order and given in Table D.2, through ε.

Scaling	M_g	M_p
Low-Mach	ε	1
Full-Mach	1	$1/\varepsilon$

Table D.3: *Orders of the pseudo Mach numbers in low and full Mach scalings.*

As a result the equation features terms of order one with eventually a power of the expansion parameter ε to figure out the effective order of the grouping. The dependency on ε reflects a crucial information on the physics of the different terms, materializing the scaling of the equation.
In order to distinguish them, the dimensionned variables are noted with the exponent $\star$. This allows to decompose any quantity thanks to its order of magnitude g^0 and a new dimensionless variable g

$$g^\star = g^0 g \tag{D.15}$$

If g is of order one by design, g^0 is not necessarily and should be replaced by a reference order of magnitude (from Table D.2) thanks to the correspondences defined above, exhibiting the order in ε and the scale separation.

D.1.2.2 Pseudo Mach numbers

The flow characteristic velocity v_h^0 allows to define pseudo Mach numbers, which are dimensionless velocities. The usual Mach number is the ratio of the fluid macroscopic velocity to the speed of sound. The latter corresponds to the maximum speed of a perturbation, which is in fact the (agitation) velocity of the underlying molecules at the microscopic level: the relation $c = \sqrt{\gamma r T}$ is the link between these two visions. So the Mach number can be seen as the ratio of a macroscopic "ordered" velocity to a microscopic "disordered" velocity.
By analogy, we define the pseudo-Mach number M_i of species i as the ratio between the hydrodynamic velocity v_h^0 and the microscopic velocity of the species v_i^0:

$$M_i = \frac{v_h^0}{v_i^0}. \tag{D.16}$$

Two cases can occur, depending on if v_h^0 is closer to the microscopic velocity of the particles or to that of the gas, which are given in Table D.3.
These pseudo-Mach numbers will appear in the following dimensionless equations. Depending on the scaling case, we will express all of them depending on the one that is closer to 1.
From now, we assume the case of a Full-Mach scaling:

[K5] $$M_g \sim 1$$

with the corresponding order of $M_g = \epsilon^{-1}$.

D.1.2.3 Choice of a reference frame and peculiar velocities

The hydrodynamic velocity is chosen *a priori* as the reference frame: this frame is non-inertial but still a classical choice for kinetic studies (Ferziger and Kaper 1972).
The hydrodynamic velocity $\boldsymbol{v}_h^\star$ is defined in Eq. (D.11) so that the peculiar velocities of $i \in \{p, g\}$ read in this frame:

$$\boldsymbol{c}_i^\star = \boldsymbol{C}_i^{\star \boldsymbol{v}_h^\star} + \boldsymbol{v}_h^\star \tag{D.17}$$

This choice is paradoxical to study the flow itself but relevant to detail the drift of particles in the mean flow.
In the plasma case, the heavy species had most of the mass so that their mean velocity was equal at first order to the hydrodynamic velocity, therefore canceling their drift velocity. Here, the hydrodynamic velocity receives contributions at the same order from both species so that no drift velocity cancels by construction.
The change of reference frame for dimensionless velocities read in the context of the full-Mach scaling [K5]:

$$\begin{aligned} \boldsymbol{c}_p &= \boldsymbol{C}_p^{\boldsymbol{v}_h} + \frac{1}{\varepsilon} M_g \boldsymbol{v}_h \\ \boldsymbol{c}_g &= \boldsymbol{C}_g^{\boldsymbol{v}_h} + M_g \boldsymbol{v}_h \end{aligned} \tag{D.18}$$

After defining the notation $\beta = M_g^{-1}$, we have the dimensionless hydrodynamic velocity from Eq. (D.11):

$$\begin{array}{ll} \left(\int m_p^\star f_p^\star \mathrm{d}\boldsymbol{c}_p^\star \quad + \quad \int m_g^\star f_g^\star \mathrm{d}\boldsymbol{c}_g^\star\right) & \boldsymbol{v}_h^\star = \int m_p^\star f_p^\star \boldsymbol{c}_p^\star \mathrm{d}\boldsymbol{c}_p^\star + \int m_g^\star f_g^\star \boldsymbol{c}_g^\star \mathrm{d}\boldsymbol{c}_g^\star \\ \left(m_p^0 \frac{n_p^0}{(v_p^0)^3}(v_p^0)^3\rho_p + m_g^0 \frac{n_g^0}{(v_g^0)^3}(v_g^0)^3\rho_g\right) v_h^0 \boldsymbol{v}_h = n_p^0 v_p^0 \rho_p \boldsymbol{v}_p & + n_g^0 v_g^0 \rho_g \boldsymbol{v}_g \end{array} \tag{D.19}$$

which reads after simplification:

$$(\alpha\rho_p + \rho_g)\boldsymbol{v}_h = \varepsilon\,\alpha\beta\rho_p\boldsymbol{v}_p + \beta\rho_g\boldsymbol{v}_g. \tag{D.20}$$

when defining $\alpha = \frac{m_p^0 n_p^0}{m_g^0 n_g^0}$ the ratio of the particle and gas volume fractions. We insist on the fact that the dimensionless quantity α is of order of one.

D.1.2.4 Species drift velocities

In the hydrodynamic reference frame, the motion of the gas and the disperse phase can be interpreted as a species diffusion, which is the main upheaval of the nanometric two-phase model: the approach is that of a multi-species mixture.
The drift velocities in the hydrodynamic reference frame $\boldsymbol{V}_i^{\boldsymbol{v}_h}$ are macroscopic velocities, therefore computed by a kinetic integral:

$$\begin{aligned} \rho_g \boldsymbol{V}_g^{\boldsymbol{v}_h} &= \int m_g f_g \boldsymbol{C}_g^{\boldsymbol{v}_h} \mathrm{d}\boldsymbol{C}_g^{\boldsymbol{v}_h} \\ \rho_p \boldsymbol{V}_p^{\boldsymbol{v}_h} &= \int m_p f_p \boldsymbol{C}_p^{\boldsymbol{v}_h} \mathrm{d}\boldsymbol{C}_p^{\boldsymbol{v}_h} \end{aligned} \tag{D.21}$$

where the change of frame Eq. (D.20) allows to exhibit the scaling:

$$(\alpha\rho_p + \rho_g)\boldsymbol{v}_h = \varepsilon\,\alpha\beta \int m_p f_p \left(\boldsymbol{C}_p^{\boldsymbol{v}_h} + \tfrac{1}{\varepsilon} M_g \boldsymbol{v}_h\right) \mathrm{d}\boldsymbol{C}_p^{\boldsymbol{v}_h} + \beta \int m_g f_g \left(\varepsilon \boldsymbol{C}_g^{\boldsymbol{v}_h} + M_g \boldsymbol{v}_h\right) \mathrm{d}\boldsymbol{C}_g^{\boldsymbol{v}_h} \tag{D.22}$$

which finally yields:

$$0 = \varepsilon\alpha\beta\rho_p \boldsymbol{V}_p^{\boldsymbol{v}_h} + \rho_g \boldsymbol{V}_g^{\boldsymbol{v}_h}. \tag{D.23}$$

This intrinsic equation translates momentum conservation.
Now that the reference frame is chosen, we may simplify the notations

$$\begin{aligned} \boldsymbol{C}_g^{\boldsymbol{v}_h} &= \boldsymbol{C}_g, & \boldsymbol{V}_g^{\boldsymbol{v}_h} &= \boldsymbol{V}_g, \\ \boldsymbol{C}_p^{\boldsymbol{v}_h} &= \boldsymbol{C}_p, & \boldsymbol{V}_p^{\boldsymbol{v}_h} &= \boldsymbol{V}_p, \end{aligned} \tag{D.24}$$

keeping in mind that the relation Eq. (D.23) applies, in the hydrodynamic reference frame.

D.1.3 Kinetic modeling of a mixture

All the interactions between particles and molecules can be described through the collisions.

D.1.3.1 General case

Kinetic theory may be generalized to several species (see for instance Bond et al. 1965): the evolution of the NDF $f_i^\star$ of each species $i \in [\![1, N]\!]$ is described by its own Boltzmann equation, in which all the possible collisions must be accounted for:

$$\partial_{t^\star} f_i^\star + \boldsymbol{c}_i^\star \cdot \partial_{\boldsymbol{x}^\star} f_i^\star + \boldsymbol{F}^\star \cdot \partial_{\boldsymbol{c}_i^\star} f_i^\star = \sum_{j=1}^{N} \mathcal{J}_{ij}^\star(f_i^\star, f_j^\star)\ , \qquad i \in [1, N] \tag{D.25}$$

where $\boldsymbol{F^\star}_i$ is the force per unit mass on species i e.g. gravity, Lorentz force or inertial force. The collision operator of species j on species i reads in most general form:

$$\mathcal{J}_{ij}^\star(f_i^\star, f_j^\star) = \iint (f_i^{\star'} f_j^{\star'} - f_i^\star f_j^\star) \mid \boldsymbol{c}_i^\star - \boldsymbol{c}_j^\star \mid \sigma_{ij}^\star \mathrm{d}\boldsymbol{\omega} \mathrm{d}\boldsymbol{c}_j^\star\ , \qquad (i, j) \in [\![1, N]\!]^2 \tag{D.26}$$

where the quantities after collision have the exponent $'$. The cross-sections read:

$$\sigma_{ij}^\star = \sigma_{ij}^\star(\mu_{ij}^\star, |\boldsymbol{c}_i^\star - \boldsymbol{c}_j^\star|^2/(kT^0), \boldsymbol{\omega}\cdot\boldsymbol{e}) \tag{D.27}$$

which depend on the relative kinetic energy of the colliding particles, on the angle between the relative velocities, and on the reduced mass:

$$\boldsymbol{\omega} = (\boldsymbol{c}_i^{\star'} - \boldsymbol{c}_j^{\star'})/|\boldsymbol{c}_i^{\star'} - \boldsymbol{c}_j^{\star'}| \tag{D.28}$$

$$\boldsymbol{e} = (\boldsymbol{c}_i^\star - \boldsymbol{c}_j^\star)/|\boldsymbol{c}_i^\star - \boldsymbol{c}_j^\star| \tag{D.29}$$

$$\mu_{ij}^\star = m_i^\star m_j^\star/(m_i^\star + m_j^\star). \tag{D.30}$$

In the equation of each species, the usual mono-species Boltzmann collision operator is included in the summation for $j = i$, while the other operators $j \neq i$ ensure the coupling between the species.

D.1.3.2 Particular case of a disperse two-phase flow

We now consider a disperse two-phase flow, where the inclusions are nanometric and in free molecular regime, so that the flow can be treated as a multi-species gas. The kinetic equations of the mixture are inspired from Eq. (D.25):

$$\begin{cases} \mathscr{D}_g^\star(f_g^\star) = \mathscr{J}_{gg}^\star(f_g^\star, f_g^\star) + \mathscr{J}_{gp}^\star(f_g^\star, f_p^\star) \\ \mathscr{D}_p^\star(f_p^\star) = \mathscr{J}_{pp}^\star(f_p^\star, f_p^\star) + \mathscr{J}_{pg}^\star(f_p^\star, f_g^\star) \end{cases} \tag{D.31}$$

where the collision terms are obtained by taking $i, j \in g, p$ in Eq. (D.26) and where the transport operator is noted:

$$\mathscr{D}_i^\star(f_i^\star) = \partial_{t^\star} f_i^\star + \boldsymbol{c}_i^\star \cdot \partial_{\boldsymbol{x}^\star} f_i^\star + \boldsymbol{F}^\star \cdot \partial_{\boldsymbol{c}_i^\star} f_i^\star\ , \qquad i \in \{g, p\} \tag{D.32}$$

We now write the dimensionless equations, in the chosen reference frame.

D.1.3.3 Coordinate change

The dimensionless recasting and the change in reference frame translate into a change in coordinates:

$$(t^\star, \boldsymbol{x}^\star, \boldsymbol{c}_i^\star) \to (t, \boldsymbol{x}, \boldsymbol{C}_i) \tag{D.33}$$

where the dimensionless variables result from the reference variable choice:

$$\begin{aligned} &t = t^\star/t^0, \\ &\boldsymbol{x} = \boldsymbol{x}^\star/l^0, \text{ and} \\ &v_i^0 \boldsymbol{C}_i = \boldsymbol{c}_i^\star - \boldsymbol{v}_h^\star. \end{aligned} \tag{D.34}$$

The resulting differential operators read for species $i \in \{p, g\}$:

$$\begin{aligned} \partial_{t^\star} &= \frac{1}{t^0}\partial_t - \frac{v_h^0}{t^0}\partial_t \boldsymbol{v}_h \cdot \frac{1}{v_i^0}\boldsymbol{\partial}_{\boldsymbol{C}_i} \\ \partial_{\boldsymbol{x}^\star} &= \frac{1}{l^0}\partial_{\boldsymbol{x}} - \frac{v_h^0}{l^0}\partial_{\boldsymbol{x}} \boldsymbol{v}_h \cdot \frac{1}{v_i^0}\boldsymbol{\partial}_{\boldsymbol{C}_i} \\ \partial_{\boldsymbol{c}_i^\star} &= \frac{1}{v_i^0}\boldsymbol{\partial}_{\boldsymbol{C}_i} \end{aligned} \tag{D.35}$$

D.1.3.4 Transport operator

The Boltzmann transport operators $i \in \{g, p\}$ from Eq. (D.31) read:

$$\begin{aligned} \mathscr{D}_i^\star(f_i^\star) &= \frac{1}{t^0}\partial_t f_i^\star - \frac{1}{t^0}\frac{v_h^0}{v_i^0}\partial_t \boldsymbol{v}_h \cdot \boldsymbol{\partial}_{\boldsymbol{C}_i} f_i^\star \\ &\quad + v_i^0(\boldsymbol{C}_i + M_i \boldsymbol{v}_h) \cdot \frac{1}{l^0}\partial_{\boldsymbol{x}} f_i^\star - v_i^0(\boldsymbol{C}_i + M_i \boldsymbol{v}_h)\frac{1}{l^0}\frac{v_h^0}{v_i^0}\partial_{\boldsymbol{x}} \boldsymbol{v}_h \cdot \boldsymbol{\partial}_{\boldsymbol{C}_i} f_i^\star \\ &\quad + F^0 \boldsymbol{F} \cdot \frac{1}{v_i^0}\boldsymbol{\partial}_{\boldsymbol{C}_i} f_i^\star \\ &= \frac{1}{t^0}\partial_t f_i^\star - \frac{1}{t^0} M_i \partial_t \boldsymbol{v}_h \cdot \boldsymbol{\partial}_{\boldsymbol{C}_i} f_i^\star \\ &\quad + \frac{v_h^0}{M_i}(\boldsymbol{C}_i + M_i \boldsymbol{v}_h) \cdot \frac{1}{t^0 v_h^0}\partial_{\boldsymbol{x}} f_i^\star - (\boldsymbol{C}_i + M_i \boldsymbol{v}_h)\frac{1}{l^0}\frac{l^0}{t^0}\partial_{\boldsymbol{x}} \boldsymbol{v}_h \cdot \boldsymbol{\partial}_{\boldsymbol{C}_i} f_i^\star \\ &\quad + \frac{v^0}{t^0}\boldsymbol{F} \cdot \frac{1}{v_i^0}\boldsymbol{\partial}_{\boldsymbol{C}_i} f_i^\star \end{aligned} \tag{D.36}$$

The NDF $f_i^\star$ can be replaced by f_i as it is on both sides, which is equivalent to dividing the equation by $n_i^0(v_i^0)^{-3}$. The hydrodynamic total derivative is noted:

$$\frac{\mathrm{D}}{\mathrm{D}t} = \partial_t + \boldsymbol{v}_h \cdot \partial_{\boldsymbol{x}} \tag{D.37}$$

so that the transport operators read:

$$\begin{aligned}\mathscr{D}_i^\star(f_i) = \quad & \frac{1}{t^0}\partial_t f_i \\ & + \frac{1}{t^0 M_i}(\boldsymbol{C}_i + M_i \boldsymbol{v}_h) \cdot \partial_{\boldsymbol{x}} f_i \\ & + \left(\frac{M_i}{t^0}\boldsymbol{F} - \frac{M_i}{t^0}\frac{\mathrm{D}\boldsymbol{v}_h}{\mathrm{D}t}\right) \cdot \boldsymbol{\partial}_{\boldsymbol{C}_i} f_i \\ & - \frac{1}{t^0}\left(\boldsymbol{\partial}_{\boldsymbol{C}_i} f_i \otimes \boldsymbol{C}_i\right) : \partial_{\boldsymbol{x}} \boldsymbol{v}_h.\end{aligned} \tag{D.38}$$

Their definitive dimensionless form is obtained after division by $(t^0)^{-1}$ and by substation of the orders of magnitude far from one:

$$\begin{cases} \mathscr{D}_g(f_g) = \partial_t f_g + \dfrac{1}{M_g}\left(\boldsymbol{C}_g + M_g \boldsymbol{v}_h\right) \cdot \partial_{\boldsymbol{x}} f_g + M_g \boldsymbol{F}_{\overline{G}} \cdot \boldsymbol{\partial}_{\boldsymbol{C}_g} f_g - \left(\boldsymbol{\partial}_{\boldsymbol{C}_g} f_g \otimes \boldsymbol{C}_g\right) : \partial_{\boldsymbol{x}} \boldsymbol{v}_h \\ \mathscr{D}_p(f_p) = \partial_t f_p + \dfrac{\varepsilon}{M_g}\left(\boldsymbol{C}_p + \dfrac{M_g}{\varepsilon}\boldsymbol{v}_h\right) \cdot \partial_{\boldsymbol{x}} f_p + \dfrac{M_g}{\varepsilon}\boldsymbol{F}_{\overline{G}} \cdot \boldsymbol{\partial}_{\boldsymbol{C}_p} f_p - \left(\boldsymbol{\partial}_{\boldsymbol{C}_p} f_p \otimes \boldsymbol{C}_p\right) : \partial_{\boldsymbol{x}} \boldsymbol{v}_h \end{cases} \tag{D.39}$$

where $\boldsymbol{F}_{\overline{G}} = \boldsymbol{F} - \frac{\mathrm{D}\boldsymbol{v}_h}{\mathrm{D}t}$ is the net external force in the chosen reference frame.

D.2 Linearization of the collision operators

D.2.1 Description of collision operators

Collision operators must be scaled as they explicitly depend on ε while the change in reference frame is unnoticeable as collisions can be written in any reference frame.

D.2.1.1 Collisions within a phase

We consider the case of intra-phase collisions, corresponding to operators $\mathcal{J}_{ii}^\star$ defined in Eq. (D.26):

$$\begin{aligned}\mathcal{J}_{ii}^\star(f_i^\star, f_i^\star) &= \iint (f_i^{\star'} f_i^{\star'} - f_i^\star f_i^\star) \mid \boldsymbol{C}_i^\star - \boldsymbol{C}_i^{\diamond\star} \mid \sigma_{ii}^\star \mathrm{d}\boldsymbol{\omega}\mathrm{d}\boldsymbol{C}_i^{\diamond\star} \\ &= \iint \frac{n_i^0}{(v_i^0)^3} \times \frac{n_i^0}{(v_i^0)^3}(f_i' f_i' - f_i f_i) v_i^0 \mid \boldsymbol{C}_i - \boldsymbol{C}_i^\diamond \mid \sigma_{ii}^0 \sigma_{ii} \mathrm{d}\boldsymbol{\omega}(v_i^0)^3 \mathrm{d}\boldsymbol{C}_i^\diamond\end{aligned} \tag{D.40}$$

The division by $(t^0)^{-1}$ and f_i^0 is performed similarly as for the transport operators:

$$t^0 \frac{1}{f_i^0}\mathcal{J}_{ii}^\star = t^0 \frac{1}{f_i^0}\frac{n_i^0}{(v_i^0)^3} n_i^0 v_i^0 \sigma^0 \iint (f_i' f_i' - f_i f_i) \mid \boldsymbol{C}_i - \boldsymbol{C}_i^\diamond \mid \sigma_{ii} \mathrm{d}\boldsymbol{\omega}\mathrm{d}\boldsymbol{C}_i^\diamond \tag{D.41}$$

The relation Eq. (D.12) allows to replace the cross-section σ_{ii}^0 and to use the mean free path orders of magnitude

$$\begin{aligned}&\text{Gas:} && t^0 v_g^0 n_g^0 \sigma_{gg}^0 = \frac{1}{\varepsilon} t_g^0 v_g^0 \frac{1}{l_{gg}^0} = \frac{1}{\varepsilon} \\ &\text{Particles:} && t^0 v_p^0 n_p^0 \sigma_{pp}^0 = \varepsilon t_p^0 v_p^0 \frac{1}{l_{pp}^0} = \varepsilon\end{aligned} \tag{D.42}$$

The notation $\mathcal{J}_{ii}$ now designates the dimensionless intra-phase collision operator for species $i \in \{g, p\}$:

$$\mathcal{J}_{ii} = \iint (f_i' f_i' - f_i f_i) \mid \boldsymbol{C}_i - \boldsymbol{C}_i^\diamond \mid \sigma_{ii} \mathrm{d}\boldsymbol{\omega}\mathrm{d}\boldsymbol{C}_i^\diamond \tag{D.43}$$

D.2.1.2 Collisions between particles of different phases

In the case of inter-phase collisions, the orders of magnitude of the velocity differences are not the same for $\mathcal{J}_{gp}$ and for $\mathcal{J}_{pg}$, which are treated separately:

$$\begin{aligned}\mathcal{J}_{gp}^{\star}(f_g^{\star},f_p^{\star}) &= \iint \frac{n_g^0}{(v_g^0)^3}\times\frac{n_p^0}{(v_p^0)^3}(f_g^{'}f_p^{'}-f_gf_p)v_g^0 \mid \boldsymbol{C}_g-\frac{v_p^0}{v_g^0}\boldsymbol{C}_p \mid \sigma_{gp}^0\sigma_{gp}\mathrm{d}\boldsymbol{\omega}(v_p^0)^3\mathrm{d}\boldsymbol{C}_p\\ \mathcal{J}_{pg}^{\star}(f_p^{\star},f_g^{\star}) &= \iint \frac{n_p^0}{(v_p^0)^3}\times\frac{n_g^0}{(v_g^0)^3}(f_p^{'}f_g^{'}-f_pf_g)v_g^0 \mid \frac{v_p^0}{v_g^0}\boldsymbol{C}_p-\boldsymbol{C}_g \mid \sigma_{pg}^0\sigma_{pg}\mathrm{d}\boldsymbol{\omega}(v_g^0)^3\mathrm{d}\boldsymbol{C}_g\end{aligned} \tag{D.44}$$

and the dimensionless residuals read:

$$\begin{aligned}&\text{Gas :} && t^0v_g^0n_p^0\sigma_{gp}^0=\frac{1}{\varepsilon}t_g^0v_g^0\frac{\varepsilon}{l_{gg}^0}=1\\ &\text{Particles :} && t^0v_g^0n_g^0\sigma_{pg}^0=\frac{1}{\varepsilon}t_g^0v_g^0\frac{1}{\varepsilon l_{gg}^0}=\frac{1}{\varepsilon^2}\end{aligned} \tag{D.45}$$

The dimensionless inter-phase collision operators are now noted $\mathcal{J}_{ij}^{\varepsilon}$ to recall that they still depend on ε, though they are scaled:

$$\begin{aligned}\mathcal{J}_{gp}^{\varepsilon}(f_g,f_p) &= \iint (f_g^{'}f_p^{'}-f_gf_p) \mid \boldsymbol{C}_g-\varepsilon\boldsymbol{C}_p \mid \sigma_{gp}^{\varepsilon}\mathrm{d}\boldsymbol{\omega}\mathrm{d}\boldsymbol{c}_p\\ \mathcal{J}_{pg}^{\varepsilon}(f_p,f_g) &= \iint (f_p^{'}f_g^{'}-f_pf_g) \mid \varepsilon\boldsymbol{C}_p-\boldsymbol{C}_g \mid \sigma_{pg}^{\varepsilon}\mathrm{d}\boldsymbol{\omega}\mathrm{d}\boldsymbol{C}_g\end{aligned} \tag{D.46}$$

These operators may indeed be expanded versus ε, due to the dependency of the cross-sections $\sigma_{ij}^{\varepsilon}$, $i\neq j$: the leading order of the collision terms is at most 1 thanks to the dimensionless recasting but it may be smaller. This aspect must be evaluated.
Now that the collision operators are scaled, let us write the phase equations:

$$\left\{\begin{array}{l}\mathscr{D}_g(f_g)=\dfrac{1}{\varepsilon}\left(\mathcal{J}_{gg}(f_g,f_g)+\varepsilon\mathcal{J}_{gp}^{\varepsilon}(f_g,f_p)\right)\\ \mathscr{D}_p(f_p)=\dfrac{1}{\varepsilon^2}\left(\mathcal{J}_{pg}^{\varepsilon}(f_p,f_g)+\varepsilon^3\mathcal{J}_{pp}(f_p,f_p)\right)\end{array}\right. \tag{D.47}$$

with the leading collision order being factorized. In fact, the collisions have a scaling that is remarkably different from the plasma case of Graille et al. (2009).
It is noted as expected that the gas equation has a dominant collision term resulting from gas/gas collisions, while the particle equation has a dominant collision term resulting from gas/particle collisions.

D.2.1.3 Effect of collisions on the gas

The $\mathcal{J}_{gg}$ collision term is largely dominant in the gas equation with its term at order -2 in ε. For the equation to provide relevant information (i.e. for the model to be in its validity domain), this term must be very small. This corresponds to regimes where the gas is thermalized and where a local equilibrium state can be defined. The model does not seek out-of-equilibrium regimes for the gas. Moreover, the operator which ensures this equilibrium state is a classical Boltzmann operator so that the ground state of the gas is defined by a Maxwell-Boltzmann velocity distribution (Ferziger and Kaper 1972). This distribution is perturbed only at second order by the presence of particles.
In the gas equation, the term $\mathcal{J}_{gp}^{\varepsilon}$, translating the effect of particles on the gas, is weaker but still of order 0. This term is interesting for two reasons:

- it renders the retrocoupling of particles on gas, which we aim at studying since the spray is moderately dense. In the standard theory of Brownian motion, this term is neglected and models are one-way coupling approximations;
- it gives insight on the term $\mathcal{J}_{pg}^{\varepsilon}$, which is crucial to enlighten the particle behavior, thanks to the reaction principle.

D.2.1.4 Effect of collisions on particles

The particle equation is a more unusual kinetic equation: the collision dominant term is $\mathcal{J}_{pg}^{\varepsilon}$ which renders an external coupling. The effective order of this term is not obvious and is studied in Eq. (D.67), proving to be 0 (instead of -1), so that the NDF is not dominated but close to an "equilibrium".
Such equilibrium is awkward in kinetic theory but can be interpreted at both macroscopic and microscopic scales:

- it means that the drift velocities of gas and particles are equal (to 0 thanks to Eq. (D.23)), corresponding to the vision of usual drag;
- it means that the particles have a kinetic energy at equilibrium with that of the gas: they are agitated.

This agitation results in transport. If it is isotropic, the center of mass of the disperse phase does not move, which corresponds to the usual Brownian diffusion. On the contrary, a non-isotropic diffusion can be induced if the gas has non-uniformities (since it is necessarily at equilibrium): this corresponds to thermophoresis and barophoresis. In the case of a multi-species gas, diffusiophoresis occurs (Davies 1966), which can be accounted for if each species has a kinetic equation.
The dominated collision term is the particle-particle term $\mathcal{J}_{pp}$. It has presumably a negligible effect on the dynamics of the mixture as it comes at order 1. The disperse phase is not thermalized according to the choice of the study time compared to the particle/particle collision time. However, if particle-particle collisions result in coalescence, this term has to be accounted for. The evolution of particle mass and size is unusual in kinetic theory and has presumably a strong though indirect effect on the flow dynamics.

D.2.2 Expansion of the collision operators

We now expand the collision operators versus ε. The inter-phase operators are formally analogous to mono-species ones and can be found in Ferziger and Kaper (1972): $\mathcal{J}_{gg}(f_g, f_g)$ is linearized as usual when expanding f_g by the Chapman-Enskog approach while $\mathcal{J}_{pp}(f_p, f_p)$ is not expanded and becomes the coalescence operator. But the inter-phase operators have to be expanded: this work is performed similarly as for the plasma case of Graille et al. (2009) since only the velocities play a role in both cases.

D.2.2.1 Dynamics of collisions

The dynamics of particle-gas collisions is studied as regards its dependency on ε, in order to expand the inter-phase collision operators.
The conservation of momentum reads for elastic collisions:

$$\begin{aligned} \boldsymbol{C}'_p &= \frac{\varepsilon}{m_i+\varepsilon^2}\boldsymbol{C}_g + \frac{m_p}{m_p+\varepsilon^2}\boldsymbol{C}_p + s\frac{\varepsilon}{m_p+\varepsilon^2}|\varepsilon\boldsymbol{C}_p-\boldsymbol{C}_g|\boldsymbol{\omega} \\ \boldsymbol{C}'_g &= \frac{\varepsilon^2}{m_i+\varepsilon^2}\boldsymbol{C}_g + \frac{\varepsilon m_g}{m_g+\varepsilon^2}\boldsymbol{C}_p - s\frac{m_p}{m_p+\varepsilon^2}|\varepsilon\boldsymbol{C}_p-\boldsymbol{C}_g|\boldsymbol{\omega} \end{aligned} \tag{D.48}$$

which links the post-collision peculiar velocities $\boldsymbol{C}'_p$ et $\boldsymbol{C}'_g$ to the pre-collision ones $\boldsymbol{C}_p$ et $\boldsymbol{C}_g$ and where s is a sign constant which is equal to $+1$ for operator $\mathcal{J}_{pg}$ and -1 for $\mathcal{J}_{gp}$. The relative velocities after collision have a direction:

$$\boldsymbol{\omega} = s\frac{\varepsilon\boldsymbol{C}'_p-\boldsymbol{C}'_g}{|\varepsilon\boldsymbol{C}'_p-\boldsymbol{C}'_g|} \tag{D.49}$$

in the hydrodynamic frame.
This expansion assumes that the phase velocity is not perturbed by a single collision. We may now expand the inter-phase collision operators

D.2.2.2 Average cross-section for the particles

The dimensional analysis has yielded Eq. (D.46), which allows to develop $\mathcal{J}_{pg}^{\varepsilon}$:

$$\begin{aligned} \mathcal{J}_{pg}^{\varepsilon}(f_p,f_g) = \int \sigma_{pg}\left(|\boldsymbol{\gamma}_{\mathrm{g}}|^2, \boldsymbol{\omega}\cdot\frac{\boldsymbol{\gamma}_{\mathrm{g}}}{|\boldsymbol{\gamma}_{\mathrm{g}}|}\right)|\varepsilon\boldsymbol{C}_p-\boldsymbol{C}_g| \\ \times\Big[f_p(\boldsymbol{C}'_p)f_g(\boldsymbol{C}'_g)-f_p(\boldsymbol{C}_p)f_g(\boldsymbol{C}_g)\Big]\mathrm{d}\boldsymbol{\omega}\mathrm{d}\boldsymbol{C}_g \end{aligned} \tag{D.50}$$

where the dimensionless relative kinetic energy is noted:

$$\boldsymbol{\gamma}_{\mathrm{g}} = s(\varepsilon\boldsymbol{C}_p-\boldsymbol{C}_g)/(1+\varepsilon^2/m_p)^{1/2}. \tag{D.51}$$

We now define the generalized momentum transfer cross-section (Mitchner and Kruger 1973):

$$Q_{pg}^{(l)}(|\boldsymbol{\gamma}_{\mathrm{g}}|^2) = 2\pi\int_0^{\pi}\sigma_{pg}(|\boldsymbol{\gamma}_{\mathrm{g}}|^2,\cos\theta)(1-\cos^l\theta)\sin\theta\mathrm{d}\theta \tag{D.52}$$

where θ is the angle between $\boldsymbol{\omega}$ and $\boldsymbol{e}$. For $l=1$, this cross section-represents the average momentum transferred from the gas to the particles per unit relative kinetic energy.

D.2.2.3 Expansion of $\mathcal{J}_{pg}^{\varepsilon}$

We formally expand $\mathcal{J}_{pg}^{\varepsilon}$ as in Graille et al. (2009):

$$\begin{aligned}\mathcal{J}_{pg}^{\varepsilon}(f_p,f_g)(\boldsymbol{C}_p) = & \quad \mathcal{J}_{pg}^{(0)}(f_p,f_g)(\boldsymbol{C}_p)\\ & + \varepsilon \quad \mathcal{J}_{pg}^{(1)}(f_p,f_g)(\boldsymbol{C}_p)\\ & + \varepsilon^2 \ \mathcal{J}_{pg}^{(2)}(f_p,f_g)(\boldsymbol{C}_p) + \mathscr{O}(\varepsilon^3).\end{aligned} \tag{D.53}$$

The zeroth order term $\mathcal{J}_{pg}^{(0)}(f_p,f_g)$ cancels thanks to the symmetry of the integral in Eq. (D.50):

$$\mathcal{J}_{pg}^{(0)}(f_p,f_g) = 0 \tag{D.54}$$

which results from the micro-reversibility of collisions.
The first order term $\mathcal{J}_{pg}^{(1)}$ reads after some algebra:

$$\mathcal{J}_{pg}^{(1)}(f_p,f_g) = \frac{1}{m_p}\boldsymbol{\partial}_{\boldsymbol{C}_p} f_p(\boldsymbol{C}_p)\cdot\int Q_{pg}^{(1)}(|\boldsymbol{\gamma}_{\mathrm{g}}|^2)|\boldsymbol{\gamma}_{\mathrm{g}}|\boldsymbol{\gamma}_{\mathrm{g}} f_g(\boldsymbol{\gamma}_{\mathrm{g}})\mathrm{d}\boldsymbol{\gamma}_{\mathrm{g}} \tag{D.55}$$

and the second order term $\mathcal{J}_{pg}^{(2)}$ reads:

$$\begin{aligned}\mathcal{J}_{pg}^{(2)}(f_p,f_g) = & -\frac{1}{m_p}\boldsymbol{\partial}_{\boldsymbol{C}_p}(f_p(\boldsymbol{C}_p)\boldsymbol{C}_p) : \int Q_{pg}^{(1)}(|\boldsymbol{\gamma}_{\mathrm{g}}|^2)|\boldsymbol{\gamma}_{\mathrm{g}}|\boldsymbol{C}_g f_g(\boldsymbol{\gamma}_{\mathrm{g}})\otimes\boldsymbol{\gamma}_{\mathrm{g}}\mathrm{d}\boldsymbol{\gamma}_{\mathrm{g}}\\ & + \frac{1}{4m_p^2}\partial^2_{\boldsymbol{C}_p} f_p(\boldsymbol{C}_p) : \int Q_{pg}^{(2)}(|\boldsymbol{\gamma}_{\mathrm{g}}|^2)|\boldsymbol{\gamma}_{\mathrm{g}}|(|\boldsymbol{\gamma}_{\mathrm{g}}|^2\mathbb{I} - 3\boldsymbol{\gamma}_{\mathrm{g}}\otimes\boldsymbol{\gamma}_{\mathrm{g}}) f_g(\boldsymbol{\gamma}_{\mathrm{g}})\mathrm{d}\boldsymbol{\gamma}_{\mathrm{g}}\\ & + \frac{1}{m_p^2}\partial^2_{\boldsymbol{C}_p} f_p(\boldsymbol{C}_p) : \int Q_{pg}^{(1)}(|\boldsymbol{\gamma}_{\mathrm{g}}|^2)|\boldsymbol{\gamma}_{\mathrm{g}}|\boldsymbol{\gamma}_{\mathrm{g}}\otimes\boldsymbol{\gamma}_{\mathrm{g}} f_g(\boldsymbol{\gamma}_{\mathrm{g}})\mathrm{d}\boldsymbol{\gamma}_{\mathrm{g}}\end{aligned} \tag{D.56}$$

where $\mathbb{I}$ is the unit tensor.

D.2.2.4 Average cross-section for the gas

The dimensional analysis has yielded Eq. (D.46), which allows to develop $\mathcal{J}_{gp}^{\varepsilon}$:

$$\begin{aligned}\mathcal{J}_{gp}^{\varepsilon}(f_g,f_p) = \int \sigma_{gp}\Big(\frac{m_p|\boldsymbol{C}_g-\varepsilon\boldsymbol{C}_p|^2}{m_p+\varepsilon^2}, \boldsymbol{\omega}\cdot\boldsymbol{e}\Big)|\boldsymbol{C}_g-\varepsilon\boldsymbol{C}_p|\\ \times\Big[f_g(\boldsymbol{C}'_g)f_p(\boldsymbol{C}'_p) - f_g(\boldsymbol{C}_g)f_p(\boldsymbol{C}_p)\Big]\mathrm{d}\boldsymbol{\omega}\mathrm{d}\boldsymbol{C}_p\end{aligned} \tag{D.57}$$

where the original variables $\{\boldsymbol{C}_g, \boldsymbol{C}_p, \boldsymbol{\omega}\}$ are kept.
The average momentum transfer cross-section is defined:

$$Q_{gp}^{(1)}(|\boldsymbol{C}_g|^2) = 2\pi\int_0^{\pi}\sigma_{gp}(|\boldsymbol{C}_g|^2,\cos\theta)(1-\cos\theta)\sin\theta\mathrm{d}\theta \tag{D.58}$$

which represents the average momentum transferred from the particles to the gas per unit relative kinetic energy. As a matter of conservation, we have the reciprocity relation:

$$Q_{gp}^{(1)} = Q_{pg}^{(1)} \tag{D.59}$$

where $Q_{pg}^{(1)}$ is defined in Eq. (D.52).

D.2.2.5 Expansion of $\mathcal{J}_{gp}^{\varepsilon}$

The operator $\mathcal{J}_{gp}^{\varepsilon}$ can be formally developed as follows:

$$\begin{aligned}\mathcal{J}_{gp}^{\varepsilon}(f_g,f_p)(\boldsymbol{C}_g) = & \quad \mathcal{J}_{gp}^{(0)}(f_g,f_p)(\boldsymbol{C}_g)\\ & + \quad \varepsilon \ \mathcal{J}_{gp}^{(1)}(f_g,f_p)(\boldsymbol{C}_g)\\ & + \quad \varepsilon^2 \ \mathcal{J}_{gp}^{(2)}(f_g,f_p)(\boldsymbol{C}_g) + \mathscr{O}(\varepsilon^3).\end{aligned} \tag{D.60}$$

The terms $\mathcal{J}_{gp}^{(0)}$, $\mathcal{J}_{gp}^{(1)}$ et $\mathcal{J}_{gp}^{(2)}$ of order zero, one and two respectively read after some algebra (Graille et al. 2009):

$$\mathcal{J}_{gp}^{(0)}(f_g,f_p)(\boldsymbol{C}_g) = \int f_p(\boldsymbol{C}_p)\mathrm{d}\boldsymbol{C}_p\int\sigma_{gp}\Big(|\boldsymbol{C}_g|^2, \boldsymbol{\omega}\cdot\tfrac{\boldsymbol{C}_g}{|\boldsymbol{C}_g|}\Big)|\boldsymbol{C}_g|\Big[f_g(|\boldsymbol{C}_g|\boldsymbol{\omega}) - f_g(\boldsymbol{C}_g)\Big]\mathrm{d}\boldsymbol{\omega} \tag{D.61}$$

and

$$\begin{aligned}\mathcal{J}_{gp}^{(1)}(f_g,f_p)(\boldsymbol{C}_g) = \quad & \Big(\int f_p(\boldsymbol{C}_p)\boldsymbol{C}_p \mathrm{d}\boldsymbol{C}_p\Big)\cdot \\ & \Big\{\boldsymbol{\partial}_{\boldsymbol{C}_g}\int \sigma_{gp}(|\boldsymbol{C}_g|^2, \tfrac{\boldsymbol{C}_g}{|\boldsymbol{C}_g|}\cdot\boldsymbol{\omega})\big[f_g(\boldsymbol{C}_g)-f_g(|\boldsymbol{C}_g|\boldsymbol{\omega})\big]|\boldsymbol{C}_g|\mathrm{d}\boldsymbol{\omega} \\ & +\int \sigma_{gp}(|\boldsymbol{C}_g|^2, \tfrac{\boldsymbol{C}_g}{|\boldsymbol{C}_g|}\cdot\boldsymbol{\omega})|\boldsymbol{C}_g|\big[\boldsymbol{\partial}_{\boldsymbol{C}_g}f_g(|\boldsymbol{C}_g|\boldsymbol{\omega})-\boldsymbol{\partial}_{\boldsymbol{C}_g}f_g(\boldsymbol{C}_g)\big]\mathrm{d}\boldsymbol{\omega}\Big\}\end{aligned} \tag{D.62}$$

and

$$\mathcal{J}_{gp}^{(2)}(f_g,f_p)(\boldsymbol{C}_g) = \frac{1}{m_p}K_{gp}^{2,1}(\boldsymbol{C}_g)\int f_p(\boldsymbol{C}_p)\mathrm{d}\boldsymbol{C}_p + \frac{1}{2}\boldsymbol{K}_{gp}^{2,2}(\boldsymbol{C}_g) : \int f_p(\boldsymbol{C}_p)\boldsymbol{C}_p\otimes\boldsymbol{C}_p\mathrm{d}\boldsymbol{C}_p \tag{D.63}$$

where

$$\begin{aligned}K_{gp}^{2,1}(\boldsymbol{C}_g) = \quad & \boldsymbol{\partial}_{\boldsymbol{C}_g}\cdot\int \sigma_{gp}(|\boldsymbol{C}_g|^2, \tfrac{\boldsymbol{C}_g}{|\boldsymbol{C}_g|}\cdot\boldsymbol{\omega})(\boldsymbol{C}_g-|\boldsymbol{C}_g|\boldsymbol{\omega})|\boldsymbol{C}_g|f_g(|\boldsymbol{C}_g|\boldsymbol{\omega})\mathrm{d}\boldsymbol{\omega} \\ & -|\boldsymbol{C}_g|\boldsymbol{C}_g\cdot\int \boldsymbol{\partial}_{\boldsymbol{C}_g}\sigma_{gp}(|\boldsymbol{C}_g|^2, \tfrac{\boldsymbol{C}_g}{|\boldsymbol{C}_g|}\cdot\boldsymbol{\omega})\big[f_g(|\boldsymbol{C}_g|\boldsymbol{\omega})-f_g(\boldsymbol{C}_g)\big]\mathrm{d}\boldsymbol{\omega}\end{aligned} \tag{D.64}$$

and where

$$\begin{aligned}\boldsymbol{K}_{gp}^{2,2}(\boldsymbol{C}_g) = \quad & \partial_{\boldsymbol{C}_g}^2\int \sigma_{gp}(|\boldsymbol{C}_g|^2, \tfrac{\boldsymbol{C}_g}{|\boldsymbol{C}_g|}\cdot\boldsymbol{\omega})|\boldsymbol{C}_g|\big[f_g(|\boldsymbol{C}_g|\boldsymbol{\omega})-f_g(\boldsymbol{C}_g)\big]\mathrm{d}\boldsymbol{\omega} \\ & +2\int \boldsymbol{\partial}_{\boldsymbol{C}_g}\big(\sigma_{gp}(|\boldsymbol{C}_g|^2, \tfrac{\boldsymbol{C}_g}{|\boldsymbol{C}_g|}\cdot\boldsymbol{\omega})|\boldsymbol{C}_g|\big)\otimes\big[\boldsymbol{\partial}_{\boldsymbol{C}_g}f_g(\boldsymbol{C}_g)-\boldsymbol{\partial}_{\boldsymbol{C}_g}f_g(|\boldsymbol{C}_g|\boldsymbol{\omega})\big]\mathrm{d}\boldsymbol{\omega} \\ & +|\boldsymbol{C}_g|\int \sigma_{gp}(|\boldsymbol{C}_g|^2, \tfrac{\boldsymbol{C}_g}{|\boldsymbol{C}_g|}\cdot\boldsymbol{\omega})\big[\partial_{\boldsymbol{C}_g}^2 f_g(\boldsymbol{C}_g)-\partial_{\boldsymbol{C}_g}^2 f_g(|\boldsymbol{C}_g|\boldsymbol{\omega})\big]\mathrm{d}\boldsymbol{\omega} \\ & +2|\boldsymbol{C}_g|\int \sigma_{gp}(|\boldsymbol{C}_g|^2, \tfrac{\boldsymbol{C}_g}{|\boldsymbol{C}_g|}\cdot\boldsymbol{\omega})\tfrac{\boldsymbol{C}_g}{|\boldsymbol{C}_g|}\otimes\boldsymbol{\omega}\partial_{\boldsymbol{C}_g}^2 f_g(|\boldsymbol{C}_g|\boldsymbol{\omega})\mathrm{d}\boldsymbol{\omega}.\end{aligned} \tag{D.65}$$

D.2.3 Summary of dimensionless equations

The system of equations describing the gas/particle mixture can finally be written in its dimensionless, scaled form with an explicit dependency on ε:

$$\begin{cases}\mathscr{D}_g(f_g) = \varepsilon^{-1}\mathcal{J}_{gg}(f_g,f_g) \\ \qquad +\int f_p(\boldsymbol{C}_p)\mathrm{d}\boldsymbol{C}_p\int \sigma_{gp}\Big(|\boldsymbol{C}_g|^2, \boldsymbol{\omega}\cdot\tfrac{\boldsymbol{C}_g}{|\boldsymbol{C}_g|}\Big)|\boldsymbol{C}_g|\times\Big[f_g(|\boldsymbol{C}_g|\boldsymbol{\omega})-f_g(\boldsymbol{C}_g)\Big]\mathrm{d}\boldsymbol{\omega} \\ \qquad +\varepsilon\Big(\int f_p(\boldsymbol{C}_p)\boldsymbol{C}_p\mathrm{d}\boldsymbol{C}_p\Big)\cdot\ \boldsymbol{\partial}_{\boldsymbol{C}_g}\int \sigma_{gp}(|\boldsymbol{C}_g|^2, \tfrac{\boldsymbol{C}_g}{|\boldsymbol{C}_g|}\cdot\boldsymbol{\omega})\big[f_g(\boldsymbol{C}_g)-f_g(|\boldsymbol{C}_g|\boldsymbol{\omega})\big]|\boldsymbol{C}_g|\mathrm{d}\boldsymbol{\omega} \\ \qquad +\varepsilon\Big(\int f_p(\boldsymbol{C}_p)\boldsymbol{C}_p\mathrm{d}\boldsymbol{C}_p\Big)\cdot\int \sigma_{gp}(|\boldsymbol{C}_g|^2, \tfrac{\boldsymbol{C}_g}{|\boldsymbol{C}_g|}\cdot\boldsymbol{\omega})|\boldsymbol{C}_g|\big[\boldsymbol{\partial}_{\boldsymbol{C}_g}f_g(|\boldsymbol{C}_g|\boldsymbol{\omega})-\boldsymbol{\partial}_{\boldsymbol{C}_g}f_g(\boldsymbol{C}_g)\big]\mathrm{d}\boldsymbol{\omega} \\ \qquad +\varepsilon^2\frac{1}{m_p}K_{gp}^{2,1}(\boldsymbol{C}_g)\int f_p(\boldsymbol{C}_p)\mathrm{d}\boldsymbol{C}_p \\ \qquad +\varepsilon^2\frac{1}{2}\boldsymbol{K}_{gp}^{2,2}(\boldsymbol{C}_g)\ :\int f_p(\boldsymbol{C}_p)\boldsymbol{C}_p\otimes\boldsymbol{C}_p\mathrm{d}\boldsymbol{C}_p \\ \\ \mathscr{D}_p(f_p) = \varepsilon\,\mathcal{J}_{pp}(f_p,f_p) \\ \qquad +\varepsilon^{-2}\frac{1}{m_p}\boldsymbol{\partial}_{\boldsymbol{C}_p}f_p(\boldsymbol{C}_p)\ \cdot\int Q_{pg}^{(1)}(|\boldsymbol{\gamma}_{\mathrm{g}}|^2)|\boldsymbol{\gamma}_{\mathrm{g}}|\boldsymbol{\gamma}_{\mathrm{g}}f_g(\boldsymbol{\gamma}_{\mathrm{g}})\mathrm{d}\boldsymbol{\gamma}_{\mathrm{g}} \\ \qquad -\varepsilon^{-1}\frac{1}{m_p}\boldsymbol{\partial}_{\boldsymbol{C}_p}(f_p(\boldsymbol{C}_p)\boldsymbol{C}_p)\ :\int Q_{pg}^{(1)}(|\boldsymbol{\gamma}_{\mathrm{g}}|^2)|\boldsymbol{\gamma}_{\mathrm{g}}|\boldsymbol{C}_g f_g(\boldsymbol{\gamma}_{\mathrm{g}})\otimes\boldsymbol{\gamma}_{\mathrm{g}}\mathrm{d}\boldsymbol{\gamma}_{\mathrm{g}} \\ \qquad +\varepsilon^{-1}\frac{1}{4m_p^2}\partial_{\boldsymbol{C}_p}^2 f_p(\boldsymbol{C}_p)\ :\int Q_{pg}^{(2)}(|\boldsymbol{\gamma}_{\mathrm{g}}|^2)|\boldsymbol{\gamma}_{\mathrm{g}}|\left[|\boldsymbol{\gamma}_{\mathrm{g}}|^2\mathbb{I}-3\boldsymbol{\gamma}_{\mathrm{g}}\otimes\boldsymbol{\gamma}_{\mathrm{g}}\right]f_g(\boldsymbol{\gamma}_{\mathrm{g}})\mathrm{d}\boldsymbol{\gamma}_{\mathrm{g}} \\ \qquad +\varepsilon^{-1}\frac{1}{m_p^2}\partial_{\boldsymbol{C}_p}^2 f_p(\boldsymbol{C}_p)\ :\int Q_{pg}^{(1)}(|\boldsymbol{\gamma}_{\mathrm{g}}|^2)|\boldsymbol{\gamma}_{\mathrm{g}}|\boldsymbol{\gamma}_{\mathrm{g}}\otimes\boldsymbol{\gamma}_{\mathrm{g}}f_g(\boldsymbol{\gamma}_{\mathrm{g}})\mathrm{d}\boldsymbol{\gamma}_{\mathrm{g}}\end{cases} \tag{D.66}$$

We highlight the fact that this expansion is valid for any couple of NDFs (f_g, f_p) which orders of magnitude are those defined in Table D.2.

D.3 Chapman-Enskog expansion

We now perform a Chapman-Enskog expansion of f_g, in order to assess the equilibrium states encountered by the mixture. The Chapman-Enskog technique is detailed in § 3.4.3 for the classical case of a single species fluid.

D.3.1 Chapman-Enskog formalism

D.3.1.1 Perturbation of f_g

The reference time scale was defined in Eq. (D.7) to ensure that the gas is thermalized. The Chapman-Enskog expansion is therefore relevant, it is by the way classical as it is performed about a Maxwell-Boltzmann distribution.
The following form is assumed for the gas NDF:

$$\begin{aligned} f_g &= f_g^{(0)} + f_g^{(1)} + f_g^{(2)} + \mathscr{O}(\varepsilon^3) \\ &= f_g^{(0)}(1 + \varepsilon\phi + \varepsilon^2\phi^{(2)} + \mathscr{O}(\varepsilon^3)). \end{aligned} \tag{D.67}$$

The order shift between gas and particle equations in Eq. (D.66) is such that it may be solved with the sole expansion of the gas function: the particle phase is decoupled from the gas one leading orders so that they can be solved and injected back into the particle equations.

D.3.1.2 Remarks on the drift velocities

Considering the relation on drift velocities given in Eq. (D.67), we may apply the expansion of f_g:

$$\begin{aligned} 0 = &\ \varepsilon\,\alpha\beta\rho_p \boldsymbol{V}_p^{\boldsymbol{v}_h} + \rho_g \boldsymbol{V}_g^{\boldsymbol{v}_h} \\ 0 = &\ \varepsilon\,\alpha\beta\rho_p \boldsymbol{V}_p^{\boldsymbol{v}_h} + \int m_g f_g^{(0)}(1 + \varepsilon\phi + \varepsilon^2\phi^{(2)} + \mathscr{O}(\varepsilon^3))\boldsymbol{C}_g \mathrm{d}\boldsymbol{C}_g \\ 0 = &\ \varepsilon\,\alpha\beta\rho_p \boldsymbol{V}_p^{\boldsymbol{v}_h} \\ &+ m_g \int f_g^{(0)} \boldsymbol{C}_g \mathrm{d}\boldsymbol{C}_g \\ &+ \varepsilon\, m_g \int f_g^{(0)} \phi \boldsymbol{C}_g \mathrm{d}\boldsymbol{C}_g \\ &+ \varepsilon^2\, m_g \int f_g^{(0)} \phi^{(2)} \boldsymbol{C}_g \mathrm{d}\boldsymbol{C}_g + \mathscr{O}(\varepsilon^3) \end{aligned} \tag{D.68}$$

where the f_g^0 is centered to have $\int m_g f_g^{(0)} \boldsymbol{C}_g \mathrm{d}\boldsymbol{C}_g = 0$ so that v_h can be written to exhibit its real scale:

$$0 = \alpha\beta\rho_p \boldsymbol{V}_p^{\boldsymbol{v}_h} + m_g \int f_g^{(0)} \phi \boldsymbol{C}_g \mathrm{d}\boldsymbol{C}_g + \varepsilon\, m_g \int f_g^{(0)} \phi^{(2)} \boldsymbol{C}_g \mathrm{d}\boldsymbol{C}_g + \mathscr{O}(\varepsilon^3) \tag{D.69}$$

which proves that the gas drift velocity $\boldsymbol{V}_g$ depends on the perturbation ϕ which is natural.
We get at order one:

$$\rho_g \boldsymbol{V}_g = \int m_g f_g^{(0)} \phi \boldsymbol{C}_g \mathrm{d}\boldsymbol{C}_g + \mathscr{O}(\varepsilon) \tag{D.70}$$

D.3.1.3 Transport operator expansion versus f_g

The gas transport operator $\mathscr{D}_g$ given in Eq. (D.39) is linear in the NDF and can be expanded straightforward. The particle transport operator $\mathscr{D}_p$ is not modified since f_p is not expanded. The transport operators read:

$$\left\{ \begin{aligned} \mathscr{D}_g(f_g) &= \mathscr{D}_g(f_g^{(0)}, \phi, \phi^{(2)}) \\ &= \partial_t\big[f_g^{(0)}(1 + \varepsilon\phi + \varepsilon^2\phi^{(2)})\big] \\ &\quad + \frac{1}{M_g}(\boldsymbol{C}_g + M_g \boldsymbol{v}_h) \cdot \partial_{\boldsymbol{x}}\big[f_g^{(0)}(1 + \varepsilon\phi + \varepsilon^2\phi^{(2)})\big] \\ &\quad + M_g \boldsymbol{F}_{\overline{G}} \cdot \boldsymbol{\partial}_{\boldsymbol{C}_g}\big[f_g^{(0)}(1 + \varepsilon\phi + \varepsilon^2\phi^{(2)})\big] \\ &\quad - \Big(\boldsymbol{\partial}_{\boldsymbol{C}_g}\big[f_g^{(0)}(1 + \varepsilon\phi + \varepsilon^2\phi^{(2)})\big] \otimes \boldsymbol{C}_g\Big) : \partial_{\boldsymbol{x}} \boldsymbol{v}_h \\ \mathscr{D}_p(f_p) &= \partial_t f_p \\ &\quad + \frac{\varepsilon}{M_g}\left(\boldsymbol{C}_p + \frac{M_g}{\varepsilon}\boldsymbol{v}_h\right) \cdot \partial_{\boldsymbol{x}} f_p \\ &\quad + \frac{M_g}{\varepsilon} \boldsymbol{F}_{\overline{G}} \cdot \boldsymbol{\partial}_{\boldsymbol{C}_p} f_p \\ &\quad - \big(\boldsymbol{\partial}_{\boldsymbol{C}_p} f_p \otimes \boldsymbol{C}_p\big) : \partial_{\boldsymbol{x}} \boldsymbol{v}_h \end{aligned} \right. \tag{D.71}$$

The gas transport operator depends *a priori* on the time derivative and the gradients of all the parts of f_g.

D.3.2 Expansion of the collision terms about the gas equilibrium

D.3.2.1 Gas-gas collision operator expansion

The gas-gas collision operator $\mathcal{J}_{gg}$ does not depend on ε by itself so that $\mathcal{J}_{gg}(f_g, f_g)$ can be expanded by bilinearity of $\mathcal{J}_{gg}$:

$$\begin{aligned}\mathcal{J}_{gg}(f_g, f_g) = \quad & \mathcal{J}_{gg}(f_g^{(0)}, f_g^{(0)}) \\ & +\varepsilon\left(\mathcal{J}_{gg}(f_g^{(0)}\phi, f_g^{(0)}) + \mathcal{J}_{gg}(f_g^{(0)}, f_g^{(0)}\phi)\right) \\ & +\varepsilon^2\left(\mathcal{J}_{gg}(f_g^{(0)}\phi^{(2)}, f_g^{(0)}) + \mathcal{J}_{gg}(f_g^{(0)}\phi, f_g^{(0)}\phi) + \mathcal{J}_{gg}(f_g^{(0)}, f_g^{(0)}\phi^{(2)})\right) \\ & +\mathscr{O}(\varepsilon^3)\end{aligned} \tag{D.72}$$

D.3.2.2 Gas-particle collision operator expansion

The gas-particle collision operator $\mathcal{J}_{gp}$ has been linearized as $\mathcal{J}_{gp}^{\ \varepsilon} = \mathcal{J}_{gp}^{(0)} + \varepsilon\mathcal{J}_{gp}^{(1)} + \varepsilon^2\mathcal{J}_{gp}^{(2)}$ in Eq. (D.60). The final expansion of $\mathcal{J}_{gp}^{\ \varepsilon}(f_g, f_p)$ is performed thanks to the linearity of $\mathcal{J}_{gp}^{(1)}$ and $\mathcal{J}_{gp}^{(2)}$:

$$\begin{aligned}\mathcal{J}_{gp}^{\ \varepsilon}(f_g, f_p) = \quad & \mathcal{J}_{gp}^{(0)}(f_g^{(0)}, f_p) + \varepsilon\mathcal{J}_{gp}^{(0)}(f_g^{(0)}\phi, f_p) + \varepsilon^2\mathcal{J}_{gp}^{(0)}(f_g^{(0)}\phi^{(2)}, f_p) \\ & +\varepsilon\mathcal{J}_{gp}^{(1)}(f_g^{(0)}, f_p) + \varepsilon^2\mathcal{J}_{gp}^{(1)}(f_g^{(0)}\phi, f_p) \\ & +\varepsilon^2\mathcal{J}_{gp}^{(2)}(f_g^{(0)}, f_p) + \mathscr{O}(\varepsilon^3)\end{aligned} \tag{D.73}$$

The zeroth order term in $\mathcal{J}_{gp}^{(0)}(f_g, f_p)$ vanishes for isotropic functions which is the case of $f_g^{(0)}$ which is the Maxwell-Boltzmann distribution:

$$\mathcal{J}_{gp}^{(0)}(f_g^{(0)}, f_p) = 0 \tag{D.74}$$

The following orders are obtained by replacing the Chapman-Enskog form in Eq. (D.61):

$$\begin{aligned}\mathcal{J}_{gp}^{(0)}(f_g^{(0)}\phi, f_p) = \quad & \int f_p(\boldsymbol{C}_p)\mathrm{d}\boldsymbol{C}_p \int \sigma_{gp}\Big(|\boldsymbol{C}_g|^2, \boldsymbol{\omega}\cdot\tfrac{\boldsymbol{C}_g}{|\boldsymbol{C}_g|}\Big)|\boldsymbol{C}_g| \\ & \times\Big[\big[f_g^{(0)}\phi\big](|\boldsymbol{C}_g|\boldsymbol{\omega}) - \big[f_g^{(0)}\phi\big](\boldsymbol{C}_g)\Big]\mathrm{d}\boldsymbol{\omega}\end{aligned} \tag{D.75}$$

and

$$\begin{aligned}\mathcal{J}_{gp}^{(0)}(f_g^{(0)}\phi^{(2)}, f_p) = \quad & \int f_p(\boldsymbol{C}_p)\mathrm{d}\boldsymbol{C}_p \int \sigma_{gp}\Big(|\boldsymbol{C}_g|^2, \boldsymbol{\omega}\cdot\tfrac{\boldsymbol{C}_g}{|\boldsymbol{C}_g|}\Big)|\boldsymbol{C}_g| \\ & \times\Big[\big[f_g^{(0)}\phi^{(2)}\big](|\boldsymbol{C}_g|\boldsymbol{\omega}) - \big[f_g^{(0)}\phi^{(2)}\big](\boldsymbol{C}_g)\Big]\mathrm{d}\boldsymbol{\omega}\end{aligned} \tag{D.76}$$

Let us now expand $\mathcal{J}_{gp}^{(1)}(f_g, f_p)$ about the Maxwell-Boltzmann distribution by injecting Eq. (D.67) in Eq. (D.62) which yields, when neglecting terms of order above two:

$$\begin{aligned}\mathcal{J}_{gp}^{(1)}(f_g, f_p) = \quad & \Big(\int f_p(\boldsymbol{C}_p)\boldsymbol{C}_p\mathrm{d}\boldsymbol{C}_p\Big)\cdot \\ & \Big\{\boldsymbol{\partial}_{\boldsymbol{C}_g}\int \sigma_{gp}(|\boldsymbol{C}_g|^2, \tfrac{\boldsymbol{C}_g}{|\boldsymbol{C}_g|}\cdot\boldsymbol{\omega})\big[f_g^{(0)}(\boldsymbol{C}_g) - f_g^{(0)}(|\boldsymbol{C}_g|\boldsymbol{\omega})\big]|\boldsymbol{C}_g|\mathrm{d}\boldsymbol{\omega} \\ & +\int \sigma_{gp}(|\boldsymbol{C}_g|^2, \tfrac{\boldsymbol{C}_g}{|\boldsymbol{C}_g|}\cdot\boldsymbol{\omega})|\boldsymbol{C}_g|\big[\boldsymbol{\partial}_{\boldsymbol{C}_g}f_g^{(0)}(|\boldsymbol{C}_g|\boldsymbol{\omega}) - \boldsymbol{\partial}_{\boldsymbol{C}_g}f_g^{(0)}(\boldsymbol{C}_g)\big]\mathrm{d}\boldsymbol{\omega}\Big\}\end{aligned} \tag{D.77}$$

where again isotropy considerations yield:

$$\begin{aligned}\mathcal{J}_{gp}^{(1)}(f_g^{(0)}, f_p) = \Big(\int f_p(\boldsymbol{C}_p)\boldsymbol{C}_p\mathrm{d}\boldsymbol{C}_p\Big)\cdot \int \sigma_{gp}(|\boldsymbol{C}_g|^2, \tfrac{\boldsymbol{C}_g}{|\boldsymbol{C}_g|}\cdot\boldsymbol{\omega})|\boldsymbol{C}_g| \\ \times\big[\boldsymbol{\partial}_{\boldsymbol{C}_g}f_g^{(0)}(|\boldsymbol{C}_g|\boldsymbol{\omega}) - \boldsymbol{\partial}_{\boldsymbol{C}_g}f_g^{(0)}(\boldsymbol{C}_g)\big]\mathrm{d}\boldsymbol{\omega}\end{aligned} \tag{D.78}$$

The second term $\mathcal{J}_{gp}^{(1)}(f_g^{(1)}, f_p)$ results from $f_g^{(0)}\phi$ and reads:

$$\begin{aligned}\mathcal{J}_{gp}^{(1)}(f_g^{(1)}, f_p) = \quad & \Big(\int f_p(\boldsymbol{C}_p)\boldsymbol{C}_p\mathrm{d}\boldsymbol{C}_p\Big)\cdot \\ & \Big\{\boldsymbol{\partial}_{\boldsymbol{C}_g}\int \sigma_{gp}(|\boldsymbol{C}_g|^2, \tfrac{\boldsymbol{C}_g}{|\boldsymbol{C}_g|}\cdot\boldsymbol{\omega})\big[\big[f_g^{(0)}\phi\big](\boldsymbol{C}_g) - \big[f_g^{(0)}\phi\big](|\boldsymbol{C}_g|\boldsymbol{\omega})\big]|\boldsymbol{C}_g|\mathrm{d}\boldsymbol{\omega} \\ & +\int \sigma_{gp}(|\boldsymbol{C}_g|^2, \tfrac{\boldsymbol{C}_g}{|\boldsymbol{C}_g|}\cdot\boldsymbol{\omega})|\boldsymbol{C}_g|\big[\boldsymbol{\partial}_{\boldsymbol{C}_g}\big[f_g^{(0)}\phi\big](|\boldsymbol{C}_g|\boldsymbol{\omega}) - \boldsymbol{\partial}_{\boldsymbol{C}_g}\big[f_g^{(0)}\phi\big](\boldsymbol{C}_g)\big]\mathrm{d}\boldsymbol{\omega}\Big\}\end{aligned} \tag{D.79}$$

Let us finally expand $\mathcal{J}_{gp}^{(2)}(f_g, f_p)$ about the Maxwell-Boltzmann distribution by injecting Eq. (D.67) in Eq. (D.63) which yields, when neglecting terms of order above two:

$$\mathcal{J}_{gp}^{(2)}(f_g^{(0)}, f_p) = \frac{1}{m_p} K_{gp}^{2,1}(\boldsymbol{C}_g) \int f_p(\boldsymbol{C}_p) \mathrm{d}\boldsymbol{C}_p + \frac{1}{2} \boldsymbol{K}_{gp}^{2,2}(\boldsymbol{C}_g) \,:\, \int f_p(\boldsymbol{C}_p) \boldsymbol{C}_p \otimes \boldsymbol{C}_p \mathrm{d}\boldsymbol{C}_p \tag{D.80}$$

with

$$\begin{aligned} K_{gp}^{2,1}(\boldsymbol{C}_g) = \; & \boldsymbol{\partial}_{\boldsymbol{C}_g} \cdot \int \sigma_{gp}(|\boldsymbol{C}_g|^2, \tfrac{\boldsymbol{C}_g}{|\boldsymbol{C}_g|} \cdot \boldsymbol{\omega})(\boldsymbol{C}_g - |\boldsymbol{C}_g|\boldsymbol{\omega})|\boldsymbol{C}_g| f_g^{(0)}(|\boldsymbol{C}_g|\boldsymbol{\omega}) \mathrm{d}\boldsymbol{\omega} \\ & -|\boldsymbol{C}_g| \boldsymbol{C}_g \cdot \int \boldsymbol{\partial}_{\boldsymbol{C}_g} \sigma_{gp}(|\boldsymbol{C}_g|^2, \tfrac{\boldsymbol{C}_g}{|\boldsymbol{C}_g|} \cdot \boldsymbol{\omega}) \big[f_g^{(0)}(|\boldsymbol{C}_g|\boldsymbol{\omega}) - f_g^{(0)}(\boldsymbol{C}_g) \big] \mathrm{d}\boldsymbol{\omega} \end{aligned} \tag{D.81}$$

and with

$$\begin{aligned} \boldsymbol{K}_{gp}^{2,2}(\boldsymbol{C}_g) = \; & 2 \int \boldsymbol{\partial}_{\boldsymbol{C}_g} \big(\sigma_{gp}(|\boldsymbol{C}_g|^2, \tfrac{\boldsymbol{C}_g}{|\boldsymbol{C}_g|} \cdot \boldsymbol{\omega}) |\boldsymbol{C}_g| \big) \otimes \big[\boldsymbol{\partial}_{\boldsymbol{C}_g} f_g^{(0)}(\boldsymbol{C}_g) - \boldsymbol{\partial}_{\boldsymbol{C}_g} f_g^{(0)}(|\boldsymbol{C}_g|\boldsymbol{\omega}) \big] \mathrm{d}\boldsymbol{\omega} \\ & + |\boldsymbol{C}_g| \int \sigma_{gp}(|\boldsymbol{C}_g|^2, \tfrac{\boldsymbol{C}_g}{|\boldsymbol{C}_g|} \cdot \boldsymbol{\omega}) \big[\partial_{\boldsymbol{C}_g}^2 f_g^{(0)}(\boldsymbol{C}_g) - \partial_{\boldsymbol{C}_g}^2 f_g^{(0)}(|\boldsymbol{C}_g|\boldsymbol{\omega}) \big] \mathrm{d}\boldsymbol{\omega} \\ & + 2|\boldsymbol{C}_g| \int \sigma_{gp}(|\boldsymbol{C}_g|^2, \tfrac{\boldsymbol{C}_g}{|\boldsymbol{C}_g|} \cdot \boldsymbol{\omega}) \tfrac{\boldsymbol{C}_g}{|\boldsymbol{C}_g|} \otimes \boldsymbol{\omega} \partial_{\boldsymbol{C}_g}^2 f_g^{(0)}(|\boldsymbol{C}_g|\boldsymbol{\omega}) \mathrm{d}\boldsymbol{\omega} \end{aligned} \tag{D.82}$$

where $\boldsymbol{K}_{gp}^{2,2}$ is also simplified thanks to isotropy.

D.3.2.3 Particle-gas collision operator expansion

The particle-gas collision operator $\mathcal{J}_{pg}$ is considered in its linearized form $\mathcal{J}_{pg}^{\varepsilon}$ from Eq. (D.53). The whole term $\mathcal{J}_{pg}^{(0)}$ vanishes under micro-reversibility and the two remaining terms $\mathcal{J}_{pg}^{(1)}$ and $\mathcal{J}_{pg}^{(2)}$ are expanded by linearity to get the expression of $\mathcal{J}_{pg}^{\varepsilon}(f_p, f_g)$ after Chapman-Enskog expansion:

$$\mathcal{J}_{pg}^{\varepsilon}(f_p, f_g) = \varepsilon \mathcal{J}_{pg}^{(1)}(f_p, f_g^{(0)}) + \varepsilon^2 \mathcal{J}_{pg}^{(1)}(f_p, f_g^{(1)}) + \varepsilon^2 \mathcal{J}_{pg}^{(2)}(f_p, f_g^{(0)}) + \mathscr{O}(\varepsilon^3) \tag{D.83}$$

where it is remarkable that the second order disequilibrium term $\phi^{(2)}$ does not appear at a significant order in $\mathcal{J}_{pg}^{\varepsilon}(f_p, f_g)$.
It is checked that $\mathcal{J}_{pg}^{(1)}(f_p, f_g^{(0)})$ cancels for an isotropic distribution as a matter of symmetry with $\mathcal{J}_{gp}^{(1)}(f_g^{(0)}, f_p)$:

$$\mathcal{J}_{pg}^{(1)}(f_p, f_g^{(0)}) = 0 \tag{D.84}$$

The first order in f_g reads:

$$\mathcal{J}_{pg}^{(1)}(f_p, f_g^{(1)}) = -\frac{1}{m_p} \boldsymbol{\partial}_{\boldsymbol{C}_p} f_p(\boldsymbol{C}_p) \cdot \int Q_{pg}^{(1)}(|\boldsymbol{\gamma}_\mathrm{g}|^2) |\boldsymbol{\gamma}_\mathrm{g}| \boldsymbol{\gamma}_\mathrm{g} \phi f_g^{(0)}(\boldsymbol{\gamma}_\mathrm{g}) \mathrm{d}\boldsymbol{\gamma}_\mathrm{g} \tag{D.85}$$

and is the dominant non-trivial term that describes particle-gas collisions in the particle equation.
Let us define a collision frequency from the average momentum transfer cross-section given in Eq. (D.52):

$$\nu_{pg} = \frac{1}{T^0} \int Q_{pg}^{(1)}(|\boldsymbol{\gamma}_\mathrm{g}|^2) |\boldsymbol{\gamma}_\mathrm{g}|^3 f_g^{(0)}(\boldsymbol{\gamma}_\mathrm{g}) \mathrm{d}\boldsymbol{\gamma}_\mathrm{g} \tag{D.86}$$

where $f_g^{(0)}(\boldsymbol{\gamma}_\mathrm{g}) = n_g \exp\left[-\boldsymbol{\gamma}_\mathrm{g} \cdot \boldsymbol{\gamma}_\mathrm{g}/(2T^0)\right] / \left(2\pi T^0\right)^{3/2}$. We get after some algebra the following expression:

$$\mathcal{J}_{pg}^{(2)}(f_p, f_g^{(2)}) = f_g^{(0)} \frac{\nu_{pg}}{3m_p} \Big(\boldsymbol{\partial}_{\boldsymbol{C}_p} \cdot (f_p \boldsymbol{C}_p) + \frac{T^0}{m_p} \partial_{\boldsymbol{C}_p}^2 f_p \Big) \tag{D.87}$$

which can be interpreted as a Fokker-Planck operator, which is a pseudo-collision-operator as described in § 8.4.2.2.

D.3.3 Summary of the different collision term expansions

The collision terms of the gas equation and those of the particle equation have been put in dimensionless form and expanded, yielding their order in ε and allowing to sort them:

1. The dimensionless collision term hierarchy is presented in Eq. (D.47);
2. The terms, resulting from the expansion versus collision probabilities (velocity differences and cross-sections) are hierarchized in Eq. (D.53) and Eq. (D.60);

3. The terms resulting from the gas NDF expansion are hierarchized in Eq. (D.72), Eq. (D.73), and Eq. (D.83).

The final order of the resulting terms is deduced from the order of the operator in the phase equation, the order of the expanded term and the order of the gas disturbance $f_g^{(k)}$. They are organized in Table D.4 as regards the two letters and the order of the operator is recalled from Eq. (D.47):

$$\begin{cases} \mathscr{D}_g(f_g) = \dfrac{1}{\varepsilon}\left(\mathscr{J}_{gg}(f_g, f_g) + \varepsilon \mathscr{J}^{\varepsilon}_{gp}(f_g, f_p)\right) \\ \mathscr{D}_p(f_p) = \dfrac{1}{\varepsilon^2}\left(\mathscr{J}^{\varepsilon}_{pg}(f_p, f_g) + \varepsilon^3 \mathscr{J}_{pp}(f_p, f_p)\right). \end{cases} \tag{D.88}$$

		Partenaire de collision : Gaz			Collision partner: particle			
Gas Eq.	$\mathscr{J}_{gg}(X,Y)$	$f_g^{(0)}$	$f_g^{(1)}$	$f_g^{(2)}$	X \ $\mathscr{J}^{\varepsilon}_{gp}$	$\mathscr{J}^{(0)}_{gp}(X, f_p)$	$\mathscr{J}^{(1)}_{gp}(X, f_p)$	$\mathscr{J}^{(2)}_{gp}(X, f_p)$
	$f_g^{(0)}$	Thermalized	$\mathscr{J}_{gg}(f_g^{(1)}, f_g^{(0)})$	$\mathscr{J}_{gg}(f_g^{(2)}, f_g^{(0)})$	$f_g^{(0)}$	Isotropy	$\mathscr{J}^{(1)}_{gp}(f_g^{(0)}, f_p)$	$\mathscr{J}^{(2)}_{gp}(f_g^{(0)}, f_p)$
	$f_g^{(1)}$	$\mathscr{J}_{gg}(f_g^{(0)}, f_g^{(1)})$	$\mathscr{J}_{gg}(f_g^{(1)}, f_g^{(1)})$	Neglected	$f_g^{(1)}$	$\mathscr{J}^{(0)}_{gp}(f_g^{(1)}, f_p)$	$\mathscr{J}^{(1)}_{gp}(f_g^{(1)}, f_p)$	Neglected
	$f_g^{(2)}$	$\mathscr{J}_{gg}(f_g^{(0)}, f_g^{(2)})$	Neglected	Neglected	$f_g^{(2)}$	$\mathscr{J}^{(0)}_{gp}(f_g^{(2)}, f_p)$	Neglected	Neglected
Particle Eq.	X \ $\mathscr{J}^{\varepsilon}_{pg}$	$\mathscr{J}^{(0)}_{pg}(f_p, X)$	$\mathscr{J}^{(1)}_{pg}(f_p, X)$	$\mathscr{J}^{(2)}_{pg}(f_p, X)$	$\mathscr{J}_{pp}(f_p, f_p)$ + coalescence (not treated)			
	$f_g^{(0)}$	Micro-revers.	Isotrope	Fok.-Planck				
	$f_g^{(1)}$		th/baroph.	Négligé				
	$f_g^{(2)}$		Neglected	Neglected				

Table D.4: *Origin of the different collision terms after expansion.*

D.4 Transcription of the scale hierarchy

All the terms of System (D.31) are completely expanded as regards ε. And terms of a given order can only compensate with all the other terms of the same order. So that the main system can be split into equations of consistent orders.

D.4.1 Order ε^{-1}

D.4.1.1 Gas equation

In the gas equation, the leading order term is the gas-gas collision term as expected. For the approach to be relevant, the term $\mathscr{J}^{(0)}_{gg}$ must be null, corresponding to a Maxwell-Boltzmann distribution for $f_g^{(0)}$ so that the equilibrium state of the gas is equivalent to the equation:

$$\mathscr{J}^{(0)}_{gg}(f_g^{(0)}, f_g^{(0)}) = 0 \tag{D.89}$$

which describes the evolution of the gas at order -1. As expected, this equation is decoupled from that of the particles, which are not agitated enough to perturb the gas.

D.4.1.2 Particle equation

At order -1, we get a condition for the particles which translates their mechanical equilibrium:

$$M_g \boldsymbol{F}_{\overline{G}} \cdot \boldsymbol{\partial}_{\boldsymbol{C}_p} f_p = 0. \tag{D.90}$$

D.4.2 Order ε^{0}

D.4.2.1 Gas equation

Both the transport Eq. (D.71) and the collision Eq. (D.72) operators from the gas equations yield terms of order ε^0:

$$\begin{aligned} &\partial_t f_g^{(0)} + \frac{1}{M_g}(\boldsymbol{C}_g + M_g \boldsymbol{v}_h) \cdot \partial_{\boldsymbol{x}}(f_g^{(0)}) \\ &\quad + \boldsymbol{v}_h \cdot \partial_{\boldsymbol{x}} f_g^{(0)} - \left(\boldsymbol{\partial}_{\boldsymbol{C}_g} f_g^{(0)} \otimes \boldsymbol{C}_g\right) : \partial_{\boldsymbol{x}} \boldsymbol{v}_h = \mathscr{J}_{gg}(f_g^{(0)}\phi, f_g^{(0)}) + \mathscr{J}_{gg}(f_g^{(0)}, f_g^{(0)}\phi) \end{aligned} \tag{D.91}$$

This equation yields the first order gas disequilibrium perturbation ϕ by linking it to the equilibrium state $f_g^{(0)}$.

D.4.2.2 Particle equation

The zeroth order equation for the particles features the gas/particle coupling which is investigated:

$$\begin{aligned}\underbrace{\partial_t f_p^{(0)} + \boldsymbol{v}_h \cdot \partial_{\boldsymbol{x}} f_p}_{1} - \underbrace{\left(\boldsymbol{\partial}_{\boldsymbol{C}_p} f_p^{(0)} \otimes \boldsymbol{C}_p\right) : \partial_{\boldsymbol{x}} \boldsymbol{v}_h}_{2} = \quad & f_g^{(0)} \frac{\nu_{pg}}{3m_p} \Big(\underbrace{\boldsymbol{\partial}_{\boldsymbol{C}_p} \cdot (f_p \boldsymbol{C}_p)}_{3} + \underbrace{\frac{T^0}{m_p} \partial^2_{\boldsymbol{C}_p} f_p}_{4} \Big) \\ & \underbrace{- \frac{1}{m_p} \boldsymbol{\partial}_{\boldsymbol{C}_p} f_p(\boldsymbol{C}_p) \cdot \int Q_{pg}^{(1)}(|\boldsymbol{\gamma}_{\mathrm{g}}|^2) |\boldsymbol{\gamma}_{\mathrm{g}}| \boldsymbol{\gamma}_{\mathrm{g}} \phi f_g^{(0)}(\boldsymbol{\gamma}_{\mathrm{g}}) \mathrm{d}\boldsymbol{\gamma}_{\mathrm{g}}}_{5}\end{aligned} \tag{D.92}$$

The terms of the equation can be interpreted, from left to right:

1. free transport or streaming at the hydrodynamic velocity;
2. particle pressure;
3. first Fokker-Planck term (drag force);
4. second Fokker-Planck term (isotropic diffusion);
5. out-of-equilibrium transport fluxes.

These terms allow to compute the particle perturbation function $f_p^{(1)}$ since it is in the r.h.s.
We focus on the out-of-equilibrium transport fluxes: the average momentum transfer cross-section $Q_{pg}^{(1)}(|\boldsymbol{\gamma}_{\mathrm{g}}|^2)$ is integrated versus the gas first order perturbation ϕ.

D.4.3 Order ε

This level of resolution is required to assess ϕ and therefore the gas velocity perturbation which drives the out-of-equilibrium transport fluxes of Eq. (D.92).

D.4.3.1 Gas equations

The gas equation reads at this order:

$$\begin{aligned}&\partial_t f_g^{(0)}\phi + \frac{1}{M_g}(\boldsymbol{C}_g + M_g \boldsymbol{v}_h) \cdot \partial_{\boldsymbol{x}}(f_g^{(0)}\phi) + \boldsymbol{v}_h \cdot \partial_{\boldsymbol{x}} f_g^{(0)}\phi - \left(\boldsymbol{\partial}_{\boldsymbol{C}_g} f_g^{(0)}\phi \otimes \boldsymbol{C}_g\right) : \partial_{\boldsymbol{x}} \boldsymbol{v}_h \\ &= \mathcal{J}_{gg}(f_g^{(0)}\phi^{(2)}, f_g^{(0)}) + \mathcal{J}_{gg}(f_g^{(0)}\phi, f_g^{(0)}\phi) + \mathcal{J}_{gg}(f_g^{(0)}, f_g^{(0)}\phi^{(2)}) + \mathcal{J}_{gp}^{(0)}(f_g^{(1)}, f_p) + \mathcal{J}_{gp}^{(1)}(f_g^{(0)}, f_p) \\ &= \mathcal{J}_{gg}(f_g^{(0)}\phi^{(2)}, f_g^{(0)}) + \mathcal{J}_{gg}(f_g^{(0)}\phi, f_g^{(0)}\phi) + \mathcal{J}_{gg}(f_g^{(0)}, f_g^{(0)}\phi^{(2)}) \\ &\quad + \int f_p(\boldsymbol{C}_p) \mathrm{d}\boldsymbol{C}_p \int \sigma_{gp}\Big(|\boldsymbol{C}_g|^2, \boldsymbol{\omega} \cdot \tfrac{\boldsymbol{C}_g}{|\boldsymbol{C}_g|}\Big) |\boldsymbol{C}_g| \times \Big[\big[f_g^{(0)}\phi\big](|\boldsymbol{C}_g|\boldsymbol{\omega}) - \big[f_g^{(0)}\phi\big](\boldsymbol{C}_g)\Big] \mathrm{d}\boldsymbol{\omega} \\ &\quad + \Big(\int f_p(\boldsymbol{C}_p)\boldsymbol{C}_p \mathrm{d}\boldsymbol{C}_p\Big) \cdot \int \sigma_{gp}(|\boldsymbol{C}_g|^2, \tfrac{\boldsymbol{C}_g}{|\boldsymbol{C}_g|} \cdot \boldsymbol{\omega}) |\boldsymbol{C}_g| \big[\boldsymbol{\partial}_{\boldsymbol{C}_g} f_g^{(0)}(|\boldsymbol{C}_g|\boldsymbol{\omega}) - \boldsymbol{\partial}_{\boldsymbol{C}_g} f_g^{(0)}(\boldsymbol{C}_g)\big] \mathrm{d}\boldsymbol{\omega}\end{aligned} \tag{D.93}$$

and allows to solve for the first order perturbation of the gas Maxwell distribution ϕ. Still it depends on the second order perturbation $\phi^{(2)}$.

D.4.3.2 Particle equation

The particle equation reads at this order:

$$\frac{1}{M_g} \boldsymbol{C}_p \cdot (\partial_{\boldsymbol{x}} f_p) = \mathcal{J}_{pp} + \mathcal{J}_{pg}^{(0)}(f_p, f_g^{(3)}) + \mathcal{J}_{pg}^{(1)}(f_p, f_g^{(2)}) + \mathcal{J}_{pg}^{(2)}(f_p, f_g^{(1)}) \tag{D.94}$$

This order in the particle distribution is not needed. We do not further the development at higher orders since they are not needed for the study.

D.4.4 Resolution strategy

Accordingly to the Chapman-Enskog technique, a cascading resolution is required to find out the desired perturbation terms.

D.5 Model analysis

D.5.1 Resulting gas hierarchy

In order to solve for the perturbations ϕ and $\phi^{(2)}$, we now present the resolubility criterion technique, as described in § 3.4.3.3.
Let us write:

$$\mathscr{F}(\phi) = \frac{1}{f_g^{(0)}}\left[\mathcal{J}_{gg}(f_g^{(0)}\phi, f_g^{(0)}) + \mathcal{J}_{gg}(f_g^{(0)}, f_g^{(0)}\phi)\right] \tag{D.95}$$

so that Eq. (D.89), Eq. (D.91), and Eq. (D.93) can be written as a system which can be solved by successive substitutions:

$$\begin{aligned}
\mathscr{F}(\phi) &= \frac{1}{M_p f_g^{(0)}}\boldsymbol{C}_g \cdot \partial_{\boldsymbol{x}} f_g^{(0)} \\
\mathscr{F}(\phi^{(2)}) &= \frac{1}{f_g^{(0)}}\Big[\partial_t f_g^{(0)} + \frac{1}{M_p}\boldsymbol{C}_g \cdot \partial_{\boldsymbol{x}}(f_g^{(0)}\phi) + \boldsymbol{v}_h \cdot \partial_{\boldsymbol{x}} f_g^{(0)} \\
&\quad - \left(\boldsymbol{\partial}_{\boldsymbol{C}_g} f_g^{(0)} \otimes \boldsymbol{C}_g\right) : \partial_{\boldsymbol{x}}\boldsymbol{v}_h - 2\mathcal{J}_{gg}(f_g^{(1)}, f_g^{(1)})\Big] \\
\mathscr{F}(\phi^{(3)}) &= \frac{1}{f_g^{(0)}}\Big[\partial_t f_g^{(0)}\phi + \frac{1}{M_p}\boldsymbol{C}_g \cdot (\partial_{\boldsymbol{x}} f_g^{(0)}\phi^{(2)}) + \boldsymbol{v}_h \cdot \partial_{\boldsymbol{x}} f_g^{(1)} + M_p \boldsymbol{F}_{\overline{G}} \cdot \boldsymbol{\partial}_{\boldsymbol{C}_g} f_g^{(0)} \\
&\quad - \left(\boldsymbol{\partial}_{\boldsymbol{C}_g} f_g^{(1)} \otimes \boldsymbol{C}_g\right) : \partial_{\boldsymbol{x}}\boldsymbol{v}_h - \mathcal{J}_{gg}(f_g^{(0)}\phi^{(2)}, f_g^{(0)}\phi) - \mathcal{J}_{gg}(f_g^{(0)}\phi, f_g^{(0)}\phi^{(2)}) \\
&\quad - \mathcal{J}_{gp}^{(0)}(f_g^{(0)}\phi, f_p) - \mathcal{J}_{gp}^{(1)}(f_g^{(0)}, f_p)\Big]
\end{aligned} \tag{D.96}$$

The resolution of the hierarchy with a resolubility criterion, as discussed in § 8.4.2.3 for a Fokker-Planck equation, is here possible but more difficult: the expansion in the gradients can in particular not be performed analytically. The further study of the hierarchy is not performed in the present work and is left for a future communication.

D.5.2 Particle equation with coalescence

The equation describing the evolution of particles is Eq. (D.92). To treat coalescence, the equation can be derived with the additional particle-particle collision term $\mathcal{J}_{pp}$. This operator can be written as a classical kinetic coalescence operator, but the particles may not be in free flight (i.e. the FMR presented in § 8.5) between two collisions so that the general form of Eq. (8.72) must be used:

$$\begin{aligned}
\mathfrak{C}(f_p, f_p, p_2) = &\frac{1}{2}\iiint_{\boldsymbol{x}^\star, \boldsymbol{c}^\star, \theta^\star} \int_{v^\star \in [0, v]} f_p^\diamond f_p^\star p_2 \, |\boldsymbol{c}^\diamond - \boldsymbol{c}^\star| \, \beta(v^\diamond, v^\star) J \mathrm{d}v^\star \mathrm{d}\boldsymbol{x}^\star \mathrm{d}\boldsymbol{c}^\star \\
&+ \iiint_{\boldsymbol{x}^\star, \boldsymbol{c}^\star, \theta^\star} \int_{v^\star} f_p f_p^\star p_2 \, |\boldsymbol{c} - \boldsymbol{c}^\star| \, \beta(v, v^\star) \mathrm{d}v^\star \mathrm{d}\boldsymbol{x}^\star \mathrm{d}\boldsymbol{c}^\star.
\end{aligned} \tag{D.97}$$

where $p_2(t, \boldsymbol{r}, \boldsymbol{c}^\star, v^\star, \boldsymbol{c}^\diamond, v^\diamond)$ is the two-point PDF, driven by its own evolution equation given in Eq. (8.74). The two-point NDF formalism introduced in § 8.4.5 is indeed more versatile and can treat coalescence whatever the regime.

D.5.3 Conclusion: a unified model for moderately dense nano-micro disperse two-phase flows

We finally have the following set of kinetic equations to describe a moderately dense nano-micro polydisperse two-phase flow:

$$\left\{\begin{aligned}
&\partial_t f_g^{(0)} + \frac{1}{M_g}(\boldsymbol{C}_g + M_g \boldsymbol{v}_h) \cdot \partial_{\boldsymbol{x}}(f_g^{(0)}) + \boldsymbol{v}_h \cdot \partial_{\boldsymbol{x}} f_g^{(0)} \\
&\qquad - \left(\boldsymbol{\partial}_{\boldsymbol{C}_g} f_g^{(0)} \otimes \boldsymbol{C}_g\right) : \partial_{\boldsymbol{x}}\boldsymbol{v}_h = \mathcal{J}_{gg}(f_g^{(0)}\phi, f_g^{(0)}) + \mathcal{J}_{gg}(f_g^{(0)}, f_g^{(0)}\phi) \\
&\partial_t f_p^{(0)} + \boldsymbol{v}_h \cdot \partial_{\boldsymbol{x}} f_p - \left(\boldsymbol{\partial}_{\boldsymbol{C}_p} f_p^{(0)} \otimes \boldsymbol{C}_p\right) : \partial_{\boldsymbol{x}}\boldsymbol{v}_h = \\
&\qquad f_g^{(0)} \frac{\nu_{pg}}{3m_p}\left(\boldsymbol{\partial}_{\boldsymbol{C}_p} \cdot (f_p \boldsymbol{C}_p) + \frac{T^0}{m_p}\partial^2_{\boldsymbol{C}_p} f_p\right) \\
&\qquad - \frac{1}{m_p}\boldsymbol{\partial}_{\boldsymbol{C}_p} f_p(\boldsymbol{C}_p) \cdot \int Q_{pg}^{(1)}(|\boldsymbol{\gamma}_{\mathrm{g}}|^2)|\boldsymbol{\gamma}_{\mathrm{g}}|\boldsymbol{\gamma}_{\mathrm{g}} \phi f_g^{(0)}(\boldsymbol{\gamma}_{\mathrm{g}}) \mathrm{d}\boldsymbol{\gamma}_{\mathrm{g}} \\
&\qquad + \mathfrak{C}(f_p, f_p, p_2) \\
&\partial_t p_2 + \partial_{\boldsymbol{r}}\left(p_2 \partial_t \boldsymbol{r} - p_2 \boldsymbol{D}_{\boldsymbol{2}} \cdot \partial_{\boldsymbol{r}} \cdot \left(\frac{\Phi_2}{kT_g}\right) - \boldsymbol{D}_{\boldsymbol{2}} \cdot \partial_{\boldsymbol{r}} p_2\right) = 0
\end{aligned}\right. \tag{D.98}$$

and Eq. (D.93) must be considered in addition to solve ϕ.
In order to yield a model for a gas-particle mixture with a significant mass loading the expansion of gas and particle NDFs based on their peculiar mass ratio is proven to be feasible, with a technique adapted from plasmas (Graille et al. 2009).

D.5.4 Prospects and limits

D.5.4.1 Validity domain as regards particle sizes

We aim at connecting the modeling up to the level of usual, non-Brownian particles. The behavior of the model must be assessed for these big droplets i.e. for very small values of ε, and the Williams-Boltzmann equation with the usual closures are to be retrieved.

D.5.4.2 Treatment of two-way coupling

The reference frame that is chosen in § D.1.2.3 for the kinetic model is based on the hydrodynamic velocity i.e. the ensemble velocity. This allows the model to account naturally for the strong coupling between the two phases, since the velocity that is solved is the hydrodynamic velocity while the gas and particle ones are treated with an additional drift velocity.

D.5.4.3 Estimation of the cross-sections

The kinetic model previously derived describes the gas-particle interactions directly through kinetic collision terms: the cross-sections characterize the physics of the collisions and their evaluation and modeling is crucial for the model. Assumption [K3] is therefore a weak point of the model and should be consolidated or refined.

D.5.4.4 Resolution difficulties

The hierarchy that has been written above is difficult to solve because of it large phase space and of its numerous couplings. We keep in mind that the behavior of moderately dense coalescing two-phase flows can be treated with the above comprehensive model whatever the size of the particles. In the following chapter, we build a more tractable model by unifying the diffusive model for Brownian particles and the kinetic-based model for ballistic particles.

References

Abbas, M. (2008). *Auto-diffusion de particules dans un écoulement cisaillé: Des interactions hydrodynamiques aux effets collisionnels*. Ph. D. thesis, Institut National Polytechnique de Toulouse. *(p. 97)*

Abbas, M., E. Climent, O. Simonin, and M. Maxey (2006). Dynamics of bidisperse suspensions under stokes flows: Linear shear flow and sedimentation. *Physics of Fluids 18*, 121504. *(p. 97)*

Abdulle, A. (2002). Fourth order Chebyshev methods with recurrence relation. *SIAM Journal on Scientific Computing 23*(6), 2041–2054. *(p. 243)*

Abgrall, R., A. Larat, and M. Ricchiuto (2011). Construction of very high order residual distribution schemes for steady inviscid flow problems on hybrid unstructured meshes. *Journal of Computational Physics 230*(11), 4103–4136. *(p. 233)*

Abrahamson, J. (1975). Collision rates of small particles in a vigorously turbulent fluid. *Chemical Engineering Science 30*, 1371–1379. *(p. 103)*

Abramowitz, M. and I. Stegun (1964). *Handbook of Mathematical Functions with Formulas, Graphs, and Mathematical Tables* (ninth Dover printing, tenth GPO printing ed.). New York: Dover. *(p. 244, 296)*

Abramzon, B. and W. Sirignano (1989). Droplet vaporization model for spray combustion calculations. *Int. J. Heat Mass Transfer 32*, 1605–1618. *(p. 95, 357, 359, 360)*

Achim, P. (1999). *Simulation de collisions, coalescence et rupture de gouttes par une approche Lagrangienne: application aux moteurs à propergol solide*. Ph. D. thesis, Université de Rouen. *(p. 81, 83, 86)*

Agarwal, R., K. Yun, and R. Balakrishnan (2001). Beyond Navier–Stokes: Burnett equations for flows in the continuum–transition regime. *Physics of Fluids 13*, 3061. *(p. 90)*

Ahmadi, G. (2009). Lagrangian versus eulerian method for nano-particles. In *Modelling and Computation of Nanoparticles in Fluid Flows*, Number 1 in Lectures of the von Karman Institute, pp. 1–74. NATO RTO AVT 169. *(p. 186)*

Aït Atmane, Y. (2012). *Synthèse de nanoparticules d'aluminium et enrobage par des polymères pour des applications énergétiques*. Ph. D. thesis, Université Paris Diderot. *(p. 23)*

Alavi, S. and D. Thompson (2006). Molecular dynamics simulations of the melting of aluminum nanoparticles. *The Journal of Physical Chemistry A 110*(4), 1518–1523. *(p. 25)*

Alderliesten, M. (2004a). Mean particle diameters. part i: Evaluation of definition systems. *Particle & Particle systems Characterization 7*(1-4), 233–241. *(p. 61)*

Alderliesten, M. (2004b). Mean particle diameters. part ii: standardization of nomenclature. *Particle & particle systems characterization 8*(1-4), 237–241. *(p. 61)*

Allaire, G. (2005). *Analyse numérique et optimisation: Une introduction à la modélisation mathématique et à la simulation numérique*. Ed. Ecole Polytechnique. *(p. 239)*

Alopaeus, V., M. Laakkonen, and J. Aittamaa (2006). Solution of population balances with breakage and agglomeration by high-order moment-conserving method of classes. *Chemical Engineering Science 61*(20), 6732–6752. *(p. 120)*

Ambroso, A., C. Chalons, F. Coquel, T. Galié, E. Godlewski, P. Raviart, and N. Seguin (2008). The drift-flux asymptotic limit of barotropic two-phase two-pressure models. *Communications in Mathematical Sciences 6*(2), 521–529. *(p. 77)*

Ambroso, A., C. Chalons, and P. Raviart (2012). A Godunov-type method for the seven-equation model of compressible two-phase flow. *Computers & Fluids 54*, 67–91. *(p. 75)*

Amsden, A. A., P. J. O'Rourke, and T. D. Butler (1989). Kiva II, a computer program for chemically reactive flows with sprays. Technical Report LA-11560-MS, Los Alamos National Laboratory, Los Alamos, New Mexico. *(p. 87, 106, 363)*

Anderson, J. (1995). *Computational fluid dynamics*, Volume 206. McGraw-Hill. *(p. 225)*

Andries, P., J. Bourgat, P. Le Tallec, and B. Perthame (2002). Numerical comparison between the boltzmann and ES-BGK models for rarefied gases. *Computer methods in applied mechanics and engineering 191*(31), 3369–3390. *(p. 91)*

Anthoine, J. (2000). *Experimental and numerical study of aeroacoustic phenomena in large solid propellant boosters, with application to the Ariane 5 solid rocket motor*. Ph. D. thesis, Université Libre de

Bruxelles. *(p. 40, 42)*

Anthoine, J., J.-M. Buchlin, and J.-F. Guéry (2000). Experimental and numerical investigations of nozzle geometry effect on the instabilities in solid propellant boosters. In 36^{th} *AIAA/ASME/SAE/ASEE Joint Propulsion Conference and Exhibit*, Cincinnati, OH. *(p. 41, 42)*

Apte, S., K. Mahesh, P. Moin, and J. Oefelein (2003). Large-eddy simulation of swirling particle-laden flows in a coaxial-jet combustor. *International Journal of Multiphase Flow 29*(8), 1311–1331. *(p. 363)*

Apte, S., M. Martin, and N. Patankar (2009). A numerical method for fully resolved simulation (FRS) of rigid particle–flow interactions in complex flows. *Journal of Computational Physics 228*(8), 2712–2738. *(p. 70, 71)*

Apte, S. and V. Yang (2000). Turbulent flame dynamics of homogeneous solid propellant in a rocket motor. *Proceedings of the Combustion Institute 28*(1), 903–910. *(p. 24)*

Apte, S. and V. Yang (2003). A large-eddy simulation study of transition and flow instability in a porous-walled chamber with mass injection. *Journal of Fluid Mechanics 477*, 215–225. *(p. 50)*

Ashgriz, N. and P. Givi (1987). Coalescence collision of fuel droplets. In 25^{th} *Aerospace Sciences Meeting*, Reno, NV. *(p. 103)*

Ashgriz, N. and J. Poo (1990). Coalescence and separation in binary collisions of liquid droplets. *Journal of Fluid Mechanics 221*, 183–204. *(p. 83)*

Avalon, F. and D. Lambert (2000). Montage VALDO : premiers essais de mise au point et de qualification. Technical Report RF 5/00064 DEFA, ONERA. *(p. xviii, 42)*

Avalon, F. and D. Lambert (2010). Mesures de vitesse par sonde à film chaud sur le montage de simulation en gaz froid VECLA. Technical Report 2/17456 DEFA, ONERA. *(p. 39)*

Avalon, F. and L. Lebon (1993). Étude de la turbulence sur le montage VECLA pour un écoulement en transition. Technical Report 6/2486EY DEFA, ONERA. *(p. 39)*

Avalon, G., G. Casalis, and J. Griffond (1998). Flow instabilities and acoustic resonance of channels with wall injection. In *34th AIAA/ASME/SAE/ASEE Joint Propulsion Conference and Exhibit. (p. 42)*

Avalon, G., B. Ugurtas, F. Grisch, and A. Bresson (2000). Numerical computations and visualization tests of the flow inside a cold gas simulation with characterization of a parietal vortex-shedding. In 36^{th} *AIAA/ASME/SAE/ASEE Joint Propulsion Conference and Exhibit*, Cincinnati, OH. *(p. 50)*

Averin, V., V. Arkhipov, I. Vasenin, N. Dyachenko, and V. Trofimov (2003). Effect of a sudden change in cross-sectional area of the solid rocket motor duct on coagulation of condensed particles. *Combustion, Explosion, and Shock Waves 39*(3), 316–322. *(p. 38)*

Azarov, I. and M. Veshchunov (2010). Development of the new approach to the Brownian coagulation theory : transition regime. *J. Engineering Thermophysics 19*(3), 128–137. *(p. 205)*

Babinsky, E. and P. Sojka (2002). Modeling drop size distributions. *Progress in energy and combustion science 28*(4), 303–329. *(p. 61, 117)*

Babuk, V., V. Vassiliev, and V. Sviridov (2001). Propellant formulation factors and metal agglomeration in combustion of aluminized solid rocket propellant. *Comb. Sc. and Tech. 163*, 261–289. *(p. 27)*

Baer, M. and J. Nunziato (1986). A two-phase mixture theory for the deflagration to detonation (DDT) transition in reactive granular materials. *Int. J. Multiphase Flow 12*, 861–889. *(p. 75)*

Balian, R. (1992). *From microphysics to macrophysics*, Volume 1. Springer. *(p. 88)*

Ballereau, S., D. Ballion, F. Godfroy, and O. Orlandi (2005). Note de synthèse des simulations échelle 1 de l'impact d'une PTFS3 3D sur les niveaux ODP 3ème bouffée. Technical Report A5-NT-1122000-01270, SNPE. *(p. 21, 52)*

Ballereau, S. and F. Godfroy (2009). Two minutes inside the Ariane 5's SRMs : Effect of different sources of pressure oscillations during operation. In 60^{th} *International Astronautical Congress*, South Korea. *(p. 42, 46)*

Ballereau, S., F. Godfroy, S. Gallier, O. Orlandi, J. Thepenier, E. Robert, and N. Cesco (2011). Evaluation method of thrust oscillations in large SRM – application to segmented SRM's. In 47^{th} *AIAA/ASME/SAE/ASEE Joint Propulsion Conf.*, San Diego, CA. *(p. 42)*

Ballereau, S., F. Godfroy, J. Guéry, and D. Ribereau (2003). Assessment on analysis and prediction method applied on thrust oscillations of Ariane 5 solid rocket motor. In *AIAA/ASME/SAE/ASEE* 39^{th} *Joint Propulsion Conference and Exhibit*, Huntsville, AL. *(p. 17, 22, 42, 45)*

Balthasar, M. and M. Frenklach (2005). Detailed kinetic modeling of soot aggregate formation in laminar premixed flames. *Combustion and Flame 140*(1), 130–145. *(p. 121)*

Baranger, C. (2004a). *Modélisation, étude mathématique et simulation des collisions dans les fluides complexes*. Ph. D. thesis, École Normale Supérieure de Cachan. *(p. 87)*

Baranger, C. (2004b). Modelling of oscillations, breakup and collisions for droplets: the establishment of kernels for the tab model. *Mathematical Models and Methods in Applied Sciences 14*(05), 775–794. *(p. 87)*

Baranger, C., G. Baudin, L. Boudin, B. Després, F. Lagoutière, E. Lapébie, and T. Takahashi (2005). Liquid jet generation and break-up. *Numerical Methods for Hyperbolic and Kinetic Equations 7*, 149–

176. IRMA Lect. Math. Theor. Phys. (EMS Publ. House). *(p. 87)*

Barbee, T. (1985). Multilayer synthesis by physical vapor deposition. *Synthetic Modulated Structures*, 313–337. *(p. 22, 23)*

Barberon, T. and P. Helluy (2005). Finite volume simulation of cavitating flows. *Computers & fluids 34*(7), 832–858. *(p. 78)*

Bardos, C., F. Golse, and D. Levermore (1991). Fluid dynamic limits of kinetic equations. i.formal derivations. *Journal of Statistical Physics 63*. *(p. 90, 91)*

Baron, P. and K. Willeke (2001). Aerosol measurement: principles, techniques, and applications. *(p. 187)*

Batchelor, G. (1972). Sedimentation in a dilute dispersion of spheres. *J. Fluid Mech. 52*, 245–268. *(p. 202)*

Batchelor, G. (1982). Sedimentation in a dilute polydisperse system of interacting spheres. Part 1. General theory. *J. Fluid Mech. 119*, 379–408. *(p. 202)*

Batchelor, G. (1986). Note on Onsager symmetry of the kinetic coefficients for sedimentation and diffusion in a dilute bidispersion. *J. Fluid Mech. 171*, 509–517. *(p. 202)*

Batchelor, G. and C.-S. Wen (1982). Sedimentation in a dilute polydisperse system of interacting spheres. Part 2. Numerical results. *J. Fluid Mech. 124*, 495–528. *(p. 202)*

Batsura, I., G. Kruglikov, and V. Arutiunov (1981). Morphology of experimental pneumoconiosis developing after exposure to lunar soil. *Biull. Eksp. Biol. Med. 92*(9), 376. *(p. 187)*

Baum, E. and M. Denison (2012). Characterization of solid propellants by damped combustion oscillations. *Combustion and Flame 159*(2), 854 – 858. *(p. 40, 50)*

Beard, K. V. and S. N. Grover (1974). Numerical collision efficiencies for small raindrops colliding with micron size particles. *Journal of Atmospheric Sciences 31*, 543–550. *(p. 82)*

Beck, J. and A. Watkins (2002). On the development of spray submodels based on droplet size moments. *Journal of Computational Physics 182*, 586–621. *(p. 28)*

Beckstead, M. (1987). Evidences for distributed combustion. In *24th JANNAF Combustion Meeting*, Volume 1, Johns-Hopkins Univ. MD. *(p. 30)*

Beckstead, M. (2002). Modeling aluminum combustion. In *RTO AVT/VKI Special course on Internal Aerodynamics in Solid Rocket Propulsion*. *(p. 30, 31)*

Beckstead, M., K. Puduppakkam, P. Thakre, and V. Yang (2007). Modeling of combustion and ignition of solid-propellant ingredients. *Progress in Energy and Combustion Science 33*(6), 497–551. *(p. 24, 30)*

Beddini, R. (1977). A reacting turbulent boundary layer approach to solid propellant erosive burning. Technical report, DTIC Document. *(p. 39)*

Beddini, R. (1981). *Analysis of Injection-induced Flows in Porous-walled Ducts with Application to the Aerothermochemistry of Solid-propellant Motors*. Ph. D. thesis, Rutgers University. *(p. 26, 39, 52)*

Beddini, R. (1986). Injection-induced flows in porous-walled ducts. *AIAA journal 24*(11), 1766–1773. *(p. 39)*

Belt, R. and O. Simonin (2009). Quadrature method of moments for the pdf modeling of droplet coalescence in turbulent two-phase flow. In *ASME Conference Proceedings*, pp. 783–793. *(p. 103, 120)*

Ben-Dakhlia, R., V. Giovangigli, and D. Rosner (2002). Soret effects in laminar counterflow spray diffusion flames. *Combust. Theory and Modelling 6*, 1–17. *(p. 118)*

BenDakhlia, R. (2001). *Combustion stationnaire et instationnaire de mélanges diphasiques*. Ph. D. thesis, École Centrale Paris. *(p. 117)*

BenDakhlia, R. and V. Giovangigli (2000). Multiradii modeling of counterflow spray diffusion flames. *In Proc. Combustion Inst. 28*, 1039–1045. *(p. 117, 119)*

Benkiewicz, K. and A. Hayashi (2002). Aluminum dust ignition behind reflected shock wave: two-dimensional simulations. *Fluid dynamics research 30*(5), 269–292. *(p. 53, 356)*

Béreux, F. (1996). Zero-relaxation limit versus operator splitting for two-phase fluid flow computations. *Comput. Methods in Appl. Mech. and Engin. 133*, 93–124. *(p. 269)*

Béreux, F. and L. Sainsaulieu (1997). A Roe-type Riemann solver for hyperbolic systems with relaxation based on time-dependent wave decomposition. *Numerische Mathematik 77*, 183–145. *(p. 269)*

Berger, M. and J. Oliger (1984). Adaptive mesh refinement for hyperbolic partial differential equations. *Journal of computational Physics 53*(3), 484–512. *(p. 233)*

Berthon, C. (2005). Stability of the MUSCL schemes for the Euler equations. *Commun. Math. Sci. 3*(2), 133–157. *(p. 250, 251, 253)*

Berthon, C. (2006). Numerical approximations of the 10-moment Gaussian closure. *Math. Comp. 75*(256), 1809–1831. *(p. 157, 230, 250)*

Bertier, N., B. Courbet, D. Dutoya, F. Vuillot, and P. Sagaut (2004). Large eddy simulation of a subsonic flow over a cavity on general unstructured grids. *AIAA journal* (Paper n textsuperscripto2004-0679). *(p. 322)*

Bhatnagar, P., E. Gross, and M. Krook (1954). A model for collision processes in gases. I. Small amplitude processes in charged and neutral one-component systems. *Physical Review 94*, 511–525. *(p. 91)*

Biagioni, M. and H. Austruy (1996). Propellant and process for Ariane 5 boosters. In *5th Int. Symp.*

Propulsion in Space Transportation, Paris. *(p. 16)*

Bico, J. and D. Quéré (2002). Self-propelling slugs in a tube. *J. Fluid Mech 467*, 201. *(p. 58)*

Billet, G., V. Giovangigli, and G. de Gassowski (2008). Impact of volume viscosity on a shock/hydrogen bubble interaction. *Comb. Theory Mod. 12*, 221–248. *(p. 53, 237, 274)*

Bird, G. A. (1994). Molecular gas dynamics and the direct simulation of gas flows. *Oxford Science Publications 42*. *(p. 106, 107)*

Bisetti, F., G. Blanquart, M. Mueller, and H. Pitsch (2012). On the formation and early evolution of soot in turbulent nonpremixed flames. *Combustion and Flame 159*(1), 317–335. *(p. 121, 185)*

Blanquart, G., P. Pepiot-Desjardins, and H. Pitsch (2009). Chemical mechanism for high temperature combustion of engine relevant fuels with emphasis on soot precursors. *Combustion and Flame 156*(3), 588–607. *(p. 185)*

Blanquart, G. and H. Pitsch (2009). Analyzing the effects of temperature on soot formation with a joint volume-surface-hydrogen model. *Combustion and Flame 156*(8), 1614–1626. *(p. 185)*

Bocanegra, P. (2007). *Études expérimentales et modélisation de la combustion des nuages de particules micrométriques et nanométriques d'aluminium.* Ph. D. thesis, Université d'Orléans. *(p. xvii, 22, 23, 25, 31, 32)*

Bockhorn, H. (1994). Soot formation in combustion (mechanisms and models). *Springer series in chemical physics*. *(p. 185)*

Bohbot, J., N. Gillet, and A. Benkenida (2009). IFP-C3D: an unstructured parallel solver for reactive compressible gas flow with spray. *Oil & Gas Science and Technology 64(3)*, 309–335. *(p. 232, 247)*

Boileau, M. (2007). Ph. D. thesis, Institut National Polytechnique de Toulouse. *(p. 103)*

Boileau, M., C. Chalons, J.-F. Bourgouin, C. Terrier, F. Laurent, S. de Chaisemartin, and M. Massot (2010). Robust numerical schemes for Eulerian spray DNS and LES in two-phase turbulent flows. In 7^{th} *International Conference on Multiphase Flows*, Tampa, FL, USA, pp. 1–15. Available at http://hal.archives-ouvertes.fr/hal-00498182/en/. *(p. 133, 154, 230)*

Boileau, M., C. Chalons, F. Laurent, S. de Chaisemartin, and M. Massot (2010). Robust numerical schemes for Eulerian spray DNS and LES in two-phase turbulent flows. In *Proceedings of the Summer Program 2010, Center for Turbulence Research, Stanford University*, Center for Turbulence Research, Stanford University, pp. 359–370. *(p. 154)*

Boileau, M., G. Staffelbach, B. Cuenot, T. Poinsot, and C. Bérat (2008). LES of an ignition sequence in a gas turbine engine. *Combustion and Flame 154*(1), 2–22. *(p. 3, 103, 232)*

Boltzmann, L. (1872). Weitere Studien über das Wärmegleichgewicht unter Gasmolekülen. *Sitz. Akad. Wiss. Wien 66*, 275–370. *(p. 89, 91, 94)*

Bond, J., K. Watson, and J. Welch (1965). *Atomic Theory of Gas Dynamics*. Addison-Wesley. *(p. 376)*

Bouchut, F. (1994). On zero pressure gas dynamics. In *Advances in kinetic theory and computing*, pp. 171–190. River Edge, NJ: World Sci. Publishing. *(p. 111, 112)*

Bouchut, F., S. Jin, and X. Li (2003). Numerical approximations of pressureless and isothermal gas dynamics. *SIAM J. Num. Anal. 41*, 135–158. *(p. 112, 230, 250, 251, 275, 292, 293)*

Bove, S., T. Solberg, and B. Hjertager (2005). A novel algorithm for solving population balance equations: the parallel parent and daughter classes. Derivation, analysis and testing. *Chemical Engineering Science 60*(5), 1449–1464. *(p. 120)*

Brain, J., M. Curran, T. Donaghey, and R. Molina (2009). Biologic responses to nanomaterials depend on exposure, clearance, and material characteristics. *Nanotoxicology 3*(3), 174–180. *(p. 187)*

Braithwaite, P. C., M. W. Beckstead, and R. L. Raun (1984). Measurements of distributed combustion. In 21^{st} *JANNAF Combustion meeting*, Sunnyvale, CA. *(p. 30)*

Brayner, R. (2008). The toxicological impact of nanoparticles. *Nano Today 3*(1), 48–55. *(p. 186)*

Brazier-Smith, P., S. Jennings, and J. Latham (1972). The interaction falling water drops : coalescence. *Proceedings of the Royal Society 326*, 393–408. *(p. 83)*

Briand, R. (2003). Note de synthèse des calculs VSP/combustion. Technical Report 593/2003/SME/DPS/CER, SME. *(p. 31)*

Briley, W. and H. McDonald (1977). Solution of the multidimensional compressible Navier-Stokes equations by a generalized implicit method. *Journal of Computational Physics 24*(4), 372–397. *(p. 228)*

Brooks, K. and M. Beckstead (1995). Dynamics of aluminum combustion. *Journal of Propulsion and Power 11*(4), 769–780. *(p. 30)*

Brown, R. (1828). A brief account of microscopical observations made in the months of june, july and august 1827, on the particles contained in the pollen of plants; and on the general existence of active molecules in organic and inorganic bodies. *Philosophical Magazine 4*(21), 161–173. *(p. 192)*

Brown, R., R. Dunlap, S. Young, and R. Waugh (1981). Vortex shedding as a source of acoustic energy in segmented solid rockets. *Journal of Spacecraft and Rockets 18*, 312–319. *(p. 17, 21, 41, 46)*

Brown, R., C. Kolb, R. Yetter, F. Dryer, and H. Rabitz (1995). Kinetic modeling and sensitivity analysis for B/H/O/C/F combination systems. *Combustion and Flame 101*(3), 221–238. *(p. 22)*

Bucher, P., R. A. Yetter, F. L. Dryer, E. P. Vicenzi, T. P. Parr, and D. M. Hanson-Parr (1999). Condensed-phase species distribution about Al particles reacting in various oxidizers. *Combustion and Flame 117*(1–2), 351–361. *(p. 29)*

Buckmaster, J., T. Jackson, L. Massa, and M. Ulrich (2005). Response of a burning heterogeneous propellant to small pressure disturbances. *Proceedings of the Combustion Institute 30*(2), 2079–2086. *(p. 40)*

Burakov, V. A. and S. F. Sandu (1997). Mathematical modeling of the dynamics of slagging and thermochemical destruction of carbon composite thermal protective materials in high-temperature two-phase flow. *Combustion, Explosion, and Shock Waves 33*(4), 472–481. *(p. 32)*

Burman, E. and L. Sainsaulieu (1995). Numerical analysis of two operator splitting methods for an hyperbolic system of conservation laws with stiff relaxation terms. *Comput. Methods in Appl. Mech. and Engrg. 128*, 291–314. *(p. 269)*

Burton, J., R. Melcher, and H. Krier (2000). Combustion of aluminum particles in solid-rocket motor flows. In V. Yang, T. Brill, W. Ren, and P. Zarchan (Eds.), *Solid Propellant Chemistry, Combustion, and Motor Interior Ballistics*, pp. 723–747. *(p. 30)*

Burton, T. and J. Eaton (2005). Fully resolved simulations of particle-turbulence interaction. *Journal of Fluid Mechanics 545*(1), 67–111. *(p. 26)*

Butcher, J. (1987). *The numerical analysis of ordinary differential equations: Runge-Kutta and general linear methods*. Wiley-Interscience. *(p. 237)*

Buzea, C., I. Pacheco, and K. Robbie (2007). Nanomaterials and nanoparticles: sources and toxicity. *Biointerphases 2*(4). *(p. 184, 186, 187)*

Cagnon, B., J.-C. Chastenet, J.-F. Guéry, and F. Godfroy (1997). Programme oscillations de poussée 1996, base de données numérique. Technical Report 5823/97/SNPE/DFP/CER, SME. *(p. 41)*

Cai, W., F. Ma, and V. Yang (2003). Two-phase vorticoacoustic flow interactions in solid-propellant rocket motors. *Journal of Propulsion and Power 19*(3), 385–396. *(p. 51, 284)*

Callen, H. and R. Greene (1952). On a theorem of irreversible thermodynamics. *Physical Review 86*, 702–710. *(p. 192)*

Calvo, J. and P. Jabin (2011). Large time asymptotics for a modified coagulation model. *Journal of Differential Equations 250*(6), 2807–2837. *(p. 178)*

Candel, S. (1990). *Mécanique des fluides* (second ed.). Paris: Dunod. *(p. 12, 353, 354)*

Candel, S., F. Lacas, R. C., and N. Darabiha (1999). Group combustion in spray flames. *Multiphase Science and Technology 11*, 1–18. *(p. 32)*

Candel, S. and T. Poinsot (1990). Flame stretch and the balance equation for the flame area. *Combustion Science and Technology 70*(1-3), 1–15. *(p. 76)*

Canneviere, K. (2003). *Simulation numérique directe de la combustion turbulente diphasique: Application à l'étude de la propagation et de la structure des flammes*. Ph. D. thesis, INSA de Rouen. *(p. 360)*

Capecelatro, J. and O. Desjardins (2013). An Euler-Lagrange strategy for simulating particle-laden flows. *J. Comp. Phys. 238*, 1–31. *(p. 109)*

Carrillo, J., T. Goudon, and P. Lafitte (2008). Simulation of fluid and particles flows: Asymptotic preserving schemes for bubbling and flowing regimes. *Journal of Computational Physics 227*(16), 7929–7951. *(p. 238)*

Casalis, G., G. Avalon, and J.-C. Pineau (1998). Spatial instability of planar channel flow with fluid injection through porous walls. *Phys. Fluids 10*(10), 25–58. *(p. 42, 284)*

Casalis, G., G. Boyer, and E. Radenac (2011). Some recent advances in the instabilities occurring in long solid rocket motors. *AIAA journal*. *(p. 42, 284)*

Casalis, G., J. Griffond, G. Avalon, B. Ugurtas, and F. Vuillot (2000). Instability and resonance in a system simulating the solid propellant motors behaviour. In 2^{nd} *European Conference on Launcher Technology*, Rome. *(p. 42)*

Caveny, L., K. Kuo, and B. Shackelford (1980). Thrust and ignition transients of the space shuttle solid rocket motor. *J. Spacecraft and Rockets 17*(6), 489–494. *(p. 38)*

Cercignani, C. (1988). *The Boltzmann equation and its applications*. New York: Springer-Verlag. *(p. 92, 97)*

Cercignani, C. (2000). *Rarefied gas dynamics: from basic concepts to actual calculations*, Volume 21. Cambridge University Press. *(p. 91)*

Cercignani, C., R. Illner, and M. Pulvirenti (1994). *The mathematical theory of dilute gases*. New York: Springer-Verlag. *(p. 92)*

CERFACS (2011). AVBP Handbook. `http://www.cerfacs.fr/~avbp/AVBP_V6.X/HANDBOOK/handbook.php`. *(p. 232)*

Cerqueira, S. (2012). *Étude du couplage aéro-mécanique au sein des moteurs à propergol solide*. Ph. D. thesis, Mines ParisTech. *(p. 21, 41, 50, 52)*

Cesco, N. (1997). *Etude et modélisation de l'écoulement diphasique à l'intérieur des propulseurs à poudre*. Ph. D. thesis, École Nationale Supérieure de l'Aéronautique et de l'Espace. *(p. 31, 38, 49, 51)*

Cesco, N., G. Lavergne, and J. Estivalezes (1996). Simulation of the two-phase flow in solid rocket motors. In *32nd ASME/SAE/ASEE Joint Propulsion Conference and Exhibit. (p. 32, 51)*

Chalons, C., R. Fox, and M. Massot (2010). A multi-gaussian quadrature method of moments for gas-particle flows in a LES framework. *Center for Turbulence Research*, 347–358. Available at http://www.stanford.edu/group/ctr/Summer/SP10/6_05_chalons.pdf. *(p. 3, 131)*

Chalons, C., D. Kah, and M. Massot (2012). Beyond pressureless gas dynamics : Quadrature-based velocity moment models. *Communication in Mathematical Sciences 10*, 1241–1272. Available at http://hal.archives-ouvertes.fr/hal-00535782. *(p. 111, 131)*

Chandrasekar, S. (1943). Stochastic problems in physics and astronomy. *Rev. Mod. Phys. 15*(1), 1–89. *(p. 192, 197, 200)*

Chang, I. (1980). One- and two-phase nozzle flows. *AIAA Journal 18*(12), 1455–1461. *(p. 119)*

Chaouat, B. (1994). *Modélisation et simulation des écoulements turbulents dans les propulseurs à propergol solide*. Ph. D. thesis, Université de Paris VI. *(p. 50)*

Chaouat, B. and R. Schiestel (2000). Turbulence stress transport modelling for flow prediction in solid rocket motors. In 2^{nd} *European Conference on Launcher Technology*, Rome. *(p. 42)*

Chaouat, B. and R. Schiestel (2005). A new partially integrated transport model for subgrid-scale stresses and dissipation rate for turbulent developing flows. *Physics of Fluids 17*, 065106. *(p. 50, 52, 102)*

Chapman, S. (1916). On the law of distribution of molecular velocities, and on the theory of viscosity and thermal conduction, in a non-uniform simple monoatomic gas. *Phil. Trans. R Soc. A*(216), 279–348. *(p. 92)*

Chapman, S. (1918). On the kinetic theory of a gas. part ii: A composite monoatomic gas: Diffusion, viscosity, and thermal conduction. *Phil. Trans. R Soc. A*(217), 115–197. *(p. 92)*

Chapman, S. and T. Cowling (1939). *The mathematical theory of non-uniform gases*. Cambridge University Pr. *(p. 92)*

Chapman, S. and T. G. Cowling (1970). *The Mathematical Theory of Non Uniform Gases*. Cambridge Mathematical Library. *(p. 92)*

Chapman, S. and T. G. Cowling (1990). *The mathematical theory of nonuniform gases* (third ed.). Cambridge Mathematical Library. Cambridge: Cambridge University Press. An account of the kinetic theory of viscosity, thermal conduction and diffusion in gases, In co-operation with D. Burnett, With a foreword by Carlo Cercignani. *(p. 92)*

Charles, F. (2009). *Modélisation mathématique et étude numérique d'un aérosol dans un gaz raréfié. Application à la simulation du transport de particules de poussière en cas d'accident de perte de vide dans ITER*. Ph. D. thesis, ENS Cachan. *(p. 371)*

Charles, F., S. Dellacherie, and J. Segré (2012). Kinetic modeling of the transport of dust particles in a rarefied atmosphere. *Mathematical Models and Methods in Applied Sciences 22*(4). *(p. 371)*

Charles, F. and L. Desvillettes (2009). Small mass ratio limit of Boltzmann equations in the context of the study of evolution of dust particles in a rarefied atmosphere. *Journal of Statistical Physics 137*(3), 539–567. *(p. 371)*

Charru, F. (2011). *Hydrodynamic Instabilities*. Cambridge University Press. *(p. 41)*

Chase, M., C. Davies, J. Downey, D. Frurip, R. McDonald, and A. Syverud (1985). JANAF thermochemical tables, Third edition. *J. Phys. Chem. Ref. Data 14*, 1432–1440. *(p. 49)*

Chassagne, F. (2007). *Contribution à la modélisation de la combustion de blocs de propergol solide aluminisé après éclatement d'un propulseur*. Ph. D. thesis, École Nationale Supérieure de Mécanique et d'Aérotechnique. *(p. 24)*

Chatzi, E. and C. Kiparissides (1992). Dynamic simulation of bimodal drop size distributions in low-coalescence batch dispersion systems. *Chemical Engineering Science 47*(2), 445 – 456. *(p. 190)*

Chavanis, P.-H., P. Laurençot, and M. Lemou (2004). Chapman-Enskog derivation of the generalized Smoluchowski equation. *Physica A: Statistical Mechanics and its Applications 341*, 145–164. *(p. 199)*

Chedevergne, F., G. Casalis, and T. Ferraille (2006). Biglobal linear stability analysis of the flow induced by wall injection. *Phys. of Fluids 18*, 1–14. *(p. 50)*

Chedevergne, F., G. Casalis, and J. Majdalani (2012). Direct Numerical Simulation and biglobal stability investigations of the gaseous motion in solid rocket motors. *Journal of Fluid Mechanics 706*, 190–218. *(p. 50, 52, 284)*

Chen, D., S. Luh, T. Liu, G. Wu, and H. Perng (1993). Combustion study of boron-based fuel-rich solid propellant. *International Journal of Energetic Materials and Chemical Propulsion 2*(1–6). *(p. 19)*

Cheng, C., R. Vigil, and R. Fox (2008). Multivariate Population Balance Equations for functional nanoparticle formation stabilized by amphiphilic block copolymer directed assembly. In *The 2008 Annual Meeting. (p. 189)*

Cheng, J., C. Yang, and Z.-S. Mao (2012). CFD-PBE simulation of premixed continuous precipitation incorporating nucleation, growth and aggregation in a stirred tank with multi-class method. *Chemical Engineering Science 68*(22), 469–480. *(p. 120)*

Chesnel, J., J. Reveillon, T. Ménard, and F. Demoulin (2012). Subgrid analysis of liquid jet atomization. *Atomization and Sprays 21*, 711–736. *(p. 71)*

Chibbaro, S. and J. Minier (2008). Langevin PDF simulation of particle deposition in a turbulent pipe flow. *Journal of Aerosol Science 39*(7), 555–571. *(p. 107)*

Chorin, A. J. (1968). Numerical solution of the Navier-Stokes equations. *Math. Comp. 22*, 745–762. *(p. 91)*

Chu, W., V. Yang, and J. Majdalani (2003). Premixed flame response to acoustic waves in a porous-walled chamber with surface mass injection. *Combustion and Flame 133*(3), 359–370. *(p. 284)*

Chung, T. (2010). *Computational fluid dynamics*. Cambridge university press. *(p. 225)*

Churg, A., B. Stevens, and J. Wright (1998). Comparison of the uptake of fine and ultrafine TiO_2 in a tracheal explant system. *American Journal of Physiology-Lung Cellular and Molecular Physiology 274*(1), L81–L86. *(p. 187)*

Clavin, P. (1996). Etude analytique de l'amortissement des ondes acoustiques longitudinales dans une chambre avec injection pariétale, programme ASSM 5 axe stabilité de fonctionnement. Technical report, IRPHE. *(p. 36)*

Clavin, P. and D. Lazimi (1992). Theoretical analysis of oscillatory burning of homogeneous solid propellant including non-steady gas phase effects. *Combustion Science and Technology 83*(1-3), 1–32. *(p. 40)*

Clift, R., J. Grace, and M. Weber (1978). *Bubbles, Drop and Particles*. Academic Press, New York. *(p. xviii, 80, 360)*

Cohen, N. (1983). A pocket model for aluminum agglomeration in composite propellants. *AIAA J. 21*(5), 720–725. *(p. 27, 30)*

Colin, O. (2000). *Simulations aux grandes échelles de la combustion turbulente prémélangée dans les statoréacteurs*. Ph. D. thesis, Institut National Polytechnique de Toulouse. *(p. 232)*

Colin, O. and M. Rudgyard (2000). Development of high-order Taylor-Galerkin schemes for LES. *J. Comp. Physics 162*, 338–371. *(p. 231)*

Connors, K. (1990). *Chemical kinetics: the study of reaction rates in solution*. Wiley-VCH. *(p. 173)*

Corcoran, A., V. Hoffmann, and E. Dreizin (2013). Aluminum particle combustion in turbulent flames. *Combustion and Flame 160*, 718–724. *(p. 30)*

Cottet, G. and S. Mas-Gallic (1990). A particle method to solve the Navier-Stokes system. *Numerische Mathematik 57*(1), 805–827. *(p. 70)*

Courbet, B., C. Benoit, V. Couaillier, F. Haider, M. Le Pape, and S. Péron (2011). Space discretization methods. *Aerospace Lab 2*, 1–14. *(p. 231, 246, 322)*

Couton, D., F. Plourde, and S. Doan Kim (1996). Cold gas simulation of a solid propellant rocket motor. *AIAA Journal 34*(12), 1462–1464. *(p. 41)*

Couzinet, A. (2008). *Approche PDF jointe fluide-particule pour la modélisation des écoulements turbulents diphasiques anisothermes*. Ph. D. thesis, Institut National Polytechnique de Toulouse. *(p. 102, 157)*

Crowe, C., M. Sharma, and D. Stock (1977). The particle-source-in cell (PSI-CELL) model for gas-droplet flows. *J. Fluids Eng. 99*(2), 325–332. *(p. 106)*

Crowe, C., M. Sommerfeld, and Y. Tsuji (1998). *Multiphase flows with droplets and particles*. Boca Raton, Fl. CRC Press. *(p. 57, 64, 67, 68, 94, 106, 166)*

Crowe, C. and P. Willoughby (1967). A study of particle growth in a rocket nozzle. *AIAA Journal 5*(7), 1300–1304. *(p. 38)*

Crowe, C., R. Woolfolk, R. Dunlap, R. Hermsen, and P. Willoughby (1964). Dynamics of two-phase flows in rocket nozzles. Technical report, DTIC Document. *(p. 1, 37, 53)*

Culick, F. (1966a). Acoustic oscillations in solid propellant rocket chambers. *Astronautica Acta 12*(2), 113–125. *(p. 15, 40, 43, 50)*

Culick, F. (1966b). Rotational axisymmetric mean flow and damping of acoustic waves in a solid propellant rocket. *AIAA Journal 4*(8), 1462–1464. *(p. 36, 52)*

Culick, F. (1975). Stability of three-dimensional motions in a combustion chamber. *Combust. Sci. and Tech. 10*, 109–124. *(p. 45)*

Culick, F. (1988). Combustion instabilities in liquid-fueled propulsion systems – an overview. In *Combustion Instabilities in Liquid-Fueled Propulsion Systems, AGARD CP-450*. *(p. 15)*

Culick, F. and K. Magiawala (1979). Excitation of acoustic modes in a chamber by vortex shedding. *Journal of Sound and Vibration 64*(3), 455–457. *(p. 42)*

Culick, F. and V. Yang (1992). Prediction of the stability of unsteady motions in solid-propellant rocket motors. In *Nonsteady Burning and Combustion Stability of Solid Propellants*, Volume 143, pp. 719–779. Washington, DC: American Institute of Aeronautics and Astronautics. *(p. 40)*

Cunningham, E. (1910). On the velocity of steady fall of spherical particles through fluid medium. In *Proceedings of the Royal Society of London*, Volume 83 of *A*, pp. 357–365. *(p. 205)*

Curtiss, C. and J. Hirschfelder (1952). Integration of stiff equations. *Proceedings of the National Academy of Sciences of the United States of America 38*(3), 235. *(p. 234)*

d'Almeida, G. and L. Schütz (1983). Number, mass and volume distributions of mineral aerosol and soils

of the Sahara. *Journal of Applied Meteorology 22*, 233–243. *(p. 184)*

Daniel, E. (2000). Eulerian approach for unsteady two-phase solid rocket flows with aluminum particles. *Journal of Propulsion and Power 16*(2), 309–317. *(p. 119)*

Dargaud, J. (2013). *Simulation numérique de l'onde de souffle et du bruit de jet au décollage d'un lanceur*. Ph. D. thesis, École Centrale de Lyon. *(p. 33, 321)*

Dash, S. and R. Thorpe (1981). Shock-capturing model for one-and two-phase supersonic exhaust flow. *AIAA Journal 19*(7), 842–851. *(p. 119)*

Davenas, A. (1995). Solid propellant environmental issues : a European perspective. In *31st ASME/SAE/ASEE Joint Propulsion Conference and Exhibit. (p. 19)*

Davies, C. (1945). Definitive equations for the fluid resistance of spheres. *Proc. Phys. Soc. 57*(4), 259. *(p. xx, 205)*

Davies, C. (1966). *Aerosol Science*. Academic Pr. *(p. 380)*

Davies, G., O. Flanagan, R. Hillier, D. Hitchings, and S. Lord (1994). Hydraulic shock loading due to supercavitating projectiles. In *Abstract of the* 20^{th} *International Symposium on Shock Waves. (p. 78)*

de Chaisemartin, S. (2009). *Polydisperse evaporating spray turbulent dispersion : Eulerian model and numerical simulation*. Ph. D. thesis, Ecole Centrale Paris. http://tel.archives-ouvertes.fr/tel-00443982/en/. *(p. xix, 2, 3, 62, 65, 74, 108, 111, 112, 115, 127, 129, 134, 139, 227, 228, 229, 230, 233, 245, 254, 255, 259, 275, 281, 291, 292, 294, 331, 357)*

de Chaisemartin, S., L. Fréret, D. Kah, F. Laurent, R. Fox, J. Reveillon, and M. Massot (2009). Eulerian models for turbulent spray combustion with polydispersity and droplet crossing. *Comptes Rendus Mécanique 337*, 438–448. Special Issue "Combustion for Aerospace Propulsion". *(p. 112, 115)*

de Chaisemartin, S., F. Laurent, M. Massot, and J. Reveillon (2007). Evaluation of Eulerian Multi-Fluid versus Lagrangian methods for ejection of polydisperse evaporating sprays by vortices. *Annual report of European Project TIMECOP-AE*, 1–56. http://hal.archives-ouvertes.fr/hal-00169721/en/. *(p. 115)*

De Gennes, P., F. Brochard-Wyart, and D. Quéré (2003). *Capillarity and wetting phenomena: drops, bubbles, pearls, waves*. Springer. *(p. 58)*

De Luca, L., C. Bonnal, O. Haidn, S. Frolov, L. Merotto, L. Galfetti, and G. Colombo (2011). Characterization of nAl powders for rocket propulsion. In *Advances in aerospace sciences (EUCASS)*. Paris: EDP Sciences, TORUS PRESS. *(p. 24)*

De Luca, L., L. Galfetti, F. Severini, L. Meda, G. Marra, A. Vorozhtsov, V. Sedoi, and V. Babuk (2005). Burning of Nano-Aluminized composite rocket propellants. *Comb., Expl., and Sh. Waves 41*(6), 680–692. *(p. 31)*

De Luca, L. and E. Price (1992). *Nonsteady burning and combustion stability of solid propellants*, Volume 143. AIAA (American Institute of Aeronautics & Astronautics). *(p. 40)*

Delhaye, J. (2008). *Thermohydraulique des réacteurs*. EDP Sciences. *(p. 59)*

Delhaye, J. M. and J. M. Achard (1977). On the use of averaging operators in two-phase flow modeling. *ASME, 1*, 289–332. *(p. 75)*

Della Pieta, P., F. Godfroy, and J.-F. Guéry (2001). Couplage fluide/structure appliqué en propulsion solide. In *XVème Congrès Français de Mécanique*, Nancy. *(p. 50)*

DeLuca, L., L. Galfetti, G. Colombo, F. Maggi, A. Bandera, V. Babuk, and V. Sinditskii (2010). Microstructure effects in aluminized solid rocket propellants. *Journal of propulsion and power 26*(4), 724–733. *(p. 22, 23)*

Demoulin, F., P. Beau, G. Blokkeel, A. Mura, and R. Borghi (2007). A new model for turbulent flows with large density fluctuations: Application to liquid atomization. *Atomization and Sprays 17*(4), 315–345. *(p. 71)*

Derksen, J. (2012). Dense suspensions-solid–liquid interactions at the particle scale. *Progress in Computational Fluid Dynamics, an International Journal 12*(2), 103–111. *(p. 72)*

Descombes, S., M. Duarte, T. Dumont, V. Louvet, and M. Massot (2011). Adaptive time splitting method for multi-scale evolutionary partial differential equations. *Confluentes Mathematici 3*, 1–31. http://hal.archives-ouvertes.fr/hal-00587036. *(p. 274)*

Descombes, S. and M. Massot (2004). Operator splitting for nonlinear reaction-diffusion systems with an entropic structure: singular perturbation and order reduction. *Numer. Math. 97*(4), 667–698. *(p. 239, 273)*

Deshpande, S., P. Kulkarni, and A. Ghosh (1998). New developments in kinetic schemes. *Computers & Mathematics with Applications 35*(1), 75–93. *(p. 229)*

Desjardins, O. and J. Capecelatro (2011). Large-scale Eulerian-Lagrangian simulations of turbulent particle-laden riser flows. *Bulletin of the American Physical Society 56. (p. 106)*

Desjardins, O., R. Fox, and P. Villedieu (2008). A quadrature-based moment method for dilute fluid-particle flows. *Journal of Computational Physics 227*(12), 6313–6350. *(p. 2, 298)*

Desjardins, O., V. Moureau, and H. Pitsch (2008). An accurate conservative level set/ghost fluid method for simulating turbulent atomization. *Journal of Computational Physics 227*(18), 8395–8416. *(p. 71)*

Desjardins, O. and P. Pepiot (2009). Analysis of dense particulate flow dynamics using a euler-lagrange approach. *Bulletin of the American Physical Society 54. (p. 106)*

Desvillettes, L. (1993). Some applications of the method of moments for the homogeneous Boltzmann and Kac equations. *Archive for rational mechanics and analysis 123*(4), 387–404. *(p. 92)*

D'Herbigny, F. X. and P. Villedieu (2001). Etude expérimentale et numérique pour la validation d'un modèle de coalescence. Technical Report RF 1/05166 DMAE, ONERA. *(p. 81, 173, 304, 350)*

Dichiara, A. (2012). *Etude chronologique de la formation de nanotubes de carbone par CVD d'aérosol à l'aide de diagnostics in situ: des premiers instants à la fin de la croissance.* Ph. D. thesis, Institut National Polytechnique de Toulouse. *(p. 185)*

Dichiara, A. and J. Bai (2012). The growth of carbon nanotube multilayers on ceramic μ-particles by catalytic chemical vapour deposition. *Diamond and Related Materials*, 52–58. *(p. 185)*

Dichiara, A., J. Yuan, S. Yao, A. Sylvestre, and J. Bai (2012). CVD synthesis of Carbon Nanotube-Graphene Nanosheet hybrids and their application in polymer composites. *Journal of Nanoscience and Nanotechnology 12*(9), 6935–6940. *(p. 185)*

Dodin, Z. and T. Elperin (2002). On the collision rate of particles in turbulent flow with gravity. *Physics of Fluids 14*, 2921. *(p. 103)*

Doisneau, F., J. Dupays, F. Laurent, and M. Massot. A unified model for nano-micro polydisperse sprays with coalescence. *In preparation. (p. 5)*

Doisneau, F., J. Dupays, A. Murrone, F. Laurent, and M. Massot (2011). Eulerian VS Lagrangian simulation of unsteady two-way coupled coalescing two-phase flows in solid propellant combustion. In 3^{rd} *INCA Colloquium*, Toulouse - France. *(p. 5)*

Doisneau, F., J. Dupays, A. Murrone, F. Laurent, and M. Massot (2013). Eulerian VS Lagrangian simulation of unsteady two-way coupled coalescing two-phase flows in solid propellant combustion. *C. R. Mec. 341*, 44–54. Special issue "Combustion for Aerospace Propulsion". *(p. xviii, 4, 5, 69, 234, 270)*

Doisneau, F. and F. Laurent (2013). Analytical and numerical study of a bimodal coalescing spray. *In preparation for Math. Models and Methods in Appl. Sc.*, 1–12. *(p. 4, 178)*

Doisneau, F., F. Laurent, J. Dupays, and M. Massot (2011). Two-way coupled simulation of acoustic waves in polydispersed coalescing two-phase flows: application to Solid Rocket Motor instabilities. In 4^{th} *EUCASS. (p. 5, 284)*

Doisneau, F., F. Laurent, A. Murrone, J. Dupays, and M. Massot (2010). Optimal Eulerian model for the simulation of dynamics and coalescence of alumina particles in solid propellant combustion. In *Proceedings of the 7th International Conference on Multiphase Flows, ICMF 2010*, Tampa - Florida USA. http://hal.archives-ouvertes.fr/hal-00498215/en/. *(p. 4)*

Doisneau, F., F. Laurent, A. Murrone, J. Dupays, and M. Massot (2013). Eulerian Multi-Fluid models for the simulation of dynamics and coalescence of particles in solid propellant combustion. *J. Computational Physics 234*, 230–262. *(p. 4, 5, 139, 162, 269, 316, 369)*

Doisneau, F., E. Montreuil, J. Dupays, A. Murrone, and F. Laurent (2013). Secondary break-up for aerospace applications with cedre. *In preparation for Int. J. of Multiphase Flows. (p. 363, 368, 369)*

Doisneau, F., A. Sibra, J. Dupays, A. Murrone, F. Laurent, and M. Massot (2013). An efficient and accurate numerical strategy for two-way coupling in unsteady polydisperse moderately dense sprays: application to Solid Rocket Motor instabilities. *J. Prop. Power*, 1–40. in press. *(p. 4, 124, 269, 270)*

Doisneau, F., A. Sibra, F. Laurent, J. Dupays, and M. Massot (2011). Numerical strategy for two-way coupling in unsteady polydisperse moderately dense sprays. In 47^{th} *AIAA/ASME/SAE/ASEE Joint Propulsion Conf. (p. 4, 124, 270)*

Doisneau, F., O. Thomine, F. Laurent, A. Vié, J. Dupays, and M. Massot (2012). Eulerian modeling and simulation of small scale trajectory crossing and coalescence for moderate-Stokes-number spray flows. In *Proceedings of the Summer Program 2012*, Center for Turbulence Research, Stanford University, pp. 365–374. *(p. 5)*

Dokhan, A., E. Price, J. Seitzman, and R. Sigman (2002). The effects of bimodal aluminum with ultrafine aluminum on the burning rates of solid propellants. *Proceedings of the Combustion Institute 29*(2), 2939–2946. *(p. 24)*

Dombard, J. (2011). *Direct Numerical Simulation of non-isothermal dilute sprays using the Mesoscopic Eulerian Formalism.* Ph. D. thesis, Institut National Polytechnique de Toulouse. *(p. 3, 64, 101, 232, 254)*

Donaldson, K., V. Stone, C. Tran, W. Kreyling, and P. Borm (2004). Nanotoxicology. *Occupational and Environmental Medicine 61*(9), 727–728. *(p. 185)*

Donea, J. and A. Huerta (2003). *Finite element methods for flow problems.* John Wiley&Sons. *(p. 231)*

Donea, J., A. Huerta, J.-P. Ponthot, and A. Rodríguez-Ferran (2004). Arbitrary Lagrangian–Eulerian methods. In *Encyclopedia of Computational Mechanics*, pp. 413–437. Wiley Online Library. *(p. 232)*

Dorey, L. (2012). *Modélisation des phénomènes couplés combustion-formation des suies-transferts radiatifs dans les chambres de combustion de turbine à gaz.* Ph. D. thesis, École Centrale Paris. *(p. 185, 322)*

Doriath, G. and B. D'Andrea (1996). New solid propellants formulations and production processes. In *5th Int. Symp. Propulsion in Space Transportation*, Paris. *(p. 21)*

Dotson, K., S. Koshigoe, and K. Pace (1997). Vortex shedding in a large solid rocket motor without inhibitors at the segment interfaces. *Journal of Propulsion and Power 13*(2), 197–206. *(p. 17, 46)*

Dowd, K., C. Severance, and M. Loukides (1998). *High performance computing* (second ed.). O'Reilly & Associates, Inc. *(p. 226)*

Drake, R. L. (1976). Similarity solutions for homogeneous and nonhomogeneous aerosol balance equations. *Journal of Colloid and Interface Science 57*(3), 411 – 423. *(p. 190)*

Dreizin, E. (2003). Effect of phase changes on metal-particle combustion processes. *Combustion, Explosion, and Shock Waves 39*(6), 681–693. *(p. 29)*

Dreizin, E., D. Keil, W. Felder, and E. Vicenzi (1999). Phase changes in boron ignition and combustion. *Combustion and Flame 119*(3), 272–290. *(p. 22)*

Drew, D. and S. Passman (1999). *Theory of Multicomponent Fluids*, Volume 135. New York: Springer-Verlag. *(p. 57, 60, 75, 76, 89, 92)*

Druzhinin, O. (1994). Concentration waves and flow modification in a particle-laden circular vortex. *Phys. Fluids 6*, 3276–3284. *(p. 77, 137)*

Druzhinin, O. (1995). On the two-way interaction in two-dimensional particle laden flows: the accumulation of particles and flow modification. *J. Fluid Mechanics 297*, 49–76. *(p. 77, 137)*

Druzhinin, O. (2001). The influence of particle inertia on the two-way coupling and modification of isotropic turbulence by microparticles. *Physics of Fluids 13*(12), 3738–3755. *(p. 103)*

Duarte, M. (2011). *Adaptive numerical methods in time and space for the simulation of multi-scale reaction fronts*. Ph. D. thesis, École Centrale Paris. http://tel.archives-ouvertes.fr/tel-00667857. *(p. 237, 238, 239, 240, 243, 274)*

Duarte, M., Z. Bonaventura, M. Massot, A. Bourdon, S. Descombes, and T. Dumont (2012). A new numerical strategy with space-time adaptivity and error control for multi-scale streamer discharge simulations. *J. Comp. Phys. 231*(3), 1002–1019. *(p. 233, 238, 274)*

Duarte, M., M. Massot, S. Descombes, C. Tenaud, T. Dumont, V. Louvet, and F. Laurent (2012). New resolution strategy for multi-scale reaction waves using time operator splitting, space adaptive multi resolution and dedicated high order implicit/explicit time integrators. *SIAM J. on Sci. Comp. 34*(1), 76–104. *(p. 283, 284)*

Duffin, R., L. Tran, D. Brown, V. Stone, and K. Donaldson (2007). Proinflammogenic effects of low-toxicity and metal nanoparticles in vivo and in vitro: highlighting the role of particle surface area and surface reactivity. *Inhalation toxicology 19*(10), 849–856. *(p. 187)*

Dufour, G. (2005). *Modélisation Multi-Fluide eulérienne pour les écoulements diphasiques à inclusions dispersées*. Ph. D. thesis, Université Paul Sabatier Toulouse III. *(p. 81, 83, 98, 99, 100, 139, 140, 142, 145, 228, 243, 291)*

Dufour, G., M. Massot, and P. Villedieu (2003). Study of a secondary break-up model for sprays. *C. R. Math. Acad. Sci. Paris 336*(5), 447–452. *(p. 99, 363, 369)*

Dufour, G. and P. Villedieu (2005). A second-order Multi-Fluid model for evaporating sprays. *M2AN Math. Model. Numer. Anal. 39*(5), 931–963. *(p. 140, 142, 144, 245, 291, 292)*

Dukowicz, J. K. (1980). A particle-fluid numerical model for liquid sprays. *J. Comput. Phys. 35*(2), 229–253. *(p. 106)*

Dunlap, R. and R. Brown (1981). Exploratory experiments on acoustic oscillations driven by periodic vortex shedding. *AIAA J. 19*(3), 408–409. *(p. 17, 46)*

Dunlap, R., P. Willoughby, and R. Hermsen (1974). Flowfield in the combustion chamber of a solid propellant rocket motor. *AIAA journal 12*(10), 1440–1442. *(p. 39)*

Dupays, J. (1996). *Contribution à l'étude du rôle de la phase condensée dans la stabilité d'un propulseur à propergol solide pour lanceur spatial*. Ph. D. thesis, Institut National Polytechnique de Toulouse. *(p. 2, 6, 22, 28, 41, 44, 45, 81, 165, 229)*

Dupays, J. (2000). Mass transfer effects on sound propagation in a droplet-gas mixture. In 5^{th} *International Symposium on Special Topics in Chemical Propulsion, Stresa, Italy. (p. 44, 166)*

Dupays, J. (2005). Cours d'écoulements diphasiques. ESTACA (2005). *(p. 79)*

Dupays, J. (2006a). Obtention des équations eulériennes de la phase dispersée. Technical report, ONERA. en cours de rédaction. *(p. 73, 94)*

Dupays, J. (2006b). Quelques notions de mécanique statistique appliquée à un fluide. Technical report, ONERA. en cours de rédaction. *(p. 88)*

Dupays, J., Y. Fabignon, O. Orlandi, and J. Trubert (2000). Combustion of aluminum particles in solid rocket motors. In *2nd ONERA-DLR Aerospace Symposium, Berlin, Germany. (p. 30, 31)*

Dupays, J., Y. Fabignon, P. Villedieu, G. Lavergne, and J. L. Estivalezes (2000). Some aspects of two-phase flows in solid-propellant rocket motors. In *Solid Propellant Chemistry, Combustion, and Motor Interior Ballistics*, Volume 185 of *Progress in Astronautics and Aeronautics*, pp. 859–883. AIAA. *(p. 22, 45,*

107)

Dupays, J., F. Godfroy, O. Orlandi, P. Prevot, M. Prévost, S. Gallier, S. Ballereau, and Y. Fabignon (2008). Inert condensed phase driving effect of combustion instabilities in Solid Rocket Motor. In 5^{th} *International Spacecraft Propulsion Conference*, Heraklion, Gr. *(p. 5, 22, 42, 45, 46, 51, 52, 137, 226, 284, 322, 325, 331, 333, 336)*

Dupays, J. and F. Vuillot (2002). Propagation of acoustic waves in a two-phase vaporizing mixture. *Journal of Propulsion and Power 18*(1), 222–224. *(p. 44, 166)*

Dupays, J., S. Wey, and Y. Fabignon (2001). Steady and unsteady reactive two-phase computations in solid rocket motors with Eulerian and Lagrangian approaches. In *37th AIAA/ASME/SAE/ASEE Joint Propulsion Conference and Exhibit. (p. 119, 134)*

Dupuy, M. (2012). *Etude par simulations numériques instationnaires de l'écoulement dans les moteurs à propergol solide*. Ph. D. thesis, Éc. Nat. Sup. de Mec. et d'Aérotechnique. *(p. 39, 42, 50, 52, 356)*

Duterque, J., R. Hilbert, and G. Lengellé (1999). Agglomération et combustion de l'aluminium dans les propergols solides. Technical Report RT 3/6274 DMAE/Y/DEFA, ONERA. *(p. 27)*

Duterque, J. and D. Lambert (1998). Synthèse des travaux sur l'agglomération de l'aluminium dans le propergol du MPS P230. In *3ème colloque R&T ENSMA/CNES/ONERA sur les écoulements internes en propulsion solide*, Poitiers, France. *(p. 27)*

Dutoya, D. and L. Matuszewski (2011). Thermodynamics in CEDRE. *Aerospace Lab 2*, 1–11. Available at www.aerospacelab-journal.org/al2. *(p. 355)*

Duval, R. (2002). *Transfert radiatif dans des chambres de combustion de propulseurs à propergol solide aluminisé*. Ph. D. thesis, École Centrale Paris. *(p. 28, 51)*

Duval, R., A. Soufiani, and J. Taine (2004). Coupled radiation and turbulent multiphase flow in an aluminized solid propellant rocket engine. *Journal of Quantitative Spectroscopy and Radiative Transfer 84*(4), 513–526. *(p. 28, 38, 51, 81)*

Eggers, J. and E. Villermaux (2008). Physics of liquid jets. *Reports on Progress in Physics 71*, 036601. *(p. 364)*

Einstein, A. (1905). über die von der molekularkinetischen Theorie der Wärme geforderte Bewegung von in ruhenden Flüssigkeiten suspendierten Teilchen. *Ann. Phys. 17*(8), 549–560. *(p. 192, 193)*

Einstein, A. (1926). *Investigatios on the Theory of Brownian Movement*. Dover. *(p. 193)*

Eisner, A. and D. Rosner (1985). Experimental studies of soot particle thermophoresis in nonisothermal combustion gases using thermocouple response techniques. *Combustion and Flame 61*(2), 153–166. *(p. 188)*

Elghobashi, S. (1991). Particle-laden turbulent flows – Direct simulation and closure models. *App. Sc. Research 38*, 301–314. *(p. 26, 67, 103)*

Elghobashi, S. and G. Truesdell (1992). Direct Numerical Simulation of particle dispersion in a decaying isotropic turbulence. *J. Fluid Mech. 242*, 655–700. *(p. 72)*

Emre, O. (2013). *Modeling and simulation of dense injection and spray atomization in internal combustion engines*. Ph. D. thesis, École Centrale Paris. *(p. 231)*

Enskog, D. (1917). Kinetische Theorie der Vorgänge in mässig verdünnten Gasen. I. Allgemeiner Teil. *Uppsala: Almquist & Wiksells Boktryckeri 1. (p. 91, 92)*

Epstein, P. (1924). On the resistance experienced by spheres in their motion through gases. *Phys. Rev. 23*(6), 710–733. *(p. 204)*

Ermolin, N., O. Korobeinichev, A. Tereshchenko, and V. Fomin (1982). Kinetic calculations and mechanism definition for reactions in an ammonium perchlorate flame. *Combustion, Explosion, and Shock Waves 18*(2), 180–189. *(p. 353)*

Ern, A. and V. Giovangigli (1994). *Multicomponent transport algorithms*. Berlin: Springer-Verlag. *(p. 90, 356)*

Ern, A. and V. Giovangigli (1995). Fast and accurate multicomponent transport property evaluation. *Journal of Computational Physics 120*(1), 105–116. *(p. 356)*

Errera, M., A. Dugeai, P. Girodroux-Lavigne, J.-D. Garaud, M. Poinot, S. Cerqueira, and G. Chaineray (2011). Multi-physics coupling approaches for aerospace numerical simulations. *Aerospace Lab 2*, 1–16. Available at www.aerospacelab-journal.org/al2. *(p. 50, 51, 231, 324)*

Estivalezes, J. and P. Villedieu (1996). High-order positivity-preserving kinetic schemes for the compressible euler equations. *SIAM journal on numerical analysis 33*(5), 2050–2067. *(p. 229)*

Estivalezes, J.-L. (2010). Simulations Lagrangiennes polydisperses avec collisions et coalescence sur une configuration Ariane V 2D à l'instant 107s. Technical Report RT 3/17717 DMAE, ONERA. *(p. xv, xvii, xxiii, 29, 51, 110, 322, 325, 338, 341)*

Estivalezes, J.-L. (2011). Simulations Lagrangiennes polydisperses avec et sans collision-coalescence sur une configuration Ariane V tridimensionnelle à l'instant 107s. Technical Report RT 10/17717 DMAE, ONERA. *(p. 2, 5, 51, 52, 53, 110, 134, 322, 325)*

Estrada, P. and J. Cuzzi (2008). Solving the coagulation equation by the moment method. *Astronautical*

J. 682(1), 515–526. *(p. 120, 317)*

Evelyn, A., S. Mannick, and P. Sermon (2003). Unusual carbon-based nanofibers and chains among diesel-emitted particles. *Nano Letters 3*(1), 63–64. *(p. 187)*

Fabignon, Y. (1997). Synthèse de l'activité MACADAM - modélisation du dépôt dans le MPS P230. Technical Report 89/6133 EY, ONERA. *(p. 17, 32)*

Fabignon, Y., J. Dupays, G. Avalon, F. Vuillot, N. Lupoglazoff, G. Casalis, and M. Prévost (2003). Instabilities and pressure oscillations in solid rocket motors. *Aerospace Science and Technology 7*, 191–200. *(p. 284)*

Fabignon, Y., P. Kuentzmann, F. Vuillot, M. Prévost, R. Bec, E. Robert, M. Marion, and P. Duval (2000). A survey of french research and technology program on the internal aerodynamics of segmented solid motors. In 2^{nd} *European Conference on Launcher Technology Space Solid Propulsion*, Rome. *(p. 17)*

Fabignon, Y., O. Orlandi, J. Trubert, D. Lambert, and J. Dupays (2003). Combustion of aluminum particles in solid rocket motors. In 39^{th} *AIAA/ASME/SAE/ASEE Joint Propulsion Conference and Exhibit*, Number AIAA Paper 2003-4807, Huntsville, AL. *(p. 30, 31, 188, 328)*

Faeth, G. (1983). Evaporation and combustion of spray. *Progress in Energy and Combustion Science 9*, 1–76. *(p. 360)*

Fan, R., D. Marchisio, and R. Fox (2004). Application of the direct quadrature method of moments to polydisperse gas–solid fluidized beds. *Powder technology 139*(1), 7–20. *(p. 120)*

Faure, A., J.-J. Thouraud, and J.-C. Tricot (1996). Solid propulsion: technological and economical barriers. In *5th Int. Symp. Propulsion in Space Transportation*, Paris. *(p. 17, 35)*

Faure, S., S. Martin, B. Maury, and T. Takahashi (2009). Towards the simulation of dense suspensions: a numerical tool. In *ESAIM: Proceedings*, Volume 28, pp. 55–79. *(p. 70)*

Favray, F. (1999). *Etude de l'instabilité d'un écoulement confiné. Application à un modèle hydrodynamique de propulseur à propergol solide pour lanceur spatial*. Ph. D. thesis, Université de Paris VI. *(p. 40, 41, 42)*

Fede, P. (2004). *Modélisation et simulation de l'influence de la turbulence sur les collisions dans les écoulements mono- et bi-solides*. Ph. D. thesis, Institut National Polytechnique de Toulouse. *(p. 103)*

Fede, P. and O. Simonin (2006). Numerical study of the subgrid fluid turbulence effects on the statistics of heavy colliding particles. *Physics of Fluids 18*(4), 1–17. *(p. 103)*

Fede, P., O. Simonin, and P. Villedieu (2002). Monte-Carlo simulation of colliding particles in gas-solid turbulent flows from a joint fluid-particle PDF equation. *ASME Conference Proceedings 2002*(36169), 431–438. *(p. 103)*

Fedkiw, R., T. Aslam, B. Merriman, and S. Osher (1999). A non-oscillatory Eulerian approach to interfaces in multimaterial flows (the ghost fluid method). *Journal of Computational Physics 152*(2), 457–492. *(p. 71)*

Fedlheim, D. and C. Foss (2001). *Metal nanoparticles: synthesis, characterization, and applications*. CRC Press. *(p. 185)*

Feke, D. and W. Schowalter (1984). The influence of Brownian diffusion on binary flow-induced collision rates in colloidal dispersions. *J. Colloid and Interface Sc. 106*(1), 203–214. *(p. 202)*

Féraille, T. (2004). *Instabilités de l'écoulement interne des moteurs à propergol solide*. Ph. D. thesis, École Nationale Supérieure de l'Aéronautique et de l'Espace. *(p. 45)*

Ferry, J. and S. Balachandar (2001). A fast Eulerian method for disperse two-phase flow. *Int. J. Multiphase Flow 27*(7), 1199–1226. *(p. 51, 66, 77, 133, 137)*

Ferry, J. and S. Balachandar (2002). Equilibrium expansion for the Eulerian velocity of small particles. *Powder Technology 125*(2-3), 131–139. *(p. 51, 77)*

Ferry, J. and S. Balachandar (2005). Equilibrium Eulerian approach for predicting the thermal field of a dispersion of small particles. *International Journal of Heat and Mass Transfer 48*(3-4), 681–689. *(p. 51, 77)*

Ferziger, J. H. and H. Kaper (1972). *Mathematical Theory of Transport Processes in Gases*. North-Holland. *(p. 90, 92, 93, 99, 375, 379, 380)*

Fevrier, P. (2000). *Etude numérique des effets de concentration préférentielle et de corrélation spatiale entre vitesses de particules solides en turbulence homogène isotrope stationnaire*. Ph. D. thesis, Institut National Polytechnique de Toulouse. *(p. 101)*

Fevrier, P., O. Simonin, and K. Squires (2005). Partitioning of particle velocities in a gas-solid turbulent flow into a continuous field and a spatially-uncorrelated random distribution: theoretical formalism and numerical study. *J. Fluid Mech. 533*, 1–46. *(p. 2, 51, 101, 102, 263)*

Fiedler, R., A. Haselbacher, M. Breitenfeld, P. Alexander, L. Massa, and W. Ross (2005). 3-D simulations of ignition transients in the RSRM. In 41^{st} *AIAA/ASME/SAE/ASEE Joint Propulsion Conference*, Tucson, AZ. AIAA Paper 2005-3993. *(p. 38)*

Fiedler, R., X. Jiao, A. Namazifard, A. Haselbacher, F. Najjar, and I. Parsons (2001). Coupled fluid-structure 3-D solid rocket motor simulations. In 37^{th} *AIAA/ASME/SAE/ASEE Joint Propulsion*

Conference, Number AIAA Paper 2001-3954, Salt Lake City, UT. *(p. 50)*

Finck, B. and C. Perut (1991). Propergols solides peu ou non polluants pour lanceurs spatiaux. *ESA SP-327*, 137–141. *(p. 19)*

Flandro, G. (1985). Energy balance analysis of nonlinear combustion instability. *Journal of Propulsion and Power 3*, 210–221. *(p. 40, 50)*

Flandro, G. (1986). Vortex driving mechanism in oscillatory rocket flows. *Journal of Propulsion and Power 2*, 206–214. *(p. 42, 50)*

Flandro, G. and J. Majdalani (2003). Aeroacoustic instability in rockets. *AIAA Journal 41*(3), 485–497. *(p. 50)*

Flandro, G.A. et Jacobs, H. (1973). Vortex-generated sound in cavities. In *AIAA Aero-Acoustics Conference*, Seattle, WA. *(p. 42)*

Foissac, A. (2011). *Modélisation des interactions entre gouttes en environnement hostile*. Ph. D. thesis, UPMC. *(p. 83)*

Fox, R. (2006). Bivariate direct quadrature method of moments for coagulation and sintering of particle populations. *Journal of Aerosol Science 37*, 1562–1580. *(p. 120, 129)*

Fox, R. (2008). A quadrature-based third-order moment method for dilute gas-particle flow. *Journal of Computational Physics 227*(12), 6313–6350. *(p. 130)*

Fox, R. (2009). Optimal moment sets for multivariate direct quadrature methods of moments. *Industrial and Engineering Chemistry Research 48*, 6313–6350. *(p. 129)*

Fox, R. (2012). Large-Eddy-Simulation tools for multiphase flows. *Annu. Rev. Fluid Mech. 44*, 47–76. *(p. 2, 100, 101, 102, 364)*

Fox, R., F. Laurent, and M. Massot (2008). Numerical simulation of spray coalescence in an eulerian framework: Direct quadrature method of moments and multi-fluid method. *Journal of Computational Physics 227*, 3058–3088. *(p. 2, 97, 120, 132)*

Fox, R. and P. Vedula (2009). Quadrature-Based Moment Model for moderately dense polydisperse gas-particle flows. *Industrial & Engineering Chemistry Research 49*(11), 5174–5187. *(p. 129)*

Frenklach, M. (2002). Method of moments with interpolative closure. *Chemical Engineering Science 57*(12), 2229–2239. *(p. 121)*

Frenklach, M. (2009). Modeling particle dynamics with MOMIC. In *Modelling and Computation of Nanoparticles in Fluid Flows*, Number 1 in Lectures of the von Karman Institute, pp. 1–17. NATO RTO AVT 169. *(p. 121, 317)*

Fréret, L., O. Thomine, F. Laurent, J. Reveillon, and M. Massot (2012). Direct Numerical Simulation of polydisperse evaporating sprays in 3D jet configuration using Euler-Euler and Euler-Lagrange formalisms. In *Proceedings of the Summer Program 2012*, Center for Turbulence Research, Stanford University, pp. 345–354. *(p. 246)*

Fréret, L., O. Thomine, F. Laurent, J. Reveillon, and M. Massot (2013). On the ability of the Eulerian multi-fluid model to predict preferential segregation and flame dynamics in polydisperse evaporating sprays. *Submitted to Combustion and Flame*. *(p. 72, 115)*

Fréret, L., O. Thomine, J. Reveillon, S. de Chaisemartin, F. Laurent, and M. Massot (2010). On the role of preferential segregation in flame dynamics in polydisperse evaporating sprays. *Proceedings of the CTR Summer Program 2010*, 383–392. *(p. 115, 227, 246)*

Frezzotti, A., L. Gibelli, and B. Franzelli (2009). A moment method for low speed microflows. *Cont. Mech. Thermodyn. 21*, 495–509. *(p. 91)*

Friedlander, S. (1999). Nanoparticles and their structures: the next generation. *J. Nanoparticle Res. 1*(159). *(p. 185)*

Friedlander, S. (2000). *Smoke, Dust and Haze, Fundamentals of Aerosol Dynamics*. Oxford University Press. *(p. 187, 188, 189, 191, 193, 200, 207, 208, 209)*

Friedlander, S. K. and C. S. Wang (1966). The self-preserving particle size distribution for coagulation by brownian motion. *Journal of Colloid and Interface Science 22*(2), 126 – 132. *(p. 190)*

Fuchs, N. A. (1964). *Mechanics of Aerosols*. New York: Pergamon. *(p. 187, 200, 201, 204, 205, 208, 215)*

Gaffet, E. (2008). Nanomatériaux: différentes voies de synthèse, propriétés, applications et marchés. *Actualité et dossier en santé publique 64*. *(p. 183)*

Gaffet, E. (2009). Aspects sécurité des nanomatériaux et nanoparticules manufacturés. *Editions Techniques de l'ingénieur*. *(p. 186)*

Gaffet, E. (2011). Nanomatériaux: Une revue des définitions, des applications et des effets sur la santé. comment implémenter un développement sûr. *Comptes Rendus Physique 12*(7), 648–658. *(p. 186)*

Gailliegue, K. (1998). *Etude de la phase condensée dans les propulseurs à propergol solide aluminisé*. Ph. D. thesis, Université de Paris VI. *(p. 51)*

Gallier, S. (2009). A stochastic pocket model for aluminum agglomeration in solid propellants. *Propellants, Explosives, Pyrotechnics 34*, 97–105. *(p. 27, 52)*

Gallier, S. and F. Godfroy (2009). Aluminum combustion driven instabilities in solid rocket motors. *Journal*

of Propulsion and Power 25(2), 509. *(p. 42, 43, 51)*

Gallier, S., F. Godfroy, and F. Plourde (2004). Computational study of turbulence in a subscale solid rocket motor. In 40^{th} *AIAA/ASME/SAE/ASEE Joint Propulsion Conference and Exhibit. (p. 42, 50)*

Gallier, S., J.-F. Guéry, F. Godfroy, P. Le Breton, D. Ribereau, and P. Cloutet (2002). Instabilités de fonctionnement dans les moteurs à propergol solide de grande taille. *Revue Scientifique et Technique de la Défense* (57). *(p. 17, 19, 40)*

Gallier, S., E. Radenac, and F. Godfroy (2009). Thermoacoustic instabilities in solid rocket motors. *AIAA journal* (AIAA paper 2009-5252), 4217–4227. *(p. 42, 43, 45, 51)*

Garcia, M. (2009). *Développement et validation du formalisme Euler-Lagrange dans un solveur parallèle non-structuré pour la simulation aux grandes échelles.* Ph. D. thesis, Institut National Polytechnique de Toulouse. *(p. 2, 109)*

Garg, R., C. Narayanan, D. Lakehal, and S. Subramaniam (2007). Accurate numerical estimation of interphase momentum transfer in Lagrangian–Eulerian simulations of dispersed two-phase flows. *International Journal of Multiphase Flow 33*(12), 1337–1364. *(p. 110)*

Garg, R., C. Narayanan, and S. Subramaniam (2009). A numerically convergent Lagrangian–Eulerian simulation method for dispersed two-phase flows. *International Journal of Multiphase Flow 35*(4), 376–388. *(p. 109)*

Gautschi, W. (1996). Orthogonal polynomials: applications and computation. *Acta numerica 5*, 45–119. *(p. 244, 298)*

Gazanion, B. (2014). *Étude de la transition laminaire–turbulent dans un conduit à paroi débitante.* Ph. D. thesis, Institut National Polytechnique de Toulouse. *(p. 39)*

Gelbard, F., Y. Tambour, and J. Seinfeld (1980). Sectional representations for simulating aerosol dynamics. *Journal of Colloid and Interface Science 76*(2), 541–556. *(p. 120)*

Gelfand, B. (1996). Droplet breakup phenomena in flows with velocity lag. *Progress in energy and combustion science 22*(3), 201–265. *(p. 86)*

Gen, M., Y. Frolov, and V. Storozhev (1979). Combustion of submicron aluminum particles (in argon-oxygen medium). *Combustion, Explosion, and Shock Waves 14*(5), 153–155. *(p. 22)*

Germano, M., U. Piomelli, P. Moin, and W. Cabot (1991). A dynamic subgrid-scale eddy viscosity model. *Physics of Fluids 3*, 1760–1765. *(p. 102)*

Geuzaine, C. and J.-F. Remacle (2009). Gmsh: A 3-D finite element mesh generator with built-in pre- and post-processing facilities. *International Journal for Numerical Methods in Engineering 79*, 1309–1331. *(p. 282)*

Gilbert, M., J. Allport, and R. Dunlap (1962). Dynamics of two-phase flow in rocket nozzles. *ARS Journal 32*(12), 1929–1930. *(p. 37)*

Giovangigli, V. (1999). *Multicomponent flow modeling.* Boston, MA: Birkhäuser Boston Inc. *(p. 90, 92, 354, 356)*

Giovangigli, V. and M. Massot (1998). Asymptotic stability of equilibrium states for multicomponent reactive flows. *Math. Models Methods Appl. Sci. 8*(2), 251–297. *(p. 353)*

Giraldi, L. (2006). *Sviluppo di un codice di balistica interna non stazionaria per la predizione delle prestazioni di motori a razzo a propellente solido.* Ph. D. thesis, Università di Pisa. *(p. 34)*

Giro, A. and E. Guardia (1985). Langevin and molecular dynamics simulations of Lennard-Jones liquids. *Mol. Phys. 55*(5), 1063–1074. *(p. 202)*

Glassman, I. (1960). Combustion of metals: Physical considerations, in solid propellant rocket research. In *ARS Progress Series in Astronautics and Rocketry*, pp. 253–258. New York: Academic Press. Ed. M. Summerfield. *(p. 29)*

Glassman, I. and R. Yetter (2008). *Combustion* (fourth ed.). Academic Press. *(p. 29)*

Godfroy, F. and R. Briand (2004). Rapport d'avancement des travaux diphasiques. Technical Report 25/2004/SME/DPS/CER, SME. *(p. 2, 45)*

Godfroy, F. and R. Briand (2005). Note de synthèse sur l'influence de la position moyenne de la PTFS3 sur le couplage VSO/VSP. Technical Report 420/2005/SME/DPS/CEP, SME. *(p. 42)*

Godfroy, F. and J.-F. Guéry (1997a). Influence de l'instationnarité de l'écoulement sur le mécanisme de formation du dépôt d'alumine dans le MPS P230. Technical Report 5892/97/SNPE/DFP/CER, SNPE. *(p. 32)*

Godfroy, F. and J.-F. Guéry (1997b). Unsteady Eulerian two-phase flow analysis of solid rocket motor slag. In *33rd AIAA/ASME/SAE/ASEE Joint Propulsion Conference and Exhibit*, Seattle, WA. *(p. 32, 52)*

Godfroy, F. and P.-Y. Tissier (1993). Simulation numérique du vortex-shedding dans les maquettes 1/15e du booster P230 d'Ariane 5, programme ASSM, Axe Stabilité de Fonctionnement. Technical Report 883/SNPE/S/NE/D, SNPE. *(p. 41)*

Godfroy, F. and P.-Y. Tissier (1994). CFD analysis of vortex shedding inside a subscale segmented motor. In 30^{th} *AIAA/ASME/SAE/ASEE Joint Propulsion Conference and Exhibit*, Indianapolis, IN. *(p. 41)*

Godon, J. (1984). Modélisation de la combustion normale et érosive d'un propergol composite. Technical report, ONERA. *(p. 24)*

Godon, J., J. Duterque, and G. Lengelle (1992). Solid-propellant erosive burning. *Journal of Propulsion and Power 8*(4), 741–747. *(p. 24)*

Godsave, G. (1953). Studies of the combustion of drops in a fuel spray: the burning of single drops of fuel. In *Proceedings of the 4th Symp. (International) on Combustion, The Comb. Institute*, Baltimore, pp. 818–830. *(p. 360)*

Godunov, S. (1959). A difference method for numerical calculation of discontinuous solutions of the equations of hydrodynamics. *Matematicheskii Sbornik 47*(3), 271–306. *(p. 229)*

Goncalves de Miranda, F. (2000). *Etude numérique de l'écoulement instationnaire diphasique dans les propulseurs à propergol solide d'Ariane 5*. Ph. D. thesis, École Nationale Supérieure de l'Aéronautique et de l'Espace. *(p. 41)*

Gopalakrishnan, R., T. Thajudeen, and C. Hogan (2011). Collision-limited reaction rates for arbitrarily shaped particles across the entire diffusive Knudsen number range. *J. Chem. Phys. 135*, 1–9. *(p. 205)*

Gordon, S. and B. McBride (1971). Computer program for calculation of complex equilibrium composition, rocket performance, incident and reflected shocks and Chapman-Jouguet detonations. Technical Report SP-273, NASA. *(p. 49)*

Gorenflo, R., F. Mainardi, F. Moretti, G. Pagini, and P. Paradisi (2002). Discrete random walks models for space-time fractional diffusion. *Journal of Chemical Physics 284*, 521–541. *(p. 367)*

Gorokhovski, M. and M. Herrmann (2008). Modeling primary atomization. *Annu. Rev. Fluid Mech. 40*, 343–366. *(p. 59, 71, 363, 364)*

Gorokhovski, M. and V. Saveliev (2003). Analyses of Kolmogorov's model of break-up and its application into Lagrangian computation of liquid sprays under air-blast atomization. *Phys. Fluid. 15*, 184. *(p. 365)*

Gossant, B. (1993). *Solid Propellant Combustion and Internal Ballistics of Motors in Solid Rocket Propulsion Technology*. Pergamon Pr (edited by A. Davenas). *(p. 22, 34, 40, 50)*

Gourdain, N., L. Gicquel, M. Montagnac, O. Vermorel, M. Gazaix, G. Staffelbach, M. Garcia, J. Boussuge, and T. Poinsot (2009). High performance parallel computing of flows in complex geometries: I. methods. *Computational Science & Discovery 2*(1), 015003. *(p. 226, 231, 232, 233)*

Grad, H. (1949). On the kinetic theory of rarefied gases. *Communications on pure and applied mathematics 2*(4), 331–407. *(p. 89, 91)*

Grad, H. (1958). *Principles of kinetic theory of gases*, Volume XII. Springer-Verlag. *(p. 92, 93)*

Graille, B., T. Magin, and M. Massot (2009). Kinetic theory of plasmas : Translational energy. *Mathematical Models and Methods in Applied Sciences 19*(4), 527–599. *(p. 371, 373, 379, 380, 381, 389)*

Granqvist, C. and R. Buhrman (1976). Ultrafine metal particles. *Journal of Applied Physics 47*(5), 2200–2219. *(p. 183)*

Greenberg, J. B., I. Silverman, and Y. Tambour (1993). On the origin of spray sectional conservation equations. *Combustion and Flame 93*, 90–96. *(p. 123)*

Greffet, J. (2008). *Physique statistique, introduction aux phénomènes hors-équilibre*. Cours ECP. *(p. 192)*

Griffond, J. (2001). *Instabilité pariétale et accrochage aéro-acoustique dans les conduits à parois débitantes simulant les moteurs à propergol solide d'Ariane 5*. Ph. D. thesis, École Nationale Supérieure de l'Aéronautique et de l'Espace. *(p. 36, 40, 42)*

Griffond, J. and G. Casalis (2001). On the nonparallel stability of the injection-induced two-dimensional Taylor flow. *Phys. Fluids 13*(6), 1635–1644. *(p. 36, 40, 50, 52)*

Griffond, J., G. Casalis, and J.-P. Pineau (2000). Spatial instability of flow in a semi-infinite cylinder with fluid injection through its porous walls. *Eur. J. of Mech. B - Fluids 19*, 69–87. *(p. 42)*

Grishin, S., A. Tishin, and R. Khairutdinov (1969). Nonequilibrious two-phase flow in a laval nozzle with coagulation of polydisperse condensate particles. *Fluid Dynamics 4*(2), 75–78. *(p. 1, 37, 38)*

Gromov, A., U. Förter-Barth, and U. Teipel (2006). Aluminum nanopowders produced by electrical explosion of wires and passivated by non-inert coatings: Characterisation and reactivity with air and water. *Powder technology 164*(2), 111–115. *(p. 23)*

Guazzelli, E. (2003). Microhydrodynamique - cours de base sur les suspensions. http://iusti.polytech.univ-mrs.fr/ guazzelli/publiperso/MicroH.pdf. *(p. 60)*

Guéry, J.-F., F. Vuillot, G. Avalon, F. Plourde, J. Anthoine, and B. Platet (2000). Use of cold flow experiments in the ASSM program - lessons and results. In 2^{nd} *European Conference on Launcher Technology*, Rome. *(p. 42)*

Gueyffier, D., J. Li, A. Nadim, R. Scardovelli, and S. Zaleski (1999). Volume-of-fluid interface tracking with smoothed surface stress methods for three-dimensional flows. *Journal of Computational Physics 152*(2), 423–456. *(p. 71)*

Gurr, J., A. Wang, C. Chen, and K. Jan (2005). Ultrafine titanium dioxide particles in the absence of photoactivation can induce oxidative damage to human bronchial epithelial cells. *Toxicology 213*(1), 66–73. *(p. 187)*

Gyarmathy, G. (1963). Zur Wachstumsgeschwindigkeit kleiner Flüssigkeitstropfen in einer übersättigten Atmosphäre. *Zeitschrift für Angewandte Mathematik und Physik (ZAMP) 14*(3), 280–293. *(p. 191)*

Gyarmathy, G. (1982). The spherical droplet in gaseous carrier streams: review and synthesis. *Multiphase science and technology 1*(1-4), 99–279. *(p. 191)*

Ha Minh, H. (1987). La turbulence en mécanique des fluides: aspects physiques, modélisation et simulation numérique. In *École de Printemps de Combustion*, Oléron. *(p. 39)*

Haider, F., P. Brenner, B. Courbet, and J. Croisille (2011). Efficient implementation of high order reconstruction in finite volume methods. *Finite Volumes for Complex Applications VI Problems & Perspectives*, 553–560. *(p. 226, 231, 323)*

Hairer, E., C. Lubich, and G. Wanner (2006). *Geometric numerical integration: structure-preserving algorithms for ordinary differential equations*, Volume 31. Springer. *(p. 238)*

Hairer, E. and G. Wanner (1996). *Solving ordinary differential equations. II* (second ed.). Berlin: Springer-Verlag. Stiff and differential-algebraic problems, second revised edition. *(p. 234, 243, 275)*

Hao, J., S. Dong, and H. Tan (2003). Numerical simulation of infrared radiation propertis of solid rocket engine exhaust plume. *Journal Infrared Millimeter and Waves 4*, 1–12. *(p. 33)*

Harrje, D. and F. Reardon (1972). Liquid propellant rocket combustion instability. Technical Report SP – 194, NASA. *(p. 15, 167)*

Hart, R. and F. Mc Clure (1965). Theory of acoustic instability in solid propellant rocket combustion. In 10^{th} *Int. Symp. on Combustion*, The combustion Institute. *(p. 40, 50)*

Harten, A., P. Lax, and B. van Leer (1983). On upstream differencing and Godunov-type schemes for hyperbolic conservation laws. *SIAM Review 25*(1), 35–61. *(p. 253)*

Hermsen, R. (1981a). Aluminum combustion efficiency in solid rocket motor. *AIAA Paper 81-0038*. *(p. 30)*

Hermsen, R. (1981b). Aluminum oxide particle size for solid rocket motor performance prediction. In 19^{th} *Aerospace Science Meeting*, St. Louis, MO. AIAA. *(p. 33, 37, 38, 85)*

Hermsen, R. and R. Dunlap (1969). Nucleation and growth of oxide particles in metal vapour flames. *Comb. and flame 13*, 253–261. *(p. 29)*

Hernandez, I., G. Lecocq, D. Poitou, E. Riber, and B. Cuenot (2013). Computations of soot formation in ethylene/air counterflow diffusion flames and its interaction with radiation. *C. R. Mec. 341*, 230–237. Special issue "Combustion for Aerospace Propulsion". *(p. 185)*

Herrmann, M. (2005). A Eulerian level set/vortex sheet method for two-phase interface dynamics. *J. Comput. Phys. 203*(2), 539–571. *(p. 71)*

Herrmann, M. (2010). Detailed numerical simulations of the primary atomization of a turbulent liquid jet in crossflow. *Journal of Engineering for Gas Turbines and Power 132*(6), 061506–10. *(p. 71)*

Hidy, G. (1984). Aerosols: An industrial and environmental science. *(p. 187)*

Hindmarsh, A. (1980). LSODE and LSODI, two new initial value ordinary differential equation solvers. *ACM Signum Newsletter 15*(4), 10–11. *(p. 243)*

Hinds, W. (1982). *Aerosol technology: properties, behavior, and measurement of airborne particles*. New York: Wiley-Interscience. *(p. 187)*

Hirschfelder, J., C. Curtiss, and R. Bird (1954). *Molecular theory of gases and liquids*. Wiley New York. *(p. 355)*

Hoglund, R. (1962). Recent advances in gas-particle nozzle flows. *ARS Journal 32*(5), 662–671. *(p. 37)*

Holmes, P., J. Lumley, G. Berkooz, and C. Rowley (2012). *Turbulence, Coherent Structures, Dynamical Systems and Symmetry*. Cambridge University Press. *(p. 103)*

Hsiang, L. and G. Faeth (1992). Near-limit drop deformation and secondary breakup. *International Journal of Multiphase Flow 18*(5), 635–652. *(p. 86, 100)*

Hsiang, L. and G. Faeth (1993). Drop properties after secondary breakup. *Int. J. Multiphase Flow 19*(5), 721–735. *(p. 86, 100)*

Hsiang, L. and G. Faeth (1995). Drop deformation and break-up due to shock wave and steady disturbance. *Int. J. Multiphase Flow 21*, 545–560. *(p. 364, 365)*

Huang, Y., G. Risha, V. Yang, and R. Yetter (2005). Analysis of nano-aluminum particle dust cloud combustion in different oxidizer environments. In *43rd AIAA Aerospace Sciences Meeting and Exhibit*, Reno, NV. *(p. 19, 31)*

Huang, Y., G. Risha, V. Yang, and R. Yetter (2009). Effect of particle size on combustion of aluminum particle dust in air. *Combustion and Flame 156*(1), 5–13. *(p. xvii, 31, 32)*

Huesmann, K. and E. Eckert (1968). Studies of the laminar flow and the transition to turbulence in porous tubes with uniform injection through the tube wall. *Heat and Mass Transfer 1*(1), 2–9. translated from Wärme und Stoffübertragung. *(p. 39)*

Hundsdorfer, W. and S. Ruuth (2007). IMEX extensions of linear multistep methods with general monotonicity and boundedness properties. *Journal of Computational Physics 225*(2), 2016–2042. *(p. 237)*

Hundsdorfer, W. and J. Verwer (2007). *Numerical solution of time-dependent advection-diffusion-reaction equations*, Volume 33. Springer. *(p. 237)*

Hyland, K., S. McKee, and M. Reeks (1999). Derivation of a PDF kinetic equation for the transport of particles in turbulent flows. *J. Phys. A 32*(34), 6169–6190. *(p. 102)*

Hylkema, J., M. Prevost, and G. Casalis (2011). On the importance of reduced scale Ariane 5 P230 solid rocket motor models in the comprehension and prevention of thrust oscillations. *CEAS Space Journal 1*(1), 99–107. *(p. 41, 46)*

Hylkema, J. and P. Villedieu (1998). A random particle method to simulate coalescence phenomena in dense liquid sprays. In *Proc. 16th Int. Conf. on Num. Meth. in Fluid Dyn.*, Volume 515, Arcachon, France, pp. 488–493. *(p. 96, 98, 107)*

Hylkema, J. J. (1999). *Modélisation cinétique et simulation numérique d'un brouillard dense de gouttelettes. Application aux propulseurs à poudre.* Ph. D. thesis, École Nationale Supérieure de l'Aéronautique et de l'Espace. *(p. 51, 81, 83, 98, 106, 107)*

Iliopoulos, I., Y. Mito, and T. Hanratty (2003). A stochastic model for solid dispersion in a non-homogeneous turbulent field. *International Journal of Multiphase Flow 29*, 375–394. *(p. 106)*

Ishihara, A. and M. Brewster (1993). Combustion studies of boron, magnesium, and aluminum composite propellants. *Combustion science and technology 87*(1-6), 275–290. *(p. 19)*

Ishii, M. (1975). *Thermo-fluid dynamic theory of two-phase flow.* Paris: Eyrolles. *(p. 57, 75, 76)*

Ishii, M. and T. Hibiki (2010). *Thermo-fluid dynamics of two-phase flow.* Springer. *(p. 57)*

Ivanov, G. and F. Tepper (1997). "Activated" Aluminum as a stored energy source for propellants. *International Journal of Energetic Materials and Chemical Propulsion 4*(1-6). *(p. 22, 23)*

Ivanov, N. and R. Ivanova (1976). Numerical investigation of nonequilibrium flows of mixtures of fusible metal particles and gases in a laval nozzle. *Journal of Applied Mechanics and Technical Physics 17*(2), 213–216. *(p. 38)*

Jabin, P.-E. (2002). Various levels of models for aerosols. *Mathematical Models and Methods in Applied Sciences 12*(7), 903–919. *(p. 112)*

Jackson, R. and B. Davidson (1983). An equation set for non-equilibrium two phase flow, and an analysis of some aspects of choking, acoustic propagation, and losses in low pressure wet steam. *International journal of multiphase flow 9*(5), 491–510. *(p. 37, 77)*

Jameson, A., W. Schmidt, and E. Turkel (1981). Numerical solutions of the Euler equations by finite volume methods using Runge-Kutta time-stepping schemes. *AIAA paper*. *(p. 232)*

Jay, S., F. Lacas, and S. Candel (2006). Combined surface density concepts for dense spray combustion. *Combustion and Flame 144*(3), 558–577. *(p. 76)*

Jeenu, R., K. Pinumalla, and D. Deepak (2010). Size distribution of particles in combustion products of aluminized composite propellant. *J. Prop. Power 26*, 715–723. *(p. 30)*

Jenkins, R. and R. Hoglund (1969). *A unified theory of particle growth in rocket chambers and nozzles.* USAF academy, CO: American Institute of Aeronautics and Astronautics. *(p. 38)*

Jeong, J. I. and M. Choi (2001). A sectional method for the analysis of growth of polydisperse non-spherical particles undergoing coagulation and coalescence. *Journal of Aerosol Science 32*(5), 565 – 582. *(p. 190)*

Jeong, J. I. and M. Choi (2003a). Analysis of non-spherical polydisperse particle growth in a two-dimensional tubular reactor. *Journal of Aerosol Science 34*(6), 713 – 732. *(p. 189)*

Jeong, J. I. and M. Choi (2003b). A simple bimodal model for the evolution of non-spherical particles undergoing nucleation, coagulation and coalescence. *Journal of Aerosol Science 34*(8), 965 – 976. *(p. 190)*

Jeong, J. I. and M. Choi (2005). A bimodal particle dynamics model considering coagulation, coalescence and surface growth, and its application to the growth of titania aggregates. *Journal of Colloid and Interface Science 281*(2), 351 – 359. *(p. 190)*

Jézéquel, P. and M. Prévost (2007). Étude des oscillations de poussée – campagne sur maquette LP10 30/07 particules inertes. Technical Report RT 3/12709 DMAE, ONERA. *(p. 45, 284, 331)*

Jibben, Z. and M. Herrmann (2012). A quadrature-free conservative level set RKDG for simulating atomization. *Bulletin of the American Physical Society 57*(17). *(p. 71)*

Johns, L. and R. Beckmann (1966). Mechanism of dispersed-phase mass transfer in viscous, single-drop extraction systems. *AIChE Journal 12*(1), 10–16. *(p. 31, 359)*

Johnston, W. (1995). Solid rocket motor internal flow during ignition. *Journal of Propulsion and Power 11*(3), 489–496. *(p. 38)*

Johnston, W., J. Murdock, S. Koshigoe, and P. Than (1994). Slag accumulation in the titan srmu. In 30^{th} *ASME/SAE/ASEE Joint Propulsion Conference and Exhibit. (p. 32, 119)*

Join-Lambert, A., M. Halle, and C. Dauviau (1996). Ariane 5 : Oscillations de pression EAP, synthèse des exploitations AEROSPATIALE des tirs au banc du P230. Technical Report AS-NT-1-A-1845-ASAI, AEROSPATIALE. *(p. 17)*

Jolicoeur, C., P. Roberge, and J. Fortier (1981). Separation of short fibers from bulk chrysotile asbestos fiber materials: analysis and physico-chemical characterization. *Canadian Journal of Chemistry 59*(7),

1140–1148. *(p. 185, 187)*

Jones, D. and A. Watkins (2012). Droplet size and velocity distributions for spray modelling. *Journal of Computational Physics 231*, 676–692. *(p. 28, 117)*

Joumani, Y. (2001). *Transferts radiatifs dans les moteurs à propergol solide*. Ph. D. thesis, École des Mines de Douai. *(p. 28)*

Kah, D. (2010). *Taking into account polydispersity for the modeling of liquid fuel injection in internal combustion engines*. Ph. D. thesis, École Centrale Paris. http://tel.archives-ouvertes.fr/tel-00618786. *(p. xix, 2, 3, 57, 59, 75, 77, 78, 115, 120, 122, 123, 124, 130, 132, 139, 159, 228, 230, 232, 242, 243, 247, 291, 368, 369)*

Kah, D., O. Emre, Q. Tran, S. Chaisemartin, S. Jay, F. Laurent, and M. Massot (2013). High order moment method for polydisperse evaporating spray with mesh movement: application to internal combustion engines. *in preparation for Int. J. Multiphase Flows*. *(p. 226, 231, 233)*

Kah, D., F. Laurent, L. Fréret, S. de Chaisemartin, R. Fox, J. Reveillon, and M. Massot (2010). Eulerian quadrature-based moment models for dilute polydisperse evaporating sprays. *Flow Turbulence and Combustion 85*(3–4), 649–676. *(p. 130, 245)*

Kah, D., F. Laurent, M. Massot, and S. Jay (2012). A high order moment method simulating evaporation and advection of a polydisperse liquid spray. *J. Comput. Phys. 231*(2), 394–422. *(p. 120, 122, 124, 228, 231, 269, 291, 292)*

Kaufmann, A., M. Moreau, O. Simonin, and J. Helie (2008). Comparison between Lagrangian and Mesoscopic Eulerian modelling approaches for inertial particles suspended in decaying isotropic turbulence. *Journal of Computational Physics 227*(13), 6448–6472. *(p. 101, 254, 263)*

Kaufmann, A., O. Simonin, and T. Poinsot (2004). Direct numerical simulation of particle-laden homogeneous isotropic turbulent flows using a two-fluid model formulation. In *5th Int. Conf. on Multiphase Flow*, Yokohama, Japan. *(p. 101, 103)*

Kee, R., F. Rupley, and J. Miller (1990). The chemkin thermodynamic data base. Technical report, Sandia National Labs., Livermore, CA (USA). *(p. 49)*

Kee, R., K. Yamashita, H. Zhu, and A. Dean (2011). The effects of liquid-fuel thermophysical properties, carrier-gas composition, and pressure, on strained opposed-flow non-premixed flames. *Combustion and Flame 158*(6), 1129–1139. *(p. 361)*

Kim, D., S. Park, Y. Song, D. Kim, and K. Lee (2003). Brownian coagulation of polydisperse aerosols in the transition regime. *Journal of Aerosol Science 34*(7), 859–868. *(p. 205)*

Kim, J., G. Mulholland, S. Kukuck, and D. Pui (2005). Slip correction measurements of certified PSL nanoparticles using a Nano-DMA for Knudsen number from 0.5 to 83. *J. Res. Natl. Inst. Stand. Technol. 110*, 31–54. *(p. 205)*

King, M., J. Komar, and R. Fry (1984). Fuel-rich solid propellant boron combustion. Technical report, DTIC Document. *(p. 19, 22)*

Kiss, L., J. Söderlund, G. Niklasson, and C. Granqvist (1999). New approach to the origin of lognormal size distributions of nanoparticles. *Nanotechnology 10*(1), 25. *(p. 184)*

Kliegel, J. (1959). One dimensional flow of a gas-particle system. Technical report, DTIC Document. *(p. 37)*

Knott, G., J. Buckmaster, and T. Jackson (2001). Random Packing of Heterogeneous Propellants. *AIAA Journal 39*, 678–686. *(p. xvii, 21, 22, 49)*

Knudsen, M. and S. Weber (1911). Luftwiderstand gegen die langsame Bewegung kleiner Kugeln. *Annalen der Physik 341*, 981–994. *(p. 205)*

Kolmogorov, A. (1941). On the logarithmically normal law of distribution of the size of particles under pulverization. *Dokl. Akad. Nauk. SSSR 31*, 99. *(p. 63, 363)*

Konan, N., H. Neau, O. Simonin, M. Dupoizat, and T. Le Goaziou (2010). Reactive multiphase flow simulation of Uranium Hexafluoride conversion reactor. In *Proceedings of the 7th International Conference on Multiphase Flow*, pp. 1152–1158. *(p. 119)*

Kostoglou, M. (2007). Extended cell average technique for the solution of coagulation equation. *Journal of Colloid and Interface Science 306*(1), 143–160. *(p. 317)*

Kostoglou, M. and A. Karabelas (1994). Evaluation of zero order methods for simulating particle coagulation. *Journal of colloid and interface science 163*(2), 420–431. *(p. 120)*

Kostoglou, M. and A. Karabelas (2009). On sectional techniques for the solution of the breakage equation. *Computers & Chemical Engineering 33*(1), 112–121. *(p. 317)*

Kourta, A. (1996). Acoustic mean-flow interaction and vortex-shedding in solid rocket motors. *International journal for numerical methods in fluids 22*, 449–465. *(p. 42)*

Kourta, A. (1999). Computation of vortex shedding in solid rocket motors using time-dependant turbulence model. *Journal of Propulsion and Power 15*(3), 390–400. *(p. 39)*

Kourta, A. and H. Ha Minh (1995). Turbulence et aéroacoustique dans les moteurs de fusée. In *Colloque Ecoulements propulsifs dans les systèmes de transport spatial*, Bordeaux. CNES/ONERA/CNRS.

(p. 42)

Kovalev, O. (2002). Motor and plume particle size prediction in solid-propellant rocket motors. *Journal of Propulsion and Power 18*(6), 1199–1210. *(p. 33, 61)*

Kovalev, O. and V. Fomin (1982). Analytical investigation of two-phase mixture flow in a nozzle with gasdynamic fractionation taken into account. *Combustion, Explosion, and Shock Waves 18*(5), 568–572. *(p. 38)*

Kraiko, A. and A. Shraiber (1974). Model of two-phase flow with coagulation of particles of a polydisperse use condensate in the one-dimensional approximation. *Journal of Applied Mechanics and Technical Physics 15*(2), 201–207. *(p. 38)*

Kubo, R. (1966). The fluctuation-dissipation theorem. *Reports on Progress in Physics 29*(1), 255. *(p. 192)*

Kuentzmann, P. (1969). Agglomération des particules d'alumine dans l'écoulement de tuyère d'un propergol métallisé. *La Recherche Aérospatiale* (131), 1–35. *(p. 38)*

Kuentzmann, P. (1973a). *Aérothermochimie des suspensions*. Gautier-Villars Editeur. *(p. 94, 111)*

Kuentzmann, P. (1973b). *Pertes d'impulsion spécifique dans les fusées à propergol solide*. Office Nationale d'Études et de Recherches Aérospatiales. *(p. 1, 27, 34, 37)*

Kuentzmann, P. (1991). Instabilités de combustion. In *Combustion of Solid Propellants*. AGARD. *(p. 16, 40)*

Kuentzmann, P. (1998). Synthèse scientifique des travaux ASSM-POP. In *3ème colloque sur les écoulements internes en propulsion solide*, Poitiers. R&T ENSMA/CNES/ONERA. *(p. 2)*

Kuentzmann, P. (2001). Un bilan du programme ASSM-POP. Technical Report RT-NT 1113100/0102, ONERA. *(p. 40)*

Kuentzmann, P. and A. Laverdant (1984). Détermination expérimentale de la réponse d'un propergol solide aux oscillations de pression de haute fréquence. *La Recherche Aérospatiale* (1), 39–55. *(p. 40)*

Kumar, J., M. Peglow, G. Warnecke, S. Heinrich, and L. Mörl (2006). Improved accuracy and convergence of discretized population balance for aggregation: The cell average technique. *Chemical Engineering Science 61*(10), 3327–3342. *(p. 120, 317)*

Kumar, S. and D. Ramkrishna (1996a). On the solution of population balance equations by discretization – I. A fixed pivot technique. *Chemical Engineering Science 51*, 1311–1332. *(p. 120, 317)*

Kumar, S. and D. Ramkrishna (1996b). On the solution of population balance equations by discretization – II. A moving pivot technique. *Chemical Engineering Science 51*, 1333–1342. *(p. 120, 317)*

Kumar, S. and D. Ramkrishna (1997). On the solution of population balance equations by discretization – III. Nucleation, growth and aggregation of particles. *Chemical Engineering Science 52*, 4659–4679. Festshrift for Professor M. M. Sharma. *(p. 317)*

Kuo, K. (1986). *Principles of combustion*. John Wiley and sons. *(p. 52)*

Lacaze, G., B. Cuenot, T. Poinsot, and M. Oschwald (2009). Large Eddy Simulation of laser ignition and compressible reacting flow in a rocket-like configuration. *Combustion and Flame 156*(6), 1166–1180. *(p. 232)*

Lai, F. S., S. K. Friedlander, J. Pich, and G. M. Hidy (1972). The self-preserving particle size distribution for brownian coagulation in the free-molecule regime. *Journal of Colloid and Interface Science 39*(2), 395 – 405. *(p. 190)*

Lamarque, N. (2007). *Schémas numériques et conditions limites pour la Simulation aux Grandes Échelles de la combustion diphasique dans des foyers d'hélicoptères*. Ph. D. thesis, Institut National Polytechnique de Toulouse. *(p. 103, 231)*

Landau, L. and E. Lifshitz (1988). *Fluid Mechanics* (third ed.), Volume 6 of *Theoretical physics*. MIR. *(p. 57)*

Langevin, P. (1908). Sur la théorie du mouvement brownien. *C. R. Acad. Sci. 146*, 530–533. *(p. 192)*

Langmuir, I. (1948). The production of rain by a chain reaction in cumulous clouds at temperatures above freezing. *J. Meteor. 5*, 17–192. *(p. 81, 82, 103)*

Larat, A. (2009). *Conception et analyse de schémas distribuant le résidu d'ordre très élevé. Application à la mécanique des fluides*. Ph. D. thesis, Université Sciences et Technologies-Bordeaux I. *(p. 233)*

Larat, A. and M. Massot (2014). On the multidimensional structure of the anisotropic Gaussian model for gas dynamics and particle-laden flows. *Mathematical Models and Methods in Applied Sciences, in preparation*. *(p. 157)*

Larat, A., M. Massot, and A. Vié (2012). A stable, robust and high order accurate numerical method for Eulerian simulation of spray and particle transport on unstructured meshes. In *Annual Research Briefs*, Center for Turbulence Research, Stanford University, pp. 205–216. *(p. 2, 233, 265)*

Laurent, C., G. Lavergne, and P. Villedieu (2010). Quadrature method of moments for modeling multicomponent spray vaporization. *International Journal of Multiphase Flow 36*(1), 51–59. *(p. 361)*

Laurent, F. (2006). Numerical analysis of Eulerian Multi-Fluid models in the context of kinetic formulations for dilute evaporating sprays. *M2AN Math. Model. Numer. Anal. 40*(3), 431–468. *(p. 121, 122, 139, 140, 142, 145, 242, 245)*

Laurent, F. (2013). Linear reconstruction for two-size moment Eulerian Multi-Fluid method. *In preparation for ESAIM: Math. Mod. and Num. Analysis*, 1–12. *(p. 142, 145, 147)*

Laurent, F. and M. Massot (2001). Multi-fluid modeling of laminar poly-dispersed spray flames: origin, assumptions and comparison of the sectional and sampling methods. *Comb. Theory and Modelling 5*, 537–572. *(p. 2, 77, 79, 94, 95, 96, 100, 101, 111, 114, 115, 117, 119, 123, 124, 126, 139, 161, 269, 359)*

Laurent, F., M. Massot, and P. Villedieu (2004). Eulerian Multi-Fluid modeling for the numerical simulation of coalescence in polydisperse dense liquid sprays. *J. Comp. Phys. 194*, 505–543. *(p. 2, 96, 107, 115, 116, 123, 124, 127, 139, 162, 246, 302, 303, 306, 311)*

Laurent, F., V. Santoro, M. Noskov, A. Gomez, M. Smooke, and M. Massot (2004). Accurate treatment of size distribution effects in polydispersed spray diffusion flames: Multi-Fluid modeling, computations and experiments. *Combust. Theory and Modelling 8*, 385–412. *(p. 96)*

Laurent, F., A. Vié, C. Chalons, R. O. Fox, and M. Massot (2012). A hierarchy of Eulerian models for trajectory crossing in particle-laden turbulent flows over a wide range of Stokes numbers. *Annual Research Briefs of the CTR*, 1–12. *(p. 260)*

Lavergne, G., L. Jacques, Y. Fabignon, and L. Dumas (1996). Alumine slag prediction in solid boosters. In 5^{th} *Int. Symp. Propulsion in Space Transportation*, Paris. *(p. 17)*

Law, C. (1973). A simplified theoritical model for the vapor-phase combustion of metal particles. *Combustion Science and Technology 7*, 197–212. *(p. 361)*

Le Chenadec, V. (2012). *Development of a Robust and Conservative Framework for Primary Atomization Computations*. Ph. D. thesis, Center for Turbulence Research, Stanford. *(p. 59, 363)*

Le Chenadec, V. and H. Pitsch (2013a). A 3D unsplit forward/backward Volume-of-Fluid approach and coupling to the level set method. *Journal of computational physics 233*, 10–33. *(p. 71)*

Le Chenadec, V. and H. Pitsch (2013b). A monotonicity preserving sharp interface flow solver for high density ratio two-phase flows. *submitted to Journal of computational physics*. *(p. 71)*

Le Helley, P., S. Coste, and T. Pevergne (2000). Influence of the unsteady flow on the alumina flux impinging the nozzle and the aft dome of the Ariane 5 booster. In 2^{nd} *European Conference on Launcher Technology*, Rome. *(p. 32)*

Le Métayer, O. (2003). *Modélisation et résolution de la propagation de fronts perméables. Application aux fronts d'évaporation et de détonation*. Ph. D. thesis, Université de Provence. *(p. 78)*

Le Touze, C., A. Murrone, E. Montreuil, and H. Guillard (2012). Numerical methods on unstructured meshes for the simulation of sprays within liquid rocket engines. In 20^{th} *ECCOMAS conference*, Vienna, Austria. *(p. 2, 6, 134, 231, 233, 246, 291, 322, 323, 324)*

Lebas, R., T. Menard, P. Beau, A. Berlemont, and F. Demoulin (2009). Numerical simulation of primary break-up and atomization: DNS and modelling study. *International Journal of Multiphase Flow 35*(3), 247–260. *(p. 71)*

Lecanu, M. (2005). *Couplage multi-physique: combustion turbulente-Rayonnement-Cinétique chimique*. Ph. D. thesis, École Centrale Paris. *(p. 53)*

Leduc, J. (2010). *Etude physique et numérique de l'écoulement dans un dispositif d'injection de turbine Pelton*. Ph. D. thesis, École Centrale de Lyon. *(p. 71)*

Lee, Y. and R. Beddini (1999). Acoustically-induced turbulent transition in solid propellant rocket chamber flowfields. *AIAA journal 51*(Paper n°99-2508), 61801. *(p. 39)*

Lefebvre, H. (1989). *Atomization and Sprays*. Hemisphere Publishing Corporation. *(p. 59, 363)*

Legrand, B., L. Catoire, C. Chauveau, and I. Gokalp (2000). Combustion of levitated aluminum in CO_2/HCl mixture. In 2^{nd} *European Conference on Launcher Technology*, Rome. *(p. 30)*

Lemonnier, H. and A. Rowe (1988). Another approach in modelling cavitating flows. *Journal of Fluid Mechanics 195*(1), 557–580. *(p. 59)*

Lemonnier, H. and S. Selmer-Olsen (1992). Experimental investigation and physical modelling of two-phase two-component flow in a converging-diverging nozzle. *International journal of multiphase flow 18*(1), 1–20. *(p. 59)*

Lempert, D., G. Manelis, and G. Nechiporenko (2009). The ways for development of environmentally safe solid composite propellants. In *Progress in Propulsion Physics*, pp. 63–80. Paris: EUCASS advances in aerospace sciences book ser., EDP Sciences, TORUS PRESS. *(p. 20)*

Lennard-Jones, J. (1924). On the determination of Molecular Fields. *Proc. R. Soc. Lond. A 106*(738), 463–477. *(p. 202)*

Lepercq-Bost, É., M. Giorgi, A. Isambert, and C. Arnaud (2008). Use of the capillary number for the prediction of droplet size in membrane emulsification. *Journal of membrane science 314*(1), 76–89. *(p. 58)*

Lepercq-Bost, É., M. Giorgi, A. Isambert, and C. Arnaud (2010). Estimating the risk of coalescence in membrane emulsification. *Journal of Membrane Science 357*(1), 36–46. *(p. 58)*

Lessard, P., F. Beaupre, and P. Brousseau (2001). Burn rate studies of composite propellants containing

ultra-fine metals. *Energetic materials – Ignition, combustion and detonation*, 1–88. *(p. 24)*

LeVeque, R. (2002). *Finite volume methods for hyperbolic problems*. Cambridge Texts in Applied Mathematics. Cambridge: Cambridge University Press. *(p. 228, 230, 250, 291)*

Levermore, C. (1996). Moment closure hierarchies for kinetic theories. *J. Stat Phys. 83*(5/6), 1021–1065. *(p. 91)*

Levermore, C. and W. Morokoff (1998). The Gaussian moment closure for gas dynamics. *SIAM J. Appl. Math. 59*(1), 72–96. *(p. 91, 153, 154, 155)*

Leyvraz, F. (2003). Scaling theory and exactly solved models in the kinetics of irreversible aggregation. *Physics Reports 383*(2-3), 95 – 212. *(p. 190)*

Lhuillier, D. (1992). Ensemble averaging in slightly non-uniform suspensions. *European journal of mechanics. B, Fluids 11*(6), 649–661. *(p. 75)*

Lhuillier, J. (1966). Les instabilités dans les moteurs-fusées à propergol solide : les instabilités acoustiques. *Doc Air-Espace 98*, 3–18. *(p. 16)*

Li, A. and G. Ahmadi (1995). Computer simulation of particle deposition in the upper tracheobronchial tree. *Aerosol science and technology 23*(2), 201–223. *(p. 186)*

Liang, Y. and M. Beckstead (1998). Numerical simulation of quasi-steady, single aluminum particle combustion in air. In *36th Aerospace Sciences Meeting & Exhibit*, Reno, NV. *(p. 29, 30)*

Liou, M. (1996). A sequel to AUSM: AUSM$^+$. *Journal of Computational Physics 129*(2), 364–382. *(p. 229)*

Liou, M. and C. Steffen (1993). A new flux splitting scheme. *Journal of Computational Physics 107*(1), 23–39. *(p. 229)*

Lippmann, M. (1990). Effects of fiber characteristics on lung deposition, retention, and disease. *Environmental Health Perspectives 88*, 311–317. *(p. 186, 187)*

Lomax, H., T. Pulliam, D. Zingg, T. Pulliam, and D. Zingg (2001). *Fundamentals of computational fluid dynamics*, Volume 246. Springer Berlin. *(p. 225)*

Loth, E. (2000). Numerical approaches for motion of dispersed particles, droplets and bubbles. *Progress in Energy and Combustion Science 26*, 161–223. *(p. 61)*

Lucas, R. (1993). *Propulsion Elements for Solid Rocket Motors in Solid Rocket Propulsion Technology*. Pergamon Pr (edited by A. Davenas). *(p. 34)*

Lupoglazoff, N. and F. Vuillot (1992). Numerical simulation of vortex-shedding phenomena in 2D test case solid rocket motors. In 30th *Aerospace and Sciences Meeting and Exhibit*, pp. Paper n°92–0776. AIAA. *(p. 50)*

Lupoglazoff, N. and F. Vuillot (1993). Synthèse des résultats obtenus sur le cas test "c2" programme ASSM axe stabilité de fonctionnement. Technical Report 40/6133 EY, ONERA. *(p. 41)*

Lupoglazoff, N. and F. Vuillot (1996). Parietal Vortex Shedding as a cause of instability for long solid propellant motors. Numerical simulations and comparisons with firing tests. *AIAA journal 21*, 1–12. Paper n° 96-0761. *(p. 40, 41, 42, 49, 50, 52, 284)*

Lupoglazoff, N. and F. Vuillot (1998a). Conception, spécifications et calculs du cas test c3 pour la validation instationnaire des modèles physiques. In *3ème colloque R&T ENSMA/CNES/ONERA sur les écoulements internes en propulsion solide*, Poitiers. *(p. 42)*

Lupoglazoff, N. and F. Vuillot (1998b). Numerical simulations of parietal vortex-shedding phenomenon in a cold flow setup. In *34th AIAA/ASME/SAE/ASEE Joint Propulsion Conference and Exhibit*. Paper n°98-3220. *(p. 41, 50)*

Lupoglazoff, N., F. Vuillot, J. Dupays, and Y. Fabignon (2000). Numerical simulations of the unsteady flow inside Ariane 5 P230 SRM booster with burning aluminum particles. In 2nd *European Conference on Launcher Technology*, Rome. *(p. 42)*

Lupoglazoff, N., F. Vuillot, J. Dupays, and Y. Fabignon (2002). Numerical simulations of the unsteady flow inside segmented solid-propellant motors with burning aluminum particles. In 40th *AIAA Aerospace Sciences Meeting and Exhibit*, Reno, NV, pp. Paper n°2002–0784. *(p. 45, 49)*

Luret, G., T. Menard, A. Berlemont, J. Reveillon, F. Demoulin, and G. Blokkeel (2010). Modelling collision outcome in moderately dense sprays. *Atomization and Sprays 20*, 41–67. *(p. 72)*

Ma, D. and G. Ahmadi (1990). A thermodynamical formulation for dispersed multiphase turbulent flows – 1 : Basic theory. *International Journal of Multiphase Flow 16*(2), 323–340. *(p. 103)*

MacCormack, R. (1969). The effect of viscosity in hypervelocity impact cratering. In *4th Aerodynamic Testing Conference*, Number Paper n°69-354, Cincinnati, OH. World Scientific. *(p. 229)*

Maggi, F., A. Bandera, L. De Luca, V. Thoorens, J. Trubert, and T. Jackson (2011). Agglomeration in solid rocket propellants: novel experimental and modeling methods. *Progress in Prop. Phys. 2*, 81–98. *(p. 30)*

Magin, T. and R. MacCormack (2009). *Hypersonic Flow*. Course, Stanford University. *(p. 91, 92, 93)*

Magni, A. and G. Cottet (2012). Accurate, non-oscillatory, remeshing schemes for particle methods. *Journal of Computational Physics 231*(1), 152–172. *(p. 70)*

Mahulikar, S., H. Sonawane, and G. Arvind Rao (2007). Infrared signature studies of aerospace vehicles.

Progress in Aerospace Sciences 43(7), 218–245. *(p. 33)*

Majdalani, J. and T. Saad (2007). The Taylor-Culick profile with arbitrary headwall injection. *Phys. of Fluids 19*(6), 1–10. *(p. 36, 52)*

Majdalani, J. and W. Van Moorhem (2001). Laminar cold-flow model for the internal gas dynamics of a slab rocket motor. *Aerospace science and technology 5*(3), 193–207. *(p. 36)*

Mallat, S. (1989). Multiresolution approximations and wavelet orthonormal bases of $L^2(R)$. *Trans. Amer. Math. Soc 315*(1). *(p. 233)*

Marble, F. (1963a). Dynamics of a gas containing small solid particles. In *5th Colloquium on Combustion and Propulsion*, Pergamon, pp. 175–213. AGARD. *(p. 111)*

Marble, F. (1963b). Nozzle contours for minimum particle-lag loss. *AIAA Journal 1*(12), 2793–2801. *(p. 1, 37)*

Marble, F. (1967). Droplet agglomeration in rocket nozzles caused by particle slip and collision. *Astronautica Acta 13*(2), 159–166. *(p. 38)*

Marble, F. (1970). Dynamics of dusty gases. *Ann. Rev. Fluid Mech. 2*, 397–446. *(p. 111, 137)*

Marble, F. and S. Candel (1977). Acoustic disturbance from gas non-uniformities convected through a nozzle. *Journal of Sound and Vibration 55*, 225–243. *(p. 28, 42)*

Marchioli, C., M. Picciotto, and A. Soldati (2006). Particle dispersion and wall-dependent fluid scales in turbulent bounded flow: Implications for local equilibrium models. *Journal of Turbulence 7*(60), 1–12. *(p. 107)*

Marchisio, D. and R. Fox (2005). Solution of population balance equations using the direct quadrature method of moments. *Journal of Aerosol Science 36*, 43–73. *(p. 2, 120, 132, 189, 317)*

Marchisio, D. and R. Fox (2007). *Multiphase reacting flows: modelling and simulation.* CISM Courses and Lectures. Udine: Springer Verlag. *(p. 120)*

Marchisio, D., J. Pikturna, R. Fox, and V. R.D. (2003). Quadrature method of moments for population-balance equations. *AIChE Journal 49(5)*, 1266–1276. *(p. 119)*

Marchisio, D., R. Vigil, and R. Fox (2003). Quadrature method of moments for aggregation-breakage processes. *J. of Colloid and Interface Sci. 258*(2), 322–334. *(p. 120)*

Marion, M., C. Chauveau, and I. Gokalp (1996). Studies on the ignition and burning of levitated aluminum particles. *Combustion Sciences and Technology 115*(4-6), 369–390. *(p. 30)*

Markutsya, S., R. Fox, and S. Subramaniam (2012). Coarse-graining approach to infer mesoscale interaction potentials from atomistic interactions for aggregating systems. *Industrial & Engineering Chemistry Research 51*(49), 16116–16134. *(p. 203)*

Markutsya, S., S. Subramaniam, R. Vigil, and R. Fox (2008). On Brownian dynamics simulation of nanoparticle aggregation. *Industrial & Engineering Chemistry Research 47*(10), 3338–3345. *(p. 203)*

Marle, C. (1982). On macroscopic equations governing multiphase flow with diffusion and chemical reactions in porous media. *Int. J. Eng. Sci. 20*, 643–662. *(p. 75)*

Marmignon, C., V. Couaillier, and B. Courbet (2011). Solution strategies for integration of semi-discretized flow equations in elsA and CEDRE. *Aerospace Lab 2*. Available at www.aerospacelab-journal.org/al2. *(p. 323)*

Martin, C. (1995). Shuttle STS-54 pressure perturbation investigation. In *31st ASME/SAE/ASEE Joint Propulsion Conference and Exhibit*, Penn State, PA. *(p. 32)*

Martinez, L. (2009). *Simulation aux grandes échelles de l'injection de carburant liquide dans les moteurs à combustion interne.* Ph. D. thesis, Institut National Polytechnique de Toulouse. *(p. 227, 232, 233)*

Mashayek, F. (1998). Direct numerical simulations of evaporating droplet dispersion in forced low mach number turbulence. *Int. J. Heat Mass Transfer 41*, 2601–2617. *(p. 72)*

Mashayek, F., N. Ashgriz, W. J. Minkowycz, and B. Shotorban (2003). Coalescence collision of liquid drops. *International Journal of Heat and Mass Transfer 46*(1), 77 – 89. *(p. 83)*

Mashayek, F. and R. Pandya (2003). Analytical description of particle/droplet-laden turbulent flows. *Prog. Energy Combust. Sci. 29*, 329–378. *(p. 102)*

Mashayek, R., F. Jaberi, R. Miller, and P. Givi (1997). Dispersion and polydispersity of droplets in stationary isotropic turbulence. *Int. J. Multiphase Flow 23*(2), 337–355. *(p. 72)*

Masi, E. (2010). *Étude théorique et numérique de la modélisation instationnaire des écoulements turbulents anisothermes gaz-particules par une approche Euler-Euler.* Ph. D. thesis, Institut National Polytechnique de Toulouse. *(p. 2, 64, 101, 157)*

Masi, E. and O. Simonin (2012). An algebraic-closure-based moment method for unsteady eulerian modeling of non-isothermal particle-laden turbulent flows in very dilute regime and high stokes number. In *7th Int. Symposium on Turbulence, Heat and Mass Transfer*, Palermo, IT. *(p. 101, 254)*

Masi, E., O. Simonin, E. Riber, P. Sierra, and L. Gicquel (2013). Development of an algebraic-closure-based moment method for unsteady Eulerian simulations of particle-laden turbulent flows in very dilute regime. *International Journal of Multiphase Flow*. *(p. 254)*

Massot, M. (1996). *Modélisation Mathématique et Numérique de la Combustion des Mélanges Gazeux.* Ph.

D. thesis, Thèse de l'Ecole Polytechnique. *(p. 90, 92, 93)*

Massot, M. (2007). Eulerian Multi-Fluid models for polydisperse evaporating sprays. In D. Marchisio and R. Fox (Eds.), *Multi-Phase Reacting Flows: Modelling and Simulation*, CISM Courses and Lectures No. 492, pp. 79–123. Springer. *(p. 102, 254)*

Massot, M., R. Knikker, C. Péra, and J. Reveillon (2004). Lagrangian/Eulerian analysis of the dispersion of evaporating sprays in non-homogeneous turbulent flows. In *5th International Conference on Multiphase Flows*, Japan. *(p. 102, 103)*

Massot, M., F. Laurent, S. de Chaisemartin, L. Fréret, and D. Kah (2009). Eulerian Multi-Fluid models: modeling and numerical methods. In *Modeling and Computation of Nanoparticles in Fluid Flows*, Number 1 in Lectures of the von Karman Institute, pp. 1–86. NATO RTO AVT 169. *(p. 112, 115, 123, 130, 281, 364, 368, 369)*

Massot, M., F. Laurent, D. Kah, and S. de Chaisemartin (2010). A robust moment method for evaluation of the disappearance rate of evaporating sprays. *SIAM J. Appl. Math. 70*(8), 3203–3234. *(p. 122, 124, 245)*

Mathiaud, J. (2006). *Étude de systèmes de type gaz-particules*. Ph. D. thesis, École normale supérieure de Cachan - ENS Cachan. Available in English at http://tel.archives-ouvertes.fr/tel-00133645/en/. *(p. 85, 90, 92, 105)*

Matous, K., H. Inglis, X. Gu, D. Rypl, T. Jackson, and P. Geubelle (2007). Multiscale modeling of solid propellants: From particle packing to failure. *Composites Science and Technology 67*(7–8), 1694–1708. *(p. 21)*

Maury, B., A. Roudneff-Chupin, and F. Santambrogio (2010). A macroscopic crowd motion model of gradient flow type. *Mathematical Models and Methods in Applied Sciences 20*(10), 1787–1821. *(p. 72)*

McGraw, R. (1997). Description of aerosol dynamics by the quadrature method of moments. *Aerosol Science and Technology 27*, 255–265. *(p. 119, 130)*

Mead, L. and N. Papanicolaou (1984). Maximum entropy in the problem of moments. *J. Math. Phys. 25*(8), 2404–2417. *(p. 122)*

Meda, L., G. Marra, L. Galfetti, S. Inchingalo, F. Severini, and L. De Luca (2005). Nano-composites for rocket solid propellants. *Comp. Sc. and Tech. 65*, 769–773. *(p. 19, 22)*

Meda, L., G. Marra, L. Galfetti, F. Severini, and L. De Luca (2007). Nano-aluminum as energetic material for rocket propellants. *Material Sc. and Eng.: C 27*, 1393–1396. *(p. 19, 22)*

Melik, D. and H. Fogler (1984). Gravity-induced flocculation. *J. Colloid and Interface Sc. 101*(1), 72–79. *(p. 202)*

Menard, T., S. Tanguy, and A. Berlemont (2007). Coupling level set/VOF/ghost fluid methods: Validation and application to 3D simulation of the primary break-up of a liquid jet. *International Journal of Multiphase Flow 33*(5), 510–524. *(p. 71)*

Mench, M., C. Yeh, and K. Kuo (1998). Propellant burning rate enhancement and thermal behavior of ultra-fine aluminum powders (Alex). In *29th International Annual Conference of ICT*, Karlsruhe, Germany. *(p. 19, 24)*

Menter, F. and Y. Egorov (2010). The scale-adaptive simulation method for unsteady turbulent flow predictions. Part 1: theory and model description. *Flow, Turbulence and Combustion 85*(1), 113–138. *(p. 50)*

Meynet, N. (2005). *Simulation numérique de la combustion d'un propergol solide*. Ph. D. thesis, Université Paris 6. *(p. 24)*

Michaelides, E. and A. Roig (2011). A reinterpretation of the Odar and Hamilton data on the unsteady equation of motion of particles. *AIChE Journal 57*(11), 2997–3002. *(p. 79)*

Miller, R. and J. Bellan (1999). Direct Numerical Simulation of a confined three-dimensional gas mixing layer with one evaporating hydrocarbon-droplet-laden stream. *Journal of Fluids Mechanics 384*, 293–338. *(p. 72)*

Miller, R. and J. Bellan (2000). Direct numerical simulation and subgrid analysis of a transitional droplet laden mixing layer. *Phys. Fluid 12*(3), 650–671. *(p. 72)*

Millikan, R. (1923). Coefficients of slip in gases and the law of reflection of molecules from the surfaces of solids and liquids. *Physical Review 21*(3), 217–238. *(p. 205)*

Minier, J. and E. Peirano (2001). The PDF approach to turbulent polydisperse two-phase flows. *Physics Reports 352*, 1–214. *(p. 102, 107)*

Misra, S., T. Tetley, A. Thorley, A. Boccaccini, and E. Valsami-Jones (2012). Engineered nanomaterials. In *Pollutants, Human Health and the Environment: A Risk Based Approach*, pp. 287–312. Wiley-Blackwell. *(p. 186)*

Mitchner, M. and C. Kruger (1973). *Partially Ionized Gases*. Wiley. *(p. 380)*

Monaghan, J. (1992). Smoothed particle hydrodynamics. *Annual review of astronomy and astrophysics 30*, 543–574. *(p. 71)*

Monin, A. and A. Yaglom (1971). *Statistical fluid dynamics*, Volume I and II. Cambridge: MIT Press.

(p. 101)

Moore, W. (1813). *A treatise on the motion of rockets*. London: G. and S. Robinson. *(p. 13)*

Moreau, M. (2006). *Modélisation numérique directe et des grandes échelles des écoulements turbulents gaz-particules dans le formalisme eulérien mésoscopique*. Ph. D. thesis, Institut National Polytechnique de Toulouse. *(p. 78, 103)*

Morel, C. (1997). *Modélisation multidimensionnelle des écoulements diphasiques gaz-liquide. Application à la simulation des écoulements à bulles ascendants en conduite verticale*. Ph. D. thesis, École Centrale Paris. *(p. 76, 78)*

Morfouace, V. and P.-Y. Tissier (1995). Two-phase flow analysis of instabilities driven by vortex-shedding in solid rocket motors. In *31st AIAA/ASME/SAE/ASEE Joint Propulsion Conference and Exhibit*, Penn State, PA. *(p. 44, 165)*

Morse, P. and K. Ingard (1987). *Theoretical acoustics*. Princeton University Press. *(p. 165, 272)*

Mossa, J.-B. (2005). *Extension polydisperse pour la description Euler-Euler des écoulements diphasiques réactifs - TH/CFD/05/74*. Ph. D. thesis, Institut National Polytechnique de Toulouse. *(p. 103, 117)*

Most, J., P. Joulain, G. Lengellé, and J. Godon (1996). Modeling of normal and erosive burning rate of a hot double-base homogeneous propellant. *Combustion and Flame 105*(1), 202–210. *(p. 24)*

Moureau, V., P. Domingo, and L. Vervisch (2011). From Large-Eddy Simulation to Direct Numerical Simulation of a lean premixed swirl flame: Filtered laminar flame-PDF modeling. *Combustion and Flame 158*(7), 1340–1357. *(p. 226)*

Moureau, V., G. Lartigue, Y. Sommerer, C. Angelberger, O. Colin, and T. Poinsot (2005). High-order methods for DNS and LES of compressible multi-component reacting flows on fixed and moving grids. *Journal of Comp. Phys. 202*(2), 710–736. *(p. 231)*

Moussa, A. (2009). *Etude mathématique et numérique du transport d'aérosols dans le poumon humain*. Ph. D. thesis, ENS Cachan. *(p. 186)*

Mueller, M., G. Blanquart, and H. Pitsch (2009a). Hybrid Method of Moments for modeling soot formation and growth. *Combustion and Flame 156*(6), 1143–1155. *(p. 121, 185)*

Mueller, M., G. Blanquart, and H. Pitsch (2009b). A joint volume-surface model of soot aggregation with the method of moments. *Proceedings of the Combustion Institute 32*(1), 785–792. *(p. 121, 185)*

Mueller, M. and H. Pitsch (2012). LES model for sooting turbulent nonpremixed flames. *Combustion and Flame 159*(6), 2166–2180. *(p. 121, 185)*

Mugele, R. and H. Evans (1951). Droplet size distribution in sprays. *Industrial & Engineering Chemistry 43*(6), 1317–1324. *(p. 61)*

Murrone, A. and P. Villedieu (2011). Numerical modeling of dispersed two-phase flows. *Aerospace Lab 2*, 1–13. *(p. 4, 107, 110, 117, 231, 321, 322, 323)*

Najjar, F., J. Ferry, B. Wasistho, and S. Balachandar (2002). Full-physics large-scale multiphase Large Eddy Simulations of flow inside solid rocket motors. In 38^{th} *Joint Propulsion Conference and Exhibit*, Indianapolis, IN. AIAA/ASME/SSAE/ASEE. *(p. 50)*

Najm, H., P. Wyckoff, and O. Knio (1998). A semi-implicit numerical scheme for reacting flow: I. stiff chemistry. *Journal of Computational Physics 143*(2), 381–402. *(p. 237)*

Nakka, R. (1984). *Solid Propellant Rocket Motor Design and Testing*. Ph. D. thesis. *(p. 36, 37)*

Nakka, R. (2012). Richard Nakka's experimental rocketry. *website*. *(p. xvii, 14)*

Netzell, K., H. Lehtiniemi, and F. Mauss (2007). Calculating the soot particle size distribution function in turbulent diffusion flames using a sectional method. *Proceedings of the Combustion Institute 31*(1), 667–674. *(p. 120, 185)*

Nicoud, F. (1995). Programme ASSM 5 : Axe PTI, Simulation numérique directe d'un écoulement avec forte injection pariétale non uniforme. Technical Report Programme ASSM5, CERFACS. *(p. 50, 52)*

Nicoud, F. and F. Ducros (1999). Subgrid-scale stress modelling based on the square of the velocity gradient. *Flow, Turbulence and Combustion 62*(3), 183–200. *(p. 102)*

Nicoud, F. and T. Poinsot (2005). Thermoacoustic instabilities: Should the Rayleigh criterion be extended to include entropy changes? *Combustion and Flame 142*(1), 153–159. *(p. 43)*

Nigmatulin, R. (1979). Spatial averaging in the mechanics of heterogeneous and dispersed systems. *Int. J. Multiphase Flow 5*, 333–385. *(p. 75)*

Nigmatulin, R. (1990). *Dynamics of multiphase media*, Volume 2. Taylor & Francis. *(p. 75, 76, 86, 111, 187)*

Ning, Z., C. Cheung, J. Fu, M. Liu, and M. Schnell (2006). Experimental study of environmental tobacco smoke particles under actual indoor environment. *Science of the Total Environment 367*(2), 822–830. *(p. 184)*

Novikov, E. and D. Dommermuth (1997). Distribution of droplets in a turbulent spray. *Phys. Rev. E. 56*, 54–79. *(p. 365)*

Olson, R. (1964). *Experimental studies of turbulent flow in a porous circular tube with uniform mass transfer through the tube wall*. Ph. D. thesis, University of Minnesota. *(p. 39)*

Olsson, E. and G. Kreiss (2005). A conservative level set method for two phase flow. *Journal of Computational Physics 210*(1), 225–246. *(p. 71)*

Oran, E. and J. Boris (2001). *Numerical simulation of reactive flow. 2nd edition*. New-York: Cambridge University Press. *(p. 53)*

Orlandi, O. (2002). *Modélisation et simulation numérique d'une goutte isolée d'aluminium*. Ph. D. thesis, Université d'Orléans. *(p. 29, 30)*

O'Rourke, P. J. (1981). *Collective drop effects on vaporizing liquid sprays*. Ph. D. thesis, Los Alamos National Laboratory 87545, University of Princeton. *(p. 28, 67, 68, 106, 107, 108)*

O'Rourke, P. J. and A. A. Amsden (1987). The TAB method for numerical calculation of spray droplet break-up. Technical Report 87545, Los Alamos National Laboratory, Los Alamos, New Mexico. *(p. 86, 87, 99, 100)*

Pai, M. (2007). *Probability density function formalism for multiphase flows*. ProQuest. *(p. 102)*

Pai, M. and S. Subramaniam (2006). Modeling interphase turbulent kinetic energy transfer in Lagrangian-Eulerian spray computations. *Atomization and Sprays 16*(7), 807–826. *(p. 71, 110)*

Pai, M. and S. Subramaniam (2009). A comprehensive probability density function formalism for multiphase flows. *Journal of Fluid Mechanics 628*, 181. *(p. 102)*

Pai, M. and S. Subramaniam (2012). Two-way coupled stochastic model for dispersion of inertial particles in turbulence. *Journal of Fluid Mechanics 700*, 29. *(p. 72, 74, 103)*

Pandya, R. and F. Mashayek (2002). Two-fluid large eddy simulation approach for particle-laden turbulent lows. *Int. J. of Heat and Mass Transfer 45*, 4753–4759. *(p. 102)*

Park, S. and K. Lee (2001). Asymptotic particle size distributions attained during coagulation processes. *Journal of Colloid and Interface Science 233*(1), 117–123. *(p. 178, 190)*

Park, S., Y. Lee, M. Jung, K. Kim, N. Chung, E. Ahn, Y. Lim, and K. Lee (2007). Cellular toxicity of various inhalable metal nanoparticles on human alveolar epithelial cells. *Inhalation toxicology 19*(S1), 59–65. *(p. 187)*

Parsons, I., P. Alavilli, A. Namazifard, A. Acharya, X. Jiao, and R. Fiedler (2000). Coupled simulations of solid rocket motors. In 36^{th} *AIAA/ASME/SAE/ASEE Joint Propulsion Conference and Exhibit*, Number Paper n°2000-3456, Cincinnati, OH. *(p. 49)*

Pecnik, R., S. Kassinos, K. Duraisamy, and G. Iaccarino (2012). Towards an accurate and robust Algebraic Structure Based Model. In *Proceedings of the Summer Program 2012*, Center for Turbulence Research, Stanford University, pp. 283–292. *(p. 102)*

Peirano, E., S. Chibbaro, J. Pozorski, and J.-P. Minier (2006). Mean-field/PDF numerical approach for polydispersed turbulent two-phase flows. *Progress in energy and combustion science 32*(3), 315–371. *(p. 107)*

Peirano, E. and B. Leckner (1998). Fundamentals of turbulent gas-solid flows applied to circulating fluidized bed combustion. *Prog. Energy Combust. Sci. 24*, 259–296. *(p. 75)*

Peirano, E. and B. Leckner (2000). A mean diameter for numerical computations of polydispersed gas-solid suspensions in fluidization. *Chemical Engineering Science 55*(6), 1189–1192. *(p. 61, 135, 333)*

Perrin, J. (1908). L'agitation moléculaire et le mouvement brownien. *Comptes rendus 146*, 967–970. *(p. 192)*

Perrin, J. (1910). Mouvement brownien et molécules. *J. Phys. Theor. Appl. 9*(1), 5–39. *(p. 192)*

Pilch, M. and C. Erdman (1987). Use of break-up time data and velocity history data to predict the maximum size of stable fragments for acceleration-induced breakup of a liquid drop. *Int. J. Multiphase Flow 13*, 741–757. *(p. 86, 364)*

Podvysotskii, A. and A. Shraiber (1975). Analysis of the nonequilibrium two-phase flow with coagulation and crushing of condensate particles for arbitrary mass and velocity distributions of the secondary drops. *Fluid Dynamics 10*(2), 249–255. *(p. 38)*

Poinsot, T. and D. Veynante (2011). *Theoretical and Numerical Combustion* (third ed.). Poinsot, T. and Veynante, D. Eds. *(p. 102, 353, 356)*

Pope, C. and J. Howard (1997). Simultaneous particle and molecule modeling (SPAMM): An approach for combining sectional aerosol equations and elementary gas-phase reactions. *Aerosol science and technology 27*(1), 73–94. *(p. 120)*

Pope, S. (2000). *Turbulent flows*. Cambridge University. *(p. 102)*

Popinet, S. and S. Zaleski (1999). A front-tracking algorithm for accurate representation of surface tension. *Int. J. Numer. Meth. Fluids 30*, 775–793. *(p. 71)*

Pottier, N. (2007). *Physique statistique hors d'équilibre - Processus irréversibles linéaires*. EDP Sciences. *(p. 87, 88, 92, 93, 192, 193, 195)*

Press, W., B. Flannery, S. Teukolsky, and W. Vetterling (1992). *Numerical Recipes in FORTRAN 77: The Art of Scientific Computing*, Volume 1. Cambridge University Press. *(p. 243, 244, 294)*

Prévost, M., Y. Dommée, and J. Maunoury (2001). Programme POP – Synthèse de la base de données expérimentales instationnaires. Technical Report RT 4/05212/DMAE, ONERA. *(p. xvii, 17)*

Prévost, M., Y. Dommée, J. Maunoury, J.-C. Traineau, F. Vuillot, and P. Duval (2000). On the representativity of small scale motor tests. In 2^{nd} *European Conference on Launcher Technology*, Rome. *(p. 41)*

Prévost, M., J. Maunoury, and P. Prévot (2000). ASSM8 2ème campagne d'essai du montage LP9 démonstrateur du vortex-shedding pariétal (VSP). Technical Report RF 9/6182/DSNA/DMAE, ONERA. *(p. 42)*

Prévost, M. and F. Vuillot (1998). Dossier de justification du montage LP9 - Futur démonstratuer du Vortex-Shedding Pariétal (VSP). Technical Report RT 1/5500.12 DMAE/Y, ONERA. *(p. 42)*

Price, E. and R. Sigman (2000). *Combustion of aluminized solid propellants*, Volume 185 of *Progress in Astronautics and Aeronautics*. AIAA. *(p. 20)*

Price, E. W. (1971). Comments on "role of aluminum in suppressing instability in solid propellant rocket motors". *AIAA Journal 9*, 987–990. *(p. 43)*

Price, E. W. (1984a). Combustion of metallized propellants. In K. Kuo and M. Summerfield (Eds.), *Fundamentals of solid propellant combustion*, pp. 479–513. AIAA. *(p. 27, 30, 167, 306)*

Price, E. W. (1984b). Experimental observations of combustion instabilities. In K. Kuo and M. Summerfield (Eds.), *Fundamentals of solid propellant combustion*, pp. 733–789. AIAA. *(p. 40, 52)*

Prosperetti, A. and G. Tryggvason (2007). *Computational methods for multiphase flow*. Cambridge University Press. *(p. 75)*

Prud'homme, R., M. Habiballah, L. Matuszewski, Y. Mauriot, and A. Nicole (2010). Theoretical analysis of dynamic response of a vaporizing droplet to acoustic oscillations. *J. Propulsion Power 26*(1), 74–83. *(p. 359)*

Puel, F., G. Févotte, and J.-P. Klein (2003). Simulation and analysis of industrial crystallization processes through multidimensional population balance equation. Part 1: a resolution algorithm based on the method of classes. *Chemical Engineering Science 58*, 3715–3727. *(p. 120)*

Puri, P. (2008). *Multi-scale modeling of ignition and combustion of micro and nano aluminum particles*. Ph. D. thesis, Penn State. Published by ProQuest. *(p. 30, 31)*

Qian, J. and C. Law (1997). Regime of coalescence and separation in droplet collision. *Journal of Fluid Mechanics 331*, 59–80. *(p. xviii, 83)*

Qian, J., G. Tryggvason, and C. Law (1997). An experimental and computational study of bouncing and deformation in droplet collision. In 35^{th} *Aerospace Sciences Meeting & Exhibit*, Number Paper n°97-0129, Reno, NV. *(p. 83)*

Qiu, J. and C. Shu (2002). On the construction, comparison, and local characteristic decomposition for high-order central WENO schemes. *Journal of Computational Physics 183*(1), 187–209. *(p. 231)*

Quéré, D. (2005). Non-sticking drops. *Reports on Progress in Physics 68*(11), 2495. *(p. 58)*

Quéré, D., J. Di Meglio, and F. Brochard-Myart (1990). Spreading of liquids on highly curved surfaces. *Science 249*(4974), 1256–1260. *(p. 58)*

Rabe, C. (2009). *Etude de la coalescence dans les rampes de spray : application au système d'aspersion des REP*. Ph. D. thesis, Univ. Paris 6. *(p. xviii, 83, 84)*

Racine, J. (1991). Subscale solid rocket motor infrared signature and particle behavior. Technical report, DTIC Document. *(p. 33)*

Radenac, E. (2011). Fluctuating energy balance for solid propellant instabilities. In *AIAA/ASME* 47^{th} *Joint Propulsion Conference*, San Diego, CA. *(p. 40, 50)*

Radenac, E. (2013). Fluctuating Energy Balance method for postprocessing multiphase flow computations. *Journal of Propulsion and Power 29*(3), 699–708. *(p. 42, 43)*

Rahman, S. (2012). *Modélisation et Simulation Numérique de Flammes Planes Instationnaires de Perchlorate d'Ammonium*. Ph. D. thesis, Université Pierre et Marie Curie. *(p. 24, 40, 49, 50, 52, 53, 353)*

Ramkrishna, D. and A. G. Fredrickson (2000). *Population Balances: Theory and Applications to Particulate Systems in Engineering*. Academic Press. *(p. 119, 120)*

Ranger, A. and J. Nicholls (1968). Aerodynamics shattering of liquid drops. *AIAA Journal 7*(2), 285–290. *(p. 86)*

Ranz, W. and W. Marshall (1952). Evaporation from drops. *Chem. Eng. Prog. 48*(3), 141–146. *(p. 81)*

Rao, K., P. Nott, and S. Sundaresan (2008). *An introduction to granular flow*. Cambridge, NY: Cambridge University Press. *(p. 92)*

Raun, R. and M. Beckstead (1993). A numerical model for temperature gradient and particle effects on Rijke burner oscillations. *Combustion and Flame 94*(1), 1–24. *(p. 42)*

Rax, J. (2005). *Physique des plasmas – Cours et applications*. Dunod. *(p. 33)*

Rayapati, N., M. Panchagnula, J. Peddieson, J. Short, and S. Smith (2011). Eulerian multiphase population balance model of atomizing, swirling flows. *Int. J. Spray and Combustion Dynamics 3*(2), 111–136. *(p. 119)*

Rayleigh, J. (1896). *The theory of sound*, Volume 2. Macmillan. *(p. 43)*

Reeks, M. (1977). On the dispersion of small particles suspended in an isotropic turbulent fluid. *J. Fluid Mech. 83*(03), 529–546. *(p. 102, 263)*

Reeks, M. (1988). The relationship between Brownian motion and the random motion of small particles in a turbulent flow. *Phys. Fluids 6*(31), 1314–1316. *(p. 192, 195)*

Reeks, M. (1991). On a kinetic equation for the transport of particles in turbulent flows. *Phys. Fluids 3*(3), 446–456. *(p. 102)*

Reeks, M. (1992). On the continuum equations for dispersed particles in nonuniform flows. *Phys. Fluids 4*(6), 1290–1303. *(p. 102)*

Reeks, M. (2005). On the probability density function equations for particle dispersion in a uniform shear flow. *Journal of Fluid of Mechanics 522*, 263–302. *(p. 102)*

Refloch, A., B. Courbet, A. Murrone, P. Villedieu, C. Laurent, P. Gilbank, J. Troyes, L. Tessé, G. Chaineray, J. Dargaud, E. Quémerais, and F. Vuillot (2011). CEDRE software. *Aerospace Lab 2. (p. 3, 225, 321)*

Rehn, B., F. Seiler, S. Rehn, J. Bruch, and M. Maier (2003). Investigations on the inflammatory and genotoxic lung effects of two types of titanium dioxide: untreated and surface treated. *Toxicology and applied pharmacology 189*(2), 84–95. *(p. 187)*

Reif, F. (1965). *Fundamentals of statistical and thermal physics*, Volume 11. McGraw-Hill New York. *(p. 87)*

Reveillon, J. (2007). DNS of spray combustion, dispersion evaporation and combustion. In *Multiphase Reacting Flows: Modeling and Simulation*, Volume 492 of *CISM Courses and Lectures*, pp. 229. Springer. Udine. *(p. 246)*

Reveillon, J., N. Bray, and L. Vervisch (1998). DNS study of spray vaporization and turbulent micromixing. In *36th Aerospace Sciences Meeting and Exhibit*, Reno NV. *(p. 72)*

Reveillon, J. and F. Demoulin (2007a). Effects of the preferential segregation of droplets on evaporation and turbulent mixing. *Journal of Fluid Mechanics 583*, 273–302. *(p. 357, 358, 359, 360)*

Reveillon, J. and F. X. Demoulin (2007b). Effects of the preferential segregation of droplets on evaporation and turbulent mixing. *J. Fluid Mech. 583*, 273–302. *(p. 5, 74, 246, 315)*

Réveillon, J., M. Massot, and C. Pera (2002). Eulerian analysis of the dispersion of vaporizing polydispersed sprays in turbulent flows. In *Proceedings of the Summer Program 2002*, Center for Turbulence Research, Stanford University, pp. 393–404. *(p. 102, 103, 113)*

Reveillon, J., C. Péra, M. Massot, and R. Knikker (2004). Eulerian analysis of the dispersion of evaporating polydispersed sprays in a statistically stationary turbulent flow. *Journal of Turbulence 5*(1), 1–27. *(p. 103)*

Reveillon, J. and L. Vervisch (2005). Analysis of weakly turbulent diluted-spray flames and spray combustion regimes. *J. Fluid Mech. 537*, 317–347. *(p. 72)*

Riber, E. (2007). *Développement de la méthode de simulation aux grandes échelles pour les écoulements diphasiques turbulents*. Ph. D. thesis, Institut National Polytechnique de Toulouse. *(p. 103)*

Riber, E., M. Garcia, V. Moureau, H. Pitsch, O. Simonin, and T. Poinsot (2006). Evaluation of numerical strategies for LES of two-phase reacting flows. Proceedings of the Summer Program 2006, Center for Turbulence Research, Stanford University. *(p. 103, 254)*

Ribereau, D. and P. Le Breton (1995). Simulation numérique des instabilités de fonctionnement observées sur un propulseur solide de type axisymétrique. In *Colloque CNES/ONERA/CNRS Ecoulements propulsifs dans les systèmes de transport spatial*, Bordeaux. *(p. 41)*

Richard, D., C. Clanet, and D. Quéré (2002). Contact time of a bouncing drop. *Nature 417*(6891), 811. *(p. 58)*

Richard, J. (2012). *Fluid-Structure interaction for aeroacoustic instabilities*. Ph. D. thesis, Institut National Polytechnique de Toulouse. *(p. 21, 50, 51)*

Richard, J. and F. Nicoud (2011). Towards the effect of the fluid structure coupling on the aeroacoustic instabilities of Solid Rocket Motors. In *10e colloque national en calcul des structures*, Giens, France. *(p. 21, 42, 49, 50, 51, 52)*

Rider, W. and D. Kothe (1998). Reconstructing volume tracking. *Journal of Computational Physics 141*(2), 112–152. *(p. 71)*

Rijke, P. (1859). LXXI. Notice of a new method of causing a vibration of the air contained in a tube open at both ends. *The London, Edinburgh, and Dublin Philosophical Magazine and Journal of Science 17*(116), 419–422. *(p. 42)*

Riley, J. and G. Patterson (1974). Diffusion experiments with numerically integrated isotropic turbulence. *Physics of Fluids 17*, 292–297. *(p. 72)*

Rimbert, N. (2010). Simple model for turbulence intermittencies based on self-avoiding random vortex stretching. *Phys. Rev. E 81*, 056315. *(p. 364, 365)*

Rimbert, N. and G. Castanet (2011). Crossover between Rayleigh-Taylor instability and turbulent cascading atomization mechanism in the bag-break-up regime. *Phys. Rev. E 84*, 016318. *(p. 364, 365,*

366, 367)

Rimbert, N., F. Doisneau, F. Laurent, D. Kah, and M. Massot (2012). Two-Layer Mesoscopic Modeling of Bag Break-up in Turbulent Secondary Atomization. In *Proceedings of the Summer Program 2012*, Center for Turbulence Research, Stanford University, pp. 335–344. *(p. 6, 100, 363)*

Rimbert, N. and O. Séro-Guillaume (2004a). Fragmentation equation and Riesz-Feller diffusion between scales. In A. Oustaloup (Ed.), *1st IFAC workshop on fractional differentiation and its application FDA04 (Bordeaux, France)*. *(p. 366, 367)*

Rimbert, N. and O. Séro-Guillaume (2004b). Log-Stable laws as asymptotic solutions to a fragmentation equation: application to the distribution of droplets in a high Weber number spray. *Phys. Rev. E. 69*, 056316. *(p. 365)*

Risken, H. (1996). *The Fokker-Planck equation: Methods of solution and applications*, Volume 18. Springer Verlag. *(p. 195)*

Ritter, H. and S. Braun (2001). High explosives containing ultrafine aluminum ALEX. *Propellants, Explosives, Pyrotechnics 26*(6), 311–314. *(p. 24)*

Roco, M. (1999). Nanoparticles and nanotechnology research. *J. Nanoparticle Res. 1*(1), 1–6. *(p. 183)*

Rogge, W., L. Hildemann, M. Mazurek, G. Cass, and B. Simoneit (1993). Sources of fine organic aerosol. 3. road dust, tire debris, and organometallic brake lining dust: roads as sources and sinks. *Environmental Science & Technology 27*(9), 1892–1904. *(p. 184)*

Rosenband, V. (2004). Thermo-mechanical aspects of the heterogeneous ignition of metals. *Combustion and Flame 137*(3), 366–375. *(p. 31)*

Rüger, M., S. Hohmann, M. Sommerfeld, and G. Kohnen (2000). Euler/Lagrange calculations of turbulent sprays: the effect of droplet collisions and coalescence. *Atomization and Sprays 10*(1), 47–81. *(p. 106, 107, 110)*

Rumsey, C. and E. Jeyapaul (2012). Pressure-strain and near-wall modeling for two-dimensional separated flows. In *Proceedings of the Summer Program 2012*, Center for Turbulence Research, Stanford University, pp. 273–282. *(p. 102)*

Sabat, M. (2015). *Eulerian modeling and numerical methods for polydisperse turbulent sprays*. Ph. D. thesis, École Centrale Paris. *(p. 5, 234)*

Sabat, M., A. Vie, A. Larat, F. Laurent, and M. Massot (2013). On the development of high order realizable schemes for the Eulerian simulation of disperse phase flows on unstructured grids: a convex-state preserving Discontinuous Galerkin method. In *Proceedings of the 8th International Conference on Multiphase Flows, ICMF 2013*, Jeju – South Korea. *(p. 5, 234)*

Sabnis, J. (2003). Numerical simulation of distributed combustion in solid rocket motors with metallized propellant. *Journal of Propulsion and Power 19*(1), 48–55. *(p. 30, 51, 137)*

Saffman, P. and J. Turner (1956). On the collision of drops in turbulent clouds. *J. Fluid Mech. 1*, 16–30. *(p. 103)*

Sagaut, P. (1998). *Introduction à la simulation des grandes échelles pour les écoulements de fluide incompressible*. Springer. *(p. 102)*

Sainsaulieu, L. (1993). An Euler system modelling vaporizing sprays in dynamics of heterogeneous combustion and reacting systems. *Progress in astronautics and aeronautics 152*, 280–305. *(p. 70)*

Sainsaulieu, L. (1995a). Equilibrium velocity distribution functions for a kinetic model of two-phase fluid flows. *Mathematical Model and Methods in Applied Science 5*(2), 191–211. *(p. 62)*

Sainsaulieu, L. (1995b). *Contribution à la modélisation mathématique et numérique des écoulements diphasiques constitués d'un nuage de particules dans un écoulement de gaz*. Habilitation à diriger les recherches. Université Paris 6. *(p. 76, 117)*

Sainsaulieu, L. and B. Larrouturou (1992). Eulerian model for dispersed two-phase flows and upwind numerical solution. Technical report, CERMICS. *(p. 76)*

Sajo, E. (2008). Evaluation of the exact coagulation kernel under simultaneous Brownian motion and gravitational settling. *Aerosol Science and Technology 42*(2), 134–139. *(p. 217)*

Sajo, E. (2010). Update and Erratum on the Numerical evaluation of the exact coagulation kernel for simultaneous Brownian motion and gravitational settling. *Aerosol Science and Technology 44*(10), 916–916. *(p. 217)*

Salita, M. (1994). Survey of recent Al_2O_3 droplet size data in solid rocket chambers, nozzles and plumes. In 31^{st} *JANNAF Combustion Subcommittee meeting*, Sunnyvale, CA. *(p. 28)*

Sambamurthi, J., E. Price, and R. Sigman (1984). Aluminum agglomeration in solid-propellant combustion. *AIAA journal 22*(8), 1132–1138. *(p. 29)*

Sanders, P., N. Xu, T. Dalka, and M. Maricq (2003). Airborne brake wear debris: size distributions, composition, and a comparison of dynamometer and vehicle tests. *Environmental science & technology 37*(18), 4060–4069. *(p. 184)*

Sangani, A., D. Zhang, and A. Prosperetti (1991). The added mass, Basset, and viscous drag coefficients in non-dilute bubbly liquids undergoing small amplitude oscillatory motion. *J. Phys. Fluids A3*, 2955–

2970. *(p. 79)*

Sanjosé, M., T. Lederlin, L. Gicquel, B. Cuenot, H. Pitsch, N. Garcia-Rosa, R. Lecourt, and T. Poinsot (2008). LES of turbulent reacting flows. *Center of Turbulence Research - Proceedings of the Summer Program*, 251–263. *(p. 226)*

Saurel, R. and R. Abgrall (1999). A multiphase Godunov method for compressible multifluid and multiphase flows. *Journal of Computational Physics 150*, 425–467. *(p. 75)*

Saurel, R., G. Huber, G. Jourdan, E. Lapébie, and L. Munier (2012). Modelling spherical explosions with turbulent mixing and post-detonation. *Physics of Fluids 24*(11), 115101–115101. *(p. 77)*

Saurel, R. and O. Le Metayer (2001). A multiphase model for compressible flows with interfaces, shocks, detonation waves and cavitation. *J. Fluid Mech. 431*, 239–271. *(p. 75)*

Scardovelli, R. and S. Zaleski (2003). Direct numerical simulation of free-surface and interfacial flow. *Annual Review of Fluid Mechanics 31*(1), 567. *(p. 71)*

Scherrer, D., F. Chedevergne, P. Grenard, J. Troyes, A. Murrone, E. Montreuil, F. Vuillot, N. Lupoglazoff, M. Huet, B. Sainte-Rose, P. Thorigny, N. Bertier, J. Lamet, T. Le Pichon, E. Radenac, A. Nicole, L. Matuszewski, and M. Errera (2011). Recent CEDRE applications. *Aerospace Lab 2*. Available at www.aerospacelab-journal.org/al2. *(p. 226, 321)*

Schiller, L. and A. Naumann (1935). A drag coefficient correlation. *V.D.I. Zeitung 77*, 318–320. *(p. 79)*

Schmelz, F. and P. Walzel (2003). Breakup of liquid droplets in accelerated gas flows. *Atomization and Sprays 13*(4), 357–372. *(p. 86)*

Schmidt, D. and C. Rutland (2000). A new droplet collision algorithm. *Journal of Computational Physics 164*(1), 62–80. *(p. 107, 108)*

Schmitt, P., T. Poinsot, B. Schuermans, and K. Geigle (2007). Large-Eddy Simulation and experimental study of heat transfer, nitric oxide emissions and combustion instability in a swirled turbulent high-pressure burner. *Journal of Fluid Mechanics 570*, 17–46. *(p. 20)*

Schowalter, W. (1982). The effect of bulk motion on coagulation rates of colloidal dispersions. *Ad. Colloid and Interface Sc. 17*, 129–147. *(p. 202)*

Schwartz, L. (1987). *Méthodes Mathématiques pour les Sciences Physiques*, Volume 3. Collection Enseignement des Sciences, Hermann, Paris. *(p. 117)*

Scippa, S., M. Biagioni, and M. Bussiere (1996). Ariane solid boosters experience. In *5th Int. Symp. Propulsion in Space Transportation*, Paris. *(p. 16)*

Scippa, S., P. Pascal, and F. Zanier (1994). Ariane 5 MPS chamber pressure oscillations full scale firings results analysis and further studies. In 30^{th} *AIAA/ASME/SAE/ASEE Joint Propulsion Conference*, Indianapolis, IN. *(p. 17)*

Seinfeld, J. H. and S. N. Pandis (1998). *Atmospheric Chemistry and Physics: From Air Pollution to Climate Change*. Rhode Saint Genès: J. Wiley, New York. *(p. 187)*

Selle, L., G. Lartigue, T. Poinsot, R. Koch, K. Schildmacher, W. Krebs, B. Prade, P. Kaufmann, and D. Veynante (2004). Compressible Large-Eddy Simulation of turbulent combustion in complex geometry on unstructured meshes. *Combustion and Flame 137*(4), 489–505. *(p. 232)*

Sellens, R. (1989). Chapter 24. drop size and velocity distributions in sprays of liquid. In P. Cheremisinoff (Ed.), *Thermal treatment of hazardous wastes*. Gulf Publishing Company. *(p. 61)*

Selva, G. (1998). *Méthodes itératives pour l'intégration implicite des équations de l'aérothermochimie sur des maillages non-structurés*. Ph. D. thesis, École Centrale Paris. *(p. 237, 239, 323)*

Shan, X., X. Yuan, and H. Chen (2006). Kinetic theory representation of hydrodynamics: a way beyond the Navier-Stokes equation. *Journal of Fluid Mechanics 550*, 413–441. *(p. 90)*

Shardt, O. and J. Derksen (2012). Direct simulations of dense suspensions of non-spherical particles. *International Journal of Multiphase Flow 47*, 25–36. *(p. 70)*

Sheu, H., W. Lee, S. Lin, G. Fang, H. Chang, and W. You (1997). Particle-bound PAH content in ambient air. *Environmental Pollution 96*(3), 369–382. *(p. 184)*

Shi, Z., L. Shao, T. Jones, and S. Lu (2005). Microscopy and mineralogy of airborne particles collected during severe dust storm episodes in Beijing, China. *J. of Geophysical Research 110*(D1), D01303. *(p. 184)*

Shraiber, A., A. Podvysotsky, and V. Dubrovsky (1996). Deformation and breakup of drops by aerodynamic forces. *Atomization and Sprays 6*(6), 667–692. *(p. 86)*

Shu, C.-W. (1998). Essentially non-oscillatory and weighted essentially non-oscillatory schemes for hyperbolic conservation laws. In *Advanced numerical approximation of nonlinear hyperbolic equations (Cetraro, 1997)*, Volume 1697 of *Lecture Notes in Math.*, pp. 325–432. Berlin: Springer. *(p. 231, 275)*

Shu, P., R. Sfozini, and W. Foster (1986). Vortex shedding from solid rocket propellant inhibitors. In *22nd AIAA/ASME/SAE/ASEE Joint propulsion Conference*. *(p. 41)*

Shuen, J., L. Chen, and G. Faeth (2004). Evaluation of a stochastic model of particle dispersion in a turbulent round jet. *AIChE Journal 29*(1), 167–170. *(p. 51)*

Sibra, A. (2011). étude d'une stratégie numérique robuste et optimisés de couplage gaz-particules en

approche eulérienne. Rapport de master recherche, École Centrale Paris. *(p. 166)*

Sibra, A. (2014). *Modeling and simulation of evaporation and combustion of aluminum droplets in a solid rocket motor with a Eulerian approach*. Ph. D. thesis, École Centrale Paris. *(p. 5, 31, 43, 44, 49, 51, 52, 245, 270, 278, 289, 337, 341, 350)*

Sibra, A., J. Dupays, F. Laurent, and M. Massot (2013). A new Eulerian Multi-Fluid model for bi-component polydisperse sprays: an essential approach to evaluate the impact of aluminum combustion on Solid Rocket Motor instabilities. In 49^{th} *AIAA/ASME/SAE/ASEE Joint Propulsion Conference*, San Jose, Ca, pp. 1–20. *(p. 142)*

Siegel, R. and J. Howell (1972). *Thermal heat transfer*. New York: McGraw-Hill. *(p. 81)*

Sierra Sanchez, P. (2012). *Modeling the dispersion and evaporation of sprays in aeronautical combustion chambers*. Ph. D. thesis, Institut National Polytechnique de Toulouse. *(p. 3, 232, 254)*

Silberberg, M. (1979). Nuclear aerosols in reactor safety. *Nuclear Energy Agency, OECD*. *(p. 211)*

Silverman, I., J. B. Greenberg, and Y. Tambour (1991). Asymptotic analysis of a premixed polydisperse spray flame. *SIAM J. Appl. Math. 51*(5), 1284–1303. *(p. 123)*

Silvestrini, J. (1996). *Simulation des grandes échelles des zones de mélange: application à la propulsion solide des lanceurs spatiaux*. Ph. D. thesis, Institut National Polytechnique de Grenoble. *(p. 50)*

Silvestrini, J., P. Comte, and M. Lesieur (1995). Simulation des grandes échelles; application aux moteurs à propergol solide segmentés. In *Conference on propulsive flows in Space Transportation Systems*, Bordeaux, France, pp. 205–220. *(p. 42, 50)*

Simmons, F. and A. DeBell (1961). Spectral radiometry and two-path pyrometry of rocket exhaust jets. Technical Report AD 257483, DTIC Document. *(p. 33)*

Simoes, M. (2006). *Modélisation eulérienne de la phase dispersée dans les moteurs à propergol solide, avec prise en compte de la pression particulaire*. Ph. D. thesis, Institut National Polytechnique de Toulouse. *(p. xvii, 3, 5, 12, 13, 16, 28, 34, 45, 51, 52, 101, 114)*

Simoes, M., P. Della Pieta, F. Godfroy, and O. Simonin (2005). Continuum modeling of the dispersed phase in solid rocket motors. In *17th AIAA Computational Fluid Dynamics Conference*, Toronto, ON. *(p. 22, 45, 51)*

Simonin, O. (1996). Continuum modelling of dispersed two-phase flows. In *Combustion and Turbulence in Two-Phase Flows*. VKI Lecture Series Program 1994-95. *(p. 101)*

Simonin, O., P. Fevrier, and J. Lavieville (2002). On the spatial distribution of heavy-particle velocities in turbulent flow: from continuous field to particulate chaos. *Journal of Turbulence 3*, 1–40. *(p. 63, 102)*

Simons, S., M. Williams, and J. Cassell (1986). A kernel for combined Brownian and gravitational coagulation. *Journal of Aerosol Science 17*(5), 789–793. *(p. 211, 217)*

Sioutas, C., R. Delfino, and M. Singh (2005). Exposure assessment for atmospheric ultrafine particles (ufps) and implications in epidemiologic research. *Environmental Health Perspectives 113*(8), 947–955. *(p. 184)*

Sirignano, W. A. (2010). *Fluid Dynamics and Transport of Droplets and Sprays*. Cambridge: Cambridge University Press. *(p. 32, 57, 72, 106, 358, 359, 360, 361)*

Smagorinsky, J. (1963). General circulation experiments with the primitive equations. i : The basic experiment. *Monthly Weather Review 91(3)*, 99–164. *(p. 102)*

Smoluchowski, M. (1916). Drei Vorträge über Diffusion, Brownsche Bewegung und Koagulation von Kolloidteilchen. *Zeitschrift für Physik 17*(321), 557–585. *(p. 188, 190, 197, 199, 200, 208)*

Smoluchowski, M. (1917). Versuch einer mathematischen Theorie der Koagulationskinetik kolloider Lösungen. *Z. phys. Chem 92*, 129–168. *(p. 208)*

Soares, T. (2011). Assessing the environmental impacts of European launchers. In *4th EUCASS*, St Petersburg. *(p. 19)*

Solonenko, O. and G. Krylov (1987). A comparative analysis for some models high temperature turbulent jets with an additive of disperse particles. In *8th International Symposium on Plasma Chemistry*, Tokyo. *(p. 81)*

Sommeijer, B., L. Shampine, and J. Verwer (1997). RKC: An explicit solver for parabolic PDEs. *J. Comput. Appl. Math. 88*, 315–326. *(p. 237)*

Sommerfeld, M. (1999). Inter-particle collisions in turbulent flows: A stochastic lagrangian model. In *Proc. Turbulence and Shear Flow Phenomena -1*, Santa Barbara, pp. 265–270. *(p. 107)*

Sommerfeld, M. (2003). Analysis of collision effects for turbulent gas-particle flow in a horizontal channel (part i and ii). *International Journal of Multiphase Flow 29*, 675–699. *(p. 110)*

Soto, K., A. Carrasco, T. Powell, K. Garza, and L. Murr (2005). Comparative in vitro cytotoxicity assessment of some manufactured nanoparticulate materials characterized by transmission electron microscopy. *Journal of Nanoparticle Research 7*(2), 145–169. *(p. 187)*

Spalding, D. (1953). The combustion of liquid fuels. In *Proceedings of the 4th Symp. (International) on Combustion, The Comb. Institute*, Baltimore, pp. 847–864. *(p. 360)*

Spicer, P., O. Chaoul, S. Tsantilis, and S. Pratsinis (2002). Titania formation by $TiCl_4$ gas phase oxidation, surface growth and coagulation. *Journal of Aerosol Science 33*(1), 17–34. *(p. 190)*

Spielman, L. (1970). Viscous interactions in brownian coagulation. *J. Colloid Interface Sci. 33*(4), 562–571. *(p. 203)*

Squires, K. and J. Eaton (1991a). Measurements of particle dispersion obtained from direct numerical simulations of isotropic turbulence. *J. Fluids Mech. 226*, 1–35. *(p. 65, 72, 102)*

Squires, K. D. and J. Eaton (1991b). Preferential concentration of particles by turbulence. *Physics of Fluids 3*, 1169–1178. *(p. xviii, 65, 102, 263)*

Srinivas, V. and S. Chakravarthy (2007). Computer model of aluminum agglomeration on burning surface of composite solid propellant. *Journal of Propulsion and Power 23*(4), 728–736. *(p. 27)*

Stefani, D., D. Wardman, and T. Lambert (2005). The implosion of the calgary general hospital: ambient air quality issues. *Journal of the Air & Waste Management Association 55*(1), 52–59. *(p. 184)*

Stella, F., F. Paglia, M. Giangi, and M. Telara (2005). Numerical simulation of pressure oscillations in solid rocket motors. In *European Conference for Aero-Space Sciences (EUCASSS)*, Moscou. *(p. 46)*

Sternbeck, J., A. Sjödin, and K. Andréasson (2002). Metal emissions from road traffic and the influence of resuspension-results from two tunnel studies. *Atmospheric Environment 36*(30), 4735–4744. *(p. 184)*

Sternin, L. (1974). *Fundamentals of gas dynamics of two-phase nozzle flows.* Moscow Izdatel'stvo Mashinostroenie. *(p. 1, 37)*

Stokes, G. (1846). *Report on recent researches in hydrodynamics. (p. 79, 193)*

Stone, V., H. Johnston, and M. Clift (2007). Air pollution, ultrafine and nanoparticle toxicology: cellular and molecular interactions. *NanoBioscience, IEEE Transactions on 6*(4), 331–340. *(p. 184)*

Strang, G. (1968). On the construction and comparison of difference schemes. *SIAM J. Num. Anal. 5*(3), 507–517. *(p. 239, 273)*

Struchtrup, H. (2005). *Macroscopic Transport Equations for Rarefied Gas Flows.* Interaction of Mechanics and Mathematics. Berlin: Springer. Approximation methods in kinetic theory. *(p. 90, 92, 99)*

Struchtrup, H. and M. Torrilhon (2003). Regularization of Grad's 13 moment equations: derivation and linear analysis. *Physics of Fluids 15*, 2668. *(p. 91)*

Subramaniam, S. (2001). Statistical modeling of sprays using the droplet distribution function. *Physics of Fluids 13*, 624. *(p. 106)*

Subramaniam, S. (2013). Lagrangian–Eulerian methods for multiphase flows. *submitted to Prog. Energy Combust. Sci. (p. 2, 109)*

Subramanian, S. (2000). Statistical representation of a spray as a point process. *Physics of Fluids 12. (p. 106)*

Summerfield, M. and H. Krier (1969). Role of aluminum in suppressing instability in solid propellant rocket motors. In *Problems of Hydrodynamics and Continuum Mechanics*, pp. 703–717. Society for Independent and Applied Mathematics. Sixtieth Anniversary Volume. *(p. 22, 43)*

Sussman, M., P. Smereka, and S. Osher (1994). *A level set approach for computing solutions to incompressible two-phase flow.* Department of Mathematics, University of California, Los Angeles. *(p. 71)*

Sutherland, W. (1893). LII. the viscosity of gases and molecular force. *The London, Edinburgh, and Dublin Philosophical Magazine and Journal of Science 36*(223), 507–531. *(p. 355)*

Sutton, G. and O. Biblarz (2011). *Rocket propulsion elements.* Wiley. *(p. 34)*

Swihart, M. and L. Catoire (2000). Thermochemistry of aluminum species for combustion modeling from ab initio molecular orbital calculations. *Combustion and Flame 121*(1), 210–222. *(p. 31)*

Talbot, L., R. Cheng, R. Schefer, and D. Willis (1980). Thermophoresis of particles in a heated boundary layer. *Journal of Fluid Mechanics 101*(4), 737–758. *(p. 188, 199)*

Tambour, Y. (1980). A sectional model for evaporation and combustion of sprays of liquid fuel. *Isr. J. Technol. 18*, 47–56. *(p. 123)*

Tandon, P. and D. Rosner (1995). Translation Brownian diffusion coefficient of large (multiparticle) suspended aggregates. *Industrial & engineering chemistry research 34*(10), 3265–3277. *(p. 188)*

Tang, K. and M. Brewster (1992). Numerical analysis of radiative heat transfer in an aluminum distributed combustion region. *Numerical Heat Transfer 22*(3), 323–342. *(p. 28, 81)*

Tang, K. and M. Brewster (2001). Nonlinear dynamic combustion in solid rockets: $L^\star$ effects. *Journal of Propulsion and Power 17*(4), 909–918. *(p. 28)*

Tanguy, S. and A. Berlemont (2005). Development of a level set method for interface tracking: application to droplet collisions. *International Journal of Multiphase Flows 31*(9), 1015–1035. *(p. 83)*

Tavernier, P., J. Boisson, and B. Crampel (1970). *Propergols hautement énergétiques.* AGARD-AG-141-70. *(p. 19, 22, 35)*

Taylor, G. (1956). Fluid flow in regions bounded by porous surfaces. *Proceedings of the Royal Society of London 234*, 455–484. *(p. 36, 52)*

Taylor, L., H. Schmitt, W. Carrier, and M. Nakagawa (2005). The lunar dust problem: from liability to asset. In *1st Space Exploration Conference: Continuing the Voyage of Discovery.* AIAA. *(p. 184)*

Tchen, C. (1947). *Mean value and correlation problems connected with the motion of small particles suspended in a turbulent fluid*. Ph. D. thesis, TU Delft. *(p. 102)*

Telara, M., L. Jacques, P. Le Helley, T. Pevergne, D. Ribereau, B. Gondouin, and N. Cesco (2005). A new concept to reduce srm pressure oscillations : the 3d frontal thermal protection. In *1st European Conference for Aero-Space Sciences (EUCASS)*, Moscou. *(p. 21)*

Temkin, S. and R. Dobbins (1966). Attenuation and dispersion of sound by particulate-relaxation processes. *The Journal of the Acoustical Society of America 40*(2), 317–324. *(p. 6, 44, 77, 166, 167, 350)*

Tennekes, H. and J. L. Lumley (1972). *A first course in turbulence*. Cambridge: M.I.T. Press. *(p. 101)*

Thomine, O. (2011). *Développement de méthodes multi-échelles pour la simulation numérique des écoulements réactifs diphasiques*. Ph. D. thesis, Université de Rouen. *(p. xviii, 5, 73, 74, 108, 246, 315)*

Tishin, A. and R. Khairutdinov (1971). Calculation of coagulation of particles of the condensate in a laval nozzle. *Fluid Dynamics 6*(5), 898–902. *(p. 38)*

Tomar, G., D. Fuster, S. Zaleski, and S. Popinet (2010). Multiscale simulations of primary atomization. *Computers & Fluids 39*(10), 1864–1874. *(p. 71)*

Toro, E. (2009). *Riemann solvers and numerical methods for fluid dynamics*. Springer. *(p. 229, 253)*

Torrilhon, M. (2010). Hyperbolic moment equations in kinetic gas theory based on multi-variate Pearson-IV distributions. *Commun. Comput. Phys. 7*(4), 639–673. *(p. 91)*

Torrilhon, M. and H. Struchtrup (2004). Regularized 13-moment equations: shock structure calculations and comparison to Burnett models. *Journal of Fluid Mechanics 513*, 171–198. *(p. 91)*

Tory, E., R. Bürger, F. Concha, and M. Bustos (1999). *Sedimentation and Thickening: Phenomenological Foundation and Mathematical Theory*, Volume 8. Springer. *(p. 72)*

Tòth, B. (2008). *Two-phase flow investigation in a cold-gas solid rocket motor model through the study of the slag accumulation process*. Ph. D. thesis, Université Libre de Bruxelles. *(p. 32, 42, 46)*

Traineau, J.-C., P. Kuentzmann, M. Prévost, P. Tarrin, and D. A. (1992). Particle size distribution measurements in a subscale motor for the Ariane 5 solid rocket booster. In 28^{th} *AIAA/ASME/SAE/ASEE Joint Propulsion Conference*, Nashville, TN. *(p. 29)*

Traineau, J.-C., M. Prévost, F. Vuillot, P. Le Breton, J. Cuny, N. Preioni, and R. Bec (1997). A subscale test program to assess the vortex shedding driven instabilities in segmented solid rocket motors. In 33^{rd} *AIAA/ASME/SAE/ASEE Joint Propulsion Conference. (p. 29, 41)*

Trautmann, T. and C. Wanner (2003). A fast efficient modified sectionnal method for simulating multicomponent collisional kinetics. *Aerosol Science and Technology 37*, 892–898. *(p. 123)*

Trubert, J.-F. (2000). Agglomeration and combustion of aluminum particles in solid rocket motors. In 2^{nd} *European Conference on Launcher Technology*, Rome. *(p. 27, 30)*

Truesdell, C. (1966). *Continuum Mechanics: The Mechanical Foundations of Elasticity and Fluid Dynamics*. Gordon & Breach. *(p. 70, 353)*

Tryggvason, G., A. Esmaeeli, J. Lu, and S. Biswas (2006). Direct numerical simulations of gas/liquid multiphase flows. *Fluid Dynamics Research 38*(9), 660–681. *(p. 71)*

Tryggvason, G., R. Scardovelli, and S. Zaleski (2010). *Direct Numerical Simulations of Gas-Liquid Multiphase Flows*. Cambridge University Press. *(p. 71)*

Tsantilis, S., H. K. Kammler, and S. E. Pratsinis (2002). Population balance modeling of flame synthesis of titania nanoparticles. *Chemical Engineering Science 57*(12), 2139 – 2156. *(p. 190)*

Tsiolkovski, K. (1903). *Issledovaniye mirovykh prostranstv reaktivnymi priborami (Study of outer space by reaction devices)*. Mashinostroyeniye. *(p. 11)*

Tsuji, Y. (2007). Multi-scale modeling of dense phase gas–particle flow. *Chemical Engineering Science 62*(13), 3410–3418. *(p. 68)*

Tsuji, Y., T. Kawaguchi, and T. Tanaka (1993). Discrete particle simulation of two-dimensional fluidized bed. *Powder technology 77*(1), 79–87. *(p. 75)*

Tsuji, Y., T. Tanaka, and S. Yonemura (1998). Cluster patterns in circulating fluidized beds predicted by numerical simulation (discrete particle versus two-fluid models). *Powder Technology 95*, 254–264. *(p. 75)*

Ugurtas, B. (2000). *Etudes numériques et expérimentales des instabilités hydrodynamiques et du couplage aéroacoustique dans un écoulement de Taylor*. Ph. D. thesis, Université de Paris VI. *(p. 40, 42)*

Ugurtas, B., G. Avalon, N. Lupoglazoff, F. Vuillot, and G. Casalis (2000). Stability and acoustic resonance of internal flows generated by side injection, solid propellant chemistry, combustion and motor interior ballistics. *AIAA Progress in Astronautics and Aeronautics Series 185*, 823–836. *(p. 42)*

Unverdi, S. and G. Tryggvason (1992). A front-tracking method for viscous, incompressible, multi-fluid flows. *Journal of computational physics 100*(1), 25–37. *(p. 71)*

Vallet, A. and R. Borghi (1999). Modélisation eulerienne de l'atomisation d'un jet liquide. *Comptes Rendus de l'Académie des Sciences-Series IIB-Mechanics-Physics-Astronomy 327*(10), 1015–1020. *(p. 76)*

Vallet, A. and R. Borghi (2002). Modélisation eulérienne de l'atomisation d'un jet liquide. *C. R. Acad.*

Sci. Computational Fluid Mechanics t. 327 (Série II b), 1015–1020. *(p. 71)*

Vallet, A., A. Burluka, and R. Borghi (2001). Development of a eulerian model for the "atomization" of a liquid jet. *Atomization and Sprays 11*(6), 619–642. *(p. 71)*

van Dongen, P. and M. Ernst (1988). Scaling solutions of Smoluchowski's coagulation equation. *Journal of Statistical Physics 50*, 295–329. *(p. 178, 190)*

Van Leer, B. (1979). Toward the ultimate conservation difference scheme V. a second-order sequel to Godunov's method. *J. Comput. Phys. 32*(1), 101–136. *(p. 229, 231, 233, 250, 253)*

Varapaev, V., Y. Shtemler, and V. Yagodkin (1973). Effect of nonparallelism on the stability of a Bickley-Schlichting jet. *Fluid Dynamics 8*(6), 966–968. *(p. 36)*

Varapaev, V. and V. Yagodkin (1969). Flow stability in a channel with porous walls. *Izv. AN SSSR. Mekhanika Zhidkosti I Gaza 4*(5), 91–95. *(p. 36, 39, 41)*

Varapaev, V. and V. Yagodkin (1970). On the stability of certain nonparallel flows of a viscous incompressible liquid in a channel. *Fluid Dynamics 5*(4), 633–636. *(p. 36)*

Vasenin, I., V. Arkhipov, V. Butov, A. Glazunov, and V. Trofimov (1986). Gas dynamics of two-phase nozzle flows. *Izd. Tomsk. Univ., Tomsk*. *(p. 37)*

Vasenin, I. M., R. K. Narimanov, A. A. Glazunov, N. E. Kuvshinov, and V. A. Ivanov (1995). Two-phase flows in the nozzles of solid rocket motors. *J. Propulsion and Power 11*(4), 583–592. *(p. 37, 118, 119)*

Venugopal, P. (2003). *Direct numerical simulation of turbulence in a model solid rocket motor*. Ph. D. thesis, Univ. Illinois at Urbana-Champaign. *(p. 50)*

Vermorel, O., S. Richard, O. Colin, C. Angelberger, A. Benkenida, and D. Veynante (2007). Multi-cycle LES simulations of flow and combustion in a PFI SI 4-valve production engine. *SAE* (2007-01-0151). *(p. 232)*

Versaevel, P. (1996). *Combustion laminaire diphasique : Etude théorique et expérimentale*. Ph. D. thesis, École Centrale Paris. *(p. 357)*

Verwer, J. and B. Sommeijer (2004). An Implicit-Explicit Runge–Kutta–Chebyshev scheme for diffusion-reaction equations. *SIAM Journal on Scientific Computing 25*(5), 1824–1835. *(p. 237)*

Veshchunov, M. (2010a). A new approach to the Brownian coagulation theory. *J. Aerosol Sc. 41*(10), 895–910. *(p. 206)*

Veshchunov, M. (2010b). On the theory of Brownian coagulation. *J. Engineering Thermophysics 19*(2), 62–74. *(p. 206, 208)*

Veshchunov, M. (2011). A new approach to the theory of Brownian coagulation and diffusion-limited reactions. preprint, `http://arxiv.org/abs/1104.2414`. *(p. 206)*

Veshchunov, M. and I. Azarov (2012). Next approximation of the random walk theory for Brownian coagulation. *J. Aerosol Sc. 47*, 70–77. *(p. 206)*

Vetel, J. (2001). *Interaction des structures pariétales sur le développement instationnaire d'écoulements cisaillés en milieu confiné - Rôle de l'injection différentielle*. Ph. D. thesis, Université de Poitiers. *(p. 41, 42)*

Vié, A. (2010). *Simulation aux grandes échelles d'écoulements diphasiques turbulents à phase liquide dispersée*. Ph. D. thesis, Institut National Polytechnique de Toulouse. http://tel.archives-ouvertes.fr/tel-00620754. *(p. xx, 103, 128, 232, 233)*

Vié, A., C. Chalons, R. Fox, F. Laurent, and M. Massot (2011). A Multi-Gaussian quadrature method of moments for simulating high-Stokes number turbulent two-phase flows. *CTR Annual Research Briefs*, 309–320. *(p. 131)*

Vié, A., C. Chalons, and M. Massot (2013). An Asymptotic Preserving numerical scheme for the Large Eddy Simulation of disperse phase flows. *Submitted to SIAM journal of Multiscale and Modelling*. *(p. 114, 238)*

Vié, A., F. Doisneau, and M. Massot (2014). On the Anisotropic Gaussian closure for the prediction of inertial particle-laden flows. *Submitted to Comm. in Comp. Phys.*. *(p. 4, 5, 153, 154, 249, 254, 315)*

Vié, A., S. Jay, B. Cuenot, and M. Massot (2013). Accounting for polydispersion in the Eulerian Large Eddy Simulation of the two-phase flow in an aeronautical-type burner. *Flow Turbulence and Combustion 90*, 545–581. *(p. 65, 103, 228, 232)*

Vié, A., F. Laurent, and M. Massot (2013). Size-velocity correlations in hybrid high order moment/multi-fluid methods for polydisperse evaporating sprays: Modeling and numerical issues. *J. of Comp. Physics 237*, 177–210. *(p. 122, 147, 148, 150)*

Vié, A., E. Masi, O. Simonin, and M. Massot (2012). On the direct numerical simulation of moderate-Stokes-number turbulent particulate flows using algebraic-closure-based and kinetic-based moment methods. In *Proceedings of the CTR Summer Program*, Center for Turbulence Research, Stanford University, pp. 355–364. *(p. 3, 5, 114, 131, 153, 266)*

Vikas, V., Z. Wang, A. Passalacqua, and R. Fox (2011). Realizable high-order finite-volume schemes for quadrature-based moment methods. *Journal of Computational Physics 230*(13), 5328 – 5352. *(p. 120)*

Villani, C. (2002). *A review of mathematical topics in collisional kinetic theory*. S. Friedlander and D.

Serre Eds. Handbook of Fluid Mechanics. *(p. 88, 89, 90, 92)*

Villedieu, P., J. J. Hylkema, G. Lavergne, B. Platet, Y. Fabignon, M. Vardelle, J.-F. Guéry, F. Godfroy, P. Le Helley, and L. Jacques (2000). Slag accumulation in solid propellant rocket motors with a submerged nozzle. In 2^{nd} *European Conference on Launcher Technology*, Rome, Italy. *(p. 32, 52)*

Vinkovic, I., C. Aguirre, S. Simoëns, and M. Gorokhovski (2006). Large Eddy Simulation of droplet dispersion for inhomogeneous turbulent wall flow. *International journal of multiphase flow 32*(3), 344–364. *(p. 107)*

Vuillot, F. (1995). Vortex-shedding phenomena in solid rocket motors. *J. Propulsion and Power 11*(4), 626–639. *(p. 21, 40, 42)*

Vuillot, F. (1998). Point sur les recherches relatives à la stabilité de fonctionnement du ps P230 d'Ariane 5. In *3eme colloque R-T sur les écoulements internes en propulsion solide*, Poitiers, FRANCE. *(p. 40, 49)*

Vuillot, F. and G. Casalis (2000). Recent advances on the stability of large segmented space boosters. In 2^{nd} *European Conference on Launcher Technology*, Rome. *(p. 42)*

Vuillot, F. and N. Lupoglazoff (1996). Combustion and turbulent flow effects in 2D unsteady Navier-Stokes simulations of oscillatory solid rocket motors – First applications. In *34th Aerospace Sciences Meeting and Exhibit*, Reno, NV. *(p. 40, 50)*

Wagner, A., H. Livbjerg, P. Kristensen, and P. Glarborg (2010). Particle emissions from domestic gas cookers. *Combustion Science and Technology 182*(10), 1511–1527. *(p. 184, 187)*

Waldman, L. (1959). über die Kraft eines inhomogenen Gases auf kleine suspendierte Kugeln. *Z. Naturforschung 14*, 589–599. *(p. 371)*

Waldman, L. and K. Schmitt (1966). Thermophoresis and Diffusiophoresis of Aerosols. In *Aerosol Science*, pp. 137–194. Academic Press: New York: Davies, C.N. *(p. 188, 204)*

Wang, L., Y. Xue, O. Ayala, and W. Grabowski (2006). Effects of stochastic coalescence and air turbulence on the size distribution of cloud droplets. *Atmospheric research 82*(1), 416–432. *(p. 103)*

Wang, Q., K. Squires, and O. Simonin (1998). Large eddy simulation of turbulent gas-solid flows in a vertical channel and modelling of particle velocity correlations. *Int. J. of Heat and Fluid Flow 19*, 505–511. *(p. 103)*

Wang, R. and R. Spiteri (2008). Linear instability of the fifth-order WENO method. *Siam J. Num. Anal. 45*(5), 1871–1901. *(p. 239, 275)*

Wang, Y. and C. Wen (1990). The effect of weak gravitational force on brownian coagulation of small particles. *J. Fluid Mech. 214*, 599–510. *(p. 202)*

Washburn, E., M. Gross, S. Smith, and S. Balachandar (2010). Fundamental simulation of aluminum droplet combustion. In 46^{th} *AIAA/ASME/SAE/ASEE Joint Propulsion Conference*, Number Paper n°2010-6677, Nashville, pp. 1–15. *(p. xvii, xxiv, 31, 347)*

Washburn, E., J. Trivedi, L. Catoire, and M. Beckstead (2008). The simulation of the combustion of micrometer-sized aluminum particles with steam. *Combustion Science and Technology 180*(8), 1502–1517. *(p. 30)*

Wasistho, B. and R. Moser (2005). Simulation strategy of turbulent internal flow in solid rocket motor. *Journal of Propulsion and Power 21*(2), 251–263. *(p. 50)*

Wen, C.-S., L. Zhang, and H. Lin (1991). The rate of coagulation of particles in a sedimenting dispersion at large Péclet number. *J. Colloid and Interface Sc. 142*(1), 257–265. *(p. 202)*

Wen, J., M. Thomson, S. Park, S. Rogak, and M. Lightstone (2005). Study of soot growth in a plug flow reactor using a moving sectional model. *Proceedings of the Combustion Institute 30*(1), 1477–1484. *(p. 120)*

Wert, K. L. (1995). A rationally-based correlation of mean fragment size for drop secondary breakup. *Int. J. Multiphase Flow 21*(6), 1063–1071. *(p. 99, 100)*

Westerdahl, D., S. Fruin, T. Sax, P. Fine, and C. Sioutas (2005). Mobile platform measurements of ultrafine particles and associated pollutant concentrations on freeways and residential streets in Los Angeles. *Atmospheric Environment 39*(20), 3597–3610. *(p. 184)*

Wheeler, J. (1974). Modified moments and Gaussian quadrature. *Rocky Mountain J. Math 4*(2), 287–296. *(p. 119, 130, 298)*

Whitesides, R., D. Purinton, J. Hengel, and S. Skelley (1995). Effects of slag ejection on solid rocket motor performance. Technical Report TM–112023, NASA. *(p. 32)*

Widener, J. and M. Beckstead (1998). Aluminum combustion modeling in solid propellant combustion products. In 34^{th} *AIAA/ASME/SAE/ASEE Joint Propulsion Conference*, Reno, NV. *(p. 29, 30)*

Wilke, C. (1950). A viscosity equation for gas mixtures. *The Journal of Chemical Physics 18*(4), 517–519. *(p. 356)*

Willeke, K. and P. Baron (1993). *Aerosol measurement*. Van Nostrand Reinhold New York. *(p. 187)*

Williams, F. A. (1958). Spray combustion and atomization. *Phys. Fluids 1*, 541–545. *(p. 95, 367)*

Williams, M. and S. Loyalka (1991). *Aerosol science: theory and practice with special applications to the*

nuclear industry. Pergamon. *(p. 187)*

Wong, G. and S. Wong (2002). A multi-class traffic flow model – An extension of LWR model with heterogeneous drivers. *Transportation Research Part A: Policy and Practice 36*(9), 827–841. *(p. 119)*

Woods, L. (1975). *The Thermodynamics of Fluid Systems*. Oxford University Press, USA. *(p. 70)*

Wright, D., R. McGraw, and D. E. Rosner (2001). Bivariate extension of the quadrature method of moments for modeling simultaneous coagulation and sintering of particle populations. *J. of Colloid and Interface Sci. 236*, 242–251. *(p. 119, 120)*

Wu, M., R. Gordon, R. Herbert, M. Padilla, J. Moline, D. Mendelson, V. Litle, W. Travis, and J. Gil (2010). Case report: Lung disease in World Trade Center responders exposed to dust and smoke: carbon nanotubes found in the lungs of World Trade Center patients and dust samples. *Environmental health perspectives 118*(4), 499. *(p. 184)*

Wunsch, D. (2009). *Theoretical and numerical study of collision and coalescence - Statistical modeling approaches in gas-droplet turbulent flows*. Ph. D. thesis, Institut National Polytechnique de Toulouse. *(p. 75, 103)*

Wunsch, D., R. Belt, P. Fede, and O. Simonin (2009). DNS/DPS of inertial droplet coalescence in Homogeneous Isotropic Turbulence and comparison with pdf model predictions using the direct quadrature method of moments. In *Proceedings of the ASME FEDSM*. *(p. 75, 103)*

Wunsch, D., P. Fede, and O. Simonin (2008). Development and validation of a binary collision detection algorithm for a polydispersed particle mixture. In *Proceedings of the ASME FEDSM 2008*. *(p. 75)*

Xu, Y. and S. Subramaniam (2006). A multiscale model for dilute turbulent gas-particle flows based on the equilibration of energy concept. *Physics of Fluids 18*(3), 033301–033301. *(p. 103)*

Xu, Y. and S. Subramaniam (2010). Effect of particle clusters on carrier flow turbulence: A direct numerical simulation study. *Flow, Turbulence and Combustion 85*(3), 735–761. *(p. 71)*

Yagodkin, V. (1967). Use of channels with porous walls for studying flows which occur during combustion of solid propellants. Volume 3, pp. 69–79. *(p. 39)*

Yamada, K., M. Goto, and N. Ishikawa (1976). Simulative study on the erosive burning of solid rocket motors. *AIAA journal 14*(9), 1170–1176. *(p. 39)*

Yan, H., Y. Yinghua, and S. Ruiqi (2001). One dimension finite difference simulation of laser ignition. *Laser Technology 5*, 002. *(p. 38)*

Yang, V., P. Vashishta, A. Nakano, R. Yetter, D. Allara, D. Dlott, T. Eden, G. Girolami, R. Kalia, and K. Kuo (2011). Nano Engineered Energetic Materials (NEEM). *(p. 22, 23)*

Yetter, R., G. Risha, and S. Son (2009). Metal particle combustion and nanotechnology. *Proceedings of the Combustion Institute 32*(2), 1819–1838. *(p. 19, 22, 24, 25, 31)*

Yoon, C. and R. Mc Graw (2004). Representation of generally mixed multivariate aerosols by the quadrature method of moments: I. Satistical foundation. *Journal of Aerosol Science 35*, 561–576. *(p. 129)*

Young, J. (1995). Fundamentals and applications of gas-particle flow. *Int. J. Multiphase Flows 21*, 175–191. *(p. 191)*

Yu, J. (2009). Pure boron particles coated for energetic propellants. *Chemical propellers and polymers 7*(006), 6–14. in Chinese. *(p. 19, 22)*

Yuan, C. and R. Fox (2011). Conditional quadrature method of moments for kinetic equations. *J. Comp. Physics 230*(22), 8216–8246. *(p. 3, 131, 132, 245, 260)*

Yuan, C., F. Laurent, and R. Fox (2012). An extended quadrature method of moments for population balance equations. *Journal of Aerosol Science 51*, 1–23. *(p. 121)*

Zaichik, L. and V. Alipchenkov (2003). Pair dispersion and preferential concentration of particles in isotropic turbulence. *Phys. Fluids 15*, 1776–1787. *(p. 263)*

Zaichik, L. and V. Alipchenkov (2008). The coagulation of aerosol particles in turbulent flow. *High Temperature 46*(5), 666–674. *(p. 208, 211, 217)*

Zaichik, L., P. Fede, O. Simonin, and V. Alipchenkov (2009). Statistical models for predicting the effect of bidisperse particle collisions on particle velocities and stresses in homogeneous anisotropic turbulent flows. *International Journal of Multiphase Flow 35*(9), 868–878. Special Issue: Point-Particle Model for Disperse Turbulent Flows. *(p. 103)*

Zaichik, L., O. Simonin, and V. Alipchenkov (2009). An Eulerian approach for Large Eddy Simulation of particle transport in turbulent flows. *Journal of Turbulence* (10), 1–21. *(p. 102)*

Zaichik, L. I., O. Simonin, and V. M. Alipchenkov (2003). Two statistical models for predicting collision rates of inertial particles in homogeneous isotropic turbulence. *Physics of Fluids 15*, 2995–3005. *(p. 103)*

Zamansky, R., F. Coletti, M. Massot, and A. Mani (2012). Buoyancy-driven turbulent flow in particle-laden fluid subject to radiation. In *Annual Research Briefs*, Center for Turbulence Research, Stanford University, pp. 217–228. *(p. 28, 53, 66)*

Zamuner, B. and R. Lecourt (1995). A numerical code for two-phase flows simulation in rocket engines – Application to the study on hollow-cone spray. In *Colloque CNES/ONERA/CNRS Ecoulements*

propulsifs dans les systèmes de transport spatial, Bordeaux. *(p. 76)*

Zel′dovich, Y. B. (1970). Gravitational instability : an approximate theory for large density perturbations. *Astronomy and Astrophysics 5*, 84–89. *(p. 111)*

Zeren, Z. (2010). *Modélisation Lagrangienne stochastique des écoulements gaz-solides turbulents avec couplage inverse en Turbulence Homogène Isotrope stationnaire*. Ph. D. thesis, Institut National Polytechnique de Toulouse. *(p. 103)*

Zeren, Z. and B. Bedat (2009). On the application of mesoscopic eulerian formalism to modulation of turbulence by solid phase. *(p. 102, 103)*

Zhang, D. and A. Prosperetti (1994). Averaged equations for inviscid disperse two-phase flow. *J. Fluid. Mech. 267*, 185–219. *(p. 75)*

Zhang, D. and A. Prosperetti (1997). Momentum and energy equations for disperse two-phase flows and their closure for dilute suspensions. *Int. J. Multiphase Flow 23*(3), 425–453. *(p. 75)*

Zhang, X. and C. Shu (2010). On maximum-principle-satisfying high order schemes for scalar conservation laws. *Journal of Computational Physics 229*(9), 3091–3120. *(p. 234)*

Zhang, X., Y. Xia, and C. Shu (2012). Maximum-principle-satisfying and positivity-preserving high order discontinuous Galerkin schemes for conservation laws on triangular meshes. *Journal of Scientific Computing 50*(1), 29–62. *(p. 234)*

Zhao, H., H. Liu, W. Li, and J. Xu (2010). Morphological classification of low viscosity drop bag break-up in a continuous air jet stream. *Phys. Fluids 22*, 114103. *(p. 365)*

Zhou, C. and J. Majdalani (2002). Improved mean-flow solution for slab rocket motors with regressing walls. *J. Prop. Power 18*(3), 703–711. *(p. 36)*

Zhou, L., W. Lin, W. Luo, and X. Huang (1994). Gas-particle flows and coal combustion in a burner/combustor with high-velocity jets. *Combustion and Flame 99*(3), 669–678. *(p. 81)*

Zhu, H., Z. Zhou, R. Yang, and A. Yu (2007). Discrete particle simulation of particulate systems: theoretical developments. *Chemical Engineering Science 62*(13), 3378–3396. *(p. 72)*

Ziegler, V. E. and B. A. Wolf (2005). Bimodal drop size distributions during the early stages of shear induced coalescence. *Polymer 46*(22), 9265 – 9273. *(p. 190)*

Ziff, R. and E. McGrady (1987). Shattering transition in Fragmentation. *Phys. Rev. Lett. 58*, 892–895. *(p. 366)*

Zucca, A., D. Marchisio, A. Barresi, and R. Fox (2006). Implementation of the population balance equation in CFD codes for modelling soot formation in turbulent flames. *Chemical Engineering Science 61*, 87–95. *(p. 185)*

Zuzio, D. (2010). *Simulation numérique directe d'écoulements diphasiques avec maillage auto adaptatif*. Ph. D. thesis, École Nationale Supérieure de l'Aéronautique et de l'Espace. *(p. 52, 71)*

Zuzio, D. and J. Estivalezes (2011). An efficient block parallel AMR method for two phase interfacial flow simulations. *Computers & Fluids 44*(1), 339–357. *(p. 71)*

Zuzio, D., J. Estivalezes, P. Villedieu, and G. Blanchard (2013). Numerical simulation of primary and secondary atomization. *C. R. Mec. 341*, 15–25. Special issue "Combustion for Aerospace Propulsion". *(p. 71)*

Zwillinger, D. (2003). *CRC standard mathematical tables and formulae*. Chapman & Hall/CRC, Boca Raton, FL. *(p. 244, 312)*

Modélisation et simulation d'écoulements diphasiques polydisperses modérément denses chargés de particules nanométriques à modérément inertielles avec coalescence: application aux moteurs à propergol solide

Dans un moteur à propergol solide, l'écoulement dépend fortement des gouttes d'alumine en suspension, dont la fraction massique est élevée. La distribution en taille des gouttes, qui s'élargit avec la coalescence, joue un rôle clef. Or résoudre des écoulements diphasiques polydisperses instationnaires avec une bonne précision sur la taille est un défi à la fois sur le plan de la modélisation et du calcul scientifique: (1) de très petites gouttes, par exemple résultant de la combustion de nanoparticules d'aluminium, subissent mouvement brownien et coalescence, (2) de petites gouttes ont leur vitesse conditionnée par leur taille de sorte qu'elles coalescent lorsqu'elles ont des tailles différentes, (3) des gouttes plus grosses peuvent se croiser par effet d'inertie et (4) toutes les gouttes interagissent de manière fortement couplée avec la phase porteuse.

En complément des approches lagrangiennes, des modèles euleriens ont été développés pour décrire la phase dispersée à un coût raisonnable, et ils permettent un couplage aisé avec la phase porteuse ainsi que la parallélisation massive des codes: les approches eulériennes sont bien adaptées aux calculs industriels. Le modèle Multi-Fluide permet la description détaillée de la polydispersion, des corrélations taille/vitesse et de la coalescence, en résolvant séparément des "fluides" de gouttes triées par taille, appelés sections. Un ensemble de modèles est évalué dans cette thèse et une stratégie numérique est développée pour effectuer des calculs industriels de moteurs à propergol solide.

(1) La physique des nanoparticules est évaluée et incluse dans un modèle de coalescence complet. Des méthodes de moments d'ordre élevé sont ensuite développées : (2) une méthode à deux moments en taille est étendue à la coalescence pour traiter la physique de la polydispersion et les développements numériques connexes permettent d'effectuer des calculs applicatifs dans le code industriel CEDRE ; (3) une méthode basée sur les moments en vitesse du deuxième ordre, un schéma de transport à l'ordre deux sur maillages structurés ainsi qu'un modèle de coalescence sont développés. Des validations académiques de la stratégie pour gouttes d'inertie modérée sont effectuées sur des écoulements complexes puis avec de la coalescence ; (4) une stratégie d'intégration en temps est développée et mise en œuvre dans CEDRE pour traiter efficacement le couplage fort, dans des cas instationnaires et polydisperses incluant de trés petites particules. L'ensemble des développements est soigneusement validé: soit par des formules analytiques ad hoc pour la coalescence et pour le couplage fort d'une onde acoustique ; soit par des comparaisons numériques croisées avec une DPS pour la coalescence et avec des simulations lagrangiennes de cas applicatifs, coalescents et fortement couplés; soit par des résultats expérimentaux disponibles sur une configuration académique de coalescence et sur un tir de moteur à échelle réduite. La stratégie complète permet des calculs applicatifs à un coût raisonnable. En particulier, un calcul de moteur avec des nanoparticules permet d'évaluer la faisabilité de l'approche et d'orienter les efforts de recherche sur les propergols chargés de nanoparticules.

Mots-clés : MOTEUR PROPERGOL SOLIDE ; SPRAY MODEREMENT DENSE ; COALESCENCE ;ATOMISATION SECONDAIRE ; CROISEMENT TRAJECTOIRE ; GOUTTE NANOMETRIQUE ; MODELE MULTI-FLUIDE EULERIEN ; METHODE MOMENT ORDRE ELEVE

Eulerian modeling and simulation of polydisperse moderately dense coalescing spray flows with nanometric-to-inertial droplets: application to Solid Rocket Motors

In solid rocket motors, the internal flow depends strongly on the alumina droplets, which have a high mass fraction. The droplet size distribution, which is wide and spreads up with coalescence, plays a key role. Solving for unsteady polydisperse two-phase flows with high accuracy on the droplet sizes is a challenge for both modeling and scientific computing : (1) very small droplets, e.g. resulting from the combustion of nanoparticles of aluminum fuel, encounter Brownian motion and coalescence, (2) small droplets have their velocity conditioned by size so they coalesce when having different sizes, (3) bigger droplets have an inertial behavior and may cross each other’s trajectory, and (4) all droplets interact in a two-way coupled manner with the carrier phase. As an alternative to stochastic-Lagrangian approaches, some Eulerian models can describe the disperse phase at a moderate cost, with an easy coupling to the carrier phase and with massively parallel codes: they are well-suited for industrial computations. The Multi-Fluid model allows the detailed description of polydispersity, size/velocity correlations and coalescence by separately solving “fluids” of sizesorted droplets, the so-called sections. In the present work, we assess an ensemble of models and we develop a numerical strategy to perform industrial computations of solid rocket motor flows.

(1) The physics of nanoparticles is assessed and included in a polydisperse coalescing model. High order moment methods are then developed : (2) a Two-Size moment method is extended to coalescence to treat accurately the physics of polydispersity and coalescence and the related numerical developments allow to perform applicative computations in the industrial code CEDRE ; (3) a second order velocity moment method is developed, together with a second order transport scheme, to evaluate a strategy for a moderately inertial disperse phase, and academic validations are performed on complex flow fields ; (4) a time integration strategy is developed and implemented in CEDRE to treat efficiently two-way coupling, in unsteady polydisperse cases including very small particles.

The developments are carefully validated, either through purposely derived analytical formulae (for coalescence and two-way acoustic coupling), through numerical cross-comparisons (for coalescence with a Point-Particle DNS, for applicative cases featuring coalescence and two-way coupling with a stochastic-Lagrangian method), or through available experimental results (for coalescence with an academic experiment, for the overall physics with a sub-scale motor firing). The whole strategy allows to perform applicative computations in a cost effective way. In particular, a solid rocket motor with nanoparticles is

computed as a feasibility case and to guide the research effort on motors with nanoparticle fuel propellants.

Keywords : SOLID ROCKET MOTOR ; MODERATELY DENSE SPRAY ; COALESCENCE ; SECONDARY BREAK-UP ; TRAJECTORY CROSSING ; NANOMETRIC DROPLET ; EULERIAN MULTI-FLUID MODELL ; HIGH ORDER MOMENT METHODS

Office National d'Études et de Recherches Aérospatiales
BP 72 - 29 avenue de la Division Leclerc
92322 CHATILLON CEDEX
Tél. : +33 1 46 73 40 40 - Fax : +33 1 46 73 41 41
http://www.onera.fr